SCHOLARLY PUBLICATIONS

A CURRENT AWARENESS BULLETIN
OF RESEARCH OUTPUT

@DTU

(98th Edition)

FEBRUARY 2021

BY: CENTRAL LIBRARY

DELHI TECHNOLOGICAL UNIVERSITY
(FORMERLY *DELHI COLLEGE OF ENGINEERING)*
GOVT. OF N.C.T. OF DELHI
SHAHBAD DAULATPUR, MAIN BAWANA ROAD
DELHI 110042

PREFACE

This is the **Ninety Eight** Issue of Current Awareness Bulletin started by Delhi Technological University, Central Library. The aim of the bulletin is to compile, preserve and disseminate information published by the faculty, students and alumni for mutual benefits. The bulletin also aims to propagate the intellectual contribution of Delhi Technological University (DTU) as a whole to the academia.

The bulletin contains information resources available in the internet in the form of articles, reports, presentations published in international journals, websites, etc. by the faculty and students of DTU. The publications of faculty and student which are not covered in this bulletin may be because of the reason that the full text either was not accessible or could not be searched by the search engine used by the library for this purpose.

The learned faculty and students are requested to provide their uncovered publications to the library either through email or in CD, etc. to make the bulletin more comprehensive.

This issue contains the information published during **February, 2020**. The arrangement of the contents is alphabetical. The full text of the article which is either subscribed by the university or available in the web is provided in this bulletin.

Central Library

CONTENTS

1. A fault-diagnosis and tolerant control technique for five-level cascaded H-bridge inverters, Pavan Mehta, Subhanarayan Sahoo and ***3.Mayank Kumar***, Electrical, DTU

2. A Fine Tuned Model of Grasshopper Optimization Algorithm with Classifiers for Optimal Text Classification, ***6.Anshu Khurana***[1] and ***3.Om Prakash Verma***[2], [1]CSE and [2]Electronics, DTU

3. A Laboratory Setup for Synchrophasor Applications, ***7.Annu Ahlawat***, ***8.Anirudh Goyal***, ***3.Saurabh Kumar Mishra*** and ***3.S T Nagarajan***, Electrical, DTU

4. A novel grayscale image encryption approach based on chaotic maps and image blocks, ***3.Ashish Girdhar***, Himani Kapur and Vijay Kumar, CSE, DTU

5. Analysis of AI Techniques for Maximum Power Point Tracking Under Partial Shading Conditions, ***7.Shagun Chaudhary*** and ***3.Alka Singh***, Electrical, DTU

6. Automation Security System, ***8.Avinash Singh***, ***8.1.Bharat Singh***, ***8.Divyanshu Rawat*** and ***3.Bhavnesh Jain***, Electrical,m DTU

7. Bioactivity reinforced surface patch bound collagen-pectin hydrogel, ***6.Himansh Goel***, ***6.Nidhi Gupta***, ***3.Deenan Santhiya***, ***6.Namit Dey***, Himadri B. Bohidar and Aditi Bhattacharya, Chemistry and Biotechnology, DTU

8. Challenges in the implementation of circular economy in manufacturing industry, ***6.Madhukar Chhimwal***, ***3.Saurabh Agrawal*** and ***3.Girish Kumar***, Mechanical & DSM, DTU

9. CLEAN AND GREEN ECONOMY FOR AIR POLLUTION, Mohit Sharma, Aditya Bhuyan and ***7.Ishan Sahajpal***, Environmental, DTU

10. Comparative Investigation of Yield and Quality of Bio-Oil and Biochar from Pyrolysis of Woody and Non-Woody Biomasses, Pranshu Shrivastava, ***3.Anil Kumar***, Perapong Tekasakul, Su Shiung Lam and Arkom Palamanit, Mechanical & Environment, DTU

11. Computational Analysis Indicates That PARP1 Acts as a Histone Deacetylases Interactor Sharing Common Lysine Residues for Acetylation, Ubiquitination, and SUMOylation in Alzheimer's and Parkinson's Disease, ***6.Rohan Gupta*** and ***3.Pravir Kumar***, Biotech, DTU

12. Design and Development of a Proficient Converter for Solar Photovoltaic Based Sustainable Power Generating System, Muhannad Alaraj, Anirudh Dube, Ibrahim Alsaidan, ***3.Mohammad Rizwan*** and Majid Jamil, Electrical, DTU

13. Design and Implementation of Grid Sequence Separator Based Control for Single-Phase Microgrid, ***6.Ankita Arora*** and ***3.Alka Singh***, Electrical, DTU

14. Design and Simulation of Ultra low loss Spiral Delay line for Integrated Optical Coherence Tomography, BHAWNA SHARMA, ***3.KAMAL KISHOR***, AMRINDRA PAL, SANDEEP SHARMA AND ROSHAN MAKKAR, Physics, DTU

15. Design of Small Wind Turbine Electric System for Household Electricity and Water Supply for Irrigation in Rural Tanzania, ***6.Isaka J. Mwakitalima***, ***3.Mohammad Rizwan*** and ***3.Narendra Kumar***, Electrical, DTU

16. Determination of optimal size of battery energy storage system (BESS) for a renewable power based microgrid, ***3.Avirup Maulik*** and ***6.Debapriya Das***, Electrical, DTU

17. Dual Input Digitally Controlled Broadband Three-Stage Doherty Power Amplifier With Back-Off Reconfigurability, ***7.1.Ayushi Barthwal***, Karun Rawat, and Shiban K. Koul, Electronics, DTU

18. Effect of Friction Stir Processing on Mechanical Properties and Wear Resistance of Tungsten Inert Gas Welded Joint of Dissimilar Aluminum Alloys, ***6.Husain Mehdi*** and ***3.R.S. Mishra***, Mechanical, DTU

19. Effect of Liquid to Binder Ratio and Curing Temperature on the Engineering Properties of the Geopolymer Concrete, ***6.Manvendra Verma*** and ***3.Nirendra Dev***, Civil, DTU

20. Effect of Specimen Preparation Technique on the Post- Liquefaction Behaviour of Fine Sand Under Cyclic Loading, Arpit Jain, Satyendra Mittal and ***3.Sanjay Kumar Shukla***, Civil, DTU

21. Enhancement and luminescence properties of Eu3+, Sm3+ co-doped KMgPO4 phosphor with variable concentration of Eu3+ for w-LEDs, ***7.SARVJEET SINGH***, Physics, DTU

22. Evaluation of the Feasibility of Recycled Concrete Aggregate for Producing Structural Concrete, Mohammad Tabrez Ali, Ibadur Rahman, ***3.Nirendra Dev*** and Priyanka Singh, Civil, DTU

23. Formulation Of Fish Feed With Multiple Ingredients Using A Software Tool Developed In Java, Pinaki Chakraborty, Tuhina Singh, ***3.Jaigopal Sharma***, Rina Chakrabarti, Biotechnology, DTU

24. Fractional Order Notch Filter for Grid-Connected Solar PV System with Power Quality Improvement, Manoj Badoni, ***3.Alka Singh***, Sandeep Pandey and ***3.Bhim Singh***, Electrical, DTU

25. Fresh and Hardened Characteristics of Basalt-Glass Hybrid Fibre Reinforced Self Compacting Concrete, ***6.Uzair Khan***, Sandeep Kumar Tripathi, Anurag, Rizwan A Khan, Civil, DTU

26. Geopolymer Concrete: A Sustainable and Economic Concrete via Experimental Analysis, ***6.Manvendra verma*** and ***3.Nirendra Dev***, Civil, DTU

27. Global, regional, national burden of breast cancer in 185 countries: evidence from GLOBOCAN 2018, ***3.Rajesh Sharma***, USME, DTU

28. Homesickness: a comparative study of defense and civilian employees and individual differences, ***3.Naval Garg***, B.K. Punia, ***8.Vanshikha Kakkar*** and Sarika Kumari, USME, DTU

29. Human Action Recognition using Prominent Camera, P. S. Kavimandan, ***3.R. Kapoor*** and K. Yadava, Electronics, DTU

30. Identifying Influential Nodes in Weighted Networks using k-shell based HookeRank Algorithm, ***8.Nipun Aggarwal*** and ***3.Sanjay Kumar***, CSE, DTU

31. Impact of Reverse Gate Oxide Stacking on Gate All Around Tunnel FET for High Frequency Analog and RF Applications, Amit Das, Vandana Nath, ***3.Sonam Rewari***, Binod Kumar Kanaujia and R. S. Gupta, Electronics, DTU

32. Impulse noise removal in color image sequences using fuzzy logic, ***6.Isha Singh*** and ***3.Om Prakash Verma***, IT, DTU

33. Incorporating Teacher's Preferences and Student Time Management in University Course Timetabling, ***3.Seba Susan*** and ***7.1.Aparna Bhutani***, IT, DTU

34. IoT in Online Banking, ***3.Malti Bansal***[1], ***8.Naman Oberoi***[2] and ***8.Mohd. Sameer***[1], [1]Electronics and [2]Mathematics, DTU

35. Levofloxacin Detection Using L-Cysteine Capped MgS Quantum Dots via the Photoinduced Electron Transfer Process, S. Z. H. Hashmi, Tarun Kumar Dhiman, ***6.Navneet Chaudhary***, Avinash Kumar Singh, Rahul Kumar, ***3.Jai Gopal Sharma***, Anil Kumar and Pratima R. Solanki, Biotechnology, DTU

36. mFlameGaze: Mobile-Based Flame Gazing for Improving Sustained Attention, ***3.Divyashikha Sethia***[1], ***3.Anil Singh Parihar***[1], ***8.Aheli Gh***osh[1], ***8.Tanish Grover***[1], ***8.Deep Diwak***ar[2], ***8.Shivam Kumar***[1] and ***8.Utkarsh Tyagi***[1], [1]CSE and [2]Electronics, DTU

37. MODELING AND ANALYSI S OF LEAN MANUFACTUR ING STRATEGIES USING ISM FUZZY MICMAC APPROACH, Mohit Tyagi, Dilbagh Panchal, ***8.Deepak Kumar*** and R. S. Walia, Mechanical, DTU

38. Multimodal cyberbullying detection using capsule network with dynamic routing and deep convolutional neural network, ***3.Akshi Kumar*** and ***6.Nitin Sachdeva***, CSE, DTU

39. Numerical study for dynamic fracture toughness of AA7075-T651 under dynamic loading, ***3.Sanjay Kumar***, Anoop Kumar Pandouria, Purnashis Chakraborty and Vikrant Tiwari, DTU

40. Phototransistor: The Story So Far, ***3.Malti Bansal*** and ***8.Raaghav Raj Maiya***, Electronics, DTU

41. PI and Fuzzy Logic Control of Single Phase Grid Connected Inverter Serving Two PV Panels, ***7.Dhruv Bhatia***, ***3.Alka Singh*** and ***3.Ankita Arora***, Electrical, DTU

42. Power Gated ECRL Adiabatic Logic Based Optimized Two-Input Multiplexer, ***8.1.Aarushi Mann***, ***8.1.Naman Malhotra***, ***8.1.Abhishek Wadhwa*** and ***3.Neeta Pandey***, Electronics, DTU

43. Profit Maximization of Multiple Active Distribution Networks Using a Fuzzy Based Approach, ***3.Avirup Maulik*** and ***7.Debapriya Das***, Electrical, DTU

44. S2NOW: Secure Social Network Ontology Using WhatsApp, Rahul Johari, Sawan Kalra, ***3.Sonika Dahiya*** and Kalpana Gupta, CSE, DTU

45. Second Order Ripple Minimization in Single Phase Single Stage On-Board PEV Charger, ***6.Aakash Kumar Seth*** and ***3.Mukhtiar Singh***, Electrical, DTU

46. Stability of fractional order fuzzy cellular neural networks with distributed delays via hybrid feedback controllers, ***6.Ajendra singh*** and ***3.Jitendra Nath Rai***, Electrical, DTU

47. STATE ESTIMATION WITH LIMITED SENSORS – A DEEP LEARNING BASED APPROACH, ***8.Yash Kumar***, ***8.Pranav Bahl*** and Souvik Chakraborty, Mechanics, DTU

48. Step-down Fibonacci switched capacitor converters- a topological design method, ***8.1.Arvind Gupta*** and ***6.Shirish Raizada***, Electrical, DTU

49. Stochastic filtering based transmissibility estimation of novel coronavirus, ***6.1.Rahul Bansala***, Amit Kumar, Amit Kumar Singh and ***6.1.Sandeep Kumar***, Electronics, DTU

50. Survey on Machine Learning and Deep Learning Applications in Breast Cancer Diagnosis, ***7.Gunjan Chugh***, ***3.Shailender Kumar*** and Nanhay Singh, CSE, DTU

51. The role of motivation theories in knowledge sharing: an integrative theoretical reviews and future research agenda, ***6.1.Asha Thomas*** and ***3.Vikas Gupta***, DSM, DTU

52. Thermodynamic Analysis of Waste to Wealth Conversion, M. Kumar and ***3.S.K. Singh***, Environmental, DTU

53. Towards the Law Enforcement of Firearms, ***8.Kushagra Yadav***, ***8.Ravneet Punia*** and ***3.NS Raghava***, CSE and Electronics, DTU

54. Virtual screening of natural compounds as combinatorial agents from indian medicinal plants against estrogen positive breast cancer, ***7.Shaleen Jain*** and ***3.Dr. Asmita Das***, Biotechnology, DTU

55. Women's Participation and Factors Affecting Their Academic Performance in Engineering and Technology Education: A Study of Ethiopia, ***6.Addissie Melak*** and ***3.Seema Singh***, Humanities, DTU

1. *Vice Chancellor*
2. *Pro Vice Chancellor*
3. *Faculty*
4. *Teaching-cum-Research Fellow*
5. *Asst. Librarian*
6. *Research Scholar*
7. *PG Scholar*
8. *Undergraduate Student*

1.1. *Ex Vice chancellor*
2.1. *Ex Pro Vice Chancellor*
3.1. *Ex Faculty*
4.1. *Alumni*
5.1 *Others*
6.1. *Ex Research Scholar*
7.1. *Ex PG Scholar*
8.1. *Ex Undergraduate Student*

Received: 27 April 2020 | Revised: 5 August 2020 | Accepted: 15 September 2020

DOI: 10.1049/cds2.12033

IET Circuits, Devices & Systems

The Institution of Engineering and Technology WILEY

ORIGINAL RESEARCH PAPER

A fault-diagnosis and tolerant control technique for five-level cascaded H-bridge inverters

Pavan Mehta[1] | **Subhanarayan Sahoo**[2] | **Mayank Kumar**[3]

[1]Electrical Engineering Department, Gujarat Technological University, Ahmedabad, India

[2]Electrical Engineering Department, Adani Institute of Infrastructure Engineering, Ahmedabad, India

[3]Electrical Engineering Department, Delhi Technological University, Delhi, India

Correspondence

Mayank Kumar, Electrical Engineering Department, Delhi Technological University, Delhi-110042, India
Email: mayankkumar@dtu.ac.in

Abstract

Reliability is a major concern for multilevel inverters (MLIs) in all industrial applications. The consequences of faults increase as the number of power semiconductor devices increases and may lead to serious damage to the overall system. To prevent such issues, an effective fault-detection technique is required. A detailed analysis is presented of five-level cascaded H-bridge MLIs under healthy and faulty conditions. A fault-detection technique based on total harmonic distortion and a normalized output voltage factor is presented. Also discussed is a fault-isolation technique based on reduction of amplitude modulation, which results in a fault-tolerant inverter. The level-shifted pulse-width modulation (LSPWM) technique is used for switching operation. LSPWM is most suitable for MLIs that require less computational effort. The presented fault-diagnosis technique can be implemented on MLI-based drives, grid-connected operations etc. without any major changes. The simulation and hardware results are presented to validate the proposed fault-detection and fault-tolerant control technique at different power factors.

1 | INTRODUCTION

Over the past decade, multilevel inverter (MLI) topologies have been one of the most highlighted areas of research in the field of power electronics. This is because intelligent MLI technology can synthesise the waveform in a staircase manner and has the inherent ability to produce output with lower total harmonic distortion (THD), lower electromagnetic interference, high power quality and reduced filter size [1,2]. With such advantages, MLIs are used in a wide range of applications such as electrical motor drives, active filters, renewable energy systems and flexible AC transmission systems [3–5]. MLIs are classified into three basic topologies: neutral point clamped (NPC) [6], flying capacitor (FC) [7,8] and cascaded H-bridge (CHB) [9]. Additional topologies that have been derived from these basic topologies to overcome certain disadvantages are active neutral point clamped [10–12], modular multilevel converter (MMC) [13] and multilevel DC link inverter [14].

The reliability of power electronics converters depends on the number of switching semiconductor devices used. The MLI gives better output voltage quality with the cost of extra static semiconductor devices. Therefore, MLI reliability is a most serious issue. Because of the switching of several power semiconductor devices, the chance for various faults to occur also increases, and it reduces reliability. The chance of a fault occurring in power semiconductor devices is higher than for any other power devices except DC link capacitors, as shown in Figure 1. According to surveys and research applied to 80 companies and more than 200 industrial processes, 21% of faults detected are in power semiconductor devices and 13% are in solders. In total, 34% of the faults in converters are caused by failure of the device module [15]. In addition to the various causes of faults, power semiconductor switch faults can be categorised into two basic types of faults—that is, open-circuit switch faults (OCSFs) and short circuit switch faults (SCSFs).

Various literature has reported on the detection of faults in power semiconductor devices. The fault-diagnostic algorithm for three-level NPC MLIs using average current Park's vector (ACPV) is presented in [16]. In the ACPV algorithm, the faulty switch leg is identified by ACPV, and the faulty switch is pointed out by the normalized average value of motor line current. An output pole voltage and current-based fault-detection technique for three-level NPC is published in [17]. This method exploits the differences between normalized output voltages and their respective control switching states. In [18,19], a vector-based diagnosis and output voltage frequency analysis is applied to find

This is an open access article under the terms of the Creative Commons Attribution License, which permits use, distribution and reproduction in any medium, provided the original work is properly cited.

© 2021 The Authors. *IET Circuits, Devices & Systems* published by John Wiley & Sons Ltd on behalf of The Institution of Engineering and Technology.

the short circuit fault in FC MLIs. A model-based predictive control technique for switch fault detection is presented in [20]. An asymmetric zero voltage state-based open-circuit fault-diagnosis technique is published in [21] for CHB MLIs. The authors have given a simpler technique based on zero voltage switching and validated for linear and nonlinear loads.

The authors of [22] have presented a short circuit fault detection method based on the comparison of output voltage with reference voltage for five-level CHB MLIs. A neural network-based fault-identification method for five-level CHB MLIs is proposed in [23]. Five multilayer perception networks are used to identify the type and location of fault. The authors of [24] have presented a simple THD-based fault-diagnosis technique for five-level CHB MLIs. The probable faulty switch is identified using normalized pole output current. For MMCs, a state observer and knowledge-based model for fault detection and reconfiguration strategy is proposed in [25]. A Kalman filter-based fault-detection technique for MMCs is presented in [26]. Some of the above-mentioned techniques has been reviewed in [27]. The fault-detection techniques are summarised in Table 1. Despite the many fault-detection techniques proposed for different MLIs using various methods, a simple and cost-effective method is required that can be implemented in existing industrial applications without making major changes.

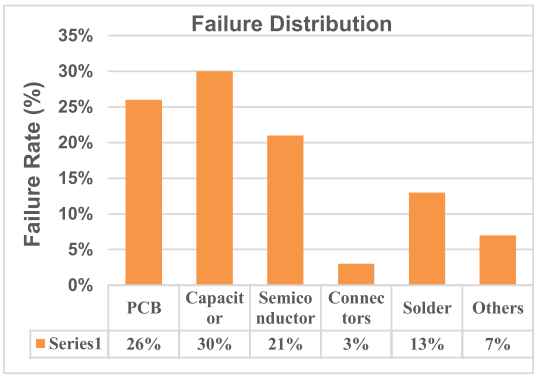

FIGURE 1 Failure rate distribution of power electronic converters

A post-fault control is mandatory to avoid multiple switch faults that may cause the shutdown of an entire operation. In fact, for a complete fault-tolerant operation, a post-fault control strategy must be implemented after fault diagnosis. The researchers have published their post-fault control algorithm. The popular controls of bypassing faulty operative cells and fundamental phase-shift compensation (FPSC) are presented in [28,29]. For balanced three-phase operation, an equal number of cells are removed to bypass the faulty cell algorithm. In this method, the load voltage is reduced to 40% of its healthy condition value, while in FPSC, to maintain balanced operation, the phase shift of the fundamental wave of all three phases will change. The reduction in voltage is not more than 23% of the healthy condition. However, it may affect the power factor. In [30–32] a space vector-based control strategy is implemented, and redundant switching states are used to overcome the fault.

An open-circuit fault-detection technique for five-level CHB MLIs is presented herein. The analysis of faulty and healthy CHB MLIs is presented in detail with respect to THD and output voltage variation. The proposed fault-diagnosis technique can be implemented with nearly any industrial applications–based MLI. Moreover, the technique is very cost-effective and can be applied to existing systems with small modifications. The investigated technique is based on THD measurement and a normalized output voltage factor. Based on the threshold calculations, a probable open-circuit switch fault can be identified within one fundamental period to the couple of fundamental periods. The proposed fault-diagnosis technique requires only one voltage sensor per phase, which is already available with any closed-loop operation-based power electronics MLI system. The post-fault control technique is proposed in order to make a completely fault-tolerant structure. The proposed fault detection and isolation method is also presented for different power factors. The technique is validated through simulation and experimental results.

TABLE 1 Summary of fault-diagnosis techniques

Sr. No.	Type of multilevel inverter	No. of levels	Fault-diagnosis technique	Type of fault resolved
1	Neutral point clamped	3	Average current Park's vector	Open circuit
		3	Output voltage and current	Open circuit
		5	Wavelet-based multiresolution analysis	Open circuit
2	Flying capacitor	5	Vector-based and output voltage frequency analysis	Short circuit
		5	Model-based predictive control	Open circuit
3	Cascaded H-bridge	5	Comparison of output voltage with reference voltage	Short circuit
		7	Asymmetric zero voltage switching	Open circuit
		5	Neural network	Open and short circuit
		5	Total harmonic distortion and normalized output current	Open circuit
4	Modular multilevel converter	N	State observer and output voltage analysis	Open circuit
		N	Kalman filter	Open circuit

2 | STRUCTURE AND SCHEMATIC OF CASCADED H-BRIDGE INVERTER

CHB MLIs have a wide range of applications compared with all other multilevel structures because of their modular structure. Series-connected H-bridge power cells can be easily added or removed, resulting in increased or decreased output voltage/power levels, respectively. MLIs consist of four switching devices with anti-parallel diodes and a DC voltage source within each power cell. The series interconnections of the power cells generate the staircase pulse-width modulated inverter output voltage waveform. Based on the DC input source, CHB MLIs are classified as one of two types, symmetric CHB MLI and asymmetric CHB MLI. If the DC source is the same for all cells in an inverter, the inverter is known as a symmetric CHB inverter. On the other hand, if the input DC source is different for each cell, the inverter is known as an asymmetric CHB inverter. In this work, symmetric CHB MLIs are used for fault detection and identification techniques. Table 2 shows the comparison of device count and reliability studies for all five-level MLI structures.

Figure 2 shows the schematic of a five-level CHB MLI. An n-level CHB MLI requires (n-1)×2 power semiconductor switching devices and (n-1)/2 separate DC sources. The cell output voltage for the first cell can be given as follows:

$$V_{CX1} = (S_1 - S_2) \times E_{DC} \quad (1)$$

where, V_{CX1} = first cell output voltage for X^{th} phase; S_1, S_2 = switching functions (0 or 1) for S_{X1}, S_{X2}; and E_{DC} = DC voltage source.

Similarly, total phase output voltage can be calculated for M cells connected in series as follows:

$$E_{OX} = V_{CX1} + V_{CX2} + V_{CX3} + - - - + V_{CXM} \quad (2)$$

This structure can synthesise five-level output according to the switching sequences mentioned for healthy conditions in Table 3. Analysis of the switching state is also helpful for OCSF studies.

TABLE 2 Device count comparison for five-level multilevel inverters

	Component count		
Component	**NPC**	**FC**	**CHB**
Power semiconductor switches	8	8	8
Feedback diodes	8	8	8
Clamping diodes	12	0	0
DC bus capacitors	4	4	2
Flying capacitors	0	6	0
Reliability while switching	NO	NO	YES
Reliability while source failure	NO	NO	YES

Abbreviations: CHB, cascaded H-bridge; FC, flying capacitor; NPC, neutral point clamped.

3 | OPEN-CIRCUIT SWITCH FAULT ANALYSIS FOR FIVE-LEVEL CASCADED H-BRIDGE INVERTER

There are many probable causes for fault occurrences in power semiconductor switching devices. The external causes of switch failures are a large and sudden sag or sudden increase from the input DC voltage source, and from the other side at load end, either short or open fault in any of the phases. The internal causes for fault can be gate driver fault, breakdown of semiconductor material, gate misfiring and thermal breakdown. All of these causes will finally lead to two categories, OCSFs and SCSFs [33]. Further, OCSF is considered for the analysis.

Figures 3 and 4 show the current path for odd and even switch faults under healthy and faulty conditions with green and red lines, respectively (solid and dashed lines, respectively, if the figure appears in black-and-white). It also shows the respective output phase voltage for faulty conditions. Note that only responsible switching states are considered for the missing respective output voltage level for a better understanding of the OCSF analysis. The green solid line represents the actual path of current in healthy condition, while the red dotted line represents the current path for faulty conditions. By applying Kirchhoff's current law, at any point in the configuration, the exact current directions for healthy and faulty conditions can be obtained for all cases. Table 3 highlights the current path for healthy and faulty conditions. It also indicates the respective

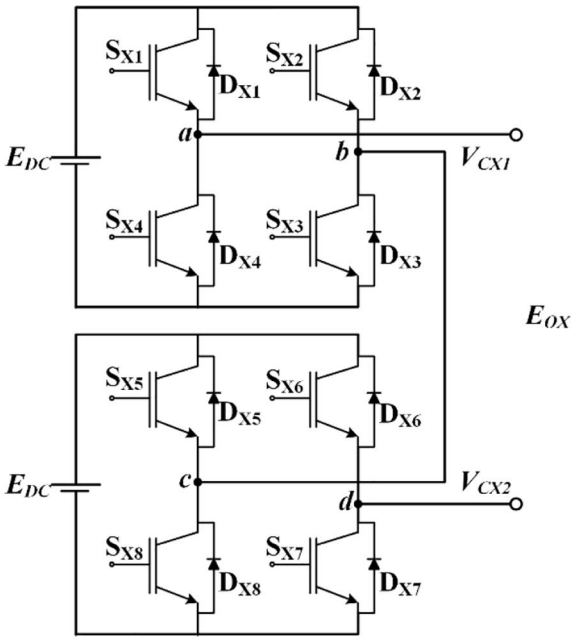

FIGURE 2 Schematic of five-level cascaded H-bridge multilevel inverter

TABLE 3 Current path and respective output voltage state under healthy and faulty switching conditions

Switch	Current path for healthy condition	Current path for faulty condition	Output voltage state (healthy)	Output voltage state (faulty)
S_{X1}	E_{DC}-S_{X1}-*a*-*d*-S_{X7}-E_{DC}-S_{X5}-*c*-*b*-S_{X3}-E_{DC}	*a*-*d*-S_{X7}-E_{DC}-S_{X5}-*c*-*b*-S_{X3}-D_{X4}-E_{DC}	$+2E_{DC}$	$+E_{DC}$
S_{X2}	E_{DC}-S_{X2}-*b*-*c*-S_{X8}-D_{X7}-*d*-*b*-S_{X3}-E_{DC}	*b*-*c*-S_{X8}-D_{X7}-*d*-*b*-S_{X3}-D_{X4}-*a*	$-E_{DC}$	0
S_{X3}	E_{DC}-S_{X1}-*a*-*d*-S_{X7}-D_{X8}-*c*-*b*-S_{X3}	*a*-*d*-S_{X7}-D_{X8}-*c*-*b*-D_{X2}-S_{X1}	$+E_{DC}$	0
S_{X4}	E_{DC}-S_{X2}-*b*-*c*-S_{X8}-D_{X7}-*d*-*b*-S_{X4}	*b*-*c*-S_{X8}-D_{X7}-*d*-*a*-D_{X1}-S_{X2}	$-E_{DC}$	0
S_{X5}	E_{DC}-S_{X5}-*c*-*b*-S_{X3}-D_{X4}-*a*-*d*-S_{X7}	*c*-*b*-S_{X3}-D_{X4}-*a*-*d*-S_{X7}-D_{X8}	$+E_{DC}$	0
S_{X6}	E_{DC}-S_{X2}-*b*-*c*-S_{X8}-E_{DC}-S_{X6}-*d*-*a*-S_{X4}-E_{DC}	E_{DC}-S_{X2}-*b*-*c*-S_{X8}-D_{X7}-*d*-*a*-S_{X4}-E_{DC}	$-2E_{DC}$	$-E_{DC}$
S_{X7}	*c*-*b*-S_{X3}-D_{X4}-*a*-*d*-D_{X6}-S_{X5}	E_{DC}-S_{X5}-*c*-*b*-S_{X3}-D_{X4}-*a*-*d*-S_{X7}	$+E_{DC}$	0
S_{X8}	E_{DC}-S_{X6}-*d*-*a*-S_{X4}-D_{X3}-*b*-*c*-S_{X8}	*d*-*a*-S_{X4}-D_{X3}-*b*-*c*-D_{X5}-S_{X8}	$-E_{DC}$	0

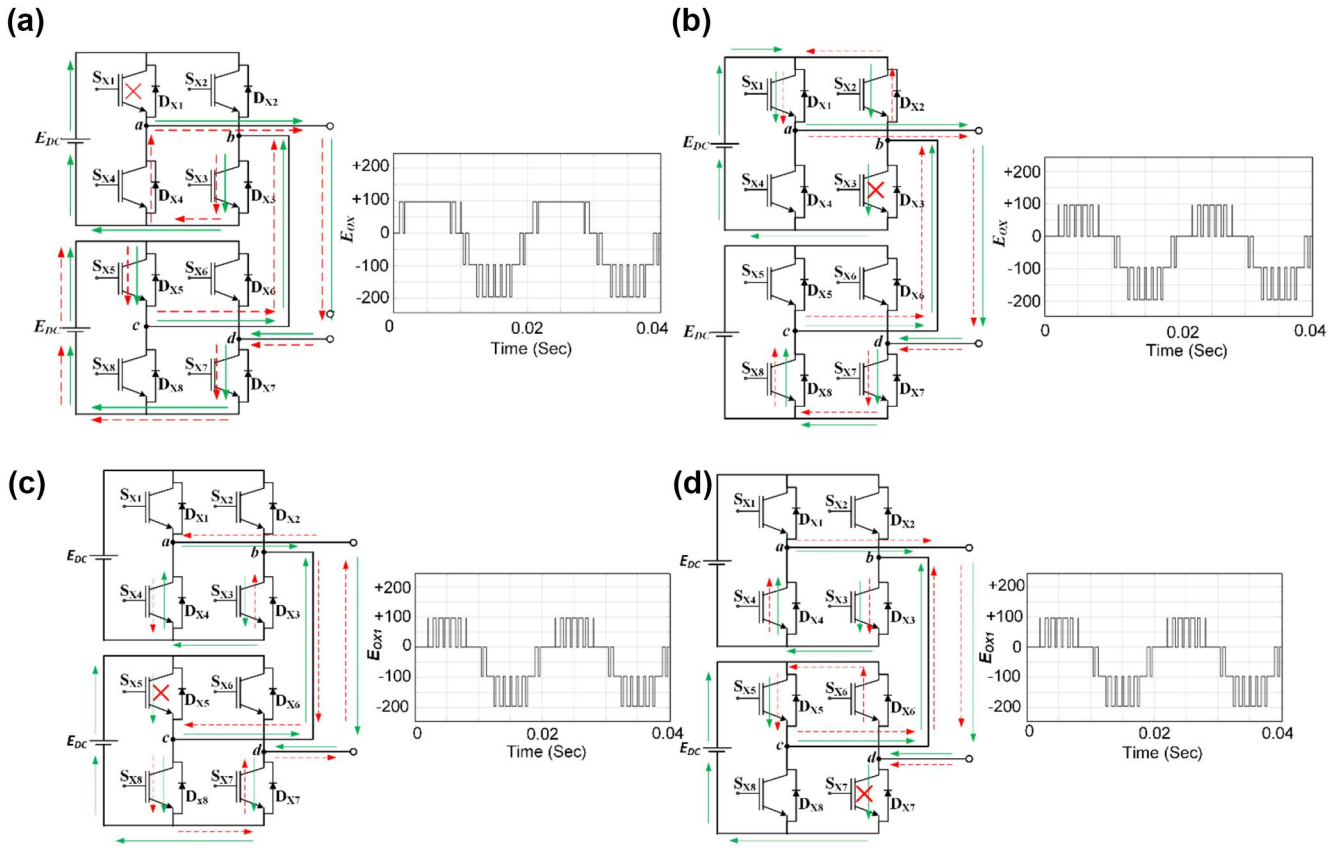

FIGURE 3 Current flows under odd number of faulty switch conditions: (a) S_{X1} (b) S_{X3} (c) S_{X5} (d) S_{X7}

missing output voltage state at the time of fault in a switching device. This analysis of the missing output voltage state will help us detect the faulty switch.

4 | OPEN-CIRCUIT FAULT DIAGNOSIS ALGORITHM

Analysis of OCSF behaviour is useful for faulty switch detection. As shown in Table 1, there are eight switches per phase for a five-level CHB MLI. For three-phase five-level CHB MLIs, three legs of single-phase bridge (i.e. 24 switches) are required, and therefore it is difficult to identify the exact OCSF location.

The fault-detection algorithm is presented in Figure 5. The process of faulty switch identification occurs in two parts: (i) THD measurement and (ii) normalized voltage factor. The first of these can identify the faulty switch phase. The THD value of the faulty switch phase will be comparatively higher than that of the other two phases. Hence, the possible switch fault locations are reduced from 24 switches to 8. Normalization of the output phase voltage is taken in the second part. Based on the normalized factor value with the threshold comparison, the probable switch fault location can be identified.

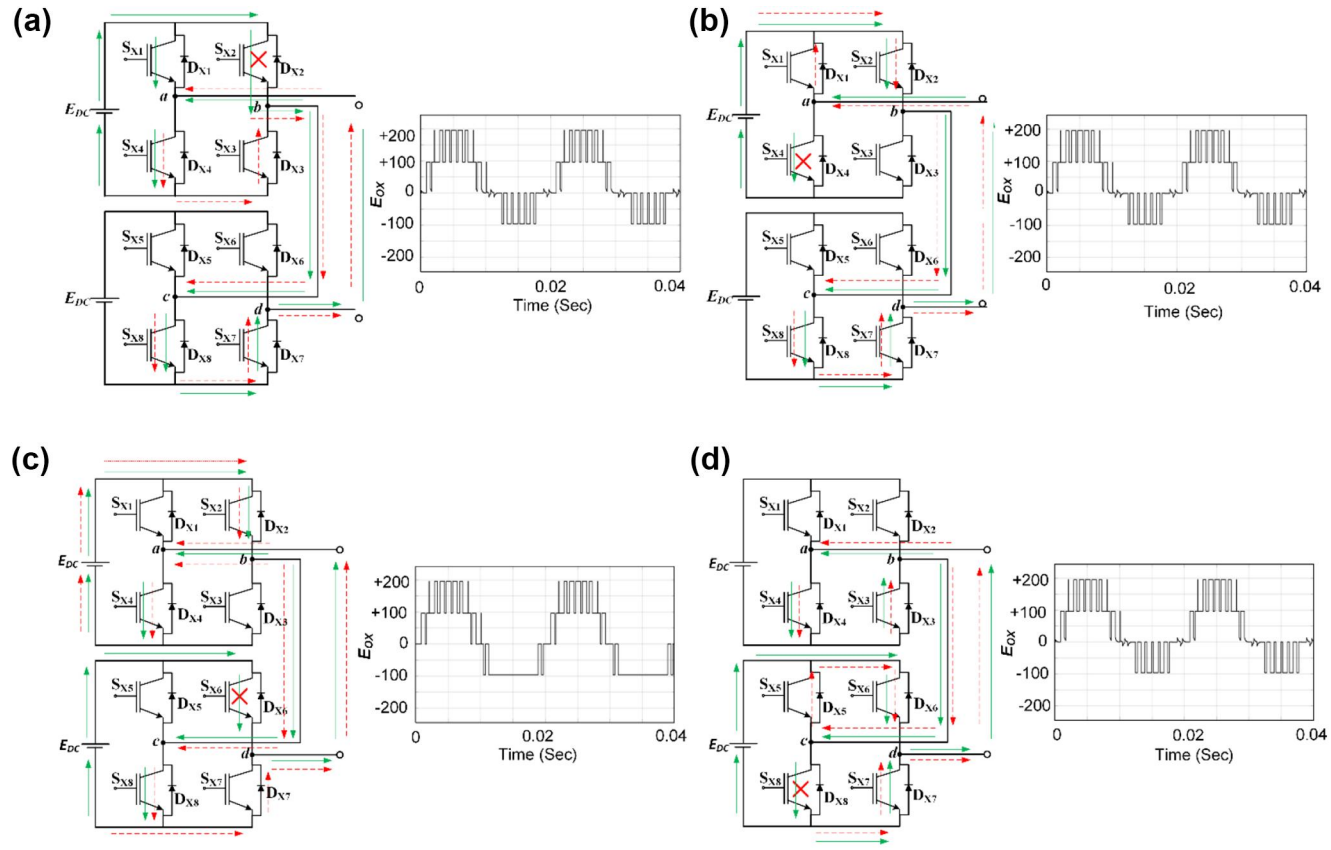

FIGURE 4 Current flows under even number of faulty switch conditions: (a) S_{X2} (b) S_{X4} (c) S_{X6} (d) S_{X8}

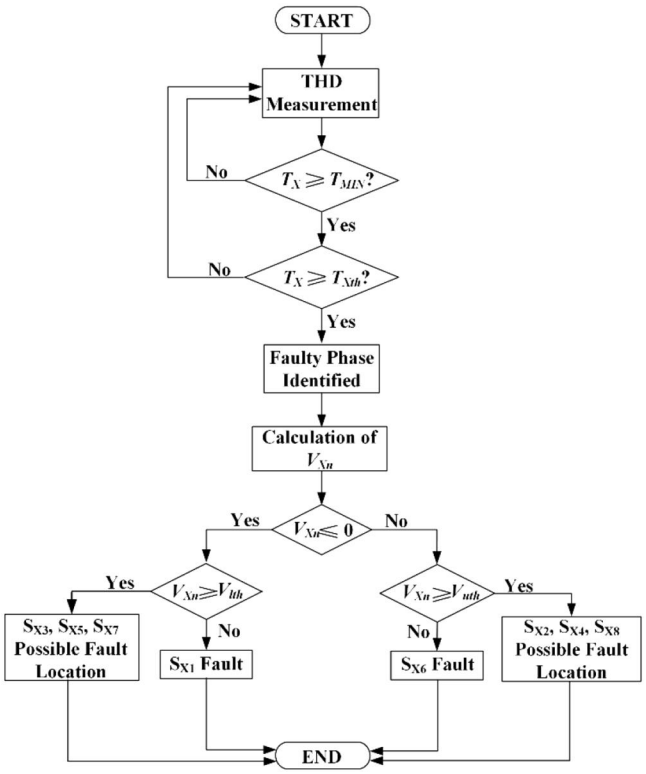

FIGURE 5 Open-circuit switch fault diagnosis algorithm

4.1 | Total harmonic distortion measurement of output phase voltage

The THD is measured from the output phase voltage using fast Fourier transform (FFT). It can be calculated as follows:

$$THD(T_X) = \frac{\sqrt{\sum_{b=2}^{b\max} E_{OXb}^2}}{E_{OX1}} \times 100 \tag{3}$$

If the OCSF occurs in any X^{th} phase switch, the THD (T_X) of that particular phase will be comparatively higher than it is for the other two phases. The value of T_X is compared with the minimum THD threshold named T_{MIN}. The measured value of T_X is compared with the switch fault THD threshold, called T_{Xth}. It is the threshold-defined value of the THD count for OSCF conditions. Once the faulty phase is identified, the normalized factor for the output phase voltage will be calculated.

4.2 | Normalized voltage factor

The normalized voltage factor (V_{Xn}) of each phase can be given as the ratio of the average voltage (V_{Xav}) of the

respective phase and the Park's transformation of the output voltage (V_S). The normalized voltage factor can be given as follows:

$$V_{Xn} = \frac{V_{Xav}}{V_S} \tag{4a}$$

where

$$V_S = V_d + V_q \tag{4b}$$

$$V_d = \frac{2}{3}V_a - \frac{1}{3}(V_b + V_c) \tag{4c}$$

$$V_q = \frac{1}{\sqrt{3}}(V_b - V_c) \tag{4d}$$

From the analysis of OCSF in Section 2, it is clear that S_{X1} and S_{X6} are the switches responsible for missing the positive-most ($+2E_{DC}$) and negative-most ($-2E_{DC}$) levels from the output phase voltages, respectively. Resultingly, the fault signatures generated by these two switches will be different from other switches. The odd switches S_{X1}, S_{X3}, S_{X5} and S_{X7} cause the production or missing of positive levels of output voltage, whereas the even-numbered switches S_{X2}, S_{X4}, S_{X6} and S_{X8} cause the production or missing of negative levels of output phase voltage. Therefore, this can be located easily at the time of fault. In the normal condition with no OCSF, the value of the normalization voltage factor is close to zero. If this value deviates from zero, then there are chances of fault. The deviation value depends on the faulty switch. If this deviation is greater than zero on the positive side, then the possible switch fault locations are S_{X2}, S_{X4}, S_{X6} and S_{X8}.

To ensure correct identification of the faulty switch, normalized voltage factor V_{Xn} is again compared with V_{uth} (upper threshold voltage) and V_{lth} (lower threshold voltage). If the result of the comparison with V_{Xn} and V_{uth} is 'NO', then the fault occurred in the switch S_{X6}, and the defined output variable d_x is zero as given in Equation (5). If the result of the comparison with V_{Xn} and V_{uth} is 'YES', then the output variable d_x is 1, and switches S_{X2}, S_{X4} and S_{X8} are the possible switch fault locations. If the deviation is less than zero (i.e. a negative value), then the possible switch fault locations are S_{X1}, S_{X3}, S_{X5} and S_{X7}. To ensure identification of the faulty switch, it is compared with V_{Xn} and V_{lth}. If the result of this comparison is 'NO', then S_{X1} is detected as the faulty switch, and another output variable, u_x, is defined as zero as given in Equation (6). If the result of this comparison is 'YES', and u_x is 1, then S_{X3}, S_{X5} and S_{X7} are the possible switch faults. The above-mentioned fault variable can be defined mathematically as follows:

$$d_x = \begin{cases} 1, \ \forall \ V_{Xn} \geq V_{uth} \\ 0, \ \forall \ V_{Xn} \geq V_{uth} \end{cases} \tag{5}$$

$$u_x = \begin{cases} 1, \forall V_{Xn} \geq V_{lth} \\ 0, \forall V_{Xn} \geq V_{lth} \end{cases} \tag{6}$$

5 | THRESHOLD ESTIMATION

The selected THD and voltage thresholds are important parameters for identifying the faulty switch. The two types of threshold used in the manuscript are as follows:

5.1 | THD threshold

Identification of the faulty phase is achieved by per-phase voltage THD threshold. The faulty phase is detected by comparison between the other two phases. The phase with higher THD compared with the other two phases is detected as the faulty phase. However, the rate of change in THD varies according to the modulation indices, and the modulation indices depend on the applications of the CHB MLI. Therefore, estimation of the THD threshold is required. The minimum value of THD in healthy condition for a five-level CHB ML inverter is considered as the reference threshold level. The plot of THDs for a five-level CHB ML inverter at various modulation indices under healthy and faulty conditions are shown in Figure 6a. The THD threshold based on the reference THD at healthy condition can detect the faulty phase up to modulation index 0.45 for faults in S_{X1} or S_{X6}. Thereafter, the threshold level is changed according to the reference or healthy THD condition for other modulation indices. The values of THD for all other switch fault conditions are much higher than they are for healthy conditions.

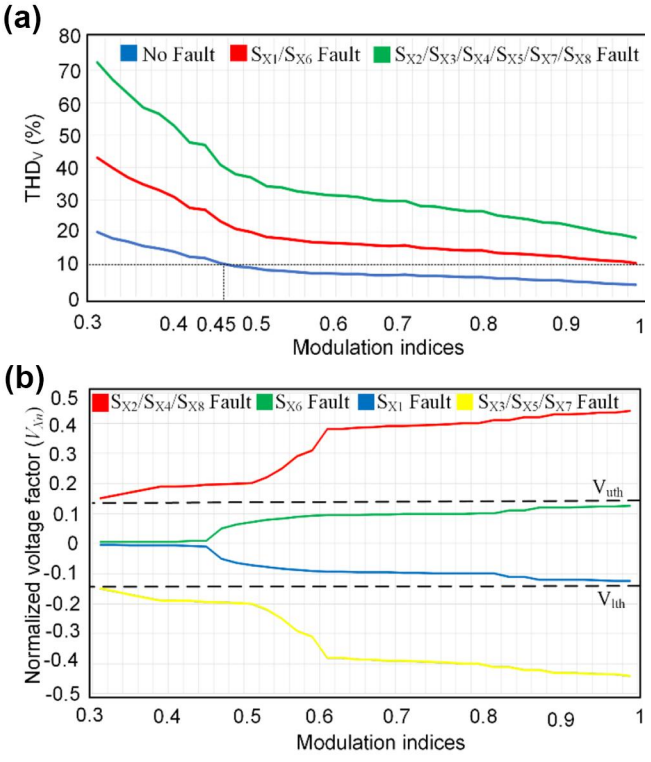

FIGURE 6 Variation of (a) total harmonic distortion with respect to modulation index and (b) normalized voltage with respect to modulation index for five-level cascaded H-bridge multilevel inverter

5.2 | Normalized voltage thresholds

After detection of the faulty phase, the normalized output voltage is calculated with respect to (4a), and further fault variables are defined using Equations (5) and (6). However, these thresholds vary according to the modulation index and resulting changes in output voltage. Figure 6b shows the relation between modulation indices and normalized voltage. If the value of V_{Xn} is greater than V_{uth}, then the probable faulty switches are S_{X3}, S_{X5} and S_{X7} (indicated by the red line). On the other side, if the value of V_{Xn} is lower than V_{uth}, then the faulty switch is S_{X1}. If the value of V_{Xn} is less than V_{lth}, then the probable faulty switches are S_{X2}, S_{X4} and S_{X8} (indicated by the yellow line). On the other side, if the value of V_{Xn} is higher than V_{lth}, then the faulty switch will be S_{X6}. The selected threshold gives a precise result up to modulation index 0.3.

6 | POST-FAULT CONTROL TECHNIQUE

The faulty switch must be isolated to ensure healthy operation of the remaining structure as well as to avoid a deterioration in system performance. If the fault is not cured within a specified time interval, it may cause the failure of other switching devices. The proposed control algorithm is based on reduction in the actual modulation indices (M_i). Once the faulty switch of any phase is identified, the Mi of all three phases will be reduced, and therefore the five-level inverter will operate as a three-level inverter. M_i can be defined as follows:

$$M_i = \frac{M_m}{(n-1) \times M_c} \tag{7}$$

where, M_m, M_C = magnitude of modulation and carrier wave.

Once the fault is identified, M_i is changed to produce the three-level output as shown in Figure 7. Switching states also show modification with changes in M_i. Table 4 presents the updated switching strategy after considering a fault in switch S_{X1}. The switching states are modified according to the switch fault that occurs. The normalized factor leads to selection of the appropriate switching state according to the faulty switch. The three-level output voltage will operate the load continuously but at low output power. The proposed faulty switch isolation algorithm can provide post-fault control for all possible switch faults. A fault in S_{X1} and S_{X6} can be detected within a short period, as their fault signatures are different. For a switch fault in S_{X3}, S_{X5} and S_{X7}, the priority of the fault is selected in ascending order. For illustration, if the fault occurred in switch S_{X5}, then according to the algorithm, the value of V_{Xn} is greater than V_{uth}, and the probable faulty switches are S_{X3}, S_{X5} and S_{X7}. Now, the fault-isolation algorithm assumes that the fault has occurred in S_{X3}. Meanwhile, the switching function and related expected output voltage are not similar. Based on this comparison, the next probable switch is selected, switching function and average output voltages are compared, and the faulty switch is isolated. However, this increases fault-isolation time by up to one fundamental cycle, which would be allowed for OCSFs. Fault isolation can also be achieved with different power factors.

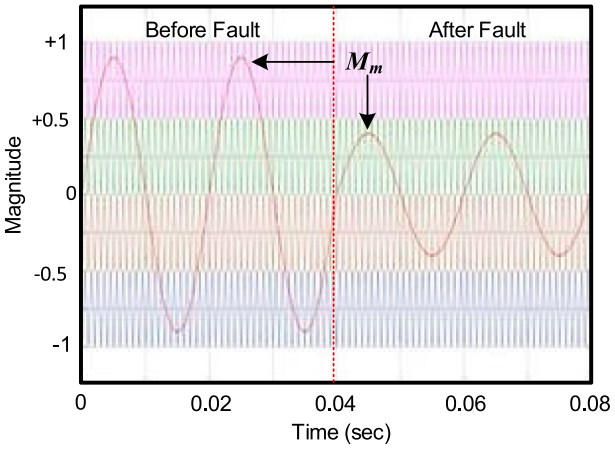

FIGURE 7 Switching technique after fault

TABLE 4 Modified switching states

	Modified switching states							
Output voltage	S_{X1}	S_{X2}	S_{X3}	S_{X4}	S_{X5}	S_{X6}	S_{X7}	S_{X8}
$+E_{DC}$	0	0	I	I	I	0	I	0
0	0	0	I	I	0	0	I	I
$-E_{DC}$	0	I	0	I	0	0	I	I

7 | RESULTS AND DISCUSSION

7.1 | Total harmonic distortion measurement of output phase voltage

Figure 8 shows THD for all three phases where S_{A1} is under fault. It can be seen that the THD count for phase-A is reduced from 24 switches to 8. After identification of the faulty phase, the normalized voltage factor is calculated.

7.2 | Normalized voltage factor

The normalized output voltage factor has almost a zero value for the no-fault condition. Small values are caused by noise or disturbances that can be handled within the defined thresholds and prevent false fault diagnosis. Figure 9 shows the fault created by removing the gate pulse of S_{A1} at time $t = 0.04$s. The normalized factor value goes to the negative region.

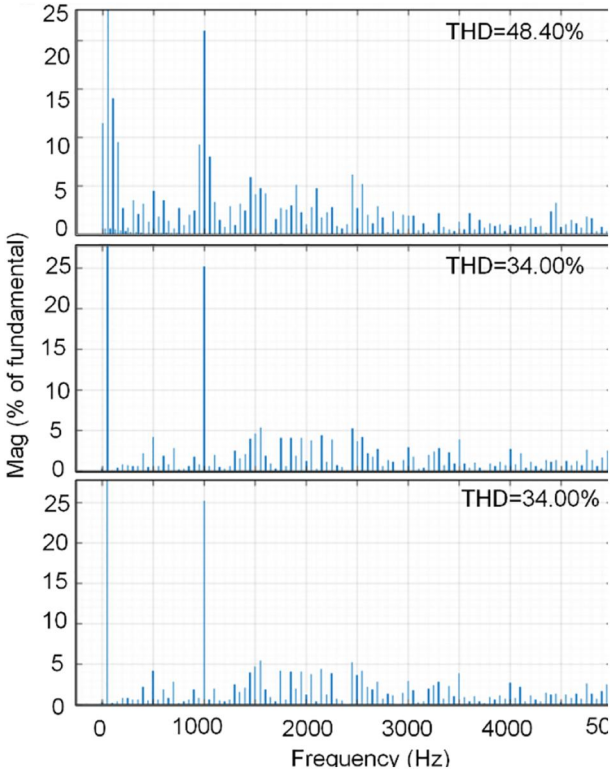

FIGURE 8 Total harmonic distortion for output voltage with S_{A1} fault

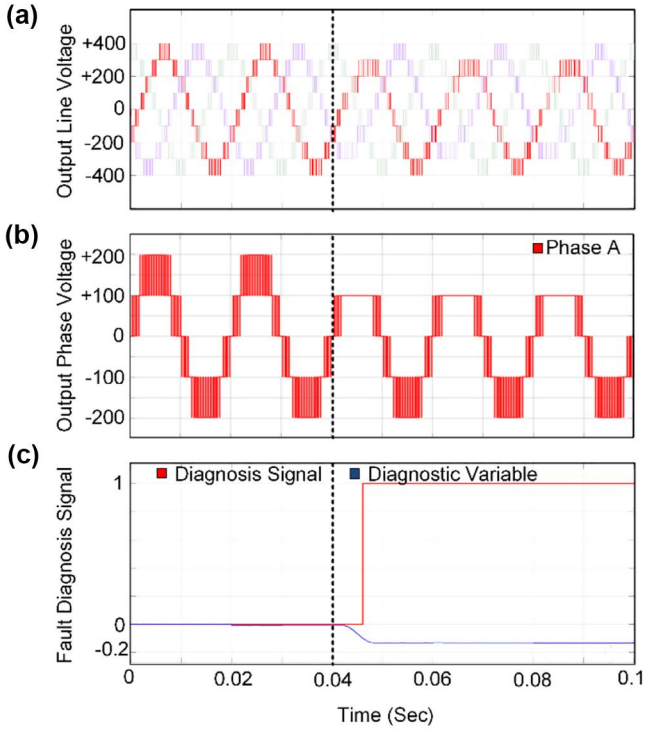

FIGURE 9 Fault detection for S_{A1} fault

However, it is within the limit of the defined threshold u_x obtained by Equation (6). Therefore, it is confirmed that S_{A1} is a faulty switch. It can be notice that the fault-detection signal goes high only when the faulty switching state arrives. Therefore, the fault signal may take time, up to one switching period, to indicate the fault, as shown in Figure 9. In Figure 10, the fault is created in S_{B6} (phase B). This switch is the cause for the production of the $-2E_{DC}$ level. The normalized voltage factor will have a positive value within the threshold limit defined as d_x in Equation (5). Similarly, the fault signal can be obtained for each switch. We can also notice that the time of fault detection for each switch will be different and depends on the respective switching state. Similarly, if the fault occurs in switch S_{A3}, then the normalized voltage factor exceeds the defined threshold limit u_x as given by Equation (6). Therefore, S_{A3}, S_{A5} and S_{A7} will be the possible switch fault locations.

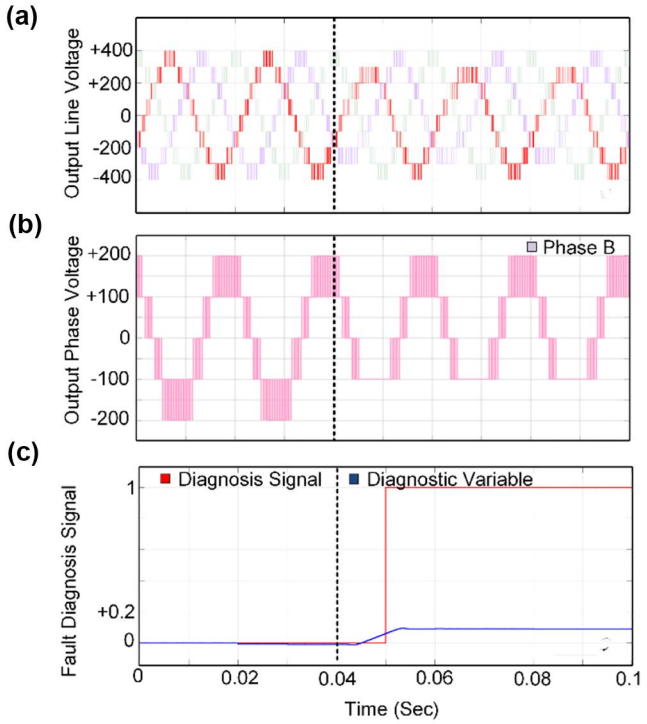

FIGURE 10 Fault detection for S_{B6} fault

7.3 | Post-fault control

A fault has occurred at time $t = 0.04$ s. After the faulty phase is identified by THD threshold, the normalization voltage factor is calculated for the faulty output voltage waveform. Based on this, the post-fault action will be taken by isolating the faulty switch from the remaining healthy system, and the predefined switching state for each possible switch fault will be implemented. The reduced value of M_i generates the three-level output shown in Figure 11a for OCSF in S_{A1} with a 0.9 power factor. The technique works effectively with different power factors. Figures 11b,c show the result of the post-fault operation for an OCSF in S_{A5} with power factors of 0.8 and 0.7, respectively. The new switching state is implemented on all

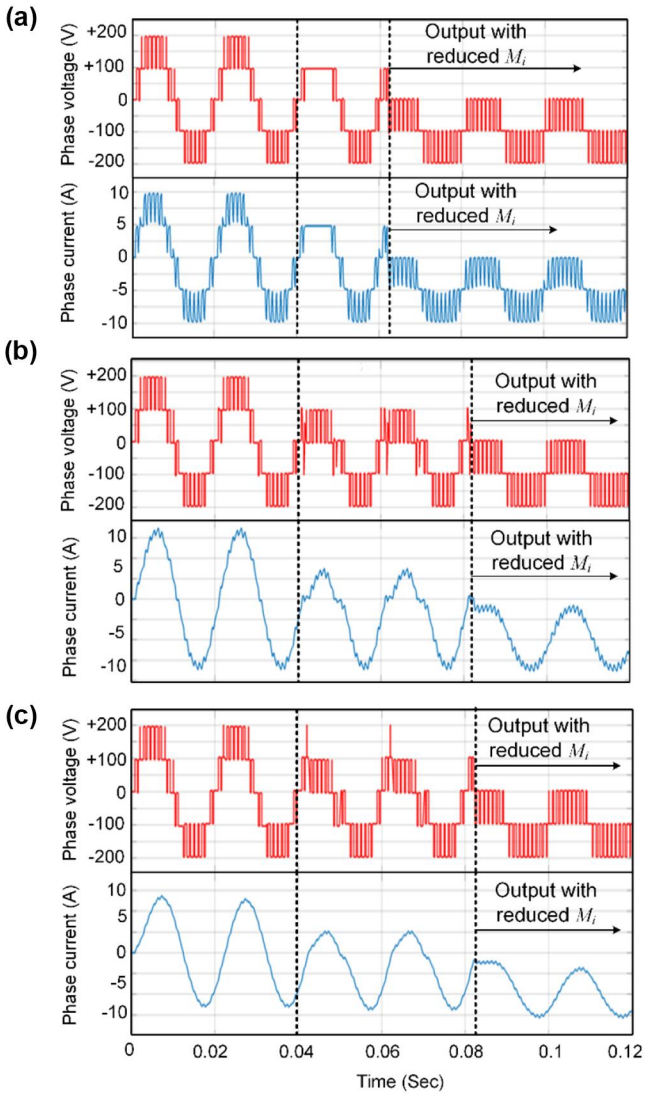

FIGURE 11 Post-fault control with output voltage and current (a) S_{A1} fault with 0.9 power factor (b) S_{A5} fault with 0.8 power factor (c) S_{A5} fault with 0.7 power factor

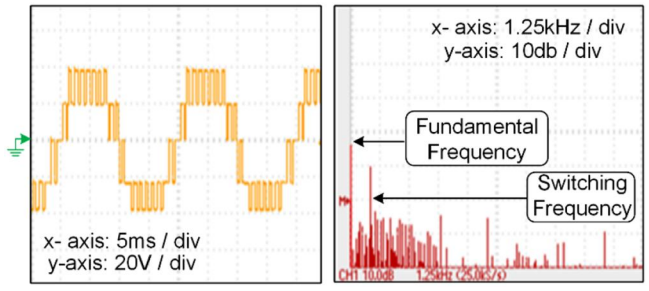

FIGURE 12 Output voltage and total harmonic distortion under healthy conditions

three phases to maintain balanced current among them. However, the output power is reduced with the reduction in modulation indices.

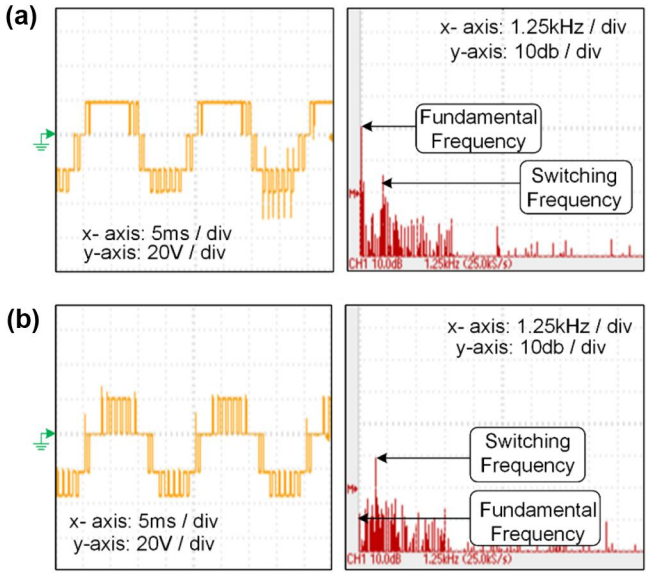

FIGURE 13 (a) Output voltage and total harmonic distortion for S_{A1} fault (b) Output voltage and total harmonic distortion for S_{A3}, S_{A5} and S_{A7}

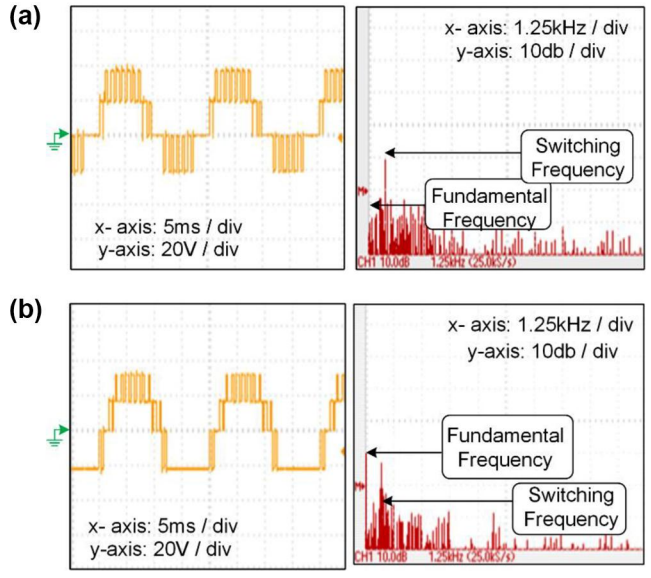

FIGURE 14 (a) Output voltage and total harmonic distortion for S_{A2}, S_{A4} and S_{A8} faults (b) Output voltage and total harmonic distortion for S_{A6} fault

8 | HARDWARE IMPLEMENTATION

The fault-diagnosis technique and post-fault control are validated through the prototype of a five-level CHB MLI. Each H-bridge cell is connected with a 20 V DC supply. TLP250 optocouplers are used as gate drivers and isolation from the controller to the power MOSFETs. The ZMPT 100 voltage sensor is used for measurement of output voltage. One voltage sensor per phase is required for implementing this technique. The open-circuit fault is created by removing the gating signals of the respective switches. The FFT plot under respective

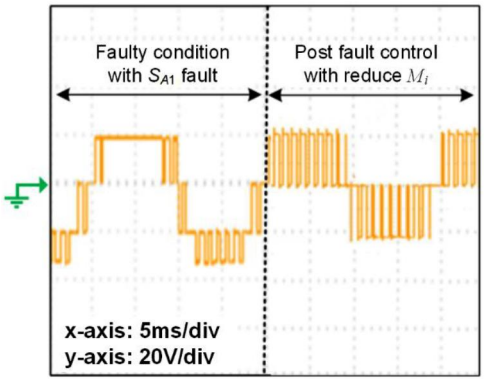

FIGURE 15 Output voltage under S_{A1} fault and post-fault control

switch faults is also captured for the analysis of OCSF faults using THD.

The output voltage waveform and voltage THD under healthy condition are shown in Figure 12. In healthy condition, the output voltage contains a higher fundamental component than that of any switch fault condition, as can be seen in Figure 13a. It can also be observed that the odd number switch faults S_{X3}, S_{X5} and S_{X7} generate nearly the same THD content, as their output voltage patterns are the same as those shown in Figure 13b. Similarly, the even-numbered switch faults S_{X2}, S_{X4} and S_{X8} generate nearly the same THD content as shown in Figure 14. The normalization factor can be calculated from Equation (4), and the faulty switch can be identified. After identification of the faulty switch, the post-fault control method is applied. As shown in Figure 15, once the faulty switch is identified by the post-fault control algorithm, it is bypassed. The modulation indices decrease, and therefore the five-level inverter output is converted into three-level output, resulting in a reduction in overall average output voltage. The inverter will now work as a three-level inverter.

9 | CONCLUSIONS

A THD and normalized voltage factor-based fault-detection technique is proposed. This five-level MLI fault-diagnosis technique can be implemented for any application. The proposed technique has a very simple control algorithm and is also very cost-effective. It does not require many hardware and software changes to existing systems. The fault-isolation algorithm is tested with different power factors. It only requires one voltage sensor per phase, which is already available for any closed-loop operation. The faulty phase can be detected in one fundamental cycle by THD thresholds. The faulty switches other than S_{X1} and S_{X6} are detected and isolated within a couple fundamental cycles. This time duration can be allowed for an open-circuit fault. However, it cannot be implemented for short circuit faults, as it requires sudden actions. The simulation and hardware results support the reliability of the proposed technique.

ORCID

Pavan Mehta https://orcid.org/0000-0002-4211-487X
Mayank Kumar https://orcid.org/0000-0001-9286-5666

REFERENCES

1. Rodríguez, J., et al.: Multilevel voltage-source-converter topologies for industrial medium voltage drives. IEEE Trans. Ind. Electron. 54(6), 2930–2945 (2007)
2. Akagi, H.: Multilevel converters: fundamental circuits and systems. Proc. IEEE. 105(11), 2048–2065 (2017)
3. Daher, S., Schmid, J., Antunes, F.L.M.: Multilevel inverter topologies for stand-alone PV systems. IEEE Trans. Ind. Electron. 55(7), 2703–2712 (2008)
4. Rodríguez, J., Lai, J.S., Peng, F.Z.: Multilevel inverters: a survey of topologies, controls, and applications. IEEE Trans. Ind. Electron. 49(4), 724–738 (2002)
5. Kouro, S., et al.: Recent advances and industrial applications of multilevel converters. IEEE Trans. Ind. Electron. 57(8), 2553–2580 (2010)
6. Rodriguez, J., et al.: A survey on neutral-point-clamped inverters. IEEE Trans. Ind. Electron. 57(7), 2219–2230 (2010)
7. El-hosainy, A., et al., A review of multilevel inverter topologies, control techniques and applications. In: 19th International Middle East Power Systems Conference (MEPCON), pp. 1265–1275. Cairo (2017)
8. Dargahi, S., et al.: Flying-capacitor stacked multicell multilevel voltage source inverters: analysis and modelling. IET Power Electron. 7(12), 2969–2987 (2014)
9. Venkataramanaiah, J., Suresh, Y., Panda, A.K.: A review on symmetric, asymmetric, hybrid and single DC sources based multilevel inverter topologies. Renew. Sustain. Energy Rev. 76, 788–812 (2017)
10. Mehta, P., Kunapara, A., Karelia, N.: Improvement in switching strategy used for even loss distribution in ANPC multilevel inverter. Proc. Technol. 21, 386–392 (2015)
11. Li, C., et al.: Hybrid modulation concept for five-level active-neutral-point-clamped converter. IEEE Trans. Power Electron. 32(12), 8958–8962 (2017)
12. Mehta, P., Kumar, M.: Capacitor voltage balancing and THD analysis in ANPC multilevel inverter. In: IEEMA Engineer Infinite Conference (eTechNxT), pp. 1–5. New Delhi, India (2018)
13. Dekka, A., et al.: Evolution of topologies, modelling, control schemes, and applications of modular multilevel converters. IEEE Trans. Emerg. Sel. Topics Power Electron. 5(4), 1631–1656 (2017)
14. Su, G.-J.: Multilevel DC-link inverter. IEEE Trans. Ind. Appl. 41(3), 848–854 (2005)
15. Shaoyong, Y., et al.: Condition monitoring for device reliability in power electronic converters: a review. IEEE Trans. Power. Electron. 25(11), 2734–2752 (2010)
16. Cruz, S.M.A., Mendes, A.M.S., Abadi, M.B.: "Fault diagnostic algorithm for three-level neutral point clamped AC motor drives, based on the average current Park's vector. IET Power Electron. 7(5), 1127–1137 (2014)
17. Mendes, A.M.S., Abadi, M.B., Cruz, S.M.Â.: Method to diagnose open-circuit faults in active power switches and clamp-diodes of three-level neutral-point clamped inverters. IET Power Electron. 10(7), 623–632 (2016)
18. Richardeau, F., Baudesson, P., Meynard, T.A.: Failures-tolerance and remedial strategies of a PWM multicell inverter. IEEE Trans. Power Electron. 17(6), 905–912 (2002)
19. Lezana, P., Aguilera, R., Rodríguez, J.: Fault detection on multicell converter based on output voltage frequency analysis. IEEE Trans. Ind. Electron. 56(6), 2275–2283 (2009)
20. Druant, J., et al.: Adding inverter fault detection to model-based predictive control for flying-capacitor inverters. IEEE Trans. Ind. Electron. 62(4), 2054–2063 (2015)
21. Sim, H.W., Lee, J.S., Lee, K.B.: Detecting open-switch faults: using asymmetric zero-voltage switching states. IEEE Ind. Appl. Mag. 22(2), 27–37 (2016)

22. Ouni, S., et al.: A fast and simple method to detect short circuit fault in cascaded h-bridge multilevel inverter. In: 2015 IEEE International Conference on Industrial Technology (ICIT), pp. 866–871. Seville (2015)
23. Khomfoi, S., Tolbert, L.M.: Fault diagnostic system for a multilevel inverter using a neural network. IEEE Trans. Power Electron. 22(3), 1062–1069 (2007)
24. Mehta, P., Kumar, M., Sahoo, S.: Fault diagnosis in five-level CHB inverter using normalisation factor and THD analysis. In: 8th IEEE India International Conference on Power Electronics (IICPE), pp. 1–5. Jaipur, India (2018)
25. Li, B., et al.: Fault diagnosis and tolerant control of single IGBT open-circuit failure in modular multilevel converters. IEEE Trans. Power Electron. 31(4), 3165–3176 (2016)
26. Deng, F., et al.: Fault detection and localization method for modular multilevel converters. IEEE Trans. Power Electron. 30(5), 2721–2732 (2015)
27. Lezana, P., et al.: Survey on fault operation on multilevel inverters. IEEE Trans. Ind. Electron. 57(7), 2207–2218 (2010)
28. Aleenejad, M., et al.: Reduced number of auxiliary H-bridge power cells for post-fault operation of three phase cascaded H-bridge inverter. IET Power Electron. 12(11), 2923–2931 (2019)
29. Rodríguez, J., et al.: Operation of a medium-voltage drive under faulty conditions. IEEE Trans. Ind. Electron. 52(4), 1080–1085 (2005)
30. Wei, S. et al.: Control method for cascaded H-bridge multilevel inverter with faulty power cells. In: 18th Annual IEEE Applications of Power Electronics Conference Expo. 1, pp. 261–267. Miami Beach, FL (2003)
31. Correa, P., Rodriguez, J.: Control strategy reconfiguration for a multilevel inverter operating with bypassed cells. In: IEEE International Symposium on Industrial Electronics, pp. 3162–3167. Vigo (2007)
32. Correa, P., Pacas, M., Rodríguez, J.: Modulation strategies for fault-tolerant operation of H-bridge multilevel inverters. In: IEEE International Symposium on Industrial Electronics, Montreal, QC, pp. 1589–1594. Canada (2006)
33. Chokhawala, R. S., Catt, J., Kiraly, L.: A discussion on IGBT short-circuit behaviour and fault protection schemes. IEEE Trans. Ind. Appl. 31(2), 256–263 (1995)

How to cite this article: Mehta P, Sahoo S, Kumar M. A fault-diagnosis and tolerant control technique for five-level cascaded H-bridge inverters. *IET Circuits Devices Syst*. 2021;1–11. https://doi.org/10.1049/cds2.12033

2020 IEEE 17th India Council International Conference (INDICON) | 978-1-7281-6916-3/20/$31.00 ©2020 IEEE | DOI: 10.1109/INDICON49873.2020.9342432

A Fine Tuned Model of Grasshopper Optimization Algorithm with Classifiers for Optimal Text Classification

Anshu Khurana
Department of Computer Science and Engineering
Delhi Technological University
Delhi, India
anshuchugh@gmail.com

Om Prakash Verma, Member, IEEE
Department Of Electronics and Communication
Delhi Technological University
Delhi,India
opverma.dce@gmail.com

***Abstract*—Text classification is widely used application of natural language processing and machine learning classifier. Tuning hyper-parameters of the classifier in machine learning is difficult and important step. The tuning of hyper-parameters means selection of the optimal hyper-parameters of the algorithm. Many approaches for tuning of the parameters have been tested and applied in the literature for the improvisation of the classification performance. Further, the feature selection using machine learning is a major task, dealing with high-dimensional dataset. In this paper, we proposed a hybrid model of tuned Grasshopper optimization algorithm with classifiers. Grasshopper optimization algorithm works on the mimic behavior of grasshoppers. The aim of this meta-heuristic approach is to determine the minimal feature subset from all features to improve the classification performance. For tuning of the classifiers, we have used random search technique. The classifiers chosen for classification are K-Nearest Neighbor and Support Vector Machine. Five multi-class datasets are used to evaluate the performance of the model in terms of Accuracy and AUC curve. All results are computed with 10-fold-cross validation method. The evaluated results of the proposed model is compared with other algorithms, which verifies the performance of our technique. The proposed model outperformed among all the compared state-of-the-art techniques.**

***Index Terms*—Feature Selection, Random Search, Optimal Text classification, Tuned Grasshopper Optimization algorithm, Tuned classifiers.**

I. Introduction

Hyper-parameter optimization is the process of determining the optimal parameter value before the beginning of the training process. The main objective of hyper-parameter tuning is to generate the optimum model for a given problem. Hyper-parameter can be obtained using several ways. One way is to give parameters to objective function to estimate the loss [6]. Other way is to obtain the generalized optimization performance of the model is the use of cross-validation [5]. From past few years, focus is on applying the techniques optimization techniques namely Grid search (GS) [10], Bayesian optimization [27], gradient based optimization [7] and Random search (RS) [5]. Feature selection algorithms emphasizes on the selection of important features, hence improves model accuracy [24]. There exist many nature inspired algorithms which are used to optimize features, namely: Genetic Algorithm (GA) [17], Particle Swarm Optimization (PSO) [28], Grey Wolf optimization (GWO) [8], Multiverse optimiser (MVO) [9] and many more. The rise in classification accuracy rely on the selected number of parameters needs to be tuned and regions of search space of the chosen algorithm. Thus, in hyper-parameter tuning the main problem lies in the fact to choose the different approach from the existing state-of-the art approaches. Grasshopper optimization algorithm is a new optimizer proposed by [23]. GOA works on the mimic behavior of grasshoppers. In study [2], researchers proposed a simultaneous approach for feature selection and parameter optimization using classical GOA. We proposed tuned GOA for feature selection which helps to improve classification accuracy.

For the classification problem, the supervised classifier are used. Support Vector Machine (SVM) [13] and k-Nearest Neighbor (k-NN) [10] are familiar, high-powered and influential classifiers. For fine tuning of the parameters of classifiers we chose RS technique. The advantage of RS over GS is that fewer combination are required to evaluate the solution, hence high-dimensionality does not cause problem for the technique. The rest part of the paper is formalized in the following manner. Related literature is presented in section II. The theoretical foundations of the proposed model is elucidate in section III. The complete method

Anshu Khurana, Delhi Technological University, India .
Om Prakash Verma, Delhi Technological University, India (e-mail: opverma.dce@gmail.com).

978-1-7281-6916-3/20/$31.00 ©2020 IEEE

Authorized licensed use limited to: DELHI TECHNICAL UNIV. Downloaded on February 15,2021 at 09:54:34 UTC from IEEE Xplore. Restrictions apply.

with flowchart is explained in IV. Datasets description and performance measure used to evaluate the model, is explained in V. Next section VI, shows the complete analysis of results with statistical comparison. Finally, conclusion of the paper is culminate in section VII.

II. Related Literature

Text classification is the branch of natural language processing. It can be applied to various text mining applications. Text classification can be binary classification [1] used in various task namely: spam filtering, opinion mining, information retrieval and many more. Multi-class classification is used where classification of more than two classes are required [19]. Tuning the parameters of the algorithms used for classification can improve the classification performance [22]. The main aim of hyper-parameter optimization is to control the parameters to improve the text classification performance. There are so many ways to tune parameters. First approach followed many years back was trying the different sets of values using hit and trial method [20] to obtain the acceptable parameters values. The second approach followed is grid search [29]. Grid search is a slow optimization algorithm which generates results after the several parameter combination. The third approach is the use of meta-heuristic algorithms, which are based on biological phenomena [4], [3]. Some used meta-heuristic algorithms in state-of-the-art are GA [21], GWO [13] , MVO [12], [9] , ACO [26] .

In [10], authors applied grid search to k-NN classifier for tuning the parameters with BM25 similarity. They proved that using BM25 similarity measure approach is a fast tuning method and proved it by comparing with other conventional approaches. The study in [2], proposed a technique of performing parameter tuning and feature selection simultaneously using GOA on SVM model. The authors compared their proposed model with other techniques and proved the performance in terms of classification accuracy. In [13] Ibrahim et al., proposed approach of using grasshopper optimizer for feature selection and parameter tuning for SVM classifier. The authors have compared the model accuracy with other meta-heuristics feature selection technique and proved the model is yielding better efficiency. The research in [22], shows the generalized model for optimizing the parameters of SVM classifier. The authors have tested their model on 15 medical diagnosis dataset. They have made the conclusion that estimation of distribution algorithms are best for the parameter tuning of SVM classifier. In [21], the authors have proposed GA-SVM model. They have used GA for feature weighting and parameters tuning for SVM. The authors proved the model efficiency by comparing their proposed technique with other feature weighting techniques. In research [15], authors proposed novel hybrid technique of nature-inspired and ensemble classifiers. They have used Bio-geography Based Optimization algorithm for feature selection technique and ensemble classifier for classifying the text. The authors have compared the classification performance with other state-of-the-art techniques and found that proposed technique outperformed among all the techniques.

The main motivation of the paper lies in the fact that tuning of GOA improved the classification performance, generating optimal feature subset. We perform classification performance using tuned SVM and k-NN classifiers. All datasets are run for 200 iterations using 10-fold-cross validation. To verify our model we compared the propose model with state-of-the-art models.

III. Theoretical Foundations

A. Grasshopper optimization

The Grasshopper Optimization algorithm [23] lies in the domain of nature inspired algorithm, established on the mimic behavior of grasshoppers. Following three components are responsible which affects the flying path of grasshoppers: Gravity power (G_j), Air advection (A_j) and social interaction (S_j) where j is the j-th individual. GOA social interaction is defined as in Equation 1:

$$S_j = \sum_{i=1, i\neq j}^{N} s(d_{ji})\hat{d_ji} \tag{1}$$

where d_{ji} is the distance measure between the j-th and i-th grasshopper, calculated as d_{ji}= $|x_i - x_j|$, S is a function which refers to the power of social forces, and $\hat{\mathbf{d}}_{\mathbf{ji}}$ is the unit vector between j-th and i-th grasshopper. The function 's' define the direction of a grasshopper defined as:-

$$s(r) = fe^{-r/l'} - e^{-r} \tag{2}$$

where 'f' refers to the intensity of attraction and "l'" represents the length scale. l' is the parameter which we selected for tuning in this research. The value of this function is the cause of attraction and repulsion in grasshopper. The swarm model is adjusted and designed which generates optimization algorithm. The mathematical model of search during interaction of the grasshopper is defined as in Equation

$$X_i^y = C(\sum_{j=1, j\neq i}^{N} C\frac{ub_y - lb_y}{s} s(|x_j^y - x_i^y|)\frac{x_j - x_i}{y_{ij}}) + \hat{T_y} \tag{3}$$

where, ub_y refers to the upper bound value in the y-th dimension, lb_y refers to the lower bound value in the y-th dimension, $\hat{T_y}$ is the value of y-th dimension in the best solution or target solution and C is decreasing co-efficient to shrink the repulsion area, attraction area and comfort area. The c parameter is responsible for the convergence of swarm so as to reach to the target.

In GOA algorithm, assumption is made that best solution obtained so far is the target solution. During the

Authorized licensed use limited to: DELHI TECHNICAL UNIV. Downloaded on February 15,2021 at 09:54:34 UTC from IEEE Xplore. Restrictions apply.

interaction between the grasshoppers and finding the target, the best solution gets updated if better solution is found. The parameter C is calculated as:

$$C = C_{max} - l\frac{C_{max} - C_{min}}{L'} \tag{4}$$

Where, L' signifies the maximum number of iteration, l is the current iteration, C_{max}=5, C_{min}= 0.00005. So, in this paper we have tuned l' from Equation 2 and L', C_{max}, C_{min} from Equation 4.

B. Classifiers

After completing literature survey, we selected two classifiers for the classification task namely: K-Nearest Neighbor (k-NN) and Support Vector Machine (SVM). We performed hyper-parameter tuning using random search technique to improve the classification accuracy. The k-NN approach is applied to various research areas like pattern recognition [16], text categorization [30]. The k-NN technique is based on the training of k instances present in the training set. These k instances will classify d documents that are similar to them (k-nearest neighbor). The majority voting method is used to classify document d, depends on the category which is common in the neighboring documents.

The improvement in the algorithm lies in the distance of a neighbor, more close neighbor influence the category of classification. The weight of the document is the main criteria to calculate the similarity score in the testing set. If testing document d is similar to more than one k nearest neighbor, then resulting weight is calculated by summing up the weights of all documents of the similar category. The sorting of similarity score is performed, and the top ranked category is the final category of the test document [25]. For the efficient working we need to know the appropriate value of k [14]. In our tuning method of random search the best value is obtained at k=7. The other parameters which yields best value are p (Eucledian distance)=2, Weight=distance.

The other classifier chosen for classification is SVM. In this paper, we consider the Gaussian kernel for SVM. The advantage of this kernel is that it can handle more number of kernels when compared to other kernels [11]. The random search technique tuned cost (c) and gamma (γ) parameters. The range for cost hyper-parameter is 2^{-2} to 2^{15} and gamma is 2^{-15} to 2^{5}. We have performed 200 runs for each classifier with 10-fold cross-validation. The tuning optimizer is very much dependent on the nature of the problem. According to the literature survey, it can be seen that random search is a good tuning model in most of the scenarios. It's process simplicity and computation time is also an advantage of using this model. On comparing different techniques, namely, manual search, random search, grid search, evolutionary algorithms and Artificial Neural Network, random search performed the best and hence was selected by authors as the model to tune the parameters of the classifiers.

IV. Method

As stated before, the goal of this research is to know the effectiveness of the tuned GOA for feature selection, and RS used for hyper-parameter optimization for the two classifiers. We employed other feature selection techniques to verify the efficiency namely: classical GOA, MVO and GWO. We have used 10-fold-cross validation method for generalizing the result. Accuracy and ROC measure was used to evaluate the working of the proposed model. In this Paper, we have optimize the parameter of Gaussian kernel [11], (γ), of SVM classifier. The parameter of SVM, cost (C), is also tuned. The accuracy and ROC curve values are used as fitness function to measure the effectiveness. Higher values indicate the propitious hyper-parameter values. Many experiments are employed using meta-heuristic techniques for feature selection and parameter optimization [13], [2]. Tuning parameters helps to improve classification performance [10]. Tuned GOA is formalized to produce reduced dataset with all essential features. Reducing the dataset helps to improve the classification accuracy. Reduced dataset is streamed to the tuned classifiers to generate the classification results. The model starts working after finalizing the parameter range for tuning of GOA and classifier. The parameters that are tuned in GOA algorithm using meta-optimization technique is present in Equation 2 and 4. The process of data normalization is performed on selected features. The updation of population is performed using the equation.

$$X_i = c * r[\sum_{k=1}^{N} c\frac{ub - lb}{2} s(|X_k - X_i|)X_k - X_i/d_{ki}] + S \tag{5}$$

After preprocessing, the vector is divided for the selected features and parameters of classifiers. The dataset is divided into training and testing parts. The subset of features are trained and then tested accuracy and AUC score and testing part. To train the model, we employed the set trained vectors and determine the objective functions. We terminate the process after setting the maximum iteration. Parameters that are tuned, range and best values obtained are mentioned in Table I. The flowchart of the methodology is explained in Figure 1. The Algorithm followed is explained in the Figure 2.

V. Experimental Setup

A. Dataset

In our research, we have used five multi-class dataset from UCI repository [18]. The description of dataset is given in Table II. It can be seen that the datasets which we have chosen are varied datasets in terms of number of features, number of classes and number of instances. Our priority focused on high-dimensionality

Authorized licensed use limited to: DELHI TECHNICAL UNIV. Downloaded on February 15,2021 at 09:54:34 UTC from IEEE Xplore. Restrictions apply.

TABLE I: Tuning Parameters

Technique	Parameters tuned	Range	Best value
GOA	l'	0-4	3.1
	C_{min}	N/A	0.00005
	C_{max}	N/A	5
	L'	N/A	200
k-NN	k	1-10	7
	p	1-3	2
	weight	uniform	distance
SVM	c	2^{-2} to 2^{15}	2^{11}
	γ	2^{-15} to 2^{5}	2^{2}

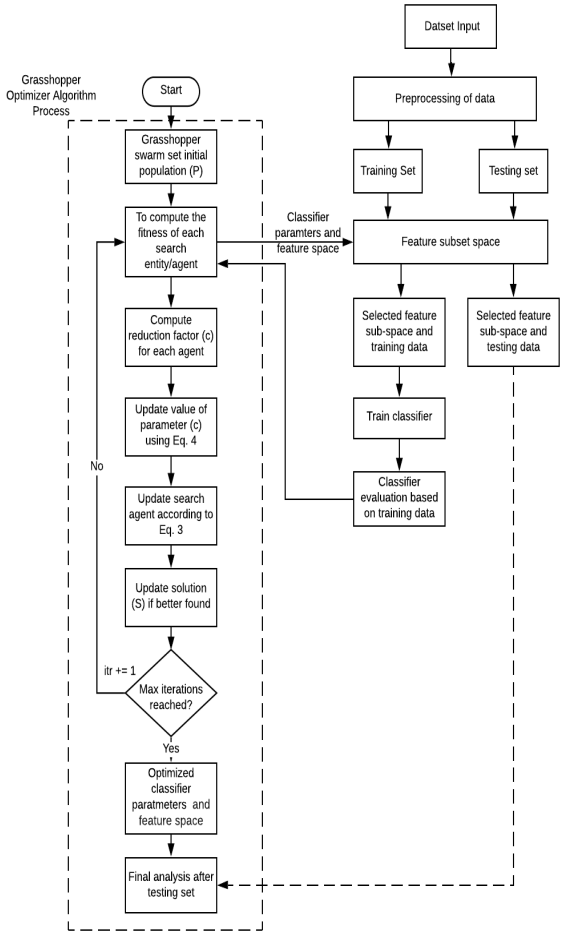

Fig. 1: Flow process of the model.

datasets. For training/testing method, we have applied 10-fold-cross validation. Each dataset is performed with 200 runs to evaluate the results. Teaching Assistant evaluation is referred as TAE in future Tables.

B. Objective functions

To evaluate the performance of the proposed model we have computed our results on two objective functions namely: Accuracy and Area Under Curve (AUC).

Parameter(s): P - Initialize control parameters: tuned GoA parameters, tuned classifier parameters, upper band(ub), lower band(lb), maximum number of iterations(T), desired number of features(f)
Output: O - Target solution(S)
//Grasshopper algorithm parameters to be tuned
Meta-optimization technique applied for tuning
C_{min}: 0.00005
C_{max}: 5
l: Range [0-4]
L: 200
j $\leftarrow$ 0
Initialize X_i: set of random vectors with initial population, where i = 1, 2, . . . , n), each member with the dimension of 1×f having integer elements in the valid interval of [lb,ub].
while $j < T$ **do**
  Compute c via below equation
  while *Member-iterated* $<$ *Population-size* **do**
    Update X_i using equation 5
    Round-up the vales of X_i to the most nearest integer
    Check the outlier values and modify them with random values lies in the provided valid interval.
    Evaluate the duplicate features and modify them.
    Calculate classification error rates of both the classifiers (tuned[k-NN and SVM]) and analyze the fitness values.
    //Parameter tuning of classifiers is done using random search technique
  end
  Update S if better solution is found in population.
  j = j+1
end
return S

Fig. 2: Tuned Grasshopper Algorithm used for feature selection

TABLE II: Description of multi-class dataset

Dataset	Features	instances	Classes
Glass	9	214	6
Cleveland	13	303	4
Arrhythmia	297	452	16
Libras	90	360	15
Teaching Assistant evaluation	5	151	3

Authorized licensed use limited to: DELHI TECHNICAL UNIV. Downloaded on February 15,2021 at 09:54:34 UTC from IEEE Xplore. Restrictions apply.

Accuracy is defined as the ratio of correctly classified to the total number of classes. It is calculated as:

$$Accuracy = (TN+TP)/(TP+FP+FN+TN) \quad (6)$$

where, -TP refers to true positive value which signifies that the positive predicted instance lies in the positive class in its correct actual state.
-FN refers to false negative value which signifies that instance which is predicted negative actually present in the positive class.
-FP is false positive value which signifies that positive predicted instance belongs actually to the negative class.
-TN refers to true negative value which signifies that negatively predicted instance belongs actually to the negative class.
Receiver operating characteristics (ROC) curve is graphically plotted by taking True positive rate (TPR) at y-axis and False positive rate (FPR) at x-axis. Area under curve (AUC) is actual area that falls under the region of ROC curve.

VI. Results

In this research, we have implemented all the algorithms on Windows 10 64-bit OS, Intel® Core™ i5-5200U CPU @2.20GHz processor. Results are computed on jupyter notebook using python. All the algorithms are set to run for 200 iterations with 10-fold-cross validation. In Table III, we compared accuracy measure of our model with other feature selection techniques namely: classical GOA, MVO, GWO and Grid search. We have consider two classifiers tuned k-NN and tuned SVM for the classification task. We found that datasets like Glass and arrhythmia which are high-dimensional datasets produced accuracy 15-20% higher, datasets like cleveland and TAE shows arise in accuracy for 10 to 15% higher. We have considered varied datasets for the generalization of the model. Higher accuracy indicates the better classification performance with optimal parameters. In Table IV comparison of the proposed technique is performed with other proposed researches [2], [13] and [21]. We concluded that our research produced better results than all the techniques with good accuracy rise.
In Figure. 3, AUC plot of Glass dataset is shown. All the techniques are represented with different colours. It can be seen that AUC for glass dataset produces similar results with both tuned classifiers. Tuned GOA and SVM with 85% score shows rise of 3% when compared to classical GOA-SVM technique and 14% rise when compared to GWO-SVM technique.
In Figure. 4, represent the AUC plot for arrhythmia dataset. The dataset is high-dimensional dataset and producing good results with our model. AUC score is 90% with tuned GOA and tuned SVM. The rise of score in our model is from 9% to 25%. Our model perform best with high-dimensional as well as low-dimensional datasets. 10-fold-cross validation method is applied for computation of all the results.

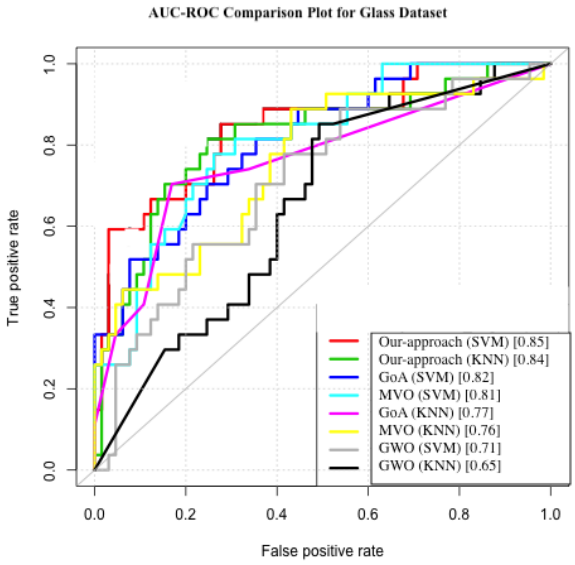

Fig. 3: AUC plot of Glass dataset

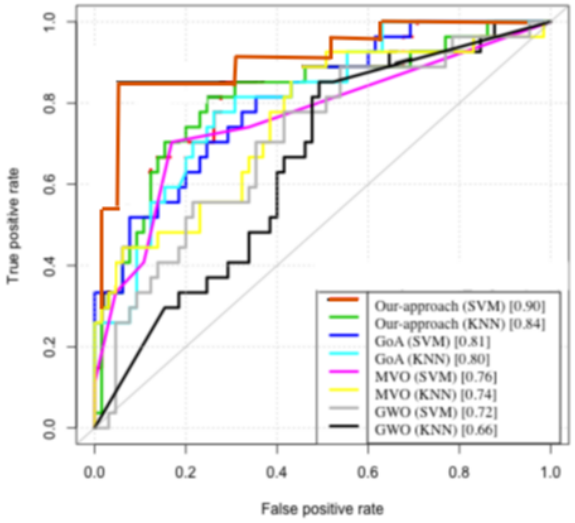

Fig. 4: AUC plot of arrhythmia dataset

VII. Conclusion

In this paper, we proposed a novel approach of tuned GOA with tuned classifiers. The tuned GOA is used for feature selection to decrease the problem caused due to high-dimensionality, and increase the classification performance. We have used random search technique for the parameter optimization of the two classifiers- k-NN and SVM. Tha Gaussian kernel of

Authorized licensed use limited to: DELHI TECHNICAL UNIV. Downloaded on February 15,2021 at 09:54:34 UTC from IEEE Xplore. Restrictions apply.

TABLE III: Accuracy results for the various techniques

Dataset	GOA		MVO		GWO		Grid search		Our approach	
	k-NN	SVM	k-NN	SVM	k-NN	SVM	k-NN	SVM	k-NN	SVM
Glass	61.8	67.1	64.7	64.2	50.9	60.2	56.4	55.1	78.3	83.2
Cleveland	52.1	54.7	50.9	47.0	53.4	56.6	54.1	52.9	66.2	60.6
Arrhythmia	55.0	68.3	64.1	71.4	60.6	68.0	62.4	61.6	76.1	82
Libras	76.4	85.2	75.3	85.8	79.7	84.1	72.1	76	86.6	90.2
TAE	62.9	57.6	68.8	54.1	69.9	54.4	55.6	49.4	71.3	60.3

TABLE IV: Comparison of Accuracy results

Dataset	[2]		[13]		[21]		Our research	
	k-NN	SVM	k-NN	SVM	k-NN	SVM	k-NN	SVM
Glass	68.2	68.5	73.3	70.8	66.2	65.3	78.6	83.5
Cleveland	50.2	53.3	51.6	57.7	40.1	51.0	66.4	60.6
Arrhythmia	70.5	66.5	56.3	50.3	48.1	45.5	76.1	82.3
Libras	89.2	87.5	92.5	90.1	75.6	70.1	86.6	90.2
TAE	50.1	56.1	76.2	70	67.3	60.2	71.3	60.3

SVM is used for hyper-parameter optimization. We have tested the proposed model on 5-real-world datasets from UCI by computing classification accuracy and AUC measure. In the different performance measure, our model performed better then other state-of-the-art techniques. The best accuracy was obtained with high-dimensional dataset, although proposed model worked good with low-dimensional dataset as well. For the future work, our research will focus on training deep neural networks using tuned meta-heuristic algorithms. The proposed algorithm with different algorithms can also be applied in other areas like image classification, pattern recognition.

REFERENCES

[1] Charu C Aggarwal and ChengXiang Zhai. A survey of text classification algorithms. In *Mining text data*, pages 163–222. Springer, 2012.

[2] Ibrahim Aljarah, Al-Zoubi Ala'M, Hossam Faris, Mohammad A Hassonah, Seyedali Mirjalili, and Heba Saadeh. Simultaneous feature selection and support vector machine optimization using the grasshopper optimization algorithm. *Cognitive Computation*, 10(3):478–495, 2018.

[3] Ibrahim Aljarah, Hossam Faris, and Seyedali Mirjalili. Optimizing connection weights in neural networks using the whale optimization algorithm. *Soft Computing*, 22(1):1–15, 2018.

[4] Ibrahim Aljarah, Hossam Faris, Seyedali Mirjalili, and Nailah Al-Madi. Training radial basis function networks using biogeography-based optimizer. *Neural Computing and Applications*, 29(7):529–553, 2018.

[5] James Bergstra and Yoshua Bengio. Random search for hyper-parameter optimization. *Journal of machine learning research*, 13(Feb):281–305, 2012.

[6] Marc Claesen and Bart De Moor. Hyperparameter search in machine learning. *arXiv preprint arXiv:1502.02127*, 2015.

[7] Shadi Diab. Optimizing stochastic gradient descent in text classification based on fine-tuning hyper-parameters approach. a case study on automatic classification of global terrorist attacks. *arXiv preprint arXiv:1902.06542*, 2019.

[8] Eid Emary, Hossam M Zawbaa, Crina Grosan, and Abul Ella Hassenian. Feature subset selection approach by gray-wolf optimization. In *Afro-European conference for industrial advancement*, pages 1–13. Springer, 2015.

[9] Hossam Faris, Mohammad A Hassonah, Al-Zoubi Ala'M, Seyedali Mirjalili, and Ibrahim Aljarah. A multi-verse optimizer approach for feature selection and optimizing svm parameters based on a robust system architecture. *Neural Computing and Applications*, 30(8):2355–2369, 2018.

[10] Raji Ghawi and Jürgen Pfeffer. Efficient hyperparameter tuning with grid search for text categorization using knn approach with bm25 similarity. *Open Computer Science*, 9(1):160–180, 2019.

[11] Taciana AF Gomes, Ricardo BC Prudêncio, Carlos Soares, André LD Rossi, and André Carvalho. Combining meta-learning and search techniques to select parameters for support vector machines. *Neurocomputing*, 75(1):3–13, 2012.

[12] Rahul Hans and Harjot Kaur. Binary multi-verse optimization (bmvo) approaches for feature selection. *International Journal of Interactive Multimedia & Artificial Intelligence*, 6(1), 2020.

[13] Hadeel Tariq Ibrahim, Wamidh Jalil Mazher, Osman N Ucan, and Oguz Bayat. A grasshopper optimizer approach for feature selection and optimizing svm parameters utilizing real biomedical data sets. *Neural Computing and Applications*, 31(10):5965–5974, 2019.

[14] Anshu Khurana and Om Prakash Verma. Pso based optimal text classification using tuned k-nn and feature weighting. *International Journal of Information Systems & Management Science*, 1(1), 2018.

[15] Anshu Khurana and Om Prakash Verma. Novel approach with nature-inspired and ensemble techniques for optimal text classification. *Multimedia Tools and Applications 10.1007/s11042-020-09013-2*, 2020.

[16] Munish Kumar, MK Jindal, and RK Sharma. k-nearest neighbor based offline handwritten gurmukhi character recognition. In *2011 International Conference on Image Information Processing*, pages 1–4. IEEE, 2011.

[17] Riccardo Leardi and Amparo Lupianez Gonzalez. Genetic algorithms applied to feature selection in pls regression: how and when to use them. *Chemometrics and intelligent laboratory systems*, 41(2):195–207, 1998.

[18] Moshe Lichman et al. Uci machine learning repository, 2013.

[19] Li Ma and Suohai Fan. Cure-smote algorithm and hybrid algorithm for feature selection and parameter optimization based on random forests. *BMC bioinformatics*, 18(1):169, 2017.

[20] Miha Pavlinek and Vili Podgorelec. Text classification method based on self-training and lda topic models. *Expert Systems with Applications*, 80:83–93, 2017.

[21] Anh Viet Phan, Minh Le Nguyen, and Lam Thu Bui. Feature weighting and svm parameters optimization based on genetic algorithms for classification problems. *Applied Intelligence*, 46(2):455–469, 2017.

Authorized licensed use limited to: DELHI TECHNICAL UNIV. Downloaded on February 15,2021 at 09:54:34 UTC from IEEE Xplore. Restrictions apply.

[22] Alfonso Rojas-Domínguez, Luis Carlos Padierna, Juan Martín Carpio Valadez, Hector J Puga-Soberanes, and Héctor J Fraire. Optimal hyper-parameter tuning of svm classifiers with application to medical diagnosis. *IEEE Access*, 6:7164–7176, 2017.

[23] Shahrzad Saremi, Seyedali Mirjalili, and Andrew Lewis. Grasshopper optimisation algorithm: theory and application. *Advances in Engineering Software*, 105:30–47, 2017.

[24] Muhammad Atif Tahir, Ahmed Bouridane, and Fatih Kurugollu. Simultaneous feature selection and feature weighting using hybrid tabu search/k-nearest neighbor classifier. *Pattern Recognition Letters*, 28(4):438–446, 2007.

[25] Chris Thornton, Frank Hutter, Holger H Hoos, and Kevin Leyton-Brown. Auto-weka: Combined selection and hyperparameter optimization of classification algorithms. In *Proceedings of the 19th ACM SIGKDD international conference on Knowledge discovery and data mining*, pages 847–855, 2013.

[26] Youchuan Wan, Mingwei Wang, Zhiwei Ye, and Xudong Lai. A feature selection method based on modified binary coded ant colony optimization algorithm. *Applied Soft Computing*, 49:248–258, 2016.

[27] Ziyu Wang, Frank Hutter, Masrour Zoghi, David Matheson, and Nando de Feitas. Bayesian optimization in a billion dimensions via random embeddings. *Journal of Artificial Intelligence Research*, 55:361–387, 2016.

[28] Cheng-San Yang, Li-Yeh Chuang, Jung-Chike Li, and Cheng-Hong Yang. Chaotic maps in binary particle swarm optimization for feature selection. In *2008 IEEE Conference on Soft Computing in Industrial Applications*, pages 107–112. IEEE, 2008.

[29] XiaoLi Zhang, XueFeng Chen, and ZhengJia He. An aco-based algorithm for parameter optimization of support vector machines. *Expert Systems with Applications*, 37(9):6618–6628, 2010.

[30] Xiao-Feng Zhong, Shi-Ze Guo, Liang Gao, Hong Shan, and Jing-Hua Zheng. An improved k-nn classification with dynamic k. In *Proceedings of the 9th International Conference on Machine Learning and Computing*, pages 211–216, 2017.

Authorized licensed use limited to: DELHI TECHNICAL UNIV. Downloaded on February 15,2021 at 09:54:34 UTC from IEEE Xplore. Restrictions apply.

A Laboratory Setup for Synchrophasor Applications

Annu Ahlawat
Department of Electrical Engineering
Delhi Technological University
Delhi, India
annuahlawat014@gmail.com

Anirudh Goyal
Department of Electrical Engineering
Delhi Technological University
Delhi, India
anirudhgoyal136@gmail.com

Saurabh Kumar Mishra
Department of Electrical Engineering
Delhi Technological University
Delhi, India
saurabhkumarmishra98@gmail.com

S T Nagarajan
Department of Electrical Engineering
Delhi Technological University
Delhi, India
stnagarajan@dce.ac.in

2020 IEEE 17th India Council International Conference (INDICON) | 978-1-7281-6916-3/20/$31.00 ©2020 IEEE | DOI: 10.1109/INDICON49873.2020.9342147

***Abstract*—Phasor Measurement Units (PMU) are being deployed in power grids all over the world recently for monitoring and control of power grids. Recently many applications of PMU are being reported in literature for estimation of power system parameters like inertia, damping, online transmission line parameters etc., however, their access to the PMU data from the grid operators is extremely difficult for verification the estimates and application development by research community. Therefore, there is a necessity to develop a laboratory scale PMU data architecture so that new PMU applications can be developed and tested in laboratories. In this paper, we have developed a low cost laboratory scale setup of PMU architecture for development of PMU applications on MATLAB platform, based on an open source software developed by Grid Protection Alliance, Delft University of technology and Power world simulator.**

Keywords— PMU, PDC, WAMS, IEEE Std. C37.118, Synchrophasor

I. INTRODUCTION

The growing demands of electricity causes highly extensive and interconnected large electric power system, which mainly consist of generating power stations, transmission lines and electricity distribution systems. Due to occurrence of Blackouts in power grid in the recent past, there is a renewed interest to make the power system resilient from external and internal disturbances. Phasor Measurement Unit is one such device developed (PMU) for deeper insight in the operation of power grid [1].

Phasor Measurement Units are high speed power system devices that can provide the synchronized measurements of electrical quantities. Recently, Phasor measurement units are being deployed over power grids, popularly known as the wide area measurement system (WAMS) or wide area monitoring and control system (WAMPCS). WAMS is an intelligent power system device setup, which are capable of providing highly precise and synchronized phasor data of the power grid in real time [2]. In WAMS there are two main components, first one is the Phasor Measurement Units (PMUs) and the other one, Phasor Data Concentrators (PDCs), which are interconnected with communication technologies and time synchronized with Global Positioning Systems (GPS) [3], [4].

PMUs have high reporting rate in the order of 30-60 frames per seconds while traditional SCADA system provides one measurement in every 2-3 seconds. Therefore, due to high resolution of PMU, helps in analyzing dynamic events occurred in power grid. PMUs have two major functions, first is to measure the analog signal and sample into digital form to estimate the phasor quantity of the signal such as, phasors of voltage and current, frequency and rate of change of frequency (ROCOF) with a real time tag. Second, is to transmit the estimate quantity at a fixed reporting rate over a communication protocol to higher level device at local or remote location. Time synchronization is achieved from a Global Positioning Systems (GPS) receivers which is based on Coordinated Universal Time (UTC). The estimation part is still evolving with research community and industry, whereas the transmission part has been standardized by IEEE standards.

In view of the increased deployment of PMUs across the globe in power grids, it is necessary for introduction of PMU topics in power engineering education at graduate level itself. Most of the educational institutions imparting power education do not have a PMU laboratory setup at this point of time. Further, setting up a laboratory for study involving a PMU shall be expensive for graduate level programs in educational institutions which do not have access to real time simulators. An attempt has been done in this regard previously for low cost, with FPGA and Raspberry pi by [5].

In this paper, a low cost laboratory setup involving only the simulation of PMU and communication architecture with open source software such as Synchro-measurement Application Development Framework developed by Matija naglich at Delft University of Technology [6], PMU connection tester [7] and Open PDC from Grind Protection Alliance [8], free student version of Power World simulator and Power World Dynamic studio [9] and an application developed on MATLAB platform at Delhi Technological University has been explained. This setup does not require an expensive real time simulator and the data transmission architecture can be studied in detail with this setup, which

978-1-7281-6916-3/20/$31.00 ©2020 IEEE

Authorized licensed use limited to: DELHI TECHNICAL UNIV. Downloaded on February 15,2021 at 09:55:51 UTC from IEEE Xplore. Restrictions apply.

helps in understanding the performance of the synchro phasor measurement units in power systems.

II. WAMS Based On Phasor Measurement System

As shown in Fig. 1, WAMS infrastructure basically consists of the following units:

- Phasor Measurement Unit (PMU)
- Global Positioning System (GPS)
- Phasor Data Concentrator (PDC)
- Communication Channels
- Control centre

PMUs are normally installed in substations across the power grid. These devices are connected to CTs (Current Transformers) and PTs (Potential Transformers) so that the line current and voltages are directly fed to these devices. The internal hardware of PMU consisting of anti-aliasing filters, A/D converters, phase-locked oscillator, phasor microprocessor and GPS receiver. The data from PMU is filtered and sampled before the input data is processed for estimating its phasor value, to overcome the problem of leakage and aliasing of the data. Thus the waveform which are fed to PMUs are captured in samples and the resulting estimate of measurement quantity is known as Synchrophasor. The collected measurement data are aligned by GPS time tag.

Phasor Data Concentrator (PDC) receives all the Synchrophasor data from PMUs installed at different locations in power grid.

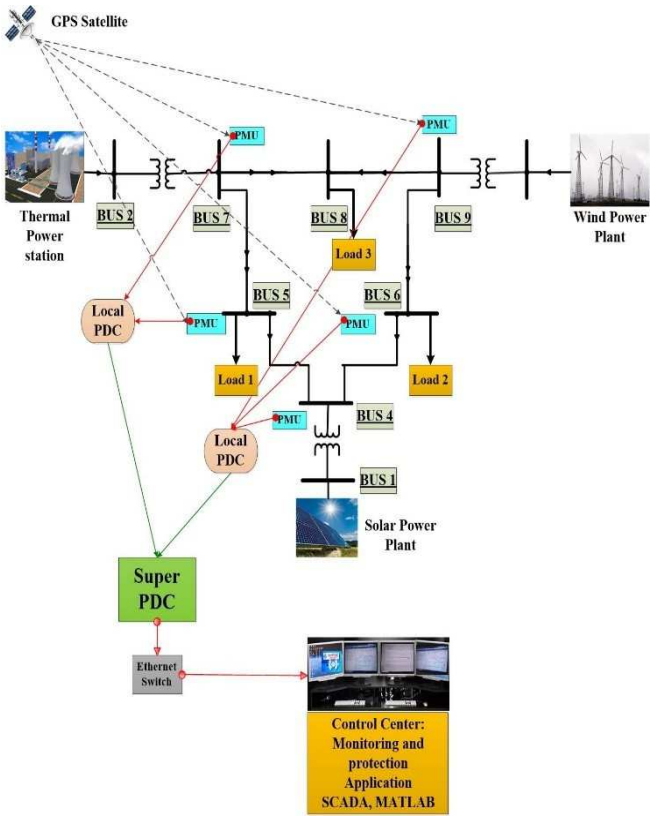

Fig. 1. Typical Architecture of PMUs and PDCs.

The standard for communication protocols are defined for real-time synchronized phasor measurement by IEEE standard C37.118.x.2011, and data exchange takes place between various connected PMUs, PDCs and other power applications. The 2005 version of communication protocol IEEE Standard involves both measurements of synchro phasor data and real-time transfer of synchronized data. The IEEE Standard C37.118-2005 was separated into two standards that accomplished the aforementioned tasks i.e., IEEE C37.118.1 2011 is defined for measurement and estimation of synchro phasor data between PMUs and connected power equipment, whereas IEEE C37.118.2-2011 is meant for synchro phasor data transfer between PMU and PDC [10][11], as shown in Fig 2.

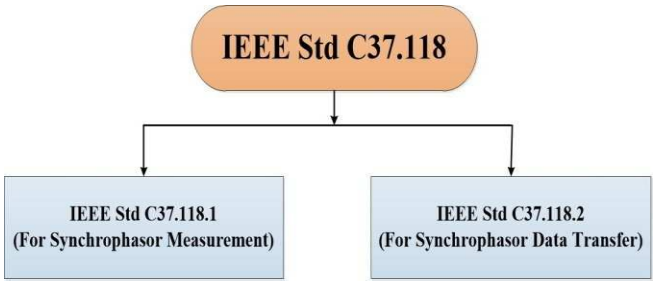

Fig. 2. Standard communication protocols.

The communication between PMU and PDC incorporates a set of four types of message types:
Data, Configuration, Header and Command.
The first three of these i.e., the data, configuration and header message types are transmitted from PMU and PDC serving as a data source, and the last message type i.e., the command is being received by the PMU from PDC.

Synchronized data from various connected local PDCs are connected to Super Phasor Data Concentrator (Super PDC) at control center through Ethernet switch. This concentrated data by Super PDC is sent for control, monitoring and protection applications. The synchronized data with time stamped from super PDC is also send to Historian Software to store data for future requirements purpose.

III. Laboratory Setup Architecture

A laboratory scale synchrophasor data transmission IT architecture has been developed on open source products. A setup consisting of a simulator for Power system, transmission of PMU data as per IEEE Standard through TCP/IP over Ethernet switch, Phasor Data Concentrator and an application software in MATLAB has been built with,

1. Student version of Power World Simulator (PWS).
2. Free version of Power World Dynamic Studio (PWDS).
3. Open source software Open PDC and PMU connection tester from Grid Protection Alliance.
4. Open source Parser software SADF from Delft University of Technology.

Authorized licensed use limited to: DELHI TECHNICAL UNIV. Downloaded on February 15,2021 at 09:55:51 UTC from IEEE Xplore. Restrictions apply.

5. Synchrophasor Application Tool (SAT), a MATLAB based add on application developed at Delhi Technological University.

The following steps give the procedure of setup in two desktop PCs:

Step 1: Power World simulator is an interactive offline simulation software for analysis of Power system. Fig. 3 shows the simulation of WSCC 9 buses, 3 generators system that has been simulated in Power World Simulator Software using data given in Annexure. The simulation was performed in first desktop PC.

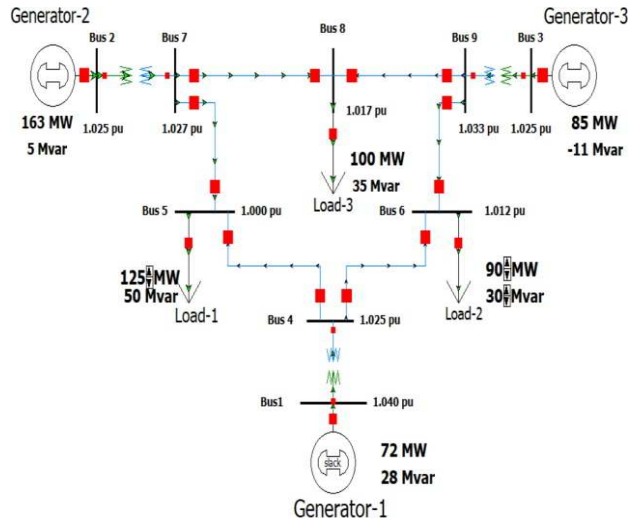

Fig. 3. WSCC 9 Bus, 3 Machine system in Power World Simulator software.

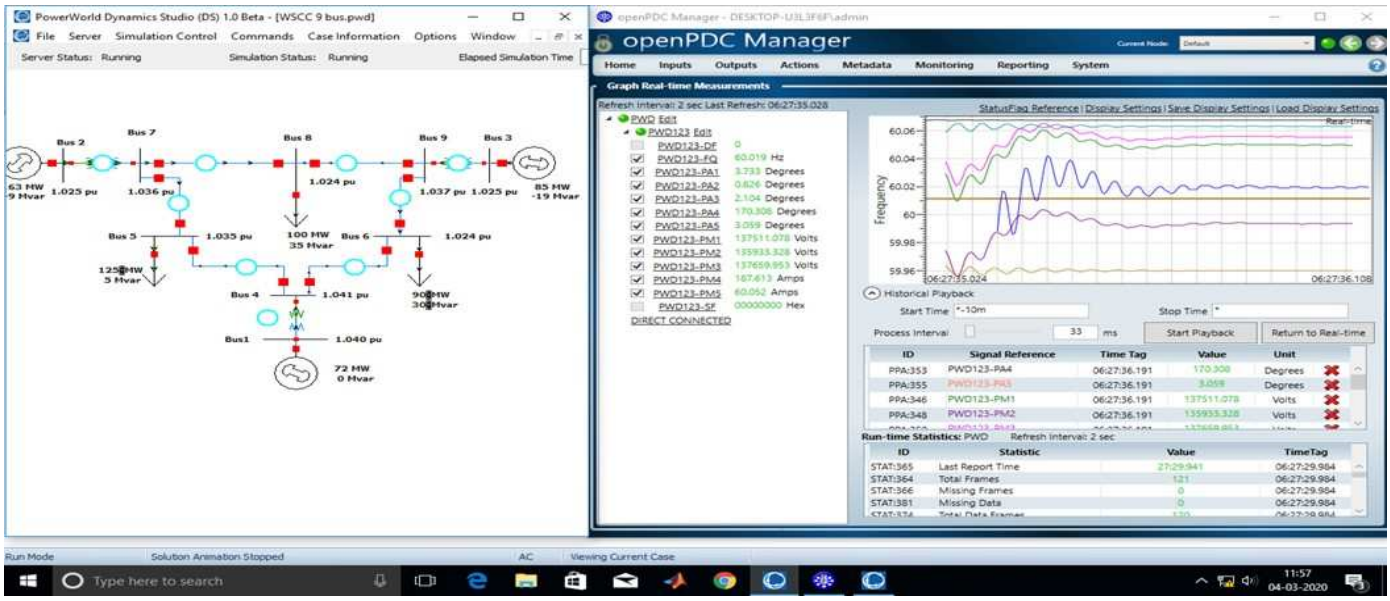

Fig. 4. Data transferred from Power World Simulator to Open PDC through Power World Dynamic Studio.

Step 2: To transfer the virtual PMU data from various substations in the simulation of step 1, Power World Dynamic Studio software was installed in desktop 1. This software was used to configure the data frame rate and PMU ID and IP address with port numbers for transmission of data as per IEEE standard C37.118.2.2011 as in Fig. 4. In this setup GPS clocks were not used for synchronization, instead local PC clock time was used.

Step 3: PMU Connection Tester software was used to test the live stream data from first desktop PC is being received or not, from the simulated power system. The open PDC software from Grid Protection Alliance, implements a number of standard phasor protocols which can be used to receive data from devices. In this paper, IEEE C37.118.2 (2011) protocol for synchro phasor measurement units has been used for communication between these interconnected systems. The Open PDC software, PMU connection tester and application software like MATLAB are installed on second desktop PC.

Step 4: Parser software is required for decoding the embedded values in the protocol for analysis of the power system data. The Synchrophasor Application framework (SADF) has been developed for use with MATLAB at Delft University. This developed tool helps to parse the voltage and current flow in the simulated IEEE 9Bus system. For this purpose, the open source software SADF was installed on second desktop PC. The IP address and port numbers were configured to receive the streaming data from the Open PDC in the same desktop PC.

Step 5: A new MATLAB add on application software SAT was developed at named Synchrophasor application tool which has user friendly graphical interface in comparison to SADF software. This application has been used to plot the voltage, current and calculated power at from different buses from the simulation of power system in Power World simulator. This software gives a virtual control room setup for monitoring various parameters of the grid in real time.

Authorized licensed use limited to: DELHI TECHNICAL UNIV. Downloaded on February 15,2021 at 09:55:51 UTC from IEEE Xplore. Restrictions apply.

The designed Synchrophasor application tool is available online at github/skmprohunt/Synchrophasor- Application-Tool. The front look of this application framework is shown in Fig. 5.

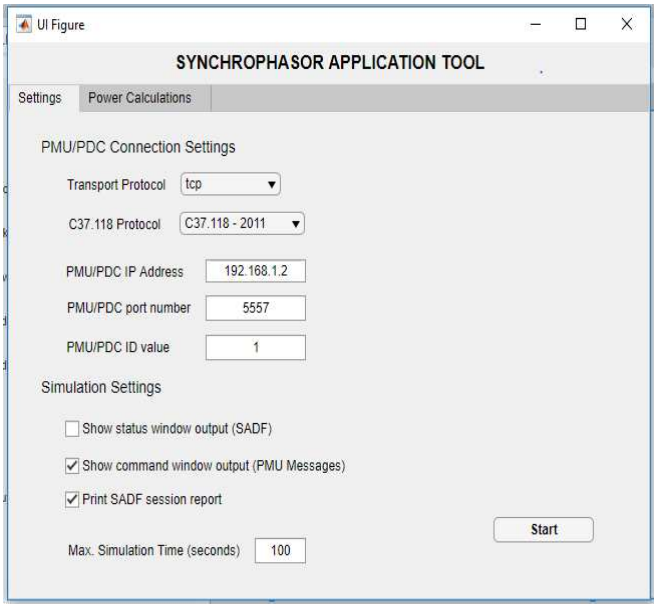

Fig. 5. Front page of Synchrophasor Application tool.

The overall schematic representation of the setup is given in Fig. 6. System I and System II are the two desktop PCs on which the open source software are installed.

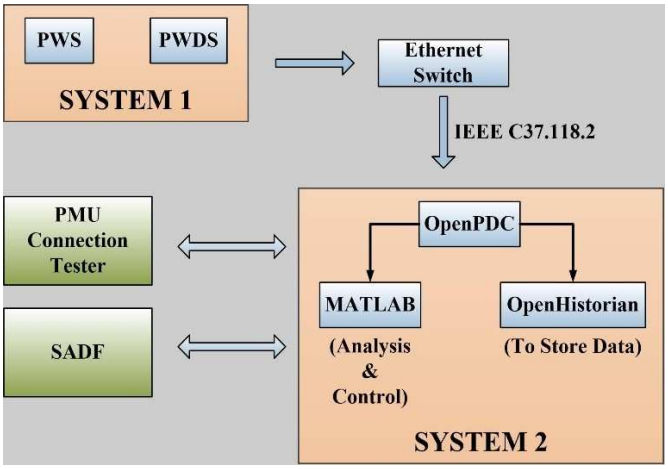

Fig. 6. Overall schematic representation.

IV. Simulation Results

In testing of setup, IEEE 3-machine 9-bus system has been simulated and it was assumed that all the three generator buses and transmission line buses have PMUs from which we can obtain synchronized measurement phasor data of voltage and current. Then, from received data the active power and reactive power was calculated to study the power flow in the designed system.

The setup developed was tested for two types of states in IEEE 9 bus Power system.

Steady state condition: A Load flow study was performed as off line simulation in PWS. Real time transfer of data to PDC was performed with PWDS. The active power flow of branch 7-8 and branch 9-8 has been monitored in SAT as shown in Fig. 7. From the load flow result it was observed that, power transfer from bus 7 to bus 8 was 78.845 MW and from bus 9 to bus 8 was 21.658 MW. Fig. 8 and Fig. 9 show the plot observed in SAP tool developed in real time.

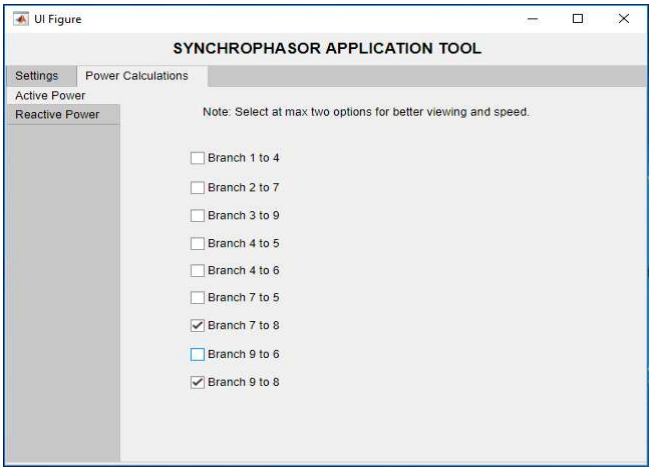

Fig. 7. Synchrophasor application tool branch selection page.

The selection of the relevant branch results in viewing of the data in real time in SAT. The constant line shows the steady power flow in the selected lines.

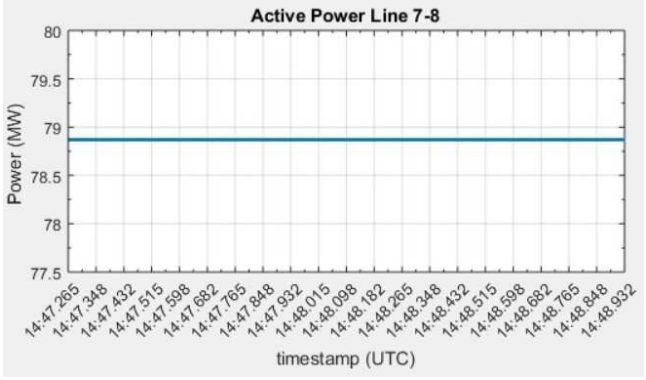

Fig. 8. Active power waveform of branch 7-8.

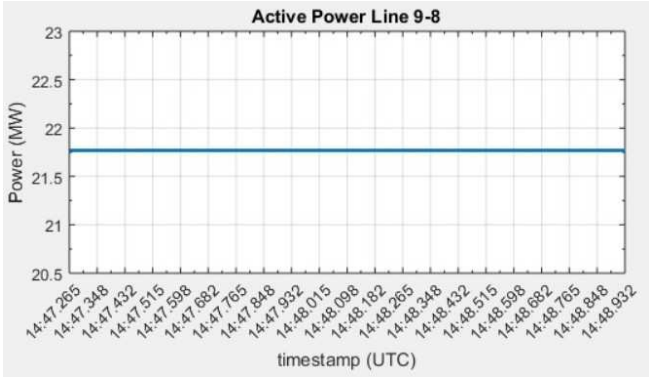

Fig. 9. Active Power waveform of branch 9-8.

Authorized licensed use limited to: DELHI TECHNICAL UNIV. Downloaded on February 15,2021 at 09:55:51 UTC from IEEE Xplore. Restrictions apply.

Before any fault being applied the constant power is obtained from both sides to supply the required load at bus 8 as in Fig. 10.

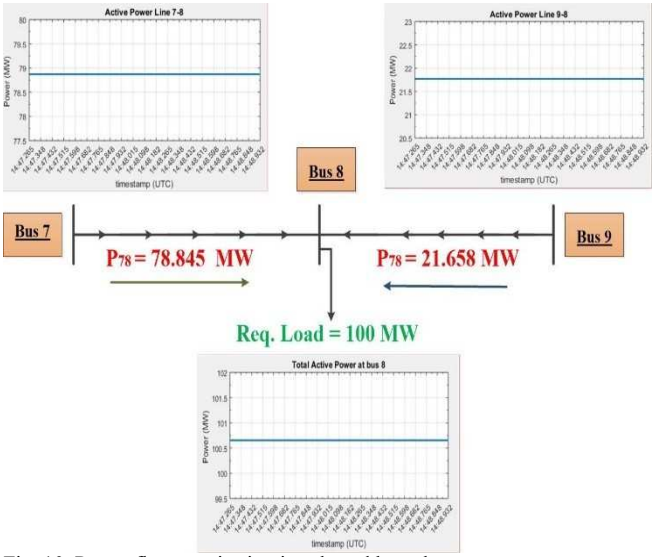

Fig. 10. Power flow monitoring in selected branches.

Transient condition: A three phase balanced fault has been applied in branch 4 to 5 at 20 sec and the fault was cleared after 0.1 sec at 20.10 sec. The resultant active power waveforms observed in the SAP are shown in Fig. 11 to Fig. 14.

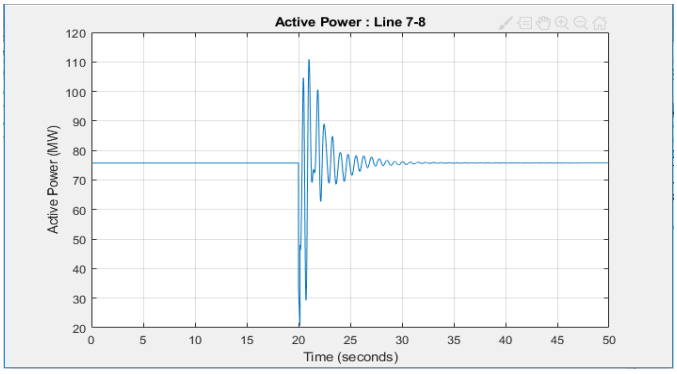

Fig. 11. Plot of transients in branch 7-8 in PWS.

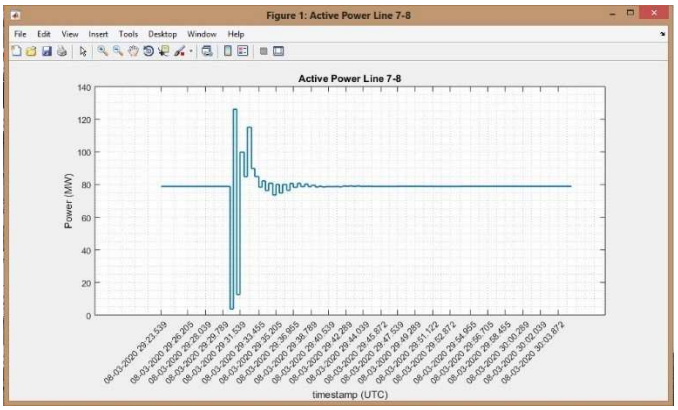

Fig. 12. Plot of transients in branch 7-8 in SAT.

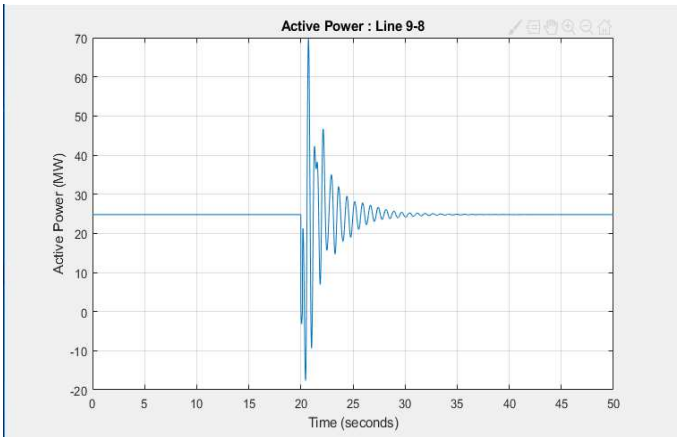

Fig. 13. Plot of transients in branch 9-8 in PWS.

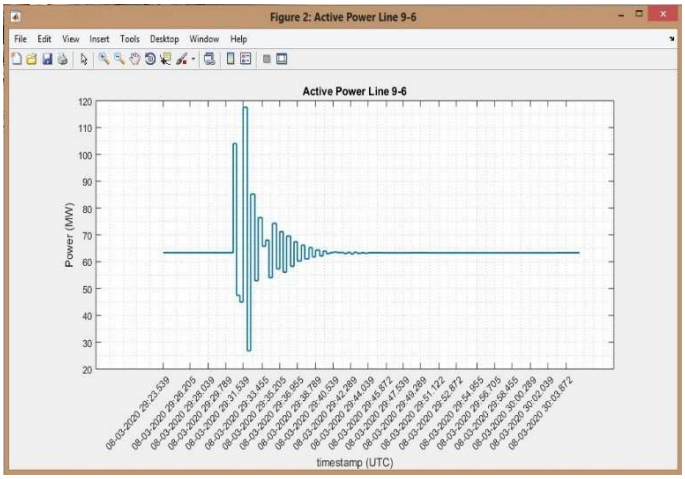

Fig. 14. Plot of transients in branch 9-6 in SAT.

V. CONCLUSION

In this paper we have developed the laboratory scale setup of PMU architecture for development of PMU applications in MATLAB platform. IEEE 9 Bus, 3 machine power system has been simulated in free version of commercial Power World Simulator and PMU data has been transferred to Open PDC from Power World Dynamic Studio. The data from PDC has been parsed with open source software and loaded in MATLAB workspace. For monitoring and analysis purpose a Synchrophasor application tool has been developed in MATLAB. This tool provides the calculation of active power and reactive power flow in the branches in real time. The developed tool has been tested for the resultant waveforms of active power flow for the selected branches. The response of a three phase fault applied and the changes in the active power flow has been observed. The developed setup can be replicated at educational institutions for power system education involving PMUs.

Authorized licensed use limited to: DELHI TECHNICAL UNIV. Downloaded on February 15,2021 at 09:55:51 UTC from IEEE Xplore. Restrictions apply.

VI. APPENDIX

The data used for simulation as shown below are in per unit values with base values as 100MVA base power, 230KV base voltage and 60Hz system frequency [8].

A. Basic Data of WSCC generating units

Parameters for the two-axis model of the synchronous machines are shown in Table I as follows. All values are given on the same system base MVA

TABLE I. RULES DATA OF GENERATING UNIT

Unit no.	H	X_d	X'_d	X_q	X'_q	T'_{do}	T'_{qo}
Gen1	23.64	0.1460	0.0608	0.0969	0.0969	8.96	0.310
Gen2	6.40	0.8958	0.1198	0.8645	0.1969	6.00	0.535
Gen3	3.01	1.3125	0.1813	1.2578	0.2500	5.89	0.600

B. Power and Voltage Set Points on each bus

Loads are modeled as a constant PQ load with parameters as shown in Table II.

TABLE II. DATA OF LOAD AND GENERATING UNIT POWER

Bus No.	Bus Type	Voltage (pu)	Load		Generator		
			MW	*MVAR*	*MW*	*MVAR*	*Unit No.*
1	Swing	1.040	0	0	-	-	Gen1
2	PV	1.025	0	0	163	-	Gen2
3	PV	1.025	0	0	85	-	Gen3
4	Transformer	-	0	0	0	0	-
5	PQ	-	125	50	0	0	-
6	PQ	-	90	30	0	0	-
7	Transformer	-	0	0	0	0	-
8	PQ	-	100	35	0	0	-
9	Transformer	-	0	0	0	0	-

C. Data of transmission lines

The transmission lines are modelled using equivalent pi model data are shown in Table III as follows.

TABLE III. DATA OF TRANSMISSION LINES

From Bus	*To Bus*	*R Resistance (pu)*	*X Reactance (pu)*	*B Susceptance (pu)*
1	4	0.0000	0.0576	0.0000
4	6	0.0008	0.0128	0.1342
6	9	0.0390	0.1700	0.3580
3	9	0.0000	0.0586	0.0000
9	8	0.0119	0.1008	0.2090
8	7	0.0085	0.0720	0.1490
7	2	0.0000	0.0625	0.0000
7	5	0.0320	0.1610	0.3060
4	5	0.0008	0.0128	0.1342

REFERENCES

[1] A.G. Phadke, and J. S. Thorp, "Synchronized Phasor Measurements and Their Applications," Springer, 2008.

[2] Monti, C. Muscas, and F. Ponci, "Phasor Measurement Units and Wide Area Monitoring Systems," Elsevier, 2016

[3] A. G. Phadke, J. S. Thorp, and M. G. Adamiak, "A New Measurement Technique for Tracking Voltage Phasors, Local System Frequency, and Rate of Change of Frequency," in IEEE Power Engineering Review, vol. PER-3, no. 5, pp. 23-23, May 1983, doi: 10.1109/MPER.1983.5519136.

[4] Reynaldo F. Nuqui, and Arunphadke, "Phasor measurement unit placement Technology for complete and incomplete observability", IEEE Transactons on power Delivery, Vol. 20, No. 4, October, 2005, pp 2381-2388.

[5] A. Mohemmed, R. Mickey, A. L. Akhila, and S. Ashok, "Open source implementation of IEEE C37.118-2011 protocol and serial communication interface for an FPGA based phasor measurement unit," 2017 2nd IEEE International Conference on Recent Trends in Electronics, Information & Communication Technology (RTEICT), Bangalore, 2017, pp. 308-313, doi: 10.1109/RTEICT.2017.8256606.

[6] Synchro-measurement Application Development Framework: an IEEE Standard C37.118.2-2011 Supported MATLAB Library, available github.com/matijanaglich/SADF_IEEE_C37.118.2-2011.

[7] PMU connection tester Grid Protection Alliance available at : github.com/GridProtectionAlliance/PMUConnectionTester

[8] Open PDC from Grid Protection Alliance available at:github.com/GridProtectionAlliance/openPDC.

[9] Power World Simulator free version available from powerworld glover overbye sarma site.

[10] IEEE Standard for Synchrophasor Measurements for Power Systems," in IEEE Std C37.118.1-2011 (Revision of IEEE Std C37.118-2005) , vol., no., pp.1-61, 28 Dec. 2011.

[11] IEEE Standard for Synchrophasor Data Transfer for Power Systems," in IEEE Std C37.118.2-2011 (Revision of IEEE Std C37.118-2005) , vol., no., pp.1-53, 28 Dec. 2011.

Authorized licensed use limited to: DELHI TECHNICAL UNIV. Downloaded on February 15,2021 at 09:55:51 UTC from IEEE Xplore. Restrictions apply.

Applied Physics B (2021) 127:39
https://doi.org/10.1007/s00340-021-07585-x

Applied Physics B
Lasers and Optics

A novel grayscale image encryption approach based on chaotic maps and image blocks

Ashish Girdhar[1] · Himani Kapur[2] · Vijay Kumar[3]

Received: 11 October 2020 / Accepted: 4 February 2021
© The Author(s), under exclusive licence to Springer-Verlag GmbH, DE part of Springer Nature 2021

Abstract
Image encryption converts a meaningful image into some random arrangement of pixel intensities. That means, the intelligible property of an image is destroyed. Taking into consideration excessively large time and space complexity required by the image encryption algorithm using multiple chaotic systems, this paper proposes an image encryption method in which employs three chaotic sequence to achieve fairly high level of encryption. Novelty of the proposed approach lies in the designed algorithm to achieve both permutation and substitution processes of image encryption. In the end, a comparison in the coefficient correlation values is drawn to evaluate the performance of the proposed algorithm with respect to many lately proposed image encryption schemes.

1 Introduction

To convey a message, an image is more helpful than text. Content of an image is easily understood by anybody present in any corner of the world. However, to convey some information using text, two pre-requisites are required. First, the receiver must be a literate person (images are understood by illiterates as well); second, sender and receiver must be well versed with at least one common language. Thus, image is generally preferred over text. However, advances of information technology have brought everyone on the planet on Internet. Which is why, images used in communication are vulnerable to attacks. One of the feasible solutions is cryptography. Cryptography converts a meaningful image into some random collection of pixel intensities (called encrypted image); making it look like some random noise. With only correct and precise keys, the encrypted image can be decrypted to give the original image back. Encrypted image reveals nothing to the intruders. For an additional layer of security, the encrypted image is added to naïve looking 2D or 3D image [25]. Encryption of plain image can be carried out in optical and digital domain. Optical encryption methods use fractional Fourier transform [26, 27], double random phase encoding [28], wavelength multiplexing [29] and other multiplexing methods [30, 31]. However, as pointed out in [28] some inherent weaknesses of optical methods inhibit their use in image encryption. The proposed image encryption uses digital methods to encrypt image and is based on two chaotic maps—Ikeda map and logistic map.

As reported in a recent survey on image encryption [1], in the 2018 only, about a thousand plus publications have been found related to the field of image encryption. Hence, area of image encryption has piqued the interests of researchers and is continuing to do so. While encrypted image can be sent directly over the communication channel, it can be hidden inside a cover media in an invisible manner [2]. A typical image encryption model consists of two stages—permutation and substitution as pointed out in [3] which is shown in Fig. 1. In the present paper, a novel image encryption algorithm is proposed which utilises two chaotic maps—Ikeda map and logistic chaotic map. Diffusion or substitution is carried out at pixel level while confusion is done at the pixel level while the confusion or permutation is done at the bit level.

The structure of the proposed paper is as follows. Chaotic maps and their advantages are discussed in Sect. 2. A brief review of related image encryption methods is presented in Sect. 3. The proposed algorithm is presented in detail in Sect. 4. Results obtained from simulation of proposed

✉ Ashish Girdhar
ashishgirdhar410@gmail.com

[1] CSED, Delhi Technological University, Delhi, India

[2] G.G.S.S.S., Kaithal, Haryana, India

[3] CSED, National Institute of Technology Hamirpur, Hamirpur, Himachal Pradesh, India

Published online: 24 February 2021

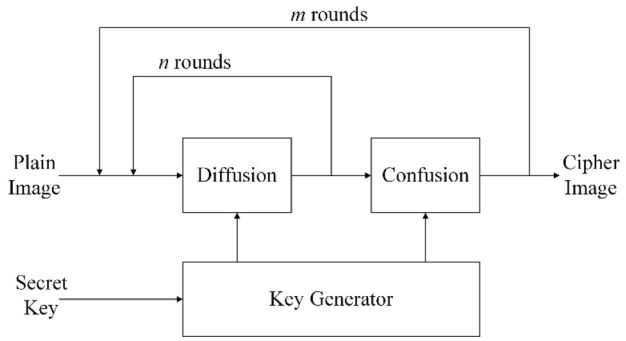

Fig. 1 Skeleton of a typical image encryption procedure

algorithm and comparisons with state of the art approaches is presented in detail in Sect. 5, followed by conclusion in Sect. 6.

2 Chaotic maps

Chaotic maps exhibit various favourable characteristics which make them suitable to be used in image encryption process. These characteristics are—pseudo-randomness, extreme sensitivity towards any change in initial conditions (or control parameters) and ergodicity. In the proposed paper, two chaotic maps are used.

2.1 Ikeda map

The original chaotic map was proposed by Kensuke Ikeda during his experiment [4]. Complex Ikeda map is defined in 2D space as follows:

$$x_{n+1} = 1 + \mu(x_n \cos t_n - y_n \sin t_n), \tag{1}$$

$$y_{n+1} = \mu(x_n \sin t_n - y_n \cos t_n), \tag{2}$$

$$t_n = 0.4 - \frac{6}{1 + x_n^2 + y_n^2}, \tag{3}$$

where μ is control parameter. 2D Ikeda map exhibits chaotic behaviour when $\mu \geq 0.6$. To obtain xy chaotic attractors of Ikeda map, $\mu = 0.9$ is chosen. Twenty starting points were taken and their trajectories were traced as shown in Fig. 2.

In this figure, as can be observed $x \in (-40, 35)$ and $y \in (-30, 30)$. To use Ikeda map for diffusion process of image encryption, these chaotic sequences were taken down to range (0,1).

2.2 Logistic chaotic map

Logistic chaotic map is the most popular chaotic map used in several image encryption algorithms. Mathematically, 1D logistic chaotic map is defined as follows:

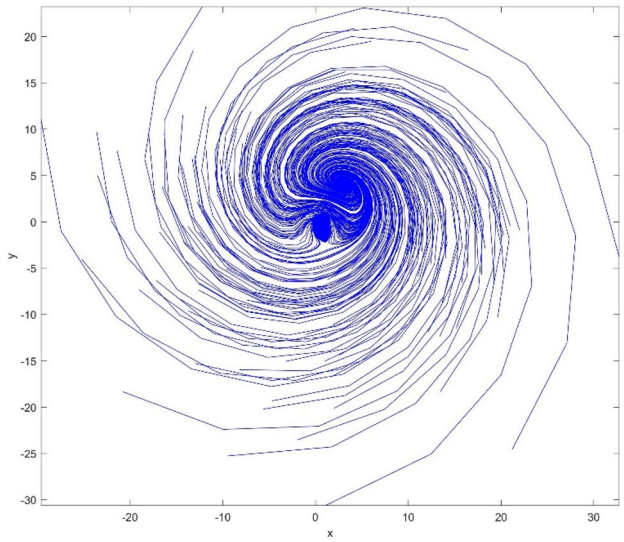

Fig. 2 Chaotic attractors of Ikeda map

$$x_{n+1} = \mu x_n (1 - x_n), \tag{4}$$

where μ is the control parameter. For $\mu > 3.569945$, the system goes into chaotic state [5]. Bifurcation diagram obtained by implementing 1D logistic map in Matlab has been shown in Fig. 3. As can be observed, for the specified range of μ, chaos is exhibited by the map.

Chaotic sequence obtained from 1D logistic map is used in the confusion or permutation process of the proposed image encryption algorithm. A brief review of the above two chaotic maps used in image encryption is presented in next section.

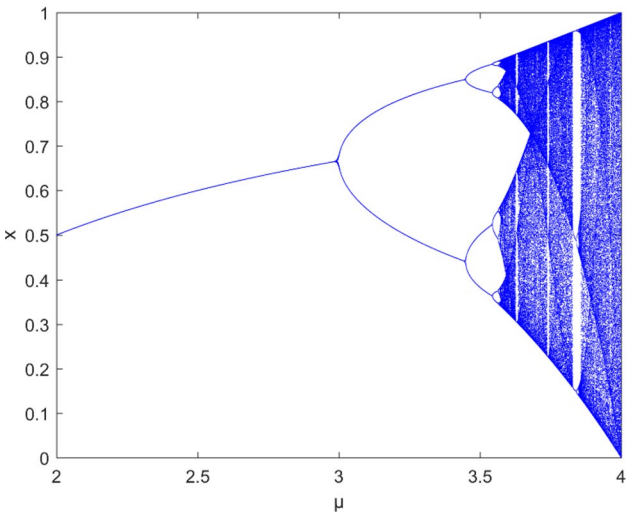

Fig. 3 Bifurcation diagram of logistic map obtained in Matlab

3 Related works

While logistic chaotic map is used in various image encryption techniques proposed so far in the literature; use of Ikeda map for construction of chaotic sequences in image encryption is limited to a very few image encryption algorithms [6]. Since the present work is for the image encryption of grayscale images using Ikeda map, literature review of grayscale image encryption schemes using Ikeda map is presented.

Jia [7] used only Ikeda map for both phases-pixel shuffling (using the sort indices) and pixel substitution. The results obtained from simulation of the algorithm were shown to be robust against the histogram analysis, correlation analysis and key sensitivity analysis. Zhu et al. [8] proposed a bit level permutation than a pixel level permutation. In their approach, Arnold cat map has been used for permutation and for diffusion, logistic map has been used. Mannai et al. [9] proposed discretised version of Ikeda system. Chaotic sequence obtained from discretised Ikeda map is XORed with the plain image pixels to obtain encrypted image. Alshibani et al. [10] used a mix of three Arnold transform, Henon map and Ikeda map for diffusion phase of grayscale images. In this paper, DNA encoding of pixels of plain image and masking key was done. Exclusive OR operation was performed between DNA sequences of plain image and that of masking key. Masking key was obtained using sort operation on the chaotic sequences of Henon map and Ikeda map. Parvees et al. [11] proposed colour image encryption algorithm using Ikeda map and logistic map. For each colour channel, separate chaotic sequences from Ikeda map and logistic map were generated. Şekertekin et al. [12] used Ikeda map for permutation and Henon map for diffusion. Becheikh et al. [13] used 1D Ikeda map and T-function for generation of a S-box which is used for grayscale image encryption. The proposed S-box was proved to have various essential properties such as bijectivity, bit independence criterion (BIC), nonlinearity, strict avalanche criterion (SAC), differential and linear approximation probability. Hikal et al. [14] proposed encryption scheme for palm print images. Since palm print images carry unique information of palm lines, shape, and texture of an individual; these are most reliable biometric authenticators. In addition, decryption process should be able to give back the exactly same plain image because a loss of even a pixel may cause the palm print matching mechanism to fail. The authors used a mix of three chaotic maps—Arnold's cat map (for confusion) and Ikeda map and enhanced Lorenz map for diffusion of pixels in confused (or permutated) image. Li et al. [15] obtained two chaotic sequences from Ikeda map and used one chaotic sequence for confusion phase and other for diffusion phase. In their approach, the authors proposed a novel approach for encrypting a Preview-Region-Image. The encrypted image and encrypted preview image are placed in Ciphered image. First, the encrypted Preview-Region-Image is decrypted and afterwards encrypted image. This is useful as it saves time in decrypting only the images of interest and not all encrypted images. A recent research by Girdhar et al. [16] applied XOR operations on chaotic sequences obtained from Lorenz and Rossler hyperchaotic system and colour image pixels and very nice results were obtained.

There are a few things that can be observed from this literature review:

- XOR operation on chaotic sequences and image pixel value results in encrypted image.
- Use of Ikeda map increases randomness in plain image.
- As pointed in the review, modification at bit level is preferred over the pixel level.

Keeping the above-mentioned points in mind, an image encryption algorithm is proposed in the next section.

4 Image encryption algorithm

A brief overview of the approach is shown in Fig. 4. A plain image is taken on which diffusion is done using chaotic sequence from Ikeda map and confusion is done using chaotic sequence from logistic map.

As the proposed image encryption process consists of two phases—diffusion and confusion, the encryption algorithm is explained in two parts—first diffusion process followed by confusion.

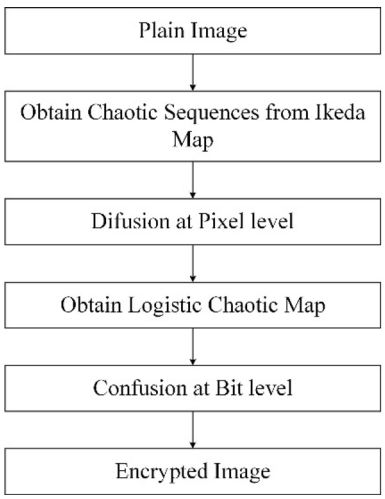

Fig. 4 Brief layout of image encryption algorithm

4.1 Diffusion process

1. Read plain image (I) of dimension ($M \times N = R$).
2. Divide I into two vertical halves—I_1 and I_2 each of size $M \times (N/2)$.
3. Next, obtain chaotic sequences from Ikeda map of size $R/2$.
4. To ensure that the chaotic sequences have unique value, algorithm in [17] is used. This results in two chaotic sequences—x, y which are unique with values lying in [1, $R/2$].
5. Reshape both x and y arrays to be of same dimension as that of I_1 and I_2.
6. Apply sort operation on x and y arrays in column wise direction and keep sort_indices in separate arrays as shown in Fig. 5. It is to be kept in mind that the unsorted x and y arrays will be used in the algorithm and sort operation is done to obtain the sort_indices of these two arrays.
7. Next, using sort_indices_y array, perform bitXOR operation on I_1 and x to obtain I_1'. This step is explained in Fig. 6.
8. Similarly, using sort_indices_x array, perform bitXOR operation on I_2 and y to obtain I_2'.
9. I_1' and I_2' are combined to form I'.
10. Now, I' is divided into two horizontal halves—I_3 and I_4 each of size $(M/2) \times N$.
11. Again, x and y arrays are reshaped to be same dimension as that of I_3 and I_4.
12. Apply sort operation on x and y arrays in row wise direction and keep sort_indices in separate arrays as shown in Fig. 7. Again, unsorted x and y arrays will be used in the algorithm and sort operation is done to obtain the sort_indices of these two arrays.
13. Now, using sort_indices_x, bitXOR is performed between I_3 and y arrays to obtain I_3'. This step is explained in Fig. 8.
14. Similarly, using sort_indices_y, I_4 and x arrays are bitXORed to give I_4'.
15. Afterwards, I_3' and I_4' are combined to give encrypted image after diffusion (EI_D). EI_D is then taken to the confusion phase.

4.2 Confusion process

Following steps are performed over the encrypted image after diffusion (EI_D) in this process.

1. All intensity levels of the plain image (I) are added to form S.
2. Next, S is divided by suitable power of 10 so that newly formed $S < 1$.
3. Add S to the initial value of logistic chaotic map so that a unique chaotic sequence is generated for every plain image.

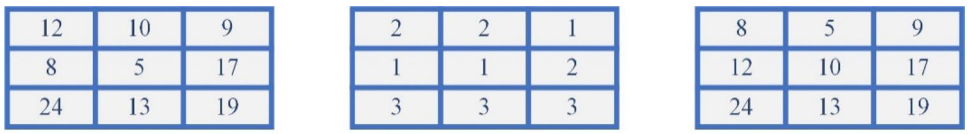

Fig. 5 Sort **a** y array in vertical direction to obtain **b** sort_indices_y array and **c** sorted_y array

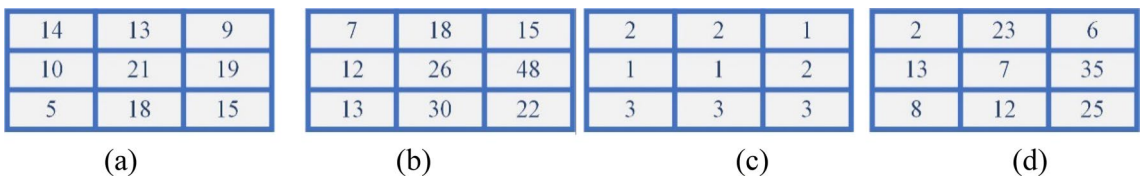

Fig. 6 BitXOR operation on **a** I_1 and **b** x using **c** sort_indices_y to obtain **d** I_1'

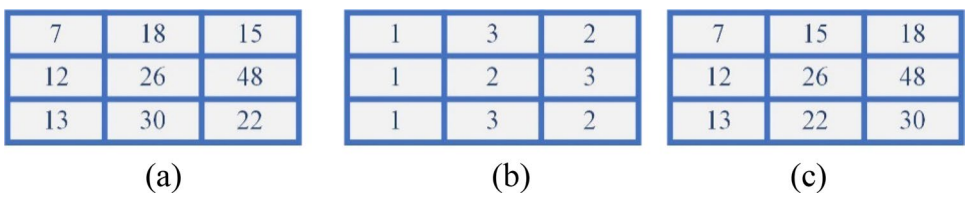

Fig. 7 Sort **a** x array in horizontal direction to obtain **b** sort_indices_x array and **c** sorted_x array

24	31	15
8	14	10
16	29	5

(a)

12	10	9
8	5	17
24	13	19

(b)

1	3	2
1	2	3
1	3	2

(c)

20	22	5
0	11	27
8	14	8

(d)

Fig. 8 bitXOR operation on **a** I_3 and **b** y using **c** sort_indices_x to obtain **d** I_3'

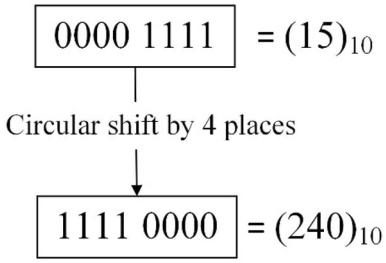

Fig. 9 Right circular shift by four places changes pixel intensity from $(15)_{10}$ to $(240)_{10}$

4. Apply modulo-by-8 operation on the chaotic sequence generated from the above written step, resulting in a chaotic sequence from the range [0, 7].
5. Pixel value from EI_D is read and converted to binary bits in a 8-bit representation.
6. Read a value from chaotic sequence and perform right circular shift on the binary bit representation. This is the permutation step and it not only permutes the binary bits of a pixel but also changes the pixel value. An example of this step is shown in Fig. 9 where a pixel value of $(15)_{10}$ is converted to $(240)_{10}$, considering value = 4.
7. Repeat the entire process of all pixel intensities in the EI_D.
8. Afterwards, convert all binary bit representations to decimal intensities to receive the final encrypted image.

The entire process of the confusion process is summarised in Fig. 10.

To decrypt the encrypted image, exact secret key is to be used and the entire process of encryption is to repeated, but in reverse order. This implies that, first confusion process is done on the encrypted image. During the confusion phase, first decimal valued intensities are converted to the binary bit representations of 8 bits. Exact same chaotic sequence is generated using the same initial conditions. Perform right circular shift on the binary bit representations to get EI_D. Next, diffusion process is repeated with steps performed in reverse order to get decrypted image which is exactly same to I.

5 Results obtained from simulation

The proposed algorithm was implemented in Matlab and run on a i7 processor with an 8-GB RAM. Table 1 shows plain, encrypted and decrypted images. As can be observed in the table, encrypted image is seemingly a random image and does not reveal anything.

5.1 Key space and key sensitivity

As the proposed image encryption uses two secret keys for Ikeda map generation and one for logistic map generation, each having precision up to 10^{-15} decimal places, 10^{45} ($=10^{15}\times10^{15}\times10^{15}$) brute force attacks would be required to break the system. Large key space ensues safety from brute force attackers. Next, key sensitivity can be ensured by decrypting encrypted image with a slightly modified key. If the decryption process fails to decrypt the encrypted image, then sensitivity of secret key is realised (Fig. 11).

5.2 Statistical analysis

Encrypted images are attacked by statistical analysers to extract information about it. Statistical information about encrypted image is extracted to examine if a seemingly noisy image is carrying any meaningful message or not. This is done by obtaining histogram of the encrypted image and drawing correlations among the pixels.

5.2.1 Histogram analysis

Histogram drawn for a true random image would have absolutely uniform histogram bars [16] because frequency of all pixel intensities is equal. An ideal histogram is shown in Fig. 12 where height of pixel intensities is exactly same.

Histogram for both plain image of baboon and respective encrypted image was obtained as shown in Fig. 13. Uniformity in histogram of encrypted image of baboon can be observed from the figure.

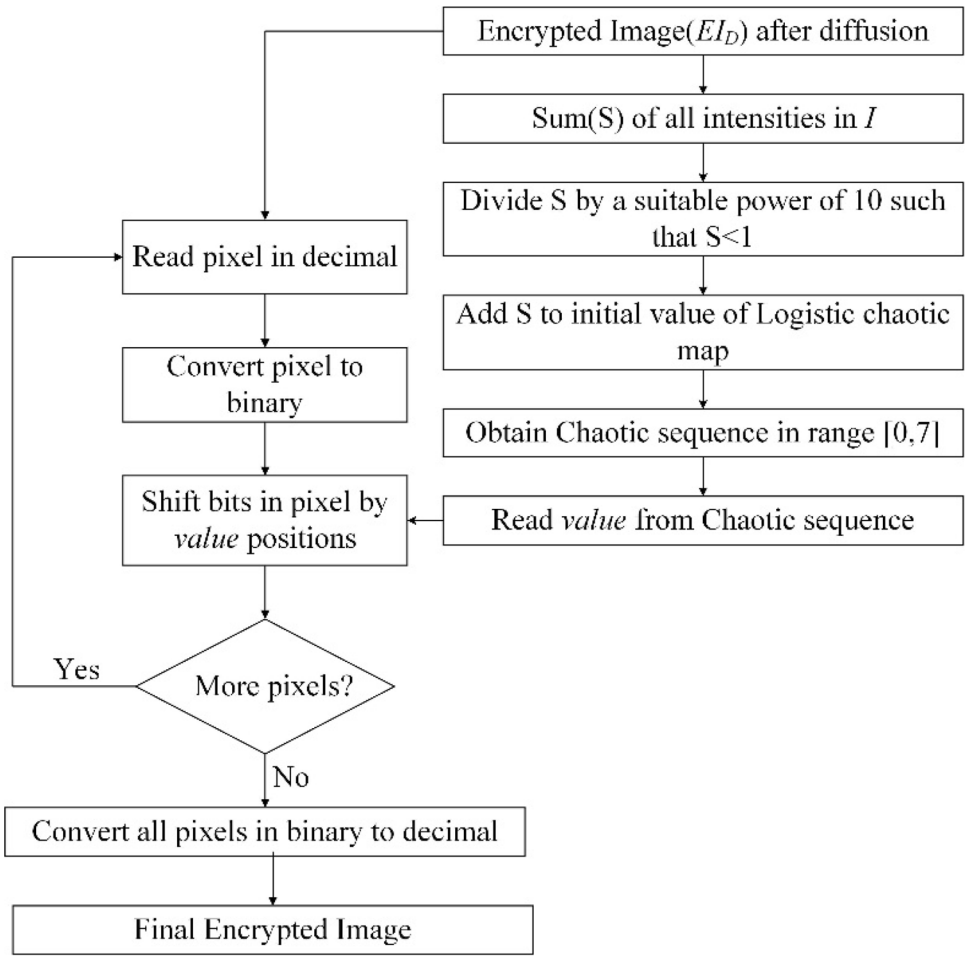

Fig. 10 Confusion process of the proposed approach

5.2.2 Correlation analysis

In a plain image, correlations among adjacent pixels in vertical, horizontal and diagonal directions exist in such a way that the correlation coefficient ≈ 1. However, the encryption algorithm should be able to destroy the correlations among pixels in all three directions. Calculation of correlation coefficient is done using formula mentioned in [16]. Correlation coefficient between neighbouring pixels in horizontal direction x and y is calculated as follows:

$$E(x) = \frac{1}{T}\sum_{i=1}^{T} x_i, \tag{5}$$

where $E(x)$ is the mean value of pixel intensities of total number of pixels which are selected randomly from image.

After finding $E(x)$, deviation from mean value and covariance is calculated using the following formula:

$$D_x = \frac{1}{T}\sum_{i=1}^{T} (x_i - E(x))^2, \tag{6}$$

$$\operatorname{cov}(x,y) = \frac{1}{T}\sum_{i=1}^{T} \big(x_i - E(x)\big)\big(y_i - E(y)\big), \tag{7}$$

Using deviation and covariance values, correlation coefficient is calculated as follows:

$$r_{xy} = \frac{\operatorname{cov}(x,y)}{\sqrt{D_x}\sqrt{D_y}}. \tag{8}$$

Table 2 was obtained for correlation coefficient among pixels of both plain image and encrypted image in horizontal, vertical and diagonal directions for 3000 pixels chosen randomly.

It can be observed from this table that the correlations among neighbouring pixels in horizontal vertical and diagonal directions have been destroyed. Hence, significant descent in correlation coefficient values in encrypted images (Fig. 14).

It is evident from the figure, that pixels are very closely related in plain image of Baboon in horizontal, vertical and diagonal direction. However, pixel intensities are sparsely located from one another in the encrypted image.

Table 1 Plain, encrypted and decrypted images

Plain Image	Encrypted Image	Decrypted Image
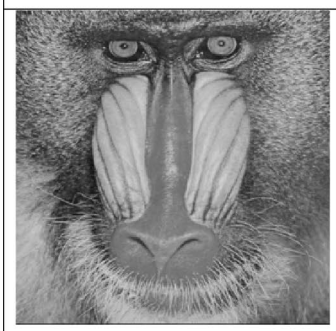	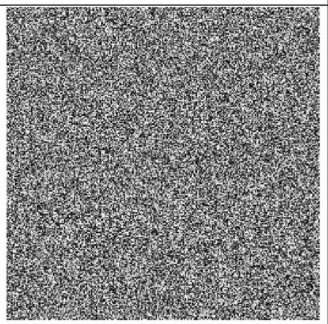	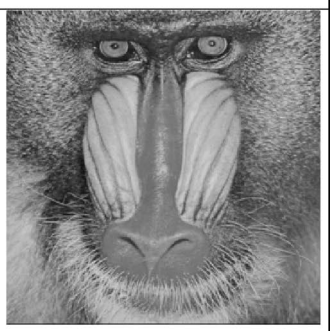
	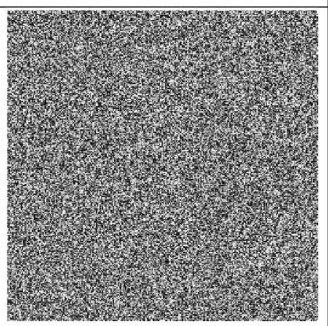	
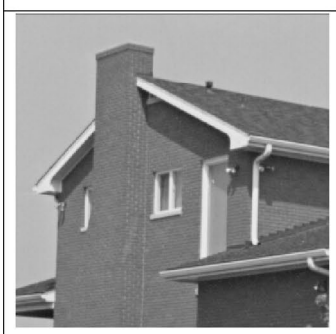	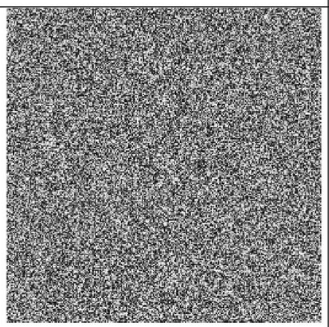	
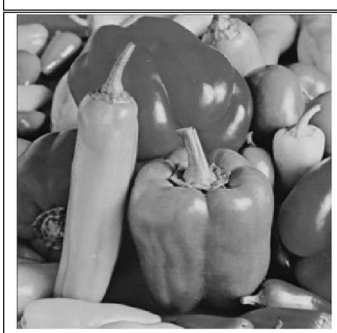	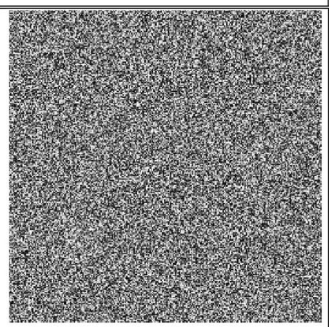	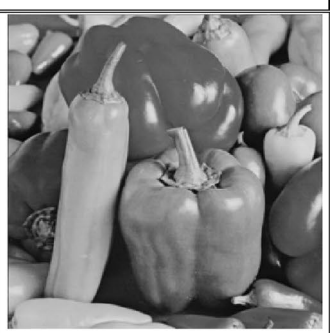
	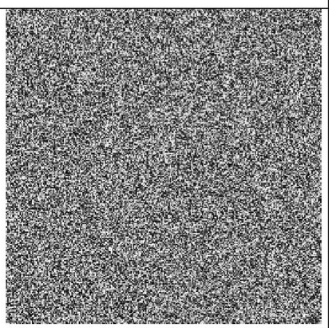	

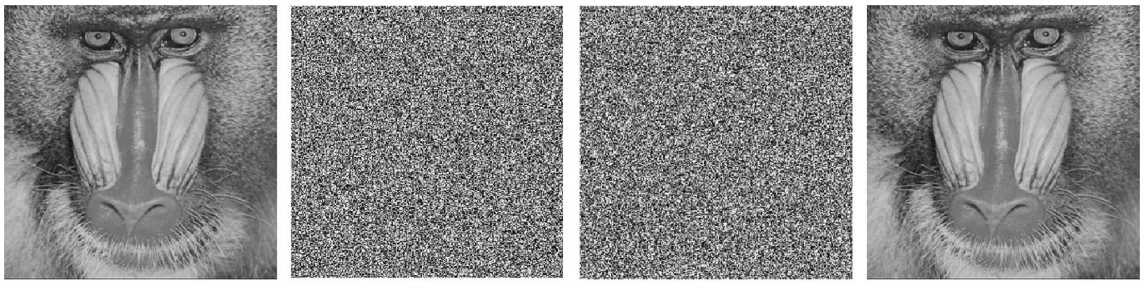

Fig. 11 **a** Plain image, **b** encrypted image, decrypted image using **c** wrong key and **d** right key

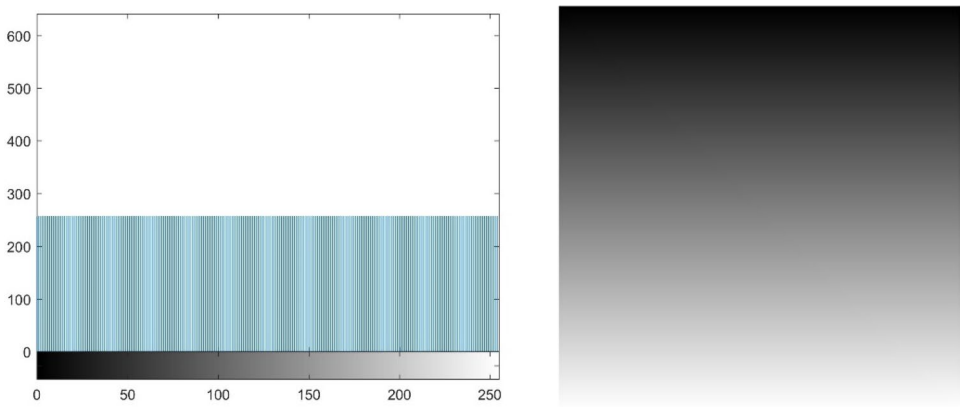

Fig. 12 Uniform histogram bars (**a**) obtained for a truly random image (**b**)

Thus, correlations of plain image are destroyed completely by the proposed encryption algorithm.

A comparison with some recent research works in the area of image encryption is shown in Table 3. As can be observed that the encrypted images obtained from proposed image encryption algorithm is able to reduce the correlations among pixels in the best manner. This is because confusion process of the proposed image encryption algorithm works at the bit level. Whereas, all the image encryption algorithms against which comparison is being done, do not perform any operation at bit level. Thus, it can be deduced that operations carried out at bit level encrypt image in a much better way.

5.3 Differential attack analysis

Differential attack analysis is conducted by attackers to establish a relationship between plain image and encrypted image. To determine potency of encryption algorithm to withstand this attack, two parameters—number of pixels change rate (NPCR) and unified average changing intensity (UACI) are determined. Evaluation of NPCR and UACI is done using two encrypted images. A pixel is chosen at random in plain image and changed to form a new plain image. Then, both plain image and new plain image are encrypted to receive two encrypted images E_1 and E_2. Using following formulae and E_1 and E_2, value of NPCR and UACI is determined [18] and mentioned in Table 4:

$$D(i,j) = \begin{cases} 0 \text{ if } E_1(i,j) = E_2(i,j) \\ 1 \text{ otherwise} \end{cases}, \tag{9}$$

$$\text{NPCR} = \frac{\sum_{i=1}^{N}\sum_{j=1}^{M} D(i,j)}{N \times M} \times 100, \tag{10}$$

$$\text{UACI} = \frac{\sum_{i=1}^{N}\sum_{j=1}^{M} \frac{E_1(i,j)-E_2(i,j)}{255}}{N \times M}. \tag{11}$$

5.4 Information entropy analysis

Information entropy is a measure of randomness in a system. Higher value of information entropy of a system, higher is the randomness or disturbance in the system.

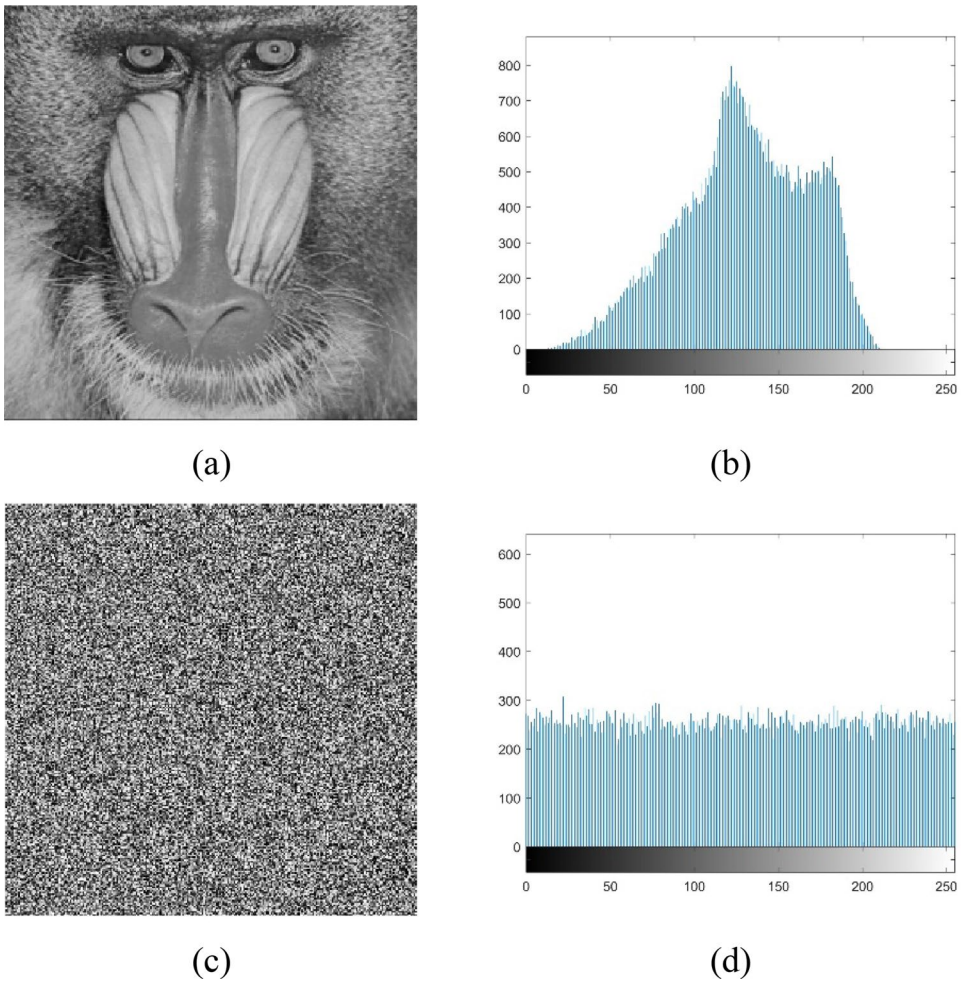

Fig. 13 Histogram of plain image (**a**) in (**b**); encrypted image (**c**) in (**d**)

Table 2 Correlation coefficient of neighbouring pixels in horizontal, vertical and diagonal directions

Image name	Horizontal	Vertical	Diagonal
Plain Baboon	0.874	0.826	0.784
Encrypted Baboon	−0.003	−0.009	0.0005
Plain marbles	0.978	0.982	0.965
Encrypted marbles	0.001	0.008	0.004
Plain hut	0.978	0.953	0.936
Encrypted hut	0.001	−0.007	0.002
Plain peppers	0.963	0.970	0.936
Encrypted peppers	−0.002	0.0001	−0.001
Plain boat	0.958	0.956	0.928
Encrypted boat	−0.0002	0.00007	0.004

Information entropy of an image is calculated using the following formula [19]:

$$H(m) = \sum_{i=0}^{2^n-1} p(m_i)\log_2 \frac{1}{p(m_i)}. \quad (12)$$

where $p(m_i)$ is probability of appearance of m_i in image and n represents different grey planes. Since a grayscale image contains eight planes, the maximum value of entropy of using formula stated above comes out to be 8. Hence, as close to 8, entropy of an image is, as close to being random the image is. Table 5 lists information entropy values of plain and encrypted images. It can be seen from the table that the information entropy of the images has increased as a result of the encryption algorithm.

5.5 Encryption speed

Speed is another parameter to determine the potency of an image encryption algorithm. Since speed of a procedure is highly dependent on hardware on which it is implemented, a point-to-point comparison cannot be made. Nevertheless, encryption times (in terms of ms) as put up by some research works are taken and compared with the proposed algorithm as jotted down in Table 6. Speed of the proposed algorithm is measured in Matlab using commands tic and toc.

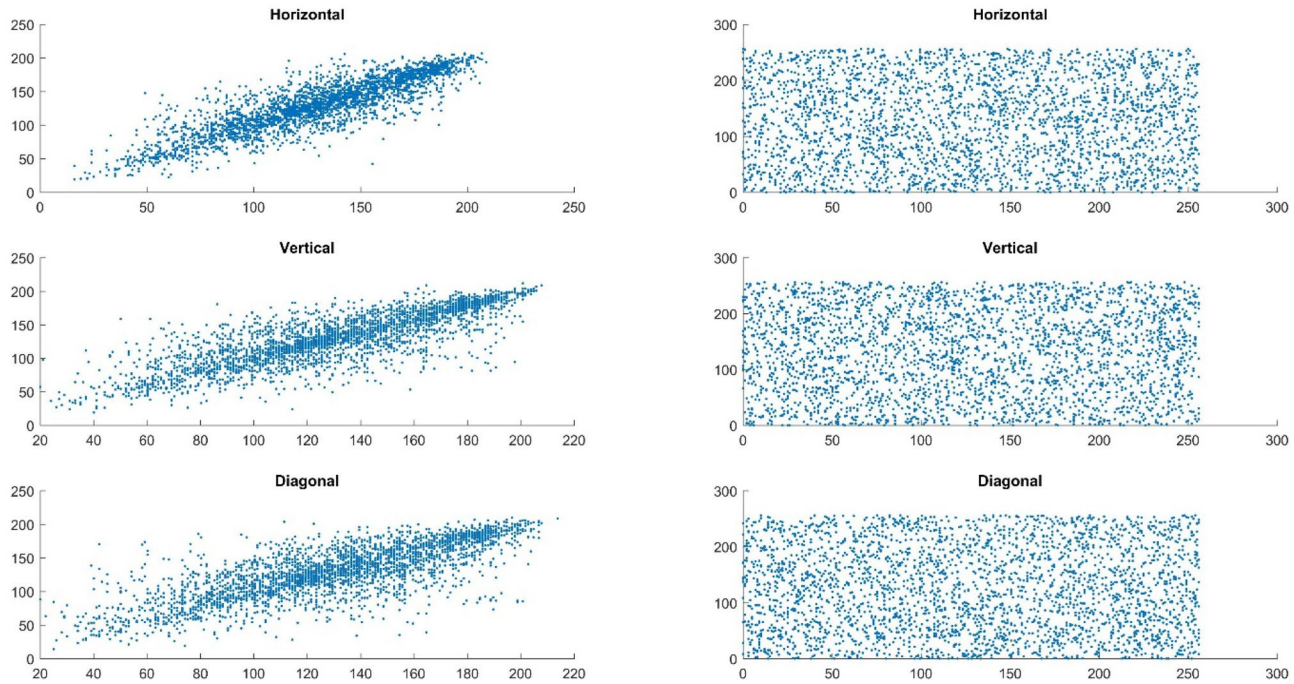

Fig. 14 Correlation coefficient plots for plain (on left) and encrypted image (on right) of Baboon

Table 3 Comparison in terms of correlation coefficient with some recent works

Direction	Proposed work	[20]	[21]	[22]	[23]	[24]
Vertical	0.0000718	−0.0568	−0.0130	0.0305	0.0034	0.000697
Horizontal	−0.00022	0.0456	0.0096	−0.0432	−0.0024	−0.00031
Diagonal	0.000597	−0.0202	−0.0132	0.0275	0.0030	−0.00022

Table 4 NPCR and UACI values for encrypted images of respective plain images

Image name	Parameter	Value
Baboon	NPCR	99.609
	UACI	33.463
Marbles	NPCR	99.737
	UACI	33.434
Hut	NPCR	99.655
	UACI	33.438
Peppers	NPCR	99.587
	UACI	33.762
Boat	NPCR	99.671
	UACI	33.482

As can be observed, the proposed image encryption takes suitably less time in encrypting a plain image as compared to other research works.

Table 5 Information entropy of plain and encrypted images

Image name	Plain	Encrypted
Baboon	7.229	7.998
Marbles	5.728	7.998
Hut	6.496	7.997
Peppers	7.580	7.997
Boat	7.457	7.997

6 Conclusion

The proposed image encryption algorithm encrypts a given plain grayscale image using Ikeda map at pixel level and logistic map at bit level. Encrypted image is obtained by applying bitXOR operations on horizontal and vertical halves of the plain image and the applying circular shift operations bitwise on all pixel intensities of confused image. The proposed image encryption algorithm has been simulated and the results are evaluated under differential, statistical and brute force attacks. Comparison with some

Table 6 Comparison in terms of encryption speed (in ms)

Proposed work	[20]	[21]	[32]	[33]	[34]	[35]
405.85	727.40	392	1184	3284	150	2837

recent works of grayscale image encryption algorithms is also presented. The novelty of the proposed work lies in the manner in which encryption algorithm is applied. Only two chaotic sequences are used for producing such promising results. Blocking and halving is not new, however, unequal halving has not been done prior to the best knowledge of the authors. Introducing more and more chaotic sequences increases both time and space complexity. Hence, this novel grayscale algorithm is the need of the hour and will entice the audience and readers to create efficient and less complex (in terms of time and space) grayscale image encryption algorithm.

References

1. C. Li, Y. Zhang, E.Y. Xie, When an attacker meets a cipher-image in 2018: a year in review. J. Inf. Secur. Appl. **48**, 102361 (2019)
2. A. Girdhar, V. Kumar, Comprehensive survey of 3D image steganography techniques. IET Image Proc. **12**(1), 1–10 (2018)
3. Y. Wang, K.-W. Wong, X. Liao, G. Chen, A new chaos-based fast image encryption algorithm. Appl. Soft Comput. **11**(1), 514–522 (2011)
4. K. Ikeda, Multiple-valued stationary state and its instability of the transmitted light by a ring cavity system. Opt. Commun. **30**(2), 257–261 (1979)
5. L. Liu, Q. Zhang, X. Wei, A RGB image encryption algorithm based on DNA encoding and chaos map. Comput. Electr. Eng. **38**(5), 1240–1248 (2012)
6. P.R. Sankpal, P.A. Vijaya, Image encryption using chaotic maps: a survey. 2014 Fifth international conference on signal and image processing (2014)
7. X. Jia, Image encryption using the Ikeda map. 2010 International conference on intelligent computing and cognitive informatics (2010)
8. Z.-L. Zhu, W. Zhang, K.-W. Wong, H. Yu, A chaos-based symmetric image encryption scheme using a bit-level permutation. Inf. Sci. **181**(6), 1171–1186 (2011)
9. O. Mannai, R. Bechikh, H. Hermassi, R. Rhouma, S. Belghith, A new image encryption scheme based on a simple first-order time-delay system with appropriate nonlinearity. Nonlinear Dyn. **82**(1–2), 107–117 (2015)
10. D.R. Alshibani, S.A. Qassir, Image enciphering based on DNA exclusive-OR operation union with chaotic maps. 2016 Al-Sadeq international conference on multidisciplinary in IT and communication science and applications (AIC-MITCSA) (2016)
11. M.M. Parvees, J.A. Samath, I.K. Raj, B.P. Bose, A colour byte scrambling technique for efficient image encryption based on combined chaotic map: image encryption using combined chaotic map. 2016 International conference on electrical, electronics, and optimization techniques (ICEEOT) (2016)
12. Y. Sekertekin, O. Atan, An image encryption algorithm using Ikeda and Henon chaotic maps. 2016 24th Telecommunications forum (TELFOR) (2016)
13. R. Becheikh, O. Mannai, R. Rhouma, S. Belghith, A novel family of strong S-Box based on Ikeda map and T-function. 2017 IEEE/ACS 14th international conference on computer systems and applications (AICCSA) (2017)
14. N.A. Hikal, M.M. Eid, A new approach for palmprint image encryption based on hybrid chaotic maps. J. King Saud Univ. Comput. Inf. Sci. **32**(7), 870–882 (2018)
15. C. Li, G. Luo, C. Li, A novel scheme for the preview of the image encryption based on chaotic Ikeda map. Int. J. Netw. Secur. **20**(6), 1105–1114 (2018)
16. A. Girdhar, V. Kumar, A RGB image encryption technique using Lorenz and Rossler chaotic system on DNA sequences. Multimed. Tools Appl. **77**(20), 27017–27039 (2018)
17. A.C. Dăscălescu, R.E. Boriga, A novel fast chaos-based algorithm for generating random permutations with high shift factor suitable for image scrambling. Nonlinear Dyn. **74**(1–2), 307–318 (2013)
18. Y. Wu, J.P. Noonan, S. Agaian, NPCR and UACI randomness tests for image encryption. Cyber J. Multidiscip. J. Sci. Technol. J. Sel. Areas Telecommun. **1**(2), 31–38 (2011)
19. M.B. Farah, R. Guesmi, A. Kachouri, M. Samet, A novel chaos based optical image encryption using fractional Fourier transform and DNA sequence operation. Opt. Laser Technol. **121**, 105777 (2020)
20. S. Somaraj, M.A. Hussain, Performance and security analysis for image encryption using key image. Indian J. Sci. Technol. **8**(35), 1–4 (2015)
21. Y. Suryanto, M.T. Suryadi, K. Ramli, A secure and robust image encryption based on chaotic permutation multiple circular shrinking and expanding. J. Inf. Hiding Multimed. Signal Process. **7**(4), 697–713 (2016)
22. G.A. Sathish kumar, K.B. Bagan, N. Sriraam, Image encryption based on diffusion and multiple chaotic maps. Int. J. Netw. Secur. Appl. **3**(2), 181–194 (2011)
23. J.D.D. Nkapkop, J.Y. Effa, J.S.A.E. Fouda, M. Alidou, L. Bitjoka, M. Borda, A fast image encryption algorithm based on chaotic maps and the linear diophantine equation. Comput. Sci. Appl. **1**(4), 232–243 (2014)
24. S.F. Yousif, Grayscale image confusion and diffusion based on multiple chaotic maps. 2018 1st International scientific conference of engineering sciences - 3rd scientific conference of engineering science (ISCES) (2018)
25. A. Girdhar, V. Kumar, A reversible and affine invariant 3D data hiding technique based on difference shifting and logistic map. J. Ambient Intell. Humaniz. Comput. **10**(12), 4947–4961 (2019)
26. P. Refregier, B. Javidi, Optical image encryption based on input plane and Fourier plane random encoding. Opt. Lett. **20**(7), 767–769 (1995)
27. M.A. Mohamed, A.S. Samarah, M.I. Fath Allah, Optical encryption techniques: an overview. Int. J. Comput. Sci. Issues IJCSI **11**(2), 125–129 (2014)
28. A. Alfalou, C. Brosseau, Optical image compression and encryption methods. Adv. Opt. Photon. **1**(3), 589–636 (2009)
29. G. Situ, J. Zhang, Multiple-image encryption by wavelength multiplexing. Opt. Lett. **30**(11), 1306–1308 (2005)

30. J.F. Barrera, R. Henao, M. Tebaldi, R. Torroba, N. Bolognini, Multiplexing encryption-decryption via lateral shifting of a random phase mask. Opt. Commun. **259**(2), 532–536 (2006)
31. J.F. Barrera, R. Henao, M. Tebaldi, R. Torroba, N. Bolognini, Multiplexing encrypted data by using polarized light. Opt. Commun. **260**(1), 109–112 (2006)
32. P. Ping, F. Xu, Z.J. Wang, Image encryption based on non-affine and balanced cellular automata. Signal Process. **105**, 419–429 (2014)
33. R. Enayatifar, A.H. Abdullah, I.F. Isnin, Chaos-based image encryption using a hybrid genetic algorithm and a DNA sequence. Opt. Lasers Eng. **56**, 83–93 (2014)
34. G. Ye, K.-W. Wong, An efficient chaotic image encryption algorithm based on a generalized Arnold map. Nonlinear Dyn. **69**, 2079–2087 (2012)
35. X. Wang, C. Jin, Image encryption using Game of Life permutation and PWLCM chaotic system. Opt. Commun. **285**, 412–417 (2012)

Publisher's Note Springer Nature remains neutral with regard to jurisdictional claims in published maps and institutional affiliations.

Analysis of AI Techniques for Maximum Power Point Tracking Under Partial Shading Conditions

Shagun Chaudhary
Department of Electrical Engineering
Delhi Technological University
Delhi, India
shagun.chaudhary43@gmail.com

Alka Singh
Department of Electrical Engineering
Delhi Technological University
Delhi, India
alkasingh.eed@gmail.com

2020 IEEE 17th India Council International Conference (INDICON) | 978-1-7281-6916-3/20/$31.00 ©2020 IEEE | DOI: 10.1109/INDICON49873.2020.9342154

***Abstract*— With the increasing injection of renewables into the grid, PV has gained extensive attention. Multiple MPPT techniques have been and are being currently developed for an efficient tracking of the Maximum Power Point (MPP). The conventional tracking techniques do not work satisfactorily under the partial shading conditions and this has led to the use of artificial intelligence (AI) based techniques. These techniques guarantee a better response and a reduced deviation than the former. In this paper a comparative analysis is performed on Fuzzy Logic, Artificial Neural Network (ANN) and Adaptive Neuro Fuzzy Inference System (ANFIS) based control techniques. AI based controllers can track the MPP with a desirable amount of accuracy under randomly varying irradiance conditions. The performance of compared techniques has been verified with the help of simulations for multiple test cases, the simulated results confirm that ANFIS based controller outperforms the FLC and ANN based controllers.**

Keywords*— *Photovoltaic (PV), Partial Shading, MPPT, Fuzzy Logic Controller (FLC), ANN, ANFIS

I. INTRODUCTION

Non-conventional energy resources have been in the limelight since their invention. They have gained a preference over the conventional resources owing to their idea of a clean and green approach towards the environment. Due to the abundant availability of solar energy, the demand for renewables has been more inclined towards PV. Easy installation procedures and maintenance have further added to it. The output of a PV array depends mainly upon the irradiance and the operating temperature of the PV array [1]. However, there are other parameters governing the output of PV as well, such as the orientation of module, mounting type, the efficiency of solar cells, etc [2]. A major part of the cost of PV systems is formed by the power converter and the inverter [3]. However, it has been observed that these converters are not much immune to failures and thus there exists a need for reliable power converters [4].

During the design process, it is assumed that the array will operate under constant irradiation. However, there is sensitivity in PV arrays towards shading. This shade could be due to trees, building, clouds passing by and thus leads to the limiting of PV output power, especially in the case of series connection [5]. In order to reduce the effect of the shaded cells, acting as hotspots being in reverse biased mode, bypass diodes are used [6]. Partial shading results into an overall reduction of the power produced by the PV array. It also introduces non-linearities in the P-V and I-V characteristics of the array due to multiple local MPPs [7].

During partial shading, the conventional MPP tracking techniques fail due to the occurrence of multiple local peaks owing to the presence of bypass diodes [8]. AI techniques emerge out to be an alternative to the existing MPP techniques under these non-linear and complex scenarios. A comparative analysis of MPP tracking using AI techniques, namely fuzzy logic, ANN and ANFIS, is presented in this paper.

Modelling of PV array is presented in Section-II, while boost converter design is discussed in Section-III. Section-IV is dedicated to AI based control techniques compared in this work. Simulation results are discussed and analyzed in Section-V. Finally, based on the analysis, conclusions are provided in Section-VI.

II. MODELLING OF PV ARRAY

The mathematical modelling of PV array was done based on the one-diode equivalent model of a PV cell, as depicted by Fig. 1.

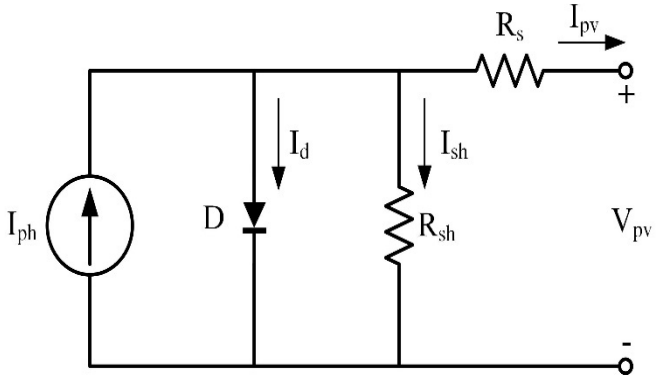

Fig. 1. One diode equivalent model of PV cell

The output current of the PV cell is represented by (1).

$$I = I_{ph} - I_d - I_{sh} \quad (1)$$

where, I denotes the output current of the PV cell; I_{ph} is the photo-current; I_d, the diode current and I_{sh}, the current flowing through the shunt resistance of the PV cell.

978-1-7281-6916-3/20/$31.00 ©2020 IEEE

Authorized licensed use limited to: DELHI TECHNICAL UNIV. Downloaded on February 15,2021 at 09:57:56 UTC from IEEE Xplore. Restrictions apply.

The photo-current generated by the PV cell can be obtained by (2):

$$I_{ph} = I_{sc}[1 + K_i(T_{op} - T_{ref})]\frac{G}{G_{ref}} \quad (2)$$

where, I_{sc} represents the short circuit current of the PV cell(A), K_i is the short-circuit current temperature coefficient(%/°C), T_{op} and T_{ref} stand for the operating and reference temperatures(K) respectively. G refers to the irradiance on which the PV cell is being operated while G_{ref} denotes the reference value of irradiance, usually taken as 1000 W/m^2.

The diode current is calculated using (3):

$$I_d = I_o(e^{\frac{V+IR_S}{AV_T}} - 1) \quad (3)$$

where, I_o signifies the reverse saturation current(A), A is the ideality factor of the diode and V_T, the thermal voltage is defined by (4).

$$V_T = \frac{kT_{op}}{q} \quad (4)$$

where, k is the Boltzmann's constant which can be equated to 1.38×10^{-23} m^2 kg s^{-2} K^{-1}; T is the operating temperature of the cell(K) and q is the charge on an electron i.e. equivalent to 1.6×10^{-19} C.

The reverse saturation current of the diode can be calculated as given by (5):

$$I_o = I_{rs} \exp\left[\left(\frac{1}{T_{op}} - \frac{1}{T_{ref}}\right)\frac{Egq}{Ak}\right]\left(\frac{T_{op}}{T_{ref}}\right)^3 \quad (5)$$

where, I_{rs} denotes the reverse current and E_g the energy band gap(eV).

The current through the shunt resistance is given by (6).

$$I_{sh} = \frac{V+IR_S}{R_{sh}} \quad (6)$$

where, R_s and R_{sh} represent the series and shunt resistances of the PV cell.

For a PV array, (1) can be modified as shown in (7).

$$I = N_p I_{ph} - N_p I_o\left(e^{\frac{V+IR_S\frac{Ns}{Np}}{AV_t}} - 1\right) - \frac{V+IR_S\left(\frac{N_S}{N_p}\right)}{R_{sh}\left(\frac{N_S}{N_p}\right)} \quad (7)$$

where, Ns and N_p represent the number of modules in series and parallel.

The block diagram of a PV array with MPPT controller is shown in Fig. 2. The voltage and current signals of PV array are used by MPPT controller to track the maximum power by regulating the duty cycle of boost converter based on the algorithm used. Boost converter is another important module of a PV system, whose design details are discussed in next section.

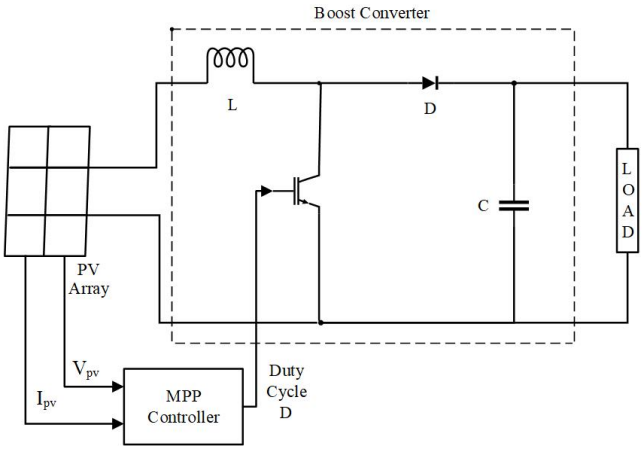

Fig. 2. Block diagram of PV array with MPPT controller

The PV array used in this work consists of 6 modules of Vikram Solar ELDORA VSP.60.AAA.03, each rated for 250W. The six modules have been divided into two parallel strings with each string consisting of 3 modules in series. The associated specifications of the PV array are given in Table I.

TABLE I. PARAMETERS OF PV ARRAY

Specifications	Rating
Maximum Power	1.5 kW
Voltage at MPP	91.84 V
Current at MPP	16.32 A
Rated Open-Circuit Voltage	112.32 V
Rated Short-Circuit Current	17.5 A

III. BOOST CONVERTER DESIGN

The boost converter design focuses on calculating the optimum value of two main components (L, C) of the boost converter i.e. inductor and capacitor. The inductance and capacitance values of which can be calculated using (8) and (9).

$$L = \frac{V_{mpp} \times D}{\Delta I_{pv} \times f} \quad (8)$$

$$C = \frac{P_{pv}}{2\pi f \times \Delta V_o} \quad (9)$$

For a switching frequency of 10 kHz and current as well as voltage ripple as 10% and 1% respectively, the inductance and capacitance are calculated as 6.3 mH and 218 µF.

IV. CONTROL TECHNIQUES

Control technique plays a pivotal role in governing the MPP tracking process. The partial shading condition is a highly non-linear condition, therefore the controller which can handle the non-linearity in a better way ought to be used. Therefore, in this work, a comparative analysis is performed on AI based controller which are known for their capability to handle non-linear conditions in a much better way as compared to their conventional counterparts. The three techniques compared in

Authorized licensed use limited to: DELHI TECHNICAL UNIV. Downloaded on February 15,2021 at 09:57:56 UTC from IEEE Xplore. Restrictions apply.

this paper to find the optimum value of duty cycle are described as follows:

A. Fuzzy Logic Controller

Fuzzy logic controllers (FLCs) have been extensively used in control applications due to their inherent capability to handle non-linearity and imprecision. It makes use of linguistic control strategy based on expert knowledge to handle uncertainties better than the conventional controllers [9-10]. In 1965, Zadeh propounded the fuzzy set theory. His work provided a framework to a formal system of mathematical logic based on linguistic terms. Mamdani and his colleagues took the lead from Zadeh's seminal papers and extended the work as pioneering research in the field of fuzzy logic control. The basic block diagram of a FLC is represented by Fig. 3.

In the proposed fuzzy control scheme, the ratio of ΔP and ΔI is used as error (e), while change in error (Δe) is evaluated by subtracting previous instant error from current error as shown by (10) and (11):

$$e(k) = \frac{\Delta P(k)}{\Delta I(k)} \tag{10}$$

$$\Delta e(k) = e(k) - e(k-1) \tag{11}$$

The output of the FLC is incremental change in duty cycle (ΔD). The duty cycle is continuously regulated by this incremental change in duty cycle as shown in Fig. 3.

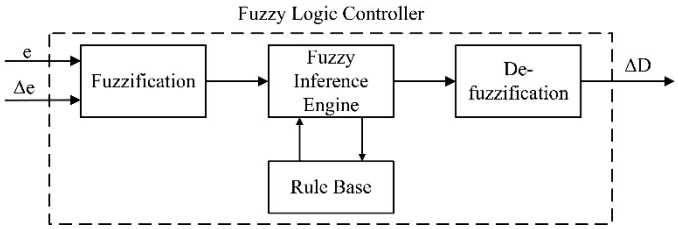

Fig. 3. Block diagram of Fuzzy Logic Controller

In the proposed controller, the universe of discourse is uniformly divided into seven fuzzy levels namely NL (negative large), NM (negative medium), NS (negative small), ZE (zero), PS (positive small), PM (positive medium), and PL (positive large) for each of the inputs and output as shown in Fig. 4.

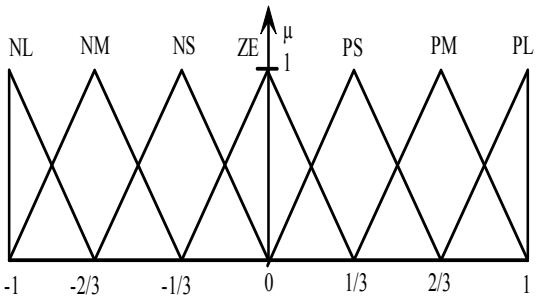

Fig. 4. Membership functions (MFs) for inputs and output

The rule base is designed based on the knowledge of the process as given in Table II.

TABLE II. RULE BASE FOR FUZZY LOGIC CONTROLLER

e/ Δe	NL	NM	NS	ZE	PS	PM	PL
NL	ZE	ZE	ZE	PL	PL	PL	PL
NM	ZE	ZE	ZE	PM	PM	PM	PM
NS	ZE	ZE	ZE	PS	PS	PS	PS
ZE	PS	PM	ZE	ZE	ZE	NM	NS
PS	NS	NS	NS	NS	ZE	ZE	ZE
PM	NM	NM	NM	NM	ZE	ZE	ZE
PL	NL	NL	NL	NL	ZE	ZE	ZE

B. Artificial Neural Network Controller

Artificial Neural Network (ANN) mimics the behaviour of human brain and is one of the prominent artificial intelligence (AI) based control techniques, which can be used as universal approximator and can handle the non-linearity of practical process in an effective way [11].

In this paper, an ANN having two neurons in input layer, one neuron in output layer and 10 neurons in hidden layer are taken to train the network as depicted in Fig. 5. The hidden layer neurons use tan-hyperbolic activation functions, while linear activation function is used in output layer. The network is trained with Levenberg Marquardt error back propagation algorithm using supervised learning.

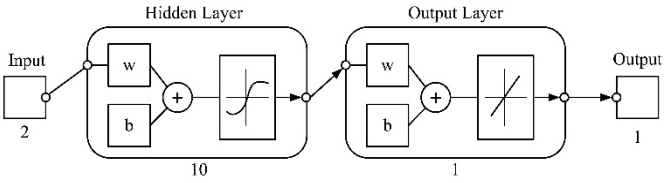

Fig. 5. Block diagram of Artificial Neural Network

C. Adaptive Neuro-Fuzzy Inference System Controller

An adaptive neuro-fuzzy inference system (ANFIS) combines the two earlier discussed techniques i.e. fuzzy logic and ANN based controllers. This combination of the two provides a better response owing to its enhanced adaptivity to handle dynamic and non-linear variations in input conditions [12]. Fig. 6 represents the block diagram of ANFIS combining the modules of FLC and ANN.

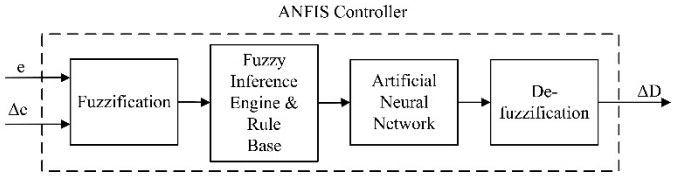

Fig. 6. Block diagram of Adaptive Neuro Fuzzy Inference System

Authorized licensed use limited to: DELHI TECHNICAL UNIV. Downloaded on February 15,2021 at 09:57:56 UTC from IEEE Xplore. Restrictions apply.

A Takagi-Sugeno fuzzy inference system (FIS) based on the test data provided is used to design ANFIS controller. In this work, seven generalized bell membership functions for each of the inputs i.e. error and change in error are selected as represented in Fig. 7. These membership functions are capable of handling non-linear distribution in a better way.

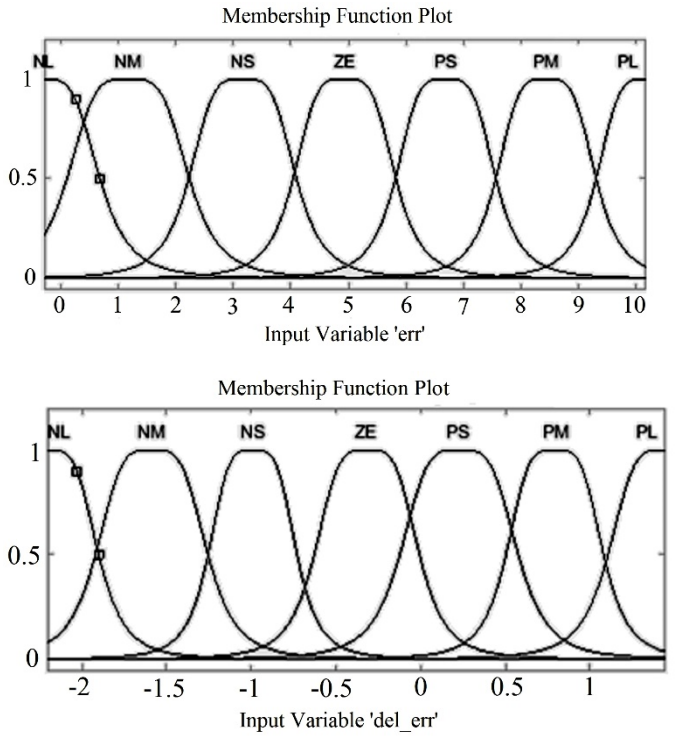

Fig. 7. Membership functions for error and change in error of ANFIS based controller

The FIS has been designed using grid partitioning while implementing the hybrid optimization method. The grid partitioning method is used when the inputs and the input membership functions involved are comparatively less. Unlike in fuzzy systems where the rules are added manually, the ANFIS controller adapts its rules according to the given dataset. This inherent prediction capability is attributed by the presence of the ANN within the ANFIS controller.

V. Simulation Results

The performance of three controllers discussed in previous section is analyzed through rigorous simulations. Simulation results are analyzed in following two subsections under various test conditions:

A. 4-Test Cases Under Partial Shading

The behaviour of the three controllers is examined under four cases as shown in the Fig. 8. Case-1 represents the condition of uniform irradiance at standard test conditions (STC). Cases 2, 3 and 4 represent some of the possible scenarios during partial shading conditions, i.e. top-shading, bottom shading and patch shading, respectively. P-V and I-V characteristics under these four test conditions are depicted in Fig. 9 and Fig. 10, respectively.

The performance of AI based controllers is analyzed on various parameters such as shading losses, mismatch losses, fill factor and tracking efficiency and performance indices based on various errors. In all the cases, the performance of ANFIS based controller is observed to surpass others as represented in Table III and Table IV. ANFIS being a hybrid version of ANN and FLC has an upper edge in performance as compared to other two controllers.

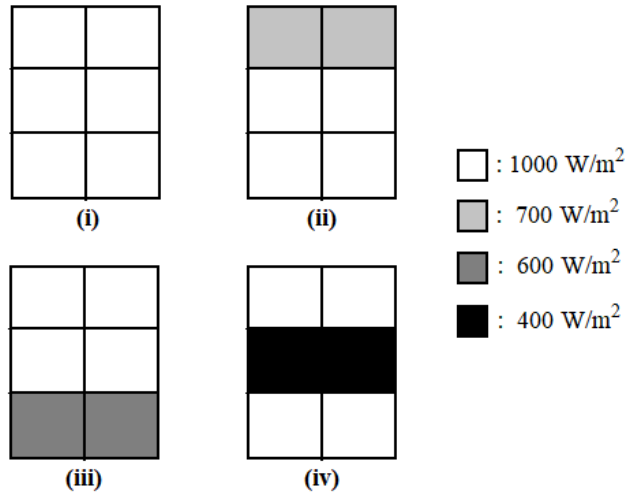

Fig. 8. Four test cases of partial shading (i) Case-1, Uniform irradiation (ii) Case-2, Top shading (iii) Case-3, Bottom shading (iv) Case-4, Patch shading

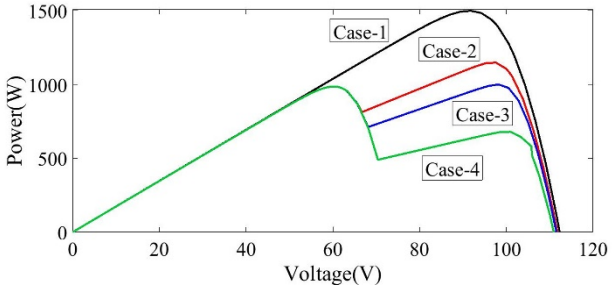

Fig. 9. P-V characteristics under test cases

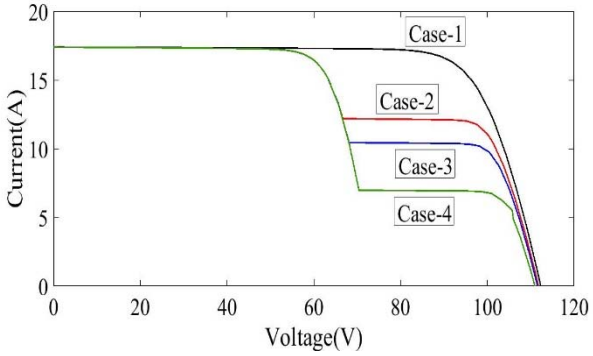

Fig. 10. I-V characteristics under test cases

Authorized licensed use limited to: DELHI TECHNICAL UNIV. Downloaded on February 15,2021 at 09:57:56 UTC from IEEE Xplore. Restrictions apply.

TABLE III. ANALYSIS OF LOSSES, FILL FACTOR AND TRACKING EFFICIENCY IN THE FOUR TEST CASES

Cases	Control Technique	Shading Losses(W)	% Shading Losses	Mismatch Losses(W)	% Mismatch Losses	Fill Factor	% Tracking Efficiency
Case-1	FLC	3.125	0.2083	3.125	0.2083	0.7657	99.79
	ANN	3	0.2	3	0.2	0.7658	99.8
	ANFIS	2.5	0.1667	2.5	0.1667	0.7660	99.83
Case-2	FLC	519.25	34.62	369.25	27.35	0.5017	85.43
	ANN	519.25	34.61	369.25	27.35	0.5017	85.43
	ANFIS	519	34.6	369	27.33	0.5018	85.45
Case-3	FLC	667.143	44.48	467.14	35.93	0.4260	83.28
	ANN	667.14	44.47	467.14	35.93	0.4260	83.29
	ANFIS	638.75	42.58	438.75	33.75	0.4406	86.13
Case-4	FLC	667.21	44.48	357.21	30.02	0.4260	84.43
	ANN	667.21	44.48	357.21	30.017	0.4260	84.43
	ANFIS	638.85	42.59	328.85	27.63	0.4405	87.3

TABLE IV. COMPARISON ON THE BASIS OF PERFORMANCE INDICES

Cases	Control Technique	ITAE	IAE	ISE (10^3)	ITSE (10^3)
Case-1	FLC	0.674	13.06	7.506	0.045
	ANN	0.674	13.05	7.511	0.045
	ANFIS	0.674	13.05	7.511	0.045
Case-2	FLC	7.205	59.45	17.65	1.943
	ANN	7.207	59.45	17.64	1.943
	ANFIS	7.197	59.38	17.62	1.939
Case-3	FLC	5.176	42.28	8.377	0.8653
	ANN	5.176	42.28	8.378	0.8653
	ANFIS	4.286	35.51	4.774	0.3775
Case-4	FLC	4.754	38.87	7.235	0.7311
	ANN	4.754	38.87	7.234	0.7311
	ANFIS	3.864	32.11	5.413	0.486

B. Performance under Dynamic Conditions (EN50530 Test)

EN50530 is a standard MPP tracking efficiency test. It involves dynamic changes in the input irradiance and tests the effectivity of the controller to track the MPP during the same. Under this test, either a trapezoidal or a staircase configuration of irradiance is chosen, and the response of the controllers is observed. In this work, the staircase pattern is used as shown in Fig. 11.

Further, to test the robustness of AI based controllers, the staircase pattern of dynamic irradiance is applied in two modes, i.e., gradual step change and sudden step change. The tracked power under dynamic irradiance with FLC, ANN and ANFIS controller is shown in Fig. 12.

Table V summarizes the performance of the three controllers under dynamically varying irradiance condition. The irradiance is changed after every 1 second during initial 5 seconds and thereafter it changes after every 0.5 second. The performances of ANN and ANFIS controllers are quite close to each other in terms of power being tracked and better than FLC in most of the cases.

When the performance is analyzed in terms of rise time, settling time, and peak overshoot/ undershoot, ANFIS based MPPT controller outperforms the other two controllers in most of the cases as evident from Table V.

The above analysis strengthens the candidature of ANFIS based controller in tracking MPP among the discussed AI based control techniques under dynamic variation in irradiance.

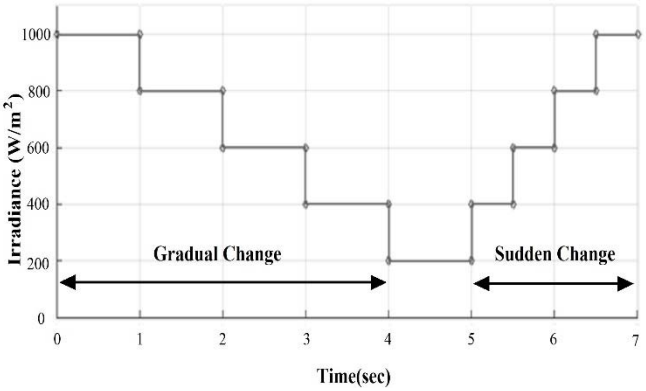

Fig. 11. Staircase pattern of dynamic variation in irradiance

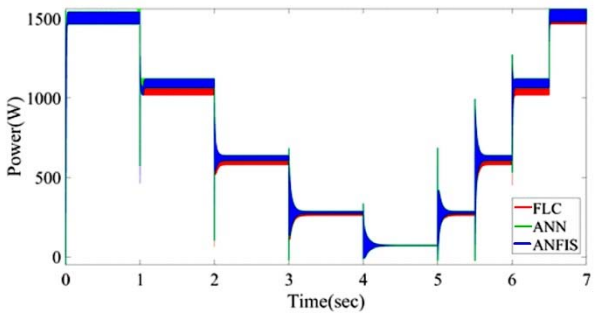

Fig. 12. Power under dynamic irradiance with FLC, ANN and ANFIS

Authorized licensed use limited to: DELHI TECHNICAL UNIV. Downloaded on February 15,2021 at 09:57:56 UTC from IEEE Xplore. Restrictions apply.

TABLE V. ANALYSIS UNDER DYNAMICALLY VARYING IRRADIANCE

Control Technique	Power Tracked (W)	Rise Time (sec)	Settling Time (sec)	% Overshoot /Undershoot
0-1 sec				
FLC	1503.05	0.007	0.025	0.00
ANN	1502.5	0.007	0.025	0.00
ANFIS	1503	0.007	0.025	0.00
1-2 sec				
FLC	1044.25	0.006	0.03	17.55
ANN	1092.5	0.001	0.05	15.33
ANFIS	1092.5	0.004	0.02	14.41
2-3 sec				
FLC	592.5	0.0025	0.05	12.23
ANN	620.5	0.001	0.16	6.52
ANFIS	622.5	0.002	0.05	8.43
3-4 sec				
FLC	265.25	0.001	0.14	62.30
ANN	279	0.001	0.15	46.24
ANFIS	279.5	0.002	0.17	53.48
4-5 sec				
FLC	67.78	0.001	0.4	100.00
ANN	71	0.001	0.36	100.00
ANFIS	71.25	0.0001	0.3	100.00
5-5.5 sec				
FLC	265.75	0.0025	0.2	50.5
ANN	279	0.002	0.15	50.53
ANFIS	280.75	0.002	0.18	48.86
5.5-6 sec				
FLC	592.71	0.0001	0.14	68.7
ANN	621.5	0.0001	0.1	59.29
ANFIS	621.85	0.0001	0.13	57.59
6-6.5 sec				
FLC	1044.28	0.0001	0.04	19.7
ANN	1093	0.0001	0.022	14.36
ANFIS	1092.75	0.0001	0.04	16.22
6.5-7 sec				
FLC	1503	0.0001	0.015	3.13
ANN	1520	0.002	0.015	2.63
ANFIS	1520.5	0.003	0.0125	2.59

VI. CONCLUSIONS

The comparative analysis of AI techniques for MPP tracking with multiple test cases under partial shading and dynamic irradiance conditions is presented. Simulation results confirm that ANFIS controller emerges out to be the best performer in comparison with FLC and ANN. ANFIS based controller tracks the maximum power with best efficiency among the three controllers discussed in this paper. As the ANFIS controller integrates the salient features of ANN and FLC, hence it can outperform the other counterparts under randomly varying irradiance conditions with gradual and sudden step change. The robustness of ANFIS controller is more dominant in terms of power tracking under sudden step changes. Conclusively, the simulated results have verified that ANFIS based controller under partial shading condition and dynamic irradiance variation has maintained its consistency in MPP tracking, in terms of both performance as well as in robustness.

REFERENCES

[1] M. Orkisz, "Estimating effects of individual PV panel failures on PV array output," IEEE Trans. Ind. Appl., vol. 54, no. 5, pp. 4825-4832, Sept./Oct. 2018.

[2] J. D. Rhodes, C. R. Upshaw, W. J. Cole, C. L. Holcomb and M. E. Webber, " A multi-objective assessment of the effect of solar PV array orientation and tilt on energy production and system economics", Sol. Energy, vol. 108, pp. 28–40, 2014.

[3] "Renewable Energy Technologies: Cost Analysis Series – Solar Photovoltaics". International Renewable Energy Agency vol. 1, issue 4/5, 2012.

[4] A. Ristow, M. Begovic´, A. Pregelj, and A. Rohatgi, "Development of a methodology for improving photovoltaic inverter reliability", IEEE Trans. Ind. Electron., vol. 55, pp. 2581–2592, 2008.

[5] S. Guo, T. Walsh, A. Aberle and M. Peters, "Analysing partial shading of PV modules by circuit modelling", 38th IEEE Photovoltaic Specialists Conference, pp. 2957-2960, 2012.

[6] J. C. Teo, H. G. T. Rodney, V. H. Mok, V. K. Ramachandaramurthy and C. K. Tan, "Impact of Partial Shading on the P-V Characteristics and the Maximum Power of a Photovoltaic String", Energies, vol. 11, no .7, pp. 1-22, 2018.

[7] A. Djalab, N. Bessous, M. M. Rezaoui and I. Merzouk, "Study of the Effects of Partial Shading on PV Array" International Conference on Communications and Electrical Engineering (ICCEE), pp. 1-5, 2018.

[8] A. Mohapatra, B. Nayak, P. Das and K. B. Mohanty, "A review on MPPT techniques of PV system under partial shading condition", Renew Sustain Energy Rev, vol. 80, pp. 854–67, 2017.

[9] C. C. Lee, "Fuzzy logic in control systems: Fuzzy logic controller- part I", IEEE trans. on system, man and cybernatics vol 20, no. 2, Mar/ Apr 1990.

[10] R. Singh, A. K. Singh and P. Kumar, "Self-tuned approximated simplest fuzzy logic controller based shunt active power filter," International Conference on Energy Economics and Environment (ICEEE*)*, pp. 1-6, 2015.

[11] Simon Haykin " Neural Networks - A comprehensive foundation", 2nd ed., Prentice Hall International, New Jersey, 1999.

[12] R. K. Kharab, S. L. Shimi, S. Chatterji and M. F. Ansari, "Modeling of solar PV module and maximum power point tracking using ANFIS", Renewable and Sustainable Energy Reviews, vol. 33, pp. 602-612, 2014.

Authorized licensed use limited to: DELHI TECHNICAL UNIV. Downloaded on February 15,2021 at 09:57:56 UTC from IEEE Xplore. Restrictions apply.

Automation Security System

Avinash Singh[1], Bharat Singh[2], Divyanshu Rawat[3], Bhavnesh Jaint[4]

Department of Electrical Engineering, Delhi Technological University, NEW DELHI

Abstract**—** *Security systems has seen a rapid rise in its place in research and development, in the field of home automation and industries. This is a field where development occurs regularly yet still always leave some room for growth. In this paper, an endeavour has been made to develop advanced automation security system with ultrasonic range module, stepper motor and GSM module to detect theft. When a person comes within the range of the system, along with an alarm buzz and led indication, an alert message is sent using GSM module touser's mobile. Use of stepper motor and ultrasonic module in system also provides an omni directional security of home detection. This system also very economical yet simple to implement. The system successfully developed, implemented and tested and that we found that its working is satisfactory. The abstract should summarize the content of the paper. Try to keep the abstract below 250 words. Do not make references nor display equations in the abstract. The journal will be printed from the same-sized copy prepared by you. Your manuscript should be printed on A4 paper (21.0 cm x 29.7 cm). It is imperative that the margins and style described below be adhered to carefully. This will enable us to keep uniformity in the final printed copies of the Journal. Please keep in mind that the manuscript you prepare will be photographed and printed as it is received. Readability of copy is of paramount importance.*

Keywords**—** ***ATmega-328 Microcontroller, Stepper Motor, Buzzer alarm, GSM SIM900.***

I. INTRODUCTION

In this era, need for security makes many folks quest for ways to safeguard their property. Many systems assure limited security in both indoor and/or outdoor environments. But, variety of them has very complicated connectivity and so the implementation cost reaches high values. In some of the cases this makes system highly inaccessible for the users. This includes hard and complicated locks or camera/sensor operated systems that are not economically viable. Furthermore such camera/sensor based systems are prone to blind spots intruder can take advantage of. This produces a requirement for security with decent number of varied systems integrated together, with as less resources as possible. This paper attempts to tackles these obstacles. The system proposed can be utilised in both security and safety of non-public sectors like homes, work places or other site that user wishes to protect. Security provides protection to our life and variable assets. Hence, we made an endeavour to develop an industrial security system with AVR microcontroller-At mega 328. Intruder is detected using ultrasonic sensor using its object detection capabilities [1]. Ultrasonic sensor is mounted on top of stepper motor. This stepper motor is rotated step by step using microcontroller and uses step angle to determine direction of intrusion [[3]]. Microcontroller, interfaced to GSM-SIM900 [[4]], sends distance and directional information of detection through GSM. Proposed system hence will be able to avoid problem of blind spots while being economical due to minimal design implemented.

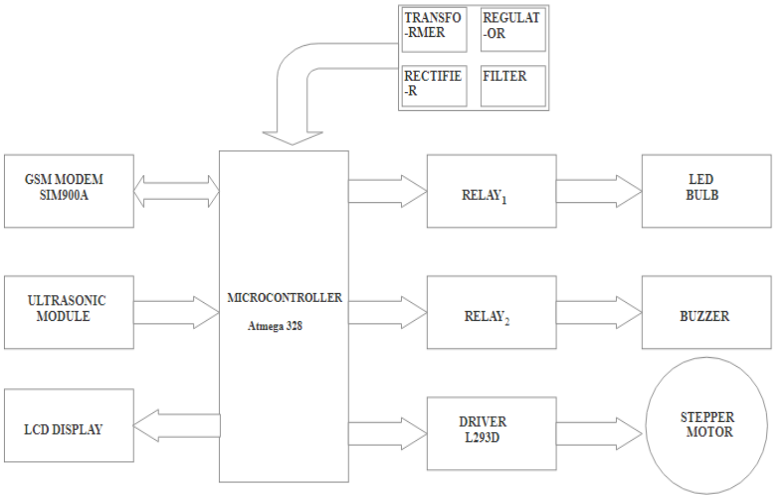

FIGURE 1: Block Diagram ATmega 328

II. LITERATURE SURVEY

As per the National Crime Records Bureau (NCRB), 2,44,119 cases of robbery, theft, burglary, dacoity, among others, happens in residential premises in 2017. This was a jump of over 10% from 2016 when the amount of such cases stood at 2,20,854. The loss thanks to these thefts and burglaries are staggering. In 2017, value of property stolen from residential premises was in more than Rs. 2065 crores, a 40% jump from Rs. 1,475 crores stolen the previous year [1].

A literature survey of GSM based Security system is conducted and presented: -

M. Sravan Kumar, M.Mounika proposed a system that uses GSM module, IR LED and Gas detector interfaced to OP AMP LM324.Whenever there is physical detection in IR LED or smoke detection through fire in gas detector, OP AMP will notify the user through GSM module [[5]]. B.Rama Murthy, O.Jagadish, proposed a home locker consisting of fingerprint scanner module and password protection through keypad and seven segment display and alert system through GSM using Arduino Uno. System will the alert the user if one enters wrong fingerprint data or password[[6]].E. Isa and N. Sklavos developed a password protected, camera monitored, home locker system with a GSM based alert system, using Arduino Uno, protection. System will alert the user when some enters wrong password 3 times or when someone not closes the door within predefined time. It alert user through sound, camera image and SMS sent through GSM [[7]]. Abhishek S. Parab and Amol Joglekar constructed an system with 8051 microcontroller, attached on the door, using magnetic relay alerts user through GSM if the door is opened in the absence of the user. Whenever door is opened magnetic rely, which acts like a switch, turns ON causing microcontroller to notify user through GSM [[8]]. B.Lakshmi Prathyusha and J.Anusha developed an all-round security system with object, fire, gas, voice and magnetic relay for door movements. User is alerted through GSM if any of the sensors in activated due to some intrusion. All sensors are controlled through Arduino Uno [[9]]..

III. PROPOSED WORK

As per the research conducted, conventional security system has developed in many areas but still consists a drawback of having blind spots. Whether it is a proximity sensor or a camera they can be easily avoided if approached in their blind spot. This can be avoided using many sensors but then system loses its economic viability. This paper attempts to tackle this obstacle, by proposing a 360 degree/omni directional security system with no blind spots. Using same Atmega 328 and ultrasonic sensor but with modification through inclusion of stepper motor onto which ultrasonic module is mounted rotating it step by step to whole 360 degree, thus providing an all-round security. Combining this technique with conventional security methods enhances its all around capabilities. Additionally using GSM module and simple AVR commands user can be alerted of distance as well as direction (in terms of steep angle of stepper motor) along with alert through an alarm buzz and led indication.

3.1 Development of Hardware

The block Diagram of the Industrial security System with ATmega 328 microcontroller, ultrasonic sensor and sending alert massage with GSM Technology and the schematic diagram in figure. The Industrial security consists of the mainly following units. They are:-

1. Ultrasonic ranging module
2. Positive voltage regulator
3. Character LCD
4. GSM Module
5. Microcontroller ATmega328

The description of each of these units and their interfacing with ATmega328 as presented below.

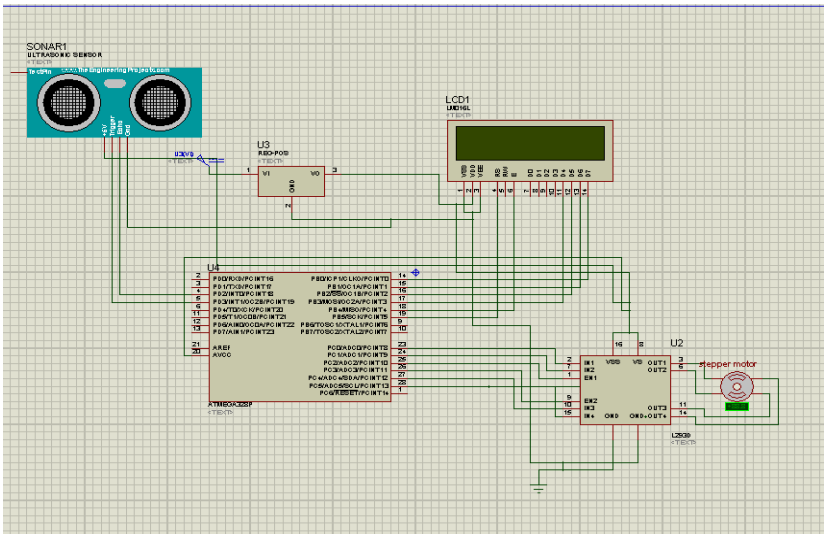

FIGURE 2. Simulation diagram of working model

3.2 Ultrasonic Ranging Module (HC - SR04)

Ultrasonic ranging module HC - SR04 provides object detection from 2cm - 400cm, with a ranging accuracy that can reach up to 3mm. This module includes ultrasonic transmitters, receiver and negative feedback circuit. The basic principle of work:

IO trigger, for a minimum of 10 micro seconds (μs), used to start the ranging module.

The Module automatically sends eight 40 kHz and detect whether there's a pulse signal back.

If the signal is received, through high level, time of high output IO duration is that the time from sending ultrasonic to returning.

Test distance can be calculated as = (high level time × velocity of sound (340M/S) /2.

FIGURE 3. Ultasonic Ranging Module (HC-SR04)

3.3 GSM modem – sim900

The worldwide System for Mobile communications (GSM) is the most used and popular standard in the world of mobile phones. Wireless communication module SIM900 which supports the standard of GSM is produced by SIMCOM Company and is employed within the developed application. To send the alert messages by implementing its commands within the software program. Featuring an industry-standard interface, the SIM900 delivers GSM/GPRS 850/900/1800/1900MHz performance for voice, SMS, Data, and Fax in a small form. Proposed system uses TX, RX pins for connection with microcontroller so that direct connection without the use of serial port can be established.

FIGURE 4: GSM Module SIM900

3.4 ATmega 328 Microcontroller

The ATmega328 is a single-chip device. It is an 8-bit microcontroller with 28 Pins. Manufactured by Atmel, a part of AVR family, it follows RISC Architecture and has a flash type program memory of 32KB.It has an EEPROM memory of 1KB and its SRAM memory is of 2KB.It has 8 Pin for ADC (Analog to digital converter) operations, which consists of Port A (PA0 – PA7). It also has 3 built in Timers, two of them are 8 Bit timers while the third one is 16-Bit Timer. Its operates in the range of3.3V to 5.5V but normally 5V is used as a standard. Atmega328 is known for its cost efficiency, low power dissipation, programming lock for security purposes, real timer counter with separate oscillator. Most commonly used in Embedded Systems applications with some applications in robotic, and many other applications.

FEATURES:
No. of pins: 28
CPU: RISC 8-bits AVR
Operating Voltage: 1.8 to 5.5V
Program Memory: 32KB
Program Memory Type: Flash
SRAM: 2048 byte
EEPROM: 2048 byte
ADC: 10-Bit
No. of ADC Channel: 8
Timer(3):16-Bit Timer(1)
8-Bit Timer(2)
I/O pin: 23
Oscillation: up to 20 MHz
Minimum Operating Temperature: -40 C to +85 C

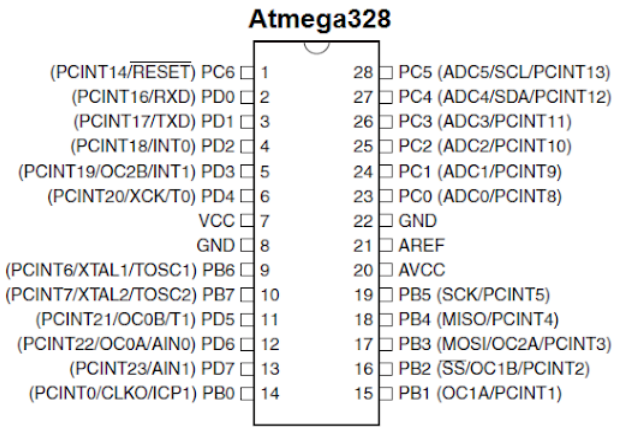

FIGURE 5. Atmega 328 Microcontroller

3.5 16*2 Alphanumeric Lcd Display

The LCD has been implemented to display the detected distance and angle which is also being sent to the user. It can exhibit 16*2 or 32 ASCII characters with 2 character lines where each line having 16. It has 8 data pins used in carrying the data from user to character LCD. Every Character has its unique bit code in accordance to ASCII format and is implemented to display characters on LCD. Other pins include enable, read/write and register selector. Ground, VCC, VO (LCD contrast) and Anode and cathode. Whenever the enable pin is low, the LCD is OFF and it is ON if the pin is high. The read/write pin, if high, reads the info from LCD and if low, writes data in it. The register select pin decides the sort of knowledge transferred through the info pins. If it is high, a character is written in LCD and if the low, command is sent to LCD.VCC is the power supply, which is 5V. VO sets contrast and brightness for the LCD display.

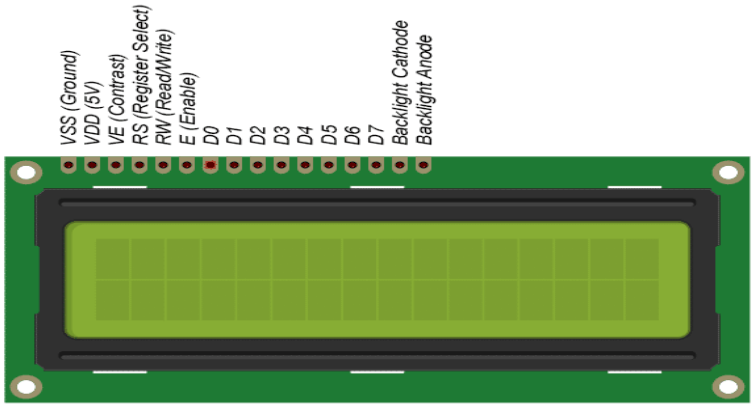

FIGURE 6: 16*2 LCD

3.6 Stepper Motor & L293D Driver IC

Stepper motors are DC motor that rotates in discrete step Stepper motor consists of many coils that are grouped together to form the phases. In order to rotate the stepper motor coils are energized phase wise using computerized sequences. Each phase is energized sequentially and each phase rotates rotor by some degree which is termed as step angle. Stepper motor used in the project has a step angle of 1.8 degree in or 200 turns per rotation. Other settings are also available including 24

and 48 turns per rotation. There are two types of stepper motor- unipolar and bipolar. Unipolar are energized in a constant manner. One coil will be positive while other is negative. Meanwhile in bipolar motors H-bridge connectivity is used for bidirectional functioning of motor.

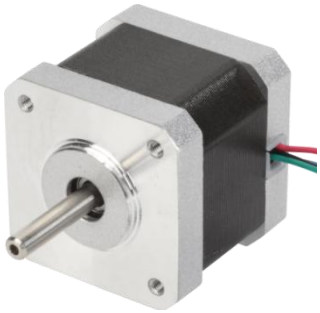

FIGURE 6: Stepper Motor

L293D (16 pin IC) is a Motor Driver IC which allows motors, be it stepper or DC, to drive on either directions. It is required as microcontroller itself cannot provide enough power for operation of stepper motor. It works on the concept of H-bridge. H-bridge is type of circuit with capabilities to allow voltage to change polarities which is essential in rotating the motor in both direction. It requires a supply of 5V for its functioning. The stepper motor rotates with the help of the driver IC.

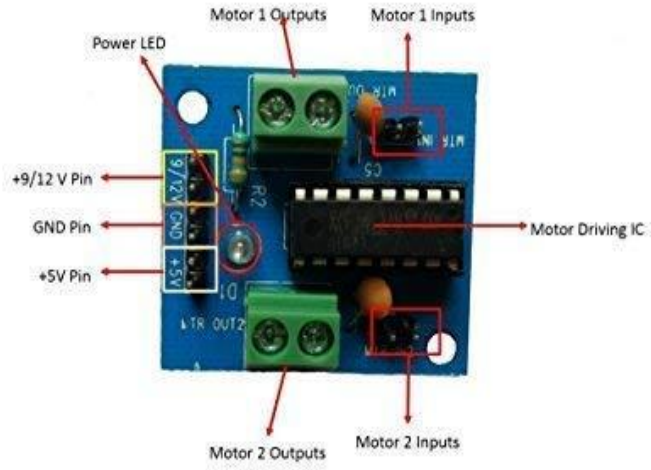

FIGURE 7: Motor Driver (L293D)

IV. SYSTEM DESIGN

The system is fully controlled by the microcontroller and it continuously monitors the sensors, detector and GSM modem.

Microcontroller repeatedly rotates stepper motor through L293D driver IC. Motor completes 1 revolution in 200 steps in accordance with its step angle 1.8 degree. Angle or Tracking is calculated based difference between variable "new angle" and "set angle" with "set angle" fixed at 0 and "new angle" calculated from number of pulses send to stepper motor.

Ultrasonic is mounted on top of stepper motor where object detection takes place and distance is calculated as (time* 0.34)/2 where 0.34 is speed of sound in cm/µs. When distance calculated is less than 10 cm then an alarm will buzz off along with activation of GSM. In that instant then it will send the "AT +CMGS ="USER MOBILE NUMBER" to GSM modem through serial port.

GSM modem will send the detected distance as well its direction of detection in terms of angle.

V. TEST AND RESULTS

System is tested for ultrasonic sensors ability to detect distance while being in motion. For this, Ultrasonic sensor is rotated through stepper motor and distance detected is observed at different measurements. Data for this observation is shown below.

TABLE 1
DATA COLLECTED FROM OBSERVATIONS

MEASURED DISTANCE (in cm)	SMS DISTANCE(in cm)	Error(in cm)	Error (in %)
5	7.36	2.36	47.2
10	12.97	2.95	29.5
15	18	3	20
20	23.41	3.53	17.05
25	28.22	3.22	10.48
30	31.87	1.87	6.23
35	36.77	1.77	4.91
37	39.08	2.08	5.62
40	42.36	2.36	5.90
45	47.86	2.86	6.35

Below graph and above table are use to show the existence error in cm and %.

Plotting the graph between measured distance (in cm) and error (in %):-

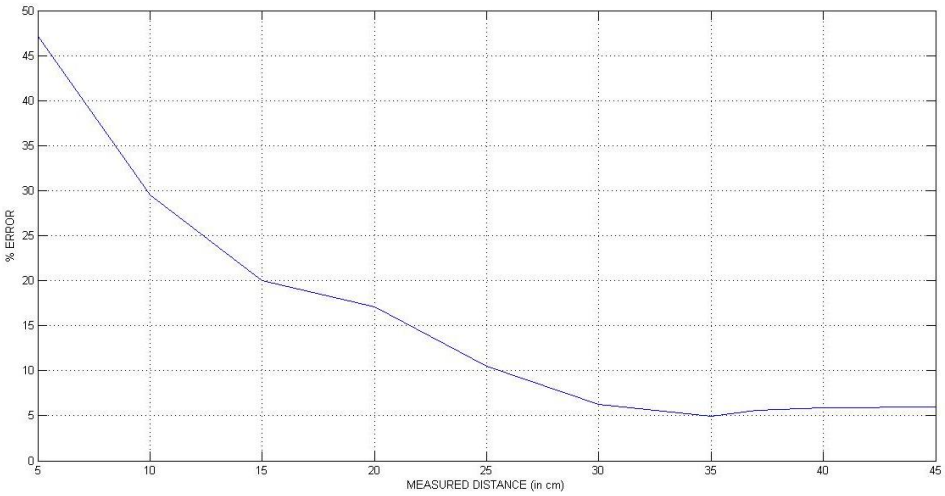

GRAPH: Plotted of Data collected from observations

According to data and graph, accuracy decreases as distance is increased, and achieves a near constant accuracy in the range of 4-5% in the terms of percent error starting from 35 cm.

VI. OUR WORKING MODEL

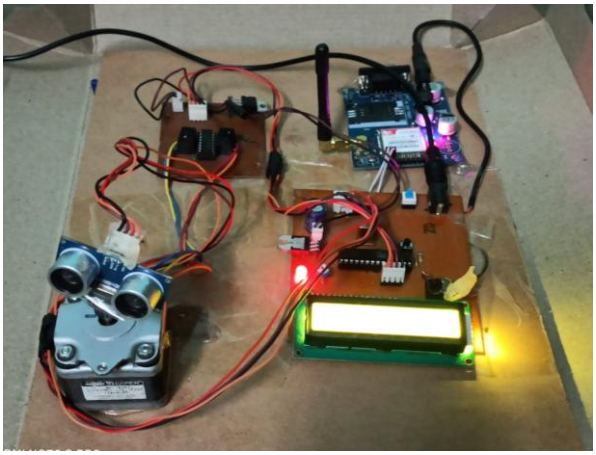

FIGURE 8: Project Designed

VII. OUTPUT OR RESULT

The distance (in cm) and angle (in degree) of the object which is detected by our model /through the SMS in the mobile (owner mobile) is:-

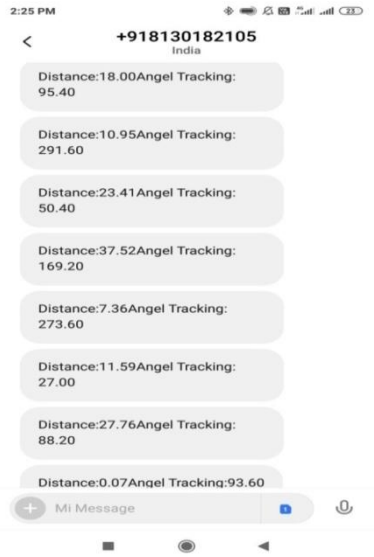

VIII. CONCLUSION AND FUTURE WORK

This security system is tested and implemented using ULTRASONIC RANGE, STEPPER MOTOR and GSM as an advance security over 360-degree angle in particular range. And we found systems' working is satisfactory. The systems having advanced features like its portable and low cost and standalone system. Our future work of this paper is planned to a develop in addition with some important equipment like:-

Wireless camera to help in identifying type of threat which is detected by the system and also some additional sensors like fire or gas sensors will enhance security prospects of this work when implanted with 360-degree detection.

REFERENCES

[1] https://www.indiatoday.in/impact-feature/story/every-3-minutes-a-burglary-robbery-or-a-break-in-is-taking-place-in-india-and-its-time-we-reconsidered-the-safety-levels-of-our-homes-1621113-2019-11-21

[2] R.Vairavan, S.Ajithkumar, L.ShabinAshiff, C.Godwin Jose "Obstacle avoidance robotic vehicle using ultrasonic sensor, Arduino controller", Published in International Research Journal of Engineering and Technology (IRJET),Volume 5, Issue 2, Feb-2018, pp.2140-2143.

[3] R.Harisudhan, M.Ganeshkumar, A.Udhaya Prakash, P.Sathiya "Stepper motor control using Arduino Atmega-328 microcontroller", International Journal for Scientific Research & Development, Volume 2, Issue 12, 2015, pp.778-780.

[4] KhinSu Hlaing, HlaYamin, MyoSuSuTheint "Electricity Meter Reading using GSM" Published in International Journal of Trend in Scientific Research and Development (IJTSRD), Volume3, Issue5, August 2019, pp.952-955.

[5] M.SravanKumar, M.Mounika,L.RamyaPavani, E.Ranadeep, B.Siddhartha, K.B.V.S.R.Subramanyam, "Gsm based industrial security system", International Journal Of Current Engineering And Scientific Research (IJCESR), Volume2, Issue5, 2015, pp.33-38

[6] B.Rama Murthy, O.Jagadish, K.TanveerAlam, V. Mahammad Dada, K. Priyanka Gandhi, "Development of GSM Based Advanced Alert Home Locker SafetySecurity System Using Arduino UNO", International Journal of Scientific Research in Science and Technology (IJSRST),Volume4, Issue2, 2018, pp.1154-1160

[7] E. Isa, N. Sklavos, "Smart Home Automation: GSM Security System Design & Implementation", Journal of Engineering Science and TechnologyReview (JESTR), Volume 10, Issue 3, 2017, pp.170-174.

[8] Abhishek S. Parab, Amol Joglekar, "Implementation of Home Security System using GSM module and Microcontroller", International Journal of Computer Science and Information Technologies (IJCSIT), Volume 6, Issue 3, 2015, pp.2950-2953.

[9] B. Lakshmi Prathyusha1, J.Anusha, D.saiLalitha, D.Venkata Krishna, "Home Security System Based on GSM and Voice Module", International Research Journal of Engineering and Technology (IRJET), Volume 05, Issue 03, Mar-2018, pp.2434-2437

[10] https://www.moglix.com/embeddinator-l293d-motor-driving-module/mp/msnrkrepxeeg9n

[11] https://avrgeeks.com/16x2-lcd-interfacing-atmega16/

International Journal of Biological Macromolecules 174 (2021) 240–253

Contents lists available at ScienceDirect

International Journal of Biological Macromolecules

journal homepage: http://www.elsevier.com/locate/ijbiomac

Bioactivity reinforced surface patch bound collagen-pectin hydrogel

Himansh Goel [a,1], Nidhi Gupta [a,b,1], Deenan Santhiya [a,*], Namit Dey [a,c], Himadri B. Bohidar [b,*], Aditi Bhattacharya [d]

[a] Department of Applied Chemistry, Delhi Technological University, New Delhi, India
[b] School of Physical Science, Jawaharlal Nehru University, New Delhi, India
[c] Department of Biotechnology, Delhi Technological University, New Delhi, India
[d] Department of Biochemistry, All India Institute of Medical Science, New Delhi, India

ARTICLE INFO

Article history:
Received 9 November 2020
Received in revised form 23 January 2021
Accepted 25 January 2021
Available online 27 January 2021

Keywords:
Hybrid composite hydrogel
Bioactive glass
Amphotericin-B
Bioactivity
Surface-patch binding

ABSTRACT

In this report, we discuss the design of a novel collagen/pectin (CP) hybrid composite hydrogel (CPBG) containing *in-situ* mineralized bioactive glass (BG) particles to simulate an integrative 3D cell environment. Systematic analysis of the CP sol revealed collagen and pectin molecules interacted regardless of both possessing similar net negative charge through the mechanism of surface patch binding interaction. Fourier transform infrared spectroscopy (FTIR) and thermogravimetric analysis (TGA) confirmed this associative interaction which resulted in the formation of a hybrid crosslinked network with the BG nanoparticles acting as pseudo crosslink junctions. Scanning Electron Microscopy (SEM), Energy Dispersive X-Ray Analysis (EDAX) and Transmission Electron Microscopy (TEM) results confirmed uniform mineralization of BG particles, and their synergetic interaction with the network. The *in-vitro* bioactivity tests on CPBG indicated the formation of bone-like hydroxyapatite ($Ca_{10}(PO_4)_6(OH)_2$) microcrystals on its surface after interaction with simulated body fluid. This hydrogel was loaded with a model antifungal drug amphotericin-B (AmB) and tested against *Candida albicans*. The AmB release kinetics from the hydrogel followed the Fickian mechanism and showed direct proportionality to gel swelling behavior. Rheological analysis revealed the viscoelastic compatibility of CPBG for the mechanical load bearing applications. Cell viability tests indicated appreciable compatibility of the hydrogel against U2OS and HaCaT cell lines. FDA/PI on the hydrogel portrayed preferential U2OS cell adhesion on hydrophobic hydroxyapatite layer compared to hydrophilic surfaces, thereby promising the regeneration of both soft and hard tissues.

© 2021 Elsevier B.V. All rights reserved.

1. Introduction

The architecture of native soft tissue to bone enthesis or interface is complicated due to its unique physiological composition and inherently poor healing capacity. Interface tissue engineering represents an attractive integrative strategy for functionally cementing soft and hard tissue and thereby improving the well-being of people exposed to its injuries [1]. Based on the numerous published reports, it is realized that future biomaterials must possess specific material properties in terms of design, composition, structure and functional features suitable for composite tissue graft [1,2]. One such type of promising biomaterials are the hydrogels, three-dimensional cross-linked network possessing the capability of holding large amount of interstitial water while maintaining structural integrity. Hydrogels have excellent biological properties due to their ability to mimic the extracellular matrix. Their aqueous environment allows for the transport of substances such as nutrients and by-products of cell metabolism. Hydrogels have gained considerable attention in the past due to their widespread use in the medical field, particularly in various tissue regeneration applications [3]. They have an added advantage of positioning them at the target diseased site, thus enhancing the bioavailability of the incorporated drug. Many synthetic polymers have been explored in the fabrication of hydrogels [4]; however, the importance of natural biopolymers in the fabrication of biomaterials for tissue engineering has gained limited attention due to obvious reasons. Since the extracellular matrix (ECM) is mainly composed of collagen and proteoglycans, natural polymers have become popular candidate biomaterials for bone tissue engineering [3]. Pectin, a plant originated heterogeneous polysaccharide having a chemical structure similar to alginate, provides interesting properties as artificial ECM [5] as well as scaffold for neo bone formation after coupling with calcium phosphate [6,7]. Importantly, easy to process pectin possesses anti-cancer and anti-inflammatory properties [8,9]. Collagen, an abundant protein of vertebrate, is not only the main component of bone ECM, but also is the load-bearing tissue of the muscles [10]. Due to these unique characteristics, both of these biopolymers

* Corresponding authors.
E-mail addresses: deenan.santhiya@dce.ac.in (D. Santhiya), bohi0700@mail.jnu.ac.in (H.B. Bohidar).
[1] HG and NG contributed equally.

https://doi.org/10.1016/j.ijbiomac.2021.01.166
0141-8130/© 2021 Elsevier B.V. All rights reserved.

are adequately placed for both soft and hard tissue engineering as well as for the formulations of tissue regenerative medicine in a variety of forms [10,11].

Recently, the concept of design and applications of two polyelectrolyte based hybrid hydrogels has gained attention [10,12]. For example, a polyelectrolyte made up of 3-acrylamidopropyltrimethylammonium chloride (APTAC), acrylamide and 2-acrylamido-2-methyl-1-propanesulfonic acid sodium salt (AMPS) monomers complements the perylene monoimide (PMI)-based-chromophores amphiphile for photocatalytic hydrogen production [12]. Herein collagen and pectin results in the synergetic self-assembly of networks based on favorable surface charge to participate in selective surface patch binding. Interestingly, macromolecules possessing similar net charge can also interact by an associative mechanism through surface patch binding where the heterogeneous charge distribution on one of these allows for the surface selective associative interaction with its partner overcoming the same charge repulsion between segments [13]. Such associative interactions are predominantly noticed in polyampholyte-polyelectrolyte pairs. The persistence length of the polymer plays a key role in facilitating this type of binding [14]. A typical example is the development of dual gelling injectable hydrogel reported by Vo et al. [15] and the biotherapeutic pectin collagen composites [10] which suggests pectin as a compatible component for collagen in formulating scaffold with an increase in thermal stability of about 14 °C as compared to native collagen (62 °C). Moreover, pectin acts as an efficient inhibitor for resisting the action of collagenase on collagen, and in turn, increases its structural stability [10]. Pectin is also well known to interact with protein molecules through the freely available amino groups by lowering the effective glycation targets [10]. Apart from this, composites of polymers and bioglass as well as calcium carbonate [16] particles have also been increasingly developed as both soft and hard tissue regenerating materials due to their superior bioactivity, biocompatibility, biodegradability and better cell adhesion ability [16,17]. The inorganic particles can synergistically interact with the polymer network either through physical or chemical forces, which effectively improves the mechanical property and stability of the resultant composite hydrogels [18,19]. Different inorganic particles in the form of hydroxyapatite, calcium phosphate [20] and silica-based bioactive glass [18,21–25] have been explored in the past for bone tissue engineering applications. Of these, in the present report, we have utilized the bone regenerative ability of third-generation biomaterial *i.e.*, bioactive glass as inorganic particles by *in-situ* mineralizing them in a dual-polymer based hybrid hydrogel system.

Highly cross-linked hydrogels were interacted with bioactive glass prepared previously through photopolymerization of gelatin methacryloyl [18] and poly(ethylene glycol) dimethacrylate [21]. Applications of various formulations of bioglass for tissue engineering have been clearly shown in the literature. Recently, injectable and self-healing Au-based 4-arm thiol terminated poly(ethylene glycol) dynamic hydrogel containing bioactive glass nanoparticles for bone regeneration has been proposed [22]. Carbohydrate based hydrogel such as dextran [23] and β-chitin with the incorporation of bioactive glass has also been reported. Recently, stimuli-responsive thermo-gelling chitosan–collagen–bioactive glass hybrids [24] as well as chitosan-beta-glycerophosphate salt formulations combined with bioactive glass nanoparticles [25] have been developed as a potential injectable system for tissue engineering. It is pertinent to note that most of the reported procedures till date use the pre-prepared bioactive glass as a reinforcing agent in the composite hydrogel. In contrast, in the present work, *in-situ* mineralized bioactive glass was incorporated into the hybrid hydrogel, a protocol which imparts sufficient novelty to this work. Moreover, during mineralization, ion contents function as an essential parameter of crosslinking allowing hydrogel properties to be controlled such as calcium from calcium carbonate particles has been reported by Abalymov et al. to serve as a crosslinker in hydrogel [16].

Microbial infection is a severe health issue concerning tissue regeneration, wound healing and recovery after surgery. Infection can prolong the healing process, leading to tissue morbidity and sepsis [26]. Candida species are the most common pathogen related to such type of infection [26,27] in various parts of the body including skin, mouth, gastrointestinal tract, vascular system and wounds related to both soft and hard tissues [28]. It may lead to serious complications or may even cause death [28]. Amphotericin-B (AmB) is a broad-spectrum antifungal drug effective against a wide range of most frequently occurring fungal infections including candida species [28,29]. To overcome its well-known side effects [29], novel AmB delivery methods are being developed. For example, Shu et al. [29] conjugated AmB with polypeptide hydrogel to increase its solubility in aqueous media. Demirci et al. [28] synthesized levan based hydrogel for controlled release of AmB. Sosa et al. [27] reported AmB loaded pluronic (P407) thermo-reversible gel for the dermal and vaginal treatment of candidiasis.

To the best of our knowledge, first time an attempt has been made for the *in-situ* mineralization of bioactive glass in collagen-pectin based hybrid hydrogel matrix. The novelty of the work lies in the fact that one of the bioactive glass precursors namely calcium acetate, acts as the pseudo crosslinker and results in hydrogel formation, regardless of the fact that both biopolymers carried net charge of same polarity. This procedure excludes the need of any external crosslinker. It is postulated that the proposed hybrid composite hydrogel matrix not only would remain helpful in both soft and hard tissue engineering but also prevent microbial infections.

2. Experimental section

2.1. Materials

For the fabrication of hydrogels, pectin with esterification 55% to 70% was purchased from Sigma-Aldrich, USA, and collagen was obtained from Sisco Research Laboratories (P) Ltd., Mumbai, India. Additionally, the precursors tetraethyl orthosilicate (TEOS), triethyl phosphate (TEP), sodium acetate and calcium acetate monohydrate, used for the *in-situ* mineralization of bioactive glass (BG) particles, were obtained from Sigma-Aldrich, USA. Hank's Balanced Salt solution (simulated body fluid (SBF)) purchased from Sigma-Aldrich, USA was used for *in-vitro* bioactivity test. Test microorganism, namely *Candida albicans* MCC1151, was obtained from National Centre for Microbial Resource, Pune, India. The broad spectrum antifungal drug amphotericin-B (AmB) was procured from Pharmaceutical and Research Laboratories (P) Ltd., Bangalore, India. Cell studies were carried out using U2OS, a human osteoblast-like osteosarcoma cell line and HaCaT, which is an adult keratinocyte cell line were obtained from National Institute of Immunology, Delhi and National Centre for Cell Science, Pune, India, respectively. For all the experimental work, Milli-Q water was used. All reagents used in these experiments were of analytical reagent (AR) grade of high purity. All procedures were performed at room temperature of 25 °C unless otherwise stated.

2.2. Synthesis of hybrid hydrogels

2.2.1. Preparation of collagen/pectin solution

Initially, collagen and pectin solutions were prepared in 10 mM Trizma buffer at pH 8.0 by continuous stirring for 1 h at a desired concentration and composition ratio. The freshly prepared solutions were analyzed to study the best fit composition ratio for the synthesis of hydrogel. The identification code of the samples used in this study is represented as xC:yP which refers to a given sample containing x mg/mL of collagen and y mg/mL of pectin, respectively (ESI Table S1).

2.2.2. Control hydrogels

Initially, a homogenous 1:1 (v/v) solution of collagen and pectin, each having a concentration of 5% (w/v) was prepared in 10 mM Trizma buffer at pH 8.0 by continuous stirring for 1 h. Thereafter, calcium

Table 1
Various compositions of CPCa hydrogel series.

Precursor	Various compositions of CPCa hydrogels							
	CPCa_20	CPCa_25	CPCa_40	CPCa_50	CPCa_60	CPCa_75	CPCa_90	CPCa_100
Calcium acetate	0.053 M	0.066 M	0.106 M	0.133 M	0.160 M	0.199 M	0.239 M	0.266 M

acetate solution was added dropwise from its stock solution to obtain the desired concentrations (25%, 50%,75% and 100% (w/v)) (Table 1). The concentration of stock calcium acetate solution was maintained at 63.6% (w/v) based on our previous report on 45S5 bioglass composition [30]. Interestingly, gel formation was noticed during the dropwise addition of the required amount of calcium acetate solution to the collagen/pectin solution. Hydrogel synthesis was carried out in 3 mL glass vials and the total gel volume was maintained at 1 mL (Scheme 1). The obtained gel was kept in a water bath at 37 °C for 24 h, lyophilized overnight and preserved in the desiccator. A control hydrogel series (CPCa) using different concentrations of calcium acetate were made and named according to their respective Ca^{2+} content as CPCa_25, CPCa_50, CPCa_75, and CPCa_100.

2.2.3. Hydrogel series containing BG particles

Initially, a 1:1 homogenous solution of collagen/pectin was prepared as mentioned in the previous section. Then, BG precursors, namely TEOS, TEP, sodium acetate and calcium acetate were sequentially added dropwise (Table 2), at ambient condition with an interval of 30 min while maintaining the required concentrations, to obtain the 45S5 composition (Scheme 1). Here again, during the dropwise addition of calcium acetate, gel formation was noticed, which was stored as mentioned in Section 2.2.2.

It is pertinent to note that considering 45S5 composition as 100% [30] bioactive glass particles were also mineralized by varying the precursor concentration from 25% to 100% (w/v) (Table 2) in the hydrogel matrix. The obtained hydrogel series (CPBG) containing *in-situ* mineralized bioactive glass were named as CPBG_25, CPBG_50, CPBG_75, CPBG_100 as per the concentration of BG precursors used.

2.2.4. Drug loading

The broad-spectrum antifungal drug amphotericin-B (AmB) was loaded by soaking the as prepared lyophilized hydrogels (1 cm diameter and 1 cm thick (CPCa and CPBG series)) in 1000 μL (0.5 mg/mL) drug solution for 6 h. The obtained hydrogels were named as CPCa_25_AmB, CPCa_50_AmB, CPCa_75_AmB, CPCa_100_AmB, CPBG_25_AmB, CPBG_50_AmB, CPBG_75_AmB and CPBG_100_AmB.

2.3. Characterization of hydrogels

2.3.1. Turbidity measurement

Turbidity measurements of collagen/pectin solution at 10 times dilution (for various compositions reported in ESI Table S1) were performed on a UV–Vis spectrophotometer (Model CE7300, Cecil Instruments, UK) operating at 400 nm which was calibrated to 100% transmittance (T) against deionized water. Turbidity was calculated as 100 − T%.

2.3.2. Zeta potential measurement

Zeta potential measurement of collagen/pectin solution at 10 times dilution (for various compositions mentioned in ESI Table S1) was recorded using a Zetasizer (Model ZSP, Malvern Instruments, UK). An average of three zeta potential readings was taken for each sample.

2.3.3. Fourier transform infrared spectroscopy (FTIR)

FTIR spectra were recorded by mixing the required lyophilized hydrogel sample with potassium bromide in the ratio of 1:100 and pelleted. Then the spectra were recorded using NICOLET 380 FTIR spectrometer operating in the spectral range of 4000–400 cm^{-1} with the resolution of 1 cm^{-1} in transmission mode.

2.3.4. Thermogravimetric analysis (TGA)

To investigate the thermal stability of hydrogel samples Perkin Elmer thermogravimetric analyzer, TGA 4000 was used. The samples were heated from room temperature to 800 °C at a heating rate of 10 °C/min under nitrogen atmosphere by maintaining a nitrogen flow rate of 20 mL/min.

2.3.5. Morphological studies

The surface morphology of various lyophilized samples was recorded using scanning electron microscope (SEM) (ZEISS EVO MA15). For lyophilization, the samples were frozen overnight at −20 °C and then lyophilized (SP Scientific Benchtop Pro) at −86 °C, ~40 mT vacuum for 10 h in a freeze dryer. The samples were gold coated and then observed in the SEM at an accelerating voltage of 5 kV at 10,000 magnifications. The hydrogels were also subjected to Energy Dispersive X-Ray Analysis (EDAX) operated at the voltage of 20 kV using (ZEISS EVO MA15) to investigate the presence of Si, P, Na, Ca ions in various samples. Additionally, *in-situ* mineralized bioactive glass particles and the porosity of the hydrogel matrix were also characterized using a transmission electron microscope (TEM) (Tecnai G2 200 KV HRTEM SEI HOLLAND) operating at an accelerating voltage of 200 kV.

2.3.6. Swelling studies and kinetic analysis

The swelling measurement of the hydrogels (1 cm dia. and 1 cm thick) was examined in simulated body fluid (SBF) buffer at 25 °C. At a pre-determined interval, the hydrogels were taken out, the excess surface liquid was wiped using a filter paper (Whatman filter paper grade, No. 2), and the weight of swollen hydrogel was measured using Sartorius BSA 2245 balance as per the standard procedure [28].

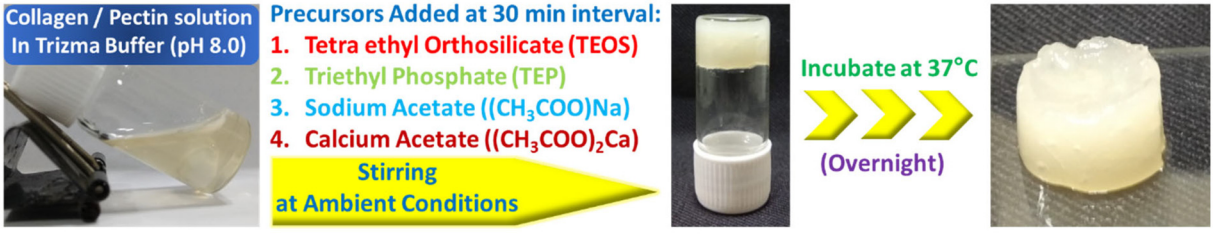

Scheme 1. Schematic illustration for the synthesis of collagen/pectin hybrid composite hydrogel containing *in-situ* mineralized bioactive glass particles.

Table 2
Various compositions of bioactive glass precursors used in CPBG hydrogel series.

BG precursors	Compositions of bioactive glass precursors in various CPBG hydrogels							
	CPBG_20	CPBG_25	CPBG_40	CPBG_50	CPBG_60	CPBG_75	CPBG_90	CPBG_100
Tetraethyl orthosilicate	0.089 M	0.111 M	0.178 M	0.222 M	0.267 M	0.333 M	0.400 M	0.445 M
Triethyl phosphate	0.011 M	0.014 M	0.022 M	0.027 M	0.033 M	0.041 M	0.049 M	0.055 M
Sodium acetate	0.155 M	0.194 M	0.31 M	0.387 M	0.465 M	0.581 M	0.697 M	0.775 M
Calcium acetate	0.053 M	0.066 M	0.106 M	0.133 M	0.160 M	0.199 M	0.239 M	0.266 M

Thereafter, the swelling ratio (S), equilibrium buffer content (EBC), swelling kinetic analysis (dS/dt) and buffer diffusion coefficient (D) was determined as discussed in ESI S1. Additionally, disintegration of CPCa_25 and CPBG_25 hydrogels (1 cm dia. and 1 cm thick) were also monitored after swelling equilibrium in SBF overnight followed by determining the weight loss in the sample (% disintegration) at the end of each preset time point.

2.3.7. Rheological analysis

Pre-formed gels/hydrogels were used for the rheological characterization using a stress controlled AR-500 rheometer (TA Instruments, U.K.) equipped with cone-plate geometry (2°, 25 mm). A constant stress of 1 Pa and truncation gap of 58 μm was maintained in all the measurements. Rheology experiments were performed with the objective to map the viscoelastic profiles of various concentrations of CP solution mixtures (ESI Table S1), CPCa_25 and CPBG_25. In order to thermally equilibrate the sample with the instrument a waiting time of 10 min was used. The mechanical spectra were measured by isothermal temperature sweep experiments which yielded the storage (G′) and loss modulus (G″) as a function of angular frequency (ω) in the range of 1 to 100 rad/s.

2.3.8. Bioactivity test

In-vitro bioactivity of various hydrogel samples was performed by monitoring the formation of bone-like hydroxyapatite on the surface of bioglass as per the procedure described by Kokubo et al. [31]. The room dried hydrogel samples containing bioglass particles of size 1 cm dia. and 1 cm thick was immersed in simulated body fluid (SBF) of volume 10 mg/mL. The samples were incubated at 37 °C under sterile conditions by changing the SBF solution every 3 days in order to avoid the effect of a decrease in cationic concentration in the SBF solution, which otherwise may decrease the ease of hydroxyapatite formation. After the required interval of time, the samples were removed, washed with Milli-Q water thrice and lyophilized. They were further characterized using FTIR, XRD, SEM and BET analysis.

2.3.9. Brunauer–Emmett–Teller (BET) analysis

The porosity textural properties of various lyophilized hydrogel samples were evaluated using BET based nitrogen adsorption and desorption techniques. The adsorption-desorption isotherm was analyzed using nitrogen as adsorptive gas (N_2, cross-sectional area 0.162 nm^2) at −196 °C (Quantachrome Autosorb-1C TCD analyzer, Model ASICX-TCD6). As per the standard BET protocol, before analysis, the sample was degassed under vacuum at 200 °C for 6 h. The surface area and pore-size distribution were determined using the Brunauer–Emmett–Teller (BET) equation on the nitrogen adsorption data and Barret–Joyner–Halenda (BJH) method applied to the desorption branch of the isotherm, respectively.

2.3.10. Drug entrapment analysis

To estimate the percentage AmB entrapment efficiency in CPCa and CPBG series, equal-sized hydrogel samples (1 cm dia. and 1 cm thick) were crushed, weighed, suspended in water for 24 h, centrifuged and subjected to quantitative analysis using UV–vis spectrophotometer (Agilent Technologies Carry 300 UV–vis) to determine the change in the absorbance at a characteristic wavelength of 320 nm as per the procedure described by Hudson et al. [32]. Experiments were conducted in triplicates and the entrapment efficiency was calculated as follows

$$\text{Drug entrapment efficiency } (\%) = \frac{\text{Actual drug content}}{\text{Total drug content}} \times 100 \quad (1)$$

2.3.11. Drug release kinetics

To determine AmB release kinetics [32], as representative samples CPCa_25_Amp and CPBG_25_Amp hydrogels (1 cm diameter and 1 cm thick) were immersed in 10 mg/mL of SBF. Immersed samples in SBF solution were shaken at 80 rpm in a water shaker bath at 37 °C. Further, at pre-determined intervals, 1 mL of solution was taken out and subjected to quantitative analysis by UV–visible Spectroscopy to determine the release content of AmB drug in SBF at a characteristic wavelength of 320 nm. Further, the released amount of AmB was determined by comparing the absorbance value with the previously plotted dilution series calibration curve. Finally, cumulative drug released percentage against time was plotted. Experiments were conducted with required volume corrections and in triplicates. Further, the drug release mechanism was analyzed for the sample along with kinetics using various drug release models as described in ESI S2.

2.3.12. Cell studies

Biocompatibility of the drug (AmB) loaded hydrogels under study were evaluated against both human osteoblast like osteosarcoma (U2OS) and keratinocyte (HaCaT) cell lines. The cellular viability was monitored through both 3-(4,5-dimethylthiazol-2-yl)-2,5-diphenyl tetrazolium bromide (MTT) and Lactate dehydrogenase (LDH) assay after 24 h. While the cellular proliferation ability of the U2OS cells were explored in the 3D cell culture construct of the CPBG_25 hydrogel. The detailed procedure can be found in ESI S3.

2.3.13. Antifungal susceptibility tests

The fungicidal properties of AmB loaded various hydrogels were studied against *Candida albicans*. Herein, disk diffusion assay (AATCC-30) was carried out by placing a drug-loaded hydrogel pellet into the well present in the middle of the agar plates of considered fungal strain culture. The plates were then incubated for 24 h at 37 °C and then observed for the zone of inhibition. Experiments were conducted in triplicates along with appropriate controls.

3. Results and discussion

3.1. Interaction studies

It is important to understand the interaction of collagen with pectin before discussing the details of hydrogel characterization. The relative biopolymer content is an important parameter that affects the complexation mechanism so the degree of associative interaction between the two biopolymers was evaluated as function of the biopolymer content through turbidity test. Turbidity is directly proportional to concentration (number density of particles) of solutes present in the solution, interparticle interaction, and their conformation. In a typical experiment,

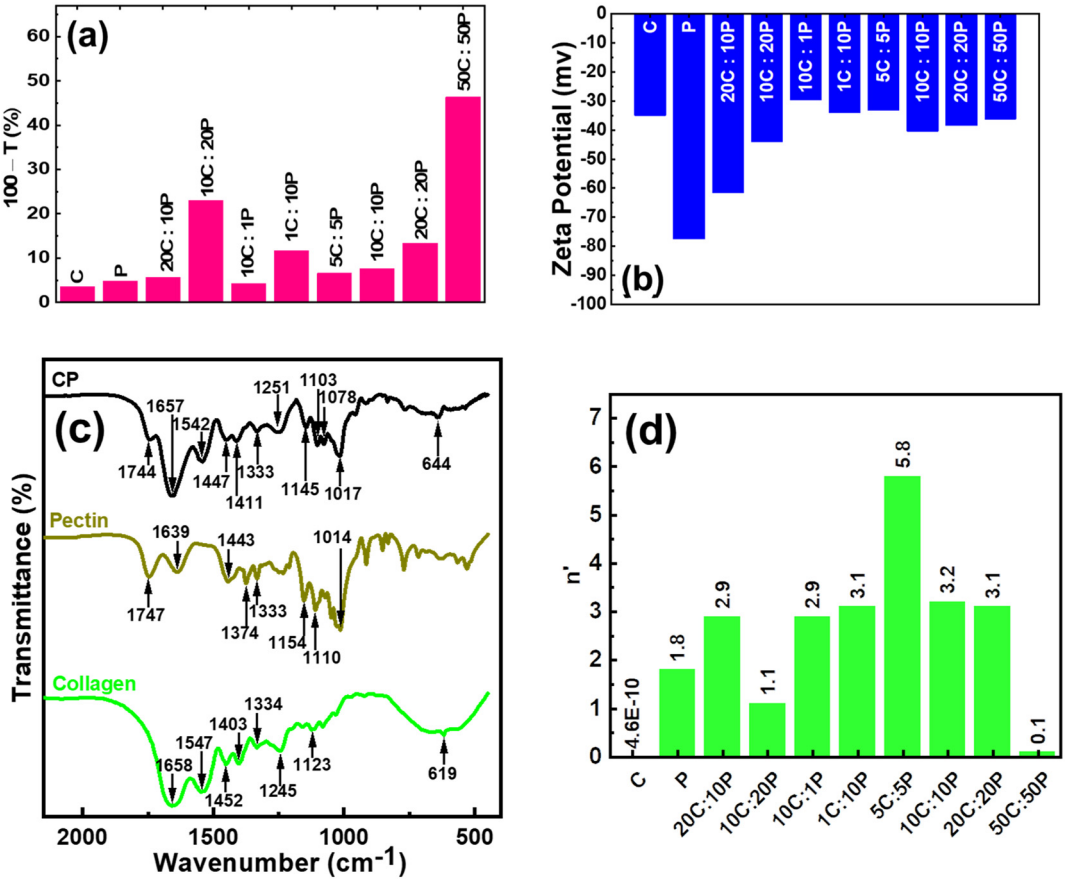

Fig. 1. (a) Turbidity measurement and (b) zeta potential measurement for various compositions of collagen/pectin mixture in Trizma buffer (10 mM, pH-8.0) (c) FTIR spectra for lyophilized collagen (C), pectin (P) and collagen/pectin (CP) blend. (d) The frequency dependence data fitted to the stress relaxation power law function, $G'(\omega) \approx \omega^{n'}$ where $0 < n' < 1$ reflects the gel behavior. The value of n′ close to 0 for the collagen and pectin in 1:1 ratio with 50 mg/mL each, implied the gel nature of the system.

the turbidity value was found to increase with the concentration of collagen and pectin in 1:1 (v/v) mixing ratio sample (Fig. 1a). Higher turbidity value for samples at this mixing ratio indicated dominant interaction between the two biopolymers that promoted complexation. Corresponding zeta potential measurements (Fig. 1b) revealed least negative values for these samples.

As per the well-known protein-polysaccharide interaction phenomena, since collagen and pectin both carry the same net charge they are considered as non-interacting biopolymers [33]. However, interestingly, in the present investigation regardless of same charge polarity, these biopolymers formed a single phase by self-organizing in the medium with the help of existing physical forces in a milieu of electrostatic repulsion. Recently, there are reports of stable soft matter synthesized with biopolymers of same polarity [13], which showed remarkable tenability in their physical properties. This is another case of same family. These physical forces could be any or a combination of the following: excluded volume, hydrogen bonding, hydrophobic, ion-bridging, van der Waals interactions *etc.* as proposed by Dickinson [33]. A lesser known interaction, called the surface selective patch binding, has been shown to be responsible in the formation of inter-polymer complexes [34]. A clear manifestation of this is noticed in the 50C:50P sample that showed maximum turbidity and minimum zeta potential (Fig. 1a and b). Since pectin is a polyanionic biopolymer, and collagen is a polyampholyte, the positively charged patches on collagen will selectively bind to the negatively charged segments of pectin overcoming the inter-segment like-charge repulsion. This is facilitated by the heterogeneous charge distribution on collagen. Many proteins have shown binding with same polarity polyelectrolytes through this interaction protocol [13]. The recorded FTIR spectra (Fig. 1c) of collagen (C) [11] and pectin (P) [9] are consistent with the literature data. In the collagen-pectin (CP) sample, the characteristic —C=O stretching of pectin appeared as a small shoulder at 1744 cm^{-1} whereas, peaks ascribed to amide I of collagen at 1658 cm^{-1} and carboxylate group ($—COO^-$) of pectin at 1639 cm^{-1} overlapped at 1657 cm^{-1} as a strong and sharp peak in the spectrum. Amide II bond of collagen at 1547 cm^{-1} appeared at 1542 cm^{-1}. The $—COO^-$ symmetrical stretching observed at 1442 cm^{-1} and 1403 cm^{-1} for collagen was noticed at 1411 cm^{-1} in the case of CP sample. Amide III of pure collagen was seen at 1245 cm^{-1}, which shifted to 1251 cm^{-1} for the CP sample. The above mentioned changes in FTIR footprint of the characteristic functional groups clearly indicate the existence of inter-polymer binding in the CP samples. These results confirmed collagen and pectin molecules existed as a hybrid complex prior to the formation of a stable hydrogel.

3.2. Rheological studies on collagen/pectin sol

Rheology measurements were performed to probe the viscoelastic properties of the sol pre-formed biopolymer blends (ESI Table S1) as a function of the mixing ratio. In the isothermal frequency sweep studies, the dispersion behavior of the in-phase (G′, storage) and out-of-phase (G″, loss) modulus were observed at a constant oscillatory stress. This frequency dependence data was fitted to the stress relaxation power-law function given by $G'(\omega) \sim \omega^{n'}$, where $0 < n' < 1$ is considered as the reflection of the viscoelastic nature of the gel [35]. The variation in the value of n' with change in the mixing ratio of collagen and pectin depicted (Fig. 1d) that collagen and pectin in the ratio of 1:1 (50 mg/mL each) possessed best gel forming ability. Hence, this particular composition was used to make a series of following hydrogels. A

control hydrogel series-I (CPCa) named after the respective Ca^{2+} crosslinker content as CPCa_25, CPCa_50, CPCa_75, CPCa_100 (Table 1), and a hydrogel series II (CPBG) containing bioactive glass (BG) designated as CPBG_25, CPBG_50, CPBG_75, and CPBG_100 (Table 2) as per the concentration of BG precursors, were prepared and used. The corresponding hydrogels loaded with amphotericin-B (AmB) were named as CPCa_25_AmB, CPCa_50_AmB, CPCa_75_AmB, CPCa_100_AmB, CPBG_25_AmB, CPBG_50_AmB, CPBG_75_AmB and CPBG_100_AmB.

3.3. FTIR analysis

Functional group analysis on various control and composite hydrogels was performed using FTIR. Interestingly, in CPCa_100 (Fig. 2a) amide I peak appeared at the higher wavenumber of 1675 cm^{-1} compared to CP sol (1657 cm^{-1}) evidencing chemical interaction between C═O and Ca^{2+} ions [36], as well as amide II of CP sol at 1542 cm^{-1} slightly shifted to the higher wavenumber at 1555 cm^{-1}. Peaks attributed to $-COO^-$ symmetrical stretching at 1411 cm^{-1} and 1447 cm^{-1} of CP sample merged with higher intensity and appeared at 1420 cm^{-1} for CPCa_100. Amide III Peak of CP at 1251 cm^{-1} shifted to a lower wavenumber at 1239 cm^{-1} in the case of CPCa_100. Here again, the changes observed in the characteristic frequencies of CPCa_100 is attributed to inter as well as intramolecular physical forces. In the case of CPBG_100, the intensity of amide I peak decreased and centered around 1652 cm^{-1} and the amide II band were seen at 1565 cm^{-1} compared to CPCa_100. $-COO^-$ symmetrical stretching at 1420 cm^{-1} of CPCa got split as a triplet (1475 cm^{-1}, 1447 cm^{-1} and 1413 cm^{-1} respectively) indicating chemical interaction with the added inorganic components. It is pertinent to highlight that the existence of the characteristic bioglass peaks [37–39] such as at 1342 cm-1 (P═O), 1102 cm^{-1} (Si—O—C), 1024 cm^{-1} (P—O—C, Si—O, P═O, Si—O—Si), 470 cm^{-1} (Si—O—Si) in the FTIR spectrum of CPBG_100 confirm the *in-situ* mineralization of bioglass in the hydrogel matrix. In addition, it is interesting to note that with the increase in the concentration of crosslinker in CP matrix, amide I band at 1655 cm^{-1} of CPCa_25 gradually shifted towards the higher wavenumber and finally appeared at 1675 cm^{-1} in the case of CPCa_100 sample (ESI Fig. S1a).

Similarly, in the case of CPBG (ESI Fig. S1b) as bioglass precursor concentration increases, the peak corresponds to $-COO^-$ symmetrical stretching observed at 1413 cm^{-1} in the case of CPBG_25 got split as a triplet namely at 1475 cm^{-1}, 1447 cm^{-1} and 1413 cm^{-1} for CPBG_100 signifying chemical interaction with the bioglass precursors. Once again, the intensity of the peak corresponding to Si—O—Si at 465 cm^{-1} increased with the concentration of bioglass precursors. It is noteworthy that peak corresponding to Si—O—C at 1102 cm^{-1} appeared uniquely in the CPBG_100 spectrum compared to the FTIR spectra of CP and CPCa_100.

3.4. TGA analysis

A comparative study on the thermal stability of CP, CPCa and CPBG series (Fig. 2b and ESI Fig. S3) demonstrated multiphase degradation behavior of the samples under investigation. In general, some initial weight loss occurred for all samples up to 135 °C due to the evaporation of bound water. The main decomposition of the backbone chains occurred above 135 °C due to breaking of protein chain and peptide bond [40]. CP blend starts to degrade at 152 °C and showed the lowest residual weight *i.e.*, 10.8 wt% among various CPCa and CPBG samples. In summary, compared to CPCa series (CPCa_25 (13.5 wt%), CPCa_50 (25.1 wt%), CPCa_75 (31.4 wt%) and CPCa_100 (35.7 wt%)), CPBG series samples showed degradation above 195 °C, and showed higher residual weights for CPBG_25, CPBG_50, CPBG_75, and CPBG_100 samples *i.e.* 18 wt%, 24.7 wt%, 39.2 wt%, 44.8 wt% respectively (ESI Fig. S3). This result clearly indicates the improved thermal stability of the CP hydrogels after cross-linking with calcium ions (referred as CPCa hydrogels) and *in-situ* mineralization of bioglass particles in the CPBG matrix. Therefore, it is necessary to realize that bioglass particles played the role of (pseudo-) crosslinkers by strategically locating themselves at the junctions of the network, which reinforced mechanical strength of the hydrogel.

3.5. Morphological studies

SEM micrographs of lyophilized hydrogel CPCa and CPBG series are depicted in Fig. 3a–h. In general, SEM images of both CPCa and CPBG samples show porous rough surface structure. Interestingly, pore size determination carried out on the SEM images of hydrogels using ImageJ analysis (ESI Fig. S4) indicated a decrease in mean pore diameter from 31.3 to 10.2 μm for CPCa with an increase in Ca^{2+} concentration. Shrinkage in pore size could be attributed to the increase in crosslinking density of Ca^{2+} ions within the matrix. A similar trend was also observed for CPBG samples, for which pore size decreased from 47.8 to 2.6 μm with increase in the concentration of BG precursor. Importantly, existence of the porous morphology indicated presence of a large amount of water before lyophilization, which is the characteristic nature of a

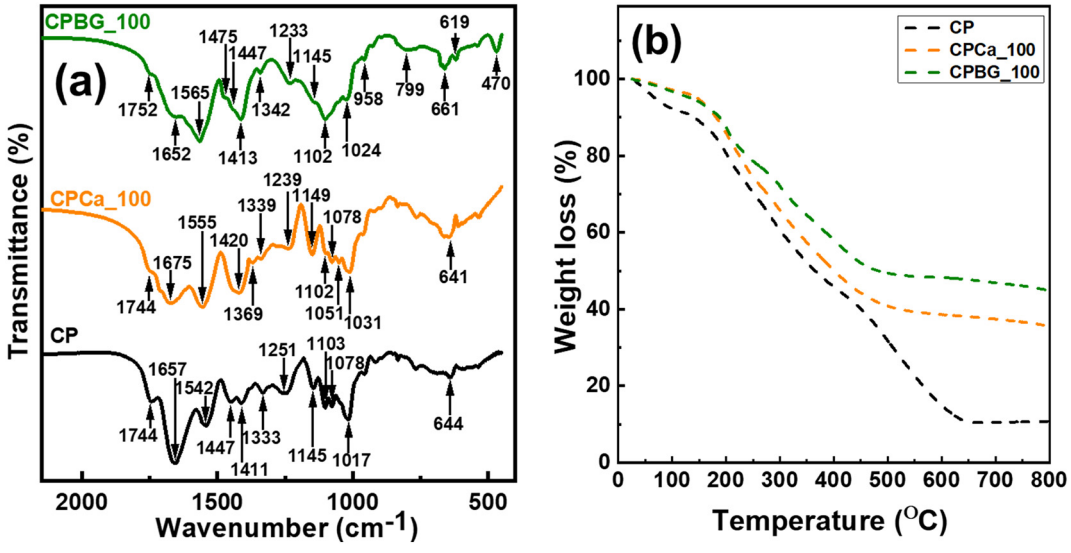

Fig. 2. (a) FTIR spectra and (b) Thermogravimetric analysis of CP, CPCa_100 and CPBG_100.

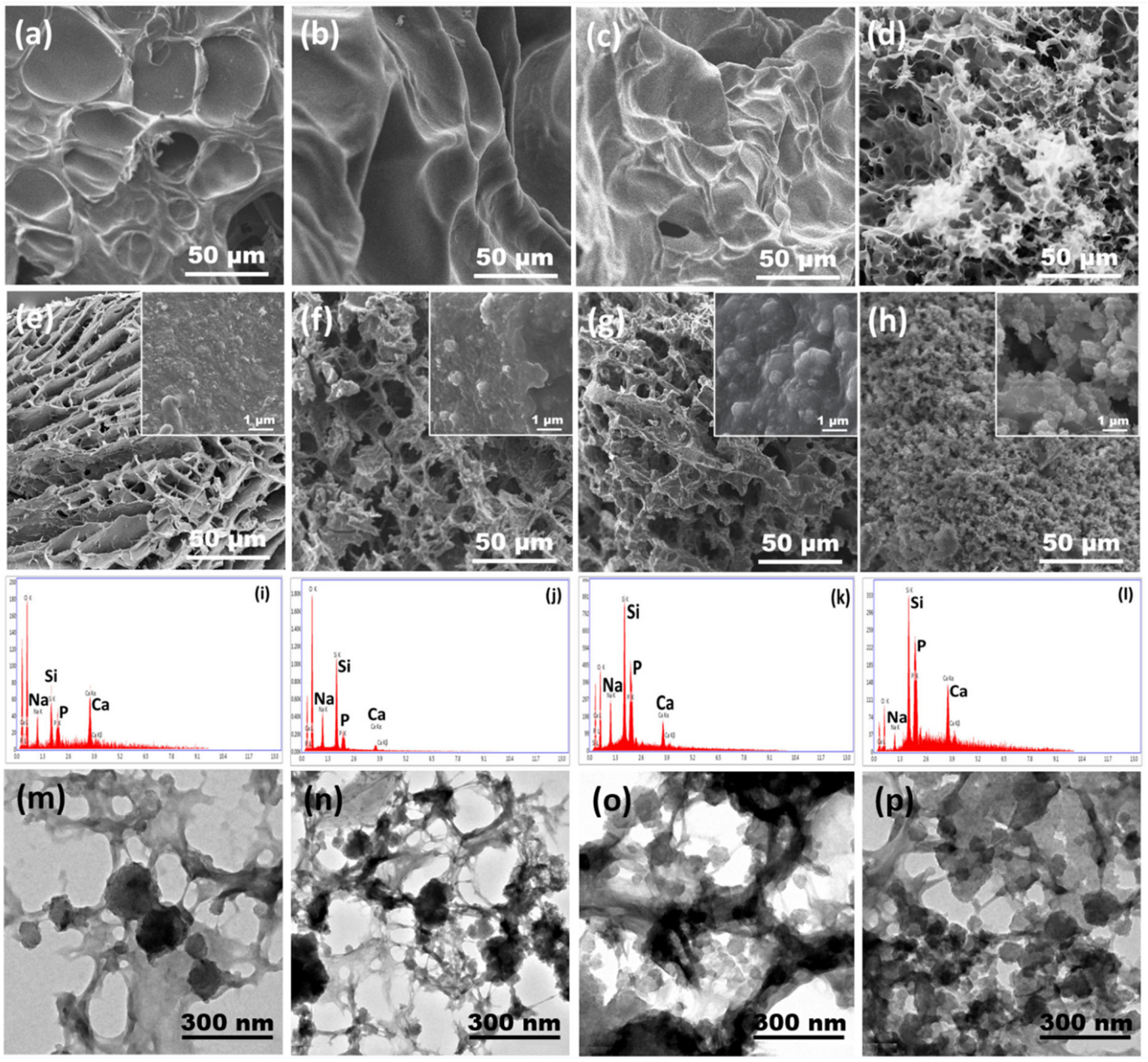

Fig. 3. SEM images of (a) CPCa_25, (b) CPCa_50, (c) CPCa_75, (d) CPCa_100, (e) CPBG_25, (f) CPBG_50, (g) CPBG_75 and (h) CPBG_100 at 250× (inset in fig. (e)–(h) shows corresponding BG particles in hydrogel at 15k×). SEM-EDAX spectra of (i) CPBG_25, (j) CPBG_50, (k) CPBG_75 and (l) CPBG_100. TEM images of (m) CPBG_25, (n) CPBG_50, (o) CPBG_75 and (p) CPBG_100.

hydrogel. Further, at higher magnification (15k×) assorted dense globular structures of various size embedded throughout the hydrogel matrix (Fig. 3e–h inset) were visualized. The mean pore size of CPCa hydrogels were smaller than those of CPBG hydrogels except for CPCa_100 (10.2 μm) and CP_BG 100 (2.6 μm) (ESI Fig. S4) samples. In the case of CPCa, Ca^{2+} ions are crosslinkers whereas in CPBG series Ca^{2+} containing BG nano-particles are the crosslinkers, which function as a multiple inorganic binding sites in CP matrix and hence provides larger pore size to CPBG series. However, the reported smaller pore size of CPBG_100 compared to CPCa_100 is attributed to multiple crosslinking sites provided by the largest number of smallest BG particles mineralized in the hydrogel matrix (Fig. 3h). The pseudo-crosslinking attribute of bioglass nanoparticles is clearly manifested here. Interestingly, EDAX spectra (Fig. 3i–l) revealed the existence of Si, P, Na, and Ca elements on these globular structures. These observations confirmed mineralization of bioglass particles in the CP matrix due to the interaction between BG precursors and CP matrix; in good agreement with the findings of FTIR spectra (Fig. 2a). Due to the bioglass mineralization, the surface of CPBG hydrogel samples was rough in comparison to their corresponding control sample. It is also pertinent to note that with an increase in BG precursor concentration, the distribution of BG particles increased in the hydrogel matrix making these more homogenous (Fig. 3e–h inset). Similar to SEM micrographs of CPBG hydrogels (Fig. 3e–h), TEM micrographs of CPBG hydrogels (Fig. 3m–p) confirmed the porous structure of the hydrogel containing higher number of bioglass particles for the CPBG_25 to CPBG_100. Interestingly, a decrease in BG particle size (94.3 to 45.5 nm) was reported by ImageJ analysis (ESI Fig. S5) of TEM micrographs with increase in the amount of BG precursors. This observation indicates that as the concentration of BG precursors increases, a higher number of nucleation sites

are generated and consequently, an increase in the number of BG particles with the corresponding decrease in their particle size was facilitated.

3.6. Swelling studies and kinetic analysis

The swelling ability of dried hydrogel samples for both CPCa and CPBG series were monitored in SBF buffer owing to evaluation of their application in tissue engineering (Fig. 4, ESI Table S2 and Fig. S6).

Significantly, Ca^{2+} ions act as a crosslinker for collagen and pectin molecules during the formation of both CPCa and CPBG hydrogel series. In CPBG series, Ca^{2+} ions also participate as one of the precursors for the *in-situ* bioactive glass mineralization in the hydrogel network in addition to crosslinking. Swelling ratio for both the hydrogel systems showed inverse proportionality to crosslinker density.

Noticeably, crosslinking also influenced both the molecular structure and swelling properties of the hydrogel system. As the crosslinker density increases, the hydrogel network becomes stiffer and compact as well as the pore size becomes smaller, and a drop in swelling was recorded. These results are in line with the reported morphology studies (Fig. 3). Interestingly, highest swelling ratio of CPCa_25 (mean pore size 31.3 μm) was reported as compared to the CPBG_25 sample (mean pore size 47.8 μm).

It might be attributed to the mineralization induced stiffness in the CPBG_25 that hindered the polymeric chain mobilization and stretching enough to hold greater amount of buffer thereby, decreasing the swelling capacity. In addition, the decrease in the swelling capacity of CPCa hydrogels in SBF with increasing crosslinker concentration could also be due to development of osmotic pressure caused by the unequal distribution of various ions in the SBF medium and the hydrogel network. It may be noted that ions attached to the hydrogel network are partly immobile and considered to be separated from the external solution through a semi-permeable membrane [41]. Within the polymeric gel network, the development of osmotic pressure is much lower, when the difference of counter ions in the gel phase and SBF solution increases. On the other hand, with the increase in concentration of crosslinker in hydrogel matrix, the difference between the concentration of counter ions in the gel and solution phase decreases, thus causing a decrease in the equilibrium solvent uptake of hydrogel sample (ESI Table S2). For the CPBG series, comprised of polymeric network and *in-situ* mineralized BG that consist of various inorganic ions. Here, difference in the concentration of counter ions in the gel and solution phase is relatively less, therefore, a drastic decrease in equilibrium buffer content (EBC %) is observed in comparison to CPCa sample series. It also accounted for the drastic reduction in the swelling ability, as observed through swelling kinetics analysis of the hydrogel (CPBG) using second-order equation (phenomenological model, ESI Eq. (3)). The t/S_{eq} *versus* t graph reflected the decrease in the values of initial swelling rate (r_0), the swelling rate (k_s), and degree of swelling equilibrium (S_{eq}) with the increase in crosslinker concentration (ESI Table S2 and Fig. S6).

Based on previous findings analysis of swelling ability mechanisms of both the hydrogel series could be characterized either by Fick's second law or by a more advanced equation of anomalous diffusion [41]. Power-law (ESI Eq. (5)) was used to determine the nature of solvent diffusion into the hydrogel and a straight line was obtained by plotting ln (F) *versus* ln(t) for the initial stages of swelling (60%), shown in ESI Fig. S6a, c. The slope of this line displays swelling exponent 'n' and its intercept gives swelling constant 'k', tabulated in ESI Table S2. The 'n' value is correlated with mechanism that drives the diffusion process and its values for CPCa and CPBG series, was found between 0.44 and 0.55 close to what is expected for Fickian diffusion. In the case of Fickian diffusion, the polymer chains have a higher mobility and the solvent penetrates easily into the gel matrix, and the solvent diffusion rate is clearly slower than the polymer chain relaxation rate. Here equilibrium is attained linearly with the square-root of time (t). For anomalous diffusion, the polymer chains are not sufficiently mobile to permit diffusion of solvent into the gel core since both diffusion and polymer chain relaxation rate are comparable with equilibrium approaching with t^{n-1} time-dependence [42]. The diffusion constant 'k' decay markedly from 0.66 to 0.37 in CPCa, and 0.45 to 0.04 in CPBG series with increasing crosslinker concentration. The diffusion coefficients (D) given in ESI Table S2 were calculated from ESI Eqs. (5)–(6). For the same measurement conditions in all hydrogel systems, yield remarkably consistent D values in the range of 10^{-5} to 10^{-6} cm^2/s, an optimum range for the biomedical application of the hydrogel system [43]. It is accepted that physical entanglement of the collagen-pectin hybrid chains with the inorganic silica network of bioactive glass provided cohesive nature to the hydrogel system and significantly improved structural integrity of the hydrogel and decreased stress relaxation. This helped in enhancing its ability to withstand the osmotic pressure for longer duration (ESI Fig. S6) particularly, in case of CPBG_25 gel. The hydrogel disintegration studies carried out on CPCa_25 and CPBG_25 (ESI Fig. S7) revealed a steep rise in percentage dispersion of CPCa_25. Whereas, dispersion of CPBG_25 is slow compared to CPCa_25 due to the multi-centered crosslinking nature of BG particles. The maximum disintegration of CPCa_25 (100%) and CPBG_25 (80%) was observed on day 7 and day 15 respectively.

3.7. Rheological analysis

Although the value of G′ (ω) and G″ (ω) was found to be quite low reflecting the fragile nature of the collagen/pectin blend in 1:1 ratio at 50 mg/mL each however, it possessed gel forming ability among others (Fig. 1d). These were considered further for evaluating the effect of

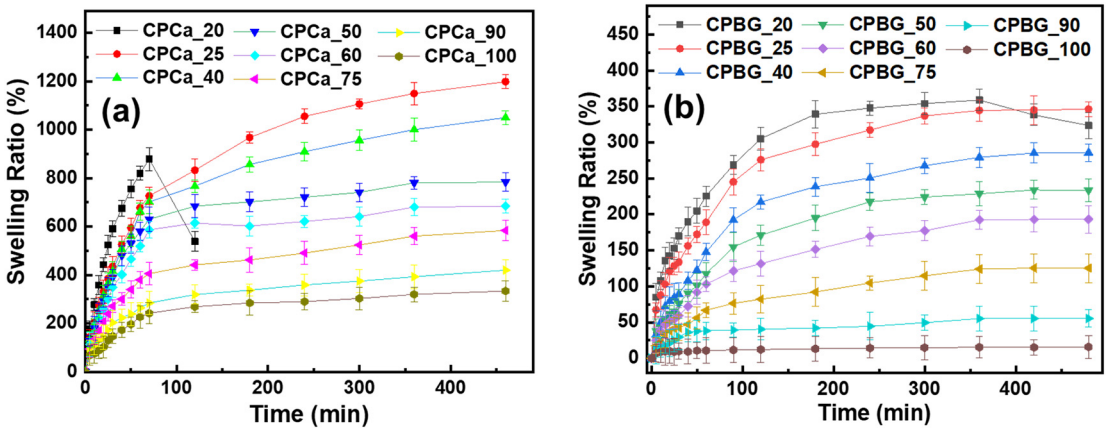

Fig. 4. Swelling studies up to 8 h in simulated body fluid on (a) control hydrogels, (b) hydrogels containing *in-situ* mineralized bioactive glass particles.

calcium crosslinker and as a template for the *in-situ* mineralization of bioactive glass. Evidence of the formation of solid like network (CPCa_25) was observed which showed G′ > G″ over the entire frequency range (ESI Fig. S8) confirming elastic response of the CP hydrogel with high storage modulus. The increase in mechanical strength of the gel phase after crosslinking in the CP hydrogel implied the existence of a well-formed network structure. The value of n' for CPBG_25 after the *in-situ* mineralization of bioactive glass revealed gain in elasticity corresponding to control CPCa_25 hydrogel, thus suitable for the load bearing applications. Therefore, bioglass particles do play the role of pseudo-crosslinkers by positioning them at the junction zones. It could also be justified on the basis of the presence of silica inorganic polymeric structure incorporation into biopolymeric hydrogel network of CPBG_25. Moreover, tan delta was found to be invariant of frequency (ESI Fig. S8), which clearly implies the uniformity of energy dissipation at all deformations, which is a clear indication of sample homogeneity in agreement with SEM (Fig. 3e).

3.8. Hydrogel formation mechanisms

Unlike the usual attraction of opposite charges, interaction between selective portions of two different macromolecules carrying similar net polarity is gaining momentum in the synthesis of potential novel materials. Herein, the formation of such inter-macromolecular aggregates purely depends on various physical environments around these polymer chains in the solution such as solution pH, ionic strength, temperature, polymer charge density and polymer mixing ratio. In the present work, we report one such type of interaction between collagen

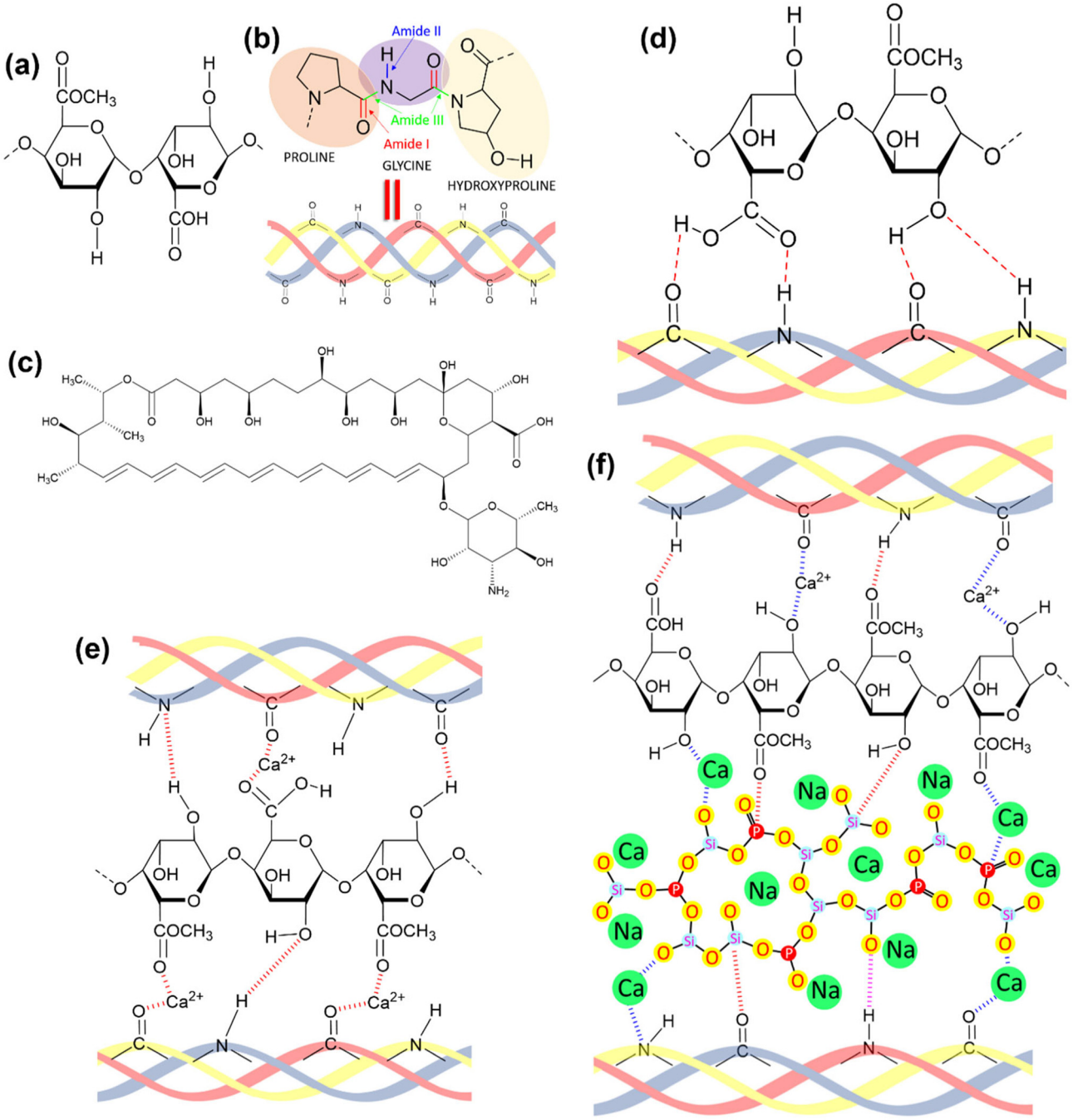

Scheme 2. Schematic representation of representative structure of (a) pectin, (b) collagen and (c) amphotericin-B (AmB), (d) surface patch binding of collagen and pectin, (c) calcium crosslinked interaction between collagen and pectin (CPCa) and (d) *in-situ* mineralization of bioglass particles showing multicentered crosslinking between collagen and pectin.

and pectin (Scheme 2d) that regardless of similar net negative charges, bind to each other and forms complex gel. The complexation of pectin and collagen was noted at 1:1 mixing ratio at pH 7 as evidenced by highest turbidity (50%) and least zeta potential values (−39 mV) (Fig. 1a and b) compared to respective individual solutions. Precisely, interaction of these macromolecules is evidenced by FTIR (Fig. 1c) through amide I, amide II and amide III of collagen and $-COO^-$ and —OH groups of pectin by physical forces (Scheme 2a–b). In detail, pectin (Scheme 2a), a polysaccharide is a strong polyelectrolyte, whereas collagen (Scheme 2b), a protein is polyampholyte. When two of these biopolymers are associating, regardless of similar charge/polarity, the protein partner collagen being a polyampholyte containing positive and negative patches expose its positively charged patches and associates with pectin molecules. Although there is a same polarity repulsion while the positive surface patches will attract the negatively charged segment of its binding partner and then result in localized contact and localized electrostatic attraction. The resulted phenomenon is called as surface patch binding (SPB) as demonstrated by Bohidar et al. [13]. Further, the addition of crosslinker (Ca^{2+}) to the collagen-pectin (CP) system strengthens their association through chemical interaction between —C=O as well as $-COO^-$ groups of CP system and Ca^{2+} ions (Scheme 2e) in addition to the physical forces. As a result, the growth of insoluble macromolecular aggregates (complex coacervation) increases with entrapping water molecules leading to hydrogel (CPCa) formation. It is worthy to note that in another class of soft matter (coacervation) interpolymer complex formation is shown to be governed by surface patch binding mechanism in polymers of same polarity. To this end, in CPBG system, addition of BG precursors in CP system not only enhances complex formation through chemical interaction, but also result in *in-situ* mineralization of BG nanoparticles as evidenced from the FTIR spectra of CPBG_100 (Scheme 2f). It is worth mentioning that network former precursors of bioglass *i.e.* tetraethyl orthosilicate and triethyl phosphate are also negatively charged [38] so, surface patch binding phenomena facilitate in forming nucleation sites on the CP aggregates. The process further leads to tightened complexation between collagen and pectin by entrapping water molecules in the interstitial space favoring the formation of a pervading network structure.

3.9. Bioactivity test

Detailed structural analysis revealed that CPBG_25 possessed an adequate mechanical strength and pore size for cell attachment as well as oxygen and nutrient transport, therefore chosen for the biological response studies. Bioactivity of CPBG_25 in SBF was monitored over 30 days by XRD, FTIR and SEM (Fig. 5a–f). Interestingly, on immersion in SBF (Fig. 5a) broad hump in the XRD spectra in the 2θ range of 15° to 30° disappeared along with the emergence of two new peaks at 31.7° and 45.5°. These new XRD peaks signaled for an interfacial activity on the hydrogel surface in contact with SBF. As the interaction time of the hydrogel with SBF prolonged to 7 days, the intensity of the above newly emerged peaks at 24 h increased and further, many new peaks were noticed after 30 days. The observed reflections in the corresponding spectra are in good agreement with the JCPDS file no. 01-072-1243, which reveals that the formed microcrystals on the surface of CPBG_25 after interaction with SBF are of bone-like hydroxyapatite ($Ca_{10}(PO_4)_6(OH)_2$). Literature evidences a similar type of bioactive behavior in BG embedded hydrogels [44,45].

FTIR data (Fig. 5b) also supports the bioactivity of the CPBG hydrogel series by indicating the disappearance of characteristic polymer peaks with the simultaneous appearance of characteristic peaks corresponding to hydroxyapatite during interaction with SBF. In fact, after 30 days of interaction with SBF, FTIR spectrum of CPBG_25 sample demonstrated the absence of the —C=O stretching peak at 1745 cm^{-1} and reduced intensity of the peak at 1419 cm^{-1} due to COO^- symmetrical stretching of the polymer matrix (Figs. 2a and 5b). Further, a small peak corresponding to P=O at 1329 cm^{-1}; a broad peak at 1096 cm^{-1} masked region of Si—O—C, P—O, and Si—O as well as small characteristic peak at 800 cm^{-1} due to the ring structure of silicate network appeared [30,37–39]. Importantly, a reported intensive peak at 471 cm^{-1} after 30 days interaction with SBF represents the phosphate ion [30,37–39] compared to 0 to 7 days interaction with SBF. These observations strongly support the XRD spectra obtained after 30 days of interaction of CPBG_25 sample with SBF solution and confirmed the hydroxyapatite formation. Further, SEM micrographs (Fig. 5c–d, ESI Fig. S9) showed the appearance of a few hydroxyapatite crystals on the hydrogel surface after 1 day of interaction with SBF (ESI Fig. S9a). Interestingly, further soaking the hydrogel for 7 days and 30 days showed an increase in the aggregation of the microcrystals covering a larger surface area (Fig. 5d, ESI Fig. S9b). These morphological analyses are in line with XRD and FTIR data [46,47] and confirm the bioactivity of the CPBG hydrogels.

Brunauer–Emmett–Teller (BET) analysis was carried out on CPCa_25, CPBG_25 and CPBG_25 after interaction with SBF for 7 days, as shown in Fig. 5e, ESI Fig. S10. From ESI Fig. S10, it is evident that the obtained BET isotherm of CPCa_25 belongs to type III with the H2 hysteresis loop whereas, CPBG_25 sample shows isotherm of type *V* with similar hysteresis loop (H2). These results revealed that the hydrogel cross-linked with only Ca^{2+} ions were of narrow and wide sectional interconnected macropores. On the other hand, the hydrogel obtained after the *in-situ* mineralization of bioglass (CPBG_25) contained interconnected mesopores. Herein, the observed difference in porosity of CPCa_25 and CPBG_25 is mainly due to the BG nanoparticle content of CPBG_25. Interestingly, a reported decrease in BET pore volume (Fig. 5e) and pore diameter with an increase in surface area of CPBG_25 compared to CPCa_25 is due to the BG mineralization in collagen/pectin hydrogel matrix. These observations are also consistent with FTIR, SEM and TEM results (Figs. 2–3). In the case of CPBG_25 after interaction with SBF for 7 days, the pore volume and pore diameter increase whereas the surface area decreases. This is due to the bioactivity of BG particles present in the CP matrix as well as its simultaneous swelling activity in SBF solution as evidenced by SEM (Fig. 5c–d, ESI Fig. S9).

3.10. Drug release studies

The amphotericin-B (AmB) encapsulation efficiency of the hydrogel CPBG_25 was found to be 81.2% and the corresponding drug release profile was analyzed based on the reported encapsulation efficiency. The initial phase of AmB release (Fig. 6a) showed a burst release of 32.5% in the first 10 min due to drug dissolution from the hydrogel surface. Such type of reported AmB release behavior from CPBG_25 is known to provide immediate relief at the initial stages of healing treatment due to the high content of drug release [8]. After 10 min, the drug release profile becomes gradual up to 360 min. Here, the duration of gradual drug release was observed to be equal to the time taken for complete swelling of the hydrogel (Fig. 4b). After 360 min the AmB release becomes constant (88%) for 24 h. The reported drug release behavior shows that release of AmB from hydrogel is proportional to the swelling behavior of the hydrogel and favors Fickian diffusion release mechanism.

Further, the drug release mechanism and its kinetics were analyzed by fitting the obtained drug release data with various existing mathematical modellings as shown in ESI Fig. S11. Out of various correlation coefficients (r^2) obtained, the highest correlation value was observed in the case of Peppas model, which describes the drug release from a polymeric system. The observed n value in our case is 0.29 which is lower than 0.5 and corresponds to the Fickian diffusion release mechanism in which solvent penetration is the rate-limiting step [48].

3.11. Antifungal studies

Antifungal activity of various hydrogels was evaluated by disk diffusion assay against *Candida albicans* and the zone of inhibition (Fig. 6b)

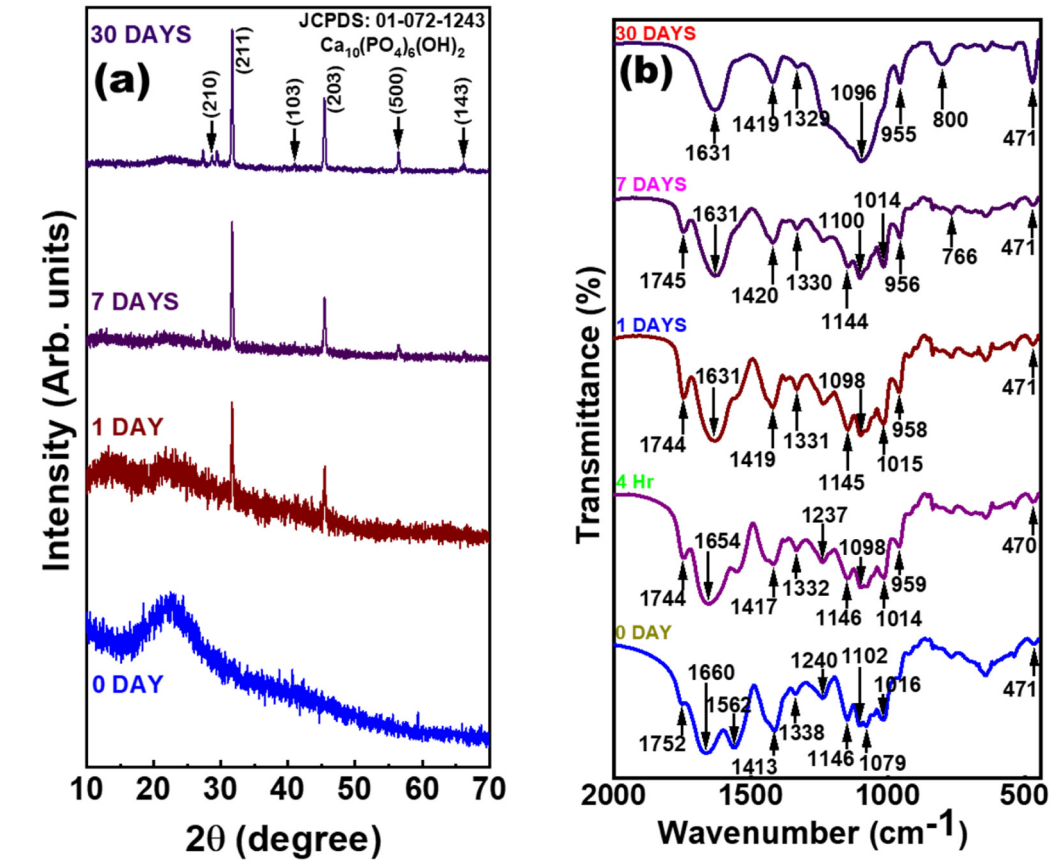

(e)

Sample	Pore Diameter (nm)	Pore Volume (ccg^{-1})	BET Surface Area (m^2g^{-1})
CPCa_25	18.8	0.091	19.44
CPBG_25	5.6	0.032	22.84
CPBG_25_HAP_7 DAYS	9.8	0.045	18.65

Fig. 5. (a) XRD spectra, (b) FTIR spectra and (c–d) SEM images (at 5k×) for CPBG_25 on interaction with SBF for (c) 0 and (d) 30 days. FTIR spectrum of CPBG_25 after 4 h interaction with SBF is also shown in (b). (e) Table shows textural parameters (pore diameter, pore volume and surface area) of hydrogels obtained after fitting the nitrogen adsorption desorption isotherm to BJH equation.

was monitored. Interestingly, in all the hydrogel samples (CPCa and CPBG) containing AmB, anti-microbial activity was reported. A positive control, pure AmB and negative controls, hydrogels (CPCa and CPBG) without AmB were used. Positive control showed 32.5 mm zone of inhibition while negative control does not give any zone of inhibition (data not shown). In the case of hydrogel samples with AmB, the reported minimum zone of inhibition was less as compared to the positive control. It can be justified based on the drug release profile of the hydrogel. Further, the minimum zone of inhibition for CPCa and CPBG decreases with the crosslinker concentration while individual comparison reflected that CPCa samples possessed slightly higher zone of inhibition than corresponding CPBG hydrogels. As the network connectivity for hydrogel samples increases (as observed in SEM images (Fig. 3)), the pore size decreases and lesser content of drug diffuse out and show lesser anti-microbial activity [49,50]. In brief, the lesser the content of BG particles or calcium the diffusion of the drug is higher and consequently resulting in a higher antifungal property. Noticeably, higher the bioglass mineralization, proportionally the crystalline hydroxyapatite formation is high that acts as a barrier in the release of drug from the hydrogel system [39]. In addition, the crosslinking ability of BG particles with the CP matrix is more substantial in comparison with Ca^{2+}, as explained in Section 3.5.

3.12. Cell culture studies. Cellular viability assay

The cellular viability of hydrogel powder samples was evaluated through MTT assay with increasing sample concentration (10 µg/mL, 50 µg/mL and 100 µg/mL) against U2OS and HaCaT cell lines for 24 h (Fig. 7a–b). In general, the cellular viability was observed above 80% for all the hydrogel samples. Importantly, the MTT assay results exhibited that the concentration of crosslinker or the content of the BG particle does not influence the viability of both the cells. Herein, untreated U2OS and HaCaT cells grown in DMEM media were considered as control with 100% cellular viability. It is pertinent to mention that the reported cellular viability by MTT assay is greater than the control (untreated), which is due to the uncertainty in the cellular proliferation for longer duration [49]. Additionally, as shown in Fig. 7c, MTT assay results are in good agreement with the LDH assay on the representative

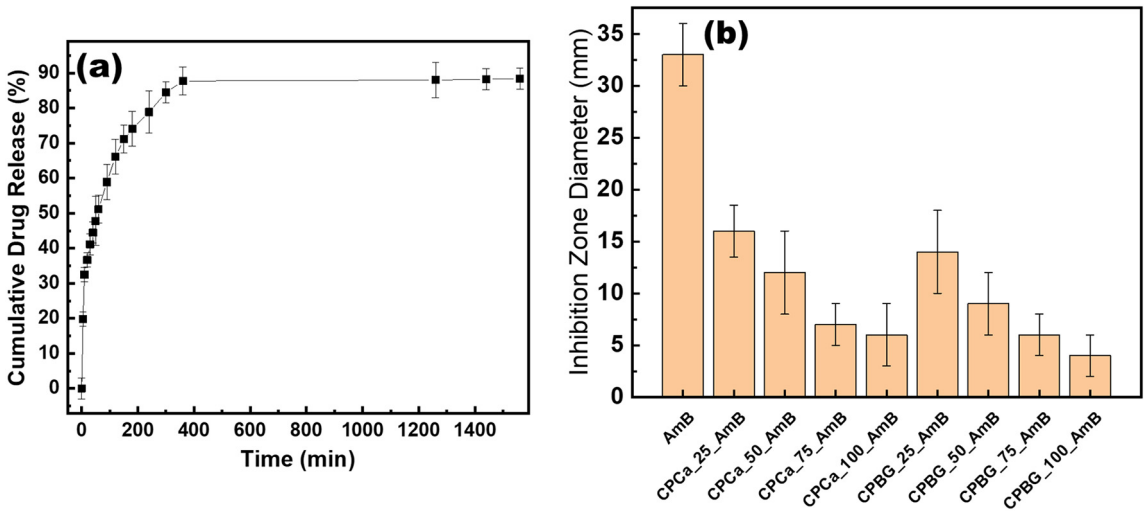

Fig. 6. (a) Cumulative drug release of amphotericin-B (AmB) from the hydrogel CPBG_25_AmB. (b) Disk diffusion assay for pure AmB (500 μg), CPCa_25_AmB, CPCa_50_AmB, CPCa_75_AmB, CPCa_100_AmB, CPBG_25_AmB, CPBG_50_AmB, CPBG_75_AmB and CPBG_100_AmB.

hydrogel CPBG_25_AmB and its corresponding control CPCa_25_AmB using U2OS and HaCaT cell lines for 24 h. Importantly, LDH assay results confirm that there is no considerable cytotoxicity imposed by both samples *i.e.* CPCa_25_AmB and CPBG_25_AmB. These findings validate the cytocompatibility of the hydrogel samples with both U2OS and HaCaT cell lines and are in good agreement with earlier reports [47,51].

3.13. FDA/PI assay

Cell viability for U2OS cells on interaction with hydrogels CPCa_25_AmB and CPBG_25_AmB was investigated by fluorescence images of FDA/PI staining for 1, 3 and 7 days (Fig. 8 and ESI Fig. S12). Initially, on day 1, most of the cells exhibited viability indicating low cytotoxicity for both the hydrogels. These results are in good agreement with MTT assay and LDH assay (Fig. 7). However, on 3rd day, only CPBG_25 showed more cell viability as compared to CPCa_25. The presence of viable cells and well-spread morphology of CPBG_25 indicates that the hydrogel can support cell adhesion due to hydroxyapatite formation (Fig. 5). In the case of CPCa_25, more inferior cell adhesion and lower cell viability might be due to relatively lower stiffness of the sample and absence of bioactivity as compared to CPBG_25 (Fig. 8) [47]. Further, at 7th day, in CPBG_25 the morphology of the cells was

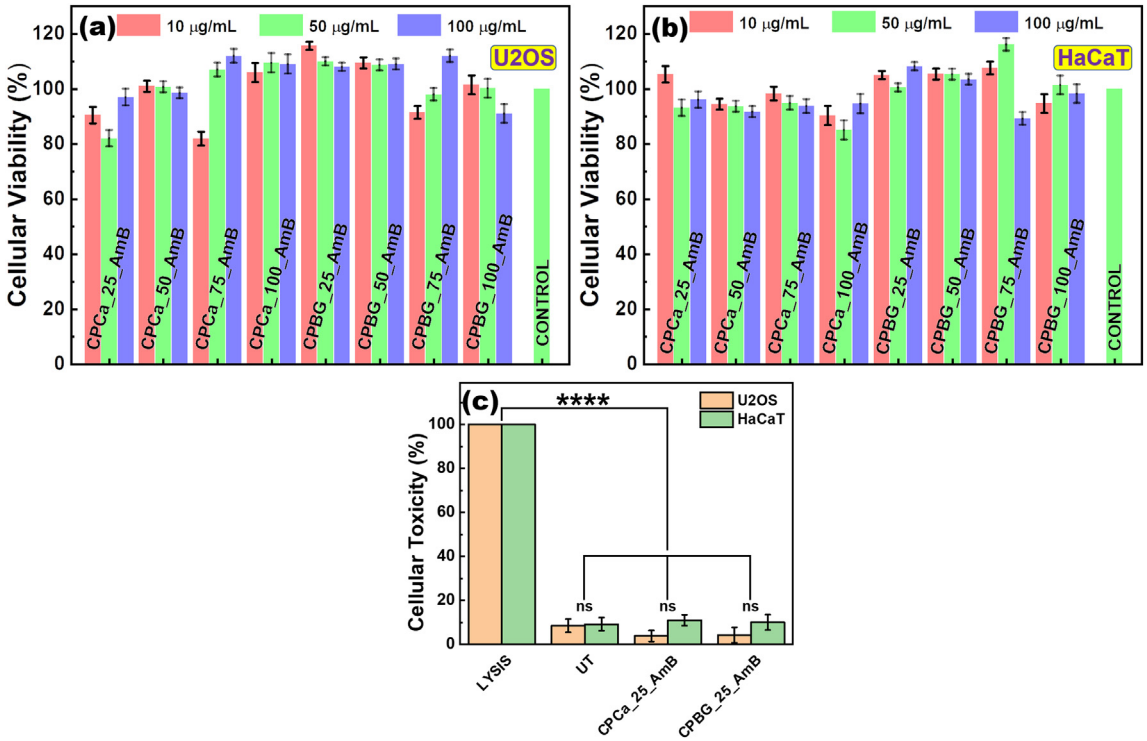

Fig. 7. Demonstration of biocompatibility for various hydrogels against U2OS and HaCaT cell lines by (a and b) MTT assay (10 μg/mL (pink), 50 μg/mL (green) and 100 μg/mL (purple)) and (c) LDH assay at 100 μg/mL sample concentration. The statistical analysis was carried out through graph pad prism 8.4.3 software using two-way ANOVA followed by Turkey's multiplicative comparison test. MTT assay of different samples on HaCaT and U2OS cell lines shows no significant cytotoxicity below or at sample concentration of 100 μg/mL ($p > 0.05$). In LDH release for various samples significant difference was assumed for $p < 0.05$, $^{****}p < 0.0001$. (For interpretation of the references to color in this figure legend, the reader is referred to the web version of this article.)

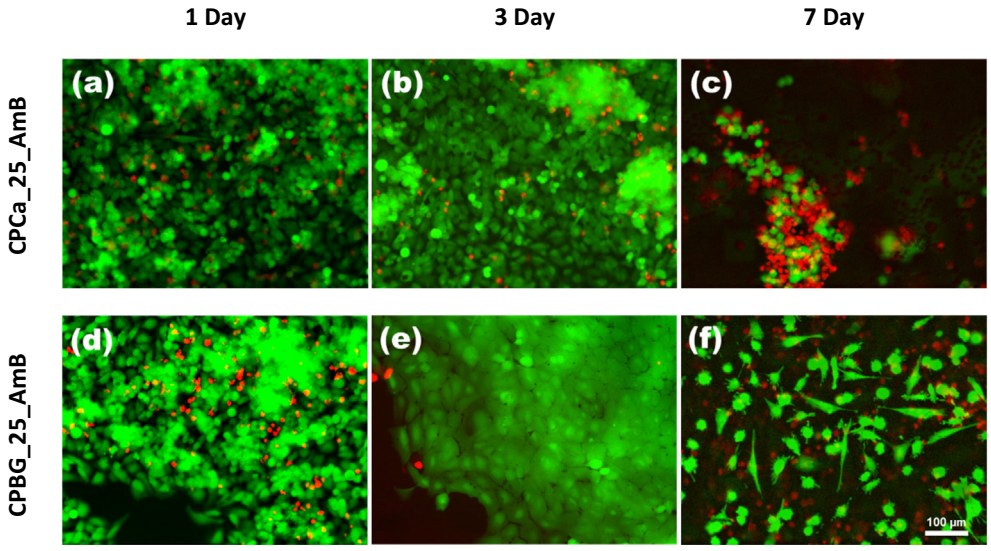

Fig. 8. Fluorescence images for cell viability analysis using fluorescein diacetate (FDA) (green)-propidium iodide (PI) (red) staining of U2OS cell cultured for 1,3 and 7 days with (a–c) CPCa_25 and (d–f) CPBG_25 hydrogels. (For interpretation of the references to color in this figure legend, the reader is referred to the web version of this article.)

highly branched due to cytoplasmic extensions, showing adhesion on the hydrogel whereas, in the case of CPCa_25, the cell viability decreases. The cytoplasmic extensions observed in CPBG_25 at the 7th day conclude that the presence of bioglass particles and the corresponding bioactivity profoundly influence the cell morphology. The observed higher U2OS cell adherence on hydrophobic hydroxyapatite layer compared to hydrophilic surfaces is well reported in literature [47,52–54]. Further in line with the *in-vitro* disintegration study (ESI Fig. S7), the lower number of cells observed on day 7 can be attributed to the disintegration of the hydrogel in media by day 7. Most cells might have dispersed and removed from wells when media was replaced every 2 days.

4. Conclusion

In this investigation, collagen-pectin based hybrid composite hydrogel containing BG nanoparticles was synthesized successfully without any external crosslinkers. The fact that, at the molecular level surface patch binding interaction between collagen and pectin, irrespective of both carrying similar net charge, favored multi-centered crosslinking that was synergetic with the additional crosslinking provided by *in-situ* mineralized BG nanoparticles, is one of the unique features of the hybrid composite hydrogel containing interconnected macropores. The Fickian swelling behavior of the macroporous hydrogel (sample CPBG_25) combined with its high mechanical strength not only favored free solvent mobility but also acted as controlled release of its drug cargo. Importantly, the macroporous hydrogel exhibited *in-vitro* bioactivity in SBF solution by the formation of bone like hydroxyapatite ($Ca_{10}(PO_4)_6(OH)_2$) microcrystals. In addition, the hydrogel was also biocompatible with U2OS and HaCaT cell lines showing higher U2OS cell adherence on hydroxyapatite layer. The observed characteristic bone bonding ability and excellent biocompatibility of the macroporous hybrid composite hydrogel promises as a suitable candidate for tissue regeneration in future.

CRediT authorship contribution statement

HG: Methodology, Resources, Investigation and Validation. NG: Conceptualization, Methodology, Investigation, Validation, Writing - review and editing. ND and AB: Investigation, specifically for performing *in-vitro* experiments. DS: Supervision, Review and editing. HBB: Supervision, Review and editing.

Declaration of competing interest

Authors declare no conflict of interest.

Acknowledgement

We would like to thank Delhi Technological University, Delhi to provide basic lab facilities and financial support. Thanks to the Department of Science and Technology (DST) project grant No.: EMR/2017/001222 Dated 03/01/2019, Government of India for financial support. We sincerely thank for the valuable contributions by Dr. Munia Ganguli, CSIR-IGIB, Delhi for the cell culture studies. We would like to acknowledge CIF-IIT Delhi, USIC-Delhi University, Delhi for providing various characterization facilities.

Appendix A. Supplementary data

Supplementary data to this article can be found online at https://doi.org/10.1016/j.ijbiomac.2021.01.166.

References

[1] A. Seidi, M. Ramalingam, I. Elloumi-Hannachi, S. Ostrovidov, A. Khademhosseini, Gradient biomaterials for soft-to-hard interface tissue engineering, Acta Biomater. 7 (2011) 1441–1451.
[2] Y.J. No, M. Castilho, Y. Ramaswamy, H. Zreiqat, Role of biomaterials and controlled architecture on tendon/ligament repair and regeneration, Adv. Mater. 32 (2020) 1904511.
[3] L.R. Feksa, E.A. Troian, C.D. Muller, F. Viegas, A.B. Machado, V.C. Rech, Hydrogels for biomedical applications, in: Nanostructures Eng, Cells, Tissues Organs, Elsevier, 2018 403–438.
[4] H. B. Bohidar, P. Dubin, Y. Osada, Polymer gels: fundamentals and applications, ed. HB Bohidar, P. Dubin and Y. Osada, ACS Symposium Series, vol. 833 (2002).
[5] F. Munarin, S.G. Guerreiro, M.A. Grellier, M.C. Tanzi, M.A. Barbosa, P. Petrini, P.L. Granja, Pectin-based injectable biomaterials for bone tissue engineering, Biomacromolecules. 12 (2011) 568–577.
[6] G. Iviglia, C. Cassinelli, D. Bollati, F. Baino, E. Torre, M. Morra, C. Vitale-Brovarone, Engineered porous scaffolds for periprosthetic infection prevention, Mater. Sci. Eng. C. 68 (2016) 701–715.
[7] G. Iviglia, C. Cassinelli, E. Torre, F. Baino, M. Morra, C. Vitale-Brovarone, Novel bioceramic-reinforced hydrogel for alveolar bone regeneration, Acta Biomater. 44 (2016) 97–109.
[8] N. Gupta, H. Goel, D. Santhiya, C.M. Srivastava, S. Mishra, P. Rai, Aqueous-phased electrospun bioactive glass mineralized gelatin-pectin hybrid composite fiber matrix for 7-dehydrocholesterol delivery, Chemistry Select. 5 (2020) 4364–4370.
[9] S. Cui, B. Yao, M. Gao, X. Sun, D. Gou, J. Hu, Y. Zhou, Y. Liu, Effects of pectin structure and crosslinking method on the properties of crosslinked pectin nanofibers, Carbohydr. Polym. 157 (2017) 766–774.

[10] G.C. Jayakumar, N. Usharani, K. Kawakami, J.R. Rao, B.U. Nair, Studies on the physico-chemical characteristics of collagen-pectin composites, RSC Adv. 4 (2014) 63840–63849.
[11] F. Wenpo, L. Gaofeng, F. Shuying, Q. Yuanming, T. Keyong, Preparation and characterization of collagen-hydroxyapatite/pectin composite, Int. J. Biol. Macromol. 74 (2015) 218–223.
[12] H. Sai, A. Erbas, A. Dannenhoffer, D. Huang, A. Weingarten, E. Siismets, K. Jang, K. Qu, L.C. Palmer, M.O. De La Cruz, Chromophore amphiphile–polyelectrolyte hybrid hydrogels for photocatalytic hydrogen production, J. Mater. Chem. A 8 (2020) 158–168.
[13] J. Pathak, E. Priyadarshini, K. Rawat, H.B. Bohidar, Complex coacervation in charge complementary biopolymers: electrostatic versus surface patch binding, Adv. Colloid Interf. Sci. 250 (2017) 40–53.
[14] J. Pathak, K. Rawat, H.B. Bohidar, Surface patch binding and mesophase separation in biopolymeric polyelectrolyte–polyampholyte solutions, Int. J. Biol. Macromol. 63 (2014) 29–37.
[15] T.N. Vo, S.R. Shah, S. Lu, A.M. Tatara, E.J. Lee, T.T. Roh, Y. Tabata, A.G. Mikos, Injectable dual-gelling cell-laden composite hydrogels for bone tissue engineering, Biomaterials. 83 (2016) 1–11.
[16] A. Abalymov, L. Van der Meeren, M. Saveleva, E. Prikhozhdenko, K. Dewettinck, B. Parakhonskiy, A.G. Skirtach, Cells-grab-on particles: a novel approach to control cell focal adhesion on hybrid thermally annealed hydrogels, ACS Biomater. Sci. Eng. 6 (2020) 3933–3944.
[17] M. Erol-Taygun, I. Unalan, M.I.B. Idris, J.F. Mano, A.R. Boccaccini, Bioactıve glass-polymer nanocomposites for bone tissue regeneration applications: a review, Adv. Eng. Mater. 21 (2019) 1900287.
[18] J. Zheng, F. Zhao, W. Zhang, Y. Mo, L. Zeng, X. Li, X. Chen, Sequentially-crosslinked biomimetic bioactive glass/gelatin methacryloyl composites hydrogels for bone regeneration, Mater. Sci. Eng. C. 89 (2018) 119–127.
[19] M.S. Saveleva, K. Eftekhari, A. Abalymov, T.E.L. Douglas, D. Volodkin, B. V Parakhonskiy, A.G. Skirtach, Hierarchy of hybrid materials—the place of inorganics-in-organics in it, their composition and applications, Front. Chem. 7 (2019) 179.
[20] M.H. Kim, B.S. Kim, H. Park, J. Lee, W.H. Park, Injectable methylcellulose hydrogel containing calcium phosphate nanoparticles for bone regeneration, Int. J. Biol. Macromol. 109 (2018) 57–64.
[21] J.A. Killion, S. Kehoe, L.M. Geever, D.M. Devine, E. Sheehan, D. Boyd, C.L. Higginbotham, Hydrogel/bioactive glass composites for bone regeneration applications: synthesis and characterisation, Mater. Sci. Eng. C. 33 (2013) 4203–4212.
[22] A. Gantar, N. Drnovšek, P. Casuso, A. Pérez-San Vicente, J. Rodriguez, D. Dupin, S. Novak, I. Loinaz, Injectable and self-healing dynamic hydrogel containing bioactive glass nanoparticles as a potential biomaterial for bone regeneration, RSC Adv. 6 (2016) 69156–69166.
[23] P. Nikpour, H. Salimi-Kenari, F. Fahimipour, S.M. Rabiee, M. Imani, E. Dashtimoghadam, L. Tayebi, Dextran hydrogels incorporated with bioactive glass-ceramic: nanocomposite scaffolds for bone tissue engineering, Carbohydr. Polym. 190 (2018) 281–294.
[24] C.D.F. Moreira, S.M. Carvalho, H.S. Mansur, M.M. Pereira, Thermogelling chitosan–collagen–bioactive glass nanoparticle hybrids as potential injectable systems for tissue engineering, Mater. Sci. Eng. C. 58 (2016) 1207–1216.
[25] D.S. Couto, Z. Hong, J.F. Mano, Development of bioactive and biodegradable chitosan-based injectable systems containing bioactive glass nanoparticles, Acta Biomater. 5 (2009) 115–123.
[26] A.S. Veiga, J.P. Schneider, Antimicrobial hydrogels for the treatment of infection, Biopolymers. 100 (2013) 637–644.
[27] L. Sosa, A.C. Calpena, M. Silva-Abreu, L.C. Espinoza, M. Rincón, N. Bozal, O. Domenech, M.J. Rodríguez-Lagunas, B. Clares, Thermoreversible gel-loaded amphotericin B for the treatment of dermal and vaginal candidiasis, Pharmaceutics. 11 (2019) 1–18.
[28] T. Demirci, M.E. Hasköylü, M.S. Eroğlu, J. Hemberger, E. Toksoy Öner, Levan-based hydrogels for controlled release of Amphotericin B for dermal local antifungal therapy of Candidiasis, Eur. J. Pharm. Sci. 145 (2020) 105255.
[29] C. Shu, T. Li, W. Yang, D. Li, S. Ji, L. Ding, Amphotericin B-conjugated polypeptide hydrogels as a novel innovative strategy for fungal infections, R. Soc. Open Sci. 5 (2018) 171814.
[30] D. Santhiya, H.K. Alajangi, F. Anjum, S. Murugavel, M. Ganguli, Bio-inspired synthesis of microporous bioactive glass-ceramic using CT-DNA as a template, J. Mater. Chem. B 1 (2013) 6329–6338.
[31] T. Kokubo, H. Takadama, How useful is SBF in predicting in vivo bone bioactivity? Biomaterials. 27 (2006) 2907–2915.
[32] S.P. Hudson, R. Langer, G.R. Fink, D.S. Kohane, Injectable in situ cross-linking hydrogels for local antifungal therapy, Biomaterials. 31 (2010) 1444–1452, https://doi.org/10.1016/j.biomaterials.2009.11.016.
[33] E. Dickinson, Stability and rheological implications of electrostatic milk protein–polysaccharide interactions, Trends Food Sci. Technol. 9 (1998) 347–354.
[34] Y. Xu, M. Mazzawi, K. Chen, L. Sun, P.L. Dubin, Protein purification by polyelectrolyte coacervation: influence of protein charge anisotropy on selectivity, Biomacromolecules. 12 (2011) 1512–1522.
[35] H.A. Barnes, A Handbook of Elementary Rheology, University of Wales, 2000.
[36] I. Fraeye, T. Duvetter, E. Doungla, A. Van Loey, M. Hendrickx, Fine-tuning the properties of pectin-calcium gels by control of pectin fine structure, gel composition and environmental conditions, Trends Food Sci. Technol. 21 (2010) 219–228.
[37] N. Gupta, D. Santhiya, Role of cellulose functionality in bio-inspired synthesis of nano bioactive glass, Mater. Sci. Eng. C. 75 (2017) 1206–1213.
[38] N. Gupta, D. Santhiya, A. Aditya, K. Badra, Dendrimer templated bioactive glass-ceramic nanovehicle for gene delivery applications, RSC Adv. 5 (2015) 56794–56807.
[39] N. Gupta, D. Santhiya, A. Aditya, Tailored smart bioactive glass nanoassembly for dual antibiotic: in vitro sustained release against osteomyelitis, J. Mater. Chem. B 4 (2016) 7605–7619.
[40] B.H. León-Mancilla, M.A. Araiza-Téllez, J.O. Flores-Flores, M.C. Piña-Barba, Physicochemical characterization of collagen scaffolds for tissue engineering, J. Appl. Res. Technol. 14 (2016) 77–85.
[41] N.V. Gupta, H.G. Shivakumar, Investigation of swelling behavior and mechanical properties of a pH-sensitive superporous hydrogel composite, Iran. J. Pharm. Res. 11 (2012) 481.
[42] F. Ganji, S. Vasheghani-Farahani, E. Vasheghani-Farahani, Theoretical description of hydrogel swelling: a review, Iran. Polym. J. (English Ed. 19 (2010) 375–398.
[43] A. Martinez-Ruvalcaba, J.C. Sánchez-Díaz, F. Becerra, L.E. Cruz-Barba, A. González-Álvarez, Swelling characterization and drug delivery kinetics of polyacrylamide-co-itaconic acid/chitosan hydrogels, Express Polym Lett 3 (2009) 25–32.
[44] M.H. Misbah, M. Santos, L. Quintanilla, C. Günter, M. Alonso, A. Taubert, J.C. Rodríguez-Cabello, Recombinant DNA technology and click chemistry: a powerful combination for generating a hybrid elastin-like-statherin hydrogel to control calcium phosphate mineralization, Beilstein J. Nanotechnol. 8 (2017) 80.
[45] R. Lakshmi, S. Sasikumar, Influence of needle-like morphology on the bioactivity of nanocrystalline wollastonite – an in vitro study, Int. J. Nanomedicine 10 (2015) 129–136.
[46] T.E.L. Douglas, W. Piwowarczyk, E. Pamula, J. Liskova, D. Schaubroeck, S.C.G. Leeuwenburgh, G. Brackman, L. Balcaen, R. Detsch, H. Declercq, K. Cholewa-Kowalska, A. Dokupil, V.M.J.I. Cuijpers, F. Vanhaecke, R. Cornelissen, T. Coenye, A.R. Boccaccini, P. Dubruel, Injectable self-gelling composites for bone tissue engineering based on gellan gum hydrogel enriched with different bioglasses, Biomed. Mater. 9 (2014).
[47] T.E.L. Douglas, M. Dziadek, J. Schietse, M. Boone, H.A. Declercq, T. Coenye, V. Vanhoorne, C. Vervaet, L. Balcaen, M. Buchweitz, F. Vanhaecke, F. Van Assche, K. Cholewa-Kowalska, A.G. Skirtach, Pectin-bioactive glass self-gelling, injectable composites with high antibacterial activity, Carbohydr. Polym. 205 (2019) 427–436, https://doi.org/10.1016/j.carbpol.2018.10.061.
[48] J. Hernandez-Montelongo, N. Naveas, S. Degoutin, N. Tabary, F. Chai, V. Spampinato, G. Ceccone, F. Rossi, V. Torres-Costa, M. Manso-Silvan, B. Martel, Porous silicon-cyclodextrin based polymer composites for drug delivery applications, Carbohydr. Polym. 110 (2014) 238–252.
[49] N. Gupta, D. Santhiya, S. Murugavel, A. Kumar, A. Aditya, M. Ganguli, S. Gupta, Effects of transition metal ion dopants (Ag, Cu and Fe) on the structural, mechanical and antibacterial properties of bioactive glass, Colloids Surf. A Physicochem. Eng. Asp. 538 (2018) 393–403.
[50] F. Wahid, C. Zhong, H.-S. Wang, X.-H. Hu, L.-Q. Chu, Recent advances in antimicrobial hydrogels containing metal ions and metals/metal oxide nanoparticles, Polymers (Basel). 9 (2017) 636.
[51] G. Tommasi, S. Perni, P. Prokopovich, An injectable hydrogel as bone graft material with added antimicrobial properties, Tissue Eng. - Part A. 22 (2016) 862–872.
[52] R. Goldshmid, D. Seliktar, Hydrogel modulus affects proliferation rate and pluripotency of human mesenchymal stem cells grown in three-dimensional culture, ACS Biomater. Sci. Eng. 3 (2017) 3433–3446.
[53] W.S. Huang, I.M. Chu, Injectable polypeptide hydrogel/inorganic nanoparticle composites for bone tissue engineering, PLoS One 14 (2019) 1–17.
[54] T. Jiang, G. Xu, X. Chen, X. Huang, J. Zhao, L. Zheng, Impact of hydrogel elasticity and adherence on osteosarcoma cells and osteoblasts, Adv. Healthc. Mater. 8 (2019) 1–11.

The current issue and full text archive of this journal is available on Emerald Insight at:
https://www.emerald.com/insight/1746-5664.htm

Challenges in the implementation of circular economy in manufacturing industry

Madhukar Chhimwal
Department of Mechanical, Production and Industrial Engineering, Delhi Technological University, Delhi, India

Saurabh Agrawal
Delhi School of Management, Delhi Technological University, Delhi, India, and

Girish Kumar
Department of Mechanical, Production and Industrial Engineering, Delhi Technological University, Delhi, India

Received 22 July 2020
Revised 8 November 2020
31 December 2020
Accepted 16 January 2021

Abstract

Purpose – The circular economy concepts are useful for resource conservation, eliminating waste and enhancing the efficiency of production to improve the sustainability of the system. The application of CE in Indian manufacturing industry is in nascent stage. India's manufacturing sector significantly contributes to the economic development of the nation; therefore, this study aims to identify and analyze the sustainability related challenges faced during the implementation of the circularity concept.

Design/methodology/approach – Comprehensive survey of literature and the use of Pareto analysis yield ten significant challenges which are further analyzed using fuzzy-Decision-Making Trial and Evaluation Laboratory approach.

Findings – Findings revealed that noncompliance of environmental laws, revenue generation, design issues owing to technological limitations and less preference to refurbished and reused product are some of the major challenges to the CE practices in the manufacturing industry.

Research limitations/implications – The results will help the researchers and practitioners in strategic decision-making for the improved application of circularity in the production process.

Originality/value – This paper contributes to the identification and prioritization of sustainability-related challenges faced during the implementation of a novel concept by a developing economy.

Keywords Operations management, Supply chain management, Circular economy, Challenges, Manufacturing industry, Fuzzy DEMATEL, Sustainability

Paper type Research paper

Funding: This research received no specific grant from any funding agency in the public, commercial or not-for-profit sectors.

© Emerald Publishing Limited
1746-5664
DOI 10.1108/JM2-07-2020-0194

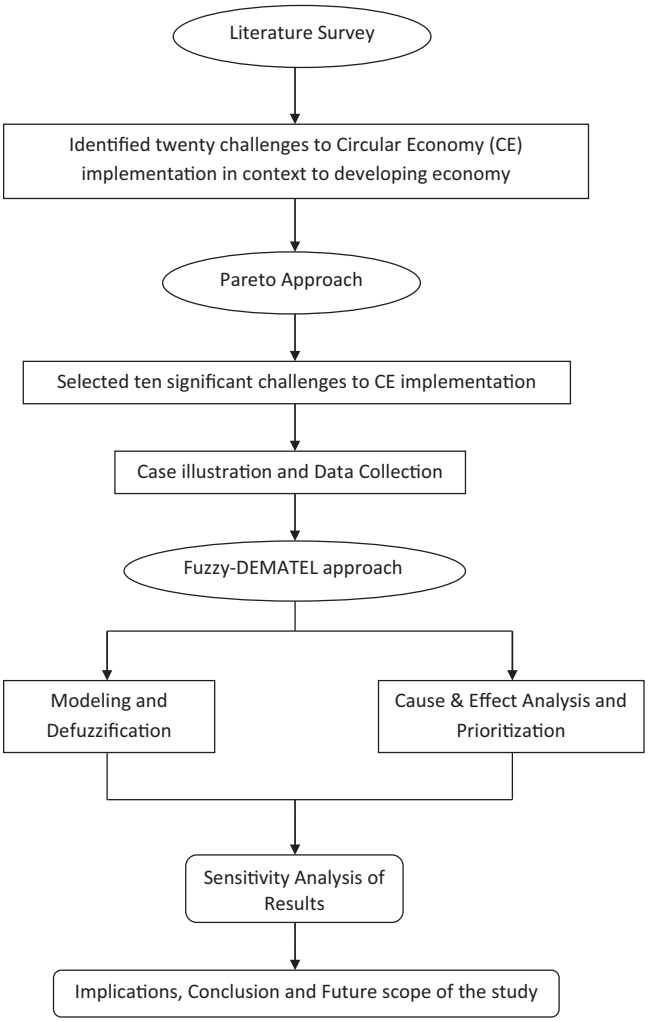

Graphical Abstract

1. Introduction

Manufacturing sector in India is witnessing a faster growth and is set to increase its share from 16% to 25% to the gross domestic product (GDP) of the nation by the year 2022 (IBEF, 2019; Iyer, 2018). Government of India (GOI) has launched "Make in India" program to boost this sector and make India a global manufacturing hub (Mehta and Rajan, 2017). This initiative will not only offer a global recognition to the Indian economy but also create several million job opportunities (CII, 2015). India is now seen as a huge market of investment owing to rapidly increasing middle class population. Various incentives offered

by the government and incubation of skilled labor at lower wages are some lucrative measures for foreign companies to invest in India (Kumar *et al.*, 2019a). In the recent past, GOI has made various amendments in the national policy of manufacturing to provide a pathway to the multi-national companies to invest in Indian manufacturing sector. Looking at the future growth of manufacturing in India and the limited availability of natural resources, there is a need of development of such business models in the manufacturing industry which can develop product more sustainably (Mathivathanan *et al.*, 2019).

Circular economy (CE) is a sustainability approach which optimizes the use of resources while empowering companies to gain profits from deliverables to market (Kumar *et al.*, 2019b). Within past few years, the concept of CE has gained much interest among the researchers, academicians and policymakers because of the stress toward a sustainable development (De Angelis, 2020; Tsai *et al.*, 2020; Mashud *et al.*, 2020a, 2020b, 2020c). The major advantages of the application of CE concept is resource conservation, lesser energy consumption and reduced emission of greenhouse gasses thereby abating the reliance of the economy on natural resources (Tseng *et al.*, 2020; Vasiljevic-Shikaleska *et al.*, 2017). Implementation of CE models may be helpful in overcoming the environmental, societal and economic issues (Upadhyay *et al.*, 2019). In the recent past many researchers have worked in this area to establish a connection of CE concept with the current sustainable supply chain business models (Mashud *et al.*, 2020a, 2020b, 2020c). Koh *et al.* (2017) proposed a circular framework to assess the interconnectedness of the environmental, economic and social capital of supply chain resources. Bocken *et al.* (2016) addressed issues related to product design and business model strategies that could help to the implementation of CE models. Rizos (2017) focused on enhancing the knowledge and understanding of the challenges and enablers that small and medium enterprises' (SME) experience during the implementation of CE business models. However, their study was specific to European context. Jaeger and Upadhyay (2020) identified barriers to CE model adoption in the manufacturing industry of Norway and investigated that the focus of manufacturers is mostly on recycling and waste reduction.

CE is a vast concept and it works on the principle of 6R (reuse, repair, refurbish, redesign, remanufacture and recycle) for any type of production and consumption model (Jawahir and Bradley, 2016; Agrawal *et al.*, 2015). By adopting this principle in the production and consumption process, CE will aim at minimizing the use of raw materials and the dependence on primary energy (Ethirajan *et al.*, 2020). The transition from a linear model to a circular economic model is of disruptive nature and certainly requires radical changes and new solutions in which current ways of working need to be changed and new ideas and practices should be followed to build products more sustainably (Mathivathanan *et al.*, 2019; Mashud *et al.*, 2020a, 2020b, 2020c). The concept of CE is in nascent stage and there are several challenges coming with the implementation of this concept that organizations need to face in today's business environment which need to be addressed in a systematic way. The review of literature on Circular Supply Chain Management (CSCM) conducted by Farooque *et al.* (2019) showed that comprehensive integrated view of CSCM is still missing, and therefore, the authors addressed various dimensions related to the incorporation of CE principle in supply chain management. The authors also highlighted the importance of identifying drivers and challenges to CSCM in near future and elucidated that knowledge gap in this area is large which could have a critical impact on the society and on the industry.

In proposed study, effort has been made to explore and analyze the challenges pertaining to the implementation of CE concept in Indian manufacturing industry. For the identification of significant challenges Pareto approach is incorporated in the study. Pareto

analysis is a statistical tool which is used for the ranking of the factors according to their frequency of occurrence (Craft and Leake, 2002). This approach identifies the challenges which are mainly responsible for CE implementation (Kumar *et al.*, 2019b). The relative importance has been analyzed by assigning rating to the individual challenge using Fuzzy-Decision-Making Trial and Evaluation Laboratory (DEMATEL) approach (Gupta *et al.*, 2019). The concept of fuzzy logic is used to remove uncertainty in the data arising from human judgment (Azadegan *et al.*, 2011). The purpose of using DEMATEL approach is to reflect causal relationship among the challenges (Rajput and Singh, 2019). The key objectives of the study are as follows:

- to explore CE in the perspective of Indian manufacturing industry;
- to identify and prioritize the challenges to the application of CE concept in Indian manufacturing industry; and
- to analyze the importance of challenges and perform the sensitivity analysis.

Further, the article comprises of "literature review" in Section 2, stating contribution made by various authors in the building up of CE concept. This section also constitutes the comprehensive review of the challenges related to CE implementation. Section 3 comprises of the research methodology adopted for the identification and prioritization of significant CE challenges. Section 4 "Case Illustration" constitutes the application of proposed methodology in the adoption of CE practices in the Indian manufacturing context. The results of analysis are summarized in Section 5 and sensitivity analysis is performed and described in Section 6. The theoretical, practical and global implication of the study is illustrated in Section 7. Finally, the conclusion is drawn from the results of the analysis and further scope of the study is provided in Section 8.

2. Literature review

The following section comprises of the review of the CE concept, its implementation and the challenges encountered during its process of implementation.

2.1 Circular economy

Pearce and Turner (1989) first established the concept of a CE based on the previous studies conducted by Boulding (1966). Boulding (1966) considered the economy as a circular system where the dependence of the economy on natural resources and the environment is weakened and keeping the resources available rather disposing them; thus closing the loop of material during the product lifecycle. Kirchherr *et al.* (2017) analyzed 114 definitions of the CE which were based on 17 components so as to create transparency regarding the current scenario of the CE concept. Urbinati *et al.* (2017) proposed a classification of CE Models into two types based on the adoption proportion of circularity: the value proposed to the customer; and the different ways of interacting with the supplier to enhance the value network. Kalmykova *et al.* (2018) provided an overview of the literature on CE theoretical approaches, strategies and implementation cases. Geissdoerfer *et al.* (2017) discussed the performance of circular models based on the three dimensions of sustainability which are important for its implementation at organizational level. Geisendorf and Pietrulla (2017) talked about different concepts related to the CE and how these concepts help in achieving circularity in the business model. Many researchers have discussed several concepts and definitions related to CE but few of them have highlighted its pathway of implementation and challenges faced during the process of adoption. Therefore, review of literature is

conducted to get an insight of the knowledge related to its process of adoption and the challenges faced during its implementation.

2.2 CE implementation

CE concept application started in Germany in the year 1996, with the passing of the law that emphasized on efficient waste management and proper disposal of waste to minimize environmental degradation (Lu and Halog, 2020; Nelles *et al.*, 2016). Thereafter, comprehensive legal framework of CE strategy was developed by the Government of Japan that directs the society on how to recycle used products (Morioka *et al.*, 2005). In China, the CE concept is projected as a new sustainable development strategy rather than considering it as an enhanced environmental regulation policy (Geng and Doberstein, 2008; Hasan *et al.*, 2020). Ghisellini *et al.* (2016) performed a comprehensive literature review and discussed CE origin along with the principles and challenges in the transition toward CE business models. Sousa-Zomer *et al.* (2018) focused on the implementation of CE at the micro-industrial level where a manufacturing organization from the developing economies was considered to explore the cleaner production practices and eco-design principles adoption. Lieder and Rashid (2016) proposed a concomitant top-down and bottom-up approach in which the interest of all the stakeholders were aligned in a single direction to achieve the benefits from the implementation of CE. The government bodies and the policymakers emphasize on environmental benefits of CE, while the industries look for economic benefits neglecting the concern for environment (Jayakumar *et al.*, 2020). Thus, a concurrent approach is necessary for the alignment of interest to obtain maximum benefits from CE implementation.

2.3 Challenges in implementation of circular economy

A critical analysis of the challenges affecting CE application and their mutual interaction can facilitate the manufacturing sector of emerging economies in the smooth transition from linear to circular business model. Therefore, a comprehensive review of literature is conducted to explore the challenges and solutions during CE implementation.

Shi *et al.* (2008) identified the challenges during the adoption of cleaner production practices by the Chinese SME's and prioritized them. Their study revealed the top three challenges as lack of policies pertaining to economic inducement; improper enforcement of environmental taxes and high initial investment of capital cost. Geng and Doberstein (2008) explored a series of challenges to the implementation of CE concept in China and categorized them into three groups: technological advancement, public participation and refined policies. Xia *et al.* (2015) focused on the execution of remanufacturing of automotive parts in China and the internal challenges encountered during its implementation. Ritzén and Sandström (2017) identified five different categories of challenges in the transition to CE which were analyzed in relation to innovation management and exemplified by the need to integrate distinctive perspectives and domains in the industry. Another major challenge to the application of CE practices is improper utilization of suitable economic and financial instruments by the government (Wang *et al.*, 2008). Poor enforcement of the laws related to environmentally friendly practices and noncompliance with these rules and regulation leads to a major shift from the CE perspective of manufacturing. Xue *et al.* (2010) found that only 16.7% of the interviewed officials had just heard of CE in a study conducted in China which clearly indicates lack of CE awareness among the officials.

During the past few years, environmental regulations and production standards have become stern and are so-called "green challenges" for international trade (Jalilian and Mirghafoori, 2020). These challenges affect the trading revenue of developing countries, as they require a complete reformation of the technical input and also the application of

green practices in the production model (Su *et al.*, 2013). Agyemang *et al.* (2019) explored drivers and barriers to CE implementation in Pakistan automobile manufacturing industry. The findings revealed that profitability, cost reduction and concern for environment are the top three drivers and unawareness, financial constraint and lack of expertise are the top three barriers in implementing CE. Moktadir *et al.* (2018) identified and prioritized the drivers of sustainable manufacturing in the leather industry of Bangladesh. The authors used graph theory and matrix approach to examine the drivers and found that knowledge of CE is essential for its smooth implementation. Cezarino *et al.* (2019) explored the relationship between CE and Industry 4.0 as a contribution to management decision and identified limitations to its implementation in Brazil. Lack of communication between public and private institutions, efficacy in consolidating industrial policies and investment in remanufacturing process are some of the major limitations to its implementation. In Indian context only a few studies have been carried out in this area. Govindan and Hasanagic (2018) identified 39 challenges affecting CE application, grouped them into the interior or exterior environment and then classified into eight categories: government, economic, technological, knowledge and skill issues, management issues, CE framework issues, cultural and social issues and market issues. Mangla *et al.* (2017) identified thirty challenges in the application of sustainable production and consumption model in the supply chain by adopting fuzzy analytic hierarchy process (AHP) approach. Mittal and Sangwan (2014) elicited the use of nonrenewable sources of energy by the manufacturing firm causes a serious problem of locating waste disposal. The studies pertaining to Indian context failed to identify significant challenges in the implementation of CE as a novel business strategy for the manufacturing sector. Therefore, this study focuses on the identification of significant challenges and their prioritization for the implementation of a novel concept in a developing economy like India.

3. Research methodology

Section 3 presents the methodologies adopted in the study for the identification and prioritization of signicant challenges related to CE implementation in manufacturing industry. The use of Pareto analysis for the identification of signicant challenges is illustrated in the subsection 3.1. Subsection 3.2 deals with the application of Fuzzy logic along with DEMATEL approach to prioritize the significant CE challenges for the implementation in manufacturing industry. A research framework portraying the various steps involved in this study and the methods adopted for the generation of fruitful results is shown in Figure 1.

3.1 Pareto analysis

The selection of significant challenges from those identified through literature survey is done using Pareto analysis. It is also sometimes referred to as 80/20 rule. Regarding this 80/20 principle, Svensson and Wood (2006) in their theory stated that "a small percentage of a total is responsible for a large proportion of total outcome." However, this concept has its own limitations. As a small percentage of key inputs is responsible for a large percentage of output, so companies should not narrow down their operations just by relying on the key inputs rather they should also consider the other input variables depending upon the application and requirement of variables (Craft and Leake, 2002). Empirical observation is the fundamental basis for the application of Pareto analysis and should not be considered as a mandatory rule for actions. Pareto analysis is widely used by academicians and industry practitioners. Talib *et al.* (2015) used Pareto approach to trace the frequency of occurrence of every possible critical success factors (CSF's) in SCM literature. Kumar *et al.* (2019b) used "Pareto Analysis" tool to shortlist and arrange the critical factors for the smooth

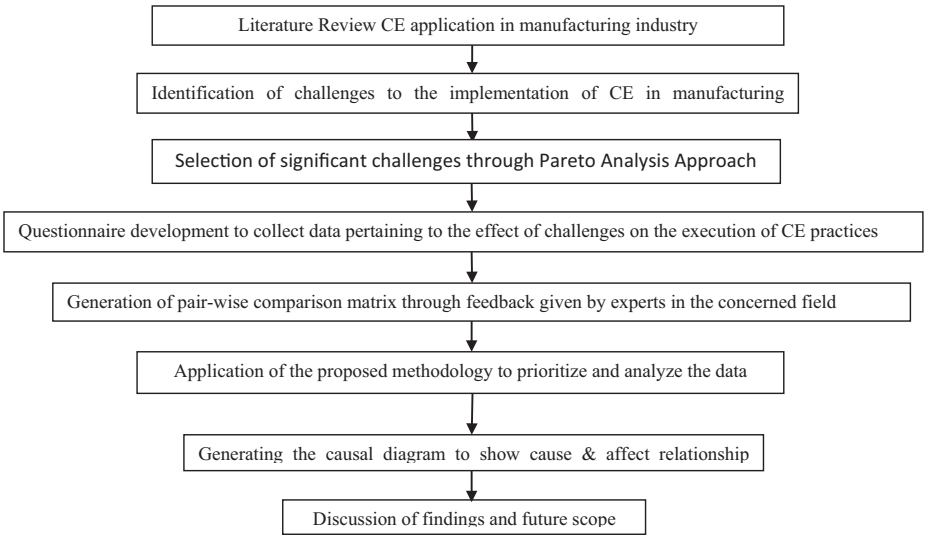

Figure 1.
Research framework

implementation of agile manufacturing. Karuppusami and Gandhinathan (2006) used "Pareto analysis" as a quality tool to sort and arrange the CSF's of total quality management according to the order of criticality. Fotopoulos *et al.'s* (2011) and Bamford and Greatbanks' (2005) studies establish that Pareto analysis can be regarded as a proven useful selection technique in management decision-making. According to Garg and Garg (2013), Pareto analysis can be used by managers as an improvement technique to select vital few from the useful many.

The current study is framed to identify the significant challenges for implementation of CE principles in Indian Manufacturing industry. This study takes into consideration the exploratory and the descriptive nature of analysis. To achieve the desired research objectives, this study is conducted in two phases. First, a comprehensive literature survey is undertaken to ensure that no important challenge is ignored. Second, Pareto analysis approach is applied to shortlist the important challenges identified through literature survey which are prioritized using Fuzzy-DEMATEL approach.

The main literature sources are the online databases, namely, Web of Science, Google Scholar, Science-Direct, Scopus, Springer, Emerald, Taylor and Francis, Wiley and Inderscience. Time-explicit and term sensitive search criteria is applied to yield the desired literature. The time frame chosen to gather the relevant literature is from the year 2000 to 2020 as research toward the implementation of environmental oriented techniques was mainly conducted in past two decades. The keywords used to extract the suitable papers are: barriers, challenges, CE barriers, circular supply chain barriers, CE challenges, close loop supply chain barriers, CE implementation.

There are several challenges to the application of CE that may vary depending upon the type of industry, sector and region in which they may occur. Table 1 shows the classification of the challenges into internal or external and the region and sector in which they originate.

The relevant literature collected is further analyzed using Pareto Analysis to separate the "Vital Few" from the "Useful Many" by prioritizing the frequency of

Table 1. Challenges to the application of circular economy

Types	Challenges	Interior/exterior	Stakeholder	Industry/ market	References
Legislative norms	$C_{1.1}$ Lack of standardization system	Interior	Organization	China	Elia *et al.* (2017), Su *et al.* (2013), Geng *et al.* (2012), Kirchherr *et al.* (2017), Ivanovic (2019), Saroha *et al.* (2018), Hughes (2017), Muradin and Foltynowicz (2019), Pauliuk (2018), Kumar and Suganya (2019), Li and Yu (2011), Goyal *et al.* (2018),Venkatesh and Luthra (2016), Zhu *et al.* (2017)
	$C_{1.2}$ Laws pertaining to circular economy practices are implemented inadequately	Exterior			Jaeger and Upadhyay (2020), Li and Yu (2011), Su *et al.* (2013), Pauliuk (2018)
	$C_{1.3}$ Noncompliance of environmental laws	Exterior			Ma and Ortolano (2000), Elia *et al.* (2017), Geng *et al.* (2012), Kirchherr *et al.* (2017), Ivanovic (2019), Saroha *et al.* (2018), Hughes (2017), Muradin and Foltynowicz (2019), Pauliuk (2018), Kumar and Suganya (2019), Li and Yu (2011), Goyal *et al.* (2018), Venkatesh and Luthra (2016), Zhu *et al.* (2017)
Economic profitability	$C_{2.1}$ Lack of economic inducement	Exterior	Government	China	Shi *et al.* (2008), Su *et al.* (2013), Geng *et al.* (2012), Kirchherr *et al.* (2017), Ivanovic (2019), Saroha *et al.* (2018), Hughes (2017), Muradin and Foltynowicz (2019), Pauliuk (2018), Kumar and Suganya (2019), Goyal *et al.* (2018),Venkatesh and Luthra (2016), Zhu and Geng (2013)
	$C_{2.2}$ High capital investment cost	Interior	Organization		Geng and Doberstein (2008), Shi *et al.* (2008), Kirchherr *et al.* (2017), Ivanovic (2019), Saroha *et al.* (2018), Hughes (2017), Muradin and Foltynowicz (2019), Pauliuk (2018), Kumar and Suganya (2019), Goyal *et al.* (2018),Venkatesh and Luthra (2016), Zhu *et al.* (2017)
	$C_{2.3}$ Complexity in deciding the final price of product	Interior	Organization		Lieder and Rashid (2016), Kirchherr *et al.* (2017)
Technological obstructions	$C_{3.1}$ Design issues owing to technological limitations	Interior	Organization	General, China	Geng and Doberstein (2008), Su *et al.* (2013), Geng *et al.* (2012), Kirchherr *et al.* (2017), Ivanovic (2019), Saroha *et al.* (2018), Hughes (2017), Muradin and Foltynowicz (2019)
	$C_{3.2}$ Managing product quality through recovered parts	Interior	Organization		Geng *et al.* (2012), Saroha *et al.* (2018), Hughes (2017), Muradin and Foltynowicz (2019)
Information challenge	$C_{4.1}$ Lack of information sharing	Interior	Society	Developing countries	Jaeger and Upadhyay (2020), Geng *et al.* (2012), Kumar and Suganya (2019)
	$C_{4.2}$ Fallacious information	Interior	Society		Su *et al.* (2013), Muradin and Foltynowicz (2019)

(*continued*)

Table 1.

Types	Challenges	Interior/exterior	Stakeholder	Industry/ market	References
Effective management	$C_{5.1}$ Unproductive management and poor administration	Interior	Organization	China	Su *et al.* (2013)
	$C_{5.2}$ Uneven distribution of work among the members of hierarchy	Interior	Organization		Shahbazi *et al.* (2016)
Operational lagging	$C_{6.1}$ Lack of infrastructure and unavailability of advance tool	Interior	Organization	General, developing countries	Su *et al.* (2013), Geng *et al.* (2012), Kirchherr *et al.* (2017), Ivanovic (2019), Saroha *et al.* (2018), Hughes (2017)
Market enhancement	$C_{7.1}$ Inefficient take back mechanism	Interior	Organization,	General	Ghisellini *et al.* (2016)
	$C_{7.2}$ Lack of Standardization of refurbished or remanufactured products	Exterior	Supplier Society		Van Weelden *et al.* (2016)
Cultural and social issues	$C_{8.1}$ Coordination with supply chain partners	Interior	Organization,	Developing countries	Cezarino *et al.* (2019), Kirchherr *et al.* (2017), Ivanovic (2019), Saroha *et al.* (2018), Hughes (2017)
	$C_{8.2}$ Less preference by customers to refurbish or reused product	Exterior	supplier Society		Kirchherr *et al.* (2017), Ivanovic (2019), Saroha *et al.* (2018), Hughes (2017), Muradin and Foltynowicz (2019)
Environmental awareness	$C_{9.1}$ Environmental awareness among the stakeholders	Interior and exterior	Organization society	Developing countries	Agyemang *et al.* (2019)
	$C_{9.2}$ Improper mapping of the environment laws with CE Practices	Interior and exterior	Organization		Moktadir *et al.* (2018), Geng *et al.* (2012)
Return on investment	$C_{10.1}$ Revenue generation	Interior	Organization	General	Muradin and Foltynowicz (2019), Pauliuk (2018), Kumar and Suganya (2019), Ivanovic (2019)

occurrence. The four steps of Pareto Analysis, as suggested by Swink *et al.* (2014) are as follows:

- identify the CE challenge categories;
- classify the CE challenges and calculate their individual percentage of occurrence;
- sort the CE challenges in descending order based on their individual percentage of occurrence; and
- represent the data graphically and recognize the significant CE challenges from those identified through literature survey.

To obtain desired results, this study incorporates empirically tested challenges as they are more reliable and valid. The statistically tested challenges are listed in Table 1. Further, a judgmental procedure is applied where the challenges with almost the same connotation are grouped and assigned a single domain name. Finally, 20 challenges were selected for Pareto Analysis with a total occurrence of 103. Table 2 shows the individual occurrence of challenges along with the source of literature.

Table 3 shows the CE challenges occurrence percentage in descending order. Applying the Pareto analysis approach, the first ten challenges which accounted for 82% of the total occurrence are represented as the "vital few" while the remaining ten challenges which hold only 18% of the total occurrence are regarded as "useful many." The outcome of Pareto analysis did not exactly yield into 80/20 split as Christopher (2011) suggests that market business may vary depending upon the strategy applied.

To sum up the findings of Pareto Analysis, these "10 vital CE challenges" are extremely important because to effectively implement CE nationwide one must distinguish the "vital few" from the "useful many" which are responsible for a larger impact on the industry as compared to the other "10 useful many challenges." This will not only help the supply chain managers in effective decision-making but will also save time and resources as they need to focus their efforts only on the "10 vital CE challenges." Figure 2 represents the individual occurrence percentage and the total percentage of occurrence of "vital CE challenges" and the "useful many CE challenges."

3.2 Fuzzy DEMATEL approach

Many organizations adopt the policy of grouping the experts from various fields and hence, collectively prepare a solution to the real world problem. Experts give their opinion on a particular situation based on their domain knowledge and experience. Multi-criteria decision-making (MCDM) is a technique which consists of setting criteria, evaluation of criteria weights and execution of a ranking method (Opricovic and Tzeng, 2003). MCDM techniques such as AHP, analytic network process (ANP), Vlse Kriterijumska OptimizacijaI Kompromisno Resenje, technique for order of preference by similarity to ideal solution (TOPSIS), elimination and choice expressing reality and preference ranking organization method for enrichment evaluation have been used in the past to rank the factors but none of the techniques can classify the factors into cause and effect groups (Chandra and Kumar, 2020; Khalilzadeh *et al.*, 2020; Rashidi, 2020). DEMATEL is used as a MCDM technique as this approach can transform the cause and effect relationship of the factors into an intelligent structural model of the system (Tian *et al.*, 2019). This approach aims to identify the most important criteria which can severely affect other criteria in the system (Jaiswal *et al.*, 2020). It is based on digraph or directional graph. Digraphs are used to represent the contextual relations among the factors of the system and each value on the digraph shows the degree of influence of individual factor (Singh *et al.*, 2020). Fuzzy set theory is used along

Challenges	References	Occurrence
1. Lack of standardization system	Elia *et al.* (2017), Su *et al.* (2013), Geng *et al.* (2012), Kirchherr *et al.* (2017), Ivanovic (2019), Saroha *et al.* (2018), Hughes (2017), Muradin and Foltynowicz (2019), Pauliuk (2018), Kumar and Suganya (2019), Li and Yu (2011), Goyal *et al.* (2018),Venkatesh and Luthra (2016), Zhu *et al.* (2017)	14
2. Noncompliance of environmental laws	Ma and Ortolano (2000), Elia *et al.* (2017), Geng *et al.* (2012), Kirchherr *et al.* (2017), Ivanovic (2019), Saroha *et al.* (2018), Hughes (2017), Muradin and Foltynowicz (2019), Pauliuk (2018), Kumar and Suganya (2019), Li and Yu (2011), Goyal *et al.* (2018), Venkatesh and Luthra (2016), Zhu *et al.* (2017)	14
3. Lack of economic inducement	Shi *et al.* (2008), Su *et al.* (2013), Geng *et al.* (2012), Kirchherr *et al.* (2017), Ivanovic (2019), Saroha *et al.* (2018), Hughes (2017), Muradin and Foltynowicz (2019), Pauliuk (2018), Kumar and Suganya (2019), Goyal *et al.* (2018),Venkatesh and Luthra (2016), Zhu *et al.* (2017)	13
4. High capital investment cost	Geng and Doberstein (2008), Shi *et al.* (2008), Kirchherr *et al.* (2017), Ivanovic (2019), Saroha *et al.* (2018), Hughes (2017), Muradin and Foltynowicz (2019), Pauliuk (2018), Kumar and Suganya (2019), Goyal *et al.* (2018),Venkatesh and Luthra (2016), Zhu *et al.* (2017)	12
5. Design issues owing to technological limitations	Geng and Doberstein (2008), Su *et al.* (2013), Geng *et al.* (2012), Kirchherr *et al.* (2017), Ivanovic (2019), Saroha *et al.* (2018), Hughes (2017), Muradin and Foltynowicz (2019)	8
6. Lack of infrastructure and unavailability of advance tool.	Su *et al.* (2013), Geng *et al.* (2012), Kirchherr *et al.* (2017), Ivanovic (2019), Saroha *et al.* (2018), Hughes (2017)	6
7. Less preference to reused or refurbished products	Kirchherr *et al.* (2017), Ivanovic (2019), Saroha *et al.* (2018), Hughes (2017), Muradin and Foltynowicz (2019)	5
8. Coordination with supply chain partners	Cezarino *et al.* (2019), Kirchherr *et al.* (2017), Ivanovic (2019), Saroha *et al.* (2018), Hughes (2017)	5
9. Managing product quality through recovered parts	Geng *et al.* (2012), Saroha *et al.* (2018), Hughes (2017), Muradin and Foltynowicz (2019)	4
10. Revenue generation	Muradin and Foltynowicz (2019), Pauliuk (2018), Kumar and Suganya (2019), Ivanovic (2019)	4
11. Inadequate implementation of CE laws	Jaeger and Upadhyay (2020), Li and Yu (2011), Su *et al.* (2013), Pauliuk (2018)	4
12. Lack of information sharing	Jaeger and Upadhyay (2020), Geng *et al.* (2012), Kumar and Suganya (2019)	3
13 Complexity in deciding final price of product	Lieder and Rashid (2016), Kirchherr *et al.* (2017)	2
14. Fallacious information	Su *et al.* (2013), Muradin and Foltynowicz (2019)	2
15. Improper mapping of the environment laws with CE Practices	Moktadir *et al.* (2018), Geng *et al.* (2012)	2
16. Unproductive management and poor administration	Su *et al.* (2013)	1
17. Uneven distribution of work	Shahbazi *et al.* (2016)	1
18. Inefficient take back mechanism	Ghisellini *et al.* (2016)	1

(*continued*)

Table 2. Grouping of CE challenges

Challenges	References	Occurrence
19. Lack of Standardization of refurbished or remanufactured products	Van Weelden *et al.* (2016)	1
20. Environmental awareness among the stakeholders	Agyemang *et al.* (2019)	1

Table 2.

S. no.	Challenge	Occurrence	Percentage of occurrence (%)	Collective percentage of occurrence (%)
1	Lack of standardization system	14	13.59	13.59
2	Noncompliance of environmental laws	14	13.59	27.18
3	Lack of economic inducement	13	12.62	39.8
4	High capital investment cost	12	11.65	51.45
5	Design issues owing to technological limitations	8	7.7	59.15
6	Lack of infrastructure and unavailability of advance tool	6	5.82	64.97
7	Less preference to reused or refurbished products	5	4.85	69.82
8	Coordination with supply chain partners	5	4.85	74.67
9	Managing product quality through recovered parts	4	3.88	78.55
10	Revenue generation	4	3.88	82.43
11	Inadequate implementation of CE laws	4	3.88	86.31
12	Lack of information sharing	3	2.91	89.22
13	Complexity in deciding final price of product	2	1.94	91.16
14	Fallacious information	2	1.94	93.1
15	Improper mapping of the environment laws with CE practices	2	1.94	95.04
16	Unproductive management and poor administration	1	0.97	96.01
17	Uneven distribution of work	1	0.97	96.98
18	Inefficient take back mechanism	1	0.97	97.95
19	Lack of standardization of refurbished or remanufactured products	1	0.97	98.92
20	Environmental awareness among the stakeholders	1	0.97	100

Table 3.
Vital few and useful many CE challenges

with DEMATEL approach to avoid loss of information owing to the uncertainty arising from human judgment thus removing ambiguity from the data collected (Chang *et al.*, 1998; Chen and Chiou, 1999).

Tian *et al.* (2019) proposed a DEMATEL methodology for the selection of take back patterns of vehicle scrap parts for the ordered implementation of reverse logistics process in China. Khompatraporn and Somboonwiwat (2017) studied the supply chain of Thai automotive industry and identified ten factors affecting its competitiveness by using Fuzzy

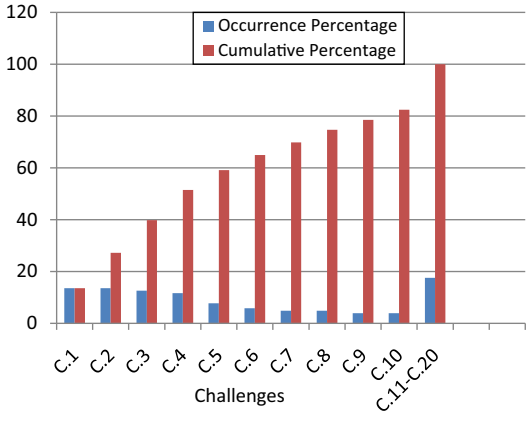

C1- Lack of standardization system
C2- Non compliance of environmental law
C3- Lack of economic inducement
C4- High capital investment cost
C5- Design issues
C6- Lack of infrastructure and advance to
C7- Less preference to reused products
C8- Coordination with SC partners
C9- Managing product quality
C10- Revenue generation
C11-20 - Inadequate CE laws, Lack of information sharing, Complex price, Falla information, Improper mapping of CE law ,Unproductive management, Uneven distribution of work, Inefficient take back mechanism, Lack of Standardization, Lack

Figure 2.
Pareto analysis of circular economy (CE) challenges

DEMATEL approach. Govindan *et al.* (2015) examined the causal interaction among GSCM practices and performance using intuitionist fuzzy sets as applied to DEMATEL approach. Lin (2013) explored the influential factors among eight different criteria of three important GSCM practices and analyzed them using Fuzzy DEMATEL method. Chang *et al.* (2011) incorporated Fuzzy DEMATEL in their study to find the most influential factors during the selection of suitable SCM suppliers. Wu and Lee (2007) used Fuzzy logic and DEMATEL approach to develop global managers competency by way of segmenting a set of competencies into some portions involving the vagueness of human judgments. Büyüközkan and Çifçi (2012) proposed an evaluation framework for green suppliers by examining GSCM dimensions using hybrid MCDM approach based on Fuzzy DEMATEL, Fuzzy ANP and Fuzzy TOPSIS approach.

The Fuzzy DEMATEL approach has been applied in the proposed study. Fuzzy set, F in Y is an ordered set of pairs, i.e. $F = \{(y, \mu F(y))\}$, $y \epsilon Y$; where $\mu F(y)$ denotes the membership of the function, and $Y = \{y\}$ relates to a set of points represented by y (Bellman and Zadeh, 1970). The membership function $\mu F(y)$ signifies the measure of acceptance that y is an element belonging to F. It is presumed that $\mu F(y) \epsilon [0, 1]$, where $\mu F\{y) = 1$ depicts that y is definitely an element of F, while $\mu F\{y) = 0$ represents *y* is not an element of F. A fuzzy number $\hat{N}$ corresponds to a fuzzy set $\{(y, \mu_{\hat{N}}(y))\}$, where the value of y always lie on the real line and $\mu_{\hat{N}}(y)$ is the membership function which shows the probability of the fuzzy number N lying within the real interval [l, *r*].

Triangular fuzzy number (TFN) $\hat{N}$ is represented as a set of (l, m, *r*) and $\mu_{\hat{N}}$ is the membership function denoted as in Figure 3. The different values of the membership function can be expressed as per equation (1):

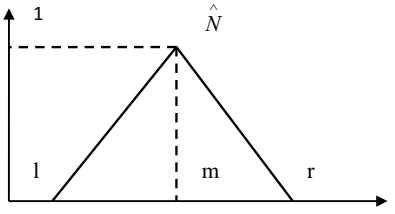

Figure 3.
Triangular fuzzy number

$$\mu_{\hat{N}}(y) = \begin{Bmatrix} 0, & y < a \\ (y-a)/(b-a), & a \le y \le b \\ (c-y)/(c-b), & b \le y \le c \\ 0, & y > c \end{Bmatrix} \quad (1)$$

The concept of TFN has been used to find idyllic solutions from group decision-making. A TFN is represented by its height, spread, shape and its relative position on the *x*-axis (Chen and Hwang, 1992). Defuzzification is a process to convert uncertain spatial data into crisp values which consider all the parameters as stated by Chen and Hwang (1992). Defuzzification can be generally performed by centroid or center-of-gravity method. The centroid method cannot differentiate among two fuzzy numbers with equivalent crisp value, even if the shape of the fuzzy numbers is different (Opricovic and Tzeng, 2003). Instead, Converting Fuzzy data into Crisp Scores (CFCS) defuzzification method is used to obtain a better crisp value (Opricovic and Tzeng, 2003). In this method, the equivalent fuzzy scores are converted into crisp numbers involving the computation of right and left score by the fuzzy maximum and fuzzy minimum, respectively and the total score is computed by calculating the average weight according to the membership functions (Opricovic and Tzeng, 2003). The step wise defuzzification process is presented below:

- Step 1. Compute normalized values of the Triangular fuzzy matrix with fuzzy number (l_{ij}, m_{ij}, r_{ij}) using equations (2) to (4):

$$r_i^{\max} = \max r_{ij}, l_i^{\min} = \min l_{ij}$$

$$\Delta_{\min}^{\max} = r_i^{\max} - l_i^{\min}$$

Compute for all alternatives *as*, a_j=*1, 2, 3, . . ., J*

$$y_{lj} = \left(l_{ij} - l_i^{\min}\right) / \Delta_{\min}^{\max} \quad (2)$$

$$y_{mj} = \left(m_{ij} - l_i^{\min}\right) / \Delta_{\min}^{\max} \quad (3)$$

$$y_{rj} = \left(r_{ij} - l_i^{\min}\right) / \Delta_{\min}^{\max} \quad (4)$$

- Step 2. Compute left (ls) and right (rs) normalized values, for j = 1, 2, . . .J using equations (5) and (6):

$$y_j^{ls} = y_{mj}\left(1 + y_{mj} - y_{lj}\right) \quad (5)$$

$$y_j^{rs} = y_{rj}\left(1 + y_{rj} - y_{mj}\right) \quad (6)$$

- Step 3. Compute total normalized crisp value, for j = 1,2,. . .,J using equation (7):

$$y_j^{crisp} = \left[y_j^{ls}\left(1 - y_j^{ls}\right) + y_j^{rs} y_j^{rs}\right] / \left[1 - y_j^{ls} + y_j^{rs}\right] \quad (7)$$

- Step 4. Compute crisp values, for j = l,2,. . .,J using equation (8):

$$f_{ij} = l_i^{\min} + y_j^{crisp} \Delta_{\min}^{\max} \tag{8}$$

Following the above process, each of the allocated fuzzy numbers is converted into crisp value. A performance matrix containing fuzzy elements, $f_{ij} = (l_{ij}, m_{ij}, r_{ij})$, j = 1,2. . .J, i ϵ $\widetilde{n}$, is converted into crisp numbers f_{ij}, j = 1,2. . .J, $i = 1,. . .,n,$ (where n represents the total number of criteria, $n > \widetilde{n}$). In most of the studies, DEMATEL has been applied on crisp data while in the proposed study the application of DEMATEL approach has been extended on the data gathered through human perception. Further, the DEMATEL method comprises of the following (Fontela and Gabus, 1976):

- Step 1. Development of direct-relation matrix

Develop a matrix of direct relations by tabulating the responses of various experts. "Direct Relation Matrix" $A_{n\times n}$ (where n stands for the total number of factors) is constructed by establishing a pairwise comparison among factors. Each value of matrix $A_{n\times n}$ is represented by a_{ij} which depicts the level of influence of criterion i on j. The averaged value of matrice A is developed by calculating the mean scores of all the "H" experts where "w_k" denotes the significant weight of kth expert [Refer equation (9)]:

$$a_{ij} = \frac{\sum_{k=1}^{H} w_k y_{ij}^k}{\sum_{k=1}^{H} w_k} \tag{9}$$

- Step 2. Representation of triangular fuzzy numbers

Responses are expressed in linguistic terms. According to Li (1999), the linguistic variable may be classified as no influence, very less influence, less influence, moderate influence and high influence. These linguistic terms are assigned an influence score which is represented in the form of TFNs. The value of influence score varies from 0 to 4 with no influence being assigned 0 value and high influence is represented with a score of 4. The score of influence of various linguistic terms with their corresponding TFN is shown in Table 6:

- Step 3. Convert the triangular fuzzy numbers into initial direct relation matrix

TFNs can be used to assign values to fuzzy linguistic variables which are then converted into crisp values using the CFCS method. The crisp value in the initial direct relation matrix can be calculated by following the equations (2)–(8) using CFCS defuzzification method:

- Step 4. Normalizing the direct relation matrix

To normalize the matrix of direct relation equations (10) and (11) are applied. This results in the formation of an averaged direct relation matrix:

$$Y = k \times A \tag{10}$$

$$k = \frac{1}{\max \sum_{j=1}^{n} a_{ij}}, 1 \le i \le n \tag{11}$$

- Step 5. Construct total relation matrix

The matrix of total relation "T" can be obtained by using the equation (12). The corresponding identity matrix is represented by "I."

$$T = Y(I - Y)^{-1} \tag{12}$$

- Step 6. Generating the causal diagram.

The causal diagram is generated by the values of summation of rows and summation of columns for each criterion which is represented as D and R, respectively. To obtain the values of D and R for each row and column, equation (13) to (15) are used:

$$T = [t_{ij}]_{n\times n}, \mathrm{i,j} = 1, 2, \ldots, \mathrm{n} \tag{13}$$

$$D = \left[\sum_{j=1}^{n} t_{ij}\right]_{n\times 1} = [t_i]_{n\times 1} \tag{14}$$

$$R = \left[\sum_{i=1}^{n} t_{ij}\right]_{1\times n} = [t_j]_{1\times n} \tag{15}$$

A cause and effect diagram is obtained by plotting the data set of (D + R, D-R), where (D + R) represents the horizontal axis vector or "Prominence" which is used to obtain the ranking of the criterion and (D-R) depicts the vertical axis or "Relation" which shows the category in which the criteria will fall.

4. Case illustration of Indian manufacturing industry

Section 4 comprises of the discussion related to the application of proposed methodology in the adoption of CE practices in the Indian manufacturing context.

4.1 Indian manufacturing industry

Rise in the per capita income, growth in population, rapid urbanization and changing lifestyle ensures a strong building up of manufacturing sector in India. According to a report published by IBEF, India will come out as world's fifth largest consumer market by 2025 with an average consumption expected to rise by four times during 2005–2025. The Indian Government aims to achieve 25% of its GDP share by manufacturing sectors till 2022 as against 16% current share (IBEF, 2019). This will attract manufacturers from all over the world to invest and establish their manufacturing unit in India thus creating 100 million new employment opportunities in this sector by 2022 and making India a global manufacturing hub.

India being a developing nation, hence sustainability becomes a major issue to meet the demand of majority of population. Therefore, it is the right time to examine the research and novel activities to help Indian manufacturing sector in developing their approach and the essential techniques/methods to adopt circular models effectively. An attempt has been made to explore and identify the challenges related to the implementation of CE practices in Indian manufacturing context by using Fuzzy-DEMATEL as the method for the prioritization of these challenges.

4.2 Data collection

This study uses survey method to collect data from different experts by distributing a questionnaire among the supply chain professionals of 75 different manufacturing organizations located in the National Capital Region (NCR) of India. Three experts each from

academia and manufacturing based multi-national companies located in Delhi-NCR reviewed the preliminary draft of the questionnaire. Experts commented on the intelligibility, subject and illustration of the survey questionnaire. Suggestions were incorporated and improvements in the questionnaire were completed before distributing for data collection. Google form was used to develop the questionnaire. This questionnaire consists of all the ten significant challenges identified through extensive literature survey after applying Pareto analysis approach. The professionals were asked to rate these challenges on a five point Likert scale (e.g. 1 = no influence and 5 = extremely high influence) illustrating the influence of each challenge on the implementation of CE principle in their manufacturing organization.

The second stage comprises of the filling up of pair-wise comparison matrix consisting of ten significant challenges. Six experts from operation, environment, logistics, procurement, store and marketing department were selected to fill the responses. The experts were chosen in a way so that every domain of the CE is included while gathering the information related to its implementation. Therefore, the experts are selected from the operations, logistics, procurement, store, marketing and environment fields. These experts were selected from industry, academia and not for profit organizations to reflect their knowledge and experience in the outcome of the study and provide better solutions to its implementation. The weight of each expert was expressed as a linguistic value shown in Table 4.

In this study the questionnaire was distributed among the supply chain professionals in two phases. First, a total of 200 emails were sent to the professionals of different manufacturing organization and responses received were analyzed. In addition, 100 emails were sent to the other organization to gather sufficient number of responses. A total of 300 emails were sent to the companies engaged in the manufacturing sector which are having a minimum annual turnover of 100 million Indian rupees and employees ranging between 200 and 1,000. Out of 90 responses received 15 were incomplete and, therefore, not considered for evaluation. Overall 75 responses were used for the purpose of analysis with a response rate of 25%. Most of the respondents either belonged to middle level management or top management of the organization which are dealing with strategic part of management. A nonresponse bias was checked by splitting the responses into two groups based upon the date on which response is received. A total of 40 responses were received before the due date and 35 were received after. A *t*-test was performed to check for any significant difference in the samples of the two groups. With a p value greater than 0.05 ($p > 0.05$) the results did not yield any significant difference between the samples of both the groups in terms of annual turnover, number of employees and their designation.

5. Results and discussion

The fuzzy DEMATEL approach is used to evaluate the relative weightage of the challenges. Ten significant challenges to the application of CE in the perspective of the manufacturing

Experts	Linguistic variable	Significance weight	Crisp weights
Expert 1 (Operation dept)	Medium	(0.3, 0.5, 0.7)	0.5
Expert 2 (Environment dept)	High	(0.5, 0.7, 0.9)	0.7
Expert 3 (Logistics dept)	Medium	(0.3, 0.5, 0.7)	0.5
Expert 4 (Procurement dept)	Low	(0.1, 0.3, 0.5)	0.3
Expert 5 (Store dept)	Low	(0.1, 0.3, 0.5)	0.3
Expert 6 (Marketing dept)	High	(0.5, 0.7, 0.9)	0.7

Table 4. Importance weight of experts

industry were selected through literature survey and responses obtained from survey questionnaire. They are classified as: (C.1) lack of standardization system; (C.2) noncompliance of environmental laws; (C.3) lack of economic inducement; (C.4) high capital investment cost; (C.5) design issues owing to technological limitation; (C.6) lack of infrastructure and unavailability of advance tool; (C.7) less preference to refurbish and reused product; (C.8) coordination with neighborhood organization; (C.9) managing product quality through recovered parts; and (C.10) revenue generation.

The responses of the experts were tabulated in the form of pairwise comparison matrix to evaluate the influence of each challenge. This yields to a direct relation matrix presented in Table 5 which shows the interrelationship between challenges.

The linguistic term used for the corresponding influence score are shown as TFNs in Table 6.

The data elements of direct relation matrix are shown as corresponding TFNs in Table 7. The responses that are shown as TFNs are defuzzified into a crisp value which obtains the f_{ij}. The logical formulae as given in the equations (2)–(8) are used to compute the initial direct-relation matrix.

The next step is normalizing the initial direct relation matrix using the equations (10) and (11). This results in the formation of a generalized direct relation matrix. The total relation matrix can be acquired from the generalized direct relation matrix by following equation (12). The total relation matrix is presented as Table 8.

The sum of each row and sum of each column of the total relation matrix are separately computed using equations (13)–(15) and are denoted as D and R, respectively. If (D-R) is positive, criterion belongs to the cause category and if the value comes out to be negative, the criterion falls into the effect group. The horizontal axis of the causal diagram is represented by "D + R" which illustrates the relative significance of a criterion. (D + R)

Table 5. Direct-relation matrix

	C.1	C.2	C.3	C.4	C.5	C.6	C.7	C.8	C.9	C.10
C.1	0	2	3	1	3	4	3	1	2	3
C.2	1	0	4	1	1	4	3	1	1	4
C.3	0	3	0	0	0	2	4	0	0	4
C.4	3	1	1	0	4	1	3	0	4	3
C.5	4	3	3	2	0	4	4	3	0	4
C.6	0	2	3	1	1	0	3	2	0	3
C.7	0	3	1	0	2	2	0	3	1	3
C.8	1	2	0	1	3	1	3	0	1	1
C.9	4	1	4	3	3	4	3	3	0	4
C.10	1	3	3	0	3	4	3	0	0	0

Table 6. Linguistic terms and corresponding triangular fuzzy number

Linguistic term	Influence score	Triangular fuzzy no.
No influence	0	(0.0, 0.1, 0.3)
Very less influence	1	(0.1, 0.3, 0.5)
Less influence	2	(0.3, 0.5, 0.7)
Moderate influence	3	(0.5, 0.7, 0.9)
High influence	4	(0.7, 0.9, 1.0)

	C.1	C.2	C.3	C.4	C.5	C.6	C.7	C.8	C.9	C.10
C.1	0	(0.3,0.5,0.7)	(0.5,0.7,0.9)	(0.1,0.3,0.5)	(0.5,0.7,0.9)	(0.7,0.9,1.0)	(0.5,0.7,0.9)	(0.1,0.3,0.5)	(0.3,0.5,0.7)	(0.5,0.7,0.9)
C.2	(0.1,0.3,0.5)	0	(0.7,0.9,1.0)	(0.1,0.3,0.5)	(0.1,0.3,0.5)	(0.7,0.9,1.0)	(0.5,0.7,0.9)	(0.1,0.3,0.5)	(0.1,0.3,0.5)	(0.7,0.9,1.0)
C.3	(0.0,0.1,0.3)	(0.5,0.7,0.9)	0	(0.0,0.1,0.3)	(0.0,0.1,0.3)	(0.3,0.5,0.7)	(0.7,0.9,1.0)	(0.0,0.1,0.3)	(0.0,0.1,0.3)	(0.7,0.9,1.0)
C.4	(0.5,0.7,0.9)	(0.1,0.3,0.5)	(0.1,0.3,0.5)	0	(0.7,0.9,1.0)	(0.1,0.3,0.5)	(0.5,0.7,0.9)	(0.0,0.1,0.3)	(0.7,0.9,1.0)	(0.5,0.7,0.9)
C.5	(0.7,0.9,1.0)	(0.5,0.7,0.9)	(0.5,0.7,0.9)	(0.3,0.5,0.7)	0	(0.7,0.9,1.0)	(0.7,0.9,1.0)	(0.5,0.7,0.9)	(0.0,0.1,0.3)	(0.7,0.9,1.0)
C.6	(0.0,0.1,0.3)	(0.3,0.5,0.7)	(0.5,0.7,0.9)	(0.1,0.3,0.5)	(0.1,0.3,0.5)	0	(0.5,0.7,0.9)	(0.3,0.5,0.7)	(0.0,0.1,0.3)	(0.5,0.7,0.9)
C.7	(0.0,0.1,0.3)	(0.5,0.7,0.9)	(0.1,0.3,0.5)	(0.0,0.1,0.3)	(0.3,0.5,0.7)	(0.3,0.5,0.7)	0	(0.5,0.7,0.9)	(0.1,0.3,0.5)	(0.5,0.7,0.9)
C.8	(0.1,0.3,0.5)	(0.3,0.5,0.7)	(0.0,0.1,0.3)	(0.1,0.3,0.5)	(0.5,0.7,0.9)	(0.1,0.3,0.5)	(0.5,0.7,0.9)	0	(0.1,0.3,0.5)	(0.1,0.3,0.5)
C.9	(0.7,0.9,1.0)	(0.1,0.3,0.5)	(0.7,0.9,1.0)	(0.5,0.7,0.9)	(0.5,0.7,0.9)	(0.7,0.9,1.0)	(0.5,0.7,0.9)	(0.5,0.7,0.9)	0	(0.7,0.9,1.0)
C.10	(0.1,0.3,0.5)	(0.5,0.7,0.9)	(0.5,0.7,0.9)	(0.0,0.1,0.3)	(0.5,0.7,0.9)	(0.7,0.9,1.0)	(0.5,0.7,0.9)	(0.0,0.1,0.3)	(0.0,0.1,0.3)	0

Table 7.
Triangular fuzzy numbers

signifies the "Prominence" and (D-R) attributes to the "relation" of a criterion. Table 9 shows the corresponding value of (D + R) and (D-R) for the ten challenges considered.

Therefore, the causal diagram is generated by plotting the data set of (D + R, D-R), shown in Figure 4. The causal diagram provides the ability to understand how far the individual challenges affect the application of CE principles in the manufacturing industry.

Findings revealed that challenges such as noncompliance of environmental laws (C.2), lack of economic inducement (C.3), lack of infrastructure and unavailability of advance tool

Table 8.
Total relation matrix

	C.1	C.2	C.3	C.4	C.5	C.6	C.7	C.8	C.9	C.10
C.1	0.1915	0.4071	0.3501	0.1994	0.3250	0.4359	0.3996	0.2479	0.2311	0.4136
C.2	0.2151	0.3045	0.3309	0.1832	0.2559	0.4043	0.3698	0.2269	0.2142	0.3886
C.3	0.1829	0.4017	0.2075	0.1563	0.2149	0.3633	0.3473	0.1963	0.1592	0.3686
C.4	0.3030	0.4110	0.3064	0.1588	0.3391	0.3711	0.3971	0.2403	0.2771	0.4191
C.5	0.3505	0.5244	0.3912	0.2548	0.2752	0.4909	0.4669	0.3366	0.2264	0.4882
C.6	0.1844	0.3742	0.3015	0.1687	0.2369	0.2589	0.3446	0.2348	0.1637	0.3603
C.7	0.1995	0.4187	0.2725	0.1671	0.2854	0.3606	0.2688	0.2754	0.1870	0.3876
C.8	0.1962	0.3534	0.2245	0.1652	0.2704	0.2920	0.3292	0.1582	0.1832	0.2902
C.9	0.3627	0.4817	0.4062	0.2884	0.3835	0.5059	0.4703	0.3448	0.2017	0.5032
C.10	0.2188	0.4337	0.3231	0.1732	0.2953	0.4052	0.3671	0.2180	0.1798	0.2900

Table 9.
The prominence and relation vectors (CASE 1)

Challenges	D	R	D-R	D + R	Rank(D + R)
C.1	3.2012	2.4047	0.7965	5.6059	8
C.2	2.8934	4.1103	−1.2169	7.0037	1
C.3	2.5979	3.1138	−0.5159	5.7117	7
C.4	3.2231	1.9149	1.3082	5.138	9
C.5	3.805	2.8815	0.9235	6.6865	3
C.6	2.6279	3.888	−1.2601	6.5159	5
C.7	2.8226	3.7608	−0.9382	6.5834	4
C.8	2.4626	2.4793	−0.0167	4.9419	10
C.9	3.9482	2.0236	1.9246	5.9718	6
C.10	2.9043	3.9094	−1.0051	6.8137	2

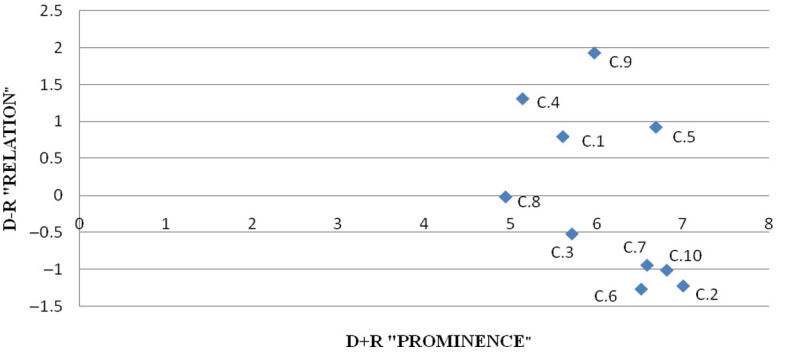

Figure 4.
CAUSAL diagram

(C.6), less preference to refurbish and reused product (C.7), coordination with neighborhood organization (C.8) and revenue generation (C.10) fall into the effect group because these challenges are easily influenced by the rest of the challenges as the individual value of (D-R) for each challenge is negative. While lack of standardization system (C.1), high capital investment cost (C.4), design issues owing to technological limitation (C.5) and managing product quality through recovered parts (C.9) belong to the cause category because these challenges have a larger value of (D) in comparison to the value of (R). (D + R) score signifies the relative importance, as value of D denotes how much it influences other factors and R depicts the degree to which it is influenced by others. Noncompliance of environmental laws (C.2) has the highest (D + R) score, therefore, should be considered as the major challenge in the CE application. Revenue generation (C.10), Design issues owing to technological limitation (C.5), less preference to refurbish and reused product (C.7) and lack of infrastructure and unavailability of advance tool (C.6) rank after noncompliance of environmental laws (C.2) in the (D + R) ranking; therefore, these are considered as relatively less important challenges. Furthermore, the (D-R) score of managing product quality through recovered parts (C.9) is the highest in the causal diagram (Figure 4) which means that it will greatly influence other challenges during the application of CE practices in the manufacturing industry. High capital investment cost (C.4), design issues owing to technological limitation (C.5) and lack of standardization system (C.1) are having less influence on other challenges as compared to managing product quality through recovered parts (C.9). The overall prioritization of the challenges is as:

C.2 > C.10 > C.5 > C.7 > C.6 > C.9 > C.3 > C.1 > C.4 > C.8

The finding of the study is also supported by earlier research. Lieder and Rashid (2016) found noncompliance of environmental laws as the major challenge toward CE application in the manufacturing industry. Geng and Doberstein (2008) in their article on the application of CE concept at the regional level in China, revealed that weak economic inducement from the government make it difficult for the small and medium enterprises to implement CE practices at the regional level.

Franklin-Johnson *et al.* (2016) suggested that the amount of revenue generated by the application of CE practices in the supply chain could be considered as one of the major challenges because cost incurred in recycling and remanufacturing of the products is quite high. Technological limitations owing to complex design and material composition of a product make it a greater challenge for the successful and cost-effective recovery and reuse of a product (Pringle *et al.*, 2016). Shahbazi *et al.* (2016) revealed that managing product quality through recovered parts is one of the major challenge that increase the chances of lack of interest among the employees toward the CE application. Pan *et al.* (2014) found that higher initial cost related to the investment in the area of cutting-edge technology, skilled manpower and better facilities for production are significantly becoming major challenge toward the application of CE. Su *et al.* (2013) suggests that lack of standardization system to measure the performance of CE-oriented practices could create obstruction in its application globally. Ghisellini *et al.* (2016) considers inefficient take-back mechanism as a major market issue. To overcome this barrier it is necessary to have an effective coordination among the supply chain partners and full support of all the stakeholders. The findings of Agyemang *et al.* (2019) revealed that unawareness, financial constraint and lack of expertise are the top three challenges in implementing CE in the automobile industry of Pakistan. Cezarino *et al.* (2019) identified lack of communication between public and private institutions, ineffectiveness in consolidating industrial policies and investment in remanufacturing process are some of the major challenges to CE implementation in the Brazilian manufacturing industry. The study conducted by Moktadir *et al.* (2018) focusing on CE

implementation in leather industry of Bangladesh found that the knowledge of CE is essential for its implementation. The findings of this study are similar to the other studies identifying challenges to CE implementation, and therefore, the results are generalized in context to emerging economies.

6. Sensitivity analysis

Sensitivity analysis is performed by varying the weight assigned to a particular expert or by changing the influential rating among various CE challenges so as to check the robustness of the model. In this paper, sensitivity analysis is carried out for Fuzzy-DEMATEL results by altering the weight of expert 1. Primarily expert 1 is assigned "medium" (0.3, 0.5, 0.7) significance weight. This situation is represented by "Case 1." During the sensitivity analysis of the above model the significance weight of Expert 1 is modified to "low" (0.1, 0.3, 0.5) and we call it "Case 2." In another situation, the weight of Expert 1 is changed to "high" (0.5, 0.7, 0.9) and represent it as "Case 3" without altering the weight of the remaining experts. The outcomes of the other two cases are shown in Table 10. Figure 5 portrays the steadiness of the model. From the results of sensitivity analysis as represented in Figure 5, it is interpreted that the peak and trough in each of the cases remain same. As there is no considerable change occurring in the ranking of the most important challenges to CE, the

Table 10. Prominence and relation vector (CASES 2 and 3)

	CASE 2		CASE 3	
Challenges	D + R	Rank	D + R	Rank
C.1	5.4868	8	6.777768	7
C.2	6.815395	1	8.136412	1
C.3	5.568633	7	6.694243	8
C.4	5.051109	9	6.243098	9
C.5	6.546153	3	7.838396	3
C.6	6.383685	5	7.700172	5
C.7	6.435442	4	7.824168	4
C.8	4.825126	10	5.963813	10
C.9	5.871386	6	7.078272	6
C.10	6.664718	2	7.848311	2

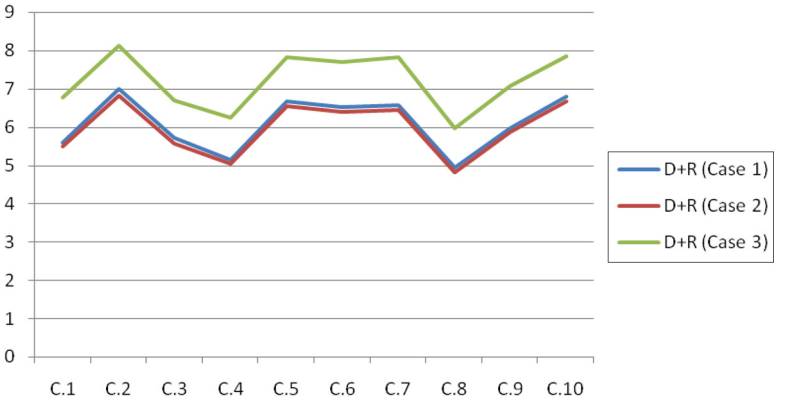

Figure 5. Sensitivity analysis of the ranking of the challenges corresponding to the change of "significance weight" of Expert 1

model has least sensitivity to the alteration in the weight of expert 1. In the future, sensitivity analysis can be performed by altering the weights of remaining experts.

7. Implications of study

The identification of significant challenges in the context to developing economies leads to theory building of the implementation phase of CE under different scenarios. Ten significant challenges were identified and prioritized to rank them according to the degree of criticality in context of developing economies. These challenges can have a major theoretical implication on the future research conducted in the direction of adopting sustainable development practices. The findings of this study will help the researchers to build a conceptual framework for the smooth transition toward CE in emerging economies.

The study is conducted in Indian context, as it is a developing economy having a large consumer base with a rapidly increasing population. Because of such a high population increasing rate and limited availability of resources, studies related to the challenges and solutions for the implementation of sustainable business model can help emerging economies to strive toward sustainable development. Participation of each and every stakeholder is required for its effective implementation. Policies need to be framed by the government to support the smoother implementation of CE in the manufacturing industry (Agrawal *et al.*, 2014). For example, in Germany law related to efficient waste management was passed in the year 1996 to minimize environment degradation (Nelles *et al.*, 2016). In Japan, a comprehensive legal framework for CE implementation was developed that directed the society toward reuse and recycling of used products (Morioka *et al.*, 2005). The past literature on the framing of policies illustrates that the government needs to regularly monitor the other stakeholders involved in the effective implementation of CE.

The outcomes of the research could be useful for those organizations planning to adopt sustainable manufacturing practices in their day to day business. The findings can be useful for the organization to understand the degree of severity of each challenge. The causal relationship among the challenges of CE implementation could assist the managers and practitioners to analyze and develop effective strategies for its successful transition. Further the ranking of the challenges could help the management to channelize their action and work on the important challenges that could significantly affect its implementation. In future, the findings could help the enterprises to understand the need of adopting sustainable business models and what benefits can be gained from its implementation.

8. Conclusion and future scope

The concept of CE is in nascent stage and requires utmost attention by the researchers and practitioners for its successful application in the manufacturing industry. This concept is a solution to many serious problems like waste generation, resource scarcity and sustainable economic benefits. Application of CE in the manufacturing industry entails serious challenges to the enterprise and researchers need to find ways for its successful application. Therefore, this study is focused to a developing economy having a huge customer base and manufacturing sector almost contributing one fourth in the GDP. It is necessary for a country like India to implement such business models in the manufacturing sector that could foster toward a sustainable development.

This study selected ten challenges for the CE application in the manufacturing industry of India. Based on the exhaustive literature review it has been seen that very limited work has been conducted in the context to developing economies. Analysis of the findings revealed that noncompliance of environmental laws, revenue generation, design issues owing to technological limitation and inefficient take-back mechanism are some of the major

challenges to the application of CE practices in the Indian manufacturing industry. The findings of this study are significant to Indian context; however, studies related to the challenges in CE implementation have yielded similar results in context to other emerging economies (Agyemang *et al.*, 2019; Cezarino *et al.*, 2019; Jaeger and Upadhyay, 2020; Moktadir *et al.*, 2018).

The novelty of this study and the contribution made to the literature is summarized as follows:

- The study contributes to the identification of sustainability related challenges faced during the implementation of a CE concept by a developing economy.
- This study also includes the prioritization of significant challenges to CE implementation faced by the manufacturing industry of a developing economy.
- This research also proposed a methodology that could evaluate and explore these challenges for CE application.

Finally, the findings of this research will help the researchers and managers to develop a framework for the successful application of CE in the context of manufacturing industry. The implementation of this novel concept is not just seen as a trillion dollar business but will also create several million job opportunities that will be regarded as a major upliftment for the society. Therefore, manufacturing organization should take prior action in this direction to prevent the obstruction caused by these challenges on the implementation of the CE concept in the Indian manufacturing industry.

This kind of approach can also be used for some other industries such as textiles, automobile, pharmaceuticals, etc. Some of the limitations of this study are: the study was conducted by collecting data from only six experts. In the future, more experts could be assigned to provide data pertaining to the study. The analysis was done considering only ten challenges to CE application. Researchers may consider more challenges to have an effective application. Apart from Fuzzy-DEMATEL approach, other techniques that could predict the interrelationship among the criterion can be used.

References

Agrawal, S., Singh, R.K. and Murtaza, Q. (2014), "Forecasting product returns for recycling in Indian electronics industry", *Journal of Advances in Management Research*, Vol. 11 No. 1, pp. 102-114.

Agrawal, S., Singh, R.K. and Murtaza, Q. (2015), "A literature review and perspectives in reverse logistics", *Resources, Conservation and Recycling*, Vol. 97, pp. 76-92.

Agyemang, M., Kusi-Sarpong, S., Khan, S.A., Mani, V., Rehman, S.T. and Kusi-Sarpong, H. (2019), "Drivers and barriers to circular economy implementation: an explorative study in Pakistan's automobile industry", *Management Decision*, Vol. 57 No. 4, pp. 971-994.

Azadegan, A., Porobic, L., Ghazinoory, S., Samouei, P. and Saman Kheirkhah, A. (2011), "Fuzzy logic in manufacturing: a review of literature and a specialized application", *International Journal of Production Economics*, Vol. 132 No. 2, pp. 258-270.

Bamford, D.R. and Greatbanks, R.W. (2005), "The use of quality management tools and techniques: a study of application in everyday situations", *International Journal of Quality and Reliability Management*, Vol. 22 No. 4, pp. 376-392.

Bellman, R.E. and Zadeh, L.A. (1970), "Decision-making in a fuzzy environment", *Management Science*, Vol. 17 No. 4, p. B-141.

Bocken, N.M.P., de Pauw, I., Bakker, C. and van der Grinten, B. (2016), "Product design and business model strategies for a circular economy", *Journal of Industrial and Production Engineering*, Vol. 33 No. 5, pp. 308-320.

Boulding, K. (1966), *The Economy of the Coming Spaceship Earth*, New York, NY.

Büyüközkan, G. and Çifçi, G. (2012), "A novel hybrid MCDM approach based on fuzzy DEMATEL, fuzzy ANP and fuzzy TOPSIS to evaluate green suppliers", *Expert Systems with Applications*, Vol. 39 No. 3, pp. 3000-3011.

Cezarino, L.O., Liboni, L.B., Oliveira Stefanelli, N., Oliveira, B.G. and Stocco, L.C. (2019), "Diving into emerging economies bottleneck: industry 4.0 and implications for circular economy", *Management Decision*, available at: https://doi.org/10.1108/MD-10-2018-1084

Chandra, D. and Kumar, D. (2020), "Prioritizing the vaccine supply chain issues of developing countries using an integrated ISM-fuzzy ANP framework", *Journal of Modelling in Management*, Vol. 15 No. 1, pp. 112-165.

Chang, Y.H., Yeh, C.H. and Cheng, J.H. (1998), "Decision support for bus operations under uncertainty: a fuzzy expert system approach", *Omega*, Vol. 26 No. 3, pp. 367-380.

Chang, B., Chang, C.W. and Wu, C.H. (2011), "Fuzzy DEMATEL method for developing supplier selection criteria", *Expert systems with Applications*, Vol. 38 No. 3, pp. 1850-1858.

Chen, L.H. and Chiou, T.W. (1999), "A fuzzy credit-rating approach for commercial loans: a Taiwan case", *Omega*, Vol. 27 No. 4, pp. 407-419.

Chen, S. and Hwang, C. (1992), "Fuzzy multiple attribute decision making methods", *Fuzzy Multiple Attribute Decision Making*, Springer, Berlin, Heidelberg, pp. 289-486.

Craft, R.C. and Leake, C. (2002), "The Pareto principle in organizational decision making", *Management Decision*, Vol. 40 No. 8, pp. 729-733.

De Angelis, R. (2020), "Circular economy: laying the foundations for conceptual and theoretical development in management studies", *Management Decision*, available at: https://doi.org/10.1108/MD-05-2019-0587

Elia, V., Gnoni, M.G. and Tornese, F. (2017), "Measuring circular economy strategies through index methods: a critical analysis", *Journal of Cleaner Production*, Vol. 142, pp. 2741-2751.

Ethirajan, M., Arasu, M.T., Kandasamy, J., Vimal, K.E.K., Nadeem, S.P. and Kumar, A. (2020), "Analysing the risks of adopting circular economy initiatives in manufacturing supply chains", *Business Strategy and the Environment*, No. April, pp. 1-33.

Farooque, M., Zhang, A., Thurer, M., Qu, T. and Huisingh, D. (2019), "AC", *Journal of Cleaner Production*, Vol. 228, available at: https://doi.org/10.1016/j.jclepro.2019.04.303

Fontela, E. and Gabus, A. (1976), "Current perceptions of the world problematique", *World Modeling: A Dialogue*, North-Holland Publishing Company, Amsterdam/Oxford.

Fotopoulos, C., Kafetzopoulos, D. and Gotzamani, K. (2011), "Critical factors for effective implementation of the HACCP system: a Pareto analysis", *British Food Journal*, Vol. 113 No. 5, pp. 578-597.

Franklin-Johnson, E., Figge, F. and Canning, L. (2016), "SC", *Journal of Cleaner Production*, Vol. 133, available at: https://doi.org/10.1016/j.jclepro.2016.05.023

Garg, P. and Garg, A. (2013), "An empirical study on critical failure factors for enterprise resource planning implementation in Indian retail sector", *Business Process Management Journal*, Vol. 19 No. 3, pp. 496-514.

Geisendorf, S. and Pietrulla, F. (2017), "The circular economy and circular economic concepts-a literature analysis and redefinition", *Thunderbird International Business Review*, pp. 1-12.

Geissdoerfer, M., Savaget, P., Bocken, N.M.P. and Hultink, E.J. (2017), "The circular economy – a new sustainability paradigm?", *Journal of Cleaner Production*, Vol. 143, pp. 757-768.

Geng, Y. and Doberstein, B. (2008), "'Developing the circular economy in China: challenges and opportunities for achieving' leapfrog development", *International Journal of Sustainable Development and World Ecology*, Vol. 15 No. 3, pp. 231-239.

Geng, Y., Fu, J., Sarkis, J. and Xue, B. (2012), "Toward a national circular economy indicator system in China: an evaluation and critical analysis", *Journal of Cleaner Production*, Vol. 23 No. 1, pp. 216-224.

Ghisellini, P., Cialani, C. and Ulgiati, S. (2016), "A review on circular economy: the expected transition to a balanced interplay of environmental and economic systems", *Journal of Cleaner Production*, Vol. 114, pp. 11-32.

Govindan, K. and Hasanagic, M. (2018), "A systematic review on drivers, barriers, and practices toward circular economy: a supply chain perspective", *International Journal of Production Research*, Vol. 56 Nos 1/2, pp. 278-311.

Govindan, K., Khodaverdi, R. and Vafadarnikjoo, A. (2015), "Intuitionistic fuzzy based DEMATEL method for developing green practices and performances in a green supply chain", *Expert Systems with Applications*, Vol. 42 No. 20, pp. 7207-7220.

Goyal, S., Esposito, M. and Kapoor, A. (2018), "Circular economy business models in developing economies: lessons from India on reduce, recycle, and reuse paradigms", *Thunderbird International Business Review*, Vol. 60 No. 5, pp. 729-740.

Gupta, S., Soni, U. and Kumar, G. (2019), "Computers and industrial engineering green supplier selection using multi-criterion decision making under fuzzy environment: a case study in automotive industry", *Computers and Industrial Engineering*, Vol. 136 No. 140, pp. 663-680.

Hasan, M.R., Mashud, A.H.M., Daryanto, Y. and Wee, H.M. (2020), "A non-instantaneous inventory model of agricultural products considering deteriorating impacts and pricing policies", *Kybernetes*, available at: https://doi.org/10.1108/K-05-2020-0288

Hughes, R. (2017), "The EU circular economy package – life cycle thinking to life cycle law?", *Procedia Cirp)*, Vol. 61, pp. 10-16.

IBEF (2019), "Report on manufacturing in India", available at: www.ibef.org/download/manufacturing-april-2019.pdf (accessed 25 May 2019).

Ivanovic, O.M. (2019), "Ecological responsibility and sustainable development as preconditions for development of the concept of circular economy", *Green Business: Concepts, Methodologies, Tools, and Applications*, IGI Global, pp. 1-16.

Iyer, A. (2018), "Moving from industry 2.0 to industry 4.0: a case study from India on leapfrogging in smart manufacturing", *Procedia Manufacturing*, Vol. 21, pp. 663-670.

Jaeger, B. and Upadhyay, A. (2020), "Understanding barriers to circular economy: cases from the manufacturing industry", *Journal of Enterprise Information Management*, Vol. 33 No. 4, pp. 729-745.

Jaiswal, P., Singh, A., Misra, S.C. and Kumar, A. (2020), "Barriers in implementing lean manufacturing in Indian SMEs: a multi-criteria decision-making approach", *Journal of Modelling in Management*, available at: https://doi.org/10.1108/JM2-12-2019-0276

Jalilian, N. and Mirghafoori, S.H. (2020), "Presenting sustainable supply chain fuzzy rotation matrix framework to manage business challenges in the context of sustainable supply chain management", *Journal of Modelling in Management*, Vol. 15 No. 1, pp. 35-49.

Jawahir, I.S. and Bradley, R. (2016), "Technological elements of circular economy and the principles of 6R-based closed-loop material flow in sustainable manufacturing", *Procedia CIRP*, Vol. 40, pp. 103-108.

Jayakumar, J., Jayakrishna, K., Vimal, K.E.K. and Hasibuan, S. (2020), "Modelling of sharing networks in the circular economy", *Journal of Modelling in Management*, Vol. 15 No. 2, pp. 407-440.

Kalmykova, Y., Sadagopan, M. and Rosado, L. (2018), "Circular economy – from review of theories and practices to development of implementation tools", *Resources, Conservation and Recycling*, Vol. 135 No. February 2017, pp. 190-201.

Karuppusami, G. and Gandhinathan, R. (2006), "Pareto analysis of critical success factors of total quality management: a literature review and analysis", *The TQM Magazine*, Vol. 18 No. 4, pp. 372-385.

Khalilzadeh, M., Karami, A. and Hajikhani, A. (2020), "The multi-objective supplier selection problem with fuzzy parameters and solving the order allocation problem with coverage", *Journal of Modelling in Management*, Vol. 15 No. 3, pp. 705-725.

Khompatraporn, C. and Somboonwiwat, T. (2017), "Causal factor relations of supply chain competitiveness via fuzzy DEMATEL method for Thai automotive industry", *Production Planning and Control*, Vol. 7287 No. May, pp. 1-14.

Kirchherr, J., Reike, D. and Hekkert, M. (2017), "Resources, conservation and recycling conceptualizing the circular economy: an analysis of 114 definitions", *Resources, Conservation and Recycling*, Vol. 127 No. 9, pp. 221-232.

Koh, S.C.L., Gunasekaran, A., Morris, J., Obayi, R. and Ebrahimi, S.M. (2017), "Conceptualizing a circular framework of supply chain resource sustainability", *International Journal of Operations and Production Management*, Vol. 37 No. 10, pp. 1520-1540.

Kumar, V., Sezersan, I., Garza-Reyes, J.A., Gonzalez, E.D.R.S. and Al-Shboul, M.A. (2019), "Circular economy in the manufacturing sector: benefits, opportunities and barriers", *Management Decision*, Vol. 57 No. 4, pp. 1067-1086.

Kumar, R., Singh, K. and Jain, S.K. (2019), "Agile manufacturing: a literature review and Pareto analysis", *International Journal of Quality and Reliability Management*, Vol. 37 No. 2, pp. 207-222.

Kumar, P.S. and Suganya, S. (2019), "Systems and models for circular economy, circular economy in textiles and apparel", available at: https://doi.org/10.1016/b978-0-08-102630-4.00008-x

Li, R.J. (1999), "Fuzzy method in group decision making", *Computers and Mathematics with Applications*, Vol. 38 No. 1, pp. 91-101.

Lieder, M. and Rashid, A. (2016), "Toward circular economy implementation: a comprehensive review in context of manufacturing industry", *Journal of Cleaner Production*, Vol. 115, pp. 36-51.

Lin, R.J. (2013), "Using fuzzy DEMATEL to evaluate the green supply chain management practices", *Journal of Cleaner Production*, Vol. 40, pp. 32-39.

Li, J. and Yu, K. (2011), "A study on legislative and policy tools for promoting the circular economic model for waste management in China", *Journal of Material Cycles and Waste Management*, Vol. 13 No. 2, pp. 103-112.

Lu, T. and Halog, A. (2020), "Toward better life cycle assessment and circular economy: on recent studies on interrelationships among environmental sustainability, food systems and diet", *International Journal of Sustainable Development and World Ecology*, Vol. 27 No. 6, pp. 515-523.

Ma, X. and Ortolano, L. (2000), *Environmental Regulation in China: Institutions, Enforcement, and Compliance*, Rowman and Littlefield Publishers.

Mangla, S.K., Govindan, K. and Luthra, S. (2017), "Prioritizing the barriers to achieve sustainable consumption and production trends in supply chains using fuzzy analytical hierarchy process", *Journal of Cleaner Production*, Vol. 151, pp. 509-525.

Mashud, A.H.M., Roy, D., Daryanto, Y. and Ali, M.H. (2020a), "A sustainable inventory model with imperfect products, deterioration, and controllable emissions", *Mathematics*, Vol. 8 No. 11, pp. 1-21.

Mashud, A.H.M., Wee, H.M., Huang, C.V. and Wu, J.Z. (2020b), "Optimal replenishment policy for deteriorating products in a newsboy problem with multiple just-in-time deliveries", *Mathematics*, Vol. 8 No. 11, pp. 1-18.

Mashud, A.H.M., Wee, H.M., Sarkar, B. and Chiang Li, Y.H. (2020c), "A sustainable inventory system with the advanced payment policy and trade-credit strategy for a two-warehouse inventory system", *Kybernetes*, available at: https://doi.org/10.1108/K-01-2020-0052

Mathivathanan, D., Mathiyazhagan, K., Noorul Haq, A. and Kaippillil, V. (2019), "Comparative study on adoption of sustainable supply chain management practices in Indian manufacturing industries", *Journal of Modelling in Management*, Vol. 14 No. 4, pp. 1006-1022.

Mehta, Y. and Rajan, A.J. (2017), "Manufacturing sectors in India: outlook and challenges", *Procedia Engineering)*, Vol. 174, pp. 90-104.

Mittal, V.K. and Sangwan, K.S. (2014), "Prioritizing barriers to green manufacturing: environmental, social and economic perspectives", *Procedia CIRP*, Vol. 17, pp. 559-564.

Moktadir, M.A., Rahman, T., Rahman, M.H., Ali, S.M. and Paul, S.K. (2018), "Drivers to sustainable manufacturing practices and circular economy: a perspective of leather industries in Bangladesh", *Journal of Cleaner Production*, Vol. 174, pp. 1366-1380.

Morioka, T., Tsunemi, K., Yamamoto, Y., Yabar, H. and Yoshida, N. (2005), "Eco-efficiency of advanced loop-closing systems for vehicles and household appliances in Hyogo eco-town", *Journal of Industrial Ecology*, Vol. 9 No. 4, pp. 205-221.

Muradin, M. and Foltynowicz, Z. (2019), "The circular economy in the standardized management system", *Amfiteatru Economic*, Vol. 21 No. 13 (Special Issue).

Nelles, M., Grünes, J. and Morscheck, G. (2016), "Waste management in Germany – development to a sustainable circular economy?", *Procedia Environmental Sciences)*, Vol. 35, pp. 6-14.

Opricovic, S. and Tzeng, G.-H. (2003), "Defuzzification within a multicriteria decision model", *International Journal of Uncertainty, Fuzziness and Knowledge-Based Systems*, Vol. 11 No. 5, pp. 635-652.

Pan, S.Y., Du, M.A., Huang, I.T., Liu, I.H., Chang, E.E. and Chiang, P.C. (2014), "Strategies on implementation of waste-to-energy (WTE) supply chain for circular economy system: a review", *Journal of Cleaner Production*, Vol. 108, pp. 1-13.

Pauliuk, S. (2018), "Critical appraisal of the circular economy standard BS 8001:2017 and a dashboard of quantitative system indicators for its implementation in organizations", *Resources, Conservation and Recycling*, Vol. 129 No. 9, pp. 81-92.

Pearce, D.W. and Turner, R.K. (1989), *Economics of Natural Resources and the Environment*, Italian edition 1991 by Il Mulino, Bologna, Hemel Hempstead, Harvester Wheatsheaf, London.

Pringle, T., Barwood, M. and Rahimifard, S. (2016), "The challenges in achieving a circular economy within leather recycling", *Procedia CIRP*, Vol. 48, pp. 544-549.

Rajput, S. and Singh, S.P. (2019), "Industry 4.0 – challenges to implement circular economy", *Benchmarking: An International Journal*, available at: https://doi.org/10.1108/BIJ-12-2018-0430

Rashidi, K. (2020), "AHP versus DEA: a comparative analysis for the gradual improvement of unsustainable suppliers", *Benchmarking: An International Journal*, Vol. 27 No. 8, pp. 2283-2321.

Ritzén, S. and Sandström, G.Ö. (2017), "Barriers to the circular economy – integration of perspectives and domains", *Procedia CIRP*, Vol. 64, pp. 7-12.

Rizos, V. (2017), "Circular economy: definitions, processes and impacts".

Sanghi, S. and Srija, A. (2015), "Make in India and the potential for job creation", *Confederation of Indian Industry*, pp. 23-32.

Saroha, M., Dixit Garg, D. and Luthra, S. (2018), "Key issues and challenges in circular supply chain management implementation-a systematic review", *International Journal of Applied Engineering Research*, Vol. 13 No. 9, pp. 91-104.

Shahbazi, S., Wiktorsson, M., Kurdve, M., Jönsson, C. and Bjelkemyr, M. (2016), "Material efficiency in manufacturing: Swedish evidence on potential, barriers and strategies", *Journal of Cleaner Production*, Vol. 127, pp. 438-450.

Shi, H., Peng, S.Z., Liu, Y. and Zhong, P. (2008), "Barriers to the implementation of cleaner production in Chinese SMEs: government, industry and expert stakeholders' perspectives", *Journal of Cleaner Production*, Vol. 16 No. 7, pp. 842-852.

Singh, C., Singh, D. and Khamba, J.S. (2020), "Analyzing barriers of green lean practices in manufacturing industries by DEMATEL approach", *Journal of Manufacturing Technology Management*, Vol. 32 No. 1, available at: https://doi.org/10.1108/JMTM-02-2020-0053

Sousa-Zomer, T.T., Magalhães, L., Zancul, E., Campos, L.M.S. and Cauchick-Miguel, P.A. (2018), "Cleaner production as an antecedent for circular economy paradigm shift at the micro-level: evidence from a home appliance manufacturer", *Journal of Cleaner Production*, Vol. 185, pp. 740-748.

Su, B., Heshmati, A., Geng, Y. and Yu, X. (2013), "A review of the circular economy in China: moving from rhetoric to implementation", *Journal of Cleaner Production*, Vol. 42, pp. 215-227.

Svensson, G. and Wood, G. (2006), "The Pareto plus syndrome in top marketing journals: research and journal criteria", *European Business Review*, Vol. 18 No. 6, pp. 457-467.

Swink, M., Melnyk, S.A., Cooper, M.B. and Hartley, J.L. (2014), *Managing Operations*, McGraw-Hill/Irwin, New York, NY.

Talib, M.S.A., Hamid, A.B.A. and Thoo, A.C. (2015), "Critical success factors of supply chain management: a literature survey and Pareto analysis", *EuroMed Journal of Business*, Vol. 10 No. 2, pp. 234-263.

Tian, G., Liu, X., Zhang, M., Yang, Y., Zhang, H., Lin, Y., Ma, F., Wang, X., Quf, T. and Lig, Z. (2019), "SC", *Journal of Cleaner Production*, Vol. 220, available at: https://doi.org/10.1016/j.jclepro.2019.01.086

Tsai, F.M., Bui, T.D., Tseng, M.L., Lim, M.K., Wu, K.J. and Mashud, A.H.M. (2020), "Assessing a hierarchical sustainable solid waste management structure with qualitative information: Policy and regulations drive social impacts and stakeholder participation", *Resources, Conservation and Recycling*, p. 105285.

Tseng, M.L., Chiu, A.S.F., Liu, G. and Jantaralolica, T. (2020), "Circular economy enables sustainable consumption and production in multi-level supply chain system", *Resources, Conservation and Recycling*, Vol. 154 No. 11, p. 104601.

Upadhyay, A., Akter, S., Adams, L., Kumar, V. and Varma, N. (2019), "Investigating 'circular business models' in the manufacturing and service sectors", *Journal of Manufacturing Technology Management*, Vol. 30 No. 3, pp. 590-606.

Urbinati, A., Chiaroni, D. and Chiesa, V. (2017), "Toward a new taxonomy of circular economy business models", *Journal of Cleaner Production*, Vol. 168, available at: https://doi.org/10.1016/j.jclepro.2017.09.047

Vasiljevic-Shikaleska, A., Gjozinska, B. and Stojanovikj, M. (2017), "The circular economy – a pathway to sustainable future", *Journal of Sustainable Development 2*, Vol. 7 No. 17, pp. 0-191.

Venkatesh, V.G. and Luthra, S. (2016), "Role of sustainable procurement in sustainable manufacturing operations: an Indian insight", *Strategic Management of Sustainable Manufacturing Operations*, IGI Global, pp. 132-148.

Wang, G.H., Wang, Y.X. and Zhao, T. (2008), "Analysis of interactions among the barriers to energy saving in China", *Energy Policy*, Vol. 36 No. 6, pp. 1879-1889.

Wu, W.W. and Lee, Y.T. (2007), "Developing global managers' competencies using the fuzzy DEMATEL method", *Expert systems with Applications*, Vol. 32 No. 2, pp. 499-507.

Van Weelden, E., Mugge, R. and Bakker, C. (2016), "Paving the way toward circular consumption: exploring consumer acceptance of refurbished mobile phones in the Dutch market", *Journal of Cleaner Production*, Vol. 113, pp. 743-754.

Xia, X., Govindan, K. and Zhu, Q. (2015), "Analyzing internal barriers for automotive parts remanufacturers in China using grey-DEMATEL approach", *Journal of Cleaner Production*, Vol. 87 No. 1, pp. 811-825.

Xue, B., Chen, X., Geng, Y., Guo, X., Lu, C., Zhang, Z. and Lu, C. (2010), "Resources, conservation and recycling survey of officials' awareness on circular economy development in China: based on municipal and county level", *Resources, Conservation and Recycling*, Vol. 54 No. 12, pp. 1296-1302.

Zhu, Q. and Geng, Y. (2013), "Drivers and barriers of extended supply chain practices for energy saving and emission reduction among Chinese manufacturers", *Journal of Cleaner Production*, Vol. 40, pp. 6-12.

Zhu, X., Wang, J. and Tang, J. (2017), "Recycling pricing and coordination of WEEE dual-channel closed-loop supply chain considering consumers' bargaining", *International Journal of Environmental Research and Public Health*, Vol. 1 No. 12, p. 1578.

Corresponding author
Girish Kumar can be contacted at: girish.kumar154@gmail.com

For instructions on how to order reprints of this article, please visit our website:
www.emeraldgrouppublishing.com/licensing/reprints.htm
Or contact us for further details: **permissions@emeraldinsight.com**

CII-ITC Centre of Excellence
for Sustainable Development

Confederation of Indian Industry

Cleaner Air
Better Life

CLEAN AND GREEN ECONOMY FOR AIR POLLUTION

ACTIONABLE SOLUTIONS FOR WASTE-TO-WEALTH FROM CROP RESIDUE

CII-ITC Centre of Excellence for Sustainable Development

Confederation of Indian Industry

Disclaimer:

Copyright © 2021 Confederation of Indian Industry (CII). All rights reserved.

No part of this publication may be reproduced, stored in, or introduced into a retrieval system, or transmitted in any form or by any means (electronic, mechanical, photocopying, recording or otherwise), in part or full in any manner whatsoever, or translated into any language, without the prior written permission of the copyright owner. CII has made every effort to ensure the accuracy of the information and material presented in this document. Nonetheless, all information, estimates and opinions contained in this publication are subject to change without notice, and do not constitute professional advice in any manner.

Furthermore, the opinions expressed do not necessarily reflect those of, Clean Air Fund and Bloomberg Philanthropies nor should they be attributed to them.

Neither CII nor any of its office bearers or analysts or employees accept or assume any responsibility or liability with respect to the information provided herein. However, any discrepancy, error, etc. found in this publication may please be brought to the notice of CII for appropriate correction.

Published by Confederation of Indian Industry (CII), The Mantosh Sondhi Centre; 23, Institutional Area, Lodi Road, New Delhi 110003, India,

Tel: +91-11-24629994-7, Fax: +91-11-24626149; Email: info@cii.in; Web: www.cii.in

CII-ITC Centre of Excellence for Sustainable Development

Confederation of Indian Industry

Cleaner Air Better Life

Clean and Green Economy for Air Pollution

Actionable Solutions for Waste-to-Wealth from Crop Residue

Mohit Sharma, Aditya Bhuyan, Ishan Sahajpal

Technology Assessment Report
January 2021

CII National Initiative: Cleaner Air - Better Life

CII - ITC Centre of Excellence for Sustainable Development
New Delhi

CII-ITC Centre of Excellence for Sustainable Development

Confederation of Indian Industry

Acknowledgement

We are thankful to Seema Arora (Deputy Director General, Confederation of Indian Industry) for her leadership at CII to enable this study. We are grateful to Nitin Prasad (Chairman, CII Cleaner Air Better Life and Chairman, Shell India), Mr Tejpreet S. Chopra (Co-Chairman, CII Cleaner Air Better Life and CEO, Bharat Light & Power), Ms Rhea Singhal (Founding Member, India CEO Forum for Clean Air and CEO, Ecoware) for extending their leadership support to convene a stakeholder dialogue series focussed on scaling ex-situ solutions.

This study could not be completed without the invaluable inputs and data from entrepreneurs and enterprises working on innovative technology and business solutions- Mr Sukhbeer Singh (Farm2Energy), Mr Sukhmeet Singh (A2P Energy), Mr Sunil Singhal (BIO-CH4), Ms Shriti Pandey (Strawcture Eco), Mr Puneet Kashyap (GBDSGNS Foundation), Mr Ankur Kumar (Kriya Labs), Mr Tarun Jami (GreenJam BuildTech), and Mr Aayush Marwaha (Saras Dairy). We also thank experts at Indian Oil, Bureau of Indian Standards and NTPC who enriched discussions at our stakeholder dialogues and provided useful inputs for shaping this study.

Finally, we are thankful to Mr George Varughese (Independent Advisor, CII) who provided feedback at various stages of this project and kept the entire team motivated and focussed during field visits and stakeholder dialogues.

About the Authors

Mohit Sharma | Aditya Bhuyan | Ishan Sahajpal

Mohit Sharma is an applied researcher with ten years of experience working across multi-disciplinary domains of climate and air quality, energy studies, economic modelling, and policy research. Mohit earned his master's degree in Sustainable Energy from Technical University of Denmark and is a Chemical Engineer by background.

Ishan Sahajpal is an Environmental Engineer with masters from Delhi Technological University. He started his career with CII's Crop Residue Management Programme and liaises between project leads for research and field implementation.

Aditya Bhuyan is a postgraduate from TERI University with specialisation in environmental studies and is a Geologist by background.

Both Aditya and Ishan are part of the data and research team for CII's Crop Residue Management Programme under CII's Cleaner Air Better Life initiative.

Supported by

CLEAN AIR FUND

Bloomberg Philanthropies

CII-ITC Centre of Excellence for Sustainable Development

Confederation of Indian Industry

CONTENTS

	Executive Summary	I - II
1.	Background: Air pollution and Biomass Management Ecosystem	1 - 2
2.	Introduction: Assessment of Ex-Situ Management Solutions	3
3.	Methodology for Assessing Actionable Solutions	4
4.	Delivery Models for Waste to Wealth from Agricultural Waste	5
	4.1 Straw Aggregation	5 - 7
	4.2 Agriculture and Rural Energy	7 - 13
	4.3 Construction Elements	14 - 17
	4.4 Pulping and Packaging Solutions	17 - 18
	4.5 Solid Fuels and Energy Recovery	19 - 21
5.	Key Findings and Recommendations for Scaling Solutions	22 - 24
	References	25 - 26

EXECUTIVE SUMMARY

In the absence of a large momentum for change required to move away from dominant rice-wheat monoculture in the breadbasket of India, management of rice straw inside the field (in-situ) through direct reuse by farmers and management outside the field (ex-situ) are the only practical choices for addressing the burning issue which causes peak pollution across severely polluted cities of the Indo-Gangetic plains. While in September 2020, we produced evidence of the change taking place in the heart of Punjab and Haryana across 102 villages intervened by CII, this report further focusses on ex-situ management solutions. These set of solutions need to be scaled for addressing 1/3rd of the rice straw or approximately 13 million tonne rice straw, while the remaining 2/3rd is filled by in-situ management solutions. We target ex-situ use cases that are not only actionable and environmentally sound but also make an economic sense to all stakeholders. Some of these perhaps, make more economic sense than others due to higher value addition in the process. But market situations are equally responsible for what works on the field and what does not. These include prices of raw materials or final products and market/consumer awareness levels which are key factors that determine the project's success. The aggregation model, once scaled, can address a host of such challenges and unlock all other delivery models along with the supply chain of biomass management. The aggregation model, detailed and evaluated here, can add significant economic value to farmers as well as rural entrepreneurs, creating increased income and livelihood opportunities in rural areas. It is estimated from field data that the straw aggregation model can bring down the cost of ex-situ operations at the farmer's end by 34%, bringing it at par with other methods. This is a significant finding and government may immediately prioritise this activity by-

1. Bringing the this activity (akin to bio-CNG) under the priority lending schemes of national banks
2. Ensuring an insurance cover to rural straw banks set up by the aggregators for insulating them from risk of fire hazards

The SATAT initiative is an encouraging step from the Government to ensure offtake and a minimum guaranteed price for bio-CNG. But ensuring the offtake of bio-fertilisers which make up for 43% revenues from bio-CNG model {Internal Rate of Return (IRR) at 29%} will be crucial for its viability. Analysis shows that even with a 50% offtake of bio-fertiliser from bio-CNG plant, the net worth of project goes down by 72% and payback period nearly doubles. Also, one composting pit of 30x10 ft can support small-marginal farmers with an additional income of INR 30,000 per year at zero capital cost and even without a microbial solution. Therefore, marketing support for bio-fertilisers is crucial and needs the following support-

1. Schemes for promotion and market development assitance to bio-fertilisers from crop residue akin to the City Compost Policy by Government of India
2. National Agricultural Co-operative Marketing Federation of India Ltd. (NAFED) and similar agencies can be roped in for their Pan-India network to propagate and distribute green-manure through nation-wide network of outlets.

Total Mixed Ration (TMR) feed pellets are found to be highly profitable (IRR at 36%), albeit requiring very careful planning by rural entrepreneurs for local availability of filler material. Scaling this model will require-

1. Scheme from NDDB for knowledge support to rural entrepreneurs willing to set up TMR feed pellet units based on rice straw
2. Mass awareness creation for dairy farmers across Punjab and Haryana to remove their misconceptions about nutritional value of rice straw (non-basmati varieties)

Three key material uses of rice straw are evaluated in this study - construction panels, blocks and pulp. All three are found to have excellent returns with IRR greater than 100%. Efforts are still underway to develop bio-char

reactors for improving environmental performance of the bio-char making process, which can arrest more than 90% emissions. With these specific material uses of rice straw, which are rapidly evolving on the field, new standards/certifications are proposed for the following products and processes-

1. Use of crop residue or lingo-cellulosic materials in construction bricks and blocks
2. Standards and certification for torrefaction reactors to produce bio-char and bio-coal in consultation with technology developers
3. Certification for green manure and liquid bio-fertilisers from Ministry of Agriculture akin to the successful German model
4. Separate route for testing procedures to certify green building materials will be desirable

In addition, the following step is also proposed for marketing and promoting already existing products from rice straw-

1. Public-cum-private procurement of construction materials from rice straw which already have a demonstrated track record of working on the ground and are evaluated in this study, including construction blocks, panels, and other such products

Finally, the Solid-fuel Pellets (SFP) model is demonstrated to work from operator and end-use market perspectives i.e. co-firing in industrial boilers (55% IRR) and thermal power plants (TPP) (73% IRR). Key difference from all other models is that the SFP model is highly sensitive to market prices and operation becomes unviable beyond landed price of rice straw greater than INR 2/kg and pellet prices lower than INR 4.5 /kg. Given the fact that necessary guidance has already been provided on co-firing by concerned authorities and regulatory agencies, Government may consider -

1. Mandating all TPP units to start consuming at least 5% rice straw-based SF pellets using competitive bidding
2. A new policy mandate, akin to Government of India's fly ash directive, can be issued for use of straw-based SF pellets within a certain radius
3. Industrial boilers can be given a choice to co-fire SF pellets as well as directly the rice straw as long as adequate emission control systems are in place

1. BACKGROUND: AIR POLLUTION AND BIOMASS MANAGEMENT ECOSYSTEM

Smoke from agricultural burning in the breadbasket of India leads to peak pollution episodes across Northern India as a result of huge quantum of rice straw burnt across agrarian states in a relatively short period in the winter months of October and November. Agricultural burning has risen to dominance with intensification of agriculture across agrarian states dominated by rice-wheat monoculture (Badarinath et al 2006), narrowing of time window[1] from groundwater conservation policies (Singh et al 2020a) and lack of an adequate biomass management ecosystem to handle surplus agricultural waste (CII-NITI 2018).

Atmospheric brown clouds from open agricultural burning coupled with unfavourable weather conditions (temperature inversion during winters and blocking effect of Himalayas) exacerbate air quality situation across the already polluted National Capital Region and surrounding areas which are highly urbanised (Saikawa et al 2019). Living in areas with intense crop residue burning is associated with three-fold increase in acute respiratory infection and averting crop residue burning across North Western States can save India INR 10,500 Crore over 5 years (Chakrabarti et al 2019). The problem of crop residue burning in the year 2020 was also compounded by labour shortage due to the COVID-19 crisis. As a result, second highest active fire detections were observed[2] across the four rice-growing states in the region—Punjab, Haryana, Madhya Pradesh, and Uttar Pradesh (See Figure 1) for the post-monsoon period since Visible Infrared Imaging Radiometer Suite (VIIRS) sensor on the Suomi NPP satellite collected data for the first time in 2012 (NASA Earth Observatory 2020).

Reducing surplus rice straw by moving away from rice to more sustainable cropping systems, in favour of more diverse agriculture, is the first choice to address crop residue burning but this requires system-wide changes in agriculture and has not yielded results despite years of efforts. We are, therefore, only left with a practical choice to add economic value to this agricultural waste through direct reuse at the field (in-situ management) and recycling outside field (ex-situ management). In-situ management is a part of the broad conservation tillage techniques defined as any form of tillage that minimises the number of tillage passes, where soil aggregate disruption is reduced, and a minimum of 30% of the soil surface covered with residues (Carter 2005). It can provide several benefits such as soil conservation, economic advantages associated with reductions in crop establishment time and energy use, reduction in soil sheet erosion and nonpoint pollution, and enhanced storage or retention of soil organic matter and improvement of soil quality at the soil surface (Singh et al 2018). Most of these benefits are established through field data in our study (Sharma et al 2020) of CII Crop Residue Management Programme across 105 villages of Punjab and Haryana where more than 87% farmers practiced improved crop residue management practices in 2019 based on their economic advantages. But in-situ has its own limitations and based on our learnings, about one-third of farmers find it difficult to rely fully on in-situ methods. This is the case with-

- Fields with hard soils where feasibility of in-situ management techniques remains limited
- Fields with sandy or sand-loamy soils and alternate crop rotation (e.g. rice-potato-sunflower) where in-situ management is either not cost-effective or it compromises the productivity for subsequent crop
- Farmers who want to provide a gap between application of rice straw to field

Ex-situ is an essential component of the biomass management system in addition to in-situ management by farmers and needs to be developed as a back-up option. Therefore, scaling ex-situ solutions and accompanying supply chains and creating market awareness on these solutions is highly desirable.

[1]25% increase in the post-monsoon rice crop production in Punjab during 2002-2016

[2]Despite good adoption rate of in-situ management practice in the last few years

Challenges for ex-situ are compounded by the fact that rice straw is one of the most difficult types of biomass to be processed owing to its inherent characteristics such as high silica and lignin content. This limits its economic viability in many applications as compared to other types of biomass or crop residue such as wheat, cotton, sugarcane etc.

Prime motivation for this study is therefore to understand the economic viability of these solutions. Also, most of these solutions are still at a nascent stage of development. Long-term support to these solutions is therefore necessary through dedicated policy and financial measures.

Figure 1. Active fire counts observed by Visible Infrared Imaging Radiometer Suite (VIIRS) sensor on the Suomi NPP satellite in October-November for years 2012-2020.

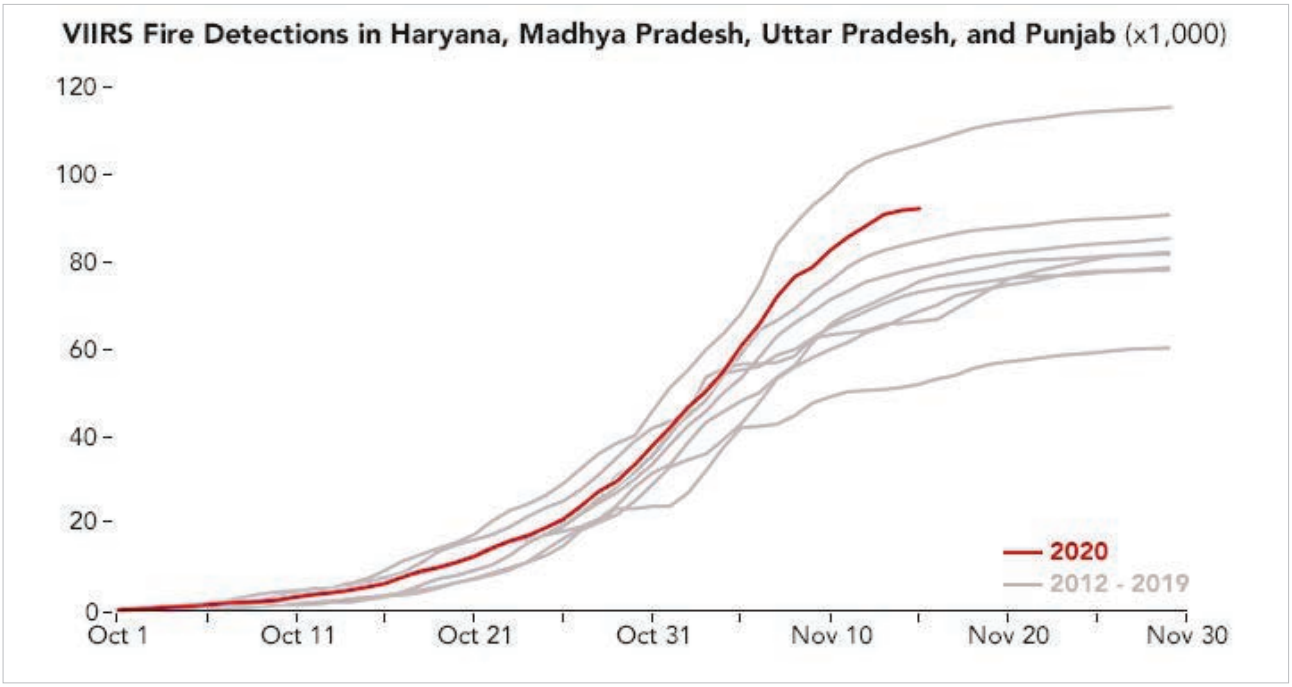

Source: NASA Earth Observatory (2020)

2. INTRODUCTION: ASSESSMENT OF EX-SITU MANAGEMENT SOLUTIONS

As most ex-situ management solutions for rice straw were either under development or trials on field, their economic viability was questionable. Solutions were screened based on their environmental merits and technology readiness level and a detailed assessment of shortlisted solutions was undertaken. The key research question for the team was to understand whether the shortlisted solutions are economically viable? Detailed cost analysis helps to shed light on the critical aspect of these business models i.e. economic viability with respect to the market situation. The price fluctuations and unsteady supply hampered new technologies and delivery models from gaining momentum. Figure 2 provides an overview of biomass management system and various solutions as part of this system which are being assessed under this study. Section 3 provides a brief summary of the methodology and key strategies used to assess actionable ex-situ solutions. Key lessons from the field on how these solutions are being tried by various entrepreneurs and assessment of the respective delivery models are captured in section 4 under relevant subsections. These subsections are focussed on-

- Straw aggregation for delivering biomass to the user facility
- Agriculture and rural energy for specific applications of rice straw within the rural economy i.e. compost, bio-char, animal feed and bio-CNG
- Construction elements for use of rice straw in building/construction
- Pulping and packaging solutions from pulping of rice straw which also opens up possibilities for use of rice straw in various packaging solutions
- Solid fuels and energy recovery focussed on pelletisation of rice straw to solid fuels and energy recovery in industrial boilers and thermal power plants

Finally, the findings are concluded along with actionable recommendations in Section 5.

Figure 2. Process diagram of biomass management system with specific elements under scope of this study.

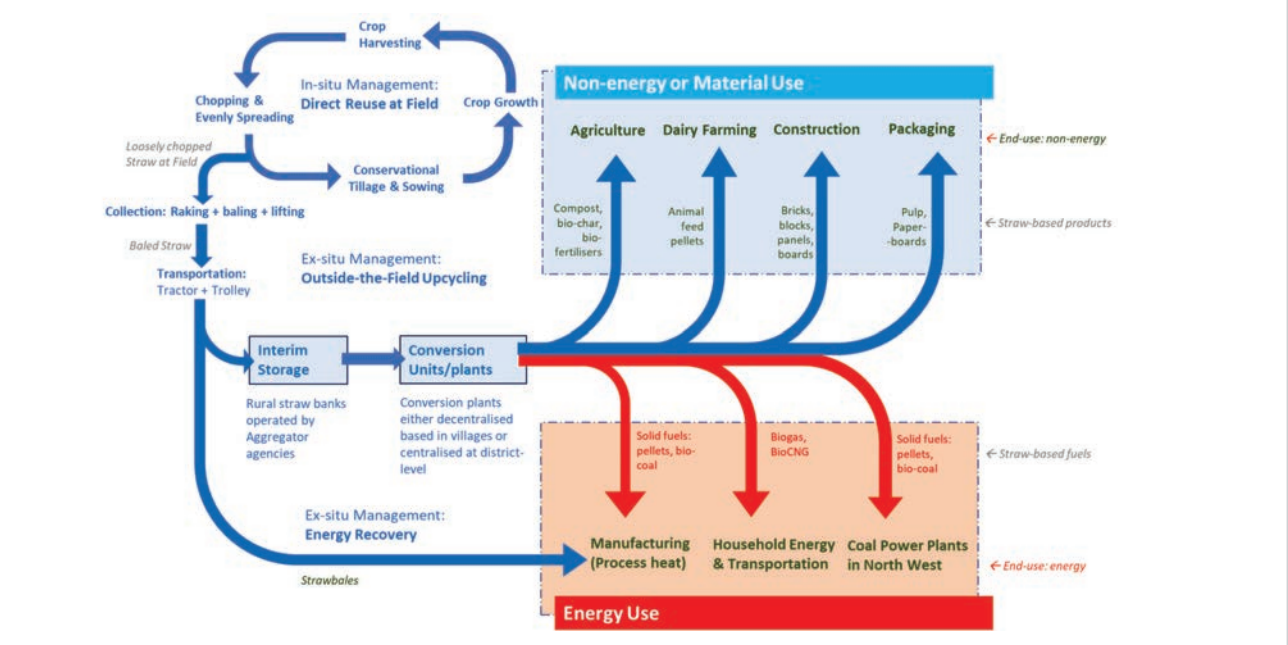

Source: Cleaner Air - Better Life (2021) Analysis

3. METHODOLOGY FOR ASSESSING ACTIONABLE SOLUTIONS

The methodology for this study followed a combination of approaches. These included-

1. Field visits and interactions with rural entrepreneurs working to develop delivery models on the ground across Punjab and Haryana
2. Stakeholder dialogue series (See Figure 3) was organised virtually in May-June 2020 to understand the challenges being faced for scaling up delivery models and get inputs from a wider group of stakeholders including industry experts
3. Data collection from select enterprises and a detailed cost-benefit assessment in order to understand economic viability or market readiness of these solutions

Field visits were undertaken by the research team across multiple locations in Punjab and Haryana in the winter of 2019 to build an understanding of multiple solutions being tried out by rural entrepreneurs on the ground. These entrepreneurs were then further invited to present their ideas for scaling delivery models to manage rice straw at the dialogues series focusing on specific components of the biomass management ecosystem.

Key indicators such as Pay Back Period (PBP), Net Present Value (NPV) and Internal Rate of Return (IRR) have been used to assess economic viability of various delivery models along the biomass management supply chains. PBP is computed from annual cashflows and initial investments of these delivery models but does not reflect the time value of money. Therefore, Discounted Cash Flows (DCFs) of these delivery models were modelled for a realistic scenario to understand the project's viability from an investment perspective. DCF and NPV values have been used to integrate time value of money[3] into the annual cash flows and are useful tools which aide financial decisions. Due to limitation of the NPV method to compare projects with similar initial investment outlays, project IRRs were computed to compare economic viability of different delivery models. IRR is essentially the discount rate at which NPV of the project reaches zero value or DCF of the project equals initial investment. Sensitivity analyses are subsequently performed on discounted cash flows and NPV to understand impact of key assumptions or market situations such as prices of raw material and final products. All cost components e.g. labour, land, energy, chemical inputs, transportation, equipment/plant, storage, packaging, raw materials etc. have been considered for building these investment models.

Figure 3. Timeline of stakeholder dialogue series undertaken to undertsand challenges faced by enterprises to scale various technologies and delivery models for rice straw management in North West Region.

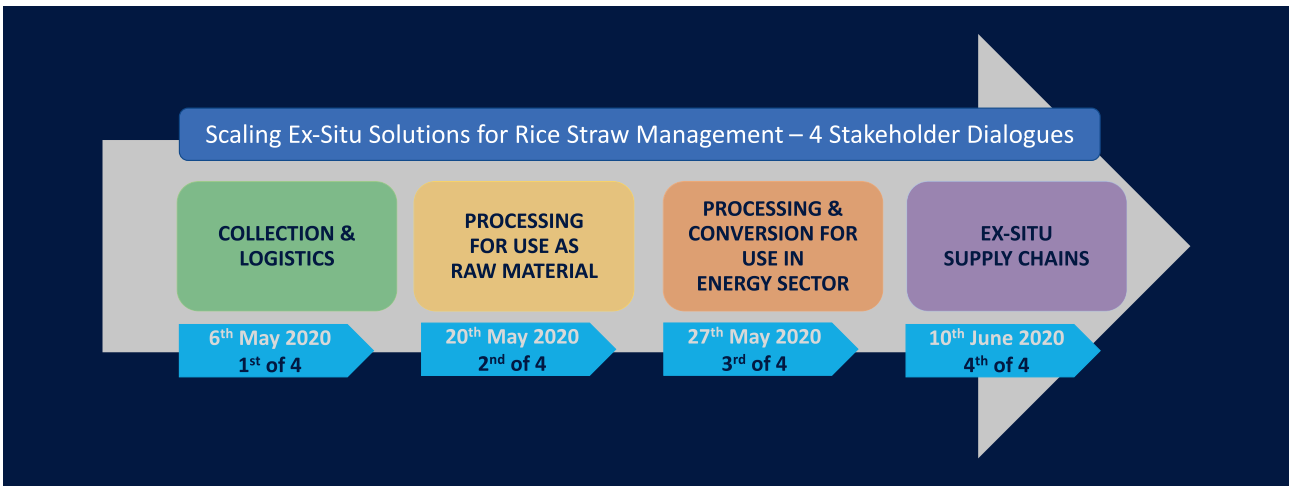

Source: Cleaner Air - Better Life (2021)

[3]standard discount rate of 8% is utilised across assessed delivery models.

4. DELIVERY MODELS FOR WASTE TO WEALTH FROM AGRICULTURAL WASTE

Figure 4. Round Strawbales stacked in pyramid shaped rows at rural straw bank in Ludhiana, Punjab

4.1 Straw Aggregation

Straw aggregation is a specialised business that is yet to be scaled as a lucrative business model across rural North West. It is the backbone of biomass management ecosystem and is a very specialised business as it requires experiential knowledge of best practices to collect/bale, stack, store and transport biomass in order to meet requirements of the user. These best practices include-

- Optimal moisture level[4] before baling chopped straw
- Compression force applied on different layers of bale
- Proper stacking (See Figure 4) with criss-cross layers and pyramid forms for stacking round bales
- Safe distance between rows for proper access and shielding from the risk of fire

The above considerations[5] are important so that biomass degradation (from rainwater seepage, microbial activity etc.) and risk of fire are minimal during storage. There are a few credible enterprises, such as Farm2Energy, who have successfully demonstrated the aggregation model across Punjab and Haryana. Rural straw banks typically store 1000-100,000 tonnes of biomass in the form of bales. Baling of biomass is necessary to ensure efficient supply chains. As the rice harvesting period lasts only for 15-20 days, interim storage at rural

[4]20-25% requiring drying of straw for two sunny days
[5]above list is not exhaustive for scope of this study

locations is crucial for the uninterrupted supply of biomass to user entities including industrial boilers, conversion facilities for solid fuel pellets, bio-CNG plants etc. (See figure 2). As per our estimate, 100-1000 straw banks will be needed across the two states if ex-situ is to fill the gap for an estimated one third of surplus rice straw which needs to be planned for ex-situ management.

Cost data for study has been acquired from Farm-to-Energy which is active across Punjab and Haryana. Cost data was then modelled from the operator's perspective. As depicted in Figure 5, key steps involved in the process include-

1. Collection from the field (raking and baling)
2. Transportation from the field using tractor-pulled trolleys
3. Stacking and interim storage at the rural straw banks which are set up by aggregator agencies in proximity of their catchment area (within 5-10 kilometres of central location)
4. Final transportation of baled straw to user facilities using trucks

For building the biomass aggregation case, capacity of the rural straw bank was assumed to be 60,000 tonnes rice straw in a season or year requiring capital investment of INR 4.5 Crore. Investment included hardware for all the steps outlined in figure 5 e.g. rakers, balers, fork lifters etc. The catchment area for this particular size of rural straw bank was spread roughly over 100 square kilometres. Due to efficiency considerations, final transportation to user facility was limited to a distance of 150 kilometers and an average transportation charge of INR 525 per tonne of baled straw has been used.

Figure 5. Process flow for straw aggregation model for collection and uninterrupted supply of rice straw by aggregation agency.

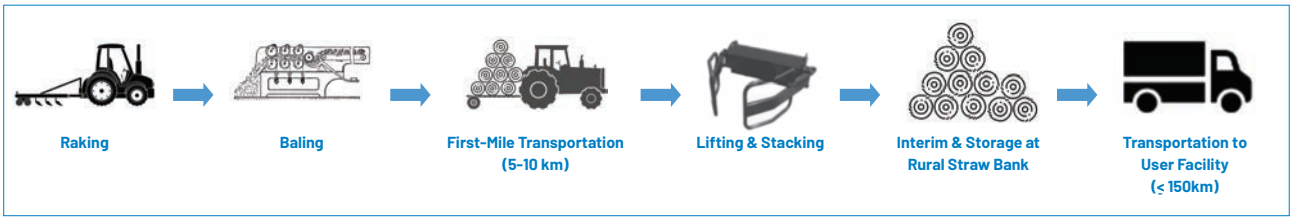

Source: Cleaner Air - Better Life (2021) Analysis

Based on learnings from 102 villages across Punjab and Haryana, as detailed in our study (Sharma et al 2020) published in September 2020, it costs the farmer INR 1985 per acre or using a standard factor of 2.5 tonne per acre - INR 794 per tonne rice straw. This is the typical amount charged by a service provider for evacuating agricultural waste from the field but under the aggregator model used by Farm2Energy, the operator of straw bank or aggregator does not charge any money from farmers for this service. Hence the inherent assumption for modelling this process was that while cost to farmer for availing baling and evacuation service is fixed at INR 794 per tonne rice straw, a premium of a similar amount is being paid to the farmer by aggregator (Farm2Energy here). Project cash flows were further analysed for different scenarios as depicted in Figure 6 where the farmer is being paid a premium which is either lower or more than this value. It is worth noting that it costs the aggregator approximately INR 650 per tonne of biomass for operations ranging from collection from field till stacking of bales at the site of interim storage or rural straw bank.

As depicted in Figure 6, the project is viable (or cummulative net prsent value of inventment over a 10 year period is postive), if farmer premium is limited to a threshold value of approx. INR 850 per tonne of biomass. For the standard assumption of farmer's premium at INR 795 per tonne, net present worth of the project is postive (INR 2.3 Crore) and the project is found to be viable.

Figure 6. Investment model for aggregation unit or rural straw bank with scenarios for different levels of farmer's premium on the rice straw.

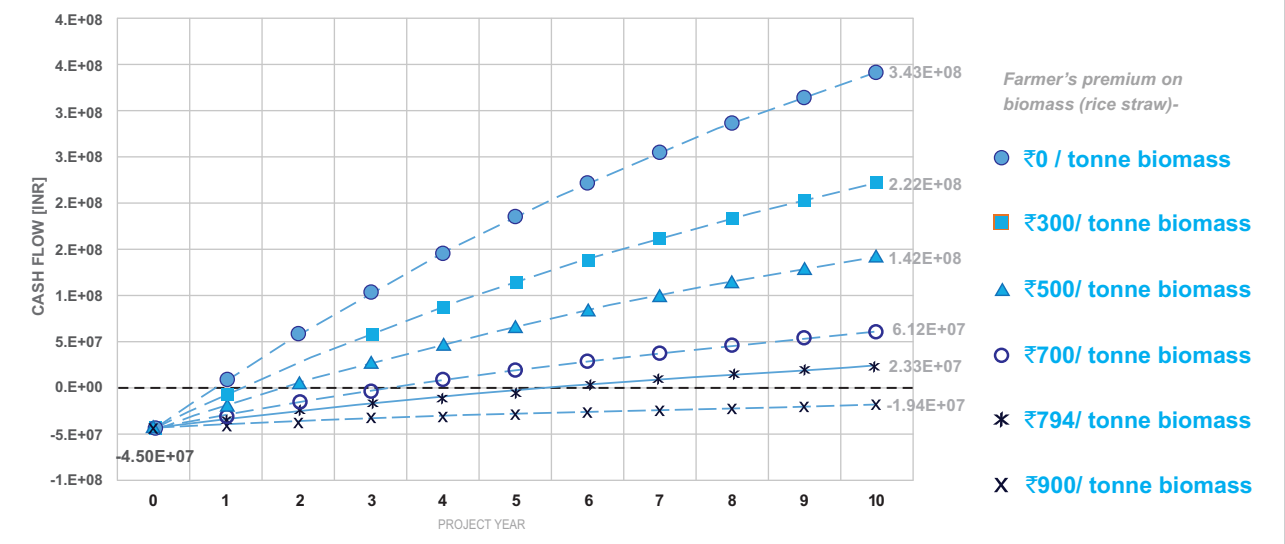

Source: Cleaner Air - Better Life (2021) Analysis

Although the simple payback period is 4.4 years, discounted cash flow analysis indicates that the project yields postive returns in 5.5 years (at 8% discount rate) which is a more realistic timeline for its break-even point from an investment perspective. The internal rate of return for the project is 18% which is a useful indicator of its economic vialbilty for comparison with other models whose initial investment outlay and cash flows are very different from the aggregator model.

Evidently, for scenarios where the farmer's premium is lower than INR 795 per tonne, the project is viable throughout and its value increases with a decrease in this premium. If the aggregator charges farmer the same rate as a private service provider of farm machinery (full amount of INR 795 per tonne for their services or in other words, zero premium), project value at the end of 10 years is found to be 7.6 times the initial investment (INR 34.4 Crores).

In addition to the above insights from cost analysis, there is a significant risk of a fire hazard which exists at rural straw banks maintained by enterprises for collection and aggregation of biomass in rural areas.

Subsequent sub-sections of the report dwell on various conversion and use cases including energy as well as material applications. Although generated in a relateively short time window, straw is typically stored year-round either at rural straw banks or onsite storage attached to user facilities. Longer storage periods inevitably accrue losses due to degradation of paddy straw and 20% decrease in the Calorific Value (Singh et al 2020b) within a year of storage, which has been documented. While this is a significant loss for energy applications, it is worth noting that even lower grade biomass can be utilised in selected material applications e.g. manufacturing building/construction elements which are also covered in the subsequent subsections.

4.2 Agriculture and Rural Energy

There are several possible applications for rice straw within the agricultural sector and rural economy besides its direct reuse at field by the farmer (formally, in-situ management). These methods are preferable over other methods discussed in subsequent subsections as they do not require transportation of straw or final products to longer distances outside the rural areas. However, these methods have their own limitations for scaling to the entire region and given the huge quantum of straw generation, role of other methods cannot be denied in the overall biomass management ecosystem.

Key methods for this include-

1. Composting for conversion to green manure
2. Pyrolysis for conversion to bio-char
3. Chopping/shredding for dry animal fodder and mixing (with supplements) for Total Mixed Ration (TMR) to animals (with further option of pelletisation)
4. Biomethanation for conversion to biogas and further purification of biogas and subsequently compression to bio-CNG

Composting is possible in multiple forms or configurations. These key methods can be classified as-

1. In-situ composting: This form of composting is undertaken simultaneously along with in-situ management. Inoculum with microbial culture is sprayed onto the field to accelerate composting but this requires chopped and evenly spread straw on the field which is either retained as a mulch layer or incorporated into the soil.
2. Ex-situ pit composting: Manually outside the field in small pits with or without microbial inoculum and vermicultures
3. Ex-situ windrow composting: Composting outside the field at scale with tractor-pulled farm implements with or without microbial inoculum and vermicultures

Different composting techniques and microbial solutions are currently under trial with farmers. While all techniques have their own limitations and benefits, focus of this study is on the ex-situ techniques. Pit composting requires near-zero capital, but it is labour intensive for operations such as- digging the pit, turning the compost bed etc. For a composting pit of 30x10 square feet size, farmers can compost roughly about 30-45 tonne of rice straw in a year (assuming 4-6 batches in a year). Assuming a conservative price of manure at INR 3/kg and four batches in a year, net benefit to the farmer from setting up one such compost pit is estimated around INR 29,881[6]. This model can further be scaled using larger areas for composting and mechanised means for turning the compost beds (windrow composting).

Composting has significant potential for treating rice straw and generating value for farmers but there are barriers such as limited land availability with farmers for composting and limited use of green manure by farmers who are into intensive agriculture with heavy dependence on chemical inputs. Some of these challenges for popularising and scaling bio-fertilisers have been revisited under biomethanation where bio-fertiliser is a key by-product along with biogas or bio-CNG and significantly impacts cash flow of this delivery model.

Bio-char, which is the main product of pyrolysis process, is used as a soil conditioner on agricultural land for a standalone application or application along with fertilisers and green manure. It has high potential as a soil conditioner in areas of North West where soil is deficient in organic Carbon. Secondary literature mentions that if residues are converted into bio-char, 50% of initial biomass Carbon can be recovered as compared to only 3% during open burning (Venkatesh et al 2018). Although a crude form of bio-char kilns which can control 40-60% emissions as compared to open burning exists, technology development for more efficient reactors which can further reduce it to 95% are in progress. The proposed reactor from Takachar, once fully developed, will be able to consume 2-5 tonnes of rice straw per day. Lack of standards and certifications for such reactors (as it is neither a boiler nor gasifier) and marketing barriers for organic inputs are key challenges speculated by technology developers.

Animal feed in the forms of - (1) dry fodder and (2) balanced animal diets with addition of nutrients, formally known as Total Mixed Ration (TMR), are two major routes through which rice straw can add value to the rural economy in North West and revive decentralised dairy farming. Presently, India faces a net deficit of 35.60 % green fodder, 10.95 % dry fodder and 44.00 % concentrate feed ingredients (IGFRI 2015). Surplus paddy straw can be used directly or by treating the straw with protein or nitrogenous compounds (Kumar et al 2014).

In Punjab and Haryana, farmers have traditionally been feeding the cattle with wheat straw and their preference for wheat straw over rice straw is based

[6]Total revenues and operational expenditure in a year is estimated at INR 63,840 and INR 33,959 respectively.

on a flawed perception of poor nutrient value associated with non-basmati rice straw. We analysed the samples of rice straw from the two states in the laboratory at Saras Dairy Plant in Hanumangarh, Rajasthan[7] for their nutrient[8] values and preliminary analysis of these findings, summarised in Figure 7, show us that these nutrient values are quite comparable[9]. This helps in busting the myth associated with lower nutrient value of rice straw. Also, silica content of both biomass types is compared in Figure 7 and although Silica content is higher for rice straw (average 5% compared to 2% in wheat straw), it is manageable for this application.

Figure 7. Comparison of total digestible nutrients (A) and silica content (B) of rice straw vis-a-vis wheat straw across North Western Region.

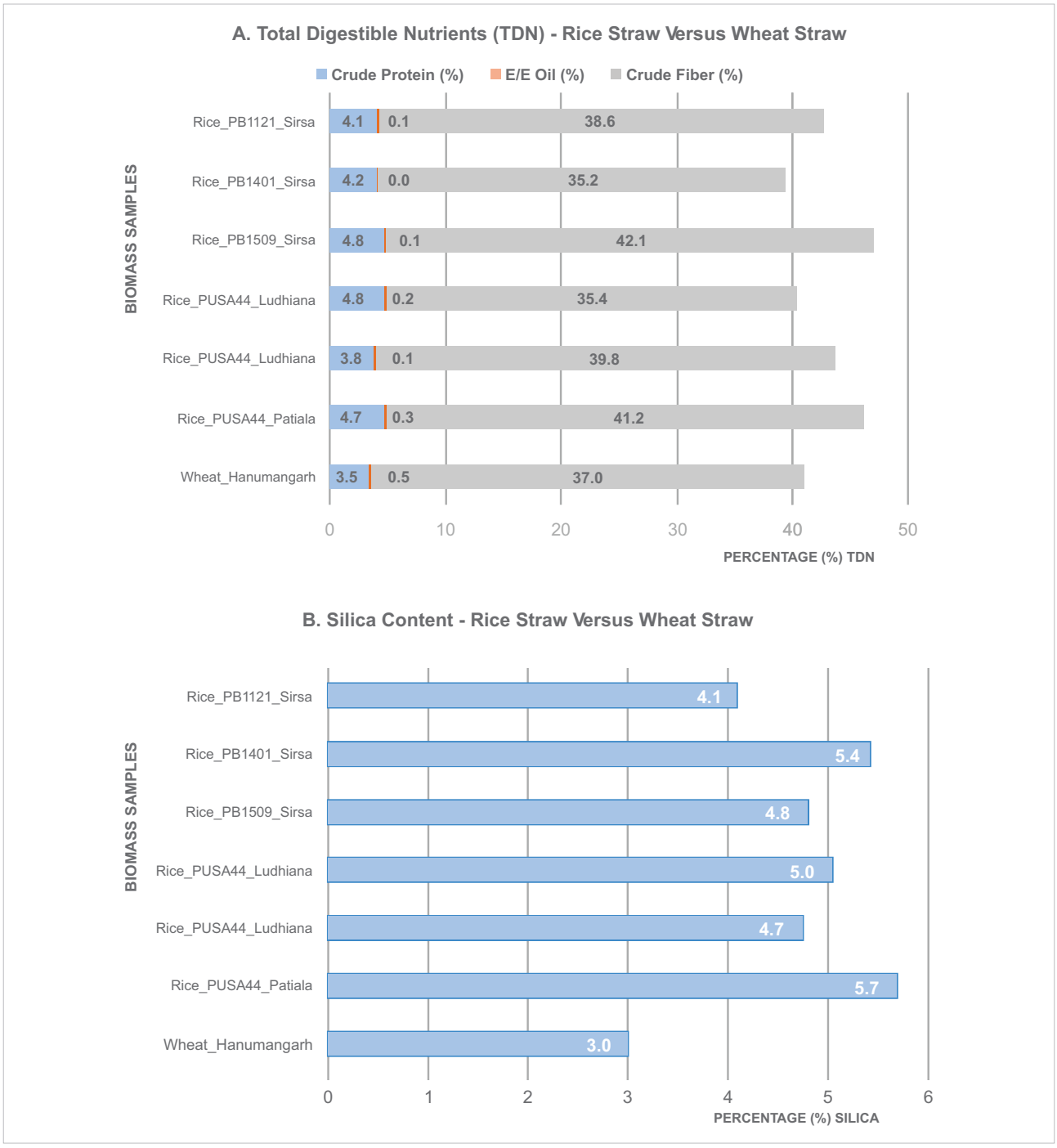

Source: Cleaner Air - Better Life (2021) Analysis

[7]Close to Haryana border

[8]Protein, fats and fibre

[9]Reference nutrient values of wheat straw from Hanumangarh are used for comparison.

Rice straw bales are already being transported by local entrepreneurs from Haryana and Punjab to the bordering and straw scarce state of Rajasthan as they are able to fetch good prices there and dairy farmers have absolutely no problem feeding rice straw to their animals. But transporting bulky straw bales to far away distances is not very efficient as the shelf life of straw bales is low. Also, treated rice straw feed enhances milk and meat yield when compared with untreated rice straw (Wanapat et al, 2009).

Therefore, converted rice straw TMR pellets as a balanced diet with the addition of other required nutrients or filler materials is seen as an emerging delivery model. SARAS Dairy's plant in Hanumangarh (see Figure 8) has in fact been producing TMR from wheat straw and piloted use of rice straw with support from National Dairy Development Board (NDDB), India. Our research team visited this plant located in Hanumangarh in the winter of 2019. Capacity of this plant is 50 tonnes per day (tpd) TMR. TMR based animal feed produced from this plant is supplied across Rajasthan in the form of pellets or briquettes and has been beneficial to dairy farmers whose access to green fodder is limited and helps them in maintaining the pH of cattle stomach and increase the quality and yield of milk. Key challenges faced by plant engineers during the piloting phase with rice straw and learnings from this are summarised below-

- Due to silica and fibre content of rice (See figure 7), grinding and feeder units face frequent jams causing the entire plant to breakdown. Wide and large feeders can solve the jamming problem.
- Metallurgy for grinding units was adjusted with specialised blades for rice straw and additional mechanical supports were added to conveyer feed systems.
- Optimal moisture is crucial and high moisture in rice straw can also lead to similar challenges.
- Moreover, there are widespread misconceptions in the dairy industry regarding particle size at which straw should be grinded. Rather than grinding rice straw down to 1-3 mm size, a particle size of 6-12 mm is suitable for animal digestion.
- The above consideration also reduces chances of mechanical wear and damage in grinding and feeding units

Figure 8. Total Mixed Ration (TMR) plant at SARAS Dairy in Hanumangarh, Rajasthan.

These summarised learnings are also applicable to entrepreneurs setting up units at smaller scales. TMR mixer can be set up by the rural entrepreneur for making the formulated TMR with addition of proteins, mineral mixture, molasses etc. TMR mixture produced can be in the loose form or can be densified into pellets for increasing shelf life of the product, easier handling and efficient transportation to longer distances. Appropriate design of onsite storage and location criteria are important considerations for cost-effective transportation and access to market/consumers. TMR mixers are available in the market in varying sizes (2-8 m^3) and can even be mounted to tractors (>50HP tractor). There are, in fact, 208 small TMR mixers (mainly based on wheat straw) which have been operating in Punjab as of 2019 and the capital cost for these is 3-5 lakh with 50% capital subsidy[10].

For this study, a medium sized (24 tpd TMR) plant was considered for developing the investment model. As shown in Figure 9, the capital investment needed for this scale is INR 1.6 Crore. Three key steps in the process include-

1. Grinding of rice straw to fine particles
2. Batch mixing with filler materials as per a predesigned formulation
3. Processing mixer in Roll-type extrusion pellet mill

Figure 9. Total Mixed Ration (TMR) feed pellet investment model with scenarios for different prices of raw materials: rice straw and filler materials.

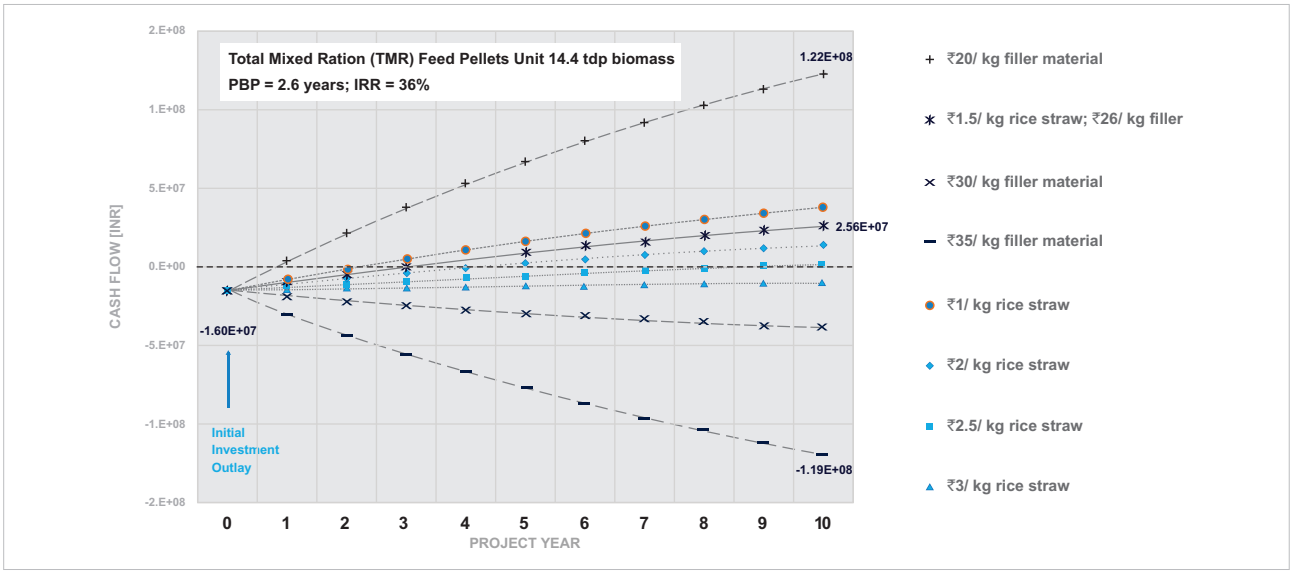

Source: Cleaner Air - Better Life (2021) Analysis

The proposed plant, which is under development, will consume about 14.4 tonne rice straw in a day which is 60%[11] of the overall TMR formulation and 40% filler materials are added. Annual cash flows from the unit have been estimated at INR 62 lakh based on detailed data from the project developer at GBDSGNS Foundation based in Raikot block (Ludhiana, Punjab). Given the fact that, prices of filler materials and rice straw are prone to market situations, further sensitivity on these has been carried out. For an average price of filler materials at INR 26 per kg (refer the TMR formulation in Table 1.) and rice straw at INR 1.5/ kg, the project PBP is estimated at 2.6 years while based on discounted cash flow analysis, actual break-even is achieved in 3.5 years' time period (with net present worth of INR 2.56 Crore). It can be seen from Figure 8 that the TMR pelletisation investment model is highly sensitive to the market price of filler materials. With the average price going up from INR 26 /kg to INR 30/ kg the project becomes completely unviable[12]. Project viability is good for rice straw prices ranging from INR 1-2 /kg.

[10]based on inputs at CII stakeholder dialogue series in May-June 2020
[11]By weight
[12]Negative NPV

Feed constituents and their prices vary from place to place depending on specific nutritional requirements of dairy animals as well as local availability of filler materials.

Table 1. Filler materials with prices for considered formulation of TMR pellets

S.N.	Filler Material	Composition [Percentage by Weight]	Price [INR/Kg]
1	Corn	2-5%	40-60
2	Maize	10-15%	12-20
3	Millets	2-5%	50-80
4	Mustard	10-15%	20-30
5	Barley	3-5%	50-60
6	De - oiled Cake	5-8%	29
7	Urea	1%	10-15
8	Salt	1%	15-20

Source: Data collected from GBDSGNS Foundation

Biomethanation is a key route for decentralised delivery models in an agrarian state to meet the future needs of energy most sustainably. The team visited the fully commercialised plant by Sampurn Agri Ventures in Fazilka, Punjab (40 tpd capacity) which is a zero-liquid discharge plant and has been in operation for last the 5 years (See Figure 11). Green manure produced by the plant approved by Punjab Agriculture University has shown significant benefits for improving crop yield and soil health in the field. Based on the same technology (dry digestor technology based on dual phase biomethanation process) and data collected from the technology provider, investment model for bio-CNG was developed. The analysed model processes rice straw at 70 tpd and has a catchment area of 100 km. For delivering purified and compressed bio-CNG, the capital requirement is INR 38 crore. Bio-methanation of rice straw can save significant amount of import duties from avoided crude oil and gas imports. It is therefore also part of Government of India's SATAT Initiative. Biofuels have the potential to reduce our fuel import bill by Rs. 1 lakh crore (GoI 2020). But it is a rather less known fact that bio-fertilisers (liquid bio-fertiliser and green manure combined) produced from biomethanation can potentially substitute 40% of the total fertiliser consumption[13], reducing a burden of INR 20,000-30,000 crore spent by Government of India on fertiliser subsidies. Both need to be seen in light of the fact that bio-fertilisers contribute to 43% of all the revenues. Therefore, they play a crucial role in the plant's economic viability. Yearly cash flows from the assessed Bio-CNG model are as follows-

1. Bio-CNG: INR 12.2 crore for 2.6 kilo tonne Bio-CNG per year (57% of all revenues)
2. Manure: INR 5.6 crore for 14 kilo tonne manure per year (26% of all revenues)
3. Liquid fertiliser: INR 3.5 crore per year for 3500 kilo litre fertilisers in a year (16% of all revenues)

[13]Stakeholder inputs at CII Stakeholder dialogue series for scaling ex-situ solutions

Promoting a bio-CNG model therefore requires equal emphasis from an agricultural perspective, if not less, and equal amount of efforts from agricultural agencies in order to improve viability and scale this delivery model across the North West region.

As depicted in Figure 10, net present value of the project is INR 42 crore at an internal rate of return at 29%. As per the assured price and 100% offtake of bio-CNG guaranteed by GoI under its SATAT initiative and assuming 100% bio-fertiliser offtake, it takes the project a little less than 4 years to reach break-even point. The simple payback period is 3.2 years. But if bio-fertiliser's offtake is zero, the model becomes completely unviable and findings reveal that NPV of the project will in turn be INR -19 crore. Even if the plant is able to sell half the bio-fertilisers it generates (or fetch half the assumed[14] market prices), the project is just viable at NPV of INR 11.4 crore with break-even in 7 years. Due to high economic value created by the bio-CNG model, it is also relatively far less sensitive to fluctuations in landed prices of rice straw in comparison to solid-fuel pellets (See Section 4.5).

Figure 10. Bio-CNG investment model with scenarios for raw material price and bio-fertiliser offtake.

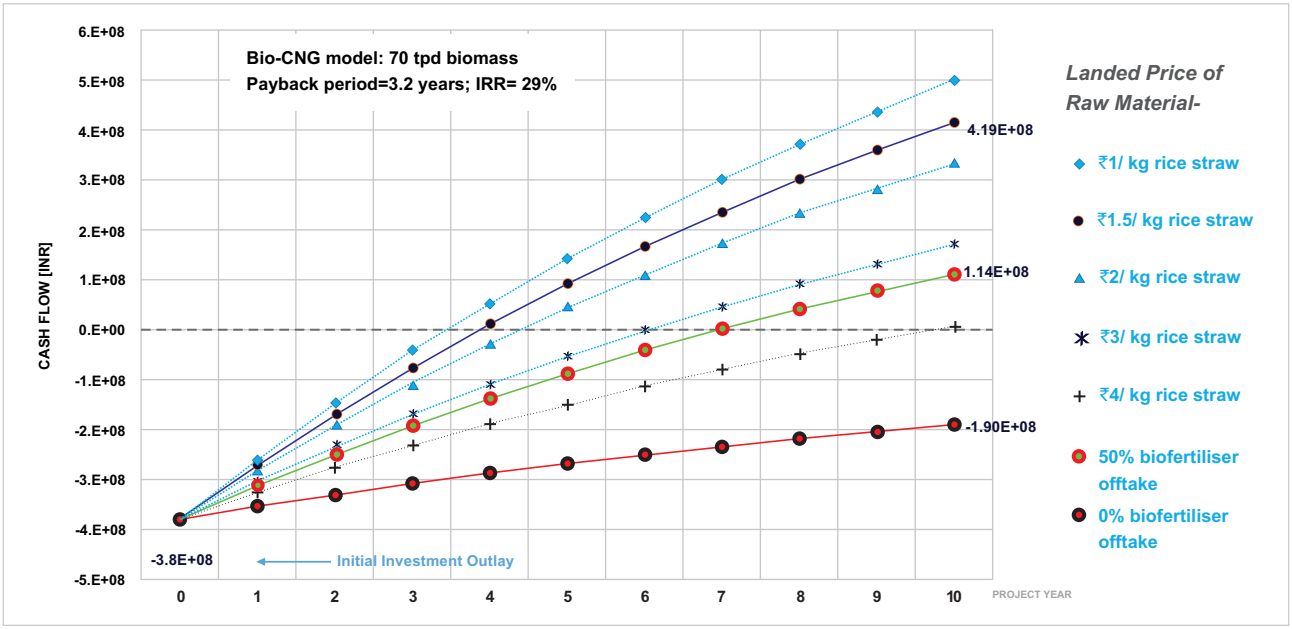

Source: Cleaner Air - Better Life (2021) Analysis

From the above analysis, it is clear that despite bio-CNG's good rate of return, it is very difficult to scale this delivery model due to inherent challenges in the offtake of bio-fertilisers, especially in agrarian states of Punjab and Haryana where farmers are predominantly dependent on chemical fertilisers and disproportionate subsidies on fertilisers which are the biggest stumbling block for scaling bio-CNG.

[14]Manure at INR 4/ kg and liquid fertiliser at INR 10/ litre

Figure 11. Bio-fertilser offtake is crucial for viability of Bio-CNG model: Sampurn Agri Venture's Bio-CNG plant in Fazilka, Punjab with green manure from plant being cured in open as seen in the foreground

4.3 Construction Elements

Solutions for use of agricultural residues in building/construction applications are fast emerging and are driven by demand for affordable housing as well as natural building materials with low embodied energy. As rice straw is turned into construction elements, its application becomes carbon neutral or carbon negative depending on the actual use and specific context. In this study two application of rice straw in building/construction (See Figure 12) are being assessed-

1. Agrocrete bricks or blocks from rice straw, lime sludge and other industrial waste
2. Strawboards or construction panels from rice straw and non-formaldehyde-based binder

Unlike solutions considered in previous subsections, these are at a very nascent stage of development, but they are being demonstrated on the field. They are being assessed as a part of this study because-

- They have a high potential to address the air pollution challenge at scale due to rampant demand for construction materials in future. Floor space demand in India is projected to grow as much as 7 times for urban residential buildings and 3 times for commercial buildings by 2050 (Rue Du Can 2019)
- They can reduce global warming by avoiding extraction of virgin materials in construction/buildings. Natural buildings can even lower energy demand by improving the Building Envelop Energy Efficiency (BEEE), but this varies with actual use case[15].

[15]Agrocrete claims that every 'square metre' of wall made up Agrocrete blocks amounts to 38 Kg CO2e of carbon captured, 8 Kg CO2e GHGs saved annually due to improved BEEE.

- Going a step further, they can store carbon in building walls for hundreds of years and hence have negative carbon emissions over the lifecycle of their use
- Degradation of biomass over longer storage periods does not limit its use unlike energy applications where degraded straw implies significantly lower calorific value. Also, it is possible to have wet storage (with water sprinklers) which helps reducing the risk of fire hazards at storage sites

Figure 12. Agrocrete blocks and strawboard panels from Strawcture Eco

Picture on the right courtesy - https://www.thebetterindia.com/187863/uttar-pradesh-girl-quits-us-job-sustainable-homes-stubble-burning-india/

Agrocrete blocks, being assessed for their economic viability, have been developed by Greenjam BuildTech as a patented technology. Greenjam uses rice straw along with lime sludge, steel flakes and other industrial waste streams in different proportions to manufacture Agrocrete. Agrocrete bricks have a compressive strength of 7.5 Megapascal (Mpa), lighter density (1400 kg/m^3) and thermal conductivity of 0.4 Watt per metre-Kelvin (W/m-K). Agrocrete blocks also have good water resistance with less than 10% water absorption. Traditional bricks have thermal conductivity ranging from 0.4-0.7 W/m-K. depending on size of brick (Dondi et al 2004). Compressive strength of traditional red bricks ranges from 3.5 to 35MPa with widely used bricks having a strength of 5-7.5 MPa (BIS 2017).

Manufacturing process of Agrocrete blocks is very simple and is similar to conventional brick making process. A small plant manufacturing 1000 blocks a day costs approximately INR 5-6 lac in capital investment. Due to the simple manufacturing process, it is possible to design a hyper-local model and engage rural entrepreneurs. Market awareness of the product is found to be a major challenge for scaling its use. Building codes also partially impact product offtake in the market. Bureau of Indian Standards (BIS)'s standard IS: 2185 which provides the

guidelines for building blocks/bricks does not recognise biomass as a raw material for bricks/blocks. This also implies that use of BIS symbol for blocks is not possible despite comparable or even better characteristics as compared to red bricks.

Strawboards and construction panels from rice straw and other agricultural residues are being produced by Strawcture Eco as a replacement of wood or other concrete material. Strawcture Eco had constructed an area of 15000 square feet across six Indian cities with these panels by 2019. It has a further building capacity for manufacturing of 300,000 square meter of the panel boards in 2020-21. Strawcture Eco is building 250-300 square feet sized small houses under the Pradhan Mantri Awas Yojana, and will have a capacity to build 2300 houses from the new factory. It has targeted to sell an additional 50,000 m^2 of panels in the market directly to builders and architects. Processing of the straw into compressed boards is done with the help of a non-formaldehyde-based binding solution[16] at a certain temperature and pressure. Thermal conductivity of such panels made from wheat straw, rice straw and sugarcane bagasse is approximately 0.09 Watts per metre-kelvin (W/m-K). It is possible for the conversion unit of straw boards/panel to utilise a variety of biomass depending on location. Density of panels ranges from 750-1100 kg/m^3 depending on types-

1. Interior grade panel
2. Exterior grade panel
3. High-density flooring grade panel

While indoor panels are approved by standards, two tests were pending for exterior panels at the time of writing this report. Price of an interior 18 mm panel made from rice straw is INR 50 per square feet in comparison to a plywood material (INR 60 per square feet). Also, it is 15% lower than gypsum and cement boards. Although the panel boards are approved by the Building Material Council of India, there is no formal information to back up the fact that bio-composite panels are similar in performance to conventional building materials.

Figure 13. Investment Model for Construction Blocks and Panels

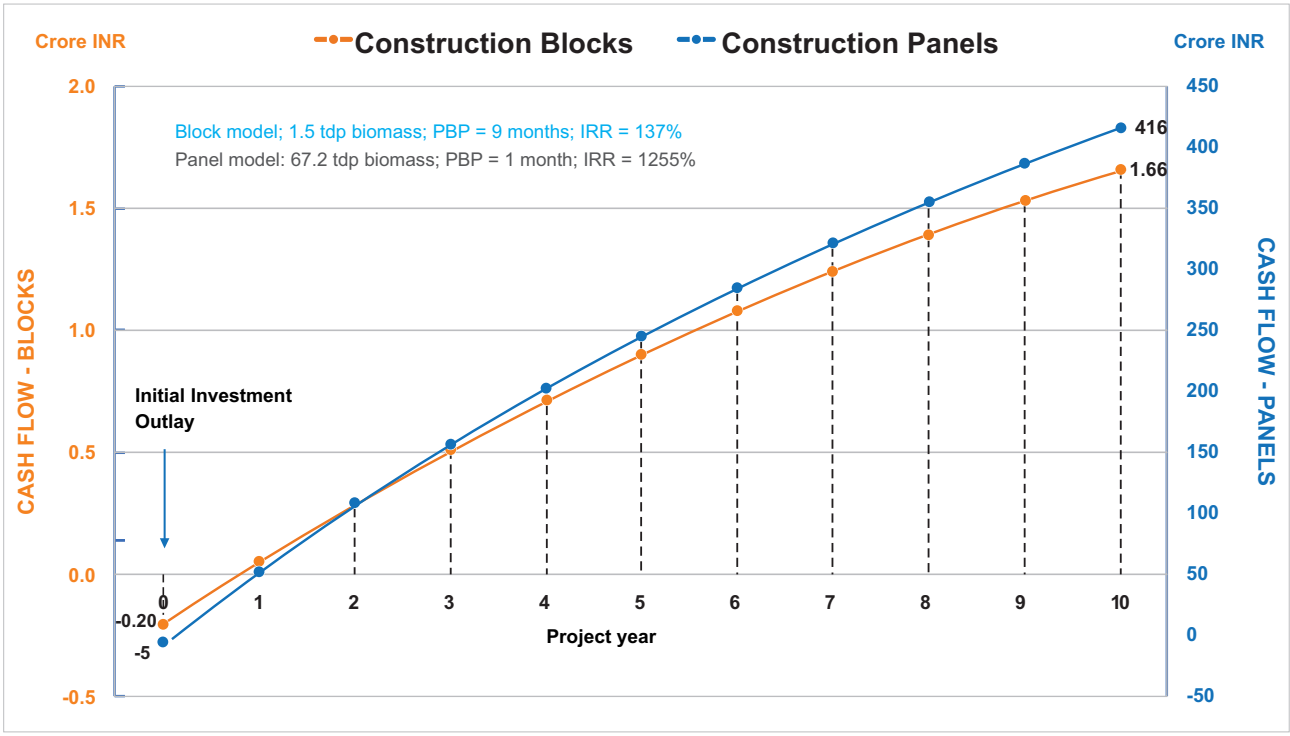

Source: Cleaner Air - Better Life (2021) Analysis

[16] outsourced from third party

For both models described, scaling is difficult due to lack of market/consumer awareness and market opportunities. Investment models (blocks consuming 1.5 tpd biomass and panels consuming 67 tpd biomass) for both were developed based on detailed data collection from both start-ups and results have been presented in Figure 13. It should be noted that although both models are shown in the same figure, discounted cash flows for the two models are not comparable, as the scale/sizes and initial investment outlays for both are very different. It is clear that both models have a very high potential for scaling and yield high returns and break even in few months, albeit, with the key assumption that both products are sold in the market immediately which is not a very realistic scenario given the current market situation. Usually, these construction elements are produced as per requirement and not as the continuous process with 300 operational days in a year as assumed in this analysis. Nonetheless, it shows that both models have very high potential if market opportunities exist. Sensitivity analysis over price of rice straw if further undertaken, in Figure 14 found that both these models, unlike other investment models presented in this study, are not very sensitive to price of straw and NPVs remain positive (INR 0.9-1.8 crore for blocks and INR 382-423 crore for panels) for the entire range of rice straw landed prices: INR 1-4 per kg used for this evaluation. Another observation can be made here is that construction panels are less sensitive to fluctuations between the two.

Figure 14. Sensitivity analysis over raw material prices

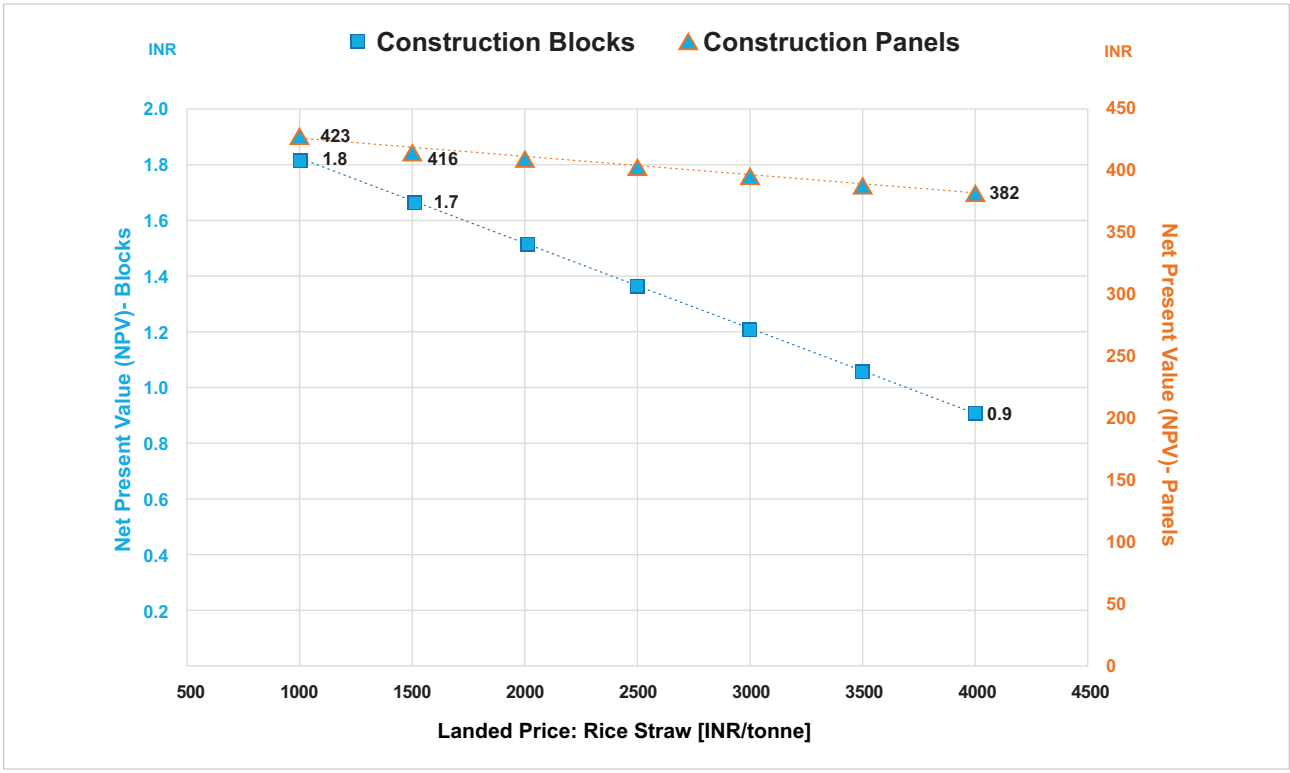

Source: Cleaner Air - Better Life (2021) Analysis

4.4 Pulping and Packaging Solutions

Once processed into pulp, rice straw can be converted to multiple products such as paperboards for packaging, disposable tableware, crafts etc. Besides addressing the air pollution problem, it can also be a solution to plastics pollution. Kriya Labs has developed the process of producing pulp from rice straw through a Chemi-thermo-mechanical process which has two crucial components-

1. Pulping system
2. Water recycling system

Much like other material applications discussed in prior subsections, chipped rice straw is first prewashed to remove any dirt and silica. Softening of the chipped straw is the next step which involves treating it in a reactor with minimum doses of chemicals. The softened material goes through a mechanical refiner which applies a shear on the fibres and separates them. This step turns the cooked material into pulp which is suitable for moulding into different forms and shapes.

The conversion ratio of straw to pulp is 0.62 which means almost 625 kg of pulp is produced with every tonne of straw processed. The pulp so produced can be moulded in the form of sheets, boards, disposable tableware or other packing materials. Since the whole process of pulping involves multiple washing steps, it is quite water-intensive, so the water recycling system has a crucial role in the entire process.

The water recycling system deals with liquor generated at each step separately. All the chemicals used in the cooking step are consumed during the cooking itself and hence there is no need for any special step for their removal, leaving only organic and inorganic residues from rice straw. The system is a combination of decanting and selective filtration. Liquor is removed from the pulp in a certain proportion along with the solid in a certain proportion from this liquor. This solid is the only waste generated in the process and is an amalgamation of fine bits of lignin and silica from rice straw. It can potentially be used as a fertilizer or binding material in the construction industry. Treated water is analysed and suitable to be fed back into the process to ensure zero liquid discharge.

Figure 15. Investment model for pulping unit and scenarios for landed price of raw material

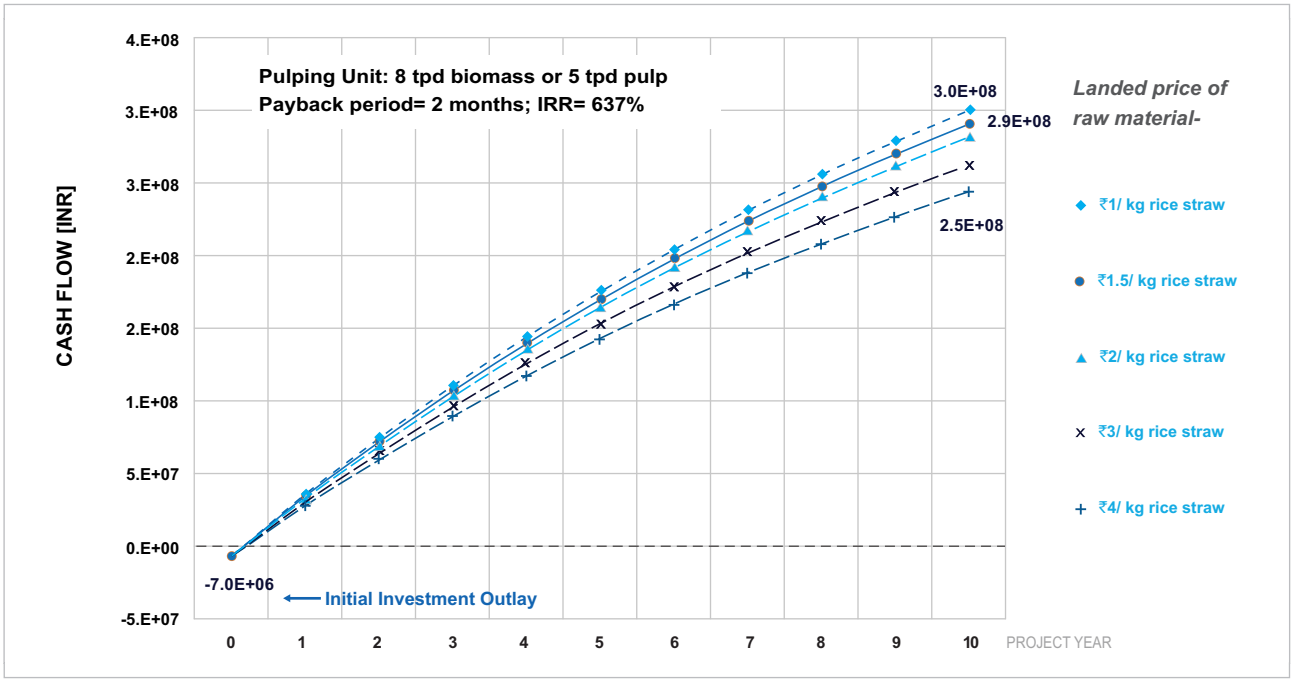

Source: Cleaner Air - Better Life (2021) Analysis

As depicted in Figure 15, the investment model and discounted cash flow analysis for pulping unit producing 5 tpd pulp has been undertaken. The project has a short payback period of 2 months, if 100% offtake of pulp is ensured at INR 40 per kg market price. The unit requires an initial investment of INR 70 lacs, consumes 8 tpd rice straw and yields a high NPV of INR 29 crore (IRR at 637 %).

4.5 Solid Fuels and Energy Recovery

There are multiple ways in which energy values of rice straw can be extracted or rather, rice straw can be converted into different energy carriers or products. Three key pathways include-

1. **Mechanical processing:** grinding straw to finer particle sizes and further densification to meet needs of the final user
2. **Thermal processing:** based on process parameters and air supply, these are further categorised into pyrolysis, torrefaction and gasification
3. **Biological processing:** biomethanation and fermentation to second generation liquid bio-fuels

Multiple energy carriers generated from the above pathways can also interlink these pathways or these energy carriers can be further used for generating electricity, but all of these excessively complex layers mean loss of energy and efficiency with each step. Also, there are inherent challenges associated with handling and processing of rice straw for energy such as-

1. Storage of biomass for year-round supply is essential but baled biomass undergoes degradation with time, causing a dip in the calorific value of rice straw. Evidence shows a 20% decrease in the calorific value over a one year period (Singh et al 2020b). As the caloric value of rice straw is already lower compared to other biomass types such as wheat, cotton, sugarcane etc., this compounds the challenges associated with energy use of rice straw.
2. The high silica and lignin content in rice straw implies that cost for processing rice straw is higher compared to other biomass types and increases with particle size requirement. This effect is already documented for the case of dedicated bio-power plants and rice straw to bio-ethanol technologies in the CII-NITI (2018).

Therefore, two delivery models i.e. 'solid fuel pellets' and 'direct firing of bales for energy recovery in industrial boilers' are considered as affordable and actionable solutions[17] in this study. For reasons mentioned under point 1, rice straw needs to be either fired directly into the boilers (wherever possible) or densified into pellets for increasing its shelf life.

Densification of biomass into Solid Fuel Pellets (SFP) also has an advantage over loose straw due to higher density and better heat conductivity. This in turn increases the efficiency of transportation and energy extraction at end-use, whether it is an industrial boiler for process heat, thermal power plant for electricity generation or in purpose-built cook stove or oven.

Crushing, mixing, drying, grinding and pelletisation are key steps involved in the process which require specialised machinery. Experiences from A2P, a bio-energy start-up active in Punjab show that-

- Use of innovative methods such as machine learning for mapping industrial boilers or use of pellets and modified equipment helped reduce cost by 12%
- Focus on different kinds of biomass may ease some of the supply chain bottlenecks for year-round availability of feedstock and address issues related to the low calorific value of rice straw.
- Wear and tear in the shredding unit (due to higher silica content of rice straw) is a significant cost factor for a pelletisation plant with greater than 1 tpd scale. Research and development for the right metallurgy and indigenous design of machinery is therefore crucial and collaboration with local entrepreneurs for customised solutions is desirable.

Calorific value of rice straw-based solid-fuel pellets is found to be 3400-3500 Kcal/Kg which his comparable to washed coal (3500-3800 Kcal/Kg). It can therefore easily substitute coal in many applications. Pellets can further be torrefied for 25-30% higher energy value (comparable to imported coal) and a higher shelf life but this entails additional cost.

Various specific interventions have been made on this issue after Ministry of Power's advisory (MoP 2017) directed power generators to utilise 5-10% rice straw by co-firing with coal in existing thermal power plants. MoP advisory also assures generators that any

[17]Refer Subsection 4.2 biomethanation of rice straw

MoP advisory also assures generators that any increase in cost of generation will not be taken into account for the purpose of determining priority or merit order for electricity dispatch. Guidance in this regard was issued by the Central Electricity Authority (CEA) in the same year (CEA 2017). The Ministry of New and Renewable Energy (MNRE) has further clarified that generators can even avail non-solar Renewable Purchase Obligations (RPOs) (MNRE 2019). Subsequently, an order was issued by the Central Electricity Regulatory Commission (CERC) for methodology to estimate electricity generated from biomass in biomass co-fired thermal power plants (CERC 2020)

NTPC invited bids for biomass pellets for two years' supply of 1000 tpd in 2018 with a capping of price at INR 5,500/tonne for conventional pellets and INR 6,600/tonne for torrefied pellets. However, NTPC received only 240 tpd material within the capping price. Subsequent tenders have been invited without the price capping. As per NTPC, supply constraints for pellets have not led to significant co-firing so far. Total potential within NTPC plants alone is estimated to be 20 million tonne per annum at 10% co-firing. Technology readiness also exists in industrial boilers for direct firing of rice straw. Several aggregators provide ready to fire feedstock to industrial boilers. In addition, grated boilers or pulsating grate boilers have made it possible to directly fire bales in boilers without any operational challenges.

Figure 16. Investment model for pelletisation unit for use of solid-fuel pellets in industrial boilers with process energy requirement and coal-based thermal power plants

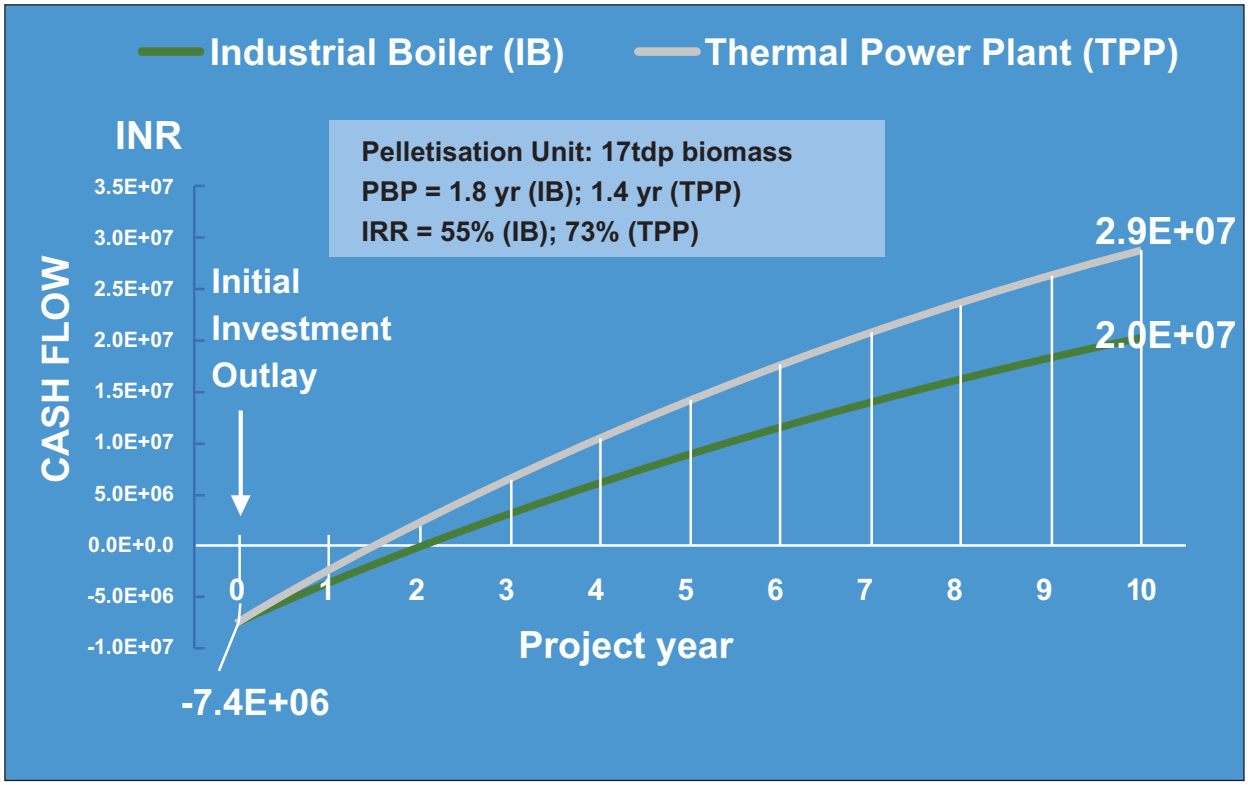

Source: Cleaner Air Better Life (2021) Analysis

The investment model has been developed to assess viability of pelletisation and as depicted in Figure 16, two different scenarios with use of pellets in industrial boilers and thermal power plants have been plotted. Essentially, the key difference between the two models is-

- Additional maintenance cost (assumed to 30% higher for TPP use case) to operator for meeting the particle size requirement as detailed in CEA 2019 guidance document
- The market price of SPF which is assumed to be INR 5 per kg for the use case of industrial boilers (IB) and INR 5.5 per kg for the use case of thermal power plants (TPP)

It can be seen in Figure 16 that the project payback period ranges 1.4-1.8 years depending on SFP configuration. Despite higher maintenance cost, the payback for the TPP use case is marginally higher over IB use case. The project NPV for this pelletisation unit (INR 74 lac capital investment) is INR 2 crore and 2.9 crore for industrial boiler use case and TPP use case respectively. Further, in figure 17, sensitivities have been performed for the use case of TPP over different-

1. Landed rice straw prices for operator of the pelletisation unit
2. Price of solid fuel pellets paid by thermal generators

It can be seen that discounted cash flows of the project in Figure 17 are very sensitive to both of these market prices. The project becomes completely unviable for rice straw prices over INR 2 per kg and pellet prices lower than INR 4.5 per kg.

Figure 17. Sensitivity analysis for (A) landed price of rice straw and (B) solid-fuel pellet price paid by thermal power generator

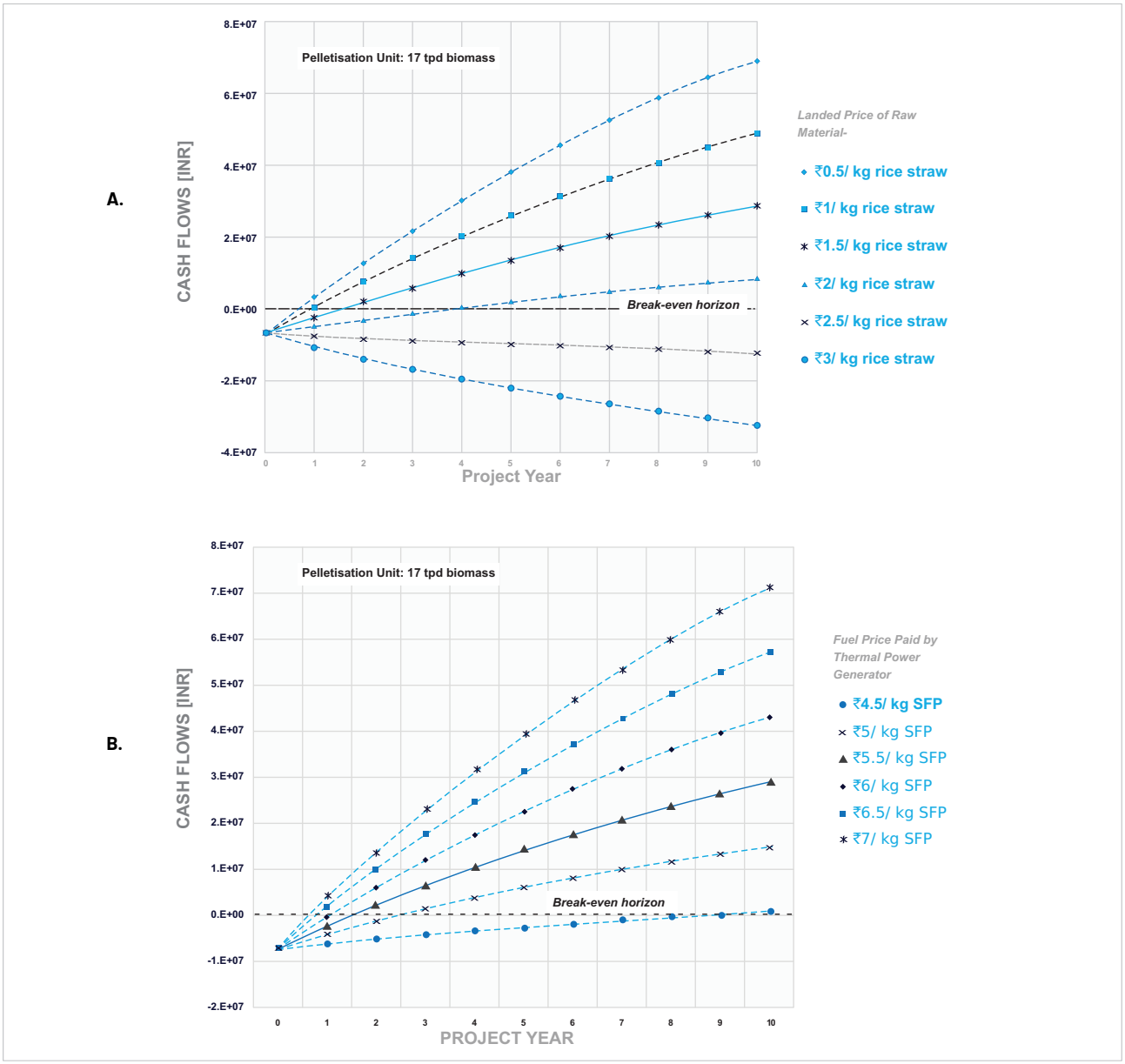

Source: Cleaner Air Better Life (2021) Analysis

5. KEY FINDINGS AND RECOMMENDATIONS FOR SCALING SOLUTIONS

Key findings with respect to various delivery models discussed throughout Section 4 point to special consideration and customization required in the design of equipment for handling and treating rice straw in North Western states due to its special characteristics: high lignin and silica content. But the biomass management infrastructure which is suited to rice straw can handle almost any crop residue. Also, there is a definite need for more entrepreneurs from diverse backgrounds to join and pool skill sets to overcome technological barriers.

Straw aggregation is a specialised business as it requires a wide array of best practices (See Section 4.1) to be integrated into the business model and needs robust quality control to be able to meet requirements of the user facility. This delivery model will be able to make an economic case for farmers as well rural entrepreneurs. Economic viability exists without even considering any capital subsidies for balers and the venture is profitable with an Internal Rate of Return (IRR) at 18% and benefits to farmers worth INR 1985 per acre. It is in fact the only actionable model which could significantly bring down the cost of ex-situ management at the farmer's end to INR 2924 per acre (from INR 4629 per acre under the conventional model) close to the cost of conventional route which involves burning (INR 2948 per acre). Serving as the very backbone of all subsequent ex-situ management operations, this activity needs to be brought under the priority lending scheme of national banks and also make sure that business risks of enterprises can be covered under insurance schemes. Depending on the size, 100-1000 rural straw banks will be required across Punjab and Haryana e.g. with the scale of delivery model considered in the analysis (which is 60,000 tonnes biomass per year), approximately 200 such units would be required across the two states.

The report presents specific cases of composting, bio-char, animal feed and bio-CNG which can add significant value to the rural economy. Scaling of composting, bio-char and Bio-CNG require promotion and mass awareness among farmers on use of bio-fertilisers for agriculture. Use of green manure remains limited to horticulture in agrarian states. The analysis shows that without using any capital or mirobial solution at all, the farmer can easily earn INR 30,000 in a year with a small composting pit of 30x10 ft. Composting is especially relevant for small-marginal farmers and can even be scaled with the help of specialised equipment on degraded lands.

Standards and certifications for reactors producing bio-char, which do not exist in the country, can affect how bio-char technologies of the future evlove and need to be carefully designed in consultation with technology developers. Also, marketing challenges are being faced in bio-char akin to green manure or bio-fertiliser due to the farmer's heavy reliance on chemical inputs in the reigon.

Non-basmati varieties of rice straw are already being used as animal fodder/feed in the Eastern states of India. Rice straw from Punjab and Haryana is even being transported to the neighbouring state of Rajasthan and sold to farmers who face scarcity of straw. There are perception issues among farmers in Punjab and Haryana which hinder them from adopting rice straw as diet for their cattle. Our rapid analysis of a few samples of rice straw from Ludhiana, Patiala and Sirsa geographies confirm these misconceptions. Values of various nutrients such as proteins, fats and fibre are found to be comparable with wheat straw. A business model (24 tpd feed pellet based on rice straw) being developed by rural entrepreneurs at the GBDSGNS Foundation in Ludhiana has been considered for evaluation of this use case. The TMR feed pellet project has good viability with IRR at 36% and achieves break even in 3 years. This model is only viable for landed price of rice straw less than or equal to approximately INR 2.5 per kg but has been found very sensitive to the prices of filler materials used in TMR pellets. Even slight fluctuations in the prices of filler materials (which depend on local availability of these) could render the TMR feed pellet project unviable and hence project viability can vary from place to place.

While standard assumption of the average price for formulation used in the model is INR 26 per kg, the project becomes unviable at the price of INR 30 per kg.

Bio-CNG can be a great source of clean energy for the rural economy and the assessed model has been found to yield good returns with an IRR at 29% assuming an assured offtake of bio-CNG as well as bio-fertlisers produced during operation. Guaranteed offtake exists only for bio-CNG (under biofuel policy by Government of India). It is found that with no offtake of bio-fertlisers produced in the process, bio-CNG model becomes completely unviable with a negative NPV (INR - 19 crore). Even with a 50% offtake of biofertilisers, net worth of the project is reduced by 72% and payback period nealry doubles.

Therefore, promotion of green manure and bio-fertiliser from agricultral waste or crop residues needs to be the focus of Government policies of unlocking the potential of three technologies: composting, bio-char as well as bio-CNG. Following recommedations are being made for this-

- Green-manure quality certification guidelines needed from Ministry of Agriculture akin to the successful German Model.
- National Agricultural Co-operative Marketing Federation of India Ltd. (NAFED) and similar agencies can be roped in for their Pan-India network to propagate and distribute green-manure through nation-wide network of outlets.

Three key and less popular cases for giving rice straw a new life or converting it into high value-added products have been presented in this study. Typically, crop residue is seen as a waste and this is perhaps why harnessing or recovering energy from rice straw seems like a logical choice. The study finds that material applications of rice straw are equally well suited when compared to energy usage. This is both as a result of inherent properties of rice straw and nature of these processes. Some of these processes, e.g. construction blocks, allow for degraded/wet biomass and are not impacted by lowering of energy value over time. With the right formulation, rice straw makes strong construction blocks and compressive strength is observed to be comparable or more than the commonly used red bricks in India.

Insulation properties of construction elements from straw are far better than conventional materials and their greenhouse gas footprint is either neutral or negative depending on the use case.

Construction and pulping models evaluated in this study have been found highly desirable from an investment perspective and can substitute virgin materials in numerous applications. Our analysis finds that construction panels, blocks and pulp from rice straw are also are found to have IRR greater than 100% albeit with assumptions that all these products (blocks, panels and pulp) are sold at fixed market prices (either lower or equal to prices of conventional products in markets). These three models are also least affected by fluctuations in prices of rice straw. Market awareness related challenges are speculated to be the key barriers when it comes to scaling the use of rice straw in manufacturing of construction elements and hence public/private procurement of these materials and other ways of promotion will be pivotal for the success of these models in future.

Although standards for construction panels or strawboard exist, standards for use of crop residues or lignocellulosic materials in construction bricks/blocks do not exist in the country as of now. As a result, blocks/bricks from crop residues are also not eligible for the eco-mark from Bureau of Indian Standard (BIS). Even if standards exist, e.g. in case of panels, it takes a long time to get green products certified and separate testing guidelines for fast tracking these procedures for green building materials are desirable.

Lastly, the solid-fuel pellets model evaluated in this study shows that despite good market feasibility, this segment has not been picking up as a result of a number of factors such as-

- The customisation required in different units, especially in grinding unit, needs specialised expertise in metallurgy and the learning curve for any start-up is very high. It is similar in the case of TMR feed pellets as well.

- The lack of backward linkages and fluctuations in straw prices are also responsible for poor viability

The latter is true especially in the case of the SF pellets model. Viability and returns have been found excellent for both use cases-

1. Industrial boilers (PBP= 1.8 years, NPV= INR 2.0 crore)
2. Thermal power plants (PBP=1.4 years, NPV= INR 2.9 crore)

Although initial investment for the SF pelletisation unit meeting requirement of the above two markets is essentially the same, a higher operation expenditure is required to produce SF pellets for TPP plants. Our assumption on a slightly higher price being paid by TPPs yielding higher returns, may not necessarily be the case. Analysis shows that the solid-fuel pellets model is most sensitive to fluctuation in straw prices and becomes unviable beyond INR 2 per kg of rice straw. Also, it becomes unviable beyond a price point of INR 4.5/kg for SF pellet. This justifies the recent lifting of capping for SF pellets by NTPC at INR 5.5/ kg. Despite this, NTPC is not able to ensure the seamless supply of pellets. Observing this in the light of the facts below, it can be said that locational criterion and competitive bidding need to be reconsidered for supply for SF pellet to thermal generators.

- SF pellet model in this study only evaluates the viability for supplying within 150 km radius of the SF plant
- Bids are being invited for supplying pellets in NTPC plants across locations in India.

A New policy mandate, akin to Government of India's fly ash directive, could be issued for use of straw-based SF pellets within a certain radius. NTPC has already set the precedent but other private generators in the North Western region and industrial boilers in Punjab and Haryana need to follow and start utilising pellets in a small amount up to 10-15%. Taking these insights into consideration and given the fact that necessary guidance has already been provided on this matter by concerned authorities and regulatory agencies (e.g. MoP, MNRE, CERC and CEA as discussed on Section 4.5); Government may consider mandating all such units to start consuming at least 5% rice straw-based SF pellets. Industrial boilers could be given a choice to co-fire SF pellets as well as rice straw directly as long as adequate emission control systems are in place and order.

REFRENCES

Badarinath K. V. S., Chand T. R. K and Prasad V. K. 2006 Agriculture crop residue burning in the Indo-Gangetic Plains – A study using IRS-P6 AWiFS satellite data, Current Science Association, Volume 91, No. 8, pages 1085-1089. https://www.jstor.org/stable/24093988?seq=1

Bureau of Indian Standards (BIS). 2007. IS1077: 1992 Reaffirmed 2007, Common burnt clay building bricks - specification (Fifth revision). https://law.resource.org/pub/in/bis/S03/is.1077.1992.pdf

Bureau of Indian Standards (BIS). Aug 2005. IS 2185-1(2005), Concrete masonry units — specification, PART 1 Hollow and solid concrete blocks (Third Revision). https://www.iitk.ac.in/ce/test/IS-codes/is.2185.1.2005.pdf

Central Electricity Authority (CEA). 2017. Advisory for utilizing biomass in coal based thermal power plants. Ministry of Power, Government of India.
https://cea.nic.in/reports/others/thermal/tetd/Biomass%20Utilization%20Advisory.pdf

CII-NITI (2018). CII-NITI Aayog 'Biomass Management Report'. Report of the Task Force on Biomass Management. February 2018. New Delhi, India. http://niti.gov.in/content/task-force-biomass-management

Confederation of India Industry. May-June 2020. Stakeholder Inputs. Stakeholder Dialogue Series: Scaling Ex-situ Solutions for Rice Straw Management in Punjab & Haryana.

Dondi M, Mazzanti F, Principi P, Raimondo M, Zanarini G. 2004 Thermal Conductivity of Clay Bricks. Journal of Materials in Civil Engineering, Volume16, Pages 8-14. https://core.ac.uk/download/pdf/37835971.pdf

Government of India. 2020. Rs. 2 lakh crore to be invested for setting up 5000 Compressed bio-gas in the country, says Petroleum Minister at MoU signing event for setting up 900 CBG plants. Ministry of Petroleum & Natural Gas, Government of India. https://pib.gov.in/PressReleaseIframePage.aspx?PRID=1674428, Accessed 20 Nov 2020.

Ministry of Power (MoP), Government of India. 2017. Policy for Biomass Utilization for Power Generation through Co-firing in Pulverized Coal Fired Boilers,
https://cea.nic.in/old/reports/others/thermal/tetd/policy_biomass_utilization.pdf.2017

Mavi M.S, Singh G, Singh B.P , Sekhon B.S, Choudhary O.P, Sagi S, Berry R.
Interactive effects of rice-residue biochar and N-fertilizer on soil functions and crop biomass in contrasting soils. Journal of soil science and plant nutrition, vol.18 no.1 2018. http://dx.doi.org/10.4067/S0718-95162018005000201

Ministry of New and Renewable Energy (MNRE), Government of India. Sept 2019. Clarification regarding power generated from co-firing of biomass in thermal power plant as renewable energy,
https://mnre.gov.in/img/documents/uploads/a408798f3a8f44d8952f1cf49a542f2e.pdf

Central Electricity Regulatory Commission (CERC), Government of India. Feb 2020. Methodology for Estimation of Electricity Generated from Biomass in Biomass Co-fired Thermal Power Plants.
http://www.cercind.gov.in/2020/orders/SO12-SM-18-02-20.pdf

Gummert M, Van Hung N, Chivenge P, Douthwaite B. 2020. Sustainable Rice Straw Management. Springer. ISBN 978-3-030-32373-8. https://www.springer.com/gp/book/9783030323721#aboutBook

Indian grassland and fodder research institute, Indian Council of Agricultural Research. Vision 2050. July 2015
http://www.igfri.res.in/cms/Publication/Miscellaneous/IGFRI,%20Jhansi%20(Vision%202050).pdf

Kumar, A., V. K. Singh, Narender and R. Kumar, 2014: Utilization of paddy straw as animal feed. Forage Res., 40(3): 154-158.

M.R. Carter, CONSERVATION TILLAGE, Editor(s): Daniel Hillel, Encyclopedia of Soils in the Environment, Elsevier, 2005, P 306-311, ISBN 9780123485304, https://doi.org/10.1016/B0-12-348530-4/00270-8

Saikawa E, Panday A, Kang S, Gautam R, Zusman E, Cong Z, Somanathan E, Adhikary B. 2019 Air Pollution in the Hindu Kush Himalaya. The Hindu Kush Himalaya Assessment Pages 339-387. https://link.springer.com/chapter/10.1007/978-3-319-92288-1_10

Rue du can Stephane de la, Khandekar Aditya, Abhyankar Nikit, Phadke Amol, Khanna Nina Zeng, Fridley David, Zhou Nan. Jan 2019. Modeling India's energy future using a bottom-up Model. Applied Energy 238 (2019) 1108-1125. https://doi.org/10.1016/j.apenergy.2019.01.065

Singh B.P, Setia R, Wiesmeier M, Kunhikrishnan A, Chapter 7 - Agricultural Management Practices and Soil Organic Carbon Storage, Soil Carbon Storage Modulators, Mechanisms and Modeling. 2018, Pages 207-244. https://www.sciencedirect.com/science/article/pii/B978012812766700007X?via%3Dihub

Singh B, McDonald A.J, Srivastava A.K, Gerard B. 2019 Tradeoffs between groundwater conservation and air pollution from agricultural fires in northwest India. Nature Sustainability, volume 2, pages 580–583. https://www.nature.com/articles/s41893-019-0304-4

Singh M, Brar Y.S, Singh H, Sharma K.K. 2020. Challenges in Paddy Straw Procurement and its Effect on Cost of Power Generation. Journal of Shanghai Jiaotong University, ISSN: 1007-1172, https://shjtdxxb-e.cn/challenges-in-paddy-straw-procurement-and-its-effect-on-cost-of-power-generation/.

Sharma M, Sahajpal I, Bhuyan A. Sep 2020. Impacts of Learnings from Crop Residue Management Programme. CII Cleaner Air Better Life. https://sustainabledevelopment.in/wp-content/uploads/2020/09/CRM_Report-1.pdf

Venkatesh G, Gopinath K.A, Reddy K.S, Reddy B.S, Prasad J.V.N.S, Rao G.R.. March 2018. Biochar Production and its Use in Rainfed Agriculture: Experiences from CRIDA. National Innovations in Climate Resilient Agriculture, ICAR-Central Research Institute for Dryland Agriculture. http://icar-crida.res.in/Pubs/Biochar%20Research%20Bulletin%20March%202018.pdf

NASA Earth Observatory. Nov 2020. A Busy Season for Crop Fires in Northwestern India. https://earthobservatory.nasa.gov/images/147547/a-busy-season-for-crop-fires-in-northwestern-india

Wanapat M, Pilajun R, Kongmun P 2009. Ruminal ecology of swamp buffalo as influenced by dietary sources. Animal Feed Science and Technology, Volume 151, Issues 3–4, 26 May 2009, Pages 205-214. https://www.sciencedirect.com/science/article/abs/pii/S0377840109000376?via%3Dihub

Confederation of Indian Industry

The Confederation of Indian Industry (CII) works to create and sustain an environment conducive to the development of India, partnering Industry, Government, and civil society through working closely with Government on policy issues, interfacing with thought leaders, and enhancing efficiency, competitiveness and business opportunities for industry.

For 125 years, CII has been working on shaping India's development journey and, this year, more than ever before, it will continue to proactively transform Indian industry's engagement in national development. The premier business association has more than 9100 members, from the private as well as public sectors, and an indirect membership of over 300,000 enterprises from around 288 national and regional sectoral industry bodies.

With 68 offices, including 9 Centres of Excellence in India, and 11 overseas offices in Australia, China, Egypt, France, Germany, Indonesia, Singapore, South Africa, UAE, UK, and USA, as well as institutional partnerships with 394 counterpart organizations in 133 countries, CII serves as a reference point for Indian industry and the international business community.

Confederation of Indian Industry
The Mantosh Sondhi Centre
23, Institutional Area, Lodi Road, New Delhi – 110 003 (India)
T: 91 11 45771000 / 24629994-7 • F: 91 11 24626149 • E: info@cii.in • W: www.cii.in

cii.in/facebook | cii.in/twitter | cii.in/linkedin | cii.in/youtube

---

CII-ITC Centre of Excellence for Sustainable Development

CII-ITC Centre of Excellence for Sustainable Development is a not-for-profit, industry-led institution that helps business become sustainable organisations. It is on a mission to catalyse innovative ideas and solutions, in India, and globally, to enable business, and its stakeholders, in sustainable value creation.

It's knowledge, action and recognition activities enable companies to be future ready, improve footprints profiles, and advocate policymakers andlegislators to improve standards of sustainable business through domestic and global policy interventions.

CESD leverages its role of all-inclusive ecosystem player, partnering industry, government, and civil society. It has been a pioneer of environment management systems, biodiversity mapping, sustainability reporting, integrated reporting, and social & natural capital valuation in India, thus upgrading business in India to sustainable competitiveness.

With two locations in India, CESD operates across the country and has also been active in parts of South and South East Asia, Middle East, and Africa. It has held institutional partnerships and memberships of the United Nations Global Compact, Global Reporting Initiative, International Integrated Reporting Council, Carbon Disclosure Project, development agencies of Canada, the USA, the UK, and Germany.

Delhi | Mumbai
www.sustainabledevelopment.in
/ciicesd

energies

MDPI

Article

Comparative Investigation of Yield and Quality of Bio-Oil and Biochar from Pyrolysis of Woody and Non-Woody Biomasses

Pranshu Shrivastava [1], Anil Kumar [2,3], Perapong Tekasakul [4], Su Shiung Lam [5] and Arkom Palamanit [6,7,*]

1 Energy Technology Program, Faculty of Engineering, Prince of Songkla University, Hat Yai, Songkhla 90110, Thailand; shri.pranshu@gmail.com
2 Department of Mechanical Engineering, Delhi Technological University, Delhi 110042, India; anilkumar76@dtu.ac.th
3 Centre for Energy and Environment, Delhi Technological University, Delhi 110042, India
4 Department of Mechanical Engineering, Faculty of Engineering, Prince of Songkla University, Hat Yai, Songkhla 90110, Thailand; perapong.t@psu.ac.th
5 Pyrolysis Technology Research Group, Higher Institution Centre of Excellence (HICoE), Institute of Tropical Aquaculture and Fisheries (AKUATROP), University Malaysia Terengganu, Kuala Nerus 21030, Terengganu, Malaysia; lam@umt.edu.my
6 Energy Technology Program, Department of Specialized Engineering, Faculty of Engineering, Prince of Songkla University, 15 Karnjanavanich Rd., Hat Yai, Songkhla 90110, Thailand
7 Energy Technology Research Center, Faculty of Engineering, Prince of Songkla University, 15 Karnjanavanich Rd., Hat Yai, Songkhla 90110, Thailand
* Correspondence: arkom.p@psu.ac.th

Abstract: This study investigated the quantitative and qualitative attributes of liquid product and biochar obtained from pyrolysis of woody biomass (rubberwood sawdust (RWS)) and non-woody biomasses (oil palm trunk (OPT) and oil palm fronds (OPF)). The prepared biomass was pyrolyzed at temperatures of 500 °C, 550 °C, and 600 °C by using an agitated bed pyrolysis reactor, and then the yields and characteristics of liquid product and biochar were determined. The results showed that liquid product and biochar yields were in the respective ranges of 35.94–54.40% and 23.46–25.98% (wt.). Pyrolysis of RWS at 550 °C provided the highest liquid yield. The energy content of the water free liquid product was in the range 12.19–22.32 MJ/kg. The liquid product had a low pH and it mainly contained phenol groups as indicated by GC-MS. The biochars had high carbon contents (75.07–82.02%), while their oxygen contents were low (14.22–22%). The higher heating value (HHV) of biochar was in the range 26.42–29.33 MJ/kg. XRF analysis revealed that inorganic elements had higher contents in biochar than in the original biomass. The slagging and fouling indexes of biochar were also different from those of the biomass. High carbon content of the biochar confirms potential for its use in carbon sequestration. The specific surface of biochar was lower than that of biomass, while the average pore diameter of biochar was larger than for raw biomass as revealed by BET and SEM. These results on liquid product and biochar obtained from RWS, OPT, and OPF demonstrate that they are promising feedstocks for biofuels and other value-added products.

Keywords: biomass; biochar; bio-oil; oil palm biomass; pyrolysis; rubberwood biomass

check for updates

Citation: Shrivastava, P.; Kumar, A.; Tekasakul, P.; Lam, S.S.; Palamanit, A. Comparative Investigation of Yield and Quality of Bio-Oil and Biochar from Pyrolysis of Woody and Non-Woody Biomasses. *Energies* **2021**, *14*, 1092. https://doi.org/10.3390/en14041092

Academic Editor: Sihyun Lee
Received: 27 January 2021
Accepted: 16 February 2021
Published: 19 February 2021

Publisher's Note: MDPI stays neutral with regard to jurisdictional claims in published maps and institutional affiliations.

Copyright: © 2021 by the authors. Licensee MDPI, Basel, Switzerland. This article is an open access article distributed under the terms and conditions of the Creative Commons Attribution (CC BY) license (https://creativecommons.org/licenses/by/4.0/).

1. Introduction

Biomass is a promising resource for reducing the reliance on fossil fuel resources such as coal, crude oil, and natural gas. This is because biomass can be converted into various products such as biofuels, bioenergy, bio-products, and biochemical products [1]. Currently, bioenergy is gaining interest in many countries, both developed and developing, especially those with high biomass potential. Previous studies have reported that heavy utilization of fossil fuels has negative impacts on the environment, such as climate change and global warming [2,3]. Moreover, heavy reliance on fossil fuels is associated with low energy security and sustainability, particularly in countries that need to import their fossil

fuels [4]. Thus, increased utilization of alternative and renewable energy resources is a most appropriate way to reduce dependency on fossil fuels and the associated impacts [5]. Alternative energy sources are sought to replace the fossil fuels. The sources of alternative energy cover nuclear energy and renewable energy (i.e., wind, hydro, solar, and biomass). Conventionally, distribution of alternative energy and renewable energy resources differs from country to country due to a number of factors. Biomass is well known as a valuable renewable resource of biofuel, bioenergy, and biorefinery products. This is because biomass can be harvested, stored, managed, and processed. Compared to fossil fuels, biomass energy gives lesser or eVen zero carbon emissions. Additionally, bioenergy is very advantageous for heat and power generation among the renewable and alternative energy resources. This is because management, storage, and transportation of solid biomass can be performed easily. Also, bioenergy can be compared to other renewable energy resources in terms of reliability, accessibility, cost of the technologies, affordability, and technicalities. In addition, applications of biomass following the concept of circular bioeconomy and bioenergy also provide many benefits to the local people in an area or country [6]. For each country, the potential of biomass depends on several factors such as location, weather, agricultural activity, and agro-industrial processes. Thus, the applications of biomass for biofuels, bioenergy, and bio-products need to be pursued from local perspectives.

Biomass is an emerging feedstock in the bioenergy systems and the bioeconomy in Thailand. This is because Thailand has available large quantities of biomass from residues and wastes generated from harvesting and processing of agricultural products, such as rice, corn, cassava, and oil palm fruit bunches. The replantation of crops and plants also generate a huge amount of biomass. For example, the southern part of Thailand is very rich in abundant rubberwood and oil palm biomasses. In 2018, Thailand had plantation areas of rubber and oil palm trees of 3.68 and 0.78 million hectares, respectively, and the southern part contributed 69.7% and 87.3% of these areas, respectively [7]. Replantation to replace old rubber trees and processing of rubberwood provide various biomasses from roots, branches, bark, and rubberwood sawdust (RWS). On replantation of oil palm trees, large amounts of oil palm trunks and oil palm fronds with leaves are generated. Applications of these biomasses in Thailand are not yet extensive. Thus, there is high potential to make use of these biomasses. Besides this, oil palm biomass also comes from the processing of oil palm fruit bunches to produce crude palm oil. This processing generates huge amounts of biomasses, such as palm kernel shell, oil palm fiber, and empty fruit bunches [8–11]. Some rubberwood and oil palm biomasses have been used as solid fuels for heat and power generation in conventional processes, namely by combustion. However, the potential of these biomasses for alternative uses in producing biofuels, bio-products, and value-added products is still high and challenging. Valorization of biomass can be performed by various conversion technologies, such as thermochemical and biochemical processes [12,13]. Biomass pyrolysis an emerging conversion process among the alternatives. Pyrolysis is a thermochemical conversion process that can be applied to biomass for producing bio-oil, biochar, and synthesis gas. These biofuels are gaining interest as potential substitutes for fossil fuels.

Pyrolysis of lignocellulosic biomasses obtained from woody and non-woody feedstocks is widely applied and has been investigated in many studies [5,14–16]. They indicate that the yield and characteristics of pyrolysis products, including bio-oil, biochar, and pyrolysis gas, strongly depend on many factors such biomass properties and composition, operating conditions, and reactor type [17–19]. There are some previous studies on characterization of the products obtained from pyrolysis along with a comparison of woody and non woody biomasses. Some studies have also investigated the upgrading of bio-oil and biochar for further value-added applications [15,20,21]. According to those previous studies, production of high bio-oil yield should be performed with biomass having high cellulose and hemicellulose contents. On the other hand, pyrolysis of biomass with high lignin content tends to give a high biochar yield [22,23]. Fast pyrolysis is preferred for converting biomass into bio-oil with high yield and quality. For liquid fuel applications, the

bio-oil must contain little water, ash, and solids, while the energy content should be high, and the pH and viscosity at appropriate levels [24–26]. Realistically, producing bio-oil of high quality by fast pyrolysis is relatively complicated and costly. Therefore, increasing the value of bio-oil by transforming it into value-added products is essential and has gained attention [17,27]. Besides fast pyrolysis, other studies have assessed biomass conversion by slow pyrolysis. Compared to fast pyrolysis, the yield and quality of bio-oil or liquid product are low from the slow process. However, the liquid product or bio-oil obtained from slow pyrolysis can be applied or upgraded as liquid fuel and value-added products. The bio-oil or liquid product with appropriate chemical compounds can be applied to improve the flavor and odor of food on in agricultural and animal farms [28,29]. The biochar can be applied as solid fuel, bio-filter, activated carbon, and bio-fertilizer. Biochar with a high energy content and a low ash content, as well as appropriate fuel properties, can be used as a solid fuel in forms of briquettes or pellets [15]. Likewise, biochar with high specific surface and suitable pore structure can be modified into activated carbon and used as bio-filter [30]. Moreover, biochar with a high ash content and high in inorganic elements is an alternative material for soil improvement [5]. Only few recent studies have examined the yield and characteristics of pyrolysis products from rubberwood and oil palm biomass using slow pyrolysis [21,31,32], and there are not many studies that have investigated characteristics of pyrolysis products (liquid and biochar) using slow pyrolysis at higher temperatures (above 500 °C) of two different lignocellulosic biomasses of woody and non-woody types [5,33–56].

Therefore, the objectives of this study were to investigate the yield and the characteristics of liquid product and biochar obtained from pyrolysis of woody biomass (rubberwood sawdust (RWS)) and of non-woody biomasses (oil palm trunk (OPT) and oil palm frond (OPF)) using an agitated bed pyrolysis reactor. The present work focuses on comprehensive feedstock characterization, followed by an investigation of product yields at pyrolysis temperatures from 500 °C to 600 °C; and finally, an in-depth characterization of the liquid product and the biochar. The liquid product parameters investigated were the basic properties, energy content, elemental composition, and chemical compounds. Then, the elemental composition and energy content of biochar were determined. Carbon sequestration in the biochar was analyzed in order to assess the recalcitrant nature of biochar, which can be applied for soil improvement. Moreover, X-ray Fluorescence (XRF) analysis was used to distinguish the inorganic compounds or oxides in the biochar ash, which helps to predict the slagging and fouling indices for solid fuel applications by combustion. The results from this study will be beneficial for further applications of liquid products and biochars from the pyrolysis of RWS, OPT, and OPF.

2. Materials and Methods

2.1. Biomass Preparation

The samples of non-woody biomass (OPT, OPF) were taken from Krabi Province, Thailand, whereas woody biomass was in the form of RWS obtained from a rubberwood processing factory located at Khlong Ngae, Sadao district, Songkhla province, Thailand. A chopping machine (MCH-420, Machinery789, Lamphun, Thailand) was used to chop the fresh OPT (with bark) and OPF (without leaves) into smaller size of around 4–5 mm. The freshly chopped OPT and OPF, and raw RWS were dried in a solar greenhouse dryer for a week to reduce the moisture content below 10% (wt.). A grinding machine (model YPS-102, Bonny, Bangkok, Thailand) equipped with 1 mm sieve was used to grind the dried samples. The ground biomass was stored in sealed plastic bags until use.

2.2. Biomass Physicochemical Properties Determination

The physicochemical properties of biomass samples were determined following the standard procedures listed in Table 1.

Table 1. Biomass physicochemical properties characterization.

Analysis	Procedure	Standard
Bulk density	Based on the mass and volume ratio, the bulk or apparent density of the ground biomass was determined. A cylindrical container with a particular inside diameter and volume (1000 mL) was used for this method. The samples were filled in the container up to a certain height and tapped down from top to maintain the proper top surface. The net weight was then reported for each sample, and the bulk density was determined.	-
Thermogravimetric analysis (TGA)	Thermogravimetric analysis (TGA) and derivative thermogravimetric analysis (DTG) were applied using a thermogravimetric analyzer (Perkin Elmer, Waltham, MA, USA). The observations were performed at temperatures ranging from 50 to 1000 °C and at a heating rate of 10 °C/min under a nitrogen gas atmosphere.	ASTM E1131
Proximate analysis	A macro thermogravimetric analyzer (TGA 701, LECO, USA) was used for proximate analysis, including moisture content, volatile matter, fixed carbon content and ash content.	ASTM D7582
Ultimate analysis	A CHNS/O Analyzer (FLASH 2000, Thermo Scientific, Monza, Italy) was used to analyze the basic elemental composition of each sample, including carbon (C), hydrogen (H), nitrogen (N), and sulfur (S). The oxygen content was determined by calculating a difference.	EN 15104 and ASTM D4239
Lignocellulosic analysis	The acid detergent fiber (ADF), neutral detergent fiber (NDF), and acid detergent lignin (ADL) were used to determine the percentage of cellulose, hemicellulose, and lignin. Cellulose content = ADF–ADL Hemicellulose content = NDF–ADF Lignin content = ADL Extractives = 100 − (Cellulose + Hemicellulose + Lignin)	-
Higher heating value (HHV)	This was estimated by the following formula: $HHV(MJ/kg) = 0.3491C+1.1783H+0.1005S - 0.1034O - 0.0151N - 0.0211Ash$ where, C, H, O, N, S and Ash are from the elemental composition found by proximate analysis and ultimate analysis.	-
Lower heating value (LHV)	Estimated from the formula: $LHV_{dry}(MJ/kg) = HHV_{dry} - 2.442 \times 8.936 \frac{H}{100}$ where H is hydrogen (% wt.) on dry basis.	-

2.3. Experimental Setup

Figure 1 shows schematically the agitated bed pyrolysis system used in this work. The system consists of a reactor, proportional–integral–derivative (PID) controlled heating system, magnetic coupling driver operated with electrical motor, cyclone for char collection, 3-stage condensation unit, water cooling bath, and nitrogen gas supply system. The cylindrically shaped reactor was made from SUS316 stainless steel with 13 cm diameter, 15 cm height, and 5 mm thickness. A 3 kW electrical heater was used as the heat source for the reactor. K-type thermocouple probes were used to measure the temperature during the pyrolysis. The biomass feedstock inside the reactor was continuously stirred by a mixing blade attached to a magnetic coupling driver, which was controlled by an electrical motor (25 W, 4RK25GN-C, Zhengke Electromotor Co., Ltd., Zhejiang, China). N_2 gas was supplied from the bottom of the reactor in a controlled manner. The vapors formed inside the reactor exited from the top of the reactor and entered the cyclone chamber. The solid particles were separated from the condensable pyrolysis vapors in the cyclone chamber, after which the vapors passed through a 3-stage series of shell-and-tube condensers. Cold water was supplied to the condensers from a cooling water bath, which could control the water temperature within 5–27 °C. The condensed liquid was collected in the collectors connected to the bottom of each condenser. The experimental setup used in this work was designed, implemented, and installed at the Prince of Songkla University, Hat Yai, Songkhla province, Thailand.

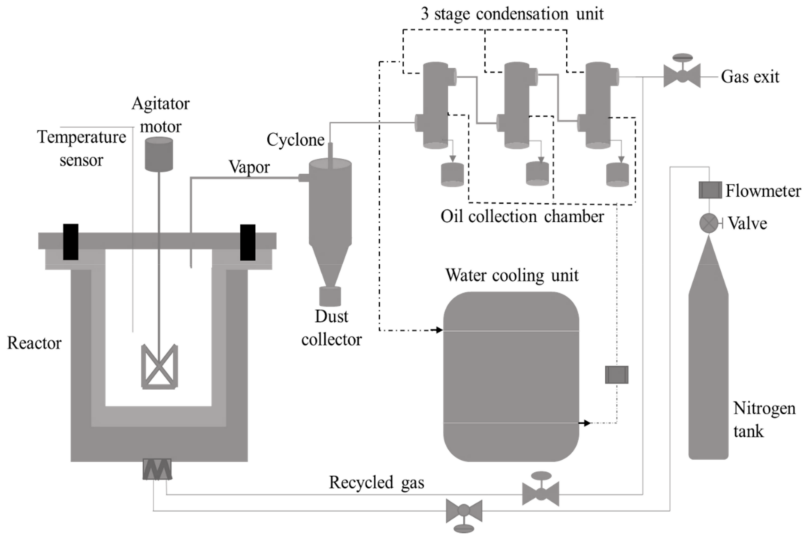

Figure 1. Schematic of the experimental setup.

2.4. Experimental Procedure

The reaction chamber was preheated to 90 °C before feeding the samples in the reactor, to prevent initial thermal losses. A 100 g sample was filled into the reactor chamber from the top and continuously stirred by the mixing blade at a speed of 10 rpm. N_2 gas was supplied to the reaction chamber at the rate of 2 L/min to maintain an inert atmosphere throughout the thermal decomposition of biomass. The biomass was partly converted into vapors in an inert atmosphere and condensed to liquid form in the collection chambers. Once the biomass temperature reached the highest treatment temperature (HTT), the N_2 gas flow rate was increased to 5 L/min to prevent any secondary reactions. Vapors were condensed in the condensers by flowing cold water at 10 °C with a flow rate of 5 L/min. The biomass was pyrolyzed for 45 min in each experiment in order to maximize the thermal decomposition or biomass conversion. The condensable and incondensable vapors were collected in the forms of liquid and gaseous products, respectively. The biochar remained in the reaction chamber as solid residue. The yields of liquid product and biochar were directly determined by weighing. The yield of pyrolysis gas was eValuated by subtraction. The properties of the liquid product, biochar, and pyrolysis gas were analyzed.

2.5. Products Analyses

2.5.1. Determination of Liquid Product Properties

Basic Properties

The water content of the liquid product was determined by the Karl-Fisher volumetric technique using Metrohm 758 KFD Titrino instrument, Herisau, Switzerland. The pH of the sample was determined using UB-10 Denver Instrument (Vernon Hills, IL, USA) pH meter at room temperature [46]. The density was calculated based on standard procedure (ASTM D-4052) using a 25 mL density bottle [47,48]. The liquid product was treated to 775 °C, cooled, and weighed in order to find the ash content based on ASTM D-482 [46,48]. The solid content was measured using the technique of vacuum filtration. Three grams of bio-oil were mixed with ethanol and filtered through a pre-dried Whatman No. 2 filter paper. The filter paper with the solid residue was pre-dried for 15 min with ambient air and then dried for 30 min with hot air in an oven at 105 °C. The solid content was weighed and recorded as a mass ratio, after keeping the filter paper in a desiccator for 30 min (wt. %) [15,49].

Ultimate Analysis

The ultimate analysis determined carbon, hydrogen, nitrogen, and sulfur contents using a CHNS analyzer (Flash 2000, Thermo Scientific, Monza, Italy) following the standard

procedures ASTM D-4239 and EN 15104 at the Office of Scientific Instruments and Testing (OSIT), Prince of Songkla University, Thailand. The HHV was calculated on a dry basis, as given in Table 1.

Gas Chromatography Mass Spectrometry (GC-MS)

A quadrupole detector and a DB-1MS capillary column (30 mm × 0.25 mm internal diameter × 0.25 µm thickness) were used on determining the chemical composition of the liquid product by gas chromatography–mass spectrometry (GC-MS) Agilent Technologies 5977A, Santa Clara, CL, USA). The initial temperature of the oven was set at 70 °C and held for 2 min, then increased to 250 °C at 5 °C/min and held for 10 min. The injector temperature was 250 °C. The injected sample volume (10% bio-oil in ethanol) was 1 µL. In the MS, full scan electron ionization (EI) was used, and standard mass spectra at 70 eV ionization energy were scanned from 35 to 550 m/z. Using the NIST14 and WILEY10 libraries, computer matching of the mass spectra was performed, and retention times of known species injected into the chromatographic column were used for peak identification.

2.5.2. Determination of Biochar Properties

Proximate Analysis, Ultimate Analysis, and Higher Heating Value (HHV)

The proximate analysis, ultimate analysis, and HHV were done as per the standards and procedures shown in Table 1.

Carbon Sequestration and Recalcitrance

The index R_{50} was used to eValuate the thermal recalcitrance of biochar. It can be obtained from TG analysis of biochar, as recently proposed by Harvey et al. [50]:

$$R_{50,biochar} = \frac{T_{50,biochar}}{T_{50,graphite}} \quad (1)$$

where $T_{50,biochar}$ and $T_{50,graphite}$ are the temperatures corresponding to 50% weight loss by oxidation/volatilization, for biochar and graphite, respectively. TG thermograms are corrected for water and ash content to obtain the temperatures directly. The final carbon retained in the solids is termed carbon sequestration (CS) potential. It is calculated by subtracting the carbon loss during pyrolysis from the initial C in raw biomass and multiplying by the recalcitrance (R_{50}) of C in the biochar as follows.

$$CS(\%) = \frac{M(g) \times Yield(\%) \times C\%_{Biochar} \times R_{50}}{M(g) \times C\%_{Feedstock}} \quad (2)$$

where M is weight of the feedstock.

Ash Composition, Slagging and Fouling Indexes

The biomass samples were analyzed with an X-ray fluorescence spectrometer (Zetium, PANalytical, Eindhoven, The Netherlands). The chemical compositions were based on high-temperature ash analysis (normalized to 100 wt. %). The ashing of the biochar obtained from pyrolysis temperature of 550 °C was done at 825 °C for 3 h. The analysis was carried out using XRF to determine the oxides SiO_2, Al_2O_3, Fe_2O_3, TiO_2, CaO, MgO, K_2O, Mn_3O_4, SO_3, and Na_2O. Slagging index (SI) and fouling index (FI) were estimated using Equations (4) and (5) [51]:

$$\text{Slagging index SI (wt. \%)} = (B / A) \times S^d \quad (3)$$

$$\text{Fouling index FI (wt. \%)} = (B/A) \times (Na_2O + K_2O) \quad (4)$$

where,

$$B/A = \text{base/acid ratio} = \frac{\text{wt. \%}(Fe_2O_3 + CaO + MgO + Na_2O + K_2O)}{\text{wt. \%}(SiO_2 + Al_2O_3 + TiO_2)} \quad (5)$$

S^d = wt. % of sulfur in dry feedstock

Surface Morphology

The structure, morphology, and pore distribution on the surface of biochar were examined by scanning electron microscopy (SEM) (JSM-5800 LV, JEOL, Tokyo, Japan). Before SEM observations, all the samples were sputter coated with gold. Under high-vacuum conditions, the SEM used an acceleration voltage of 20 kV and a secondary electron detector (SE2) with a magnification of 500×. The working distance was 10–15 mm, and 1024 × 768 pixel images were recorded.

BET Surface Area

Brunauer–Emmett–Teller (BET) (ASAP2460, Micromeritics, GA, USA) analysis was used to determine the specific surface of biochar based on static volumetric N_2 gas adsorption. Samples were pre-treated at temperature from 80 °C to 200 °C for 15 h under vacuum, and isothermal adsorption-desorption was fit with static volumetric model. Both the carrier gas and the adsorbed gas were N_2. The pore volume was obtained using the multi-condensation-point adsorption isotherm (p/p_0 = 0.05−0.03, >200 points). The pore structure was determined from the adsorption isotherm and the average pore width was estimated as 4 V/A, where the pore volume is "V" while "A" denotes its surface area.

3. Results

3.1. Characteristics of Raw Biomass

Initial characteristics of the raw samples are listed in Table 2. The physicochemical properties of the biomass influence the bio-product yields during the pyrolysis [1–3]. All the biomass samples tested had high volatile matter contents. RWS had the most volatile matter and the least ash, which should lead to a large liquid yield [4,5]. It was noted that the RWS had a greater fixed carbon content than OPT or OPF. The portion that can be converted into biochar is the fixed carbon in a biomass. Biomass with a high fixed carbon content is necessary for making biochar. The ultimate analysis results were consistent with the proximate analyses. The carbon and hydrogen contents of RSW and OPT were relatively high among typical biomasses (e.g., wheat straw, oak wood, corn stalk, corncob, rice husk, cassava rhizomes, cassava stalk, wood sawdust, bamboo, and birch wood) [1,6–9]. Biomass with high contents of carbon and hydrogen usually has high HHV and LHV [3,10]. The contents of nitrogen and sulfur in the biomasses tested were low. Low nitrogen and sulfur contents in a biomass help preventing partial formation of NO_x and SO_x during combustion of the biomass [3,11].

The bulk density was the least for OPF followed by OPT and RWS, and this is an essential parameter for designing the pyrolysis reactor. The mass of biomass in the reaction chamber directly affects the volume of biomass and thus the heat transfer during pyrolysis. The bulk density of a biomass also relates to its energy density (MJ/m^3), storage space requirement, and costs of handling and transport [7,12,13]. TGA curve represents the thermal decomposition in four main stages, and also the decomposition trends of a lignocellulosic biomass containing cellulose, hemicellulose, and lignin. Initially, biomass weight decreases merely due to the eVaporation of moisture, from 90 °C to 150 °C. In the second stage, there was a gradual decrease in the biomass weight possibly due to the eVaporation of light volatile compounds, which lasted until 300 °C. Then the next stage comprised significant thermal decomposition of the biomass from 300 °C. to 550 °C. The last stage constituted prolonged decomposition of lignin, which is a tough compound to break down completely [14–16]. All feedstocks show similar trends in the TGA analysis, in Figure 2.

Table 2. Characterization of biomass samples.

Property or Component	Type of Biomass		
	OPT	**OPF**	**RWS**
Proximate Analysis			
Moisture Content (wt. %, wet basis)	7.07 ± 0.04	6.48 ± 0.03	7.13 ± 0.02
Volatile Matter (wt. %, dry basis)	71.14 ± 0.20	71.31 ± 0.30	75.98 ± 0.26
Fixed Carbon (wt. %, dry basis)	15.42 ± 0.22	16.68 ± 0.28	15.21 ± 0.24
Ash (wt. %, dry basis)	6.38 ± 0.02	5.24 ± 0.03	1.68 ± 0.01
Ultimate Analysis (wt. %, Dry Basis)			
Carbon	45.79 ± 0.07	44.95 ± 0.15	47.55 ± 0.23
Hydrogen	6.15 ± 0.02	5.89 ± 0.06	6.22 ± 0.02
Nitrogen	1.47 ± 0.01	0.40 ± 0.01	0.32 ± 0.01
Oxygen *	46.33 ± 0.07	48.71 ± 0.01	45.91 ± 0.26
Sulphur	1.47 ± 0.01	0.06 ± 0.01	0.03 ± 0.01
Lignocellulosic Component (wt. %, Dry Basis)			
Cellulose	47.81 ± 0.36	48.56 ± 0.28	56.91 ± 0.47
Hemicellulose	23.19 ± 0.14	22.41 ± 0.42	15.21 ± 0.28
Lignin	9.52 ± 0.09	13.15 ± 0.08	17.44 ± 0.16
Extractives	19.48 ± 0.16	15.88 ± 0.38	10.44 ± 0.44
Element (mg/kg)			
Silicon (Si)	3560	1694	2538
Iron (Fe)	1589	2722	189
Calcium (Ca)	5432	7095	5164
Magnesium (Mg)	2789	2035	1058
Sodium (Na)	1065	250	68
Potassium (K)	9610	3240	5037
Higher and Lower Heating Values (MJ/kg)			
HHV	23.22 ± 0.23	22.52 ± 0.41	23.77 ± 0.19
LHV	21.88 ± 0.18	21.24 ± 0.37	22.42 ± 0.47
Other Properties			
Molecular Formula	$CH_{1.597}O_{0.759}$	$CH_{1.559}O_{0.813}$	$CH_{1.556}O_{0.725}$
H/C Molar Ratio	1.59	1.55	1.55
O/C Molar Ratio	0.75	0.81	0.72
Bulk Density (kg/m^3)	150.97 ± 0.36	220.68 ± 0.31	293.58 ± 0.29

* oxygen by difference.

3.2. Effects of Temperature on Product Yields

The products obtained from OPT, OPF, and RWS in an agitated pyrolysis process at 500 °C, 550 °C, and 600 °C are shown in Figures 3–5, respectively. The yields of liquid product, biochar, and pyrolysis gas were in the ranges 35.94–54.40% wt., 23.46–26.98% wt., and 21.58–40.60% wt., respectively. The RWS treated at 550 °C gave the most liquid at 54.40% by weight, while OPF and OPT treated at the same temperature provided 44.86% and 44.48% liquid by weight, respectively. Therefore, the quantity of liquid product depends upon the type of feedstock as well as on the treatment temperature. There is higher liquid yield from woody biomass than from non-woody biomass, because of thermal decomposition of the high cellulose and hemicellulose contents in woody biomass. The amount of liquid product increases with pyrolysis temperatures from 500 °C to 550 °C. However, a steep decrease in liquid yield was noticed when the temperature was further increased to 600 °C. This is possibly due to secondary reactions of the vapors from the biomass, which significantly reduced the yield of liquid product. A high yield of liquid product and a low yield of biochar from RWS are due to the low ash content of this woody biomass, which reduces the secondary reactions in the reaction chamber. It has been

observed in prior studies that the inorganic compounds present in non-woody biomass (i.e., ash content) act as catalysts in biomass decomposition [5,15]. This is likely the reason for getting lesser liquid yields and more non-condensable gases compared to woody biomass [46,56–63]. However, previous studies have indicated that the bio-oil yield of pyrolysis depends not only on the composition and properties of the biomass, but also on the operating parameters and type of the reactor [48,63–68]. Using moving bed reactors, biomass pyrolysis at a high heating rate gave bio-oil production exceeding 47 (wt. %) [48,69]. In comparison to fixed bed reactors, biomass pyrolysis with moving bed reactors usually provides higher bio-oil yields [68,70].

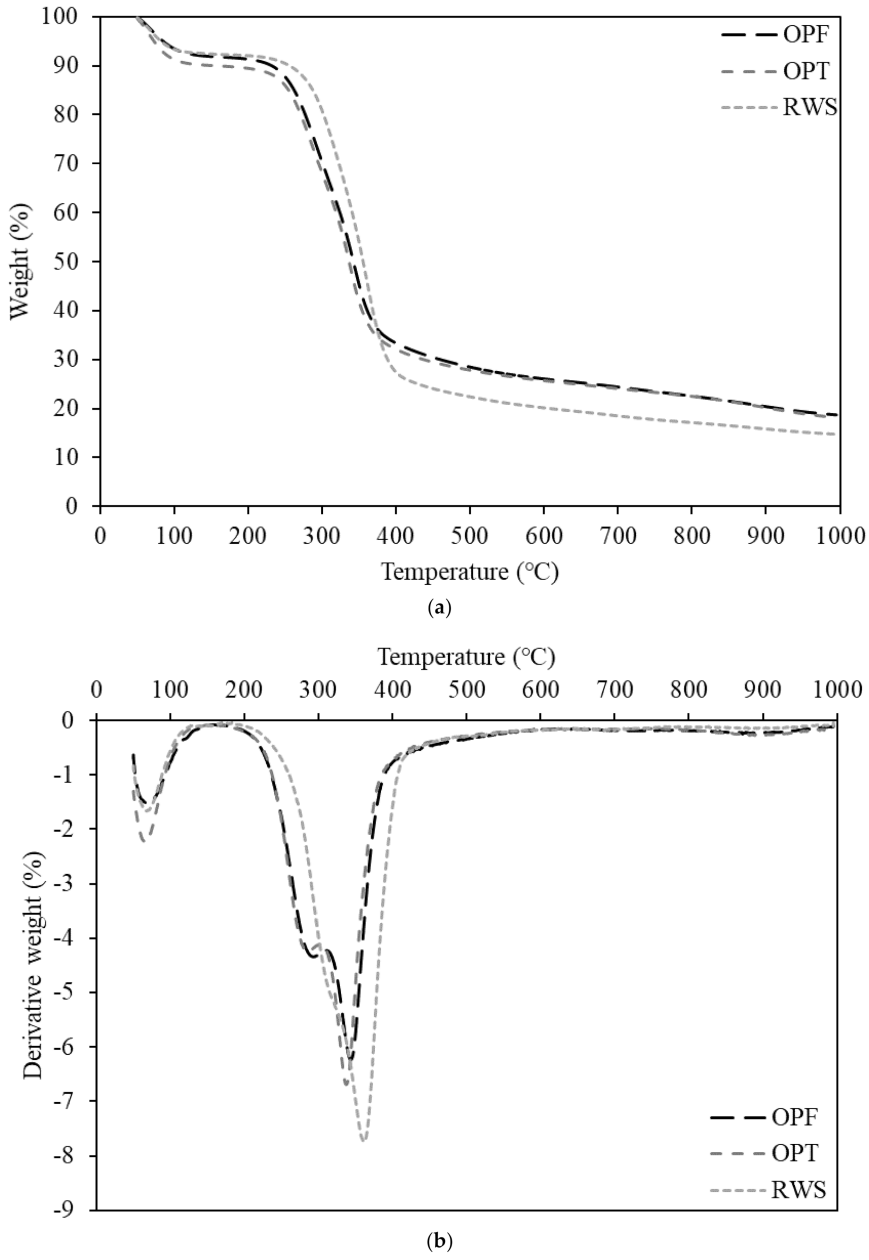

Figure 2. (**a**) TGA and (**b**) DTG for the biomass samples.

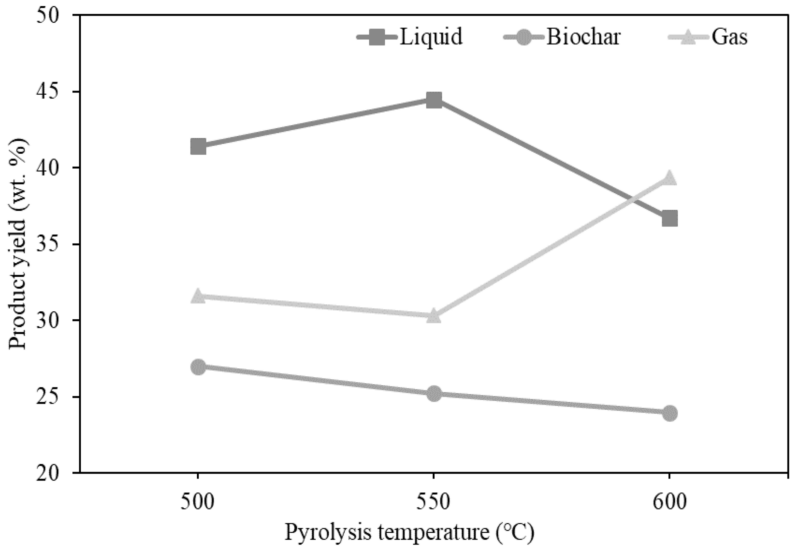

Figure 3. Effects of temperature on pyrolysis yields from oil palm trunk (OPT).

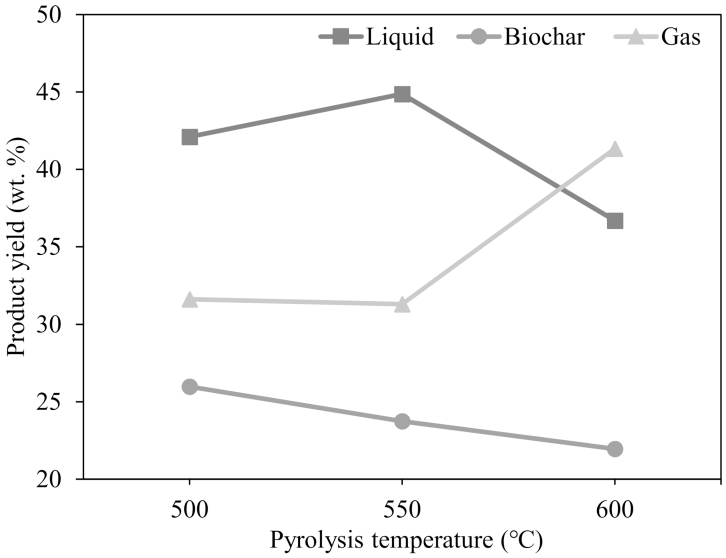

Figure 4. Effects of temperature on pyrolysis yields from oil palm frond (OPF).

On considering the effects of reaction temperature on bio-product yields, an increase in temperature leads to lower char yield and increased non-condensable gas yield. Similar results have been observed in many previous studies [5,47,52,70–73], irrespective of the type of biomass or the pyrolysis reactor type. The decrease in biochar product yield with increasing temperature was likely due to more initial decomposition of the lignocellulosic feedstock at a higher temperature and/or secondary degradation of char formed before it is extracted from the reaction zone. Secondary thermal cracking of the eVolved vapors from pyrolysis of biomass was likely increasing gas yields at the higher temperatures. Therefore, the optimum temperature for the pyrolysis, to obtain the most liquid from either woody or non woody biomass, is 550 ± 10 °C. In comparison, biomass pyrolysis with a high fixed carbon content gives a high biochar yield. The highest biochar yield at 500 °C was obtained from OPT (25.98 wt. %) and the least from RWS (23.67 wt. %). The biochar yield decreased due to more thermal decomposition of lignocellulosic components when temperature was increased further [5]. The gas yield, however, showed the opposite pattern. It decreased on increasing temperature from 500 °C to 550 °C because the condensable gases were converted to bio-oil or liquid product. However, the gas yield increased at

600 °C probably because of the increased extent of secondary reactions inside the reactor at higher temperatures, which formed non condensable vapors. The highest and lowest yields of gas at 600 °C were 39.35 wt. % and 32.39 wt. % from OPT and RWS, respectively. The liquid could be used as a chemical feedstock or a low speed engine fuel [74,75] while the solid product (biochar) might be used as soil recalcitrant, absorbent, or co-firing fuel in boilers [76–78].

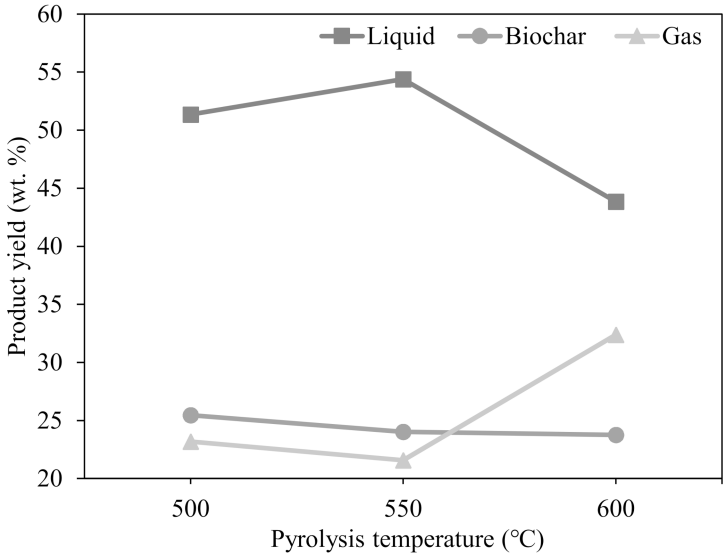

Figure 5. Effects of temperature on pyrolysis yields from rubberwood sawdust (RWS).

3.3. Physicochemical Properties of Products

Detailed analyses of the products are discussed in the next subsections.

3.3.1. Liquid Product

Water Content

The preliminary properties of liquid product obtained from pyrolysis of OPT, OPF, and RWS at 500 °C, 550 °C and 600 °C are shown in Table 3. The liquid product contains 52.89–72.84% (wt.) water. These results indicate that for OPT, OPF, and RWS, pyrolysis temperature significantly affected water content in the liquid product. The liquid product from RWS pyrolysis showed less water than those of OPT and OPF, because of the woody nature of RWS: It had the least initial moisture content in the biomass. The water content of the liquid product depends on the initial moisture and oxygen content in biomass, as concluded in prior studies. The reaction between the oxygen and hydrogen in the feedstock forms water that condenses into the liquid product [15,79]. The heating rate was around 20 °C/min (considered as slow pyrolysis), due to which the water content of liquid product is slightly high. Previous studies have shown results consistent with this current study, with water content in liquid product exceeding 50% (wt.) for slow pyrolysis [5,80,81]. Moreover, the water content in liquid product not only depends on the moisture content but is also influenced by pyrolysis conditions, such as vapor residence time and pyrolysis reaction temperature [5,45,82]. A high water content has both merits and demerits, as high water content in the liquid product helps reduce its viscosity and improves stability. Simultaneously, a high water content in the liquid product also reduces the HHV of the yield [83,84]. However, the water content can be reduced by fuel upgrading.

Table 3. Basic properties of liquid product.

Type of Biomass	Pyrolysis Temperature (°C)	Properties of Liquid Product				
		Water Content (wt. %)	Ash Content (wt. %)	pH Value	Density (kg/m^3)	Solid Content (wt. %)
OPT	500	70.84 ± 0.22	0.08 ± 0.02	2.91 ± 0.02	1011 ± 0.01	0.02 ± 0.01
	550	67.99 ± 0.59	0.09 ± 0.01	2.96 ± 0.01	1008 ± 0.02	0.04 ± 0.02
	600	65.16 ± 0.81	0.09 ± 0.02	2.98 ± 0.01	1003 ± 0.01	0.05 ± 0.01
OPF	500	67.96 ± 0.32	0.05 ± 0.01	2.67 ± 0.04	1013 ± 0.02	0.03 ± 0.02
	550	65.11 ± 0.13	0.07 ± 0.02	2.59 ± 0.03	1007 ± 0.02	0.05 ± 0.03
	600	64.13 ± 0.30	0.08 ± 0.04	2.64 ± 0.02	1001 ± 0.01	0.06 ± 0.02
RWS	500	59.30 ± 0.21	0.02 ± 0.01	2.15 ± 0.03	1012 ± 0.02	0.05 ± 0.05
	550	54.80 ± 0.34	0.03 ± 0.01	2.18 ± 0.02	1009 ± 0.02	0.06 ± 0.03
	600	52.89 ± 0.70	0.05 ± 0.01	2.15 ± 0.02	1006 ± 0.01	0.07 ± 0.01

pH, Solids Content, Ash Content, and Density

The pH, solids content, ash content, and density of liquid product at different pyrolysis temperatures for OPT, OPF, and RWS are shown in Table 3. The pH of the liquid product was in the range 2.15–2.98. The acidic nature of bio-oil is due to oxidation of hydrocarbon groups in hemicellulose and cellulose. During the pyrolysis, volatile vapors released from the reaction chamber condensed into liquid product that might contain some lighter solid particles. In this study, there was very little solids content (less than 0.07% (wt.)) found in the liquid products, because of the high thermal decomposition of lignocellulosic biomass at high reaction temperatures. Fuels with solid contents less than 0.25% (wt.) are acceptable, however an ideal fuel would not contain any solids [85]. The liquid yield from RWS contains less ash than those from OPT and OPF. The ash content in the liquid product was in the range 0.02–0.09% (wt.), which is consistent with the solids' contents. High ash content in a liquid fuel (the liquid pyrolysis product) can cause high wear in pumps and injectors, and deposits and corrosion in combustion equipment due to the possible presence of alkali metals [49]. The density of the liquid product was in the range 1,001–1,012 kg/m^3. The normal range of densities of the liquid product from pyrolysis is 1,000–1,300 kg/m^3 [86]. The density of the liquid product affects the energy value of the oil or fuel. As the density increases, the energy content also tends to increase.

Ultimate Analysis and Energy Content of the Liquid Product

The ultimate analyses of liquid products from OPT, OPF, and RWS are shown in Table 4. In the liquid products the contents of C, H, N, S, and O were in the ranges 13.75–26.54, 9.38–10.39, 0.12–0.24, <0.01, and 12.99–16.74 (wt. %), respectively. Pyrolysis of RWS provided a liquid product with higher contents of carbon and hydrogen than in those from OPT and OPF. The carbon content in liquid from woody biomass is higher for higher temperatures than from non-woody biomass, but the hydrogen content shows the opposite trend. This is possibly due to decarboxylation and dehydration reactions during the processing, involving breakage of bonds at high temperatures [87]. The sum of hydrogen and carbon contents in the liquid product was in the range 23.89–36.11% (wt.). The sum of hydrogen and carbon contents was higher for woody biomass because of the high cellulose content in RWS. The thermal decomposition of cellulose at higher temperatures gave more hydrogen and carbon in the liquid product [88]. The oxygen content is high because of slow exothermic decomposition of xylan, which leads to slow conversion of hemicellulose linkages into condensable vapors [52]. RWS possesses less oxygen than the other tested non-woody biomasses. The high hydrogen and carbon contents with a low oxygen content of bio-oil enhance fuel properties, especially by increasing HHV of

the liquid product [5]. Regarding contents of nitrogen and sulphur, it was found that the liquid product contained low amounts of nitrogen and sulphur since the biomasses used in this study had low nitrogen and sulphur contents. Lower nitrogen and sulphur contents enable the liquid product from this work to be upgraded for value added applications. The HHV of bio-oil was in the range 12.19–22.32 MJ/kg when calculated on water free basis. The HHV of bio-oil from RWS is better than those from OPF and OPT. The HHV of bio-oils obtained in this study are comparable with prior studies, in which HHV has been within 17–28 MJ/kg [5,15,67,89]. The variations are due to differences in type of biomass, compositions of biomasses, and type of pyrolysis process. Moreover, the bio-oil HHVs in the studies done by Palamanit et al. [5] and Sakulkit et al. [15] that performed pyrolysis of oil palm biomass were in the range 16–23 MJ/kg.

Table 4. Ultimate analysis of liquid product.

Biomass	Pyrolysis Temperature (°C)	Ultimate Analysis (wt. %, As Water Free Basis)					
		Carbon	Hydrogen	Nitrogen	Sulphur	* Oxygen	** HHV
OPT	500	13.75 ± 0.20	6.20 ± 0.19	0.16 ± 0.00	<0.01	12.99 ± 0.02	12.19 ± 0.15
	550	14.62 ± 0.30	6.46 ± 0.21	0.23 ± 0.00	<0.01	14.41 ± 0.24	14.28 ± 0.18
	600	15.37 ± 0.21	6.77 ± 0.17	0.24 ± 0.00	ND	16.10 ± 0.37	16.61 ± 0.23
OPF	500	15.31 ± 0.18	6.40 ± 0.23	0.18 ± 0.18	<0.01	13.48 ± 0.41	13.97 ± 0.19
	550	17.30 ± 0.13	6.08 ± 0.12	0.20 ± 0.01	<0.01	14.90 ± 0.24	16.01 ± 0.17
	600	17.34 ± 0.36	6.15 ± 0.26	0.12 ± 0.01	ND	15.83 ± 0.24	17.10 ± 0.09
RWS	500	22.85 ± 0.25	6.09 ± 0.07	0.12 ± 0.01	ND	14.95 ± 0.28	18.53 ± 0.20
	550	24.64 ± 0.08	6.38 ± 0.21	0.13 ± 0.01	ND	17.12 ± 0.30	21.89 ± 0.14
	600	26.54 ± 0.10	6.65 ± 0.18	0.12 ± 0.01	ND	16.74 ± 0.09	22.32 ± 0.13

* Oxygen estimated as a difference and then converted to water free basis using molecular weight balance method. ** HHV calculated on water free basis. ND means not detected.

Chemical Compounds

The GC-MS was also used to analyze the condensable compounds from pyrolysis at 550 °C in the liquid product for OPT, OPF, and RWS. It can be inferred from the results of GC-MS that the liquid products of pyrolysis are highly complex and consist of hundreds of different forms of organic compounds. Table 5 lists the major compounds and their peak area percentages for the liquid products obtained at 550 °C from OPT, OPF, and RWS. The results indicate that the main chemical compounds of the liquid product samples were oxygenated compounds such as phenols, phenol derivatives and anhydro-sugars. The biomass cellulose and hemicellulose could decompose into glucopyranoses (anhydro-sugars) and heterocyclic compounds (furan and furan derivatives, and acetic acid). From lignin, oxygenated aromatic compounds such as phenols and phenolic derivatives were devolatilized to the liquid product [67,90]. Anhydro-sugars are bicyclic monosaccharides with 1,6- and 1,5-anhydro rings for hexoses and 1,4- and 1,5-rings for pentoses, respectively, which are formed by thermochemical decomposition of monosaccharides or polysaccharides such as cellulose, hemicellulose, and amylose [91]. The presence of aromatic and oxygenated compounds in the liquid product is due to biomass biopolymer remnants from cellulose and hemicellulose in the liquid product. The lignin is hemicellulose-covalently bonded and polysaccharide-crosslinked and is thus extremely rigid and strong. In addition, lignin consists mostly of aromatic rings; the bio-oil derived from lignin is therefore rich in aromatic compounds. The results obtained from GC-MS are consistent with the elemental compositions of these biomasses and physicochemical characterizations of the liquid products.

Table 5. Main compounds in liquid products obtained from pyrolysis at 550 °C.

Compounds	Peak Area (%)		
	OPT	**OPF**	**RWS**
Phenol	21.79	10.24	7.46
3-Penten-2-one, 3,4-dimethyl-	9.87	N/D	N/D
Butyric acid hydrazide	4.19	2.65	N/D
2-Cyclopenten-1-one, 2-hydroxy-3-methyl-	3.81	4.12	5.02
o-Cresol	3.31	1.10	1.34
p-Cresol	2.83	N/D	N/D
Phenol, 2-methoxy-	2.84	4.40	4.99
1,3-Propanediamine	2.62	1.86	N/D
Creosol	2.15	1.55	1.95
Catechol	2.10	N/D	1.68
1,2-Benzenediol, 3-methoxy-	2.10	2.60	2.29
Propanoic acid, 2-methyl-, propyl ester	2.07	N/D	2.26
Phenol, 4-ethyl-2-methoxy-	1.92	1.88	2.16
Phenol, 2,6-dimethoxy-	1.83	11.32	11.72
3,5-Dimethoxy-4-hydroxytoluene	1.59	3.21	4.23
1,3-Benzenediol	N/D	5.12	5.09
2-Pentanone, 1-(2,4,6-trihydroxyphenyl)	2.15	2.99	2.67
5-tert-Butylpyrogallol	1.42	3.08	2.29
(E)-2,6-Dimethoxy-4-(prop-1-en-1-yl) phenol	1.42	1.54	1.62
Anhydro-sugar	N/D	8.14	7.79

N/D means not detected.

3.3.2. Biochar

Proximate Analysis

Table 6 displays the proximate analysis results for the biochars from various pyrolysis temperatures of OPT, OPF, and RWS. The moisture content, volatile matter, fixed carbon content, and ash content of the biochars are within 3.74–4.61 wt. %, 10.25–16.16 wt. %, 71.69–76.70 wt. %, and 6.89–11.44 wt. %, respectively. It was observed that the moisture content of biochar was not zero after pyrolysis, matching results of the study conducted by Kabir et al. (2017), in which moisture content of biochar was in the range 3.06–4.42 wt. % [67]. However, the moisture content and volatile matter of biochar decreased with pyrolysis temperature. This is because the volatile matter changed to low molecular weight liquid and gas rather than biochar as the temperature increased [92]. There is a decreasing trend in volatile matter of biochar with pyrolysis temperature. This is because of the thermal decomposition of volatile matter present in the biomass to lower molecular weight liquid and gas components [92]. The volatile content is found to be in the range 10.25–16.16% (wt.), because of the complexity involved in thermal decomposition of lignin at low pyrolysis temperature. The high lignin content in the woody biomass results in more volatile matter in the biochar produced, in this study.

Less volatile matter gave a higher carbon content in the biochar. Biochar with high fixed carbon content is favorable for solid fuel applications because it has a high energy content [5,92,93]. High fixed carbon content of biochar also improves its storage stability compared to raw biomass, since biomass hemicellulose and cellulose contribute to microbial decomposition during storage [94]. OPT's ash content was higher than those of RWS and OPF, which is consistent with the raw biomass gross proportions. The ash is a non-volatile matter and non-combustible part of biomass and biochar [95]. The increased ash content in biochar was attributed to destructive volatilization at higher pyrolysis temperatures of lignocellulosic components [96].

Table 6. Proximate analyses of biochar samples.

Type of Biomass	Pyrolysis Temperature (°C)	Proximate Analysis (wt. %, As Received Basis)			
		Moisture Content	Volatile Matter	Fixed Carbon	Ash Content
OPT	500	3.85 ± 0.01	13.02 ± 0.75	71.69 ± 0.42	11.44 ± 0.87
	550	3.74 ± 0.04	12.72 ± 0.25	72.51 ± 0.23	11.03 ± 0.29
	600	4.61 ± 0.04	11.41 ± 0.60	72.69 ± 0.65	11.29 ± 0.41
OPF	500	4.58 ± 0.05	14.05 ± 1.14	74.06 ± 1.06	7.31 ± 0.30
	550	4.13 ± 0.04	12.43 ± 0.18	75.42 ± 0.23	8.02 ± 0.20
	600	4.17 ± 0.13	10.25 ± 0.27	76.70 ± 0.74	8.88 ± 0.55
RWS	500	3.41 ± 0.07	16.16 ± 0.18	73.29 ± 0.60	7.14 ± 0.43
	550	3.76 ± 0.03	14.56 ± 0.28	74.48 ± 0.28	7.20 ± 0.11
	600	3.74 ± 0.03	13.06 ± 0.14	76.31 ± 0.27	6.89 ± 0.41

Ultimate Analysis and Energy Content

The elemental compositions of the biochar are shown in Table 7. The C, H, N, S and O contents of the biochars were in the ranges of 75.07–82.02 wt. %, 1.59–3.45 wt. %, 0.35–1.78 wt. %, 0.03–0.40 wt. % and 14.22–22.00 wt. %, respectively. The carbon content was lower for RWS and OPF than for OPT. Due to the extensive thermal decomposition at higher temperatures, the pyrolysis temperature had a strong impact on the biochar. Biomass pyrolysis provided biochar with a high carbon and a low oxygen content, close to the results of previous studies [68]. High pyrolysis temperature caused losses of hydrogen and oxygen by the cleavage of weak bonds in the biomass, or by dehydration and decarboxylation reactions [97]. Owing to the incorporation of nitrogen into complex structures that are heat resistant and not easily volatilized, the nitrogen and sulfur contents of the biochar were relatively low [98]. Biochar's higher heating value (HHV) was in the range 26.42–29.33 MJ/kg, and RWS had a higher HHV than OPT or OPF. The higher carbon content and lower oxygen content of the biochar resulted in higher HHV, while the presence of elements C, H, and O in biomass resulted in higher levels of char formation [99]. High biochar HHV is suitable for solid fuel applications for both heat and power generation, as these properties help reduce airborne waste and energy losses [100].

Table 7. Ultimate analyses and energy contents of biochars.

Type of Biomass	Pyrolysis Temperature (°C)	Ultimate Analysis (wt. %, Dry Basis)					
		Carbon	Hydrogen	Nitrogen	Sulphur	Oxygen *	HHV
OPT	500	77.53 ± 0.11	3.45 ± 0.13	0.43 ± 0.01	0.04 ± 0.01	18.63 ± 0.71	28.82 ± 0.52
	550	79.35 ± 0.13	1.87 ± 0.05	1.78 ± 0.01	0.38 ± 0.01	16.65 ± 0.75	27.96 ± 0.38
	600	82.02 ± 0.14	1.59 ± 0.04	1.78 ± 0.01	0.40 ± 0.01	14.22 ± 0.42	28.79 ± 0.21
OPF	500	75.07 ± 0.01	2.41 ± 0.01	0.43 ± 0.01	0.11 ± 0.01	22.00 ± 0.51	26.61 ± 0.22
	550	76.41 ± 0.02	1.80 ± 0.04	0.40 ± 0.01	0.09 ± 0.01	21.31 ± 0.82	26.42 ± 0.39
	600	78.34 ± 0.01	1.91 ± 0.01	0.46 ± 0.01	0.11 ± 0.01	19.19 ± 0.51	27.43 ± 0.22
RWS	500	76.65 ± 0.01	2.71 ± 0.06	0.41 ± 0.01	0.04 ± 0.01	20.21 ± 0.41	27.70 ± 0.23
	550	78.59 ± 0.35	3.30 ± 0.02	0.49 ± 0.01	0.09 ± 0.01	17.63 ± 0.02	29.33 ± 0.02
	600	80.19 ± 0.02	2.09 ± 0.06	0.35 ± 0.01	0.03 ± 0.01	17.35 ± 0.23	28.50 ± 0.12

* Oxygen by difference.

Surface Morphology and Specific Surface Area

Figure 6A–F shows the surface characteristics of the biomass and biochar derived from OPT, OPF, and RWS at a pyrolysis temperature of 550 °C. The surface of biomass samples was smooth without any ridges or pores in Figure 6A,C,E. Biochar formed by the pyrolysis process is shown in Figure 6B,D,F; many well-defined pores were created,

probably by the volatilization of organic compounds [101]. Consequently, more void space and higher porosity are eVident on the surfaces of the biochars. The biochar from RWS had more pores than those from OPT and OPF. The BET surface areas of biomasses and biochar samples prepared at 550 °C were determined and are shown in Table 8. At the high 500 °C temperature, the BET surface area of biochar was decreased from that of the biomass. The BET surface area of biochar from OPT was higher than those of biochars from RWS or OPF.

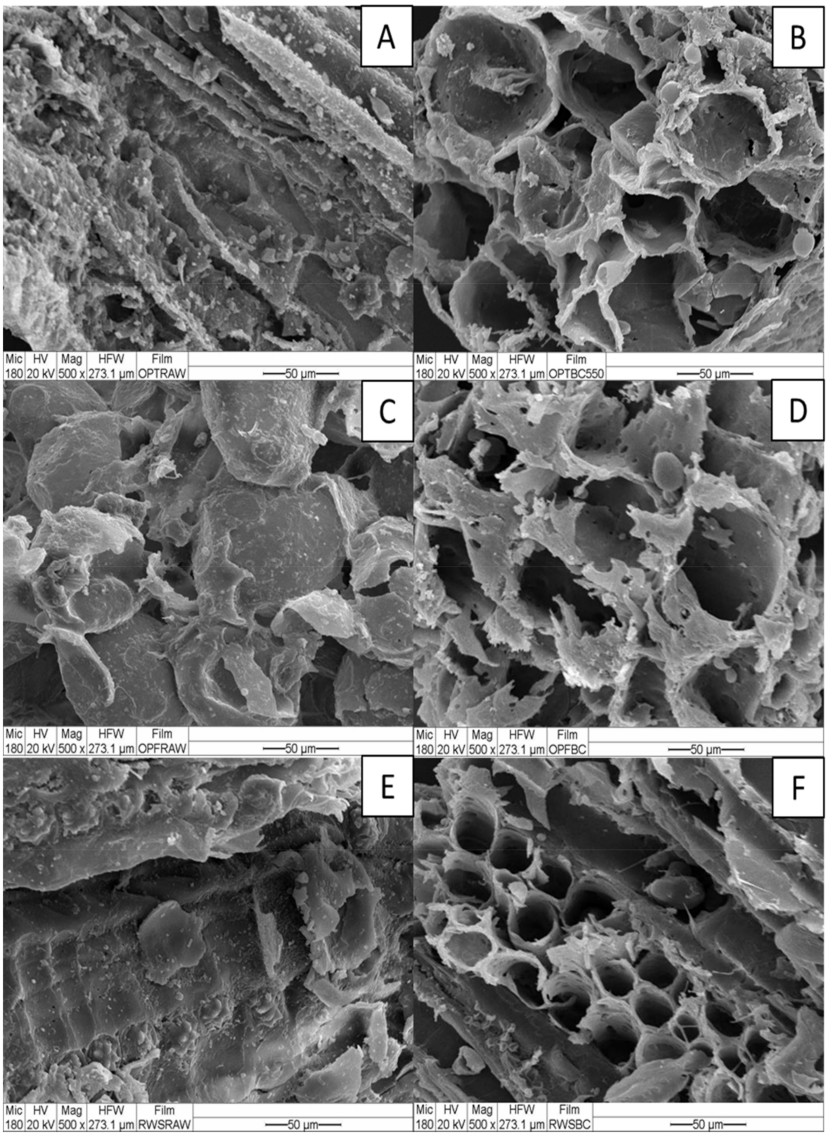

Figure 6. SEM photographs of (**A**) OPT, (**B**) OPT biochar, (**C**) OPF, (**D**) OPF biochar, (**E**) RWS, (**F**) RWS biochar.

Table 8. Specific surface areas and average pore diameters of biomasses and biochars pyrolyzed at 550 °C.

Name of Sample	BET Surface Area (m^2/g)	Average Pore Diameter (nm)
OPT	3.8034	99.9636
OPT biochar	0.3629	142.7742
OPF	3.127	96.4568
OPF biochar	0.3358	160.6406
RWS	4.7785	113.8839
RWS biochar	0.4854	175.7577

This is possibly due to the thermal decomposition of OPT biomass and also the woody nature of RWS. The TGA curve showed the weight loss percentage for OPT at 550 °C to decline more than that of RWS. The large pore size of biochar is caused by the progressive degradation of organic materials or lignocellulose content, including cellulose, hemicelluloses, and lignin. Also, high temperatures facilitated the release of volatile materials and created more pores, resulting in larger pores in the biochar [102]. Previous work has reported that when the heating rate was more than 10 °C/min, volatiles were formed inside the particles and released from the surface, which resulted in opened fiber structures leading with cavities, and this corresponded to a low BET surface area but a large pore diameter for the biochar when compared with the initial biomass [103]. High porosity of biochar is beneficial for bio-filter applications and soil mixing, and also for use as a solid fuel.

Recalcitrance and Stability

The functionality of atmospheric carbon sequestration in soil is crucially dependent on the ability of biochar to resist biotic and abiotic degradation (termed recalcitrance). The recalcitrant nature of biochar is eValuated by an index (R_{50}) based on a model developed by Harvey et.al. (2012). The R_{50} index is based on the energy usage for thermal oxidation at 50% weight loss of biochar [50]. The temperatures at which R_{50} is calculated are obtained from water and ash content-corrected TG thermograms of biochar and were found in the range 422–476 °C for all the biochars of this study. The calculated R_{50} for biochar from all feedstocks fell in a range of 0.49–0.53. Previous studies showed that the recalcitrance of biochar is mainly determined by the pyrolysis temperature, as indicated in Table 9 [50,104]. Biochar recalcitrance is connected to aromatic C, which increases with pyrolysis temperature and N loss caused by the higher temperature pyrolysis [105]. The reaction temperature has dominating control of recalcitrant nature of biochar. Carbon sequestration potential (CS) was eValuated using the R_{50} index and carbon contents from the ultimate and proximate analyses. Lower pyrolysis temperature produces more char, but a large amount of biochar C will be abiotically or microbially mineralized because of its poor recalcitrance [104,106]. Pyrolysis temperatures past 550 °C on the other hand, generate less biochar, but the recalcitrance of biochar formed is higher than of biochar from lower pyrolysis temperature [107]. The C sequestration potential is primarily determined by the biomass feedstock's intrinsic molecular structure, which may not be very varied [108]. The carbon sequestration capacity of the biochar for $R_{50} > 0.7$ is considered to be similar as those of graphite or soot [50]. The biochar obtained at 600 °C possessed higher capacity to sequestrate carbon, but the solid yield at 600 °C was found to be the least among all the experimental runs.

Table 9. Recalcitrant nature of biochar.

Type of Biomass	Pyrolysis Temperature (°C)	Carbon Sequestration			
		Carbon (% wt.)	Fixed Carbon (wt. %)	R_{50}	CS (%)
OPT	550	79.35 ± 0.13	72.51 ± 0.23	0.49	18.70
OPF	550	76.41 ± 0.02	75.42 ± 0.23	0.51	21.41
RWS	550	78.59 ± 0.35	74.48 ± 0.28	0.53	22.49

Ash Composition, and Slagging and Fouling Indexes of Biochar

K_2O and SiO_2 are viewed as the major oxide compounds influencing slacking index and fouling index. When comparing the magnitudes of these effects, K_2O should be of more concern because of its outstanding concentration of over 20 wt. % (compared to around 18 wt. % of SiO_2), which is also much higher than of the other compounds in Table 10. This is because K is a crucial nutrient in flowering fertilizers for fruit bearing palm plantations [109]. After burning, the K in ash can react to form KCl and K_2SO_4 with impurities present in the biochar, which will lower the ash melting temperature. This

improves the adhesion of fly ash particles that would otherwise cause the formation of slag in boiler heat transfer sections [110,111]. The suggested categories by slagging index (SI) are slight (<0.6), moderate (0.6–2.0), high (2.0–2.6), and extremely high (>2.6) and for fouling index (FI) they are slight (<0.6), high (0.6–40), and extremely high (>40) [112]. While the biochars of this study have very high SI and Fi, they can be used as cofiring substances in combustion chambers. The high SiO_2 contents in biochars from pyrolysis are possibly due to the comparatively heavier mass and more stable shape of silica oxide compared with the other mineral oxides [113]. For further use of biochar as co-firing fuel, addition of another high Si content biomass would benefit by lowering the tendency of slagging and fouling in the combustion chamber. Also, removal of potassium can be done to decrease slagging and fouling in combustion.

Table 10. Ash composition, and slagging and fouling indexes of biochar samples.

Oxides (wt. %)	Biochar		
	OPT	**OPF**	**RWS**
Fe_2O_3	2.991	4.92	1.124
CaO	12.625	14.069	11.361
MgO	5.155	5.383	9.096
Na_2O	1.169	1.118	0.541
K_2O	23.877	24.829	20.002
SiO_2	18.11	19.889	18.575
Al_2O_3	0.686	0.643	0.676
TiO_2	1.411	0.672	0.16
B/A	2.27	2.37	2.17
Sd	0.09	0.09	0.38
SI	0.20	0.21	0.82
FI	56.79	61.57	44.58

4. Conclusions

This study investigated yields and characteristics of liquid product and biochar obtained from pyrolysis of rubberwood sawdust (RWS), oil palm trunk (OPT), and oil palm frond (OPF) under various run conditions using an agitated bed pyrolysis reactor. The results indicate that the yields and characteristics of liquid product and biochar obtained from biomass samples vary widely. The yields of liquid product and biochar were in the ranges 35.94–54.40% and 23.46–25.98% (wt.), respectively. The highest liquid yield was obtained from pyrolysis of RWS at 550 °C. The energy content of the water-free liquid product or bio-oil was relatively low, due to the low carbon and hydrogen contents in the bio-oil. The results of GC-MS analysis showed high content of phenol groups in the liquid product. The biochars had high carbon contents (75.07–82.02%) and low oxygen contents (14.22–22%). Consequently, the higher heating values of biochars were high (26.42–29.33 MJ/kg). However, for solid fuel applications of biochar, particularly those from OPT and OPF have concerns regarding slagging and fouling, due to high contents of some oxides in biochar ashes as revealed by XRF. Aside for potential fuel applications, the biochars also have potential for use in carbon sequestration. The results also indicate that pyrolysis of biomass gave enlarged average pore diameters to the biochar, while its surface area was decreased from that of raw biomass, as revealed by BET and SEM.

Author Contributions: Conceptualization, methodology, experimentation, original draft preparation, P.S.; writing, proof reading, A.K.; supervision, P.T.; reviewing and editing, S.S.L.; conceptualization, visualization, investigation, writing, proof reading, A.P. All authors have read and agreed to the published version of the manuscript.

Funding: This research received no external funding.

Data Availability Statement: Not applicable.

Acknowledgments: The authors express their sincere appreciation to Graduate School, Prince of Songkla University, and Interdisciplinary Graduate School of Energy Systems (IGS-Energy), Prince of Songkla University, for partially financial support. The authors also thank to Energy Technology Research Centre, Faculty of Engineering, Prince of Songkla University, for partially financial support. This study was also supported by Office of Scientific Instrument and Testing (OSIT), Prince of Songkla University for testing the properties of biomass and products.

Conflicts of Interest: The authors declare no conflict of interest.

References

1. British Petroleum Company. BP Statistical Review of World Energy. 2019. Available online: https://www.bp.com/content/dam/bp/business-sites/en/global/corporate/pdfs/energy-economics/statistical-review/bp-stats-review-2019-full-report.pdf (accessed on 16 September 2020).
2. Kumar, A.; Kumar, N.; Baredar, P.; Shukla, A. A review on biomass energy resources, potential, conversion and policy in India. *Renew. Sustain. Energy Rev.* **2015**, *45*, 530–539. [CrossRef]
3. Johnsson, F.; Kjärstad, J.; Rootzén, J. The threat to climate change mitigation posed by the abundance of fossil fuels. *Clim. Policy* **2019**, *19*, 258–274. [CrossRef]
4. Rathore, D.; Nizami, A.-S.; Singh, A.; Pant, D. Key issues in estimating energy and greenhouse gas savings of biofuels: Challenges and perspectives. *Biofuel Res. J.* **2016**, *3*, 380–393. [CrossRef]
5. Palamanit, A.; Khongphakdi, P.; Tirawanichakul, Y.; Phusunti, N. Investigation of yields and qualities of pyrolysis products obtained from oil palm biomass using an agitated bed pyrolysis reactor. *Biofuel Res. J.* **2019**, *6*, 1065–1079. [CrossRef]
6. Davis, S.J.; Lewis, N.S.; Shaner, M.; Aggarwal, S.; Arent, D.; Azevedo, I.L.; Benson, S.M.; Bradley, T.; Brouwer, J.; Chiang, Y.-M.; et al. Net-zero emissions energy systems. *Science* **2018**, *360*, eaas9793. [CrossRef]
7. Office of Agricultural Economics. Agricultural Statistics of Thailand. 2018. Available online: http://www.oae.go.th/view/1/Home/EN-US (accessed on 6 September 2020).
8. Yusoff, S. Renewable energy from palm oil-innovation on effective utilization of waste. *J. Clean. Prod.* **2006**, *14*, 87–93. [CrossRef]
9. Shuit, S.H.; Tan, K.T.; Lee, K.T.; Kamaruddin, A.H. Oil palm biomass as a sustainable energy source: A Malaysian case study. *Energy* **2009**, *34*, 1225–1235. [CrossRef]
10. Sulaiman, F.; Abdullah, N.; Gerhauser, H.; Shariff, A. An outlook of Malaysian energy, oil palm industry and its utilization of wastes as useful resources. *Biomass Bioenergy* **2011**. [CrossRef]
11. Loh, S.K. The potential of the Malaysian oil palm biomass as a renewable energy source. *Energy Convers. Manag.* **2017**, *141*, 285–298. [CrossRef]
12. Azwar, E.; Mahari, W.A.W.; Chuah, J.H.; Vo, D.-V.N.; Ma, N.L.; Lam, W.H.; Lam, S.S. Transformation of biomass into carbon nanofiber for supercapacitor application. A review. *Int. J. Hydrogen Energy* **2018**, *43*, 20811–20821. [CrossRef]
13. Lam, S.S.; Su, M.H.; Nam, W.L.; Thoo, D.S.; Ng, C.M.; Liew, R.K.; Yek, P.N.Y.; Ma, N.L.; Vo, D.V.N. Microwave Pyrolysis with Steam Activation in Producing Activated Carbon for Removal of Herbicides in Agricultural Surface Water. *Ind. Eng. Chem. Res.* **2018**, *58*, 695–703. [CrossRef]
14. Anwar, Z.; Gulfraz, M.; Irshad, M. Agro-industrial lignocellulosic biomass a key to unlock the future bio-energy: A brief review. *J. Radiat. Res. Appl. Sci.* **2014**, *7*, 163–173. [CrossRef]
15. Sakulkit, P.; Palamanit, A.; Dejchanchaiwong, R.; Reubroycharoen, P. Characteristics of pyrolysis products from pyrolysis and co-pyrolysis of rubber wood and oil palm trunk biomass for biofuel and value-added applications. *J. Environ. Chem. Eng.* **2020**, *8*, 104561. [CrossRef]
16. Shrivastava, P.; Khongphakdi, P.; Palamanit, A.; Kumar, A.; Tekasakul, P. Investigation of physicochemical properties of oil palm biomass for eValuating potential of biofuels production via pyrolysis processes. *Biomass Convers. Biorefin.* **2020**, 1–15. [CrossRef]
17. Pawar, A.; Panwar, N.L.; Salvi, B.L. Comprehensive review on pyrolytic oil production, upgrading and its utilization. *J. Mater. Cycles Waste Manag.* **2020**, *22*, 1712–1722. [CrossRef]
18. Ronsse, F.; Van Hecke, S.; Dickinson, D.; Prins, W. Production and characterization of slow pyrolysis biochar: Influence of feedstock type and pyrolysis conditions. *GCB Bioenergy* **2012**, *5*, 104–115. [CrossRef]
19. Abhijeet, P.; Swagathnath, G.; Rangabhashiyam, S.; Rajkumar, M.A.; Balasubramanian, P. Prediction of pyrolytic product composition and yield for various grass biomass feedstocks. *Biomass Convers. Biorefin.* **2020**, *10*, 663–674. [CrossRef]
20. Kan, T.; Strezov, V.; eVans, T.J. Lignocellulosic biomass pyrolysis: A review of product properties and effects of pyrolysis parameters. *Renew. Sustain. Energy Rev.* **2016**, *57*, 1126–1140. [CrossRef]
21. Foong, S.Y.; Liew, R.K.; Yang, Y.; Cheng, Y.W.; Yek, P.N.Y.; Mahari, W.A.W.; Lee, X.Y.; Han, C.S.; Vo, D.-V.N.; Van Le, Q.; et al. Valorization of biomass waste to engineered activated biochar by microwave pyrolysis: Progress, challenges, and future directions. *Chem. Eng. J.* **2020**, *389*, 124401. [CrossRef]
22. Wang, D.; Jiang, P.; Zhang, H.; Yuan, W. Biochar production and applications in agro and forestry systems: A review. *Sci. Total Environ.* **2020**, *723*, 137775. [CrossRef] [PubMed]
23. Veiga, T.R.L.A.; Lima, J.T.; Dessimoni, A.L.D.A.; Pego, M.F.F.; Soares, J.R.; Trugilho, P.F. Different Plant Biomass Characterizations for Biochar Production. *Cerne* **2017**, *23*, 529–536. [CrossRef]

24. Rueangsan, K.; Suwapaet, N.; Pattiya, A. Bio-oil production by fast pyrolysis of cassava residues in a free-fall reactor using liquid media-assisted condensation. *Energy Sources Part. A Recover. Util. Environ. Eff.* **2018**, *40*, 615–622. [CrossRef]
25. Güngör, A.; Önenç, S.; Uçar, S.; Yanik, J. Comparison between the "one-step" and "two-step" catalytic pyrolysis of pine bark. *J. Anal. Appl. Pyrolysis* **2012**, *97*, 39–48. [CrossRef]
26. Kilic, M.; Pütün, E.; Pütün, A.E.; Kılıç, M. Optimization of Euphorbia rigida fast pyrolysis conditions by using response surface methodology. *J. Anal. Appl. Pyrolysis* **2014**, *110*, 163–171. [CrossRef]
27. Oni, B.A.; Oziegbe, O.; Olawole, O.O. Significance of biochar application to the environment and economy. *Ann. Agric. Sci.* **2019**, *64*, 222–236. [CrossRef]
28. Czernik, S.; Bridgwater, A.V. Overview of Applications of Biomass Fast Pyrolysis Oil. *Energy Fuels* **2004**, *18*, 590–598. [CrossRef]
29. Jahirul, M.I.; Rasul, M.G.; Chowdhury, A.A.; Ashwath, N. Biofuels Production through Biomass Pyrolysis—A Technological Review. *Energies* **2012**, *5*, 4952–5001. [CrossRef]
30. Biswas, B.; Pandey, N.; Bisht, Y.; Singh, R.; Kumar, J.; Bhaskar, T. Pyrolysis of agricultural biomass residues: Comparative study of corn cob, wheat straw, rice straw and rice husk. *Bioresour. Technol.* **2017**, *237*, 57–63. [CrossRef]
31. Mahari, W.A.W.; Zainuddin, N.F.; Chong, C.T.; Lee, C.L.; Lam, W.H.; Poh, S.C.; Lam, S.S. Conversion of waste shipping oil into diesel-like oil via microwave-assisted pyrolysis. *J. Environ. Chem. Eng.* **2017**, *5*, 5836–5842. [CrossRef]
32. Kong, S.; Lam, S.S.; Yek, P.N.Y.; Liew, R.K.; Ma, N.L.; Osman, M.S.; Wong, C.C. Self-purging microwave pyrolysis: An innovative approach to convert oil palm shell into carbon-rich biochar for methylene blue adsorption. *J. Chem. Technol. Biotechnol.* **2019**, *94*, 1397–1405. [CrossRef]
33. Abnisa, F.; Daud, W.M.A.W. A review on co-pyrolysis of biomass: An optional technique to obtain a high-grade pyrolysis oil. *Energy Convers. Manag.* **2014**, *87*, 71–85. [CrossRef]
34. Mohammed, I.Y.; Abakr, Y.A.; Hui, J.N.X.; Alaba, P.A.; Morris, K.I.; Ibrahim, M.D. Recovery of clean energy precursors from Bambara groundnut waste via pyrolysis: Kinetics, products distribution and optimisation using response surface methodology. *J. Clean. Prod.* **2017**, *164*, 1430–1445. [CrossRef]
35. Sareekam, N.; Kamarudin, S.K.; Kasmuri, N.H. Optimization of Bio Oil from Palm Oil Fronds Via Fast Pyrolysis. *Indian J. Sci. Technol.* **2016**, *9*. [CrossRef]
36. Asadullah, M.; Ab Rasid, N.S.; Kadir, S.A.S.A.; Azdarpour, A. Production and detailed characterization of bio-oil from fast pyrolysis of palm kernel shell. *Biomass Bioenergy* **2013**, *59*, 316–324. [CrossRef]
37. Ruengvilairat, P.; Tanatavikorn, H.; Vitidsant, T. Bio-Oil Production by Pyrolysis of Oil Palm Empty Fruit Bunch in Nitrogen and Steam Atmospheres. *J. Sustain. Bioenergy Syst.* **2012**, *2*, 75–85. [CrossRef]
38. Mao, Y.; Dong, L.; Dong, Y.; Liu, W.; Chang, J.; Yang, S.; Lv, Z.; Fan, P. Fast co-pyrolysis of biomass and lignite in a micro fluidized bed reactor analyzer. *Bioresour. Technol.* **2015**, *181*, 155–162. [CrossRef] [PubMed]
39. Imran, A.; Bramer, E.A.; Seshan, K.; Brem, G. An overview of catalysts in biomass pyrolysis for production of biofuels. *Biofuel Res. J.* **2018**, *5*, 872–885. [CrossRef]
40. Chen, J.; Liang, J.; Wu, S. Lignin-rich biomass of cotton by-products for biorefineries via pyrolysis. *Bioresour. Technol.* **2016**, *218*, 402–409. [CrossRef]
41. Wang, Y.; Zeng, Z.; Tian, X.; Dai, L.; Jiang, L.; Zhang, S.; Wu, Q.; Wen, P.; Fu, G.; Liu, Y.; et al. Production of bio-oil from agricultural waste by using a continuous fast microwave pyrolysis system. *Bioresour. Technol.* **2018**, *269*, 162–168. [CrossRef]
42. Guedes, R.E.; Luna, A.S.; Torres, A.R. Operating parameters for bio-oil production in biomass pyrolysis: A review. *J. Anal. Appl. Pyrolysis* **2018**, *129*, 134–149. [CrossRef]
43. Leng, L.; Huang, H. An overview of the effect of pyrolysis process parameters on biochar stability. *Bioresour. Technol.* **2018**, *270*, 627–642. [CrossRef]
44. Kurnia, J.C.; Jangam, S.V.; Akhtar, S.; Sasmito, A.; Mujumdar, A.S. Advances in biofuel production from oil palm and palm oil processing wastes: A review. *Biofuel Res. J.* **2016**, *3*, 332–346. [CrossRef]
45. Guda, V.K.; Toghiani, H. Altering bio-oil composition by catalytic treatment of pinewood pyrolysis vapors over zeolites using an auger-packed bed integrated reactor system. *Biofuel Res. J.* **2016**, *3*, 448–457. [CrossRef]
46. Pattiya, A. Bio-oil production via fast pyrolysis of biomass residues from cassava plants in a fluidised-bed reactor. *Bioresour. Technol.* **2011**, *102*, 1959–1967. [CrossRef]
47. Sirijanusorn, S.; Sriprateep, K.; Pattiya, A. Pyrolysis of cassava rhizome in a counter-rotating twin screw reactor unit. *Bioresour. Technol.* **2013**, *139*, 343–348. [CrossRef]
48. Sukiran, M.A.; Loh, S.K.; Bakar, N.A. Production of Bio-oil from Fast Pyrolysis of Oil Palm Biomass using Fluidised Bed Reactor. *J. Energy Technol. Policy* **2016**, *6*, 52–62.
49. Oasmaa, A.; Peacocke, C. *A Guide to Physical Property Characterisation of Biomass-Derived Fast Pyrolysis Liquids*; Technical Research Centre of Finland, Bergsmansgården: Espoo, Finland, 2001.
50. Harvey, O.R.; Kuo, L.-J.; Zimmerman, A.R.; Louchouarn, P.; Amonette, J.E.; Herbert, B.E. An Index-Based Approach to Assessing Recalcitrance and Soil Carbon Sequestration Potential of Engineered Black Carbons (Biochars). *Environ. Sci. Technol.* **2012**, *46*, 1415–1421. [CrossRef]
51. Tan, C.; Saritpongteeraka, K.; Kungsanant, S.; Charnnok, B.; Chaiprapat, S. Low temperature hydrothermal treatment of palm fiber fuel for simultaneous potassium removal, enhanced oil recovery and biogas production. *Fuel* **2018**, *234*, 1055–1063. [CrossRef]

52. Pattiya, A.; Suttibak, S. Production of bio-oil via fast pyrolysis of agricultural residues from cassava plantations in a fluidised-bed reactor with a hot vapour filtration unit. *J. Anal. Appl. Pyrolysis* **2012**, *95*, 227–235. [CrossRef]
53. McKendry, P. Energy production from biomass (part 2): Conversion technologies. *Bioresour. Technol.* **2002**, *83*, 47–54. [CrossRef]
54. Mishra, R.K.; Mohanty, K. Pyrolysis kinetics and thermal behavior of waste sawdust biomass using thermogravimetric analysis. *Bioresour. Technol.* **2018**, *251*, 63–74. [CrossRef] [PubMed]
55. Widjaya, E.R.; Chen, G.; Bowtell, L.; Hills, C. Gasification of non-woody biomass: A literature review. *Renew. Sustain. Energy Rev.* **2018**, *89*, 184–193. [CrossRef]
56. Pattiya, A.; Suttibak, S. Influence of a glass wool hot vapour filter on yields and properties of bio-oil derived from rapid pyrolysis of paddy residues. *Bioresour. Technol.* **2012**, *116*, 107–113. [CrossRef]
57. Uzun, B.B.; Varol, E.A.; Pütün, E. Pyrolysis: A Sustainable Way from Biomass to Biofuels and Biochar. In *Biochar*; Amsterdam University Press: Amsterdam, The Netherlands, 2016; pp. 239–265.
58. Mishra, R.K.; Mohanty, K. Pyrolysis characteristics, fuel properties, and compositional study of *Madhuca longifolia* seeds over metal oxide catalysts. *Biomass Convers. Biorefin.* **2020**. [CrossRef]
59. Brar, J.S.; Singh, K.B.; Wang, J.; Kumar, S. Cogasification of Coal and Biomass: A Review. *Int. J. For. Res.* **2012**, *2012*, 1–10. [CrossRef]
60. McKendry, P. Energy production from biomass (part 1): Overview of biomass. *Bioresour. Technol.* **2002**, *83*, 37–46. [CrossRef]
61. Quan, C.; Gao, N.; Song, Q. Pyrolysis of biomass components in a TGA and a fixed-bed reactor: Thermo-chemical behaviors, kinetics, and product characterization. *J. Anal. Appl. Pyrolysis* **2016**, *121*, 84–92. [CrossRef]
62. Basu, P. Analytical Techniques. *Biomass Gasif. Pyrolysis Torrefaction* **2018**, 479–495. [CrossRef]
63. Huang, X.; Cao, J.-P.; Zhao, X.-Y.; Wang, J.-X.; Fan, X.; Zhao, Y.-P.; Wei, X.-Y. Pyrolysis kinetics of soybean straw using thermogravimetric analysis. *Fuel* **2016**, *169*, 93–98. [CrossRef]
64. Das, P.; Ganesh, A.; Wangikar, P. Influence of pretreatment for deashing of sugarcane bagasse on pyrolysis products. *Biomass Bioenergy* **2004**, *27*, 445–457. [CrossRef]
65. Fahmi, R.; Bridgwater, A.; Darvell, L.; Jones, J.; Yates, N.; Thain, S.; Donnison, I. The effect of alkali metals on combustion and pyrolysis of Lolium and Festuca grasses, switchgrass and willow. *Fuel* **2007**, *86*, 1560–1569. [CrossRef]
66. Müller-Hagedorn, M.; Bockhorn, H.; Krebs, L.; Müller, U. A comparative kinetic study on the pyrolysis of three different wood species. *J. Anal. Appl. Pyrolysis* **2003**, *69*, 231–249. [CrossRef]
67. Kabir, G.; Din, A.M.; Hameed, B. Pyrolysis of oil palm mesocarp fiber and palm frond in a slow-heating fixed-bed reactor: A comparative study. *Bioresour. Technol.* **2017**, *241*, 563–572. [CrossRef]
68. Bensidhom, G.; Ben Hassen-Trabelsi, A.; Alper, K.; Sghairoun, M.; Zaafouri, K.; Trabelsi, I. Pyrolysis of Date palm waste in a fixed-bed reactor: Characterization of pyrolytic products. *Bioresour. Technol.* **2018**, *247*, 363–369. [CrossRef] [PubMed]
69. Madhu, P.; Livingston, T.S.; Kanagasabapathy, H. Flash Pyrolysis of Lemon Grass (*Cymbopogon flexuosus*) for Bio-oil Production in an Electrically Heated Fluidized Bed Reactor. *Waste Biomass Valorization* **2017**, *9*, 1037–1046. [CrossRef]
70. Şensöz, S.; Can, M. Pyrolysis of Pine (*Pinus brutia* Ten.) Chips: 1. Effect of Pyrolysis Temperature and Heating Rate on the Product Yields. *Energy Sources* **2002**, *24*, 347–355. [CrossRef]
71. Tsai, W.T.; Lee, M.K.; Chang, Y.M. Fast pyrolysis of rice straw, sugarcane bagasse and coconut shell in an induction-heating reactor. *J. Anal. Appl. Pyrolysis* **2006**, *76*, 230–237. [CrossRef]
72. Lee, Y.; Park, J.; Ryu, C.; Gang, K.S.; Yang, W.; Park, Y.-K.; Jung, J.; Hyun, S. Comparison of biochar properties from biomass residues produced by slow pyrolysis at 500 °C. *Bioresour. Technol.* **2013**, *148*, 196–201. [CrossRef]
73. Sokoto, M.A.; Biswas, B.; Kumar, J.; Bhaskar, T. Slow pyrolysis of Defatted Seeds Cakes of African star apple and silk cotton for production of bio-oil. *Renew. Energy* **2020**, *146*, 1710–1716. [CrossRef]
74. Callegari, A.; Bolognesi, S.; Cecconet, D.; Capodaglio, A.G. Production technologies, current role, and future prospects of biofuels feedstocks: A state-of-the-art review. *Crit. Rev. Environ. Sci. Technol.* **2020**, *50*, 384–436. [CrossRef]
75. Sukumar, V.; Manieniyan, V.; Senthilkumar, R.; Sivaprakasam, S. Production of bio oil from sweet lime empty fruit bunch by pyrolysis. *Renew. Energy* **2020**, *146*, 309–315. [CrossRef]
76. Kappler, G.; De Souza, D.M.; Moraes, C.A.M.; Modolo, R.C.E.; Brehm, F.A.; Wander, P.R.; da Cruz Tarelho, L.A. Conversion of Lignocellulosic Biomass Through Pyrolysis to Promote a Sustainable Value Chain for Brazilian Agribusiness. In *Lignocellulosic Biorefining Technologies*; Wiley: Hoboken, NJ, USA, 2020; pp. 265–283.
77. Azni, A.A.; Ghani, W.A.W.A.K.; Idris, A.; Ja'Afar, M.F.Z.; Salleh, M.A.M.; Ishak, N.S. Microwave-assisted pyrolysis of EFB-derived biochar as potential renewable solid fuel for power generation: Biochar versus sub-bituminous coal. *Renew. Energy* **2019**, *142*, 123–129. [CrossRef]
78. Maguyon-Detras, M.C.; Migo, M.V.P.; Van Hung, N.; Gummert, M. Thermochemical Conversion of Rice Straw. In *Sustainable Rice Straw Management*; Springer: Cham, Switzerland, 2019; pp. 43–64.
79. Pimenidou, P.; Dupont, V. Characterisation of palm empty fruit bunch (PEFB) and pinewood bio-oils and kinetics of their thermal degradation. *Bioresour. Technol.* **2012**, *109*, 198–205. [CrossRef] [PubMed]
80. Chen, T.; Wu, C.; Liu, R.; Fei, W.; Liu, S. Effect of hot vapor filtration on the characterization of bio-oil from rice husks with fast pyrolysis in a fluidized-bed reactor. *Bioresour. Technol.* **2011**, *102*, 6178–6185. [CrossRef] [PubMed]

81. Gómez, N.; Banks, S.; Nowakowski, D.; Rosas, J.; Cara, J.; Sánchez, M.; Bridgwater, A. Effect of temperature on product performance of a high ash biomass during fast pyrolysis and its bio-oil storage eValuation. *Fuel Process. Technol.* **2018**, *172*, 97–105. [CrossRef]
82. Odetoye, T.E.; Onifade, K.R.; Abubakar, M.S.; Titiloye, J.O. Pyrolysis of Parinari polyandra Benth fruit shell for bio-oil production. *Biofuel Res. J.* **2014**, *1*, 85–90. [CrossRef]
83. Zhang, W.; Yuan, C.; Xu, J.; Yang, X. Beneficial synergetic effect on gas production during co-pyrolysis of sewage sludge and biomass in a vacuum reactor. *Bioresour. Technol.* **2015**, *183*, 255–258. [CrossRef]
84. Bardalai, M.; Mahanta, D. Characterisation of Biochar Produced by Pyrolysis from Areca Catechu Dust. *Mater. Today Proc.* **2018**, *5*, 2089–2097. [CrossRef]
85. Oasmaa, A.; Elliott, D.; Muller, S. Quality control in fast pyrolysis bio-oil production and use. *Environ. Prog. Sustain. Energy* **2009**, *28*, 404–409. [CrossRef]
86. Feng, F.; Liu, W.Y.; Chen, Y.S. Study on derivatives of gambogic acid. *J. China Pharm. Univ.* **2005**, *36*, 302–305.
87. Akhtar, J.; Amin, N.S. A review on operating parameters for optimum liquid oil yield in biomass pyroly-sis. *Renew. Sustain. Energy Rev.* **2012**, *16*, 5101–5109. [CrossRef]
88. Alvarez, J.; Amutio, M.; Lopez, G.; Bilbao, J.; Olazar, M. Fast co-pyrolysis of sewage sludge and lignocellulosic biomass in a conical spouted bed reactor. *Fuel* **2015**, *159*, 810–818. [CrossRef]
89. Suttibak, S.; Sriprateep, K.; Pattiya, A. Production of Bio-oil via Fast Pyrolysis of Cassava Rhizome in a Fluidised-Bed Reactor. *Energy Procedia* **2012**, *14*, 668–673. [CrossRef]
90. Mushtaq, F.; Abdullah, T.A.T.; Mat, R.; Ani, F.N. Optimization and characterization of bio-oil produced by microwave assisted pyrolysis of oil palm shell waste biomass with microwave absorber. *Bioresour. Technol.* **2015**, *190*, 442–450. [CrossRef]
91. Yoshida, T. Synthesis of polysaccharides having specific biological activities. *Prog. Polym. Sci.* **2001**, *26*, 379–441. [CrossRef]
92. Thangalazhy-Gopakumar, S.; Adhikari, S.; Ravindran, H.; Gupta, R.B.; Fasina, O.; Tu, M.; Fernando, S.D. Physiochemical properties of bio-oil produced at various temperatures from pine wood using an auger reactor. *Bioresour. Technol.* **2010**, *101*, 8389–8395. [CrossRef]
93. Nudri, N.A.; Bachmann, R.T.; Ghani, W.A.W.A.K.; Sum, D.N.K.; Azni, A.A. Characterization of oil palm trunk biocoal and its suitability for solid fuel applications. *Biomass Convers. Biorefin.* **2019**, *10*, 45–55. [CrossRef]
94. Wilk, M.; Magdziarz, A.; Kalemba, I. Characterisation of renewable fuels' torrefaction process with different instrumental techniques. *Energy* **2015**, *87*, 259–269. [CrossRef]
95. Angin D Effect of pyrolysis temperature and heating rate on biochar obtained from pyrolysis of saf-flower seed press cake. *Bioresour. Technol.* **2013**, *128*, 593–597. [CrossRef]
96. Tsai, W.-T.; Liu, S.-C.; Chen, H.-R.; Chang, Y.-M.; Tsai, Y.-L. Textural and chemical properties of swine-manure-derived biochar pertinent to its potential use as a soil amendment. *Chemosphere* **2012**, *89*, 198–203. [CrossRef]
97. Zhang, J.; Liu, J.; Liu, R. Effects of pyrolysis temperature and heating time on biochar obtained from the pyrolysis of straw and lignosulfonate. *Bioresour. Technol.* **2015**, *176*, 288–291. [CrossRef]
98. Pereira, R.C.; Kaal, J.; Arbestain, M.C.; Lorenzo, R.P.; Aitkenhead, W.; Hedley, M.; Macias, F.D.; Hindmarsh, J.P.; Agulló, J.A.M. Contribution to characterisation of biochar to estimate the labile fraction of carbon. *Org. Geochem.* **2011**, *42*, 1331–1342. [CrossRef]
99. Obernberger, I.; Thek, G. Physical characterisation and chemical composition of densified biomass fuels with regard to their combustion behaviour. *Biomass Bioenergy* **2004**, *27*, 653–669. [CrossRef]
100. Liu, Z.; Quek, A.; Hoekman, S.K.; Balasubramanian, R. Production of solid biochar fuel from waste biomass by hydrothermal carbonization. *Fuel* **2013**, *103*, 943–949. [CrossRef]
101. Shaaban, A.; Se, S.-M.; Dimin, M.; Juoi, J.M.; Husin, M.H.M.; Mitan, N.M.M. Influence of heating temperature and holding time on biochars derived from rubber wood sawdust via slow pyrolysis. *J. Anal. Appl. Pyrolysis* **2014**, *107*, 31–39. [CrossRef]
102. Lua, A.C. A detailed study of pyrolysis conditions on the production of steam-activated carbon derived from oil-palm shell and its application in phenol adsorption. *Biomass Convers. Biorefin.* **2019**, *10*, 523–533. [CrossRef]
103. Chen, B.; Zhou, D.; Zhu, L. Transitional Adsorption and Partition of Nonpolar and Polar Aromatic Contaminants by Biochars of Pine Needles with Different Pyrolytic Temperatures. *Environ. Sci. Technol.* **2008**, *42*, 5137–5143. [CrossRef]
104. Zimmerman, A.R. Abiotic and Microbial Oxidation of Laboratory-Produced Black Carbon (Biochar). *Environ. Sci. Technol.* **2010**, *44*, 1295–1301. [CrossRef]
105. Spokas, K.; Koskinen, W.; Baker, J.; Reicosky, D. Impacts of woodchip biochar additions on greenhouse gas production and sorption/degradation of two herbicides in a Minnesota soil. *Chemosphere* **2009**, *77*, 574–581. [CrossRef]
106. Cheng, C.-H.; Lehmann, J.; Thies, J.E.; Burton, S.D.; Engelhard, M.H. Oxidation of black carbon by biotic and abiotic processes. *Org. Geochem.* **2006**, *37*, 1477–1488. [CrossRef]
107. Worasuwannarak, N.; Sonobe, T.; Tanthapanichakoon, W. Pyrolysis behaviors of rice straw, rice husk, and corncob by TG-MS technique. *J. Anal. Appl. Pyrolysis* **2007**, *78*, 265–271. [CrossRef]
108. Mašek, O.; Brownsort, P.; Cross, A.; Sohi, S. Influence of production conditions on the yield and environmental stability of biochar. *Fuel* **2013**, *103*, 151–155. [CrossRef]
109. Rankine I, Fairhurst TH Management of phosphorus, potassium and magnesium in mature oil palm. *Better Crop Int.* **1999**, *13*, 11.
110. Wang, X.; Liu, Y.; Tan, H.; Ma, L.; Xu, T. Mechanism Research on the Development of Ash Deposits on the Heating Surface of Biomass Furnaces. *Ind. Eng. Chem. Res.* **2012**, *51*, 12984–12992. [CrossRef]

111. Abdullah, N.; Sulaiman, F. The properties of the washed empty fruit bunches of oil palm. *J. Phys. Sci.* **2013**, *24*, 117–137.
112. Zhu, Y.; Niu, Y.; Tan, H.; Wang, X. Short Review on the Origin and Countermeasure of Biomass Slagging in Grate Furnace. *Front. Energy Res.* **2014**, *2*. [CrossRef]
113. Omar, F.N.; Mohammed, M.A.P.; Baharuddin, A.S. Effect of Silica Bodies on the Mechanical Behaviour of Oil Palm Empty Fruit Bunch Fibres. *BioResources* **2014**, *9*, 7041–7058. [CrossRef]

Made available through a Creative Commons CC-BY-NC-ND License

ACS OMEGA

ACS AUTHORCHOICE

http://pubs.acs.org/journal/acsodf

Article

Computational Analysis Indicates That PARP1 Acts as a Histone Deacetylases Interactor Sharing Common Lysine Residues for Acetylation, Ubiquitination, and SUMOylation in Alzheimer's and Parkinson's Disease

Rohan Gupta and Pravir Kumar*

Cite This: https://dx.doi.org/10.1021/acsomega.0c06168

Read Online

ACCESS | Metrics & More | Article Recommendations

ABSTRACT: ***Aim/Hypothesis***: Lysine residues are known for the post-translational modifications (PTMs) such as acetylation, ubiquitination, and SUMOylation. In acetylation, histone deacetylase (HDAC) and its interactors cause transcriptional deregulation and cause mitochondrial dysfunction, apoptosis, inflammatory response, and cell-cycle impairment that cause brain homeostasis and neuronal cell death. Other regulatory PTMs involved in the pathogenesis of neurodegenerative diseases (NDDs) are ubiquitination and SUMOylation for the degradation of the misfolded proteins. Thus, we aim to investigate the potential acetylation/ubiquitination/SUMOylation crosstalk sites in the HDAC interactors, which cause NDDs. Furthermore, we aim to identify the influence of PTMs on the structural features of proteins and the impact of putative lysine mutation on disease susceptibility. Last, we aim to examine the impact of the putative mutation on acetylated lysine for ubiquitination and SUMOylation. ***Results***: Herein, we integrate 1455 genes, 3094 genes, and 1940 genes related to HDAC interactors, Alzheimer's disease (AD), and Parkinson's disease (PD), respectively. Furthermore, the protein−protein interaction and PTM integrations from different databases identified 32 proteins that are associated with HDAC, AD, and PD with 1489 potential lysine-modified sites. HDAC interactors poly(ADP-ribose) polymerase 1 (PARP1), nucleophosmin (NPM1), and cyclin-dependent kinase 1 (CDK1) involved in the progression of NDDs and 64 and 75% of PTM sites in PARP1, NPM1, and CDK1 fall into coiled and ordered regions, respectively. Moreover, 15 putative lysine sites have been found in the crosstalk and K148, K249, K528, K637, K700, and K796 of PARP1 are crosstalk hotspots. ***Conclusion***: The loss of acetylated hotspot sites results in the loss of ubiquitination and SUMOylation function on nearby sites, which is relatively higher when compared to the gain of function.

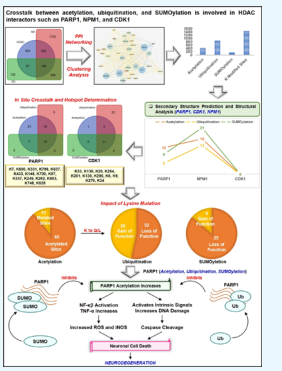

1. INTRODUCTION

Neurodegenerative diseases (NDDs) such as Alzheimer's disease (AD), Parkinson's disease (PD), Huntington's disease (HD), amyotrophic lateral sclerosis (ALS), frontotemporal dementia, and multiple sclerosis occur due to the progressive loss of neuronal cells, which causes synaptic dysfunction and memory impairment. AD and PD are the two most prevalent forms of NDDs in older people.[1] Recent studies demonstrated the potential role of post-translational modifications (PTMs) such as acetylation/deacetylation, methylation/demethylation, ubiquitination, SUMOylation, phosphorylation, and others in the pathogenesis of NDDs.[2] These PTMs cause transcriptional alteration, which leads to mitochondrial dysfunction, apoptosis and autophagic cell death, DNA damage response, inflammatory response, cell-cycle dysregulation, stress response, and microglial activation, which are prominent features of AD and PD.[3,4] Among different PTMs, acetylation of essential regulatory proteins via lysine acetyltransferase (HATs/KATs) promotes the euchromatin structure and leads to transcriptional activation.[5−8] Acetylation of lysine residues neutralizes the charges on histone proteins, increasing the chromatin accessibility for transcription factors, which is called euchromatin or relaxed chromatin structure.[9] Transcriptional activation of regulatory proteins reverses cellular processes' impairment, which restores synaptic functions and learning ability.[10]

On the contrary, histone deacetylases (HDACs) are a class of lysine deacetylases that reverse the process of acetylation and cause transcriptional repression, which causes neurodegeneration.[11] Along with acetylation, ubiquitination and SUMOylation are two other significant PTMs, which are involved in the pathogenesis of NDDs. Ubiquitination plays an essential role in the clearance of accumulated toxic proteins in

Received: December 18, 2020
Accepted: February 12, 2021

Downloaded via DELHI TECHNOLOGICAL UNIV on February 23, 2021 at 06:46:52 (UTC).
See https://pubs.acs.org/sharingguidelines for options on how to legitimately share published articles.

© XXXX The Authors. Published by American Chemical Society

Table 1. Mechanism of HDAC Interactors Involved in AD and PD Pathogenesis in Acetylation, Ubiquitination, and SUMOylation

HDAC interactor	acetylation	ubiquitination	SUMOylation
NPM1	NPM1 acetylation through p300 modulates its subcellular localization and promotes its binding with transcriptionally active RNA polymerase II[21]	impaired BRCA1-BARD1 ubiquitin ligase causes NPM1 downregulation through p-STAT5, which in turn enhances cell survival[22]	ARF and TRIM28 coexpression enhances NPM1 SUMOylation and alters its centrosomal localization, which suppressed the centrosome amplification[23]
HIF1A	acetylation of HIF1A at K709 through p300 increases its stability and decreases polyubiquitination[24]	HIF1A ubiquitination at K63 through STUB1 causes its proteasomal degradation[25]	SUMOylation of HIF1A changes its turnover rate through E3 SUMO ligase, which reduces its transcriptional activity[26]
CASP8	HDAC inhibitor increases Ku70 acetylation and thus decreases FLIP/Ku70 association and increases caspase 8activation[27]	increased Ku70 acetylation triggers FLIP polyubiquitination and causes its degradation through the proteasome[27]	SUMOylation of caspase 8 at K156 alters its nuclear localization but does not interfere in its activation[28]
ERK1	acetylated ERK1 at K72 enhances the enzymatic activity and affects ATP binding[29]	PHD domain of E3 ligase MEKK1 acts as an upstream activator of ERK1 and JNK, which promotes their degradation through the proteasomal pathway[30]	SUMOylation of nNOS at K725 and K739 enhances NO production, which is required for ERK1/2 activity in nNOS-positive neurons[31]
PARP1	P300/CREB-induced PARP1 acetylation causes coactivation of NF-$\kappa\beta$-dependent transcription[32]	polyubiquitination of PARP1 at K48 regulates its degradation[33]	SUMOylation of PARP1 at K486 through SUMO1 and SUMO3 decreases its p300-mediated acetylation, which restrains transcriptional coactivator functions[34]
AKT1	acetylation of Akt at K163 and K377 increases the neuronal differentiation[35]	E3 Ligase TRAF6 promotes Ak1 polyubiquitination at K63 and promotes membrane localization and its phosphorylation[36]	decreases Akt SUMOylation at K276 and K301 and affects Akt-induced Bcl-X alternative splicing[37]
ERBB2	acetylation of ERBB2 increases its stability[38]	ubiquitination of ERBB2 through E3 ligase CHIP decreases its stability and facilitates its proteasomal degradation[39]	SUMOylation of ERBB2 at K23 promotes its transcriptional repression[40]
DNMT1	DNMT1 is destabilized with Tip60-induced acetylation[41]	acetylation of DNMT1 triggers ubiquitination with UHRF1 and promotes its proteasomal degradation[41]	SUMOylation of DNMT1 enhances demethylase activity *in vivo* and modulates its interaction with HDAC[42]
MYC	P300-mediated Myc acetylation increases the transcriptional activity and control Myc protein turnover[43]	USP28-induced Myc ubiquitination promotes its stability and promotes its degradation through interaction with FBW7γ[44]	K52, K148, K157, and K317 SUMOylation of Myc promotes its degradation regulated by PIAS1 and RNF4[45]
APP	increased H3 and H4 acetylation of APP enhances its transcriptional activity, which increases EGR1 and c-FOS expression[46]	enhanced ubiquitination of APP decreases its full-length expression and thus decreases Aβ generation[47]	SUMOylation of APP decreases Aβ production, whereas SENP1 and SENP2 decrease APP SUMOylation[48]
GAPDH	GAPDH acetylation at K256 increases its activity in glucose response[49]	S-nitrosylation of B23 at cysteine 275 enhances b23-SIAH1 binding through the decreased E3 ligase activity of SIAH1 and exerts neuroprotective effects[50]	
CDK1	acetylation of CDK1 at K33 requires CDK1: cyclin B binding[51]	CDK master target of SUMOylation. Inhibition of CDK1 SUMOylation alters its status on CDK1 and its interacting proteins. Decreased CDK1 SUMOylation enhances its activity[52]	TRAP1 silencing enhances CDK1 ubiquitination, increases MAD2 degradation, and decreases nuclear translocation of the CDK1/cyclin B complex[53]

https://dx.doi.org/10.1021/acsomega.0c06168
ACS Omega XXXX, XXX, XXX−XXX

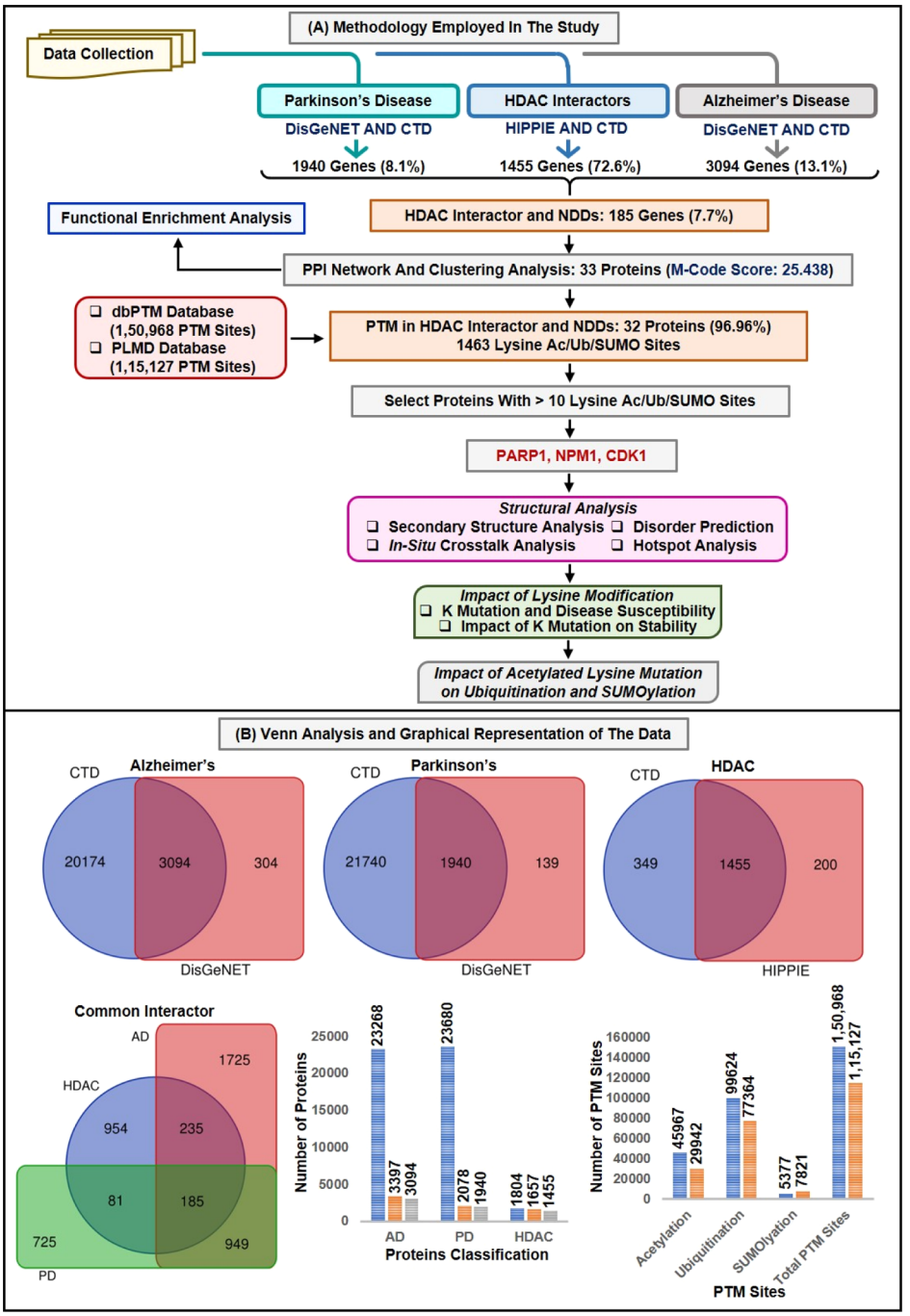

Figure 1. (A) Brief description of the methodology in the current study and (B) interactive Venn analysis of AD, PD, and HDAC interactors collected during the data extraction from different databases. For AD and PD, databases such as CTD and DisGeNET were used, whereas for HDAC interactors, databases such as CTD and HIPPIE were used. The figure also shows the Venn analysis of common genes involved in AD, PD, and HDAC interactors. Later on, bar graph analysis of protein extracted from databases for AD, PD, and HDAC interactors is given in the figure. The blue color in the graph represents the CTD database. The orange color represents the DisGeNET database for AD and PD and the HIPPIE database for HDAC interactors. Similarly, gray color represents the common among them. In the second bar graph, the blue color denotes the dbPTM database, whereas the orange color represents the PLMD database.

the brain through the ubiquitin−proteasome system (UPS), where any impairment in ubiquitination is known to exaggerate the neurodegenerative malignancies.[12] Similarly, SUMOylation is a process that involves the addition of a small ubiquitin-related modifier (SUMO) protein to the lysine side chain of regulatory proteins, which assists in protein folding and the clearance of toxic protein aggregates through chaperone-mediated autophagy, macroautophagy, and proteolytic systems.[13] Thus, targeting acetylation, ubiquitination, and SUMOylation pathways provides a new mechanism toward neuroprotection. Recent studies demonstrated the implementation of PTM crosstalk in the progression of NDDs, where negative crosstalk at the same site between different lysine modifications or commonly called as *in situ* crosstalk, has been highlighted on different occasions.[14,15] Previous studies confirmed that HDAC and its interactors play a crucial role

https://dx.doi.org/10.1021/acsomega.0c06168
ACS Omega XXXX, XXX, XXX−XXX

in the PTMs, such as acetylation, ubiquitination, and SUMOylation in neurodegeneration. For example, the noncovalent attachment of SUMO-2 to repressor element-1 silencing the transcription factor corepressor 1 (CoREST1) causes transcriptional activation and changes the acetylation level of coREST1/lysine (K)-specific demethylase 1 (LSD1)/HDAC target genes.[16] Similarly, decreased HDAC activity promotes the acetylation of Htt protein and also causes an increase in Ube2e3, SUMo2, and USp28 expression. Furthermore, decreased HDAC expression causes increased proteasomal degradation of mHtt aggregates due to the increased activity of HDAC interactor IkappaB kinase (IKK).[17] Tao et al. (2017) demonstrated that in APP/PS1 mice, acute Aβ increases the protein inhibitor of activated STAT 1 (PIAS1) and Mcl-1 expression through MAPK/ERK signaling activation. Increased PIAS1 expression enhances HDAC1 SUMOlyation in rat hippocampus.[18] Table1 describes the mechanism of different HDAC interactors in acetylation, ubiquitination, and SUMOylation. Our previous studies confirmed the role of lysine residues in ubiquitination[19] and acetylation,[20] which enables us to investigate the crosstalk between acetylation, ubiquitination, and SUMOylation at HDAC interactors. Moreover, acetylation, ubiquitination, and SUMOylation individual *in situ* crosstalk have been demonstrated in different large-scale proteome studies. However, crosstalk between the three has not been discussed until now, and the possible effect of acetylation on ubiquitination and SUMOylation is still unexplored.

Herein, we integrated AD- and PD-related genes with HDAC interactors and identified the HUB genes through the protein−protein interaction (PPI) network and clustering analysis. Furthermore, we examined the molecular functions and biological pathways in which shared genes (AD, PD, and HDAC) were involved. Last, PTM data were integrated through dbPTM and PLMD databases on 32 proteins, which are the regulatory sequences. Afterward, the proteins with high frequency for acetylation, ubiquitination, and SUMOylation were extracted among the 32 selected proteins. Finally, structural features and crosstalk sites were identified along with the impact of putative lysine mutation on disease susceptibility and protein stability. Last, our study investigates the potential implementation of the loss of crucial lysine residues on ubiquitination and SUMOylation function. Thus, to the best of our knowledge, this is the first study that deals with the crosstalk of acetylation with ubiquitination and SUMOylation simultaneously among HDAC interactors.

2. MATERIALS AND METHODS

2.1. Integration of PPI of HDAC, AD, and PD Genes. Data from two databases, such as DisGeNET (https://www.disgenet.org/)[54] and The Comparative Toxicogenomics Database (CTD) (http://ctdbase.org/),[55] were collected for genes associated with the progression of AD and PD. Similarly, information related to HDAC interactors was extracted from two databases, such as CTD and HIPPIE (http://cbdm-01.zdv.uni-mainz.de/~mschaefer/hippie/).[56] The databases were searched for duplicates, and redundancy in data was removed manually (Figure 1A). The proteins that were common in two databases were selected, and Venn analysis was carried out through Bioinformatics & Evolutionary Genomics Venn creator (http://bioinformatics.psb.ugent.be/webtools/Venn/) in order to identify common proteins in AD, PD, and HDAC interactors (Figure 1B). Furthermore, the PPI network and clustering analysis of proteins were carried out with the STRING database (https://string-db.org/)[57] and The Cytoscape Software (https://cytoscape.org/).[58]

2.2. Molecular Function and Biological Pathway Analysis of HDAC Interactors. Gene set enrichment analysis was performed to extract the information related to molecular functions and biological pathways in which the defined set of genes (HDAC interactors) were involved. The gene set's molecular functions were determined through a freely available software known as FunRich (http://www.funrich.org/).[59] Furthermore, signal transduction pathways in which the genes were involved were determined with the Kyoto encyclopedia of genes and genomes (KEGG) pathway database (https://www.genome.jp/kegg/).[60]

2.3. Integration of PTM Sites. Two databases, such as dbPTM (http://dbptm.mbc.nctu.edu.tw/)[61] and protein lysine modification database (PLMD) (http://plmd.biocuckoo.org/),[62] were used to extract the information of PTM (acetylation, ubiquitination, and SUMOylation) on regulatory proteins. Once the data were extracted, they were combined manually, and redundancy in PTM sites was removed. The PTM sites are sorted out according to PTM and modification sites.

2.4. Structural Analysis of Regulatory Proteins. *2.4.1. Secondary Structure Prediction.* PTM influences the secondary structure of the protein, which regulates its biological functions. We extracted the protein secondary structure information from DISOPRED3 (http://bioinf.cs.ucl.ac.uk/psipred/)[63] on both PTM and nonPTM lysine residues. DISOPRED3 is an open-source tool created by the UCL Department of Computer Science: Bioinformatics Group. The output was classified into three categories, such as coiled, helix, and strand.

2.4.2. Disorder Prediction. The sequences for regulatory proteins containing PTMs were extracted from the PMLD database. Structural order and disorder for these proteins were predicted through DISOPRED3, which uses PSIPRED software for disorder prediction. The extracted data were separated into two categories, such as the ordered region and the disordered region, as analyzed from the output.

2.4.3. PTM Crosstalk. *In situ* crosstalk analysis was performed to check the competition of PTMs on the same site. Data collected from PLMD and dbPTM were used to identify different PTMs on the same amino acid residues. The residues which have more than one PTM were selected for further analysis.

2.4.4. Hotspot Analysis. For all the identified PTM crosstalk sites, a motif of +7 and −6 amino acid stretch was extracted from the PLMD database from the corresponding protein sequence. For each identified acetylation site, the frequency of the probable PTM site was calculated in the vicinity for the defined motif. Every motif containing ≥2 lysine residues, excluding the central lysine residue, was called a PTM hotspot region. Furthermore, if a motif contained ≥2 PTMs on the same site, it will be considered a PTM crosstalk hotspot.

2.5. Impact of Lysine Modification. *2.5.1. Acetylated Lysine Mutation and Disease Susceptibility.* The functional impact of lysine mutations was studied with the help of online tools such as PMut (http://mmb.irbbarcelona.org/PMut/),[64] PolyPhen2 (http://genetics.bwh.harvard.edu/pph2/),[65] PANTHER (http://www.pantherdb.org/tools/csnpScoreForm.jsp),[66] and SNAP2 (https://rostlab.org/services/snap/).[67] The obtained results were transformed into numerical values

https://dx.doi.org/10.1021/acsomega.0c06168
ACS Omega XXXX, XXX, XXX−XXX

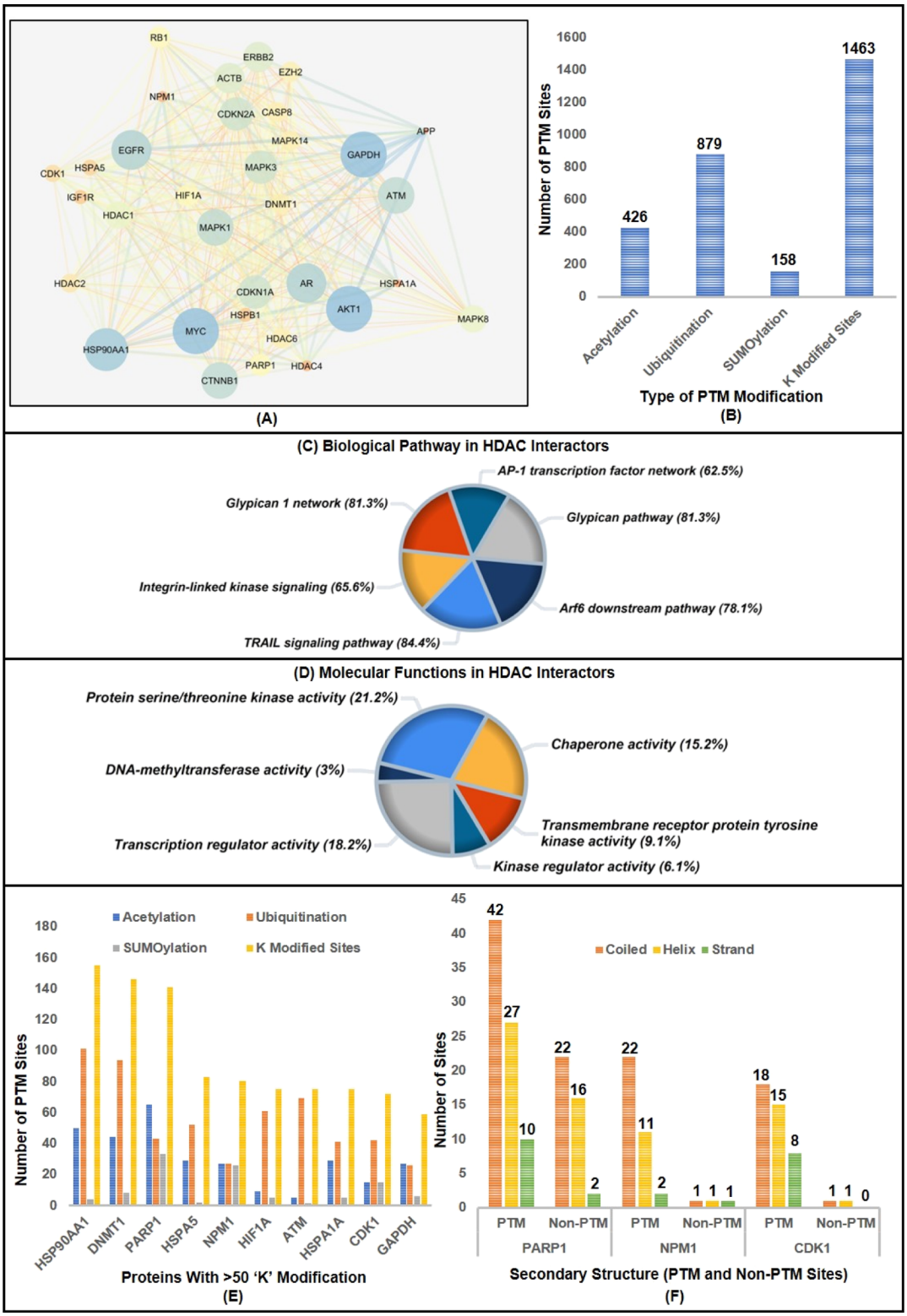

Figure 2. (A) PPI network of cluster 1 including 33 proteins extracted from the core PPI network after clustering analysis, (B) graphical representation of acetylation, ubiquitination, and SUMOylation sites in the protein present in cluster 1, (C) molecular functions of top 33 proteins involved in HDAC interactors, AD, and PD, (D) biological pathway analysis of HDAC interactors involved in the pathogenesis of AD and PD, (E) stack-bar representation of "K"-modified sites, and (F) secondary structure representation in PARP1, CDK1, and NPM1.

in order to visualize them on the stack bar graph. The particular mutation is said to be disease susceptible if its confidence score is greater than or equal to "3", which is called a threshold value.

2.5.2. Involvement of Acetylated Lysine Mutation on Protein Stability. The protein structure was analyzed for force field energy upon lysine mutation. The lysine residue was mutated into glutamine (Q) and leucine (L), and their total

https://dx.doi.org/10.1021/acsomega.0c06168
ACS Omega XXXX, XXX, XXX−XXX

Table 2. Functional Enrichment Analysis (Biological Pathways and Molecular Functions) Involved in Top Interacting HDAC Interactors[a]

Molecular Function	Number of Genes	Percentage of Genes	Fold Enrichment	P-Value	Mapped Genes
MOLECULAR FUNCTION					
Protein serine/threonine kinase activity	7	21.21	12.78	9.58384E-07	ATM; CDK1; MAPK8; AKT1; MAPK1; MAPK3; MAPK14;
Transcription regulator activity	6	18.18	3.96	0.0035	HDAC1; EZH2; HDAC2; HDAC4; RB1; HDAC6;
Transcription factor activity	2	6.06	1.31	0.45	MYC; HIF1A;
Transmembrane receptor protein tyrosine kinase activity	3	9.09	29.50	0.000142	IGF1R; ERBB2; EGFR;
Chaperone activity	5	15.15	21.83	3.04388E-06	HSPB1; HSPA5; NPM1; HSPA1A; HSP90AA1;
DNA-methyltransferase activity	1	3.03	138.29	0.0072	DNMT1;
BIOLOGICAL PATHWAY					
Glypican pathway	26	81.25	3.82	6.10568E-13	AR; HSPB1; ATM; **CDK1**; **NPM1**; CTNNB1; HSPA1A; MAPK8; MYC; IGF1R; HDAC1; HIF1A; APP; AKT1; HDAC2; CASP8; MAPK1; ERBB2; MAPK3; CDKN2A; RB1; HSP90AA1; EGFR; CDKN1A; GAPDH; MAPK14;
TRAIL signaling pathway	27	84.37	4.00	2.91586E-14	AR; HSPB1; ATM; **CDK1**; **NPM1**; CTNNB1; HSPA1A; MAPK8; MYC; IGF1R; HDAC1; **PARP1**; HIF1A; APP; AKT1; HDAC2; CASP8; MAPK1; ERBB2; MAPK3; CDKN2A; RB1; HSP90AA1; EGFR; CDKN1A; GAPDH; MAPK14;
Glypican 1 network	26	81.25	3.94	2.93211E-13	AR; HSPB1; ATM; **CDK1**; **NPM1**; CTNNB1; HSPA1A; MAPK8; MYC; IGF1R; HDAC1; HIF1A; APP; AKT1; HDAC2; CASP8; MAPK1; ERBB2; MAPK3; CDKN2A; RB1; HSP90AA1; EGFR; CDKN1A; GAPDH; MAPK14;
Integrin-linked kinase signaling	21	65.62	6.31	7.17368E-14	AR; HSPB1; ATM; **CDK1**; **NPM1**; CTNNB1; MAPK8; MYC; HDAC1; **PARP1**; HIF1A; AKT1; HDAC2; CASP8; MAPK1; MAPK3; CDKN2A; RB1; HSP90AA1; CDKN1A; MAPK14;
AP-1 transcription factor network	20	62.5	6.33	4.19493E-13	AR; HSPB1; ATM; **CDK1**; **NPM1**; CTNNB1; MAPK8; MYC; HDAC1; HIF1A; AKT1; HDAC2; CASP8; MAPK1; MAPK3; CDKN2A; RB1; HSP90AA1; CDKN1A; MAPK14;
Arf6 downstream pathway	25	78.12	3.82	3.54199E-12	AR; HSPB1; ATM; **CDK1**; **NPM1**; CTNNB1; HSPA1A; MAPK8; MYC; IGF1R; HDAC1; HIF1A; AKT1; HDAC2; CASP8; MAPK1; ERBB2; MAPK3; CDKN2A; RB1; HSP90AA1; EGFR; CDKN1A; GAPDH; MAPK14;

[a]In the above table, the blue color highlights the involvement of key HDAC interactors such as PARP1, CDK1, and NPM1 in the biological pathways. The table observed that CDK1 and NPM1 were involved in the glypican pathway, glypican 1 network, AP-1 transcription factor network, and Arf6 downstream pathway. Similarly, CDK1, PARP1, and NPM1 were involved in the TRAIL signaling pathway and integrin-linked kinase signaling.

energy was calculated with the help of an online prediction tool, that is, DynaMut (http://biosig.unimelb.edu.au/dynamut/).[68] The variation in the energy was estimated to observe the impact of lysine mutation on poly(ADP-ribose) polymerase 1 (PARP1) protein stability.

2.6. Crosstalk Analysis of Acetylated Lysine with Ubiquitination and SUMOylation. To investigate the contribution of lysine in acetylation, ubiquitination, and SUMOylation on the nearby sites, substitute lysine residue to glutamine (Q) and leucine (L). MutPred2 (http://mutpred.mutdb.org/),[69] an online tool, was used to predict the physical significance of lysine mutation on acetylation, ubiquitination, and SUMOylation. The same tool was also used to predict the affected motifs and pathogenic score upon lysine mutation with either glutamine or leucine. Furthermore, BDM-PUB (http://bdmpub.biocuckoo.org/)[70] and SUMOgo (http://predictor.nchu.edu.tw/SUMOgo/)[71] were employed to predict the potential ubiquitination and SUMOylation on nearby sites, respectively. The sites which are affected due to modification of lysine by either glutamine or leucine were tallied. The affected sites were classified into two groups that are gain in function on nearby sites and loss of function on nearby sites.

3. RESULTS AND DISCUSSION

3.1. Integration of Data and PTM Sites. After collecting data for HDAC interactors from two databases, such as HIPPIE and CTD, Venn analysis was performed to investigate the common interactors among both databases. A total of 1657 proteins were obtained from HIPPIE, and 1804 proteins were collected from the CTD database. The HDAC interactors were associated with class I, class II, and class IV HDACs. Venn analysis demonstrated that there are 1455 (72.6%) proteins that were common in both the databases. Similarly, for AD- and PD-associated protein, data were collected from CTD and DisGeNET. In CTD, 23268 and 23680 proteins were associated with AD and PD, respectively, whereas in DisGeNET, 3397 and 2078 proteins were involved in the pathogenesis of AD and PD, respectively. Furthermore, Venn analysis demonstrated the involvement of 3094 (13.1%) and 1940 (8.1%) proteins that were common in both the databases. Furthermore, HDAC interactor, AD, and PD data were combined manually to check the common proteins among them. A total of 185 proteins (7.7%) were found to be involved in the pathogenesis of AD and PD, which are associated with HDAC interactors.

Moreover, the PPI network and clustering analysis demonstrated the involvement of 33 proteins as top-ranked proteins (Figure 2A), which are associated with HDAC

https://dx.doi.org/10.1021/acsomega.0c06168
ACS Omega XXXX, XXX, XXX−XXX

Table 3. List of HDAC Interactors Having More Than 50 Lysine-Modified Sites (Acetylation, Ubiquitination, and SUMOylation)[a]

	Acetylation	Ubiquitination	SUMOylation	K Modified Sites
HSP90AA1	50	101	4	155
DNMT1	44	94	8	146
PARP1	65	43	33	141
HSPA5	29	52	2	83
NPM1	27	27	26	80
HIF1A	9	61	5	75
ATM	5	69	1	75
HSPA1A	29	41	5	75
CDK1	15	42	15	72
GAPDH	27	26	6	59

[a]The proteins marked in blue color and filled with gray color indicate that proteins have individual acetylation, ubiquitination, and SUMOylation sites more than 10.

interactors and the pathogenesis of NDDs. Furthermore, 150,968 PTM sites and 115,127 PTM sites were collected from the dbPTM database and PLMD database, respectively. A total of 45,967 and 29,942 acetylation sites, 99,624 and 77,364 ubiquitination sites, and 5377 and 7821 SUMOylation sites were extracted from the dbPTM and PLMD database. The extracted PTM sites were mapped to respective proteins. A total of 1463 potential acetylation (426), ubiquitination (879), and SUMOylation (158) sites were identified among 32 potential proteins for crosstalk analysis (Figure 2B).

3.2. Different Molecular Functions and Biological Pathways Followed by Top Interacting HDAC Partners. A total of 33 proteins identified through clustering analysis involving HDAC interactors, AD, and PD were subjected to the gene set enrichment analysis. Through this, molecular functions and biological processes involved in the pathogenesis of AD and PD through HDAC interaction were determined. The cutoff *p*-value for identifying the molecular function and biological pathways was set at less than 0.05, as shown in Table 2. Among molecular functions, protein serine/threonine kinase activity (21.21%), transcription regulator activity (18.18%), transcription factor activity (6.06%), transmembrane receptor protein tyrosine kinase activity (9.09%), chaperone activity (15.15%), and DNA-methyltransferase activity (3.03%) were highly enriched having a *p*-value less than 0.05 (Figure 2C). Similarly, among different biological pathways, glypican pathway (81.25%), TNF-related apoptosis-inducing ligand (TRAIL) signaling pathway (84.37%), glypican 1 network (81.25%), integrin-linked kinase signaling (65.62%), AP-1 transcription factor network (62.50%), and ADP-ribosylation factor 6 (Arf6) downstream pathway (78.12%) (Figure 2D). However, from Table 1, it is observed that only two pathways, such as the TRAIL signaling pathway and integrin-linked kinase signaling, constitute nucleophosmin (NPM1), cyclin-dependent kinase 1 (CDK1), and PARP1 (highlight in blue script with a green fill). Thus, the above-said pathways were crucial in the AD and PD pathogenesis with HDAC interactors.

3.3. Structural Characterization of PARP1, NPM1, and CDK1. For crosstalk analysis, a protein should be selected on the basis that the individual frequency of acetylation, ubiquitination, and SUMOylation is ≥10 (Table 3). Thus, PARP1, NPM1, and CDK1 were found to be the most prominent proteins for crosstalk between acetylation, ubiquitination, and SUMOylation (Figure 2E). Secondary structure analysis of PARP1, NPM1, and CDK1 revealed the importance of the coiled structure as compared to helix and strand in the PTM region. A coiled region regulates protein interactions and aggregation propensity, and thus mutations, which impair coiled regions and deregulate aggregation and protein activity, whereas mutations, which increase the coiled structure, enhance aggregation propensity.[72] In PARP1, 42 PTM sites fall into the coiled region, whereas 22 and 18 PTM sites formed a coiled structure in NPM1 and CDK1, respectively. Furthermore, our analysis demonstrates that the frequency of the helix structure is greater in PARP1 (27), NPM1 (11), and CDK1 (15) PTM sites as compared to that in nonPTM sites (Figure 2F) (Table 4). However, in NPM1, the frequency of strands is almost equal in both PTM and nonPTM sites.

Table 4. List of PTM and NonPTM Sites of PARP1, NPM1, and CDK1 (HDAC Interactors) in Coiled, Helix, and Strand Regions

	PARP1		NPM1		CDK1	
	PTM	nonPTM	PTM	nonPTM	PTM	nonPTM
coiled	42	22	22	1	18	1
helix	27	16	11	1	15	1
strand	10	2	2	1	8	0

PTMs preferred disordered regions as compared to the ordered region, which affect their functions and interactions. Furthermore, the involvement of PTM in the disordered region influences disorder to order transition, thus altering protein's stability and its associated mechanisms. This mechanism could be beneficial in diversifying the functional effect of protein by forming new structural sites or PPI by proving a binding region. Interestingly, our analysis of PTM sites revealed that 75% of sites fall in the ordered region, whereas 25% of sites fall in the disordered region (Figure 3A). Our data suggest that there is no PTM site in the disordered region for CDK1. Similarly, PARP1 has 12 acetylation, 9 SUMOylation, and 5 ubiquitination sites falling in the disordered region, whereas NPM1 has 16 acetylation, 21 SUMOylation, and 13 ubiquitination sites falling in the disordered region. Although previous studies reported that acetylation, ubiquitination, and SUMOylation preferred the ordered region, and thus, PARP1 has more acetylation and ubiquitination sites in the ordered region, which is 53 and 38, respectively. However, in NPM1, the number of acetylation sites in the ordered region is less than that of the disordered region, whereas the number of ubiquitination sites in the ordered region (18) is higher than that of ubiquitination sites in the disordered region (13). Similarly, the SUMOylation sites of PARP1 in the ordered region (24) are greater than that in the disordered region (9), whereas the SUMOylation sites

https://dx.doi.org/10.1021/acsomega.0c06168
ACS Omega XXXX, XXX, XXX−XXX

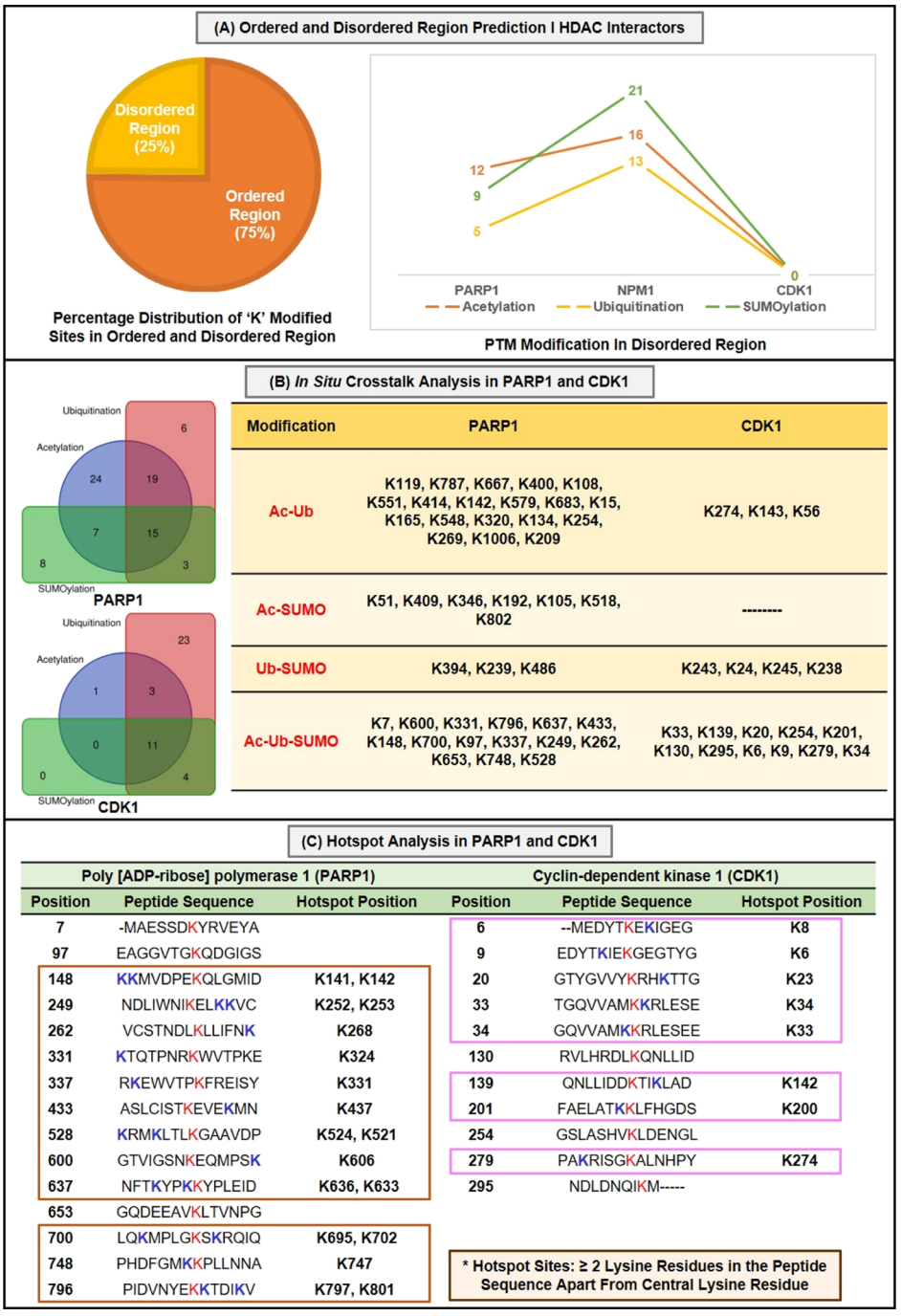

Figure 3. (A) Classification of PTM sites of PARP1, NPM1, and CDK1 into the ordered and disordered region, (B) crosstalk analysis between acetylation, ubiquitination, and SUMOylation in PARP1, CDK1, and NPM1, and (C) identification of hotspot regions in PARP1 and CDK1.

of NPM1 in the ordered region (5) are less than that in the disordered region (21). Thus, our study demonstrates the deviation in NPM1, whereas PARP1 data go well with the previously reported literature for acetylation, ubiquitination, and SUMOylation. Moreover, to identify PTM hotspots and crosstalk hotspots and their susceptibility to neurodegeneration, we separated the proteins based on PTM sites and hotspot sites. *In situ* crosstalk analysis in PARP1 revealed 15 potential acetylation/ubiquitination/SUMOylation sites, 19 acetylation/ubiquitination sites, 7 acetylation/SUMOylation sites, and 3 ubiquitination/SUMOylation sites. Similarly, in CDK1, there are 11 acetylation/ubiquitination/SUMOylation sites, 3 acetylation/ubiquitination sites, and 4 ubiquitination/SUMOylation sites (Figure 3B). The acetylation/ubiquitination/SUMOylation crosstalk sites of CDK1 and PARP1 were selected to identify crosstalk hotspots. Later on, we selected high-density stretches containing the +7 and −6 motif starch, excluding the central PTM. Our analysis observed that K148, K249, K528, K637, K700, and K796 have crosstalk hotspots in PARP1, whereas no such hotspot has been observed in CDK1 (Figure 3C).

3.4. Impact of Lysine Mutation on PARP1. The disease susceptibility of putative lysine mutation, either with glutamine or with leucine, was investigated through mutational analysis tools such as PANTHER, PMut, PolyPhen2, and SNAP2. Our results observed that all sites have an impact on disease

https://dx.doi.org/10.1021/acsomega.0c06168
ACS Omega XXXX, XXX, XXX−XXX

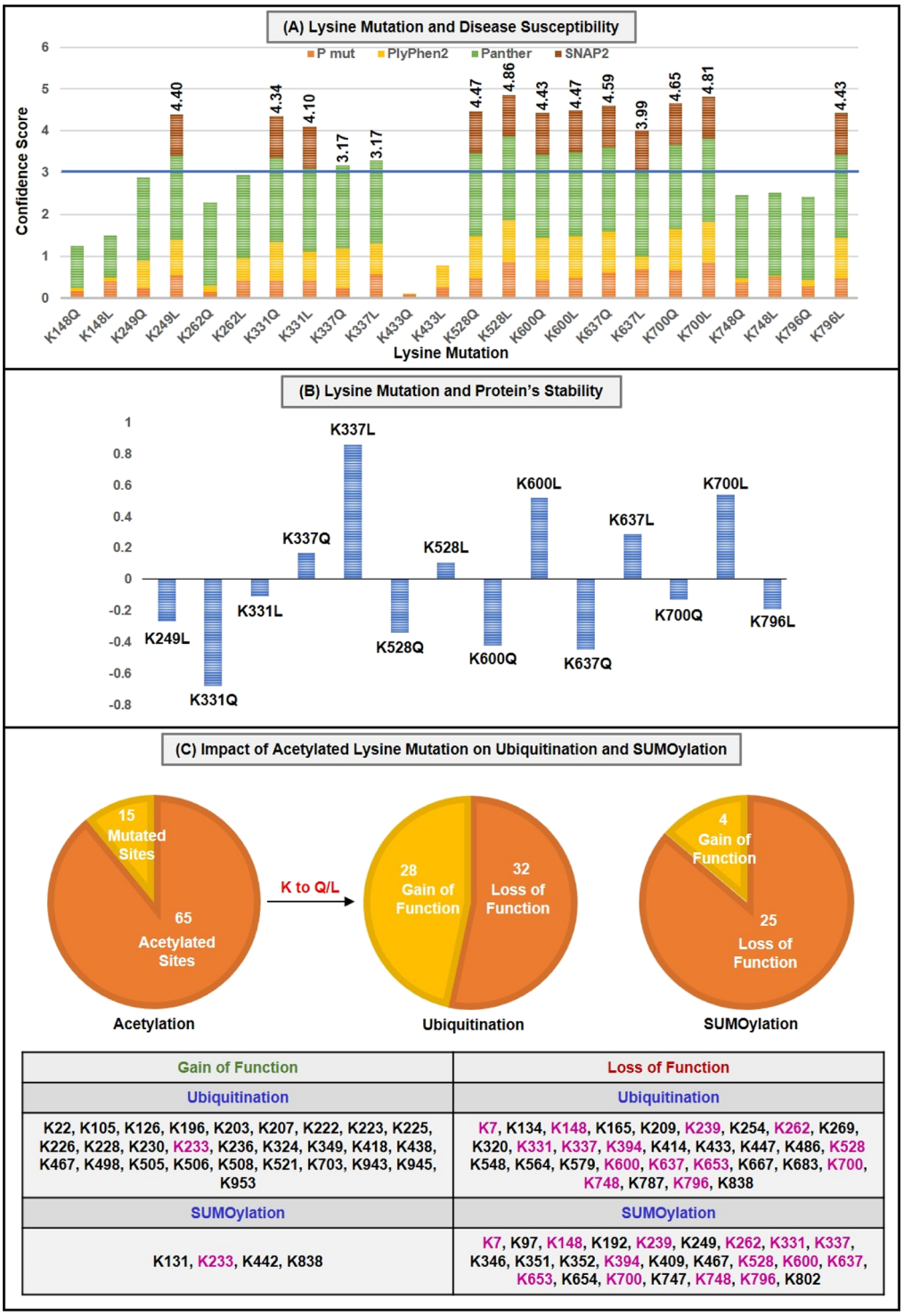

Gain of Function	Loss of Function
Ubiquitination	Ubiquitination
K22, K105, K126, K196, K203, K207, K222, K223, K225, K226, K228, K230, K233, K236, K324, K349, K418, K438, K467, K498, K505, K506, K508, K521, K703, K943, K945, K953	K7, K134, K148, K165, K209, K239, K254, K262, K269, K320, K331, K337, K394, K414, K433, K447, K486, K528 K548, K564, K579, K600, K637, K653, K667, K683, K700, K748, K787, K796, K838
SUMOylation	SUMOylation
K131, K233, K442, K838	K7, K97, K148, K192, K239, K249, K262, K331, K337, K346, K351, K352, K394, K409, K467, K528, K600, K637, K653, K654, K700, K747, K748, K796, K802

Figure 4. (A) Impact of lysine mutation in hotspot sites on disease susceptibility. The selected lysine residues such as K148, K249, K262, K331, K337, K433, K528, K600, K637, K700, K748, and K796 were subjected to mutation with both glutamine and leucine. Afterward, the mutations were checked for their impact on disease susceptibility. The results indicate that mutations such as K249L, K331Q, K331L, K337Q, K337L, K528Q, K528L, K600Q, K600L, K637Q, K637L, K700Q, K700L, and K796L have a pathogenic score above 3 (taken as reference). (B) Impact of lysine mutation on protein stability. Afterward, the selected disease-susceptible mutations were subjected to investigate their impact on protein structure stability. The results indicate that mutations such as K337Q, K337L, K528L, K600L, K637L, and K700L have a positive energy value and increase the protein stability. Similarly, K249L, K331Q, K331L, K528Q, K600Q, K637Q, K700Q, and K796L have a negative energy value and thus decrease the stability of the protein. (C) Investigation of acetylated lysine residue mutations on ubiquitination and SUMOylation. Here, the results suggest that out of a total of 65 potential lysine sites, 15 sites were mutated and predicted the change in ubiquitination and SUMOylation states of the PARP1. The results suggested that a total of 28 sites result in a gain of ubiquitination, whereas 32 sites exhibit loss of ubiquitination when mutated with either glutamine or leucine. Similarly, 4 sites result in a gain of SUMOylation, whereas 25 sites exhibit loss of SUMOylation when mutated with both glutamine and leucine. Furthermore, K233 exhibits gain of both ubiquitination and SUMOylation, whereas 14 sites result in a loss of both ubiquitination and SUMOylation as represented with pink color in the figure.

https://dx.doi.org/10.1021/acsomega.0c06168
ACS Omega XXXX, XXX, XXX−XXX

susceptibility. However, K249, K331, K337, K528, K600, K637, K700, and K796 have a high confidence score on disease susceptibility. The highly intolerant mutation that is disease susceptible is shown in Figure 4A and Table 5. The mutational

Table 5. Impact of PARP1's "K" Putative Mutation to Either Q or L on Disease Susceptibility Predicted with the Help of PMut, PolyPhen2, Panther, and SNAP2

Residue	Pmut	PolyPhen2	Panther	SNAP2	Confidence
K148Q	0.16	0.075	1	0	1.235
K148L	0.39	0.097	1	0	1.487
K249Q	0.23	0.656	2	0	2.886
K249L	0.54	0.86	2	1	4.4
K262Q	0.15	0.138	2	0	2.288
K262L	0.42	0.529	2	0	2.949
K331Q	0.42	0.924	2	1	4.344
K331L	0.41	0.696	2	1	4.106
K337Q	0.24	0.935	2	0	3.175
K337L	0.56	0.731	2	0	3.291
K433Q	0.08	0.005	0	0	0.085
K433L	0.26	0.522	0	0	0.782
K528Q	0.47	1	2	1	4.47
K528L	0.86	1	2	1	4.86
K600Q	0.43	1	2	1	4.43
K600L	0.48	0.999	2	1	4.479
K637Q	0.61	0.988	2	1	4.598
K637L	0.68	0.318	2	1	3.998
K700Q	0.66	0.997	2	1	4.657
K700L	0.84	0.979	2	1	4.819
K748Q	0.38	0.084	2	0	2.464
K748L	0.51	0.01	2	0	2.52
K796Q	0.28	0.148	2	0	2.428
K796L	0.47	0.961	2	1	4.431

"Probably Begin" and "Neutral" Marked as 0
"Possible Damage" Marked as 1
"Probably Damaging" and "Effect" Marked as 2

analysis study also revealed that the mutation of K249, K331, and K796 residue with leucine decreases PARP1 stability, whereas the mutation of K331, K528, K600, K637, and K700 with glutamine decreases PARP1 stability. However, the decrease in PARP1 stability at K331 is higher when mutated with glutamine as compared to mutation with leucine (Figure 4B). Thus, the investigation suggests that mutation with glutamine on crosstalk sites impacts the stability of PARP1 to a great extent as compared to leucine.

3.5. Crosstalk between Acetylation, Ubiquitination, and SUMOylation. Herein, we investigated the impact of an acetylated lysine residue on ubiquitination and SUMOylation, either at the same location or at the nearby sites. Our data revealed that putative mutation in 15 lysine-acetylated sites (K7, K97, K148, K249, K262, K331, K337, K433, K528, K600, K637, K653, K700, K748, and K796) out of a total of 65 acetylated sites in PARP1 affects the process of ubiquitination to a great extent as compared to SUMOylation (Table 6). Table 6 demonstrates the functional impact of putative lysine residue mutation on acetylation, ubiquitination, and SUMOylation. Furthermore, the collective results depict the role of putative lysine mutation on other cellular functions. The results revealed that mutation in K7, K249, K337, K528, and K796 results in loss of acetylation on the same site, whereas the loss of lysine on K637 results in loss of acetylation at K633. Similarly, the loss of putative lysine residue on K7 results in loss of ubiquitination at K7, whereas the loss of putative lysine residue on K600 results in the loss of SUMOylation at K600. Furthermore, our analysis demonstrates that putative mutation in lysine either with glutamine or with leucine at K528 results in loss of acetylation at K528, loss of ubiquitination at K528, and loss of SUMOylation at K524 with ELME000051, ELME000231, ELME000336, and PS00005 as the affected motifs. The results collectively show the importance of K528 of PARP1, which regulates acetylation, ubiquitination, and SUMOylation collectively in NDDs such as AD and PD. Furthermore, SUMOgo and BDM-PUB predict 117 SUMOylation sites and 80 ubiquitination sites, respectively. The cutoff value for SUMOylation and ubiquitination prediction was set at 0.5 and 1.5, respectively, which filters 12 SUMOylation sites and 39 ubiquitination sites in PARP1. Through the *in silico* approach, we substitute the lysine residue with glutamine and leucine, which promotes the neutral side chain and hydrophobic side chain, respectively. The predicted residues were then compared with the integrated ubiquitination and SUMOylation residues.

Here, we classified the affected ubiquitination and SUMOylation sites into two groups, which are the gain of function on nearby sites and loss of function on nearby sites. Our prediction demonstrated that the loss of crucial lysine residue alters the ubiquitination function to a great extent as compared to SUMOylation. In ubiquitination, 28 sites resulted in a gain of function, whereas 32 sites resulted in the loss of function. Similarly, in SUMOylation, only 4 sites were predicted to gain in function, whereas 25 sites resulted in the loss of function (Figure 4C). Furthermore, our results suggest that the loss of lysine residue at crucial sites either with glutamine or with leucine resulted in both ubiquitination and SUMOylation gain in function at K233. Similarly, 14 sites (K7, K148, K239, K262, K331, K337, K394, K528, K600, K637, K653, K700, K748, and K798) predicted to the loss in function for both ubiquitination and SUMOylation upon lysine substitution with either glutamine or leucine.

4. CONCLUSIONS

NDDs such as AD and PD are best characterized as progressive loss of neuronal cells leading to memory deficits and cognitive dysfunction. Mounting evidence suggests the possible implementation of PTMs in the pathogenesis of NDDs. One important PTM is acetylation, which is the process of the addition of the acetyl group to the N-terminal lysine residue. Acetylation and deacetylation are reversible processes, which are carried out with the help of HATs and HDAC enzymes, respectively. HATs/HDACs promote euchromatin and heterochromatin structure, respectively, which is involved in the transcriptional regulation. Apart from acetylation, ubiquitination and SUMOylation are two important PTMs, which help in the removal of misfolded toxic protein aggregates such as β-amyloid (Aβ) and α-synuclein. The common characteristic feature of acetylation, ubiquitination, and SUMOylation is the involvement of the lysine (K) residue, and thus, crosstalk between three PTMs becomes a fascinating topic for research. Studies indicate that the acetylation of PARP1 leads to its hyperactivation, which will intensify oxidative stress and cause mitochondrial dysfunction and subsequently neuronal cell death through parthanatos. Mounting evidence indicates that PARP1 acetylation increases Aβ and α-synuclein aggregates, which increases neurotoxicity.[78] Studies demonstrated that the activation of PARP1 decreases Aβ clearance and increases AIF expression. Love et al. (1999) first reported the activation of PARP1 in brain samples of AD patients. The authors conducted immunostaining analysis, which indicated the increased levels of PAR in AD patients in frontal and temporal lobes as compared to control patients.[79] Similarly, Abeti et al. (2011) in mixed cultures of

https://dx.doi.org/10.1021/acsomega.0c06168
ACS Omega XXXX, XXX, XXX−XXX

Table 6. Physical Significance of Lysine (K) Residue in PARP1 Acetylation, Ubiquitination, and SUMOylation through an Online Analysis Tool Known as MutPred2 (http://mutpred.mutdb.org/)[a]

lysine residue	mutation	affected molecular mechanism ($p \leq 0.05$)	affected motifs	pathogenic score
K7	Lys(K)-Gln(Q)			0.273
	Lys(K)-Leu(L)	loss of intrinsic disorder, **loss of acetylation at K7**, loss of phosphorylation at Y9, loss of methylation at K7, **loss of ubiquitination at K7**	ELME000149, PS00005	0.517
K97	Lys(K)-Gln(Q)			0.196
	Lys(K)-Leu(L)			0.383
K148	Lys(K)-Gln(Q)		ELME000155, PS00347	0.545
	Lys(K)-Leu(L)	gain of loop, altered transmembrane protein		0.742
K249	Lys(K)-Gln(Q)			0.479
	Lys(K)-Leu(L)	altered coiled, loss of intrinsic disorder, gain of loop, loss of helix, altered disordered interface, **loss of acetylation at K249**	ELME000002	0.737
K262	Lys(K)-Gln(Q)			0.453
	Lys(K)-Leu(L)	altered coiled		0.771
K331	Lys(K)-Gln(Q)			0.272
	Lys(K)-Leu(L)	altered transmembrane protein		0.575
K337	Lys(K)-Gln(Q)	**loss of acetylation at K337**	ELME000064, ELME000117, ELME000133, ELME000136, ELME000159	0.694
	Lys(K)-Leu(L)	**loss of ascetylation at K337**		0.825
K433	Lys(K)-Gln(Q)			0.113
	Lys(K)-Leu(L)			0.385
K528	Lys(K)-Gln(Q)			0.370
	Lys(K)-Leu(L)	loss of intrinsic disorder, **loss of acetylation at K528**, loss of strand, loss of helix, **loss of SUMOylation at K524**, **loss of ubiquitination at K528**, loss of methylation at K528	ELME000051, ELME000231, ELME000336, PS00005	0.687
K600	Lys(K)-Gln(Q)	**loss of SUMOylation at K600**, gain of GPI-anchor amidation at N599	PS00005	0.718
	Lys(K)-Leu(L)	**loss of SUMOylation at K600**		0.862
K637	Lys(K)-Gln(Q)	gain of strand, **loss of acetylation at K633**, altered transmembrane protein	ELME000163, ELME000233	0.713
	Lys(K)-Leu(L)	**loss of acetylation at K633**, altered transmembrane protein	ELME000120, ELME000233	0.886
K653	Lys(K)-Gln(Q)			0.273
	Lys(K)-Leu(L)			0.489
K700	Lys(K)-Gln(Q)			0.499
	Lys(K)-Leu(L)	altered coiled	ELME000333	0.768
K748	Lys(K)-Gln(Q)			0.562
	Lys(K)-Leu(L)	altered coiled		0.775
K796	Lys(K)-Gln(Q)	**loss of acetylation at K796**, altered transmembrane protein, altered coiled, gain of proteolytic cleavage at D791	ELME000020, ELME000120, ELME000173, ELME000233	0.546
	Lys(K)-Leu(L)	altered ordered interface, **loss of acetylation at K796**, altered transmembrane protein, altered coiled, gain of proteolytic cleavage at D791		0.776

[a]In the given table, the pathogenic score represents the probability that the amino acid substitution is pathogenic. A score threshold of 0.50 would suggest pathogenic for a particular substitution. However, a threshold of 0.68 yields a false positive rate of 10%, whereas a threshold of 0.80 yields a false positive rate of 5%.

hippocampal neurons and glial cells from a Sprague-Dawley rat concluded that PARP1 activation leads to oxidative stress in the presence of Aβ and causes metabolic failure and neuronal death.[80] Furthermore, Li et al. (2010) in ischemic mice demonstrated that PARP1 causes nuclear translocation of AIF, which results in neuronal cell death, whereas in another study conducted on rats, it was concluded that PARP1 increased expression causes suppression of the AIF protein expression.[81] In the 1-methyl-4-phenyl-1,2,3,6-tetrahydropyridine mouse model of PD, FAF1 plays a key role in PARP-1-dependent necrosis in response to oxidative stress. Furthermore, FAF1 depletion prevented PARP1-linked downstream events such as mitochondrial depolarization and nuclear translocation of AIF.[82] (Figure 5A).

In this study, we have examined the PTMs and their crosstalk in HDAC interactors, which are involved in the progression of NDDs such as AD and PD. The interactors of HDAC and proteins involved in AD and PD were collected from different databases such as HIPPIE, CTD, and DisGeNET. Venn analysis and PPI interaction of HDAC interactors, AD, and PD demonstrated the involvement of the top 33 proteins. Gene set enrichment analysis of 33 proteins confirmed the involvement of six different molecular functions and biological pathways in the pathogenesis of AD and PD through HDAC interactors. Protein serine/threonine kinase activity (21.21%), transcription regulator activity (18.18%), transcription factor activity (6.06%), transmembrane receptor protein tyrosine kinase activity (9.09%), chaperone activity (15.15%), and DNA-methyltransferase activity (3.03%) were the top-ranked molecular functions performed by HDAC interactors having a p-value less than 0.05. Similarly, glypican pathway (81.25%), TRAIL signaling pathway (84.37%), glypican 1 network (81.25%), integrin-linked kinase signaling (65.62%), AP-1 transcription factor network (62.50%), and Arf6 downstream pathway (78.12%) were the top-ranked biological pathways involved in the pathogenesis of AD and PD. Lately, 150,968 PTM sites from dbPTM and 115,127 PTM sites from PLMD were integrated to 32 proteins in which

https://dx.doi.org/10.1021/acsomega.0c06168
ACS Omega XXXX, XXX, XXX−XXX

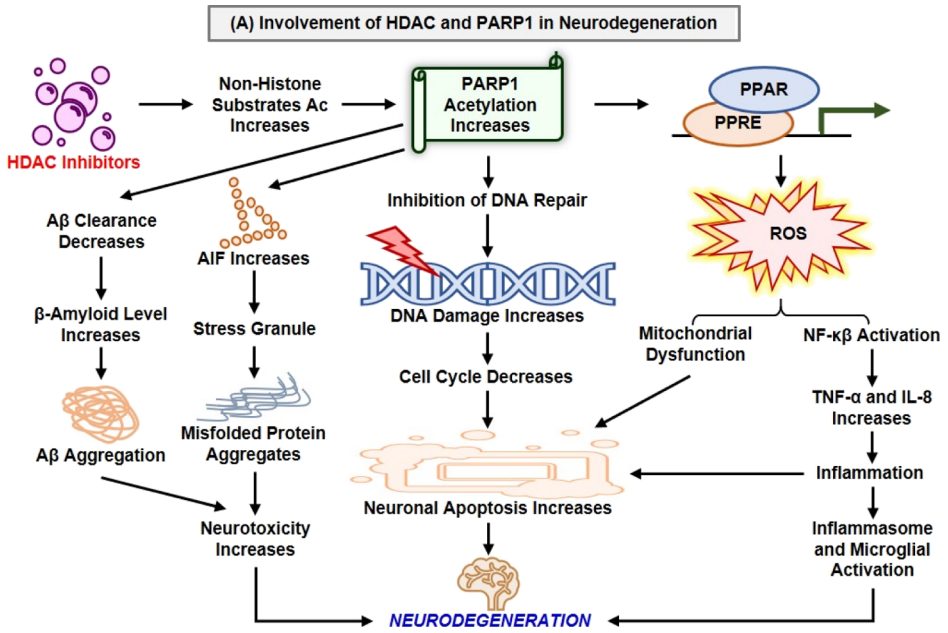

Figure 5. (A) Mechanism of PARP1 acetylation in NDDs. HDAC inhibitors increase the level of PARP1 acetylation and lead to PARP1 activation. This level is involved in the pathogenesis of AD.[73,74] Increased PARP1 acetylation levels induce increased levels of AIF expression and decreased levels of Aβ clearance, which in turn increase neurotoxicity by increasing the levels of misfolded protein aggregates.[75−77] Similarly, the increased PARP1 acetylation causes inhibition of DNA repair and increased ROS activity, which decreases the cell-cycle activity and increases the mitochondrial function, respectively. The decreased cell-cycle regulation and increased mitochondrial dysfunction cause increased neuronal apoptosis, which results in memory impairment and cognitive defects. Increased ROS activity by increased PARP1 acetylation leads to NF-$\kappa\beta$ activation, which increases proinflammatory cytokine release and results in microglial activation.

1489 were acetylation, ubiquitination, and SUMOylation sites. Among the 32 proteins, only three proteins, such as PARP1, NPM1, and CDK1, have individual acetylation, ubiquitination, and SUMOylation frequency greater than 10. Secondary structure prediction confirmed that 42, 22, and 18 PTM sites formed coiled structure in PARP1, NPM1, and CDK1, respectively, demonstrating that the probability of the PTM site is higher in the coiled region as compared to that in the helix and strand region. However, in NPM1, the probability of forming a strand region is higher as compared to that in PARP1 and CDK1. Further investigation revealed that 75% of PTM sites were associated with the ordered region, whereas 25% of PTM sites were associated with the disordered region. Thus, it will be concluded that the PTM distribution is higher in the ordered region as compared to that in the disordered region. Furthermore, crosstalk analysis of acetylation, ubiquitination, and SUMOylation sites in PARP1 revealed that 19 PTM sites were associated with acetylation and ubiquitination crosstalk. Similarly, acetylation-SUMOylation (7 sites), ubiquitination-SUMOylation (3 sites), and acetylation-ubiquitination-SUMOylation (15 sites) were identified. Hotspot analysis identified that K148, K249, K528, K637, K700, and K796 have potential crosstalk sites having $\geq$2 potential lysine residue in the vicinity of +7 and −6 motif sequence. In order to predict crucial crosstalk sites, the impact of putative lysine mutation on disease susceptibility was predicted, which demonstrated that among hotspot sites, K249L, K528Q, K528L, K637Q, K637L, K700Q, K700L, and K796L were involved in the progression of NDDs. Furthermore, our study investigated the role of putative lysine mutation on ubiquitination and SUMOylation, which shows that putative mutation in the lysine residue will result in the loss of SUMOylation and ubiquitination function. However, the gain of function after putative lysine mutation will also be observed, but the frequency is low as compared to the loss of function. In conclusion, K249, K331, K337, K528, K600, K637, K700, and K796 of PARP1 play a vital role in ubiquitination, acetylation, and SUMOylation crosstalk, which can potentially be useful for newer leads into acetylation mechanism, HDAC interactions, disease progression, biomarkers, or as a therapeutic target. Furthermore, from this study, we also concluded that site-specific inhibition of PARP1 acetylation (K249, K331, K337, K528, K600, K637, K700, and K796) and simultaneous activation of ubiquitination and SUMOylation at the same residues rescue neuronal cell death that is involved in AD pathology..

AUTHOR INFORMATION

Corresponding Author

Pravir Kumar − *Molecular Neuroscience and Functional Genomics Laboratory, Department of Biotechnology, Delhi Technological University (Formerly DCE), Delhi 110042, India;* orcid.org/0000-0001-7444-2344; Phone: +91-9818898622; Email: pravirkumar@dtu.ac.in, kpravir@gmail.com

Author

Rohan Gupta − *Molecular Neuroscience and Functional Genomics Laboratory, Department of Biotechnology, Delhi Technological University (Formerly DCE), Delhi 110042, India*

Complete contact information is available at: https://pubs.acs.org/10.1021/acsomega.0c06168

Author Contributions

P.K. and R.G. conceived and designed the manuscript. R.G. has collected, analyzed, and critically evaluated these data. P.K.

https://dx.doi.org/10.1021/acsomega.0c06168
ACS Omega XXXX, XXX, XXX−XXX

and R.G. have prepared figures and tables. P.K and R.G. analyzed the entire data and wrote the manuscript.

Notes

The authors declare no competing financial interest.

■ ACKNOWLEDGMENTS

We would like to thank the senior management of the Delhi Technological University for constant support and encouragement. This study was funded by the Delhi Technological University (Established under Govt. of Delhi Act 6 of 2009), Delhi-110042, India.

■ ABBREVIATIONS

PTMs, post-translational modifications; HDAC, histone deacetylase; NDDs, neurodegenerative diseases; PARP1, poly(ADP-ribose) polymerase 1; NPM1, nucleophosmin; CDK1, cyclin-dependent kinase 1; AD, Alzheimer's disease; PD, Parkinson's disease; HD, Huntington's disease; ALS, amyotrophic lateral sclerosis; HATs, histone acetyltransferases; HDACs, histone deacetylases; UPS, ubiquitin proteasome system; SUMO, small ubiquitin-related modifier; CoREST1, repressor element-1 silencing transcription factor corepressor 1; LSD1, lysine (K)-specific demethylase 1; IKK, IkappaB kinase; PIAS1, protein inhibitor of activated STAT 1; CTD, Comparative Toxicogenomics Database; KEGG, Kyoto Encyclopedia of Genes and Genomes; PLMD, protein lysine modifications database; Arf6, ADP-ribosylation factor 6; TRAIL, TNF-related apoptosis-inducing ligand; HSP90AA1, heat shock protein 90α; DNMT1, DNA methyltransferases 1; HSPA5, heat shock protein family A (Hsp70) member 5; HIF1A, hypoxia-inducible factor 1-alpha; ATM, ataxia-telangiectasia mutated; HSPA1A, heat shock 70 kDa protein 1; GAPDH, glyceraldehyde 3-phosphate dehydrogenase

■ REFERENCES

(1) Dawson, T. M.; Golde, T. E.; Lagier-Tourenne, C. Animal Models of Neurodegenerative Diseases. *Nat. Neurosci.* **2018**, *21*, 1370.
(2) Didonna, A.; Benetti, F. Post-Translational Modifications in Neurodegeneration. *AIMS Biophys.* **2016**, *3*, 27.
(3) Barrett, P. J.; Timothy Greenamyre, J. Post-Translational Modification of α-Synuclein in Parkinson's Disease. *Brain Res.* **2015**, *1628*, 247.
(4) Buuh, Z. Y.; Lyu, Z.; Wang, R. E. Interrogating the Roles of Post-Translational Modifications of Non-Histone Proteins. *J. Med. Chem.* **2018**, *61*, 3239.
(5) Bannister, A. J.; Kouzarides, T. Regulation of Chromatin by Histone Modifications. *Cell Res.* **2011**, *21*, 381.
(6) Eberharter, A.; Becker, P. B. Histone Acetylation: A Switch between Repressive and Permissive Chromatin. Second in Review on Chromatin Dynamics. *EMBO Rep* **2002**, *3*, 224.
(7) Görisch, S. M.; Wachsmuth, M.; Tóth, K. F.; Lichter, P.; Rippe, K. Histone Acetylation Increases Chromatin Accessibility. *J. Cell Sci.* **2005**, *118*, 5825.
(8) Hassan, A. H.; Prochasson, P.; Neely, K. E.; Galasinski, S. C.; Chandy, M.; Carrozza, M. J.; Workman, J. L. Function and Selectivity of Bromodomains in Anchoring Chromatin-Modifying Complexes to Promoter Nucleosomes. *Cell* **2002**, *111*, 369.
(9) Mujtaba, S.; He, Y.; Zeng, L.; Yan, S.; Plotnikova, O.; Sachchidanand; Sanchez, R.; Zeleznik-Le, N. J.; Ronai, Z.; Zhou, M. M. Structural Mechanism of the Bromodomain of the Coactivator CBP in P53 Transcriptional Activation. *Mol. Cell* **2004**, *13*, 251.
(10) Esteves, A. R.; Palma, A. M.; Gomes, R.; Santos, D.; Silva, D. F.; Cardoso, S. M. Acetylation as a Major Determinant to Microtubule-Dependent Autophagy: Relevance to Alzheimer's and Parkinson Disease Pathology. *Biochim. Biophys. Acta, Mol. Basis Dis.* **2019**, *1865*, 2008.
(11) Sharma, S.; Sarathlal, K. C.; Taliyan, R. Epigenetics in Neurodegenerative Diseases: The Role of Histone Deacetylases. *CNS Neurol. Disord.—Drug Targets* **2019**, *18*, 11.
(12) Kumar, D.; Ambasta, R. K.; Kumar, P. Ubiquitin Biology in Neurodegenerative Disorders: From Impairment to Therapeutic Strategies. *Ageing Res. Rev.* **2020**, *12*, 101078.
(13) Yau, T.-Y.; Molina, O.; Courey, A. J. SUMOylation in Development and Neurodegeneration. *Development* **2020**, *147*, dev175703.
(14) Olsen, C. A. An Update on Lysine Deacylases Targeting the Expanding "Acylome.". *ChemMedChem* **2014**, *9*, 434.
(15) Sabari, B. R.; Zhang, D.; Allis, C. D.; Zhao, Y. Metabolic Regulation of Gene Expression through Histone Acylations. *Nat. Rev. Mol. Cell Biol.* **2017**, *18*, 90.
(16) Ouyang, J.; Shi, Y.; Valin, A.; Xuan, Y.; Gill, G. Direct Binding of CoREST1 to SUMO-2/3 Contributes to Gene-Specific Repression by the LSD1/CoREST1/HDAC Complex. *Mol. Cell* **2009**, *34*, 145.
(17) Jia, H.; Kast, R. J.; Steffan, J. S.; Thomas, E. A. Selective Histone Deacetylase (HDAC) Inhibition Imparts Beneficial Effects in Huntington's Disease Mice: Implications for the Ubiquitin-Proteasomal and Autophagy Systems. *Hum. Mol. Genet.* **2012**, *21*, 5280.
(18) Tao, C. C.; Hsu, W. L.; Ma, Y. L.; Cheng, S. J.; Lee, E. H. Epigenetic Regulation of HDAC1 SUMOylation as an Endogenous Neuroprotection against Aβ Toxicity in a Mouse Model of Alzheimer's Disease. *Cell Death Differ.* **2017**, *24*, 597.
(19) Kumar, D.; Kumar, P. Integrated Mechanism of Lysine 351, PARK2, and STUB1 in AβPP Ubiquitination. *J. Alzheimer's Dis.* **2019**, *68*, 1125.
(20) Gupta, R.; Ambasta, R. K.; Kumar, P. Identification of Novel Class I and Class IIb Histone Deacetylase Inhibitor for Alzheimer's Disease Therapeutics. *Life Sci* **2020**, *256*, 117912.
(21) Shandilya, J.; Swaminathan, V.; Gadad, S. S.; Choudhari, R.; Kodaganur, G. S.; Kundu, T. K. Acetylated NPM1 Localizes in the Nucleoplasm and Regulates Transcriptional Activation of Genes Implicated in Oral Cancer Manifestation. *Mol. Cell. Biol.* **2009**, *29*, 5115.
(22) Ren, Z.; Aerts, J. L.; Vandenplas, H.; Wang, J. A.; Gorbenko, O.; Chen, J. P.; Giron, P.; Heirman, C.; Goyvaerts, C.; Zacksenhaus, E.; Minden, M. D.; Stambolic, V.; Breckpot, K.; De Grève, J. Phosphorylated STAT5 Regulates P53 Expression via BRCA1/BARD1-NPM1 and MDM2. *Cell Death Dis.* **2016**, *7*, No. e2560.
(23) Neo, S. H.; Itahana, Y.; Alagu, J.; Kitagawa, M.; Guo, A. K.; Lee, S. H.; Tang, K.; Itahana, K. TRIM28 Is an E3 Ligase for ARF-Mediated NPM1/B23 SUMOylation That Represses Centrosome Amplification. *Mol. Cell. Biol.* **2015**, *35*, 2851.
(24) Geng, H.; Liu, Q.; Xue, C.; David, L. L.; Beer, T. M.; Thomas, G. V.; Dai, M. S.; Qian, D. Z. HIF1α Protein Stability Is Increased by Acetylation at Lysine 709. *J. Biol. Chem.* **2012**, *287*, 35496.
(25) Ferreira, J. V.; Soares, A. R.; Ramalho, J. S.; Pereira, P.; Girao, H. K63 Linked Ubiquitin Chain Formation Is a Signal for HIF1A Degradation by Chaperone-Mediated Autophagy. *Sci. Rep.* **2015**, *5*, 1.
(26) Berta, M. A.; Mazure, N.; Hattab, M.; Pouysségur, J.; Brahimi-Horn, M. C. SUMOylation of Hypoxia-Inducible Factor-1α Reduces Its Transcriptional Activity. *Biochem. Biophys. Res. Commun.* **2007**, *360*, 646.
(27) Kerr, E.; Holohan, C.; McLaughlin, K. M.; Majkut, J.; Dolan, S.; Redmond, K.; Riley, J.; McLaughlin, K.; Stasik, I.; Crudden, M.; Van Schaeybroeck, S.; Fenning, C.; O'Connor, R.; Kiely, P.; Sgobba, M.; Haigh, D.; Johnston, P. G.; Longley, D. B. Identification of an Acetylation-Dependant Ku70/FLIP Complex That Regulates FLIP Expression and HDAC Inhibitor-Induced Apoptosis. *Cell Death Differ* **2012**, *19*, 1317.
(28) Besnault-Mascard, L.; Leprince, C.; Auffredou, M. T.; Meunier, B.; Bourgeade, M. F.; Camonis, J.; Lorenzo, H. K.; Vazquez, A. Caspase-8 Sumoylation Is Associated with Nuclear Localization. *Oncogene* **2005**, *24*, 3268.

https://dx.doi.org/10.1021/acsomega.0c06168
ACS Omega XXXX, XXX, XXX−XXX

(29) Wu, J. Y.; Xiang, S.; Zhang, M.; Fang, B.; Huang, H.; Kwon, O. K.; Zhao, Y.; Yang, Z.; Bai, W.; Bepler, G.; Mary Zhang, X. Histone Deacetylase 6 (HDAC6) Deacetylates Extracellular Signal-Regulated Kinase 1 (ERK1) and Thereby Stimulates ERK1 Activity. *J. Biol. Chem.* **2018**, *293*, 1976.
(30) Lu, Z.; Xu, S.; Joazeiro, C.; Cobb, M. H.; Hunter, T. The PHD Domain of MEKK1 Acts as an E3 Ubiquitin Ligase and Mediates Ubiquitination and Degradation of ERK1/2. *Mol. Cell* **2002**, *9*, 945.
(31) Du, C. P.; Wang, M.; Geng, C.; Hu, B.; Meng, L.; Xu, Y.; Cheng, B.; Wang, N.; Zhu, Q. J.; Hou, X. Y. Activity-Induced SUMOylation of Neuronal Nitric Oxide Synthase Is Associated with Plasticity of Synaptic Transmission and Extracellular Signal-Regulated Kinase 1/2 Signaling. *Antioxid. Redox Signaling* **2020**, *32*, 18.
(32) Hassa, P. O.; Haenni, S. S.; Buerki, C.; Meier, N. I.; Lane, W. S.; Owen, H.; Gersbach, M.; Imhof, R.; Hottiger, M. O. Acetylation of Poly(ADP-Ribose) Polymerase-1 by P300/CREB-Binding Protein Regulates Coactivation of NF-KB-Dependent Transcription. *J. Biol. Chem.* **2005**, *280*, 40450.
(33) Wang, T.; Simbulan-Rosenthal, C. M.; Smulson, M. E.; Chock, P. B.; Yang, D. C. H. Polyubiquitylation of PARP-1 through Ubiquitin K48 Is Modulated by Activated DNA, NAD+, and Dipeptides. *J. Cell. Biochem.* **2008**, *104*, 318.
(34) Messner, S.; Schuermann, D.; Altmeyer, M.; Kassner, I.; Schmidt, D.; Schär, P.; Müller, S.; Rottiger, M. O. Sumoylation of Poly(ADP-ribose) Polymerase 1 Inhibits Its Acetylation and Restrains Transcriptional Coactivator Function. *FASEB J* **2009**, *23*, 3978.
(35) Iaconelli, J.; Lalonde, J.; Watmuff, B.; Liu, B.; Mazitschek, R.; Haggarty, S. J.; Karmacharya, R. Lysine Deacetylation by HDAC6 Regulates the Kinase Activity of AKT in Human Neural Progenitor Cells. *ACS Chem. Biol.* **2017**, *12*, 2139.
(36) Yang, W.-L.; Wang, J.; Chan, C.-H.; Lee, S.-W.; Campos, A. D.; Lamothe, B.; Hur, L.; Grabiner, B. C.; Lin, X.; Darnay, B. G.; Lin, H.-K. The E3 Ligase TRAF6 Regulates Akt Ubiquitination and Activation. *Science* **2009**, *325*, 1134−1138.
(37) Risso, G.; Pelisch, F.; Pozzi, B.; Mammi, P.; Blaustein, M.; Colman-Lerner, A.; Srebrow, A. Modification of Akt by SUMO Conjugation Regulates Alternative Splicing and Cell Cycle. *Cell Cycle* **2013**, *12*, 3354.
(38) Scott, G. K.; Marx, C.; Berger, C. E.; Saunders, L. R.; Verdin, E.; Schäfer, S.; Jung, M.; Benz, C. C. Destabilization of ERBB2 Transcripts by Targeting 3′ Untranslated Region Messenger RNA Associated HuR and Histone Deacetylase-6. *Mol. Cancer Res.* **2008**, *6*, 1250.
(39) Xu, W.; Marcu, M.; Yuan, X.; Mimnaugh, E.; Patterson, C.; Neckers, L. Chaperone-Dependent E3 Ubiquitin Ligase CHIP Mediates a Degradative Pathway for c-ErbB2/Neu. *Proc. Natl. Acad. Sci. U.S.A.* **2002**, *99*, 12874.
(40) Brix, D. M.; Tvingsholm, S. A.; Hansen, M. B.; Clemmensen, K. B.; Ohman, T.; Siino, V.; Lambrughi, M.; Hansen, K.; Puustinen, P.; Gromova, I.; James, P.; Papaleo, E.; Varjosalo, M.; Moreira, J.; Jäättelä, M.; Kallunki, T. Release of Transcriptional Repression via ErbB2-Induced, SUMO-Directed Phosphorylation of Myeloid Zinc Finger-1 Serine 27 Activates Lysosome Redistribution and Invasion. *Oncogene* **2019**, *3*, ra80.
(41) Du, Z.; Song, J.; Wang, Y.; Zhao, Y.; Guda, K.; Yang, S.; Kao, H. Y.; Xu, Y.; Willis, J.; Markowitz, S. D.; Sedwick, D.; Ewing, R. M.; Wang, Z. DNMT1 Stability Is Regulated by Proteins Coordinating Deubiquitination and Acetylation-Driven Ubiquitination. *Sci. Signal.* **2010**, *3*, ra80.
(42) Lee, B.; Muller, M. T. SUMOylation Enhances DNA Methyltransferase 1 Activity. *Biochem. J.* **2009**, *421*, 449.
(43) Faiola, F.; Liu, X.; Lo, S.; Pan, S.; Zhang, K.; Lymar, E.; Farina, A.; Martinez, E. Dual Regulation of C-Myc by P300 via Acetylation-Dependent Control of Myc Protein Turnover and Coactivation of Myc-Induced Transcription. *Mol. Cell. Biol.* **2005**, *25*, 10220.
(44) Popov, N.; Wanzel, M.; Madiredjo, M.; Zhang, D.; Beijersbergen, R.; Bernards, R.; Moll, R.; Elledge, S. J.; Eilers, M. The Ubiquitin-Specific Protease USP28 Is Required for MYC Stability. *Nat. Cell Biol.* **2007**, *9*, 765.
(45) González-Prieto, R.; Cuijpers, S. A. G.; Kumar, R.; Hendriks, I. A.; Vertegaal, A. C. O. C-Myc Is Targeted to the Proteasome for Degradation in a SUMOylation-Dependent Manner, Regulated by PIAS1, SENP7 and RNF4. *Cell Cycle* **2015**, *14*, 1859.
(46) Hendrickx, A.; Pierrot, N.; Tasiaux, B.; Schakman, O.; Kienlen-Campard, P.; De Smet, C.; Octave, J. N. Epigenetic Regulations of Immediate Early Genes Expression Involved in Memory Formation by the Amyloid Precursor Protein of Alzheimer Disease. *PLoS One* **2014**, *9*, No. e99467.
(47) Scuderi, C.; Steardo, L.; Esposito, G. Cannabidiol Promotes Amyloid Precursor Protein Ubiquitination and Reduction of Beta Amyloid Expression in SHSY5YAPP+ Cells through PPARγ Involvement. *Phyther. Res.* **2014**, *28*, 1007.
(48) Maruyama, T.; Abe, Y.; Niikura, T. SENP1 and SENP2 Regulate SUMOylation of Amyloid Precursor Protein. *Heliyon* **2018**, *4*, No. e00601.
(49) Li, T.; Liu, M.; Feng, X.; Wang, Z.; Das, I.; Xu, Y.; Zhou, X.; Sun, Y.; Guan, K. L.; Xiong, Y.; Lei, Q. Y. Glyceraldehyde-3-Phosphate Dehydrogenase Is Activated by Lysine 254 Acetylation in Response to Glucose Signal. *J. Biol. Chem.* **2014**, *289*, 3775.
(50) Lee, S. B.; Kim, C. K.; Lee, K. H.; Ahn, J. Y. S-Nitrosylation of B23/Nucleophosmin by GAPDH Protects Cells from the SIAH1-GAPDH Death Cascade. *J. Cell Biol.* **2012**, *199*, 65.
(51) Deota, S.; Rathnachalam, S.; Namrata, K.; Boob, M.; Fulzele, A.; Radhika, S.; Ganguli, S.; Balaji, C.; Kaypee, S.; Vishwakarma, K. K.; Kundu, T. K.; Bhandari, R.; Gonzalez de Peredo, A.; Mishra, M.; Venkatramani, R.; Kolthur-Seetharam, U. Allosteric Regulation of Cyclin-B Binding by the Charge State of Catalytic Lysine in CDK1 Is Essential for Cell-Cycle Progression. *J. Mol. Biol.* **2019**, *431*, 2127.
(52) Xiao, Y.; Lucas, B.; Molcho, E.; Schiff, T.; Vigodner, M. Inhibition of CDK1 Activity by Sumoylation. *Biochem. Biophys. Res. Commun.* **2016**, *478*, 919.
(53) Sisinni, L.; Maddalena, F.; Condelli, V.; Pannone, G.; Simeon, V.; Li Bergolis, V.; Lopes, E.; Piscazzi, A.; Matassa, D. S.; Mazzoccoli, C.; Nozza, F.; Lettini, G.; Amoroso, M. R.; Bufo, P.; Esposito, F.; Landriscina, M. TRAP1 Controls Cell Cycle G2−M Transition through the Regulation of CDK1 and MAD2 Expression/Ubiquitination. *J. Pathol.* **2017**, *243*, 123.
(54) Piñero, J.; Bravo, Á.; Queralt-Rosinach, N.; Gutiérrez-Sacristán, A.; Deu-Pons, J.; Centeno, E.; García-García, J.; Sanz, F.; Furlong, L. I. DisGeNET: A Comprehensive Platform Integrating Information on Human Disease-Associated Genes and Variants. *Nucleic Acids Res* **2017**, *45*, D833−D839.
(55) Davis, A. P.; Grondin, C. J.; Johnson, R. J.; Sciaky, D.; McMorran, R.; Wiegers, J.; Wiegers, T. C.; Mattingly, C. J. The Comparative Toxicogenomics Database: Update 2019. *Nucleic Acids Res* **2019**, *47*, D948.
(56) Alanis-Lobato, G.; Andrade-Navarro, M. A.; Schaefer, M. H. HIPPIE v2.0: Enhancing Meaningfulness and Reliability of Protein-Protein Interaction Networks. *Nucleic Acids Res* **2017**, *45*, D408−D414.
(57) Szklarczyk, D.; Morris, J. H.; Cook, H.; Kuhn, M.; Wyder, S.; Simonovic, M.; Santos, A.; Doncheva, N. T.; Roth, A.; Bork, P.; Jensen, L. J.; Von Mering, C. The STRING Database in 2017: Quality-Controlled Protein-Protein Association Networks, Made Broadly Accessible. *Nucleic Acids Res* **2017**, *45*, D362−D368.
(58) Cline, M. S.; Smoot, M.; Cerami, E.; Kuchinsky, A.; Landys, N.; Workman, C.; Christmas, R.; Avila-Campilo, I.; Creech, M.; Gross, B.; Hanspers, K.; Isserlin, R.; Kelley, R.; Killcoyne, S.; Lotia, S.; Maere, S.; Morris, J.; Ono, K.; Pavlovic, V.; Pico, A. R.; Vailaya, A.; Wang, P. L.; Adler, A.; Conklin, B. R.; Hood, L.; Kuiper, M.; Sander, C.; Schmulevich, I.; Schwikowski, B.; Warner, G. J.; Ideker, T.; Bader, G. D. Integration of Biological Networks and Gene Expression Data Using Cytoscape. *Nat. Protoc.* **2007**, *2*, 2366.
(59) Pathan, M.; Keerthikumar, S.; Ang, C. S.; Gangoda, L.; Quek, C. Y. J.; Williamson, N. A.; Mouradov, D.; Sieber, O. M.; Simpson, R. J.; Salim, A.; Bacic, A.; Hill, A. F.; Stroud, D. A.; Ryan, M. T.; Agbinya, J. I.; Mariadason, J. M.; Burgess, A. W.; Mathivanan, S.

https://dx.doi.org/10.1021/acsomega.0c06168
ACS Omega XXXX, XXX, XXX−XXX

FunRich: An Open Access Standalone Functional Enrichment and Interaction Network Analysis Tool. *Proteomics* **2015**, *15*, 2597.
(60) Kanehisa, M.; Furumichi, M.; Tanabe, M.; Sato, Y.; Morishima, K. KEGG: New Perspectives on Genomes, Pathways, Diseases and Drugs. *Nucleic Acids Res* **2017**, *45*, D353.
(61) Huang, K. Y.; Lee, T. Y.; Kao, H. J.; Ma, C. T.; Lee, C. C.; Lin, T. H.; Chang, W. C.; Huang, H. Da. DbPTM in 2019: Exploring Disease Association and Cross-Talk of Post-Translational Modifications. *Nucleic Acids Res* **2019**, *47*, D298.
(62) Xu, H.; Zhou, J.; Lin, S.; Deng, W.; Zhang, Y.; Xue, Y. PLMD: An Updated Data Resource of Protein Lysine Modifications. *J. Genet. Genom.* **2017**, *44*, 243.
(63) Jones, D. T.; Cozzetto, D. DISOPRED3: Precise Disordered Region Predictions with Annotated Protein-Binding Activity. *Bioinformatics* **2015**, *31*, 857.
(64) López-Ferrando, V.; Gazzo, A.; De La Cruz, X.; Orozco, M.; Gelpí, J. L. PMut: A Web-Based Tool for the Annotation of Pathological Variants on Proteins, 2017 Update. *Nucleic Acids Res.* **2017**, *45*, W222.
(65) Adzhubei, I.; Jordan, D. M.; Sunyaev, S. R. Predicting Functional Effect of Human Missense Mutations Using PolyPhen-2. *Curr. Protoc. Hum. Genet.* **2013**, *76*, 7.
(66) Mi, H.; Huang, X.; Muruganujan, A.; Tang, H.; Mills, C.; Kang, D.; Thomas, P. D. PANTHER Version 11: Expanded Annotation Data from Gene Ontology and Reactome Pathways, and Data Analysis Tool Enhancements. *Nucleic Acids Res* **2017**, *45*, D183.
(67) Hecht, M.; Bromberg, Y.; Rost, B. Better Prediction of Functional Effects for Sequence Variants. *BMC Genom.* **2015**, *16*, 1.
(68) Rodrigues, C. H. M.; Pires, D. E. V.; Ascher, D. B. DynaMut: Predicting the Impact of Mutations on Protein Conformation, Flexibility and Stability. *Nucleic Acids Res* **2018**, *46*, W350.
(69) Pejaver, V.; Urresti, J.; Lugo-Martinez, J.; Pagel, K. A.; Lin, G. N.; Nam, H. J.; Mort, M.; Cooper, D. N.; Sebat, J.; Iakoucheva, L. M.; Mooney, S. D.; Radivojac, P. Inferring the molecular and phenotypic impact of amino acid variants with MutPred2. *Nat. Commun.* **2020**, *11*, 5918.
(70) Cai, B.; Jiang, X. Computational Methods for Ubiquitination Site Prediction Using Physicochemical Properties of Protein Sequences. *BMC Bioinf.* **2016**, *17*, 1.
(71) Chang, C. C.; Tung, C. H.; Chen, C. W.; Tu, C. H.; Chu, Y. W. SUMOgo: Prediction of Sumoylation Sites on Lysines by Motif Screening Models and the Effects of Various Post-Translational Modifications. *Sci. Rep.* **2018**, *8*, 1.
(72) Fiumara, F.; Fioriti, L.; Kandel, E. R.; Hendrickson, W. A. Essential Role of Coiled Coils for Aggregation and Activity of Q/N-Rich Prions and PolyQ Proteins. *Cell* **2010**, *143*, 1121.
(73) Martire, S.; Mosca, L.; d'Erme, M. PARP-1 Involvement in Neurodegeneration: A Focus on Alzheimer's and Parkinson's Diseases. *Mech. Ageing Dev.* **2015**, *146*, 53.
(74) Cohen-Armon, M.; Visochek, L.; Rozensal, D.; Kalal, A.; Geistrikh, I.; Klein, R.; Bendetz-Nezer, S.; Yao, Z.; Seger, R. DNA-Independent PARP-1 Activation by Phosphorylated ERK2 Increases Elk1 Activity: A Link to Histone Acetylation. *Mol. Cell* **2007**, *25*, 297.
(75) Strosznajder, J. B.; Czapski, G. A.; Adamczyk, A.; Strosznajder, R. P. Poly(ADP-Ribose) Polymerase-1 in Amyloid Beta Toxicity and Alzheimer's Disease. *Mol. Neurobiol.* **2012**, *46*, 78.
(76) Kauppinen, T. M.; Suh, S. W.; Higashi, Y.; Berman, A. E.; Escartin, C.; Won, S. J.; Wang, C.; Cho, S. H.; Gan, L.; Swanson, R. A. Poly(ADP-Ribose)Polymerase-1 Modulates Microglial Responses to Amyloid *β*. *J. Neuroinflammation* **2011**, *8*, 1.
(77) Gorman, A. M. Neuronal Cell Death in Neurodegenerative Diseases: Recurring Themes around Protein Handling. *J. Cell Mol. Med.* **2008**, *12*, 2263.
(78) Narne, P.; Pandey, V.; Simhadri, P. K.; Phanithi, P. B. Poly(ADP-Ribose)Polymerase-1 Hyperactivation in Neurodegenerative Diseases: The Death Knell Tolls for Neurons. *Semin. Cell Dev. Biol.* **2017**, *63*, 154.
(79) Love, S.; Barber, R.; Wilcock, G. K. Increased Poly(ADP-Ribosyl)Ation of Nuclear Proteins in Alzheimer's Disease. *Brain* **1999**, *122*, 247.
(80) Abeti, R.; Abramov, A. Y.; Duchen, M. R. *β*-Amyloid Activates PARP Causing Astrocytic Metabolic Failure and Neuronal Death. *Brain* **2011**, *134*, 1658.
(81) Zhao, Y. J.; Wang, J. H.; Fu, B.; Ma, M. X.; Li, B. X.; Huang, Q.; Yang, B. F. Effects of 3-Aminobenzamide on Expressions of Poly(ADP Ribose) Polymerase and Apoptosis Inducing Factor in Cardiomyocytes of Rats with Acute Myocardial Infarction. *Chin. Med. J.* **2009**, *122*, 1322.
(82) Yu, C.; Kim, B. S.; Kim, E. FAF1 Mediates Regulated Necrosis through PARP1 Activation upon Oxidative Stress Leading to Dopaminergic Neurodegeneration. *Cell Death Differ* **2016**, *23*, 1873.

https://dx.doi.org/10.1021/acsomega.0c06168
ACS Omega XXXX, XXX, XXX−XXX

sustainability

MDPI

Article

Design and Development of a Proficient Converter for Solar Photovoltaic Based Sustainable Power Generating System

Muhannad Alaraj [1], Anirudh Dube [2,*], Ibrahim Alsaidan [1], Mohammad Rizwan [1,3] and Majid Jamil [2]

[1] Department of Electrical Engineering, College of Engineering, Qassim University, Buraydah 52571, Qassim, Saudi Arabia; Muhannad@qu.edu.sa (M.A.); Alsaidan@qu.edu.sa (I.A.); MR.Khan@qu.edu.sa (M.R.)
[2] Department of Electrical Engineering, Jamia Millia Islamia, Delhi-110025, India; mjamil@jmi.ac.in
[3] Department of Electrical Engineering, Delhi Technological University, Delhi-110042, India
* Correspondence: anirudhdube12@gmail.com

Abstract: The demand for renewable energy resources is invigorated due to various issues primarily related to energy security, energy sustainability, and greenhouse gas emissions. The proper utilization of renewable energy resources has certain challenges due to the varying nature of meteorological parameters and atmospheric aerosols. Therefore, it is of utmost importance to extract the maximum power from the photovoltaic systems with the help of proficient converters. Here, a coupled inductor based highly efficient synchronous interleaved boost converter is designed and developed for the grid integrated photovoltaic system. The proposed converter contains an Insulated Gate Bipolar Transistor (IGBT) switch in place of the conventional diode to maintain zero leakage current, bared minimum switching losses, and improved conduction time thereby enhancing the overall efficiency and reliability of the system. In addition, the proposed system topology is simple to implement and is capable of controlling power at both the generation as well as the load sides. The results obtained are validated with the help of a laboratory prototype under practical scenarios like varying temperature and solar irradiance. Further, an intelligent technique based on modified particle swarm optimization is utilized to extract the maximum power from the photovoltaic system. Moreover, the power quality indices were monitored and analyzed at the point of common coupling and at the grid level which vets the effectiveness of the proposed topology.

Keywords: solar photovoltaic system; sustainable power generation; energy security; converter; renewable energy resources

Citation: Alaraj, M.; Anirudh, D.; Alsaidan, I.; Rizwan, M.; Jamil, M. Design and Development of a Proficient Converter for Solar Photovoltaic Based Sustainable Power Generating System. *Sustainability* **2021**, *13*, 2045. https://doi.org/10.3390/su13042045

Academic Editor: Detlef Schulz
Received: 11 January 2021
Accepted: 10 February 2021
Published: 14 February 2021

Publisher's Note: MDPI stays neutral with regard to jurisdictional claims in published maps and institutional affiliations.

Copyright:© 2021 by the authors. Licensee MDPI, Basel, Switzerland. This article is an open access article distributed under the terms and conditions of the Creative Commons Attribution (CC BY) license (http://creativecommons.org/licenses/by/4.0/).

1. Introduction

The enhancement of the power electronics components in various applications of the renewable energy sector leads to the requirement of efficient components or configurations so as to obtain better results. Power electronics components play a vital role in transforming power supply and renewable energy resources-based applications [1]. The selection of the accurate topology plays a vital role in building efficient configuration. The entire effectiveness of the solar photovoltaic (PV) system depends on the tracking of the Maximum Power Point Tracking (MPPT), selecting the efficient DC-DC boost converter, and implementation of the efficient configuration of the inverter with control strategies for the grid connected PV system. Significant work has been done in the field of MPPT for its various types and applications [2–5], its superior or improved versions with high accuracy, and fast-tracking under different environmental conditions [6–8]. In [9], a modified MPPT algorithm for reducing the inter harmonics present while tracking maximum power point is proposed whereas, a new concept called boost MPPT system is based on non-linear dynamics so as to track global MPPT without any additional external circuitry is provided in [10].

Equally advanced work has been carried out by researchers on DC-DC boost converters. Some topologies with high efficiency, cost-effective, and high step-up are proposed in [11,12]. A comprehensive review of DC-DC converters topologies based on five major drives and accordingly classifying their area of applications is reported in [13]. A comprehensive analysis of the DC-DC converters is provided in [14,15]. A novel high step-up DC-DC converter is provided in [16]. A comparative study of diverse non-isolated DC-DC boost converters is provided [17]. DC-AC converter or inverter topology is also the key factor for a photovoltaic system. In [18], a review of the various inverter topologies or single-phase systems is provided. Specific investigations on inverter topologies have also been done by many researchers. Few of them include multilevel inverter topology [19], transformer-less type inverter topology [20], enhanced z-source [21], and online variable topology [22]. The paper [23] provides the recent trends in inverter topologies. In [24], the disturbance control strategy for LCL filter type grid-connected inverters is focused. The performance of the proposed control method was compared with other conventional control techniques for proving its effectiveness and stability. The matter of fact is that the advancement and researches done with respect to MPPT, DC-DC converters, and DC-AC converters are substantial and grooming with day-to-day advancement in technology. Researchers are focusing on cost-effective, efficient, reliable, and sustainable topology so as to get the most power at the least cost. However, issues pertaining to grid integration, like power quality, also need to be addressed for maintaining a stable and secure system. The power quality responses of grids under usual and unusual conditions with grid-connected solar water pumps have been analyzed [25]. In the paper [26], the power quality issues at the distribution grid after integration of roof-top solar PV system are presented. The recent developments in the grid-connected solar PV system are highlighted [27]. A detailed review of the topologies available in the literature is provided [28]. In the paper [29], emphasis is given to the recent integration requirements related to power quality (PQ) issues. The paper also proposed the control for mitigating PQ concerns whereas the paper [30] discussed the design of fuzzy based space vector PWM controller for mitigations of the power quality issues in the grid connected converters.After reviewing the existing research, some limitations were observed in the area of loss minimization on the DC side and ripple reduction at the DC link capacitor. Also, many researchers have used additional power control devices such as UPQC, DSTATCOM, etc., which enhance the additional cost of the system. Controlling the power on the DC side can enhance the conversion efficiency and thereby reduce the DC ripples present at the DC link capacitor.

The present paper emphasizes the efficient topology of the DC-DC converter so that the maximum power loss can be controlled and maximum efficiency can be obtained on the DC side with reduced ripples present at the input of the inverter. A synchronous interleaved boost converter was developed and presented in this paper. Efforts were made to develop the prototype in the laboratory and test it for the grid integrated solar PV system. Among the various intelligent controllers, the PSO based MPPT controller and the synchronous frame reference (SRF) based phased lock loop (PLL) control strategy for grid synchronization and control were used in this paper. The key objectives of this proposed configuration are as follows:

- This proposed synchronous interleaved boost converter has a switch in place of the diode in the conventional method, which reduced the switching losses across the diode and thus making a more reliable system as compared to the conventional type of interleaved boost converter available.
- This system topology is simple to implement and is capable of controlling power on both sides, that is, on the generation side as well as on the load side. On the generation side, the optimum power was tracked using PSO-based MPPT and then the DC link losses were reduced by using switches in place of diode whereas maintaining the power quality, power factor, and power management on the load side makes the system robust and practical.

- In case of deviation in the load condition or deviation in the generation side due to solar irradiance, the proposed configuration coordinates with the power generation through the solar PV system and accordingly feeds continuous accessible power to the load to maintain the stability of the system. However, if any deficiency of power occurred from the solar PV system, the same shall be fulfilled by the existing grid power.

The response of grid and total harmonics distortion present in the grid after integration of the proposed system is also recorded in this paper.

The paper is organized as follows: Section 1 describes the Introduction which includes proposed DC-DC boost converter and its advantages over the conventional type boost converter,system configuration and its hardware prototype.Section 2 discusses the results obtained from the proposed system. Section 3 concludes the paper. Authors contribution and references are mentioned thereafter in the paper.

1.1. Proposed DC-DC Boost Converter

The basic architecture of the grid integrated solar PV system has mainly three segments which are the DC side, AC side, and DC link as shown in Figure 1. Onthe DC side, the main components are solar PV array and DC-DC converter with MPPT controller; the AC side includes the inverter, filter, and isolation transformer with the AC controller and decoupling capacitor or DC link capacitor, which acts as a link between the DC side and AC side.

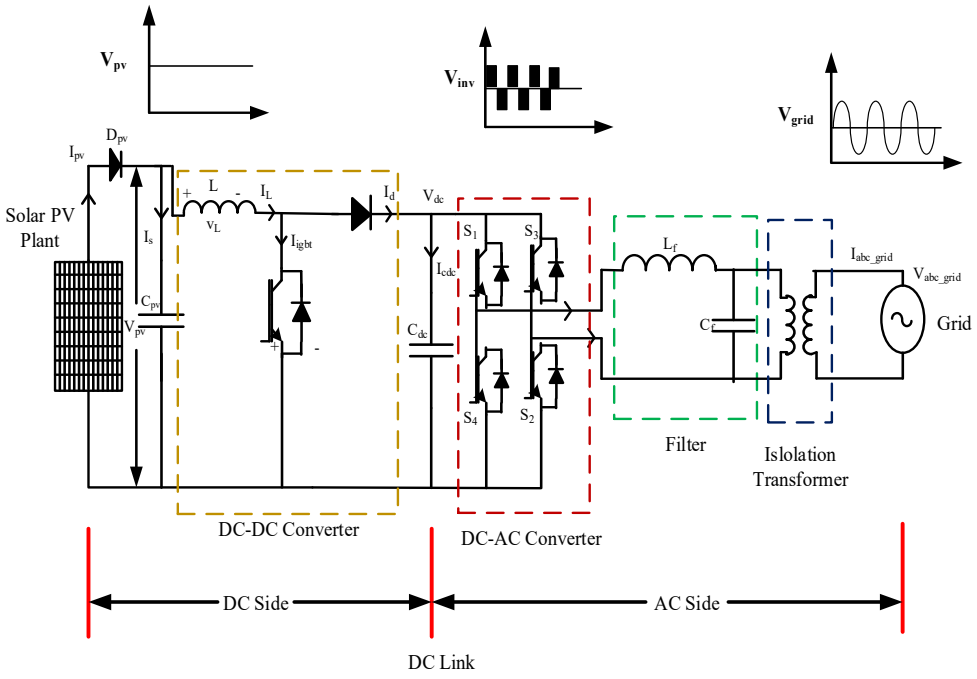

Figure 1. Basic architecture of DC-DC boost converter in grid integrated solar PV system.

The prime focus was given to the DC part of the architecture in this paper. Hence, emphasis was given to the MPPT controller for catering to the real-time variation and to the DC-DC converter for reducing losses and maintaining fewer ripples at the DC link capacitor so as to achieve better results on the AC side of the system.

The selection of topology and further choosing its hardware components required for implementing the same to design the DC-DC converter plays a significant part in formulating the dynamic system. The selection is based on various factors like voltage rating, on-state resistance, current flowing, and switching frequency. The culling of the switching device to be used in the DC-DC converter depends on the intercepting voltage, on-state

resistance, and switching frequency. MOSFET and IGBT are the most prominent components used as a switching device. If the intercept voltage is below 700 V, then it is preferable to use MOSFET because it provides low conduction loss. Above 700 V voltage level, IGBT is the better choice. The IGBT based control switch was used in this paper.

1.2. Benefits of Interleave Boost Converter (IBC) over Traditional Boost Converter (TBC)

A traditional boost converter is one having one IGBT/MOSET switch, a diode, and an inductor placed in the manner shown in Figure 2. The traditional boost converter has the voltage gain represented as:

$$V_{gain} = \frac{V_o}{V_{dc}} = \frac{1}{1-D} \quad (1)$$

where,
D stands for the duty ratio
and current across inductor I_L is given as:

$$I_L = \frac{I_o}{1-D} \quad (2)$$

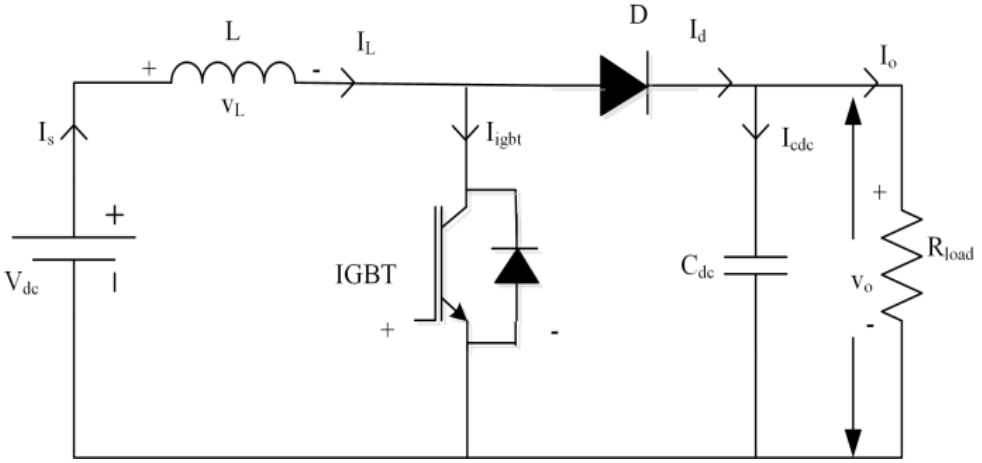

Figure 2. Conventional Boost Converter.

At duty ratio, D = 0.5, the current and voltage stress experienced by the diode and IGBT switch is within permissible limits whereas at a high value of duty ratio or high voltage gain, that is, D > 0.7, the diode conducts for a prolonged time as compared to the desired value and thus causes an enormously high current and voltage stress[31]. Also, the power loss afterward, over the diode, becomes steeply high at such duty ratios. Thus, photovoltaic applications having large voltage gain and involved in high power capabilities do not suit the use of the conventional type boost converter.

Interleaving the boost convert makes it the special type of boost converter where the current entering into the input gets divided into two paths so as to diminish the conduction losses and hence increases the effectiveness of the scheme.

Figure 3 illustrates the typical boost converter with the interleaved facility where the input current (I_o) is divided into two paths having current I_{L1} and I_{L2}.

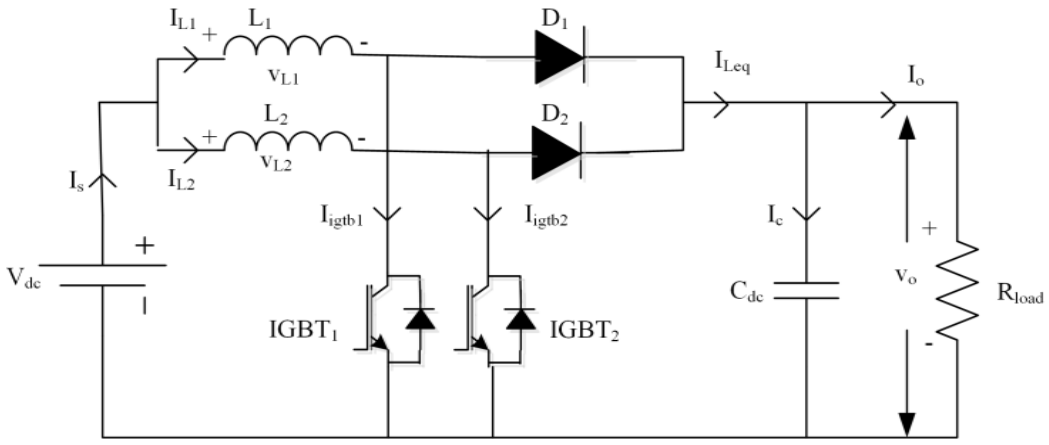

Figure 3. Interleaved Boost Converter.

The value of the inductor also gets reduced. The expressions for IBC are:

$$V_o = \frac{V_{dc}}{1-2D} \tag{3}$$

where,

D is the duty ratio

and inductor current I_L is given as:

$$I_L = \frac{I_o}{1-2D} \tag{4}$$

The proficient ripple frequency at the capacitor's output also improved due to interleaving and thus reduces the ripple voltage conveniently at the converter's output. Also, as compared to the CBC, the IBC is able to handle more power.

1.3. Synchronous and Non-Synchronous Means of Operation

The fundamental operation of the converter with traditional boosting capabilities and interleaving is usually based on the non-synchronous mode. In the non-synchronous mode of operation, the converter contains the combination of IGBT/MOSFET and diode. However, during the synchronous mode of operation, the diode is substituted by the switch, either IGBT or MOSFET, thereby reducing the losses, and hence the efficiency of the converter gets enhanced. The loss calculations of boost converter under synchronous and non-synchronous mode are analyzed [32]. There are two sources of power loss across IGBT/MOSFET one is power loss across the resistive elements of the MOSFET and the second is the dissipation of power due to the switching losses. Further, the size of MOSFET is conversely proportional to the resistance loss. More is the size of the MOSFET, less will be the resistance loss. This resistance is called on-resistance (R_{on}). The second loss is the switching loss. When MOSFET toggles on and off, the inherent freeloading capacitance accumulates and then disperses the energy at each interval. The switching frequency is directly proportional to this loss and thus with the enhancement in the size of the MOSFET, its capacitance also enhances resulting in enhancement of switching loss. The expression for the same is as below:

Power loss across IGBT/MOSFET:

$$P_{mf} = P_{Ron} + P_{sw} = \left[\left(\frac{DR_{on}}{(1-D)^2 R}\right) + \left(\frac{1}{2} f C_o R\right)\right] P_o \tag{5}$$

where, D stands for the duty ratio, R_{on} represents the on-resistance of MOSFET, f denotes the switching frequency, C_o represents the capacitance at the output of the MOSFET and Po is the output power and power loss across the diode is given as:

$$P_D = P_{fv} + P_{Rf} = \left[\left(\frac{V_F}{V_o}\right) + \left(\frac{R_F}{(1-D)R}\right)\right] P_o \quad (6)$$

where, V_F represents the forward voltage drop, R_F stands for the forward resistance of the dynamic diode and Vo is the output voltage.

Loss across the inductor (P_L) and capacitor (P_C) is given as:

$$P_L = \frac{R_L}{(1-D)^2 R} P_o \quad (7)$$

$$P_C = \frac{DR_C}{(1-D)R} P_o \quad (8)$$

Therefore, as the synchronous mode of operation is adopted, the power loss across the diode as represented in Equation (6) gets replaced by the power loss across the MOSFET as represented in Equation (5) making the synchronous configuration more efficient.

1.4. Circuit Diagram of Synchronous Interleave Boost Converter

In the present paper, the boost converter with the interleaved facility is proposed, which is working in the synchronous mode of operation. This synchronous interleaved boost converter (SIBC) has a dual advantage, that is, the advantage of interleaving the input current thereby reducing the losses and second operating in the synchronous mode, that is, by replacing the diode with the IGBT/MOSFET. The circuit design of the prospective model is demonstrated in Figure 4.

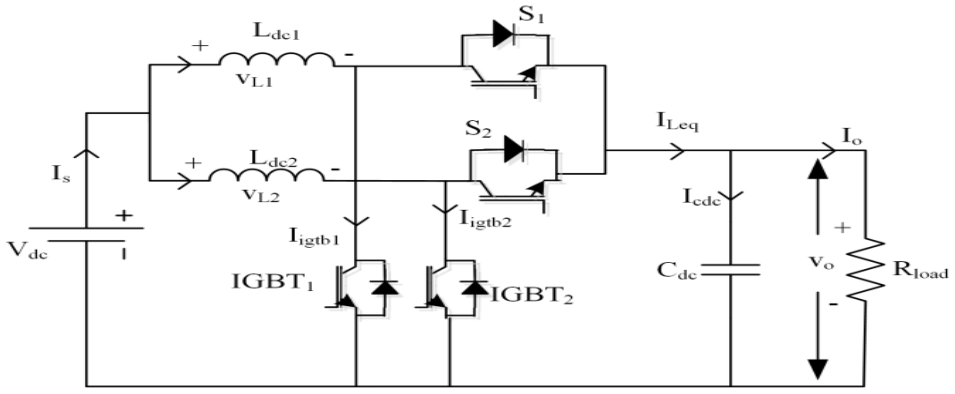

Figure 4. Synchronous Interleaved Boost Converter.

As observed from Figure 4, the two IGBTs and the two diodes were replaced with the two MOSFETs/switches say S_1 and S_2. Due to interleaving the inductor L is divided into two parallel inductors having values L_{dc1} and L_{dc2}. The output voltage (V_o) and load current (I_o) was derived and is represented as:

$$V_o = \frac{V_{dc}(T + \Delta_t)}{T(1-2D) + \Delta_t)} \quad (9)$$

$$I_o = \frac{I_o(T + \Delta_t)}{T(1-2D) + \Delta_t)} \quad (10)$$

where,

T is the total duration of time the converter is conducting and Δ_t is the incremental time of conduction.

1.5. System Configuration and Hardware Setup

The configuration of the synchronous boost converter-based grid connected solar PV system is shown in Figure 5. The system consists of the 1.5 kW grid integrated solar PV system, a highly efficient synchronous interleaved boost converter having two shunt connected inductors having a value of 2.3 mH, input capacitance of 470μF each, and output capacitance of 1200 μF. The diodes were replaced with the IGBT based switches, which are denoted as S_1 and S_2 respectively. The three-stack voltage source converter having three IGBTs branches containing two switch ports was connected with the boost converter with the DC link capacitance having a value of 1200 μF.

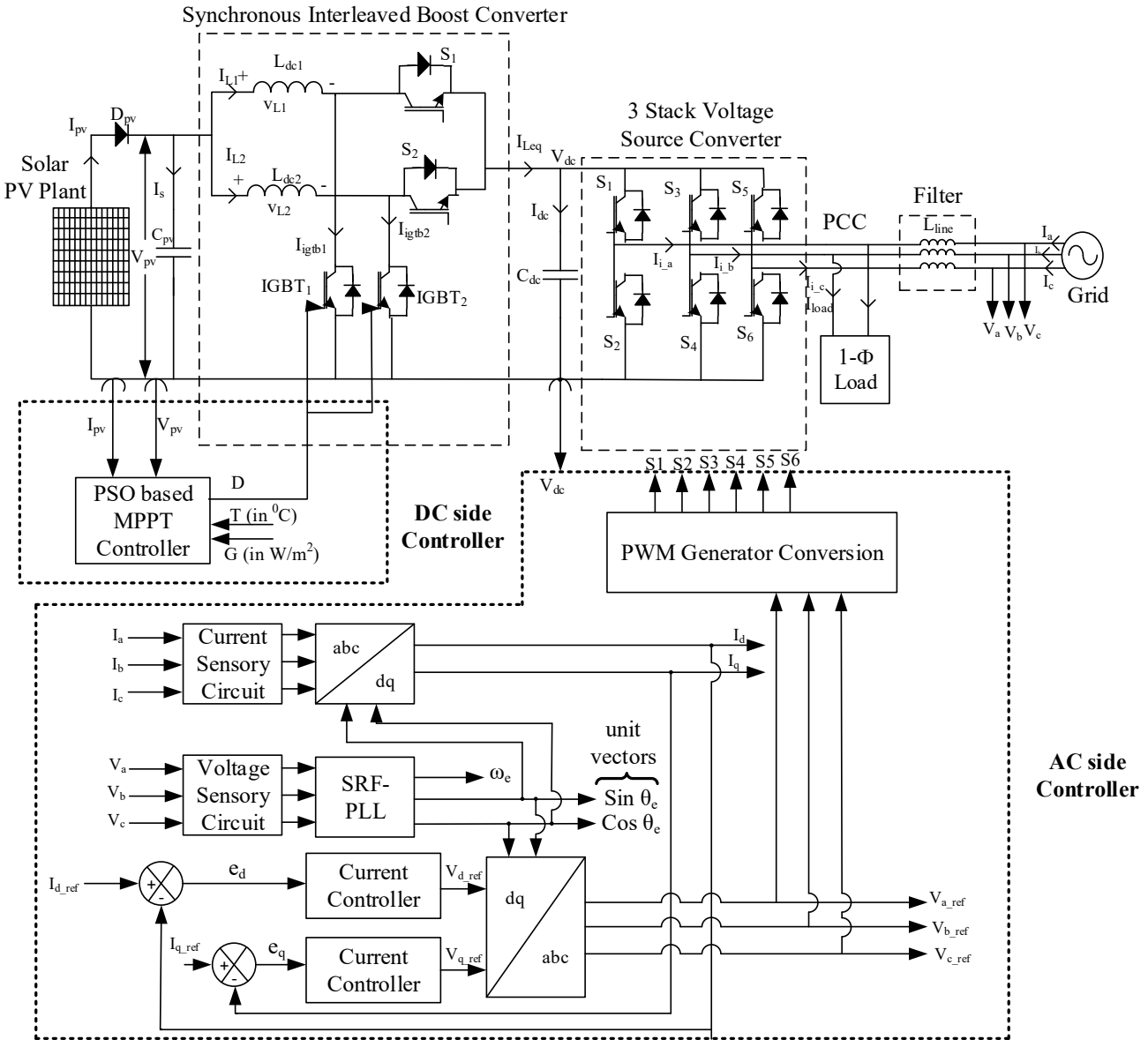

Figure 5. Architecture of grid integrated solar PV system.

The technique used for tracking the maximum power point in the proposed configuration is particle swarm optimization (PSO), which is used to generate pulses and regulate the switches of the boost converter. The PSO was selected due to its faster response in case of the partial shading conditions of PV modules. The typical PSO method may be described using the following equations:

$$v_{i(k+1)} = w(k)v_i(k) + c_1 r_1\left(l_{best} - x_i(k)\right) + c_2 r_2\left(g_{best} - x_i(k)\right) \quad (11)$$

$$x_i(k+1) = x_i(k) + v_i(k+1) \quad (12)$$

This algorithm is an intuitive method that is used for optimization by calculating the fitness function and then continuously amending the local best (LB) and global best (GB) points thus assuring the chasing of global maxima if the situation of partial shading conditions persists.

The AC side controller also plays a vital role in grid synchronism. The foremost requirement for grid synchronism is to measure the grid voltage (V_{grid}), phase angle (Φ), and frequency (f) and match with the voltage, phase angle, and frequency of the inverter output respectively. In this paper, the phase lock loop (PLL) based method has been used due to its advantage of well-established and simple configuration to implement. The synchronous reference frame phase lock loop (SRF-PLL) used for the control at the AC side is shown in Figure 6. The SRF-PLL determines the phase and frequency of the grid voltage. The outputs of the SRF-PLL are the sine and cosine signals with unit magnitude. These are known as the unit vectors and are utilized to produce reference signals. The SRF-PLL is capable of handling disturbances like DC offset, unbalance, and harmonics.

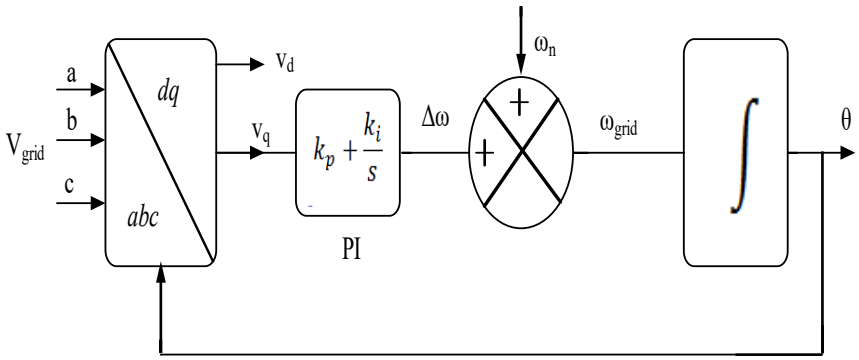

Figure 6. Basic synchronous reference frame phase lock loop (SRF-PLL).

The hardware prototype was developed wherein the control was provided with the help of a dSPACE DSP board 1104 [33], which is used as an interface between the hardware components and the computer-based algorithms for control strategies. The complete hardware setup is illustrated in Figure 7.

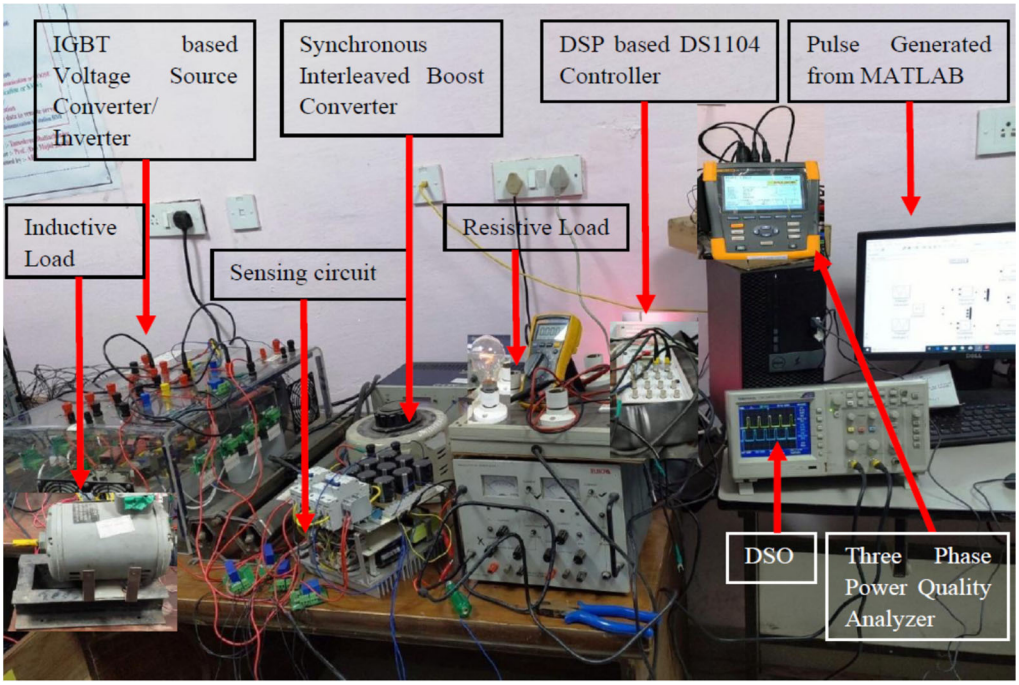

Figure 7. Hardware laboratory prototype of the proposed research.

The hardware archetype of the synchronous interleaved boost converter was established after theoretical study and carrying out the simulation and the replica of the same is demonstrated in Figure 8.

The hardware of the synchronous interleaved boost converter consists of the two-leg IGBT, DC link capacitor, input capacitor, HRC fuses for protection, and input inductor. The rating of the same is given in Table 1.

For sensing the current and voltage of the PV system and the grid, the sensory circuit was designed. This sensory circuit shall sense the actual value of the current and voltage and feed to the computer-based controller through dSPACE 1104.

Figure 8. Hardware replica of synchronous interleaved boost converter.

Table 1. Hardware Components Parameters.

S. No.	Description of the Item	Qnty.	Specification
1.	Two-leg IGBT	2 Nos.	SKM100GB12T4, 1200 V, 100 A
2.	DC Link Capacitor	1 No.	1200 μF, 500 V. 100 kΩ resistor is connected across capacitor.
3.	Interleaved Inductor	2 Nos.	2.5 mH
4.	HRC fuse	2 Nos.	500V, 100 kA, 10 × 38, IEC269
5.	Input Capacitor	1 No.	470 μF

The current is sensed using the sensor, LEM LA 25 P and the voltage through the sensor, LEM LV 25 P.

The three-phase, 10 kVA, 415 V AC, 50 Hz,with a switching frequency capability of up to 20 kHz, three-stack voltage source converter was designed for the proposed configuration. The proposed voltage source converter can cater the DC voltage range from 200 V to 800 V. The Semikron make SKM100GB12T4 IGBT having a pair of switches was used as one leg and four such legs were configured, one for each phase R, Y, and B, and one leg spare for either grounding purposes or as a standby. The Semikron IGBT driver circuit was used for driving the IGBT. The hardware realization of the voltage source converter is shown in Figure 9.

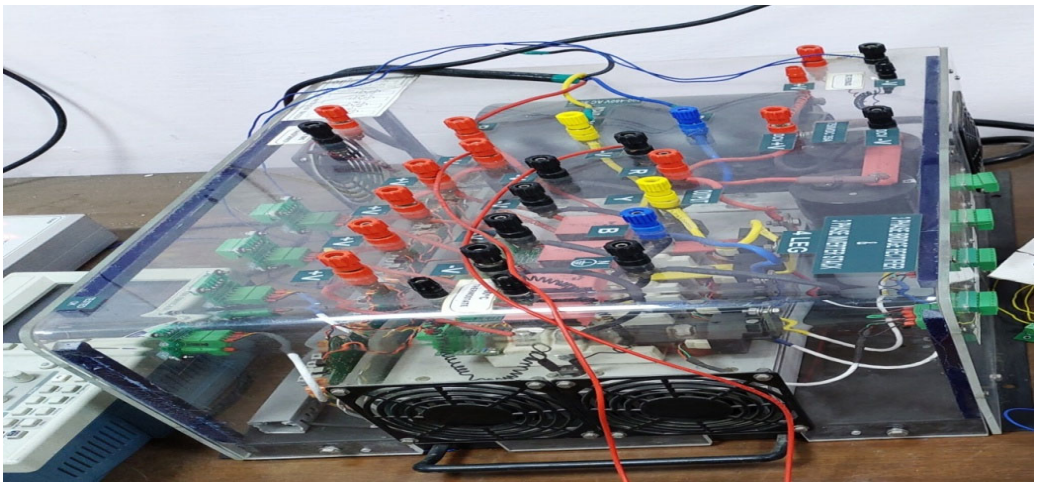

Figure 9. Hardware realization of voltage source converter.

2. Results and Discussions

The 100 kWp solar PV system was designed and simulated with a solar PV module of rating 305 Wp each. A total of five modules were linked in sequence and 66 such strings were connected in shunt to form an array. A total of five modules were linked in sequence and 66 such strings were connected in a shunt to form an array. The variation of irradiance and temperature was considered under this study for vetting the response of the proposed system under different environmental uncertainties.

For analysis, the same, the 1.5 kW hardware archetype was established in the research lab. The DS1104 DSP board was based on a 64-bit PowerPC type PPC603e processor. The board included analog to digital (A/D), digital to analog (D/A) converters, and digital incremental encoder interfaces. The controller was designed using MATLAB Simulink and the pulses generated were provided to fire the IGBTs in the hardware setup using dSPACE Control Desk software [33]. The controlling of the firing angle and other controls was done using dSPACE graphical user interface GUI software. With this GUI, it was possible to see the real-time output and any changes in the controller could be observed on a real-time basis. The pulses given to the IGBTs of the synchronous boost

converter are shown in Figure 10, whereas the 1.5 kW solar PV modules installed on a roof top were used for providing DC power to the proposed prototype, which is illustrated in Figure 11.

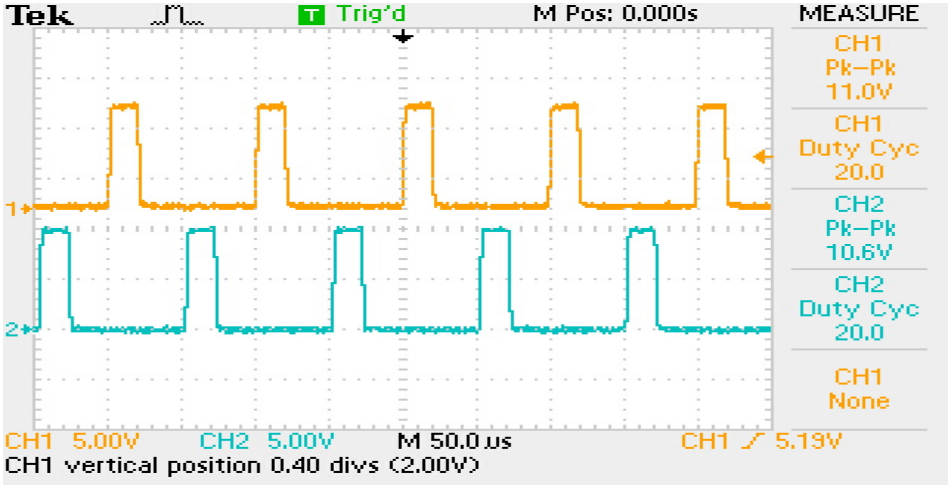

Figure 10. Pulse output from dSPACE 1104.

The magnitude of irradiance considered was 1000 W/m² initially and it varied over the time period. The simulation was done for 2.5 s. At time t = 0.6 s, the irradiance varied to the level of 200 W/m² and then started rising to attain the value of 1000 W/m² at time t = 1.7 s. Then, to vet the variation of the temperature, the temperature was initially considered as 25 °C till t = 2 s. After 2 s, the temperature rose to 50 °C. Figure 12 depicts the responses received from the photovoltaic system under different environmental conditions.

Figure 11. Solar PV modules.

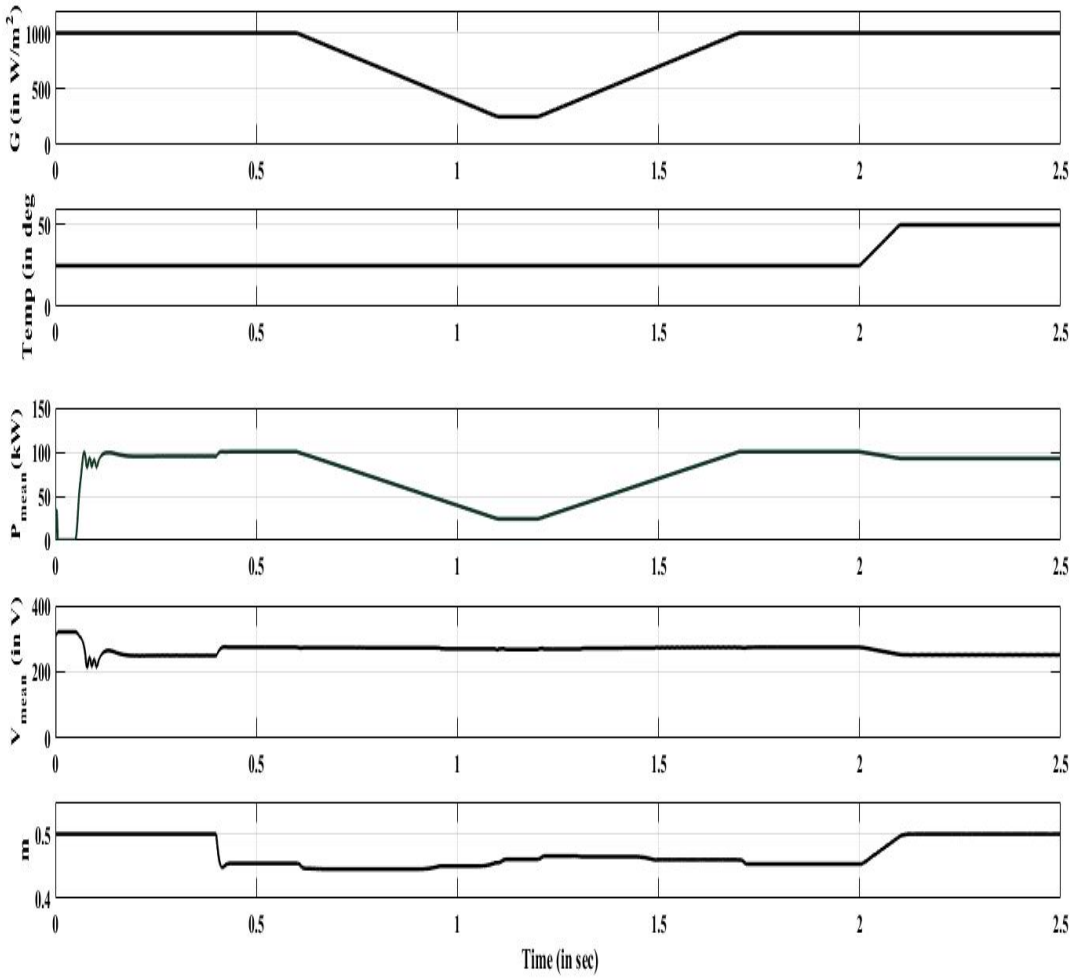

Figure 12. Response of the solar PV system under varying environmental conditions.

It was observed that as the irradiance value dipped, the corresponding voltage and power also dropped in the same respect, which shows the direct relationship between the irradiance and voltage. However, with the increase in temperature, the voltage and power reduced, which illustrates the inverse relationship between the temperature and voltage till the standard temperature condition (STC) of the PV module.

The synchronous interleaved boost converter configuration was implemented for this grid tied solar PV system. For verifying the reliability and robustness of the proposed system, a comparative analysis of the synchronous mode of operation and non-synchronous conventional type of boost converter was carried out. The simulation results obtained are shown in Figure 13. The response in black color denotes the non-synchronous mode whereas the response obtained in magenta color is the proposed synchronous mode of operation. The response clearly depicts the stability and efficient regulation of the ripples of the output voltage waveform from the synchronous mode of operation as compared to the non-synchronous mode.

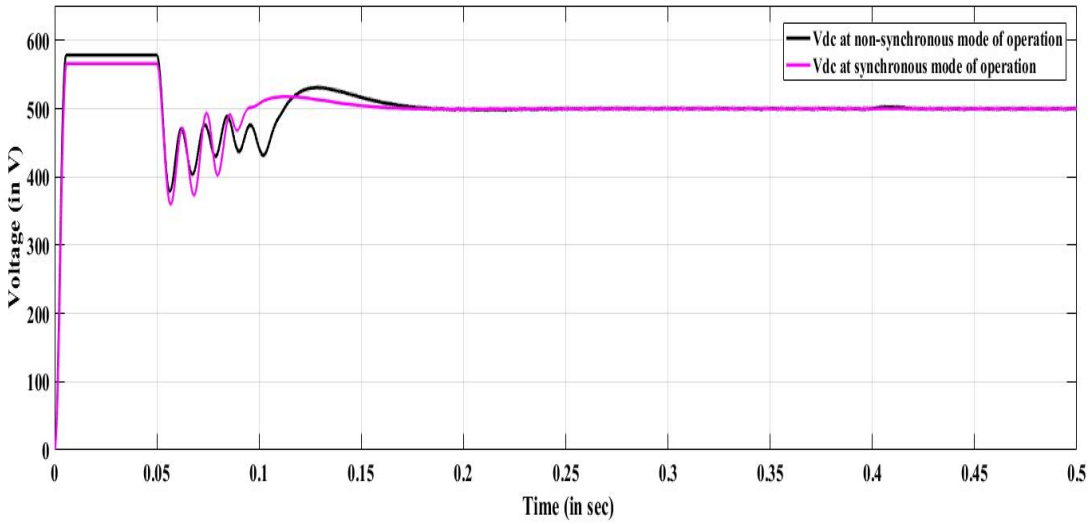

Figure 13. Synchronous vs. non-synchronous mode of operation for boost converter.

The simulation results illustrate the presence of fewer ripples in voltage for the DC link capacitor when functioning in the synchronous mode of operation and it is stabled in early time with stable voltage. Also, the average magnitude of the DC voltage measured is greater in the case of the synchronous mode of operation as compared to the non-synchronous boost converter. The voltage at the output of the voltage source converter is after the DC link capacitor was measured and is shown in Figure 14.

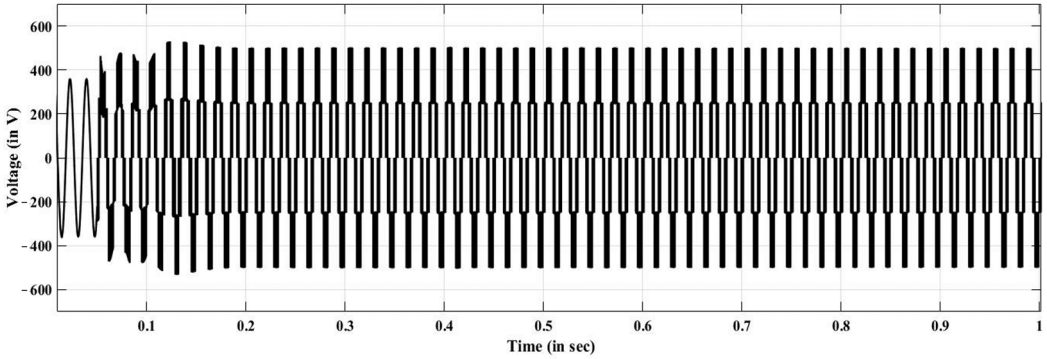

Figure 14. Voltage profile at the output of VSC.

It was observed that the conversion efficiency of the proposed converter configuration was recorded to be more than 93% under different duty ratios. To synchronize the output response received through voltage source converter with the power grid, the synchronous reference frame phase lock loop-based AC control scheme with PI controller was implemented. The complete AC control scheme is demonstrated in Figure 15.

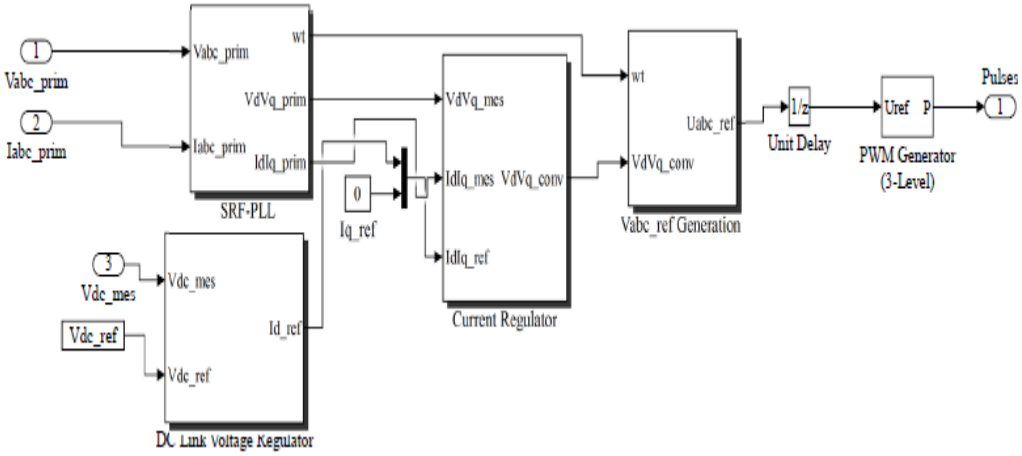

Figure 15. AC side controller.

The sensory circuit senses the three-phase voltages (V_a, V_b, and V_c) and currents (I_a, I_b, and I_c) from the grid and fed into the control scheme. Then these three-phase voltage signals are converted into the two-phase stationary frame using abc to $\alpha\beta$ transform using Equation (13).

$$\begin{bmatrix} V_\alpha \\ V_\beta \end{bmatrix} = \begin{bmatrix} \frac{2}{3} & -\frac{1}{3} & -\frac{1}{3} \\ 0 & \frac{1}{\sqrt{3}} & -\frac{1}{\sqrt{3}} \end{bmatrix} \begin{bmatrix} V_a \\ V_b \\ V_c \end{bmatrix} \tag{13}$$

Then these stationary frame values Vα and Vβ transform into the rotating reference frame. This conversion is called $\alpha\beta$ to dq transformation. This is carried out using Equation (14).

$$\begin{bmatrix} V_d \\ V_q \end{bmatrix} = \begin{bmatrix} \cos\theta_e & \sin\theta_e \\ -\sin\theta_e & \cos\theta_e \end{bmatrix} \begin{bmatrix} V_\alpha \\ V_\beta \end{bmatrix} \tag{14}$$

where θ_e is the estimated angle calculated from the synchronous reference frame-based phase lock loop. The PI controller is used in association with the PLL so that the value of V_d is terminated or zero at steady state and the grid voltage is preferably aligned with the q-axis of the rotating reference frame. After the process of PLL, the outcome received is the estimated frequency, which is represented here as ω_e and estimated angle θ_e. This estimated angle is multiplied with the sine and cosine factor to generate unit vectors Sinθ_e and Cosθ_e respectively.

The system acts as nonlinear due to the rotating reference frame which is transformed from the stationary reference frame. The value of V_d is calculated using Equation (14) and is given as:

$$V_d = V_\alpha \cos\theta_e + V_\beta \sin\theta_e \tag{15}$$

Differentiate equation 6.14 with respect to θ_e

$$\frac{dV_d}{d\theta_e} = -V_\alpha \omega_e \sin\theta_e + \frac{dV_\alpha}{d\theta_e}\cos\theta_e + V_\beta \omega_e \cos\theta_e + \frac{dV_\beta}{d\theta_e}\sin\theta_e \tag{16}$$

The estimated frequency is given by:

$$\omega_e = -K_p V_d - K_i \int V_d dt + C \tag{17}$$

$$\frac{d\omega_e}{d\theta_e} = -K_p \frac{dV_d}{d\theta_e} - K_i V_d \tag{18}$$

$$\frac{d\omega_e}{d\theta_e} = P_1 \cos\theta_e + P_2 \sin\theta_e \quad (19)$$

Where,

$$P_1 = -K_p \frac{dV_\alpha}{d\theta_e} - K_p V_\beta \omega_e - K_i V_\alpha$$
$$P_2 = -K_p \frac{dV_\beta}{d\theta_e} - K_p V_\alpha \omega_e - K_i V_\beta \quad (20)$$

Equation (19) is a nonlinear equation. V_α and V_β are quadrature signals wherein V_β lags 90° with respect to V_α.The I_{d_ref} is generated by comparing the actual assessment of voltage at DC link (V_{dc}) and reference value V_{dc_ref} in DC link controller whereas I_{q_ref} is generated by evaluating the reference value reactive power in the grid using a Q controller based on the dips present in the grid and then this reference value is given to the inner current loop to generate the same.

Figure 16 displays the voltage and current profile at the output of the grid integrated solar PV inverter. Figure 17 is the voltage and current profile of the grid where the voltage level at the grid side is considered at the primary distribution system, which is at 20 kV voltage level which can be stepped down with the help of a distributed transformer for further integration into the distribution side and consumer load.

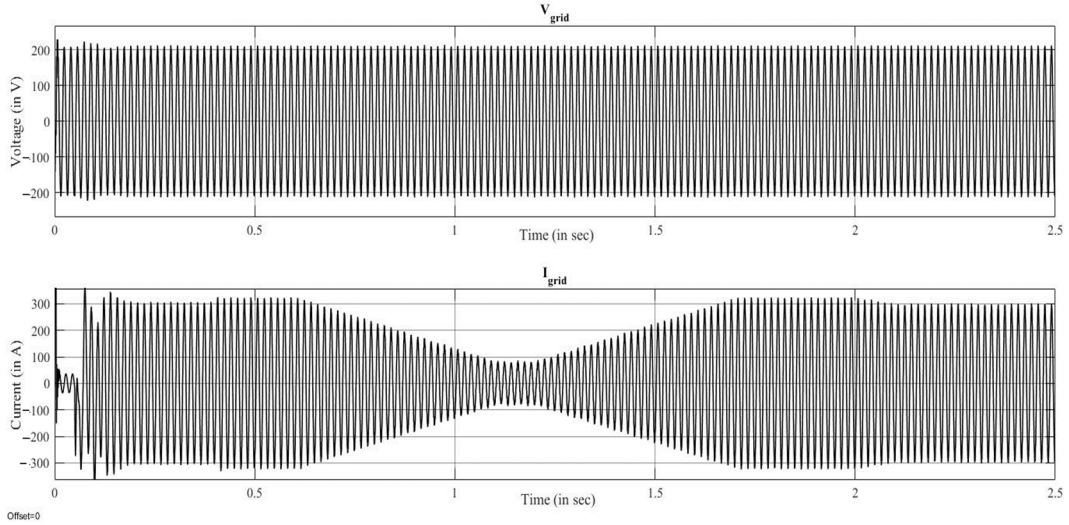

Figure 16. Voltage and current profile at the output of the grid tied VSC.

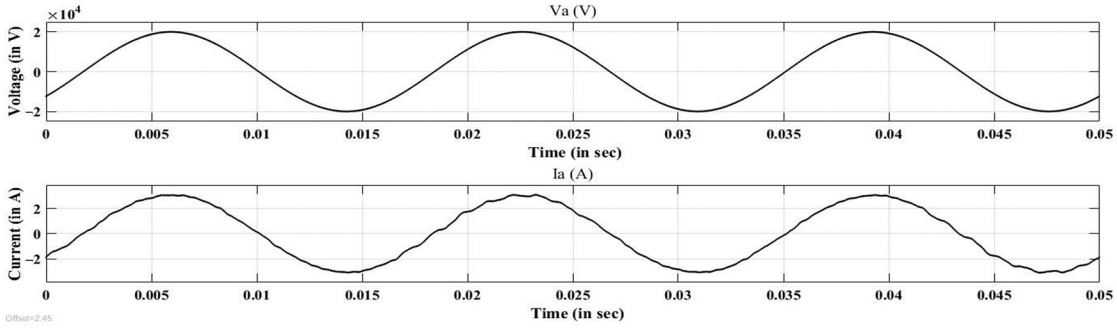

Figure 17. Voltage and current profile at the grid side.

The voltage and current at inverter output and point of common coupling of the distributed network was recorded using Fluke Energy and Power meter and is illustrated in Figure 18 and Figure 19 respectively.

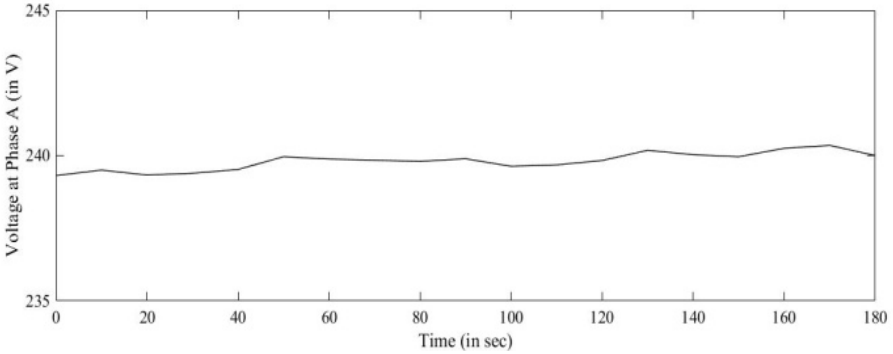
Voltage at Phase A (in V)
245
240
235
0
20
40
60
80
100
120
140
160
180
Time (in sec)

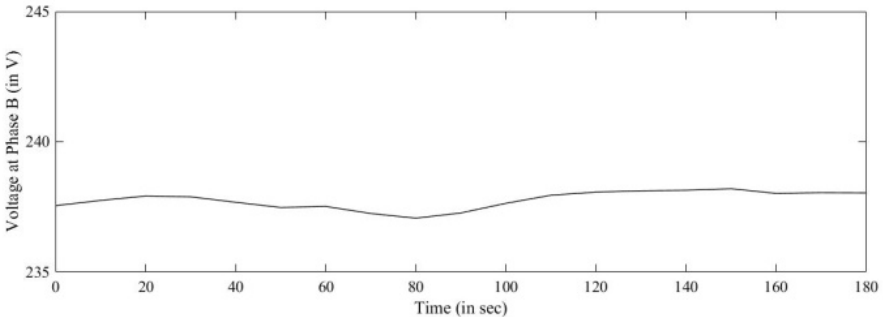
Voltage at Phase B (in V)
245
240
235
0
20
40
60
80
100
120
140
160
180
Time (in sec)

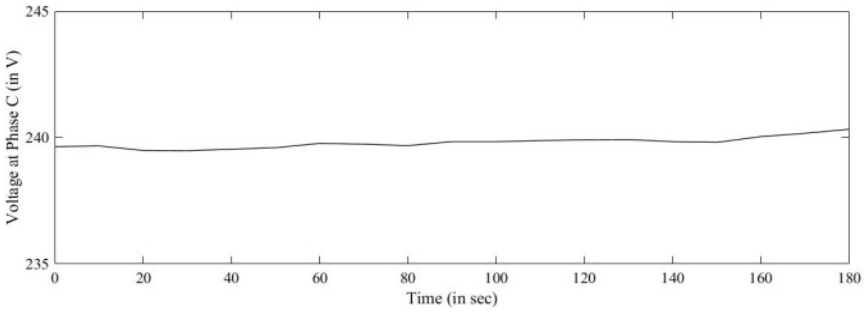
Voltage at Phase C (in V)
245
240
235
0
20
40
60
80
100
120
140
160
180
Time (in sec)

(**a**)

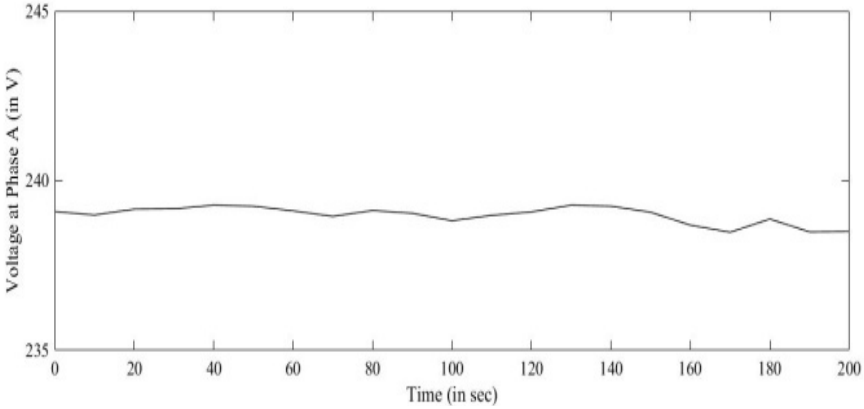
Voltage at Phase A (in V)
245
240
235
0
20
40
60
80
100
120
140
160
180
200
Time (in sec)

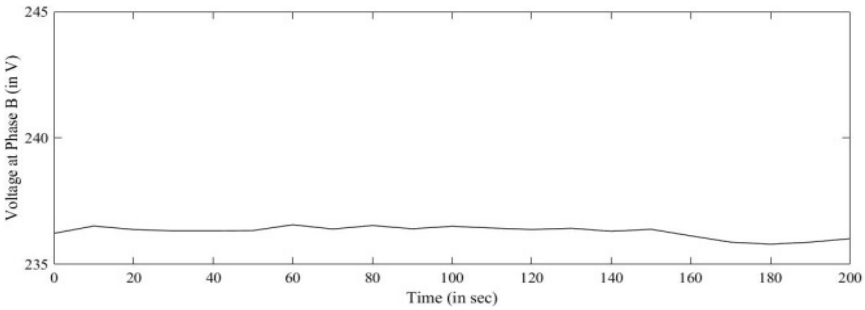
Voltage at Phase B (in V)
245
240
235
0
20
40
60
80
100
120
140
160
180
200
Time (in sec)

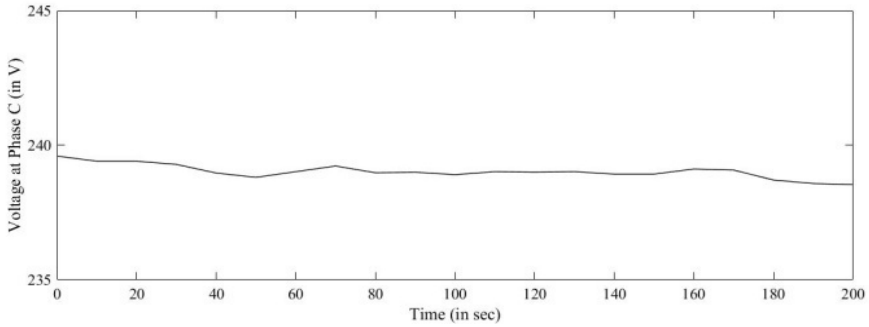

(**b**)

Figure 18. Voltage waveform of (**a**) output of inverter (**b**) at PCC.

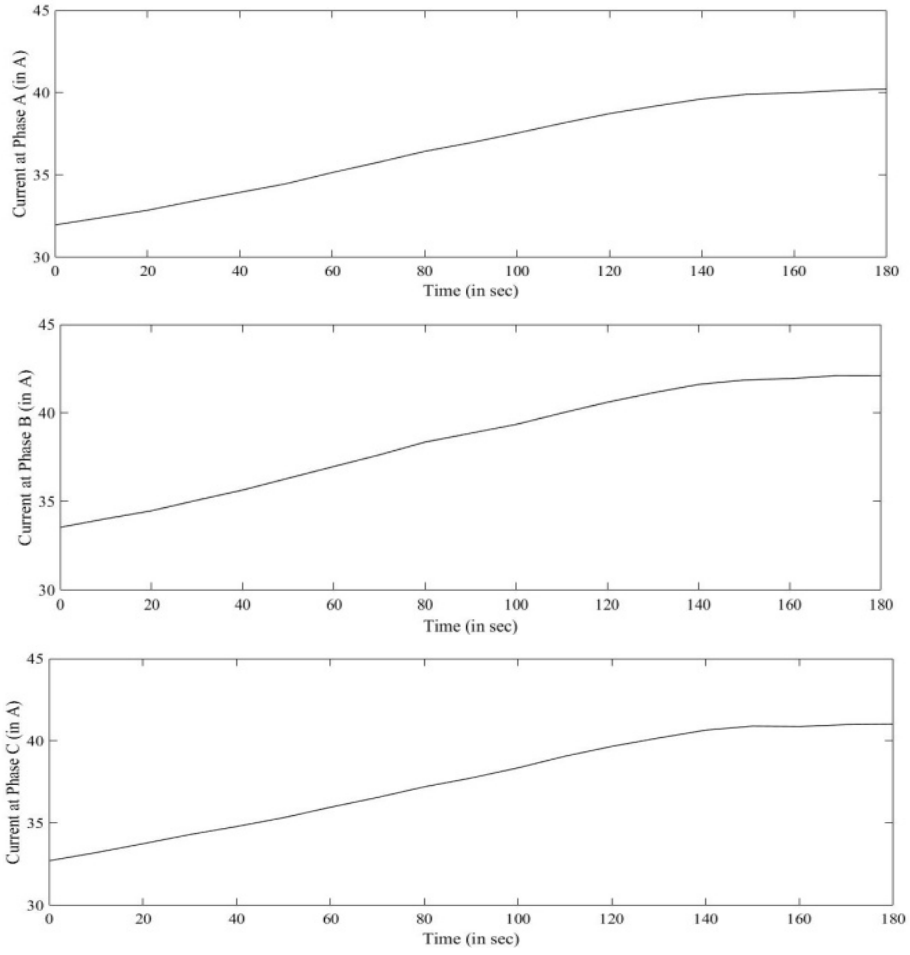

(**a**)

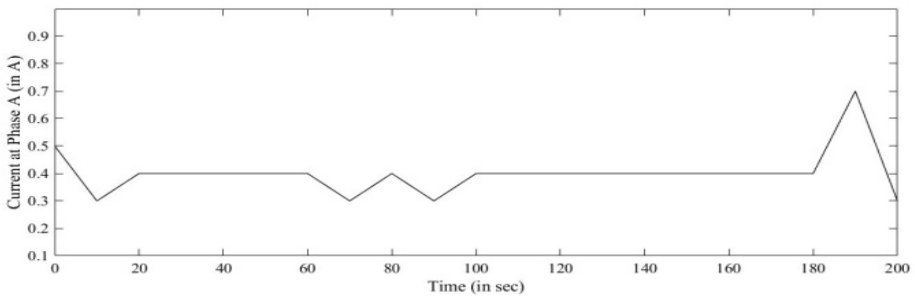

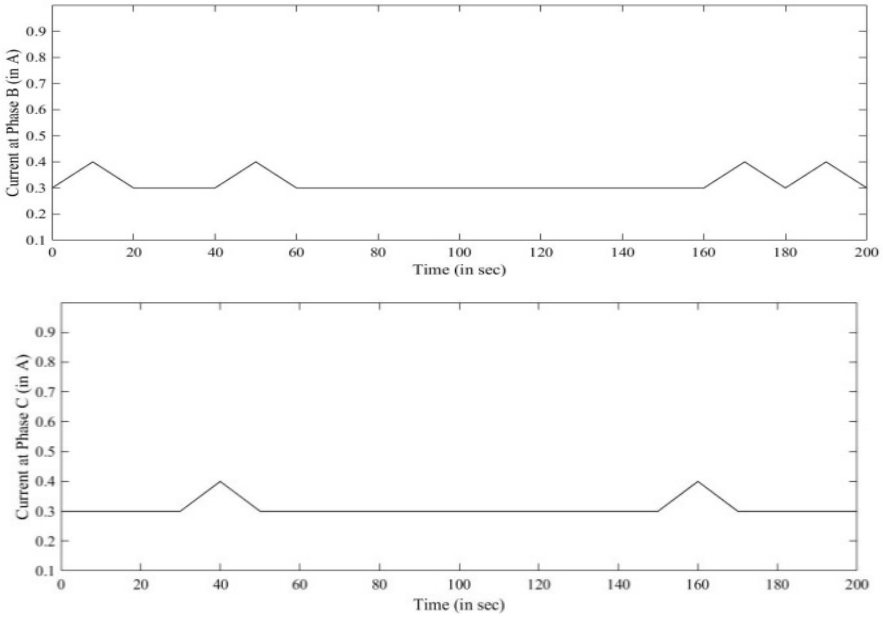

(**b**)

Figure 19. Current waveform of (a) output of inverter (b) at PCC.

It was observed from the Figure 18 that the average magnitude of the output voltage at each phase of the inverter (V_{i_abc}) with respect to time is near to the value 240V or line voltage of 415 V. Moreover the distortions at grid voltage (V_{grid_abc}) are more as compared to the inverter output voltage. To mitigate the difference in each phase voltage, an SRF-PLL based controller was used. Similarly, the response of rms phase current injected into the grid by voltage source converter and the grid current at each phase has was observed and is shown in Figure 19.

During the observations of the behavior of the current waveform, it is seen that small ripples were present in the grid current. However, at certain fractions of a second, the current from the inverter becomes constant with no ripples or distortions. The role of SRF-PLL based controller used is to regulate the injected current into the grid so as to maintain the constant level of the current waveform.

It is significant to measure and analyze the power wave of the grid before injecting the inverter current into the grid or before grid connection. The power wave at each phase is to be observed so as to reduce the error difference between the grid voltages and inverter output voltage and thus making the phase match with each other. The same conditions are for each phase current of the grid and inverter.

Figure 20 shows the power wave of the grid depicting the general trends of variations of the waveform.

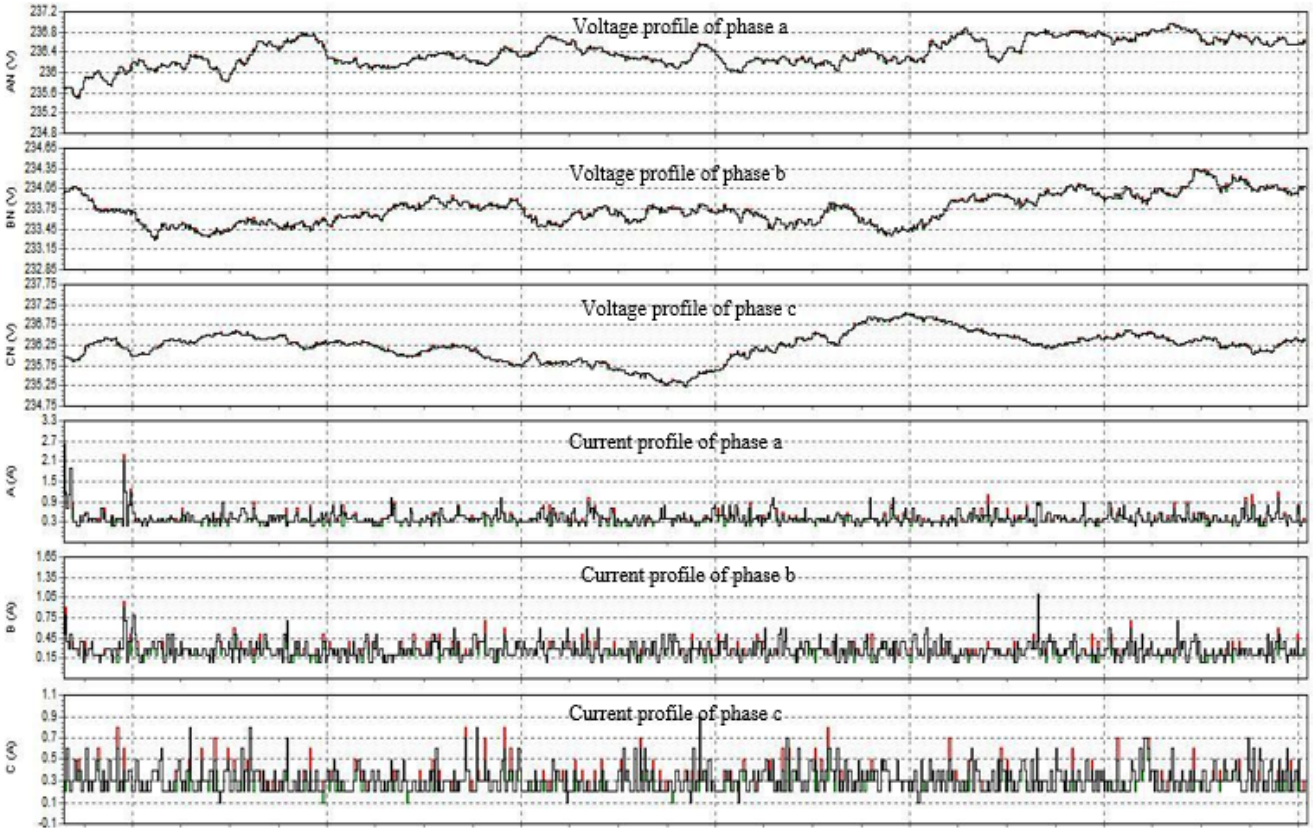

Figure 20. Power wave of the distribution grid.

The graphical result shows an assessment of frequency, which is nearly sinusoidal in nature with a measured value of nearly 50 Hz. However, some difference was observed in the frequency of grid and inverter. The inverter frequency is nearly 50 Hz constant as presented in Figure 21 whereas the frequency varies for the grid but it was observed that the frequency variations of the grid were well within the limit as per the IEEE 519 [34].Figure 22 shows the frequency spectrum at the point of common coupling (PCC) during the time span at a different number of events. Here, total 10 numbers of events were observed. It was observed that the frequency variation is from 50.03 Hz to 50.11 Hz out of which maximum times the value of frequency observed is f= 50.09 Hz, which compiles as per IEEE 519 standard.

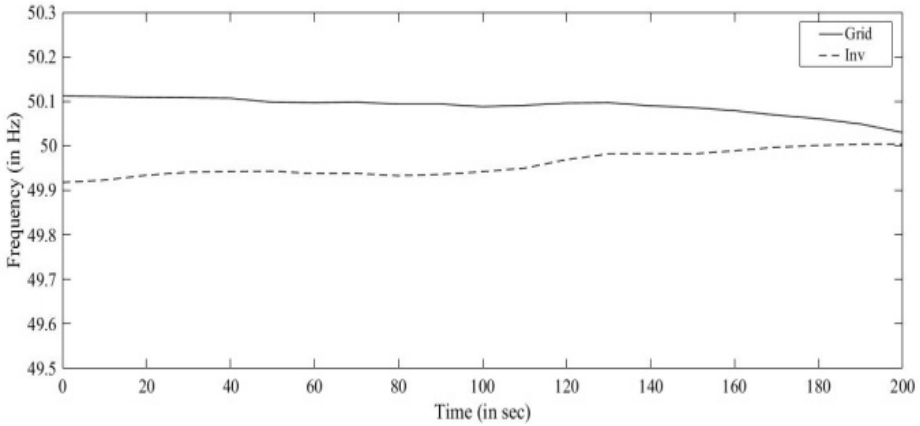

Figure 21. Frequency analysis of grid and inverter.

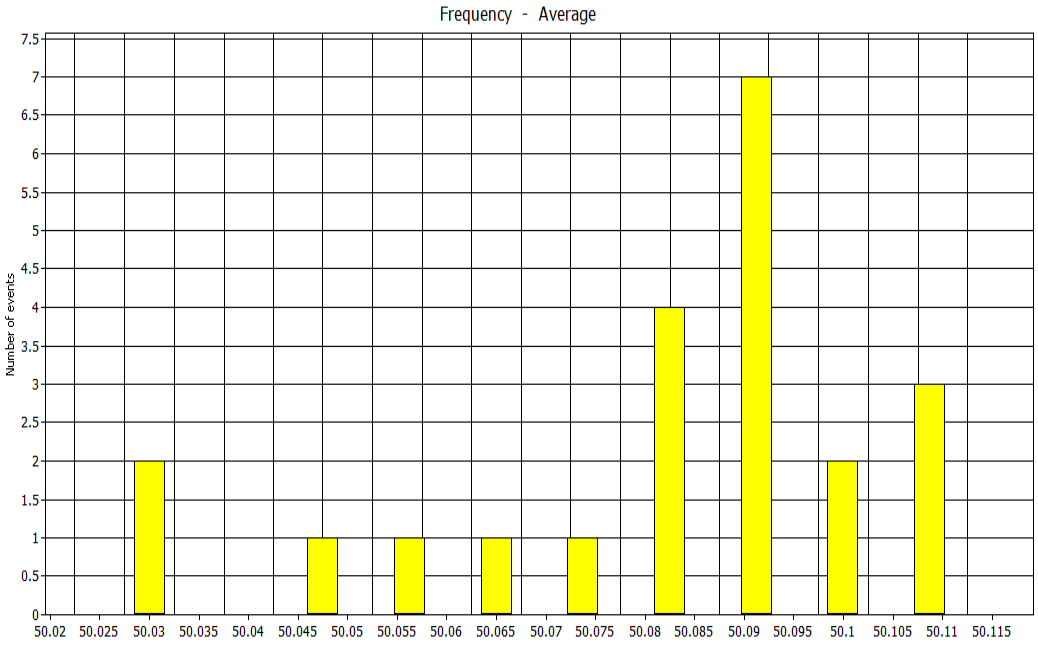

Figure 22. Frequency spectrum of grid.

The graph in Figures 23 and 24 depicts the three-phase current and voltage analysis of the solar system and the grid side. It is seen from the figures that the waveform for solar system is pure sinusoidal whereas some notches has been observed at the tip point of the graphs as shown in Figure 24.

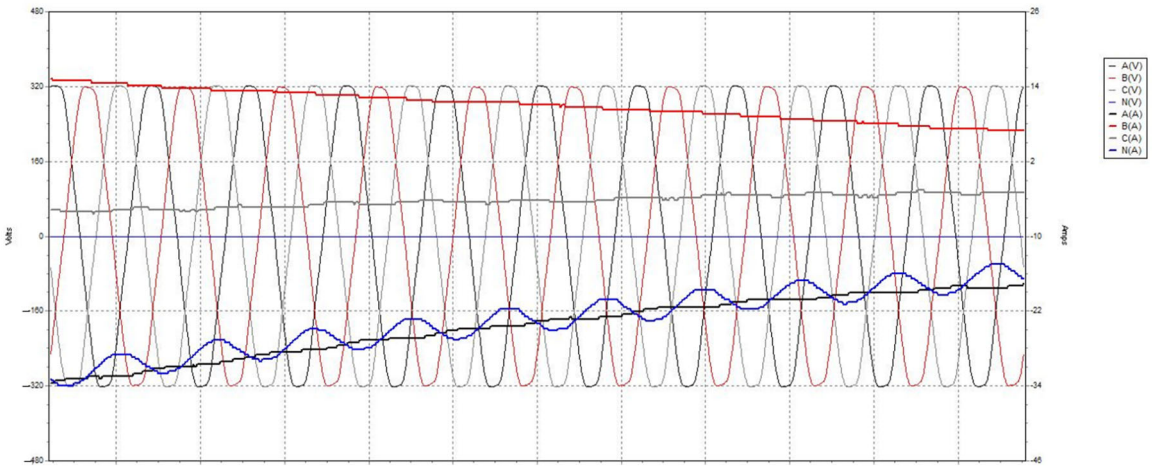

Figure 23. Current and voltage profile of solar PV system.

Due to load variation at the grid, the voltage profile of the grid side varies and some distortions and notches at the edge points were observed. To compensate for these variations, IGBTs of the inverter/VSC were fired so as to mitigate the distortions. However, the grid voltage and current are always the references while calculating the compensation or error signals. If the grid fails, the reference point value stands at zero and hence, the inverter shall not get the power and go in islanding mode of operation.

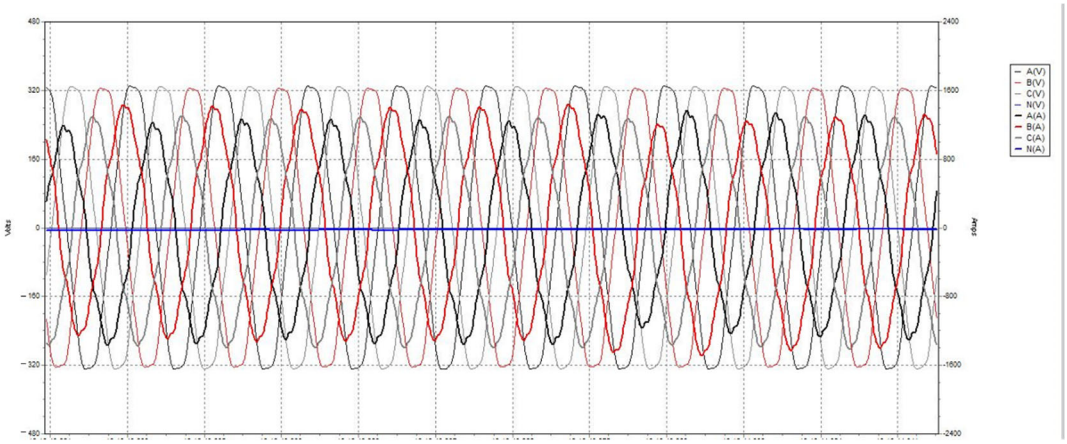

Figure 24. Current and voltage of profile of grid.

The harmonic analysis of the grid side was also an important factor while the integration of the solar system takes place into the grid. For catering to the harmonics present in the grid, IEEE Std. 929-2000 [35] has to be followed. The analysis of the harmonics on the grid side was observed and is shown in Figure 25. It is seen that thethird, fifth, and seventh harmonics were present at each phase of the voltage. The 6n±1 harmonic is always present in the grid system, which can be viewed in the harmonics analysis of the grid. It can be seen in Figure 25 that the harmonics present were approx. 3.4% which is less than the 5% THD and hence complies with the IEEE 519 standard.

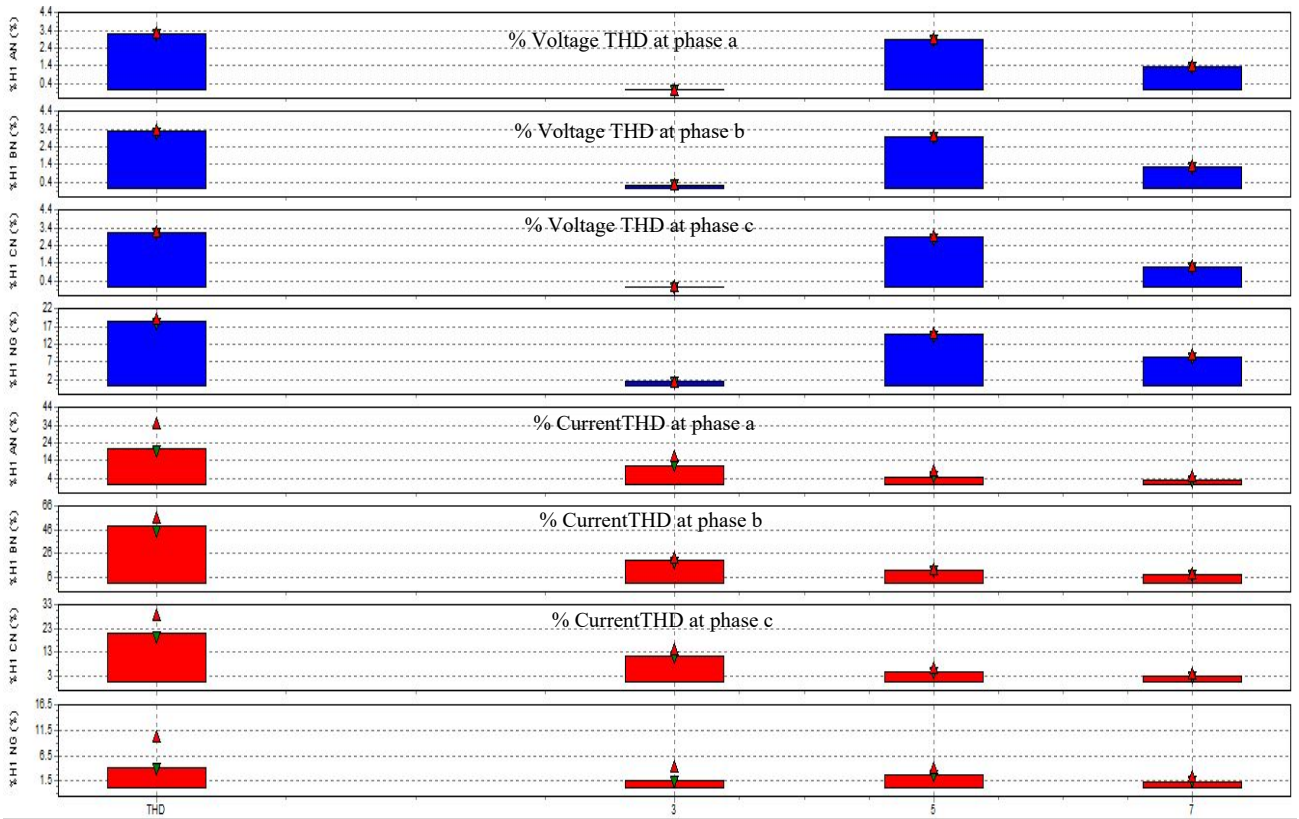

Figure 25. Harmonics analysis in grid.The system was tested with a nonlinear load of 1 HP motor and resistive bulb load in the stand-alone as well as grid-connected mode, but no transients were observed during both modes of operations. However, some voltage drop was observed when load enhances.

The transients present in the network current travels in the distribution grid which is interconnected with the solar inverter. Hence, the current profile of the grid gets

distorted, which is in general 120° out of phase with each other. This happens due to variation in the load side power demand As a whole, it can be concluded that the grid current and voltage have sinusoidal behavior, and the same is required if grid integration is to take place with a stable frequency. It is further noticed that if there is any deviation from normal operating conditions, like failure of the reference grid, the inverter isolates from the grid and stops injecting voltages into the grid.

The active power feed from the grid tied inverter after receiving from the solar PV plant through the DC-DC converter is shown in Figure 26. It is observed that the power dipped at time t=0.6 s and then resumed to the desired level at t=1.6 s. This is due to the variation of irradiance at the generation side of the system. Also, at t=2 s, a slight plunge was observed due to the variation in the temperature of the system at the input side. The results show that the power on the demand side varies as per the conditions on the generation side. The active power is directly proportional to the irradiance and hence a steep depletion was observed as recorded in Figure 26 whereas, it is inversely proportional to the temperature so trivial moderation was traced during such a time period.

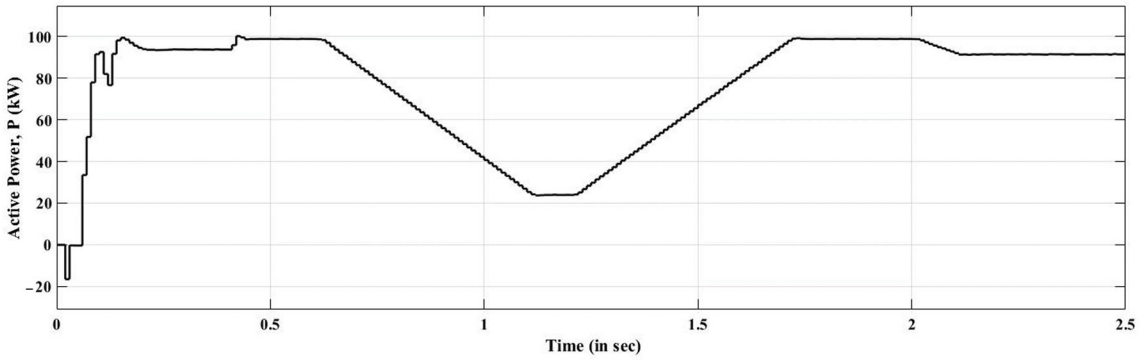

Figure 26. Active power received at the output of the grid tied inverter.

3. Conclusion

The proposed grid-connected model contains mainly a synchronous mode interleave boost converter, which has both advantages, that is, interleaved and synchronous operation due to which the more efficient system is obtained at the DC side. To cater to the irradiance variation on the DC side, the PSO based MPPT topology has been employed so as to track the maximum power point. The four-legged IGBT based VSC was used in the proposed model. For vetting the robustness of the proposed methodology and analysis of the solar PV system integrated into the distribution system, the system was designed and developed in Simulink environment. The system was simulated under distinct values of irradiance and temperature to examine the behavior of the proposed topology in the actual situation. A laboratory prototype of a 1.5 kW system was designed to analyze the system performance. The voltage, current and active power generated from the proposed scheme was observed under the variation of irradiance and temperature. The comparison of the synchronous mode and non-synchronous mode of the boost converter was recorded. It was seen that the proposed boost converter topology has fewer ripples and lesser stable time as compared to the conventional boost converters including interleaved facilities. The output voltage of the boost converter gets stabilized in a fraction of seconds. The conversion efficiency of the proposed converter topology was recorded to be more than 93% under different duty cycles. The frequency analysis of the grid was also remarked upon. The comparison of the frequency response of the grid tied inverter and utility grid was plotted and it was observed that the frequency response of the inverter is almost constant and disturbance-free with the local source being a little higher as compared to the grid frequency response. It is found that the variation of the frequency was from 50 Hz to 50.11 Hz, which is not beyond the boundaries as per the IEEE 519 standard. The

synchronous reference frame-based phase lock loop control strategy with PI controller was implemented to control and regulate the AC power and worked synchronously with the distribution grid. The analysis of the total harmonics distortion (THD) was carried out and recorded after the integration of the solar PV system with the distribution grid. It was observed that the third, fifth, and seventh harmonics were spotted but all were <5%, which is well within the range and complying with the IEEE standard 519.

Author Contributions: Conceptualization, A.D., M.R. and M.J.; Methodology, A.D., M.A. and M.R.; Validation, A.D. and M.J.; Formal Analysis, M.A., A.D., I.A. and M.R.; Resources, M.R. and M.A.; Writing—Original Draft, A.D. and M.R.; Writing—Review and Editing, A.D., I.A., M.R. and M.J.; Visualization, A.D.; Supervision, M.R. and M.J.; Funding Acquisition, M.A., I.A., and M.R. All authors have read and agreed to the published version of the manuscript.

Funding: Researchers would like to thank the Deanship of Scientific Research, Qassim University for funding publication of this project.

Acknowledgments: Researchers would like to thank the Deanship of Scientific Research, Qassim University for funding the publication of this project.

Conflicts of Interest: The authors declare no conflict of interest.

References

1. Rashid, M.H. *Power Electronics Circuits, Devices and Applications*, 3rd ed.; Pearson: London, UK, 2006.
2. Subudhi, B.; Pradhan, R. *A Comparative Study on Maximum Power Point Tracking Techniques for photovoltaic Power Systems*; IEEE Transactions on Sustainable Energy: Piscataway Township, NJ, USA, 2013; Volume 4, pp. 89–98.
3. Nabil, K.; Nazih, M.; Rachid, O. General review and classification of different MPPT Techniques. *Renew. Sustain. Energy Rev.* **2017**, *68*, 1–18.
4. Alivarani, M.; Byamakesh, N.; Priti, D.; Kanungo, B.M. A review on MPPT techniques of PV system under partial shading condition. *Renew. Sustain. Energy Rev.* **2017**, *80*, 854–867.
5. Ahmed, J.; Salam, Z. An Enhanced Adaptive P&O MPPT for Fast and Efficient Tracking Under Varying Environmental Conditions. *IEEE Trans. Sustain. Energy***2018**, *9*, 1487–1496.
6. Wang, Y.; Li, Y.; Ruan, X. High-Accuracy and Fast-Speed MPPT Methods for PV String Under Partially Shaded Conditions. *IEEE Trans. Ind. Electron.***2016**, *63*, 235–245.
7. Peng, B.; Ho, K.; Liu, Y. A Novel and Fast MPPT Method Suitable for Both Fast Changing and Partially Shaded Conditions. *IEEE Trans. Ind. Electron.* **2018**, *65*, 3240–3251.
8. Li, X.; Wen, H.; Jiang, L.; Xiao, W.; Du, Y.; Zhao, C. An Improved MPPT Method for PV System with Fast-Converging Speed and Zero Oscillation. *IEEE Trans. Ind. Appl.* **2016**, *52*, 5051–5064.
9. Sangwongwanich, A.; Blaabjerg, F. Mitigation of Interharmonics in PV Systems with Maximum Power Point Tracking Modification. *IEEE Trans. Power Electron.* **2019**, *34*, 8279–8282.
10. Shaw, P. Modelling and analysis of an analogue MPPT-based PV battery charging system utilising dc–dc boost converter. *IET Renew. Power Gener.***2019**, *13*, 1958–1967, doi:10.1049/iet-rpg.2018.6273.
11. Liu, H.; Hu, H.; Wu, H.; Xing, Y.; Batarseh, I. Overview of High-Step-Up Coupled-Inductor Boost Converters. *IEEE J. Emerg. Sel. Top. Power Electron.* **2016**, *4*, 689–704.
12. Li, W.; He, X. Review of Nonisolated High-Step-Up DC/DC Converters in Photovoltaic Grid-Connected Applications. *IEEE Trans. Ind. Electron.* **2011**, *58*, 1239–1250.
13. Forouzesh, M.; Siwakoti, Y.P.; Gorji, S.A.; Blaabjerg, F.; Lehman, B. Step-Up DC–DC Converters: A Comprehensive Review of Voltage-Boosting Techniques, Topologies, and Applications. *IEEE Trans. Power Electron.* **2017**, *32*, 9143–9178.
14. Mousavi, A.; Das, P.; Moschopoulos, G. A Comparative Study of a New ZCS DC–DC Full-Bridge Boost Converter with a ZVS Active-Clamp Converter. *IEEE Trans. Power Electron.* **2012**, *27*, 1347–1358.
15. Asim, A.; Aamir, A.; Hang, S.C.; Ahmad, E.; Nasrudin, A.R. Comparative analysis of high voltage gain DC-DC converter topologies for photovoltaic systems. *Renew. Energy***2019**, *136*, 1147–1163.
16. Annop, N.; Sudarat, K. A Novel High Step-up DC-DC Converter for Photovoltaic Applications. *Procedia Comput. Sci.* **2016**, *86*, 409–412.
17. Dileep, G.; Singh, S.N. Selection of non-isolated DC-DC converters for solar photovoltaic system. *Renew. Sustain. Energy Rev.* **2017**, *76*, 1230–1247.
18. Joydip, J.; SahaHiranmay; Konika, D.B. A review of inverter topologies for single-phase grid-connected photovoltaic systems. *Renew. Sustain. Energy Rev.* **2017**, *72*, 1256–1270.
19. Amamra, S.; Meghriche, K.; Cherifi, A.; Francois, B. Multilevel Inverter Topology for Renewable Energy Grid Integra-tion. *IEEE Trans. Ind. Electron.* **2017**, *64*, 8855–8866.

20. Li, W.; Gu, Y.; Luo, H.; Cui, W.; He, X.; Xia, C. Topology Review and Derivation Methodology of Single-Phase Transformerless Photovoltaic Inverters for Leakage Current Suppression. *IEEE Trans. Ind. Electron.* **2015**, *62*, 4537–4551.
21. Li, T.; Cheng, Q. A comparative study of Z-source inverter and enhanced topologies. *CES Trans. Electron. Mach. Syst.* **2018**, *2*, 284–288.
22. Wu, F.; Sun, B.; Duan, J.; Zhao, K. Online Variable Topology-Type Photovoltaic Grid-Connected Inverter. *IEEE Trans. Ind. Electron.* **2015**, *62*, 4814–4822.
23. Raveendhra, D.; Pathak, M.K. Recent trends in solar PV inverter topologies. *Solar Energy***2019**, *183*, 57–73.
24. Saleem, M.; Choi, K.-Y.; Kim, R.-Y. Resonance damping for an LCL filter type grid-connected inverter with active disturbance rejection control under grid impedance uncertainty. *Int. J. Electron. Power Energy Syst.***2019**, *109*, 444–454, doi:10.1016/j.ijepes.2019.02.004.
25. Shankar, V.A.; Umashankar, S.; Sanjeevikumar, P.; Mihet-Popa, L.; Fedák, V.; Ramachandaramurthy, V.K. Power Quality Performance Analysis of grid tied PV fed Parallel Pumping System under Normal and Vibrating Condition. *Energy Procedia***2018**, *145*, 497–503, doi:10.1016/j.egypro.2018.04.092.
26. Kharrazi, A.; Sreeram, V.; Mishra, Y. Assessment techniques of the impact of grid-tied rooftop photovoltaic generation on the power quality of low voltage distribution network-A review. *Renew. Sustain. Energy Rev.***2020**, *120*, 109643, doi:10.1016/j.rser.2019.109643.
27. Hariri, M.H.M.; Desa, M.K.M.; Masri, S.; Zainuri, M.A.A.M. Grid-Connected PV Generation System—Components and Challenges: A Review. *Energies***2020**, *13*, 4279, doi:10.3390/en13174279.
28. Naidu, R.P.K.; Meikandasivam, S. Power quality enhancement in a grid-connected hybrid system with coordinated PQ theory& fractional order PID controller in DPFC. *Sustain. Energy Grids Netw.* **2020**, *21*, doi:10.1016/j.segan.2020.100317.
29. Al-Shetwi, A.Q.; Hannan, M.A.; Jern, K.P.; Alkahtani, A.A.; Abas, A.E.P. Power Quality Assessment of Grid-Connected PV System in Compliance with the Recent Integration Requirements. *Electronics***2020**, *9*, 366, doi:10.3390/electronics9020366.
30. Teekaraman, Y.; Kuppusamy, R.; Baghaee, H.R.; Vukobratović, M.; Balkić, Z.; Nikolovski, S. Current Compensation in Grid-Connected VSCs using Advanced Fuzzy Logic-based Fluffy-Built SVPWM Switching. *Energies***2020**, *13*, 1259, doi:10.3390/en13051259.
31. Revathi, B.S.; Prabhakar, M. Non isolated high gain DC-DC converter topologies for PV applications–A comprehensive review. *Renew. Sustain. Energy Rev.* **2016**, *66*, 920–933.
32. Hinov, N.; Arnaudov, D.; Valchev, V.; Vuchev, S. *Comparative Loss Analysis of Boost and Synchronous Boost DC-DC Con-Verters*; XXVI International Scientific Conference Electronics (ET): Sozopol, Bulgaria, 2017; pp. 1–4.
33. dSPACE DS-1104. *Hardware Installation and Configuration and Control Desk Experiment Guide*; dSPACE: Paderborn, Germany, 2004.
34. IEEE Guide for Harmonic Control and Reactive Compensation of Static Power Convertors, IEEE 519-1981, April 1981.
35. Recommended Practice for Utility Interface of Photovoltaic Systems, IEEE Std 929-2000, 2000.

Design and Implementation of Grid Sequence Separator Based Control for Single-Phase Microgrid

Ankita Arora
Dept. of Electrical Engineering
Delhi Technological University
Delhi, India
arora.ankita09@gmail.com

Alka Singh
Dept. of Electrical Engineering
Delhi Technological University
Delhi, India
alkasingh.eed@gmail.com

2020 IEEE 17th India Council International Conference (INDICON) | 978-1-7281-6916-3/20/$31.00 ©2020 IEEE | DOI: 10.1109/INDICON49873.2020.9342103

***Abstract*—This paper proposes a Grid Sequence Separator (GSS) based control in standalone and grid connected mode for 1-ϕ PV integrated battery energy storage system (BESS). The proposed model serves many functions such as reactive power compensation, power balance, harmonic removal in source current and continuity of supply power in standalone mode. Battery is connected at the DC Link through bidirectional buck-boost converter. The smooth transfer from grid connected to standalone mode (GTS) and standalone to grid connected mode (STG) is achieved through static transfer switch (STS). GSS has been designed in αβ frame which removes in-loop filters problems causing time delays thereby improving its transient performance. This makes the bandwidth of the system wider making the PLL transition control faster. It has been employed for control of shunt compensator to extract fundamental load current accurately. The absence of in-loop delays remarkably improves its performance which is validated using simulation results.**

Keywords— ***Grid Sequence Separator, Phase Locked Loop, Shunt Compensation, Power quality, Battery Energy Storage System***

I. INTRODUCTION

Renewable energy sources (RES) are becoming more and more popular because of increasing price of fossil fuels and their high depletion rate and environmental degradation due to pollution. The RES with energy storage system form an integral part of the microgrid which provide energy to the local loads [1]. The seamless transition between Grid to Islanding (GTI) and Islanding to Grid (ITG) should take place fast without producing large variations in voltage and current waveforms. A smooth transition should be ensured irrespective of the change of control in both the modes. Hence, efficient control methods are needed to eliminate the above disturbances during transition from GTI to ITG mode [2].

There are many seamless transition techniques in literature which deals with GTI and ITG modes. For achieving synchronization of microgrid to the main grid, the Phase Locked Loop (PLL) is the conventional and accepted approach. Good PLL techniques provide improved performance under polluted grid or sudden grid disturbances such as voltage sag, swell and presence of harmonics. It also plays a very crucial role in tracking the grid phase angle and frequency by generating the synchronizing signal during change of mode. A PLL needs to be suitably designed to avoid unnecessary transients in voltage and current waveforms under sudden disturbances. Therefore, PLL plays a very important role and only an efficient PLL can ensure efficient performance of synchronization and de-synchronization during islanding and grid mode [3].

Due to constantly changing solar irradiation, Photovoltaic (PV) with grid connected systems normally employ boost converter and maximum power point tracking (MPPT) algorithms such as Perturb & Observe (P&O), Incremental Conductance (Inc-Cond) and other intelligent techniques to track the maximum power [4,5]. Also, PV integrated microgrid employs energy storage system such as battery that constantly controls load demand and generation variations and also inhibits the fluctuation caused in the distribution system due to intermittent nature of PV, thus improving the robustness of the whole system.

It is also well known that distribution systems employ extensive use of power electronics based non-linear loads. Hence, it is natural that the power quality issues have become a major concern in grid connected PV systems. The elimination of harmonics from the source current injected due to non-linear loads is based on the principle of shunt compensation. The controller is designed and controlled to be able to extract the fundamental estimated load current for making sinusoidal reference current for grid.

Many control techniques in literature have been discussed for effective shunt compensation in PV based microgrid [6-11]. Z.Arani et.al have discussed Multi-resonator Notch Frequency control [6], X. Guo et.al discussed Multiple complex coefficient Filter based Microgrid [7], Adaptive power management based microgrid is discussed in [8]. Performance of any microgrid is highly dependent on the control algorithm employed for Shunt Compensation and the type of PLL used. The robustness of microgrid is discussed in [9] and emphasize on the effective design of controller to achieve this. Therefore, PLL and active shunt compensator control must be designed which are resistant to grid disturbances, load disturbances and achieve good dynamic and steady state response. Here GSS control based Microgrid is discussed in this paper [10-11].

Grid Sequence Separator Control (GSS) based shunt compensator and PLL is based on designing the Delayed Signal Cancellation (DSC) time lag operators in stationary frame. The stationary frame called $\alpha\beta$ frame eliminates the delay in the control loop and thus improving the dynamic response of the system. It effectively reduces the steady state error to zero. It shows higher resistance to lower order harmonics and thus there

978-1-7281-6916-3/20/$31.00 ©2020 IEEE

Authorized licensed use limited to: DELHI TECHNICAL UNIV. Downloaded on February 15,2021 at 09:57:07 UTC from IEEE Xplore. Restrictions apply.

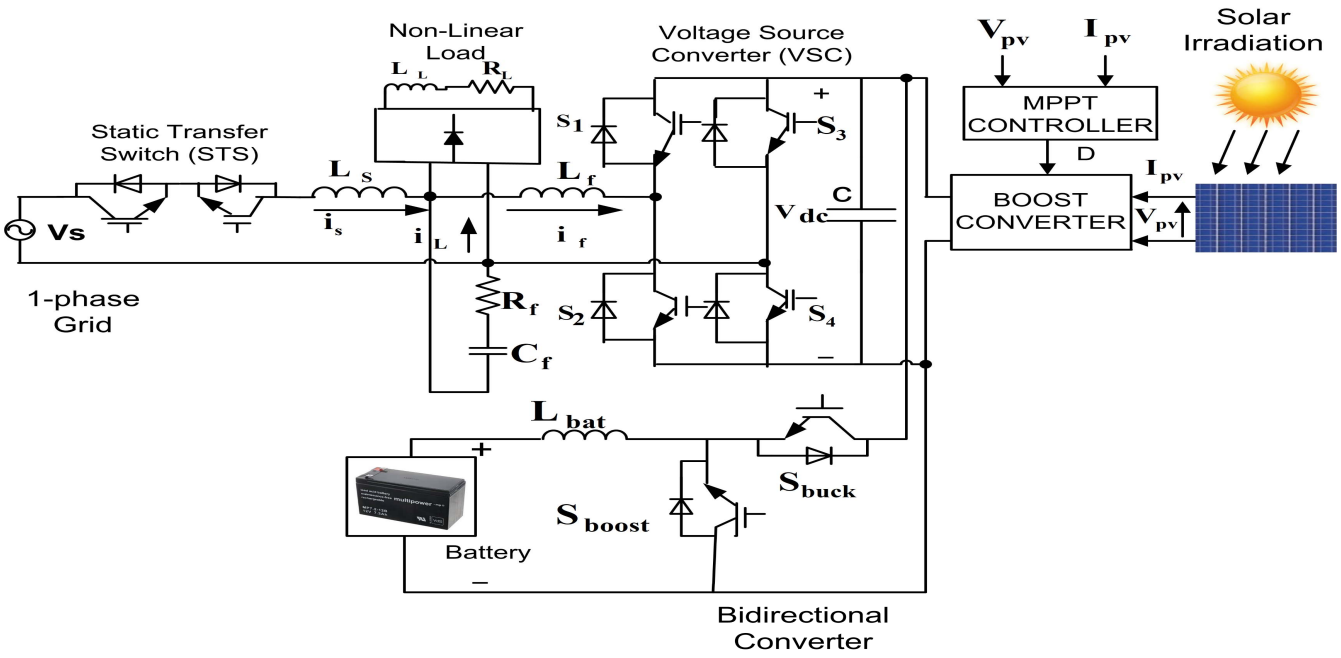

(a)

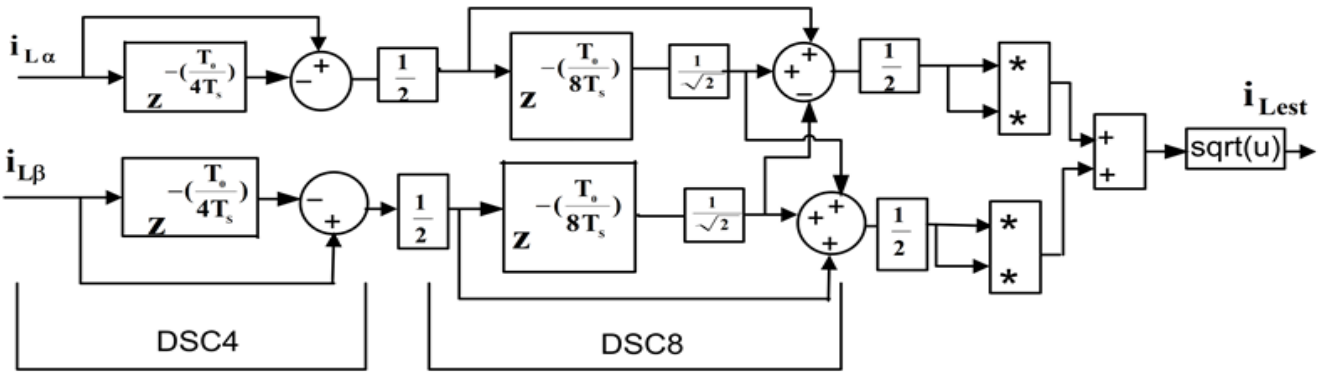

(b)

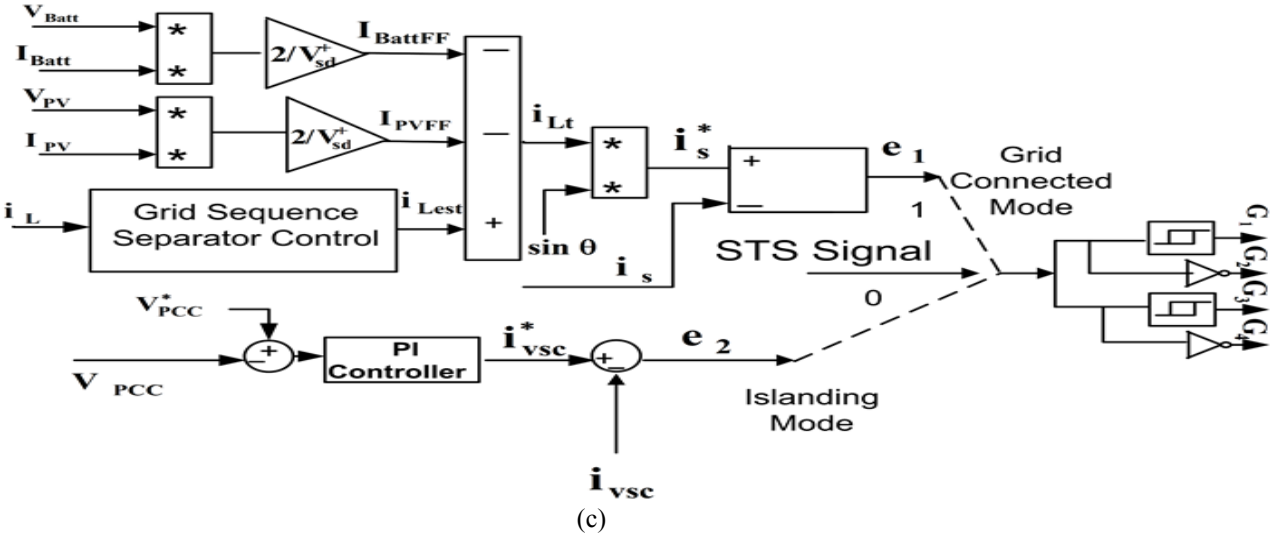

(c)

Fig. 1. (a) Block Diagram of PV Based Microgrid (b) Grid Sequence Separator Control (c) Control Diagram of PV Based Microgrid

Authorized licensed use limited to: DELHI TECHNICAL UNIV. Downloaded on February 15,2021 at 09:57:07 UTC from IEEE Xplore. Restrictions apply.

is no requirement of Low Pass Filter to filter out these harmonics. In $\alpha\beta$ frame, the α component is used to extract the sine component and β component is used extract the cosine component. Here, only two DSC operators with delay of T/4 and T/8 are used to remove harmonics till 13th order. Therefore, this technique is advantageous to the DSC technique. The whole paper is divided as follows. Section II provides the system configuration. GSS operation is discussed in Section III. Section IV gives the Simulink results and the last section summarizes the conclusion.

II. System Configuration

The PV based microgrid with battery energy storage system is connected to a distribution system feeding non-linear load and the system is simulated in MATLAB environment. The schematic block diagram and the control developed in grid connected and islanding mode is shown in Fig. 1(a). The battery dynamics are controlled by using bidirectional converter connected to the DC Link of Voltage Source Converter (VSC). The Static Transfer Switch (STS) is connected for smooth transfer between both the modes and allows for power flow in both the directions. An interfacing inductor is connected for the elimination of current ripples and RC filter is connected at the PCC for reduction of voltage ripples.

III. Grid Sequence Separator Control

Grid Sequence Separator (GSS) is an advanced version of Delayed Signal Cancellation (DSC) technique which operates in $\alpha\beta$ frame rather than in dq frame. The DSC filter is the time delayed version of the original signal added to the original signal to cancel the effect of harmonics [11]. DSC in dq frame is defined as

$$i'_{Ldq} = \frac{1}{2}\left[i_{Ldq}(t) + i_{Ldq}\left(t - \frac{T_o}{n}\right)\right] \quad (1)$$

where T_o is the fundamental time period of the load current and n is the delay factor.

Assuming that the connected load is non-linear in nature, the load current with harmonic order h' can be represented in dq frame as

$$i_{Ld}^{h'} = I_h \cos(h'wt) \quad (2)$$

$$i_{Lq}^{h'} = I_h \sin(h'wt) \quad (3)$$

where $h' = h - 1$, h represents harmonic order in $\alpha\beta$ frame.

From (1), (2) and (3) and using trigonometric properties we get

$$i'_{Ldq} = I_h\left[\cos\left(h'wt - \frac{h'\pi}{n}\right) + j\sin\left(h'wt - \frac{h'\pi}{n}\right)\right]\cos\left(\frac{h'\pi}{n}\right) \quad (4)$$

Converting the above rectangular coordinate form in Euler form and polar form we get

$$i_{Ldq}^{h'} = \cos(\frac{h'\pi}{n}).e^{-j\frac{\pi h'}{n}} I_h e^{jh'wt} \quad (5)$$

$$= \cos\left(\frac{h'\pi}{n}\right) \angle -\frac{\pi h'}{n} \quad (6)$$

By choosing the proper value of n and h', any harmonic order can be removed. Since the harmonic order h' in dq frame is one less than h when represented in $\alpha\beta$ frame, therefore fifth harmonic in $\alpha\beta$ frame is removed when $h' = -6$ and n=4. Similarly, the 11th harmonic in $\alpha\beta$ frame is removed by $h' = -12$ and n=8. Like this using various combination of delay factor any harmonics order can be removed. Here the suitable number of DSC blocks are connected in series which create unwanted delays. Therefore, to avoid delays within the control loop in dq frame, it is mapped in to $\alpha\beta$ frame where in-loop drawback has been eliminated. This is the basic principle of GSS based Control. When DSC filter is relocated to $\alpha\beta$ frame from dq frame we get,

$$\begin{bmatrix} i'^{h}_{L\alpha}(t) \\ i'^{h}_{L\beta}(t) \end{bmatrix} = \frac{1}{2}\left\{\begin{bmatrix} i^{h}_{L\alpha}(t) \\ i^{h}_{L\beta}(t) \end{bmatrix}\begin{bmatrix} \cos(\frac{2\pi}{n}) & -\sin(\frac{2\pi}{n}) \\ \sin(\frac{2\pi}{n}) & \cos(\frac{2\pi}{n}) \end{bmatrix}\begin{bmatrix} i^{h}_{L\alpha}\left(t - \frac{T_o}{n}\right) \\ i^{h}_{L\beta}\left(t - \frac{T_o}{n}\right) \end{bmatrix}\right\} \quad (7)$$

Therefore, we can observe that the delay factor of 2 is used to eliminate the effect of dc offset while the delay factor of 4 is used to eliminate the effect of negative sequence, fifth harmonic and seventh harmonic. Delay factor of 8 eliminates the effect of 11th and 13th harmonic. All delay factors are connected in parallel form which reduces the sample time delay as contrast to DSC. The GSS based control is shown in Fig. 1 (b) connected in cascaded form. Therefore, now there is no need of bulky tuned LC filters to remove 5th, 7th ,11th and 13th harmonics. Also, it removes the problem of tuning LC passive filters which has disadvantage of causing resonance with the supply systems. The GSS control avoids the problem of causing unwanted in-loop delays and lag in the system.

A. Current Based Control

The estimated current from the GSS filter is calculated as

$$i_{Lest} = \sqrt{i_{L\alpha}^2 + i_{L\beta}^2} \quad (8)$$

The PV and Battery contribution reflected in the grid is shown by

$$i_{PVFF} = \frac{2*P_{PV}}{V_{sd}^+} \quad (9)$$

$$i_{BattFF} = \frac{2*P_{Batt}}{V_{sd}^+} \quad (10)$$

The total current drawn from the grid is obtained by

$$i_{Lt} = i_{Lest} - i_{PVFF} - i_{BattFF} \quad (11)$$

The V_{sq} obtained from the synchronization controller is applied as input to the PI controller which provides the error in angular frequency (Δω). This angular frequency error is added to the natural frequency (ω_n) to get the estimated angular frequency.

$$\omega_{est} = \omega_n + \Delta\omega \quad (12)$$

Authorized licensed use limited to: DELHI TECHNICAL UNIV. Downloaded on February 15,2021 at 09:57:07 UTC from IEEE Xplore. Restrictions apply.

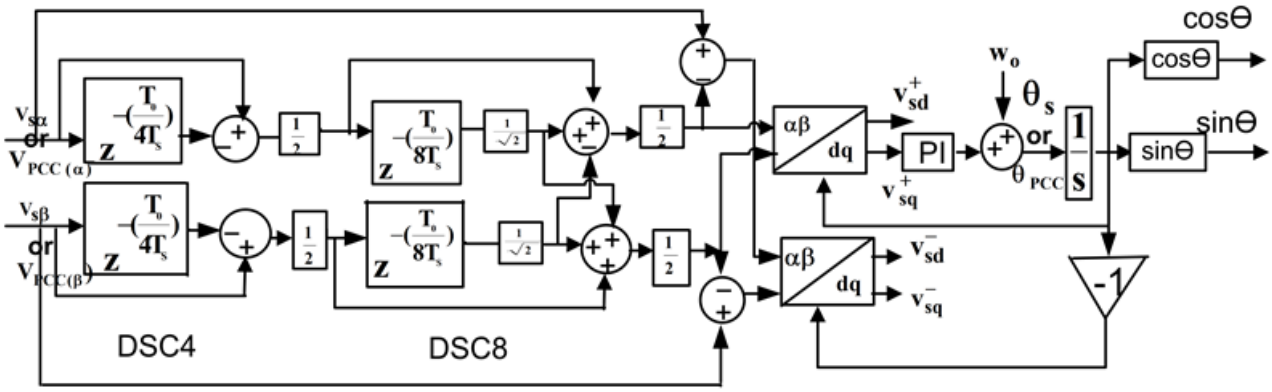

Fig. 2. Synchronization Controller in grid connected Mode and Islanding Mode

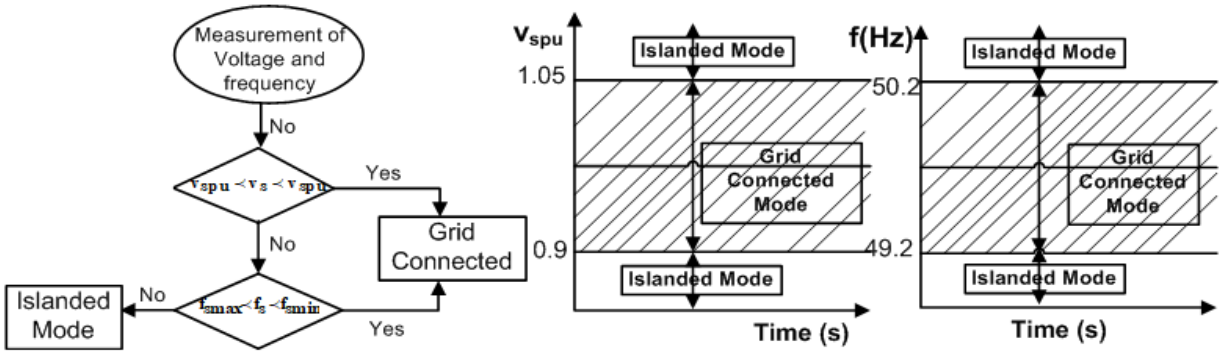

(a) (b)

Fig. 3. (a) Flow chart (b) Graphical representation for smooth transition between grid connected and Islanding Mode

The estimated frequency (ω_{est}) is integrated to get the grid voltage angle (θ_{est}) .

$$\int \omega_{est}\, dt = \theta_{est} \tag{13}$$

The estimated voltage angle (θ_{est}) is used to get the unit in-phase template and the quadrature template for generation of reference signal

$$i_s^* = i_{Lt} * sin\theta \tag{14}$$

The difference between the actual source current and the reference source current is given to the hysteresis controller for the generation of pulses in current control mode. The above control is illustrated in Fig. 1(c).

B. Voltage Based Control

The aim of the islanded control is to have smooth transition from grid connected to islanded mode. The schematic diagram of the synchronization controller is shown in Fig. 2. The controller is used to operate the PV Based Battery integrated system either in islanding mode and grid connected mode. The magnitude of voltage (v_s) and frequency (f_s) generated by the grid must be comparable with that generated by PCC voltage (V_{PCC}) and frequency (f_{PCC}) measured at PCC.

If the voltage and frequency are within the range (i.e. $0.9 < V_s(pu) < 1.05$ and $49.2\,Hz < f_s < 50.2\,Hz$) then '1' signal is given to the STS and when mismatch takes place then '0' signal is given to the STS and seamless transition to islanding mode is achieved as illustrated in flow chart in Fig. 3 (a) and graphical representation in Fig. 3 (b). In islanded mode, the reference PCC voltage is generated as

$$V_{PCC}^* = V_{MPCC} sinwt \tag{15}$$

The PCC voltage generated is compared with the sensed PCC Voltage and is fed to the PI controller and generates the reference VSC current.

$$v_{ePCC} = V_{PCC}^* - V_{PCC} \tag{16}$$

The PI controller output at 'm' instant is calculated as

$$i_{vsc}^*(m) = i_{vsc}^*(m-1) + K_{pv}\{v_{ePCC}(m) - v_{ePCC}(m-1)\} + K_{iv} v_{ePCC} \tag{17}$$

Authorized licensed use limited to: DELHI TECHNICAL UNIV. Downloaded on February 15,2021 at 09:57:07 UTC from IEEE Xplore. Restrictions apply.

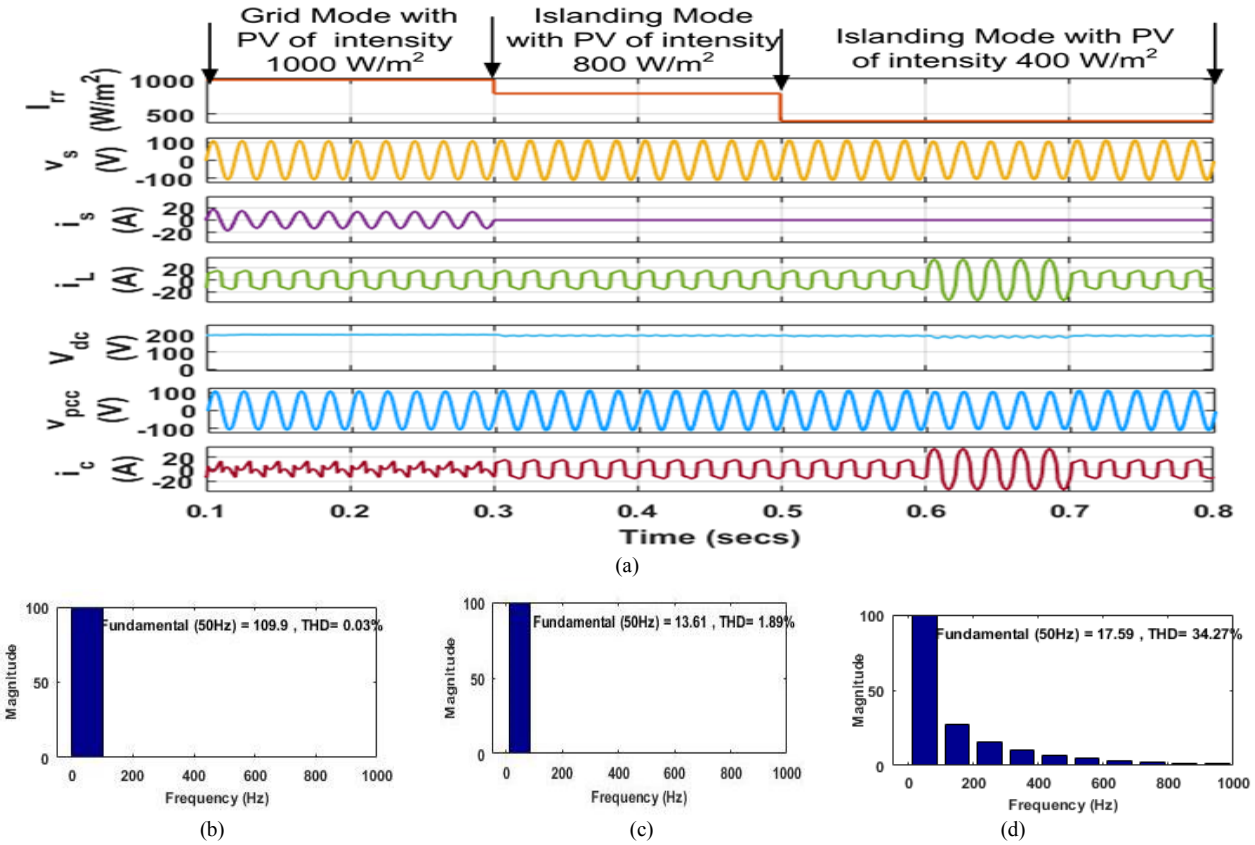

Fig. 5. (a) Simulation of GSS based Control in PV based Microgrid (b) THD in Supply voltage (b) THD in Supply current (c) THD in Load Current

The reference VSC current is compared with the sensed VSC current and given to the hysteresis controller for generation of PWM pulses.

IV. Results and Discussion

The performance is analysed and discussed under changing irradiation and changing load conditions. Power-Voltage (P- V) and Current Voltage (I-V) curves of module is shown in Fig. 4. The system parameters are listed in Table I.

TABLE I. System Parameters

Maximum power of PV array at 1000 W/m^2	750 W
1-phase grid Supply	110 V (rms)
Interfacing Inductor	3 mH
Ripple Filter	R=15Ω C= 6μF
DC Bus Voltage	200 V
Battery Rating	120 V, 1000 Ah
Load Rating	R= 5Ω, L= 40 mH
Source Inductance	1 mH

A. Grid Connected Mode

The grid connected mode is simulated till 0.3 s. The waveforms of solar irradiation (I_{rr}), grid voltage (v_s), source current (i_s), load current (i_L), DC Link voltage (V_{dc}),PCC

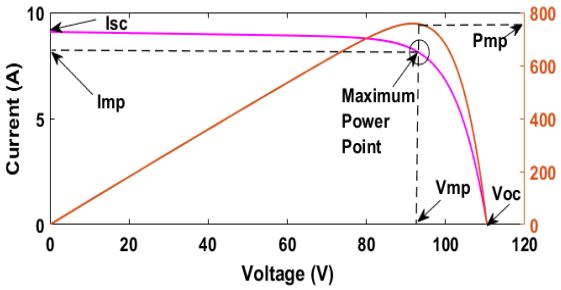

Fig. 4. P-V and I-V curves of the PV Module

voltage (V_{pcc}) and Compensator current (i_c) are shown in Fig. 5(a). The source current is observed to be sinusoidal and free of harmonics as the compensating current is sending the neutralizing current to cancel the harmonics injected by the non-linear load. The THD in source voltage is 0.09 %, THD in source current is found to be 1.89% with load THD of 34.27% as shown in Fig. 5(b-d).

Fig. 6 illustrates the waveforms of solar irradiation (I_{rr}), PV power (P_{pv}), grid power (P_s), load power (P_L) and battery power (P_{batt}). Under solar irradiation intensity of 1000 W/m2, the PV is delivering power of 700 W and grid delivers power of 650 W. Out of 1350 W delivered, the 900 W power is absorbed by the load and the remaining 450 W power is used for charging

Authorized licensed use limited to: DELHI TECHNICAL UNIV. Downloaded on February 15,2021 at 09:57:07 UTC from IEEE Xplore. Restrictions apply.

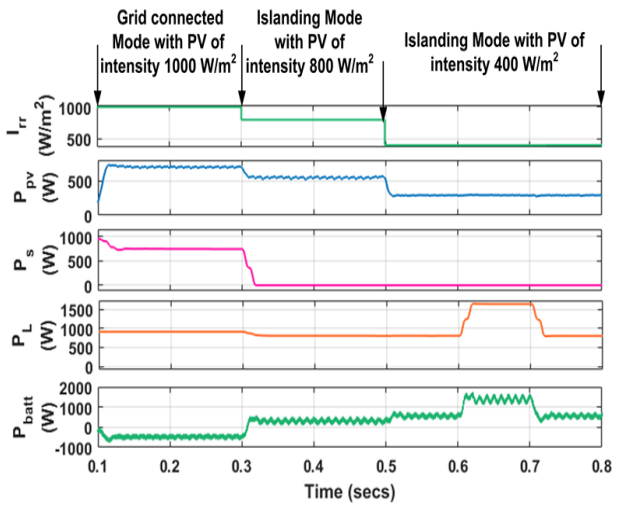

Fig. 6. Steady State Power balance in grid connected and islanded mode

the battery. Under the battery charging mode, the battery takes 7 A current and the voltage is increased to 122.4 V and SOC is also increased shown in Fig. 7.

B. Islanding Mode

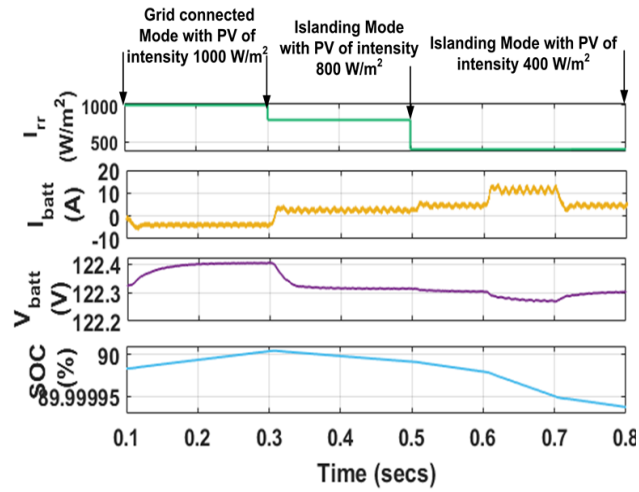

Fig. 7. Battery current (I_{batt}), voltage (V_{batt}) and State of Charge (SOC) in grid connected and islanding mode

In islanding mode, the voltage control mode is used. Here the load demand is met by both PV system and Battery energy storage system. This mode is observed under varying solar irradiation and load disturbance.

1) Under solar irradiation of 800 W/m²: The PCC voltage is sinusoidal and now the load demand is met by both PV system and Battery energy storage system. The load demand of 900 W is met by PV power of 700 W and battery of 200 W. The battery is discharging with current of 4A and the battery is discharged to voltage of 122.3 V and the SOC has also decreased.

2) Under solar irradiation of 400 W/m²: Under low solar irradiation of 400 W/m², the battery power is increased to 300 W and the Battery charging current has further increased to 7A and PV power is reduced to 600 W to meet the load demand of 900 W. When the load disturbance is caused, the load current is increased to 25 A for which also load power is increased to 1600 W. Since the irradiation is reduced to 400 W/m², therefore the load power of 1600 W is provided by the battery with 1000 W and solar power of 600 W.

Under islanding mode, the PCC voltage is found to be sinusoidal. Here also the battery has discharged and SOC has also reduced.

B. GSS based PLL Performance under voltage sag, swell and distorted grid

The GSS performance is observed under voltage sag, swell and distorted grid conditions in Fig. 8. It has been found that the source current is found to be sinusoidal under all voltage disturbances of sag, swell and distorted grid. Under normal grid voltage of 110 V, the supply current is found to be 16 A. When the voltage sag is introduced, the voltage is decreased to 100 V and the supply current also decreases to 14 A to meet the load demand. When the voltage is increased to 120 V, the supply current also increases to 17 A to meet the load demand. When the distorted grid with 5th and 7th harmonics is observed, the supply current is found to be sinusoidal. The results conclude that it works good under above voltage

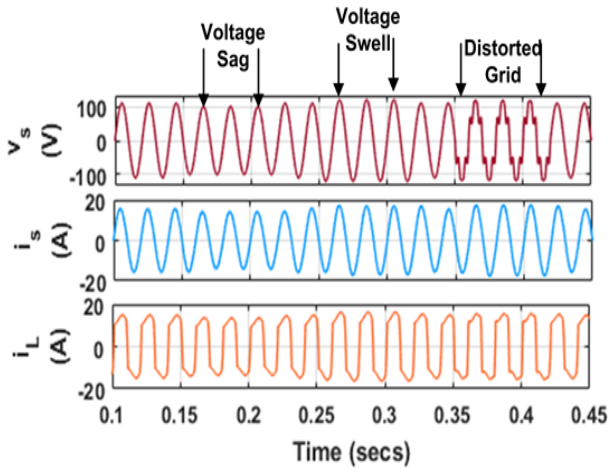

Fig. 8. GSS performance under voltage sag, swell and distorted grid disturbances

V. Conclusion

The seamless transition of Grid Connected to Islanding Mode (GTI) using Grid Sequence Separator (GSS) Based Control is studied in this paper. A single-phase PV integrated Battery Energy storage system is realized. The control algorithm is designed and tested for both Phase Locked Loop and shunt compensator is found to work satisfactorily well. The controller has the capability to cancel the harmonics being injected to the supply current side when used for compensation purpose. Moreover, it has maintained the supply current THD within 5% as per IEEE 519 and IEEE-1547 grid code. The other feature of the designed controller is exploited in synchronization. Its working as a PLL is quite effective and

Authorized licensed use limited to: DELHI TECHNICAL UNIV. Downloaded on February 15,2021 at 09:57:07 UTC from IEEE Xplore. Restrictions apply.

capability to synchronize and de-synchronize with the grid efficiently under both the modes is remarkable. The bidirectional buck-boost converter has efficiently regulated the dc link voltage to 200 V and controlled the dynamics of battery current and voltage.

ACKNOWLEDGEMENT

The authors are thankful to the DST, SERB for the sponsored project (EMR/2016/001874).

REFERENCES

[1] K. Macken, K. Vanthournout, J. VandenKeybus, G. Deconinck, R. Belmans, "Distributed Control of Renewable Generation Units with Integrated Active Filter", *IEEE Transactions on Power Electronics*, vol. 19, no. 5, 2004.

[2] Y. Karimi, H. Oraee, J. M. Guerrero, "Decentralized Method for Load Sharing and Power Management in a Hybrid Single/Three-Phase-Islanded Microgrid Consisting of Hybrid Source PV/Battery Units", *IEEE Trans. Power Electron.*, vol. 32, no. 8, pp. 6135-6144, 2017.

[3] S. Kumar, B. Singh, B.C. Pal, L. Xiu, A.A Durra, "Energy Efficient Three-Phase Utility Interactive Residential Microgrid With Mode Transfer Capabilities at Weak Grid Conditions*", IEEE Transactions on Industrial Applications*, vol. 55, no. 6, 2019.

[4] A. Arora, P. Gaur, "Comparison of ANN and ANFIS based MPPT Controller for grid connected PV systems", 2015 Annual IEEE India Conference (INDICON), pp. 1-6, 2015.

[5] T. Esram, P.L. Chapman, "Comparison of Photo voltaic Array Maximum Power Point Tracking Techniques", *IEEE Transactions on Energy Conversion*, vol. 22, no. 2, pp. 439-449, 2007.

[6] Preetha Sreekumar, Vinod Khadkikar, "Adaptive Power Management Strategy for Effective Volt–Ampere Utilization of a Photovoltaic Generation Unit in Standalone Microgrids", *IEEE Trans. Ind. Appl.*, vol. 54, no. 2, pp. 1784-1792, 2018.

[7] X. Guo, W. Wu, Z. Chen, "Multiple-complex coefficient-filter-based phase-locked loop and synchronization technique for three-phase grid-interfaced converters in distributed utility networks", *IEEE Trans. Ind. Electron.*, vol. 58, no. 4, pp. 1194-1204, Apr. 2011.

[8] Z. D. Arani, S. A. Taher, A. Ghasemi, M. Shahidehpour, "Application of multiresonator notch frequency control for tracking the frequency in low inertia microgrids under distorted grid conditions", *IEEE Trans. Smart Grid*, vol. 10, no. 1, pp. 337-349, 2019.

[9] S. Kumar, B. Singh, "Seamless Operation and Control of Single-Phase Hybrid PV-BES-Utility Synchronized System", *IEEE Trans. on Ind. Appl., Vol. 55, no. 2, 2019.*

[10] H.A. Hamed, A.F. Abdou, E. Bayoumi E.E. El-Kholy, "Effective design and implementation of GSS-PLL under voltage dip and phase Interruption," *IET Power Electron.*, vol. 11, no. 6, pp. 1018-1028, 2018.

[11] Yi Fei Wang, Yun Wei Li, "Grid Synchronization PLL Based on Cascaded Delayed Signal Cancellation", Power Electronics IEEE Transactions on,vol. 26, no. 7, pp. 1987-1997,2011.

Authorized licensed use limited to: DELHI TECHNICAL UNIV. Downloaded on February 15,2021 at 09:57:07 UTC from IEEE Xplore. Restrictions apply.

Design and Simulation of Ultra low loss Spiral Delay line for Integrated Optical Coherence Tomography

BHAWNA SHARMA,[1,*] KAMAL KISHOR,[2] AMRINDRA PAL,[1] SANDEEP SHARMA,[3] AND ROSHAN MAKKAR[4]

[1]*Electronics & Communication Engineering, DIT University, Dehradun-248009, Uttarakhand,*
[2]*Department of Physics, Delhi Technological University, (Formerly Delhi College of Engineering), Bawana road, Delhi-110042, India*
[3]*Centre for Reliability Sciences and Technology, Department of Electronics Engineering, Chang Gung University, Taoyuan, 33302, Taiwan*
[4]*Photonics Division, Society for Applied Microwave Electronics & Engineering Research, IIT Bombay Campus, Powai, Mumbai, Maharashtra, India*

Abstract: We report a design of 55 cm long spiral delay line at 850 nm wavelength. Propagation characteristics were simulated and analysed with fully vectorial Eigen Mode Expansion (EME) method. Bending losses were calculated and analysed for the optimization of minimum bending radius for reported structure. We have also simulated and analysed excess loss for a broadband of 200 nm at 850 nm operating wavelength. An excess loss of less than 0.2 dB is reported for the structure over the entire bandwidth range. The structure was further simulated for individual Transverse Electric (TE) and Transverse Magnetic (TM) modes and the analysis showed better results for TM mode. Reported structure is easy to fabricate, ultra-low loss and also broadband over 200 nm with a foot print of only 6×6 sq. mm. So, this design will improvise the reference arm section and will enhance the depth scanning of integrated optics based optical coherence tomography system**.**

Keywords: Spiral delay line, OCT, silicon nitride, integrated optics

1. Introduction

Photonic integrated components have recently gained wide interest in medical and industrial applications [1][2]. One such biomedical application is optical coherence tomography (OCT). OCT is a non-contact imaging technique which works on the principle of low coherence interferometry [3]. The generic OCT system consists of a broadband monochromatic light source which is directed on to a 2×2 fibre optic coupler in order to split the incident power evenly into the sample and reference arm. Light from the reference arm is sent upon a reference delay and redirected back whereas light from the sample arm is sent to a scanning mechanism which is structured to focus the beam on the sample. The recombined light from the sample and reference arms gives rise to interference pattern only when constructive interference takes place. The scanning depth of sample is controlled by the delay in the reference arm for deep scanning [4].

Optical delay lines (ODL) are important components which are used to provide a timed delay in a system. When these ODLs are implemented using integrated chips they show various advantages such as reduced cost, size, weight and power consumption [5]. They have various applications such as optical beam forming networks for antenna arrays, imaging processing units, radio on fibre links and devices, OCT systems and sensing units. There are different techniques to obtain optical delay in photonic integrated circuits such as integrated grating [6] delay lines(IGDL) wherein the spatial structure or refractive index parameter undergoes a periodic change mainly by modulating its structural parameters such as waveguide width and height or by modulating its effective refractive index [7], photonic crystal waveguides (PhCWs) based delay lines in which the photonic crystals consist of periodic optical micro and nano structures resulting in manipulation of light propagation while maintaining its efficiency [8], micro ring resonators(MRR) having the advantage of compact size and scalability consists of cascaded optical ring resonators for obtaining tuneable delay lines mainly in side coupled integrated space sequence of resonators(SCISSSOR) or coupled resonator optical waveguides (CROW) fashion and optical waveguide spiral delay lines which are simple length dependent delay structures that can be implemented using various material technologies such as Indium Phosphide (InP), silicon nitride (Si_3N_4) and silicon on insulator(SOI) [9].

While PhCWs offer wide bandwidth but incur high propagation losses, MRRs offer small foot print but usually have narrow bandwidth and bandwidth delay product is rather small. IGDLs offer compact resonant delay lines but fabrication is rather challenging and insertion loss is also high. Spiral delay lines are most promising candidate as they offer optimal area utilization with low loss, large bandwidth and does not require any external control. Moreover, these delay lines can be easily integrated with other components.

Various components in OCT system can be integrated on a chip so as to miniscule the existing fibre optic based OCT system. Numerous research groups have designed various components on an integrated optics platform for

Research Square

Preprints are preliminary reports that have not undergone peer review. They should not be considered conclusive, used to inform clinical practice, or referenced by the media as validated information.

OCT system. Yurtsever et al. reported a Mach-Zehnder interferometer (MZI) based integrated circuit consisting of numerous y-splitters and 190mm reference arm using Si_3N_4 / SiO_2 waveguides at 1320 nm. Upon its realization, the system was used to scan different layers of finger tip [10]. Cascaded MZI with tunable couplers-based delay line with delay tuning range of 124 ps was reported at 1550 nm central wavelength [11]. Recently cascaded MRRs on Si_3N_4platform was proposed. These structures showed a maximum delay tuning range of 394.6 ps @ 2GHz bandwidth using continues tuning method [12].

In this paper, a spiral reference ODL for depth scanning in integrated optics-based OCT system is reported. This reference delay line is designed for 850 nm central wavelength using Si_3N_4 and SiO_2 waveguides. The proposed structure is compact, low loss, broadband and long enough to provide deep scanning for OCT system. This structure was modelled for FV mode type and was found to be broadband over 200 nm bandwidth with an excess loss of 0.17dB. The structure was further simulated for individual TE and TM mode and minimum bending radius is also calculated. Comparative analyses for all three modes were done and it is found that TM mode being the most promising candidate with minimal propagation losses. The reported compact reference delay line upon realization along with integrated directional coupler [10-11] will completely replace the bulky fiber-based interferometer in a Fourier domain OCT system.

2. Waveguide design and modelling

The reported spiral structured optical delay line is designed for integrated optics OCT system at 850 nm central wavelength to compensate for the time delay required in the reference arm. The waveguides used in our structure are based on $Si_3N_4$and SiO_2technology called Triplex.We preferred channel buried waveguide geometry to achieve low propagation losses and better mode confinement. Smaller bending radius is required to miniaturize the device, so we encapsulated Si_3N_4 between SiO_2 layersdue to having medium refractive index contrast between$Si_3N_4(1.98)$ and $SiO_2(1.45)$. Schematic of waveguide structure is shown in Figure 1.

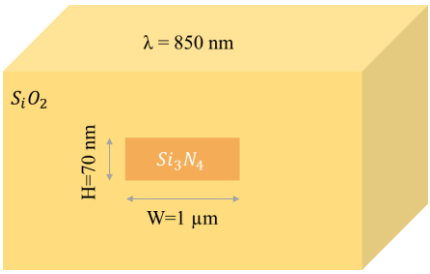

Fig:1: Illustration of channel buried waveguide at 850 nm wavelength

Reference delay lines for OCT prefer single mode operation as multimode might alter its axial resolution and sensitivity. To optimize the width and thickness of waveguide core for single mode operation, we have done modelling of waveguide using fully vectorial Finite Difference Mode (FDM) solver of Fimmwave simulation tool. Effective indices were calculated at the lower spectral end i.e. 750 nm of the broadband structure. The calculated effective indices for TE and TM mode as a function of waveguide core width (W) and thickness (H) are shown in Figure 2.

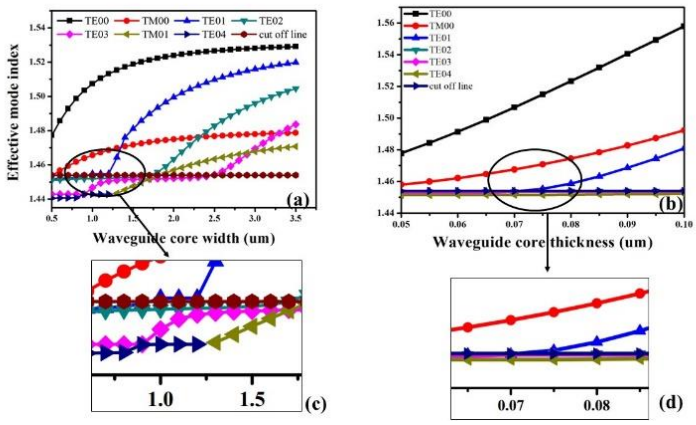

Fig:2: Mode effective index calculations of waveguide core (a) width and (b) thickness for TE and TM modes at 750 nm wavelength

It has been observed from the figure 2(a) that for waveguide core width below 1.2 µm only fundamental TE and TM mode will propagate. Also, from figure 2(b) it can be viewed that fundamental TE and TM modes will propagate for waveguide core thickness below 75 nm. So, after analysis of results, the width and thickness for single mode operation are optimised as 1 µm and 70 nm respectively.

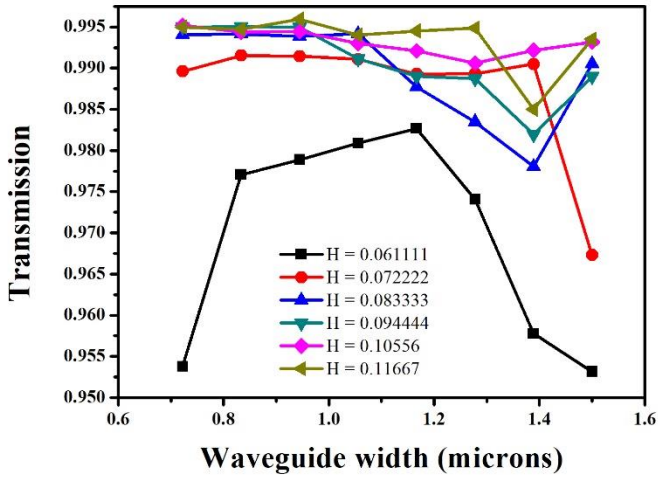

Fig 3: Normalized transmission over waveguide core width and thickness at 850 nm wavelength

Once we have achieved cut off value of waveguide core W and H, transmission below these values is an essential factor which needs to be contemplated. For this we have considered values of W ranging from 0.7 um to 1.4 µm and H ranging from 0.05 µm to 0.09 µm. A plot of waveguide W and H vs transmission at output is shown in Figure 3. It can be interpreting from the graph that best suitable values for maximum transmission below cut-off will be for W greater than 0.9 µm and H greater than 0.065 µm. So, after analysis of results, the W and H for single mode operation with transmission efficiency are optimised as 1 µm and 70 nm respectively.

3. Spiral Reference Section Design

The reported spiral delay line has been constructed using interleaved Archimedean spiral with continuous change of bending radius. General descriptive schematic for spiral reference delay line at 850 nm is shown in Fig 4. The reported structure covers an area of approximately 6×6 sq. mm.

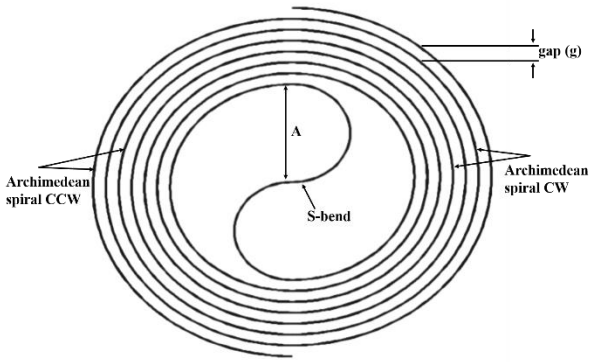

Figure 4: Descriptive illustration of reported spiral reference delay line

The structure consists of 2 set of half circles of which one set is used to bring light into the centre and other outwards towards the output. These inwards and outwards semi circles are connected to a S bend shaped structure whose radius is kept adiabatically large enough so as to have lossless transmission and change of mode location between CW and CCW spiral waveguides. Design parameters and propagation characteristics were modelled and optimized using Eigen Mode Expansion (EME) method of Fimmprop. Circular bends with a bend section along the circular path were used for designing the structure. The structure began with a set of bending arcs having 180° phase shift each for CW rotation. Each successive bending arc was set with a decreasing radius so as to form an inward spiral. A total 30 set of semi-circular bending arcs were used to form this inward spiral. Next an S-bend section was designed using two bending arcs of same radius having +180° and -180° phase shift each. The bending

section exiting the S-bend was then connected through a set of bending arcs having -180° phase shift with increasing radius for all successive arcs.

The minimum bending radius is a very significant parameter as the overall length of spiral is dependent on it. For the optimization of minimum bending radius, we have calculated the transmission and excess loss over a range of 0.5 mm to 3.5 mm. Results obtained for variation in transmission and excess loss vs bending radius is plotted in Figure 5.

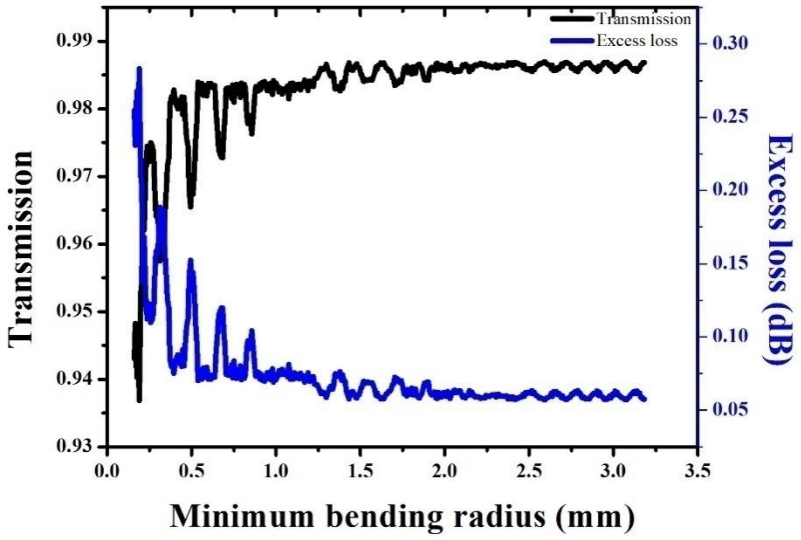

Fig. 5: Min. bending radius vs power at output

From Fig.5, it has been observed that the first constant maximum was achieved at 1.29 mm, next at 1.47 mm and then at 1.66 mm bending radius and so on. We have considered 1.47 mm as minimum bending radius as at 1.47 mm, the reported structure results with minimum excess losses for a broad range (200 nm) of spectrum.

Mathematical calculations

The length of consecutive semi circles is then related to the length of minimum bending arc by following relation.

$$A2 = (A \times 2) + dA \qquad (1)$$

Where A is the minimum bending arc length and dA is 10 µm and $A2$ is the bending arc length of consecutive semi-circle from S bend.

A multiplication factor of 2 was used for consecutive bending radius as S-bend was constructed using two bending arcs. So the next bending arcs should be wide enough such that overlapping doesn't occur. Moreover, a value of 10 µm was also added along with the multiplication factor so that coupling between consecutive arcs doesn't take place.

In general, there is a need for very accurate length parameters to be specified. Although this can be altered later on by few modifications in some parameters. The number of semi-circular arcs is mainly responsible for the overall length of spiral. For this structure, the number of half circles are taken to be 30 i.e. 30 half circle are deployed both in CW and CCW direction and the relation of each arc length can be determined by following relation

$$A_n = A_{n-1} + 10; \ for\ n = 3\ to\ 30 \qquad (2)$$

Once the length of each half arc is being determined, the overall length (L) of spiral structure can then be defined by following relation as

$$L = 2 \times \sum_{n=1}^{30} A_n \qquad (3)$$

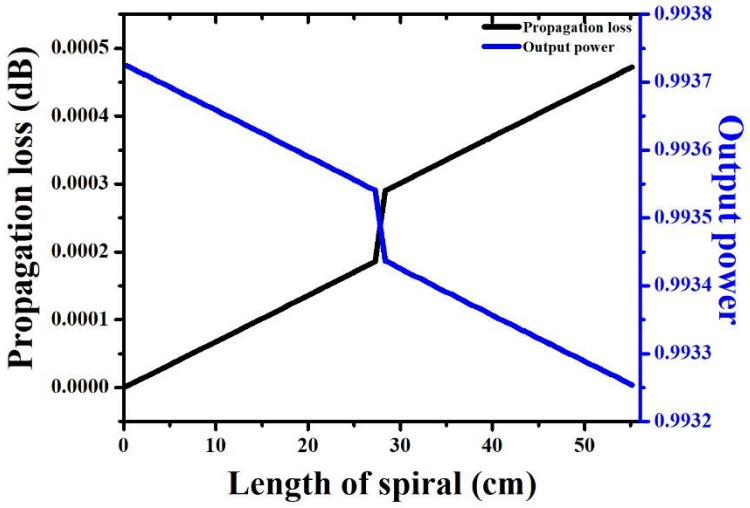

Fig.6: Length of propagation at 850 nm wavelength

Spiral structure results

For minimum bending radius of 1.47 mm, an overall delay line of 55.11 cm is accounted. The relation between length of propagation across spiral structured delay line vs power obtained and loss can be seen in Fig. 6. The overall propagation loss across the length of propagation was 0.00047 dB.

The time delay can then can be calculated by following relation

$$t_d = \frac{n_g \times L}{C} \qquad (4)$$

Where t_d is the time delay of the spiral delay line, n_g is the group effective index and *C* is the speed of light. For a delay length (L) of 55.11 cm and effective group index (n_g) of 1.62 (TE mode) and 1.51 (TM mode), a delay time of 2.35 ns and 2.19 ns is reported for this structure at 850 nm.

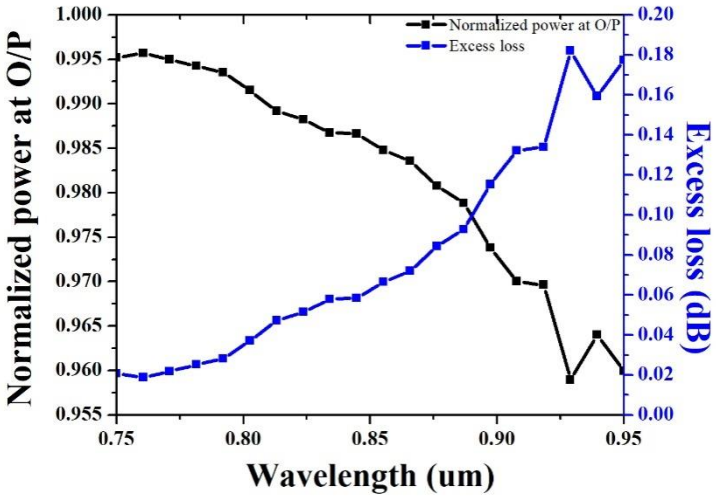

Fig. 7: Normalized power at output and excess loss for 200 nm bandwidth at 850 nm central wavelength

Now in order to analyse the structure performance, certain parameters such as its bandwidth, normalized power at output and excess loss are to be determined. The reported structure has been scanned over 200 nm i.e. from 750 nm to 950 nm at 850 nm central wavelength and is found to be broadband over this bandwidth range. Also, at 850 nm central wavelength, a normalized power of 98.64% and an excess loss of 0.06 dB is accounted. A maximum excess loss of 0.18 dB is observed across 200 nm bandwidth. The relation between bandwidth, normalized power and excess loss at 850 nm centre wavelength can be seen through Fig. 7.

2.3 Performance Analysis for TE, TM and FV modes

The calculations for the reported structure as stated above were performed for fully vectorial (FV) mode type which consists of both TE and TM modes. Now in order to study the individual mode performance for reported structure it is important to study the structural behaviour at TE and TM modes individually. Certain calculations were performed at different bending radius for all three mode types and analysis for the same is reported in Table 2. It can be seen from the calculations that for FV mode types, a constant PL is observed at all bending radius values.

For TE mode, it can be seen that an reduces PL occurs on increasing the bending radius value. A reduced PL of 0.000411dB for spiral structure length of 83.56 cm resulting a delay of 3.56 ns. The PL can be seen to be constant thereafter for spiral length of 86.06 cm, 94.30 cm and 96.88 cm resulting in a corresponding time delay of 3.67 ns, 4.02 ns and 4.13 ns respectively.

For TM mode, it is observed that for even smaller values of bending radius, reduced PL takes place. At spiral length of 14.67 cm a PL of 0.0042 dB was observed resulting in a time delay of 0.61 ns. Moreover, for increasing spiral length values, reduced PL is observed.

It can be analysed that TM mode shows best performance in comparison to other mode types while TE mode shows better performance than FV mode. The reduced performance for TE mode in comparison to TM mode may attribute due to sidewall roughness at waveguide core.

Table 1: Performance analysis for TE, TM and FV modes

Mode type	Min. bend. radius (mm)	L of spiral (cm)	Td (ns) TE	Td (ns) TM
FV	1.48	55.11	2.35	2.19
	1.66	61.88	2.64	2.46
	1.79	66.60	2.84	2.65
	1.84	68.25	2.91	2.72
	2.16	80.29	3.43	3.20
	2.41	89.38	3.81	3.56
	2.73	101.07	4.31	4.02
	3.08	112.65	4.81	4.49
TE	1.62	59.73	2.55	-
	1.81	66.74	2.85	-
	2.28	83.56	3.57	-
	2.34	86.06	3.67	-
	2.57	94.30	4.03	-
	2.64	96.88	4.14	-
TM	0.38	14.67	-	0.61
	0.72	27.41	-	1.14
	1.01	38.04	-	1.59
	1.78	51.96	-	2.17
	2.01	74.51	-	3.11
	2.23	82.89	-	3.46

3 Tolerance Analysis

The design tolerance was calculated at ±2% deviation for waveguide core width and thickness. The simulations for design tolerance were performed for FV mode type in terms of EL and PL parameters. The EL calculations were performed for 200 nm wavelength range which can be seen through Figure 8. It is observed from the plot that the maximum EL of 0.27 dB is accounted which is little higher than the original EL of 0.17 dB. Also, at 850 nm, an almost similar EL of 0.06 dB was observed for all deviation in width and thickness

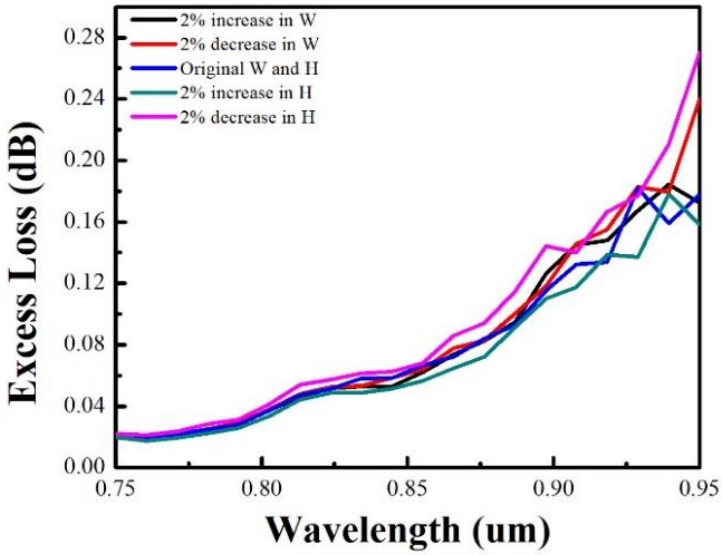

Fig. 8: Tolerance analysis for EL at 850 nm

Next PL was calculated at ±2% deviation for waveguide core width and thickness. The plot for PL in terms of its design tolerance can be seen through Figure 8. It can be seen that a constant PL was observed for entire length of propagation at all deviations in waveguide width and thickness at 850 nm central wavelength.

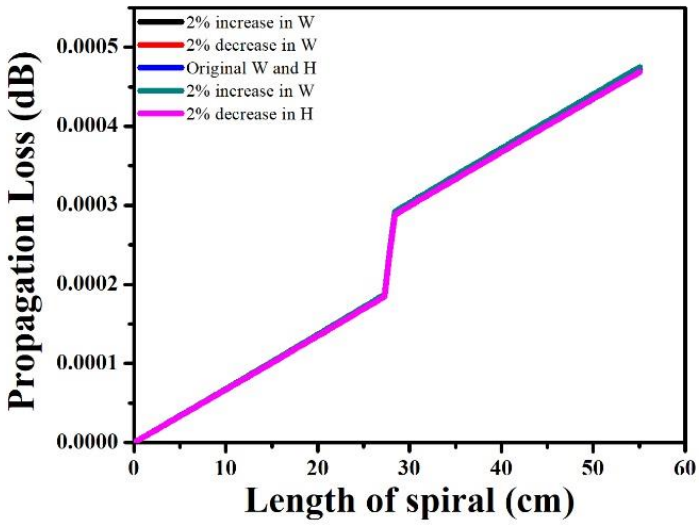

Fig. 9: Tolerance analysis for PL at 850 nm

It can be thus be analysed from Figure 8 and 9 that the reported structure is fabrication tolerant and can be used for IO based OCT systems.

The reported structure was also compared to some of the existing structure available in literature. A comparison analysis can be seen through Table 3. For Si_3N_4 material-based delay line structures, a time delay of 395 ps and 17.2 ns was observed with a loss of 3.6 dB and 0.5 dB respectively. It can be observed from the table that lowest PL was calculated for the reported spiral delay line with a compact footprint of only 6×6 mm sq. It lists the comparison of this reported spiral delay line with various state of art integrated optical delay lines over the years. Comparisons are made in terms of loss obtained, delay time acquired, material and wavelength used, length of delay structure and area occupied and bandwidth. To the author's knowledge, this is the first ever attempt to design an integrated spiral delay line at 850 nm wavelength using Si_3N_4 / SiO_2material.

Table 2: Comparison of various optical delay lines from literature and reported structure

Paper	Loss	Delay	Material	Wavelength	Length	Area
Dongdong Lin (2019)	3.6 dB	395 ps	Si_3N_4	40 GHz	NA	6.4×2 sq mm
Bykhovsky (2018)	0.5 dB	17,2 ns	Si_3N_4	1.55 um	2.59 m	17.7 mm wafer size
Yan Li(2016)	37.7dB IL/ 1.908dB/cm	2.804 ns	SOI	1.55 um	19.79 cm	1×1 mm
Chen (2015)	2.5 dB/cm	NA	Si/SiO_2	1.55 um	4 mm	0.13 ×0.13 sq mm
Chen,(2014)	0.1dB/m	NA	Si/SiO_2	NA	7m	9.5 ×9.5 sq mm
Yurtsever (2014)	NA	NA	Si_3N_4 $/SiO_2$	1320 nm	190 mm	10×33 sq mm
JingyaXie (2014)	16 dB IL, 0.013 dB/ps delay loss	1.27 ns	Si	1.55 um	NA	11.84 sq mm
Cherchi,(2014)	0.15dB/cm	NA	SOI	1.55 um	2.8 cm	NA
Stopinski(2013)	10 dB	250 ps	InP	1.55 um	2 cm	0.38 sq mm
Hansuek Lee,(2012)	0.037 dB/m	NA	Si	1570 nm	27 m	NA
This work	**0.00047 dB PL 0.18 dB IL**	**2.35 ns/ 2.19 ns**	$\boldsymbol{Si_3N_4}$ $\boldsymbol{/SiO_2}$	**850 nm**	**55.11 cm**	**6×6 sq mm**

Where IL=Insertion loss, PL=Propagation loss

4. Conclusion

In this work, design and simulation of compact spiral delay line for application as parameterized building block in integrated optics-based OCT has been presented. Simulation results show a potential of Si_3N_4 / SiO_2 material to be used for further integration of other components in OCT system. The reported delay line showed very promising results over 200nm bandwidth at 850 nm central wavelength. Over the length of propagation of 55.11 cm, an excess loss of 0.06 dB and propagation loss of 0.027 dB was accounted in an area of 6×6 sq. mm. Also, the design was analysed for TE, TM and FV mode types and their performance comparison shows TM mode to be the best candidate. The structure was also analysed in terms of its tolerance parameter and was found to be design tolerant. With further optimization with directional coupler, the system will replace the beam splitters in existing fibre optics-based OCT system.

ACKNOWLEDGEMENT

This work is supported by DIT University, Dehradun, India. The authors would like to thank Vice-chancellor and management of DIT University, India, for encouragement and support during the present research work. The authors are also thankful to Dr. Sulabha Ranade, Director General, SAMEER and Sh. S.S. Prasad, Programme Director, SAMEER for their encouragement and support for this work. One of the authors Dr. Kamal Kishor, would also like to gratefully acknowledge the financial support provided by the TIFAC-Centre of Relevance and Excellence in Fiber Optics and Optical communication at Delhi Technological University (Formerly Delhi College of Engineering, Delhi) through the Mission Reach program of Technology, Vision-2020, Government of India.

Declaration:

The authors declare no conflict of interest.

References

[1] Yadvendra Singh, Sanjeev K. Raghuwanshi, Manish Kumar, "Photonic based liquid level transmitter using Mach-Zehnder interferometer for industrial application," Proc. SPIE 10539, Photonic Instrumentation Engineering V,105391A (22 February 2018); doi: 10.1117/12.2289616.

[2] Srivastava N. K., R. Parihar and S. K. Raghuwanshi, "Efficient Photonic Beamforming System Incorporating a Unique Featured Tunable Chirped Fiber Bragg Grating for Application Extended to the Ku-Band," in *IEEE Transactions on Microwave Theory and Techniques*, vol. 68, no. 5, pp. 1851-1857, May 2020, doi: 10.1109/TMTT.2019.2961889.

[3] Fercher A. F., W. Drexler, C. K. Hitzenberger, and T. Lasser, "Optical coherence tomography-principles and applications," *Reports on Progress in Physics*, vol. 66, pp. 239–303, 2003. https://doi.org/10.1088/0034 4885/66/2/204

[4] Izatt, J. A., &Choma, M. A. (2008). Theory of Optical Coherence Tomography (book chapter), 47–72. https://doi.org/10.1007/978-3-540-77550-8_2

[5] Shahoei, Hiva & Yao, Jianping. (2014). Delay Lines.(book chapter) 10.1002/047134608X.W8234.

[6] Sharma T. et al., "Design of grating based narrow band reflector on SOI waveguide," Optik (Stuttg)., p.p 165995, 2020, doi: 10.1016/j.ijleo.2020.165995.

[7] Zhou, L., Wang, X., Lu, L., & Chen, J. (2018). Integrated optical delay lines: a review and perspective [Invited]. *Chinese Optics Letters*, *16*(10), 1–16. https://doi.org/10.3788/COL201816.101301

[8] Watcharakitchakorn, O., &Silapunt, R. (2018). Design and modeling of the photonic crystal waveguide structure for heat-Assisted magnetic recording. *Advances in Materials Science and Engineering*, *2018*. https://doi.org/10.1155/2018/8097841

[9] Stopinski, S., Malinowski, M., Piramidowicz, R., Kleijn, E., Smit, M. K., &Leijtens, X. J. M. (2013). Integrated optical delay lines for time-division multiplexers. *IEEE Photonics Journal*, *5*(5). https://doi.org/10.1109/JPHOT.2013.2280519.

[10] Yurtsever, G., Považay, B., Alex, A., Zabihian, B., Drexler, W., &Baets, R. (2014). Photonic integrated Mach-Zehnder interferometer with an on-chip reference arm for optical coherence tomography. *Biomedical Optics Express*, *5*(4), 1050. https://doi.org/10.1364/boe.5.001050

[11] Waqas, A., Melati, D., &Melloni, A. (2018). Cascaded Mach-Zehnder architectures for photonic integrated delay lines. *IEEE Photonics Technology Letters*, *30*(21), 1830–1833. https://doi.org/10.1109/LPT.2018.2865703

[12] Lin, D., Xu, X., Zheng, P., Yang, H., Hu, G., Yun, B., & Cui, Y. (2019). A Tunable Optical Delay Line Based on Cascaded Silicon Nitride Microrings for Ka-Band Beamforming. *IEEE Photonics Journal*, *11*(5), 1–10. https://doi.org/10.1109/jphot.2019.2941510

[13] Sharma, B., Kishor, K., Sharma, S., & Makkar, R. L. (2019). *Broadband SiN directional coupler at 850 nm for optical coherence tomography*. (September), 31. https://doi.org/10.1117/12.2529351

[14] Sharma, B., Kishor, K., Sharma, S., & Makkar, R. (2019). Design and Simulation of Broadband Beam Splitter on a Silicon Nitride Platform for Optical Coherence Tomography. *Fiber and Integrated Optics*, *0*(0), 1–11. https://doi.org/10.1080/01468030.2019.1639001

[15] Chen, T., Lee, H., Li, J., Painter, O., &Vahala, K. (2011). Ultra-low-loss optical delay line on a silicon chip. *Optics InfoBase Conference Papers*, *3*(May), 867. https://doi.org/10.1038/ncomms1876

[16] Xie, J., Zhou, L., Li, Z., Wang, J., & Chen, J. (2014). Seven-bit reconfigurable optical true time delay line based on silicon integration: erratum. *Optics Express*, *22*(21), 25516. https://doi.org/10.1364/oe.22.025516

[17] Chen, T., Lee, H., &Vahala, K. J. (2014). Design and characterization of whispering-gallery spiral waveguides. *Optics Express*, *22*(5), 5196. https://doi.org/10.1364/oe.22.005196

[18] Cherchi, M., Ylinen, S., Harjanne, M., Kapulainen, M., Vehmas, T., & Aalto, T. (2014). Low-loss spiral waveguides with ultra-small footprint on a micron scale SOI platform. *Silicon Photonics IX*, *8990*, 899005. https://doi.org/10.1117/12.2039940

[19] Chen, Z., Flueckiger, J., Wang, X., Zhang, F., Yun, H., Lu, Z., … Chrostowski, L. (2015). Spiral Bragg grating waveguides for TM mode silicon photonics. *Optics Express*, *23*(19), 25295. https://doi.org/10.1364/oe.23.025295

[20] Li, Y., Song, X., Xu, Y., & Li, Y. P. (2014). Spiral optical delay lines in silicon-on-insulator. *Optics InfoBase Conference Papers*, (2), 3–5. https://doi.org/10.1364/ACPC.2016.AF3G.6

[21] Bykhovsky, D., Rosenblit, M., &Arnon, S. (2018). Two-sided through-wafer interconnect for optical spiral delay line. *Journal of Modern Optics*, *65*(1), 98–103. https://doi.org/10.1080/09500340.2017.1377305

[22] Li, W., Anantha, P., Lee, K. H., Qiu, H. D., Guo, X., Goh, S. C. K., … Tan, C. S. (2018). Spiral Waveguides on Germanium-on-Silicon Nitride Platform for Mid-IR Sensing Applications. *IEEE Photonics Journal*, *10*(3), 1–7. https://doi.org/10.1109/JPHOT.2018.2829988

[23] Moralis-Pegios, M., Mourgias-Alexandris, G., Terzenidis, N., Cherchi, M., Harjanne, M., Aalto, T., … Vyrsokinos, K. (2017). On-ChipSOI delay line bank for optical buffers and time slot interchangers. *IEEE Photonics Technology Letters*, *30*(1), 31–34. https://doi.org/10.1109/LPT.2017.2773146

Design of Small Wind Turbine Electric System for Household Electricity and Water Supply for Irrigation in Rural Tanzania

Isaka J. Mwakitalima
Department of Electrical Engineering
Delhi Technological University
Delhi, India
mwakitalimaisaka0@gmail.com

Mohammad Rizwan
Department of Electrical Engineering
Delhi Technological University
Delhi, India
rizwan@dce.ac.

Narendra Kumar
Department of Electrical Engineering
Delhi Technological University
Delhi, India
narendrakumar@dtu.ac.in

2020 IEEE 17th India Council International Conference (INDICON) | 978-1-7281-6916-3/20/$31.00 ©2020 IEEE | DOI: 10.1109/INDICON49873.2020.9342555

***Abstract*—African countries including Tanzania have poor water supply infrastructure in most parts of the rural areas. Initiatives are taken by the country to resolve the issue of water supply deficiency. In Tanzania, there are some community-based water supply systems which are diesel powered and manually hand driven wind mills energy systems. There are few available renewable based electric systems in the country in such community-based water supply systems. RES-based projects such as Small-wind turbine systems (SWTESs) are globally implemented for remote off-grid applications. However, in Tanzania no SWTES that has been installed for powering water supply systems for rural dwelling. This paper presents the design of SWTES for generating electricity for water pumping supply system and domestic appliances. HOMER pro software is applied for the simulation process. This paper concludes that the off-grid SWTES is feasible beyond breakeven grid extension distance of 4.58 km while batteries have highest cost.**

Keywords—SPVS, HOMER, SWTES, water supply, wind speed, solar radiation, TNPC

I. INTRODUCTION

Modern energy services including electricity and clean water supplies are important infrastructure for improved economy and social quality of life. Global climate changes cause the shortage of water supply worldwide. This water shortage is more problematic in rural areas of developing countries [1]. Water supply for drinking and agricultural irrigation becomes scarce especially during dry seasons. Therefore, there is need to increase access to water supply infrastructure via alternative sources. Rain water is among of these alternative energy sources which can be harvested and stored for agricultural irrigation and drinking with minimal treatment. Unfortunately, large amount of this rain water is wasted [2]. Additional approach of increasing access to water supply infrastructure is by decentralized systems.

Government of Tanzania (GOT) increases access to water supply infrastructure through centralized and decentralized water supply systems. Usually, both categories of these systems are community-based systems [3]. These systems are hand driven pumps, mechanical wind mills and diesel powered generators. Firstly and in most cases, community- based systems are major projects demanding for high initial capital; and it takes long time for them to be implemented; they are normally centralized and located far away from many households and security for women is not guaranteed and little amount of water may be obtained because it depends on human effort. Mechanical pumping systems are constructed in the proximity with a water bore that requires water supply distribution network leading to additional installation costs [4]. Additionally, these mechanical systems can't supply multiple loads and have limited efficiencies. Mechanical wind water pumping systems or hand driven wind mills are common options for water supply infrastructure in off-grid locations [5] [6]. These systems can also operate less in windy sites than electric wind water pumping systems [7]. Secondly, applying fossil fuels in the traditional water pumping systems is not cost effective and environmentally friendly [8]. This situation is undesirable and thus renewable energy sources are suitable for enhancing access to water supply infrastructure in rural areas of Tanzania. Utilization of renewable energy sources in the country is at an infant stage. Non-dispatchable energy systems of solar and wind energy sources are being exploited in the country at small rate. There are few solar photovoltaic systems (SPVS) and wind mills are currently being installed in the country for the water supply community based systems. Majority are also at different planning and implementation stages [7] [9]. There is a limited installation of electric pumping systems for family level wind based energy systems. Wind-electric pumping systems are preferred due to their simplicity, versatility, more loads and utilization points may be located far away from the well by power cable. However, unlike mechanical wind pumping systems, these electric systems need higher potential of renewable energy resources [6] [10]. In addition, durability and cost-effectiveness need to be addressed carefully. Apart from the benefits of wind energy-based systems, there are environmental concerns such as visual effects, bird mortality, turbine noise, interferences and land impacts [11]. Wind turbines can be categorized according to the position of axis and installed generation capacity. Based on the axis, there are two types namely Horizontal Axis Wind Turbines (HAWTs) and Vertical Axis Wind Turbines (VAWTs) [11]. HAWTs are often used because simplified conversion of energy and maximum power output. According to the generation capacity can be classified as micro, small, medium and large wind turbine. Micro-wind turbine system can generate power of few watts starting from 20W to 500 W, applied for charging batteries on sailboats and recreational cars [12]. Small wind turbines systems operate within the wind speed 3-4 m/s and are connected with batteries for residential applications. Medium sized wind Turbine have installed capacities 20-300 KW, used in various applications. Large wind turbine systems

#1570658158-XXX-X-XXXX-XXXX-X/XX/$XX.00 ©20XX IEEE

Authorized licensed use limited to: DELHI TECHNICAL UNIV. Downloaded on February 15,2021 at 10:00:50 UTC from IEEE Xplore. Restrictions apply.

are of MW generation capacities range [13]. Basically, Residential based systems may consists of a rotor, generator plus balance of the system (BOS) components such as controllers, inverter and battery energy storage systems. Normally, residential wind energy based systems use guyed towers due to their cost effectiveness and simplicity of installations [11]**.** This study tries to bridge up such a gap of generating electricity using SWTES multiple loads of electricity and water supply systems at famer's residence in environment of Tanzania. The objective of this work is to explore the feasibility of generating electricity via SWTES for powering water pumping systems for famer's residence in rural areas of Tanzania. The designed SWTES provides electricity for household appliances. Several case studies have been done to investigate the possibility of generating electricity using wind energy based systems for community based water supply systems and for family water supply with specific load for example agricultural irrigation. In these studies a number of methods, techniques and software tools are used

In this paper, the feasibility study of off-grid SWTES has been performed for water supply infrastructure at family level for Simboya village in Mbeya region, Tanzania. Additionally, proposed off-grid and on-grid SWTES configurations have been compared economically. NPC or Life Cycle Cost (LCC) method is used for the economic comparison. HOMER pro software is used for the simulation. The study is important for high exploration of renewable energy resources in the country, supplementing major utilities infrastructures and enhancing the accessibility to electricity and water supply infrastructure in remote areas.

II. Description of Area of Study and Energy Profile Assessment

This section of the paper provides a brief description of the selected location of this study alongside with its evaluation of energy profile. This part deals with the examination of renewable energy resources and electrical load as important aspects for designing any electric generating system. Precipitation of the selected site affects the operation of water pumping systems and therefore is also considered in the design.

A. Description of Area of Study

Simboya village has been selected as area of study which is located in Mbeya region, Tanzania at latitude 8°54. 6′S and longitude 33°27.6′E. Livestock keeping and agriculture are major economic activities for this place. The River Shongo supply water for drinking and small irrigated plots owned by individual villagers. Water supply from this river is used by neighbouring village called Ikukwa. The water flow of the river falls under gravitational force and are diverted into small plots. Most parts of Mbeya region including Simboya village receive high rainfall annually. Unfortunately, the large amount of rain water is not harvested for dry season applications leading to insufficient of water supply. During dry season water supply from the Shongo River is not sufficient to fully support agricultural irrigation. Additionally, this area of study has no grid connectivity. Sufficient water supply can be achieved via distributed generation electric systems. In this work, feasibility study is made to see the possibility of providing water supply using wind electric power system for agriculturalist's residence in Tanzania. Moreover, the power obtained from this system will also be supplied to the famer's household.

B. Energy Resource Profile Assessment

Data for renewable energy resources from Simboya village are obtained from NASA-SSE. At this location average monthly wind speed at 10 m is small for electric power generation and therefore data are collected at height of 50 m considered for wind speed. Scaled annual averages for wind velocity is 4.78 m/s and maximum temperature is 24.9°C respectively. This annual wind velocity is sufficient for small wind power electricity [14]. Data for the rainfall have obtained from Tanzania Meteorological Agency (TMA) at branch of Mbeya Weather Station. Table 1 shows Data collected for energy resources and meteorological profile and Figure 1shows wind energy resource potential for proposed site.

Table 1: Data collected for energy resources and meteorological profile

Parameter	V (m/s)	Min T (°C)	Max T (°C)	R. fall (mm)
January	3.15	15.6	24.4	200.9
February	2.94	15.1	25.6	217.3
March	3.3	15.5	26.4	130.8
April	4.56	13.9	23.6	106.2
May	5.17	9.2	22.5	13.1
June	5.49	7.2	22.1	0
July	5.87	6.6	22.1	0
August	6.03	8.4	23.8	0
September	6.14	9.5	26.0	0
October	5.98	12.7	28.1	6.2
November	5.01	14.7	28.0	132.5
December	3.77	15.3	26.2	236.6

[1] V = wind velocity at 50 m, Min T = Minimum temperature, Max T= Maximum temperature, R. fall = Rainfall

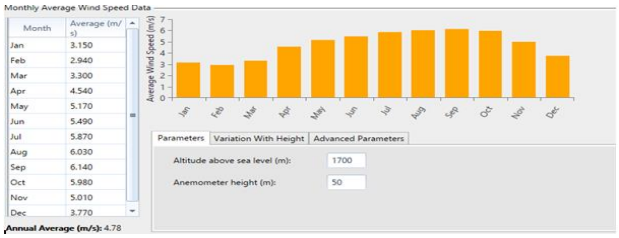

Fig. 1. Wind energy resource potential for proposed site

C. Energy Demand Profile Analysis

Water supply, electricity and cooling/ heating are main services for the family. In this study, demand for water and electricity supplies are estimated for peasant's residence. Cooling/ heating services are not considered and therefore cooling/heating appliances are not considered. Therefore, demand profile analysis of the residence is grouped into two categories, i.e. demands for water and electricity for the peasant's family. Demand estimation for water supply is subdivided into applications such as family use, irrigation for

Authorized licensed use limited to: DELHI TECHNICAL UNIV. Downloaded on February 15,2021 at 10:00:50 UTC from IEEE Xplore. Restrictions apply.

small plot and livestock. Additionally, electrical load demand is also estimated for electric appliances in the household. In other words, the designed wind based system supplies electric power to pumping equipment and household appliances. Figure 2 indicates demand profile analysis for a typical peasant's residence. Following section provides demand profile analysis for water and electricity for the peasant's residence.

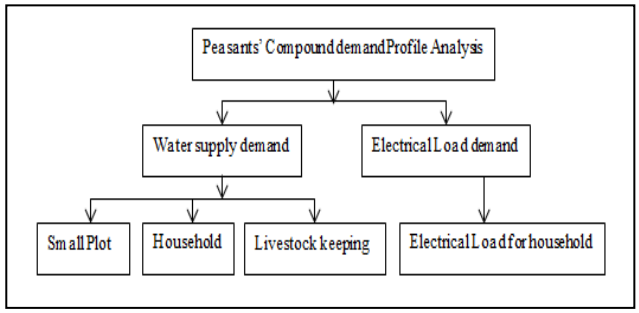

Fig. 2 . Demand profile analysis for a typical peasant's residence

1) Water demand analysis for sizing water pumping electric equipment

Required amount of water is estimated for small irrigated plot, family's internal use, and livestock keeping for the peasant's home. Amount of water for irrigation is influenced by a number of factors such as type of crop, soil type variation, soil preparation, and ways of irrigation, precipitation, humidity and cloud coverage. However, rainfall is a main factor affecting the amount of water for irrigation. Maximum water demand for irrigated plot is during dry season in the months starting from June to September. Following is important information for determining quantity of water for irrigation of a perennial crop such as sugarcane. Tables 2- 4 present the water demand analysis according for the aforementioned applications.

Table 2: Daily quantity of water for irrigated area

Characteristic	Specific assumption	Units/ remarks
Size of irrigated area	2	Acres
Area of plant spacing	1 m × 1.5 m = 1.5	m^2
Number of plants per acre	4026.86/1.5 = 2685	quantity
Total number of plants for 2 acres	2685 × 2= 5370	quantity
AVR max. amount of water at dry season	20	Litres/ plant/ day
Water for irrigation in rainy season	0	Litre/plant/day
Amount of water for irrigating 2 acres per day	20×0.001×5370 = 107.4	m^3/day

Table 3: Daily quantity of water for animal keeping

Specific livestock	Quantity	Assumed water consumption (m^3/animal/day)	Total consumption (m^3/day)
Cows	10	0.04	0.4
Oxen	2	0.03	0.06
Calves	5	0.02	0.1
Pigs	10	0.015	0.15
Sheep	20	0.008	0.16
Goats	20	0.008	0.16
Poultry	400	0.0002	0.08
		Total	1.11

Table 4: Daily water demand for the peasant's household

Family member	Parents	Children	others	Persons per household
Number	2	3	2	7

Assuming basic daily per capita water consumption is 25litres/person for rural Tanzania [15]. This amount of water is used for drinking, laundry and shower for person daily. Therefore, amount of consumed by the whole family equals to the product of per capita water consumption multiplied by number of persons in a family. Therefore total water consumption equals to 25 litres/person/day × 7= 175 litres/day = 175 x 0.001= 0.175 m^3/day

Total water consumption = 107.4 + 1.11+ 0.175 = 108.69 m^3/day

Head is refers to the total distance of pumping level and discharge level. In order to determine the capacity of pumping equipment head is assumed to be 15 m. Equation (1) was used to determine size of the pump.

$$P = Q \times \rho \times g \times H \qquad (1)\ [16]$$

Where, P is power transmitted to water, Q is water flow rate in cubic metres per second, ρ is the water density, g is acceleration due to gravity, and H is the head to raise amount of water to the storage tank.

Therefore, P = 0.0013 m^3/s × 1000 kg/m^3 × 9.81 m/s^2× 15 m = 191.3 W

Efficiency of the pump shaft η = Power output/ power input × 100 %

Assumptions made for water pumping system

Water piping system = 95%, centrifugal pump = 75% and electric motor = 85%

Combined efficiency for water pumping system is the product of the three efficiencies of the components. Combined efficiency for pumping system was calculated using (2).

Combined efficiency of the assembly = 0.95 × 0.85 × 0.75 = 0.61 (2) [17]

Power input = power output/ combined efficiency of the components assembly

Authorized licensed use limited to: DELHI TECHNICAL UNIV. Downloaded on February 15,2021 at 10:00:50 UTC from IEEE Xplore. Restrictions apply.

Power of the pumping equipment = 191.3/ 0.61 = 313.61 W or equivalent to 0.42 HP.

Total power for pump for storage of water for duration of three days
= 313. 61 × 3 = 940.8 W = 1.3 HP

Table 5: Motor selection and its specifications from Kirloskar Brother Limited

Pump model	Power KW/hp	Voltage (volts)	Head m	Discharge LPM
KS4F-1508	1.1 / 1.5	240 , 50 Hz	22	135

2) Electrical Load Analysis for the Peasant's Household

Electrical load analysis for the peasant's household is performed in addition to electric pump unit. Total electrical load is obtained by combining the types of loads. Table 6 indicates the data for appliances used for estimation of electrical load of peasant's residence. Figure indicates load profiles for the proposed site.

Table 6: Estimation of total electrical load for peasant's residence

Appliance	Rating (W)	Quantity	Duration (h)	Tot. power (W)	Tot. energy (Wh)
Energy saver lamp **I**	2	4	5	8	40
Energy saver lamp **II**	2	4	12	8	96
Fluorescent lighting	5	1	6	5	30
Television set	100	1	6	100	600
Refrigerator	300	1	12	300	2400
Phone charger	7	3	2	21	42
Electric pump	1100	1	5	1100	5500
				1.542	8,708

I= Indoor lighting, **II** = Outdoor lighting

Based on electric power applications, electrical load for water pumping system is assessed deliberately by distributing it over a twenty four hour period. Load factor in dispersed rural areas is poor and thus a load distribution is made to improve it. The assessment is carried out in Microsoft excel worksheet by customizing data templates before the detailed evaluation by HOMER pro software. Baseline peak loads during rainy and dry seasons are 0.045 kW and 0.262 kW respectively. Electrical load during dry season is higher than in rainy season due to increased irrigation activities. No electric power is required during rainy season for irrigation. SWTES supplies power for electrical appliance and internal use of water supply in the house. According to Table 1, dry season starts from June to September with zero rainfall and rainy period starts October to May. Figure 3 (a) - (c) indicates electrical load distribution according to load profiles for household electrical equipment water pumping system during dry and rain seasons from excel sheet and synthesized load profile via HOMER.

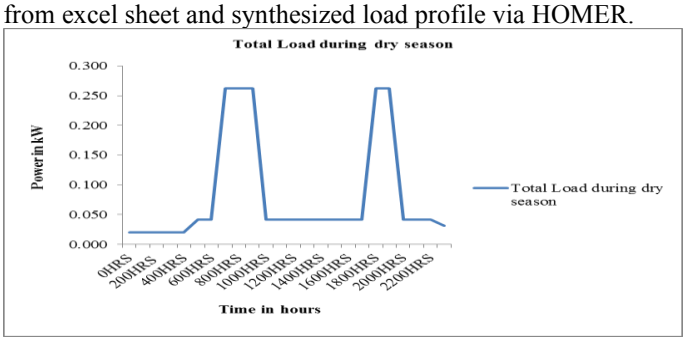

Fig. 3(a) Daily load profile during dry season

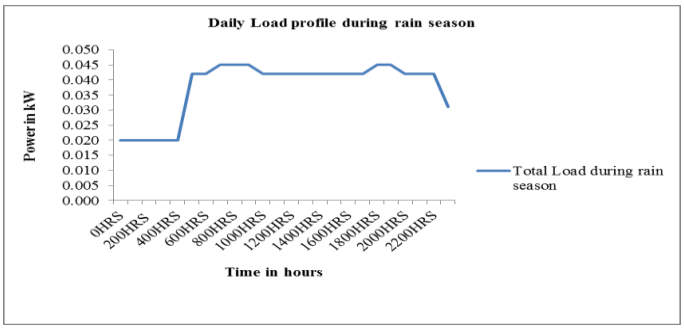

Fig. 3(b) Daily load profile during rain season

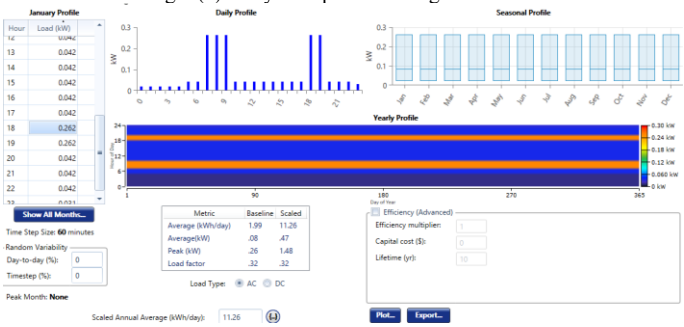

Fig. 3(c) . Synthesized data for load profile of proposed site via HOMER software.

Determining the Size of Water Storage Tank

The size of storage cistern refers to the daily water demand (Q) multiplied by number of the days (Nd) for delivering fixed supply of water. Capacity of water storage is estimated using (3).

Total capacity of storage system,

$$Ct = Q \times N\,d \qquad (3)\ [16]$$

Therefore, Ct = 108.69 m3/day × 3 days = 326.07 m3

Authorized licensed use limited to: DELHI TECHNICAL UNIV. Downloaded on February 15,2021 at 10:00:50 UTC from IEEE Xplore. Restrictions apply.

Fig. 4 indicates lock diagram for layout of SWTES supplying electricity to water pumping system and electric appliances for the peasant's household.

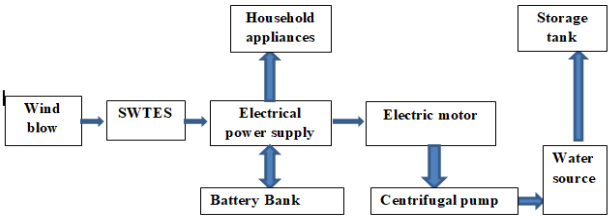

Fig. 4. Block diagram for layout of SWTES supplying electricity to water pumping system and electric appliances for the peasant's household.

III. Design of SWTES

Components of SWTES are such as rotor, generator, charge controllers, inverters and batteries. Power output from SWTES depends on air of density, swept area of the rotor and wind speed and electric power of the wind turbine. Equation (6) estimates power from WT.

$$P_w = 0.5 \times C_p \times \rho \times A \times v^3 \times \eta_t \qquad (6)\ [18]$$

Where, Pw is the wind power output, ρ is the density of air (Kg/m^3), A is the rotor swept area (m^2), v is the wind speed (m/s), C_p is the wind power coefficient and η_t is a drive train efficiency. SWTES consists of small wind turbine with a swept area of the rotor than 200 m^2 [19]

Optimum configuration of SWTES is obtained through HOMER pro software. The system configuration should be reliable and cost-effective. Cost-effectiveness and reliability of the system is defined via lowest LCC. Yearly energy generation (YEG) is one of the essential variables evaluated by HOMER. Total annual energy generation is computed using equation (5)

$$YEG = 8\,760 \int P(V).f\,(V).dV \qquad (5)\ [19]$$

Where, YEG= Yearly energy generation in kilowatt-hour (kWh) integrated with respect to a given wind velocity, P (V) = Electric power generated at a given wind velocity in watts, f (V) = Wind velocity probability density function.

The Weibull distribution function provides a broad range of wind energy resources. Wind velocity V, is expressed using Weibull distribution function. The function has two variables such as shape factor k (dimensionless) and scale factor c (m/s) can be used to estimate the wind potential. This distribution function is defined by probability density function and cumulative distribution functions in (6) and (7) respectively.

$$f(V) = k/c\ (V/c)^{k-1} \exp\,[-V/c]^k \qquad (6)\ [20]$$

Cumulative distribution function,

$$F(V) = 1 - \exp\,[-V/c]^k \qquad (7)\ [20]$$

Rayleigh distribution is a special form for Weibull distribution function with a constant value k equals to 2. In this study, for simplicity purpose analytical and empirical methods have been used to compute k and c values. Referring to the collected wind data, sum of monthly averages is given as

N = 12, $\Sigma V = 57.41$, $\Sigma V^2 = 290.7095$, Mean velocity, $V = \Sigma V/12 = 57.41/12 = 4.78$ m/s

But Variance $\sigma^2 = 1/(N-1)\ [\Sigma V^2 - (\Sigma V)^2/N] = 1/\,/\,(12-1)\ [290.7095 - (57.41)^2/12] = 1.459$

Standard deviation, $\sigma = 1.21$, k and c are computed using equations (8) and (9) respectively.

$$k = (\sigma/\text{mean } V)^{-1.086}, \qquad (8)\ [11]$$

Therefore, $k = (1.21/4.78)^{-1.086} = 4.45$,

$$c = [0.568 + (0.433)/k]^{1/k} * V \qquad (9)\ [11]$$

Therefore, $c = [0.568 + (0.433)/4.45]^{1/4.45} * 4.78 = 4.36$ m/s

Figure 5 shows a Weibull diagram that has been obtained for the proposed off-grid location using HOMER pro software.

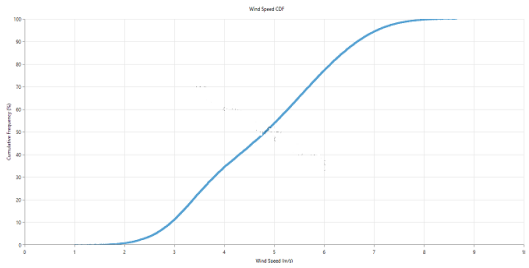

Fig. 5 Shows a Weibull diagram for the proposed off-grid location

Capacity factor (CF) of wind turbine refers to electric energy generated by the system divided by the maximum possible electric energy that would have been produced if the system operated at full installed capacity per year equivalent to duration of 8760 hours. Equation (10) is used to estimate CF.

Mathematically, $CF = 100. \dfrac{YEG}{\text{Installed capacity} \times 8760}$ (10) [19]

The total Net Present Cost (TNPC) is a parameter which gives the project's life span. NPC evaluates the amount of money at present in $ with future cash flow discount to present value based on the assumed discount rate i = 7.0 % (Bank of Tanzania). TNPC is evaluated using equation (11).

$$C_{TNPC} = \frac{TAC}{CRF\,(i,N)} \qquad (11)\ [19]$$

Where, TAC = Total annualized cost, I = Discount rate, N = Number of years of project's life time and CRF = Capacity recovery factor. CRF is calculated using equation (12).

$$CRF\,(i, N) = i\,(1+i)/\,(1+i)^N - 1 \qquad (12)\ [19]$$

HOMER assumes levelized cost of energy (LCOE) as average unit (kWh) cost of utilizable energy generated by SWTES. LCOE is defined as an overall annualized cost of electric power

Authorized licensed use limited to: DELHI TECHNICAL UNIV. Downloaded on February 15,2021 at 10:00:50 UTC from IEEE Xplore. Restrictions apply.

divided by total electrical load served or consumed. LCOE is calculated using (13).

$$\text{LCOE} = \frac{\text{Overall annualized cost}}{\text{Total electrical load consumed}} \quad (13)\ [19]$$

Renewable fraction (RF) is the electrical power fraction delivered as a load that comes from renewable energy resources (RES) which is 100% [19].

A. Simulation Results

In this study, primary load and deferrable load are combined as generic AC load for the proposed system. Electrical demand during dry season is higher than the rainy season due to increased irrigation activities. Therefore, configuration of the proposed system is designed according to the dry season load. Scaled peak power and energy consumption during rainy season are 1.48 KW and 11.26 kWh / day respectively. Figure 6 indicates schematic diagram of the proposed system while Figure 7 indicates wind turbine power curve for off-grid SWTES.

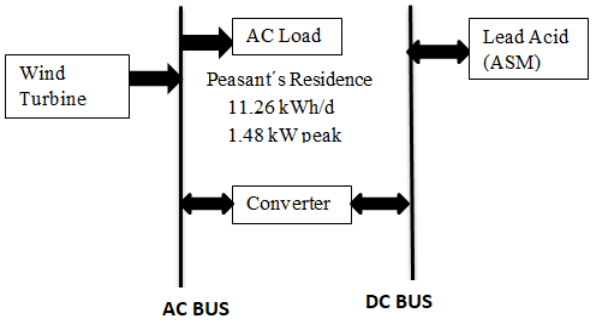

Fig. 6. Configuration of off-grid SWTES

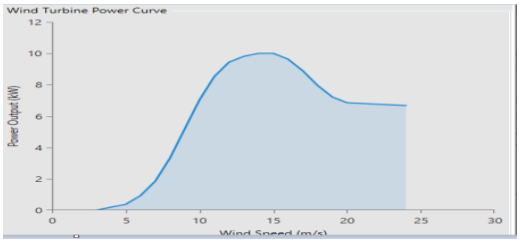

Fig. 7. Indicates wind turbine power curve for off-grid SWTES

B. SWTES Components

Apart from electrical load, this proposed system also includes main components such as wind generator, battery bank and converter. Table 7 shows technical details for the simulated SWTES and related miscellaneous input parameters. . YEG for SWETS is 3999 kWh/ year. Table 8 shows details of total cost for simulated SWTES and assumed costs based on selected components. Total NPC for SWTES is $ 106 273. 80 and LCOE is estimated to be $ 1.58/ kWh. Table 10 indicates the summary of TNPC cost per selected components for off-grid SWTES. The cost for batteries is $ 77 892. 96 (73.3%) being higher than the cost for WT which is 18 369. 80 (17.3%). The cost for converter is $ 6713.11(6.3%). SWTES has miscellaneous expenses equivalent to $ 3296. 98 (3.1%). Table 10 indicates the economics and constraints of project**.** The lifespan of the project is considered to 25 years.

Table 7 Technical details for simulated SWTES and related miscellaneous input parameters

Name of component and	Value
Generic wind turbine generator :	
Rated capacity (kW)	1-10
CF (%)	4.57
RF Wind Penetration (%)	97.3
YEP (kWh/year)	3999
Electrical consumption (kWh/year)	4 109
Hub height (m)	50
Altitude above sea level (m)	1700
Lifetime (years)	20
Average wind speed (m/s)	4.78
Availability losses (%)	2
Turbine performance losses (%)	3
Wake effect losses (%)	0.25
Electrical losses (%)	0.5
Other losses (%)	1
Shape factor, k	4.45
Scale factor, c (m/s)	4.36
Diurnal pattern strength	0.15
Wind speed duration (hours)	10
Generic lead acid batteries:	
Nominal voltage (v)	2
Nominal capacity (kWh)	1.03
Maximum capacity (Ah)	513
Number of batteries	4608
Number of strings	48
System voltage (v)	96
Initial stage charges (%)	100
Mini state of charge (%)	30
Degradation limit (%)	5
Anticipated life (Years)	2.93
Lifetime through output (kWh)	7297
Autonomy (hours)	9573
Converter:	
Rated power (kW)	10
Peak output power (kW)	1.48
Inverter efficiency (%)	95
Rectifier efficiency (%)	95

Authorized licensed use limited to: DELHI TECHNICAL UNIV. Downloaded on February 15,2021 at 10:00:50 UTC from IEEE Xplore. Restrictions apply.

Lifespan (hours)	15

Table 8: Details of TNPC for simulated SWTES and assumed costs based on selected components

Name of components			
	Wind turbine generator	Lead acid batteries	Converter
Specific cost	Cost per Kw ($)	Cost per unit ($)	Cost per kW ($)
Capital cost	10 000	150	350
Replacement cost	10 000	100	350
O & M cost	400	10	10
System cost	**Type of key system costs**		
	Initial cost ($)	TNPC ($)	LCOE ($)
	29 400	106 273.80	1.58

Table 9: Summary of TNPC cost per selected components for off-grid SWTES

Component	WT 10 kW	Batteries	Converter	Miscellaneous	
Capital ($)	10, 000	14 400	3500	1500	29 400
Replacement ($)	4946.87	49 657.06	2064.51	0	56668.44
O&M ($)	6534.36	15 682.71	1633.62	1796.98	25647.76
Fuel ($)	0	0	0	0	0
Salvage ($)	53 111.54	1646 .81	484.02	0	5442.36
Total ($)	18 369.8	77892.96	6714.11	3296.98	106 273.8
%	17.3	73.3	6.3	3.1	100

Table 10: Economics and constraints

Economics / Constraints parameters	Value
Project lifetime (Years)	25
Nominal discount rate (%)	7
Expected inflation rate (%)	3.3
System capital ($)	1500
System fixed 0 & M ($/ year)	110
Capacity shortage penalty ($/ kWh)	0
Minimum annual capacity shortage (%)	1
Operating reserve, load current time step (%)	7
Minimum RF (%)	100
Wind power output (%)	100

IV. Comparison Between Off-Grid SWTES versus Grid Extension

Simulated off-grid SWTES is economically compared with national grid extension from Tanzania Electricity Supply Company (TANESCO). HOMER computes the breakeven grid extension distance which defines the LCOE in standalone system, off-grid SWTES in particular, cheaper than an extension of the national grid. Capital cost, O & M and grid power price are $ 9500/Km, $713/year and $ 0.1/kWh respectively. The breakeven grid extension distance is 4.58 km which implies that off-grid SWTES is cheaper than the national grid from TANESCO for distance greater than the aforementioned value. Figures 8 and 9 indicate configurations for grid-connected SWTES and breakeven grid extension distance respectively.

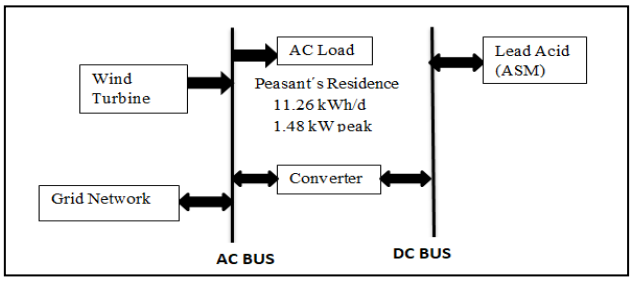

Fig. 8. Configuration of grid-connected SWTES.

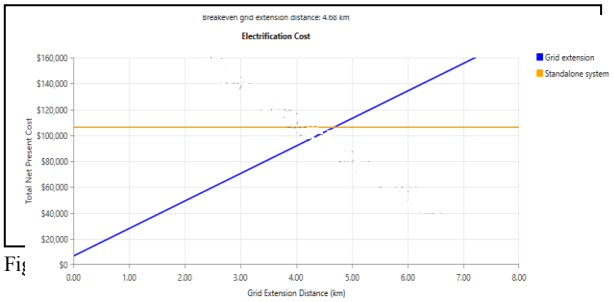

Fi

V. Conclusion

Generation of electric power from wind-turbine systems depends on several factors such as potential of wind resources, practical and functioning characteristics. In this study, SWTES has been designed by considering available wind regime at the proposed rural site. Technical and economic analysis of proposed off-grid SWTES for multiple electrical loads of peasant's compound in the rural Tanzania has been performed. Simulated SWTES intends to serve the load electricity and water supply for household and irrigation application. There is a higher demand of electricity during dry season than that of rainy season due to high demand of water supply including irrigation. Load profile during dry season has been used for designing SWTES. In this particular study, deferrable load of pumping system has been combined with the electrical appliances to form ac primary load. Scaled peak load and daily consumption are estimated to be 1.48 kW and 11.26 kWh /day respectively. For suitable CF simulated SWTES consists of higher capacity than the peak power. It includes components such as WT of 1- 10 kW, 10 k W converter with 4608 batteries. However, intermittent nature of wind energy source is a major drawback

Authorized licensed use limited to: DELHI TECHNICAL UNIV. Downloaded on February 15,2021 at 10:00:50 UTC from IEEE Xplore. Restrictions apply.

of this configuration. Off-grid SWTES requires high number of batteries and thus increasing more cost. The life span of this project has been taken to be 25 years. TNPC and LCOE are $106 273.80 and $ 1.58 respectively. SWTES is actually more cost effective compared to grid extension. SWTES is more viable beyond the breakeven grid extension distance 4.58 Km.

ACKNOWLEDGMENT

Authors are thankful to Indian Council for Cultural Relations (ICCR) and management of Delhi Technological University (DTU) for their support of the research. Appreciation is also extended to Regional Commissioner's Office in Mbeya region for the permission of doing research in Mbeya Rural District. Authors also recognize the support from administrations of Ikukwa ward, Ikukwa health centre and dwellers at Simboya village for the cooperation.

REFERENCES

[1] M. A Hanjra and M. E. Qureshi , "Global water crisis and future food security in an era of climate change." Food Policy, vol.35, no. 5, pp 365-377, 2010

[2] [2] W.M.A.Adams, Wasting the Rain (Routledge Revivals): Rivers, People and Planning in Africa, Routledge, (2014)

[3] [3] A. J. F. De Palencia and A. Pérez-Foguet , "Implementing pro-poor policies in a decentralized context: the case of the Rural Water Supply and Sanitation Program in Tanzania." Sustainability Science**,** vol.6, no1, pp 37-49, 2011

[4] [4] S.S.Chandel, M.N. Naik and R. Chandel , "Review of solar photovoltaic water pumping system technology for irrigation and community drinking water supplies." Renewable and Sustainable Energy Reviews, Vol.49, pp 1084-1099, 2015

[5] [5] M. Jaskolski, A. Davis and D. Tutwiler, "Second International Conference on Solar Energy Solutions for Electricity and Water Supply in Rural Areas.", TheAmerican University in Cairo, Egypt, October 2016

[6] [6] N.Davies, "Novel, induced flow, centrifugal water pumping system for off grid application.", Ph.D. dissertation, Dept. of Eng., University of Liverpool, 2015.

[7] [7] M.Musiba, "Assessing the potential of wind energy for electrical power generation in dodoma region, Tanzania.", Ph.D. dissertation, Dept. of Meteorology, University of Nairobi, 2013.

[8] [8] O. Badran, "Wind turbine utilization for water pumping in Jordan.", Journal of wind engineering and industrial aerodynamics, vol. 91, no. 10, pp 1203-1214, 2003.

[9] [9] H. Sarakikya, I. Ibrahim and J.Kiplagat, "Renewable energy policies and practice in Tanzania: Their contribution to Tanzania economy and poverty alleviation.", Update, vol. 177, no 337,740.00, pp 454,654.400, 2015

[10] [10] V. C. Sontake and V. R. Kalamkar, "Solar photovoltaic water pumping system-A comprehensive review." Renewable and Sustainable Energy Reviews, vol 59, pp 1038-1067, 2016

[11] [11] J. F.Manwell, J. G. McGowan and A.L. Rogers, " Wind energy explained: theory, design and application.", John Wiley & Sons, 2010

[12] [12] A.Harrouz, A. benAtialah and O. Harrouz , "Modeling of small wind energy based of PMSG in south of Algeria.", in 2012 2nd International Symposium On Environment Friendly Energies and Applications, IEEE.

[13] [13] A. Khaligh, and O. C. Onar, " Energy harvesting: solar, wind, and ocean energy conversion systems. ", CRC press, 2017.

[14] [14] A.Abu-Jasser, "An off-grid wind energy system powering a residence in Gaza.", An off-grid wind energy system powering a residence in Gaza, vol. 5, no 2, 2010.

[15] [15] K. Sattler, "Analysis of the Water Sector Reforms in Tanzania, Kenya and Uganda.", PhD dissertation, Universty of Wien, 2010.

[16] [16] M.Girma, M. "Feasibility study of a wind powered water pumping system for rural Ethiopia.", (2015).

[17] [17] D. D. Lara, G.G. Merino, B.J. Pavez and J.A. Tapia, "Efficiency assessment of a wind pumping system." , Energy Conversion and Management, vol. 52, no 2, pp 795-803, 2011

[18] [18] M. P. G. Krishnan and M. K. Arunachaleswari, "Distributed Generation Grid infrastructure using smartmeters modelled with renewable energy sources and power trading.", International Journal of Engineering Sciences and Research Technology (IJESRT), 2013.

[19] [19] R. V.Rodrigues and L. A. Rossi, "Performance of small wind turbines: simulation of electricity supply to loads connected to the public or isolated grid.", Engenharia Agrícola, vol 36, no 2, pp 281-290, 2016

[20] [20] K. Sukkiramathi and C. Seshaiah, "Analysis of wind power potential by the three-parameter Weibull distribution to install a wind turbine.", Energy Exploration and Exploitation, vol. 38, no 1, pp 158-174, 2020

Authorized licensed use limited to: DELHI TECHNICAL UNIV. Downloaded on February 15,2021 at 10:00:50 UTC from IEEE Xplore. Restrictions apply.

Determination of optimal size of battery energy storage system (BESS) for a renewable power based microgrid

Avirup Maulik
Department of Electrical Engineering
Delhi Technological University
Delhi, India
avirupmaulik@gmail.com

Debapriya Das
Department of Electrical Engineering
Indian Institute of Technology
Kharagpur, India
ddas@ee.iitkgp.ac.in

2020 IEEE 17th India Council International Conference (INDICON) | 978-1-7281-6916-3/20/$31.00 ©2020 IEEE | DOI: 10.1109/INDICON49873.2020.9342575

***Abstract*—A battery energy storage system (BESS) plays a crucial role in the proper operation of a microgrid. Larger the size of the BESS, smaller is the microgrid operating cost, but higher is the BESS's capital cost. Thus, a compromise between the operating cost and capital investment is to be reached for determining the optimal BESS size. The present work focuses on finding the optimal power and energy rating of a BESS in a microgrid. In this work, a non-trivial network with proper network parameters and network loss has been considered. A simple energy management strategy is proposed to determine the optimal dispatch strategy in the microgrid when the day-ahead forecasts of load, wind power, and solar power are available. Optimal sizing of three types of batteries, namely lithium-ion, sodium-sulfur, and lead-acid are considered. Simulation studies on a twelve-node distribution network are presented.**

Keywords*—Microgrids, distributed generation, energy storage sizing, energy management strategy

I. Introduction

Renewable sources like solar photovoltaic arrays and wind power distributed generation are being extensively used for power generation at the distribution level to counter environmental pollution and greenhouse gas emission. Power generation from renewable sources is variable, uncertain, and weather dependant. An energy storage system (ESS) is deployed in conjunction with renewable generation sources to obviate problems of power generation variability. A properly sized ESS will store energy during high availability periods of renewable power. The same will be utilized for supplying the load when there is a shortage of generation. Problems arising from intermittency of the non-dispatchable DGs can be mitigated to a large extent by this operation. Further, ESS can leverage the time of use (TOU) tariff by purchasing power at a low price from the main grid, storing it, and reselling it back to the main grid whenever the power tariff is high. ESSs can also provide ancillary services and improve power quality. Battery energy storage system (BESS) is the most widely used storage technology used in a power system as on date. A considerable amount of research work has been carried out investigating the operation of a power system with renewable sources and battery energy storage systems [1], [2].

978-1-7281-6916-3/20/$31.00 ©2020IEEE

Suitable sizing of a BESS is key to the successful and financially viable operation of a microgrid. Considerable research addressing proper sizing of BESS has been reported in the literature [3]–[11]. This paper is an extension of the work in the domain of optimal battery sizing. The salient features of this work are as follows:

1) A non-trivial network with network parameters is considered. We have considered operating constraints like network loss, bus voltage limits, line flow constraints, etc. in the formulation.
2) We have used a simple particle swarm optimization (PSO) technique to optimally dispatch the ESS and optimal sizing instead of using fuzzy expert systems trained by human expertise or genetic algorithm (GA).
3) A comparative study between the financial benefits of three types of BESS technologies, namely, lead-acid (LA), Sodium-sulfate (NaS), and Lithium-Ion (Li-ion) is presented.

The PSO technique acts as a link between the network and time-domain equations. Day-ahead forecasts of load, wind power, and solar power are required for using the proposed technique for optimal energy scheduling. The proposed method is validated on a twelve node test distribution system comprising wind and solar-based DGs, loads, and BESS. Sizing of BESS is carried out considering three different battery types - lead-acid (LA), sodium-sulfur (NAS), and lithium-ion (Li-Ion). The objective of the study is to select an optimal size and type of battery from financial considerations.

Remainder of this paper is arranged as follows. In section II, we have modeled different components of the microgrid. The problem is mathematically formulated, and the solution strategy is briefly discussed in section III. Simulation results are presented in section IV, and conclusions in section V.

II. System component modeling

We have considered a distribution network comprising loads, BESS, and renewable sources (wind and solar). The

Authorized licensed use limited to: DELHI TECHNICAL UNIV. Downloaded on February 15,2021 at 10:05:49 UTC from IEEE Xplore. Restrictions apply.

network is an 11 kV distribution network. The total peak active load is 435 kW, while the total peak reactive load is 405 kVAr. The BESS and solar power DG are coupled to the AC bus via DC/AC inverter, while the wind power DG is coupled to the AC bus via AC/AC converters. The solar and wind power DGs operate following a maximum power point tracking (MPPT) algorithm, while a central controller provides set points of the ESS for different hours. Information like day-ahead forecasts of load, wind power, solar power, and hourly grid energy price, limits of units, network connections, and parameters are fed to the central controller. The central controller then uses an energy management system algorithm to determine the ESS's hourly optimal dispatch strategy. The microgrid can exchange power in both directions while operating in grid-connected mode. In this study, the selling and buying prices of electricity are assumed to be the same.

A. Wind Turbine Model

The power output of a wind turbine can be expressed as given below [12]:

$$\begin{aligned} P_{WT}(v_w) &= 0; \quad : v_w < v_{ci}; \quad v_w > v_{co} \\ P_{WT}(v_w) &= \alpha v_w^2 + \beta v_w + \gamma \quad : v_{ci} \leq v_w \leq v_{rated} \\ P_{WT}(v_w) &= P_{rated} \quad : v_{rated} < v_w \leq v_{co} \end{aligned} \tag{1}$$

Here, v_w is the wind speed, $P_{WT}(v_w)$ is the power output of the wind turbine at a wind speed v_w, v_{ci} is the cut-in wind speed, v_{co} is the cut-off wind speed, v_{rated} is the rated wind speed, and P_{rated} is the rated power of the wind turbine. Coefficients α, β, and γ are expressible in terms of the rated power of the wind turbine, cut-in wind speed, rated wind speed, and cut-off wind speed [12].

B. Solar PV cell array DG model

In the PV system, it is assumed that a maximum power point tracker is being used. The maximum power output is given below [13]:

$$P_{solar} = \eta S I (1 - 0.005(t_0 - 25)) \tag{2}$$

Where, η is the solar cell array conversion efficiency (%), S is the array area (m^2); I is the solar radiation (kW/m^2), and t_0 is the outside air temperature (degree Celsius).

C. BESS model

In this work, three types of batteries are considered separately, lead-acid (LA), lithium-ion (Li-ion), and sodium-sulfur (NaS). Lead-acid batteries have low cost, matured technology, and are widely available [14]. Therefore, they are most commonly used. But, the disadvantages of lead-acid batteries are their short lifetime, and requirement of frequent maintenance [14]. Sodium-sulfur (NaS) batteries utilize new technology and have high power and energy densities. Therefore, they are suitable for large-scale applications. Further, they don't suffer from self-discharge problems, and their efficiency is close to 90% [14]. NaS batteries have high capital costs and require a high operating temperature of around $300°C$–$400°C$. Therefore, an additional heating arrangement is necessary [14]. Lithium-ion batteries have high efficiency, high power density, fast discharge capability, long life, and deep discharges are permitted [14]. However, they have a high cost and require circuitry for safety and protection [14]. Irrespective of the battery type considered, the BESS equations and constraints remain the same and are given below. During discharge, $P_{batt}^t > 0$ and the energy equation is given below:

$$C^t = C^{t-1} - P_{batt}^t \frac{\Delta T}{\eta_{dis}} \tag{3}$$

During charging, $P_{batt}^t < 0$ and the energy equation is given below:

$$C^t = C^{t-1} - P_{batt}^t \Delta T \eta_{chg} \tag{4}$$

Where t is the time interval under consideration, T is the time horizon in hours (24 hours in this paper), P_{batt}^t is the BESS power output at t^{th} time interval, C^t is the Energy of the BESS at the end of the t^{th} time interval, ΔT is the duration of time interval (1 hour in this paper), η_{dis} is the BESS discharge efficiency, η_{chg} is the BESS charging efficiency. Further, the energy stored in the battery at the end of t^{th} time interval must be within the minimum SOC limit, and the energy rating of the BESS represented as:

$$SOC^{min} C_{rated} \leq C^t \leq C_{rated} \tag{5}$$

The battery energy at the beginning and the end of the day must be the same:

$$C^0 = C^T \tag{6}$$

III. Problem formulation and solution strategy

A. Problem formulation

The cost of BESS comprises one time BESS capital cost and annual maintenance cost [15], [16]. The one time capital cost in turn consists of a component proportional to the energy rating of the BESS ($C1$ in $\$/kWh$) and a component proportional to the power rating of the BESS ($C2$ in $\$/kW$). Therefore, the initial capital cost ($Cost_{capital}$) of the BESS with energy rating of C_{rated} and power rating of P_{rated} is given by:

$$Cost_{capital} = C_1 C_{rated} + C_2 P_{rated} \tag{7}$$

If Rt be the interest rate for financing the BESS, Lt be the lifetime of the installed BESS, then the annual one time capital cost of the BESS $Cost_{capyrly}$ is given by:

$$Cost_{capyrly} = \frac{Rt(1+Rt)^{Lt}}{(1+Rt)^{Lt} - 1} Cost_{capital} \tag{8}$$

The installed BESS will also have a maintenance cost comprising a component proportional to the energy rating (C_3 in $\$/kWh$) and a component proportional to the power rating ($C4$ in $\$/kW$) of the BESS [15]. Therefore, the annual maintenance cost of the BESS is given by:

Authorized licensed use limited to: DELHI TECHNICAL UNIV. Downloaded on February 15,2021 at 10:05:49 UTC from IEEE Xplore. Restrictions apply.

TABLE I
BATTERY CHARACTERISTICS [15]

Battery type	Life (Yrs)	Charging efficiency (%)	Discharge efficiency (%)	C1 ($/kWh)	C2 ($/kW)	C3 ($/kWh)	C4 ($/kW)
Li-Ion	10	0.95	0.95	500	400	12.5	25
NaS	6	0.90	0.90	125	1000	1.5	3
LA	3	0.90	0.90	150	300	15	30

$$Cost_{mntyrly} = C_3 C_{rated} + C_4 P_{rated} \tag{9}$$

In this paper, the daily operating cost of the microgrid is calculated. Therefore, the total BESS cost is to be expressed in $/day. Hence, the BESS cost per day can be expressed as:

$$Cost_{BESSdaily} = \frac{1}{365}(Cost_{capyrly} + Cost_{mntyrly}) \tag{10}$$

Let K_t be the energy exchange cost between the main grid and the microgrid at any hour t. The cost of buying and selling energy is assumed to be equal in this paper. $Pgrid_t$ be the value of power exchanged between the microgrid and the main-grid for an hour t ($Pgrid_t > 0$, if the microgrid purchases power from the main grid; and $Pgrid_t < 0$, if the microgrid sells electricity to the main grid). Then, the daily cost of energy purchase from the main grid is given by:

$$Cost_{purchdaily} = \sum_{t=1}^{T} K_t Pgrid_t \Delta T \tag{11}$$

Therefore, the total daily operating cost of the microgrid is given by:

$$Cost_{daily} = Cost_{BESSdaily} + Cost_{purchdaily} \tag{12}$$

The objective is to minimize the total daily operating cost of the microgrid. Therefore, the optimization problem can be formulated as follows:

$$Minimize \quad Cost_{daily} \tag{13}$$

Constraints:

1) *Power balance constraint*:

$$P_{battit} + P_{DGit} - P_{loadit} = V_{it} \sum_{j=1}^{NB} V_{jt}[G_{ij} cos(\delta_{it} - \delta_{jt}) + B_{ij} sin(\delta_{it} - \delta_{jt})] \tag{14}$$

$$Q_{battit} + Q_{DGit} - Q_{loadit} = V_{it} \sum_{j=1}^{NB} V_{jt}[G_{ij} sin(\delta_{it} - \delta_{jt}) - B_{ij} cos(\delta_{it} - \delta_{jt})] \tag{15}$$

With $t = 1, 2, \ldots T, i \in \Omega$ where Ω is the set of all buses, V_{it} is magnitude of the voltage at bus i at time step t, δ_{it} is the phase angle of the voltage of bus i at time t, G_{ij} is the ij^{th} term of the system's conductance matrix, and B_{ij} is the ij^{th} term of the system's susceptance matrix. P_{battit}/Q_{battit}, P_{DGit}/Q_{DGit}, and P_{loadit}/Q_{loadit} respectively denote the active/reactive powers of battery, DG unit, and the load demand active/reactive power connected to bus i at a time t. For the slack bus, the term $Pgrid_t$ is also added to the left side of eqs. (14) and (15) with a positive sign.

2) *Battery constraints*: Battery constraints given by eqs. (3) to (6) should also be satisfied.

3) *Upstream grid power limits*:

$$-Pgrid^{max} \leq Pgrid_t \leq Pgrid^{max} \tag{16}$$

$Pgrid^{max}$ is the maximum power that the microgrid is allowed to exchange with the main grid.

4) *DG converter limits:*

$$\sqrt{P_{DGit}^2 + Q_{DGit}^2} \leq S_{DGi}^{max} \tag{17}$$

S_{DGi}^{max} is the kVA rating of the DG converter connected to bus i.

5) *Battery converter limits*:

$$\sqrt{P_{battit}^2 + Q_{battit}^2} \leq S_{batti}^{max} \tag{18}$$

S_{batti}^{max} is the kVA rating of the battery converter connected to bus i.

6) *Voltage limit constraints*:

$$0.90 \leq V_{it} \leq 1.10 \quad p.u \quad \forall \quad i \in \Omega \tag{19}$$

7) *Line current Limits*:

$$|I_{bt}| \leq I_b^{max} \quad \forall b \in LN \tag{20}$$

I_b and I_b^{max} are the line current and the maximum current rating of the line b, respectively. LN is the set of all lines in the network.

B. Solution strategy

The optimization is carried out at two levels. At a higher level, optimization is carried out for battery sizing. We implement a battery management system algorithm for each battery size, optimal scheduling of batteries, and a power flow solution at a lower level sub-ordinate problem. We have adopted the battery management system algorithm discussed in detail in [3] and is not repeated in this paper for brevity. The battery scheduling is carried out considering the twenty-four hours forecast of renewable generation and load demand. Battery scheduling may be carried out using a heuristic algorithm like particle swarm optimization or discrete dynamic programming discussed in [17]. The battery size may be optimized either through a discrete exhaustive search or using a heuristic algorithm.

Authorized licensed use limited to: DELHI TECHNICAL UNIV. Downloaded on February 15,2021 at 10:05:49 UTC from IEEE Xplore. Restrictions apply.

TABLE II
OPTIMAL BATTERY SIZES

Battery type	Energy rating (kWh)	Power Rating (kW)	Normalized daily capital and O&M cost of battery ($)	Daily cost of power purchase ($)	Total daily cost ($)	Daily savings with battery ($)
Li-Ion	500	200	153.6614	3.818	157.4799	11.93 %
NaS	1000	130	147.2533	-33.9817	113.2716	36.65 %
LA	500	100	136.3878	56.240	192.6276	-7.72 %

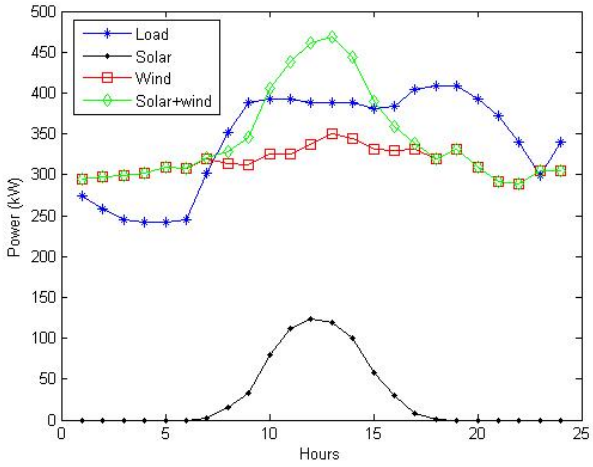

Fig. 1. Hourly variation of load demand, solar power generation, and wind power generation

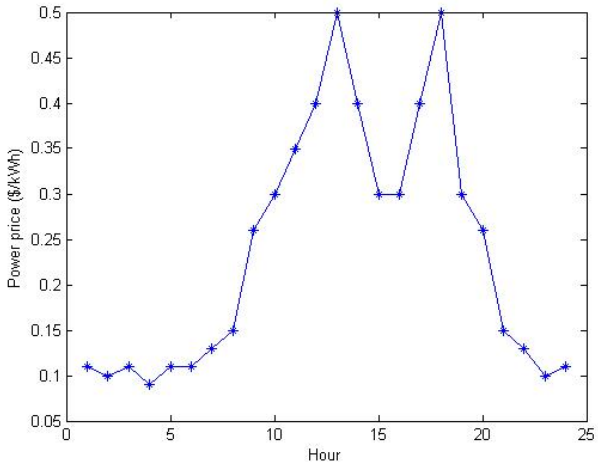

Fig. 2. Hourly variation of grid power price used for simulation study in this paper

IV. SIMULATION RESULTS

The proposed sizing methodology is applied to a test distribution network of $11kV$ with twelve nodes given in [18]. We have considered a solar PV array of $150kW$, operating at unity power factor connected to bus 2. A wind turbine DG unit of $350kW$ and operating at 0.85 power factor leading is connected to bus 9. A BESS is connected to bus 3. The hourly variations of load (RTS pattern), wind power ([19]), and solar generations (IIT Kharagpur) are shown in Fig. 1. The variation of grid energy price is taken from [20] and is shown in Fig.

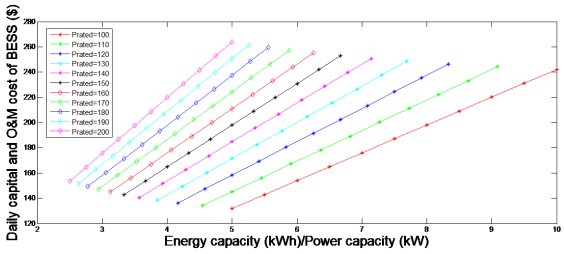

Fig. 3. Daily capital and O&M cost of BESS as a function of energy and power capacities for Li-Ion battery

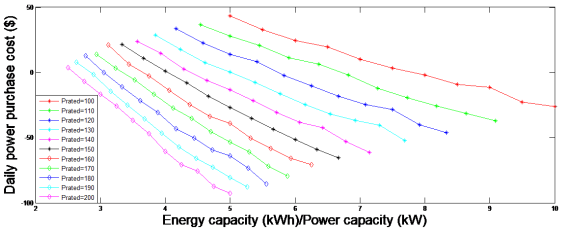

Fig. 4. Daily power purchase cost of microgrid as functions of energy and power capacities of Li-Ion battery

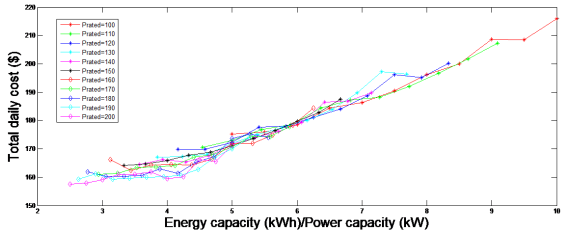

Fig. 5. Daily operating cost of microgrid as functions of energy and power rating of Li-Ion battery

2.

We have considered optimal sizing of three types of batteries- lead-acid (LA), sodium-sulfur (NaS), and lithium-ion (Li-ion). The battery details are provided in Table I [15]. A microgrid should operate stably in an islanded mode, imposing a minimum battery-size requirement on the system. The minimum sizing is based on the principle that battery should discharge or charge to ensure load and generation balance at every instant for islanded microgrid operation. The approximate minimum battery size is $100kW$, $500kWh$ using the above principle. Hence, in the simulation, we set the minimum energy and power ratings to $500kWh$ and $100kW$. The power rating is varied in steps of $10kW$, and the rating is varied up to $200kW$. The energy rating is varied in steps of $50kWh$ and varied till $1000kWh$. We considered the initial

Authorized licensed use limited to: DELHI TECHNICAL UNIV. Downloaded on February 15,2021 at 10:05:49 UTC from IEEE Xplore. Restrictions apply.

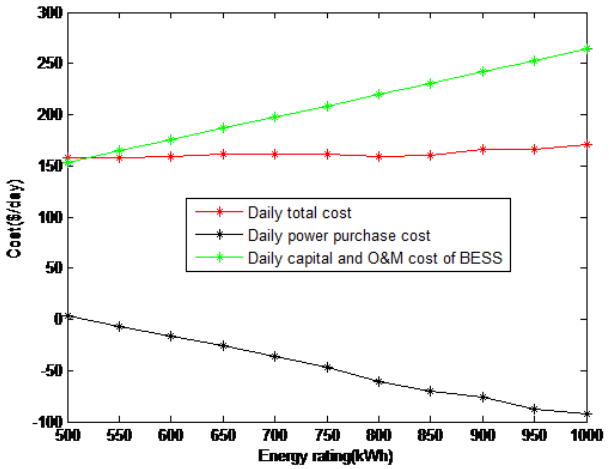

Fig. 6. Daily capital and O&M cost, daily power purchase cost, and daily total cost as a function of the energy capacity for a 200 kW Li-Ion battery

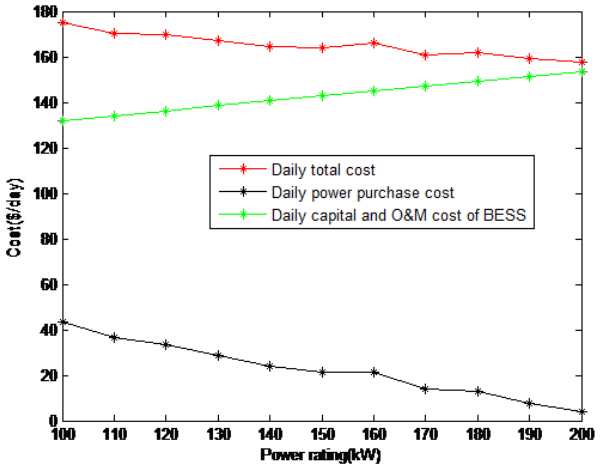

Fig. 7. Daily capital and O&M cost of BESS, daily power purchase cost, and daily total cost as a function of the power capacity for a 500 kWh Li-Ion battery

and final SOCs of the battery to be 0.6. The daily cost of operation without a BESS is \$178.81. The optimal battery sizes, daily capital cost, operation and maintenance cost of batteries, daily total cost, and the savings are given in Table II. For Li-Ion battery, the optimal size is found to be $500kWh$, $200kW$. The net saving achieved per day with installation of this battery is around 11.93% of the operation cost of the microgrid without any storage (Table II).

Fig.3 shows the daily cost of BESS (capital cost and annual O&M cost per day) as a function of both power and energy ratings for Li-Ion battery. It is seen that BESS cost increases with the power and energy rating of the battery. The variation of the daily cost of power purchase (in grid-connected mode) with energy and power ratings is shown in Fig.4. It is observed that the higher the energy and power rating of a battery,

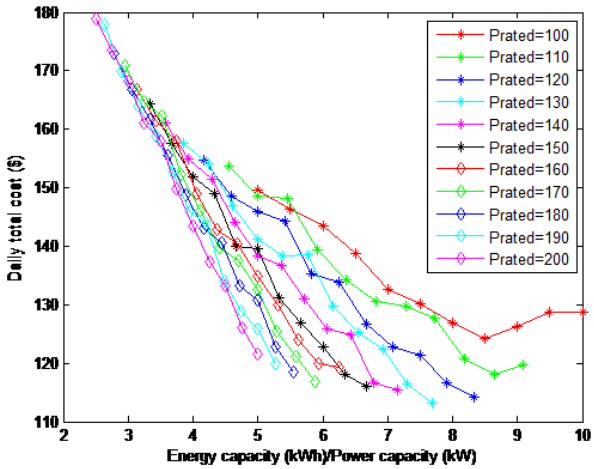

Fig. 8. Daily total cost as a function of power and energy capacities for a NaS battery

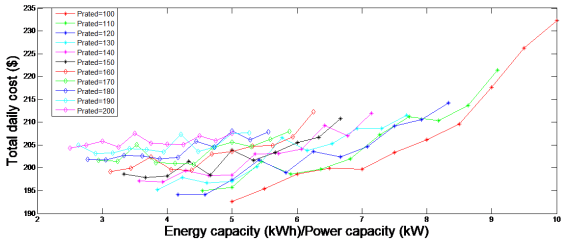

Fig. 9. Daily total cost as a function of power and energy capacities for a LA battery

the lower the cost of power purchase, because, batteries with larger power and energy ratings can store larger quantities of excess renewable generation, and cheap power during off-peak periods. This cheap stored energy can then be dispatched to feed load when there is a generation shortage, or when the power price in the main grid is high. But, for choosing the optimal battery size, the objective is to minimize the sum of the daily power purchase price and daily capital and O&M cost of the battery. Fig.5 shows the total daily cost as a function of power and energy ratings of Li-Ion battery. It is seen that the optimal size of a Li-Ion battery is $200kW$, $500kWh$. Further, the variation of the daily capital and O&M cost of the battery, the daily power purchase cost, and the total daily cost with a change of energy rating for a $200kW$ Li-Ion battery are plotted in Fig.6. It is seen that while the cost of power purchase decreases with an increasing energy rating of the battery, the daily capital and O&M cost of battery increases with a higher energy rating of the battery. Optimal size is attained when the sum of the two becomes least. Again, Fig.7 shows the variation of the daily capital and O&M cost of the battery, the daily power purchase cost, and the total daily cost with a change of power rating for a $500kWh$ Li-Ion battery.

For NaS battery, the optimal size is $1000kWh$, $130kW$. For the three types of batteries studied in this paper, the maximum

Authorized licensed use limited to: DELHI TECHNICAL UNIV. Downloaded on February 15,2021 at 10:05:49 UTC from IEEE Xplore. Restrictions apply.

saving is achieved with NaS battery. Daily saving is to the tune of 36.65% of the microgrid operation cost without any storage (Table II). Since the optimum NaS battery has a high energy rating, it stores large quantities of cheap energy from the main grid during off-peak hours. During the peak period, it sells the power to the main grid at a much higher price. Therefore, the total energy purchase cost from the main grid during off-peak hours is overcompensated by the income from selling energy to the main grid during peak hours. Therefore, the microgrid makes a net profit of $\$33.9817$ by exchanging energy with the main grid, which is reflected as a negative cost of power purchase in Table II. Fig.8 shows the total daily cost as a function of power and energy ratings of NaS battery. We observe from Fig. 8 that the optimal size for a NaS battery is $1000kWh$, $130kW$.

However, by installing LA batteries, savings cannot be achieved. Therefore, the LA battery's optimum size corresponds to the minimum energy and power rating, i.e., $500kWh$, $100kW$ (see Fig. 9). With this size, there is an increase in daily operational costs by 7.72% (Table II). Cost-benefit cannot be achieved with LA battery due to its small lifetime. Although the one-time capital cost of LA is the least out of the three battery types understudy, yet, due to its short life-span (around three years), the daily cost becomes very high, making it a financially unviable choice from a long term point of view. To summarize, it can be concluded that the following are the pattern of the optimal choices for batteries: i) Li-Ion: Low energy rating, high power rating. ii) NaS: High energy rating, low power rating. iii)LA: Low energy rating, low power rating.

V. Conclusions

In this paper, a method for optimal sizing of BESS has been presented. The use of the proposed method allows the selection of optimal energy and power ratings of the BESS. It also determines the optimal EMS for the given battery and system characteristics. In the proposed method, the non-trivial network topology is considered, and system loss is also incorporated. The proposed methodology is validated on a 12 node sample distribution network with renewable-based DG. Three different battery types, namely Li-Ion, NaS, and LA, are considered for the simulation. It is observed that maximum saving can be achieved by installing optimally rated NaS battery, while with LA; no net saving can be achieved. Moreover, it is found that due to high capital cost proportional to the energy rating of a Li-Ion battery, the optimal choice is a battery with low energy rating, and high power rating. On the other hand, the capital cost proportional to a NaS battery's power rating is very high; consequently, an optimal selection is a NaS battery with a high energy rating and low power rating. Since, with LA battery, no net savings can be achieved, an optimal choice is a LA battery with low energy and power ratings.

References

[1] K. W. Cheung and R. Rios-Zalapa, "Smart dispatch for large grid operations with integrated renewable resources," in *ISGT 2011*. IEEE, 2011, pp. 1–7.

[2] P. Samadi, H. Mohsenian-Rad, V. W. Wong, and R. Schober, "Tackling the load uncertainty challenges for energy consumption scheduling in smart grid," *IEEE Transactions on Smart Grid*, vol. 4, no. 2, pp. 1007–1016, 2013.

[3] J. P. Fossati, A. Galarza, A. Martín-Villate, and L. Fontan, "A method for optimal sizing energy storage systems for microgrids," *Renewable Energy*, vol. 77, pp. 539–549, 2015.

[4] I. Alsaidan, A. Khodaei, and W. Gao, "A comprehensive battery energy storage optimal sizing model for microgrid applications," *IEEE Transactions on Power Systems*, vol. 33, no. 4, pp. 3968–3980, 2017.

[5] X. Dui, G. Zhu, and L. Yao, "Two-stage optimization of battery energy storage capacity to decrease wind power curtailment in grid-connected wind farms," *IEEE Transactions on Power Systems*, vol. 33, no. 3, pp. 3296–3305, 2017.

[6] M. A. Abdulgalil and M. Khalid, "Enhancing the reliability of a microgrid through optimal size of battery ess," *IET Generation, Transmission & Distribution*, vol. 13, no. 9, pp. 1499–1508, 2019.

[7] H. Xie, X. Teng, Y. Xu, and Y. Wang, "Optimal energy storage sizing for networked microgrids considering reliability and resilience," *IEEE Access*, vol. 7, pp. 86 336–86 348, 2019.

[8] H. Abdeltawab and Y. A.-R. I. Mohamed, "Mobile energy storage sizing and allocation for multi-services in power distribution systems," *IEEE Access*, vol. 7, pp. 176 613–176 623, 2019.

[9] M. A. Abdulgalil, M. Khalid, and F. Alismail, "Optimal sizing of battery energy storage for a grid-connected microgrid subjected to wind uncertainties," *Energies*, vol. 12, no. 12, p. 2412, 2019.

[10] ——, "Optimizing a distributed wind-storage system under critical uncertainties using benders decomposition," *IEEE Access*, vol. 7, pp. 77 951–77 963, 2019.

[11] M. T. Elsir, M. A. Abdulgalil, A. T. Al-Awami, and M. Khalid, "Sizing and allocation for solar energy storage system considering the cost optimization," in *2019 8th International Conference on Renewable Energy Research and Applications (ICRERA)*. IEEE, 2019, pp. 407–412.

[12] W. R. Powell, "An analytical expression for the average output power of a wind machine," *Solar Energy*, vol. 26, no. 1, pp. 77–80, 1981.

[13] C. Tao, D. Shanxu, and C. Changsong, "Forecasting power output for grid-connected photovoltaic power system without using solar radiation measurement," in *The 2nd International Symposium on Power Electronics for Distributed Generation Systems*. IEEE, 2010, pp. 773–777.

[14] H. Chen, T. N. Cong, W. Yang, C. Tan, Y. Li, and Y. Ding, "Progress in electrical energy storage system: A critical review," *Progress in natural science*, vol. 19, no. 3, pp. 291–312, 2009.

[15] W. A. Omran, M. Kazerani, and M. Salama, "Investigation of methods for reduction of power fluctuations generated from large grid-connected photovoltaic systems," *IEEE Transactions on Energy Conversion*, vol. 26, no. 1, pp. 318–327, 2010.

[16] P. Komor and J. Glassmire, "Electricity storage and renewables for island power: a guide for decision makers," *International Renewable Energy Agency (IRENA), Bonn, Germany*, 2012.

[17] X. Kong, L. Bai, Q. Hu, F. Li, and C. Wang, "Day-ahead optimal scheduling method for grid-connected microgrid based on energy storage control strategy," *Journal of Modern Power Systems and Clean Energy*, vol. 4, no. 4, pp. 648–658, 2016.

[18] D. Das, H. Nagi, and D. Kothari, "Novel method for solving radial distribution networks," *IEE Proceedings-Generation, Transmission and Distribution*, vol. 141, no. 4, pp. 291–298, 1994.

[19] L. F. Ochoa, A. Padilha-Feltrin, and G. P. Harrison, "Evaluating distributed time-varying generation through a multiobjective index," *IEEE Transactions on Power Delivery*, vol. 23, no. 2, pp. 1132–1138, 2008.

[20] S. Chen, H. B. Gooi, and M. Wang, "Sizing of energy storage for microgrids," *IEEE Transactions on Smart Grid*, vol. 3, no. 1, pp. 142–151, 2011.

Authorized licensed use limited to: DELHI TECHNICAL UNIV. Downloaded on February 15,2021 at 10:05:49 UTC from IEEE Xplore. Restrictions apply.

This article has been accepted for inclusion in a future issue of this journal. Content is final as presented, with the exception of pagination.

Dual Input Digitally Controlled Broadband Three-Stage Doherty Power Amplifier With Back-Off Reconfigurability

Ayushi Barthwal, *Member, IEEE*, Karun Rawat, *Senior Member, IEEE*, and Shiban K. Koul, *Life Fellow, IEEE*

***Abstract*— This article presents a design strategy to improve the bandwidth of the three-stage Doherty Power Amplifier (DPA) by controlling the phase difference between the dual RF inputs digitally. The theory also proposes multiple back-off reconfigurability without using tuning elements and extra circuitry. The proposed theory is validated by demonstration of a dual-input three-stage DPA which is designed and implemented using Wolfspeed's GaN HEMT transistors. The measured results show a drain efficiency of 50.4 – 58% and 46.1 – 65.4% at 12 dB and 6 dB back-off respectively, over the frequency range of 550-900 MHz. Over this 350 MHz band, the drain efficiency is between 53.97% and 71.5% at saturation, corresponding to 48.3% fractional bandwidth. The measurement results also show that both the back-offs are reconfigurable by changing the drain bias of main and first auxiliary power amplifier. The modulated measurements are carried with a 10 MHz LTE signal with a PAPR of 11.75 dB. The high average efficiency of 51.6%, 54.9%, and 52.6% is reported at 600, 700, and 800 MHz, respectively, at an average power of around 30 dBm. The measurement results validate the theory proposed making the presented DPA as a potential candidate for future wireless transmitters.**

***Index Terms*— Broadband, Doherty power amplifier (DPA), efficiency enhancement, GaN, load modulation, reconfigurability, three-stage.**

I. Introduction

HIGH speed data requirements in a modern communication system have put forward a demand for a wide band signal and spectral efficient modulation schemes. Such modulation schemes increase the peak to average power ratio (PAPR) of the signals, due to which power amplifier (PA) operates at large back-off, where efficiency of conventional PA is very low. Thus, it becomes a crucial factor to improve the efficiency of PA at back-off [1]–[3]. The advancement in communication systems has also led to the addition of new frequency bands to the existing wireless spectrum along with the increase in the signal bandwidth. This poses a requirement of a PA which should not only have a potential of supporting high PAPR signals, but it should also support wide bandwidth signal at different carrier frequencies simultaneously. Several PA architectures have been proposed in the literature to cater to such need, among which Doherty Power Amplifier (DPA) is the most popular architecture because of its ease in circuit implementation [4]–[9].

The broadband conventional two-stage DPAs focus on efficiency enhancement up to 6 dB back-off [10]–[17]. With the advent of the new wireless era, the adopted modulated schemes are more complex, which further increase PAPR of signals. The multi-stage DPA provides the solution by enhancing efficiency at multiple back-off and at saturation. [18]–[23]. Among the many three-stage DPA works described, very few of them focus on bandwidth extension [24]–[28]. The quarter-wave transformers present in the load combiner limit the bandwidth performance of DPA in the back-off region. Additionally, all the broadband three-stage DPA reported have used analog splitting at the input, which provides fixed amplitude and a fixed phase at all frequencies. The use of an analog splitter restricts the bandwidth behavior of three-stage DPA. Therefore, digital splitting of input signal is required, which could provide different magnitude and phase at a different frequency in order to obtain broad bandwidth performance. Such digital splitting has been used in [14] but it enhances efficiency up to 6 dB back-off only. The mixed-signal approach for three-stage DPA has been utilized in [22], [23], but they do not propose a wideband operation.

Along with wideband capability, the DPA should also support backward compatibility in order to amplify previous existing communication standards along with the newer generation communication standards. Since the PAPR of the different communication standards are different, therefore the DPA has to amplify efficiently at different back-off levels, which demands DPA to be back-off reconfigurable. In [14], [29], a single back-off point is tuned by using different drain bias conditions for the main PA; in which [14] shows broadband performance. In [14], the DPA is implemented using bare die devices, which allow for a broadband design due to the

Manuscript received July 24, 2020; revised October 30, 2020 and December 14, 2020; accepted December 31, 2020. This work was supported by SERB Grant CRG/2018/003869, in part by SPARC Grant SPARC/2018-2019/P291/SL. This article was recommended by Associate Editor M. Onabajo. *(Corresponding author: Ayushi Barthwal.)*

Ayushi Barthwal is with the School of Engineering, Jawaharlal Nehru University, New Delhi 110067, India (e-mail: barthwal.ayushi1988@gmail.com).

Karun Rawat is with the Department of Electronics and Communication Engineering, IIT Roorkee, Roorkee 247667, India (e-mail: karun.rawat.in@ieee.org).

Shiban K. Koul is with the Centre for Applied Research in Electronics, IIT Delhi, New Delhi 110016, India (e-mail: shiban_koul@hotmail.com).

Color versions of one or more figures in this article are available at https://doi.org/10.1109/TCSI.2021.3050543.

Digital Object Identifier 10.1109/TCSI.2021.3050543

1549-8328 © 2021 IEEE. Personal use is permitted, but republication/redistribution requires IEEE permission.
See https://www.ieee.org/publications/rights/index.html for more information.

Authorized licensed use limited to: DELHI TECHNICAL UNIV. Downloaded on February 15,2021 at 10:30:47 UTC from IEEE Xplore. Restrictions apply.

This article has been accepted for inclusion in a future issue of this journal. Content is final as presented, with the exception of pagination.

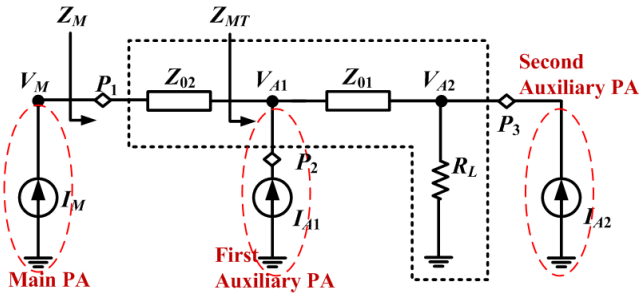

Fig. 1. Ideal schematic of three-stage DPA, with P1, P2 and P3 representing three ports.

absence of package parasitic. In order to support forward compatibility along with backward compatibility, different standards having different PAPRs are required to be handled simultaneously. This poses the requirement of multiple reconfigurable back-offs in three-stage DPA so that different standards are amplified efficiently over a wide range of frequencies.

This work demonstrates a setup in which dual RF inputs are used whose amplitude and phase-difference is controlled digitally. The proper control on parameters of dual inputs along with the selection of appropriate load combiner impedances leads to a broadband three-stage DPA. This work also proposes DPA with multiple reconfigurable back-offs. Both the back-off points are reconfigured by changing drain bias of the main and first auxiliary PA. The measurement results validate the proposed strategy.

II. Wideband Approach

The three-stage DPA consists of a main PA and two auxiliary PAs, as shown in Fig. 1. Each of the PA is represented by an ideal voltage-dependent current source, with output current as I_M, I_{A1} and I_{A2} respectively for main, first auxiliary, and second auxiliary PA. The main PA remains ON from low power level, whereas the first auxiliary PA turns ON at medium power level, and the second auxiliary PA turns ON at a high power level. These output currents are combined by a load combiner, comprised of two quarter-wave transformers having characteristic impedance Z_{01} and Z_{02}, and a load resistance R_L. The load impedance seen by the main PA, Z_M is modulated by the first and second auxiliary PA as the input power is swept from low to high level. The load modulation is achieved with the help of quarter-wave transformers, which also act as one of the prime factors in limiting the bandwidth of DPA.

The impedance seen by the main PA, Z_M is given by;

$$Z_M = Z_{02}\frac{Z_{MT} + jZ_{02}\tan(\gamma l)}{Z_{02} + jZ_{MT}\tan(\gamma l)} \tag{1}$$

where Z_{MT} is defined as

$$Z_{MT} = Z_{01}\frac{R_L + jZ_{01}\tan(\gamma l)}{Z_{01} + jR_L\tan(\gamma l)} \tag{2}$$

when both the auxiliary PAs are in OFF state, i.e. $I_{A1} = I_{A2} = 0$. The term (γl) represents the electrical length and is dependent on the frequency with a value of 90° at the center frequency.

The theory proposes a fact that if Z_{02}, Z_{01}, and R_L are made equal, Z_M becomes frequency independent when both the auxiliary PAs are OFF [28]. But when $I_{A1} \neq 0$ and $I_{A2} \neq 0$, Z_M becomes frequency-dependent. However, if one could control the amplitude and phase relations between main and auxiliary PA currents, the frequency dependency of Z_M can be reduced.

The output current of each PA changes with the applied input voltage and is given in terms of normalized input voltage (v_{in}) as:

$$I_M = \begin{cases} I_{M,\max}\left(\dfrac{v_{in}}{(1/\beta_2)}\right) & 0 \le v_{in} \le 1/\beta_2 \\ I_{M,\max} & 1/\beta_2 \le v_{in} \le 1 \end{cases} \tag{3a}$$

$$I_{A1} = \begin{cases} 0 & 0 \le v_{in} \le \dfrac{1}{\beta_1} \\ {m_1}^* {I_{M,\max}}^* \exp(-j^*\theta_1) & \dfrac{1}{\beta_1} \le v_{in} \le 1 \end{cases} \tag{3b}$$

$$I_{A2} = \begin{cases} 0 & 0 \le v_{in} \le \dfrac{1}{\beta_2} \\ {m_2}^* {I_{M,\max}}^* \exp(-j^*\theta_2) & \dfrac{1}{\beta_2} \le v_{in} \le 1 \end{cases} \tag{3c}$$

where $I_{M,max}$ is the main PA current at saturation and m_1 and θ_1 are amplitude ratio and phase difference between I_{A1} and I_M respectively; and m_2 and θ_2 are respective amplitude ratio and phase difference between I_{A2} and I_M after second auxiliary PA turns ON.

The back-off parameter is defined by β_i and is given as:

$$\beta_i = 10^{X_i/20} \tag{4}$$

where $i = 1, 2$ represents for the first and second back-off levels respectively. The variable X_i is back-off level expressed in dB, where high efficiency is required. Similar to the conventional DPA, the first auxiliary PA is OFF for $v_{in} \le 1/\beta_1$ and the second auxiliary PA is OFF for $v_{in} \le 1/\beta_2$.

The terms m_1 and θ_1 are dependent on the normalized input voltage (v_{in}) and frequency. These will be digitally controlled by two RF inputs. The term m_2 is assumed to be frequency independent presuming the broadband performance of input splitter, which splits the input power between main and second auxiliary PA, as explained in later sections. Similar to conventional three-stage DPAs [19], the output current of the second auxiliary PA, m_2 is assumed linear with respect to v_{in} and is expressed as:

$$m_2 = \frac{v_{in} - (1/\beta_2)}{1 - (1/\beta_2)} \tag{5}$$

The phase between the output current of main and second auxiliary PA, θ_2 is taken as 180° in order to have constructive phase alignment at load due to second auxiliary PA. This phase difference is obtained with the help of input splitter as discussed in later sections of this manuscript.

Authorized licensed use limited to: DELHI TECHNICAL UNIV. Downloaded on February 15,2021 at 10:30:47 UTC from IEEE Xplore. Restrictions apply.

This article has been accepted for inclusion in a future issue of this journal. Content is final as presented, with the exception of pagination.

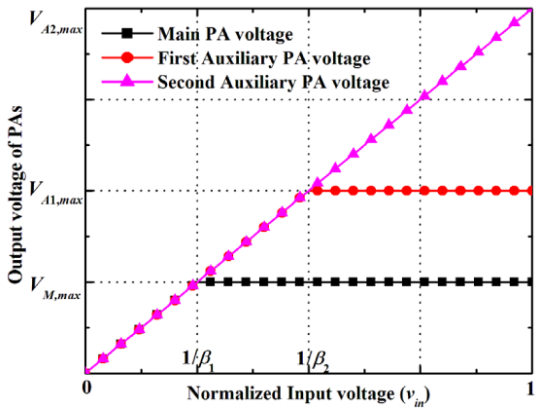

Fig. 2. Output voltage profile of PAs in three-stage DPA configuration.

A. Derivation of Load Combiner Impedances

In order to achieve peak efficiency at first back-off (v_{in} =$1/\beta_1$), the voltage across the main PA should have the maximum value, i.e. $|V_M| = V_{M,\max}$ as shown in Fig. 2. The impedance of the main PA at first back-off can be determined by the ratio of voltage across the main PA and current drawn by main PA using (3a) and is given as:

$$Z_{M,BO1} = \frac{V_{M,\max}}{I_{M,\max}}\left(\frac{\beta_1}{\beta_2}\right) = Z_{02} = Z_{01} = R_L \tag{6}$$

The load combiner impedances (Z_{01}, Z_{02}, and Z_{03}) are also made equal to the main PA impedance at first back-off to reduce frequency dependency as can be observed from (6).

B. Determination of Output Voltages of PAs in DPA Configuration

The load combiner of three-stage DPA can be represented as a three-port network as shown by the dashed box in Fig. 1. The output voltages and output currents of three-port network can be related as:

$$V_M = Z_{11}I_M + Z_{12}I_{A1} + Z_{13}I_{A2} \tag{7a}$$
$$V_{A1} = Z_{21}I_M + Z_{22}I_{A1} + Z_{23}I_{A2} \tag{7b}$$
$$V_{A2} = Z_{31}I_M + Z_{32}I_{A1} + Z_{33}I_{A2} \tag{7c}$$

The impedance parameters of a three-port network is obtained by the output voltages (V_M, V_{A1} and V_{A2}) and the output currents (I_M, I_{A1} and I_{A2}) of main and auxiliary PAs, and the respective impedance matrix is given as:

$$\begin{bmatrix} R_L & R_L e^{-j\gamma l} & R_L e^{-j2\gamma l} \\ R_L e^{-j\gamma l} & R_L e^{-j\gamma l}\cos(\gamma l) & R_L e^{-j2\gamma l}\cos(2\gamma l) \\ R_L e^{-j2\gamma l} & R_L e^{-j2\gamma l}\cos(\gamma l) & R_L e^{-j2\gamma l}\cos(2\gamma l) \end{bmatrix} \tag{8}$$

Using (8) together with (3a) and (6), V_{A1} and V_{A2} are obtained for $0 \le v_{in} \le 1/\beta_1$. It can be observed from Fig. 2 that the first auxiliary PA voltage is linear up to the second back-off and the output voltage of the second auxiliary PA is linear till saturation. Combining these facts, the first and second auxiliary PA voltage is given by:

$$|V_{A1}| = \left(\frac{v_{in}}{1/\beta_1}\right)V_{M,\max} \quad 0 \le v_{in} \le 1/\beta_2 \tag{9}$$

$$|V_{A2}| = \left(\frac{v_{in}}{1/\beta_1}\right)V_{M,\max} \quad 0 \le v_{in} \le 1 \tag{10}$$

which is valid for all frequencies.

The first auxiliary PA saturates at second back-off ($v_{in} = 1/\beta_2$) and at saturation $|V_{A1}| = V_{A1,\max}$ as shown in Fig. 2. Using (9), the maximum output voltages of main PA ($V_{M,\max}$) and first auxiliary PA ($V_{A1,\max}$) are related as:

$$V_{A1,\max} = \frac{\beta_1}{\beta_2}V_{M,\max} \tag{11}$$

Similarly, the second auxiliary PA saturates at peak power ($v_{in} = 1$) where $|V_{A2}| = V_{A2,\max}$ and the relation between maximum output voltages of main PA ($V_{M,\max}$) and second auxiliary PA ($V_{A2,\max}$) is obtained from (10) and is given by:

$$V_{A2,\max} = \beta_1 V_{M,\max} = \beta_2 V_{A1,\max} \tag{12}$$

It can be observed from (12), the maximum output voltages of all three PAs in DPA configuration are related to each other.

C. Derivation of Magnitude and Phase Relationship of the Output Current of First Auxiliary PA

This section derives the dependency of m_1 and θ_1 on frequency and input voltage.

The output voltage of the first auxiliary PA for $1/\beta_1 \le v_{in} \le 1/\beta_2$ is obtained using (3), (7b), and (8) and is written as:

$$V_{A1} = I_{M,\max}R_L\left(\beta_2 v_{in}e^{-j\gamma l} + m_1\cos(\gamma l)\,e^{-j(\theta_1+\gamma l)}\right) \tag{13}$$

The output power of PA is proportional to the square of the magnitude of the output voltage. Equating the output power of the first auxiliary PA using (9) and (13), the following equation is obtained:

$$m_1^2\cos^2(\gamma l) + 2m_1\beta_2\cos(\gamma l)\cos\theta_1 v_{in} = 0 \tag{14}$$

Solving (14), the phase difference between output currents of main and first auxiliary PA is derived as:

$$\theta_1 = \cos^{-1}\left(-\frac{m_1\cos(\gamma l)}{2\beta_2 v_{in}}\right) \tag{15}$$

Similarly, the output voltage of the main PA for $1/\beta_1 \le v_{in} \le 1/\beta_2$ is obtained using (3), (7a), and (8) as

$$V_M = I_{M,\max}R_L\left(\beta_2 v_{in} + m_1 e^{-j(\theta_1+\gamma l)}\right) \tag{16}$$

The output voltage of main PA for $1/\beta_1 \le v_{in} \le 1/\beta_2$ is maximum i.e. $|V_M| = V_{M,max}$ as shown in Fig. 2. Therefore, equating the output power of main PA using (6) and (16), the following equation is obtained

$$\frac{\beta_2^2}{\beta_1^2} = \beta_2^2 v_{in}^2 + m_1^2 + 2m_1\beta_2 v_{in}\cos(\theta_1 + \gamma l) \tag{17}$$

Authorized licensed use limited to: DELHI TECHNICAL UNIV. Downloaded on February 15,2021 at 10:30:47 UTC from IEEE Xplore. Restrictions apply.

This article has been accepted for inclusion in a future issue of this journal. Content is final as presented, with the exception of pagination.

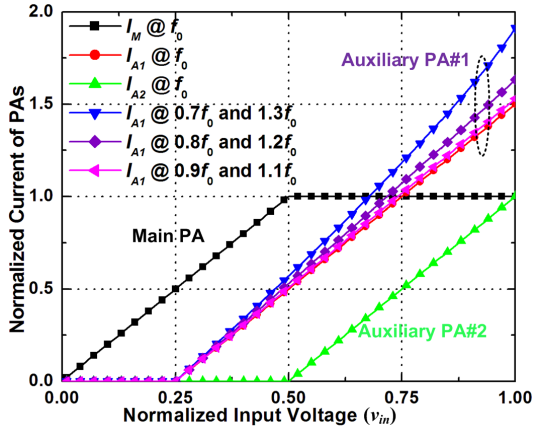

Fig. 3. Theoretical normalized amplitude of output current of PAs with respect to input drive level for $\beta 1 = 4$ and $\beta 2 = 2$.

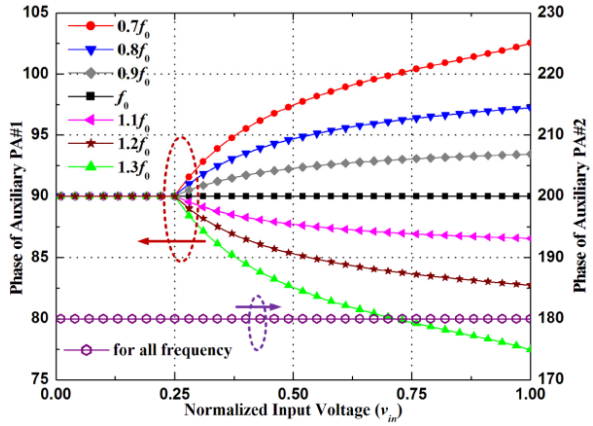

Fig. 4. Theoretical phase difference between the output currents of main & first auxiliary PA; and main & second auxiliary PA.

Using (15), the term $\cos(\theta_1 + \gamma l)$ can be rewritten as:

$$\cos(\theta_1 + \gamma l) = -\frac{m_1 \cos^2(\gamma l)}{2\beta_2 v_{in}} - \sin(\gamma l)\sqrt{1 - \frac{m_1^2 \cos^2(\gamma l)}{4\beta_2^2 v_{in}^2}} \tag{18}$$

Solving (17) and 18) for m_1, the following equation is obtained

$$m_1 = \sqrt{\frac{v_{in}^2 + 1/\beta_1^2}{1/\beta_2^2} - \sqrt{\left(\frac{v_{in}^2 + 1/\beta_1^2}{1/\beta_2^2}\right)^2 - \left(\frac{v_{in}^2 - 1/\beta_1^2}{(1/\beta_2^2)\sin(\gamma l)}\right)^2}} \tag{19}$$

It can be observed from (15) and (19) that θ_1 and m_1 are frequency and input drive level dependent.

Fig. 3 shows the dependency of the magnitude of the output current of first auxiliary PA, m_1, on input drive level for a different frequency. Similarly, Fig. 4 shows the variation of phase requirement between the output currents of main PA and first auxiliary PA, θ_1 with input drive level and frequency. The phase difference between I_M and I_{A2} is assumed to be

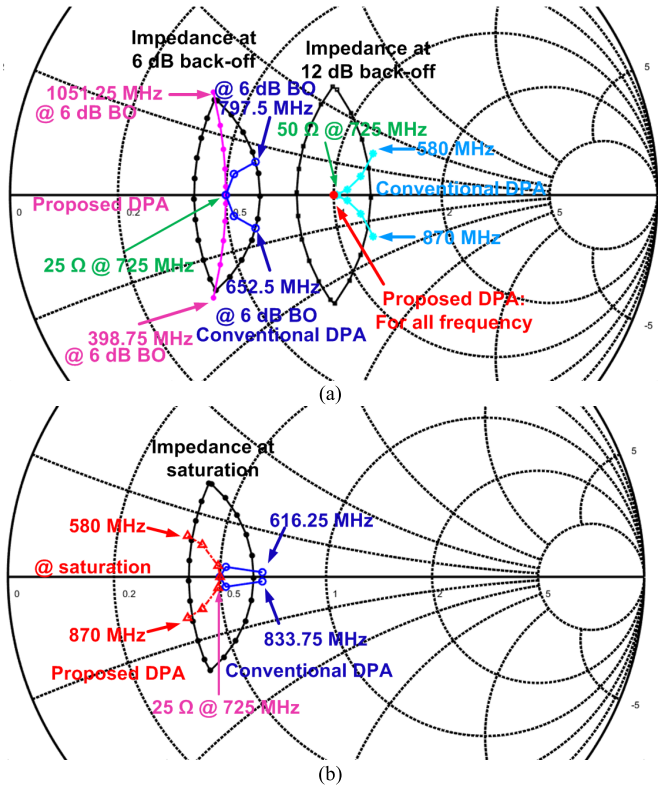

Fig. 5. Comparison between impedance of main PA in conventional and proposed DPA with respect to frequency at 12 dB, 6 dB back-off and saturation.

equal to 180° at simulated frequencies in order to align phase of the output current at load terminal, as shown in Fig. 4.

The selection of the magnitude and phase of output current of first auxiliary PA in such manner reduces the dependency of main PA impedance, Z_M on frequency even after first back-off. Fig. 5 compares the impedance seen by main PA of proposed three-stage DPA with conventional three-stage DPA [19] at first back-off (12 dB), second back-off (6 dB) and saturation. In the case of conventional three-stage DPA, the characteristic impedances of quarter-wave transmission line of load combiner are calculated using equations (1)-(4) of [19], and are obtained as Z_{02} =25 Ω, Z_{01} = (25/4) Ω, and R_L = (25/8) Ω. In the proposed DPA, the impedance values of Z_{02}, Z_{01} and R_L are taken as equal impedances of 50 ohms. The load combiner impedances of conventional DPA and proposed DPA are obtained by assuming the optimum impedance of main PA as 25 Ω.

Fig. 5 shows the 1-dB power contours [30] plotted for load variation at saturation along with 6 dB and 12 dB back-off. One can see from Fig. 5(a) that at 12 dB back-off, the main PA impedance of conventional three-stage DPA remains within 1-dB power contour for the frequency range of 580 MHz to 870 MHz, corresponding to a fractional bandwidth of 40% whereas the main PA impedance of proposed DPA is concentrated on single impedance for all frequencies.

Similarly at 6 dB back-off, the main PA impedance of conventional DPA lies within 1-dB power contour from 652.5 MHz to 797.5 MHz whereas the variation of main

Authorized licensed use limited to: DELHI TECHNICAL UNIV. Downloaded on February 15,2021 at 10:30:47 UTC from IEEE Xplore. Restrictions apply.

This article has been accepted for inclusion in a future issue of this journal. Content is final as presented, with the exception of pagination.

PA impedance of proposed DPA is within 1-dB power contour for frequency range of 398.75 MHz to 1051.25 MHz. At 6 dB back-off, the fractional bandwidth of conventional and proposed DPA is 20% and 90% respectively. At saturation, Fig. 5(b) shows that the main PA impedance of conventional DPA lies within 1-dB power contour for frequency range of 616.25 MHz to 833.75 MHz, equivalent to 30% fractional bandwidth. Similarly, the main PA impedance of proposed DPA remains within 1-dB power contour from 580 MHz – 870 MHz corresponding to 40% fractional bandwidth. One can deduce from Fig. 5 that the proposed scheme produces less variation of Z_M with frequency at 12 dB and 6 dB back-off as compared to the conventional three-stage DPA. The lesser dependency of Z_M on frequency corresponds to proper load modulation over a wide range of frequency which leads to a broadband three-stage DPA which enhances efficiency beyond 6 dB back-off.

In order to compare the fractional bandwidth in terms of drain efficiency of proposed ideal three-stage DPA with conventional three-stage DPA [19], the theoretical drain efficiency is plotted at 12 dB, 6 dB back-off, and at saturation in Fig. 6 (a)-(c). It can be seen from Fig. 6 that the proposed three-stage DPA presents much better efficiency performance at both the back-offs as well as saturation as compared to conventional DPA.

D. Back-Off Reconfiguration

The output voltage at load terminal as shown in Fig. 1 is given by $|V_{A2}|$. Using (10) and (12), the load voltage can be rewritten as:

$$|V_{A2}| = v_{in}{}^{*} V_{A2,\max} \tag{20}$$

The voltage at load terminal is a linear function of normalized input voltage and is independent of frequency. It only depends on maximum output voltage of second auxiliary PA, $V_{A2,\max}$. The maximum output voltages of PAs depend on drain bias of PAs. Therefore, one can deduce from (20) that the overall output power at saturation solely depends on drain bias of second auxiliary PA ($V_{DS,A2}$) and is independent of drain bias of main PA ($V_{DS,M}$) and first auxiliary PA ($V_{DS,A1}$).

The equation (12) can be rewritten as:

$$V_{DS,A2} = \beta_1 V_{DS,M} = \beta_2 V_{DS,A1} \tag{21}$$

which suggests that the back-off of three-stage DPA can be made reconfigurable if $V_{DS,A2}$ is kept fixed and $V_{DS,M}$ and $V_{DS,A1}$ are changed. Figs. 7(a) and 7(b) validate the fact that by changing drain bias voltages of main and first auxiliary PA and keeping $V_{DS,A2}$ constant, the reconfigurability can be achieved at β_1 and β_2 respectively.

The above section explains that if the magnitude of output current of first auxiliary PA and the phase difference between the output current of main PA and that of first auxiliary PA is controlled with frequency, along with the appropriate selection of drain bias, the three-stage DPA shows a broadband behavior for a wide range of frequency.

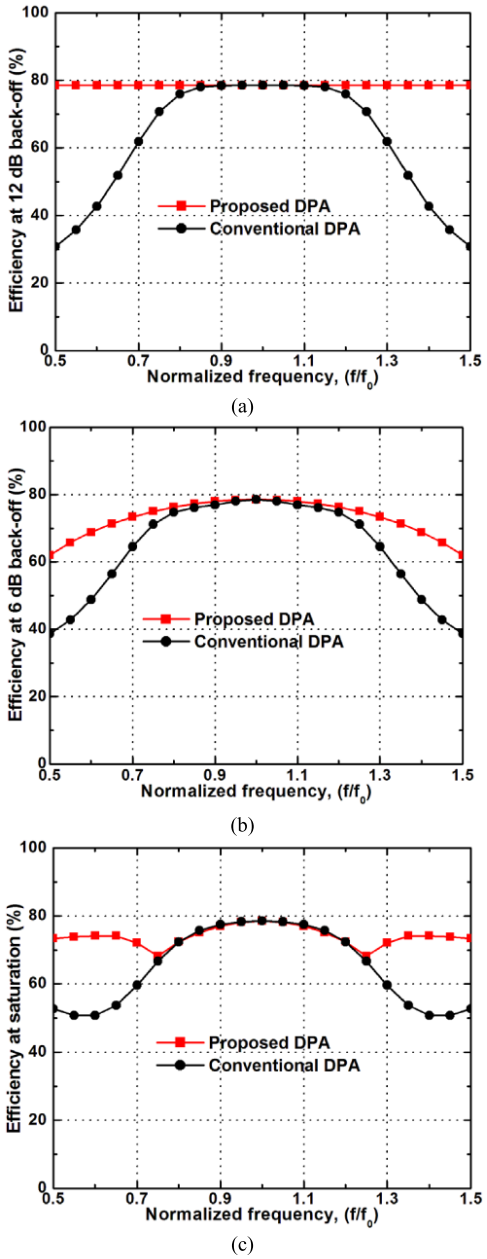

Fig. 6. Bandwidth comparison of theoretical drain efficiency of conventional and proposed DPA at (a) 12 dB back-off, (b) 6 dB back-off, and (c) saturation.

III. Design and Simulation Results

To implement the proposed theory, a dual input 16 W three-stage DPA is designed with maximum output power of main PA, first and second auxiliary PAs as 2, 6 and 8 W respectively. The schematic is shown in Fig. 8 which shows a main and two auxiliary PAs, input splitter and load combiner. The following section will give detailed design of various components designed.

A. Main and Auxiliary PA Design

All the three PAs in three-stage DPA are designed using the load-pull simulation in Keysight's Advanced Design System with three 10 W GaN HEMT CGH40010F from Wolfspeed.

Authorized licensed use limited to: DELHI TECHNICAL UNIV. Downloaded on February 15,2021 at 10:30:47 UTC from IEEE Xplore. Restrictions apply.

This article has been accepted for inclusion in a future issue of this journal. Content is final as presented, with the exception of pagination.

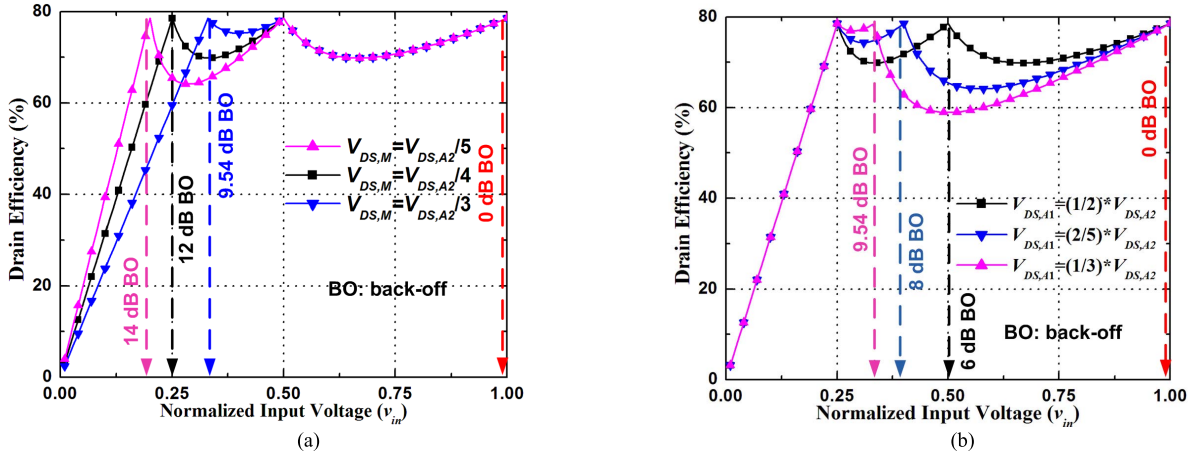

Fig. 7. Reconfigurability at (a) First back-off point by changing main PA drain bias voltage, (b) Second back-off point by changing first auxiliary PA drain bias voltage.

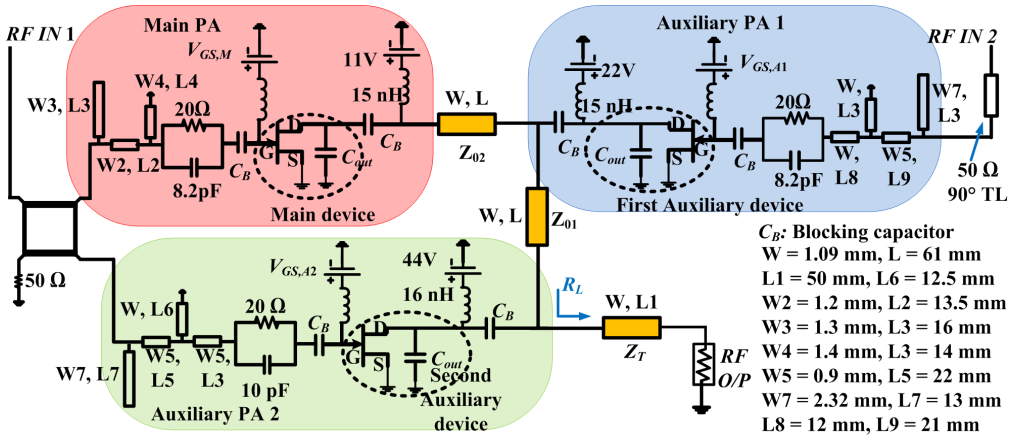

Fig. 8. Schematic of dual input three-stage DPA.

The drain bias of each device is scaled down to obtain the respective output power of 2 W, 6 W and 8 W from main PA, first auxiliary PA, and second auxiliary PA respectively. The drain bias of the second auxiliary PA is kept fixed at 44 V whereas the drain bias of the main and first auxiliary PA is varied to attain reconfiguration. To obtain high efficiency at 6 dB and 12 dB back-off, the main and first auxiliary PAs are drain biased at 11 V and 22 V, respectively. An optimum load of 25 Ω, 33.3 Ω and 100 Ω is obtained for main, first auxiliary and second auxiliary PA at 11 V, 22 V and 44 V, respectively. The output capacitance of the device, C_{out} is tuned out by the drain bias inductor. The drain bias inductor also helps in providing an open circuit towards the output of auxiliary PAs, which prevents leakage of current into auxiliary PAs at low output power levels. The double stub input matching network is used to match the input impedance of PAs to 50 Ω.

B. Input Power Divider

The schematic of dual-input broadband three-stage DPA has two RF inputs. The first RF input, *RF IN* 1 is given to a branch line coupler which divides input power equally between main and second auxiliary PA. The branch line coupler also provides a necessary phase difference of 180° between the input of main PA and second auxiliary PA in order to align the phase of output currents of respective PAs at load terminal. The second input *RF IN* 2 is given to the input of first auxiliary PA. The transmission line used at the input of first auxiliary PA provides a phase delay of 90°, such that there is zero phase difference required between *RF IN* 1 and *RF IN* 2 at the centre frequency. The amplitude and phase of the input RF signals provided at the input of *RF IN* 1 and *RF IN* 2 is controlled in order to obtain broadband performance of DPA.

C. Load Combiner

All the load combiner impedances are equal and their impedance is kept equal to 50 Ω. The length of all transmission lines in the load combiner is 90° at 725 MHz. The load combiner combines the output current of the main PA, first auxiliary PA and second auxiliary PA together to form a broadband three-stage DPA.

D. Broadband Three-Stage DPA and Its Simulated Performance

All the components are combined together to form a dual-input broadband three-stage DPA. The EM simulation of the entire DPA was carried out in ADS Momentum from Keysight.

Authorized licensed use limited to: DELHI TECHNICAL UNIV. Downloaded on February 15,2021 at 10:30:47 UTC from IEEE Xplore. Restrictions apply.

This article has been accepted for inclusion in a future issue of this journal. Content is final as presented, with the exception of pagination.

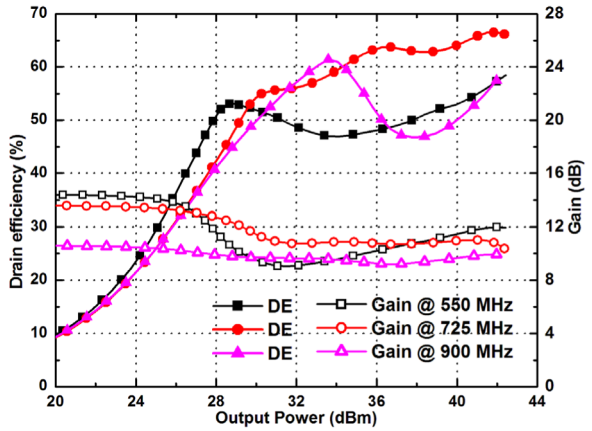

Fig. 9. Simulated drain efficiency and gain performance w.r.t. output power.

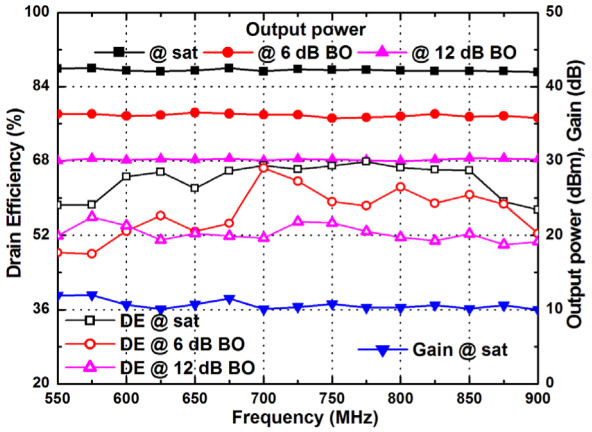

Fig. 10. Simulation performance parameters for frequency range from 550 MHz to 900 MHz.

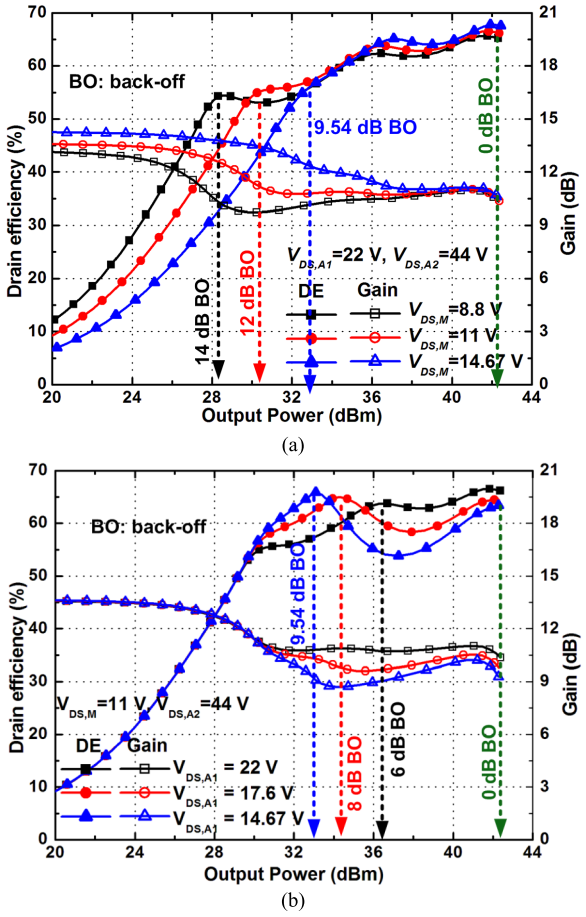

Fig. 11. Simulated results showing reconfigurability (a) at first back-off, and (b) at second back-off.

The main PA is biased in Class AB mode with drain current of 35 mA. The first auxiliary and second auxiliary PAs are biased in Class C mode with gate to source voltage as −4.2 V and −6.5 V, respectively. Such a biasing scheme is adopted to turn ON auxiliary PAs one after the other to obtain the output current profile, as shown in Fig. 3.

The overall configuration of DPA is simulated and its performance is evaluated from 550 MHz to 900 MHz. The simulated drain efficiency and gain variation with output power is shown in Fig. 9 at the centre frequency and at two corner frequencies. It can be observed from Fig. 9 that the drain efficiency is greater than 50%, 48%, and 57.5% at 12 dB back-off, 6 dB back-off and saturation, respectively. The gain at saturation is above 9.96 dB as can be observed from Fig. 9.

In order to observe the wideband capability of proposed three-stage DPA, the input power is swept individually to obtain performance parameters at different frequencies. The simulated output performances obtained at respective frequencies are plotted for the frequency range of 550 MHz to 900 MHz with a frequency gap of 25 MHz in Fig. 10. It can be seen from Fig. 10 that drain efficiency at 12 dB back-off lies between 50% and 55.97%. The respective maximum and minimum drain efficiency at 6 dB back-off is 66.4% and 48% and at saturation is 67.8% and 57.4%. The maximum gain at saturation is 11.97 dB. The output power at saturation, 12 dB back-off, and 6 dB back-off lies within ± 0.3 dB. Fig. 10 verifies the simulated broadband performance of three-stage DPA. The reconfigurability of three-stage DPA is also verified by changing the drain bias voltage of the main PA and first auxiliary PA. Figs. 11(a) and 11(b) validate that the first back-off and second back-off become reconfigurable when the drain bias voltage of the main and first auxiliary PA is changed, respectively. It can be observed from Fig. 11 that the maximum output power of DPA remains the same in all three cases, despite the change in drain bias of main and first auxiliary PA. The simulated gain is also shown for different drain biasing conditions in Figs. 11(a) and 11(b).

IV. Measurement Results

In order to validate the simulation results of the proposed dual-input three-stage DPA, the circuit was fabricated on Rogers 4350B substrate with a dielectric constant of 3.66 and a height of 20 mil with a loss tangent of 0.0037. Fig. 12 shows the photograph of the fabricated board.

The fabricated board was tested using dual-channel setup as shown in Fig. 13 in the frequency range of 550 MHz to 900 MHz. In the measurements, the dual input ports of

Authorized licensed use limited to: DELHI TECHNICAL UNIV. Downloaded on February 15,2021 at 10:30:47 UTC from IEEE Xplore. Restrictions apply.

This article has been accepted for inclusion in a future issue of this journal. Content is final as presented, with the exception of pagination.

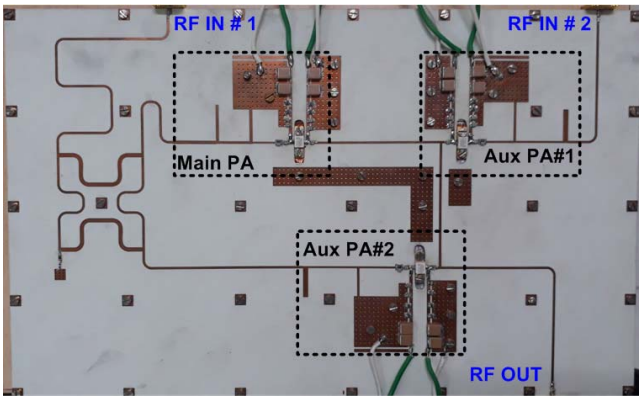

Fig. 12. Photograph of dual-input three stage DPA.

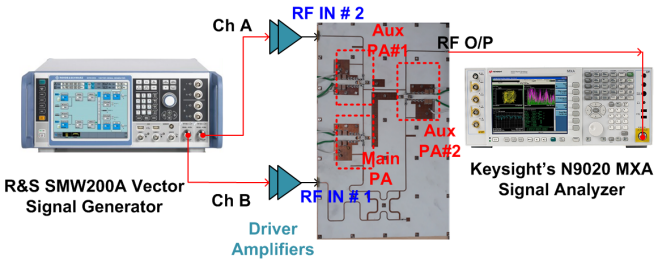

Fig. 13. Measurement set-up of dual-input digitally controlled three-stage Doherty PA measurements.

TABLE I
DIFFERENT PHASE REQUIREMENTS AT DIFFERENT FREQUENCIES

Frequency (MHz)	Phase (deg)	Phase of conv. DPA (deg)	Frequency (MHz)	Phase (deg)	Phase of conv. DPA (deg)
550	-57	0	800	40	0
600-650	-23±2	0	850	64	0
700-750	±2	0	900	94	0

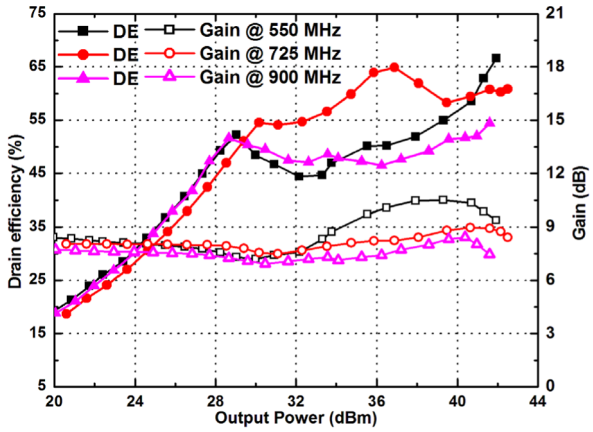

Fig. 14. Measured Drain efficiency and gain performance w.r.t output power.

the fabricated board are fed using Rohde & Schwarz (R&S) SMW200A Vector Signal Generator (VSG). The broadband linear drivers were used in both the paths to amplify the input signals to required level. The amplitude and phase between signals obtained from Channel A and Channel B of R&S SMW200A VSG were calibrated before starting measurements of dual input broadband three-stage DPA. The output power was tested using Keysight's MXA Signal Analyzer. During the measurements, the drain bias of main PA was 11 V, and first and second auxiliary PAs were biased at 22 V and 44 V respectively.

A. Continuous Wave Measurements

To assess the performance of three-stage DPA, it is tested with Continuous Wave (CW) signal at different frequencies. The optimum phase requirements used in the experiment between the two RF inputs are different from the theoretical phase difference. The theoretical derivation assumed ideal conditions such as ideal current sources, and linear output voltage variation. In practice, the transistors are non-linear, and the output voltage of a PA compresses as the input power is increased. All these factors have resulted into the change of phase difference used in measurement with a calculated phase difference. Also, the input phase difference between *RF IN* 1 and *RF IN* 2, as obtained from theoretical results, is not varied with change in input power, since no significant difference in performance was observed in the output parameters of DPA. Therefore, the phase difference was kept constant at an individual frequency for the entire input power sweep. The phase difference between the two terminals is kept different at different frequencies, as mentioned in Table I. A similar case was observed with amplitude difference between *RF IN* 1 and *RF IN* 2. There was no significant improvement observed in simulations after the variation of amplitude difference with input power drive. Therefore, the amplitude difference between *RF IN* 1 and *RF IN* 2 is kept constant at 4 dB for the complete frequency range. The *RF IN* 1 is given more power since it feeds two PAs, main PA and second auxiliary PA, respectively.

Fig. 14 shows CW performance of dual input three-stage DPA at three frequencies with output power sweep. It can be observed from the figure that the minimum drain efficiency is 50.4% and 46.1% at 12 dB and 6 dB back-off, respectively. The drain efficiency is above 53.97% at saturation. In order to measure gain of three-stage DPA, the RF power that is given at the two input terminals is summed up for obtaining total input RF power. The gain in dB is thus obtained by subtracting the overall input power in dBm from the overall output power in dBm. The gain measured at saturation is more than 7 dB for all the frequencies.

The broadband behavior of dual-input three-stage DPA is verified by measuring its performance parameters for the frequency range of 550 MHz to 900 MHz. The variation of output power and drain efficiency with different frequencies is plotted in Fig. 15 at saturated output power and at back-off levels. It can be observed that drain efficiency at 12 dB back-off is more than 50.4% over the frequency range of 550 to 900 MHz. In the same frequency band, the drain efficiency lies between 46.1% and 65.4% at 6 dB back-off. The figure also shows the maximum and minimum drain efficiency at saturation is 71.5% and 53.97% respectively. The output power at saturation lies within ±1 dB over the frequency range of 550 MHz to 900 MHz which accounts for 48.3% fractional bandwidth.

Authorized licensed use limited to: DELHI TECHNICAL UNIV. Downloaded on February 15,2021 at 10:30:47 UTC from IEEE Xplore. Restrictions apply.

This article has been accepted for inclusion in a future issue of this journal. Content is final as presented, with the exception of pagination.

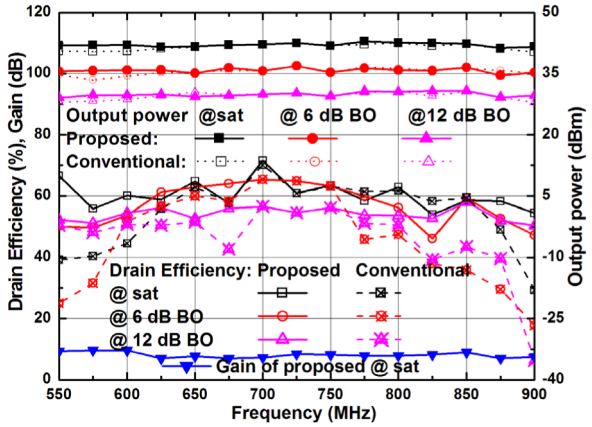

Fig. 15. Measured CW performance parameters w.r.t frequency.

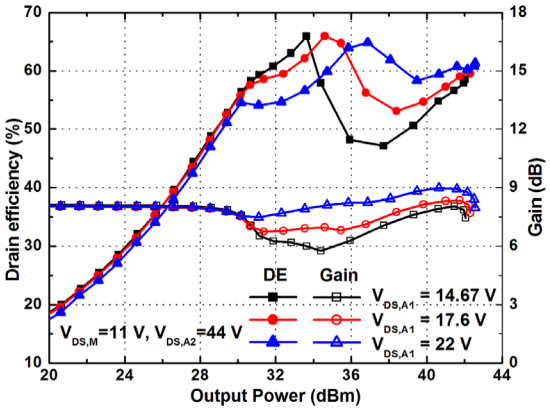

Fig. 17. Measured drain efficiency vs. output power for different first aux. PA drain bias showing reconfigurability around 6-dB back-off.

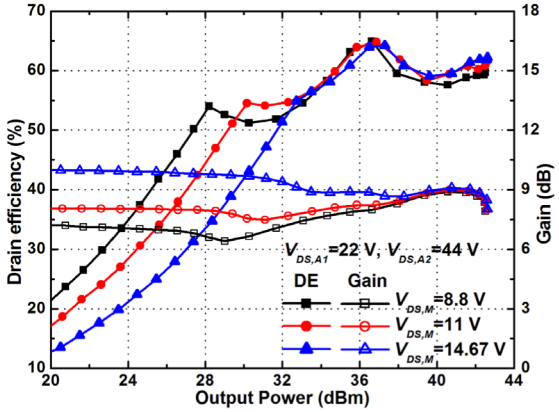

Fig. 16. Measured drain efficiency vs. output power for different main PA drain bias showing reconfigurability around 12-dB back-off.

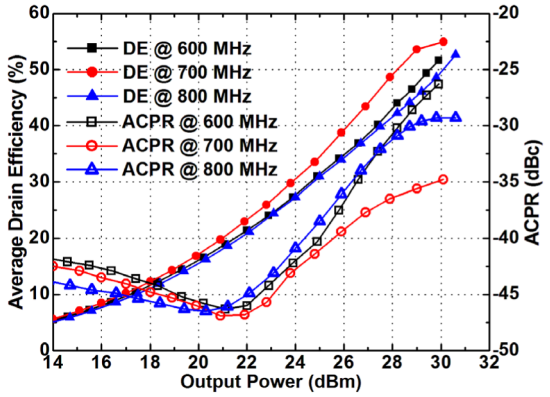

Fig. 18. Drain efficiency and ACPR measurement at different frequencies with 10 MHz LTE signal with 11.75 dB PAPR.

In order to show the comparison of proposed dual-input digital three-stage DPA with conventional three-stage DPA, the present circuit is tested for the entire frequency range with 0° phase-difference between the two RF inputs. The output power and drain efficiency for the conventional case are plotted in Fig. 15. It is clearly visible from the figure that the drain efficiency of conventional DPA degrades as one move away from center frequency. Also, the output power variation increased to ±2.5 dB over the frequency range of 550 MHz to 900 MHz. Fig. 15 also shows the measured gain of proposed three-stage DPA at saturation. In the entire frequency range, the gain is better than 7 dB.

Fig. 16 and Fig. 17 shows the measured drain efficiency variation at 725 MHz with output power for different sets of drain biasing conditions. It can be observed from Fig. 16 that 12 dB back-off point changes when the drain bias of main PA is changed from 11 V. Similarly, Fig. 17 depicts reconfigurability at 6 dB back-off when drain bias of first auxiliary PA is varied from 22 V. It can also be observed from both the figures that the peak output power remains constant since it depends only on drain bias of second auxiliary PA. The gain is also measured for different sets of drain biasing condition, and is plotted in Figs. 16 and 17. From the results, one can see that the measured performance parameters have slightly deviated from the simulated performance parameters.

The inaccurate models of transistors, especially in Class C mode and fabrication errors, can affect measurement results.

The work presented in this article is also compared with the existing broadband three-stage DPA, and the comparison is shown in Table II. The proposed dual-input three-stage DPA exhibits considerable performance over other broadband three-stage DPA.

B. Modulated Signal Measurement

The fabricated dual input three-stage DPA is also tested with Long Term Evolution (LTE) signal of 10 MHz bandwidth having a PAPR of 11.75 dB at 600 MHz, 700 MHz and 800 MHz. The adjacent channel power ratio (ACPR) is measured at an offset of 10 MHz. It can be seen from Fig. 18 that the average efficiency is 51.6% at 600 MHz with output power of 29.9 dBm. The ACPR at 600 MHz is below −26.3 dBc. At the frequency of 700 MHz, the average efficiency is reported as 54.9% at an average power of 30.1 dBm with ACPR below −34.8 dBc. Similarly, at 800 MHz, the average efficiency of 52.6% is obtained at average output power of 30.6 dBm, with an ACPR below −29.3 dBc.

Fig. 19 shows the output power spectral density (PSD) of 256 QAM signal with a bandwidth of 50 MHz having a PAPR of 11.5 dB at 600 MHz, 725 MHz, and 800 MHz before and after applying digital predistortion (DPD). The summary of DPD linearization is shown in Table III. The

Authorized licensed use limited to: DELHI TECHNICAL UNIV. Downloaded on February 15,2021 at 10:30:47 UTC from IEEE Xplore. Restrictions apply.

This article has been accepted for inclusion in a future issue of this journal. Content is final as presented, with the exception of pagination.

TABLE II
COMPARISON WITH CURRENT STATE-OF-THE-ART IN THREE-STAGE BROADBAND DPA

Ref.	Freq.	Config.	Fractional BW	Pout @ Sat (Max/Min)	Pout @ 6dB OPBO (Max/Min)	Pout @ 12dB OPBO (Max/Min)	DE @ Sat. (Max/Min)	DE @ 6 dB OPBO (Max/Min)	DE @ 12 dB OPBO (Max/Min)	Gain @ Sat. (Max./Min.)
Units	MHz	Type	%	dBm	dBm	dBm	%	%	%	dB
[24]	1600-2600	Symmetric	48	45.5-46	~39.5-40	~33.5-34	66/53	63/52	~43/40*	9.6/7.6
[25]	1850-2400	Asymmetric	25.9	~43.7/41*	~37.7/35*	~31.7/29*	~75/60*	~ 69/48*	~62/46*	~11/7.5*
[26]	730-980	Symmetric	29	~44.7/42.5*	~38.7/36.5*	~32.7/30.5*	~67/43*	~62/41*	~52/38*	~12.5/10.2*
[27]	700-950	Symmetric	30.3	44.7/42.9	38.7/36.42	32.7/30.42	78.3/60.04	67.5/51.6	~58/40*	~10.85/7.1*
[28]	600-900	Asymmetric	40	46.9/46.1	41.1/40.07	34.94/34.01	78/51.1	66.2/51.9	61.8/50	11/7
[This Work]	550-900	Asymmetric	48.3	42.9/41.3	36.9/34.6	30.8/29	71.5/53.97	65.4/46.1	58/50.4	9.66/7

*calculated from measured results plotted in respective papers.

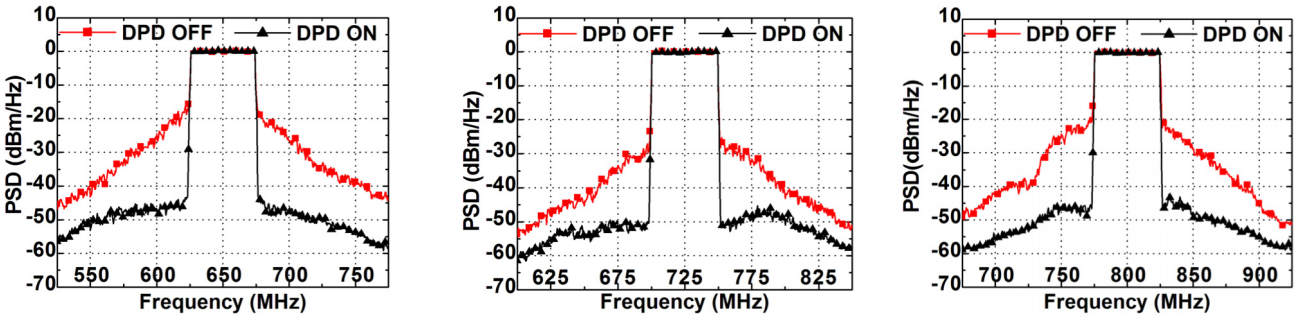

Fig. 19. Output spectrum of 50 MHz signal with 11.5 dB PAPR at (a) 650 MHz, (b) 725 MHz, and (c) 800 MHz before and after applying DPD.

TABLE III
SUMMARY OF DPD LINEARIZATION

Frequency (MHz)	Average Power (dBm)	Average Drain Efficiency (%)	ACLR at 50 MHz	
			DPD OFF	DPD ON
650	29.91	53.6	-26.8/-26.5	-46.9/-46.7
725	30.5	54.3	-33.3/-31.7	-51.8/-47.6
800	30.85	52.9	-24.4/-28.7	-46.9/-47.7

DPD results in Fig. 19 and its summary in Table III clearly show that the output signal qualifies the spectral mask after linearization. Therefore, the proposed dual-input three-stage DPA is linearizable.

V. CONCLUSION

The article presents a new methodology of introducing dual RF inputs with phase and amplitude control to improve bandwidth of three-stage DPA. Both the back-offs are made reconfigurable in three-stage DPA in order to achieve backward compatibility. The theory proposed is well-validated with the measurement results by fabricating a three-stage DPA with the maximum output power of 42 dBm. The measured outcomes fulfill the requirements of broadband, multi standard and highly efficient wireless transmitters.

REFERENCES

[1] P. Chen and S. He, "Investigation of inverse class-E power amplifier at sub-nominal condition for any duty ratio," *IEEE Trans. Circuits Syst. I, Reg. Papers*, vol. 62, no. 4, pp. 1015–1024, Apr. 2015.

[2] F. H. Raab *et al.*, "Power amplifiers and transmitters for RF and microwave," *IEEE Trans. Microw. Theory Techn.*, vol. 50, no. 3, pp. 814–826, Mar. 2002.

[3] C. Li, F. You, S. He, X. Tang, W. Shi, and J. Wang, "High-efficiency power amplifier employing minimum-power harmonic active load modulator," *IEEE Trans. Circuits Syst. II, Exp. Briefs*, vol. 66, no. 8, pp. 1371–1375, Aug. 2019.

[4] W. H. Doherty, "A new high efficiency power amplifier for modulated waves," *Proc. IRE*, vol. 24, no. 9, pp. 1163–1182, Sep. 1936.

[5] F. Raab, "Efficiency of Doherty RF power-amplifier systems," *IEEE Trans. Broadcast.*, vol. BC-33, no. 3, pp. 77–83, Sep. 1987, doi: 10.1109/TBC.1987.266625.

[6] W. Chen, S. Zhang, Y. Liu, Y. Liu, and F. M. Ghannouchi, "A concurrent dual-band uneven Doherty power amplifier with frequency-dependent input power division," *IEEE Trans. Circuits Syst. I, Reg. Papers*, vol. 61, no. 2, pp. 552–561, Feb. 2014.

[7] R. Kalyan, K. Rawat, and S. K. Koul, "A digitally assisted dual-input dual-band Doherty power amplifier with enhanced efficiency and linearity," *IEEE Trans. Circuits Syst. II, Exp. Briefs*, vol. 66, no. 2, pp. 297–301, Feb. 2019.

[8] H. Jang, P. Roblin, C. Quindroit, Y. Lin, and R. D. Pond, "Asymmetric Doherty power amplifier designed using model-based nonlinear embedding," *IEEE Trans. Microw. Theory Techn.*, vol. 62, no. 12, pp. 3436–3451, Dec. 2014.

[9] K. Rawat and F. M. Ghannouchi, "Design methodology for dual-band Doherty power amplifier with performance enhancement using dual-band offset lines," *IEEE Trans. Ind. Electron.*, vol. 59, no. 12, pp. 4831–4842, Dec. 2012.

Authorized licensed use limited to: DELHI TECHNICAL UNIV. Downloaded on February 15,2021 at 10:30:47 UTC from IEEE Xplore. Restrictions apply.

This article has been accepted for inclusion in a future issue of this journal. Content is final as presented, with the exception of pagination.

[10] D. Y.-T. Wu and S. Boumaiza, "A modified Doherty configuration for broadband amplification using symmetrical devices," *IEEE Trans. Microw. Theory Techn.*, vol. 60, no. 10, pp. 3201–3213, Oct. 2012.

[11] M. Li, J. Pang, Y. Li, and A. Zhu, "Bandwidth enhancement of Doherty power amplifier using modified load modulation network," *IEEE Trans. Circuits Syst. I, Reg. Papers*, vol. 67, no. 6, pp. 1824–1834, Jun. 2020, doi: 10.1109/TCSI.2020.2972163.

[12] X. A. Nghiem, J. Guan, and R. Negra, "Broadband sequential power amplifier with Doherty-type active load modulation," *IEEE Trans. Microw. Theory Techn.*, vol. 63, no. 9, pp. 2821–2832, Sep. 2015.

[13] K. Rawat, G. B, G. Ajmera, A. Basu, and S. K. Koul, "Design scheme for broadband Doherty power amplifier using broadband load combiner," *Int. J. RF Microw. Comput.-Aided Eng.*, vol. 25, no. 8, pp. 655–674, Oct. 2015.

[14] D. Gustafsson, C. M. Andersson, and C. Fager, "A modified Doherty power amplifier with extended bandwidth and reconfigurable efficiency," *IEEE Trans. Microw. Theory Techn.*, vol. 61, no. 1, pp. 533–542, Jan. 2013.

[15] X. Y. Zhou, S. Y. Zheng, W. S. Chan, S. Chen, and D. Ho, "Broadband efficiency-enhanced mutually coupled harmonic postmatching Doherty power amplifier," *IEEE Trans. Circuits Syst. I, Reg. Papers*, vol. 64, no. 7, pp. 1758–1771, Jul. 2017.

[16] S. Ghosh and K. Rawat, "Hybrid analog/digital continuous class B/J mode for broadband Doherty power amplifiers," *IEEE Access*, vol. 7, pp. 74986–74995, 2019.

[17] C. Liang, P. Roblin, Y. Hahn, Z. Popovic, and H.-C. Chang, "Novel outphasing power amplifiers designed with an analytic generalized Doherty–Chireix continuum theory," *IEEE Trans. Circuits Syst. I, Reg. Papers*, vol. 66, no. 8, pp. 2935–2948, Aug. 2019.

[18] A. Barthwal, G. Ajmera, K. Rawat, A. Basu, and S. K. Koul, "Design scheme for dual-band three stage Doherty power amplifiers," in *Proc. IEEE Int. Microw. RF Conf. (IMaRC)*, Dec. 2014, pp. 80–83.

[19] N. Srirattana, A. Raghavan, D. Heo, P. E. Allen, and J. Laskar, "Analysis and design of a high-efficiency multi-stage Doherty power amplifier for wireless communications," *IEEE Trans. Microw. Theory Techn.*, vol. 53, no. 3, pp. 852–859, Mar. 2009.

[20] M.-W. Lee, S.-H. Kam, Y.-S. Lee, and Y.-H. Jeong, "Design of highly efficient three-stage inverted Doherty power amplifier," *IEEE Microw. Wireless Compon. Lett.*, vol. 21, no. 7, pp. 383–385, Jul. 2011.

[21] I. Kim, J. Moon, S. Jee, and B. Kim, "Optimized design of a highly efficient three-stage Doherty PA using gate adaptation," *IEEE Trans. Microw. Theory Techn.*, vol. 58, no. 10, pp. 2562–2574, Oct. 2010.

[22] M. J. Pelk, W. C. Neo, J. R. Gajadharsing, R. S. Pengelly, and L. C. N. de Vreede, "A high-efficiency 100-W GaN three-way Doherty amplifier for base-station applications," *IEEE Trans. Microw. Theory Techn.*, vol. 56, no. 7, pp. 1582–1591, Jul. 2008.

[23] W. C. E. Neo, J. Qureshi, M. J. Pelk, J. R. Gajadharsing, and L. C. N. de Vreede, "A mixed-signal approach towards linear and efficient N-way Doherty amplifiers," *IEEE Trans. Microw. Theory Techn.*, vol. 55, no. 5, pp. 866–879, May 2007.

[24] J. Xia, W. Chen, F. Meng, C. Yu, and X. Zhu, "Improved three-stage Doherty amplifier design with impedance compensation in load combiner for broadband applications," *IEEE Trans. Microw. Theory Techn.*, vol. 67, no. 2, pp. 778–786, Feb. 2019.

[25] X. A. Nghiem, J. Guan, and R. Negra, "Design of a broadband three-way sequential Doherty power amplifier for modern wireless communications," in *IEEE MTT-S Int. Microw. Symp. Dig.*, Jun. 2014, pp. 1–4.

[26] H. Golestaneh, F. A. Malekzadeh, and S. Boumaiza, "An extended-bandwidth three-way Doherty power amplifier," *IEEE Trans. Microw. Theory Techn.*, vol. 61, no. 9, pp. 3318–3328, Sep. 2013.

[27] A. Barthwal, K. Rawat, and S. Koul, "Bandwidth enhancement of three-stage Doherty power amplifier using symmetric devices," *IEEE Trans. Microw. Theory Techn.*, vol. 63, no. 8, pp. 2399–2410, Aug. 2015.

[28] A. Barthwal, K. Rawat, and S. K. Koul, "A design strategy for bandwidth enhancement in three-stage Doherty power amplifier with extended dynamic range," *IEEE Trans. Microw. Theory Techn.*, vol. 66, no. 2, pp. 1024–1033, Feb. 2018, doi: 10.1109/TMTT.2017.2751044.

[29] D. Y.-T. Wu and S. Boumaiza, "A mixed-technology asymmetrically biased extended and reconfigurable Doherty amplifier with improved power utilization factor," *IEEE Trans. Microw. Theory Techn.*, vol. 61, no. 5, pp. 1946–1956, May 2013.

[30] S. C. Cripps, *Advanced Techniques in RF Power Amplifier Design*. Norwood, MA, USA: Artech House, 2002.

Ayushi Barthwal (Member, IEEE) received the M.Tech. degree in microwave and optical communication from Delhi Technological University (DTU), New Delhi, India, in 2012, and the Ph.D. degree in microwave engineering from IIT Delhi.

She was a Student Research Assistant under the GATE Fellowship of Ministry of Human Resource Development, Government of India. She was an Assistant Professor with Galgotias University, Greater Noida, India. She is currently an Assistant Professor with the School of Engineering, Jawaharlal Nehru University. Her current research interests include microwave active circuit design and advanced power amplifier architectures for upcoming high data rate communication.

Karun Rawat (Senior Member, IEEE) received the Ph.D. degree in electrical engineering from the University of Calgary, Canada, in 2012. He is currently an Associate Professor in the Department of Electronics and Communication at the IIT Roorkee, India. Prior to this, he was an Assistant Professor in IIT Delhi from 2013–2014 and a Scientist in the Space Applications Center, Indian Space Research Organization Ahmedabad, from 2003–2007. His current research interests are in the areas of RF power amplifier and transceiver design, nonlinear device modeling, RF CMOS, and MMIC designs. His research has resulted in more than 70 publications in journals and conferences, two published books, one book chapter, and three patents. He is the recipient of a Young Scientist Award (finalist) in the category of "Innovation in Engineering & Physical Science" from the National Academy of Science (NASI) & Scopus and Outstanding Young Faculty Award from IIT Roorkee. He is also a member of the IEEE MTT Microwave High-Power Techniques Committee (MTT-12) and the Editorial Board of Wiley journal in *RF and Microwave Computer-Aided Engineering* (RFMiCAE). He is the Founding Director and the Chairman of a start-up in the area of linearized power amplifier design and wireless solutions. He has also been part of the technical program committee of several IEEE conferences and organized workshops in IEEE IMS 2018, EuMC 2018, and APMC 2016. He was the Technical Program Committee Chair of IEEE INDICON 2017.

Shiban K. Koul (Life Fellow, IEEE) received the B.E. degree in electrical engineering from the Regional Engineering College, Srinagar, in 1977, and the M.Tech. and Ph.D. degrees in microwave engineering from IIT Delhi, New Delhi, India, in 1979 and 1983, respectively. He served as the Chairman for Astra Microwave Products Limited, Hyderabad, from 2009 to 2019, and also a Dr. R.P. Shenoy Astra Microwave Chair Professor with IIT Delhi from 2014 to 2019. He is currently an Emeritus Professor with CARE, IIT Delhi, and also the Deputy Director of strategy and planning with IIT Jammu. He has successfully completed 38 major sponsored projects, 52 consultancy projects, and 61 technology development projects. He has authored or coauthored 490 research articles, 13 state-of-the-art books, 4 book chapters, and 2 e-books. He holds 16 patents, 6 copyrights, and one Trademark. He has guided 25 Ph.D. thesis and more than 100 master's theses. His current research interests include RF MEMS, nonlinear device modeling, microwave and millimeter wave active and passive circuit design, and reconfigurable microwave circuits including antennas.

Dr. Koul is a Fellow of the Indian National Academy of Engineering, India, and the Institution of Electronics and Telecommunication Engineers (IETE), India. He served as a Distinguished Microwave Lecturer of IEEE MTT-S from 2012 to 2014. He was a recipient of numerous awards including the Indian National Science Academy (INSA) Young Scientist Award, in 1986, the Top Invention Award of the National Research Development Council for his contributions to the indigenous development of ferrite phase shifter technology, in 1991, the VASVIK Award for the development of Ka-band components and phase shifters, in 1994, Ram Lal Wadhwa Gold Medal from the Institution of Electronics and Communication Engineers (IETE), in 1995, the Academic Excellence Award from the Indian Government for his pioneering contributions to phase control modules for Rajendra Radar, in 1998, the Shri Om Prakash Bhasin Award in the field of Electronics and Information Technology, in 2009, the VASVIK Award for the contributions made to the area of Information, Communication Technology (ICT), in 2012, the Teaching Excellence Award from IIT Delhi, in 2012, the M N Saha Memorial Award from IETE, in 2013, and the IEEE MTT Society Distinguished Educator Award, in 2014. He is the Chief Editor of *IETE Journal of Research* and an Associate Editor of the *International Journal of Microwave and Wireless Technologies*, Cambridge University Press.

Authorized licensed use limited to: DELHI TECHNICAL UNIV. Downloaded on February 15,2021 at 10:30:47 UTC from IEEE Xplore. Restrictions apply.

JMEPEG
https://doi.org/10.1007/s11665-021-05549-y

©ASM International
1059-9495/$19.00

Effect of Friction Stir Processing on Mechanical Properties and Wear Resistance of Tungsten Inert Gas Welded Joint of Dissimilar Aluminum Alloys

Husain Mehdi and R.S. Mishra

Submitted: 2 October 2020 / Revised: 22 January 2021 / Accepted: 27 January 2021

In this work, we examine TIG welded joints processed with friction stir processing at tool rotational speeds (TRSs) of 700, 800, 900, 1000, and 1100 rpm, with a constant feed rate of 70 mm/min and tilt angle of 1°. The percentage improvement in the tensile strength of TIG + FSP (TF) weldments was observed to be 78.57 and 75.89%, compared with TIG welded joints with ER4043 and ER5356 filler, respectively, at a TRS of 1100 rpm. A maximum tensile strength of 196 MPa was observed in a TF welded joint with ER5356 filler, and a minimum tensile strength of 98 MPa was observed in the TIG weldment with ER4043 filler. Cleavage facets, tear ridges, and large dimples were observed in fractured specimens of TIG welded joints, whereas fine, equiaxed dimples were observed in TF welded joints. A maximum micro-hardness of 137 HV in the stir zone was observed in TF welded joints at a TRS of 1100 rpm. TF welded joints with ER5356 filler had superior wear resistance compared to TIG and TF welded joints with ER4043 filler.

Keywords micro-hardness, residual stress, tensile strength, wear resistance

1. Introduction

Demand for lightweight materials with high strength, such as aluminum alloys AA6061, AA7075, and AA2024, is continuously increasing in the aerospace and automobile industries, due to their advantages of low thermal expansion, high resistance to wear and thermal conductivity (Ref 1, 2). Fabrication of joints between dissimilar aluminum alloys can be achieved using various techniques including tungsten inert gas (TIG) welding, and the friction stir welding/processing (FSW/FSP) techniques FSW/FSP was developed by TWI in 1991(Ref 3) and is a relatively novel welding process that has shown great potential in terms of joining similar or dissimilar aluminum alloys. FSP is well known as a microstructural modification technique in which a rotating tool is inserted into a single workpiece to modify the microstructural grain structure and hence improve a specific property (Ref 4). FSP has been successfully used in many applications and has recently been applied to improve fusion welded joints. The rotational speed of the tool is an important parameter that can enhance the mechanical properties and wear resistance of an FSP sample of AS-castA356, and when the TRS increases, wear resistance is also increased (Ref 5). At a low TRS, the hardness of a welded joint of AA5754 increases. The effect of the welding speed is also a dominating factor affecting the welded joint, and when the traverse speed is increased, less heat may be encountered in the SZ, causing an equiaxed fine-grained structure with enhanced mechanical properties and reduced wear rate (Ref 6). The concurrent occurrence of abrasive and adhesive wear has been observed in the presence of deep plows, delamination, and loose metallic debris on the worn surface of a FSW joint at 45 mm/min (Ref 7). The homogenous dispersion of reinforcement particles in the AA6061 enhances its hardness and wear resistance (Ref 8). The residual stresses in a TIG welded joint were investigated, and a minimum value of residual stress was observed in the heat affected zone (HAZ), whereas compressive residual stresses were measured in the root section of the welded joint, and tensile residual stresses were observed in the weld zone and HAZ (Ref 9, 10). Numerous surface modification technologies have been developed in recent years, including micro-arc oxidation technologies, cladding technology, plasma spraying, and ion implantation technologies (Ref 11-14). FSP has been used to improve the mechanical properties and microstructure of TIG welded joints between dissimilar aluminum alloys (Ref 15-17).

In this paper, the effect of FSP on TIG welded joints of AA6061 and AA7075 with ER5356 and ER4043 filler was investigated, and the wear and mechanical properties of TF welded joints were analyzed. We focused on improvements in the mechanical properties and wear resistance of TIG welded joints due to the use of FSP. This research was motivated by the scarcity of the available literature on the TF welding process, and it is hoped that the results of this work will give rise to new approaches to enhancing the wear resistance and mechanical properties of TF welded joints, which are very widely used.

2. Materials and Methods

Plates of the base metals (AA7075 and AA6061) with dimensions of 150 × 40 × 6.2 mm were prepared with a V-groove with an angle of 75°, a root height of 1.5 mm, and a root opening of 1.5 mm. Before welding, the plates were ground and cleaned with acetone to remove any dust and oxidized

Husain Mehdi and **R.S. Mishra**, Department of mechanical engineering, Delhi Technological University, Delhi, India. Contact e-mail: husainmehdi4u@gmail.com.

Published online: 19 February 2021

layers on the plates. For the multi-pass TIG process, a plate of thickness 6.2 mm with a V-groove weld design was used, with filler wires of ER5356 and ER4043 with a diameter of 2.4 mm. The average heat inputs were 1.34 and 1.47 kJ/mm for the ER4043 and ER5356 fillers, respectively. Argon gas at 24 l/min and welding speeds of 3.4 and 4.2 mm/s were used during the welding for both fillers. A voltage of 20 V and currents of 85 and 125 A were used for the ER4043 and ER5356 fillers, respectively. It was found that good heat penetration was achieved for both filler wires during the welding process. FSP was applied after the TIG welding to improve the wear resistance and mechanical properties of the TIG welded joint. The chemical compositions of the parent materials and the filler wire are shown in Table 1.

TRSs of 700, 800, 900, 1000, 1100 rpm, a Traverse speed (TS) of 70 mm/min, a tilt angle (TA) of 1°, and a threaded cylindrical pin geometry were used during FSP. The FSP tool was made of H13 tool steel with a hardness of 475 HV. The diameters of the pin and shoulder were 5 and 19 mm, respectively, and the length of the pin was 5.5 mm. The shoulder penetration depth was adjusted to 0.7 mm, and the tool dwell time was maintained at 15 s for all specimens. The processing parameters used in FSP are shown in Table 2. A scanning electron microscope (SEM) was used to characterize the morphology of the TIG + FSP welded joints. Tensile testing was carried out at room temperature. Three tensile test specimens were prepared for each parameter, with a gauge length of 25 mm and a width of 6.25 mm (Ref 15), and the average of three results was taken. A Vickers hardness machine was used to measure the variation in the micro-hardness of the welded joints, with a load of 100 gm and a dwell time of 15 s. A wear test was performed following the ASTM G99 standard, using a pin on disk tribometer with a pin made from TIG and TF welded joints, with a rectangular cross-section of 10 × 5 mm, and a disk made of EN31 steel. All pin specimens were polished with 2000 grit abrasive paper, and the test was conducted under dry sliding conditions at room temperature. The wear specimens and the disk were cleaned with acetone, and the COF between the disk and pin was measured based on the frictional force using a stress sensor. The parameters used in the pin on disk wear test are shown in Tables 3 and 4.

3. Results and Discussions

3.1 Tensile Strength

The influence of the TRS on the mechanical properties of TIG welded joints of dissimilar Al-alloys of AA7075 and AA6061with ER5356 and ER4043 fillers was observed. The tensile specimens fractured in the HAZ and the thermo-mechanically affected zone (TMAZ), where the hardness was found to be a minimum. In other dissimilar aluminum alloys, the FSW joints failed at the location of the HAZ (Ref 18). The tensile stress in the TF joints was lower than in the parent material and showed a tendency to increase with the precipitation hardening of the parent metal. The strength and ductility of defect-free welded joints are dependent on the thermal properties of the base metal (Ref 19, 20). Coarse grains were observed to have precipitated within the grain boundary, due to dissolution of fine precipitates during the TF process, which influences the tensile properties of the weldments. The percentage elongation and ductility of the weldments were lower than those of the parent material (Ref 21). If welded joints are free from defects, then the tensile strength of the weldments is dependent only on the hardness of the FSW joints (Ref 22). The stress-strain curve of the TF joints with various TRS is shown in Fig. 1, and it can be seen that the TRS produced a higher tensile strength than the TIG welded joints. The tensile strength of TF joints increases as TRS increases; the hardness and tensile strength initially increase with an increase in TRS, up to 1100 rpm, and begin to decline with the further increase in TRS (Ref 23).

Table 1 Chemical composition of filler wire and parent material

Material	Si	Cu	Fe	Zn	Mg	Mn	Cr	Al
AA6061	0.61	0.15	0.6	0.18	0.7	0.12	0.1	Bal.
AA7075	0.45	1.3	0.31	5.2	2.3	0.11	0.15	Bal.
ER 5356	0.03	0.016	0.1	0.02	4.8	0.15	0.12	Bal.
ER 4043	5.3	0.025	0.8	0.1	0.05	…	…	Bal.

The tensile strength of the TIG welded joints with ER4043 and ER5356 fillers was observed to be 98 and 112 N/mm^2, respectively, whereas for TF welded joints with a fixed tilt angle (1°) and a traverse speed of 70 mm/min, a maximum tensile strength of 196 MPa was observed at 1100 rpm with ER5356 filler, and a minimum tensile strength of 100 MPa was observed at 700 rpm in the TF welded joint with ER4043 filler. It was concluded that the tensile properties of the FSW joints were highly affected by TRS (Ref 24). As the TRS increased, the tensile strength also increased; at lower TRSs, the heat generated in the SZ was inadequate to strain the plasticized metal which degraded the mechanical properties of the FSW joints (Ref 25).

An optimized value of the TRS was therefore necessary to generate frictional heat. A higher TRS influences the strain rate of the plasticized metal, causing a change in the precipitation and grain size in the SZ (Ref 26, 27). The average tensile strengths of the AA6061 and AA7075 base metals were observed to be 306 and 412 MPa, respectively, and the joint efficiency (Ref 28) was calculated as $\frac{\text{Tensile strength of welded joint}}{\text{Tensile strength of base material AA}_{6061}} \times 100$. The macroscopic advents of the cross-section of 12 mm weld are shown in Fig. 2. TIG welded joints are known to have defects such as porosity, large grain structures, micro cracks, and insufficient consolidation of material in the fusion zone. However, the use of TIG + FSP reduces all these defects, and based on the microstructural characterization of the grain boundary, three different zones can be identified in the TF joints: the SZ, TMAZ, and HAZ. A banding pattern appears in the SZ from the retreating side (RS), and different band geometries were observed at different values of the TRS. The grain structure in the band pattern was very small. The same result was also reported in a prior study (Ref 29). The SZ was characterized by an equiaxed, fine-grained structure due to dynamic recrystallization (DRX). DRX occurs in the SZ due to high thermal exposure and strain during FSP. The degree of heat input and material deformation was both reduced when welding speed was increased at a constant TRS (Ref 30).

Table 2 Processing parameter of TIG + FSP welded joints

Samples	Current, amp	Traverse speed, mm/min	TRS, rpm	Tilt angle
1	5.4	70	700	1°
2			800	
3			900	
4			1000	
5			1100	

Table 3 Processing parameters of pin on disk wear test

Sliding speed, m/s	Disk diameter, mm	Load, N	Disk rotational speed, rpm	Time, min	Sliding distance, m
1.68	40	20	800	10	1005.71
1.68	60	30	535	12.5	1261.07
1.68	80	40	400	15	1508.57

Table 4 Mechanical properties of TIG + FSP welded joint of AA7075 and AA6061 with different filler material

Processing parameters	Filler	Tensile strength, MPa	Joint efficiency, %	Strain, %	Hardness at stir zone, HV	Fracture location
TIG welded joint	ER 4043	98 ± 4	32.03	8.1	72	Fusion zone
TIG welded joint	ER 5356	112 ± 3	36.60	9.6	78	Fusion zone
TIG + FSP_700 rpm	ER 4043	100 ± 2	32.68	10.9	81	HAZ_AA6061
TIG + FSP_800 rpm		124 ± 3	40.52	14.8	92	HAZ_AA6061
TIG + FSP_900 rpm		135 ± 2	44.12	16.4	104	HAZ_AA6061
TIG + FSP_1000 rpm		149 ± 1	48.69	18.5	114	HAZ_AA6061
TIG + FSP_1100 rpm		175 ± 3	57.19	19.8	118	HAZ_AA6061
TIG + FSP_700 rpm	ER 5356	126 ± 2	41.18	12	100	TMAZ_AA6061
TIG + FSP_800 rpm		154 ± 1	50.33	16	112	HAZ_AA6061
TIG + FSP_900 rpm		161 ± 2	52.61	16.9	118	HAZ_AA6061
TIG + FSP_1000 rpm		183 ± 2	59.80	19	126	TMAZ_AA6061
TIG + FSP_1100 rpm		196 ± 3	64.05	20	137	HAZ_AA6061

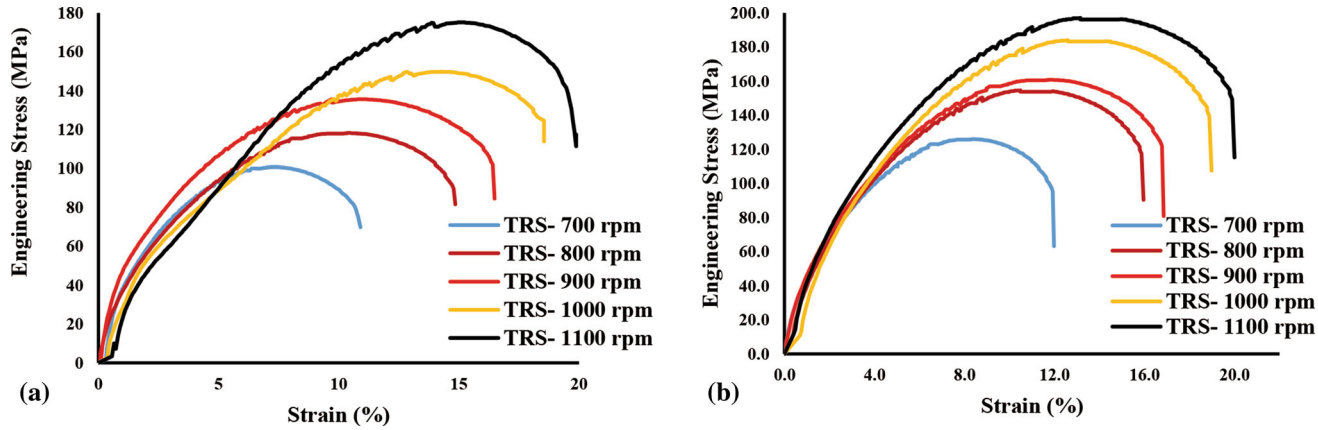

Fig. 1 Stress-strain curves of TIG + FSP welded joint of AA6061 and AA7075 under different TRS, (a) filler ER4043, (b) filler ER5356

Fig. 2 Macrostructure of the TIG + FSP welded joint of AA6061 and AA7075

3.2 Optical Micrograph of TIG and TIG + FSP Welded Joint

A superior weld quality was observed when the FSP tool was rotated on TIG welded joints, the AA7075 was placed on the RS, and AA6061 was placed on the advancing side (AS). In FSP, the frictional heat under the tool shoulder gave a higher temperature, since the material flow around the rotating tool was transferred from the AS to the RS, meaning that the temperature of the material on the AS was higher than the RS (Ref 31, 32). Due to the precipitation of Mg_2Si, the rate of dissolution on the AS was greater than that on the RS during welding. The driving force for re-precipitation increased when the stirring probe was moved away from the welding plate. A higher TRS promotes the dissolution of grains during stirring, and it was observed that the precipitates were fragmented or completely dissolved at higher values of TRS (Ref 32). The grain size in the stir zone (SZ) in the TF welded joint was much finer than the grain size in the FZ of the TIG welded joint. At high TRS (1100 rpm), the grain size in the SZ was observed to be 8-13 μm, whereas the grain size in the FZ was observed to be between 21 and 26 μm, as analyzed using Image J software and shown in Fig. 3. This may be because the materials in the DRX were exposed to a lower temperature than the materials in the SZ, far away from the TMAZ. At low temperatures, the migration velocity and grain growth rate of the grain boundaries are reduced, and the low temperature of the DRX region refines the particles of the Mg_2Si precipitate. The temperature distribution during FSP is asymmetric throughout the weldment, and the AS temperature is higher than that on the RS (Ref 33). A fine, equiaxed grain structure was observed in the SZ in the TIG + FSP welded joint due to DRX, as shown in Fig. 3.

3.3 XRD Analysis of Worn Surface

An x-ray diffractometry (XRD) evaluation of the worn surfaces of the TIG and TF welded joint was carried out with Cukα radiation at 1.518 Å, as shown in Fig. 4. Each material has a unique d-spacing, meaning that the conversion of the

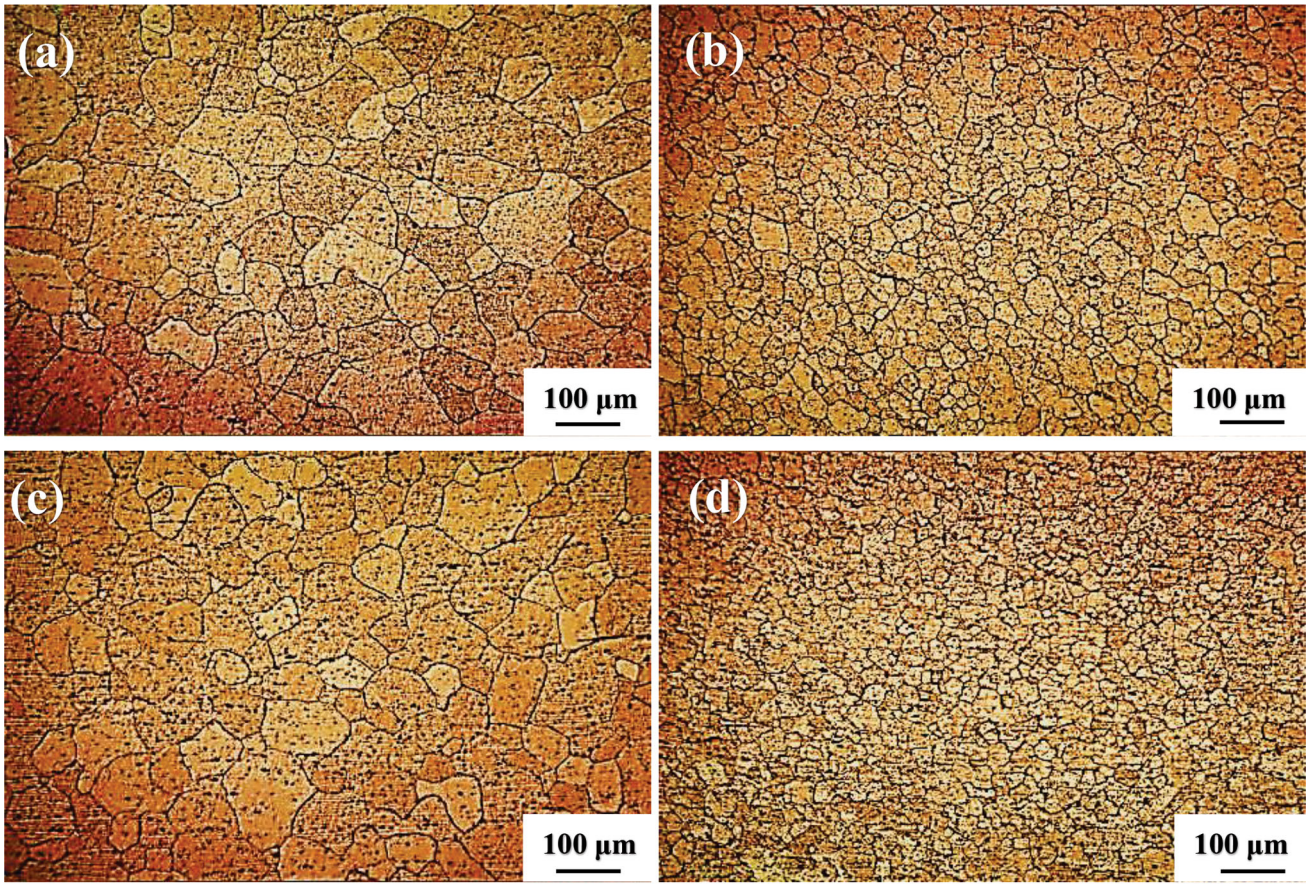

Fig. 3 Optical microstructure, (a) TIG welded joint with filler ER4043 (b) TIG + FSP welded joint with filler ER4043, (a) TIG welded joint with filler ER5356 (b) TIG + FSP welded joint with filler ER5356

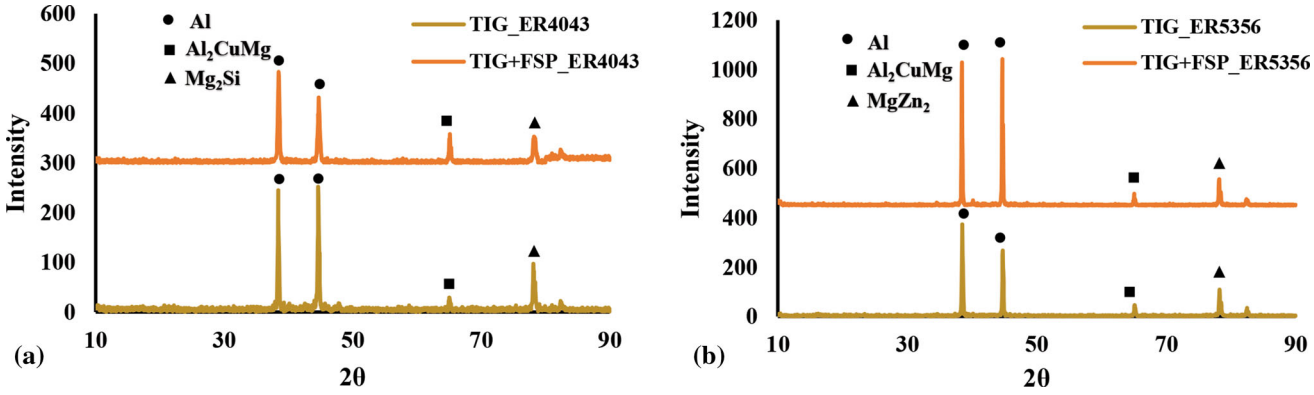

Fig. 4 XRD peaks of worn surface of TIG and TIG + FSP welded joint

diffraction peaks to d-spacing allows for identification of the material. This was achieved using d-spacing with a typical reference pattern. When wear occurs in TF welded joints, the d-spacing of the crystal is expected to decrease. Four major phases (Al, $MgZn_2$, Mg_2Si, Al_2CuMg) were found in the welded joints. When FSP was applied to the TIG welded joint, the fragmentation of precipitates the intensity of $MgZn_2$ was reduced. The penetration depth of the welded joint was calculated by $\tau = \frac{\sin\theta\cos\psi}{2\mu}$ (Ref 34), where τ = mean penetration depth, θ = Bragg peak position in degree with linear absorption coefficient, ψ = Tilt angle, μ = Linear absorption coefficient

Mg and Si undergo precipitation reactions and generate a strong precipitate of Mg_2Si in the center of the weld (Ref 17), which gives a higher tensile strength, as shown in Fig. 5. A precipitate of Al_2CuMg was found in TF weldments with both types of filler. The micro-hardness of the TF welded joints is affected by precipitate formation, strain hardening, boundary energy, and the formation of brittle intermetallic phases (Ref 35). The white precipitates indicate the presence of Cu and Mg. The large intermetallic phases visible in the microstructure graph were formed during the welding and did not contribute to hardening of the alloy (Ref 36, 37). The increase in the grain boundaries and recrystallized grains in the SZ of AA7075 and AA6061 indicate higher hardness. Due to its fine-grained structure and fine precipitates, the nugget zone was associated with high temperatures and plastic deformation.

3.4 Fracture Surface Morphology

The fractured surface morphology of the tensile test specimens for the TIG and TF joints was also investigated, as shown in Fig. 6(a), (b), (c) and (d). The fractured surface was examined using the SEM in order to understand the influence of the microstructure of the failure pattern of the welded joint. During the tensile test, a shear plane at 45° to the tensile axis was formed along the periphery of the test specimens, forming a cup-cone fracture. The coalescence of micro-voids resulted in an equiaxed dimple at the tensile fractured surface normal to the loading axis (Ref 38, 39). The fractured surfaces of the TIG welded joints with both fillers were characterized by ductile dimples and cleavage facets, indicating ductile failure. Cleavage facets are low-energy fractures that propagate along a well-defined low index crystallographic plane known as the cleavage plane.

The location of fracture in the TF welded joints was within the HAZ. An analysis of the fracture location of the welded joints is important in order to improve the mechanical properties of the welded joint. The fracture locations in the TF welded joints were not distant from the weld center and changed with the revolutionary pitch. As the revolutionary pitch increased, the fracture location of the welded joint became close to the center of the weld, and the fracture locations also depended on the process parameters of the TF welded joint (Ref 40). All of the TIG welded joints failed in the fusion zone, while the TF joints failed 12 mm away from the nugget zone,

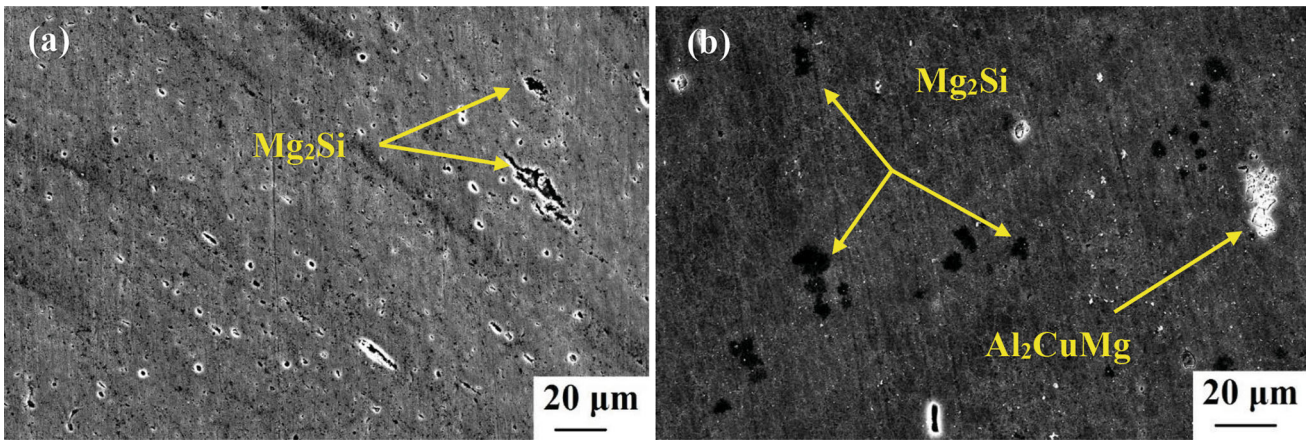

Fig. 5 SEM micrograph of TIG + FSP welded joint with filler ER4043, (a) Stir zone, (b) TMAZ

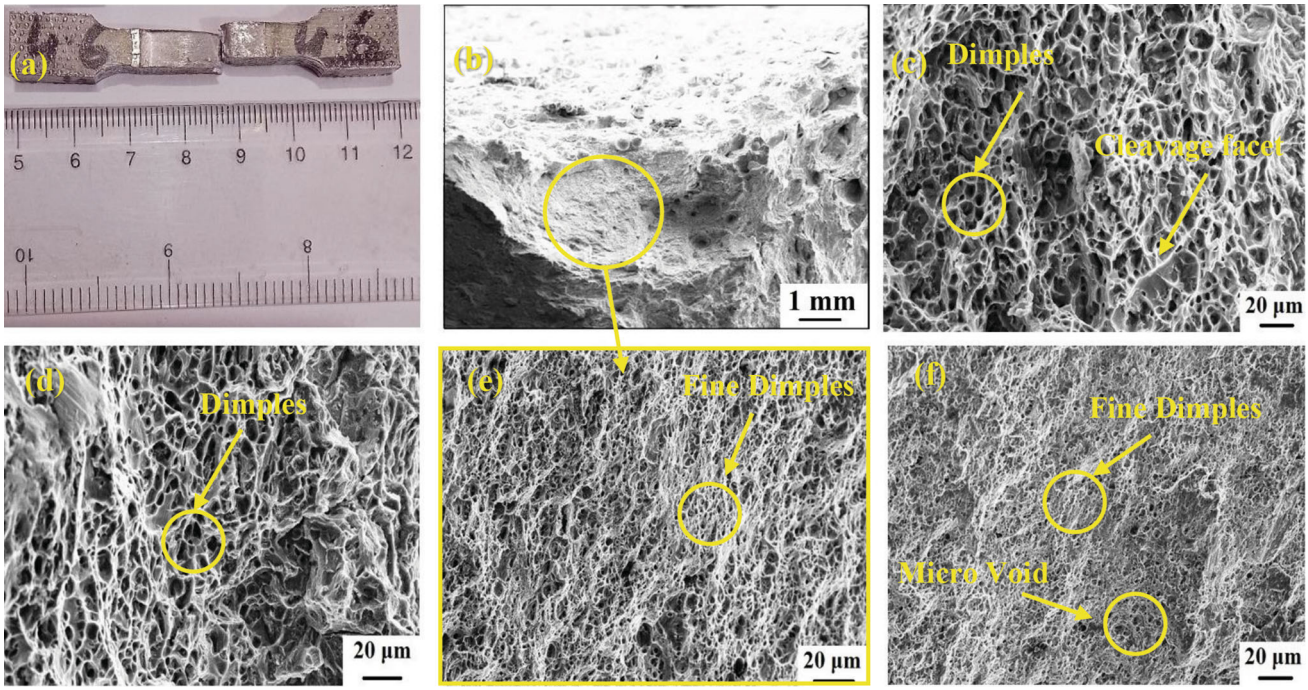

Fig. 6 Fracture surface morphology, (a) Fractured specimen, (b) Cross-section of fractured region, (c) TIG welded joint with filler 4043, (d) TIG welded joint with filler 5356, (e) TIG + FSP welded joint with filler 4043, (f) TIG + FSP welded joint with filler 5356

as fracture commenced at the interface of the HAZ and TMAZ in the RS. This type of fracture behavior can also be explained by analyzing the strain localization, grain size characteristics, and texture in the RS (Ref 41). The TF fractured surface showed tiny, equiaxed dimples, indicating ductile fracture. All the TF joints showed agglomerative and microporous ductile fractures. The microstructure of the base metals (AA6061 and AA7075) was uniform and finer than in the TIG and TF welded joints, and it was also observed from the fracture morphology that the size of the dimples in both the welded joints was larger than in the base metal; for this reason, the tensile strength of the base metal is much higher than the welded joints. Quasi-cleavage with ductile fracture was observed in the TF welded joints, and the regularly separated features on the fracture surface showed characteristics of both cleavage and plastic deformation (Ref 42). The TF samples processed at a lower TRS of 700 rpm contained large voids, located at the bottom of the TF joints, which may arise from ineffectual material mixing during the FSP process; these voids were the cause of failure in the SZ. At high values of TRS, fine, equiaxed dimples were observed. Fracture in the TF joint at high TRS was observed in the HAZ due to material softening, as confirmed by variations in the micro-hardness (Ref 43).

3.5 Micro-hardness

Figure 7 illustrates the influence of TRS on the micro-hardness of the different zones in the transverse direction of the TF welded joints. A higher compact pressure, leading to an increase in the bond strength, was observed with the ER5356 filler as compared to the ER4043 filler in the TIG welded joint, and the grain size in the WFZ with ER5356 filler was smaller than with the ER4043 filler. Due to this, the hardness in the WFZ was observed to be higher with ER5356 than with ER4043 (Ref 44). The micro-hardness of the SZ was slightly higher than in the TMAZ and HAZ, a result that was attributed to the small grain size. The decreasing trend of the micro-hardness in the TMAZ was due to the dissolution of precipitates, and a lower hardness was observed in the HAZ due to the coarsening of precipitates (Ref 45). The decrease of micro-hardness in the HAZ is due to disappearance of Guinier-Preston (GP) zone and coarsening of strengthening precipitates. Comprehensive, severe coarsening and dissolution of precipitates occurred in the TMAZ. The material experienced higher temperatures in the nugget zone, due to re-precipitation after complete dissolution took place. When the AA6061 was positioned on the AS and a low TRS was used, the transition of micro-hardness in the SZ from the 6061 aluminum alloy to the 7075 was more gradual, and more effective material mixing was observed. The minimum hardness was observed in the HAZ on the AA6061 side with ER4043 filler. Some tensile specimens with ER5356 filler failed in the HAZ, and some failed in the TMAZ on the AA6061 side. Fig. 7 shows the variation in micro-hardness from the HAZ to the TMAZ in the TF welded joints of AA7075 and AA6061, at different values of TRS. From the figure, it can be seen that the hardness value in the SZ increases when the TRS is increased. An increase in the TRS also causes an increase in hardness, due to the fine microstructure and low heat concentration (Ref 46). The micro-hardness directly affects the phase dispersion microstructure and the dislocation density. In the conventional FSW process, the high heat input and thermal cycle cause grain growth, and roughen the microstructure of the SZ. The processing parameters used in FSP predominate over the hardness value, since the hardness values are less significant in terms of affecting the mechanical properties of the weldment (Ref 17). The variation in micro-hardness also plays a significant role in the detection of the metallurgical phase in the welded region. Due to the cooling rate and solidification sequence, the micro-hardness and grain size can be used as indicators of the primary effects at

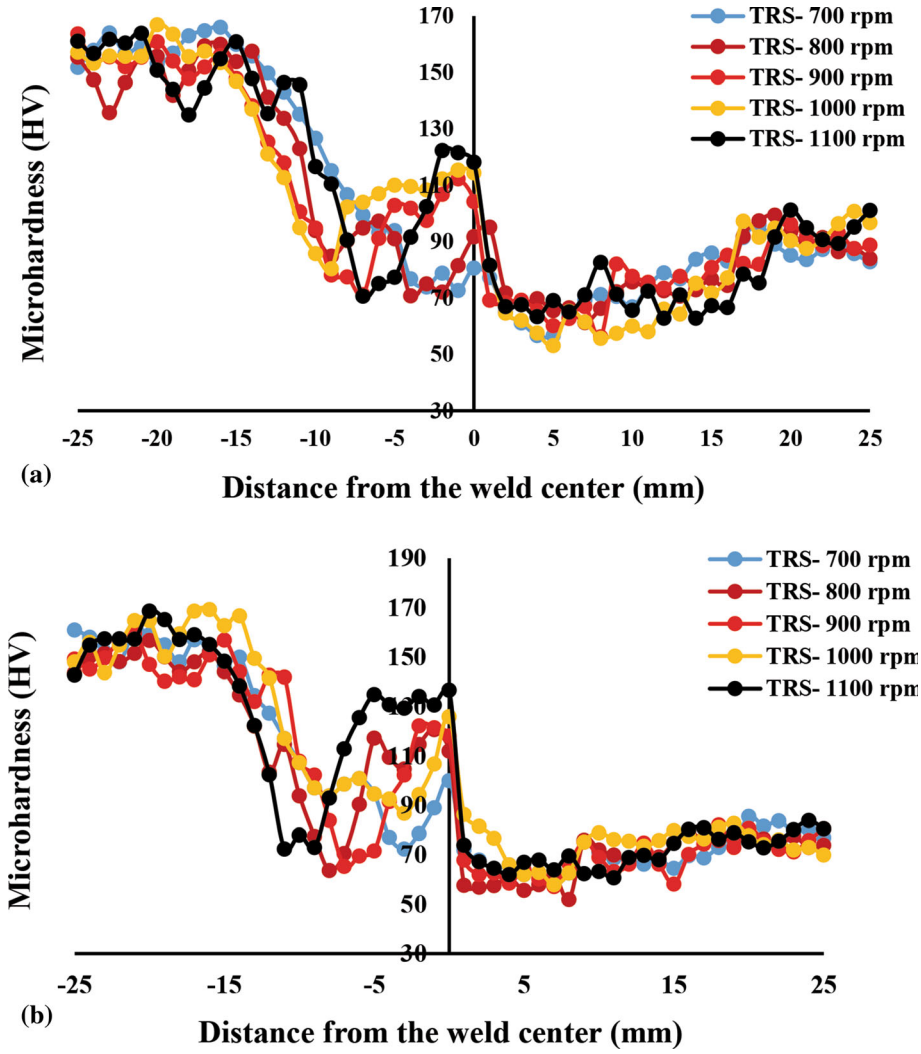

Fig. 7 Variation of micro-hardness of TIG + FSP welded joint of AA6061 and AA7075 under different TRS, (a) filler ER4043, (b) filler ER5356

the bottom and middle of the welded joint. Fig. 7 shows that when the TRS is increased, the hardness in the Stir zone increases and reaches a maximum value. A maximum hardness of 137 HV was observed at a TRS of 1100 rpm for the ER5356 filler, and the minimum hardness of 81 HV was obtained at a TRS of 700 rpm with the ER4043 filler.

3.6 Wear Test

The wear rate was calculated using a high-temperature rotary tribometer TR-20L-PHM800-DHM850 machine. Fig. 8(a), (b), (c), (d) and (e) shows the worn surface of the TF weldment with ER4043 filler at a load of 20 N and a sliding velocity of 1.68 m/s. It was found that at this sliding velocity and load, the wear debris of the welded joint was in the form of microchips, and the wear was greater. When the load was increased further to 30 N at the same sliding velocity, microchips suddenly became detached from the track. The surface deformation was increased with high micro-cutting of the welded joints. Fig. 8(f), (g), (h), (i) and (j) shows the worn surface of the TF welded joint with ER5356 filler at a load of 30 N and a sliding speed of 1.68 m/s. When the load was increased from 30 to 40 N at the same sliding speed, the deformation of the TF welded surface was higher. At a load of 40 N, the surface of the TIG + FSP welded joint contained more microchips and higher deformation.

A smooth wear track was observed at low sliding speeds, with more plastic deformation and less abrasion. Figures 9 and 10 show the variation in the wear rate against sliding distance and the COF against the rotational speed of the disk for loads of 20, 30, and 40 N for TIG and TF welded joints with ER4043 and ER5356 fillers. The wear rate was found to be higher for greater sliding distances of about 1005.71 to 1508.57 m in all specimens. The wear rate was found to be lower for the TF weldment with ER5356 filler than for ER4043, and the wear resistance was therefore reduced with ER4043 and increased with ER5356 for the TF weldment. A higher wear rate was observed in the TIG welded joints compared to the TF welded joints. A high wear rate was observed at a fixed sliding velocity of 1.68 m/s with different loads. The wear resistance increased as the TRS for FSP was increased. Hence, the AA7075 and AA6061 welded joints fabricated by TF with ER5356 filler at a TRS of 1100 rpm had the best wear resistance of all the welded joints. Fig. 11(a) and (b) shows the variation in the COF with sliding distance for the TIG and TF welded joints, at a sliding velocity of 1.68 m/s and weights of 20, 30, and 40 N, and it can

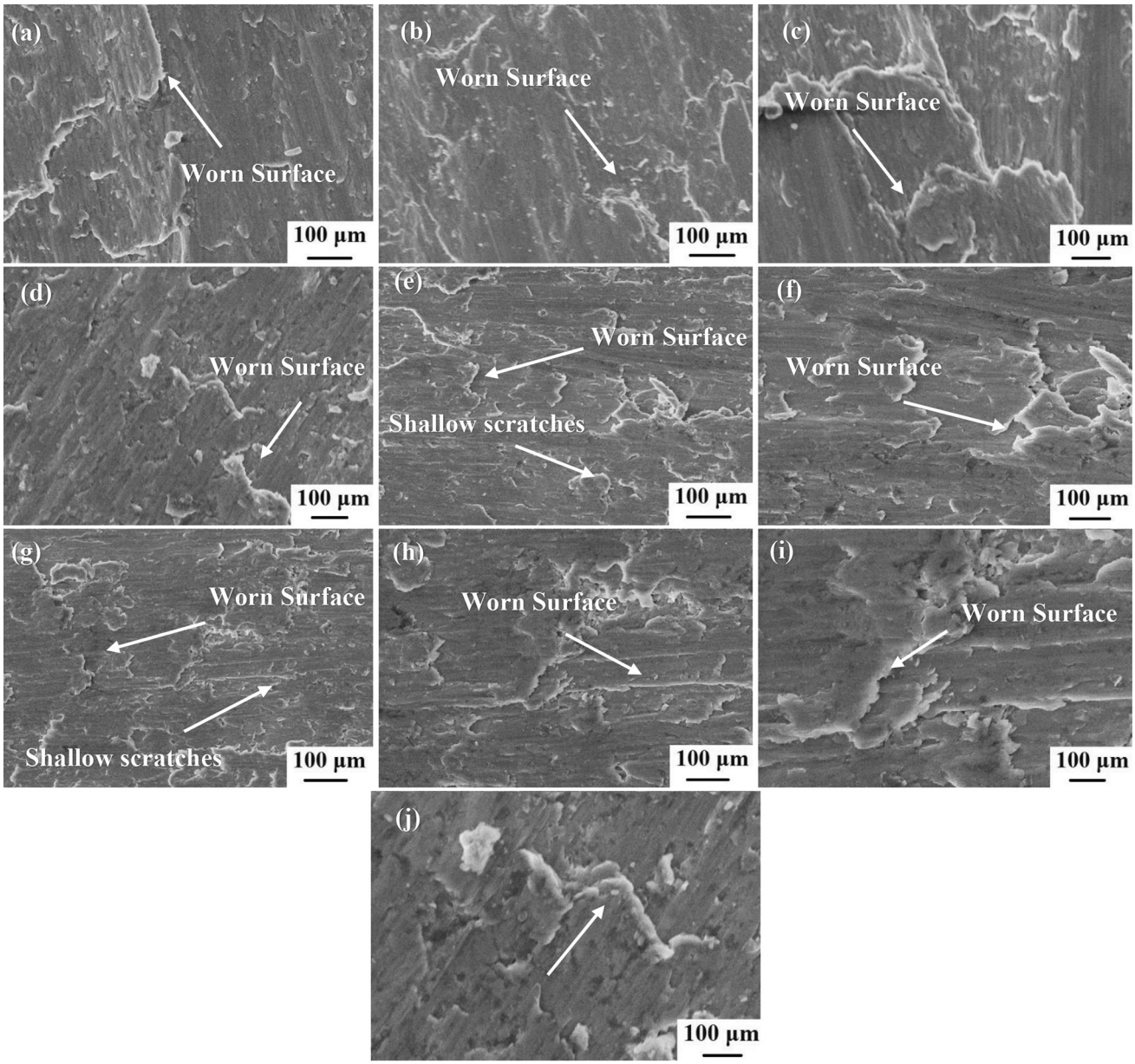

Fig. 8 Worn out surfaces of TIG and TF weldments, (a–e) TF welded joint with filler ER4043 at different TRS, (f–j) TF welded joints with filler ER5356 at different TRS

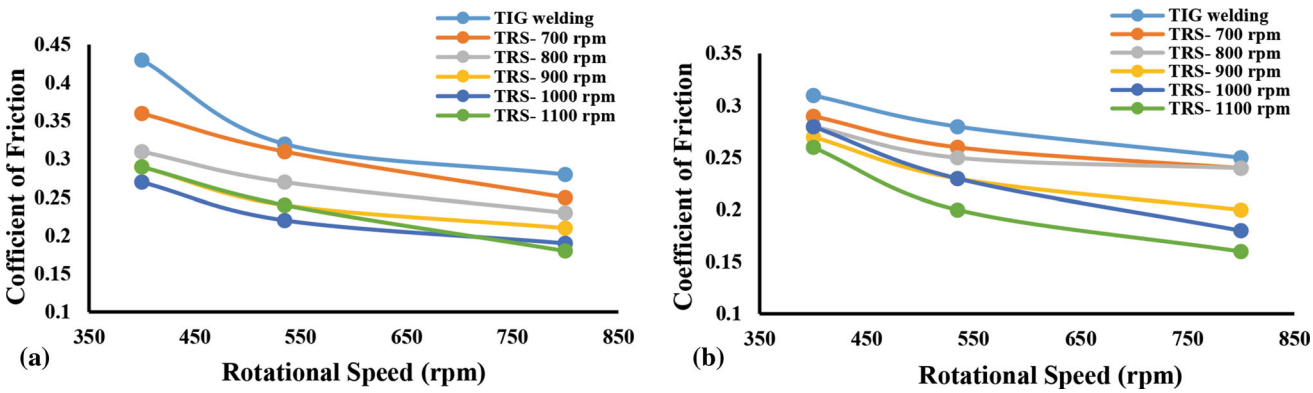

Fig. 9 Variation of COF to rotational speed TIG + FSP welded joint, (a) filler ER4043, (b) ER5356

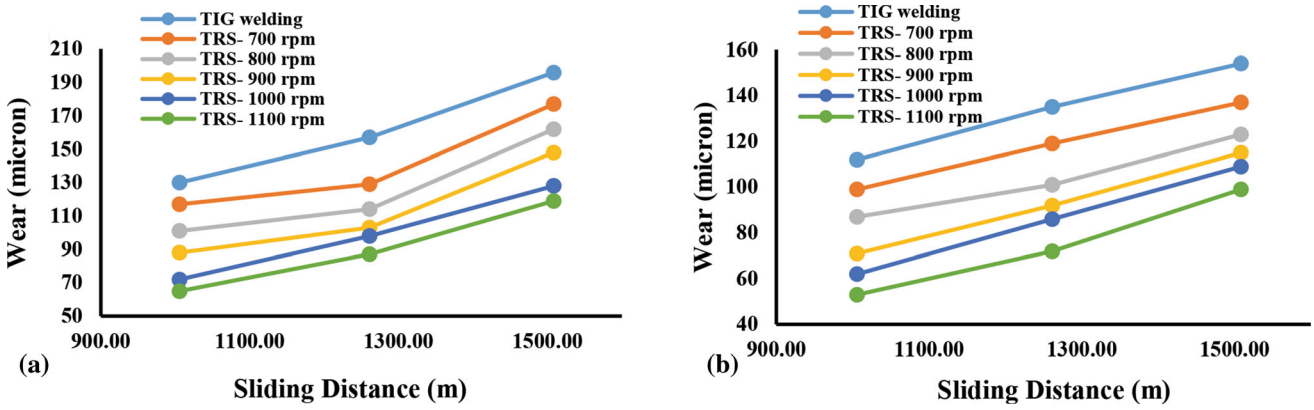

Fig. 10 Variation of Wear rate to sliding distance for TIG + FSP welded joint, (a) filler ER4043, (b) ER5356

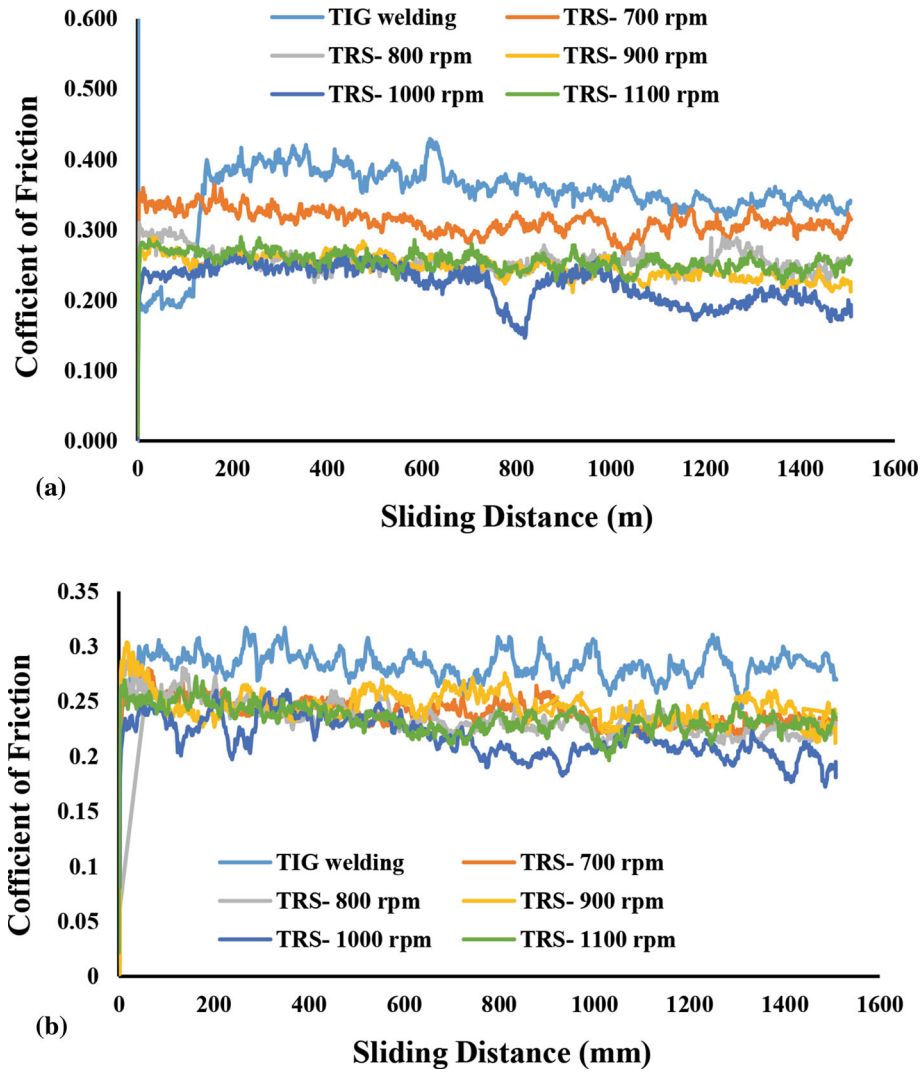

Fig. 11 Experimental results of sliding distance vs COP for TIG + FSP welded joint, (a) filler ER4043, (b) ER5356

clearly be seen that the COF of the TF weldment with ER5356 filler has a lower variation in sliding distance. The variation in the COF was higher in TIG welded joints than in TF welded joints. The average COFs for TIG and TF weldments with ER4043 filler were 0.28 and 0.238, respectively, whereas the average COFs for the TIG and TIG + FSP with ER5356 filler were 0.343 and 0.257, respectively.

At higher loads of 40 and 50 N, valleys and hills were observed on the worn surface, but these were not significantly higher at higher speeds, meaning the wear rate was more

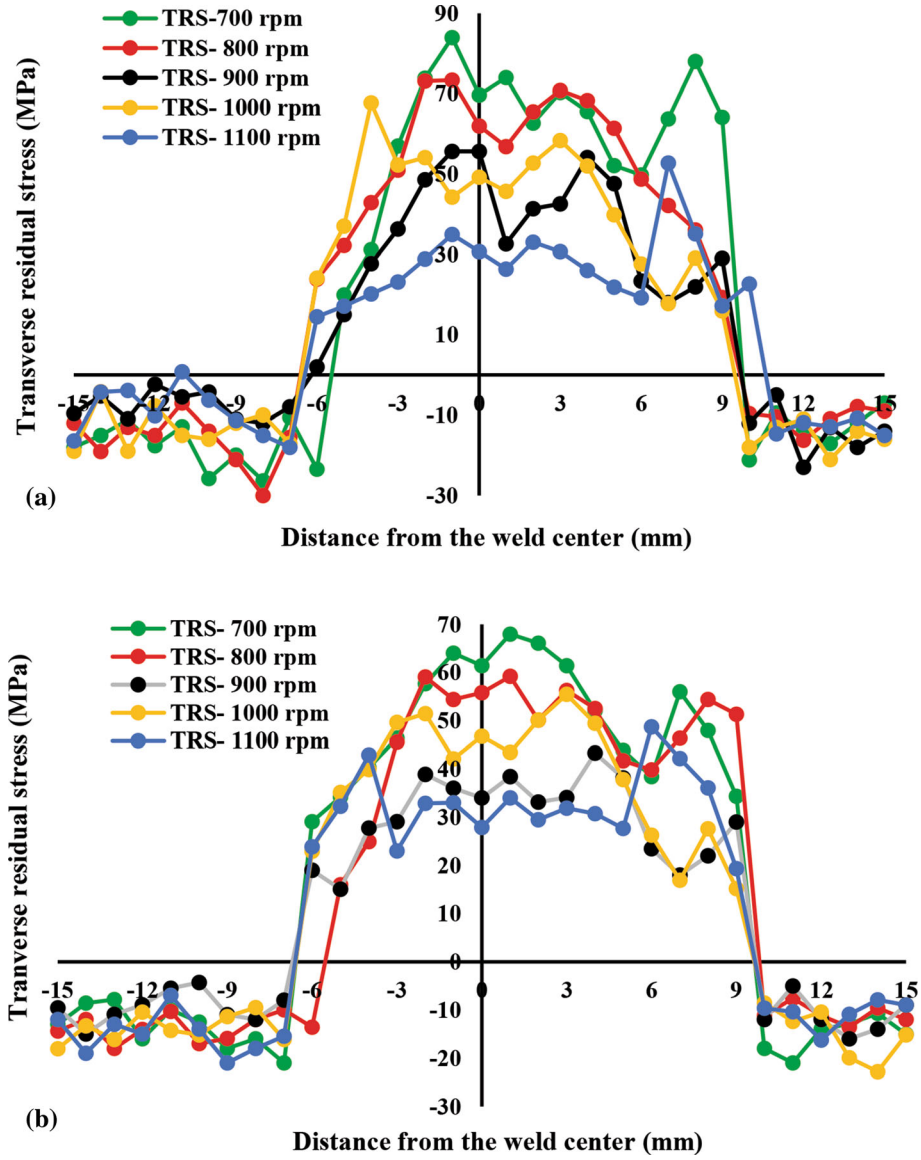

Fig. 12 Variation of residual stress of TF welded joint of AA6061 and AA7075 under different TRS, (a) filler ER4043, (b) filler ER5356

pronounced at higher speeds for the TF welded joints with both fillers. The wear rate was not much higher than for the other higher loaded weldments at a sliding speed of 1.68 m/s and a load of 10 N. At a low load of 10 N and a lower sliding speed of 1.68 m/s, the top surfaces of the TIG and TF welded specimens were not greatly affected. A low wear rate was observed at low sliding speeds and loads (Ref 47), but this increased sharply when the sliding speed was increased. Worn debris in the form of microchips was found at higher rotational speeds of the disk, and higher surface deformation was observed at lower rotational speeds. At low sliding speeds, the wear rate increased with an increase in load (Ref 48), and at higher speeds, it increased sharply with increasing loading conditions (Ref 49, 50). It can be concluded that at lower loads, wear was generally due to deformation and adhesion in the TF welded joint.

3.7 Residual Stress

In this work, the residual stress was measured using a Pulstec μ-X360 machine, which operates based on the cosα method, at the mid-section of the welded joint. The residual stresses were recorded in the transverse direction of the welded joint using XRD, with an incident angle of 35°. The incidence time for the x-ray was about 5-6 min at the weld center during the process, and the diffracted beam captured images from the workpiece at a resolution of 50 μm. Residual stresses affect the mechanical properties of the weldment: a low residual stress may improve the buckling strength, fracture strength and cracking, and can also affect the predicted life of the weldment. The residual stress distribution profile was observed to have an M shape, which was a function of the lateral distance from the weld center. This distribution occurred because behind the tool, the tensile stresses start to appear in a longitudinal direction as the weld metal cools down, while the compressive stresses produced by the expanding hot material lead to plastic strain, due to the low compressive yield strength. The magnitudes of

the transverse residual stresses may be below the yield strength of the welded joint (Ref 51). The transverse residual stresses were notably smaller in the SZ when the TRS was increased in FSP. Negative residual stresses were observed in the area of the HAZ. The residual stresses were measured at 1 mm intervals from the weld interface, and it was found that the residual stress gradually increased toward the end of the TF weld line, as shown in Fig. 12. The residual stress at the stir zone decreased with an increase in the TRS, and a minimum value of 28 MPa was observed in the TF welded joint at a TRS of 1100 rpm with ER5356 filler. From Fig. 12, several observations can be made. Firstly, the compressive residual stress was observed just outside the weld region. Secondly, a maximum tensile residual stress of 70 MPa was observed in the stir zone at a TRS of 700 MPa with ER4043 filler in the TF welded joint, and the residual stress gradually decreases in the stir zone as the TRS increases. The transverse residual stress on the AS of the TF welded joint in the SZ is slightly greater than on the RS (Ref 17).

4. Conclusions

The effect of FSP on TIG welded joints with different tool rotational speeds has been successfully fabricated, and results show that the wear resistance and mechanical properties of TIG + FSP welded joint with different filler materials have been improved as compared to TIG welded joints. The following conclusions can be made from the above results.

- The percentage improvement in the tensile strength of TIG + FSP weldments was observed to be 78.57% and 75.89%, compared with TIG welded joints with ER4043 and ER5356 filler, respectively, at a TRS of 1100 rpm
- A maximum tensile strength of 196 MPa was observed in a TIG + FSP welded joint with ER5356 filler, and a minimum tensile strength of 98 MPa was observed in the TIG weldment with ER4043 filler.
- A maximum micro-hardness of 137 HV in the stir zone was observed in TIG + FSP welded joints at a TRS of 1100 rpm.
- Cleavage facets, tear ridges, and large dimples were observed in fractured specimens of TIG welded joints, whereas fine, equiaxed dimples were observed in TIG + FSP welded joints.
- TF welded joints with ER5356 filler had superior wear resistance compared to TIG and TIG + FSP welded joints with ER4043 filler

Conflict of interest

The author declare that they have no conflict interest.

References

1. J.F. Guo, H.C. Chen, C.N. Sun, G. Bi, Z. Sun, and J. Wei, Friction Stir Welding of Dissimilar Materials Between AA6061 and AA7075 Al Alloys Effects of Process Parameters, *Mater. Des.*, 2014, **56**, p 185–192
2. S. Madhavarao, R.V. Penmetsa, G.S.V.S. Kumar, C.R. Raju, and K.T. Kumar, Investigation on Mechanical Properties of Friction Stir Welded Aa7075 and Aa6061 Joints, *Mater. Today Proc.*, 2019, **18**, p 2288–2297
3. W.M. Thomas, E.D. Nicholas, J.C. Needham, M.G. Murch, P. Templesmith, and C.J. Dawes, Friction-Stir Butt Welding. G.B. Patent 9125978.8, UK, 1991
4. S. Sirohi, C. Pandey and A. Goyal, Role of Heat-Treatment and Filler on Structure-Property Relationship of Dissimilar Welded Joint of P22 and F69 Steel, *Fusion. Eng. Des.*, 2020, **159**, p 111935
5. S.A. Alidokht, A.A. Zadeh, S. Soleymani, T. Saeid and H. Assadi, Evaluation of Microstructure and Wear Behavior of Friction Stir Processed Cast Aluminum Alloy, *Mater. Char.*, 2012, **63**, p 90–97
6. A.M. Hassan, M. Almomani, T. Qasim and A. Ghaithan, Effect of Processing Parameters on Friction Stir Welded Aluminum Matrix Composites Wear Behavior, *Mater. Manuf. Proc.*, 2012, **27**, p 1419–1423
7. N.M. Farahmand, N. Parvin and M. Bahrami, Al_2O_3 Fortifed AA6061-T6 Joint Produced via Friction Stir Welding: The Effects of Traveling Speed on Microstructure, Mechanical, and Wear Properties, *Proc. Inst. Mech. Eng. Pt. L. J. Mater. Des. Appl.*, 2017, **213**, p 534–543
8. Y. Zhao, X. Huang, Q. Li et al., Effect of Friction Stir Processing with B4C Particles on the Microstructure and Mechanical Properties of 6061 Aluminum Alloy, *Int. J. Adv. Manuf. Technol.*, 2015, **78**, p 1437–1443
9. C. Pandey, M.M. Mahapatra, P. Kumar et al., Effect of Weld Consumable Conditioning on the Diffusible Hydrogen and Subsequent Residual Stress and Flexural Strength of Multipass Welded P91 Steels, *Metall. Mater. Trans. B*, 2018, **49**, p 2881–2895
10. P.K. Taraphdar, J.G. Thakare, C. Pandey and M.M. Mahapatra, Novel Residual Stress Measurement Technique to Evaluate through Thickness Residual Stress Fields, *Mater. Lett.*, 2020, **277**, p128347
11. T.G. Santos, R.M. Miranda, V. Pedro and J. Pamies Teixeira, Modification of Electrical Conductivity by Friction Stir Processing of Aluminum Alloys, *Int. J. Adv. Manuf. Technol.*, 2011, **57**, p 511–519
12. Z.Y. Ma, Friction Stir Processing Technology: A Review, *Metall. Mater. Trans. A*, 2008, **36**, p 642–658
13. A.A.M. Silva, E. Arruti, G. Janeiro, E. Aldanondo, P. Alvarez and A. Echeverria, Material Flow and Mechanical Behaviour of Dissimilar AA2024-T3 and AA7075-T6 Aluminium Alloys Friction Stir Welds, *Mater. Des.*, 2011, **32**, p 2021–2027
14. S.T. Amancio-Filho, S. Sheikhi, J.F.D. Santos and C. Bolfarini, Preliminary Study on the Microstructure and Mechanical Properties of Dissimilar Friction Stir Welds in Aircraft Aluminium Alloys 2024–T351 and 6056–T4, *J. Mater. Proc. Technol*, 2008, **206**, p 132–142
15. H. Mehdi, Mishra RS (2020) Effect of Friction Stir Processing on Microstructure and Mechanical Properties of TIG Welded Joint of AA6061 and AA7075, *Metall. Micro Anal.*, 2020, **9**, p 403–418
16. H. Mehdi and R.S. Mishra, Investigation of Mechanical Properties and Heat Transfer of Welded Joint of AA6061 and AA7075 Using TIG + FSP Welding Approach, *J. Adv. Joint. Proc.*, 2020, **1**, p 100003
17. H. Mehdi and R.S. Mishra, Influence of Friction Stir Processing on Weld Temperature Distribution and Mechanical Properties of TIG Welded Joint of AA6061 and AA7075, *Trans. Ind. Inst. Met.*, 2020, **73**, p 1773–1788
18. M. Koilraj, V. Sundareswaran, S. Vijayan and S.R.K. Rao, Friction Stir Welding of Dissimilar Aluminum Alloys AA2219 to AA5083-Optimization of Process Parameters Using Taguchi Technique, *Mater. Des.*, 2012, **42**, p 1–7
19. O.T. Midling, L.D. Oosterkamp, and J. Bersaas, Friction Stir Welding Aluminium Process and Applications. I, in *7th International Conference and Exhibition on Aluminum, 1998, INALCO98*
20. J. Backlund, A. Norlin, and A. Andersson, Friction Stir Welding-Weld Properties and Manufacturing Techniques, in *7th International Conference and Exhibition on Aluminum, 1998, INALCO98*
21. H. Aydın, A. Bayram, A. Uguz, and K.S. Akay, Tensile Properties of Friction Stir Welded Joints of 2024 Aluminum Alloys in Different Heat-Treated-State, *Mater. Des.*, 2009, **30**, p 2211–2221
22. T. Hirata, T. Oguri, H. Hagino, T. Tanaka, S.W. Chung and Y. Takigawa, Influence of Friction Stir Welding Parameters on Grain Size and Formability in 5083 Aluminum Alloy, *Mater. Sci Eng. A*, 2007, **456**, p 344–349
23. V. Saravanan, S. Rajakumar and A. Muruganandam, Effect of Friction Stir Welding Process Parameters on Microstructure and Mechanical Properties of Dissimilar AA6061-T6 and AA7075-T6 Aluminum Alloy Joints, *Metallogr. Microstruct. Anal.*, 2016, **5**, p 476–485
24. A. Simar, Y. Brechet, B. Meester, A. Denquin, C. Gallais and T. Pardoen, Integrated Modeling of Friction Stir Welding of 6xxx Series

Al Alloys: Process, Microstructure and Properties, *Progr. Mater. Sci.*, 2012, **57**, p 95–183
25. H. Mehdi and R.S. Mishra, An Experimental Analysis and Optimization of Process Parameters of AA6061 and AA7075 Welded Joint by TIG+ FSP Welding Using RSM, *Proc. Technol. Adv. Mater.*, 2020 https://doi.org/10.1080/2374068X.2020.1829952
26. I. Dinaharan, N. Murugan and S. Parameswaran, Developing an Empirical Relationship to Predict the Influence of Process Parameters on Tensile Strength of Friction Stir Welded AA6061/0–10 wt% ZrB2 In Situ Composite, *Trans. Indian Inst. Met.*, 2012, **65**, p 159–170
27. Z.Y. Ma, S.R. Sharma and R.S. Mishra, Microstructural Modification of As-Cast Al–Si–Mg Alloy by Friction Stir Processing, *Metall. Mater. Trans. A*, 2006, **37**, p 3323–3336
28. C. Pandey, M.M. Mahapatra, P. Kumar, J.G. Thakre and N. Saini, Role of Evolving Microstructure on the Mechanical Behaviour of P92 Steel Welded Joint in As-Welded and Post Weld Heat Treated State, *J. Mater. Proc. Technol.*, 2019, **263**, p 241–255
29. K.R. Horton, Micro-hardness, Strength and Strain field Characterization of Self-reacting Friction Stir and Plug Welds of Dissimilar Aluminum Alloys (Ref dissertation). Tuscaloosa: the University of Alabama; 2011
30. F. Humphreys and M. Hatherly, *Recrystallization and Related Annealing Phenomena*, 2nd ed. Pregamon, New York, 2004
31. O.S. Salih, H. Ou, W. Sun and D.G. McCartney, A Review of Friction Stir Welding of Aluminium Matrix Composites, *Mater. Des.*, 2015, **86**, p 61–71
32. Y. Mao, L. Ke, F. Liu, C. Huang, Y. Chen and Q. Liu, Effect of Welding Parameters on Microstructure and Mechanical Properties of Friction Stir Welded Joints of 2060 Aluminum Lithium Alloy, *Int. J. Adv. Manuf. Technol.*, 2015, **81**, p 1419–1431
33. C. Hamilton, M. Kopyscianski, O. Senkov and S. Dymek, A Coupled Thermal/Material Flow Model of Friction Stir Welding Applied to Modified Aluminum Alloys, *Metall. Mater. Trans. A*, 2013, **44**, p 1730–1740
34. O.P. Oladijo, A.M. Venter, L.A. Cornish and N. Sacks, X-Ray Diffraction Measurement of Residual Stress in WC-Co Thermally Sprayed Coatings onto Metal Substrates, *Surf. Coat. Technol.*, 2012, **206**, p 4725–4729
35. H. Mehdi and R.S. Mishra, *Effect of Friction Stir Processing on Mechanical Properties and Heat Transfer of TIG Welded Joint of AA6061 and AA7075*, Technol., Def., 2020. https://doi.org/10.1016/j.dt.2020.04.014
36. Z. Zhang, H. Xu, S. Wu and Y. Liu, Effects of Combined Prestraining and Pre-aging on Natural Aging and Bakehardening Response of an Al-Mg-Si Alloy, *Acta Meta Sin.*, 2013, **26**, p 340–344. https://doi.org/10.1007/s40195-012-0239-5
37. D. Maisonnette, M. Suery, D. Nelias, P. Chaudet and T. Epicier, Effects of Heat Treatments on the Microstructure and Mechanical Properties of a 6061 Aluminium Alloy, *Mater. Sci. Eng. A*, 2011, **528**, p 2718–2724. https://doi.org/10.1016/j.msea.2010.12.011
38. C. Pandey, A. Giri and M.M. Mahapatra, Evolution of Phases in P91 Steel in Various Heat Treatment Conditions and their Effect on Microstructure Stability and Mechanical Properties, *Mater. Sci. Eng. A*, 2016, **664**, p 58–74
39. C. Pandey, N. Saini, M.M. Mahapatra and P. Kumar, Study of the Fracture Surface Morphology of Impact and Tensile Tested Cast and Forged (C&F) Grade 91 Steel at Room Temperature for Different Heat Treatment Regimes, *Eng. Fail. Anal.*, 2017, **71**, p 131–147
40. H.J. Liu, H. Fujii, M. Maeda and K. Nogi, Tensile Properties and Fracture Locations of Friction-Stir-Welded Joints of 2017–T351 Aluminum Alloy, *J. Mater. Proc. Technol.*, 2013, **142**, p 692–696
41. C. Pandey, M.M. Mahapatrab, P. Kumar and N. Saini, Study on Effect of Double Austenitization Treatment on Fracture Morphology Tensile Tested Nuclear Grade P92 Steel, *Eng. Fail. Anal.*, 2018, **96**, p 158–167
42. A. Heidarzadeh, R.V. Barenji, M. Esmaily and A.R. Ilkhichi, Tensile Properties of Friction Stir Welds of AA 7020 Aluminum Alloy, *Trans. Indian Inst. Met.*, 2015, **68**, p 757–767
43. R.I. Rodriguez, J.B. Jordon, P.G. Allison, T. Rushing and L. Garcia, Microstructure and Mechanical Properties of Dissimilar Friction Stir Welding of 6061-to-7050 Aluminum Alloys, *Mater. Des.*, 2015, **83**, p 60–65
44. M.N.M. Salleh, M. Ishak, L.H. Shah and S.R.A. Idris, The Effect of ER4043 and ER5356 Filler Metal on Welded Al 7075 by Metal Inert Gas Welding, *WIT Trans. Built. Environ.*, 2016, **166**, p 213–224
45. T. Azimzadegan and S. Serajzadeh, An Investigation into Microstructures and Mechanical Properties of AA7075-T6 during Friction Stir Welding at Relatively High Rotational Speeds, *J. Mat. Eng. Perf.*, 2010, **19**, p p1256-1263
46. P. Sevvel and V. Jaiganesh, A Detailed Investigation on the Role of Different Tool Geometry in Friction Stir Welding of Various Metals and their Alloys, in *Proceedings of the International Colloquium on Materials, Manufacturing and Metrology–ICMMM*, 2014, p 103−107
47. D.K. Dwivedi, T.S. Arjun, P. Thakur, H. Vaidya and K. Singh, Sliding Wear and Friction Behaviour of Al–18% Si–0.5% Mg Alloy, *J. Mater. Process. Technol.*, 2004, **152**, p 323–328
48. K. Kato, Wear in Relation to Friction—A Review, *Lab. Tribol. Wear*, 2000, **241**, p 151–157
49. W. Maa, J. Lua and B. Wanga, Sliding Friction and Wear of Cu–Graphite Against 2024, AZ91D and Ti6Al4V at Different Speeds, *Wear*, 2009, **266**, p 1072–1081
50. M. Yamane, T.A. Stolarskia and S. Tobeb, Influence of Counter Material on Friction and Wear Performance of PTFE–Metal Binary Coatings, *Tribol. Int.*, 2008, **41**, p 269–281
51. A.S. Altenkirch, P.J. Withers, S.W. Williams, M. Poad and S.W. Wen, Residual Stress Engineering in Friction Stir Welds by Roller Tensioning, *Sci. Technol. Weld Joint.*, 2009, **14**, p 85–192

Publisher's Note Springer Nature remains neutral with regard to jurisdictional claims in published maps and institutional affiliations.

Silicon
https://doi.org/10.1007/s12633-021-00985-w

ORIGINAL PAPER

Effect of Liquid to Binder Ratio and Curing Temperature on the Engineering Properties of the Geopolymer Concrete

Manvendra Verma [1] · Nirendra Dev

Received: 20 October 2020 / Accepted: 25 January 2021
© Springer Nature B.V. 2021

Abstract
Geopolymer concrete(GPC) is a perfect alternative to conventional cement concrete. This experimental investigation examines the physical properties, chemical properties, mechanical properties, non-destructive test, and microstructural analysis of the various geopolymer concrete samples, varying the liquid-to-binder(LBR) ratio from 0.40 to 0.70, and curing temperature from 60 °C to 120 °C. After the experimental investigation, the workability increases with the increment of the liquid-to-binder ratio in the design mix, but the mix specimen density decreases with the same. In the mechanical properties, the compressive strength optimum at the ratio of 0.60 of liquid-to-binder ratio, and the poisson's ratio increases with the increment of liquid to binder ratio from .14 to .18 consecutively. All the mixes mechanical properties got the optimum point at the ratio of 0.60 of LBR in both ambient and oven curing conditions. The curing temperature directly increases the gain strength rate at early ages, but it reduces beyond the 100 °C temperature. The drying shrinkage increases with the increment of curing temperature, similarly the modulus of elasticity increase with the increment of curing temperature, but it reduces beyond the 100 °C curing temperature. The thermal stability of the GPC specimens is higher and shows the weight remained up to 92% of the original at the 850 °C temperature.

Keywords Geopolymer concrete · Liquid-to-binder ratio · Curing condition · Compressive strength · Modulus of elasticity · Curing temperature

1 Introduction

GPC is a sustainable concrete because it uses industrial solid wastes like fly ash and slag as a binding material in the mix designs. It indirectly reduced the carbon footprints by reducing cement in concrete and became the alternative to conventional concrete [1, 2]. Geopolymer is an inorganic chemical bond between the alumina and silica and is formed after the geopolymerisation reaction. The geopolymerisation reactions occur in the highly alkaline condition, and the pozzolanic materials are activated through the reaction's alkaline condition. The pozzolanic materials are rich in silica, and alumina content would be used in the GPC as binding material [3]. The GPC mix design with the class-f fly ash has an excellent capability to replace OPC in construction industries [4]. The fly ash-based GPC has a higher solid-to-liquid ratio than the metakaolin GPC due to its porous spherical structure with a higher fineness [5]. Sodium hydroxide and sodium silicate solution are used as the alkaline liquid in the GPC mixes, and it activates the industrial solid wastes (fly ash, GGBFS) to work as a binding material in the GPC mix designs [6, 7]. The increment of alkaline solution concentration in the fresh mix decreases the workability, and the mix's workability increases with the addition of water or superplasticiser [8, 9]. The SNF-based superplasticiser got the optimum point at 1% of dosage in the GPC without affecting their strength [10] The addition of the GGBFS in the flyash-based GPC increases the strength of the mix specimens and strengthens the GPC specimens in the ambient temperature in the laboratory and field [11–14]. The geopolymer mortar shows higher drying shrinkage than the OPC mortar due to the higher mesopore volume [15]. The water absorption of the geopolymer mortar is lower compared to the OPC mortar. The higher flyash amount in the geopolymer mix reduces the drying shrinkage compared to the slag

✉ Manvendra Verma
mv075415@gmail.com

Nirendra Dev
nirendradev@dce.ac.in

[1] Department of Civil Engineering, Delhi Technological University, Delhi, India

Published online: 06 February 2021

content [14]. The flow of mortar decreases with the fine aggregate-to-binder ratio increment in the mix [16].

The NaOH is the only activator in the GPC that provides excellent mechanical properties compared to the OPC concrete [17]. The Na_2SiO_3 addition in the mix enhanced the early strength(7–28 days) of the geopolymer system [18]. The NaOH higher concentration in the mix increases concrete strength, but it reduces the fresh mix's workability [19–25]. The GGBFS content in the GPC mix forms the CSH bond if the NaOH concentration is low or less alkalinity [26, 27]. The PCE-based superplasticiser is used for the production of self-compacting concrete rather than SNF-based superplasticiser

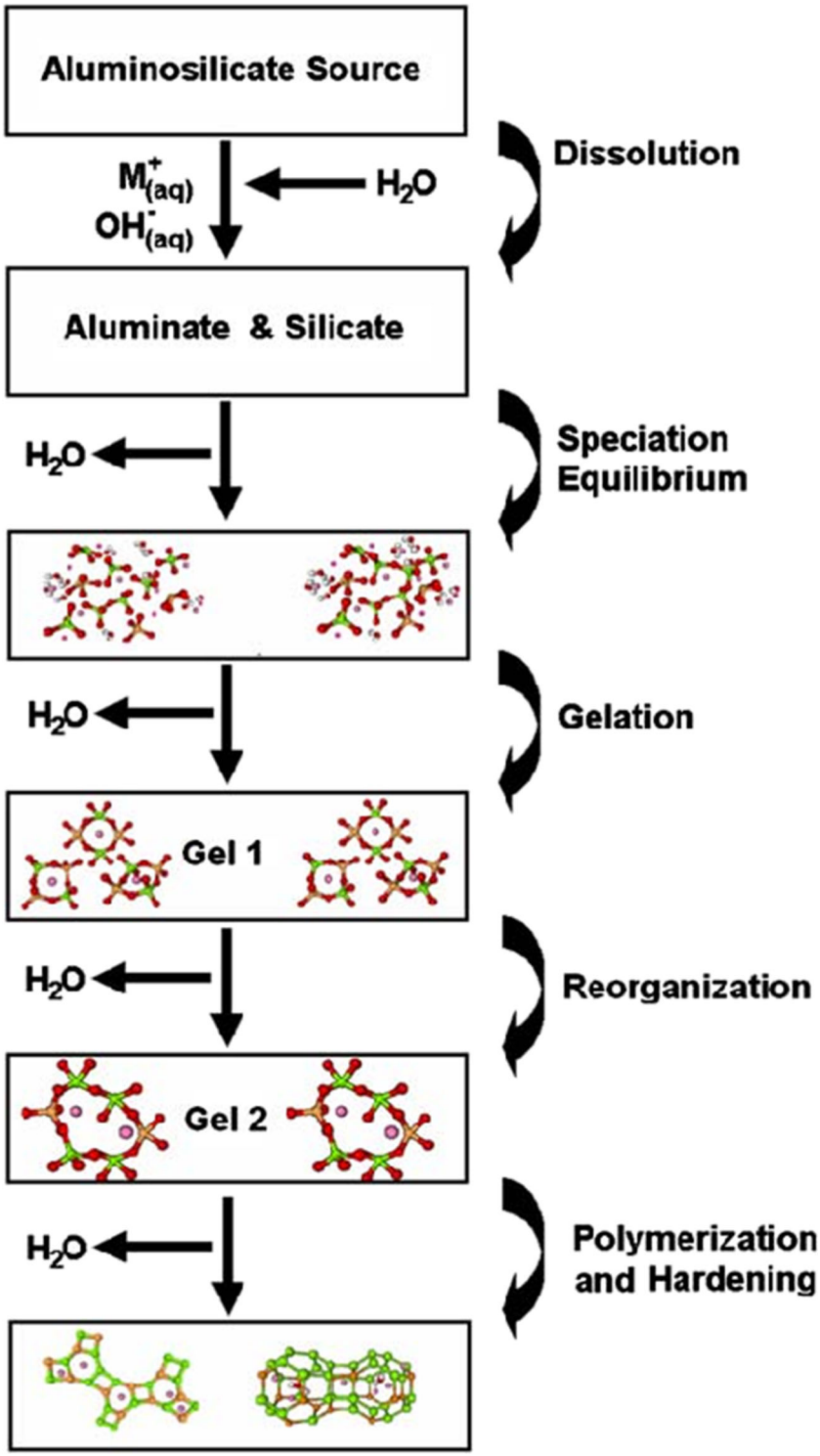

Fig. 1 Conceptual model of geopolymerisation reaction [30]

Table 1 Composition of Flyash And GGBFS

Characteristics	SiO_2	Al_2O_3	CaO	Fe_2O_3	MgO	SO_3	LOI
Flyash (%)	45.8	21.4	13.7	12.6	1.3	1.9	.1
GGBFS (%)	34.52	20.66	32.43	.57	10.09	.77	.3

[28]. The curing temperature plays a vital role in geopolymerisation reaction occurs for strength enhancement [29]. Figure 1 describes the concept of geopolymerisation reaction in the different phases. The first phase shows the dissolution of water with alkali material and hydroxides to form an alumino-silicate bond, and after that, the chemical reduces the water from the reaction and forms the end products [30].

The GGBFS addition in the mix reduces the workability, setting time, and hardening when the other content remained the same in the mix design. The GPC mix compressive strength increases with the GGBFS content increment at various ages up to 180 days. The strength development of the GGBFS blended fly ash-based GPC is cured at ambient temperature shows a similar pattern to the water-cured OPC concrete [31] when m-sand has replaced the natural sand and gives significant results with better performance of the mix samples [32]. The presence of alkali metal plays a vital role in the geopolymerisation reaction rate [33]. The GPC mix samples made by the sodium-based activator stabled up to 500 °C [34]. The GPC strength increases with the curing temperature up to 90 °C [17, 35]. Higher temperature curing increases the early strength of the GPC specimens [36]. The gain of strength is slow for 40 °C curing temperature compared to higher curing temperature [37]. The FLGC reinforced by the propylene fibers has excellent thermomechanical properties and highly durable [38–40]. The polypropylene fiber reinforced metakaolin-based GPC is highly stable against the elevated temperature, freezing-thawing, and wetting drying [41].

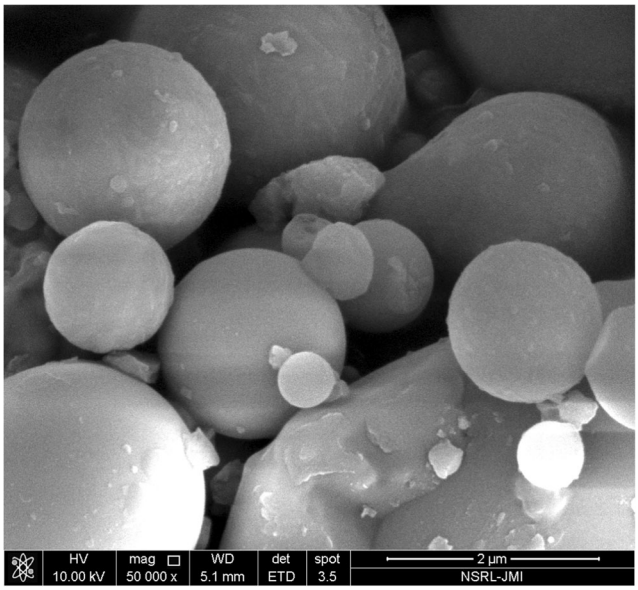

Fig. 3 SEM image of flyash

2 Materials and Tests Setup

2.1 Materials

2.1.1 Binders

Flyash is collected from the NTPC, Dadri, Gautam Buddha Nagar, Uttar Pradesh. The flyash is found in the class-c as per the ASTM C618–33512 [42]. Table 1 describes the mineral component with their percentage present in the flyash and GGBFS sample. The GGBFS is collected from the Bhilai Steel Plant, Durg, Chhattisgarh in India [43]. Figure 2 describes the XRD graphs of flyash and GGBFS, which define the crystalline mineral component intensity present in the samples. Figures 3 and 4 show the flyash and GGBFS SEM images at the 2-µm resolution, which effortlessly defines the particle size's shape. Flyash looks like a porous sphere,

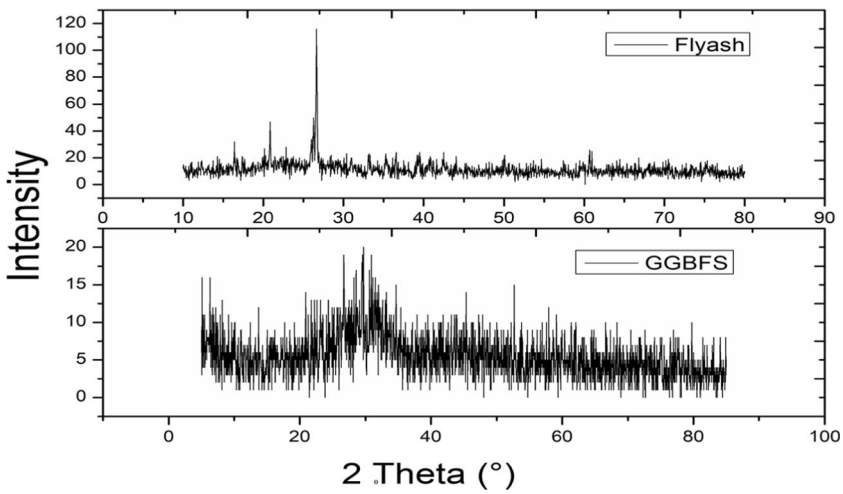

Fig. 2 XRD Pattern of Flyash and GGBFS

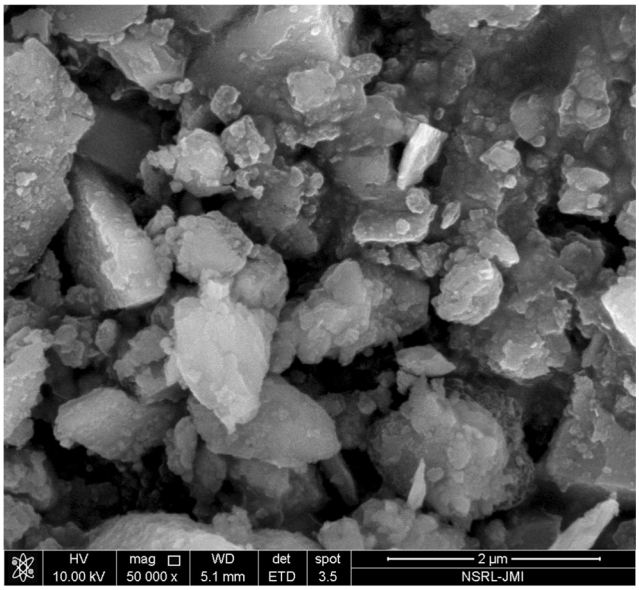

Fig. 4 SEM image of GGBFS

whereas GGBFS has an uneven shape or flaky structure of the particles.

2.1.2 Aggregates

Stone-dust or m-sand is used as a fine aggregate in the mix designs of GPC. Figures 6 and 7 show the pictures of the stone-dust and coarse aggregate, respectively. The various tests were conducted on the stone-dust sample to check the quality of the materials in the laboratory. The m-sand was a well-graded medium sand type of Zone-II with the specific gravity, bulk density, silt content, and water absorptions are 2.62, 1610 kg/m^3, 6%, and 1.21% respectively [44–52]. Locally crushed coarse aggregate was used in the GPC mix with the 10 mm and 20 mm msa. Figure **5** describes the well-graded gradation curve of stone-dust and coarse aggregate used in the experimental analysis.

Fig. 6 Picture of stone-dust or m-sand

Fig. 7 Picture of coarse aggregates

2.1.3 Alkaline Solution

NaOH and Na_2SiO_3 solution (water glass) was purchased from the Central Drug House (P) Ltd. in New Delhi-110,002 (India). These are used as an alkaline activator in the mix design, whereas, NaOH presents in the form of flakes and Na_2SiO_3 presents in the form of thick cloudy liquid. NaOH contains a minimum purity level of 96.0%, and Na_2SiO_3 contains the minimum assay of Na_2O titrimetric is 10.0%, and SiO_2, gravimetric is 25.5–28.5% in the sample. Figures 8 and 9 show NaOH and Na_2SiO_3 solution sample pictures used in the experimental laboratory analysis.

2.2 Mixing, Casting, and Curing

The mix design of the GPC could be made by the multivariate adaptive regression spline model [53, 54]. The raw materials mix in the pan mixture for five minutes initially mix the aggregates with flyash and GGBFS and pour the alkaline solution with additive water [55]. Figure **10** shows the picture of the fresh mix in pan mixture. The fresh mix

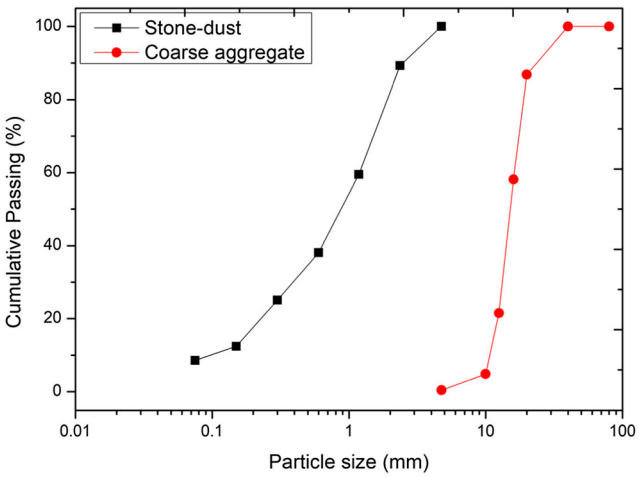

Fig. 5 Gradation curve of stone-dust and coarse aggregate

Fig. 8 Sodium hydroxide sample picture used in the experimental work

of the GPC cast in the cubes, cylinders, and prism shape molds. The sample molds open after 3 days and cured in the two conditions: 1) keep in the oven for 24 h at 60 °C, and 2) keep in the ambient area. The alkaline solution of NaOH and Na_2SiO_3 was made 24 h before the mixing of the GPC. The GPC mix designs vary the liquid-to-binder ratio in the mix from 0.40 to 0.70 and check the concrete's mechanical properties. Table 2 describes the different mix design content present in the GPC mixes, and around 750 samples cast in the laboratory to experimental analysis.

2.3 Tests Setup

2.3.1 Physical Properties

Slump test and compaction factor used for the workability of the fresh geopolymer concrete mix in which the slump apparatus is conical in shape or size of top diameter, bottom diameter, and height are 100 mm, 200 mm, and 300 mm respectively. In contrast, the compaction factor apparatus contains two conical buckets in a vertical alignment and puts a cylinder

Fig. 9 Sodium silicate sample picture used in experimental work

Fig. 10 Picture of pan mixture during concrete mixing

below conical buckets. These are the physical properties tests of geopolymer concrete mix [56, 57].

2.3.2 Chemical Properties

The chemical properties of the GPC mix samples are tested by the density and drying shrinkage. The weight of cubes samples tests the density of the mix design before the 28 days destructive test [58], and the length change of the specimens calculates the drying shrinkage after harden in the length comparator instrument [59].

2.3.3 Mechanical Properties

The mix design's mechanical properties included the compressive strength, splitting tensile, flexural strength, poisson's ratio, and modulus of elasticity. The GPC mix designs cube samples of size 150 mm*150 mm*150 mm are used to examine the specimens compressive strength. The samples tests under axial loading in Universal Testing Machine at 5.2kN/s rate of loading [60]**.** The cylindrical samples of the size diameter and height are 150 mm, and 300 mm, respectively are tested to splitting tensile strength. Transverse loads are applying the cylinder to examine the splitting tensile strength of the GPC cylinder specimen in the Universal testing machine [61]. The beam sample's size width, height, and length are 100 mm, 100 mm, and 500 mm, respectively, for testing the GPC mix design's flexural strength. The two-point load or flexural tensile test was applied to the beam specimen to examine the GPC mix specimen's flexural strength at the flexural testing machine [62]. The cylindrical samples are of size diameter of 150 mm and length of 300 mm to test the modulus of elasticity and poisons ratio of the GPC mix design. The axial load is applying to the cylinder to examine the vertical and horizontal strain of the GPC cylinder specimen in the universal testing machine for calculating the modulus of elasticity and poisons ratio [63].

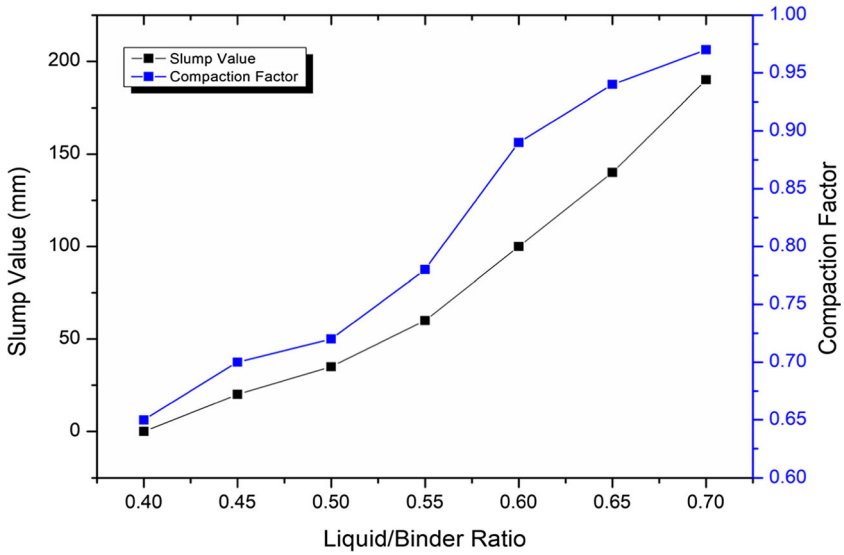

Fig. 11 Graph between the Slump value and compaction factor with the liquid-to-binder ratio

2.3.4 Non-Destructive Tests

The non-destructive tests check the strength or quality of the specimens without destruction. It includes the rebound test and UPV test. The rebound test is based on the check of surface hardness by the apparatus, and these tests are conducted on the cube samples at 7 days, 14 days, 28 days, 42 days, and 56 days after the casting. It was conducted on both types of sample cube and cylinder to test the mix sample's strength [64, 65]. The UPV test is based on the ultrasonic pulse wave velocity passes through the sample. The UPV is higher shows the better strength and quality of the GPC specimen. The test apparatus has two transducers, an electrical pulse generator, an amplifier, and an electronic timing device. The ultrasonic pulse wave transmitting through the sample by the transducers and electronic timing machine shows the time passage [66, 67].

2.3.5 Microstructural Analysis

The XRD analysis and thermogravimetric analysis do the microstructural analysis of the GPC samples. The XRD analysis shows the mineral oxides intensity presents in the sample of the GPC [68]. The TGA analysis shows the thermal stability of the sample material up to the 850 °C temperature. It works to weight the sample at the various temperature stages consecutively, whereas the temperature increases with 10 °C/min [69].

3 Results and Discussion

3.1 Effect of Liquid-to-Binder Ratio

3.1.1 Slump and Compaction Factor

In the experimental investigation, workability examines by the slump test and compaction factor in the laboratory. The slump

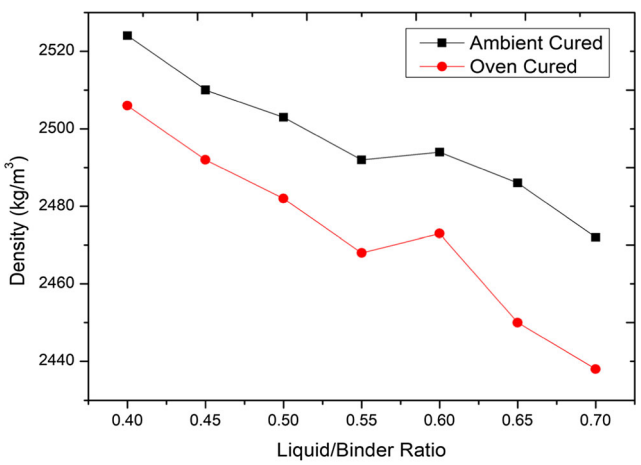

Fig. 12 Graph between density and Liquid-to-binder ratio

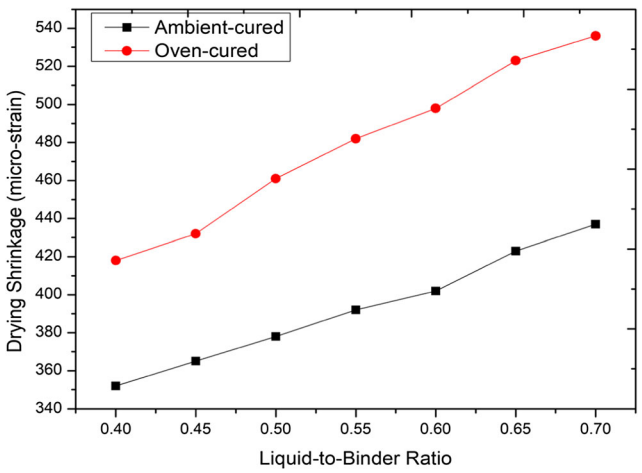

Fig. 13 Graph between drying shrinkage and liquid-to-binder ratio

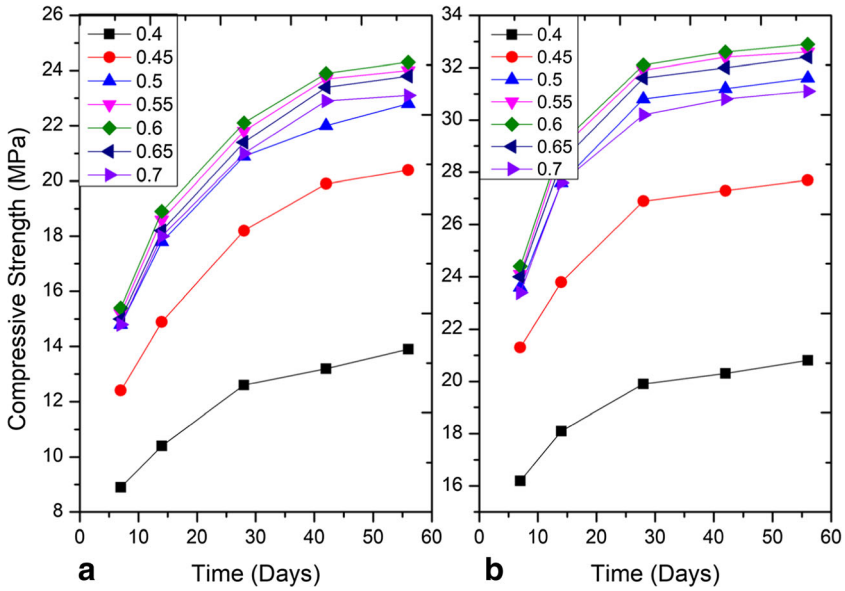

Fig. 14 Compressive strength of (**a**) ambient-cured GPC (**b**) oven-cured GPC

value increases with the increment of water content in the mix design, so the slump value increases consecutively with the increase of liquid-to-binder ratio in mixes of GPC. Similarly, the compaction factor value also increases with the increment of the liquid-to-binder ratio. Figure 11 describes the effect of the liquid-to-binder ratio on both slump value and compaction factor on the fresh mix of GPC. The workability of GPC increases with the increment of the alkaline solution/flyash ratio [70].

3.1.2 Density and Drying Shrinkage

The density and drying shrinkage of the concrete mix design shows the chemical properties of the GPC. The chemical reaction decides the density or unit weight and drying shrinkage of the GPC mix design. The density of ambient-cured GPC mix design specimens is higher compared to oven-cured specimens of the same mix designs. The density of GPC mix specimens decreases with the increment of the liquid-to-binder ratio. Figure 12 describes the variation of density with the variation of the liquid-to-binder ratio of both curing conditions. The drying shrinkage is created after the concrete's hardening due to the water's evaporation from the matrix. The drying shrinkage increases with the increment of the liquid-to-binder ratio in the GPC mix designs. The oven-cured GPC specimens show higher drying shrinkages than the ambient-cured specimens of the same mix designs. Figure 13 describes the behavior of drying shrinkage with the liquid-to-binder ratio in the design mix of GPC.

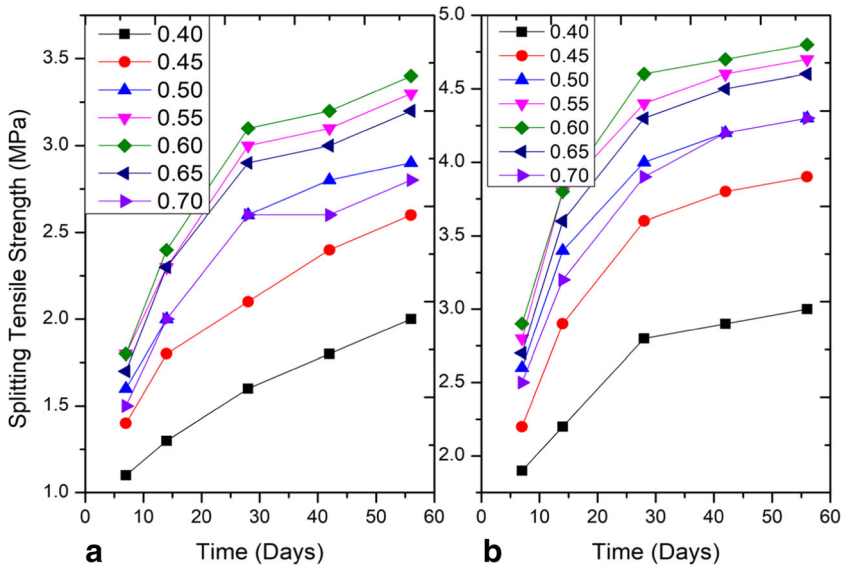

Fig. 15 Splitting tensile strength of (**a**) ambient-cured GPC (**b**) oven-cured GPC

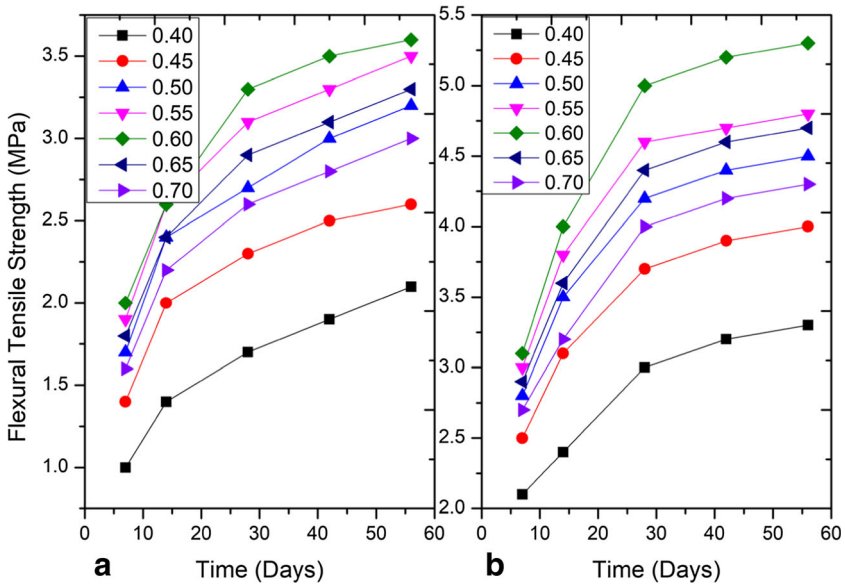

Fig. 16 Flexural Tensile Strength of (**a**) ambient-cured (**b**) oven-cured GPC

3.1.3 Compressive Strength

In the GPC mix design, the liquid-to-binder ratio plays a vital role in mechanical and durability properties. In the experimental investigation analysis, the liquid-to-binder ratio varies from 0.40 to 0.70 in the GGBFS flyash-based GPC. The compressive strength increases with the ratio's increment but beyond the 0.60 liquid-to-binder ratio decreases randomly in the mix samples. The oven-cured specimens got higher strength than the ambient-cured specimens of the same design mixes, but in both the curing condition, 0.60 liquid-to-binder ratios got the optimum compressive strength. Figure 14 describes the graph of compressive strength of different mixes of both curing conditions, in which; a) shows the ambient-cured GPC specimens, and b) shows the oven-cured GPC specimens. The compressive strength of specimens got around 85–90% and 95–98% in ambient-cured and oven-cured conditions, respectively.

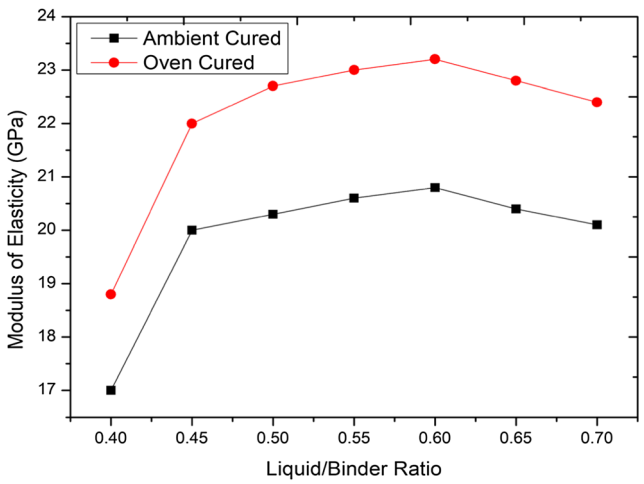

Fig. 17 Graph between Modulus of elasticity and liquid-to-binder ratio

3.1.4 Splitting Tensile and Flexural Strength

The splitting tensile measured by the statically load, applying the cylindrical sample along the UTM lateral dimension is an indirect tensile strength. The splitting tensile shows a similar strength compared to the mixed compressive strength in both curing conditions. The oven-cured specimens got higher strength compared to the ambient-cured specimens of the same design mixes. The optimum splitting tensile got at the 0.60 liquid-to-binder ratios in both curing conditions among all design mixes. Figure 15 describes the graph of splitting tensile of different design mixes in both curing conditions, in which a) shows the ambient-cured splitting tensile; and b) shows the oven-cured splitting tensile of the different GPC mix designs.

The flexural strength is used to examine the bending strength or property of the concrete. The flexural strength of GPC also has the same pattern as compressive strength, and it is around 12–18% of the compressive strength in all design mixes of GPC. The oven-cured specimens got higher flexural strength than ambient-cured for the same mix designs, and the mix design with 0.60 liquid-to-binder ratios got the optimum point of the strength. Figure 16 describes the flexural strength of the different mix designs of both curing conditions, whereas a) shows the ambient-cured strength, and b) shows the oven-cured strength of the GPC specimens.

3.1.5 Poisson's Ratio and Modulus of Elasticity

The Poisson's ratio and modulus of elasticity of the mix design measured by the testing on the cylinder specimens of size

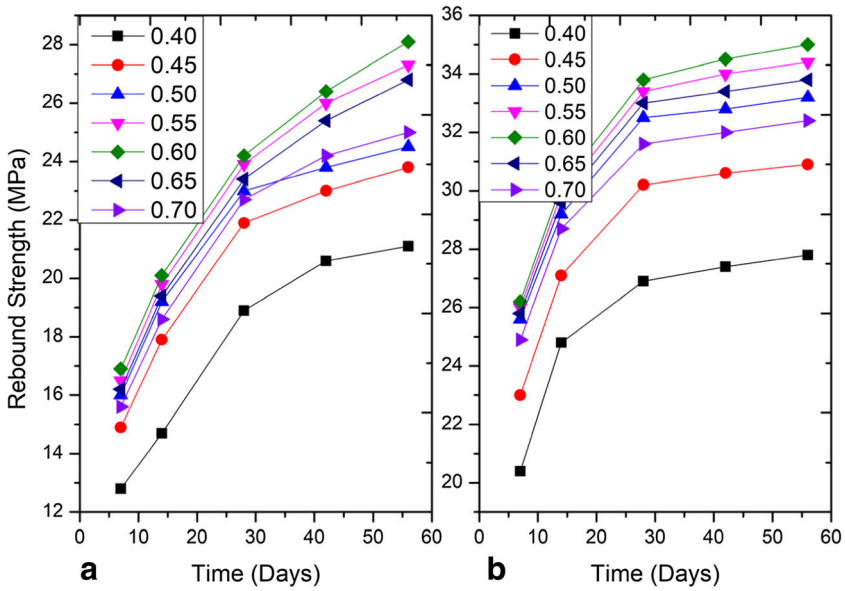

Fig. 18 Rebound strength of (**a**) ambient-cured (**b**) oven-cured GPC

length and diameter are 300 mm and 150 mm, respectively. The static load applies to the specimens along the vertical direction and measures the horizontal and vertical deformation for Poisson's ratio calculation. The modulus of elasticity of the mix design is calculated by the repetition load applying the cylindrical specimen of one-third crushing load statically and measures the elastic modulus by the secant modulus method. Figure 17 describes the graph of modulus of elasticity of both curing conditions at the different liquid-to-binder ratios in the mix designs.

3.1.6 Non-Destructive Test (Rebound Test and UPV Test)

The non-destructive test is used to check the strength or quality of the concrete specimen without destruction. It includes the rebound hammer test and UPV test. The rebound strength shows the similar compressive strength of the concrete specimens with a precision of 20% as per the IS code. It is based on the specimen's surface hardness gives the specimen strength, whereas the UPV test is used to find the strength or quality by measuring the time passage of the ultrasonic pulse wave. The time would be increasing with the reduction of quality or strength of the specimens. The crack develops inside the specimen also checked by the UPV test. Figure 18 describes the graph of rebound strength of different mixes of both cured samples, whereas a) shows the ambient-cured specimens rebound strength, and b) shows the oven-cured specimens rebound strength of the GPC. Figure 19 describes the UPV of the different

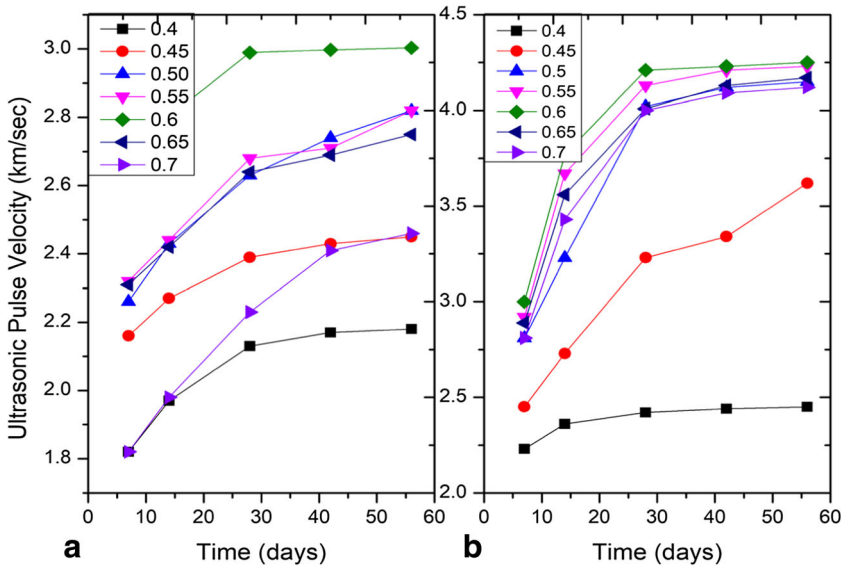

Fig. 19 Graph between the UPV and liquid-to-binder ratio (**a**) ambient-cured (**b**) oven-cured GPC

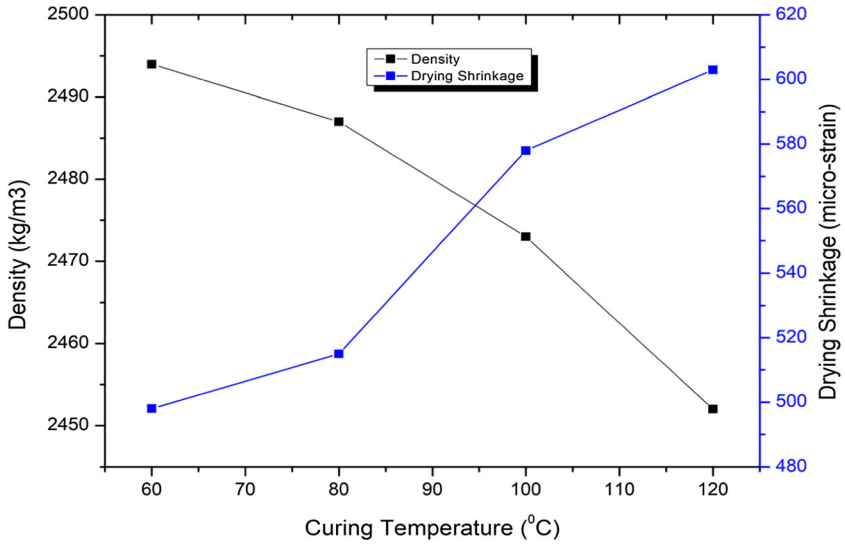

Fig. 20 Graph among the density, drying shrinkage, and curing temperature

mixes in both cured samples, whereas a) shows the ambient-cured specimens, and b) shows the oven-cured specimens of the GPC. The graph shows a similar pattern of the UPV to the rebound strength in both cured conditions. The optimum point of non-destructive strength got at the 0.60 liquid-to-binder ratios in the GPC mix design.

3.2 Effect of Curing Temperature

The curing temperature varies from 60 °C to 120 °C in the optimum GPC mix design. The chemical and mechanical properties of the GPC specimens would change with the variation of curing temperature. In the experimental analysis, to check the effect of curing temperature on the GPC mix design specimens.

3.2.1 Density and Drying Shrinkage

The density of the GPC mix specimens decreases with the increment of curing temperature. The drying shrinkage increases with the increment of curing temperature continuously from 60 °C to 120 °C. Figure 20 shows the graph of density and drying shrinkage variation with the curing temperature. The maximum drying shrinkage of GPC is 603 micro-strains at the 120 °C curing temperature.

3.2.2 Compressive Strength

The compressive strength of the GPC mix design increases with the increment of curing temperature, but it reduces beyond the 100 °C curing temperature. Figure 21 describes the variation of compressive strength with the different curing temperatures. It shows the GPC specimens cured at 100 °C

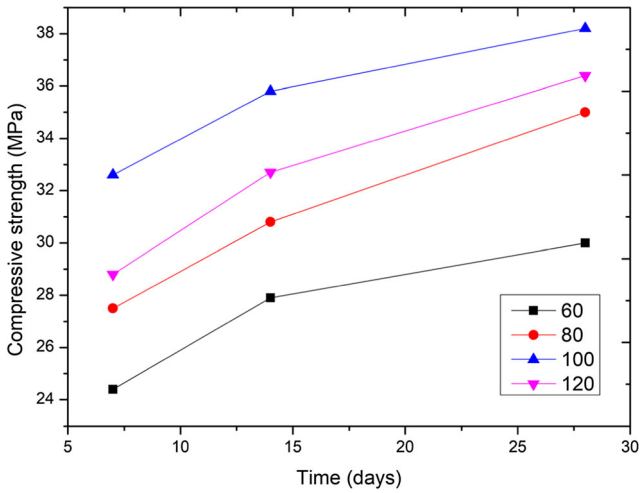

Fig. 21 Compressive strength of different temperature-cured GPC specimens

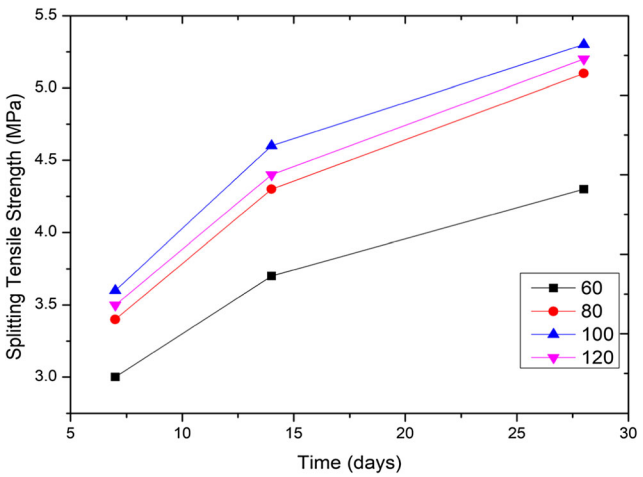

Fig. 22 Splitting tensile of different temperature-cured GPC specimens

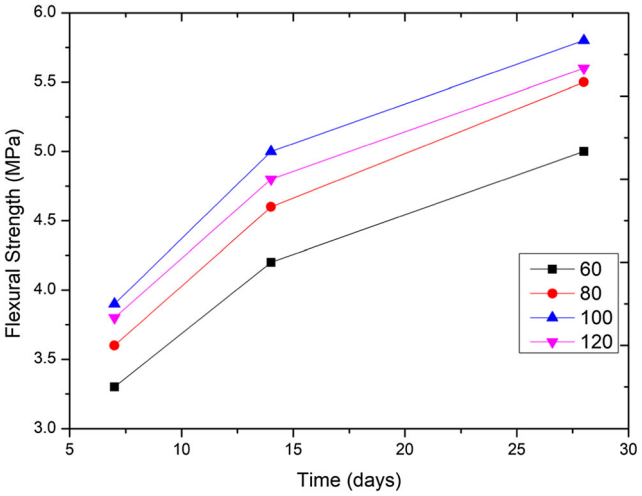

Fig. 23 Flexural strength of different temperature-cured GPC specimens

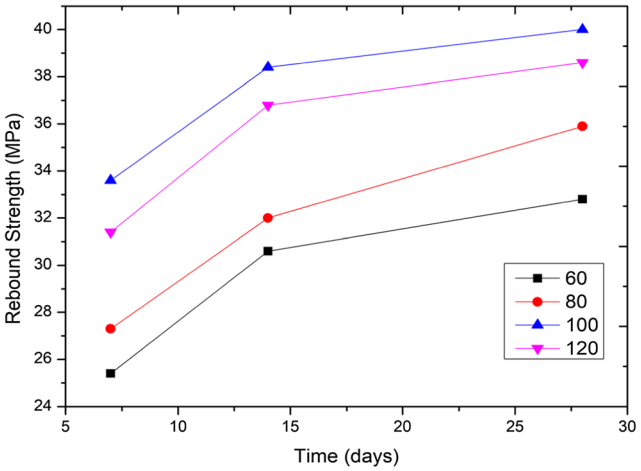

Fig. 25 Rebound strength variations with the curing temperature of GPC

got the maximum strength among all other curing temperatures. The maximum strength is 38.2 MPa at 28 days test, which is cured at 100 °C.

3.2.3 Splitting Tensile

The splitting tensile strength shows the concrete's indirect tensile, which is tested on the cylindrical specimens. The splitting tensile shows a similar pattern of strength compared to the compressive strength. The GPC specimens cured at 100 °C got the maximum strength among all other curing temperatures. The GPC specimens got the optimum point at 100 °C curing temperature, and the maximum splitting tensile is 5.3 MPa at 28 days test. Figure 22 shows the graph of splitting tensile of different temperature cured GPC specimens. The splitting tensile increases with the increment of temperature, but it reduces beyond the 100 °C curing temperature.

3.2.4 Flexural Strength

The flexural strength of the concrete shows the bending tensile strength of the specimens. The flexural strength shows a similar pattern to the compressive strength, and it got 15%–20% of the compressive of the GPC mix design. The GPC specimens got the optimum point of strength at 100 °C curing temperature. Figure 23 shows the graph of flexural strength of GPC mix at the different curing temperatures. The maximum flexural strength is 5.8 MPa at 28 days which is cured at 100 °C temperature.

3.2.5 Modulus of Elasticity

The modulus of elasticity of the concrete is an essential mechanical property of the mix design. It is calculated and tested on the cylindrical specimens as per the IS code. The modulus of elasticity directly depends on the compressive strength of the concrete. Figure 24 shows the variation of modulus of

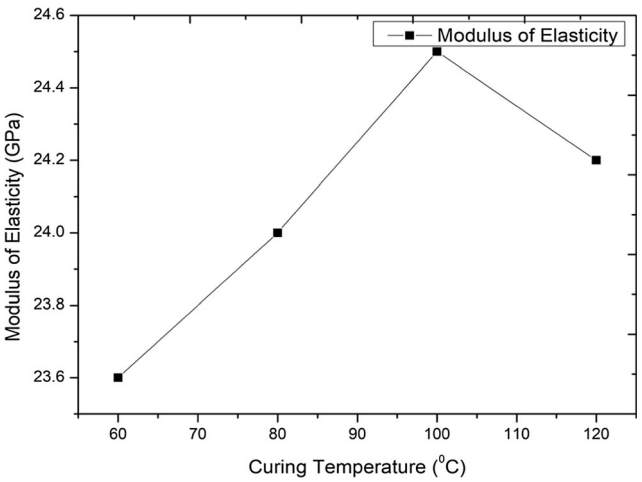

Fig. 24 Modulus of elasticity variations with the curing temperature

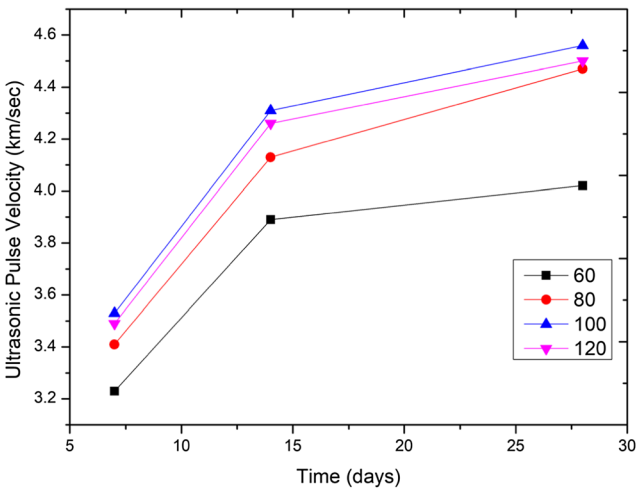

Fig. 26 UPV variation with the curing temperature of GPC

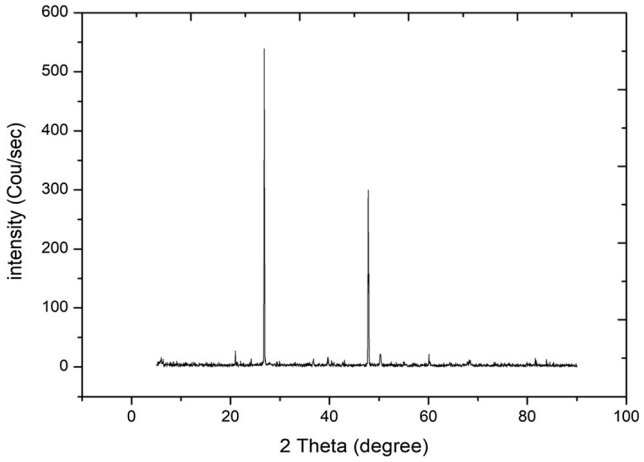

Fig. 27 XRD analysis graph of the GPC sample

elasticity with the curing temperature of the specimens. It increases with the increment of the curing temperature, but it reduces beyond the 100 °C curing temperature. The maximum modulus of elasticity is 24.5GPa at 28 days after the casting which is cured at 100 °C temperature.

3.2.6 Rebound Strength

The rebound hammer test is one of the non-destructive tests used for the strength check of the hard material's objectives. The rebound strength is based on the surface hardness of the objectives. It strikes on the surface of the specimens and gives the strength value without destruction of the specimens. Figure 25 shows the graph of the rebound strength of the GPC mix designs at various curing temperatures. It increases with the increment of curing temperature, but it reduces beyond the 100 °C curing temperature. It shows the 5–10% higher strength to the compressive strength of the mix specimens. The maximum rebound strength is 40 MPa at 28 days test which is cured at 100 °C temperature.

3.2.7 UPV Test

The UPV test is also one of the non-destructive tests for concrete specimens. It is based on the time passage reading of ultrasonic pulse waves through the objectives. The time passage of the ultrasonic pulse wave increases with the reduction of the objective strength or hardness. The UPV test easily checks the insides of the crack of the objective. The test was conducted on any size of the specimens. It is very useful in the real field of life for quality assessment of the structure. Figure 26 shows the graph of UPV variations with the curing temperatures. The UPV increases with the increment of curing temperature, but it reduces beyond the 100 °C curing temperature. The maximum UPV is 4.56 km/s at 28 days which is cured at 100 °C temperature.

3.3 Microstructural Analysis

3.3.1 X-Ray Diffraction

XRD is used to analyze the crystalline mineral oxides present in the materials. XRD shows the intensity of the oxides present in the samples described in the graphical forms. Figure **27** shows the XRD graph of the oven-cured at 100 °C of the GPC specimen. It clearly shows the peak of alumina-silicate oxides in the graph.

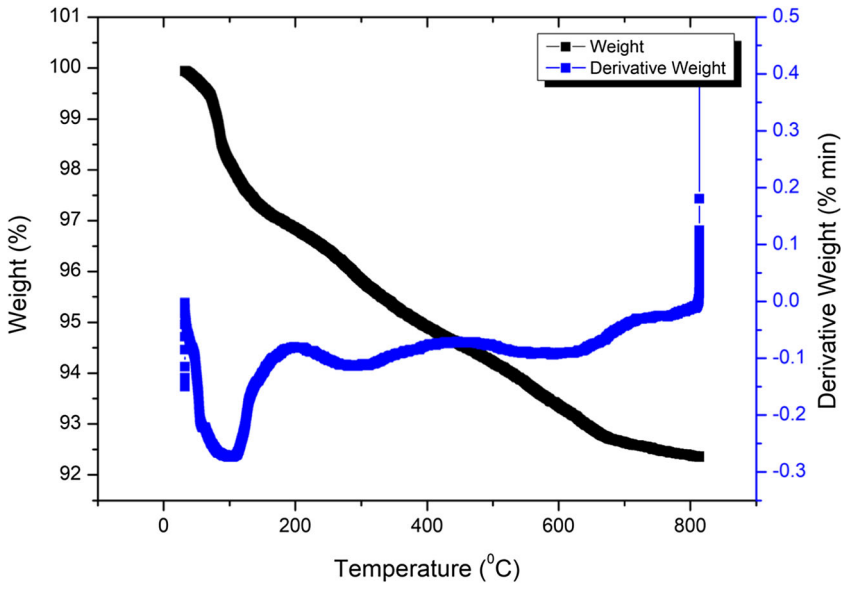

Fig. 28 TGA-DTG Graph of the GPC

Table 2 Mix Proportion

Mix Design	Liquid/Binder Ratio	Fly ash (kg/m^3)	GGBFS (kg/m^3)	Coarse Aggregate (kg/m^3)	Fine Aggregate (kg/m^3)	NaOH Solution (kg/m^3)	Sodium Silicate (kg/m^3)	Extra water (kg/m^3)
M1	0.4	303.75	101.25	1269	683	81.0 (13 M)	81.0	0
M2	0.45	303.75	101.25	1269	683	81.0 (13 M)	81.0	20.25
M3	0.50	303.75	101.25	1269	683	81.0 (13 M)	81.0	40.5
M4	0.55	303.75	101.25	1269	683	81.0 (13 M)	81.0	60.75
M5	0.60	303.75	101.25	1269	683	81.0 (13 M)	81.0	81
M6	0.65	303.75	101.25	1269	683	81.0 (13 M)	81.0	101.25
M7	0.70	303.75	101.25	1269	683	81.0 (13 M)	81.0	121.5

3.3.2 Thermo Gravimetric Analysis

Thermogravimetric analysis is used for the thermal stability of the material. The temperature increases with 10 °C/min in the machine and checks the material's weight with the various temperatures. Figure 28 shows the TGA and DTG graph of the GPC sample cured at 100 °C in the oven. It shows that the GPC sample retained up to 92% weight after the 850 °C. Initially, the weight loses around 4% up to the 200 °C and loses the weight of another 4% up to the 850 °C. Initially, the sample loses water hygroscopic water from the sample, and after, it loses the capillary water with the temperature. The DTG graph shows that the rate of water loss with temperature increment. The rate of derivative weight is initially high up to the 100 °C temperature.

4 Conclusion

The result concludes as per the experimental analysis of the GPC samples in various phases. It includes the physical properties test, chemical properties test; mechanical properties test, non-destructive test, and microstructural analysis are as follows:

- The compressive strength, splitting tensile and flexural strength got the optimum point at the 0.60 liquid-to-binder ratios in the GPC mix design. The strength increases with the increment of the liquid-to-binder ratio, but it reduces randomly beyond the 0.60 ratios. The workability of the GPC fresh mixes increases with the increment of liquid-to-binder ratio, whereas the density decreases consecutively with the increment of ratio.
- The drying shrinkage of the GPC mix specimens increases with the increment of liquid-to binder ratio, whereas the modulus of elasticity increases with the increment of ratio, but it reduces beyond the 0.60 ratios. The non-destructive test result shows similar results to the destructive test in which the rebound test shows the 5–10% higher strength to the compressive strength.
- The GPC design mix's mechanical strength increases with the curing temperature increment, but it reduces beyond the 100 °C curing temperature. The higher curing temperature increases the rate of gain strength of the GPC samples.
- The GPC specimen density decreases continuously with the increment curing temperature, whereas the drying shrinkage increases with curing temperature increment. The non-destructive test shows similar results to the compressive strength of the GPC specimens.
- The thermal stability of the GPC sample is higher up to the 850 °C temperature. It retained the weight of around 92% of the original at the 850 °C temperature. The XRD analysis shows the mineral oxide's clear intensity in the GPC sample, which is cured at the 100 °C temperature.

Acknowledgments This work is supported by the Civil Engineering Department, Delhi Technological University. Moreover, Sandeep Mishra's help for XRD analysis and Ankesh Kumar and Jawed Alam for another work related to the central instrumentation facility of the Delhi Technological University.

Funding Statement This study was funded by the Delhi Technological University, Delhi, India.

Author Contribution All authors have participated in (a) conception and design, or analysis and interpretation of the data; (b) drafting the article or revising it critically for valuable intellectual content; and (c) approval of the final version.

Data Availability The available data had been used and discussed in the manuscript.

Declarations This manuscript has not been submitted to, nor is under review at, another journal or other publishing venue.

Consent to Participate As a corresponding author or on behalf of all authors of the research paper, I consent to participate.

Consent to Publication All author of the research paper is consent to the publication.

Conflict of Interest There are no conflicts of interest or competing interests in this article.

Abbreviation *GPC,* Geopolymer Concrete; *GGBFS,* Ground Granulated Blast Furnace Slag; *NaOH,* Sodium hydroxide; Na_2SiO_3, Sodium silicate; *XRD,* X-ray diffraction; *SEM,* Scanning electronic microscope; *EDS,* Energy-dispersive X-ray spectroscopy; *OPC,* Ordinary Portland cement; *PCE,* Poly-carboxylate ester; *SNF,* Sulphonated naphthalene formaldehyde; *CSH,* Calcium silicate hydrate; *UPV,* Ultrasonic pulse velocity; *ASTM,* American standard testing materials; *TGA,* Thermogravimetric analysis; *LBR,* Liquid-to-binder ratio; *FLGC,* Flyash-based lightweight geopolymer concrete

References

1. Hassan A, Arif M, Shariq M (2019) Use of geopolymer concrete for a cleaner and sustainable environment e a review of mechanical properties and microstructure. J Clean Prod 223:704–728
2. Verma M, Dev N (2018) Geopolymer concrete : a way of sustainable construction. Int J Recent Res Asp 5(1):201–205
3. Davidovits J, Quentin S (1991) GEOPOLYMERS inorganic polymeric new materials. J Thamal Anal 37:1633–1656
4. Albitar M, Visintin P, Ali MSM, Drechsler M, Mohamed Ali MS, Drechsler M (2015) Assessing behaviour of fresh and hardened Geopolymer concrete mixed with class-F Fly ash. KSCE J Civ Eng 19:1445–1455
5. Kong DLY, Sanjayan JG, Sagoe-Crentsil K (2007) Comparative performance of geopolymers made with metakaolin and fly ash after exposure to elevated temperatures. Cem Concr Res 37: 1583–1589
6. Duxson P, Provis JL, Lukey GC, Mallicoat SW, Kriven WM, van Deventer JSJ (2005) Understanding the relationship between geopolymer composition, microstructure and mechanical properties. Colloids Surfaces A Physicochem Eng Asp 269:47–58
7. Davidovits J 30 Years of Successes and Failures in Geopolymer Applications. Market Trends and Potential Breakthroughs
8. Chindaprasirt P, Chareerat T, Sirivivatnanon V (2007) Workability and strength of coarse high calcium fly ash geopolymer. Cem Concr Compos 29:224–229
9. Li Y, Shen L, Mirmoghtadaei R, Ai L (2019) Advances in Civil Engineering Materials A Design of Experiment Approach to Study the Effects of Raw Material on the Performance of Geopolymer Concrete A Design of Experiment Approach to Study the Effects of Raw Material on the Performance of Geopolymer Co, vol. 6, no. 1
10. Verma M; Dev N (2021) Effect of SNF-Based Superplasticizer on Physical, Mechanical and Thermal Properties of the Geopolymer Concrete, *Silicon*, pp. 1–11
11. Kumar S, Kumar R, Mehrotra SP (2010) Influence of granulated blast furnace slag on the reaction, structure and properties of flyash-based geopolymer. J Mater Sci 45:607–615
12. Brough AR, Holloway M, Sykes J, Atkinson A (2000) Sodium silicate-based alkali-activated slag mortars," Cem Concr Res
13. Brough AR, Atkinson A (2002) Sodium silicate-based, alkali-activated slag mortars Part I . Strength, hydration and microstructure. Cem Concr Res 32:865–879
14. Chi M, Huang R (2013) Binding mechanism and properties of alkali-activated fly ash/slag mortars. Constr Build Mater 40:291–298
15. Lee NK, Jang JG, Lee HK (2014) Cement & Concrete Composites Shrinkage characteristics of alkali-activated fly ash/slag paste and mortar at early ages. Cem Concr Compos 53:239–248
16. Yang K-H, Song J-K (2009) Workability loss and compressive strength development of Cementless mortars activated by combination of sodium silicate and sodium hydroxide, J Mater Civ Eng
17. Nagalia G, Park Y, Abolmaali A, Aswath P (2016) Compressive strength and microstructural properties of Fly ash–based Geopolymer concrete, J Mater Civ Eng
18. Ban CC, Ken PW, Ramli M (2015) Effect of sodium silicate and curing regime on properties of load bearing Geopolymer mortar block. J Mater Civ Eng:1–9
19. Sung G et al (2015) The mechanical properties of fly ash-based geopolymer concrete with alkaline activators. Constr Build Mater 47(2013):409–418
20. Lee NK, Lee HK (2013) Setting and mechanical properties of alkali-activated fly ash/slag concrete manufactured at room temperature. Constr Build Mater 47:1201–1209
21. Nagalia G, Park Y, Abolmaali A, Aswath P (2016) Compressive Strength and Microstructural Properties of Fly Ash – Based Geopolymer Concrete, vol. 28, no. 12, pp. 1–11
22. Hardjito D, Wallah SE (2004) On the development of Fly ash-based Geopolymer concrete, ACI Mater J, pp. 467–72
23. Topark-Ngarm P, Chindaprasirt P, Sata V, P. C. and V. Sata, Pattanapong Topark-Ngarm (2015) Setting time, strength, and bond of high-calcium Fly ash Geopolymer concrete. J Mater Civ Eng 27(2011):1–7
24. Patankar SV, Ghugal YM, Jamkar SS Effect of Concentration of Sodium Hydroxide and Degree of Heat Curing on Fly Ash-Based Geopolymer Mortar Effect of Concentration of Sodium Hydroxide and Degree of Heat Curing on Fly Ash-Based Geopolymer Mortar, no. January 2015, 2014
25. Verma M, Dev N (2020) Sodium hydroxide effect on the mechanical properties of flyash-slag based geopolymer concrete. Struct Concr:1–12
26. Yip CK, Lukey GC, Provis JL, van Deventer JSJ, Van Deventer JSJ (2008) Effect of calcium silicate sources on geopolymerisation. Cem Concr Res 38:554–564
27. Yip CK, Lukey GC, Van Deventer JSJ, Van Deventer JSJ (2005) The coexistence of geopolymeric gel and calcium silicate hydrate at the early stage of alkaline activation. Cem Concr Res 35:1688–1697
28. Verma M, Nigam M (2007) Mechanical behaviour of self compacting and self curing concrete. Int J Innov Res Sci Eng Technol 6(7):14361–14366
29. Verma M, Dev N (2017) Review on the effect of different parameters on the behavior of Geopolymer concrete. Int J Innov Res Sci Eng Technol 6(6):11276–11281
30. Duxson P *et al.* (2007) Geopolymer technology: the current state of the art, *J Mater Sci*, no. 4, pp. 2917–2933
31. Deb PS, Nath P, Sarker PK (2014) The effects of ground granulated blast-furnace slag blending with fly ash and activator content on the workability and strength properties of geopolymer concrete cured at ambient temperature. J Mater 62:32–39
32. Nagajothi S, Elavenil S (2018) Strength properties of geopolymer concrete using msand by assessing their mechanical characteristics. *ARPN J Eng Appl Sci* 13(July):4028–4041
33. Van Jaarsveld JGS, Van Deventer JSJ, Lukey GC (2002) The effect of composition and temperature on the properties of fly ash-and kaolinite-based geopolymers
34. Khater HM (2014) Studying the effect of thermal and acid exposure on alkali-activated slag geopolymer, *Adv Cem Res*, vol. 26, no. 1
35. Patankar SV, Ghugal YM, Jamkar SS (2014) Effect of concentration of sodium hydroxide and degree of heat curing on Fly ash-based Geopolymer mortar," Indian J Mater Sci

36. Rovnaník P, Al SO (2010) Effect of curing temperature on the development of the hard structure of metakaolin-based geopolymer. Constr Build Mater 24(7):1176–1183
37. Heah CY, Kamarudin H, Bakri AMMA, Binhussain M, Luqman M, Nizar IK, Ruzaidi CM, Liew YM (2011) Effect of curing profile on kaolin-based Geopolymers. Phys Procedia 22:305–311
38. Wang Y, Zheng T, Zheng X, Liu Y, Darkwa J, Zhou G (2020) Thermo-mechanical and moisture absorption properties of fly ash-based lightweight geopolymer concrete reinforced by polypropylene fibers. Constr Build Mater 251:118960
39. Lin TS *et al.* (2009) Thermal-mechanical properties of short carbon fiber reinforced geopolymer matrix composites subjected to the thermal load, *J Cent South Univ Technol (English Ed.*, pp. 881–886
40. Korniejenko K, Lin W-T, Šimonová H (2020) Mechanical Properties of Short Polymer Fiber-Reinforced Geopolymer Composites. *J Compos Sci* 4(3):128
41. Aygörmez Y, Canpolat O, Al-mashhadani MM, Uysal M (2020) Elevated temperature, freezing-thawing and wetting-drying effects on polypropylene fiber reinforced metakaolin based geopolymer composites, *Constr Build Mater*, vol. 235
42. ASTM International (2019) Standard Specification for Coal Fly Ash and Raw or Calcined Natural Pozzolan for Use, *C618–19*, pp. 1–5
43. Metals P-II (2016) Yearbook 2015, vol. 2015, no. 0712, pp. 1–10
44. Bureau of Indian Standard, "Specific Gravity, Density, Voids, Absorption and Bulking," *IS 2386 (Part III)*, vol. 2386, no. October 1963, 1997
45. Bureau of Indian Standard, "Particle Size and Shape," *Is 2386(Part I)*, vol. 2386, 1997
46. Bureau of Indian Standard, "Mechanical Properties," *IS 2386(Part IV)*, vol. 2386, no. March 1964, 1997
47. Bureau of Indian Standard, "Petrographic Examination," *Is 2386(Part VIII)*, vol. 2386, 1997
48. Bureau of Indian Standard, "Coarse and Fine Aggregate from Natural Sources for Concrete," *IS 383–1970*, no. 1997, pp. 1–20, 1997
49. Bureau of Indian Standard, "MEASURING MORTAR MAKING PROPERTIES OF FINE AGGREGATE," *IS 2386 (Part VI)*, vol. 2386, no. October 1963, 1997
50. Bureau of Indian Standard, "Estimation of Deleterious Materials and Organic Impurities," *IS 2386 (Part II)*, vol. 2386, no. October 1963, 1998
51. Bureau of Indian Standard, "Alkali Aggregate Reactivity," *IS 2386(Part VII)*, 1997
52. Bureau of Indian Standard, "Soundness," *IS 2386*, 1997
53. Lokuge W, Wilson A, Gunasekara C, Law DW, Setunge S (2018) Design of fly ash geopolymer concrete mix proportions using multivariate adaptive regression spline model. Constr Build Mater 166: 472–481
54. Venkataraman S, Venkatasubramani R, Rangan BV (2012) Modified guidelines for geopolymer concrete mix design using Indian standard MODIFIED GUIDELINES FOR GEOPOLYMER CONCRETE MIX. ASIAN J Civ Eng (BUILDING HOUSING) 13(3):353–364
55. Bureau of Indian Standard, "GENERAL REQUIREMENT FOR PAN MIXTURES FOR CONCRETE," *IS 12119–1987*, no. 1999, 1999
56. ASTM International, "Standard Test Method for Slump of Hydraulic-Cement Concrete 1," *C143/C143M − 15a*, pp. 6–9, 2019
57. Bureau of Indian Standard, "METHODS OF SAMPLING AND ANALYSIS OF CONCRETE," *IS 1199–1959*, no. 2004, 1959
58. ASTM International, "Standard Test Method for Density (Unit Weight), Yield, and Air Content (Gravimetric) of Concrete," *C138/C138M − 17a*, pp. 1–6, 2019
59. ASTM: C157/C157M-08, "Standard Test Method for Length Change of Hardened Hydraulic-Cement Mortar and Concrete," *ASTM Int.*, vol. 08, no. Reapproved, pp. 1–7, 2008
60. Bureau of Indian Standard, "METHODS OF TEST FOR STRENGTH OF CONCRETE," *IS 516–1959*, 2004
61. Bureau of Indian Standard, "SPLITTING TENSILE STRENGTH OF CONCRETE - METHOD OF TEST," *IS 5816 1999*, 1999
62. Bureau of Indian Standard, "SPECIFICATION FOR APPARATUS FOR FLEXURAL TESTING OF CONCRETE," *lS9399–1979*, no. 2004, 1979
63. ASTM International, "Standard Test Method for Static Modulus of Elasticity and Poisson 's Ratio of Concrete," *C469/C469M − 14*, pp. 1–5, 2019
64. Bureau of Indian Standards, "Method of non-destructive testing of concrete-methods of test Part 2: Rebound hammer," *Is 13311–2*, no. 2004, 1992
65. ASTM International, "Rebound Number of Hardened Concrete," *C805/C805M − 18*, no. 2019, pp. 2–4, 2002
66. ASTM International, "Standard Test Method for Pulse Velocity Through Concrete ASTM C 597," *C597–16*, p. 4, 2016
67. Bureau of Indian Standard, "Non-destructive testing of concrete methods of test Part 1: Ultrasonic pulse velocity," *IS 13311 (Part1) 1992*, no. 2004, 1992
68. ASTM International, "Identification of crystalline compounds in water-formed deposits by X-ray diffraction," 2014
69. ASTM International, "Standard test method forLoss-on-drying by Thermogravimetry," *E2550–17*, vol. 11, no. 2019, pp. 1–6, 1868
70. M. S. and S. T. C. Antony Jeyasehar, G. Saravanan, "Development of fly ash based GEOPOLYMER precast concrete elements," ASIAN J Civ Eng, vol. 14, no. 4, pp. 605–615, 2013

Publisher's Note Springer Nature remains neutral with regard to jurisdictional claims in published maps and institutional affiliations.

Indian Geotech J
https://doi.org/10.1007/s40098-021-00505-y

ORIGINAL PAPER

Effect of Specimen Preparation Technique on the Post-Liquefaction Behaviour of Fine Sand Under Cyclic Loading

Arpit Jain[1] · **Satyendra Mittal**[1] · **Sanjay Kumar Shukla**[2,3]

Received: 16 September 2020 / Accepted: 28 January 2021
© Indian Geotechnical Society 2021

Abstract Understanding the post-liquefaction behaviour of fine sand helps estimate the stress–strain behaviour and deformations after the occurrence of an earthquake. Several research studies have been conducted to analyse the post-liquefaction behaviour of soil incorporating numerous factors such as relative density, origin/formation of soil, loading intensity and type of loading. The specimen preparation technique has also been found to replicate the fabric characteristics of soils that originated from rivers, offshores, wind or other agencies. In the present study, a comparison between specimens prepared through air pluviation and water sedimentation techniques has been presented for the analysis of post-liquefaction behaviour. The fine sand was collected from the Solani river, Roorkee, India, which is categorized in a high-risk earthquake zone. Strain-controlled cyclic triaxial tests were performed under undrained conditions for two different amplitudes of 0.4 mm and 0.6 mm. To simulate the earthquake aftershocks, multi-staged cyclic loading was applied to the undrained reconsolidated specimens. The results show that the maximum stress carried by the specimens constituted through the water sedimentation technique is 20% more than the air pluviated one during the final stage of the post-liquefaction. The liquefaction resistance is observed in the further rounds of loading. This study has been carried out for two different specimen preparation techniques where the cyclic stress ratio, pore water pressure and stress–strain behaviour have been compared. Through this study, the effect of strain on the post-liquefaction behaviour of fine sand can be understood for the two different soil fabrics formed through the different techniques used.

Keywords Post-liquefaction · Strain-controlled · Cyclic triaxial · Soil fabric · Cyclic stress ratio

✉ Arpit Jain
arpitjaintkg@gmail.com

Satyendra Mittal
satyendramittal@gmail.com

Sanjay Kumar Shukla
sanjaykshukla1@gmail.com; s.shukla@ecu.edu.au

[1] Department of Civil Engineering, Indian Institute of Technology, Roorkee, Uttarakhand, India

[2] School of Engineering, Edith Cowan University, Joondalup, Perth, Australia

[3] Department of Civil Engineering, Delhi Technological University, Delhi, India

Introduction

Soil failures during the Fukui earthquake (1948) in Japan, caused by soil liquefaction in which the soil under undrained conditions, in presence of repeated destabilizing forces of an earthquake, loss its strength [1]. The severity of the earthquake was visible in Niigata (1964) where the damages were significant even after the occurrence of the earthquakes [2]. Ishihara [3] discussed the post-seismic analysis of soil where residual strength was the important parameter to demarcate flow and no flow situation. Using the data of pre- and post-seismic activity, Hamada et al. [4] developed a finite-element technique to predict the magnitude and the direction of the displacement induced by seismic liquefaction. The aftermath of liquefaction can be disastrous due to slope failures and settlements, as observed by many researchers [5–7] for the post-liquefaction failures. Kokusho [8] observed the post-liquefaction failure in terms of settlements and slope failures. All the events provided a clear mindset to investigate the post-

Published online: 14 February 2021

liquefied state of soil for suitable remedial measures. The various agencies like wind, rivers and glaciers are responsible to constitute a soil stratum with a variety of soil fabrics. Also, the characteristics of soil fabric govern the stress–strain soil behaviour as observed by previous researchers. Ladd [9] depicted the importance of the method of specimen preparation where the cyclic undrained triaxial strength of cohesionless soil was observed for different techniques of specimen reconstitution. Mulinis et al. [10] carried out the fabric studies and electrical conductivity on the specimens prepared by moist tamping or moist vibratory compaction measurements that indicated the orientation and arrangement of contact between soil grains. In most cases, the dynamic strength of undisturbed specimens ranged from 0 to 45% higher than that of specimens prepared by moist tamping. Wood et al. [11] suggested the effect of depositional method on the liquefaction of the silty sand through undrained triaxial compression. Here, the specimen prepared through the water sedimentation (WS) technique exhibited completely stable behaviour than that of the dry funnel deposition (DFD) due to temporary liquefaction (period of decreasing stress difference with the axial strain; [30, 31]). This was due to the presence of a higher percentage of potentially unstable and compressible grain contact in DFD than that in the WS specimens. The experimental studies conducted by Tsukamoto et al. [14], Vaid and Sivathayalan [15] and Vaid et al. [16] supported the concept where water sedimentation method can properly generate the soil fabric of natural deposits, such as sea beach, coastal dune, and river deposits. Tatsuoka et al. [17] showed the effect of sample preparation methods on cyclic undrained stress–strain behaviour of sands using triaxial and torsional shear tests. Using the cyclic undrained behaviour, a new density index was proposed by authors from which the cyclic undrained behaviour could be estimated for different specimen preparation methods. When the soil specimens are formed through the action of gravity, it inherently acquires an anisotropic fabric as observed by Oda [18], Arthur and Menzies [19] and Ishihara and Okada [20]. Wanatowski and Chu [21] obtained the experimental results to study the effect of the specimen preparation method on the stress–strain behaviour of sand in plane-strain compression tests. Della et al. [22] performed a series of drained and undrained monotonic triaxial compression tests to observe the influence of the specimen preparation methods. The significant differences were observed for the liquefaction characteristics of soil where the changes in soil fabric were the reason for this variation. Gade and Saka [23] developed a mechanized travelling pluviator to understand the effect of sieves, deposition intensity and height of fall on the relative density and uniformity of sand specimens. Kodicherla et al. [24] studied the inherent soil fabric anisotropy and packing density of reconstituted sand for different specimen preparation techniques like dry tamping, moist tamping, dry pluviation and wet pluviation. The fabric characteristics of soil anisotropy were quantified using an image analysis approach where dry pluviation possesses higher inherent fabric anisotropy than others. This study is helpful in the preparation of large, uniform sand beds. Kwan [25] presented a review of sand reconstitution methods used for soil strength characterization using simple shear tests. The detailed study of Oda and Koishikawa [26] on the fabrics of undisturbed samples from rivers, sea beaches, and coastal dunes showed that the anisotropicity of soil fabric is due to the parallel alignments of particles. The degree of anisotropic behaviour can be predicted through the particle shape and deposition manner in natural sand grounds. Sze and Yang [27] investigated the impact of specimen preparation on the deformation pattern, pore-water pressure generation, stress–strain relationship and cyclic shear strength of saturated sand by performing a series of cyclic triaxial tests. To correlate the behaviour of laboratory reconstituted specimens to in situ soil response, Kiyota et al. [28] performed a undrained cyclic triaxial test to investigate the effect of density with changes in the soil fabric characteristics and proposed a method to evaluate the in situ liquefaction resistance based on the in situ and laboratory-measured shear wave velocities. The results showed that the different specimen reconstitution methods had limited effects on the shear behaviour in monotonic loading tests. Even small quakes after liquefaction can cause significant damages to engineered structures. To understand the stress–strain behaviour of sand at post-liquefied state, Hussain and Sachan [29] performed strain-controlled cyclic triaxial tests under undrained conditions. The multi-stage cyclic loading was provided after reconsolidation at an amplitude of 0.4 mm to simulate the aftershocks of the earthquake. Sriskandakumar et al. [30] performed the constant-volume direct shear tests on Fraser river sand, and the multiple cyclic loading was provided to simulate the effect of pre- and post-liquefaction. Here, the cyclic loading was terminated at a predetermined r_u (pore pressure ratio) level and the specimen reconsolidated for another round of cyclic loadings.

In the previous studies, the effect of specimen reconstitution was observed on the liquefaction characteristics mostly at liquefied stages but there exists a limited understanding of the post-liquefaction behaviour of soil corresponding to the different patterns of fabrics. This study presents significant outcomes for the post-liquefaction soil behaviour at different fabric characteristics using two different specimen preparation techniques. A series of undrained cyclic triaxial tests were performed on the specimens prepared using two different specimen preparation techniques, viz. water sedimentation (WS) and air

pluviation (AP) techniques. Two different amplitudes, 0.4 mm and 0.6 mm, were considered for the strain-controlled undrained cyclic triaxial tests. The multi-stage loading after suitable reconsolidation had been carried out for the aftershocks.

Materials and Methods

The fine sand used for the current study was collected from the Solani river. The properties of sand are shown in Table 1. The sand was classified as the poorly grade sand (SP) as per the Indian classification system [31]. Figure 1 shows the image of the material used. Based on field evidence, Kramer [2] categorized the poorly graded sand as liquefaction susceptible. Solani river sand used is poorly graded and hence vulnerable to liquefaction. Figure 2 shows the grain size distribution of Solani river sand. After combining the curve with the well known upper and lower limit of liquefaction, Solani sand falls in between, showing its vulnerability towards liquefaction.

Strain-controlled cyclic triaxial tests were performed on the fine sand under undrained conditions at a frequency of 0.1 Hz. The dominant frequency of seismic waves for small to large earthquakes ranges from 0.1 Hz to 1.5 Hz [32]. The specimens were prepared using water sedimentation (WS) and air pluviation (AP) techniques to impart variability in soil fabric. In the air pluviation technique, a conical funnel was used for the soil deposition, and the specimen was formed through five different layers of sand. After maintaining a constant fall height, a vertical tube connected to the conical funnel was raised continuously at the centre of the split. To obtain the required density, a gentle tapping was provided in a symmetric pattern. The second technique of water sedimentation was adopted to replicate the soil conditions in nearby rivers. Here, a calculated amount of dry sand was poured into the de-aired still water present inside the mould, under the desired density. Chaney and Mulinis [33] suggested the wet-raining preparation method for remoulding specimens by a sedimentation process and mentioned that this method may give the fabric replicating the natural alluvium environment more closely. The microscopic examination was performed by Oda et al. [34] on oven-dried sand prepared through a funnel. Here, the particle arrangements are very similar to that of in situ sand grounds such as river sand deposits. Figure 3 shows images of two different techniques used in the study. All the tests were performed at a relative density of 30% to replicate the loose condition of soil strata.

Fig. 1 Fine sand

After mounting the specimens, CO_2 was applied for 30 min to attain the optimal saturation and then water flushing was carried out. The saturation was attained by checking the B-factor (Skempton's coefficient) above 0.95. It was achieved at different combinations of confining pressure and backpressure with an increment of 20 kPa in 30 min. Then, specimens were isotropically consolidated at an effective confining pressure of 100 kPa. Before deciding the amplitude of strain-controlled mechanism, strain rate of 0.05%, 0.2%, 0.5% and 1% was provided. After observing the significant variations in pore pressure ratio, deviator stress at the amplitudes of 0.4 mm (0.28% strain rate) and 0.6 mm (0.43% strain rate), the two values were adopted. At a very low strain-rate, the variation in parameters was insignificant while at a strain rate higher than 0.5% failure was too quick to reach. Hussain and Sachan [32] also adopted an amplitude of 0.4 mm at a frequency of 0.1 Hz where the soil specimens were of SP and SP-SM type. Yamamuro and Lade [12, 13] considered the axial strain rate between 0.2 and 1% axial strain. To finalize the no. of cycles provided, the changes in pore pressure ratio vs. time, deviator stress vs. strain were observed for both the pre- and post-liquefied states. Firstly, 100 cycles were provided, but the pattern was not useful after 50 cycles. Hussain and sachan [32] considered the same 50 cycles for all the specimens. Also, to maintain the uniformity, 50 cycles were considered.

Table 1 Material used in the study

Soil type	Mean particle size (D_{50})	Coefficient of uniformity	Specific gravity	Maximum void ratio (e_{max})	Minimum void ratio (e_{min})
Fine sand (SP)	0.20 mm	1.95	2.65	0.88	0.57

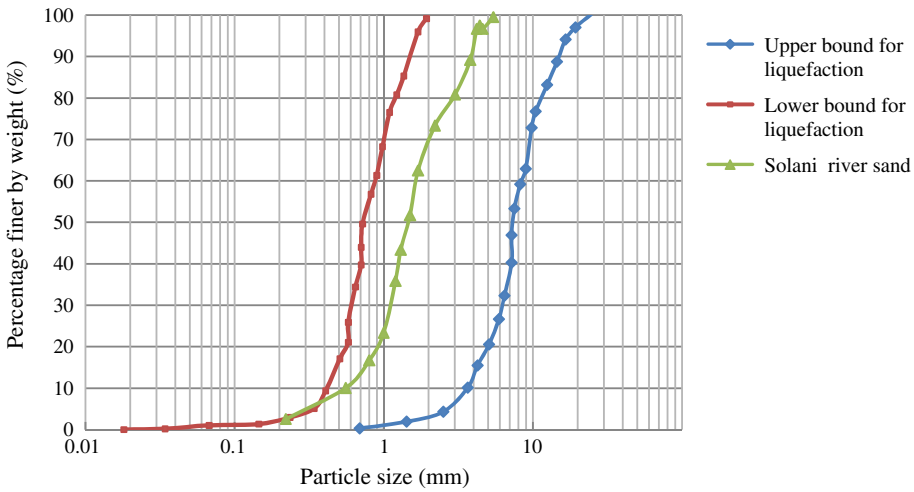

Fig. 2 Particle size distribution curve of Solani sand with upper and lower bound of liquefaction

(a) Air pluviation **(b)** Water sedimentation

Fig. 3 Specimen preparation

In this study, the amplitudes of displacement were taken as 0.4 mm and 0.6 mm for the two different specimens preparation techniques, where 50 cycles were provided for the first stage of loading. After finishing pre-liquefaction, the generated excess pore water pressure was dissipated. The specimen was reconsolidated for further rounds of loading where 35 cycles were provided at the amplitude of 0.4 mm or 0.6 mm to replicate small quakes after the occurrence of an earthquake. A total of four post-liquefaction loading stages were considered for each specimen. Figure 4 shows the test pattern followed for the post-liquefaction study on each specimen. Table 2 shows the stage and varieties of tests performed.

Results and Discussion

The significance of soil fabric characteristics through a variety of specimen preparation techniques can be well understood from this study. Even under post-liquefaction state, two different soil fabrics affect the changes in pore pressure generation and *CSR* (cyclic stress ratio) for two different axial strain rates. Two different specimen preparation techniques, for example, water sedimentation (WS) and air pluviation (AP) have been adopted to ascertain the effect of fabric characteristics. Discussion regarding the prominent failure state of pre-liquefaction and post-liquefaction is presented in the following sections based on the results obtained from the undrained cyclic triaxial test.

Variation in Pore Pressure Ratio Along with the Time

Seed and Lee [35] defined the pore pressure ratio (r_u) as the ratio of increase in pore pressure to that of the effective confining pressure. When r_u reaches unity, it signifies the initiation of liquefaction.

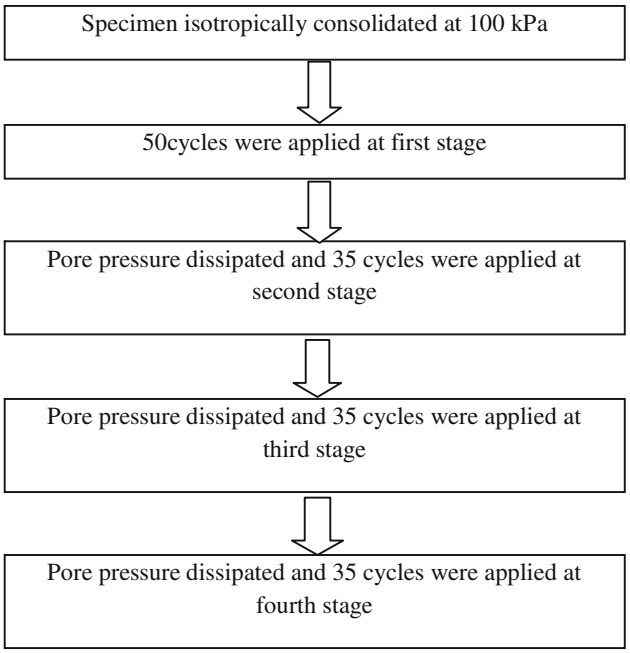

Fig.4 Test series followed for the specimen

Table 2 Details of the tests performed

Sl. no	Amplitude	Specimen preparation technique	Stages	Test code
1	0.4 mm	Air pluviation	Pre-liquefaction	AP1PL
2			Stage 1	AP1S1
3			Stage 2	AP1S2
4			Stage 3	AP1S3
5			Stage 4	AP1S4
6	0.4 mm	Water sedimentation	Pre-liquefaction	WS1PL
7			Stage 1	WS1S1
8			Stage 2	WS1S2
9			Stage 3	WS1S3
10			Stage 4	WS1S4
11	0.6 mm	Air pluviation	Pre-liquefaction	AP2PL
12			Stage 1	AP2S1
13			Stage 2	AP2S2
14			Stage 3	AP2S3
15			Stage 4	AP2S4
16	0.6 mm	Water sedimentation	Pre-liquefaction	WS2PL
17			Stage 1	WS2S1
18			Stage 2	WS2S2
19			Stage 3	WS2S3
20			Stage 4	WS2S4

$$r_u = \frac{\Delta u}{\sigma'_{3c}} (u = \text{Pore pressure}) \quad (1)$$

The stability and design problems in the engineering structures encountered using r_u where Seed [36] suggested the triggering of the liquefaction phenomenon. In this study, the initiation of liquefaction is considered when r_u reaches unity, in all of the specimens. Excess pore pressure has a significant role in the liquefaction phenomenon of the soil strata as previously studied and observed. The variety of fabrics formed through agencies like wind, river and others imparted the significant differences in pore pressure generation characteristics as explained in the earlier section.

Figure 5 shows the variation in excess pore pressure ratio (r_u) of the specimen reconstituted using the water sedimentation technique having staged cyclic loading at an amplitude of 0.4 mm. It can be observed that under post-liquefied staged loading conditions, as the stages increased, the generation of pore pressure was comparatively low. The reason behind the less development of excess pore pressure is the readjustment of sand particles, maintaining a more stable state due to a reduction in unstable particle contacts. The undrained situation prevailed in all of the stages where there was no change in volume. Meanwhile, the generated excess pore water pressure had dissipated before each loading stage. An exciting observation can be seen in Figs. 6 and 7 where the specimens were prepared using two different specimen preparation techniques and cyclically loaded at the same amplitude of 0.6 mm. After assessing these two figures, a difference in pore pressure generation even under post-liquefied stages can be ascertained. This unstable grain contact generated higher pore pressure through air pluviation than that of the WS technique which can be seen in Figs. 6 and 7.

As observed in Fig. 8, there exist three different phases of pore water pressure for pre- and post-liquefaction phenomenon. The first phase has fast and transient development of excess pore water pressure. As shown in Fig. 8, phase 1 finished in nearly 20 s for the AP specimens and 30 s for the specimen reconstituted through the water sedimentation technique. The second phase is the stable attainment of liquefaction as here the pore pressure ratio reaches unity with a stable pattern. The third phase is of post-liquefaction state, where the cyclic loading was provided after the dissipation of excess pore water pressure developed during phase 2. The pattern of normalized excess pore water pressure is different for two techniques due to the changes in fabric. The development of pore pressure was earlier in AP specimens than that of the WS ones.

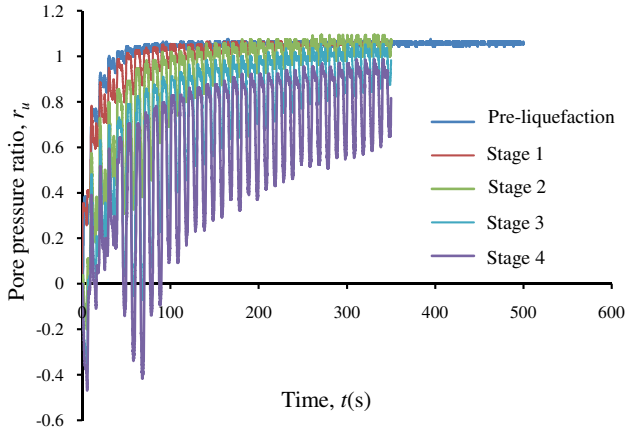

Fig. 5 Pore pressure ratio versus time variation at an amplitude of 0.4 mm for WS specimen

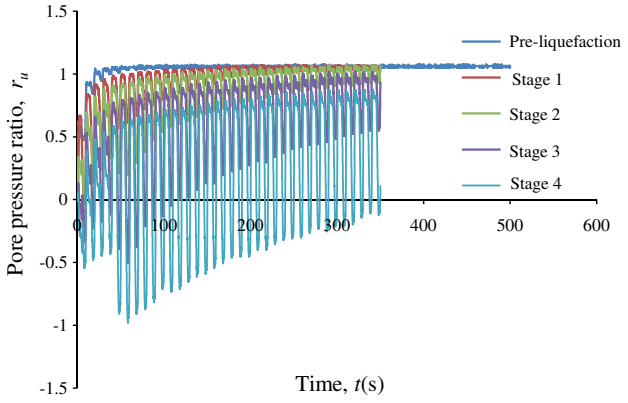

Fig. 7 Pore pressure ratio versus time variation at an amplitude of 0.6 mm for WS specimen

Variation in Deviator Stress Versus Axial Strain

A correlation between deviator stress and axial strain signifies the loading characteristics of the soil. To understand the impact of mode of soil formation on deviator stress, Figs. 9, 10, 11 and 12 are presented. These specimens are showing the results of pre-liquefaction conditions where two different amplitudes, 0.4 mm and 0.6 mm, were provided. The comparison for the deviator stress vs. strain plot can be observed for the two different specimen preparation techniques through Figs. 9 and 10, at an amplitude of 0.4 mm. The maximum deviator stress value for the AP technique here was 73.31 kPa but it was 98 kPa for the water sedimentation (WS) specimens. The rise in this value was due to the changes in soil fabric characteristics by two different specimen preparation techniques.

Ghionna and Porcino [37] compared the cyclic liquefaction resistant curves of specimens prepared through WS and AP techniques and observed that the AP method leads to lower in situ resistance values. The same conclusion can be drawn from Figs. 11 and 12 (stages AP2PL and WS2PL), where the maximum stress is taken by WS specimen as 103 kPa while it was 71 kPa for air pluviated specimen. Here, less resistance towards liquefaction was observed in AP specimens due to the presence of the higher amount of unstable particle contact.

After comparing Figs. 10 and 12, due to the increase in the amplitude from 0.4 mm to 0.6 mm, the value of maximum stress taken should decrease but this trend was not visible here. This might be due to the errors in specimen reconstitution or inconsistency in the experiment performed. Specimen WS1PL has the maximum stress of 98 kPa which enhances to the value of 103 kPa for specimen WS2PL.

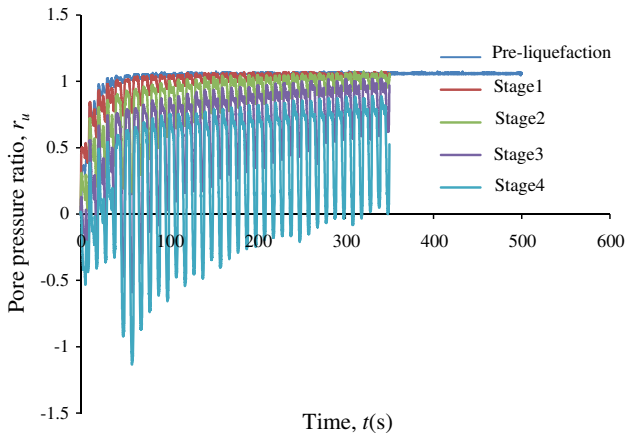

Fig. 6 Pore pressure ratio versus time variation at an amplitude of 0.6 mm for AP specimen

Deviator Stress Versus Time Variation for Pre- and Post-Liquefaction States

In this section, the progression of deviator stress has been discussed which reaches the highest value in its first cycle then starts diminishing due to the development of excess pore water pressure as shown in Fig. 13. A comparative study has been carried out between the two specimens reconstituted with water sedimentation and air pluviation techniques for both pre- and post-liquefied states. As the stages of post-liquefaction increase, the maximum stress taken by the specimen also increases. At stage AP2PL, the highest stress was 71 kPa which enhances to 208.50 kPa at the AP2S4 stage. The skeleton of the post-liquefied state is more stable. Due to the readjustment of grains, the share of unstable particle contact starts diminishing with the advancement in post-liquefied stages, which is only responsible to produce higher load-carrying capacity.

The experimental study of Zlatovic and Ishihara [38] reported that the liquefaction resistance was higher in specimens prepared by sedimentation technique than that of the dry funnel pluviation ones. This was due to the

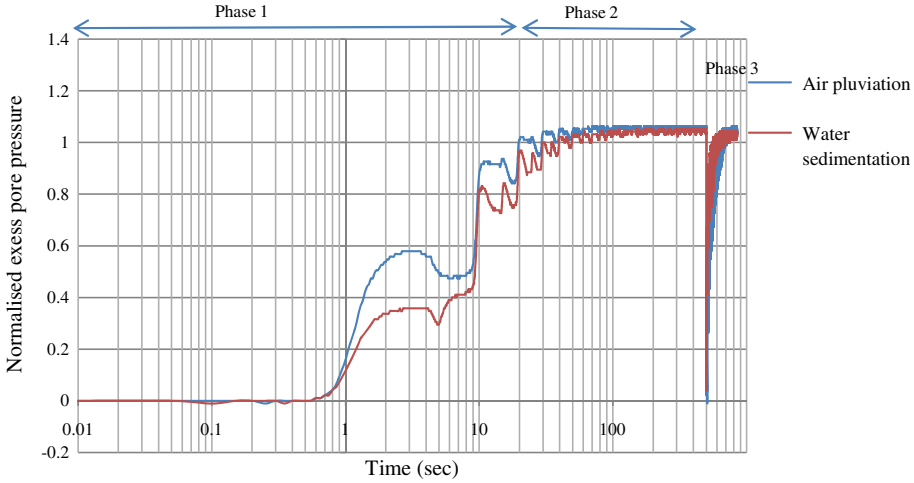

Fig. 8 Normalized excess pore pressure vs. time variation at an amplitude of 0.6 mm

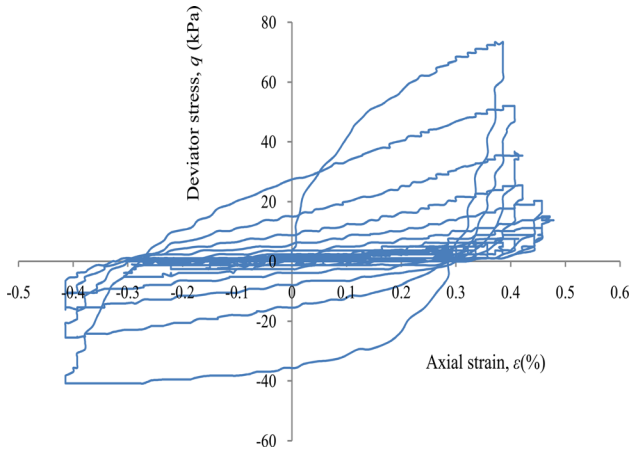

Fig. 9 Deviator stress versus axial strain variation at an amplitude of 0.4 mm for AP specimen

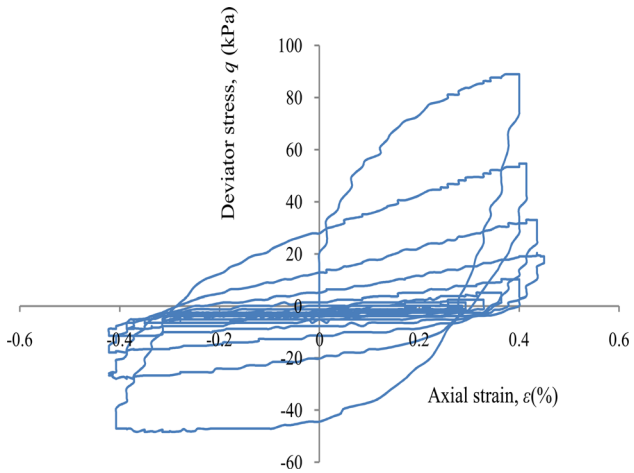

Fig. 10 Deviator stress versus axial strain variation at an amplitude of 0.4 mm for WS specimen

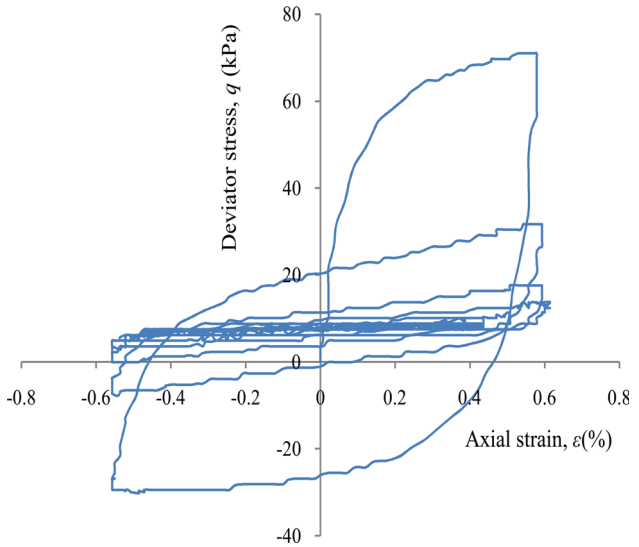

Fig. 11 Deviator stress versus axial strain variation at an amplitude of 0.6 mm for AP specimen

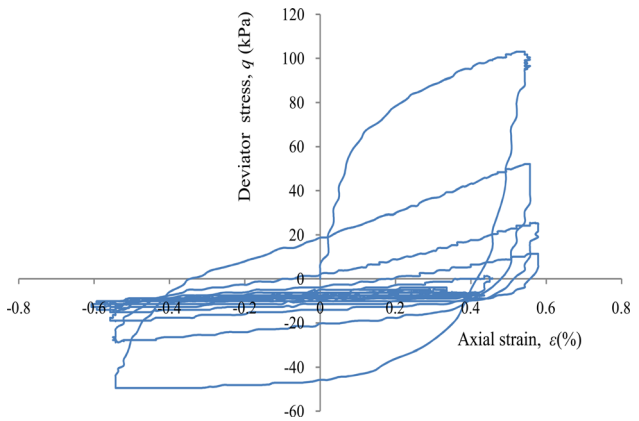

Fig. 12 Deviator stress versus axial strain variation at an amplitude of 0.6 mm for WS specimen

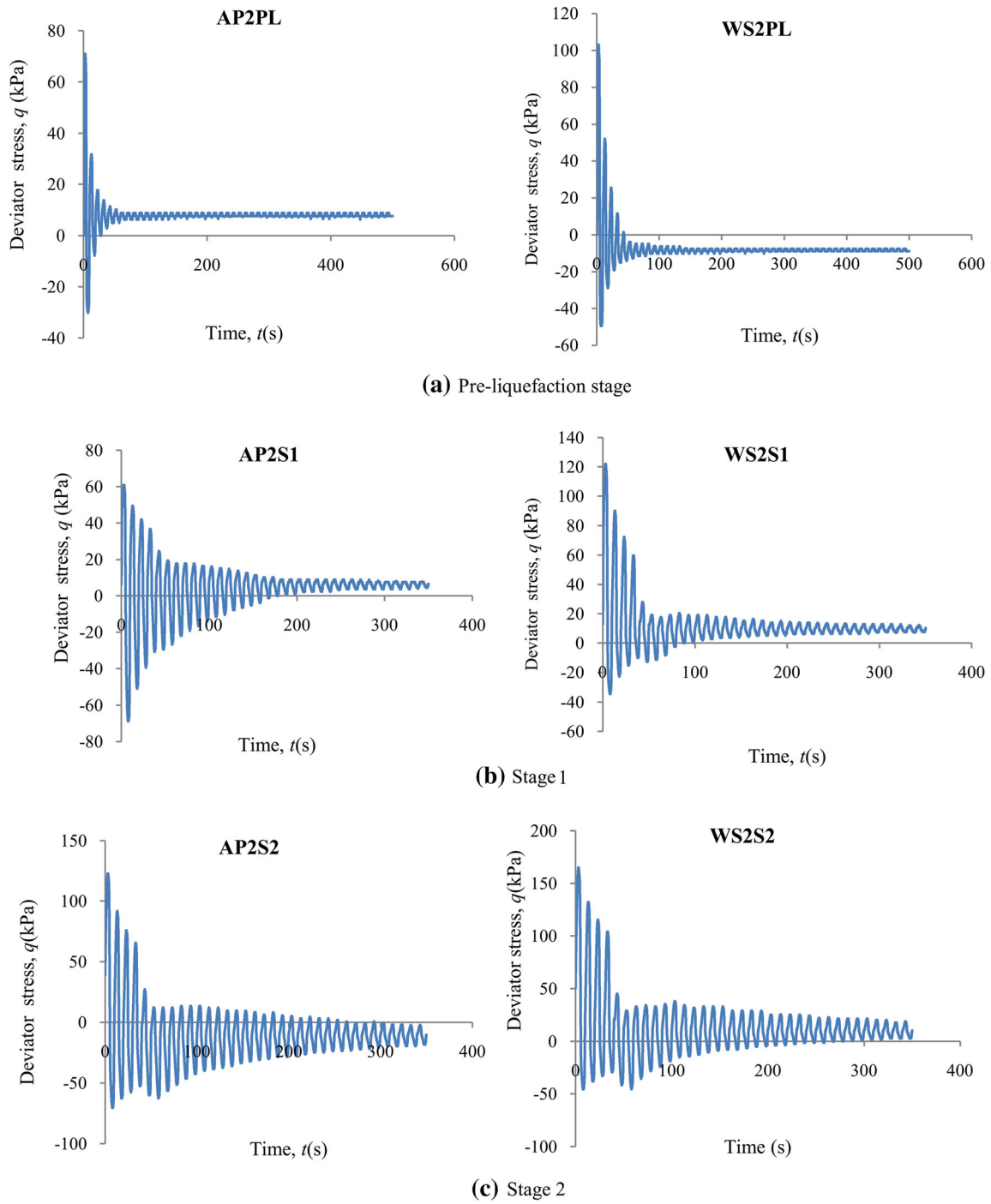

Fig. 13 Variation in deviator stress vs. time plot for the air pluviated and water sedimentated specimens, cyclically loaded at an amplitude of 0.6 mm under pre- and post-liquefied stage

higher percentage of unstable particles in the air pluviation process. This can be well understood through Table 3 where the deviator stresses are higher at all stages for WS prepared specimens. The same conclusion can be drawn from Fig. 13 also. One can certainly ensure the importance of specimen preparation techniques for both the pre- and post-liquefied stages, through these figures.

Mean Effective Stress Versus Deviator Stress Variation

The impact of specimen preparation technique on pre- and post-liquefaction can also be observed using effective stress paths under staged cyclic loading. As discussed in the earlier sections, post-liquefaction readjusts soil

Table 3 Pore pressure ratio (r_u) and load-carrying capacity

S.N	Test code	Max. stress (kPa)	PPR (r_u)
1	AP1PL	73.31	1.07
2	AP1S1	80.66	1.07
3	AP1S2	138.82	1.06
4	AP1S3	175.38	1.06
5	AP1S4	220.27	0.98
6	WS1PL	98.00	1.06
7	WS1S1	113.09	1.06
8	WS1S2	146.10	1.06
9	WS1S3	185.36	1.05
10	WS1S4	232.70	0.94
11	AP2PL	71	1.06
12	AP2S1	60.83	1.06
13	AP2S2	122.70	1.06
14	AP2S3	168.70	1.00
15	AP2S4	207.80	0.87
16	WS2PL	103.00	1.06
17	WS2S1	122.00	1.06
18	WS2S2	165.08	1.05
19	WS2S3	198.10	1.00
20	WS2S4	250.10	0.87

particles which cause the decrement in the effectiveness of unstable particles. In most of the research work, the behaviour of an unstable particle with fabric change has been observed on the pre-liquefaction. To look over the post-liquefaction behaviour more significantly, q (deviator stress) versus p' (mean effective stress) is presented in Figs. 14 and 15 for WS and AP specimens. Porcino et al. [39] and Srikandakumar et al. [22] observed the significant increment in liquefaction resistance under the post-liquefied state. Higher number of cycles were required to reach the state of liquefaction for the post-liquefaction state than that of the pre-liquefaction. In Fig. 14a, four cycles were required to diminish the p' value for the air pluviation technique. The mean effective stress was 22.6 kPa for stage WS2S4 even after 35 cycles as shown in Fig. 13b.

By using the epoxy impregnation and SEM imaging, Yamamuro et al. [40] suggested that the dry pluviation supports the specimen instability while this was absent in WS specimen. This concept seems to be applicable also at the post-liquefaction state, which can be observed by comparing Figs. 14b and 15b. Here, the highest value of p' was 165 kPa at stage WS2S4, while 136 kPa at stage AP2S4. This was only due to the changes in soil fabric characteristics and the variability in the effects of unstable particle contact.

Conclusions

The post-liquefaction soil behaviour has been studied by several researchers earlier, but through this work, one can certainly grasp an insight of picking up a suitable specimen preparation technique to replicate the natural conditions more closely. The significant effects of soil fabric structure on the pre- and post-liquefaction phenomena have been presented using the following key conclusions:

1. The generation of pore water pressure is observed to be higher in the specimens prepared using the water sedimentation technique (WS) as compared to that of the air pluviation (AP). In the last stage of post-liquefaction in WS specimen, the r_u value does not reach unity in a specific case but under the same loading condition, the AP specimen shows r_u value above 1 only due to the unique particle structural arrangement.
2. The instability caused by the unstable particle contact is found to be higher in AP specimens than that in WS specimens. Thus, the maximum stress taken by AP specimen was about 208 kPa while it was 250 kPa for the specimens constituted through water sedimentation.
3. Due to the changes in particle structure, the mean effective stress for the WS specimen is 1.21 times higher than that of the AP specimen. This is due to the fact that larger share of unstable particles reside in the fabric structure of AP specimens. Researchers can perform several experiments to observe the changes in the microscopic structure of soil fabric using the SEM (electron microscopy) analysis.
4. The maximum deviator stress at stage WS2S4 is 19% higher than that of stage AP2S4 because as the stages of post-liquefaction increase, the stability of a specimen also increases. This is mainly due to the readjustment of particle structure causing the ineffective share of unstable particles.
5. For successful engineering practices, it is important to replicate the natural soil conditions more closely using the suitable specimen preparation technique. This may help in studying the pre- and post-liquefaction failures of slopes, foundations, bridges, etc.

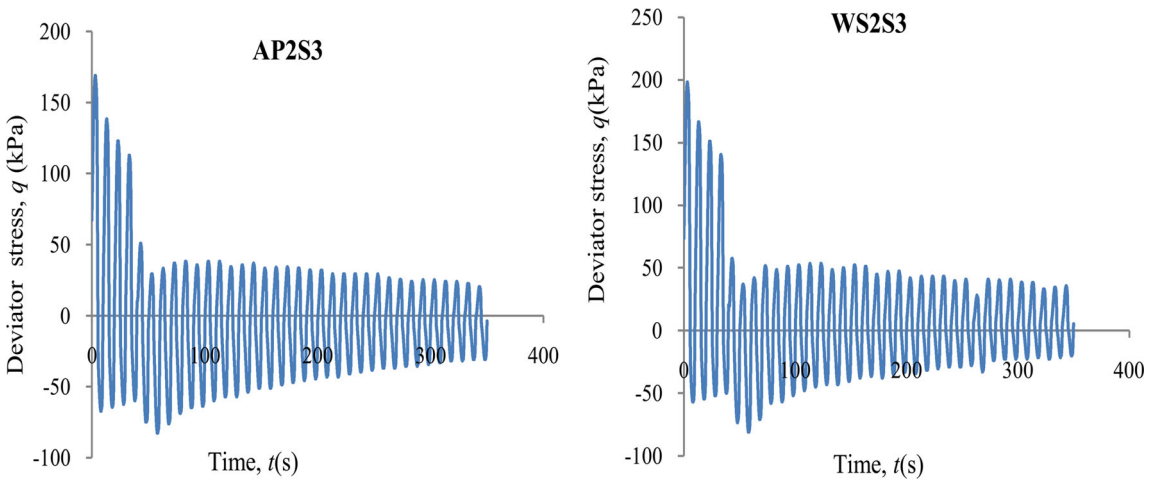

(d) Stage 3

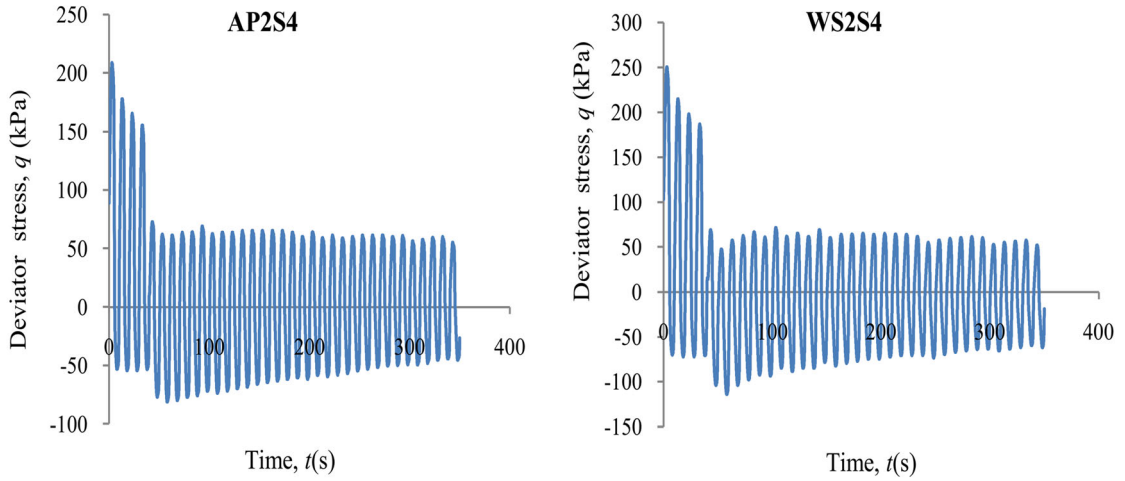

(e) Stage 4

Fig. 13 continued

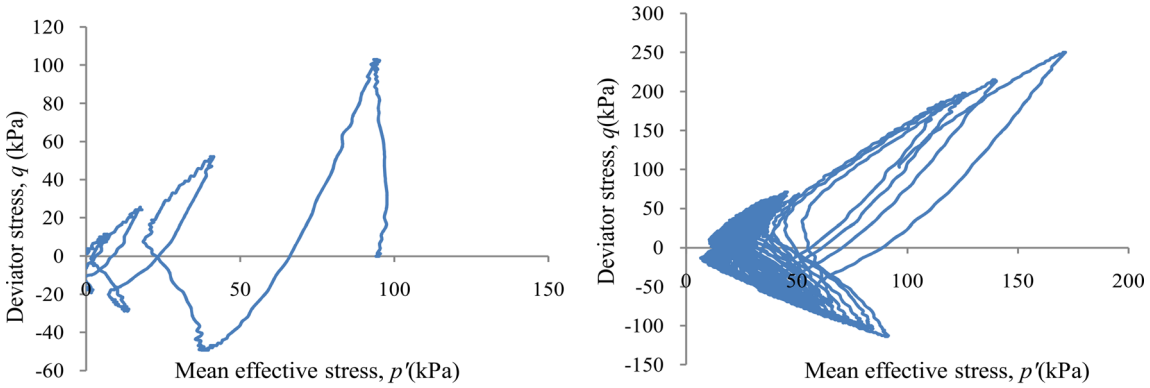

(a) Pre-liquefaction **(b)** Stage WS2S4

Fig. 14 q vs. p′ plot for the specimen prepared through water sedimentation technique

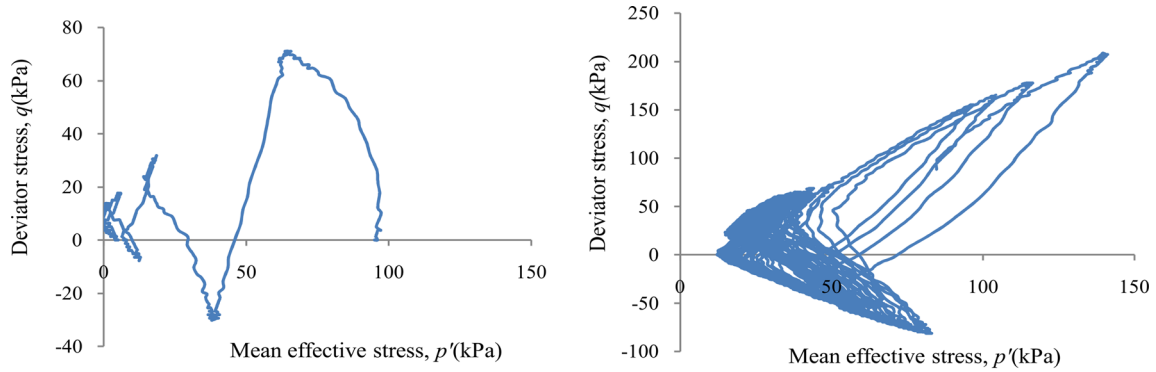

(a) Pre-liquefaction **(b)** Stage AP2S4

Fig. 15 q vs. p′plot for the specimen prepared through air pluviation technique

Acknowledgment All the experiments in this study have been performed in the Geotechnical engineering laboratory, IIT Roorkee, India. This work was supported by the Ministry of Human Resource Development, Government of India (grant no. MHR 002).

References

1. Mogami T and Kubu K (1953) The behavior of soil during vibration. In: Proceedings, 3rd International Conference on soil Mechanics and Foundation Engineering Zurich; 1:152–155.
2. Kramer SL (1996) Geotechnical earthquake engineering Prentice Hall. Upper Saddle River, NJ
3. Ishihara K (1993) Liquefaction and flow failure during earthquakes. The 33rd Rankine lecture. Geotechnique 43(3):351–415.
4. Hamada M, Towhata I, Yasuda S, Isoyama R (1987) Study on permanent ground displacement induced by seismic liquefaction. Comput Geotech 4(4):197–220
5. Vaid YP, Thomas J (1995) Liquefaction and postliquefaction behavior of sand. J Geotech Eng 121(2):163–173
6. Amini ZA, Trandafir AC (2008) Post-liquefaction shear behavior of Bonneville Silty-Sand. Geotechnical earthquake engineering, and soil dynamics 181. Geotechnical Special Publication, USA
7. Sitharam TG, Vinod JS, Ravishankar BV (2009) Post-liquefaction undrained monotonic behaviour of sands experiments and DEM simulations. Géotechnique 59(9):739–749
8. Kokusho T (1999) Water film in liquefied sand and its effects on lateral spread. J GeotechEng 125(10):817–826
9. Ladd RS (1974) Specimen preparation and liquefaction of sands. In: Proc., ASCE 100(10):1180–1184.
10. Mulinis JP, Seed HB, Chan CK, Mitchell JK, Arulanandan K (1997) Effect of sample preparation on sand liquefaction. J Geotech Eng Division 103(2):91–108
11. Wood FM, Yamamuro JA, Lade PV (2008) Effect of depositional method on the undrained response of silty sand. Can Geotech J 45(11):1525–1537
12. Yamamuro JA, Lade PV (1997) Static liquefaction of very loose sands. Can Geotech J 34(6):905–917. https://doi.org/10.1139/cgj-34-6-905
13. Yamamuro JA, Lade PV (1998) Steady state concepts and static liquefaction of silty sands. J GeotechGeoenv Eng 124(9):868–877
14. Tsukamoto Y, Ishihara K, Nonaka T (1998) Undrained deformation and strength characteristics of soils from reclaimed deposits in Kobe. Soils Found 2:47–55
15. Vaid YP, and Sivathayalan, S (1999) Fundamental factors affecting liquefaction susceptibility of sands. In: Proc., Int. Workshop on the Physics and Mechanics of Soil Liquefaction P. V. Lade and J. A. London;1999.
16. Vaid YP, Sivathayalan S, Stedman D (1999) Influence of specimen-reconstituting method on the undrained response of sand. Geotech Test J 22(3):187–195
17. Tatsuoka F, Ochi K, Fujii S, Okamoto M (1986) Cyclic undrained triaxial and torsional shear strengths of sands for different sample preparation methods. Soils Found 26(3):23–41. https://doi.org/10.3208/sandf1972.26.3_23
18. Oda M (1972) Initial fabrics and their relations to mechanical properties of granular material. Soils Found 12(1):17–36
19. Arthur JRF, Menzies BK (1972) Inherent anisotropy in a sand. Geotechnique 22(1):115–128
20. Ishihara K, Okada S (1978) Effects of stress history cyclic behavior of sand. Soils Found 18(4):31–45
21. Wanatowski D, Chu J (2008) Effect of specimen preparation method on the stress-strain behavior of sand in plane-strain compression tests. Geotech Test J. https://doi.org/10.1520/GTJ101307
22. Della N, Belkhatir M, Henni AD, Canou J, Dupla JC (2013) Laboratory assessment of saturation and sample molding effects on shear resistance and mechanical characteristics of sandy soil. Arab J Geosci 7:2969–2980. https://doi.org/10.1007/s12517-013-1046-7
23. Gade VK, Dasaka SM (2016) Development of a mechanized traveling pluviator to prepare reconstituted uniform sand specimens. J Mater Civ Eng 28(2):04015117
24. Kodicherla SPK, Gong G, Fan L (2018) Moy CKS and He J (2018) Effects of preparation methods on inherent fabric anisotropy and packing density of reconstituted sand. Cogent Eng 5:1533363
25. Kwan WS (2018) A review on sand sample reconstitution methods and procedures for undrained simple shear test. Int J Geotech Eng. https://doi.org/10.1080/19386362.2018.1461988
26. Oda M, Koishikawa I (1978) Strength anisotropy of sand ground and its significance in soil engineering. Trans JSCE 273:111–120
27. Sze HY, Yang J (2014) Failure modes of sand in undrained cyclic loading: Impact of sample preparation. J Geotechl Geoenviron Eng 140(1):152–169. https://doi.org/10.1061/(ASCE)GT.1943-5606.0000971
28. Kiyota T, Maekawa Y, Chiehyu W (2019) Using in-situ and laboratory-measured shear wave velocities to evaluate the influence of soil fabric on in-situ liquefaction resistance. Soil Dynam Earthq Eng 117:164–173. https://doi.org/10.1016/j.soildyn.2018.11.016

29. Hussain M and Sachan A (2019) Post-liquefaction reconsolidation and undrained cyclic behaviour of chang dam soil. In: IACMAG Symposium 9(5).
30. Sriskandakumar S, Wijewickreme D and Byrne PM (2012) Multiple cyclic loading response of loose air-pluviated Fraser River sand. In: Proceedings of the 15th World Conference on Earthquake Engineering Lisbon, September pp. 24–28, 2012.
31. Indian standard code, Revised 2002 Classification and identification of soils for general engineering purposes. (IS: 1498-1970).
32. Hussain H, Sachan A (2019) Dynamic characteristics of natural kutch sandy soils. Soil Dynam Earthq Eng 125:101517. https://doi.org/10.1016/j.soildyn.2019.105717
33. Chaney R, Mulinis JP (1978) Suggested method for soil specimen remolding by wet-raining. Geotech Test J ASTM 1(2):107–108
34. Oda M, Koishikawa I, Higuchi T (1978) Experimental study of anisotropic shear strength of sand by plane strain test. Soils Found 18(1):25–38
35. Seed HB, Lee KL (1966) Liquefaction of saturated sands during cyclic loading. J Soil Mech Found Div 92(6):105–134
36. Seed HB (1987) Design problems in soil liquefaction. J Geotech Eng 113(8):827–845
37. Ghionna VN, Porcino D (2006) Liquefaction resistance of undisturbed and reconstituted samples of a natural coarse sand from undrained cyclic triaxial tests. J Geotech Geoenviron Eng 132(2):194–202
38. Zlatovic S, Ishihara K (1997) Normalized behavior of very loose nonplasticsoils: effects of fabric. Soils Found 37(4):47–56
39. Porcino D, Marcianò V, Nicola GV (2009) Influence of cyclic pre-shearing on undrained behaviour of carbonate sand in simple shear tests. Geomech Geoeng: Int J 4(2):151–161
40. Yamamuro JA, Wood FM, Lade PV (2008) Effect of depositional method on the microstructure of silty sand. Can Geotech J 45(11):1538–1555

Publisher's Note Springer Nature remains neutral with regard to jurisdictional claims in published maps and institutional affiliations.

Bull Mater Sci (2021)44:22
https://doi.org/10.1007/s12034-020-02314-0

© Indian Academy of Sciences

Enhancement and luminescence properties of Eu^{3+}, Sm^{3+} co-doped $KMgPO_4$ phosphor with variable concentration of Eu^{3+} for w-LEDs

SARVJEET SINGH
Delhi Technological University, Delhi 110042, India
sarvjeetsingh779@gmail.com

MS received 14 June 2020; accepted 3 September 2020

Abstract. This study reports enhancement in emission efficiency of Eu^{3+} and Sm^{3+} co-doped $KMgPO_4$ phosphor. The sample was synthesized by a conventional solid-state reaction for the variable concentration of europium. The structural analysis of the sintered phosphor was done by using powder X-ray diffraction, also the photoluminescence behaviour, energy transformation of Sm^{3+} to Eu^{3+} and decay properties were studied throughout. It was found that the main intense peak of Sm^{3+}-doped sample reduced when increasing Eu^{3+} concentration and this shows the energy transfer between Eu^{3+} and Sm^{3+} ions, also the decay time of particle get reduced with increasing Eu^{3+} concentration. So by adjusting the energy transfer between Eu^{3+} and Sm^{3+} ions using an optimum concentration of europium ion can improve the emission efficiency and enlarge the excitation spectra and therefore, enhanced the emission efficiency under 402 nm n-UV excitation. This study shows the new methodology for developing the red-emitting phosphor with enhanced emission efficiency. The calculated CIE coordinated for co-doped phosphor was estimated to $x = 0.610$ and $y = 0.381$.

Keywords. Photoluminescence; X-ray diffraction; $KMgPO_4$: Sm^{3+}/Eu^{3+} phosphor; solid-state reaction.

1. Introduction

In w-LED, efficiency is degraded when temperature increases due to thermal effect of *p–n* junction, which accommodate temperature layer on the phosphor substrate consequently reducing the life of LEDs. So it is essential to develop new phosphor materials, which give enhanced emission efficiency without reaching the concentration quenching and thus significantly increase the lifespan of phosphor material.

In recent years, w-LED is commercially developed using the RGB phosphor under the n-UV and another method to generate white light by using the blue-chip on the RGB phosphor or single yellow (YAG: Ce^{3+}) phosphor, which gives promising results as usual [1,2]. However, these methods are having some drawbacks like poor colour rendering index, low chemical and thermal stability [3–6]. To overcome these demerits, a fusion of RGB and n-UV phosphor with improved rendering index value (Ra) was investigated to obtain w-LED [7].

Rare-earth ion Sm^{3+} act as activator and sanitizer material for the $KMgPO_4$ host lattice, which is excited by n-UV radiation efficiently. Phosphate materials are known for their tetrahedral host structure with charge stabilization, which makes it preferable luminescent material [8].

Therefore, Sm^{3+}-doped $KMgPO_4$ phosphor could be suitable material with Eu^{3+} acting as activator ion for w-LEDs. Also Eu^{3+} ion has the nearly same energy level to the Sm^{3+} ion, so it covers broad emission spectra and behaves like activator in the same host material [9,10]. However, it is known that when ions like Eu^{3+} occupy low coordinated distorted environments, the luminescence intensity significantly increased due to electric dipole transition probability [11]. These activators are studied to generate intense red light, because Sm^{3+} ion excited to $^4F_{7/2}$ level and relaxed to its $^4G_{5/2}$ level and Eu^{3+} ion has a transition from $^5D_0$ to ^7F_J (where $J = 0$ to 4). At present, mostly single doped red-emitting phosphors are used to generate red light, which have some drawbacks as mentioned above. Even though lanthanide phosphates ($LnPO_4$) have many advantages, like extremely high thermal stability, very high solubility for lanthanide ions, etc., it is always desirable to have a non-lanthanide-based phosphate host with all the properties of $LnPO_4$. This is because obtaining large quantities of lanthanides in a highly pure form is much costlier compared to main group elements like Sb and Bi [12]. Rare-earth co-doped phosphate can be a preferable material for white light in terms of extended emission efficiency and the improved lifetime.

Published online: 05 February 2021

2. Experimental

2.1 *Materials and synthesis*

Samples of $KMgPO_4$: $0.75Sm^{3+}$ and $KMgPO_4$: xSm^{3+}, yEu^{3+} (x = 0.75 and y = 0.5, 0.75, 1.00, 1.25, 1.50 mol%) co-doped phosphor were prepared by using a conventional solid-state synthesis method. The starting chemicals were highly pure potassium nitrate (K_2NO_3), ammonium dihydrogen phosphate ($NH_4H_2PO_4$), magnesium nitrate ($MgNO_3{\cdot}6H_2O$), samarium oxide (Sm_2O_3 + HNO_3) and europium oxide (Eu_2O_3). These raw materials in stoichiometric amounts were mixed in an agate mortar with acetone as wetting solution by taking the different mol% of Eu^{3+} ions. The homogeneous samples were fired at 250°C for 2.5 h, 500°C for 4 h, 700°C for 3 h and 1050°C for 2.5 h in the furnace and finally, the obtained samples were grounded in powder form for characterization of the phosphor.

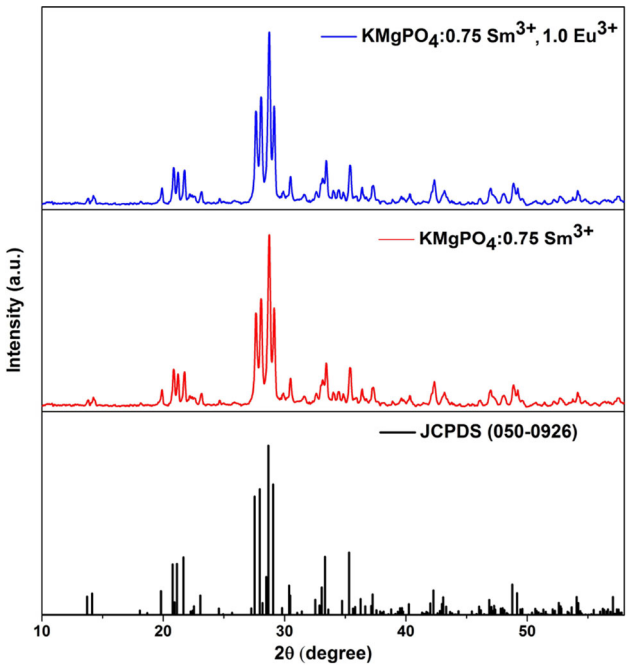

Figure 1. XRD images of $KMgPO_4$: $0.75Sm^{3+}$, $1.0Eu^{3+}$, $KMgPO_4$: $0.75Sm^{3+}$ and the JCPDS card (no. 050-0926).

2.2 *Characterization*

The X-ray diffraction (XRD) pattern of the obtained sample was measured using the Bruker D8 diffractometer with Cu-Ka (40 kV, λ = 1.54305 Å, 40 ma) and the range of 2θ is 10°–90°. Before the XRD data measurement, the sample was reheated to 100°C with an intermittent temperature rate of 4°C min^{-1}. Photoluminescence (PL) excitation (PLE) and emission spectrum of prepared samples were determined using a spectrofluorometer (RF-5301pc) equipped with a xenon light source. The decay curve of the phosphor was measured by using the Edinburgh instrument, FLS920.

3. Results and discussion

The XRD pattern of phosphor samples $KMgPO_4$: $0.75Sm^{3+}$, $1.0Eu^{3+}$, $KMgPO_4$: $0.75Sm^{3+}$ and JCPDS card (no. 050-0926) are depicted in figure 1. XRD images of the sample show the characterization FWHMs, which are similar to the JCPDS card (no. 050-0926) and this validates that Sm^{3+}- and Eu^{3+}-doped phosphor does not consist phase deformation of the host material.

3.1 *Luminescence properties*

The photoluminescence excitation spectra of $KMgPO_4$: $0.75Sm^{3+}$ phosphor observed at 602 nm is shown in figure 2a. The intense peak of the excitation spectra at 402 nm attributes to $^6H_{5/2} \rightarrow {}^4F_{7/2}$ transition [13–15]. This phosphor

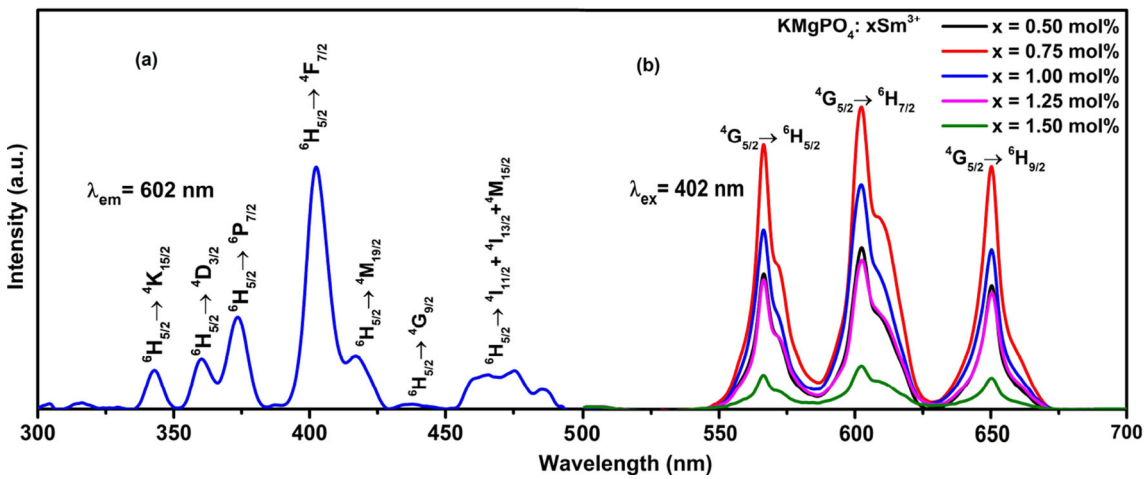

Figure 2. (**a**) PLE spectrum at 602 nm and (**b**) emission spectrum at 402 nm of Sm^{3+}-doped $KMgPO_4$ phosphor.

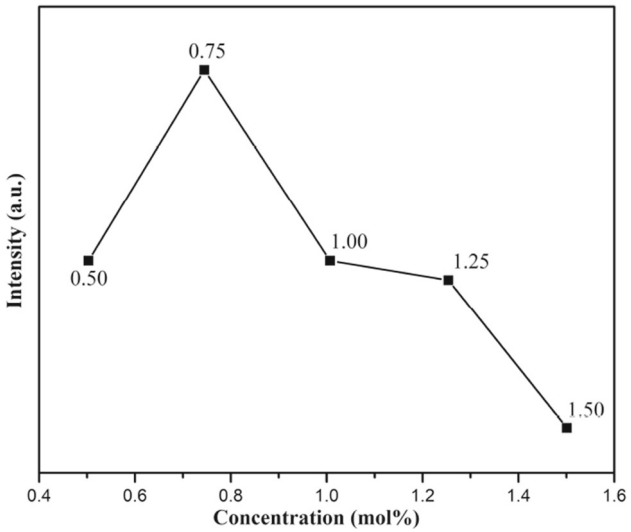

Figure 3. Photoluminescence intensity *vs.* the Sm^{3+} concentration in $KMgPO_4$ phosphor.

exhibits emission peaks at 565, 602 and 652 nm, which attributes to the $^4G_{5/2} \rightarrow {}^6H_{5/2}$, $^4G_{5/2} \rightarrow {}^6H_{7/2}$ and $^4G_{5/2} \rightarrow {}^6H_{9/2}$ transitions [16,17]. The most emission intense peak was found at 602 nm, which is in view of electrical dipole moment, and remaining two weak peaks monitored at 565 and 652 nm are in view of the purely magnetic and combined moment of electrical and magnetic, respectively [18].

From figure 2a, it was examined that characteristics peak intensity increases with increasing doping of samarium ion in $KMgPO_4$: $x Sm^{3+}$ phosphor and achieved a maximum up to 0.75 mol% and after that, it was digressed due to quenching effect (figure 3) [19]. So, the suitable concentration of the Sm^{3+} ion was found to be 0.75 mol%.

The PLE and emission spectra of the $KMgPO_4$: $0.75Sm^{3+}$, xEu^{3+} phosphor are depicted in figure 4a and b. By observing the spectra, the emission efficiency increases gradually with increase in the doping of Eu^{3+} ion up to 1 mol% and then decreases immediately due to non-radiative transition between Eu^{3+} and Sm^{3+} ions.

Figure 4a shows PLE spectra of $KMgPO_4$: $0.75Sm^{3+}$, $1.0Eu^{3+}$ phosphor expanded from 300 to 500 nm under λ_{em} of 617 nm. Peaks contributing to Sm^{3+} ions are $^6H_{5/2} \rightarrow {}^4H_{9/2}$, $^6H_{5/2}$- $\rightarrow {}^4F_{7/2}$, $^6H_{5/2} \rightarrow {}^4G_{9/2}$ and broad peak $^6H_{5/2} \rightarrow {}^4I_{11/2} + {}^4I_{13/2} + {}^4M_{15/2}$ at 346, 404, 440 and 456–496 nm, respectively. The other peak due to the Eu^{3+} ions are $^7F_0 \rightarrow {}^5H_6$, $^7F_0 \rightarrow {}^5D_4$, $^7F_0 \rightarrow {}^5L_7$, $^7F_0 \rightarrow {}^5L_6$, $^7F_0 \rightarrow {}^5D_3$ and $^7F_0 \rightarrow {}^5D_2$ originated at 325, 310, 329, 395, 414 and 420 nm, respectively [20,21].

Figure 4b shows the PL spectrum of $KMgPO_4$: $0.75Sm^{3+}$, xEu^{3+} under excitation of 402 nm, where x = 0.50, 0.75, 1.0, 1.25 and 1.50. The most intense peak observed at 602 nm caused by the transition of $^4G_{5/2}$ level to $^6H_{5/2}$ level of Sm^{3+} ion. However, other peaks are comparatively weak, so it is possible to enhance the PL spectrum. Peaks attributed to samarium ions are $^4G_{5/2} \rightarrow {}^6H_{5/2}$, $^4G_{5/2} \rightarrow {}^6H_{7/2}$ and $^4G_{5/2} \rightarrow {}^6H_{9/2}$. Other peaks attributed to Eu^{3+} ions are $^5D_0 \rightarrow {}^7F_0$, $^5D_0 \rightarrow {}^7F_1$, $^5D_0 \rightarrow {}^7F_2$, $^5D_0 \rightarrow {}^7F_3$ and $^5D_0 \rightarrow {}^7F_4$. The above result shows the enhancement in emission efficiency by covering large spectra due to Eu^{3+} ions.

3.2 *Decay curve*

Decay measurement also observed with various concentrations of Eu^{3+} ions in $KMgPO_4$: $0.75Sm^{3+}$, xEu^{3+} phosphor material. Sm^{3+} ions concentration was fixed at 0.75 mol% and when concentration increased beyond this level, the

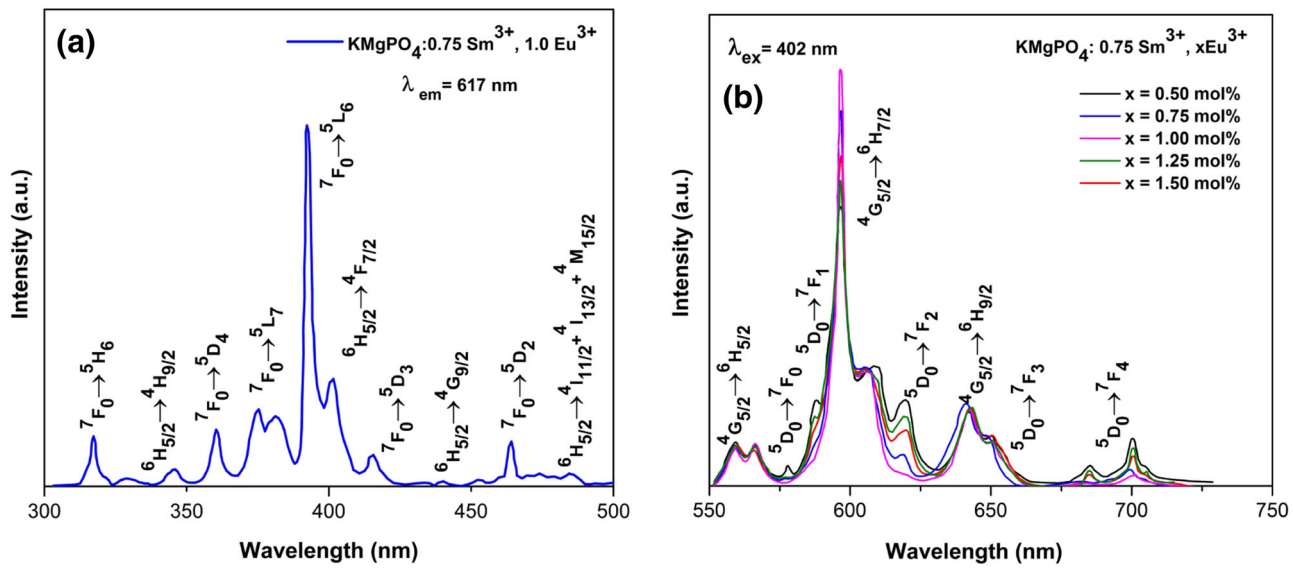

Figure 4. (**a**) PLE spectrum of $KMgPO_4$: $0.75Sm^{3+}$, $1.0Eu^{3+}$ and (**b**) PL spectra of $KMgPO_4$: $0.75Sm^{3+}$, xEu^{3+} (x = 0.50, 0.75, 1.0, 1.25, 1.50 mol%).

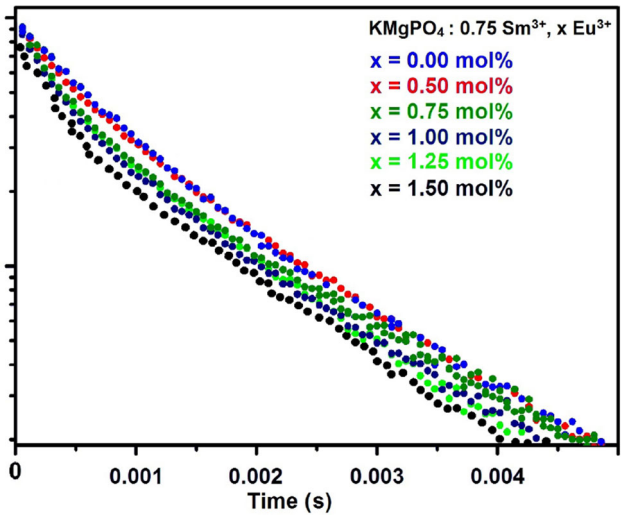

Figure 5. Decay curve of $KMgPO_4$: xSm^{3+}, yEu^{3+} ($x = 0.75$ mol% and y = 0.50, 0.75, 1.00, 1.25 and 1.50 mol%) phosphors under excitations and emission of $\lambda_{ex} = 402$ nm and $\lambda_{em} = 602$ nm.

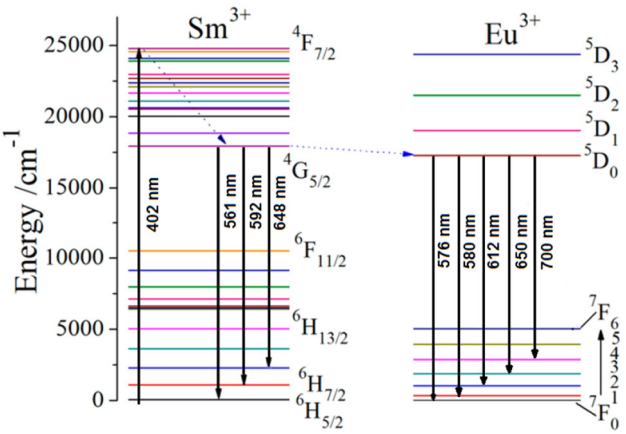

Figure 6. Energy level diagram of $KMgPO_4$: Sm^{3+}, Eu^{3+} phosphor.

decay time slightly decrease because of energy deportation between samarium ions in the form of non-radiative transition.

The decay curve (figure 5) shows the decay time of $KMgPO_4$: xSm^{3+}, yEu^{3+} ($x = 0.75$ mol% and $y = 0.5$, 0.75, 1.00, 1.25, 1.50 mol%) under excitations and emission of $\lambda_{ex} = 402$ nm and $\lambda_{em} = 602$ nm, respectively. According to Blasse and Grabmaier [22], the decay behaviour can be determined by using the following expression

$$I = I_0 e^{(-t/\tau)},$$

where I denotes the intensity at time 0 s, I_0 the intensity at time t and τ denotes the lifetime. The calculated lifetime of Sm^{3+} ions under 602 nm emission was found to be 1.23, 1.01, 0.76, 0.36 and 0.10 ms, which decreases with the Eu^{3+} concentration.

The energy transfer mechanism between Eu^{3+} and Sm^{3+} ions, energy level diagram were further studied, as shown in the figure 6. Sm^{3+} ions excited by 402 nm go to $^4F_{7/2}$ level and then come to $^4G_{5/2}$ in the form of non-radiative transition. The energy of $^4G_{5/2}$ level relax to the $^6H_{7/2}$ and $^6G_{5/2}$ level and gives emission peaks at 565 and 652 nm. Simultaneously, the energy of $^4G_{5/2}$ level is transferred to the $^5D_0$ level by means of the resonance. So the characteristics peaks obtained in emission spectra due to the transition of $^5D_0 \rightarrow {}^7F_0$, $^5D_0 \rightarrow {}^7F_1$, $^5D_0 \rightarrow {}^7F_2$, $^5D_0 \rightarrow {}^7F_3$ and $^5D_0 \rightarrow {}^7F_4$ levels in Eu^{3+} ions, therefore, enhanced the emission peak intensity in the host material. The energy level of the Sm^{3+} ions is 647 cm^{-1} more than the Eu^{3+}, so the energy transfers from Eu^{3+} ion to Sm^{3+} ions rarely happened and this make Sm^{3+} ion as a suitable sensitizer for the Eu^{3+} ion.

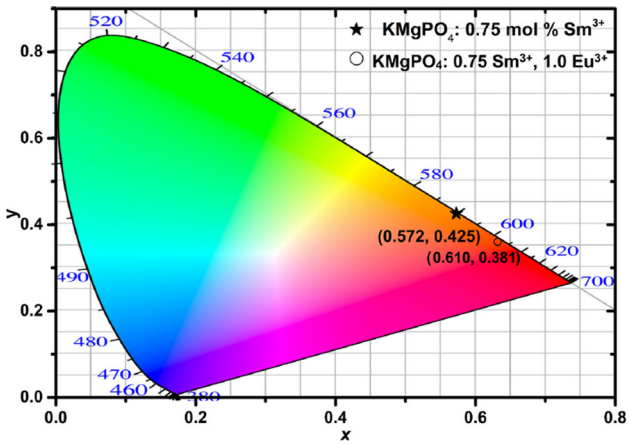

Figure 7. CIE diagram of $KMgPO_4$: $0.75Sm^{3+}$, $1.0Eu^{3+}$ phosphor.

3.3 *CIE diagram*

CIE diagram is important to decide the shading immaculateness of the acquired phosphor using the PLE spectra [23]. The CIE coordinates of the $KMgPO_4$ doped with Sm^{3+} ion is located at ($x = 0.572$, $y = 0.425$) under the 402 nm excitation and coordination of $KMgPO_4$: Sm^{3+}, Eu^{3+} co-doped phosphor located at ($x = 0.610$, $y = 0.381$) (figure 7). Shifting of coordination shows the colour phase transition from reddish-orange to pure red colour. During colour transition towards the red region when increasing the Eu^{3+} doping concentration, intensity of emission peaks did not affect. These results are matching with coordination for the red colour given by the NTSC system and hence it is suitable for the w-LED application.

4. Conclusion

This study shows that red-emitting phosphor $KMgPO_4$: Sm^{3+}, Eu^{3+} under n-UV radiation phosphor was effectively prepared by the conventional solid-state synthesis method.

The emission efficiency of phosphor increased by increasing the doping of europium without reaching the concentration quenching limit. The decay curve and PL spectra show the broad spectra area covered by the europium and samarium co-doped phosphor, because of the energy deportation between the Sm^{3+} and Eu^{3+} and hence extend the excitation spectra from 402 to 460 nm. The energy transfer mechanism from sensitizer Sm^{3+} to activator Eu^{3+} ion depends on Dexter's and Reisfeld's approximation, which states that electric multipolar quadrupole–quadrupole (q–q) interaction among the activator ions. The determined Commission internationale de l'Eclairage coordinates were estimated to $x = 0.610$, $y = 0.381$ in the pure red region. The above result confirms that the Sm^{3+}-doped $KMgPO_4$ phosphor used in w-LEDs can be replaced by Sm^{3+}, Eu^{3+} co-doped $KMgPO_4$ phosphor with enhanced emission efficiency without reaching the concentration quenching effect.

Acknowledgements

We acknowledge NPL, Delhi, and Delhi Technological University, Delhi, for providing facilities for performing experiments and characterization.

References

[1] Zheng J, Feng J, Cheng Q, Guo Z, Cai L and Chen C 2015 *J. Funct. Mater. Lett.* **8** 1550042
[2] Ratnam B V, Jayasimhadri M and Jang K 2014 *Spectrochim. Acta A Mol. Biomol. Spectrosc.* **132** 563
[3] Bai X, Caputo G, Hao Z, Freitas V T, Zhang J, Longo R L *et al* 2014 *Nat. Commun.* **5** 5702
[4] Matioli E, Brinkley S, Kelchner K M, Hu Y L, Nakamura S, DenBaars S *et al* 2012 *Light: Sci. Appl.* **1** e22
[5] Deng H, Zhao Z, Wang J, Hei Z, Li M, MiNoh H *et al* 2015 *J. Solid State Chem.* **228** 110
[6] Kim J S, Jeon P E, Park Y H, Choi J C, Park H L, Kim G C *et al* 2004 *Appl. Phys. Lett.* **85** 3696
[7] Zhou R, Wang L, Xu M and Jia D 2015 *J. Alloys Compd.* **647** 136
[8] Su Y K, Peng Y M, Yang R Y and Chen J 2012 *Opt. Mater.* **34** 1598
[9] Tsutsui T, Nakashima T, Fujita Y and Saito S 1995 *Synth. Met.* **71** 2281
[10] Lin H Y and Fang Y C 2010 *J. Am. Ceram. Soc.* **93** 3850
[11] Naidu B, Sudarsan V and Vatsa R 2009 *J. Nanosci. Nanotechnol.* **9** 2997
[12] Naidu B, Sudarsan V and Vishwanadh B 2012 *Dalton Trans.* **41** 3194
[13] Tiana Y, Liu Y, Hua R N, Na L Y and Chen B 2012 *J. Mater. Res. Bull.* **47** 59
[14] Lin H, Yang D, Liu G, Ma T, Zhai B, An Q *et al* 2005 *J. Lumin.* **113** 121
[15] Lin C C, Liu R S, Tang Y S and Hu S F 2008 *J. Electrochem. Soc.* **155** J248
[16] Carnall W T, Fields P R and Rajnak K 1968 *J. Chem. Phys.* **49** 4424
[17] Yu R, Noh H M, Moon B K, Choi B C, Jeong J H, Lee H S *et al* 2014 *J. Lumin.* **145** 717
[18] Ding B, Han C, Zheng L, Zhang J, Wang R and Tang Z 2015 *Sci. Rep.* **5** 9443
[19] Raju G S R, Yu J S, Park J Y, Jung H C and Moon B K 2012 *J. Am. Ceram. Soc.* **95** 238
[20] Carnall W T, Fields P R and Rajnak K 1968 *J. Chem. Phys.* **49** 4450
[21] Wang Z J, Li P L, Yang Z P, Guo Q and Li J 2011 *J. Optoelectron. Laser* **22** 718
[22] Blasse G and Grabmaier B C 1994 *Luminescent materials* (Berlin, Germany: Springer-Verlag) p 118
[23] Yu R, Noh H M, Moon B K, Choi B C, Jeong J H, Lee H S *et al* 2014 *J. Lumin.* **152** 133

Evaluation of the Feasibility of Recycled Concrete Aggregate for Producing Structural Concrete

Mohammad Tabrez Ali[1], *Ibadur* Rahman[1], *Nirendra* Dev[2], *and Priyanka* Singh[3]

[1]Department of Civil Engineering, Jamia Millia Islamia University, New Delhi, India
[2]Department of Civil Engineering, Delhi Technological University, New Delhi, India
[3]Department of Civil Engineering, Amity School of Engineering & Technology, Amity University Uttar Pradesh, Noida, India

Abstract. When sustainability has become a primary measure of the selection of the building materials in the construction industry over the past decades, researchers all around the world have been looking upon for alternatives to reduce the overall environmental impact of the construction materials while not compromising the strength and durability. The factors like manufacturing, reusability, recyclability, disposal etc, are the criteria of utmost attention affecting the overall life cycle impact of the construction materials. In this prospect the Recycled Concrete Aggregate (RCA) has shown up as an exceptionally viable contender for the manufacturing of concrete with several environmental benefits over the Natural Aggregate (NA) and has already been identified by industry and several government agencies across the globe. The efficient material use of RCA can potentially deliver an inferior though competent concrete in comparison to the NA while averring the criteria of sustenance. The present study delves into the calculation of the proportion of the RCA in a mix design for achieving maximum compressive strength. The experimental setup constituted the casting of concrete cubes of control mix design of M40 grade with proportions of RCA varying from 0-100 percent spread over a space of 10% with NA which were later put to tests. The thorough investigation on the casted concrete cubes lead to the conclusion that the mix design with 50% proportion of RCA in addition to 50% proportion of NA delivered the maximum compressive strength, an average value of 8.23% higher than that of the normal concrete and the highest Rebound Number, an average value of 53.92 for the M40 grade concrete thereby showcasing the feasibility of producing structural concrete with RCA. The results are asserted to be governed by the better bonding between the RCA and NA and due to the significant increase in the water retention capacity by the provision of RCA in the mix.

1 Introduction

As we know today′s world is facing major environmental problems i.e. global warming, ozone layer depletion, waste accumulation, etc. Over the last few decades the research indicates that the global climate is changing rapidly (IPCC, 2001) and also un-reveals the fact that this change will continue with time (Morgan, 2004). The increase in emissions from the building sector worldwide is estimated to rise from 8.6 gigatons of carbon dioxide ($GtCO_2$) in 2004 to 14.3 $GtCO_2$ by 2030 (Y. Hossain & Marsik, 2019). The building sector is responsible for over 40% of overall energy consumption, making a significant contribution to CO_2 emissions (Ardente et al., 2008; Zabalza Bribián et al., 2009) (D, 1999; United Nation Environment Programme, 2007) and the percentage can be as high as 70% for developing countries such as China (Hu et al., 2012). The exploitation of natural resources, in particular non-renewable resources, for

the construction purpose lead to generation of millions of tonnes of construction and demolition wastes (CDW) every year. The Environmental Protection Agency of the United States estimated the generation of debris, from the construction, demolition, and renovation of residential and non-residential buildings close to 170 million tonnes in 2003. According to Eurostat, the total amount of waste generated in the European Union in 2010 was over 2.5 billion tonnes, of which almost 35% (860 million tonnes) was derived from construction and demolition activities and 27% (672 million tonnes) belonged to mining and quarrying operations. Without any specific processing plan for these materials, this waste is sent to landfills instead of being reused and recycled in new construction (Silva et al., 2014). The social, economic and environmental indicators of sustainable development are drawing attention to the construction industry, which is a globally emerging sector, and a highly active industry in both developed and developing countries (Ortiz-rodriguez et al., 2009).

To create a deeper sense of the amount of environmental impact that is linked with the usage of building materials a review has been presented in **Ошибка! Источник ссылки не найден.**, whereby a number of commonly used building material elements have been analyzed for the Embodied Energy and

© The Authors, published by EDP Sciences. This is an open access article distributed under the terms of the Creative Commons Attribution License 4.0 (http://creativecommons.org/licenses/by/4.0/).

Table 1. Embodied Energy and Embodied Carbon of typical construction materials-Comparative Data based on LCA (Christoforou et al., 2016).

Assembly/Material	Ref	Embodied energy	Unit	Embodied carbon	Unit	Info.
Adobe Brick	(Christoforou et al., 2015)	0.033	MJ/kg	1.76E-3	$kgCO^2e/kg$	Cradle-to-site, On-site production, use of straw as fibre material
Adobe Brick	(Christoforou et al., 2015)	0.078	MJ/kg	5.41E-3	$kgCO^2e/kg$	Cradle-to-site, On-site production, use of straw as fibre material
Adobe Brick	(Christoforou et al., 2015)	0.170	MJ/kg	1.29E-2	$kgCO^2e/kg$	Cradle-to-site, Off-site production, use of straw as fibre material
Adobe Brick	(Christoforou et al., 2015)	0.033	MJ/kg	1.70E-3	$kgCO^2e/kg$	Cradle-to-site, On-site production, use of sawdust as fibre material
Adobe Brick	(Christoforou et al., 2015)	0.077	MJ/kg	5.30E-3	$kgCO^2e/kg$	Cradle-to-site, On-site production, use of sawdust as fibre material
Adobe Brick	(Christoforou et al., 2015)	0.169	MJ/kg	1.28E-2	$kgCO^2e/kg$	Cradle-to-site, Off-site production, use of sawdust as fibre material
Common Brick	(Hammond & Jones, 2011)	3.0 6.9	MJ/kg MJ/brick	0.24 0.55	$kgCO^2e/kg$ $kgCO^2e/brick$	Cradle-to-gate Cradle-to-gate
Ceramic Brick	(Andrew Alcorn, 2001)	2.7 5310	MJ/kg MJ/m^3	-	-	
Concrete Block	(Andrew Alcorn, 2001)	0.9 12.5	MJ/kg MJ/block	-	-	
Fired Clay Brick	(Venkatarama Reddy & Jagadish, 2003)	4.25	MJ/brick	-	-	
Fired Clay Brick	(Cabeza et al., 2013)	2.0-3.4	GJ/m^3	-	-	
Fired Clay Brick	(Praseeda et al., 2015)	1.2-4.05	MJ/kg	-	-	Fired clay bricks (i.e. table moulded, wire cut, country brick)
Stabilized Rammed Earth Wall	(Cabeza et al., 2013)	0.45-0.60	GJ/m^3	-	-	
Hollow Concrete Block	(Venkatarama Reddy & Jagadish, 2003)	1.32-1.62	MJ/block			7-10% cement

Embodied Carbon content based on LCA assessment. This impact can however be reduced by the help of reusable construction with a low demand for primary resources. Reusable blocks with recycled brick aggregate, reusable blocks with recycled aggregates (RA), reusable blocks with natural aggregate (NA), and regular concrete wall have great potential in reducing the overall construction and demolition impact(Pešta et al., 2020; Vẋquez & RILEM Technical Committee 217-PRE, 2013). A study (M. U. Hossain et al., 2016) revealed that the use of coarse recycled aggregates obtained from the CDW in Hong Kong reduced the greenhouse gases footprints up to 65% and saved up to 58% of the energy consumption. To encourage and promote the use of RA, government agencies the world over have often introduced levies and legislation in an attempt to overcome barriers, with varying degrees of success. The European Union Directive No. 2008/98/CE (Council, 2008) encourages the reuse and recycling of waste materials.

1.1 Recycled Concrete Aggregate (RCA)

There is a reuse market for RA derived from CDW in landscaping, road construction (unbound sub-base and base layers, hydraulically bound layers, bituminous surface pavements), cementitious mortars and concrete (Hansen, 1992). The application of RCA derived from CDW, as shown in **Ошибка! Источник ссылки не найден.** and **Ошибка! Источник ссылки не найден.**, in the construction work has become a subject of priority throughout many places especially in USA and several EU countries. Critical studies are being made to understand the characteristics of RCA to encourage the optimum and wide use of this potent sustainable option as an economic concrete ingredient and as one of the solutions in preserving the environment. Generally, the obstacles to using recycled aggregate concrete (RAC) for realistic structures are lower mechanical and durability properties in comparison with that of natural

aggregate concrete (NAC) (Bui et al., 2018; Dimitriou et al., 2018; McGinnis et al., 2017). The use of 100% RCA for replacing natural coarse aggregates in new concrete, unless carefully managed and controlled, is likely to have a negative influence on most concrete properties due to the presence of adhered old cement mortar on the surface of RCA, which could contain a significant amount of fully hydrated cement paste leading to its lower density, higher porosity, higher water absorption, lower strength and lower abrasion resistance (Bui et al., 2018; Silva et al., 2014; Xuan et al., 2016; Zhan et al., 2019). The adhered and loose mortars contribute to the angularity, rough surface texture and high absorption of fine RCA particles (Evangelista & de Brito, 2014).

RCA also contain more micro-cracks caused by the crushing process, and more interfacial transition zones (ITZs) in the matrix between the old cement mortar and the virgin aggregate in RCA (Kong et al., 2010; Kou et al., 2011; Lotfi et al., 2014; Poon et al., 2004; Tam & Tam, 2008).

Many studies have reported that the strength development rate of RCA concrete is higher than that of NA, especially at the later age (e.g. 28 days) due to the remnant of non-hydrated old cement adhered on the surfaces of RCA particles which react with water (Evangelista & de Brito, 2007; Gesoglu et al., 2015; Kurad et al., 2017; Poon et al., 2004). It has been reported that the influence of RCA replacement level on concrete compressive strength is significantly influenced by the initial moisture condition of RCA. Previous studies have reported a significant increase in water permeability, sorptivity and water absorption capacity for the concrete when over 50% of NA was replaced by RCA (Alexandridou et al., 2018; Zaharieva et al., 2003). Depending on the moisture level the compressive strength can be reduced by up to 30% or increase up to 20% for 100% aggregate replaced by RCA. In their study (Etxeberria et al., 2007) reported that the use of 100% recycled coarse aggregates results in 20-25% less compression strength, 2-10% less tensile strength and 16-17% lower modulus of elasticity than conventional concrete at all ages with the same effective w/c ratio. Lowering the w/c ratio improves the compressive strength of concrete containing RCA (Beltrán et al., 2014; Gesoglu et al., 2015). Some studies have also indicated the benefits of the use of TSMA (two-stage mixing approach) in producing concrete with high compressive strength (Brand et al., 2015; Tam & Tam, 2008).

The creep of concrete containing RCA is found to be proportional to the amount of RCA as the higher amount of RCA in concrete mixture increased the degree of potential creep (Tam & Tam, 2007). In their study (Zaharieva et al., 2003) proposed the use of fine recycled aggregate to be restricted and to use extended curing using a moist environment as another way of increasing the durability of RAC. A possible use of admixtures such as fly ash or silica fume could decrease significantly porosity and permeability of RAC (Verian et al., 2018).

2 Experimental Study

2.1 Goal

The strength evaluation of concrete blocks casted using RCA as coarse aggregates is carried upon in this study to propose the suitability of usage of RCA in producing structural concrete. The study targets the comparison of compressive strength and hardness of sixty-six concrete blocks with varying concentrations of RCA and NA as coarse aggregate. This includes the comparison of test results for addressing and ascertaining the impact of adding RCA in concrete and to calculate the optimum concentration of RCA with NA to achieve substantial amount of strength for a defined grade of concrete to be put to use as structural concrete.

Fig. 1. Demolished Concrete.

Fig. 2. Dismantling of Building.

2.2 Materials

Coarse Aggregate-

- RCA- The aggregates (**Ошибка! Источник ссылки не найден.**) are recycled and derived after demolishing old concrete blocks of size 150 mm of varying strengths used for testing concrete in the concrete lab in Jamia Millia Islamia University, New Delhi, India, in the past and were discarded after their testing as shown in **Ошибка! Источник ссылки не**

Table 2. Varying proportions of RCA with NA as coarse aggregates.

S. No.	Recycled Coarse Aggregate (%)	Fresh Coarse Aggregate (%)	Designation	Total No. of Concrete Cubes
1.	0	100	S0	6
2.	10	90	S10	6
3.	20	80	S20	6
4.	30	70	S30	6
5.	40	60	S40	6
6.	50	50	S50	6
7.	60	40	S60	6
8.	70	30	S70	6
9.	80	20	S80	6
10.	90	10	S90	6
11.	100	0	S100	6

найден.. The concrete cubes were dismantled using a hammer (**Ошибка! Источник ссылки не найден.**) and the aggregates were screened and graded afterward (Bureau of Indian Standards (BIS), 1963).

- NA- The natural aggregates used are of fineness modulus of 7.71 ((BIS), 1970; Bureau of Indian Standards (BIS), 1963) **Ошибка! Источник ссылки не найден.**.

Fig. 3. Recycled Concrete Cubes.

Fig. 4. Crushing of Concrete Cubes using Hammer.

Fig. 5. Recycled Concrete Aggregate (RCA).

Fine Aggregate- Natural river sand of fineness modulus value of 2.486 ((BIS), 1970; Bureau of Indian Standards (BIS), 1963) **Ошибка! Источник ссылки не найден.** is used as fine aggregate.

Binding Material- Ordinary Portland Cement (OPC) Wonder 43 grade cement (Bureau of Indian Standard(BIS), 2013) was selected and used as the binding material for the casting of concrete blocks. The tests conducted on cement includes normal consistency test (IS 4031- Part IV, 1988), setting time test (IS 4031- Part V, 1988) including initial and final setting time measurements and the compressive strength test of cement (IS: 4031 (Part 6), 2005). The results of the tests conducted have been tabulated in **Ошибка! Источник ссылки не найден.**.

2.3 Experimental Setup

The present study in its intended goal involves the casting of concrete blocks (of size 150 mm) with varying percentages of RCA (as coarse aggregate) spaced over an interval of 10% from 0-100% with NA (as coarse aggregate) and fine aggregates combined together using a binding material shown in **Ошибка! Источник ссылки не найден.**. The concrete mix design of M-40 grade concrete (STANDARDS, 1982) was selected and a total number of sixty-six concrete blocks were casted, six cubes for every concentration of RCA, placed in a separate designated group as shown in **Ошибка! Источник ссылки не найден.**. The constituent materials put to use in the mix design were subjected to

different tests to assure the quality and strength of the concrete cubes.

After casting the concrete blocks were de-molded and half of the concrete cubes (33 cubes) were cured for duration of 28 days and the other half for duration of 90 days as shown in **Ошибка! Источник ссылки не найден.**. The cubes cured for 28 days were air dried for 24 hours, shown in **Ошибка! Источник ссылки не найден.**, and at first put to Non-Destructive Test (Rebound Hammer Test) (Indian Standards, 1992) as shown in **Ошибка! Источник ссылки не найден.**, to study the behavior of RCA, added in different proportions, on the hardness of the concrete cubes. These cubes were later put to the compression strength test (IS 456, 2000; IS 516:2014, 2004), as shown in **Ошибка! Источник ссылки не найден.**, to calculate the compressive strength of the blocks at 28 and 90 days of curing interval to visualize the impact of RCA on the concrete cube strength. The results have been compiled in **Ошибка! Источник ссылки не найден.** and **Ошибка! Источник ссылки не найден.** respectively for concrete cubes after curing time of 28 days and 90 days.

Fig. 6. Casting of concrete cubes of size 150 mm.

Fig. 7. Curing of concrete cubes.

Fig. 8. Rebound Hammer T.

Fig. 9. Compressive Strength Test using Compression Machine.

Fig. 10. Concrete blocks left for air drying.

3 Results & Discussion

3.1 Compressive Strength

The results obtained from compressive tests on concrete samples after curing duration of 28 days and 90 days are given in **Ошибка! Источник ссылки не найден.** and **Ошибка! Источник ссылки не найден.**. These results are also depicted graphically in **Ошибка! Источник ссылки не найден.** showing a comparison of the compressive strengths after different curing time durations. These results show an incremental variation mainly from 10-50% of RCA replacement and a decrement in strength from 60-100 % of RCA replacement in the concrete matrix. As can be observed from results and as seen in **Ошибка! Источник ссылки не найден.** and **Ошибка! Источник ссылки не найден.**, the compressive strength of concrete at 28 and 90 days having 10% RCA is more than the compressive strength of M-40 grade normal concrete with a value of 0.39% and 5.28% respectively which rises up to 8.32% and 13.98% respectively for the concrete with a 50% RCA replacement. A peak average value of 52.3 MPa and 55 MPa respectively for S5 designation specimens is reached for 50% RCA. However, it was anticipated that the increase in the RCA content will eventually cause the compressive strength of the concrete cubes to fall due to the high water absorption of RA that creates a porous interfacial transition zone (ITZ). The true reason for the

Table 3. Test results of Cement mortar.

S. No.	Cement Type	Normal Consistency (%)	Initial Setting Time (min)	Final Setting Time (min)	Compressive Strength (MPa)
1.	Wonder Cement OPC 43 Grade	33	35	312	44.32

Table 4. Results of Sieve Analysis of coarse aggregates ((BIS), 1970; Bureau of Indian Standards (BIS), 1963).

S.No	Sieve Size (mm)	Weight Retained (gm)	Percentage wt. retained (%)	Cumulative percentage wt. retained	Percentage wt. passing
1.	40	0	0	0	100
2.	20	3550	71	71	29
3.	10	1450	29	100	0
4.	4.75	0	0	100	0
5.	2.36	0	0	100	0
6.	1.18	0	0	100	0
7.	0.6	0	0	100	0
8.	0.3	0	0	100	0
9.	0.15	0	0	100	0
		Total= 771		Fineness Modulus= 7.71	

Table 5. Results of Sieve Analysis of fine aggregates ((BIS), 1970; Bureau of Indian Standards (BIS), 1963).

S.No	Sieve Size (mm)	Weight Retained (gm)	Percentage wt. retained (%)	Cumulative percentage wt. retained	Percentage wt. passing
1.	10	11	0.55	0.55	99.45
2.	4.75	74	3.70	4.25	95.75
3.	2.36	80	4.00	8.25	91.75
4.	1.18	158	7.90	16.15	83.84
5.	0.6	254	12.70	28.85	71.15
6.	0.3	1234	61.70	90.55	9.45
7.	0.15	189	9.45	100.00	0
		Total= 248.60		Fineness Modulus= 2.486	

justification of this pattern of elevation of compressive strength is not yet confirm and could be attributed to a better concrete mix with lower void ratio due to a better grading of aggregates. A further research is proposed on the account of the physical and chemical properties of the virgin concrete used for recycling of aggregates.

The compressive strength of concrete having 60% RCA at 28 and 90 days is more than the compressive strength of normal concrete which was rather already predicted. The percentage increase in the strength of concrete having 60% RCA with the normal concrete at 28 and 90 days is 2.61% and 10.88% respectively. But the strength is less than 50% RCA made concrete. The fall in compressive strength continues at a varying pace for the concrete blocks with 60-100% proportion of RCA in the matrix. The compressive strength of concrete having 100% RCA comes out to be the least which is an inevitable result because of the inferior quality of the aggregates. The percentage decrease in the strength of concrete having 100% RCA with the normal concrete at 28 and 90 days comes out to be 11.85% and 0.62% respectively from **Ошибка! Источник ссылки не найден.** and **Ошибка! Источник ссылки не найден.**. The inferior concrete though has a significant compressive strength. The drop in the compressive strength is attributed to the rise in the content of the RCA with hydrated cement leading to improper mixing and bonding of aggregates with the fresh cement and fine aggregates, adding further to the voids in the concrete matrix.

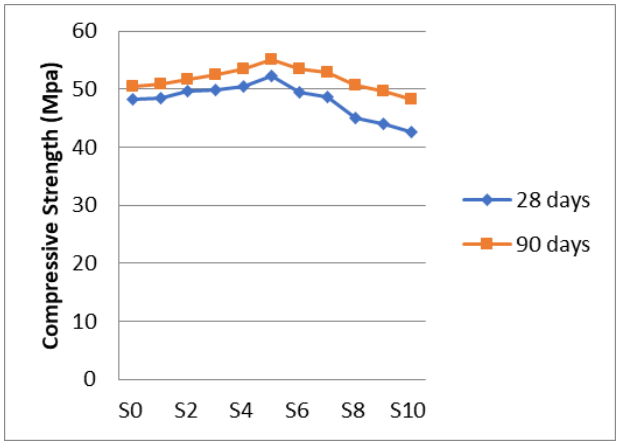

Fig. 11. Variation of compressive strength of concrete cubes with varying proportions of RCA for different curing duration.

Table 6. Results of Compressive Strength test of concrete cubes after 28 days of curing.

S.No	Sample	Cube 1	Cube 2	Cube 3	Average (KN)	Average (N/mm2)	Percentage Variation
1.	S0	1141	1107	1010	1086	48.27	0.04
2.	S1	1090	1100	1080	1090	48.44	0.39
3.	S2	1120	1105	1130	1118.33	49.70	3.0
4.	S3	1130	1122	1110	1120.83	49.81	3.23
5.	S4	1144	1130	1125	1133.16	50.36	4.37
6.	**S5**	**1170**	**1205**	**1155**	**1176.67**	**52.30**	**8.32**
7.	S6	1240	1060	1042	1114	49.51	2.61
8.	S7	1173	1108	1001	1094	48.62	0.76
9.	S8	1020	1005	1010	1011.67	44.96	-6.8
10.	S9	986.3	1037	950	991.10	44.05	-8.7
11.	S10	970	960.5	940	956.83	42.53	-11.85

Table 7. Results of Compressive Strength test of concrete cubes after 90 days of curing.

S.No	Sample	Cube 1	Cube 2	Cube 3	Average (KN)	Average (N/mm2)	Percentage Variation
1.	S0	1135	1155	1125	1138.3	50.5	4.66
2.	S1	1129	1145	1160	1144.6	50.8	5.28
3.	S2	1145	1167	1175	1162.3	51.6	6.94
4.	S3	1155	1175	1210	1180	52.4	8.60
5.	S4	1205	1210	1190	1201.6	53.4	10.67
6.	**S5**	**1245**	**1220**	**1250**	**1238.3**	**55.0**	**13.98**
7.	S6	1170	1195	1235	1200	53.5	10.88
8.	S7	1215	1195	1160	1190	52.8	9.43
9.	S8	1160	1175	1090	1141.6	50.7	5.07
10.	S9	1130	1090	1140	1120	49.7	3.0
11.	S10	1085	1135	1035	1085	48.22	-0.62

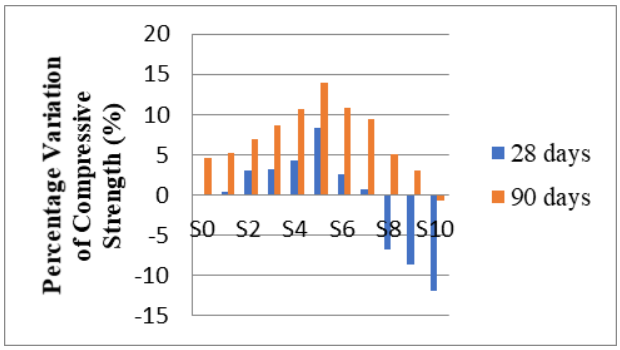

Fig. 12. Percentage variation of compressive strength of concrete cubes with varying proportions of RCA with respect to M-40 grade concrete.

3.2 Rebound Hammer Number

Result of NDT conducted on 33 concrete cube specimens of size 150 mm are given in **Ошибка! Источник ссылки не найден.** and are represented graphically in **Ошибка! Источник ссылки не найден.**. The hardness of the concrete blocks are in alignment with their compressive strength portraying a similar trend of an increase in the bond strength from 10-50% concentration of RCA, from RH number value of 47.27 extending to a peak value of 53.92 for a S5 (50% concentration of RCA) concrete group. The value drop for concrete blocks with the RCA proportions of 60-100% from 53.32 to 47.12 respectively. Rebound Hammer Test also validates the Compressive Strength Test, as the variation between rebound hammer number (RH number) and compressive strength values in the **Ошибка! Источник ссылки не найден.** is almost less than 10% in all the cases.

Their is still no affirm reason for the dominating results and the kind of variation shown of the hardness for a 10-50% proportion of RCA mix concrete and is part of further research. However, the drop in the RH number value can be reasoned with certainty and could be attributed to the lower grade of the aggregates with high porosity and lower strength. The cement mortar adhered to the aggregates causes a poor bonding with large ITZ, altogether resulting in the decline of the bond strength of the concrete specimen.

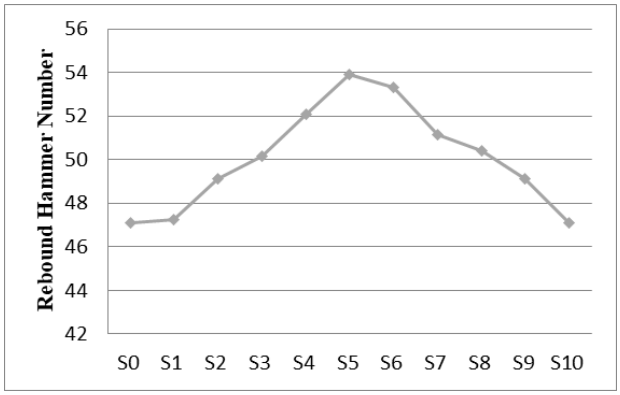

Fig. 13. Variation of Rebound Hammer Test of concrete cubes with varying proportions of RCA.

Table 8. Results of Rebound Hammer Test on concrete cubes.

Sample	S0	S1	S2	S3	S4	S5	S6	S7	S8	S9	S10
Surface 1	49.5	41.5	42.5	43.5	47	48	45	43.5	48.5	42.5	48.5
	34.5	40.5	45	44.5	51	50.5	51.5	44.5	54	45	50
	43.5	49.5	40.5	41.5	43	49.5	43	41.5	49.5	40.5	49.5
	53.5	49	49.5	43.5	63	57.5	45	43.5	50	49.5	50
	45	44.5	44	43	48	52.5	47	57	49.5	44	49.5
Surface 2	49.5	52.5	55	49	40	57	49.5	49	45.5	55	45.5
	50	49.5	53	48.5	45	56.5	50	48.5	51.5	53	48
	52	38.5	58.5	50.5	54	54	49.5	50.5	45.5	58.5	45.5
	53	49	52	50	52	60.5	49.5	50	48.5	52	48.5
	53.5	52	57.5	49.5	50	54	71	49.5	56	57.5	49
Surface 3	41	38	53.5	51.5	51	53	50	51.5	57	53.5	44
	38	48	49	49	58.5	52.5	57.5	55	48.5	49	48.5
	45	53	54	59.5	56	57.5	49	59.5	55	54	43.5
	50.5	52	54	52	56	49.5	51	52	45	54	45
	52	46.5	50	51	54.5	54.5	54	51	51.5	50	41.5
Surface 4	42	48	41.5	57	69.5	49	55	57	52.5	41.5	45
	52	54	40.5	64	59	53.5	50	64	50	40.5	50
	33	49	46.5	52.5	43	54	47	52.5	50	46.5	50
	52.5	45	49	50.5	50	55.5	63	50.5	50	49	48
	52.5	45.5	47.5	53	51.5	59.5	69	53	50	47.5	43
Average RH No.	**47.125**	**47.275**	**49.15**	**50.175**	**52.1**	**53.925**	**52.325**	**51.175**	**50.4**	**49.15**	**47.125**

Table 9. Variation of RH No. and Compressive Strength.

Average RH No.	47.125	47.275	49.15	50.175	52.1	53.925	52.325	51.175	50.4	49.15	47.125
Compressive Strength (28 days)	48.27	48.44	49.70	49.81	50.36	52.30	49.51	48.62	44.96	44.05	42.53
Variation (%)	2.4297	2.414	1.114	-0.723	3.334	3.0203	5.3777	4.9883	10.788	10.379	9.7593

4 Conclusions

The erudite based on the tests conducted on the concrete cubes delivers a number of qualitative and quantitative conclusions. The tests delivered unexpected results of compressive strength and hardness of the concrete manufactured via proportioning of RCA as coarse aggregate in varying quantities in the concrete matrix. The concrete blocks in the vicinity of 50% RCA did exceptionally well in the qualitative analysis marking the highest values of compressive and bond strengths (even higher than normal concrete) for M-40 grade. An increase up to more than 8% has been observed for concrete cube specimens having 50% RCA as compared to the normal concrete cube. Both the compressive strength and the hardness properties go analogous to each other showing similar characteristics for the concrete specimens. On the basis of the present study the authors were able to draw the following conclusions:

- It can be stated that the recycled aggregate concrete; for lean concrete < M-40 grade (IS 456, 2000), has a convenient compressive strength and bond strength, which means a convenient concrete for structural elements in concrete structures where the extent of desirable strength is not too high.
- By decreasing the water/cement ratio, recycled aggregate can achieve higher compressive strength concrete. But the workability will be very low. Therefore, it is recommended to add admixtures such as super plasticizer and silica fume, etc, into the mix.
- Selective demolition should be promoted and enacted whenever possible. This is an absolute necessity for obtaining RA with minimum level of contamination, thereby adding value to the RCA produced for its use in construction.

Old concrete and RA composition seem to play an important role on the recycled concrete's performance, though a limited chemical and mineralogical characterization of RA is available (Alexandridou et al., 2018; Limbachiya et al., 2007). The physical and chemical properties of the RCA like void ratio, hardness, strength, etc, are affected by the grade of the concrete of origin and upon the methods and level of screening and grading. To employ RCA as fine and coarse aggregates in the concrete mix design demands the determining and standardizing of the best practices for RCA and a controlled citation of these properties to address the strength requirements. The variability of building construction methods naturally means that RA sourced from construction and demolition activities will vary in quality and composition, which will indubitably produce new construction materials of varying quality (Silva et al., 2014).

5Scopes for Future Research

While the present study has shown that recycled concrete aggregate can be used as aggregate for new concrete, there is a need to obtain long-term in-service performance and life cycle cost data for concrete made with recycled aggregate concrete to assess its durability and performance. If additional research supports the use of concrete buildings then existing specification should be revised to permit and encourage the use of recycled concrete as aggregate. Using recycled aggregate in concrete mixes lead to conserve existing supplies of natural aggregates and to reduce the amount of solid waste that must be disposed of in landfills. Further testing and studies on the recycled aggregate concrete is highly recommended to indicate the strength characteristics of recycled aggregates for application in high strength concrete. Below are some of the recommendations for further studies:

- More investigations and laboratory tests are required to understand the strength characteristics of recycled aggregate. It is recommended that testing can be done on concrete slabs, beams and walls. Some mechanical properties such as creeping, shrinkage and abrasion are also recommended.
- The authors propose a further detailed study of the physical and chemical properties of the RCA recycled from the discarded concrete cubes, as part of this research, to deliberately investigate into the reason of the impact of the true parameters resulting in the observed variation of the compressive strength and hardness of the concrete.
- More trials with different particle sizes of recycled aggregate and percentage of replacement of recycled aggregate are recommended to get higher feasible strength characteristics in the RCA.
- The influence of contaminants in the demolished concrete from buildings should be carefully studied and investigated to extend life time of concrete made with recycled aggregate concrete.
- The fire-resistant property of recycled aggregates should be carefully studied with economic aspect of concrete processing and recycling.

As natural aggregate specification have been specified in building codes and are being utilised all over the world, similarly, specifications and standards are a key to the future use of recycled aggregates. Work is required to develop specifications and standards in order to create opportunities for the increased and efficient use of recycled aggregates.

The authors would like to extend their gratitude towards the Department of Civil Engineering of Jamia Millia Islamia University, New Delhi, India, for their support.

References

1. (BIS), B. of I. S. (1970). IS 383: 1970 Specification for Coarse and Fine Aggregates From Natural Sources for Concrete. Indian Standards, 1–24.

2. Alexandridou, C., Angelopoulos, G. N., & Coutelieris, F. A. Mechanical and durability performance of concrete produced with recycled aggregates from Greek construction and demolition waste plants, Journal of Cleaner Production, 176, 745–757,(2018).

3. Andrew Alcorn. Embodied energy and CO2 coefficientd for NewZealand building materials. Centre for Building Performance Research, Victoria University of Wellington, November, 4–16, (2001).

4. Ardente, F., Beccali, M., Cellura, M., & Mistretta, M.Building energy performance: A LCA case study of kenaf-fibres insulation board. Energy and Buildings, 40, 1–10,(2008).

5. Beltrán, M., Barbudo, A., Agrela, F., P. Galvin, A., & Jiménez, J. R. Effect of cement addition on the properties of recycled concretes to reach control concretes strengths. Journal of Cleaner Production, 79, 124–133, (2014).

6. Brand, A. S., Roesler, J. R., & Salas, A. Initial moisture and mixing effects on higher quality recycled coarse aggregate concrete. Construction and Building Materials, 79, 83–89,(2015).

7. Bui, N. K., Satomi, T., & Takahashi, H. Mechanical properties of concrete containing 100% treated coarse recycled concrete aggregate. Construction and Building Materials, 163, 496–507,(2018).

8. Bureau of Indian Standard(BIS). IS: 8112 – 1989, Specification for 43 grade Ordinary Portland Cement. Bureau of Indian Standards,New Delhi, 17,(2013).

9. Bureau of Indian Standards (BIS). IS : 2386 (Part I)-1963- Indian Method of test for aggregate for concrete. Part I - Particle size and shape. Indian Standards, (Reaffirmed 2002),(1963).

10. Cabeza, L. F., Barreneche, C., Miró, L., Morera, J. M., Bartolí, E., & Inés Fernández, A. Low carbon and low embodied energy materials in buildings: A review. Renewable and Sustainable Energy Reviews, 23, 536–542,(2013).

11. Christoforou, E., Kylili, A., Fokaides, P. A., & Ioannou, I. Cradle to site Life Cycle Assessment (LCA) of adobe bricks. Journal of Cleaner Production, 112, 443–452,(2016).

12. Christoforou, E., Kylili, A., Fokaides, P., & Ioannou, I. Cradle to site Life Cycle Assessment (LCA) of adobe bricks. Journal of Cleaner Production, 112,(2015).

13. Council, O. F. T. H. E. Directive 2008/98/EC of the European Parliament and of the European Council. Fundamental Texts On European Private Law, 3–30,(2008).

14. D, P. C. Agenda 21 on sustainable construction in developing countries. CIB (International Council for Research and Innovation in Building and Construction)., 120,(1999).

15. Dimitriou, G., Savva, P., & Petrou, M. F. Enhancing mechanical and durability properties of recycled

aggregate concrete. Construction and Building Materials, 158, 228–235,(2018).

16. Etxeberria, M., Vázquez, E., Mari, A., & Barra Bizinotto, M. Influence of amount of recycled coarse aggregates and production process on properties of recycled aggregate concrete. Cement and Concrete Research, 37, 735–742,(2007).

17. Evangelista, L., & de Brito, J. Mechanical behaviour of concrete made with fine recycled concrete aggregates. Cement and Concrete Composites, 29(5), 397–401,(2007).

18. Evangelista, L., & de Brito, J. Concrete with fine recycled aggregates: a review. European Journal of Environmental and Civil Engineering, 18(2), 129–172,(2014).

19. Gesoglu, M., Güneyisi, E., Oz, H., Taha, I., & Yasemin, M. T. Failure characteristics of self-compacting concretes made with recycled aggregates. Construction and Building Materials, 98, 334–344,(2015).

20. Hammond, G., & Jones, C. A BSRIA Guide. Embodied Carbon: The Inventory of Carbon and Energy. University of Bath, UK. Ice, 136,(2011).

21. Hansen, T. (1992). Recycling of demolished concrete and masonry : report of.

22. Hossain, M. U., Poon, C. S., Lo, I. M. C., & Cheng, J. C. P. Comparative environmental evaluation of aggregate production from recycled waste materials and virgin sources by LCA. Resources, Conservation and Recycling, 109, 67–77,(2016).

23. Hossain, Y., & Marsik, T. Conducting life cycle assessments (LCAs) to determine carbon payback: A case study of a highly energy-efficient house in rural Alaska. Energies, 12(9), (2019).

24. Hu, M., Weir, J. D., & Wu, T. Decentralized operation strategies for an integrated building energy system using a memetic algorithm. European Journal of Operational Research, 217(1), 185–197,(2012).

25. Indian Standards. IS 13311-2 (1992): Method of non-destructive testing of concret-methods of test, Part 2: Rebound hammer. Indian Standards,(1992).

26. IPCC, 2001: Climate change. Contribution of Working Group I to the Third Assessment Report of the Intergovernmental Panel on Climate Change [Houghton, J.T. Ding, Y. Griggs, D.J. Noguer, M. Linden, P.J. van der Dai, X. Maskell, K. Johnson, C.A.]. Cambridge University Press, 94,(2001).

27. IS: 4031 (Part 6). Methods Of Physical Tests For Hydraulic Cement Part 6 Determination Of Compressive Strength Of Hydraulic Cement Other Than Masonry Cement (First Revision). Bureau of Indian Standards,New Delhi, 1–3,(2005).

28. IS 4031- Part IV. Methods of physical tests for hydraulic cement. Part IV- Determination of consistency of standard cement paste. Bureau of Indian Standards, New Delhi, Reaffirmed in 2005,(1988).

29. IS 4031- Part V. Methods of physical tests for hydraulic cement. Part V- Determination of initial and final setting times. Bureau of Indian Standards, New Delhi, Reaffirmed in 2005,(1988).

30. IS 456. Concrete, Plain and Reinforced. Bureau of Indian Standards,New Dehli, 1–114,(2000).

31. IS 516:2014. Method of Tests for Strength of Concrete. IS : 516 - 1959 (Reaffirmed 2004), New Delhi,India,(2004).

32. Kong, D., Lei, T., Zheng, J., Ma, C., Jiang, J., & Jiang, J. Effect and mechanism of surface-coating pozzalanics materials around aggregate on properties and ITZ microstructure of recycled aggregate concrete. Construction and Building Materials, 24(5), 701–708,(2010).

33. Kou, S. C., Poon, C. S., & Agrela, F. Comparisons of natural and recycled aggregate concretes prepared with the addition of different mineral admixtures. Cement & Concrete Composites - CEMENT CONCRETE COMPOSITES, 33, 788–795,(2011).

34. Kurad, R., Silvestre, J., Brito, J., & Ahmed, H. Effect of incorporation of high volume of recycled concrete aggregates and fly ash on the strength and global warming potential of concrete. Journal of Cleaner Production, 166, 485–502,(2017).

35. Limbachiya, M. C., Marrocchino, E., & Koulouris, A. Chemical-mineralogical characterisation of coarse recycled concrete aggregate. Waste Management, 27(2), 201–208,(2007).

36. Lotfi, S., Deja, J., Rem, P., Mróz, R., Van Roekel, E., & Van Der Stelt, H. Mechanical recycling of EOL concrete into high-grade aggregates. Resources, Conservation and Recycling, 87, 117–125,(2014).

37. McGinnis, M. J., Davis, M., de la Rosa, A., Weldon, B. D., & Kurama, Y. C. Strength and stiffness of concrete with recycled concrete aggregates. Construction and Building Materials, 154, 258–269,(2017).

38. Morgan, M. R. Climate change 2001. In Weather (Vol. 59, Issue 8),(2004).

39. Ortiz-rodriguez, O., Castells, F., & Sonnemann, G. Sustainability in the construction industry: A review of recent developments based on LCA. Construction and Building Materials, 23, 28–39,(2009).

40. Pešta, J., Pavlů, T., Fortová, K., & Kočí, V. Sustainable masonry made from recycled aggregates: LCA case study. Sustainability (Switzerland), 12(4),(2020).

41. Poon, C. S., Shui, Z. H., Lam, L., Fok, H., & Kou, S. C. Influence of moisture states of natural and recycled aggregates on the slump and compressive strength of concrete. Cement and Concrete Research, 34(1), 31–36,(2004).

42. Praseeda, K., Reddy, B., & Mani, M. Embodied energy assessment of building materials in India using process and input–output analysis. Energy and Buildings, 86, 677–686,(2015).

43. Sharma, A., Saxena, A., Sethi, M., Shree, V., & Varun. Life cycle assessment of buildings: A review. Renewable and Sustainable Energy Reviews, 15(1), 871–875,(2011).

44. Silva, R. V., De Brito, J., & Dhir, R. K. Properties and composition of recycled aggregates from construction and demolition waste suitable for concrete production. Construction and Building Materials, 65, 201–217,(2014).

45. STANDARDS, Burea. O. I. Handbook on Concrete Mix Design,(1982).

46. Tam, V. W. Y., & Tam, C. M. Assessment of durability of recycled aggregate concrete produced by two-stage mixing approach. Journal of Materials Science, 42(10), 3592–3602,(2007).

47. Tam, V. W. Y., & Tam, C. M. Diversifying two-stage mixing approach (TSMA) for recycled aggregate concrete: TSMAs and TSMAsc. Construction and Building Materials, 22(10), 2068–2077,(2008).

48. United Nation Environment Programme. Buildings and Climate Change: Current Status , Challenges and Opportunities. DG Environment News Alert Dervice, 71, 1,(2007).

49. Venkatarama Reddy, B. V., & Jagadish, K. S. Embodied energy of common and alternative building materials and technologies. Energy and Buildings, 35(2), 129–137,(2003).

50. Verian, K. P., Ashraf, W., & Cao, Y. Properties of recycled concrete aggregate and their influence in new concrete production. Resources, Conservation and Recycling, 133(February), 30–49,(2018).

51. Vẋquez, E. (Professor), & RILEM Technical Committee 217-PRE. Progress of recycling in the built environment : final report of the RILEM Technical Committee 217-PRE,(2013).

52. Xuan, D., Zhan, B., & Poon, C. S. Assessment of mechanical properties of concrete incorporating carbonated recycled concrete aggregates. Cement and Concrete Composites, 65, 67–74,(2016).

53. Zabalza Bribián, I., Aranda Usón, A., & Scarpellini, S. Life cycle assessment in buildings: State-of-the-art and simplified LCA methodology as a complement for building certification. Building and Environment, 44(12), 2510–2520,(2009).

54. Zaharieva, R., Buyle-Bodin, F., Skoczylas, F., & Wirquin, E. Assessment of the surface permeation properties of recycled aggregate concrete. Cement and Concrete Composites, 25(2), 223–232,(2003).

55. Zhan, B. J., Xuan, D. X., Zeng, W., & Poon, C. S. Carbonation treatment of recycled concrete aggregate: Effect on transport properties and steel corrosion of recycled aggregate concrete. Cement and Concrete Composites, 104(July), 103360,(2019).

FORMULATION OF FISH FEED WITH MULTIPLE INGREDIENTS USING A SOFTWARE TOOL DEVELOPED IN JAVA

PINAKI CHAKRABORTY[A], TUHINA SINGH[A], JAIGOPAL SHARMA[B], RINA CHAKRABARTI[C*]

[a]*Department of Computer Science and Engineering, Netaji Subhas University of Technology, New Delhi 110078, India.*

[b]*Department of Biotechnology, Delhi Technological University, Delhi 110042, India.*

[c]*Aqua Research Lab, Department of Zoology, University of Delhi, Delhi 110007, India.*

ABSTRACT

A software tool named Interactive Fish Feed Designer (IFFD) has been developed using Java programming language for the formulation of fish feed. IFFD allows formulating fish feed with desirable protein and lipid levels using multiple ingredients. In the first step, ingredients are selected from a list. Then the ratio of the ingredients is adjusted to maintain the percentage of protein and lipid in the feed; finally, the quantity of the total feed is specified. IFFD generates a report that may be printed and referred later. Six plant-based pelleted feeds are designed using this software. The feeds are prepared with the Twin-screw Extruder. The protein and lipid contents of feeds varied from 26.90 - 38.61 and 10.31 - 12.63%, respectively. The software is interactive and user-friendly. The calculation is automatic; results are precise and clearly visualized.

KEYWORDS: Interactive Fish feed designer, Java programming language, Plant ingredients, Twin-screw extruder.

1. INTRODUCTION

Aquaculture industry has been expending globally with the diversification of cultivable species. Nutrition plays significant role in the aquaculture production. There is a growing demand of aquafeed to meet the requirement for the estimated enhanced production of already existing

J. Aqua Trop. Vol. 35, No. (1-4) 2020, Pages 149-165
© Prints Publications Pvt. Ltd.
Corresponding Author E-mail: aquarsearchlab@yahoo.co.in
http//www.printspublications.com
DOI:-http://doi.org/10.32381/JAT.2020.35.1-4.14

This article has been accepted for publication in a future issue of this journal, but has not been fully edited. Content may change prior to final publication. Citation information: DOI 10.1109/TIE.2021.3051585, IEEE Transactions on Industrial Electronics

Fractional Order Notch Filter for Grid-Connected Solar PV System with Power Quality Improvement

Manoj Badoni, *Member*, *IEEE*, Alka Singh, *Senior Member*, *IEEE*, Sandeep Pandey, Bhim Singh, *Fellow*, *IEEE*

***Abstract*- This paper deals with the development of fractional order notch filter (FONF) for a grid-connected solar photovoltaic (PV) system. The developed FONF control approach is used to estimate fundamental active constituents from the distorted load currents and hence gating pulses for operating voltage source converter (VSC) are used in the PV system. This control approach for the grid-connected solar PV system is designed to achieve several purposes such as feeding active power demand of load/grid and counter current related power quality issues at common connecting point. The power quality issues taken into consideration are harmonics distortion, reactive power burden on the system and unbalancing of connected loads. The FONF based control proposes a modified structure of an integer order notch filter. The integer order filters have limitation due to fixed integrator and differentiator term. In FONF, the power of integrator used in a notch filter, can be modified according to the application required for obtaining accurate response of the system. A prototype of the grid-connected solar PV system is developed in the laboratory using IGBTs based VSC and dSPACE MicroLabBox (DS-1202) to demonstrate the behaviour of the FONF based control. Simulation and experimental results are obtained for steady state and unbalanced loads with variation in solar irradiance. The harmonic distortions in the system are observed as per the IEEE-519 standard.**

***Index Terms* — Solar photovoltaic generation, fractional order control, notch filter, harmonics, power quality.**

NOMENCLATURE

PV	Photovoltaic.
FONF	Fractional order notch filter.
IONF	Integer order notch filter
VSC	Voltage source converter.
RESs	Renewable energy sources.
MPPT	Maximum power point tracking.
PQ	Power quality.
NLMS	Normalized least mean square.
NLMF	Normalized least mean fourth.
PCC	Point of common coupling.
R_s-L_s	Line impedance.
L_f	Interfacing inductors.
R_f-C_f	Ripple filter.
V_{dc}	DC bus voltage.
$\Gamma(\cdot)$	Gamma function.
α,β	Fractional parameters.
G_{OL}	Forward transfer function.
G_{FON}	FONF transfer function.
G_{ION}	IONF transfer function.
$\phi_{pa}, \phi_{pb}, \phi_{pc}$	Power factor angles of load currents.
$I_{pra}, I_{prb}, I_{prc}$	Phase currents.
I_{pa}, I_{pb}, I_{pc}	Active components of load currents.
I_{pavg}	Average active power component.
v_{sa}, v_{sb}, v_{sc}	PCC voltages.
u_{pa}, u_{pb}, u_{pc}	Unit in-phase components.
V_t	PCC voltage magnitude.
$y_{va}^{\cdot}$, $y_{vb}^{\cdot}$, $y_{vc}^{\cdot}$	Fundamental components of PCC voltages
i_{pdc}	DC link PI controller output.
e_{dc}	Voltage error.
V_{PV}, I_{PV},P_{PV}	PV voltage, PV current and PV power.
I_{pvf}	Dynamic reflection component.
i_{ga}, i_{gb}, i_{gc}	Sensed grid currents.
i_{la}, i_{lb}, i_{lc}	Load currents.
i_{ia}, i_{ib}, i_{ic}	VSC currents.
i_{ga}^{*}, i_{gb}^{*}, i_{gc}^{*}	Reference grid currents.
T_{r1}	Initial rise time.
T_f	Fall time during unbalancing.
T_{r2}	Final rise time.
ISE	Integral square error.

Manuscript received June 19, 2020; revised September 11, 2020, October 26, 2020, November 29, 2020 accepted December 29, 2020.

M. Badoni is with the Electrical and Instrumentation Engineering Department, Thapar Institute of Engineering and Technology, Patiala, Punjab, India (e-mail: manojbadoni23@gmail.com).

A. Singh is with the Electrical Engineering Department, Delhi Technological University, Delhi, India (e-mail: alkasingh.dr@gmail.com).

S. Pandey is with the Electrical and Instrumentation Engineering Department, Thapar Institute of Engineering and Technology, Patiala, Punjab, India (e-mail: sandeep.pandey@thapar.edu).

B. Singh is with the Electrical Engineering Department, Indian Institute of Technology, Delhi, India (e-mail: bhimsinghiitd63@gmail.com).

I. INTRODUCTION

Growing concern about global climate change and increasing electricity demand have provided an impetus to renewable energy sources (RESs). Among several RESs viz. wind power, biomass, biogas, fuel cell, small/micro-hydro, the solar photovoltaic (PV) energy conversion system is the preferred choice because of its availability, easy installation, environment friendly nature and reduced cost [1]. An installation of large-scale grid connected solar PV generating stations, is becoming more prevalent in developed as well as developing countries. Government of India has also set a goal to install solar PV generation of 100 GW by 2022 [2]-[3]. The grid-connected PV system provides a link of the PV array and the grid via a voltage source converter (VSC). These systems are often equipped with maximum power point tracking (MPPT) control to extract as much power as possible from the

0278-0046 (c) 2020 IEEE. Personal use is permitted, but republication/redistribution requires IEEE permission. See http://www.ieee.org/publications_standards/publications/rights/index.html for more information.
Authorized licensed use limited to: DELHI TECHNICAL UNIV. Downloaded on February 15,2021 at 10:31:54 UTC from IEEE Xplore. Restrictions apply.

This article has been accepted for publication in a future issue of this journal, but has not been fully edited. Content may change prior to final publication. Citation information: DOI 10.1109/TIE.2021.3051585, IEEE Transactions on Industrial Electronics

PV panel. This can be achieved by controlling the duty cycle to determine the on and off states of semiconductor device used within the DC-DC converter interfaced with the PV array [4].

Moreover, an increased use of nonlinear loads and presence of highly inductive loads have raised power quality concerns for the utility. Nonlinear loads introduce distortion in the grid currents, which leads to the distortion in the grid voltages. Large and heavy inductive loads drawing power at low power factor, cause an additional burden on the grid. Besides this, an unbalancing in the three-phase distribution network can lead to heavy neutral current on the neutral conductor, which may lead to its damage [5]. An integration of RESs with the utility grid requires various power conversion stages (power converters), which enhance harmonic distortions in the supply system. Therefore, the grid integrated solar PV system should not only be capable of feeding real power in the grid/load and also capable of mitigating power quality issues. The solution of overcoming power quality problems such as harmonics, feeding lead/lag reactive power and load unbalancing can be easily achieved with the use of active shunt compensator. The modest design, fast and stable operation make active shunt compensators very fascinating solution for load compensation over passive compensators [6]. The solution is even more attractive and cost effective when the same VSC is suitably controlled to achieve twin objectives of feeding real as well as reactive power [7]. Several work on achieving these twin objectives in the grid connected solar PV system have been mentioned in the literature. Arab *et al.* [8] have proposed a robust linear quadratic regulator with added integral action controller to obtain different functions of the solar PV system such as power line conditioner, an active power regulator and a voltage stabilizer. Modi *et al.* [9] have introduced Widrow-Hoff algorithm to achieve twin functions of grid-tied solar PV system viz. extracting maximum power from the PV array and to deliver to the load, in addition to this system, also improves power quality at the distribution system. Miranda *et al.* [10] have investigated a hybrid control to achieve uninterruptable supply irrespective of intermittent nature of solar PV array along with mitigation of power quality issues viz. harmonics and power factor correction.

The features of active shunt compensator can be incorporated in the PV array fed grid connected VSC with the help of suitable control approaches. Numerous control methods for such applications have been reported in the literature. These are conventional techniques such as instantaneous p-q theory [11], which uses αβ0 transformation (Clark transformation) comprising a real matrix that transforms three-phase voltages/currents into αβ0 stationary reference frame, power balance theory [12], an instantaneous symmetrical component theory (ISCT) [13], which has been developed to operate dual VSC to enhance power quality in the microgrid operation. The hybrid one cycle control (HOCC) [14], has been developed for three phase PFC rectifier and combines superior performance of symmetrical pulse width modulation (PWM) and a control block that can be operated in SPWM and space vector PWM (SVPWM). Numerous artificial intelligence-based controllers have been evolved for the grid-tied PV system. These are based on artificial neural network (ANN), T-S fuzzy controller and adaptive neuro fuzzy based inference system [15]-[17].

Adaptive theory-based controls have acquired notable consideration over the past decade as they avoid the need to tune and fix several parameters in real time. An automatic tuning helps to accomplish desired objectives more effectively. Numerous adaptive controls have been reported in the literature and some of them are based on multilayer fifth order generalized-integrator [18], adaptive differential evolution control [19], adaptive Laguerre filter based control [20], least mean square-Adaline based adaptive neuro-fuzzy controller [21] etc. Some other recent control approaches are based on notch filter, which are adaptive notch filter (ANF) operated multifunction control for the grid connected RES system [22]-[23] and amplitude adaptive notch filter [24]. The adaptive control strategy is embedded with the notch filter in [22]-[24] and its comparison with the integer order notch filter design. The limitation of these controllers is that only the symmetric gain curve is possible. The integer order integrator cannot provide the asymmetrical gain curve around the central frequency of notch filter.

The notch filter is usually designed for rejecting all unwanted frequencies present in the signal and selecting a frequency of interest by providing high gain at the same frequency [25]. Notch filters basically belong to a category of band pass filters or band reject filters and hence are used as selector or rejector circuits for various applications. An integer order notch and other filters have their own limitations due to their fixed integrator or differentiator term [26]. The fractional order control theory gives an opportunity to alter this fixed structure of an integer order filter and because of its flexibility and advantage fractional order filters have come into existence [27].

Using fractional order control theory, the power of integrator used in a conventional notch filter can be changed according to the designer's choice for getting a more desirable and accurate response during operation. The fractional order notch filter produces the gain term between 0db/decade and ±20 db/decade or ±40 db/decade unlike the integer order notch. Another advantage of fractional order notch filter is the possibility to obtain asymmetrical gain response curve, which is not possible in case of conventional notch filter. However, only some limited studies and research have been reported in the literature related to the operation of fractional order filters in the field of signal processing [28]-[29] but no promising work has been reported in the field of power electronics control.

In this paper, a novel structure of notch filter is developed particularly for the operation of a grid integration of solar PV system. This fractional order notch filter (FONF) is primarily used to extract fundamental weight component from the distorted load currents. The active power requirements of load/grid along with attributes of active shunt compensator such as harmonics alleviation, reactive power burden and load unbalancing are demonstrated using FONF control. A comparative simulation study and test results validate significant advantages for a precise control by reducing an overall integral square error of the system.

0278-0046 (c) 2020 IEEE. Personal use is permitted, but republication/redistribution requires IEEE permission. See http://www.ieee.org/publications_standards/publications/rights/index.html for more information.
Authorized licensed use limited to: DELHI TECHNICAL UNIV. Downloaded on February 15,2021 at 10:31:54 UTC from IEEE Xplore. Restrictions apply.

This article has been accepted for publication in a future issue of this journal, but has not been fully edited. Content may change prior to final publication. Citation information: DOI 10.1109/TIE.2021.3051585, IEEE Transactions on Industrial Electronics

Major contributions in this paper are summarized as follows.

- Development of fractional order notch filter (FONF) for grid integrated solar photovoltaic (PV) system.
- The FONF controller is developed to extract fundamental active components from the distorted load currents and to alleviate PQ problems such as harmonics, reactive power burden on the system and load unbalancing.
- Real time implementation of grid integrated PV system developed in the laboratory. Performance of FONF controller is validated on a developed prototype.
- Testing system operation in various modes such as during daytime when the sun light is available. It feeds active power to the grid/load along with taking care of certain ancillary services related to PQ. Moreover, during night, the system works as power quality compensator, taking care of several PQ issues.
- Performance parameters of FONF control for solar PV system are compared with integer order notch filter (IONF), normalized least mean square (NLMS) and normalized least mean fourth (NLMF) based control techniques [30]-[31].
- Superior performance of proposed control is demonstrated in terms of integral square error, computational complexity, fundamental weight convergence, harmonics compensation and sampling time.

II. SYSTEM DESCRIPTION

Fig. 1 shows a schematic diagram of 3-phase AC mains with small line impedance (R_s-L_S) feeding the linear/nonlinear loads connected to it. The solar PV array (1.5 kW rated power capacity) is connected at the DC link of VSC. The AC side of VSC is coupled with the point of common coupling (PCC) by using interfacing inductors (L_f). Small ripple filter (R_f-C_f) is connected at PCC, which are used to supress high frequency components generated from switching of semiconductor devices. The PCC voltages (v_s), grid currents (i_s), load currents (i_l), DC link voltage (V_{dc}), PV array voltage and PV current (V_{PV} and I_{PV}) are sensed using Hall-Effect voltage and current sensors. The FONF based control algorithm is implemented using dSPACE DS-1202 MicroLabBox and detected voltages and currents are entered using analog to digital converter (ADC) channels of controller interfacing box. System parameters are given in Appendix-A.

III. CONTROL ALGORITHM

The fractional notch filter-based control technique is evolved for power electronics interface i.e. control of VSC used in the grid-connected PV system. This is used to acquire fundamental current components from distorted load currents and to generate gating pulses of VSC used in the solar PV system. The control is developed for VSC, which feeds active power transfer to the load/grid generated from the PV array along with active compensation, which involves solving several power quality issues viz. harmonics distortion in the grid current, reactive power burden and load unbalancing. In this section, the description of fractional notch filter (FONF) with its mathematical modeling and use of FONF for the grid connected solar PV system are described in detail.

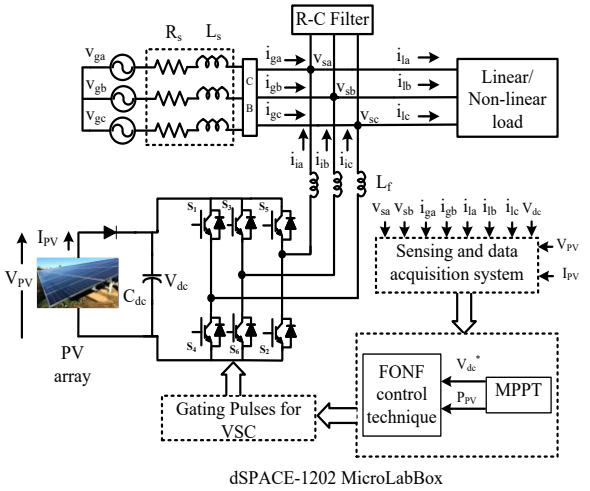

Fig. 1 System configuration of grid connected solar PV system.

A. Fractional Notch Filter Based Control Technique

To achieve twin objectives of grid integrated solar PV system for feeding load/grid along with certain ancillary functions viz. eliminating the harmonics, a fractional order-based notch filter based control strategy is deployed here. It also serves the load balancing and reactive power compensation. A novel fractional order notch filter is designed for obtaining the active constituents of load current for achieving the desired objectives. The fractional calculus control theory deals with a generalized form of both the integer and non-integer order controllers and filters. It provides additional flexibility to adjustthe power of integral and differentiator term used in a filter unlike the conventional notch and other filter design. According to Riemann-Louville [32], a fractional derivative and integral function are given as,

$$\frac{d^{\alpha}}{dt^{\alpha}}f(t) = \frac{1}{\Gamma(1-\alpha)}\frac{d}{dt}\int_0^t (t-\tau)^{-\alpha} f(\tau)d\tau \quad (1)$$

where $\Gamma(\cdot)$ is the gamma function, α is power of fractional order integrator used in a fractional order notch filter (α<0). The Laplace transform of (1) with zero initial condition gives,

$$L_0\{d_t^{\alpha} f(t)\} = s^{\alpha}F(s) \quad (2)$$

B. Structure of Fractional Order Notch Filter

Based on a definition and Laplace transformation of fractional derivative and integral term, a fractional second order notch filter with two fractional integral terms is proposed. The structure of fractional order notch filter is given in Fig. 2(a). The equivalent block illustration of fractional order notch filter (shown in Fig. 2(a)) can be represented in the form of cascaded loop as shown in Fig. 2(b). After solving the inner

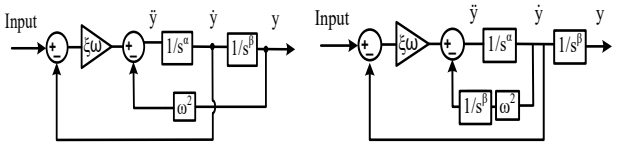

(a) (b)

Fig. 2 Fractional order notch filter (a) block diagram (b) equivalent block diagram.

0278-0046 (c) 2020 IEEE. Personal use is permitted, but republication/redistribution requires IEEE permission. See http://www.ieee.org/publications_standards/publications/rights/index.html for more information.
Authorized licensed use limited to: DELHI TECHNICAL UNIV. Downloaded on February 15,2021 at 10:31:54 UTC from IEEE Xplore. Restrictions apply.

This article has been accepted for publication in a future issue of this journal, but has not been fully edited. Content may change prior to final publication. Citation information: DOI 10.1109/TIE.2021.3051585, IEEE Transactions on Industrial Electronics

loop, the forward transfer function (TF) of the block illustration (Fig. 2(b)) is expressed as,

$$G_{OL} = \frac{\xi\omega\, s^{\beta}}{s^{\alpha+\beta}+\omega^2} \quad (3)$$

where G_{OL} is open loop TF of the filter, α and β are the fractional parameters, ξ is the damping factor and ω is the natural frequency. The outer loop (Fig. 2(b)) with unity feedback combined with the forward loop TF given in (3) provides the overall transfer function of fractional order notch filter (FONF) and it is represented as,

$$G_{FON} = \frac{\xi\omega\, s^{\beta}}{s^{\alpha+\beta}+\xi\omega\, s^{\beta}+\omega^2} \quad (4)$$

where G_{FON} is the overall TF of the fractional notch filter. The complete TF of FONF consists of two fractional parameters α and β, which can be variedin the interval (0, 2). The transfer function given in (4) is a generalized form depicting both the integer order and non-integer order notch filter. If the value of α=β=1 is taken, it results in a conventional second order notch filter having transfer function given as,

$$G_{ION} = \frac{\xi\omega\, s}{s^2+\xi\omega\, s+\omega^2} \quad (5)$$

where G_{ION} is the TF of integer order notch filter (IONF).

C. Development of FONF Control Approach for Grid-Connected PV System

Fig. 3 illustrates the block diagram of fractional order notch filter (FONF) for generating gating pulses for VSC used in the solar PV system. The active constituent of load current is required and the same can be achieved through the $\cos\emptyset$ component of the current. The power factor angle of the load currents ($\emptyset_{pa}$, $\emptyset_{pb}$ and $\emptyset_{pc}$), is obtained by substituting the current and voltages of all three phases as input to three different fractional order notch filters. As shown in the figure, the outputs of a fractional notch filter are y and $\dot{y}$ respectively. The control scheme shown in Fig. 3, provides phase angle of the voltage and current of a phase as well as component I_{pra}. The outputs of the fractional notch filters for all three phases provide the fundamental frequency components of the three phase voltages and currents. To get the active power component of each phase current (I_{pa}), the cosine of power factor angle is multiplied with the magnitude of all three phase currents (I_{pra}, I_{prb} and I_{prc}) determined using fractional order notch filter. The phase angle difference between the current and voltage gives the desired power factor. The active constituents of load current are acquired as follows,

$$I_{pa} = I_{pra}\cos\emptyset_{pa},\ I_{pb} = I_{prb}\cos\emptyset_{pb} \text{ and } I_{pc} = I_{prc}\cos\emptyset_{pc} \quad (6)$$

An average active power component (I_{pavg}) is computed from I_{pa}, I_{pb} and I_{pc} as,

$$I_{pavg} = \frac{I_{pa}+I_{pb}+I_{pc}}{3} \quad (7)$$

D. Generation of Reference Grid Currents and Gating Pulses

The voltage magnitude (V_t) at PCC is determined using phase voltages v_{sa}, v_{sb} and v_{sc} as,

$$V_t = \sqrt{\frac{2}{3}\left(v_{sa}^2 + v_{sb}^2 + v_{sc}^2\right)} \quad (8)$$

The unit in-phase vectors (u_{pa}, u_{pb} and u_{pc}) of PCC voltages are obtained using fundamental components of PCC voltages ($\dot{y_{va}}$, $\dot{y_{vb}}$ and $\dot{y_{vc}}$) and PCC voltage amplitude as,

$$u_{pa} = \frac{\dot{y_{va}}}{V_t},\ u_{pb} = \frac{\dot{y_{vb}}}{V_t} \text{ and } u_{pc} = \frac{\dot{y_{vc}}}{V_t} \quad (9)$$

The reference grid currents are obtained by active components of the load currents (I_{pa}, I_{pb} and I_{pc}) and VSC loss component (I_{pdc}). An appropriate operation of solar PV converter depends on the DC link voltage, which should be regulated at reference value. An incremental conductance (InC) based MPPT algorithm is used to obtained the reference DC link voltage (V_{dc}^*) [33]. The proportional-integral (PI) controller is used here to adjust the DC link voltage to the reference value. To accomplish the regulated DC voltage, sensed DC link voltage of VSC is compared with reference DC voltage and the voltage error (e_{dc}) produced from their comparison, is input to the PI controller, whose output is considered as the active loss component (I_{pdc}). The (10) and (11) are representing expressions of e_{dc} and I_{pdc} at k^{th} time instant as,

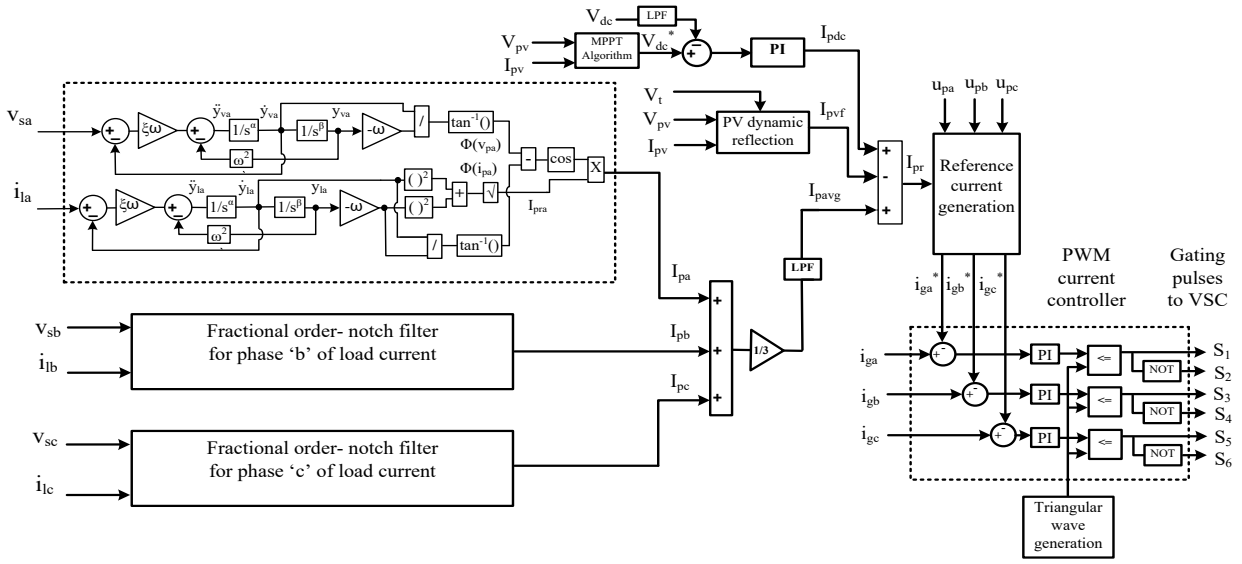

Fig. 3 Fractional order-notch filter based control technique for gating pulses generation.

0278-0046 (c) 2020 IEEE. Personal use is permitted, but republication/redistribution requires IEEE permission. See http://www.ieee.org/publications_standards/publications/rights/index.html for more information.
Authorized licensed use limited to: DELHI TECHNICAL UNIV. Downloaded on February 15,2021 at 10:31:54 UTC from IEEE Xplore. Restrictions apply.

This article has been accepted for publication in a future issue of this journal, but has not been fully edited. Content may change prior to final publication. Citation information: DOI 10.1109/TIE.2021.3051585, IEEE Transactions on Industrial Electronics

$$e_{dc}(k) = v^*_{dc}(k) - v_{dc}(k) \quad (10)$$

Output of the PI controller is given as,

$$I_{pdc}(k) = I_{pdc}(k-1) + k_{pd}\{e_{dc}(k) - e_{dc}(k-1)\} + k_{id}e_{dc}(k) \quad (11)$$

where V_{dc} and V_{dc}^* are sensed and reference DC link voltages, k_{pd} and k_{id} are proportional and integral gains of PI controller.

The dynamic performance of a solar PV system is improved by considering an additional term using reflection of the instantaneous variation in PV array power (P_{PV}=V_{PV}*I_{PV}) on the grid current (i_g). Therefore, the dynamic reflection component (I_{pvf}), which represents the contribution of PV array power, is figured as,

$$I_{pvf} = \frac{2\times P_{pv}}{V_t} \quad (12)$$

The reference grid currents are obtained as,

$$i^*_{ga} = u_{pa}\left(I_{pavg} + I_{pdc} - I_{pvf}\right) \quad (13)$$

$$i^*_{gb} = u_{pb}\left(I_{pavg} + I_{pdc} - I_{pvf}\right) \quad (14)$$

$$i^*_{gc} = u_{pc}\left(I_{pavg} + I_{pdc} - I_{pvf}\right) \quad (15)$$

These reference grid currents (i_{ga}^*, i_{gb}^* and i_{gc}^*) are compared with sensed grid currents (i_{ga}, i_{gb} and i_{gc}), therefore, current errors are obtained. These current errors are processed through PI controllers. The PI controllers outputs are compared with triangular waveform of 10 kHz frequency, which generates gating pulses for VSC.

IV. RESULTS AND DISCUSSION

The grid-tied PV system is developed and gating pulses for VSC are generated with FONF based control. The control for VSC is designed to study several functions viz. feeding active power demand of grid/load and taking care of power quality issues. Simulated and experimental results are presented here to validate the behaviour of FONF control for multifunctional grid-tied PV system. This section starts with performance of FONF control and its comparison with integer order notch filter (IONF) using FOMCON (Fractional-order Modeling and Control) toolbox of MATLAB platform, followed by experimental performance of developed PV system.

A. Performance of Fractional Order Notch Filter (FONF)

In conventional IONF, the sharpness of the gain curve of the notch filter is maximum for lower value of ξ and the gain curve is also symmetric [23], as shown in Fig. 4. It is also evident that for lower value of ξ, the speed of response is very sluggish and to speed up the response of the system, the value of ξ should be increased. The higher value of ξ, gives almost flat Bode curve at desired frequency and the nature of notch filter with sharpness at operating frequency is lost. Consequently, there is a tradeoff between these two desirable characteristics of the system, one is the speed of response and another is the sharpness of the gain curve.

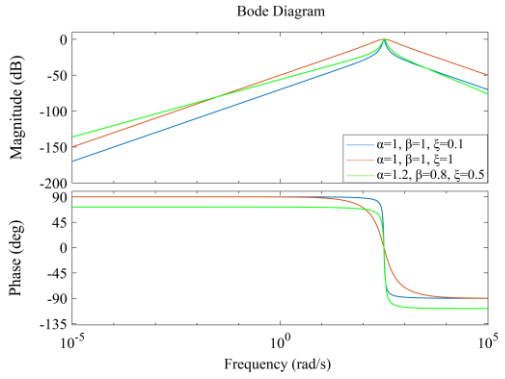

Fig. 4 Bode plot comparison of IONF (α=1, β=1, ξ=0.1 and α=1, β=1, ξ=1) and FONF (α=1.2, β=0.8, ξ=0.5) with different values of fractional parameters.

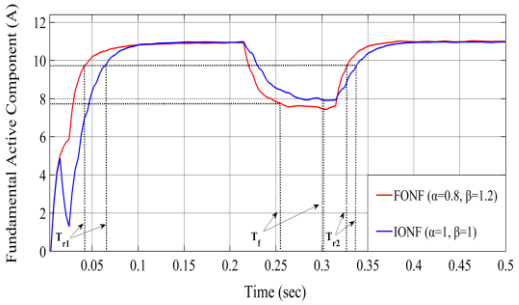

Fig. 5 Comparative performance of IONF and FONF in converging active weight component.

The proposed FONF gives an extra degree of freedom to get the both desirable characteristics sharpness of gain curve and speed of response at same time because an asymmetrical gain curve response can be achieved with the help of additional fractional order parameters. To ameliorate performance of the system, the asymmetric gain plot (not possible using conventional second order notch filter) can be achieved by varying the value of fractional parameters α and β. Suitable values of α=1.2 and β=0.8 are chosen and these provide sharp gain curve and also high speed of response. After inserting the value of fractional parameters in (4), a second order term is obtained for the denominator of transfer function while the numerator term provides the asymmetric components of gain curve. The Bode plot in Fig. 4, shows the sharpness of the gain curve does not alter, and the same nature of the curve is observed for the case of ξ=0.1 (conventional integer order notch filter). In short, the speed of response of the system has enhanced without affecting the sharpness of the gain curve with the help of asymmetric component of the fractional order notch filter. Fig. 4 shows the comparative analysis of gain curve for different values of ξ with FONF and IONF and validates the advantage of proposed fractional order notch filter. In this figure, two curves almost coincide with two different values of ξ=0.1, in case of integer order notch filter

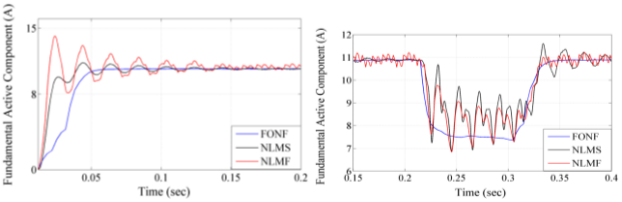

(a) (b)

Fig. 6 Convergence of fundamental active components using FONF, NLMS and NLMF under (a) steady state and (b) unbalanced loading conditions.

0278-0046 (c) 2020 IEEE. Personal use is permitted, but republication/redistribution requires IEEE permission. See http://www.ieee.org/publications_standards/publications/rights/index.html for more information.
Authorized licensed use limited to: DELHI TECHNICAL UNIV. Downloaded on February 15,2021 at 10:31:54 UTC from IEEE Xplore. Restrictions apply.

This article has been accepted for publication in a future issue of this journal, but has not been fully edited. Content may change prior to final publication. Citation information: DOI 10.1109/TIE.2021.3051585, IEEE Transactions on Industrial Electronics

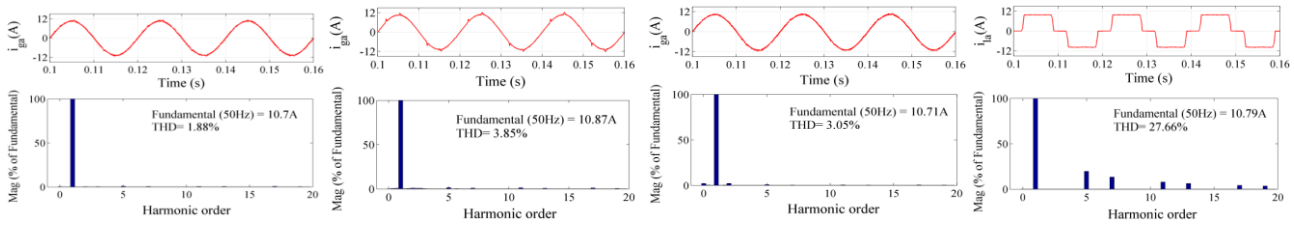

Fig. 7 Harmonic spectra of (a) grid current i_{ga} using FONF (b) grid current i_{ga} using NLMS (c) grid current i_{ga} using NLMF (d) load current i_{la}.

and ξ=0.5 in case of FONF. It indicates that for increasing the value of damping ratio ξ does not alter the sharpness of FONF and provides fast response in comparison with IONF.

B. Comparative Performances of IONF and FONF

Fig. 5 shows the output of notch filter in form of fundamental active component of the load current phase 'a'. The average value of this current is I_{pa}=11A in case of a balanced load. The initial value of rise time or to attain the 90% of reference value of fundamental component of the load current is defined as 'T_{rI}' as given in Table-I. In case of IONF, rise time T_{rI}=0.07s, while in case of FONF, it takes comparatively less time T_{rI}=0.04s. In addition to this, FONF provides a smooth pickup in initial part of the response while in case of IONF initially unwanted oscillations occur and give comparatively inferior response as shown in Fig. 5. To check the robust performance of the system, a load disturbance is injected at 0.22s, and the desired reference value of load current in case of unbalancing is shifted to I_{pa}=7.5A. The new current (under unbalanced loading condition) reference is now 3.5A below the steady state reference value of the load current and to reach 90% of span 3.5A is now denoted as the 'T_f' (fall time). The FONF control successfully attains the desired value of the load current at T_f =0.25s, and comparatively no offset present in this case. The IONF control shows the sluggish behaviour with T_f =0.30s, and as a result of this, an offset is present between the desired value and the actual value of the load current. At 0.32s, the load again acquires its previous position (steady state value) and now the load current again increases to the previous value of I_{pa}=11A. At this position, the value of time to reach I_{pa} at its final value is denoted as 'T_{r2}' and corresponding values in case of IONF and FONF are mentioned in Table-I. The overall performance of the system is evaluated here by calculating the integral square error (ISE) and the corresponding value in both the cases, is given in Table-I, which is less in case of FONF control. It is evident from the above discussion that the system with FONF based control, presents a significant improvement in the transient and steady state performances and validates its applicability in converging active fundamental component.

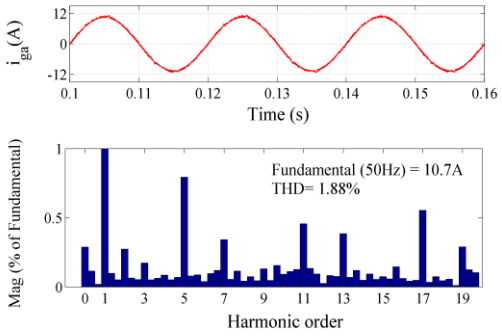

Fig. 8 Harmonic spectrum of grid current with different frequency components using FONF controller.

C. Comparative Performance of FONF with NLMS and NLMF Control Techniques

The proposed FONF controller is compared with some recently developed control techniques such as NLMS and NLMF for grid connected solar PV system. These control techniques are compared in terms of computational complexity, fundamental weight convergence, harmonics compensation and sampling time taken while implementing on dSPACE DS-1202. Figs. 6 (a) and (b) show the convergence of active fundamental load component extracted using FONF, NLMS and NLMF control techniques in balanced and unbalanced load circumstances. Fig. 6(a) illustrates the convergence under steady state loading condition, which shows approximately 10 cycles are taken by NLMS and 8 cycles are taken by NLMF, whereas convergence is very fast with FONF (achieve steady state within a cycle). Fig. 6(b) represents the convergence of fundamental active weight during load unbalancing (aftera phase of load is disconnected from t=0.2s to 0.3s), large oscillations are observed in fundamental weight using NLMS and NLMF, whereas there are almost no oscillations in weight component with FONF. Fig. 7 shows harmonics compensation capability of FONF, NLMS and NLMF. Figs. 7(a) to (c) depict harmonic spectra of the grid current (phase 'a') i_{sa}, using FONF, NLMS and NLMF. Fig. 7(d) shows harmonics spectrum of load current (phase 'a') i_{la}. The total harmonic distortions (THDs) of 3.85% and 3.05% are obtained in i_{sa} using NLMS and NLMF, whereas 1.88% THD is obtained using FONF control. The sampling times (T_s) taken by controllers FONF, NLMS and NLMF during real time implementation on dSPACE are 35μs, 50μs and 60μs, respectively, which is observed less in case of FONF controller. Hence, it is observed from above discussion that the FONF controller demonstrates superior performance

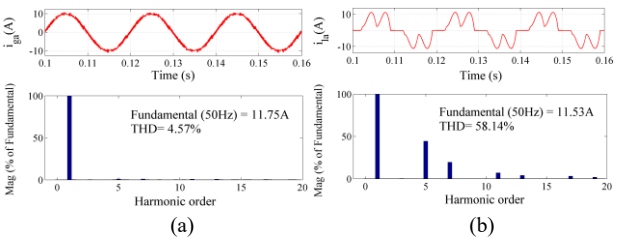

Fig. 9 Harmonic spectrum under nonlinear load with R-C parallel branch using FONF controller (a) grid current, i_{ga} (b) load current, i_{la}.

0278-0046 (c) 2020 IEEE. Personal use is permitted, but republication/redistribution requires IEEE permission. See http://www.ieee.org/publications_standards/publications/rights/index.html for more information.
Authorized licensed use limited to: DELHI TECHNICAL UNIV. Downloaded on February 15,2021 at 10:31:54 UTC from IEEE Xplore. Restrictions apply.

This article has been accepted for publication in a future issue of this journal, but has not been fully edited. Content may change prior to final publication. Citation information: DOI 10.1109/TIE.2021.3051585, IEEE Transactions on Industrial Electronics

TABLE-I
COMPARATIVE PERFORMANCE OF IONF AND FONF

Performance Parameters	IONF	FONF
Initial Rise time T_{r1} (sec)	0.07s	0.04s
Fall time during unbalancing T_f (sec)	0.25s	0.30s
Final Rise time T_{r2} (sec)	0.34s	0.32s
Integral square error, ISE	110.4	108.4

over NLMS and NLMF controllers in terms of complexity, weight convergence, harmonics compensation and sampling time. A comparison of these controllers is summarized in Table-II. Fig. 8 depicts harmonic spectrum of grid current (i_{ga}) using FONF controller, which represents clearly different frequency components present in i_{sa}, other than the fundamental component.

Fig. 9 demonstrates the performance of FONF controller for developed PV system with higher level of THD in the load current (such as computer center load). The effect of such load is created by designing a diode bridge rectifier with parallel R-C branch (R=30Ω and C=400μF) on the DC side. These results show very high THD (58.14%) in the load current and after compensation it has been reduced to 4.57% by the controller action (well within the IEEE-519 standard). Thus, the proposed FONF controller has been found to be suitable for compensating higher distortion present in large nonlinear loads also. From the above analysis, it has been observed that for load current THD< 60%, the designed setup with selected values of interfacing inductors, DC link capacitor of the compensator works well and the supply current THD reduces to < 5% level effectively as specified by the IEEE standard.

D. Experimental Results

An experimental prototype (Fig. 10) of a 3-phase grid-tied PV array system of a 1.5 kW capacity is developed to validate real time performance of fractional order notch filter (FONF) to demonstrate several functions viz. providing real power to the load/grid and alleviating power quality issues. The solar simulator (Chroma 62100 H-600S) is used as a solar PV array. The FONF control for several functions is implemented in dSPACE DS-1202 (Micro Lab Box). The PCC voltages, DC link voltage and PV voltage are sensed using Hall-Effect voltage sensors (LEM LV-25p, LEM LV-25p/sp5). The grid current, load current and PV array current are sensed using Hall-Effect current sensors (LEM LA-25p). Test results are demonstrated for steady state and unbalanced load conditions, which are recorded using DSO (4-channel, 100MHz) and power analyzer (1-phase). The FONF control is validated for harmonics alleviation, load unbalancing, power factor enhancement and variable solar irradiance at nonlinear load.

1) System Behaviour under Steady State Load Condition

Figs. 11 and 12 represent steady state behaviour of developed FONF control technique for the solar PV system. Figs. 11(a), (c) and (e) depict waveforms of the grid, load and converter currents (i_{ga}, i_{la} and i_{ia}) along with PCC voltage (v_{sa}) waveform presented above. Figs. 11(b), (d) and (f) illustrate harmonic spectra of i_{ga}, i_{la} and v_{sa}, which are presented as 3.2%, 23.6% and 3.1%. The THD in the grid current after compensation is achieved 3.2%, whereas the load current THD is very high as 23.6%. The generated power from solar PV system is delivered to the load and surplus power is transferred to the grid. These results demonstrate adequate steady state performance of developed solar PV system in terms of harmonics compensation.

TABLE-II
COMPARATIVE PERFORMANCE OF FONF, NLMS AND NLMF CONTROL TECHNIQUES

Operation		FONF	NLMS	NLMF
Type		Fractional order filtering	Adaptive filtering	Adaptive filtering
Controller Modeling		Easy (few mathematical processes required to extract fundamental weights)	complex (more mathematical processes required to obtain fundamental weights)	Complex (more mathematical processes required to obtain fundamental weights)
Convergence of active fundamental component		Fast (attain steady state within a cycle)	Very slow (attain steady state within 10 cycles)	Slow (attain steady state within 8 cycles)
Harmonic compensation	Grid current, i_{ga}	1.88% THD	3.85% THD	3.05% THD
	Load current, i_{la}	27.66% THD	27.66% THD	27.66% THD
Sampling time, T_s		35μs	50μs	60μs

0278-0046 (c) 2020 IEEE. Personal use is permitted, but republication/redistribution requires IEEE permission. See http://www.ieee.org/publications_standards/publications/rights/index.html for more information.
Authorized licensed use limited to: DELHI TECHNICAL UNIV. Downloaded on February 15,2021 at 10:31:54 UTC from IEEE Xplore. Restrictions apply.

This article has been accepted for publication in a future issue of this journal, but has not been fully edited. Content may change prior to final publication. Citation information: DOI 10.1109/TIE.2021.3051585, IEEE Transactions on Industrial Electronics

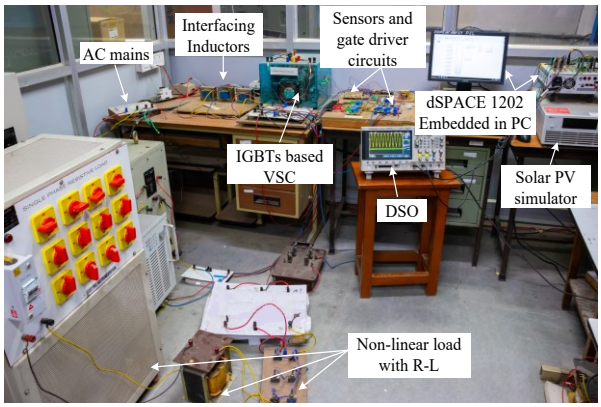

Fig. 10 Experimental setup of grid connected solar PV array system.

Figs. 12(a) to (c) represent grid power (P_g), load power (P_l) and solar PV converter power (P_i). These results demonstrate that the power generated from solar PV array is 1.51kW, which is feeding the load of capacity 205W and surplus power of 1.31kW is transferred to the grid with the control action of FONF control. Therefore, the developed control is suitably feeding the load and the grid demand along with meeting the supply current THD within acceptable confines of the IEEE-519 standard.

2) System Behaviour under Dynamic Load Condition

Fig. 13 depicts behaviour of the developed system with FONF based control, when a-phase ('c') of load is disconnected. Figs. 13(a)-(c) show the waveforms of the grid, the load and converter currents (i_{ga}, i_{gb} and i_{gc}; i_{la}, i_{lb} and i_{lc}; i_{ia}, i_{ib} and i_{ic}) along with PCC line voltage (v_{sab}) on the top of current waveforms in each result. These results are shown to present adequate performance of developed solar PV system with FONF control. The solar PV system is able to feed the load demand and to the grid along with maintaining the grid current stable and sinusoidal even under highly distorted load current and load unbalancing conditions. Fig. 13(d) depicts one phase (phase 'c') of the grid, load and compensator currents (i_{gc}, i_{lc} and i_{ic}) along with the DC link voltage (V_{dc}) in the top. This result represents that i_{gc} is maintained sinusoidal and stable even in load unbalancing and the DC link voltage is regulated at its set value with the PI controller action.

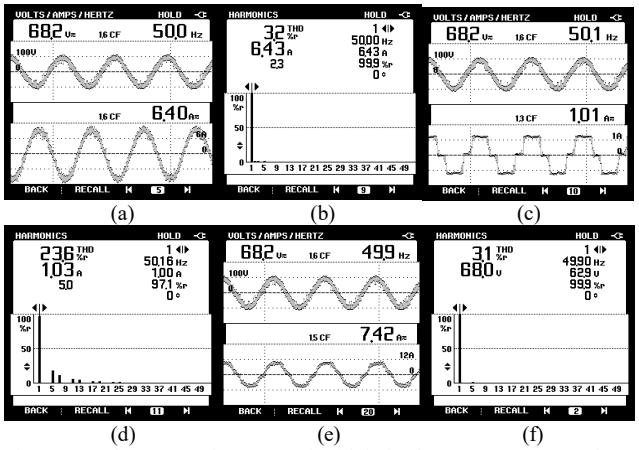

Fig. 11 Steady state performance of grid tied solar PV system (a) voltage at point of common interconnection v_{sa}, and grid current i_{ga} (b) harmonic spectrum of i_{ga} (c) v_{sa}, load current i_{la} (d) harmonic spectrum of i_{la} (e) v_{sa}, converter current i_{ia} (f) harmonic spectrum of v_{sa}.

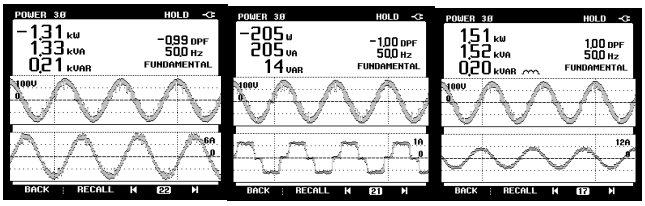

Fig. 12 Steady state performance of grid tied solar PV system (a) grid power, P_g, (b) load power, P_L and (c) solar PV power, P_i.

3) System Behaviour at Variable Solar Irradiance Condition

Fig. 14 illustrates performance of the developed system at varying solar irradiance condition. Fig. 14(a) shows the waveforms of voltage and current of PV array (V_{PV}, I_{PV}), phase 'a' of converter current (i_{ia}) and the grid current (i_{ga}). It presents the performance under condition of decreasing solar irradiance. Initially the solar irradiance is set at 1000W/m^2 and it is reduced to 500 W/m^2. Because of this condition, the solar power is reduced up to 500W, which can still be fed to meet the load demand and hence reduced power balance is transferred to the grid side. Fig. 14(b) depicts voltage and current of PV array (V_{PV}, I_{PV}), phase 'a' of converter current (i_{ia}) and the grid current (i_{ga}) with increased solar irradiance. Initially it is set at 500W/m^2 and at some instant, it is increased up to 1000W/m^2. The effect of an increased solar irradiance and lower load demand result in injecting greater active power to the grid side.

V. CONCLUSIONS

A three-phase grid connected solar photovoltaic system with FONF based control has been proposed in this work. The FONF control has been designed to accomplish twin functions of the grid-connected PV system viz. delivering active power to the load/grid and alleviating current related power quality issues at PCC. Numerous power quality issues such as harmonics distortion in the grid current, reactive power demand of the load and unbalancing load currents have been solved by the developed control system. The FONF control has been found suitable in terms of its flexibility to alter power of integrator used in the notch filter and asymmetrical gain

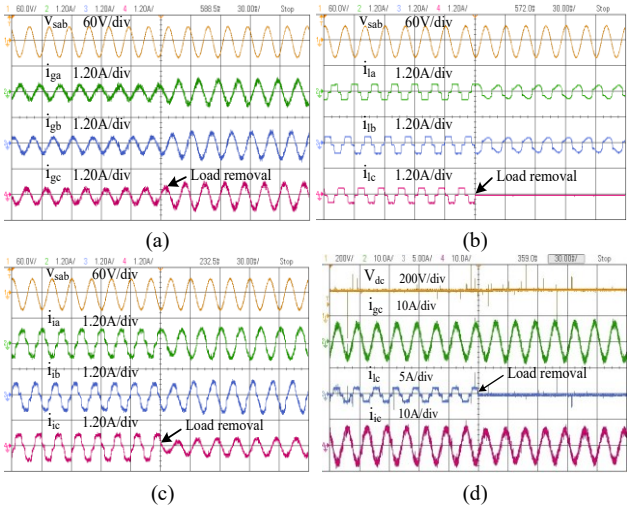

Fig. 13 Performance of the system under dynamic load condition (a) line voltage (v_{sab}), grid currents (i_{ga}, i_{gb} and i_{gc}) (b) v_{sab} , load currents (i_{la}, i_{lb} and i_{lc}) (c) v_{sab}, converter currents (i_{ia}, i_{ib} and i_{ic}) (d) DC link voltage (V_{dc}), phase 'c' of grid, load and converter currents (i_{gc}, i_{lc} and i_{ic}).

0278-0046 (c) 2020 IEEE. Personal use is permitted, but republication/redistribution requires IEEE permission. See http://www.ieee.org/publications_standards/publications/rights/index.html for more information.
Authorized licensed use limited to: DELHI TECHNICAL UNIV. Downloaded on February 15,2021 at 10:31:54 UTC from IEEE Xplore. Restrictions apply.

This article has been accepted for publication in a future issue of this journal, but has not been fully edited. Content may change prior to final publication. Citation information: DOI 10.1109/TIE.2021.3051585, IEEE Transactions on Industrial Electronics

response curve, which is not possible in case of integer order notch filter. It has been observed from the Bode plot that sharpness of developed FONF does not alter by increasing the value of damping ratio once fractional gains are appropriately decided. Moreover, this control presents fast response when compared with integer order notch filter. Performances of FONF controller have been confirmed at steady state and unbalanced load along with variation in solar irradiance considered. Experimental results demonstrate performance of FONF controller in maintaining 3.2% THD in the grid current, which is in accordance with the IEEE-519 standard for the grid interfaced PV system.

APPENDIX-A

Solar PV Irradiance 1000W/m^2, Open circuit voltage=25V, short circuit current=7.75A, MPP voltage=200V, MPP current=8.62A, AC mains: 3-phase, 110V, 50Hz, Line impedance: R_s=0.05Ω, L_s=0.8mH. DC link voltage V_{dc}=200V, interfacing inductor: L_f=3mH, Ripple filter parameters: R_f=5Ω, C_f=5μF, DC bus PI gains: k_{pd}=0.45, k_{id}=8, FONF controller parameters: α=0.8 and β=1.2.

APPENDIX-B

Discretization of FONF based control technique for developed grid integrated solar PV system:

The realization of fractional component of the FONF has been done using the approximation method given in [34]. In this method Bode magnitude plot is used with a variable slope of ±α20 (α is a real number) dB/decade unlike as a constant slope of ±20 dB/decade in case of integer order term. To achieve the desired variable slope plot, various real poles and zeros are placed alternatively on the negative real axis. The number of pole zero pair depends on the approximation order N and can be realizable with in the desired frequency band range denoted by "$\omega_l < f < \omega_h$". The phase plot for this approximation is represented by the value ±90^o. To get the desired optimal number of poles and zeros for the realization of fractional term within the permissible limit, it has been carried out according to the (A1) as,

$$\text{First pole, } p_1 = 10^{\left[\frac{\phi_{req}+45\log\omega_l}{45}+1\right]}$$
$$\text{First zero, } z_1 = 10\omega_l$$
$$\text{Second pole, } p_2 = 10^{[\log(p_1)+2-\mu]} \quad \text{(A1)}$$
$$\text{Second zero, } z_2 = 10^{[\log(z_1)+2-\mu]}$$

.

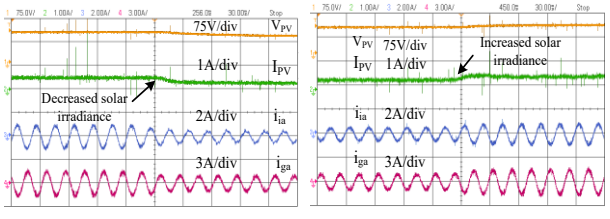

(a) (b)

Fig. 14 Performance of the system under changing variable irradiance condition (a) PV voltage (V_{PV}), PV current (I_{PV}), phase 'a' of converter and grid current under decreased solar irradiance (b) PV voltage (V_{PV}), PV current (I_{PV}), phase 'a' of converter and grid current under increased solar irradiance condition.

.

till $p_n \geq \omega_h$

where $\phi_{req} = \alpha 90^0$ is the desired phase angle, ω_l is low translational frequency, ω_h is high translational frequency and μ is design parameter.

To discretize the system, Tustin bilinear approximation method is used and the relation between continuous domain (s-domain) and the discrete domain (z-domain) according to the same method is represented as given in (A2),

$$z = e^{sT_s} \approx \frac{1+sT_s/2}{1-sT_s/2} \quad \text{(A2)}$$

After conversion from continuous domain to discrete domain the discretized form $C_d(z)$ of the continuous transfer function $C(s')$ is denoted by (A3) as,

$$C_d(z) = C(s'), \text{ where } s' = \frac{2}{T_s}\frac{z-1}{z+1} \quad \text{(A3)}$$

REFERENCES

[1] A. Reinders, P. Verlinden, W. Sark and A. Freundlich, *Photovoltaic Solar Energy: From Fundamentals to Applications*, Hoboken, NJ, USA, Wiley, 2017.

[2] R. Precup, T. Kamal, S. Z. Hassan, *Solar Photovoltaic Power Plants: Advanced Control and Optimization Techniques*, Gateway East Singapore, Springer, 2019.

[3] M. K. Hairat, S. Ghosh, "100GW solar power in India by 2022 – A critical review", *Rene. Sustain. Ener. Rev.*, vol. 73, pp.1041-1050, 2017.

[4] N. Priyadarshi, S. Padmanaban, P. K. Maroti and A. Sharma, "An extensive practical investigation of FPSO-based MPPT for grid integrated PV system under variable operating conditions with anti-islanding protection," *IEEE Sys. Journal*, vol. 13, no. 2, pp. 1861-1871, June 2019.

[5] N. Mukundan C. M., Y. Singh, S. Naqvi, B. Singh and J. Pychadathil, "Multi-objective solar power conversion system with MGI control for grid integration at adverse operating conditions," *IEEE Trans. Sust. Energy*, vol. 11, no. 4, pp. 2901-2910, 2020.

[6] M. Badoni, A. Singh, B. Singh and H. Saxena, "Real-time implementation of active shunt compensator with adaptive SRLMMN control technique for power quality improvement in the distribution system," *IET Gene. Trans. Dist.*, vol. 14, no. 8, pp. 1598-1606, 2020.

[7] R. A. Mastromauro, M. Liserre, T. Kerekes and A. Dell'Aquila, "A single-phase voltage-controlled grid-connected photovoltaic system with power quality conditioner functionality,"*IEEE Trans. Indu. Electron.*, vol. 56, no. 11, pp. 4436-4444, Nov. 2009.

[8] N. Arab, B. Kedjar, A. Javadi and K. Al-Haddad, "A multifunctional single-phase grid-integrated residential solar PV systems based on LQR control," *IEEE Trans. Ind. Applications*, vol. 55, no. 2, pp. 2099-2109, March-April 2019.

[9] G. Modi, S. Kumar and B. Singh, "Improved Widrow–Hoff based adaptive control of multiobjective PV-DSTATCOM system," *IEEE Trans. Ind. Appl.*, vol. 56, no. 2, pp. 1930-1939, March-April 2020.

[10] M. Reveles-Miranda, M. Flota-Bañuelos, F. Chan-Puc, V. Ramirez-Rivera and D. Pacheco-Catalán, "A hybrid control technique for harmonic elimination, power factor correction, and night operation of a grid-connected PV inverter," *IEEE Journal of Photovoltaics*, vol. 10, no. 2, pp. 664-675, March 2020.

[11] E. H. Watanabe, H. Akagi and M. Aredes, "Instantaneous p-q power theory for compensating nonsinusoidal systems," In *Proc. International School on Nonsinusoidal Currents and Compensation*, Lagow, 2008.

[12] B. Singh, D. T. Shahani and A. K. Verma, "Power balance theory-based control of grid interfaced solar photovoltaic power generating system with improved power quality," In *Proc. 2012 IEEE Inter. Conf. on Power Electronics, Drives and Energy Systems (PEDES)*, Bengaluru, 2012.

[13] M. V. Manoj Kumar, M. K. Mishra and C. Kumar, "A grid-connected dual voltage source inverter with power quality improvement features," *IEEE Trans. Sust. Energy*, vol.6, no. 2, pp.482-490, April 2015.

[14] A. A. M. Bento, A. Lock, E. R. C. d. Silva and D. A. Fernandes, "Hybrid one-cycle control technique for three-phase power factor control," *IET Power Electro.*, vol. 11, no. 3, pp. 484-490, 2018.

0278-0046 (c) 2020 IEEE. Personal use is permitted, but republication/redistribution requires IEEE permission. See http://www.ieee.org/publications_standards/publications/rights/index.html for more information.
Authorized licensed use limited to: DELHI TECHNICAL UNIV. Downloaded on February 15,2021 at 10:31:54 UTC from IEEE Xplore. Restrictions apply.

This article has been accepted for publication in a future issue of this journal, but has not been fully edited. Content may change prior to final publication. Citation information: DOI 10.1109/TIE.2021.3051585, IEEE Transactions on Industrial Electronics

[15] Y. Sun, S. Li, B. Lin, X. Fu, M. Ramezani and I. Jaithwa, "Artificial neural network for control and grid integration of residential solar photovoltaic systems," *IEEE Trans. Sust. Energy*, vol. 8, no. 4, pp. 1484-1495, Oct. 2017.

[16] M. Patowary, G. Panda, B. Naidu, D. Ramesh and C. Bimal, "ANN-based adaptive current controller for on-grid DG system to meet frequency deviation and transient load challenges with hardware implementation," *IET Rene. Pow. Gene.*, vol. 12, no. 1, pp. 61-71, 2018.

[17] M. Badoni, A. Singh and B. Singh, "Adaptive neurofuzzy inference system least-mean-square-based control algorithm for DSTATCOM," *IEEE Trans. Ind. Informat..*, vol. 12, no. 2, pp. 483-492, April 2016.

[18] N. Kumar, I. Hussain, B. Singh and B. K. Panigrahi, "Implementation of multilayer fifth-order generalized integrator-based adaptive control for grid-tied solar PV energy conversion system," *IEEE Trans. Ind. Informat.*, vol. 14, no. 7, pp. 2857-2868, July 2018.

[19] Z. Liu, H. Wu, W. Jin, B. Xu, Y. Ji and M. Wu, "Two-step method for identifying photovoltaic grid-connected inverter controller parameters based on the adaptive differential evolution algorithm," *IET Gene., Trans. Dist.*, vol. 11, no. 17, pp. 4282-4290, 2017.

[20] P. Shukl and B. Singh, "Grid integration of three-phase single-stage PV system using adaptive Laguerre filter based control algorithm under nonideal distribution system," *IEEE Trans. Indu. Applications*, vol. 55, no. 6, pp. 6193-6202, Nov.-Dec. 2019.

[21] S. Benhalima, A. Chandra and M. Rezkallah, "Real-time experimental implementation of an LMS-adaline-based ANFIS controller to drive PV interfacing power system," *IET Rene. Power Gene.*, vol. 13, no. 7, pp. 1142-1152, 2019.

[22] R. S. R. Chilipi, N. Al Sayari, K. H. Al Hosani and A. R. Beig, "Adaptive notch filter-based multipurpose control scheme for grid-interfaced three-phase four-wire DG inverter,"*IEEE Trans. Ind. Applications*, vol. 53, no. 4, pp. 4015-4027, July-Aug. 2017.

[23] B. Singh, K. Kant and S. R. Arya, "Notch filter-based fundamental frequency component extraction to control distribution static compensator for mitigating current-related power quality problems,"*IET Pow. Electron.*, vol. 8, no. 9, pp. 1758-1766, 2015.

[24] S. Kewat and B. Singh, "Modified amplitude adaptive control algorithm for power quality improvement in multiple distributed generation system," *IET Pow. Electron.*, vol. 12, no. 9, pp. 2321-2329, 2019.

[25] R. Schaumann and M.V. Valkenburg, "*Design of Analog Filters*," Oxford University Press, 1st ed., 2001.

[26] A. G. Radwan, A. S. Elwakil, and A. M. Soliman, "On the generalization of second-order filters to the fractional-order domain," *Journal of Circu. Sys. Comp.*, vol. 18, no. 2, pp. 361–386, 2009.

[27] A. Adhikary, S. Sen and K. Biswas, "Practical realization of tunable fractional order parallel resonator and fractional order filters," *IEEE Trans. Circuits and Systems I: Regular Papers*, vol. 63, no. 8, pp. 1142-1151, Aug. 2016.

[28] P. Ahmadi, B. Maundy, A. S. Elwakil and L. Belostotski, "High-quality factor asymmetric-slope band-pass filters: A fractional-order capacitor approach," *IET Circu. Dev. & Sys.*, vol. 6, pp. 187-197, 2012.

[29] M. Bošković, T. B. Šekara, M. R. Rapaić, B. Lutovac, M. Daković and V. Govedarica, "Novel band-pass and notch filter with dynamic damping of fractional order," In *Proc. 25th Telecommunication Forum (TELFOR)*, Belgrade, 2017.

[30] R. Rajagopal, K. Palanisamy and S. Paramasivam, "Comparative performance of normalized LMS and variable step size LMS based control for shunt active filtering," In *Proc. 9th International Conference on Advances in Computing and Communication (ICACC)*, Kochi, India, 2019, pp. 136-141.

[31] A. K. Singh, I. Hussain and B. Singh, "Double-stage three-phase grid-integrated solar PV system with fast zero attracting normalized least mean fourth based adaptive control,"*IEEE Trans. Indu. Electron.*, vol. 65, no. 5, pp. 3921-3931, May 2018.

[32] Y. Jiang and B. Zhang, "Comparative study of Riemann–Liouville and Caputo derivative definitions in time-domain analysis of fractional-order capacitor," *IEEE Transactions on Circuits and Systems II: Express Briefs*, vol. 67, no. 10, pp. 2184-2188, Oct. 2020.

[33] N. Kumar, B. Singh, B. K. Panigrahi and L. Xu, "Leaky-least-logarithmic-absolute-difference-based control algorithm and learning-based InC MPPT technique for grid-integrated PV system," *IEEE Trans. Ind. Elect.*, vol. 66, no. 11, pp. 9003-9012, Nov. 2019.

[34] A. Oustaloup, F. Levron, B. Mathieu and F. M. Nanot, "Frequency-band complex noninteger differentiator: characterization and synthesis," *IEEE Transactions on Circuits and Systems I: Fundamental Theory and Applications*, vol. 47, no. 1, pp. 25-39, Jan. 2000.

Manoj Badoni (M'18) received the B. Tech. degree in Instrumentation Engineering form University Science and Instrumentation Centre, Srinagar Garhwal, Uttrakhand in 2006, M.E. degree in Electronics Engineering from PEC, Chandigarh, India in 2008 and Ph.D degree in Electrical Engineering from DTU, Delhi, India in 2016.In 2017, he has joined Department of Electrical and Instrumentation Engineering, Thapar Institute of Engineering and Technology, Patiala, India as an Assistant Professor. His areas of research interest include power electronics, power quality, and grid integration of renewable energy sources.

Alka Singh (SM'15) received the B.E. degree in Electrical Engineering from Delhi College of Engineering, Delhi, India, in 1996, M.Tech. Degree in Power Systems from the IIT, New Delhi, India, in 2001, and the Ph.D. degree from Netaji Subash Institute of Technology (Delhi University), Delhi, India, in 2006. Currently, she is working as an Professor in the Department of Electrical Engineering, DTU, Delhi. Her research interests include power systems, and power quality. She has more than 15 years of teaching and industrial experience. She is a Life Member of the Indian Society for Technical Education.

Sandeep Pandey received the B.E. degree in electronics and instrumentation engineering from IET Devi Ahilya Vishvavidalaya, Indore, India in 2007, M.Tech degree in control systems from electrical engineering department, IIT BHU, Varanasi, India in 2013. He obtained his Ph.D from VNIT, Nagpur, India in 2019. His areas of interest are fractional order PID controller, robust control system, actuator saturation and anti-windup techniques. He is currently working as an assistant professor in the department of electrical and instrumentation engineering department of Thapar Institute of Engineering and Technology, Patiala, Punjab, India.

Bhim Singh (SM'99, F'10) was born in Rahamapur, Bijnor (UP), India, in 1956. He has received his B.E. (Electrical) from the University of Roorkee (Now IIT Roorkee), India, in 1977 and his M.Tech. (Power Apparatus & Systems) and Ph.D. from the IIT Delhi, India, in 1979 and 1983, respectively. In 1983, he joined the Department of Electrical Engineering, University of Roorkee, as a Lecturer. He became a Reader there in 1988. In December 1990, he joined the Department of Electrical Engineering, IIT Delhi, India, as an Assistant Professor, where he has become an Associate Professor in 1994 and a Professor in 1997. He has been Head of the Department of Electrical Engineering at IIT Delhi from July 2014 to August 2016 He has been Dean, Academics at IIT Delhi, August 2016 to August 2019. He is JC Bose Fellow of DST, Government of India since December 2015. He is CEA Chair Professor since January 2019. Prof. Singh has guided 95 Ph.D. dissertations, and 168 M.E./M.Tech./M.S.(R) theses. He has been filed 69 patents. He has executed more than eighty sponsored and consultancy projects. His areas of interest include solar PV grid interface systems, microgrids, power quality monitoring and mitigation, solar PV water pumping systems, improved power quality AC-DC converters.

0278-0046 (c) 2020 IEEE. Personal use is permitted, but republication/redistribution requires IEEE permission. See http://www.ieee.org/publications_standards/publications/rights/index.html for more information.
Authorized licensed use limited to: DELHI TECHNICAL UNIV. Downloaded on February 15,2021 at 10:31:54 UTC from IEEE Xplore. Restrictions apply.

Fresh and Hardened Characteristics of Basalt-Glass Hybrid Fibre Reinforced Self Compacting Concrete

Uzair Khan, Sandeep Kumar Tripathi, Anurag, Rizwan A Khan

Abstract: Proof that, just as results, self-compacting concrete is complete benchmark in the area of construction. Because of its highly profitable qualities, Self Compacting Concrete (SCC) extremely favoured and used drastically all over the construction world. SCC is that creative concrete which does not require any help of vibration for arrangements and compaction. It is shown that SCC have capability of complete filling formwork by property of flow under its self weight. Hence, it attain over all compaction, even in case of choke reinforcement. The main intent of this research paper is to find the fresh characteristics of basalt- glass hybrid fibre reinforced self-compacting concrete like T50 cm, spread flow, L-box, V funnel and hardened characteristics such as compressive strength, ultrasonic pulse velocity (UPV) and flexural strength at 7 and 28 days. Basalt-glass hybrid fibre reinforced self-compacting concrete has shown improved hardened characteristics with the addition of fibres.

Keywords: Glass Fibres (GF), Basalt Fibres (BF), Hybrid Fibre Reinforced Self Compacting Concrete (HFRSCC), Self Compacting Concrete (SCC).

I. INTRODUCTION

Durability of concrete structures was important area of interest in the early 1980's.The design engineers used proper mix design and quality control checks, yet the durability of concrete structures was not achieved. Later it was investigated that failure of concrete structures was due to improper compaction of concrete. It is required to do adequate compaction by skilled labours to produce durable concrete structures, but there was considerable deterioration in the availability of skilled labours in the construction industry of Japan *(Okamura and Ouchi 2003).* In the modern day construction heavy and congested reinforcement mesh is no longer unusual, and hence to produce heavily reinforced durable concrete structures is a major problem. This problem can be mitigated or completely eliminated by the introduction of self-compacting concrete (SCC), which compacts without the requirement of agitation or vibration. Okumura recommended the requirement of this type of concrete in 1986. Studies carried out by "Ozawa and Maekawa" at the university of Tokyo to develop SCC, which includes the fundamental investigation on the workability of concrete *(Okamura et al.1993).*

The concrete with high durability due to the water cement ratio being low in amount was termed as high performance concrete *(Gagne et al. 1989).* For the longevity of structure high durable concrete is used for gaining effective results. Therefore, Okamura and Ouchi, have changed the term for the proposed concrete, for their work, to "Self – consolidating high performance concrete".

Self-compacting concrete is highly flow able and rational which is easy to spread and compact under its self-weight without applying any external vibration. Small interstices of formwork and compounded shapes in structural members can easily be filled by self-consolidating concrete. Long distance pumping of concrete is also possible. Self-compatibility in self-compacting concrete can be achieved by limiting the maximum size of coarse aggregate and content. Chemical admixtures such as viscosity modifying admixtures (VMA) and high range water reducer (super-plasticizer), incorporating and adopting low water to binder ratios can also be commonly practiced to achieve self-compatibility in self-compacting concrete *(Okamura and Ozawa 1995).*

Self –compacting concrete is a concrete that is not separated nor bled owing to its self-weight *(Aggarwal et al. 2008).* No internal vibration for compaction is used by self-compacting concrete *(Murthy et al. 2012).* It completely includes the formwork and achieves thorough compaction even in the weighty crowded mesh of strengthening. Self-compacting concrete has various superiority over ordinary concrete in terms of productivity enhancement, general labour cost degradation, finished high-quality product with outstanding of hardened characteristics and durability.

The self-compacting concrete manufacturing technique is similar to the standard concrete, but its production requires a sufficient variety of aggregates and finely ground cemented materials along with an adequate water powder (w / p) ratio to preserve its desire workability so that the concrete does not bleed and segregate. Suitable choice of finely ground aggregates proliferates strong particle packing density and allows water content to be cut. In order to produce SCC, extremely finely ground powder [fly ash (FA) and silica fume (SF)] is required to enhance the slump quality and cohesiveness. In addition, viscosity enhancing admixtures and super plasticizer (SP) and are

Revised Manuscript Received on December 05, 2019.

Uzair Khan, Department of Civil Engineering, ABES Engineering College, Ghaziabad, India.

Sandeep Kumar Tripathi, Department of Civil Engineering, ABES Engineering College, Ghaziabad, India.

Anurag, Department of Civil Engineering, ABES Engineering College, Ghaziabad, India.

Rizwan A Khan, Department of Civil Engineering, Z. H. College Engg. & Tech., Aligarh Muslim University, Aligarh, India.

extremely needed and used in SCC production.

Hybrid fibre reinforced self-compacting concrete (HFRSCC), it is an advanced form of composite material generated by using different fibres types, shapes and sizes in a SCC *(Kumar 2017).* Adding two or more fibres to the self compacting concrete blend enhances the hardened characteristics of SCC and it is called as hybrid fibre reinforced self-compacting concrete *(Khan and Singh 2019).* With the addition of fibres, the fracture values of self-compacting concrete are elevated *(Khan et al 2019).* Polypropylene fibres enhance cement matrix bending and acts as crack arrester *(Nandhini and Manju 2017).* When fibres are used, micro cracks can be minimized. The inclusion of hybrid fibres reduces the main crack generation and maximizes failure load *(Nandhini and Manju 2017).*The authors conducted experiments on fresh and hardened characteristics of HFRSCC in the current research. The testing of ultrasonic pulse velocity (UPV) were also carried out to verify the quality of the hybrid fibre reinforced self compacting concrete thus generated.

II. EXPERIMENTAL INVESTIGATION

The fresh properties of HFRSCC such as T50cm (sec), flow spread (mm), V- funnel time (sec), L-box (h2/h1), hardened characteristics of HFRSCC such as flexural strength, ultra-sonic pulse velocity (UPV) test and compressive strength were carried out at 7 and 28 days. The proportion of basalt fibres in the current experimental program is 0.25% by volume fraction of concrete quantity, whereas glass fibres are 0%, 0.1 %, 0.2% and 0.3%. Table 1 shows the percentage of fibres used in the corresponding blend. In each blend, 6 cubes of (150 x 150 x150) mm and 6 beams of (100 × 100 × 500) mm samples has been casted in order to evaluate the flexural strength, ultra-sonic pulse velocity (UPV) test and compressive strength of HFRSCC. Table 2 shows details of the SCC mix ratio.

Table 1 Experimental programme

S. No.	Blend	Fibre proportion (%)	
		Basalt fibres (BF)	Glass fibres (BF)
1	M-BF0-GF0	0	0
2	M-BF0.25-GF0	0.25	0
3	M-BF0.25-GF0.1	0.25	0.1
4	M-BF0.25-GF0.2	0.25	0.2
5	M-BF0.25-GF0.3	0.25	0.3

Table 2 Blend ratio of SCC

Cement (kg/m^3)	Fly ash (kg/m^3)	Fine aggregates (kg/m^3)	Coarse aggregates (kg/m^3)	Water (litres)	Super plasticizer (litres)
410	205	846	602	246	7.2

III. MATERIALS USED

The present research work was completed by using 43 grade Ordinary Portland Cement (OPC). Table 3 presents the physical characteristics of Ordinary Portland Cement. Potable tap water has been used for all mixtures. Fine aggregates were used as natural river sand (zone II). The most extreme size of the coarse aggregates was restricted to 12.5 mm. In present study Master Genelium SKY 8765 was utilized as super-plasticizer .In the current paper, the hybrid blend consisted of basalt fibres and glass fibres. Table 4 provides specialized information on basalt fibres and glass fibres.

Table 3 Physical characteristics of OPC (43 Grade)

S. No.	Property	Units	Result obtained
1	Fineness (specific surface)	cm^2/gm	2340
2	Normal consistency	%	32
3	Initial setting time	minutes	65
4	Final setting time	minutes	410
5	Soundness	mm	3
6	Compressive strength 7 days 28 days	MPa	 35.50 45.10
7	Specific gravity	-	3.14

Table 4 Specialized information of basalt fibres and glass fibres

S. No.	Parameters	Basalt Fibres (BF)	Glass Fibres (GF)
1	Length (mm)	12	12
2	Density (g/cm^3)	2.65	2.6
3	Elastic Modulus (GPa)	93-100	72-85
4	Tensile Strength (MPa)	4500	2050
5	Diameter (µ)	12 micron	14
6	Appearance	Golden Brown	White

Figure 1 Chopped basalt fibres (BF)

Figure 2 Glass fibres (GF)

IV. RESULTS FOR FRESH CHARACTERISTICS OF HFRSCC

Table 5 Results of fresh characteristics of HFRSCC

Blend	% Fibres	T_{50}cm (sec)	Flow spread (mm)	L-box (h_2/h_1)	V-funnel time (sec)
M-BF0-GF0	0	3.2	760	0.97	6.7
M-BF0.25-GF0	0.25	3.5	740	0.94	7.4
M-BF0.25-GF0.1	0.35	3.7	732	0.88	8.5
M-BF0.25-GF0.2	0.45	4.1	708	0.84	8.7
M-BF0.25-GF0.3	0.55	4.5	691	0.8	9

Table 5 and graph 1-4 demonstrate the flow spread value decrease due to fibres incorporation. The logic for this situation is that owing to the dispersed fibres in the concrete, a network structure may form, which limits mixing from segregation and flow.

Compared to control blend (M-BF0-GF0), the maximum decline in flow value was observed 9.07 percent for M-BF0.25-GF0.3. The reason for this is due to the highest percentage of fibres compared to the other blends in this mix. As the flow spread value decreases, the T50 cm flow, measured in terms of time (sec) rises. The optimum flow time was found 4.3 sec for M-BF0.25-GF0.3.The L-box ((h2/h1) value reduces with the rise in fibre ratios. The decrease in the value of L-box (h2/h1) also results in a simultaneous reduction in the value of the slump flow. The optimum value for M-BF0-GF0 (SCC reinforced with basalt of 0 percent and glass fibres of 0 percent) was 0.97.The value of the V-funnel, measured as time (sec) rises as the value of the slump flow declines. Mix M-BF0.25-GF0.3 was observed to have the highest value of V-funnel, whereas M-BF0-GF0 had the minimum value.

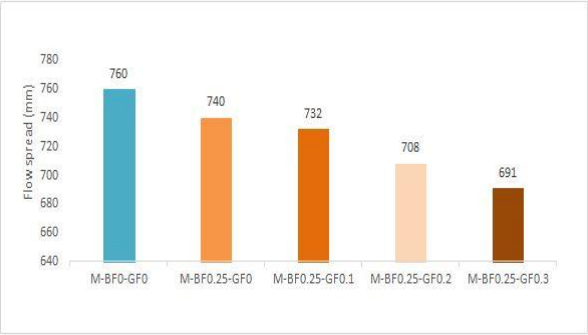

Graph 1. Results of flow spread for HFRSCC blends

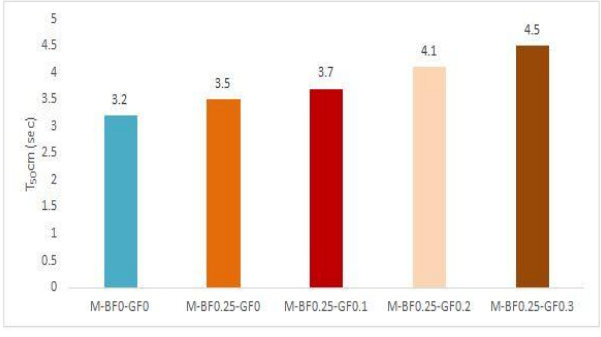

Graph 2. Results of T_{50}cm for HFRSCC blends

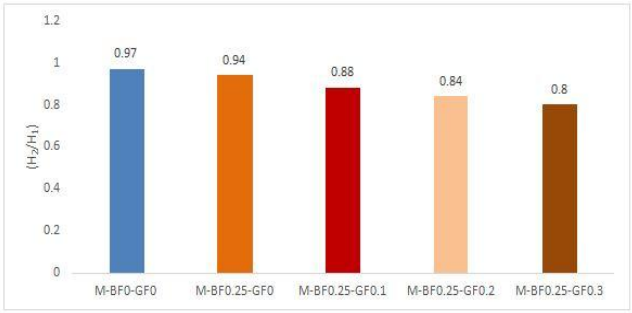

Graph 3. Results of L-box for HFRSCC blends

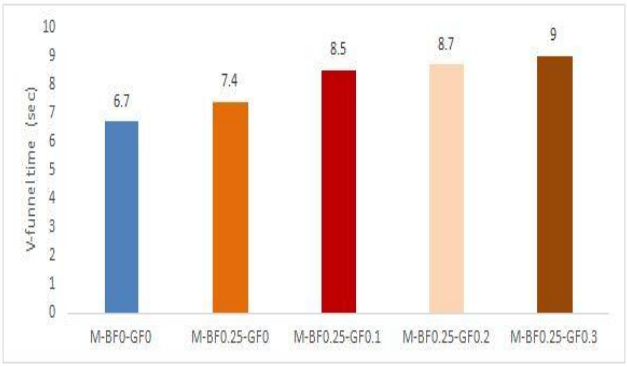

Graph 4. Results of V-funnel for HFRSCC blends

V. RESULTS FOR HARDENED CHARACTERISTICS OF HFRSCC

Samples were tested on 7 days and 28 days of normal curing to contrast the different hardened characteristics of HFRSCC blends. Table 6-7 and Graph 5-6 outline the results.

Table 6: Results for Compressive Strength

S. No.	Blend	Compressive Strength (MPa) at 7 days	Compressive Strength (MPa) at 28 days
1	M-BF0-GF0	22.01	28.61
2	M-BF0.25-GF0	24.1	31.45
3	M-BF0.25-GF0.1	24.5	31.70
4	M-BF0.25-GF0.2	24.6	32.10
5	M-BF0.25-GF0.3	24.9	32.37

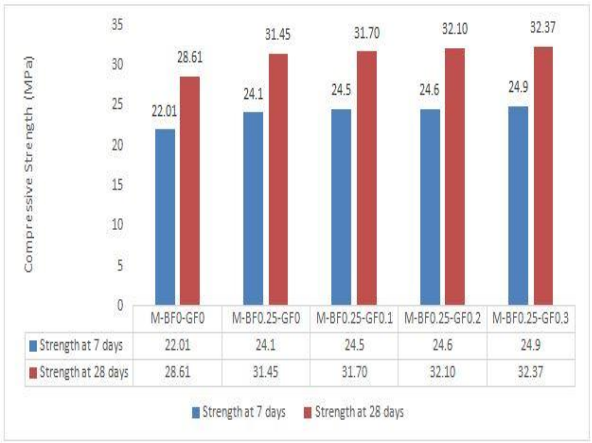

Graph 5. Results of Compressive Strength for HFRSCC blends

In comparison to the control blend (M-BF0-GF0), compressive strength was enhanced for all the blends. However, for M-BF0.25-GF0.3 mix with the mixture of 0.25% basalt fibres and 0.3% glass fibres, the optimum compressive strength was acquired. Compared with the control blend (M-BF0-GF0), compressive strength improved by 9.92 percent at 28 days of self-compacting concrete strengthened with 0.25% basalt fibres. The compressive strength of self-compacting concrete strengthened with 0.25% basalt fibres and 0.1% glass fibres (M-BF0.25-GF0.1) improved by 10.80% compared to the control blend (M-BF0-GF0). The compressive strength of self-compacting concrete strengthened with basalt fibres 0.25% and glass fibres 0.2% (M-BF0.25-GF0.2) improved by 12.19% compared to the control blend (M-BF0-GF0). The compressive strength of self-compacting concrete strengthened with basalt fibres 0.25% and glass fibres 0.3% (M-B0.25-G0.3) improved by 13.14% compared to control blend (M-BF0-GF0). In addition, with the percentage increase in glass fibres remaining continuous as basalt fibres (M-BF0.25-GF0.3), compressive strength was discovered to be nearly the same as compared to M-BF0.25-GF0.2.

Table 7: Results for Flexural Strength

S. No.	Blend	Flexural Strength (MPa) at 7 days	Flexural Strength (MPa) at 28 days
1	M-BF0-GF0	5.69	7.39
2	M-BF0.25-GF0	6.5	8.49
3	M-BF0.25-GF0.1	6.58	8.55
4	M-BF0.25-GF0.2	7.54	9.87
5	M-BF0.25-GF0.3	7.9	10.27

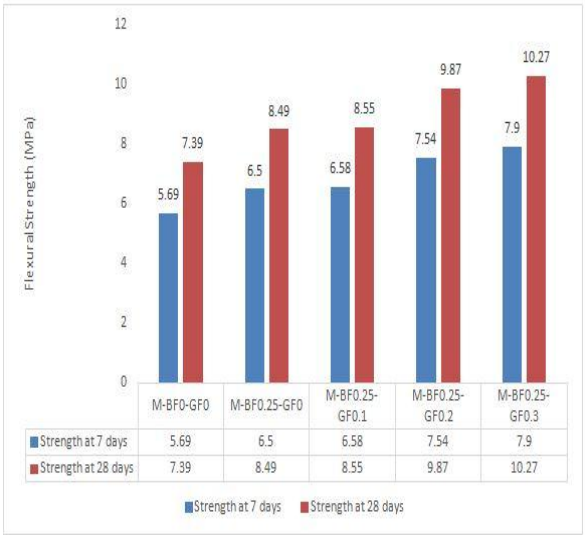

Graph 6: Results of Flexural Strength for HFRSCC blends

In comparison to the control blend (M-BF0-GF0), flexural strength was enhanced for all blends. However, for M-BF0.25-GF0.3 mix with the mixture of basalt fibres 0.25% and glass fibres 0.3%, the optimum flexural strength was acquired. Compared with the control blend (M-BF0-GF0), flexural strength improved by 14.88 percent at 28 days of self-compacting concrete strengthened with 0.25% basalt fibres. The flexural strength of self-compacting concrete strengthened with 0.25% basalt fibres and 0.1% glass fibres (M-BF0.25-GF0.1) improved by 15.69% compared to the control blend (M-BF0-GF0). The flexural strength of self-compacting concrete strengthened with basalt fibres 0.25% and glass fibres 0.2% (M-BF0.25-GF0.2) improved by 33.55% compared to the control blend (M-BF0-GF0). Further, with the percentage increase in glass fibres remaining continuous as basalt fibres (M-BF0.25-GF0.3), flexural strength was discovered increment when contrasted with the M-BF0-GF0 by 38.97%.

Table 8: Results for Ultrasonic Pulse Velocity (UPV)

S. No.	Blend	UPV (km/sec) at 7 days	UPV (km/sec) at 28 days
1	M-BF0-GF0	4.12	4.20 (Good)
2	M-BF0.25-GF0	4.24	4.27 (Good)
3	M-BF0.25-GF0.1	4.27	4.29 (Good)
4	M-BF0.25-GF0.2	4.3	4.35 (Good)
5	M-BF0.25-GF0.3	4.37	4.45 (Excellent)

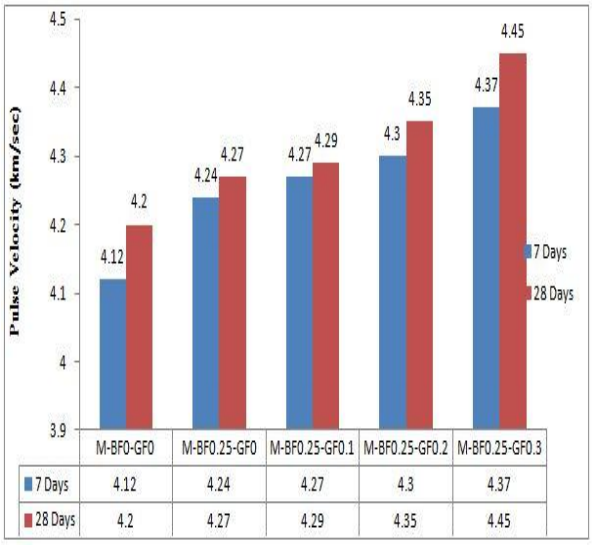

Graph 7: Variation of Pulse Velocity for HFRSCC blends

In order to examine the concrete sub-surface without damaging the surface or the integrity of the structure UPV test is found helpful. It allows the hard concrete to be comprehensively understood and quality assured. The quality of SCC strengthened with basalt fibres of 0.25 percent and glass fibres of 0.3 percent is excellent and all the others are in good condition.

VI. CONCLUSIONS

- As the percentage of fibres added increases, fresh HFRSCC properties decrease.
- For the M-BF0.25-GF0.3 blend, the highest decrease in spread flow was evaluated to be 9.07%. This may be due to the highest fibre proportion.
- By including fibres in self-compacting concrete, hardened properties such as compressive strength, ultrasonic pulse velocity and flexural strength were enhanced.
- Compared to the control blend (M-BF0-GF0), compressive strength of self-compacting concrete at 28 days improved by 9.92% with 0.25% basalt fibres.

- Compared with the control blend (M-BF0-GF0), 28 days compressive strength of self-compacting concrete strengthened with basalt 0.25% and glass fibres 0.3% (M-BF0.25-GF0.3) increased by 13.14%.
- Glass fibres inclusion increases flexural strength.
- Optimum flexural and compressive strength was found for M-BF0.25-GF0.3.
- Improving the fibre proportion has enhanced the quality of SCC.
- Self-compacting concrete strengthened with 0.25% basalt and 0.3% glass fibres has shown excellent quality.

REFERENCES

1. Aggarwal, P., R. Siddique, Y. Aggarwal, S.M. Gupta, "Self-consolidating concrete- procedure for mix design", Leonardo Electronic Journal of Practices and Technologies, 12 (2008) 15-24.
2. Bharathi, S. M. L, "Experimental study on hybrid fiber self-consolidating concrete", International Journal of Engg. Research and Modern Education, (2017) 248-254.
3. Bureau of Indian Standards IS 8112-1989 "43-Grade Ordinary Portland Cement – Specification", 2008.
4. Dhiyaneshwaran, S., P. Ramanathan, L. Bhaskar, R. Venkatasubramania, "Study on durability characteristics of self-compacting concrete with fly ash", Jordan Journal of Civil Engineers, 7 (2013).
5. EFNARC, "Specifications and Guidelines for Self-consolidating concrete", 2002.
6. Gagne, R., M. Pigeon, P.C. Aitcin, "Deicer Salt Scaling Resistance of high Performance Concrete", ACI, (1989) 122.
7. Khan, U., R.A. Khan, N.K. Pandey, A. Tyagi, "Fresh and Hardened Properties of Hybrid Fibre Reinforced Self Consolidating Concrete Containing Basalt and Polypropylene Fibres", International Journal of Recent Technology and Engineering (IJRTE), 8(2019), 3356-3361.
8. Khan,U.,S.P.Singh,"Investigation on the Strength Properties of Hybrid Fibre Reinforced Self Compacting Concrete", UKIERI Concrete Congress, Concrete:The Global builder, 2019.
9. Kumar, D.V.N., "A study on strength properties of hybrid fiber reinforced self-consolidating concrete", International Journal of Civil Engg. Research, 8 (2017) 49-55.
10. Murthy, K.N., N.A.V. Rao, R. I. V. Reddy, M.V.S. Reddy, "Mix design procedure for self-consolidating concrete", IOSR Journal of Engineering (IOSRJEN), 2(2012) 33-41.
11. Naaman, A.E., "Engineered steel fibers with optimal properties for reinforcement of cement composites", Journal of Advanced Concrete Technology, 1(2003) 241-252.
12. Nandhini, S., R. Manju, "A study on hybrid fibre reinforced self-consolidating concretes", SSRG International Journal of Civil Engg.-(ICRTCETM-2017), (2017) 283-291.
13. Okamura, H., K. Maekawa, K. Ozava, "High performance concrete", Ghihodo Publishing, 1993.
14. Okamura, H., M. Ouchi, "Self-consolidating concrete, Journal of Advanced Concrete Technology", 1(2003) 5-15.
15. Okamura, H., K. Ozawa, "Mix – design for self-consolidating concrete", Concrete Library of JSCE, 25 (1995) 107-120.
16. Pajak, M., T. Ponikiewski, "Effect of the shape of steel fibres on the mechanical properties of reinforced self-consolidating concrete", Cement Lime Concrete, 18 (2013) 335-42.
17. Pajak, M., "Investigation on flexural properties of hybrid fibre reinforced self-consolidating concrete", Procedia Engg., 161 (2016) 121 – 26.
18. Rohilla, C., K. Sharma, Kuldeep, "A study on behavior of chopped fiber reinforced self-consolidating concrete", Engg. and Technology Journal, 1(2016) 33-8.
19. Sahmaran, M., A. Yurtseven, A., I. O. Yaman, "Workability of hybrid fiber reinforced self-consolidating concrete", Building and Environment, 40(2005) 1672–77.
20. Satheskumar. K, R. Gobinath, V. Ramachandran, "Structural behaviour of self-compacting concrete with basalt fiber", International Journal of Engg. Research & Tech. (IJER.0T), 6 (2017), 689 – 97.

AUTHORS PROFILE

Uzair Khan received his B. Tech in Civil Engineering in 2012 from Integral University, M. Tech in Structural & Construction Engineering in 2018 from Dr B R Ambedkar National Institute of Technology, Jalandhar and Ph.D (Pursuing) in Civil Engineering Delhi Technological University, New Delhi in the field of Concrete Technology. He is currently working as an Assistant Professor in the Department of Civil Engineering, ABES –Engineering College, Ghaziabad. He has more than 7 years of teaching, research and educational experience and published more than 13 research papers in peer reviewed journals and conferences. His interests are Self Compacting Concrete, Concrete Composites, Fibre Reinforced Concrete and Geopolymer Concrete.

Sandeep Kumar Tripathi received his B. Tech in Environmental Engineering in 2009 from Uttar Pradesh Technical University, Lucknow, M. Tech in Environmental Engineering in 2013 from Jaypee University of Engineering and Technology, Guna, Madhya Pradesh and Ph.D (Pursuing) in Civil Engineering Jamia Millia Islamia, New Delhi in the field of Remote Sensing and GIS. He is currently working as an Assistant Professor in the Department of Civil Engineering, ABES Engineering College, Ghaziabad. He has more than 7 years of industrial, teaching, research and educational experience and published eminent research papers in peer reviewed journals. His interests are wastewater treatment and technologies, Remote Sensing, Geographic Information System.

Anurag received his B. Tech in Civil Engineering in 2019 from ABES –Engineering College, Ghaziabad. He is currently studying for higher education. His area of interest includes Self Compacting Concrete and Fibre Reinforced Concrete.

Dr. Rizwan Ahmad Khan is currently an Associate Professor in the Department of Civil Engineering at AMU Aligarh. Dr Khan earned his Ph.D. from Indian Institute of Technology, Delhi (IITD). He has more than 10 years of teaching, research and educational experience. He has guided more 40 Master's thesis and published more than 70 research papers in peer reviewed journals and conferences. His interests are Self Compacting Concrete, Concrete Composites, Fibre Reinforced Concrete and Recycling of Materials in Concrete

Research Square

Preprints are preliminary reports that have not undergone peer review.
They should not be considered conclusive, used to inform clinical practice,
or referenced by the media as validated information.

Geopolymer Concrete: A Sustainable and Economic Concrete via Experimental Analysis

Manvendra verma (mv075415@gmail.com)
Delhi Technological University https://orcid.org/0000-0002-0840-841X
Nirendra Dev
Delhi Technological University

Original Research

Keywords: Geopolymer Concrete, Flyash, GGBFS, Sustainable construction, Mechanical properties

DOI: https://doi.org/10.21203/rs.3.rs-185150/v1

License: This work is licensed under a Creative Commons Attribution 4.0 International License.
Read Full License

Abstract

Geopolymer concrete is a sustainable, economical, eco-friendly, and high-strength concrete. The GPC utilizes industrial solid wastes like flyash and slag as binding material and is activated by the alkaline solution containing NaOH and Na_2SiO_3 in the design mix. The experimental investigation analyzes both GPC and OPC concrete's physical and mechanical properties for the same mix design and analyzes the concretes cost and sustainability. After the experimental investigation, the GPC and OPC concrete's compressive strength shows similar trends at the 28 days strength, but the initial three days strength of the GPC strength is much higher than the OPC concrete, but around 28 days, the compressive strength of concrete mix got similar. The splitting tensile strength and flexural strength of the GPC specimens are slightly higher than the OPC concrete mix specimens. The OPC concrete's elastic modulus is slightly higher than the GPC mix design, whereas the Poisson ratio of the OPC concrete is slightly lower than the GPC mix designs. The GPC has less embodied energy compared to the OPC concrete. The cost of the GPC at a bulk level reduced the cost of up to 40% of the OPC concrete.

1. Introduction

GPC becomes a perfect alternative to the world's sustainable construction industry because the concrete demand is the second largest in the world after the water. The development of the country and society increases with the increment of the infrastructure. So, concrete production increases exponentially in the future with the development. In the OPC cement production, around a similar amount of carbon emission in the environment to OPC production quantity [1]. The GPC utilizes the Industrial solid wastes flyash and slag in the GPC. Flyash generates in thermal power plants as a waste product in a vast amount, but the utilization of flyash is limited to up to 50% of the production[2]. GPC shows better physical, chemical, and mechanical properties compared to the OPC cement concrete. The durability properties of the GPC are also higher than OPC concrete. GPC is highly resistant to sulfate attack compared to the OPC concrete[3]–[6]. The geopolymerisation reaction plays a vital role in the development of the strength of the GPC. Some factors affect the geopolymerisation process like curing conditions, alkaline solution content, and binding material content in the design mix.

The pozzolanic materials like flyash, GGBFS, metakaolin, and rice husk ash were used as a binding material in the geopolymer due to the high silica, and alumina content composition and compressive strength increases with the increment of Si/Al ratio[7]. The sodium hydroxide and sodium silicate mix solution was used to activate pozzolanic material to work as binding material for the geopolymerisation reaction. The GPC mix's strength increases with the increment of molarity of NaOH, but it reduces the workability[8]–[13]. Geopolymerisation reaction develops the strength of the concrete affected by the various factors and parameters[14]. The alkaline ratio also affects the mix's strength, and it increases with the Na_2SiO_3/NaOH ratio[15].

The curing condition is an essential parameter to gain strength, and the strength increases with the increment of curing temperature up to 100^0C[16][17]. The replacement of flyash by the GGBFS develops

the GPC mix's strength in the ambient curing conditions[18]. The fineness of the flyash plays a vital role in the development of strength, increases the strength, and decreases the mix's setting time [19][20]. The fineness of flyash directly reduces the porosity by increasing small particles in the mix[21][22]. In the geopolymerisation reaction, curing time directly affects the mix's early strength development, and longer curing time gives better end products after the reaction[23]. The water present in the mix was not used in the geopolymerisation endproducts so, evaporation of water from the mixture made the specimens crack-free [24]. The water content increases in the mix reduce the strength of the mix specimens[25]. The flyash and slag have a high potential for reactivity and bond formation for strength development[26]. The GPC has a very high potential to resist the acidic or sea-water environment and other extreme weather conditions[27], and it shows the future scope of the geopolymer paste as a repair of the concrete structure due to their efficiency and performance[28]. The GPC specimens have high stability against the elevated temperature than the OPC concrete samples[29]. Manufacturing sand or stone dust has a high capability to work as fine aggregate in the concrete without reducing their strength. It is also useful in the formation of high-strength GPC[30]. All the building construction constituent's alternative materials embodied energy is lower than the conventional building materials[31]. Embodied energy is used to calculate the carbon footprints used to produce material in various ways[32]. The GGBFS and flyash contents present in the concrete's mix design reduce the concrete's embodied energy [33].

2. Methods

All the constituents used in forming the GPC and OPC concrete specimens for the experimental analysis are explained separately in the paragraphs. The preliminary test on the material samples to identify the concrete laboratory properties in the civil engineering department, DTU, Delhi. The SEM and EDS test of the samples done in the nanotechnology lab, Jamia Millia Islamia, New Delhi, whereas the XRD test in the central facility laboratory, DTU, Delhi. The OPC 43 grade of cement was purchased from the JK cement to experiment with a controlled mix design[34]. In the preliminary check, the cement's quality, by testing consistency, initial and final setting time, specific gravity, fineness of the particles sizes, and soundness. The cement passes all preliminary tests as per Indian standard codes[35]–[40]. Table **1** describes the cement's properties identified through the testing sample in the concrete laboratory in the civil engineering department, DTU, Delhi. Flyash is an industrial solid waste produced from the thermal power plant by the coal ash fumes electrostatic precipitation. The particle size of the flyash somewhat lower or similar to the OPC particle size and contain high silica and alumina in the composition. Flyash brought from the national thermal power plant, Dadri, Gautam Budh Nagar, Uttar Pradesh.

Flyash used for the test is class-c type flyash in the mix design[41]. The particles of the flyash are spherical and porous, confirmed by the SEM image. Fig. 1 shows the amorphous nature of the flyash sample by the XRD graph, whereas Fig. 3 shows the porous spherical particles of the flyash by the SEM image at the 5-micron resolution. Table 2 shows the composition of the chemical constituents present in the flyash explained by the XRF test, and Fig. 4 shows the EDS graph in which describe element content present in the flyash conducted in the nanotechnology lab Jamia Millia Islamia, New Delhi.

GGBFS is produced from the steel manufacturing plant by quenching the slag from the molten iron-steel material. The waste material present in the iron or steel ores is called slag after separating the wastes from the steels' manufacturing. GGBFS also contains the high silica and alumina content in the composition. GGBFS was brought from the Bhilai steel plant, Bhilai, Chhattisgarh, India, to test and produce the GPC mix specimens. Fig. 1 shows the XRD graph of the GGBFS, which shows the sample's amorphous nature, whereas Table 2 shows the chemical composition present in the GGBFS sample. Fig. 2 describes the SEM image of the GGBFS sample at the resolution of two microns and shows the irregular shape of the particles, whereas Fig. 5 shows the EDS graph in which describes the element present in the samples.

2.1.Alkaline Solution

The alkaline solution plays a vital role in the Geopolymerisation reaction because it activates the reaction's pozzolanic binding materials and finds the end products. The alkaline solution contains the sodium hydroxide and sodium silicate solution, and it is mixed before the 20-24 hours for sampling. Sodium hydroxide was purchased from the Fisher scientific manufactured in the business park, Powai, Mumbai, Maharashtra, India. Fig. 6 shows the sample of sodium hydroxide flakes used in the mix design, whereas Fig. 7 shows the sodium silicate sample purchased from the Central Drug House (P) Ltd.

2.2. Aggregates

Aggregate is used as the concrete's skeleton because it occupies up to 85% of the concrete. Various sizes of the aggregate used in the mix are mostly classified into two categories are fine aggregates and coarse aggregates. In the coarse aggregate, two types of aggregates used are 10mm and 20mm in the design mix, whereas in fine aggregate used the crushed stone dust in the mix of both concrete. As per the Indian standard codes, to test the aggregate used quality in the mix design. In the preliminary test, check the gradation of the aggregates, zone, fineness modulus, specific gravity, water absorption, silt content, bulk density, crushing value, impact value, abrasion value, flakiness index, and elongation index of the aggregates samples[42]–[48]. Fig. 8 shows a picture of the raw material of stone dust used as fine aggregate in the mix design. Fig. 9 describes the grain-size curve on the logarithmic graph and the particle size distribution or gradation of the m-sand by the sieve analysis. The stone-dust properties found out through the test conducted in the concrete lab describes in Table 3.

As the percentage passing 600μ sieve is between 35 and 59, the sand belongs to gradation II. From the gradation curve, we find D_{10}=0.1, D_{30}=0.4, and D_{60}=1.2

$C_u = D_{60} / D_{10} = 1.2/0.1 = 12 > 6$

$C_c = D_{30}^2 / (D_{10} \times D_{60}) = 0.4^2 / (0.1 \times 1.2) = 1.33$

Thus the sand is well-graded.

Locally available materials coarse aggregates used in all mixes of concretes. The all particles size of aggregates present in the sample with their percentage and found the coarse aggregate's fineness modulus. **Fig. 10** shows the coarse aggregate sample pic, whereas Table 4 describes the coarse aggregate properties found through the laboratory tests as per the Indian standards[49]–[53]. The fineness modulus of the coarse aggregate is 7.29, calculated through the sieve analysis of the samples.

2.3.Superplasticiser

Superplasticiser is used to enhance the concrete's performance by reducing the mix design's water content and increasing the fresh mix's workability. SNF-based superplasticizer is used in the mix design of both concrete made by the Fosroc industry named SP Conplast-430 in the market[54]. Table **5** shows the properties of the SNF-based superplasticizer used in the mix.

3. Sampling And Test Setup

Specimens made of the controlled OPC concrete mix usually mix all constituents in the pan mixture for around 2 to 5 minutes and cast in the specimens mold for 24 hours. In the case of GPC, the alkaline solution mix before 20-24 hours mixing of the concrete constituents in the pan mixture and cast in the mold of the specimens with the proper compaction of casted samples. The OPC concrete specimens were cured in the water tank, but the GPC specimens were cured in the oven at 60^0C for 24 hours. The cubical, cylindrical, and beam shape specimens cast of both types of concrete for the testing. Physical and mechanical properties tested for both types of concretes. Table **6** describes the mixed proportion of all constituents used in GPC and OPC concretes' mix design.

3.1.Physical properties

The slump and compaction factor test is used for the identification of the workability of the concrete. Slump is most common for testing the concrete's workability in site or laboratory, but the compaction factor is usually used in the laboratory only. Slump is conical in shape, but the compaction factor setup made of the two conical shape buckets fitted in the vertical alignment with a standard gap and down the buckets' surface is openable. The compaction factor checks the self-compaction ability of the concrete with the gravity force[1]. Self-compacting concrete is made with the use of a PCE-based superplasticizer in the concrete mix design[55].

3.2.Density

The weight of the specimens calculates the density of both mixed specimens before the destructive tests. The cube specimen's weight decides the mixes density at the 28 days after the casting, and the mass

calculates the density to volume ratio of the cube specimens[56].

3.3.Mechanical properties test

Compressive strength of both types of concrete mixes tested by the cube sample test under the CTM machine at the 5.25kN/sec rate of the loading statically applied on the specimens. The 150mm*150mm*150 mm' cube sizes as per the Indian Standard code. The mixed samples were tested at 3, 7, 14, 28 days after the specimens casting [56], [57].

Splitting tensile is used to find the indirect tensile strength of the concrete. The cylindrical shape of size diameter*length is 150mm*300mm as per the Indian Standard codes used to find the splitting tensile of the concrete mix specimens. The 4.5kN/sec rate of loading was applied in the transverse direction of the cylindrical specimens for the test of splitting tensile of the concrete[58]. Splitting tensile is higher than the direct tensile but lower to the concrete's same mix design's flexural strength.

Flexural strength is also called a rupture of the concrete used to find the concrete specimens bending capability. If the maximum aggregate size is less than equal to 20mm, then the beam of standard size 100mm*100mm*500mm is used for the cast specimens to analyze the flexural strength. A two-point load was applied along the specimens' transverse direction for the test on the flexural testing machine[59].

Elastic modulus and the Poisson ratio of the concrete mix analyze by testing on the cylindrical specimens. The uniaxial statically load applied along the vertical direction to the cylindrical specimens and found the vertical and horizontal displacement and strength of the cylinder; from the displacements, the Poisson ratio calculated through the ratio of horizontal strain to vertical strain. The elastic modulus finds through the load applied to the cylindrical specimens about one-third of their strength and release and going continuously for the same procedure often draws the stress-strain graph and finds the elastic modulus through the chord modulus as per the American standard code.

3.4 Non-destructive tests

The Non-destructive test is also used to identify specimens' strength without any destruction, and it primarily uses the rebound hammer test and UPV test. Rebound hammer test based on the specimen's surface's penetration reflects by the surface hardness of the specimen[60]. The UPV test propagates the ultrasonic pulse in the sample and measures the time travel duration to pass the specimens. The transducers are connected on two opposite sides of specimens in which one works as an emitter, and another works as a receiver of the ultrasonic pulse wave as per the Indian standard[61].

4. Results And Discussion

All the casted specimens of the mixes of both types of concretes were tested in the machines and compared to concrete mix mechanical properties. The specimens of cubical, cylindrical, and beams were tested as per the Indian standards. The experimental work on the mix of GPC and OPC concrete was

conducted in the concrete laboratory, civil engineering department, Delhi Technological University, Delhi. It includes the slump value, compaction factor, density, compressive strength, splitting tensile, flexural strength Poisson ratio, and elastic modulus done in

4.1.Physical Properties

The slump and compaction factor test is used to analyze the workability of the fresh concrete mix. In both types of concrete, the Slump value of both concrete OPC concrete and GPC are the same 75-100mm, and the compaction factor of the OPC concrete is .89, whereas the GPC is .87 after the mixing in the pan mixture for 3-5 minutes. The concrete mix's workability increases by adding a superplasticizer in the mix without reducing concrete strength [54]. The SNF-based superplasticizer does not harm the GPC specimen's strength [62], [63]. It also increases the microstructure development [64], but it is not beneficial for the elevated temperature[65].

4.2.Density

The concrete sample cubes' weight is used to calculate density before the compressive strength test after the 28 days of casting. The density of the OPC concrete mix design increases with time, whereas the density of the GPC decreases with the same. The maximum density of GPC is 2492kg/m^3 found three days after the casting, whereas the maximum density of the OPC concrete is 2462kg/m^3 found at 28 days after the casting. The concrete density with age is the opposite case in both concrete because the GPC density decreases with increasing time but OPC concrete density increases. Fig. **11** shows the graph between the density and time in which the GPC samples density decreases with increasing time, but OPC concrete density increases with up to 28 days of tests. The density of the concrete increased by the addition of finer content in the mix-like nanoparticles materials.

4.3.Compressive Strength

The compressive strength of the GPC and OPC concretes similar in trends at the 28 days strength, but the initial three days strength the GPC strength is much higher than the OPC concrete but around 28 days the compressive strength of concrete mix got similar. GPC and OPC concrete's three-day compressive strength is 23.2MPa and 14.4MPa, respectively, whereas the 28 days compressive strength of GPC and OPC concrete is 35MPa 35.6MPa, respectively. Fig. **12** shows the graph between the compressive with the time of both concrete. The graph shows the initial strength of the GPC higher than the OPC concrete samples but shows similar strength at 28 days compressive strength. The compressive strength of OPC concrete increases by reducing water content, the addition of superplasticizer, increment of cement content, and silica fumes in the mix design. The compressive strength of the GPC depends on the various parameters are as the molarity of NaOH, alkaline ratio, curing condition, curing temperature, curing time,

water content, and superplasticizer. The compressive strength of the GPC increases with the increment of NaOH concentration in the mix design[66].

4.4.Splitting Tensile Strength

The splitting tensile strength of the concrete mix designs found by the test of the mix design's cylindrical specimens in the compression testing machine at the rate of loading is 4.5kN/sec statically. The splitting tensile strength of the GPC is higher compared to the OPC concrete mix specimens. The splitting tensile of the OPC concrete at 3, 7, 14, and 28 are 1.5MPa, 3MPa, 3.5MPa, and 3.8MPa, respectively, whereas the GPC's splitting tensile at 3, 7, 14, and 28 days are 2.6MPa, 3.2MPa, 3.9MPa, and 4.2MPa respectively. The Splitting strength of the GPC is slightly higher than the OPC concrete for the same compressive strength mix. Fig. **13** shows the splitting tensile of both concrete with the time. It shows that the GPC samples have higher splitting tensile compared to the OPC concrete samples. The GPC specimens show initial high strength at 7 days, but after the 28days show similar trends.

4.5.Flexural Strength

The flexural strength of the concrete mix designs identifies through the testing of the beam samples of the mix design in the flexural testing machine under a two-point load applied on the section of the beam at the transverse direction of the specimens. The flexural strength of the GPC specimens is slightly higher than the OPC concrete mix specimens. The OPC concrete's flexural strength at 3, 7, 14, 28 days is 1.7MPa, 3.4MPa, 3.8MPa, and 4.2MPa, respectively, whereas the GPC flexural strength at 3, 7, 14, and 28 days are 2.8MPa, 3.6MPa, 4.1MPa, and 4.7MPa respectively. Fig. **14** describes the flexural strength with the time of both concrete. It shows the GPC has higher flexural strength to OPC concrete samples at all the time of tests continuously.

4.6.Elastic Modulus and Poisson Ratio

Elastic modulus and the Poisson ratio of the concrete mix design identifies through the test of the cylindrical specimens of the mix in the compression testing machine with vertical and horizontal extension meters. The load was applied along the vertical direction of the specimens statically in the machine. To determine the lateral and linear deformation of the specimens by which got the strains after the failure. The lateral strain ratio to the linear strain shows the Poisson ratio of the concrete mix design, whereas the load applied one-third of failure to the specimens and reduce the load and continue the same procedure many times. The slope of the initial stress-strain curve describes the elastic modulus of the concrete mix designs. The GPC and OPC concrete mix design's elastic modulus was tested 28 days after the casting of the specimens molds. The OPC concrete's elastic modulus is slightly higher than the GPC mix design, whereas the Poisson's ratio of the OPC concrete is slightly lower than the GPC mix designs. The elastic modulus of the OPC concrete and GPC are 26.3GPa and 23.4GPa, respectively, whereas the

Poisson ratio of the OPC concrete and GPC are .15 and .17, respectively. **Fig. 15** shows the elastic modulus of the OPC concrete and GPC at 28 days test of samples. **Fig. 16** shows the setup to determine the Poisson's ratio of the concrete mix cylindrical samples.

Non-Destructive Tests

Rebound Strength

The rebound strength test is generally used in the field as a non-destructive test. It is based on the hammer struck on the specimen's surface with some IS code provisions and showed the rebound value. The Rebound hammer on the specimen surface continuously 10 times, then the rebound gives the average rebound value and gives the rebound strength of the specimens as per the Indian standard. The rebound strength shows similar trends to the mix's compressive strength, but the rebound strength showed a little higher value. The initial three-day strength of GPC higher than the OPC concrete mix but shows somewhat lower strength to the OPC concrete. **Fig. 17** describes the graph of rebound strength of both GPC and OPC concrete.

UPV Test

The UPV test is vital in the non-destructive test method because it directly gives the strength and cracks information in the existing structures. The UPV test needs only two opposite sides of specimens in a clean condition to propagate ultrasonic pulse waves. It plays a vital role in the strength check of the existing damaged or vulnerable structures because rebound tests are based on the surface hardness, so rebound is used only in fewer thickness specimens up to 300mm. The UPV test is mostly used in the consultancy check works of the existing concrete structures. The UPV of the specimens increases with the hardness that directly relates to the strength. **Fig. 18** describes the graph of the UPV test results of both GPC and OPC concrete mix samples. It shows similar trends of GPC and OPC concrete to the rebound strength graph.

TGA (Thermo Gravimetric Analysis)

The TGA test does the thermal analysis of the materials by increasing the temperature 10^0C per second up to 900^0C and check the derivative of weight reduction with the temperature. The apparatus and shows note the weight reduction of the material with increasing temperature in the graphical form. The two-parameter shows in a single graph with different y-axis but in the single x-axis in which one y-axis represents the derivative weight percentage and another one representing the weight percentage reduction with temperature. GPC matrix is highly stable at the elevated temperature without failure compared to the OPC concrete matrix. **Fig. 19** describes the graph of TGA-DTG of GPC concrete up to the temperature of 850^0C. It shows the weight reduction with increasing temperature, but the GPC matrix is highly stable up to 850^0C, and it shows the retained material 92% of the original at 850^0C. DTG graph shows the reduction of the weight with temperature is non-linear, and it varies from negative to positive undefinedly.

Mechanical properties correlation

The correlation generates through the data of mechanical properties produces by the destructive test in the laboratory. The linear regression analysis of data among the compressive strength, splitting tensile, and flexural tensile strength shows the correlation equation and compared it to the Indian standard correlation equations.

Correlation between the compressive strength and splitting tensile

The correlation between splitting tensile and compressive strength proposed eq. (1). It generates through the regression analysis of the data generates by the destructive testing in the laboratory. The ACI committee gives eq. (2) in the state of the art of high strength concrete[67] and a committee of euro code international gives eq. (3) in the model code 1990[68]. eq. (4) introduced by an ACI standard and report for building code requirements for structural concrete[69]. **Fig. 20** describes the graph of the correlation between the compressive strength and splitting tensile. The correlation equation produces by regression analysis of the test data.

$$\text{Proposed: } f_{st} = -.63 + .14 f_{ck} \quad (1)$$

$$ACI363R-92: f_{st} = 0.59\sqrt{f_c} \quad (1)$$

$$CEB-FIP: f_{st} = 0.301 f_c^{0.67} \quad (2)$$

$$ACI\ 318-14: f_{st} = 0.56 f_c^{0.5} \quad (3)$$

Correlation between compressive strength and flexural strength

The correlation between the compressive strength and flexural describes by the eq. (5) generates through the regression analysis of the test data. ACI committee introduces the eq. (6) in the publication of the state of the art of high strength concrete[67]. A standard report presented on the code for the design of concrete in the structure introduces the eq. (7) of correlation[69]. Australian code for the reinforced concrete design presented the correlation eq. (8), and the Indian code introduced the eq. (9) between the flexural strength and compressive strength[70],[71]. The flexural strength is always about 10%-20% of the compressive strength. The tested data also lies between these values. **Fig. 21** describes the correlation equation's graph between flexural strength and compressive strength proposed by the tested data.

$$\text{Proposed: } f_{fs} = -1.03 + .16 f_{cs} \quad (5)$$

$$ACI363R - 92: f_{fs} = 0.94\sqrt{f_c} \quad (6)$$

$$\boldsymbol{ACI\ 318 - 99: f_{fs} = 0.62\sqrt{f_c}} \quad (7)$$

$$\boldsymbol{AS\ 3600: f_{fs} = 0.6\sqrt{f_c}} \quad (8)$$

$$\boldsymbol{IS\ 456 - 2000: f_{fs} = 0.7\sqrt{f_c}} \quad (9)$$

Sustainability Analysis

Sustainable development is essential for the present scenario. A very massive amount of industrial solid wastes produces in the present time requires the usage of that waste in the development work. The usage of industrial solid wastes reduces the carbon footprints, indirectly reduces the usage of the high embodied energy products. The OPC cement's embodied energy produced by the dry process is about 4.6MJ/kg, whereas the flyash and slag have nil embodied energy. The industrial solid wastes flyash and slag used as a binder in the concrete by replacing the OPC and that wastes activated by the chemical solution of sodium hydroxide and sodium silicate. The GPC has less embodied energy compared to the OPC concrete[31]–[33], [72]–[74]. The embodied energy calculation of both concrete is shown in Table **7**. The embodied energy of all constituents of concrete calculated based on reference papers.

Cost Analysis

The concrete cost was calculated by the amount of the constituents present in the concrete mix design, and then, after calculating the rate of all individual constituent prices, the concrete mix design cost was found. The cost of the GPC at a bulk level reduced the cost of up to 40% of the OPC concrete. The cost of the OPC of $1m^3$ is Rs. 3758, whereas the cost of the GPC of $1m^3$ is Rs. 2230. Table **8** describes all calculations of the cost of the materials and concrete. The materials and concrete costs are essential in the construction industries because the construction projects' costs are always higher. The project's economy always matters and goes for the optimum point, which got the essential strength with the project's lesser cost. The GPC is economic concrete compared to the OPC concrete and also reduced pollution or carbon footprints. GPC is a new trend in the construction industry due to sustainable development properties.

Conclusion

After the experimental, sustainability, and cost investigation concluded the followings:-

- In both types of concrete, the slump value of both concrete OPC concrete and GPC are the same 75-100mm, and the compaction factor of the OPC concrete is .89, whereas the GPC is .87 after the mixing in the pan mixture for 3-5 minutes.
- The density of the OPC concrete mix design increases with time, whereas the density of the GPC decreases with the same.
- The compressive strength of the GPC and OPC concretes similar in trends at the 28 days strength, but the initial three days strength the GPC strength is much higher than the OPC concrete but around 28 days the compressive strength of concrete mix got similar.
- The splitting tensile and flexural strength of the GPC is slightly higher than the OPC concrete mix specimens. Similarly, the OPC concrete's elastic modulus is slightly higher than the GPC mix design, whereas the Poisson ratio of the OPC concrete is slightly lower than the GPC mix designs.
- The GPC has less embodied energy compared to the OPC concrete.
- The cost of the GPC at a bulk level reduced the cost of up to 40% of the OPC concrete. The cost of the OPC of $1m^3$ is Rs. 3758, whereas the cost of the GPC of $1m^3$ is Rs. 2230.

Declarations

Funding Statement

This study is supported by the Delhi Technological University, Delhi, India.

Conflict of Interest

There are no conflicts of interest or competing interests in this article.

Author Contribution

All authors have participated in (a) conception and design, or analysis and interpretation of the data; (b) drafting the article or revising it critically for valuable intellectual content; and (c) approval of the final version.

Availability of data and material

The available data had been used and discussed in the manuscript.

Compliance with ethical standard

This manuscript has not been submitted to, under review at, another journal or other publishing venue.

Consent to Participate

As a corresponding author or on behalf of all authors of the research paper, I consent to participate.

Consent to publication

All author of the research paper is consent to the publication.

Acknowledgment

The experimental test was conducted in the concrete laboratory in the civil engineering department of Delhi technological University, Delhi, India. It includes a compressive strength test, splitting tensile, flexural strength, density, slump, Poisson's ratio, and modulus of concrete mix elasticity; the XRD analysis and TGA test conducted in the central facility laboratory of DTU.

References

[1] M. Verma and N. Dev, “Geopolymer concrete : A way of sustainable construction,” *Int. J. Recent Res. Asp.*, vol. 5, no. 1, pp. 201–205, 2018.

[2] Central Electricity Authority, “Flyash generation at coal/lignite based thermal power stations and its utilization in the country,” 2019.

[3] I. Ismail, S. A. Bernal, J. L. Provis, S. Hamdan, and J. S. J. Van Deventer, “Microstructural changes in alkali-activated fly ash/slag geopolymers with sulfate exposure,” *Mater. Struct. Constr.*, pp. 361–373, 2013.

[4] C. Chotetanorm, P. Chindaprasirt, V. Sata, S. Rukzon, and A. Sathonsaowaphak, “High-Calcium Bottom Ash Geopolymer : Sorptivity, Pore Size, and Resistance to Sodium Sulfate Attack,” vol. 25, no. January, pp. 105–111, 2013.

[5] W. Gustavo *et al.*, “Fly Ash Slag Geopolymer Concrete : Resistance to Sodium and Magnesium Sulfate Attack,” *J. Mater. Civ. Eng.*, vol. 28, no. 12, pp. 1–9, 2016.

[6] M. A. R. Bhutta *et al.*, “Sulphate Resistance of Geopolymer Concrete Prepared from Blended Waste Fuel Ash,” *J. Mater. Civ. Eng.*, vol. 26, no. 11, pp. 1–6, 2014.

[7] P. Duxson *et al.*, “Understanding the relationship between geopolymer composition, microstructure and mechanical properties,” *Colloids Surfaces A Physicochem. Eng. Asp.*, vol. 269, pp. 47–58, 2005.

[8] G. Nagalia, Y. Park, A. Abolmaali, and P. Aswath, “Compressive Strength and Microstructural Properties of Fly Ash–Based Geopolymer Concrete,” *J. Mater. Civ. Eng.*, 2016.

[9] G. Sung *et al.*, “The mechanical properties of fly ash-based geopolymer concrete with alkaline activators,” *Constr. Build. Mater.*, vol. 47, no. 2013, pp. 409–418, 2015.

[10] N. K. Lee, J. G. Jang, and H. K. Lee, “Cement & Concrete Composites Shrinkage characteristics of alkali-activated fly ash/slag paste and mortar at early ages,” *Cem. Concr. Compos.*, vol. 53, pp. 239–248,

2014.

[11] P. Topark-Ngarm, P. Chindaprasirt, V. Sata, and P. C. and V. Sata, Pattanapong Topark-Ngarm, “Setting Time, Strength, and Bond of High-Calcium Fly Ash Geopolymer Concrete,” *J. Mater. Civ. Eng.*, vol. 27, no. 2011, pp. 1–7, 2015.

[12] D. Hardjito and S. E. Wallah, “On The Development of Fly Ash-based Geopolymer Concrete,” *ACI Mater. J.*, pp. 467–72, 2004.

[13] S. V. Patankar, Y. M. Ghugal, and S. S. Jamkar, “Effect of Concentration of Sodium Hydroxide and Degree of Heat Curing on Fly Ash-Based Geopolymer Mortar,” *Indian J. Mater. Sci.*, 2014.

[14] Manvendra Verma; Nirendra Dev, “Review on the effect of different parameters on behavior of Geopolymer Concrete,” *Int. J. Innov. Res. Sci. Eng. Technol.*, vol. 6, no. 6, pp. 11276–281, 2017.

[15] P. Nath and P. K. Sarker, “Effect of GGBFS on setting, workability and early strength properties of fly ash geopolymer concrete cured in ambient condition,” *Constr. Build. Mater.*, vol. 66, pp. 163–171, 2014.

[16] P. Rovnaník and S. O. Al, “Effect of curing temperature on the development of hard structure of metakaolin-based geopolymer,” *Constr. Build. Mater.*, vol. 24, no. 7, pp. 1176–1183, 2010.

[17] P. Nath and P. K. Sarker, “Flexural strength and elastic modulus of ambient-cured blended low-calcium fly ash geopolymer concrete,” *Constr. Build. Mater.*, vol. 130, pp. 22–31, 2017.

[18] S. Kumar, R. Kumar, and S. P. Mehrotra, “Influence of granulated blast furnace slag on the reaction, structure and properties of flyash-based geopolymer,” *J. Mater. Sci.*, pp. 607–615, 2010.

[19] A. Sathonsaowaphak, P. Chindaprasirt, and K. Pimraksa, “Workability and strength of lignite bottom ash geopolymer mortar,” *J. Hazard. Mater.*, vol. 168, pp. 44–50, 2009.

[20] Y. M. G. and S. V. P. S.S. Jamkar, “Effect of Fineness of Fly Ash on Flow and Compressive Strength of Geopolymer Concrete,” *Indian Concr. J.*, pp. 57–62, 2013.

[21] U. K. Salmabanu Luhar*, S. Luhar, and U. Khandelwal, “A Study on Water Absorption and Sorptivity of Geopolymer Concrete,” *SSRG Int. J. Civ. Eng.*, vol. 2, no. 8, pp. 1–10, 2015.

[22] P. S. Deb and P. K. Sarker, “Effects of Ultrafine Fly Ash on Setting, Strength, and Porosity of Geopolymers Cured at Room Temperature,” *Am. Soc. Civ. Eng.*, pp. 1–5, 2016.

[23] N. A. Lloyd and B. V Rangan, “Geopolymer Concrete with Fly Ash,” in *Second international conference on sustainable construction materials and technologies.*, 2017, no. January 2010.

[24] K. S. Finnie, D. S. Perera, O. Uchida, E. R. Vance, and K. S. Finnie, “Influence of curing schedule on the integrity of geopolymers,” *J. Mater. Sci.*, pp. 3099–3106, 2007.

[25] J. June *et al.*, “Engineering Properties of Alkali Activated Natural Pozzolan Concrete,” in *Second international conference on sustainable construction materials and technologies.*, 2010.

[26] J. G. Jang, N. K. Lee, and H. K. Lee, “Fresh and hardened properties of alkali-activated fly ash/slag pastes with superplasticizers,” *Constr. Build. Mater.*, vol. 50, pp. 169–176, 2014.

[27] K. U. Ambikakumari, M. Lahoti, and E. Yang, “Investigating the potential reactivity of fly ash for geopolymerization,” *Constr. Build. Mater.*, vol. 225, pp. 283–291, 2019.

[28] Y. D. T. C. Y. Dai, “Application of geopolymer paste for concrete repair,” *Struct. Concr.*, no. May 2018, pp. 1–11, 2017.

[29] Z. Pan, Æ. J. G. Sanjayan, J. G. Sanjayan, and A. B. V Rangan, “An investigation of the mechanisms for strength gain or loss of geopolymer mortar after exposure to elevated temperature,” *J. Mater. Sci.*, no. 44, pp. 1873–1880, 2009.

[30] D. D. Sakthidoss and T. Senniappan, “A Study on High Strength Geopolymer Concrete with Alumina-Silica Materials Using Manufacturing Sand,” *Silicon*, vol. 12, no. 3, pp. 735–746, 2020.

[31] B. V. Venkatarama Reddy and K. S. Jagadish, “Embodied energy of common and alternative building materials and technologies,” *Energy Build.*, vol. 35, no. 2, pp. 129–137, 2003.

[32] G. P. Hammond and C. I. Jones, “Embodied energy and carbon in construction materials,” *Proceedinds Inst. Civ. Eng.*, no. May, pp. 87–98, 2008.

[33] K. Kupwade-Patil, C. De Wolf, S. Chin, and J. Ochsendorf, “Impact of Embodied Energy on Materials / Buildings with Partial Replacement of Ordinary Portland Cement (OPC) by Natural Pozzolanic Volcanic Ash Impact of Embodied Energy on materials/buildings with partial replacement of ordinary Portland Cement (OP,” *J. Clean. Prod.*, no. January 2018, pp. 1–9, 2017.

[34] Bureau of Indian Standards, “43 GRADE ORDINARY PORTLAND CEMENT - SPECIFICATION,” *IS 81121989*, no. May, 1990.

[35] Bureau of Indian Standard, “Determination of Initial and Final Setting Time,” *IS 4031 (Part 5)*, vol. 4031, no. 1, pp. 3–6, 2002.

[36] Bureau of Indian Standard, “METHODS OF PHYSICAL TESTS FOR HYDRAULIC CEMENT PART II Determination of Density,” *IS 4031(Part 11)*, vol. 4031, pp. 1–2, 1995.

[37] Bureau of Indian Standard, “Fineness by dry sieving,” *IS 4031 (Part I)*, vol. 4031, 1996.

[38] Bureau of Indian Standard, “Determination of Soundness,” *IS 4031 (Part 3)*, vol. 4031, no. 1, pp. 2–7, 2002.

[39] Bureau of Indian Standard, “Determination of Consistency of Standard Cement Paste,” *IS 4031 (Part 4)*, vol. 4031, no. August 1988, 1997.

[40] Bureau of Indian Standard, “Determination of False Set,” *IS 4031 (Part 14)*, vol. 4931, 1999.

[41] ASTM International, “Standard Specification for Coal Fly Ash and Raw or Calcined Natural Pozzolan for Use,” *C618 − 19*, pp. 1–5, 2019.

[42] Bureau of Indian Standard, “Mechanical Properties,” *IS 2386(Part IV)*, vol. 2386, no. March 1964, 1997.

[43] Bureau of Indian Standard, “Estimation of Deleterious Materials and Organic Impurities,” *IS 2386 (Part II)*, vol. 2386, no. October 1963, 1998.

[44] Bureau of Indian Standard, “Coarse and Fine Aggregate from Natural Sources for Concrete,” *IS 383-1970*, no. 1997, pp. 1–20, 1997.

[45] Bureau of Indian Standard, “Particle Size and Shape,” *Is 2386(Part I)*, vol. 2386, 1997.

[46] Bureau of Indian Standard, “Specific Gravity, Density, Voids, Absorption and Bulking,” *IS 2386 (Part III)*, vol. 2386, no. October 1963, 1997.

[47] Bureau of Indian Standard, “MEASURING MORTAR MAKING PROPERTIES OF FINE AGGREGATE,” *IS 2386 (Part VI)*, vol. 2386, no. October 1963, 1997.

[48] Bureau of Indian Standard, “Soundness,” *IS 2386*, 1997.

[49] ASTM International, “Standard Test Method for Materials Finer than 75-µm (No . 200) Sieve in Mineral Aggregates by Washing,” *C117 − 17 Stand.*, no. 200, pp. 7–10, 2019.

[50] ASTM International, “Standard Test Method for Surface Moisture in Fine Aggregate,” *C70 − 13*, pp. 1–3, 2019.

[51] ASTM International, “Standard Test Method for Bulk Density (‘ Unit Weight ’) and Voids in Aggregate,” *C29/C29M − 17a*, pp. 1–5, 2019.

[52] ASTM International, “Standard Test Method for Sieve Analysis of Fine and Coarse Aggregates,” *C136/C136M − 14*, pp. 1–5, 2019.

[53] ASTM International, “Standard Test Method for Relative Density (Specific Gravity) and Absorption of Fine,” *C127 − 15*, pp. 1–6, 2019.

[54] Bureau of Indian Standards, “CONCRETE ADMIXTURES-Specification,” *IS 91031999*, vol. April, 1999.

[55] M. Verma and M. Nigam, “Mechanical Behaviour of Self Compacting and Self Curing Concrete,” *Int. J. Innov. Res. Sci. Eng. Technol.*, vol. 6, no. 7, pp. 14361–366, 2007.

[56] Bureau of Indian Standard, “METHODS OF TEST FOR STRENGTH OF CONCRETE,” *IS 516-1959*, 2004.

[57] Bureau of Indian Standard, “SPECIFICATION FOR MOULDS FOR USE IN TESTS OF CEMENT AND CONCRETE,” *IS 10086 - 1982*, no. 1952, 2008.

[58] Bureau of Indian Standard, “SPLITTING TENSILE STRENGTH OF CONCRETE - METHOD OF TEST,” *IS 5816 1999*, 1999.

[59] Bureau of Indian Standard, “SPECIFICATION FOR APPARATUS FOR FLEXURAL TESTING OF CONCRETE,” *IS9399 - 1979*, no. 2004, 1979.

[60] Bureau of Indian Standards, “Method of non-destructive testing of concrete-methods of test Part 2: Rebound hammer,” *Is 13311-2*, no. 2004, 1992.

[61] Bureau of Indian Standard, “Non-destructive testing of concrete methods of test Part 1: Ultrasonic pulse velocity,” *IS 13311 (Part1) 1992*, no. 2004, 1992.

[62] M. Albitar, P. Visintin, M. S. M. Ali, M. Drechsler, M. S. Mohamed Ali, and M. Drechsler, “Assessing Behaviour of Fresh and Hardened Geopolymer Concrete Mixed with Class-F Fly Ash,” *KSCE J. Civ. Eng.*, vol. 19, pp. 1445–1455, 2015.

[63] Manvendra Verma; Nirendra Dev, “Effect of SNF-Based Superplasticizer on Physical, Mechanical and Thermal Properties of the Geopolymer Concrete,” *Silicon*, pp. 1–11, 2021.

[64] S. Demie, M. F. Nuruddin, N. Shafiq, M. Fadhil, and N. Shafiq, “Effects of microstructure characteristics of interfacial transition zone on the compressive strength of self-compacting geopolymer concrete,” *Constr. Build. Mater.*, vol. 41, no. 2013, pp. 91–98, 2020.

[65] D. L. Y. Kong and J. G. Sanjayan, “Cement and Concrete Research Effect of elevated temperatures on geopolymer paste, mortar and concrete,” *Cem. Concr. Res.*, vol. 40, no. 2, pp. 334–339, 2010.

[66] M. Verma and N. Dev, “Sodium hydroxide effect on the mechanical properties of flyash-slag based geopolymer concrete,” *Struct. Concr.*, pp. 1–12, 2020.

[67] H. G. Russell *et al.*, “State-of-the-Art Report on High-Strength Concrete Reported by ACI Committee 363,” vol. 92, no. Reapproved, 1997.

[68] “ceb-fip-model-code-1990-design-code.pdf.” 1990.

[69] A. C. I. Committee, *Building Code Requirements for Structural Concrete (ACI 318-14)*. 2014.

[70] C. Concrete, *Reinforced Concrete Design in accordance with AS 3600—2009*. 2009.

[71] Bureau of Indian Standard, “PLAIN AND REINFORCED CONCRETE - CODE OF PRACTICE,” *IS 4562000*, no. July, 2000.

[72] J. K. R. VARSHA BN, SARANYA S, “EMBODIED ENERGY OF AGGREGATES AND MASONRY UNITS PRODUCED AROUND BENGALURU, INDIA,” *Int. J. Adv. Sci. Eng. Technol.*, vol. 6, no. 1, pp. 42–45, 2018.

[73] L. G. Breitenbach, U. Ppgem, and F. Kirch, “A case study about embodied energy in concrete and structural masonry buildings,” *J. Constr.*, vol. 13, no. 2, pp. 9–14, 2014.

[74] S. R. Anvekar, L. R. Manjunatha, S. R. Anvekar, S. Sagari, and K. Archana, “An Economic and Embodied Energy Comparison of Geopolymer, Blended Cement and Traditional Concretes,” *J. Civ. Eng. Technol. Res.*, vol. 1, no. November, pp. 33–40, 2014.

Tables

Table 1 Cement Properties

Test	Result	As per IS 4031-1998
Consistency	30%	30-35
Initial setting time	40 min	Not less than 30min.
Final setting time	1 hr 20 min	Not more than 600min
Specific gravity	3.15	3.10-3.15
Fineness	2.9%	Not exceed 10%
soundness	2mm	Not exceed 10mm

Table 2 Composition of Flyash and GGBFS

Characteristics	SiO_2	Al_2O_3	CaO	Fe_2O_3	MgO	SO_3	LOI
Flyash (%)	45.8	21.4	13.7	12.6	1.3	1.9	.1
GGBFS (%)	34.52	20.66	32.43	.57	10.09	.77	.3

Table 3 Properties of Fine Aggregate/Stone Dust (M-Sand).

S.No.	Test	Results	As Per IS
1.	Zone	Zone II	IS: 2386 (Part I)-1963
2.	Grade	Well Graded	IS: 2386 (Part I)-1963
3.	Fineness Modulus	2.756 (Medium sand)	2.6-2.9 [IS: 2386 (Part I)-1963]
4.	Specific Gravity	2.62	2.6-2.8 [IS: 2386 (Part III)-1963]
5.	Water absorption	1.21 %	Less than 3% [IS: 2386 (Part III)-1963]
6.	Silt Content	6 %	Less than 8% [IS: 2386 (Part I)-1963]
7.	Bulk density	1610 kg/m^3	IS: 2386 (Part III)-1963

Table 4 Properties of coarse Aggregate.

S. No.	Test	Results	As per IS
1.	Fineness Modulus	7.29	6 - 9 [IS: 2386 (Part I)-1963]
2.	Specific Gravity	2.79	2.6-2.8 [IS: 2386 (Part III)-1963]
3.	Water absorption	0.2%	Less than 2% [IS: 2386 (Part III)-1963]
4.	Crushing Value	23%	Less Than 30% [IS: 2386 (Part-IV)-1963]
5.	Impact Value	22%	Less Than 30% [IS: 2386 (Part-IV)-1963]
6.	Flakiness Index	24%	Less than 30% [IS: 2386 (Part I)-1963]
7.	Elongation Index	30%	Less than 45% [IS: 2386 (Part I)-1963]
8.	Abrasion value	8%	Less Than 16% [IS: 2386 (Part-IV)-1963]

Table 5 Properties of Superplasticiser.

S. No.	**Test**	**Results**
1.	Appearance	Brown liquid
2.	Specific gravity	1.18 @ 25°C
3.	Chloride content	Nil to BS 5075 / BS: EN934
4.	Air entrainment	Less than 2% additional air entrained at usual dosages.

Table 6 Mix Proportion of GPC and OPC concrete

Constituents	OPC Concrete Mix Content (kg/m^3)	Geopolymer Concrete Mix Content (kg/m^3)
OPC	370	00
Flyash	00	303.75
GGBFS	00	101.25
NaOH	00	40.5
Na_2SiO_3	00	101.25
Fine Aggregate	683	683
Coarse Aggregate	1289	1269
Water	148	40.5
Superplasticiser	3.7	4.05
Total	2493.7	2543.7

Table 7 Embodied energy calculation of GPC and OPC

Constituents	Embodied Energy (MJ/kg)	OPC Concrete		Geopolymer Concrete	
		Mix Content (kg/m^3)	Embodied Energy Content (MJ/kg)	Mix Content (kg/m^3)	Embodied Energy Content (MJ/kg)
OPC	4.6	370	1702	-	-
Flyash	0.0	-	-	303.75	00
GGBFS	0.2	-	-	101.25	31.38
NaOH	20.5	-	-	40.5	830.25
Na_2SiO_3	5.37	-	-	101.25	543.71
Fine Aggregate	0.02	683	13.66	683	13.66
Coarse Aggregate	0.22	1289	283.58	1269	279.18
Water	0.0	148	00	40.5	00
Superplasticiser	12.6	3.7	46.62	4.05	51.03
	Total	2493.7	2045.86 MJ/m^3	2543.7	1749.21 MJ/m^3

Table 8 Cost analysis of the GPC and OPC concrete

Constituents	Cost rate (Rs./kg)	OPC Concrete		Geopolymer Concrete	
		Mix Content (kg/m^3)	Cost of the Constituent ($Rs./m^3$)	Mix Content (kg/m^3)	Cost of the Constituent ($Rs./m^3$)
OPC	7.6	370	2812	-	-
Flyash	0.7	-	-	303.75	212.62
GGBFS	2.5	-	-	101.25	253.13
NaOH	10.05	-	-	40.5	407.03
Na_2SiO_3	10	-	-	101.25	1012.5
Fine Aggregate	0.25	683	170.75	683	170.75
Coarse Aggregate	0.525	1289	676.72	1269	666.23
Water	0.0	148	00	40.5	00
Superplasticiser	26.67	3.7	98.68	4.05	108.01
	Total	2493.7	Rs. 3758.15/m^3	2543.7	Rs. 2230.27/m^3

Breast Cancer Research and Treatment
https://doi.org/10.1007/s10549-020-06083-6

EPIDEMIOLOGY

Global, regional, national burden of breast cancer in 185 countries: evidence from GLOBOCAN 2018

Rajesh Sharma[1]

Received: 6 February 2020 / Accepted: 29 December 2020
© Springer Science+Business Media, LLC, part of Springer Nature 2021

Abstract

Purpose This study aims to examine the burden of breast cancer in 185 countries in 2018.

Methods The estimates of incidence, mortality, and prevalence of breast cancer were drawn from GLOBOCAN 2018. The overall burden of breast cancer was gauged using breast cancer burden index (BRCBI)—a novel index comprising age-standardized incidence rate (ASIR), age-standardized mortality rate (ASMR), mortality-to-incidence ratio (MIR), prevalence-to-incidence ratio (PIR), and prevalence-to-mortality ratio (PMR). The socioeconomic status of countries was measured using human development index (HDI)

Results Globally, breast cancer was responsible for an estimated 626,679 deaths at age-standardized rate of 13/100,000; there were 2.1 million cases diagnosed in 2018 at age-standardized rate of 46.3/100,000. The ASIR varied 22-fold from 5/100,000 (Bhutan) to 113.2/100,000 (Belgium). The ASMR varied 13-fold from 2.7/100,000 (Bhutan) to 36.9/100,000 (Fiji). The HDI exhibited a positive gradient with ASIR ($r=0.73$), PIR ($r=0.98$), and PMR ($r=0.85$); with MIR, however, it exhibited a negative association ($r=-0.83$). The BRCBI spanned from 0.70 in Somalia to 78.92 in South Korea and exhibited a positive association with HDI ($r=0.76$). An additional 46,823 female lives in 2018 and a cumulative total of 333,304 lives could have been saved over 2013–2018, had countries performed as per their HDI.

Conclusions The substantial burden of breast cancer in developing and low-resource economies calls for a holistic approach to cancer management and control that includes oncologic infrastructure to provide cost-effective screening, diagnostic, therapeutic, and palliative services, greater breast cancer awareness, and mitigation of risk factors.

Keywords Breast cancer · Incidence · Mortality · Mortality-to-incidence ratio · Prevalence-to-mortality ratio · Breast cancer burden index · GLOBOCAN

Introduction

Breast cancer is the leading malignancy in females worldwide, and its burden has grown in the last three decades, with higher incidence and survival rates in developed countries than the developing ones [1–3]. The improved treatment modalities and early detection in developed countries have improved the mortality and survival rates; in developing countries, however, survival rates are lower due to late-disease presentation, lack of oncologic infrastructure, and lack of cost-effective treatment regimens [2]. Breast cancer is linked with a multitude of modifiable risk factors (e.g., alcohol, tobacco consumption, and obesity) that relate to lifestyle [4, 5] and non-modifiable risk factors such as inherited gene mutation (e.g., BRCA 1/2), age, and familial risks [6–8].

For informed policy formulation and decision-making against breast cancer in global, regional, and national context, it is pertinent to understand the epidemiology of breast cancer burden in a cross-country context. This study investigates breast cancer's burden in 185 countries drawing upon estimates from GLOBOCAN 2018 [9, 10]. We studied the breast cancer burden in three dimensions. First, we examined the all-age, age-group-wise, and age-standardized incidence, mortality, and 5-year prevalence and made a comparative analysis between countries as per their socioeconomic development measured by human development index (HDI) [11]. Second, we constructed a

✉ Rajesh Sharma
rajesh.sharma@dtu.ac.in

[1] University School of Management and Entrepreneurship, Delhi Technological University, Delhi, India

Published online: 30 January 2021

novel index of breast cancer burden, namely breast cancer burden index (BRCBI), which is a composite of five epidemiological metrics: age-standardized incidence rate (ASIR), age-standardized mortality rate (ASMR), mortality-to-incidence ratio (MIR), prevalence-to-incidence ratio (PIR), and prevalence-to-mortality ratio (PMR). In the absence of actual survival data from low-resource economies, MIR has previously been demonstrated as a useful proxy of 5-year survival rate in a cross-country context [3, 12–14]. The new epidemiological constructs PIR and PMR, coupled with MIR, can gauge health system quality and oncologic care in different countries. Third, we identified few exemplar countries in each HDI groupings, which performed better than expected based on their HDI alone through observed-to-expected ratio (OER); based on OER, we quantified number of lives that could have been saved worldwide in 2018 and cumulatively in 2013–18.

Materials and methods

Estimates of breast cancer

We procured estimates of breast cancer burden in females for 185 countries from GLOBOCAN 2018 [9, 10, 15]. The estimates were available for three metrics: incidence, mortality, and prevalence (1-year, 3-year, and 5-year). GLOBOCAN produced age-standardized rates using World Population Reference standard. All-age and age-specific incidence and death counts are reported along with 95% uncertainty intervals (UIs) and are displayed inside square brackets; these UIs reflect uncertainties associated with cancer registry coverage and death registration, data quality, and timeliness of data reporting [9, 10, 15].

BRCBI and its components

BRCBI is an index used to compare breast cancer burden across countries; it comprises ASIR, ASMR, MIR, PIR, and PMR. We constructed an index for each of these metrics with 0 being assigned to worst-performing country and 100 being assigned to best-performing country by following formula.

$$ASIRI_i = \frac{ASIR_{99} - ASIR_i}{ASIR_{99} - ASIR_1} * 100 \quad (1)$$

In the above formula, $ASIRI_i$ denotes value of $ASIR$ index for ith country; $ASIR_{99}$ and $ASIR_1$ are 99th percentile and first percentile values of $ASIR$; $ASIR_i$ is value of $ASIR$ of ith country. For ASIR, ASMR, and MIR, high values implied worst performance and hence resulted in low value of the index; in the case of PIR and PMR, high values implied better performance; therefore, the index construction for these two indices was modified as per the following formula.

$$PMRI_i = \frac{PMR_i - PMR_1}{PMR_{99} - PMR_1} * 100 \quad (2)$$

We also assigned threshold values for countries at lowest and highest levels: countries with values lower than first percentile were assigned a minimum value of 0.1, and countries with values higher than 99th percentile were assigned a threshold value of 100[1] The BRCBI was constructed by taking geometric mean[2] of individual indices by the following formula.

$$BRCBI_i = \sqrt[5]{ASIRI_i * ASMRI_i * MIRI_i * PIRI_i * PMRI_i} \quad (3)$$

The choice of these five epidemiological constructs was governed by availability of metrics and breast cancer burden characterized by the metrics. The MIR (high MIR means low value on MIR index), for instance, has been shown to reflect 5-year survival rates in the previous literature [3, 12–14]. Similarly, higher PIR (i.e., high PIR index) in a country implies that a patient diagnosed with breast cancer lives greater number of years so that 5-year prevalence is high in relation to incidence. The PIR of breast cancer in a country would be lower than diseases such as diabetes, but the inter-country differences in PIR in diseases such as breast cancer reflect the survival rates and quality of oncologic care. Lastly, high age-standardized rates (e.g., high ASIR and ASMR and low value on respective indices) imply that countries need to improve oncologic care involving early detection, prevention, and timely, cost-effective therapeutics.

Human Development Index

Countries' comparative performance and progress against breast cancer were gauged against a country's development status measured by its HDI [11, 16]. HDI is a summary measure of three indicators: natural logarithm of gross national income per capita, education (composite construct of mean years of schooling and expected years of schooling), and life span (life expectancy at birth). A country's value was rated on a 0 (worst) to 1 (best) scale for each of these three indicators; the geometric mean of three indicators provided HDI's final value.

[1] Choosing minimum values as 1st percentile also helped in not assigning 0 value to BRCBI.

[2] An alternate index using arithmetic mean was generated; it has a pairwise correlation of $r = 0.9230$ with BRCBI (Supplementary Table S3).

Bivariate association between breast cancer metrics and HDI

The association between various breast cancer metrics and HDI was examined using bivariate regression as per the following equation.

$$y_i = \alpha + \beta x_i + \varepsilon_i \quad (4)$$

In above equation, y_i denotes breast cancer metrics, x_i denotes HDI for ith country. The expected value of breast cancer metrics is generated as follows.

$$\widehat{y}_i = \widehat{\alpha} + \widehat{\beta} x_i \quad (5)$$

The OER was calculated as $OER = \frac{y_i}{\widehat{y}_i}$. For MIR, OER lesser than one reflected better than the expected performance, whereas for PMR, an OER greater than one denoted better performance than was expected based on HDI alone.

We also tested for non-linear effects of HDI on breast cancer metrics by including a quadratic term in (5) as per the following regression.

$$y_i = \alpha + \beta x_i + \gamma x_i^2 + \varepsilon_i \quad (6)$$

The quadratic term was added if quadratic term and linear term were found to be statistically significant as per Eq. 6. The fitted model, fitted values ($\widehat{y}_i$) , and OER were thence modified accordingly.

Results

Incidence, mortality, and prevalence

Globally, breast cancer was responsible for 626,679 deaths [95% UI, 606,077–647,981] at an age-adjusted rate of 13/100,000; there were an estimated 2.1 million cases [2.0–2.2 million] in 2018 at an age-standardized rate of 46.3/100,000. East Asia was the leading region in terms of incidence with 476,509 [474,656–478,370] cases; in terms of death counts, however, South-central Asia was ranked first with 123,060 [119,256–126,986] breast cancer deaths in 2018 (Table 1). The ASIR was highest in Australia/New Zealand at 94.2/100,000, followed by Western Europe (92.6/100,000), and it was the lowest in South-central Asia (25.9/100,000). The 5-year prevalence was highest in East Asia, with 1.5 million females living with breast cancer; however, the 5-year prevalence rate was highest in developed regions led by Northern Europe (653.9/100,000) and lowest in middle Africa (30.1/100,000).

China was the leading country with 367,900 [346,754–390,335] cases and 97,972 [93,309–102,868] deaths (Supplementary Table S1). India was ranked second in terms of death counts (87,090 [84,651–89,599]) and was ranked third in terms of incidence (162,468 [158,245–166,804]) after China and United States (234,087 [232,580–235,604]). The ASIR varied more than 22-fold between countries, spanning from 5/100,000 in Bhutan to 113.2/100,000 in Belgium; the ASMR varied 13-fold between countries, ranging from 2.7/100,000 (Bhutan) to 36.9/100,000 (Fiji) (Fig. 1a, b).

Global MIR stood at 0.30, varying five-fold worldwide from 0.12 in South Korea to 0.68 in Central African Republic (Fig. 1c; Supplementary Table S1) and exhibited a negative association with HDI ($r = -0.8260$; Supplementary Table S2). Globally, PIR stood at 3.29, varying threefold between countries spanning from 1.29 in Niger to 4.29 in Norway (Supplementary Table S1). The PMR exhibited a positive association with HDI ($r = 0.8543$; Supplementary Table S2); it was comparatively higher in high/very high HDI countries led by South Korea (28.53), followed by Norway (25.72) and was lower in low/medium HDI countries (e.g., Central African Republic 1.90 and Somalia 1.93).

Age-group-wise burden

Figure 2a–d illustrates that the age-wise distribution of breast cancer incidence and mortality varied substantially across HDI groupings. In low/medium HDI countries, the incidence and mortality of breast cancer peaked in the 45–54 age group, whereas developed countries faced a substantial portion of breast cancer burden in 55-plus age groups. In low HDI countries, 55% of cases were diagnosed before the age of 50 years, claiming 50% breast cancer deaths (Supplementary Fig S1); in very high HDI countries, however, the burden of breast cancer was lowest in the young age groups (~21% cases and ~10% of deaths in under-50 age groups).

Breast cancer burden index and components

The developed countries performed poorly in terms of ASIR index (or high ASIR), whereas populous countries such as China (ASIR index:71.26), India (81.8), and low/medium HDI countries (e.g., Bhutan 100, Mongolia 99.3, and Mozambique 95.9) scored high on this index (Fig. 3; Supplementary Table S3). In contrast, the ASMR index had mixed values as per the country's development status, with majority of least developed countries and few developed countries recording best performance (i.e., low values) on the ASMR index (e.g., Gambia 100, South Korea 92.23). Notably, few developed countries scored intermediate values on this index (e.g., Luxembourg 51.3 and United Kingdom 59.6).

MIR index had a clear positive association with HDI, with a majority of developed countries recording high values on this index (e.g., Australia 100, Finland 99.9) and low/medium

Table 1 Region-wise Burden of Breast Cancer in 2018

Region	Incidence	ASIR	Deaths	ASMR	Prevalence	Prevalence rate	MIR	PIR	PMR
Australia and New Zealand	22,062 [21,721–22,408]	94.2	3,631 [3,491–3,776]	12.6	93,336	628.7	0.16	4.23	25.71
Caribbean	14,097 [13,104–15,165]	50.2	5,496 [5,101–5,922]	18.1	43,666	195.7	0.39	3.10	7.95
Central America	35,349 [34,194–36,544]	38.3	9,341 [9,075–9,615]	10.1	105,536	116.7	0.26	2.99	11.30
Central and Eastern Europe	149,024 [147,521–150,542]	54.5	49,951 [49,095–50,822]	15.5	537,230	347.6	0.34	3.60	10.76
Eastern Africa	40,310 [34,161–47,565]	29.9	20,165 [16,826–24,166]	15.4	74,870	34.3	0.50	1.86	3.71
Eastern Asia	476,509 [474,656–478,370]	39.2	119,678 [118,818–120,544]	8.6	1,472,640	182.4	0.25	3.09	12.31
Melanesia	2,116 [1,890–2,370]	49.7	1,046 [967–1,131]	25.5	4,881	94.4	0.49	2.31	4.67
Micronesia	121 [105–140]	42.5	47 [35–63]	16.3	170	64.4	0.39	1.40	3.62
Middle Africa	14,486 [11,784–17,808]	27.9	7,864 [6,431–9,616]	15.8	25,429	30.1	0.54	1.76	3.23
North America	262,347 [260,585–264,121]	84.8	46,963 [46,475–47,457]	12.6	1,102,533	600.3	0.18	4.20	23.48
Northern Africa	53,917[50,539–57,521]	48.9	20,058 [18,731–21,480]	18.4	142,739	120.6	0.37	2.65	7.12
Northern Europe	84,272[83,391–85,163]	90.1	18,063 [17,659–18,477]	14.1	347,043	653.9	0.21	4.12	19.21
Polynesia	252[214–298]	70.5	78[44–139]	21.6	630	185.3	0.31	2.50	8.08
South America	150,288 [145,986–154,716]	56.8	37,721 [36,962–38,496]	13.4	475,700	219.2	0.25	3.17	12.61
South-Central Asia	241,077 [233,926–248,447]	25.9	123,060 [119,256–126,986]	13.6	597,176	62.6	0.51	2.48	4.85
South-Eastern Asia	137,514 [132,555–142,659]	38.1	50,935 [48,966–52,983]	14.1	387,922	118.2	0.37	2.82	7.62
Southern Africa	14,820 [13,944–15,751]	46.2	5,002 [4,832–5,178]	15.6	39,393	117.1	0.34	2.66	7.88
Southern Europe	119,577 [118,199–120,972]	80.3	28,064 [27,387–28,758]	13.3	467,102	596.9	0.23	3.91	16.64
Western Africa	45,157[40,355–50,531]	37.3	20,983 [18,507–23,791]	17.8	87,584	46.2	0.46	1.94	4.17
Western Asia	55,914[54,574–57,287]	45.3	16,904 [15,791–18,095]	13.6	166,007	128.4	0.30	2.97	9.82
Western Europe	169,640[168,093–171,201]	92.6	41,629 [40,888–42,383]	15.5	703,512	715	0.25	4.15	16.90

Prevalence Rate: 5-year prevalence rate (Number of breast cancer patients per 100 000). The MIR was calculated as the ratio of all-age death counts and all-age cases of breast cancer. The PIR was calculated as the ratio of all-age 5-year prevalence and all-age incidence count. The PMR was calculated as the ratio of 5-year prevalence and all-age death counts. The estimates of breast cancer burden were drawn from GLOBOCAN 2018. The figures inside square brackets reflected 95% uncertainty intervals

Incidence: All-age new cases; Deaths: All-age deaths;

ASIR Age-standardized incidence rate (cases per 100 000), *ASMR* Age-standardized mortality rate (deaths per 100,000), *MIR* Mortality-to-incidence ratio, *PIR* Prevalence-to-incidence ratio, *PMR* Prevalence-to-mortality ratio

HDI countries recorded low values on this index (e.g., Somalia and Niger 0.1, Equatorial Guinea 3.8). PIR and PMR indices followed similar patterns as that of MIR, with developed countries recording high values and low/medium HDI countries lagging with low values. Those developed countries which performed relatively high on BRCBI also generally performed high on individual indices except for ASIR index (Fig. 3). The BRCBI varied from 0.70 in Somalia to 78.92 in South Korea and exhibited a positive correlation ($r = 0.76$) with HDI (Supplementary Table S2-S3).

Bivariate regression

The association between breast cancer burden and HDI was examined using bivariate regression with HDI as explanatory variable (Fig. 4a–f; Supplementary Table S4). The ASIR was positively and significantly associated with HDI ($R^2 = 0.5277$) with the inclusion of quadratic term significantly improving the model fit ($R^2 = 0.6448$). There was no statistically significant relationship between ASMR and HDI, neither linear nor in quadratic form (Supplementary Table S4). The MIR had an inverse relationship with HDI ($R^2 = 0.6822$), whereas PIR was positively linked with HDI ($R^2 = 0.9623$). In case of PMR, there was a statistically significant positive association with HDI, and inclusion of quadratic term significantly improved the model fit (from $R^2 = 0.7298$ *to* $R^2 = 0.8235$). The HDI had a positive and statistically significant relationship with BRCBI and could explain 57% of variation in BRCBI, and the inclusion of quadratic term marginally improved the model fit ($R^2 = 0.6029$). The relationship became slightly inverted U in shape, implying that after reaching a certain HDI level, HDI's influence on BRCBI tapers off (Fig. 4f).

A comparative analysis of OERs as per HDI

The country-wise OERs were produced as per linear regression in MIR and quadratic regression in the case of PMR (Supplementary Table S5). In terms of MIR, Syria in low HDI (OER 0.81); Guatemala in medium HDI (OER 0.65); Brazil in high HDI (OER 0.63); South Korea in very high HDI (OER 0.47) were the best performers. Notably, a heavily burdened country such as India performed relatively poor in terms of its HDI (OER 1.27); it could have saved an estimated 18,915 lives in 2018 had it performed as per its HDI.[3] In terms of PMR, Syria in low HDI (OER 1.44); Guatemala in medium HDI (OER 1.66); Libya in high HDI (OER 1.56); South Korea in very high HDI (OER 1.62) were the best performers. Notably, due to its better performance as per HDI, Brazil (OER 1.49) could save 86,593 lives over five years (2013–2018); India, in contrast, could have saved 75,420 lives had it performed as per its HDI. In very high HDI category, United States and South Korea saved 208,468 and 29,952 lives, respectively, due to their better than expected performance as per HDI.[4]

[3] Number of deaths that could be prevented in 2018 was calculated as per the following.

$$(\text{Extra Deaths})_{2018} = (\text{Incidence})_{2018}(\text{Observed MIR} - \text{Expected MIR})$$

[4] Number of lives saved as per PMR was calculated as per the following.

$$(\text{Extra Deaths})_{2013-18} = (\text{Observed Deaths})_{2018} (\text{Observed PMR} - \text{Expected PMR})$$

Discussion

Breast cancer was responsible for more than half a million deaths, and 2 million cases were estimated to be diagnosed worldwide in 2018. The ASIR exhibited positive association with HDI ($r = 0.7264$) and was the highest in developed countries (e.g., Belgium 113.2/100,000 and Luxembourg 109.2/100,000) and lowest in low/medium HDI countries (e.g., Bhutan 5/100,000 and Mozambique 14.5/100,000). Although incidence rates were the highest in developed regions, the developing countries in Asia and Africa shared a substantial portion of deaths and cases (~52% cases; ~61% deaths) in 2018. The 5-year survival rates proxied by MIR were the worst in sub-Saharan Africa (SSA) led by Central African Republic (0.68) and Equatorial Guinea (0.64). As with the previous studies [12], if we treat 1-MIR as the equivalent of 5-year survival rate, it varied from 32% in the Central African Republic to 88% in South Korea (MIR 0.12).

Consistent with previous studies [17, 18], breast cancer patients were comparatively younger in low and medium HDI countries; importantly, the proportion of younger patients diminishes with rising HDI. The developed countries had a substantial portion of breast cancer burden in 50-plus age groups (81% of cases and 89% of deaths), with low HDI countries had half the deaths and cases diagnosed before the age of 50 [19]. The age profile of breast cancer patients as per development status likely reflects higher life expectancy in developed countries, reproductive patterns, and etiologic differences [20]. In addition to younger age profile of breast cancer patients, the risk profile of breast cancer patients is also different in developing countries with a substantial portion of high-risk cancers such as triple-negative breast cancer, which has a poor prognosis [17, 21, 22].

The high incidence rates and high survival rates in developed countries (low MIR and high PIR) reflect an early detection, better cancer infrastructure, and cancer treatment in these countries [23]. The population-wide screening through breast mammograms has shown success in lowering mortality rates in developed countries [24, 25]. However, there are recent concerns over mammographic screening harms such as overdiagnosis/overtreatment, risk of secondary tumors due to ionizing radiation, and adverse psychological effects [26, 27]. Therefore, population-based mammographic screening cannot be emulated in low-resource economies due to large population sizes; younger breast cancer patients; financial, sociocultural, and logistical constraints; and competing population health problems [28, 29]. Moreover, population-based screening's success depends crucially on strength of health system to provide high-quality mammography, ensure high coverage and follow-up of screened patients, manage symptomatic patients, and provide timely access to diagnostic and therapeutic services

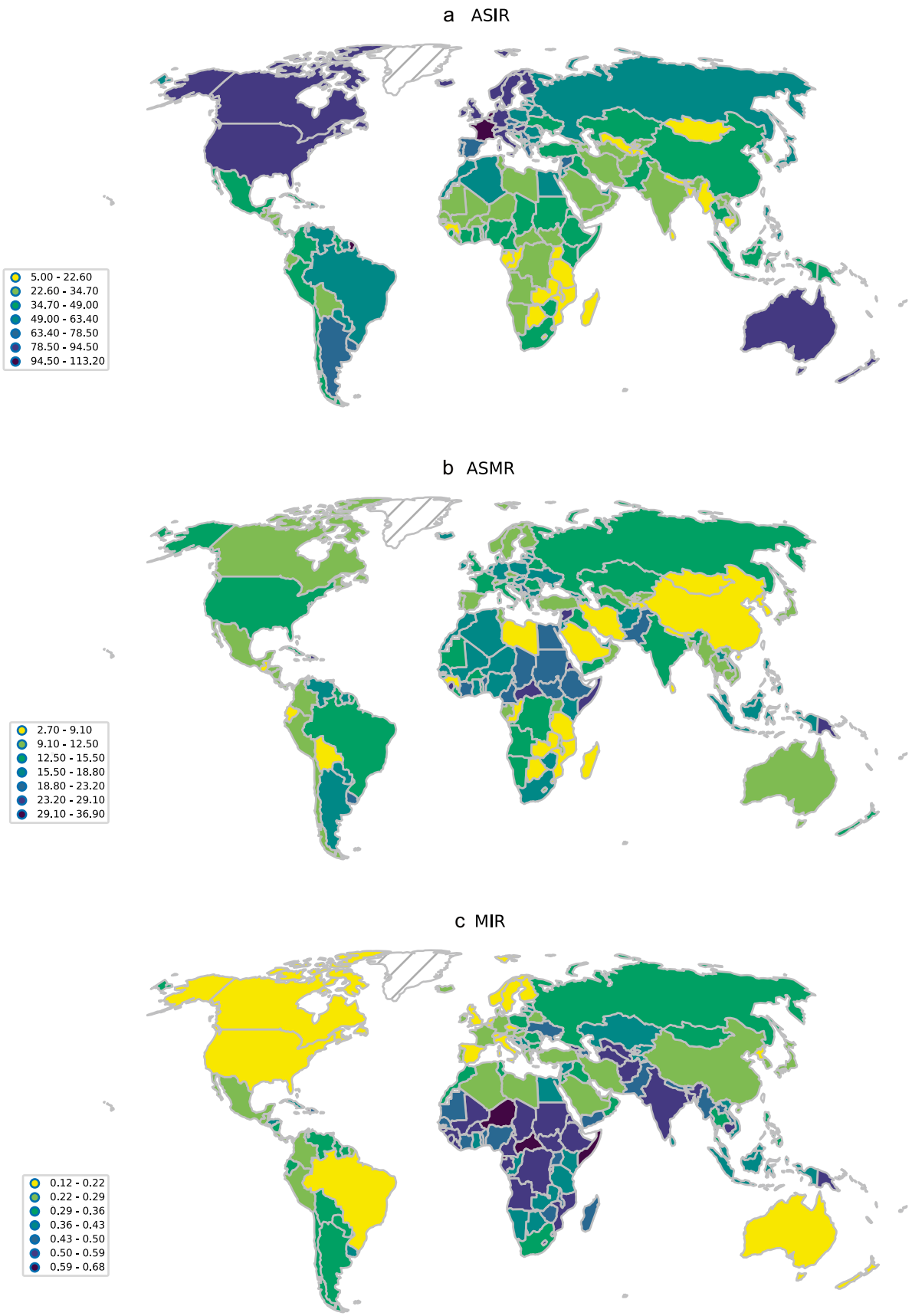
a ASIR
5.00 - 22.60
22.60 - 34.70
34.70 - 49.00
49.00 - 63.40
63.40 - 78.50
78.50 - 94.50
94.50 - 113.20
b ASMR
2.70 - 9.10
9.10 - 12.50
12.50 - 15.50
15.50 - 18.80
18.80 - 23.20
23.20 - 29.10
29.10 - 36.90
c MIR
0.12 - 0.22
0.22 - 0.29
0.29 - 0.36
0.36 - 0.43
0.43 - 0.50
0.50 - 0.59
0.59 - 0.68

◂**Fig. 1** Geographical distribution of Breast Cancer Statistics in 2018 **1a**. ASIR **1b**. ASMR **1c**. MIR. ASIR: Age-standardized incidence rate (cases per 100 000); ASMR: Age-standardized mortality rate (deaths per 100 000); MIR: Mortality-to-incidence ratio. The estimates of breast cancer burden were drawn from GLOBOCAN 2018

[30]. Low-cost screening solutions such as clinical breast examination may be considered, which have shown some success in clinical downstaging in low and medium-income countries [31–34].

The HDI exhibited a positive association with PIR ($r = 0.98$), PMR ($r = 0.85$), and negative association with MIR ($r = -0.83$). As these metrics reflect relative survival rates, this implies that higher HDI countries provide better cancer care and ensures greater survival. Previous studies have also found marked disparities in 5-year survival rates, ranging from 12% and 46% in Gambia and Uganda [35] to over 90% in developed countries such as Australia and United States [2]. Late-disease presentation is one of the primary reasons for low survival rates in developing and low-resource economies, which leads to poor prognoses and fatal outcomes [35, 36]. About 50–75% of African women presented with advanced disease [37]; in United States, however, only 11% of females were diagnosed with an advanced tumor (stage III/IV) [38]. In SSA, lack of awareness, sociocultural factors, fatalism (i.e., cancer is not curable and always results in death), and fear of mastectomy are few of the patient-specific factors resulting in delayed diagnosis [17, 39, 40].

Due to resource constraints and low awareness levels in low-resource countries, previous studies have shown that focus must be on downstaging and raising cancer awareness rather than screening asymptomatic women in low-resource countries [28, 30, 41]. Even in upper-middle-income countries such as Brazil, there is limited evidence of improved cancer mortality rates after the Ministry of Health's introduction of screening guidelines in 2004 [30]. The African Breast Cancer-Disparities in Outcomes (ABC-DO) study found that stage at diagnosis was the most potent prognostic factor and concluded that earlier stage at diagnosis and improved therapy can avert one-third of breast cancer deaths over 2020–2029 in SSA [42]. In few low-resource countries, such programs have shown some success. For instance, in a pilot study conducted in Malaysia, a program focused on training health workers and raising cancer awareness reduced advanced breast cancer detection (stage III/IV) from 60 to 35% between 1994 and 1998 [43]. Similarly, increased cancer awareness and breast examination program among trained, non-medical volunteers in rural Sudan led to greater detection of benign, early-stage, and potentially curable tumors [33].

Low HDI countries' performance was worst in terms of BRCBI (e.g., Somalia 0.70; Central African Republic 1.11) and high/very high HDI countries showed the best performance (South Korea 78.92; Brunei 74.36). Notably, apart from incidence and mortality rates, which are the most commonly considered variables of breast cancer burden, BRCBI also encompasses the burden measured by metrics such as MIR and PIR. Therefore, improvements in BRCBI can be attained through improvements in individual components (i.e., reduction of ASIR, ASMR, MIR or increases in PIR, PMR), which is linked with all facets of oncologic care from disease prevention, availability of facilities (e.g., hospitals, oncologist, drugs, imaging techniques), early detection, cost-effective diagnostic and therapeutic services, and coverage of treatment expenses.

The poor performance of low/medium HDI countries on most epidemiological metrics and BRCBI is reminiscent of other public health systems' weaknesses in these countries. First, the treatment expenses and travel and accommodation cost from pocket discourages patients from reaching healthcare providers even after noticing cancer symptoms [17, 40]. For instance, in the ABC-DO study, the treatment completion and survival rates were the highest in Namibia because of free treatment [42, 44]. Second, the treatment options are also limited in LMICs so that surgery is sometimes the only treatment option due to limited availability of chemotherapy, radiotherapy, and hormonal treatments such as Tamoxifen [17, 40, 45, 46]. Third, under-staging of breast cancer is also possible in low-income countries due to inadequate imaging techniques resulting in inappropriate treatment decisions, high costs, and side effects [42].

Limitations

This study suffers from three limitations. First, data coverage and quality from cancer registries, which have a marked effect on GLOBOCAN estimates, are far from complete in many low-resource economies. This implies that breast cancer estimates in these countries are expected to be biased, and the country-specific values of different metrics and BRCBI would be adjusted accordingly. Second, we used MIR, PIR, and PMR as the proxy measures of survival rates and quality of health care system. These are not the actual survival rates and should not be substituted with actual survival rates. In the absence of actual data, however, these three indicators can serve the dual purpose of proxy for relative survival rates and quality of health services in a country. Third, although GLOBOCAN estimates provided a snapshot of breast cancer burden in 2018, lack of consistent time series prevented us from examining the improvement/worsening of breast cancer burden in cross-country context.

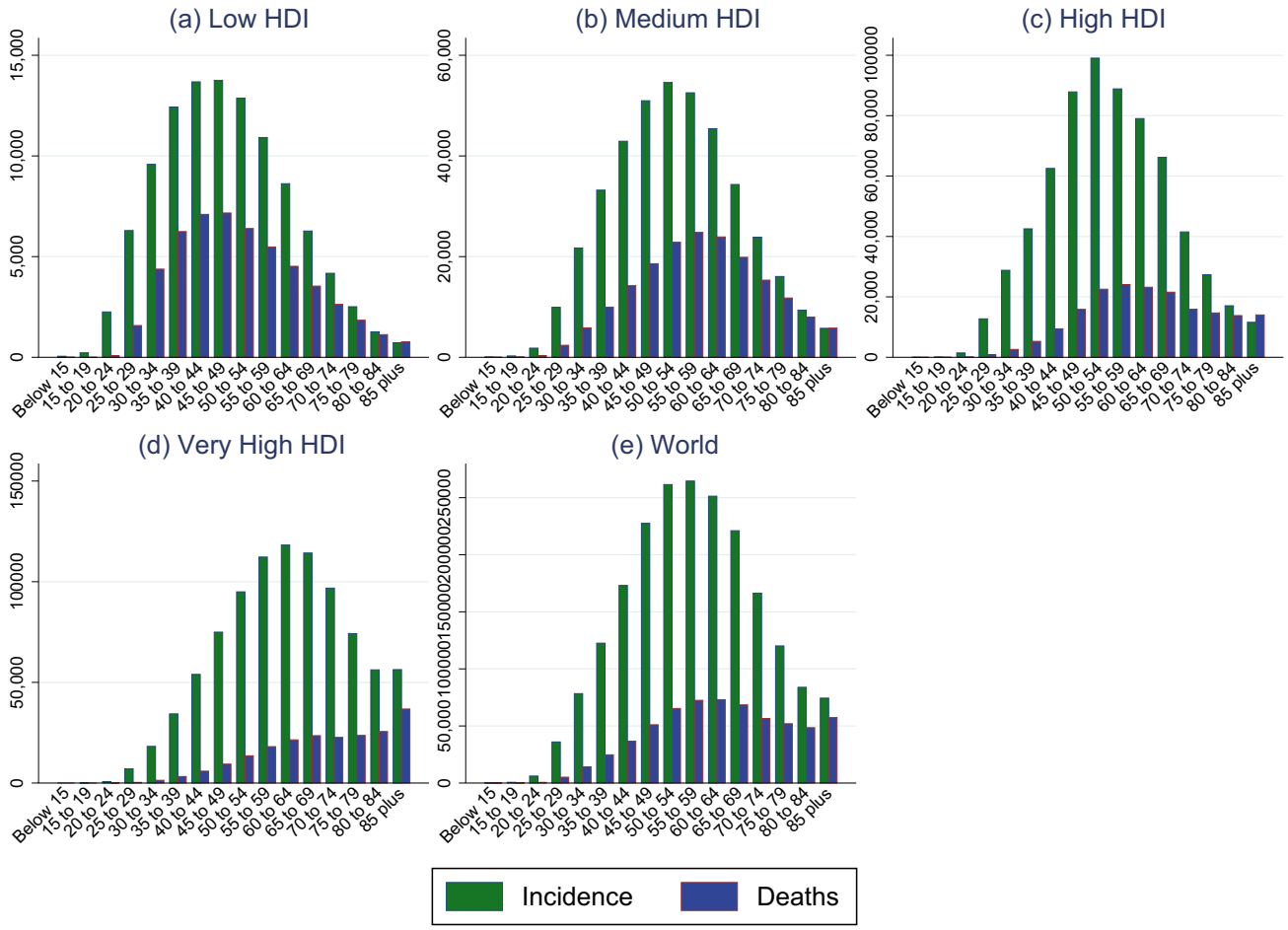

Fig. 2 Age-group-wise distribution of incidence and mortality of Breast Cancer **a**. Low HDI **b**. Medium HDI **c**. High HDI d. Very High HDI e. Global. Incidence: new cases; Deaths: deaths due to breast cancer; HDI: human development index. The estimates of breast cancer burden were drawn from GLOBOCAN 2018. The data of the human development index were taken from the United Nations Development Program. The countries were categorized as low (HDI < 0.550), medium (0.550–0.669), high (0.700–0.799), and very high (> 0.800)

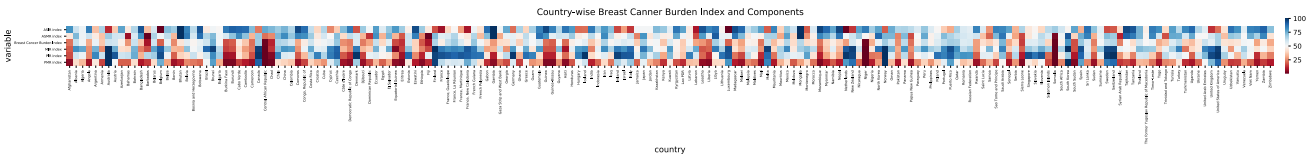

Fig. 3 Country-wise distribution of Breast Cancer Burden Index and Components. ASIR: Age-standardized incidence rate (cases per 100 000); ASMR: Age-standardized mortality rate (deaths per 100 000); MIR: Mortality-to-incidence ratio; HDI: Human development index; PIR: Prevalence-to-incidence ratio; PMR: Prevalence-to-incidence ratio; BRCBI: Breast cancer burden index. The MIR was calculated as the ratio of all-age death counts and all-age cases of breast cancer. The PIR was calculated as the ratio of all-age 5-year prevalence and all-age incidence count. The PMR was calculated as the ratio of 5-year prevalence and all-age death counts. The BRCBI was calculated as the geometric mean of ASIR index, ASMR index, MIR index, PIR index, and PMR index. The estimates of breast cancer burden were drawn from GLOBOCAN 2018

Conclusion

Low incidence and low survival rates in resource-poor countries and high incidence and high survival rates in developed countries mark the dichotomy of breast cancer burden as per HDI status of countries. The BRCBI, a novel index capturing the relative intensity of breast cancer burden on a 0 to 100 scale, is positively correlated with HDI.

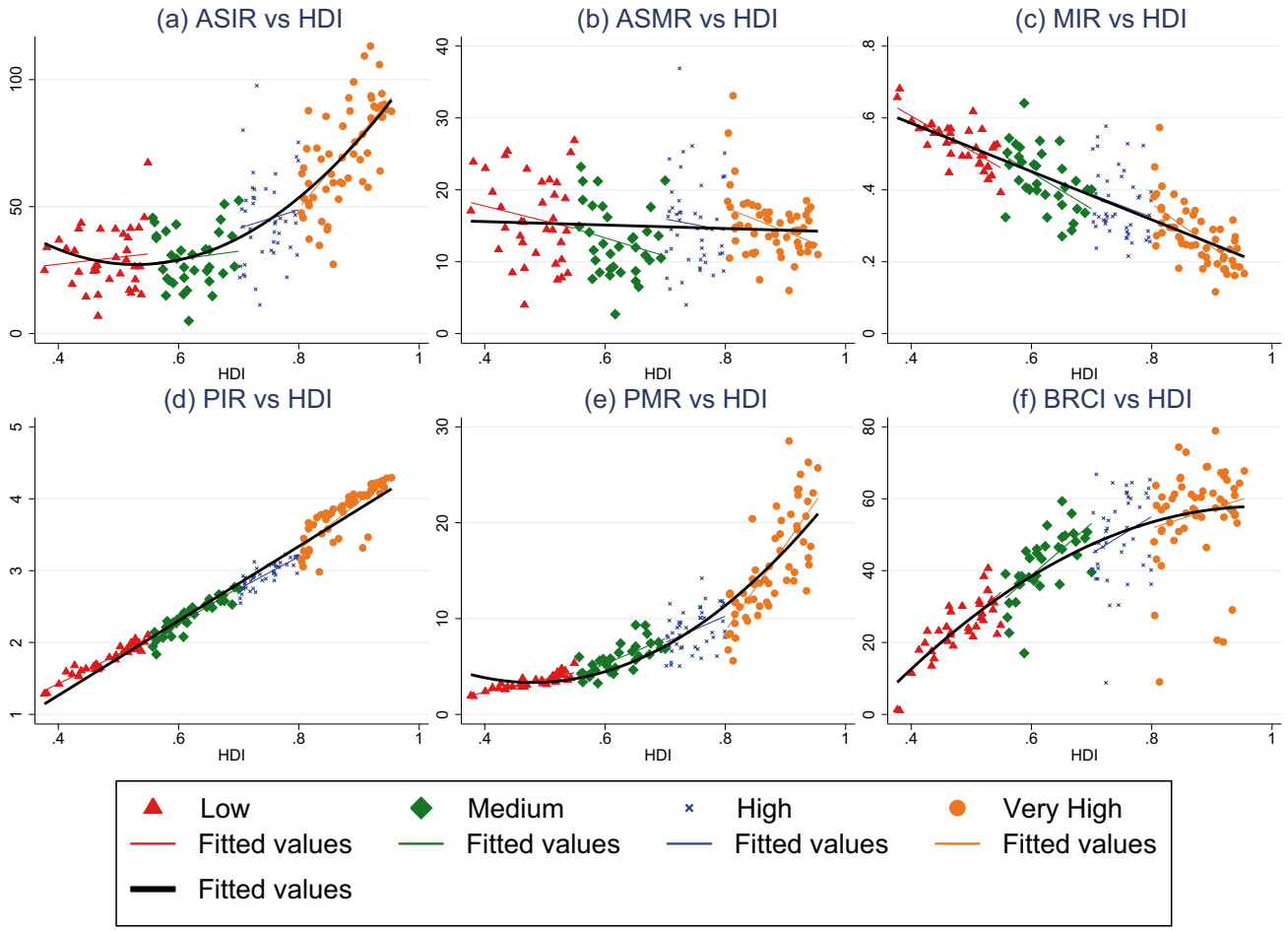

Fig. 4 Bivariate Association Between Childhood Cancer Burden and HDI **a**. ASIR vs. HDI **b**. ASMR vs. HDI **c**. MIR vs. HDI **d**. PIR vs. HDI **e**. PMR vs HDI **f**. BRCBI vs HDI. ASIR: Age-standardized incidence rate (cases per 100 000); ASMR: Age-standardized mortality rate (deaths per 100 000); MIR: Mortality-to-incidence ratio; PIR: Prevalence-to-incidence ratio; BRCBI: Breast cancer burden index; HDI: Human development index. The MIR was calculated as the ratio of all-age death counts and all-age cases of breast cancer. The PIR was calculated as the ratio of all-age 5-year prevalence and all-age incidence count. The PMR was calculated as the ratio of 5-year prevalence and all-age death counts. The BRCBI was calculated as the geometric mean of ASIR index, ASMR index, MIR index, PIR index, and PMR index. The estimates of breast cancer burden were procured from GLOBOCAN 2018. The data of human development index were taken from United Nations Development Program. The countries were categorized as low (HDI < 0.550), medium (0.550–0.669), high (0.700–0.799), and very high (> 0.800)

The burden characterized by different metrics in BRCBI shows that breast cancer poses different challenges across the development continuum, which is reflected in different incidence, mortality and survival rates, different age profiles of breast cancer patients, etiology, and prevalence of risk factors. The developed countries need to address the risk factors that result in disease onset (e.g., obesity, alcohol consumption), ensure elongated survival, and quality of life for breast cancer patients across the socioeconomic strata. In low- and medium-income countries, the breast cancer burden is expected to escalate further in future due to the westernization of lifestyles [47] (e.g., delayed marriages, low parity, low age at menarche, lack of physical activity, and poor diet), better cancer registration and cancer detection. The developing and low-resource economies, therefore, have to adopt a holistic approach to cancer management and control that requires oncologic infrastructure, cost-effective and equitable access to diagnostic, therapeutic, and palliative services, increase breast cancer awareness, and mitigate potentially modifiable risk factors that can aggravate incidence and death rates in these populations.

Supplementary Information The online version of this article (https://doi.org/10.1007/s10549-020-06083-6) contains supplementary material, which is available to authorized users.

Compliance with Ethical Standards

Conflicts of interest The authors declare that they have no conflict of interest.

Informed consent

Human and animal rights This article does not contain any studies with human participants or animals performed by any of the authors.

Informed consent The research was conducted using data available in the public domain and did not include any human participants or animals.

References

1. Global Burden of Disease Cancer Collaboration (2019) Global, Regional, and National Cancer Incidence, Mortality, Years of Life Lost, Years Lived With Disability, and Disability-Adjusted Life-Years for 29 Cancer Groups, 1990 to 2017: a systematic analysis for the global burden of disease study. JAMA Oncol 5(12):1749–1768. https://doi.org/10.1001/jamaoncol.2019.2996
2. Allemani C, Matsuda T, Di Carlo V et al (2018) Global surveillance of trends in cancer survival 2000–14 (CONCORD-3): analysis of individual records for 37 513 025 patients diagnosed with one of 18 cancers from 322 population-based registries in 71 countries. Lancet 391(10125):1023–1075
3. Sharma R (2019) Breast cancer incidence, mortality and mortality-to-incidence ratio (MIR) are associated with human development, 1990–2016: evidence from Global Burden of Disease Study 2016. Breast Cancer 26(4):428–445
4. Pérez-Solis MA, Maya-Nuñez G, Casas-González P et al (2016) Effects of the lifestyle habits in breast cancer transcriptional regulation. Cancer Cell Int 16(1):7
5. Yung RL, Ligibel JA (2016) Obesity and breast cancer: risk, outcomes, and future considerations. Clin Adv Hematol Oncol 14(10):790–797
6. Bradbury AR, Olopade OI (2007) Genetic susceptibility to breast cancer. Rev Endocr Metab Disord 8(3):255–267
7. Kim H, Choi DH (2013) Distribution of BRCA1 and BRCA2 mutations in Asian patients with breast cancer. J Breast Cancer 16(4):357–365
8. Skol AD, Sasaki MM, Onel K (2016) The genetics of breast cancer risk in the post-genome era: thoughts on study design to move past BRCA and towards clinical relevance. Breast Cancer Res 18(1):99
9. Bray F, Ferlay J, Soerjomataram I et al (2018) Global cancer statistics 2018: GLOBOCAN estimates of incidence and mortality worldwide for 36 cancers in 185 countries. CA Cancer J Clin 68(6):394–424
10. Ferlay J, Colombet M, Soerjomataram I et al (2019) Estimating the global cancer incidence and mortality in 2018: GLOBOCAN sources and methods. Int J Cancer 144(8):1941–1953
11. UNDP. Human Development Statistical Update 2018. (United nations Development Programme,2016) http://hdr.undp.org/sites/default/files/2018_human_development_statistical_update.pdf. Accessed 24 June2019
12. Vostakolaei F, Karim-Kos HE, Janssen-Heijnen ML et al (2010) The validity of the mortality to incidence ratio as a proxy for site-specific cancer survival. Eur J Public Health 21(5):573–577
13. Choi E, Lee S, Nhung BC et al (2017) Cancer mortality-to-incidence ratio as an indicator of cancer management outcomes in Organization for Economic Cooperation and Development countries. Epidemiol Health 39:e2017006
14. Sharma R (2019) The burden of prostate cancer is associated with human development index: evidence from 87 countries, 1990–2016. EPMA J 10(2):137–152
15. Ferlay J, Ervik M, Lam F et al Global Cancer Observatory. Lyon, France: International Agency for Research on Cancer. https://gco.iarc.fr/. Accessed Dec 2019 - Jan 2020
16. Human Development Database. http://hdr.undp.org/en/data#. Accessed Dec 2019
17. Brinton LA, Figueroa JD, Awuah B et al (2014) Breast cancer in Sub-Saharan Africa: opportunities for prevention. Breast Cancer Res Treat 144(3):467–478
18. Sharma R (2020) Breast cancer burden in Africa: evidence from GLOBOCAN 2018. J Public Health. https://doi.org/10.1093/pubmed/fdaa099
19. DeSantis CE, Ma J, Goding Sauer A et al (2017) Breast cancer statistics, racial disparity in mortality by state. CA Cancer J Clin 67(6):439–448
20. Gabriel CA, Domchek SM (2010) Breast cancer in young women. Breast Cancer Res 12(5):212
21. Corbex M, Bouzbid S, Boffetta P (2014) Features of breast cancer in developing countries, examples from North-Africa. Eur J Cancer 50(10):1808–1818
22. Youlden DR, Cramb SM, Yip CH, Baade PD (2014) Incidence and mortality of female breast cancer in the Asia-Pacific region. Cancer Boil Med 11(2):101
23. Youlden DR, Cramb SM, Dunn NA et al (2012) The descriptive epidemiology of female breast cancer: an international comparison of screening, incidence, survival and mortality. Cancer Epidemiol 36(3):237–248
24. Shapiro S (1997) Periodic screening for breast cancer: the HIP randomized controlled trial. JNCI Monogr 1997(22):27–30
25. Tabár L, Yen AM, Wu WY et al (2015) Insights from the breast cancer screening trials: how screening affects the natural history of breast cancer and implications for evaluating service screening programs. Breast J 21(1):13–20
26. Bleyer A, Welch HG (2012) Effect of three decades of screening mammography on breast-cancer incidence. N Engl J Med 367(21):1998–2005
27. Marmot MG, Altman DG, Cameron DA et al (2013) The benefits and harms of breast cancer screening: an independent review. Br J Cancer 108(11):2205–2240
28. Harford JB (2011) Breast-cancer early detection in low-income and middle-income countries: do what you can versus one size fits all. Lancet Oncol 12(3):306–312
29. Black E, Richmond R (2019) Improving early detection of breast cancer in sub-Saharan Africa: why mammography may not be the way forward. Glob Health 15(1):3
30. dos-Santos-Silva I, de Stavola BL, Junior NL, Nogueira MC, Aquino EM, Bustamante-Teixeira MT, Silva GA (2019) Ethnoracial and social trends in breast cancer staging at diagnosis in Brazil, 2001–14: a case only analysis. Lancet Glob Health 7(6):e784–e797
31. Mittra I, Mishra GA, Singh S et al (2010) A cluster randomized, controlled trial of breast and cervix cancer screening in Mumbai, India: methodology and interim results after three rounds of screening. Int J Cancer 126(4):976–984
32. Sankaranarayanan R, Ramadas K, Thara S et al (2011) Clinical breast examination: Preliminary results from a cluster randomized controlled trial in India. J Natl Cancer Inst 103(19):1476–1480
33. Abuidris DO, Elsheikh A, Ali M et al (2013) Breast-cancer screening with trained volunteers in a rural area of Sudan: a pilot study. Lancet Oncol 14(4):363–370
34. Song QK, Wang XL, Zhou XN et al (2015) Breast cancer challenges and screening in China: Lessons from current registry data and population screening studies. Oncologist 20(7):773–779
35. Sankaranarayanan R, Swaminathan R, Brenner H et al (2010) Cancer survival in Africa, Asia, and Central America: a population-based study. Lancet Oncol 11(2):165–173
36. Jedy-Agba E, McCormack V, Adebamowo C et al (2016) Stage at diagnosis of breast cancer in sub-Saharan Africa: a systematic review and meta-analysis. Lancet Glob Health 4(12):e923–e935

37. Abdulrahman GO, Rahman GA (2012) Epidemiology of breast cancer in Europe and Africa. J Cancer Epidemiol 2012:915610
38. Sariego J (2009) Patterns of breast cancer presentation in the United States: does geography matter? Am Surg 75(7):545–550
39. Akuoko CP, Armah E, Sarpong T, Quansah DY, Amankwaa I, Boateng D (2017) Barriers to early presentation and diagnosis of breast cancer among African women living in sub-Saharan Africa. PLoS ONE 12(2):e0171024
40. Tetteh DA, Faulkner SL (2016) Sociocultural factors and breast cancer in sub-Saharan Africa: implications for diagnosis and management. Women's Health 12(1):147–156
41. Yip CH (2019) Downstaging is more important than screening for asymptomatic breast cancer. Lancet Glob Health 7(6):e690–e691
42. McCormack V, McKenzie F, Foerster M, Zietsman A, Galukande M, Adisa C, Anele A, Parham G, Pinder LF, Cubasch H, Joffe M (2020) Breast cancer survival and survival gap apportionment in sub-Saharan Africa (ABC-DO): a prospective cohort study. Lancet Glob Health 8(9):e1203–e1212
43. Devi BC, Tang TS, Corbex M (2007) Reducing by half the percentage of late-stage presentation for breast and cervix cancer over 4 years: a pilot study of clinical downstaging in Sarawak. Malays Ann Oncol 18(7):1172–1176
44. Foerster M, Anderson BO, McKenzie F, Galukande M, Anele A, Adisa C, Zietsman A, Schuz J, dos Santos SI, McCormack V (2019) Inequities in breast cancer treatment in sub-Saharan Africa: findings from a prospective multi-country observational study. Breast Cancer Res 21(1):93
45. Clegg-Lamptey J, Dakubo J, Attobra YN (2009) Why do breast cancer patients report late or abscond during treatment in ghana? A pilot study. Ghana Med J 43(3):127–131
46. Sullivan R, Alatise OI, Anderson BO (2015) Global cancer surgery: delivering safe, affordable, and timely cancer surgery. Lancet Oncol 16(11):1193–1224
47. Porter P (2008) 'Westernising' women's risks? Breast cancer in lower income countries. N Engl J Med 358(3):213–216

Publisher's Note Springer Nature remains neutral with regard to jurisdictional claims in published maps and institutional affiliations.

The current issue and full text archive of this journal is available on Emerald Insight at:
https://www.emerald.com/insight/1934-8835.htm

Homesickness: a comparative study of defense and civilian employees and individual differences

Naval Garg
Delhi Technological University, Delhi, India

B.K. Punia
Guru Jambheshwar University of Science and Technology, Hisar, India

Vanshikha Kakkar
Delhi Technological University, Delhi, India, and

Sarika Kumari
Department of Telecommunications, New Delhi, India

Received 11 July 2020
Revised 10 October 2020
17 December 2020
20 December 2020
Accepted 27 December 2020

Abstract

Purpose – Most of the studies in the field of homesickness are confined to students; this study aims to explore the feeling of homesickness among working professionals. Also, it tends to examine individual differences in the experience of homesickness across employees of different gender, ages, experience, family type, etc. The study also aspires to compare homesickness among military and civil employees.

Design/methodology/approach – The study explores five dimensions of homesickness, namely, missing family, missing friend, rumination about home, feeling lonely and adjustment problems. The collected data is subjected to reliability, validity and confirmatory factor analysis. Further, *t*-test and analysis of variance are used to explore homesickness differences across soldiers and corporate employees.

Findings – The study reveals that homesickness is significantly higher for employees in the male, unmarried, nuclear family, above the age of 45 years, and below the graduation category. Also, defense people experience more homesickness than civilian employees.

Originality/value – This study is one of the pioneer studies that compare homesickness among defense and civilian employees. Also, variables such as type of family, the experience of employees and marital status have hardly been explored in the literature of homesickness.

Keywords Homesickness, Defense, Civilian, Individual differences

Paper type Research paper

Introduction

Homesickness is a historical phenomenon. It can be traced to the Biblical period, where its account was found in Psalm 137. In the 17th century, several narratives of homesickness emerged in which the most significant was the case of a Swiss physician. He encountered severe homesickness and immediately recovered when sent back home (Rosen, 1975). Homesickness is equally prevalent both in children and adult population. There has been ample research on school children to corroborate the fact (Stroebe *et al.*, 2016). Young adults, especially those stepping out of their homes for the first time searching for jobs, experience homesickness (Du *et al.*, 2017). Similarly, migrant workers, refugees and institutionalized

International Journal of Organizational Analysis
© Emerald Publishing Limited
1934-8835
DOI 10.1108/IJOA-07-2020-2305

people also demonstrate homesickness symptoms (Scharp *et al.*, 2016; Nauta *et al.*, 2020). Though homesickness is a common phenomenon across all age groups and cultures, adequate attention has not been paid by social science and organizational behavior researchers to study the phenomena in great depth (Nauta *et al.*, 2020). The majority of studies on homesickness are based on educational institutions (Stroebe *et al.*, 2015). In addition, research studies on the prevalence of homesickness in the organizational context are extremely rare.

Homesickness is reported to cause a detrimental effect on a person's physical, social, emotional, behavioral and cognitive well-being (English *et al.*, 2017). Ruminative and obsessive thoughts about home hinder the daily functioning of a person. At a physical level, some of the problems reported are fluctuation of the blood pressure, gastric or cardio problems, loss of sleep or too much of sleep, loss of appetite and fatigue (Stroebe *et al.*, 2016; Nauta *et al.*, 2020); at the social level, a person may develop a phobia for new people and new environment. They may restrain themselves from eye contact, conversations or sharing knowledge. At an emotional level, the person may encounter loneliness, sadness, mood swings, anger, lack of energy and motivation (Mashayekhi, 2016). At the cognitive level, they may have negative and inappropriate thoughts about the new environment or an old familiar environment that they have left behind. Constant idealizing of the home is also seen as a common symptom among migrants (Thurber and Walton, 2012). Finally, withdrawing from social life, inability to normalize life through routine, crying episodes and loss of concentration can be experienced at the behavioral level.

Despite the severe detrimental consequences of homesickness, it is often least talked about because it is perceived as embarrassment and humiliation, especially for both adults (Stroebe *et al.*, 2016). It also lacks specific clinical diagnosis and homesick people are often labeled as a patient of depression. Therefore, very little attention has been paid to understanding homesickness among soldiers (Niziurski and Berntsen, 2018). While soldiers in the armed forces are often studied for post-traumatic stress disorder, little is known about the extent to which soldiers experience homesickness during their service (Niziurski and Berntsen, 2018). Unlike civilian counterparts, defense personnel faces adverse physical and social working conditions such as extreme weather, challenging terrain, deployed in remote and isolated places, which intensify their homesick symptoms (Narang *et al.*, 2016) and make them psychologically vulnerable. Studies reveal there has also been a modest rise in suicidal tendencies among the soldiers in the defense population (Tochkov *et al.*, 2010). Some of the causes attributed to such psychological distress are lack of communication with family members, lack of intimate relationships, poor adjustment to military life and financial problems.

The civilians and defense personnel have strikingly different nature of the job, working conditions, organizational setup and hierarchies and job expectations. Contrary to civilian employees, armed forces are subject to very strict unity of command and direction, service rules with zero tolerance to deviance and establishment rules. Civilian employees enjoy liberal leave, accommodation and transfer policy. Except in emergency cases, human resource (HR) managers take care of employees' personal and familial needs while processing different employees' requests. Even those civilian workers, who stay away from their family, have greater chances of interacting and visiting their family more frequently than defense personnel. These structural, functional and operational differences are bound to influence the level of homesickness among defense and non-defense employees. These inherent variations make a strong case for a comparative study of the homesickness of these two sectors' employees. There has been limited study investigating the nature of differences in homesickness experienced by both the population. Hence, this paper tries to plug this

research gap through a comparative evaluation of homesickness among defense personnel and professional employees. The study explores the variations in the experience of five dimensions of homesickness (missing family, missing friends, having adjustment difficulties, ruminations about home and feeling lonely) among defense and civilian employees. Also, variation in overall homesickness is explored for two sets of populations.

Previous studies have explored homesickness variations based on demographic variables and personality traits (Archer *et al.*, 1998; Stroebe *et al.*, 2002; Scopelliti and Tibero, 2010; Thurber and Walton, 2012; Tochkov *et al.*, 2010). Stroebe *et al.* (2002) observe higher homesickness among women. Scopelliti and Tibero (2010) report similar levels of homesickness among male and female respondents. Thurber (1995), Eurelings-Bontekoe *et al.* (2000) and Kerns *et al.* (2008) find higher homesickness among younger respondents than older ones. Although few studies mentioned above explore homesickness based on individual differences, these studies are mainly confined to western settings. Also, most of these studies are conducted on students. Accordingly, the present study proposes a comprehensive exploration of variations in homesickness experience across a wide range of variables such as gender, marital status, age, education and type of family. It also investigates the difference in homesickness among defense and civilian employees across these demographic variables.

Literature review

Homesickness

Homesickness is defined as "a negative emotional state primarily due to separation from home and attachment persons, characterized by a longing for and preoccupation with home and often with difficulties adjusting to a new place" (Stroebe *et al.*, 2016). It is also defined as "the distress or impairment caused by an actual or anticipated separation from home" (Thurber and Walton, 2012, p. 1). Fisher *et al.* (1986) elaborated homesickness as psychological depression implicated by the bitter feeling of loss of home. Common to these and several other definitions of homesickness are negative feelings due to separation from home, relatives and friends. This separation from home and near ones have serious repercussions on the efficiency and effectiveness of the employees. Homesickness may lead to anxiety, social dysfunction and depression (Mashayekhi, 2016). English *et al.* (2017) reported a negative impact of homesickness on social interaction and psychosocial adjustment. Intense homesickness may aggravate preexisting mood and anxiety disorders. It may lead to serious mental and physical health problems (Thurber and Walton, 2012). Stroebe *et al.* (2015) elaborated that homesickness manifests at different levels, namely, emotional, cognitive, social and somatic. The emotional manifestation is in the form of yearning, loneliness, anxiety and depression. The cognitive indicator of homesickness is preoccupied thoughts of home and attachment figures, absent-mindedness and obsessionality. Withdrawal from the new environment, inability to adapt to new working conditions, Uneasiness with new colleagues, and introverted behavior are few social challenges associated with the feeling of homesickness. In addition, somatic effect includes loss of appetite, loss of weight, sleeplessness, headache, tiredness and gastric pain (Hach-Polay, 2012).

Previous scholars have discussed several theoretical perspectives to understand the complex concept of homesickness. Attachment theory explains that individuals develop an attachment with home, family members, friends and relatives through continuous interactions. The frequent interaction develops the attachment behavioral system (Stroebe *et al.*, 2015; Nauta *et al.*, 2020). Multi-causal model of homesickness assumes that both leaving the present environment and interaction with a new and unfamiliar environment

cause homesickness. The dual process model also states two stressors of homesickness. The first stressor is loss-orientation, which includes missing family members and significant others. In addition, the second factor inscribes adjustment and adaptability challenges in the new environment (Smith *et al.*, 2015; Stroebe *et al.*, 2016). The belonging theory (Baumeister and Leary, 1995) states that human beings have an inherent "need to belong." Following the belonging theory, Watt and Badger (2009) state that homesickness results from the dissolution of former social bonds and groups. The reduced control model of homesickness elaborates that the migrant does not have any control over the new environment, people and relationship. An individual lacks a mechanism to cope with new social, technological, cultural and psychological settings (Hach-Polay, 2012). Although researchers have different perspectives to understand homesickness, they are unanimous that not everyone faces a similar level of homesickness under the same conditions. Several scholars, including, Scopelliti and Tibero (2010), Thurber and Walton (2012), Tochkov *et al.* (2010), Stroebe *et al.* (2002), Stroebe *et al.* (2015) have discussed the socio-demographic-based variation in homesickness.

Homesickness and individual differences

Previous researchers have claimed that individual and dispositional factors play a pivotal role in the occurrence of homesickness (Stroebe *et al.*, 2015). Several socio-demographic variables such as gender, age, experience, education and marital status have been explored for probable variation in the feeling of homesickness. Contrary to the common belief that women experience higher homesickness, several previous studies have reported equal or lower homesickness among women than men. Researchers such as Archer *et al.* (1998) and Stroebe *et al.* (2002) reports higher homesickness among women, while other scholars, including Scopelliti and Tibero (2010), Thurber and Walton (2012), find no variation in homesickness among male and women. Interestingly, Tochkov *et al.* (2010) observe a higher level of homesickness among Indian male students than their female counterparts. Alike gender, the findings of the researchers regarding age-based variations in homesickness are not unanimous. Thurber (1995) and Kerns *et al.* (2008) find higher homesickness among younger students than older ones. Other authors, such as Fisher and Hood (1987), reports no age-based variation in homesickness.

Similarly, the experience of homesickness is reported to vary with distance from home, cultural background and academic credentials. Like age and gender, different researchers have observed distinct findings. Eurelings-Bontekoe *et al.* (2000) report that employees in their late 30s or with a work experience of six to eight years are more prone to experience homesickness than a newcomer. The authors also elaborate that people working in the same cultural settings are at less risk of homesickness than employees engaged in different cultural settings.

It is being observed that most of the studies in the domain of homesickness are restricted to students only. Only a few studies are conducted on employees engaged in professional work organizations (Eurelings-Bontekoe *et al.*, 2000; Scullion and Linehan, 2005; Hach-Polay, 2012). As previous studies are mainly confined to students, factors such as marital status, experience and education level are rarely considered in previous studies. Also, the majority of studies are conducted in western settings. The present explores homesickness among employees employed in Indian organizations with the help of a few interesting variables such as type of family (nuclear, joint and extended joint family) and academic

credentials. Based on the above theoretical foundations and studies, the following hypotheses are proposed:

H1. Homesickness varies with the age of the employees.

H2. Homesickness varies among male and female employees.

H3. Homesickness varies among married and unmarried employees.

H4. Homesickness varies with the educational level of the employees.

H5. Homesickness varies among employees belonging to nuclear, joint and extended joint families.

Homesickness among defense and civilian employees

Previous research studies in the domain of homesickness have focused on students and immigrants and has ignored another significantly vulnerable population, i.e. soldiers (Niziurski and Berntsen, 2018). Migrant workers and expatriates report serious socio-cultural and psychological adjustment issues due to homesickness (Scullion and Linehan, 2005; Hach-Polay, 2012). Maladjustment and malfunctioning are common symptoms among newly recruited migrant employees. Following the change and transition model, Hach-Polay (2012) suggested that the transition between "old roles and habits" to "new expectations and roles" is quite stressful for new employees. Homesickness seriously dampens the employees' efficiency by influencing their motivation, morale, team spirit, adaptability and aptitude (Deresky, 2010). The displacement from the point of origin leads to psychological damages and drains morale (Omi and Winnant, 2003). The impact of homesickness is proposed to higher on defense personnel because they are subjected to frequent and long assignments away from their homes. Also, soldiers face extreme geographical, climatic and stressful working conditions. The conditions are much more complex for Indian soldier, who consistently struggles with internal Maoism, cross border terrorism and violent borders. The shortage of staff, lack of modern HR practices, a strict authoritarian chain of command, frequent job rotation and lack of accommodation facility for family (nearby posting) makes things extremely challenging for Indian soldiers (Narang *et al.*, 2016).

While the empirical explorations on homesickness of defense personnel are rare, such a study has theoretical and practical relevance (Niziurski and Berntsen, 2018). The sense of homesickness influences the military people's performance (Niziurski and Berntsen, 2018; Bell and Bromnick, 1998). It invokes anxiety, stress, depression, a sense of loneliness and loss, uncertainty about family members' well-being, and other somatic symptoms (Niziurski and Berntsen, 2018; Archer *et al.*, 1998). These negative influences of homesickness breed emotional, psychological, cognitive and attentional problems for soldiers. Du *et al.* (2017) report that consistent and prolonged homesickness experience undermines the military trainees' performance and their safety and security on the battlefield. Other researchers, including, Ramsberger and Bell (2002), finds that one of the prominent reasons for soldiers leaving their job is homesickness. Flach *et al.* (2000) explain that homesickness among defense personnel is because of three basic reasons – situation at home, inability to adjust to military life and inability to cope-up with foreign military assignments. These reasons lead to attrition of 28% during military training. It has also been reported that a significant percentage of soldiers employed in short services generally do not opt for permanent commissioning owing to familial concerns. Researchers and army experts believe that the psychological health of soldiers bears immense importance for two obvious reasons. First, they render an important service of safety of people, critical installations and national

borders. Second, they carry a highly sophisticated weapon with them. Thus, the mental well-being of defense personnel is of utmost importance for several stakeholders of the country. Based on the above studies, the following hypotheses are proposed:

H6. Defense personnel experiences higher levels of homesickness.

Methodological framework

Objective and sample

The study's primary objective is to explore variation in homesickness experience across a range of demographic variables, namely, age, gender, education level, family type (nuclear, joint and extended joint) and marital status. It also tends to compare homesickness levels among defense and civil employees. Five dimensions of homesickness – "missing family, missing friends, having adjustment difficulties, ruminations about home and feeling lonely" are studied in this study. The present study is based on explorative-cum-descriptive research design. It describes the level of homesickness among defense and civilian employees. It also explores the difference in homesickness experience among two working populations, i.e. defense and civilian employees. India's estimated defense population is 4 million, and other working professionals are estimated at around 400 million. As the study requires inputs from defense personnel, convenient sampling was used to collect the data. It is also ensured that data comes from respondents of different genders, ages, experiences, etc. Cochran (1977) developed the following formula for sample size calculation. It was used to determine the appropriate sample size for the study:

$$N = z^2 p\, q/e^2$$

where z is the critical value at a given confidence level, p is the estimated proportion of an attribute present in the population, $q = p - 1$, and e is the margin of error. Here, the confidence level is 95% and the margin of error is 5% and the estimated population proportion is assumed as 0.5. The sample size derived from the formula mentioned above is 384.

Initially, emails were sent to 100 respondents, out of which 65 reverted. Thus, to achieve responses from 384 respondents, 600 emails were sent. In total, 200 emails were sent to each cluster of defense, public and private sector employees. Finally, 429 responses were received. In total, 26 questionnaires were discarded for being incomplete. Thus, the final sample comprises 403 employees engaged in Indian armed forces and other public and private companies. The demographic description of the sample is depicted in Table 1. There are 103 respondents from defense services, 173 from private sector companies and the remaining 127 from public sector enterprises. Employees of professional organizations belong to banking, insurance, business process outsourcing and oil and gas companies. The normality of data is ensured using the Kolmogorov-Smirnov test and the Shapiro-Wilk test. The significance values in both tests are above 0.05, which means tests are not significant. And hence, it could be concluded that data is normal.

Measure of homesickness

Homesickness is measured with the help of a 20-items Utrecht homesickness scale (UHS) developed and validated by Stroebe *et al.* (2002). The scale measures five dimensions of homesickness – missing family, missing friends, having adjustment difficulties, ruminations about home and feeling lonely – on a five-point rating scale ranging from "not at all" (1) to "very often" (5), where a higher score indicates a higher level of homesickness. It includes statements such as "missing people whom you can trust and can talk with",

Variable	Category	Frequency (overall)	Defense	Civilian
Gender	Male	260	70	190
	Female	143	33	110
Marital status	Married	214	59	155
	Unmarried	189	44	145
Age	Below 25 years	162	27	135
	26–35 years	115	31	84
	36–45 years	89	32	57
	Above 45 years	37	13	24
Education level	Below graduation/diploma	81	21	60
	Graduation	199	65	134
	Post-graduation	86	14	72
	Above PG	37	3	34
Family	Nuclear	77	33	44
	Joint (with parents)	188	41	147
	Extended joints (with siblings)	138	29	109

Source: Primary data

Table 1. Demographic description of sample

"missing your friends", "finding it difficult adjusting to a new situation", "feeling uncomfortable in a new situation", "feeling lost in a new situation", "having difficulties get using to new customs" and "having thoughts that an old situation was better than here and now". Several scholars, including van Vliet (2001), Zulkarnain *et al.* (2019), Thomas (2018), Stroebe *et al.* (2015), have relied on the scale. Duru and Balkis (2013) reported strong psychometric properties of the scale based on test-retest reliability, internal consistency reliability and concurrent validity.

Exploratory factor analysis

UHS was developed by Stroebe *et al.* (2002) to investigate homesickness among new students in The Netherlands and UK. Before adopting the scale for professionals, the 20 statements of the scales were subjected to stringent exploratory factor analysis (EFA), Confirmatory factor analysis (CFA), reliability and validity testing. Before EFA, Kaiser-Meyer-Olkin (KMO) and Bartlett's tests were conducted to access the sample's adequacy for factor analysis. Table 2 states that the value of KMO is greater than 0.70, and Bartlett's test of sphericity is also significant for $p < 0.05$. These values confirm that data is suitable for the application of factor analysis. Now, 20 statements of UHS were subjected to EFA using varimax rotation. Like the original UHS scale, five factors were extracted, which explains 79.401% of the total variance in

Kaiser-Meyer-Olkin measure of sampling adequacy	0.954
Bartlett's test of sphericity	
Approx. chi-square	7,298.264
df	190
Sig.	0.000

Source: Primary data

Table 2. KMO and Bartlett test

homesickness (Table 3). These five factors comprise four statements, each with factor loading greater than 0.70.

Confirmatory factor analysis

The five-dimensional model of homesickness is further evaluated through CFA using analysis of a moment structure 21. The model's fitness is analyzed with the help of chi-square, the goodness-of-fit index, comparative fit index, incremental fit index and relative fit index. The most commonly used standards to assess model fit are root mean square error of approximation (RMSEA) and root mean square residual (RMR) ≤ 0.08 (Hu and Bentler, 1999), goodness of fit (GFI) ≥ 0.90, comparative fit index (CFI) ≥ 0.90, incremental fit index (IFI) ≥ 0.90, normed fit index (NFI) ≥ 0.90 and relative fit index (RFI) ≥ 0.90 (Bentler, 1990) and χ^2/df 2>-<5). Values obtained in the present model are $\chi 2$/df = 2.914, RMSEA = 0.069, RMR = 0.066, GFI = 0.893, CFI = 0.958, IFI = 0.958, NFI = 0.937 and RFI = 0.926. GFI's value is slightly less than the threshold value of 0.90, but it is acceptable given that the χ^2/df is reported statistically significant. These results indicate that the model of the study is a good fit. An appropriate output figure has been inserted in Appendix.

Reliability and validity

Although the scale's psychometric properties were previously explored, most of the studies were based on students' samples. As the present study explores homesickness among employees, the scale's reliability and validity are again established. Cronbach's alpha (CA) and composite reliability (CR) estimates are used to measure internal consistency reliability. CA for missing family, a missing friend, feeling lonely, adjustment problem, ruminations about the home are 0.963, 0.868, 0.906, 0.916 and 0.865, respectively. CA for overall homesickness is 0.960. Hair *et al.* (1998) advocated that a value of 0.70 for CA and CR is good enough to confirm the scale's reliability. Also, CR for five dimensions of homesickness is 0.920, 0.846, 0.894, 0.883 and 0.861. Convergent validity refers to the extent to which a measure correlates positively with alternate measures of the same variable (Hair *et al.*, 2013). Convergent validity of the scale is adjudged using average variance explained (AVE) values. According to Fornell and Larcker (1981), AVE values greater than 0.70 are considered very good and values above 0.50 are good enough to ensure convergent reliability. AVE values for missing family, a missing friend, feeling lonely, adjustment problem, ruminations about the home are 0.744, 0.581, 0.682, 0.655 and 0.611, respectively. Here, all values are above a threshold value of 0.50, so it indicates good convergent validity. Discriminant validity refers to the extent to which a variable is genuinely distinct from other variables in terms of how much it correlates with different variables and how much indicators represent only a single variable (Hair *et al.*, 2013). According to the Fornell-Larcker testing system, discriminant validity can be assessed by comparing the variance captured by the construct (AVE) and the

Table 3.
Results of exploratory factor analysis

Factor	Eigen value	% of variance	Cumulative variance
Missing family	6.425	19.197	19.197
Feeling lonely	6.278	18.756	37–953
Missing friends	6.303	18.833	53.786
Adjustment problem	3.943	11.783	68.569
Rumination about home	3.625	10.832	79.401

Source: Primary data

shared variance with other constructs. Thus, the AVE levels for each construct should be greater than the squared correlation involving the constructs to confirm discriminant validity. Table 4 depicts the result of the Fornell-Larcker test, and it confirms the divergent validity of the scale.

Analysis of collected data

The data is investigated in two steps using statistical package for social sciences 21 and R-studio. First, demography-based variation in homesickness is studied using *t*-test and one-way analysis of variance. Second, the difference in homesickness among defense and civil employees is examined using a *t*-test. Homesickness of defense and non-defense employees is further compared using cross-tabulation tables. Table 1 represents the demographics distribution of the sample.

Results

Table 5 depicts that male employees experience a significantly higher level of homesickness than their female counterparts (mean for male = 3.749, mean for female = 3.308, $p < 0.05$). It is also reported that male's homesickness is significantly higher for all dimensions of homesickness. These results support the alternate *H2*. Previous researchers do not have a similar view, with some scholars reporting equal homesickness levels among men and

Variable	1	2	3	4	5
Missing family	*0.744*				
Feeling lonely	0.373	*0.682*			
Missing friends	0.441	0.520	*0.581*		
Adjustment problem	0.286	0.379	0.361	*0.655*	
Rumination about home	0.376	0.49	0.515	0.576	*0.611*

Source: Primary data, AVE values are in diagonal (Italic)

Table 4. Results of Fornell-Larcker test

Variable	Category	Mean	SD	*t*-value	Sig.
Missing family	Female	3.547	1.316	4.239	0.000*
	Male	4.063	1.080		
Missing friends	Female	3.351	1.176	4.453	0.000*
	Male	3.836	0.967		
Feeling lonely	Female	3.185	1.276	3.314	0.001*
	Male	3.586	1.095		
Adjustment problem	Female	3.174	1.143	3.564	0.000*
	Male	3.600	1.145		
Rumination about home	Female	3.281	1.194	3.352	0.001*
	Male	3.661	1.026		
Homesickness	Female	3.308	1.043	4.459	0.000*
	Male	3.749	0.896		

Note: * Sig at 0.05
Source: Primary data

Table 5. Variations in homesickness among male and female employees

women (Scopelliti and Tibero, 2010; Thurber *et al.*, 2007; Fisher and Hood, 1987). Other researchers, including Stroebe *et al.* (2002) and Archer *et al.* (1998), reported higher homesickness among female students.

Interestingly, Tochkov *et al.* (2010) investigated homesickness among male and female students studying in the US. The authors reported a higher level of homesickness among Indian men than women students. The present study supports the findings of greater homesickness among Indian men. The finding seems to support the common belief of women being more psychologically stronger than men.

Table 6 concludes that homesickness is significantly higher for married employees (mean = 3.725) than unmarried workers (mean = 3.475). The result supports the *H3* of the present study. The results are quite natural married men are more inclined to miss their families, especially spouses and children. It is also observed that three (missing friends, missing family and feeling lonely) out of five dimensions of homesickness varies significantly across married and unmarried employees.

Table 7 defines the nuclear family as a family, including spouse and children only. A joint family is considered as a family comprising of a spouse, children and parents. An extended joint family is considered a household that houses spouses, children, parents, siblings and families. The result states that homesickness varies significantly across these three types of family members. It lends support for acceptance of the fifth alternate hypothesis. Post-hoc analysis using the Scheffe test is also used for an in-depth understanding of variations in homesickness across three types of families. The results suggest significant variations across all three combinations (nuclear-joint, nuclear-extended joint and joint and extended joint). In simple words, it reflects that employees belonging to different types of families experience a significantly different level of homesickness.

Interestingly, homesickness is highest for members of the nuclear family (mean = 3.802), followed by an extended joint family (mean = 3.756) and then the joint family (mean = 3.387). The findings could be interpreted in the light of the strong desire for care and safety of spouse and children. The parents provide a conducive and flourishing environment for the appropriate socialization of the toddlers. Thus, an employee belonging to a joint family is less homesick than a nuclear family employee. The joint family offers a single-point

Table 6.
Variations in homesickness among unmarried and married employees

Variable	Category	Mean	SD	*t*-value	Sig.
Missing family	Unmarried	3.706	1.318	3.137	0.002*
	Married	4.076	1.003		
Missing friends	Unmarried	3.525	1.096	2.790	0.006*
	Married	3.821	1.021		
Feeling lonely	Unmarried	3.292	1.205	2.783	0.006*
	Married	3.616	1.123		
Adjustment problem	Unmarried	3.406	1.128	0.782	0.435
	Married	3.497	1.201		
Rumination about home	Unmarried	3.448	1.087	1.515	0.131
	Married	3.615	1.116		
Homesickness	Unmarried	3.475	0.980	2.586	0.010*
	Married	3.725	0.950		

Note: *Sig at 0.05
Source: Primary data

Variable	Category	Mean	SD	*F*-value	Sig.
Missing family	Nuclear	3.993	1.020	7.341	0.001*
	Joint	3.646	1.320		
	Extended joint	4.135	1.038		
Missing friends	Nuclear	3.811	1.018	7.921	0.000*
	Joint	3.442	1.162		
	Extended joint	3.884	0.903		
Feeling lonely	Nuclear	3.724	1.137	7.753	0.000*
	Joint	3.204	1.239		
	Extended joint	3.614	1.049		
Adjustment problem	Nuclear	3.756	1.069	5.257	0.006*
	Joint	3.271	1.216		
	Extended joint	3.519	1.100		
Rumination about home	Nuclear	3.727	1.020	3.767	0.024*
	Joint	3.371	1.145		
	Extended joint	3.626	1.065		
Homesickness	Nuclear	3.802	0.867	8.210	0.000*
	Joint	3.387	1.035		
	Extended joint	3.756	0.888		

Note: *Sig at 0.05
Source: Primary data

Table 7. Variations in homesickness based on family status

concentration to parents than an extended joint family, where parents are indulged with siblings and their children too.

Table 8 suggests that homesickness varies significantly with the age of the employees. This result supports the alternate *H1*. Homesickness increases with the age of the employees, with aged employees more vulnerable to homesickness (Table 8). Also, Scheffe test reports that employees above the age of 45 years experience a significantly different level of homesickness than employees of the other three age categories. The Scheffe test also suggests that employees of two age categories, i.e. 26–35 years and 36–45 years are equally homesick. Previous studies are not unanimous about age-based variations in homesickness. Some researchers reported no age-based differences (Fisher and Hood, 1987; Kerns *et al.*, 2008), while others pointed out a higher level of homesickness among young ones (Thurber, 1995; Thurber and Weisz, 1997). However, these studies are often being criticized for limited age-range comparisons (Poyrazli and Lopez, 2007). Most of the studies are limited to students only. The present study offers some interesting facts that older employees miss their family and friends to a greater extent. Younger people are keener to make new friends and venture out of new places. They readily use technology to connect with their family members. All these virtues may allow younger generations to cope-up with homesickness.

Table 9 observes that homesickness decreases progressively with the academic credentials of the respondents. The results state that employees with relatively lower educational qualifications are more likely to feel lonely and miss friends. The Scheffe test also suggests that employees with "below graduation" academic credentials experience a significantly different level of homesickness than workers with higher educational qualifications. It is also reported that the difference in homesickness among graduation and post-graduate employees is statistically insignificant. In India, migration for education purposes is quite high. As higher education opportunities are not available everywhere, students move to big cities to pursue their graduation and post-graduation degrees. These

Variable	Category	Mean	SD	*F*-value	Sig.
Missing family	Below 25 years	3.621	1.426	4.802	0.003*
	26–35 years	3.997	0.965		
	36–45 years	4.042	1.021		
	Above 45 years	4.256	0.871		
Missing friends	Below 25 years	3.455	1.175	4.169	0.006*
	26–35 years	3.730	0.916		
	36–45 years	3.817	1.073		
	Above 45 years	4.006	0.872		
Feeling lonely	Below 25 years	3.166	1.254	5.572	0.001*
	26–35 years	3.547	1.046		
	36–45 years	3.716	1.117		
	Above 45 years	3.682	1.135		
Adjustment problem	Below 25 years	3.334	1.171	2.238	0.083
	26–35 years	3.423	1.138		
	36–45 years	3.516	1.169		
	Above 45 years	3.864	1.122		
Rumination about home	Below 25 years	3.327	1.134	3.049	0.029*
	26–35 years	3.632	1.052		
	36–45 years	3.685	1.125		
	Above 45 years	3.689	0.956		
Homesickness	Below 25 years	3.381	1.051	4.975	0.002*
	26–35 years	3.666	0.845		
	36–45 years	3.755	0.971		
	Above 45 years	3.900	0.823		

Note: *Sig at 0.05
Source: Primary data

Table 8. Variations in homesickness based on age of the employees

students experience homesickness and learn different strategies to deal with it too. On joining the industry, such students experience less homesickness due to their prior experience of staying away from their families.

Table 10 reveals that defense personnel experience (mean = 3.980) significantly higher homesickness levels than civilians (mean = 3.460). It supports the sixth alternate hypothesis. The major contributors to high homesickness among armed forces are missing family (mean = 4.434) and rumination about home (mean = 3.900). It indicates that defense people remain mainly concerned for their family members. For civilians, major factors are missing family (3.690) and missing friends (mean = 3.517). The results are quite understandable in the light of strict leave rules (2–3 times in a year), limited usage and access to technology that hinders frequent contact with family, frequent transfers and excessive anxiety and job strain. These results could not be compared owing to the scarcity of comparative studies.

Table 11 compares the homesickness of two genders engaged in defense and civil jobs. It is being revealed that there is no significant variation in overall homesickness among female soldiers and the company's employees. However, male soldier's homesickness owing to missing family, missing friends and rumination about home is significantly higher than employees engaged in industries. It is interesting to note that male soldiers experience a higher level of homesickness than their counterparts working in the corporate world. Also, the mean value of homesickness is higher for male defense (mean = 3.99) and civilian personnel (mean = 3.60) than female employees engaged in armed forces (mean = 3.78) and professional organizations (mean = 3.28).

Variable	Category	Mean	SD	*F*-value	Sig.
Missing family	Below graduation	4.123	1.060	2.076	0.083
	Graduation	3.888	1.255		
	Post-graduation	3.761	1.129		
	Above PG	3.458	1.279		
Missing friends	Below graduation	3.895	1.023	2.969	0.019*
	Graduation	3.712	1.110		
	Post-graduation	3.412	0.985		
	Above PG	3.375	1.076		
Feeling lonely	Below graduation	3.839	1.127	3.943	0.004*
	Graduation	3.366	1.190		
	Post-graduation	3.345	1.092		
	Above PG	3.050	1.298		
Adjustment problem	Below graduation	3.700	1.147	2.320	0.056
	Graduation	3.467	1.159		
	Post-graduation	3.287	1.224		
	Above PG	3.058	1.007		
Rumination about home	Below graduation	3.660	1.120	2.013	0.092
	Graduation	3.572	1.075		
	Post-graduation	3.473	1.114		
	Above PG	3.025	1.218		
Homesickness	Below graduation	3.843	0.984	3.215	0.013*
	Graduation	3.601	0.995		
	Post-graduation	3.456	0.895		
	Above PG	3.193	0.963		

Note: *Sig at 0.05
Source: Primary data

Table 9.
Variations in homesickness based on education level of the employees

Variable	Category	Mean	SD	*t*-value	Sig.
Missing family	Defense	4.434	0.650	5.666	0.000*
	Civilian	3.690	1.277		
Missing friends	Defense	3.092	0.682	4.829	0.000*
	Civilian	3.517	1.139		
Feeling lonely	Defense	3.742	0.883	3.013	0.003*
	Civilian	3.341	1.247		
Adjustment problem	Defense	3.730	1.027	2.874	0.004*
	Civilian	3.352	1.191		
Rumination about home	Defense	3.900	0.803	4.063	0.000*
	Civilian	3.398	1.162		
Overall homesickness	Defense	3.980	0.650	4.806	0.000*
	Civilian	3.460	1.024		

Note: *Sig at 0.05
Source: Primary data

Table 10.
Variations in homesickness among defense personnel and civilian

Variable	Category	Mean	Female *t*-value	Sig.	Mean	Male *t*-value	Sig.
Missing family	Defense	4.461	4.784	0.000*	4.00	0.933	0.353
	Civilian	3.827			3.52		
Missing friends	Defense	4.114	3.626	0.000*	3.78	1.002	0.318
	Civilian	3.673			3.32		
Feeling lonely	Defense	3.757	1.939	0.054	3.53	0.743	0.458
	Civilian	3.486			3.16		
Adjustment problem	Defense	3.737	1.478	0.140	3.64	1.108	0.270
	Civilian	3.519			3.15		
Rumination about home	Defense	3.895	2.854	0.005*	3.96	1.559	0.121
	Civilian	3.524			3.24		
Homesickness	Defense	3.780	1.245	0.215	3.99	3.435	0.001*
	Civilian	3.280			3.60		

Note: *Sig at 0.05
Source: Primary data

Table 11. Variations in homesickness among defense personnel and civilian (gender)

Table 12 reported no significant variation in homesickness among unmarried employees employed in the defense and professional industry. However, married armed personnel (mean = 3.987) are significantly more homesick than married corporate employees (mean = 3.494). Also, married defense personnel (mean = 3.987) experience higher homesickness than unmarried soldiers (mean = 3.941). Married soldiers experience greater homesickness in all five dimensions of homesickness.

Table 13 highlights that homesickness among defense and civilian employees vary significantly in joint and extended families. The armed force personnel belonging to joint and extended joint families are more homesick. Nuclear family-based employees working in both sectors experience an equal level of homesickness.

Variable	Category	Mean	Unmarried *t*-value	Sig.	Mean	Married *t*-value	Sig.
Missing family	Defense	4.366	2.024	0.044*	4.446	5.020	0.000*
	Civilian	3.657			3.755		
Missing friends	Defense	3.766	0.882	0.379	4.147	4.284	0.000*
	Civilian	3.507			3.537		
Feeling lonely	Defense	3.650	1.194	0.234	3.758	1.631	0.105
	Civilian	3.265			3.492		
Adjustment problem	Defense	3.933	1.887	0.061	3.696	2.143	0.033*
	Civilian	3.366			3.323		
Rumination about home	Defense	3.983	1.989	0.048	3.886	3.194	0.001*
	Civilian	3.408			3.378		
Homesickness	Defense	3.941	1.914	0.057	3.987	3.643	0.000*
	Civilian	3.442			3.494		

Note: *Sig at 0.05
Source: Primary data

Table 12. Variations in homesickness among defense personnel and civilian (martial)

Variable	Category	Nuclear Mean	Nuclear *t*-val	Nuclear Sig.	Joint Mean	Joint *t*-val	Joint Sig.	Extended joint Mean	Extended joint *t*-val	Extended joint Sig.
Missing family	Defense	3.916	0.191	0.849	4.425	3.407	0.001*	4.482	4.212	0.000*
	Civilian	4.000			3.515			3.779		
Missing friends	Defense	4.250	1.099	0.275	4.037	2.928	0.004*	4.100	2.927	0.004*
	Civilian	3.774			3.343			3.661		
Feeling lonely	Defense	3.833	0.244	0.808	3.685	2.199	0.011*	3.757	1.635	0.104
	Civilian	3.714			3.124			3.466		
Adjustment problem	Defense	3.583	0.553	0.598	3.648	1.871	0.069	3.775	2.833	0.005*
	Civilian	3.771			3.208			3.257		
Rumination	Defense	4.166	1.100	0.083	3.861	2.434	0.016*	3.892	3.067	0.003*
	Civilian	3.690			3.288			3.352		
Homesickness	Defense	3.95	0.431	0.668	3.93	3.015	0.003*	4.00	3.415	0.001*
	Civilian	3.79			3.29			3.50		

Note: *Sig at 0.05
Source: Primary data

Table 13. Variations in homesickness among defense personnel and civilian (family)

Table 14 stated that defense and civilian employees below the age of 25 years are equally homesick. For all other age groups, defense people experience a higher level of homesickness. It is interesting to note that homesickness follows an inverted "U" shape graph for defense people. Homesickness steadily increases for three age groups, namely, below 25 years, 26–35 years and 36–45 years. After this, it decreases for the above 45 years, age group. For civilians, homesickness increases with the age of the employees.

Table 15 elaborated that defense employees, having academic degrees up to graduation, experience greater homesickness than civilian employees with the same educational credentials. Also, employees with higher academic qualifications than graduation experience an equal level of homesickness.

Variable	Category	Below 25 yr Mean	Below 25 yr Sig.	26–35 years Mean	26–35 years Sig.	36–45 years Mean	36–45 years Sig.	Above 45 yr Mean	Above 45 yr Sig.
Missing family	Defense	4.625	0.155	4.295	0.035*	4.488	0.000*	4.500	0.019*
	Civilian	3.596		3.878		3.643		3.807	
Missing friends	Defense	3.500	0.939	4.090	0.007*	4.142	0.006*	4.104	0.364
	Civilian	3.454		3.585		3.526		3.826	
Feeling lonely	Defense	3.250	0.894	3.840	0.056	3.839	0.329	3.520	0.245
	Civilian	3.164		3.429		3.606		3.980	
Adjustment problem	Defense	4.062	0.209	3.681	0.124	3.678	0.219	3.833	0.820
	Civilian	3.316		3.320		3.372		3.923	
Rumination	Defense	3.875	0.330	3.969	0.029*	4.011	0.009*	3.614	0.527
	Civilian	3.313		3.497		3.393		3.826	
Homesickness	Defense	3.862	0.356	3.975	0.012*	4.032	0.010*	3.914	0.886
	Civilian	3.369		3.541		3.508		3.873	

Note: *Sig at 0.05
Source: Primary data

Table 14. Variations in homesickness among defense personnel and civilian (age)

Table 15. Variations in homesickness among defense personnel and civilian (education)

Variable	Category	Below grad. Mean	Below grad. Sig.	Graduate Mean	Graduate Sig.	PG Mean	PG Sig.	Above PG Mean	Above PG Sig.
Missing family	Defense	4.413	0.065	4.468	0.000*	4.410	0.018*	4.000	0.449
	Civilian	3.961		3.666		3.635		3.398	
Missing friends	Defense	4.293	0.008*	4.109	0.002*	3.714	0.213	3.666	0.629
	Civilian	3.673		3.560		3.354		3.342	
Feeling lonely	Defense	4.206	0.028*	3.536	0.215	3.535	0.481	3.916	0.229
	Civilian	3.634		3.302		3.309		2.953	
Adjustment problem	Defense	4.094	0.020*	3.531	0.629	3.625	0.263	4.250	0.028*
	Civilian	3.480		3.442		3.222		2.925	
Rumination	Defense	4.094	0.008*	3.813	0.051	3.910	0.109	3.916	0.186
	Civilian	3.418		3.480		3.388		2.925	
Homesick-ness	Defense	4.220	0.009*	3.891	0.010*	3.839	0.081	3.950	0.155
	Civilian	3.633		3.490		3.381		3.109	

Note: *Sig at 0.05
Source: Primary data

Discussion and conclusion

Theoretical contribution of the study

Almost everyone experiences homesickness in their life-time, regardless of the nature of the job, age, occupation, interest, etc. (Thurber and Walton, 2012). Modern organizations have to pay significant direct and indirect costs owing to homesick employees. The direct cost includes loss of productivity, as it is reported that 10% to 15% of homesick employees face trouble in carrying out their routine jobs due to physical and psychological functioning (Stroebe *et al.*, 2002). In addition, indirect ill-effects involve psychological disturbance and absent-mindedness (Fisher and Hood, 1987), lack of concentration and ability to perform (Burt, 1993; Stroebe *et al.*, 2002), disappointing social relationships and networks, distress and functional impairment (Thurber and Walton, 2012), physiological disturbance such as loss of appetite, sleep disorder and fatigue (Van Tilburg *et al.*, 1996) and somatic disorder such as binge eating, suicidal tendency and heart complaints (Van Tilburg, 2005). Despite serious repercussions of homesickness at both individual and organizational levels, the academic field is often criticized for the scarcity of research in organizational contexts. Previous research studies are mainly confined to students (Fisher and Hood, 1987; Scopelliti and Tibero, 2010; Vergara *et al.*, 2010). A few previous studies also explored homesickness among foreigners in a new country (Eurelings-Bontekoe *et al.*, 2000; Ying, 2005; Vergara *et al.*, 2010). Unfortunately, many working professionals who face frequent geographical movements and subsequent relocations are not studied enough. The present study is strongly footed to address this research gap of lack of study of working professionals.

Homesickness, being a psychological construct, does not have a similar effect on every individual. Thus, this study empirically discusses demographic variables-based variations in homesickness. Overall, it is reported that homesickness is statistically significantly greater for men than women, married employees than unmarried employees, workers belonging to nuclear family than those of joint family, aged employees than younger ones and less educationally qualified workers than highly qualified ones. These findings could be explained with the help of attachment, belonging and the dual-process theory of homesickness. A married employee and an aged employee are poised to be more attached to

its family and children than unmarried and younger employees. Thus, greater experience of homesickness among married and aged employees is explained by attachment theory.

The present study is also one of the pioneer studies that compare homesickness among defense and civilian employees. The variations in homesickness among these two clusters of employees have also been examined on five different demographic variables. Also, defense personnel is reported to be more homesick than civilian employees. In this way, the current study expands the existing knowledge set of homesickness in at least three ways. First, it explores homesickness among working professionals. Second, it provides a deep insight into demographic variations of homesickness. And finally, it provides a comparative study of defense and non-defense employees. Probably, no previous study has undergone such a comparative study. The study reports a higher level of homesickness among soldiers than working professionals. The findings could be explained in light of the dual-process theory and reduced control theory. These models state that inability and difficulty to adapt and adjust to a new environment activates homesickness experience. It is a well-known fact that military life is relatively harder and difficult than that of working professionals. Thus, the result seems in line with existing theories of homesickness.

Another major theoretical contribution is in the domain of individual differences. Previous theories support demographical, personality and situational determinants of individual differences in one's response to a particular situation. The current study also witnesses demographics and job context-based individual differences in the experience of homesickness. It also expands the academic pursuit of human resource-related challenges of armed forces. Military studies primarily focus on the command's tactical and strategic approach, modernization of weapons and forces, defense expenditure and quick mobilization of army resources. Human resource and organization behavior studies are scares among army personnel, especially in the Indian force. In addition, it also stimulates the interest of practitioners and researchers for employee-related challenges.

Practical implications of the study

HR managers of modern organizations are devoting significant resources and time to deal with homesickness. The findings of the present study offer vital insight to develop the anti-homesickness program. Demographics-based variation indicates that several tailor-made approaches for different demographic groups are required than following a universalist approach. More efforts are required for more vulnerable groups such as aged employees and employees belonging to the nuclear family. Simple interventions such as expressing feelings (oral or writing), reassurance and involvement in physical and mental exercises may be adopted for less vulnerable groups. Highly effective techniques such as rational emotive therapy, meditation and mindfulness and gratitude and compassion practices may be used for highly homesick employees. A supportive and collaborative organizational climate and environment is a must for the successful implementation of these interventions. It is also suggested to integrate remedial pursuit in other HR functions too. Recruiters may get a fair idea of job applicants' chances of being homesick using direct questions/questionnaires or projective techniques. Relatively less educated and aged employees may be given specific training in communication-related technologies so that they can contact their families promptly and easily.

Modern HR managers rely on workplace spirituality to decrease homesickness among employees (Saxena *et al.*, 2020; Garg *et al.*, 2019). The findings of the present study will help in designing demographic group-based workplace spirituality interventions. As male and married employees are relatively more homesick, spiritual dimensions such as a sense of community, karma capital and swadharma (meaningful and meditative work) are more

suited for these vulnerable groups (Garg, 2017). Other researchers advocate gratitude-based intervention to develop resilience and vitality among employees (Garg, 2020). In addition, resilience and vitality are vital moderators of homesickness. Accordingly, it is suggested that specific gratitude interventions such as blessing count, gratitude letters and visits, opposition thinking and gratitude diary may decrease homesickness among aged employees. These practices are easy to follow but are highly effective. Gratitude practices help in the realization of good in one's life (Fredrickson, 2009). According to Fredrickson's broaden-and-build theory, gratitude broadens one's outlook and develops social, intellectual and psychological resources for an individual. These resources may help in minimizing the experience of homesickness in two ways. First, it makes an employee realize the importance and benefits of the current assignment. Although they are away from their homes and families, a grateful individual will appreciate that difficult and unknown situations are highly helpful in holistic personality development. A grateful employee or soldier will also realize the fact that this home-away job is the source of bread and butter for their family. Thus, gratefulness may transform a painful expression of homesickness into a prayerful expression of thankfulness. Second, the stated social, intellectual and psychological resources develop resilience and adaptability among employees (Garg and Sarkar, 2020). Gratitude allows an employee to adapt to the new situation with ease and thankfulness. Thus, it negates one reason for the "difficulty in adaptability" of homesickness described in the dual-process model and reduced control theory of homesickness.

The paper offers a few significant practical suggestions for decision-makers of armed forces too. The results report higher levels of homesickness among defense personnel. In addition, previous studies conclude undesirable linkage between homesickness and neuroticism (Van Heck *et al.*, 1997; Verschuur *et al.*, 2003), depression and anxiety, sense of loneliness (Archer *et al.*, 1998), cognitive and attentional problems (Du *et al.*, 2017) among soldiers. Thus, it is extremely important to frame specific policies for soldiers. Several scholars, including Drummet *et al.* (2003), suggested introducing a "buddy system" to neutralize homesickness. Based on the current study results, a married soldier may be buddied with an unmarried one, aged personnel with a younger one, etc. Such a research-based buddy system is poised to help homesick soldiers. The general perception of armed force personnel is that they are physically and mentally very strong. It restricts candid admission and free discussion on the problem of homesickness. Thus, discussion sessions, preferably in the presence of a counselor or organizational development practitioners, may bring wonders for defense people.

Social implications of the study

The findings of the study offer some interesting insights into the unique socio-cultural settings of the eastern world. The findings of lesser homesickness among women could be seen in the light of the Indian cultural and marriage system. Indian marriage system is unique in the world, in which the bride moves to the home of her in-laws. From a very young age, Indian girls are socialized for migration to their husbands' homes for the rest of their lives. They are taught that their parents' home is secondary for them, and their real home is that of their husband. This cultural upbringing may result in a lesser experience of pain and despair among women while leaving their parental home. Second, a hallmark of eastern societies is a joint or extended joint family. The findings-employees belonging to a nuclear family are more homesick than joint family employees- could benefit the joint family. The joint family system provides an appropriate avenue for rearing and caring for the family's toddlers, which remains a prime concern for a working lady. A joint family also assures an expatriate about the safety, health and welfare of its spouse and old aged parents.

Limitation, scope for future studies and conclusion

Although the study provides some interesting findings, the study is marred with a few limitations also. This present study is essentially conducted in Indian settings. In addition, few most important parameters of individual differences are national, social and cultural backgrounds. So, a similar study in different countries or different cultural settings may derive different results. Future researchers may be interested in conducting a comparative study of homesickness in eastern and western cultures. Second, the size of defense personnel is around 4 million in India, and that of employees engaged in professional organizations is more than 400 million. Thus, the results of the present study could not be generalized with such a small sample size of the study. The present study hints toward probable differences in the experience of homesickness of defense and civilian employees. However, the results require authentication with a sample of a sizeable proportion of defense and civilian employees. Third, only a handful of variables are explored in this study. Future studies may include other vital variables such as distance from home, place of posting, frequency of transfer and frequency of visit to the home. Homesickness among different personality types may also be a good area to explore. This study is also based on a cross-sectional research design, wherein data has been collected only once. Longitudinal research is certainly a better choice to avoid common method bias. Future studies may include a comparative study of different antecedents of homesickness in different demographic groups. In a nutshell, the challenge of homesickness requires a comprehensive and thoughtful approach keeping in mind that the same key cannot open all the doors. Different interventions are required for different groups.

References

Archer, J., Ireland, J., Amos, S.L., Broad, H. and Currid, L. (1998), "Derivation of a homesickness scale", *British Journal of Psychology*, Vol. 89 No. 2, pp. 205-221.

Baumeister, R.F. and Leary, M.R. (1995), "The need to belong: desire for interpersonal attachments as a fundamental human motivation", *Psychological Bulletin*, Vol. 117 No. 3, pp. 497-529.

Bell, J. and Bromnick, R. (1998), "Young people in transition: the relationship between homesickness and self-disclosure", *Journal of Adolescence*, Vol. 21 No. 6, pp. 745-748.

Bentler, P.M. (1990), "Comparative fit indexes in structural models", *Psychological Bulletin*, Vol. 107 No. 2, pp. 238-246.

Burt, C. (1993), "Concentration and academic ability following the transition to university: an investigation of the effects of homesickness", *Journal of Environmental Psychology*, Vol. 13 No. 4, pp. 333-342.

Cochran, W. (1997), *Sampling Techniques*, 3rd ed., Wiley. New York.

Deresky (2010), *International Management: managing across Borders and Cultures*, Pearson/Prentice Hall. NJ.

Drummet, A.R., Coleman, M. and Cable, S. (2003), "Military families under stress: implications for family life education", *Family Relations*, Vol. 52 No. 3, pp. 279-287.

Du, D., Derks, D., Bakker, A.B. and Lu, C. (2017), "Does homesickness undermine the potential of job resources? A perspective from work–home resources model", *Journal of Organizational Behaviour*, Vol. 37 No. 3, pp. 309-325.

Duru, E. and Balkis, M. (2013), "The psychometric properties of the Utrecht homesickness scale: a study of reliability and validity", *Egitim Arastirmalari-Eurasian Journal of Educational Research*, Vol. 52 No. 1, pp. 61-78.

English, T., Davis, J., Wei, M. and Gross, J.J. (2017), "Homesickness and adjustment across the first year of college: a longitudinal study", *Emotion*, Vol. 17 No. 1, pp. 1-5.

Eurelings-Bontekoe, E.H.M., Brouwers, E.P.M. and Verschuur, M.J. (2000), "Homesickness among foreign employees of a multinational high-tech company in The Netherlands", *Environment and Behavior*, Vol. 32 No. 3, pp. 443-456.

Fredrickson, B.L. (2009), *Positivity*, Crown, New York.

Fisher, S. and Hood, B. (1987), "The stress of the transition to university: a longitudinal study of vulnerability to psychological disturbance and homesickness", *British Journal of Psychology*, Vol. 78 No. 4, pp. 425-441.

Fisher, S., Frazer, N. and Murray, K. (1986), "Homesickness and health in boarding school children", *Journal of Environmental Psychology*, Vol. 6 No. 1, pp. 35-37.

Flach, A., De Jager, M.L. and Van de Ven, C.P.H.W. (2000), "Fight or flight? The drop-out phenomenon during initial military training: Homesickness", *The Proceedings of the 42nd Annual Conference of the International Military Testing Association Edinburgh*, available at: http://citeseerx.ist.psu.edu/viewdoc/download?doi=10.1.1.112.2616&rep=rep1&type=pdf#page=188

Fornell, C. and Larker, D. (1981), "Structural equation modeling and regression: guidelines for research practice", *Journal of Marketing Research*, Vol. 18 No. 1, pp. 39-50.

Garg, N. (2017), "Workplace spirituality and organizational commitment: an empirical exploration", *Purushartha - A Journal of Management, Ethics, and Spirituality*, Vol. 10 No. 2, pp. 8-24.

Garg, N. (2020), "Exploring the role of gratitude in developing teacher leadership in Indian universities", *International Journal of Educational Management*, Vol. 34 No. 5, pp. 881-901.

Garg, N. and Sarkar, A. (2020), "Vitality among university students: exploring the role of gratitude and resilience", *Journal of Organizational Effectiveness: People and Performance*, Vol. 7 No. 3, pp. 321-337, doi: 10.1108/JOEPP-03-2020-0041.

Garg, N., Punia, B. and Jain, A. (2019), "Workplace spirituality and job satisfaction: exploring the mediating effect of organization citizenship behaviour", *Vision: The Journal of Business Perspective*, Vol. 23 No. 3, pp. 287-296.

Hach-Polay, D. (2012), "When home isn't home – a study of homesickness and coping strategies among migrant workers and expatriates", *International Journal of Psychological Studies*, Vol. 4 No. 3, pp. 62-72.

Hair, J.F., Ringle, C.M. and Sarstedt, M. (2013), "Partial least squares structural equation modeling: rigorous applications, better results and higher acceptance", *Long Range Planning*, Vol. 46 Nos 1/2, pp. 1-12.

Hair, J.E., Jr, Anderson, R.E., Tatham, R.L. and Black, W.C. (1998), *Multivariate Data Analysis*, Prentice-Hall. Upper Saddle River, NJ.

Hu, L.T. and Bentler, P.M. (1999), "Cutoff criteria for fit indexes in covariance structure analysis: conventional criteria versus new alternatives", *Structural Equation Modeling: A Multidisciplinary Journal*, Vol. 6 No. 1, pp. 1-55.

Kerns, K., Brumariu, L. and Abraham, M. (2008), "Homesickness at summer camp: associations with the mother-child relationship, social self-concept, and peer relationships in middle childhood", *Merrill-Palmer Quarterly*, Vol. 54 No. 4, pp. 473-498.

Mashayekhi, S. (2016), "The integrating effect of homesickness, attachment and spiritual wellbeing on international students' mental health in Malaysia", PhD thesis, Universiti Teknologi Malaysia, Faculty of Education.

Narang, G.S., Goswami, P. and Sharma, A. (2016), "Best HR practice in the corporate sector and the indian armed forces: a comparative study", *International Research Journal of Humanities, Engineering, and Pharmaceutical Sciences*, Vol. 11 No. 1, pp. 23-30.

Nauta, M.H., Aan Het Rot, M., Schut, H. and Stroebe, M. (2020), "Homesickness in social context: an ecological momentary assessment study among 1st-year university students", *International Journal of Psychology*, Vol. 55 No. 3, pp. 392-397.

Niziurski, J.A. and Berntsen, D. (2018), "A prospective study of homesickness in soldiers during military deployment", *Personality and Individual Differences*, Vol. 120 No. 1, pp. 81-86.

Omi, M. and Winnant, H. (2003), *Racial Formation in the United States*, Routledge, London.

Poyrazli, S. and Lopez, M. (2007), "An exploratory study of perceived discrimination and homesickness: a comparison of international students and american students", *The Journal of Psychology*, Vol. 141 No. 3, pp. 263-280.

Ramsberger, P.F. and Bell, D.B. (2002), "What we know about AWOL and desertion: a review of the professional literature for policymakers and commanders", U.S. Army Research Institute Special Report 51.

Rosen, G. (1975), "Nostalgia: a 'forgotten' psychological disorder", *Psychological Medicine*, Vol. 5 No. 4, pp. 340-354.

Saxena, A., Garg, N., Punia, B.K. and Prasad, A. (2020), "Exploring role of Indian workplace spirituality in stress management: a study of oil and gas industry", *Journal of Organizational Change Management*, Vol. 33 No. 5, available at: https://doi.org/10.1108/JOCM-11-2019-0327

Scharp, K.M., Paxman, C.G. and Thomas, L.J. (2016), "I want to go home": homesickness experiences and social support-seeking practices", *Environment and Behavior*, Vol. 48 No. 9, pp. 1175-1197.

Scopelliti, M. and Tibero, L. (2010), "Homesickness in university students: the role of multiple place attachment", *Environment and Behavior*, Vol. 42 No. 3, pp. 335-350.

Scullion, H. and Linehan, M. (2005), *International Human Resource Management: A Critical Text*, Palgrave Macmillan, Basingstoke.

Smith, B., Hanrahan, S., Anderson, R. and Abbott, L. (2015), "Predicting homesickness in residential athletes", *Journal of Clinical Sport Psychology*, Vol. 9 No. 2, pp. 138-155.

Stroebe, M., Schut, H. and Nauta, M. (2015), "Homesickness: a systematic review of the scientific literature", *Review of General Psychology*, Vol. 19 No. 2, pp. 157-171.

Stroebe, M., Schut, H. and Nauta, M.H. (2016), "Is homesickness a mini-grief? Development of a dual-process model", *Clinical Psychological Science*, Vol. 4 No. 2, pp. 344-358.

Stroebe, M., van Vliet, T., Hewstone, M. and Willis, H. (2002), "Homesickness among students in two cultures: antecedents and consequences", *British Journal of Psychology*, Vol. 93 No. 2, pp. 147-168.

Thomas, D. (2018), "Factors that contribute to homesickness among students of Thailand", *Kasetsart Journal of Social Sciences*, available at: https://doi.org/10.1016/j.kjss.2018.07.011

Thurber, C.A. (1995), "The experience and expression of homesickness in preadolescent and adolescent boys", *Child Development*, Vol. 66 No. 4, pp. 1162-1178.

Thurber, C.A. and Walton, E.A. (2012), "Homesickness and adjustment in university students", *Journal of American College Health*, Vol. 60 No. 5, pp. 415-419, doi: 10.1080/07448481.2012.673520.

Thurber, C.A. and Weisz, J.R. (1997), "Describing boys' coping with homesickness using a two-process model of control", *Anxiety Stress Coping*, Vol. 10 No. 2, pp. 181-202.

Thurber, C.A., Patterson, D.R. and Mount, K. (2007), "Children's adjustment to hospitalization: is homesickness a factor?", *Child Health Care*, in press.

Tochkov, K., Levine, L. and Sanaka, A. (2010), "Variation in the prediction of cross-cultural adjustment by Asian-Indian students in the United States", *College Student Journal*, Vol. 44 No. 3, pp. 677-689.

Van Heck, G.L., Vingerhoets, A.J.J.M., Voolstra, A., Gruijters, I., Thijs, H. and Van Tilburg, M.A.L. (1997), "Personality, temperament, and homesickness", in Van Tilburg, M.A.L. and Vingerhoets, A.J.J.M. (Eds), *Psychological Aspects of Geographical Moves: Homesickness and Acculturation Stress*, Tilburg University Press, Tilburg, pp. 181-196.

Van Tilburg, M.A. (2005), "The psychological context of homesickness", in Van Tilburg, M.A.L. and Vingerhoets, A.J.J.M. (Eds), *Psychological Aspects of Geographical Moves: Homesickness and Acculturation Stress*, Tilburg University Press, Tilburg, The Netherland, pp. 35-48.

Van Tilburg, M.A.L., Vingerhoets, A.J.J.M. and VanHeck, G.L. (1996), "Homesickness: a review of the literature", *Psychological Medicine*, Vol. 26 No. 5, p. 899.

Van Vliet, A. (2001), *Homesickness: Antecedents, Consequences, and Mediating Processes*, Utrecht University Press, Utrecht.

Vergara, M., Smith, N. and Keele, B. (2010), "Emotional intelligence, coping responses, and length of stay as correlates of acculturative stress among international university students in Thailand", *Procedia – Social and Behavioral Sciences*, Vol. 5, pp. 1498-1504.

Verschuur, M.J., Eurelings-Bontekoe, E.H.M., Spinhoven, P. and Duijsens, I.J. (2003), "Homesickness, temperament and character", *Personality and Individual Differences*, Vol. 35 No. 4, pp. 757-770.

Watt, S.E. and Badger, A.J. (2009), "Effects of social belonging on homesickness: an application of the belongingness hypothesis", *Personality and Social Psychology Bulletin*, Vol. 35 No. 4, pp. 516-530.

Ying, Y. (2005), "Variation in acculturative stressors over time: a study of Taiwanese students in the United States", *International Journal of Intercultural Relations*, Vol. 29 No. 1, pp. 59-71.

Zulkarnain, Z., Debby, D., Elvi, Y. and Maya, Y. (2019), "Homesickness, locus of control and social support among first-year boarding-school students", *Psychology in Russia: State of the Art*, Vol. 12 No. 2, pp. 134-145.

Appendix

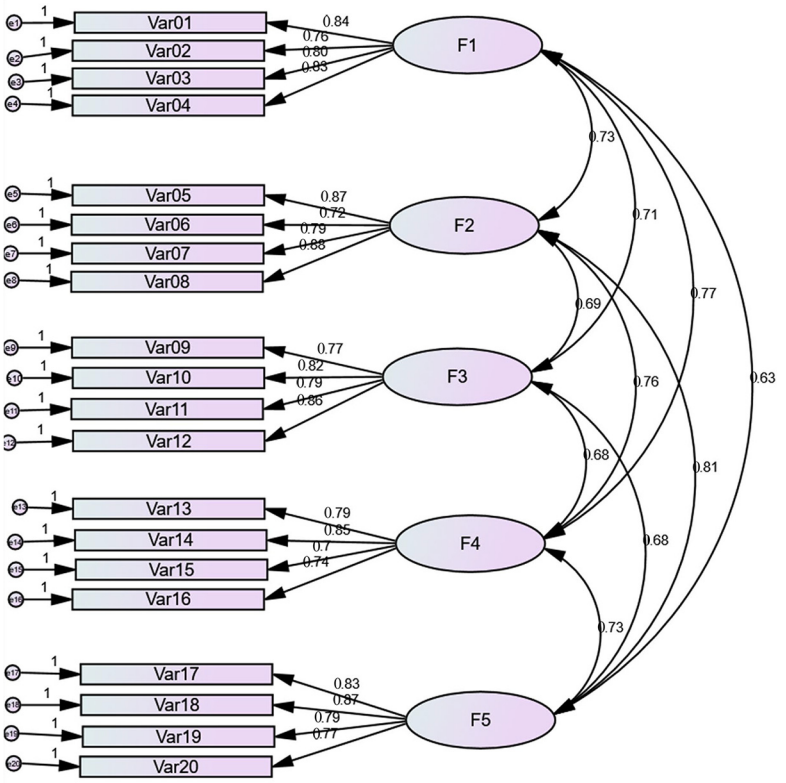

Figure A1.
CFA output

Corresponding author
Naval Garg can be contacted at: naval.garg@dtu.ac.in

For instructions on how to order reprints of this article, please visit our website:
www.emeraldgrouppublishing.com/licensing/reprints.htm
Or contact us for further details: **permissions@emeraldinsight.com**

International Journal of Engineering

Journal Homepage: www.ije.ir

Human Action Recognition using Prominent Camera

P. S. Kavimandan*[a], R. Kapoor[b], K. Yadav[a]

[a] *Indira Gandhi Delhi Technical University for Women, Delhi, India*
[b] *Delhi Technological University, Delhi, India*

PAPER INFO

Paper history:
Received 19 August 2020
Received in revised form 03 November 2020
Accepted 05 November 2020

Keywords:
Action Recognitio
Modified Bag-of-Words
Prominent camer
Support Vector Machine

ABSTRACT

Human action recognition has undoubtedly been under research for a long time. The reason being its vast applications such as visual surveillance, security, video retrieval, human interaction with machine/robot in the entertainment sector, content-based video compression, and many more. Multiple cameras are used to overcome human action recognition challenges such as occlusion and variation in viewpoint. The use of multiple cameras overloads the system with a large amount of data, thus a good recognition rate is achieved with cost (in terms of both computation and data) as the overhead. In this research, we propose a methodology to improve the action recognition rate by using a single camera from multiple camera environments. We applied a modified bag-of-visual-words based action recognition method with the Radial Basis Function-Support Vector Machine (RBF-SVM) as a classifier. Our experiment on a standard and publicly available dataset with multiple cameras shows an improved recognition rate compared to other state-of-the-art methods.

***doi**: 10. 5829/ije.2021.34.02b.14*

1. INTRODUCTION

The development of technology has made the camera a very easily available gadget, to the point that almost everybody these days uses a digital camera for capturing pictures or recording videos on a daily basis. In profession video recording for film production many cameras are in use simultaneously. The director of the film decides which camera has captured the best scene for a particular moment. But it is not always possible for a human administrator to be present for making such decisions. Thus, an automated machine that can decide which camera has produced the best scene can be valuable. The best information depends on the best view which in turn depends on several points. A view from one angle for a particular action may not be a good view from another angle for that same action. Thus the analysis of the video is required to select the best camera for the particular action. With the advent of technology and the rising number of videos, analyzing a video for the purpose of action recognition has gained tremendous importance in the field of computer vision. Action recognition is quite helpful especially in fields such as surveillance, security, robotics, etc. It also plays a vital role in intelligent systems. The aim here is to identify the category of actions performed in the video from the viewpoint of a selected camera.

In this work, we propose a methodology to recognize human actions performed by an actor by selecting a prominent camera in the multi-camera scenario. This technique helps to avoid the data processing captured by all the cameras. We rely here on the principle that different cameras capture different views, all of which are not good enough to recognize the action. Thus, we develop a score for each of the cameras based on two factors: limb visibility and limb movement. Depending on the score, one of the cameras is chosen as the 'prominent camera and selected for further processing. To testify the methodology, standard databases such as IXMAS [23] are used. The structure of the remaining paper is as follows: literature survey is discussed in Section 2; Section 3 explains the methodology in detail; in Section 4 results are discussed; followed by a conclusion and future work in Section 5.

*Corresponding Author Email: *pranoti.sk@gmail.com* (P. S. Kavimandan)

Please cite this article as: P. S. Kavimandan, R. Kapoor, K. Yadav, Human Action Recognition using Prominent Camera, International Journal of Engineering, B: Applications Vol. 34, No. 02, (2021) 427-432

2. RELATED WORKS

Action recognition from multiple views has been broadly studied in two approaches, the 2D approach and the 3D approach. 2D approaches deal with methods that use data from multiple cameras captured independently; whereas 3D approaches deal with multiple cameras that have been set up at a fixed location [1]. 2D approaches can be divided into two categories. First, the view independent category where data from all cameras is captured independently. And then either action is represented with view-invariant features [2-5] or several classifiers are fused for classification [6]. In Yilmaz and Shah [2], a moving camera is used for capturing data. Thus along with humans, the camera trajectory is also moving. Authors proposed the geometry of dynamic scenes to recognize human action in a number of challenging sequences. Ashraf et al. [3] have used the notion of projective depth to implement the view-invariant action recognition method. Projective depth is unaffected by the camera's orientation and thus has been used to recognize similar actions. In Junejo et al. [4], self similarity descriptors are used since, according to the authors, they are very stable and do not require a correlation between multiple views. A novel action descriptor is constructed using a temporal Laplacian Eigen map that converts view-dependent videos to a stylistic invariant embedded manifold for every single view in Lewandowski et al. [5]. Ahmad and Lee [6] proposed a novel method to recognize human action from a random view by combining features from silhouettes and optical flow.

Other approaches used universal classifiers to recognize actions from the data received from each camera [7-10]. A novel algorithm based kernelized structural SVM is used as a classifier to recognize human action from a random view in Wu and Jia [7]. Zhu et al. [8] proposed a novel multi-sensor fusion method and the universal classifier random forest is used for action recognition. Action videos are represented as prototypes of human body postures using self-organizing maps that are spatially related in Iosifidis et al. [9]. Subsequently, action classification is done using multi-layer perceptrons in a Neural Network. Wang et al. [10] used cross-view action recognition with a K-NN-like classifier. Local features extracted from the input video form a bag of word using k-means clustering. The action is recognised bases on the transfer probability between visual words.

3D approaches usually combine all the visual information (2D human poses) gathered from each camera to represent it in the form of features that are eventually used for action recognition. Thus actions are represented as consecutive 2D human poses. Volumetric data helps to generate a system that is robust as proposed by Pierobon et al. [11]. It also helps to overcome the problem of self-occlusion that is obvious in the multi-camera environment. They have used only posture dependent characteristics as descriptors. Weinland et al. [12] have introduced Motion History Volumes (MHV) as a descriptor that is viewpoint independent. They used Fourier transforms in cylindrical co-ordinates around a vertical axis to align and compare their results. Another representation such as spherical harmonics has been used as a descriptor by Kazhdan et al. [13] with the purpose of avoiding calculations for the optimal alignment which are unfeasible. Their descriptor is rotation invariant. Gkalelis et al. [14] have used fuzzy vector quantization (FVQ) and linear discriminant analysis (LDA) to model and recognize different human movements. They have exploited rich data in multi-view videos and have used Discrete Fourier Transform (DFT), since it is circular and shift-invariant, to solve correspondence issues between training and testing samples. Holte et al. [15] took advantage of intensity and depth maps both captured by SwissRanger SR4000 camera. According to them this combination and the use of Motion Context (HMC) as an action descriptor improved the detection quality. Holte et al. [16] again used HMC along with 3D Motion Context (3D-MC) as the motion descriptor. Few authors, Feizi [17] and Sezavar et al. [18] have implemented Convolution Neural Network (CNN) for their methodologies, but Support Vector Machine (SVM) seems to be the better choice since the main focus is to reduce the computation time and cost [19]. Approaches based on 3D methods are found to be superior to approach based on 2D methods concerning recognition accuracy [20]. To deal with the important challenges in human action recognition such as variation in viewpoint and occlusion, the basic solution is to use multiple cameras, and thus literature concerning multiple cameras has been studied. But multiple camera usage hampers the complexity and running time of the system. To deal with it, in this research paper, we propose a human recognition technique to chose a prominent camera from the multi camera environment. We propose to gather initial data from multiple cameras but to process the data only from a prominent camera.

3. METHODOLOGY

Figure 1 shows the block diagram of the proposed methodology. The video along with the action expected

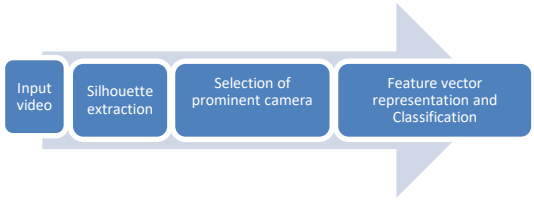

Figure 1. Flowchart of the proposed methodology

to be recognized is given as input. From the action, video silhouettes are extracted from all of the available cameras. Based on extracted silhouettes, information regarding limb visibility and movements can be discovered. We later calculate two scores namely, temporal score and spatial score for each camera. Based on the combination of these scores, a total score for each camera is calculated. The camera with the highest score is chosen as the most prominent camera, and the feature vector is represented for that prominent camera. These feature vectors act as input to the RBF-SVM classifier to recognize human action.

3. 1. Silhouettes Extraction The initial step in the methodology is silhouette extraction. This step requires background subtraction. Background subtraction has its own set of challenges such as variations in lighting, noise, etc. In the proposed methodology, the background has been modeled using a very popular technique known as the Gaussian Mixture Model (GMM) [21] since it is considered to be the most trustworthy background estimation method. This GMM technique is an adaptive mixture model that helps to deal with the problem of lighting variations, motion repetition, etc.

3. 2. Selection of a Prominent Camera To select a prominent camera, first of all, a score for each camera is developed for every camera on two factors. One is the limb movement and the other is limb visibility. We rely on the fact that when limb movement is significant, we can say that the silhouettes in the video will also move significantly. Thus a good motion of limbs indicates that the camera capturing it has a good chance of recognizing the action successfully and in lesser time. Lesser time here implies that the data from the camera other than the prominent camera need not be processed. A camera will develop a good score if it captures significant limb movement. This is called a score for temporal measure (C_t). Since we are interested in the limb movements, we picked out cameras which views show significant variations in movement, be it anywhere in the camera view. To calculate the limb movement, we need to develop the Motion Energy Image (MEI) [22]. MEI is found out using the following Equation (1):

$$MEI(x,y) = \bigcup_{t=0}^{\tau-1} B(x,y,t) \quad (1)$$

where, *B(x, y, t)* is a sequence of a binary images that highlights the area where motion has occurred. Let the most prevalent frame concerning the number of pixels be denoted by $B_{max}(x,y)$, thus we define the confidence score of the camera for temporal measure C_t by the following Equation (2):

$$C_t = 1 - \frac{\sum_{x,y} B_{max}(x,y)}{\sum_{x,y} MEI(x,y)} \quad (2)$$

The other fact that we rely on is that when limb visibility is good, the silhouettes tend to generate a concave profile. To find out the concavity of the shape, we define a spatial measure called a confidence score for the spatial measure $C_s$as given in Equation (3):

$$C_s = 1 - \frac{Vol_{st}}{Vol_{ch}} \quad (3)$$

where Vol_{st} is the Spatio-temporal volume and Vol_{ch} is the convex hull. Both C_t and $C_s$scores are delimited by 1, to always keep them positive. Both of these confidence scores for each camera are multiplied to calculate Confidence Score for a camera (C_c). Thus Confidence Score for a camera (C_c) is a combination of the Confidence score for temporal measure (C_t) and the Confidence score for spatial measure (C_s) as shown in Equation (4):

$$C_c = C_t . C_s \quad (4)$$

Thus we get the final score of each camera. Based on this score, the camera with the highest score will be chosen as the 'prominent camera' and feature vectors from that particular camera are processed further rather than processing data from all cameras. To recognize an action, we are using the modified bag-of-visual-words method described in literature [23].

3. 3. Feature Vector Representation and Classification Bag-of-visual-words methods are popular but these methods fail to preserve the information related to the geometry of the structure. Thus the method described in literature [23] is used to overcome this drawback. According to this method, a Harris 3D detector has been used to extract spatiotemporal points of interest.

The Histogram of Oriented Gradients (HOG) and Histogram of Optical Flow (HOF) descriptors are used to express interest points. Thus a bag-of-visual-word is created using these spatiotemporal interest points for representing an action and the contribution of cluster points is calculated. Depending on the difference among them the contextual distance among the points of a cluster is determined. Directed graphs are then created which are described by Laplacian. A Radial Basis Function Support Vector Machine (RBF-SVM) is fed with the feature vector corresponding to those Laplacians for action recognition.

4. RESULT DISCUSSION

The dataset used for validation is IXMAS [24]. It consists data of 11 actions performed by 5 male and 5 female actors from five static cameras. Figure 2(a-e) shows frames from the IXMAS dataset, and the actor here, namely ‘Daniel’, is acting a 'kick'. In Figure 3(a-e) the same actor is acting a 'punch'. Frames of all five cameras

have been shown for both of the actions, kick and punch in the figures. Figure 4(a-d) shows the result of the computation of temporal and spatial confidence scores C_t and C_s for different cameras. Table 1 shows temporal and spatial scores C_t and C_s calculated for all the five cameras, Camera 0-Camera 4 of the IXMAS dataset for

(a) Camera 0 (b) Camera 1 (c) Camera 2 (d) Camera 3 (e) Camera 4

Figure 2. (a-e) Frames from IXMAS dataset with actor Daniel acting 'kick' in all 5 cameras

(a) Camera 0 (b) Camera 1 (c) Camera 2 (d) Camera 3 (e) Camera 4

Figure 3. (a-e) Frames from IXMAS dataset with actor Daniel acting 'punch' in all 5 cameras, (a) C_t = 0.62, (b) C_t = 0.48, (c) C_s = 0.58, (d) C_s = 0.50

(a) (b) (c) (d)

Figure 4. Figure showing scores for different cameras; (a) C_t score for Daniel's kick action in Camera 0 (Figure 2 a); (b) C_t score for Daniel's kick action in Camera 2 (Figure 2 c); (c) C_s score for Daniel's punch action in Camera 0 (Figure 3 a); (d) C_s score for Daniel's punch action in Camera 3 (Figure 3 d)

TABLE 1. Temporal and spatial scores C_t and C_s and the final confidence score C_c calculated for all 5 cameras Camera 0-Camera 4 of IXMAS dataset. Prominent camera's Confidence score C_c is highlighted.

Action	Camera 0			Camera 1			Camera 2			Camera 3			Camera 4		
	Ct	Cs	Cc	Ct	Cs	Cc	Ct	Cs	Cc	Ct	Cs	Cc	Ct	Cs	Cc
Check watch	0.38	0.22	0.083	0.55	0.42	0.231	0.49	0.50	0.245	0.60	0.45	0.270	0.29	0.45	0.130
Cross arms	0.30	0.27	0.081	0.50	0.53	0.265	0.54	0.55	0.297	0.59	0.50	0.295	0.42	0.66	0.277
Scratch head	0.33	0.40	0.132	0.52	0.32	0.166	0.56	0.51	0.285	0.55	0.61	0.335	0.45	0.45	0.202
Sit down	0.54	0.52	0.280	0.53	0.56	0.296	0.52	0.58	0.301	0.56	0.60	0.336	0.32	0.28	0.089
Get up	0.28	0.35	0.098	0.52	0.55	0.286	0.50	0.52	0.260	0.51	0.49	0.249	0.49	0.52	0.254
Turn Around	0.34	0.47	0.159	0.36	0.45	0.162	0.45	0.57	0.256	0.52	0.59	0.306	0.27	0.31	0.083
Walk	0.53	0.50	0.265	0.55	0.49	0.269	0.53	0.49	0.259	0.56	0.50	0.280	0.30	0.42	0.126
Wave	0.50	0.58	0.290	0.45	0.59	0.265	0.42	0.54	0.226	0.60	0.58	0.348	0.49	0.60	0.294
Punch	0.55	0.58	0.319	0.58	0.61	0.353	0.45	0.48	0.216	0.49	0.50	0.245	0.52	0.60	0.312
Kick	0.62	0.58	0.359	0.60	0.58	0.348	0.48	0.50	0.240	0.52	0.45	0.234	0.49	0.54	0.264

10 actions such as checking the watch, crossing arms, scratching head, sitting down, getting up, turning around, walking, waving, punching and kicking. Prominent camera's confidence score C_c is highlighted. Figure 5 shows the graphical results for C_t, C_s, and C_c of all the five cameras for 10 actions in the IXMAS dataset. It can be noted from the graph that no single camera can be labeled as a prominent camera. It depends on the action to be recognized as in which camera would be the prominent camera. Table 2 shows the comparison of the proposed method with the other methods. As can be seen from the table, Camera 0 gives a good accuracy of 90.8% while recognizing the action 'Kick'. Camera 1 is good for actions 'Get up' and 'Punch' whereas Camera 2 for 'Cross arms' with an accuracy of 90.6% and 92.4% respectively. For all other actions, Camera 3 gives a worthy accuracy of 91.2%. Thus, we can also observe that if the prominent camera is chosen for action recognition, significant computation can be avoided by not processing the data from cameras other than the prominent camera.

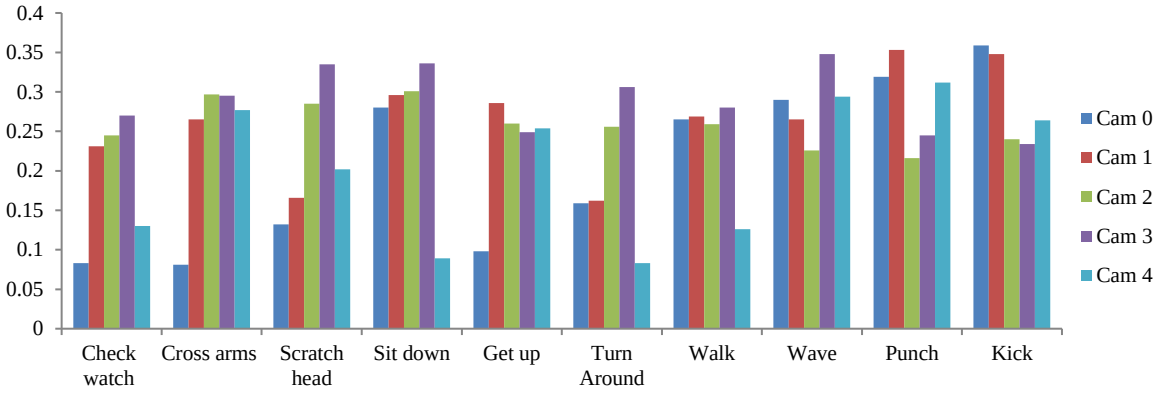

Figure 5. Shows the graphical results for confidence score C_c of all the five cameras for 10 actions in the IXMAS dataset

TABLE 2. Comparison of Proposed Method with other methods

Method	Accuracy (in Percentage)				
	Camera 0	**Camera 1**	**Camera 2**	**Camera 3**	**Camera 4**
Junejo I. et al. [4]	74.8	74.5	74.8	70.6	61.2
Wu, X. et al. [7]	86.5	83.8	86.1	84.5	87.4
Wang J. et al. [10]	88.4	85.3	88.3	86.5	87.2
Proposed Method	90.8 (Kick)	90.6 (Get Up, Punch)	92.4 (Cross Arms)	91.2 (All other actions)	90.6

5. CONCLUSION AND FUTURE WORK

In this paper, we have worked on the methodology of recognizing an action in an environment with multiple cameras. When multiple cameras are considered, along with their advantages comes the major disadvantage of computing time and cost because of the large amount of data. In our proposed methodology we have used the single camera with the most significant information for action recognition. We have given a score to each camera and based on this score the camera with the most significant information is chosen. As shown in Table 1, the prominent camera has been highlighted in yellow. The prominent camera may differ depending on the action, for example, the prominent camera in case of the action 'Checking watch' is Camera number 3 whereas, for the action 'Kich' it is Camera number 0. Thus, we processed the data from only a prominent camera among all the cameras to reduce the processing time and cost. In the future, we can fuse information from more than one prominent camera to further improve the recognition rate.

6. REFERENCES

1. Iosifidis, A., Anastasios T. and Ioannis P., "Multi-view Human Action Recognition: A Survey." 2013 Ninth International Conference on Intelligent Information Hiding and Multimedia Signal Processing (2013), 522-525, doi: 10.1109/IIH-MSP.2013.135.

2. Yilmaz A. and Shah M., "Recognizing human actions in videos acquired by uncalibrated moving cameras" Tenth IEEE International Conference on Computer Vision (ICCV'05) Volume 1, Beijing, (2005), 150-157, doi: 10.1109/ICCV.2005.201.
3. Ashraf, N., Sun, C. and Hassan, F., "View Invariant Action Recognition Using Projective Depth" ***Computer Vision and Image Understanding***, Vol. 123, (2014) doi.:10.1016/j.cviu.2014.03.005.
4. Junejo, I., Dexter, E., Laptev, Ivan and Pérez, P., "View-Independent Action Recognition from Temporal Self-Similarities," In IEEE Transactions on Pattern Analysis and Machine Intelligence, Vol. 33, No. 1, (2011), 172-185, doi.: 10.1109/TPAMI.2010.68.
5. Lewandowski, M., Dimitrios, M. and Jean-Christophe, N., "View and Style-Independent Action Manifolds for Human Activity Recognition." ECCV (2010). doi.org/10.1007/978-3-642-15567-3_40
6. Ahmad, M. and Lee, S. W., "HMM-based human action recognition using multiview image sequences", In Proceedings - 18th International Conference on Pattern Recognition, ICPR 2006, (2006), 263-266. doi.:10.1109/ICPR.2006.630
7. Wu, X. and Jia, Y., "View-Invariant Action Recognition Using Latent Kernelized Structural SVM", Fitzgibbon A., Lazebnik S., Perona P., Sato Y., Schmid C. (eds) Computer Vision – ECCV 2012, Lecture Notes in Computer Science, Vol. 7576. (2012) Springer, Berlin, Heidelberg. doi.: 10.1007/978-3-642-33715-4_30
8. Zhu, F., Shao, L. and Lin, M. "Multi-view action recognition Using local similarity random forests and sensor fusion", ***Pattern Recognition Letters***. Vol. 34, (2013) 20-24. doi.: 10.1016/j.patrec.2012.04.016.
9. Iosifidis, A., Tefas, A. and Pitas, I., "View-Invariant Action Recognition Based on Artificial Neural Networks," ***IEEE Transactions on Neural Networks and Learning System***s, Vol. 23, No. 3, (2012). 412-424, doi.: 10.1109/TNNLS.2011.2181865.
10. Wang, J., Zheng, H., Gao, J. and Cen, J., "Cross-View Recognition based ona Statistical Translation Framework", ***IEEE Transactions on Circuits and Systems for Video Technology***, Vol 26, (2014) doi. : 10.1109/TCSVT.2014.2382984
11. Pierobon, M. Marcon, M., Sarti, A. and Tubaro, S., "3-D Body Posture Tracking For Human Action Template Matching," 2006 IEEE International Conference on Acoustics Speech and Signal Processing Proceedings, Toulouse, (2006) doi.: 10.1109/ICASSP.2006.1660389.
12. Weinland, D., Ronfard, R. and Boyer, E., "Free viewpoint action recognition using motion history volumes", ***Computer Vision and Image Understanding***, Vol. 104, No. 2-3, (2006), 249-257, doi :https://doi.org/10.1016/j.cviu.2006.07.013
13. Kazhdan, M.M., Funkhouser, T.A., and Rusinkiewicz, S., "Rotation Invariant Spherical Harmonic Representation of 3D Shape Descriptors", Symposium on Geometry Processing, (2003) doi.:10.2312/SGP/SGP03/156-165
14. Gkalelis, N. Nokilaidis, N. and Pitas, I., "View independent human movement recognition from multi-view video exploiting a circular invariant posture representation", IEEE International Conference on Multimedia and Expo, (2009), 394-397. doi.: 10.1109/ICME.2009.5202517.
15. Holte M.B., Moeslund, T.B. and Fihl, P., "View-invariant gesture recognition using 3D optical flow and harmonic motion context", ***Computer Vision and Image Understanding***, Vol. 114, No. 12, (2010), 1353-136, https://doi.org/10.1016/j.cviu.2010.07.012
16. Holte, M.B., Moeslund, T., Nikolaidis, N. and Pitas, I., "3D Human Action Recognition for Multi-view Camera Systems", International Conference on 3D Imaging, Modeling, Processing, Visualization and Transmission, (2011), 342-349. doi.: 10.1109/3DIMPVT.2011.50.
17. Feizi, A., "Convolutional Gating Network for Object Tracking", ***International Journal of Engineering, Transactions A: Basics***, Vol. 32, No. 7, (2019), 931-939, https://dx.doi.org/10.5829/ije.2019.32.07a.05
18. Sezavar, A., Farsi, H. and Mohamadzadeh, S., "A Modified Grasshopper Optimization Algorithm Combined with CNN for Content Based Image Retrieval," ***International Journal of Engineering, Transactions A: Basics***, Vol. 32, No. 7, (2019), 924-930, https://dx.doi.org/10.5829/ije.2019.32.07a.04
19. Anding, K., Kuritcyn, P. and Garten, D., "Using artificial intelligence strategies for process-related automated inspection in the production environment", ***Journal of Physics: Conference Series***, Vol. 772, (2016). doi.:10.1088/1742-6596/772/1/012026.
20. Holte, M.B., Moeslund, T., Tran, C. and Trivedi M.M., "Human Action Recognition using Multiple Views: A Comparative Perspective on Recent Developments", MM'11-Proceedings of the 2011 ACM Multimedia Conference and Co-Located Workshops, (2011), doi.: 10.1145/2072572.2072588
21. Chen, Z. and Ellis, T.J., "A self-adaptive Gaussian mixture model", ***Computer Vision and Image Understanding***., (2014), Vol. 122, 35-46. https://doi.org/10.1016/j.cviu.2014.01.004
22. Bobick, A.F. and Davis, J.W., "The recognition of human movement using temporal templates," ***IEEE Transactions on Pattern Analysis and Machine Intelligence***, Vol. 23, No. 3, (2001), 257-267. doi.: 10.1109/34.910878.
23. Mishra, O., Kapoor, R. and Tripathi, M.M., "Human Action Recognition Using Modified Bag of Visual Word based on Spectral Perception", ***International Journal of Image, Graphics and Signal Processing***, Vol 11, (2019), 34-43. doi.: 10.5815/ijigsp.2019.09.04.
24. Weinland, D., Ronfard, R. and Boyer, E., "Free viewpoint action recognition using motion history volumes", ***Computer Vision and Image Understanding***, Vol. 104, No. 2-3, (2006), 249-257. doi: https://doi.org/10.1016/j.cviu.2006.07.013

Persian Abstract

چکیده

تشخیص عمل انسان بدون شک مدتهاست که تحت تحقیق بوده است. دلیل آن، کاربردهای گسترده آن مانند نظارت بصری، امنیت، بازیابی ویدئو، تعامل انسان با ماشین / ربات در بخش سرگرمی، فشرده‌سازی فیلم مبتنی بر محتوا و موارد دیگر است. از چندین دوربین برای غلبه بر چالش‌های تشخیص عملکرد انسان مانند انسداد و تغییر در دیدگاه استفاده می‌شود. استفاده از چندین دوربین سیستم را با مقدار زیادی داده بیش از حد بار می‌کند، بنابراین میزان شناخت خوبی با هزینه (از نظر محاسبه و داده) به عنوان سربار حاصل می‌شود. در این تحقیق، ما یک روش برای بهبود میزان تشخیص عملکرد با استفاده از یک دوربین منفرد از چندین محیط دوربین پیشنهاد می‌کنیم. ما یک روش اصلاح شده عمل مبتنی بر کلمات تصویری اصلاح شده با ماشین بردار عملکرد پشتیبانی-شعاعی (RBF-SVM) را به عنوان طبقه‌بندی اعمال کردیم. آزمایش ما بر روی یک مجموعه داده استاندارد و در دسترس عموم با چندین دوربین، میزان تشخیص بهتر در مقایسه با سایر روش‌های پیشرفته را نشان می‌دهد.

arXiv:2102.04304v1 [cs.SI] 23 Jan 2021

Identifying Influential Nodes in Weighted Networks using k-shell based HookeRank Algorithm

Nipun Aggarwal[a], Sanjay Kumar[a]

[a]*Department of Computer Science and Engineering, Delhi Technological University, Main Bawana Road, New Delhi-110042, India*

Abstract

Finding influential spreaders is a crucial task in the field of network analysis because of numerous theoretical and practical importance. These nodes play vital roles in the information diffusion process, like viral marketing. Many real-life networks are weighted networks, but relatively less work has been done for finding influential nodes in the case of weighted networks as compared to unweighted networks. In this paper, we propose k-shell based HookeRank (KSHR) algorithm to identify spreaders in weighted networks. First, we propose weighted k-shell centrality of node (u) by using k-shell value of u, k-shell value of its neighbors (v), and edge weight (w_{uv}) between them. We model edges present in the network as springs and edge weights as spring constants. Based on the notion of Hooke's law of elasticity, we assume a force equal to weighted k-shell value acts on each node. In this arrangement, we formulate KSHR centrality of each node using associated weighted k-shell value and the equivalent edge weight by taking care of series and parallel combination of edges up to 3-hop neighbors from the source node. The proposed algorithm finds influential nodes that can spread the information to the maximum number of nodes in the network. We compare our proposed algorithm with popular existing algorithms and observe that it outperforms them on many real-life and synthetic networks suing Susceptible-Infected-Recovered (SIR) information diffusion model.

Keywords: Complex networks, Centrality measure, Epidemic Spreading, Influential spreaders, Social networks, Weighted networks

1. Introduction

In our day to day life, we come across numerous complex networks like communication networks, social networks, biological networks, and the world wide web network [1]. Such networks consist of a large number of nodes with non-trivial properties leading to a variety of research problems [2]. Complex networks can be modeled as graphs $G = (V, E)$ where V corresponds to set of nodes, E represents edges between nodes. Many complex networks are weighted networks where edges are associated with some weight, where weight refers to the duration or frequency of communication, collaboration, friendship, or trade between two entities [3]. For example, in social networks, the weight of an edge can be a function

Email address: nipundtu@gmail.com (Nipun Aggarwal)

of time, affection, and exchange of services between two persons [4]. In other weighted networks, the weight often expresses the potential or capability of the tie [5]. In airport networks, the edge weight between the two cities can refer to the number of direct flight services between them. Usually, information or diseases are more likely to be transferred between the nodes having high or frequent interactions.

Finding influential spreaders is one of the prominent research problem in the field of complex networks analysis [7]. Influential nodes play crucial roles in many spreading phenomena like viral marketing, influence maximization [6], rumor control [9], epidemic spreading [10]. The action of influential spreaders can lead to maximizing the information coverage in the advertisement of the products and viral marketing, whereas minimizing the damage in case of rumor or epidemic spreading in the network. Influence maximization [14] aims to choose a constant number (k) of influential nodes as seed nodes such that information originating from them can reach to the maximum number of nodes in the network due to cascade trigger through word-of-mouth strategy. The influence maximization activity comprises of two phase: identifying the seed spreaders, and information diffusion phase. Researchers have effectively applied various epidemic spreading methods to model information diffusion in networks to assess influence spread arises due to trigger from the selected seed nodes [11]. Identifying influential nodes problem on unweighted networks has been extensively studied in recent years. However, it is relatively less explored for the weighted networks. The majority of such methods on weighted systems are just extension of existing methods on unweighted methods by bringing edge weight into the picture. In this paper, we propose a k-shell decomposition and Hooke's law of elasticity based algorithm named as KSHR for locating the influential spreaders in the weighted network. Our algorithm considers the influence of nodes in a setting where edges are demonstrated as springs and edge-weights are displayed as flexibility coefficients. We model edge weights as spring constants. The edges present in the system are displayed as springs, which are associated in arrangement and equal. They lengthen by a separation under the influence of an expected steady power adhering to Hooke's law of flexibility, and this is the identical spread separation between nodes in the system.

The contributions of our work are as follows:

1. We introduce a new algorithm for weighted k-shell decomposition and use the weighted k-shell value of a node as stretch value for the edges connected to that node in a setting where the weighted graph is modeled as springs.
2. Based on the notion of weighted k-shell centrality and Hooke's law of elasticity in the case of complex weighted networks, we propose the KSHR algorithm to identify influential nodes.
3. The experimental results on real-life and synthetic network datasets based on various performance parameters reveal that the proposed algorithm performs reasonably well compared to other existing popular methods.

The rest of the paper is organized as follows: Section 2 presents the related weighted centrality, related applications of modeling the edge of the graph as the spring, and information diffusion model. Section 3 discusses the performance matrices and data-sets used in this paper. In Section 4, we describe the proposed algorithm, time complexity of the algorithm, and its simulation on a toy network. Section 5 discusses the experimental

results on each performance parameter for various datasets. Finally, in Section 6, we conclude our study.

2. Preliminary

2.1. Node Centrality

The underlying models in the field of impact maximization have significantly been advancements in the field of unweighted networks where all edges are similarly significant. In real networks, these edges are related with weights that should be thought of while calculating the quality of these nodes during a pattern of information diffusion. At the point when we think about these parts of topology, we can accumulate insights into what is generally useful for the expansion of information propagation. The early advances in weighted networks were through centralities like DegreeRank utilized for unweighted networks, by extra weighing of these edges to accomplish a weighted DegreeRank [16]. In a similar way, different centralities taken from unweighted networks, advancing into a technique for weighted graphs through numerical changes adjusting the weighted calculations. Betweenness centrality thinks about the most limited way of a node in an unweighted graph, and it was stretched out for weighted rendition giving the weighted-betweenness centrality [17, 18]. In view of the thought of the voting method, analysts have proposed influence calculation in unweighted just as weighted networks where the nodes getting the maximum votes in each round as spreader nodes [19, 20, 21]. The h index is a proportion of the impact of analysts dependent on the quantity of references got, and by expanding edge weight, Yu et al. proposed a weighted h-index centrality [22]. Weighted-eigenvector centrality is appropriate in a weighted network and depends on the way that a node is significant if its neighbors are likewise celebrated and finds the centrality for a node as an element of the centrality of its neighbors [23].

2.2. Spring-based edges

Eades [24] proposed to display the edges of the network as springs to draw graphs by limiting expected potential energy. This technique was later refined by Fruchterman et al. [25], where they model nodes as electrical charges and edges as associating springs. The electrical charges cause these nodes to repulse one another. One of the most well known calculations for drawing graphs is Kamada and Kawai's strategy, which models the edges of the graph as springs acting observing Hooke's Law [26, 27]. The strategy increases the length of the spring between any two nodes by limiting a worldwide cost variable. We contend the relevance of the spring-based model to quantify the centrality of the nodes and to discover persuasive spreaders.

2.3. Weighted K shell

The first K-shell was applicable to just unweighted graphs [28]. It is a classical calculation that has been utilized to discover influential nodes. The expected augmentation of the calculation on weighted networks was performed by consideration of weights on biological networks by Eidsaa [29]. The calculation was additionally stretched out based on interaction and a hybrid k-core methodology was created [30]. These centralities were improved by taking neighboring k-shells and figuring the consolidated result by Maji and Wei [31, 32]. We propose a weighted K-shells method that performs better in our context.

2.4. Information Diffusion Model

SIR Model: In this paper, we employ the popular stochastic susceptible-infected-recovered (SIR) model as the information propagation model [33]. The SIR model partitions nodes of the network into three classes: susceptible (S), infected (I), and recovered (R). Susceptible are those nodes that are supposed to receive the information from their infected neighbor. In this model, the selected seed nodes are initially in an infected state, and all other nodes are in a susceptible state. In each subsequent iteration, the infected nodes influence their susceptible neighbors with a probability of β. Infected nodes at the following timestamp enter the recovered stage with a probability of γ. Once a node is in recovered state, it can't infect its neighbors further. Hence, according to this model, the amount of influence spread caused by the selected seed nodes can be estimated by counting the number of nodes who got infected and then later recovered in the subsequent stage of the SIR simulation.

3. Datasets and Performance Metrics

3.1. Performance Metrics

In this paper, we adopt a variety of evaluation matrices to reasonably analyze the performance of the proposed algorithm and other existing popular algorithms. The following evaluation matrices are included in our study:

(i) Influence spread or number of active nodes: It counts the total number of nodes that became active or infected at the end of the simulation of the information diffusion model, which caused due to the cascade effect triggered by the initial spreaders. In the SIR model of information dissemination, the selected seed nodes are initially infected nodes. They try to infect their susceptible neighbors with the rate β. This process continues till the state of nodes keeps on changing, and at the end, the total number of nodes during the diffusion process which converts from susceptible state to infected state and then to recovered state are counted to measure the influence spread. It is one of the most important parameters to judge the effectiveness of an influence maximization algorithm as it directly measures the overall spread of the information in the network originating from the selected spreaders.

(ii) Kendall tau correlation (τ) :- Kendall tau correlation [**?**] measures the ordinal association between two measured quantities in statistics. It is utilized to determine the precise spreading influence of the selected spreader nodes. In our case, the Kendall tau correlation is used to find the correlation between the rank list (R_1) generated by various algorithms of the influence maximization with the natural ranking list (R_2) generated by the SIR Model. For a pair of seed nodes, if $x_i > y_j$ in the list R_1, and $x_i > y_j >$ in actual rank list R_2 then such pair is known as concordant pair otherwise it is called discordant pair. The value of Kendall tau correlation lies in the range [-1, 1]. Kendall tau correlation (τ) between two ranked list R_1 and R_2 is computed using the following formula:

$$\tau(R_1, R_2) = \frac{n_{con} - n_{dis}}{\frac{1}{2}n(n-1)} \tag{1}$$

where n_{con} is the number of concordant pairs, n_{dis} is the number of discordant pairs and n is total number of nodes in both lists L_1 and L_2.

(iii) Average distance between spreaders (L_s): This metric computes the average shortest path distance between the selected spreaders. The high value of the average distance between spreaders implies that the spreaders are chosen from the diverse locations in the network and therefore, can propagate information to a significant portion of the system. The following equation computes the average distance between spreaders (L_s):

$$L_s = \frac{1}{\frac{|S|(|S|-1)}{2}} \sum_{u,v \in S \ u \neq v} d_{uv} \tag{2}$$

where S represents the set of nodes and d_{uv} represents the shortest path distance between a pair of seed nodes u and v in S.

3.2. Datasets used

Table 1: Real world data-sets for simulation

S.No.	Dataset Name	Description	#Nodes	#Edges
1	Newman-CondMat [36]	This is the co-authorship network of reprints posted to the Condensed Matter section of the arXiv E-Print Archive.	16264	47594
2	US-Airports [37]	The data is downweighted from the Bureau of Transportation Statistics (BTS) Transtats site (Table T-100; id 292) with the following filters: Geography=all; Year=2010; Months=all; and columns: Passengers, Origin, Destination	2939	15677
3	Bitcoin [38]	The datasets contains the details of the members of Bitcoin OTC rate other members in a scale of -10 (total distrust) to +10 (total trust) in steps of 1.	5881	35592
4	Facebook-like [35]	This is a weighted dataset originates from an online community for students at the University of California, Irvine	1899	13838
5	p2p-Gnutella [40]	A sequence of snapshots of the Gnutella peer-to-peer file sharing network from August 2002.	6301	20777
6	Barabasi-2000 [34]	An undirected randomly weighted network based on growth and preferential attachment in scale-free networks.	2000	7984
7	Barabasi-9000 [34]	An undirected randomly weighted network based on growth and preferential attachment in scale-free networks.	9000	35984

4. Methodologies

Hooke's law is stated as follows:

$$F = k.x \tag{3}$$

In this section, we present the depiction of the edges present in the network as springs, which are associated in series and parallel, and present the proposed KSHR algorithm. In a weighted network, weights commonly imply that the higher the weight, the stronger is the association. The same is valid for our KSHR centrality, since we know from Hooke's law that more is the constant of the spring(k) and less is the force (F), lower is the spring stretched (x) as in eq. 3. When we visualize the edges of the graphs as springs, where their edge-weight takes the role of spring constant k, the separation (x) is the parameter

to be minimised between the nodes for the influence maximization. By calculating the separation (x), we can accommodate the various paths that exist between any pair of nodes. We describe the definition of spring terminology below.

Parallel: When Springs are put in parallel, they end up as a joint spring with the complete elasticity of another spring of a spring stretched that can be displayed utilizing the fact that the spring is certainly much stiffer.

Series: It is conceivable to include the commitments of the springs in series. The Springs in series make a progressively increasing spring that will in general stretch more than the springs that are connected.

4.1. Distance Calculation

When two springs of different spring constants, k_1 and k_2 respectively are placed in series with each other, we get:

$$\frac{1}{k_{eq}} = \frac{1}{k_1} + \frac{1}{k_2} \tag{4}$$

When two springs of different spring constants, k_1 and k_2 respectively are placed in parallel with each other, we get:

$$k_{eq} = k_1 + k_2 \tag{5}$$

This means in an actual network is that springs in series are stiffer if the strength of ties in the individual connections is strong. It also implies that more connections from one node to another, add up a single connection, as seen in case of parallel connections. Now the equivalent distance between any of these nodes, under a constant force is given as:

$$x = \frac{f}{k} \tag{6}$$

where $f = weighted - k_shellvalue$ and k = weight of the edge between node i and j When we model edges present in the graph as springs, which are associated in series and parallel.

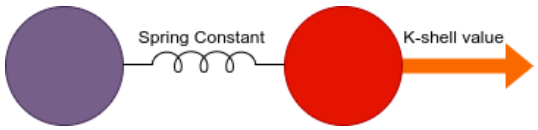

Figure 1: Calculating the heuristic separation between two nodes dependent on weights of the edges, being displayed utilizing springs and assessing to a solitary spring, adhering to Hooke's Law of Elasticity

As shown in Fig. 1, an amount of force acts on each node and hence causes the springs to be stretched. For our method, we consider a constant force acting on each node, which is given by its weighted k-shell value. Thus, the force on every node is given

as $F_0 = wkshell[node]$, which stretches the edges connected to it. We propose a novel weighted k-shell value in this paper.

Our model assumes the node(i) is associated with direct neighbor node (j) with a spring constant k equal to edge weight of w_{ij}. This gives us $k = w_{ij}$ as the spring constant of direct neighbors. By exploiting series and parallel combination of springs, for a given source node we can consider its indirect neighbors as well for the information spread. The value of spring constant k_{eq} for indirect neighbors can be computed using the formula for series and parallel combinations (Eq. 4, and 5). Now, using the value of k_{eq}, we compute equivalent spring stretch distances (x) for direct and indirect neighbors. In our algorithm, we consider the indirect neighbors up to 3-hops by utilizing a Breadth first traversal (BFS) for a given source node (i). Let us consider the node (i) with which our BFS starts and j as one of its indirect neighbors. We calculate the spring constant (k_{eq}) between nodes i and j. The stretch distance (x) between nodes i and j, is given by Eq. 6. Our overall objective here is to minimise the value of stretch distance (x) for the neighbor because a less stretch distance shall mean an increased spreading potential of seed node i implying that information spread by i can easily reach j. Thus, restating the same as follows:

$$\frac{1}{x} = \frac{k}{f} \tag{7}$$

Assuming $f = wkshell[node]$, we can easily see that the full measure of distance in this network is relative. We need to maximise the value of $1/x$ so that the spreading can happen and we name the average of this value as $kshr_value$ of the given node i when connected to all nodes j such that $j \epsilon N_i^3$, where N_i^3 signifies the neighbors upto 3 hops.

$$kshr_value[i] = \frac{(\sum_{j \epsilon N_i^3} w_{ij})}{wkshell[i]} \tag{8}$$

4.2. Calculation of K-Shell Value

$$wk_i = k_shell[i] + \sum_{j \epsilon N_i} \sqrt{w_{ij} * k_shell[j]} \tag{9}$$

Algorithm 1 Weighted K-shell Algorithm

Require: *Graph*

```
1: function WKShells(G)
2:     nodes ← list(G.nodes())
3:     wkshell ← {}
4:     for node in nodes do
5:         wkshell[node] ← kshell[node]
6:         neighbors ← list(G.neighbors(node))
7:         s ← 0
8:         for neighbor in neighbors do
9:             wij ← G[node][neighbor][weight]
10:            s+ = √(wij ∗ kshell[neighbor])
11:        end for
12:        wkshell[node]+ = s
13:    end for
14:    return wkshell
15: end function
```

4.3. Proposed algorithm

The explanation of the algorithm is as follows:

1. We create a *kshr_value* dictionary and initialize for all nodes as in Step 1.
2. Since we wish to minimize x, the stretch distance of the string. We instead maximize $1/x = k/f$ as in Eq. 7. Hence, we create a dictionary named as *spring_constant* of constants from Step 4 and 5 to calculate k.
3. Our BFS happens for 3 hops from the start node in the complete loop from 7 to 13, here N_i^3 denotes all neighbors upto 3 hops.
4. The BFS takes the nodes that have not been visited and initializes them to the value of the parent and combines them in series in Step 9 using equation 4.
5. All the nodes that occur again in the BFS traversal are assumed to be in a parallel connections and add up to the spring constant as in Step 11 as in eq. 5.
6. We calculate the inverse distance for the node by finding the equivalent spring constant (k_{eq} between the neighbor and the current node and dividing it by the node's weighted K-shell value as in step 16 given by Eq. 7.
7. The KSHR Value is calculated based on the addition of these individual distances given by Eq. 8.
8. As, the objective of influence maximization is to select top c nodes, where c is a constant. Here, the top c nodes are the nodes having the maximum KSHR score values in the ranking, and such nodes can be chosen as the influential spreaders.
9. We sort the KSHR value dictionary and return it so that top nodes can be chosen as influential spreaders.

4.4. Time Complexity Analysis

The time complexity of this algorithm is calculated as follows. We traverse on each node of the graph and venture to 3 hops of its neighbors. The steps from line 15-34 give us a time complexity of $O(k^3.n)$. If we assume hat the diameter of the network is fairly large, the average value of $k = n^{1/d}$. Thus giving a loose upper bound of $O(n^{\frac{d+3}{d}}$. In sparse graphs, k is a constant with much lower magnitude and the average complexity is of the order of $O(n)$

Algorithm 2 KSHR Algorithm

```
1: function KSHR(G)
2:     kshr_value ← {}
3:     for each node in graph do
4:         kshr_value[node] ← 0
5:         spring_constant ← {}
6:         N_i^3 ← THREE_HOP_NEIGHBORS(G, node)
7:         for neighbor in N_i^3 perform BFS do
8:             if neighbor in series then
9:                 use Eq 4 for series combination
10:            else
11:                use Eq 5 for parallel combination
12:            end if
13:        end for
14:        wkshell = WKSHELLS(G)
15:        for neighbor in N_i^3 do
16:            kshr_value[node]+ = spring_constant[neighbor]/wkshell[node]
17:        end for
18:    end for
19:    sort(kshr_values)
20:    return kshr_value
21: end function
```

5. Results and Analysis

We perform the experiment of the proposed KSHR method along with the contemporary centrality measures like weighted- degree, weighted betweenness centrality, weighted eigenvector centrality, and weighted voteRank. The investigation has been performed on a toy network and three real-world networks of different nature, application, and size that are listed in Tab 1. We use the SIR model to compute the final infected scale, $f(t_c)$, as a function of spreaders fraction and final infected scale in terms of increasing timestamps. The results were averaged over SIR 100 simulations. For simplicity and to maintain consistency in the analysis for all data-sets, we chose infection rate (β) as 0.01, meaning that when a node is infected, then it can infect 1% of its neighbors randomly.

5.1. Simulation of the proposed algorithm on a toy network

In this section, we simulate the working of the proposed KSHR method using a toy network, as depicted in Fig. 2. The toy network that we use is randomly weighted and has 11 nodes with different edge weights. The force acting on each node is assumed to be equal to the weighted-k-shell value of the node. The traditional K-shell value of the nodes is indicated using colors in Fig. 2. The red colored nodes have K-shell value 3, the blue colored nodes have value 2, and the green colored nodes have a K-shell value 1. The traditional K-shell value will help us calculate the weighted K-shell value as in Eq. 9.

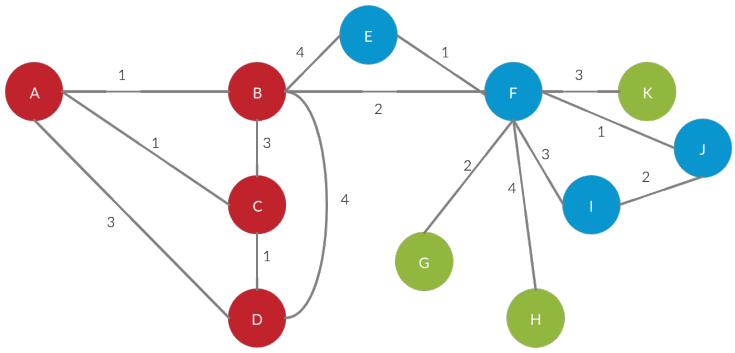

Figure 2: Weighted toy network with 11 nodes to simulate the proposed KSHR centrality

Nodes are connected using weighted-edges represented as springs, based on our algorithm. We aim to find the equivalent spring between all direct and indirect neighbors of a given node using series and parallel spring combination. This relation between series and parallel is illustrated through the example of nodes B and F in this case. As shown in Fig. 3, the spring between B and E is in series with the spring from E to F. The resulting value of resulting spring $B-E-F$ is found using eq. 4. This resulting spring $B-E-F$ is in parallel to the spring between B and F and the net spring between B and F is given by eq. 5.

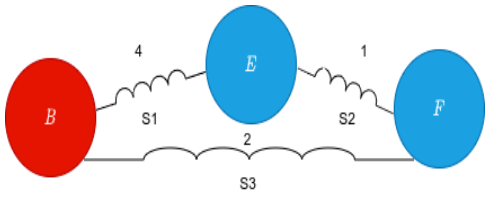

Figure 3: Spring S1 and S2 are in series and the resulting spring is in parallel with S3

Let us consider the steps of the algorithm for a sample node B to find the KSHR-value of B and understand the working of KSHR centrality. Now, we begin processing the algorithm by taking the node B and compute the spring constant for the 1-hop neighbors of B, namely A, C, E, D, and F using the series connection of the spring. After the 1-hop neighbors are covered and we get the 2-hop neighbors by combination series in parallel similar to the example of B, E, and F above. A similar calculation is performed taking all

nodes in the network as the start and performing the computation using series and parallel combination of the direct and indirect weighted edges to calculate the KSHR-value given by eq. 8. Table 2 summarises the computed KSHR-values and F is determined to be the top node for the toy-network.

Table 2: Results on the toy network

Node	K-Shell	WK-Shell	KSHR-Score
A	3	14.660254037844386	0.40297842100090797
B	3	40.88098600800384	1.0447729815375513
C	3	15.928203230275507	0.3469518067328419
D	3	20.660254037844386	0.5588701059990411
E	2	54.61172454625088	0.3578790830315174
F	2	10.342416792648603	3.356840317431281
G	1	3.0	0.36995550589091647
H	1	3.8284271247461903	0.36995550589091647
I	2	8.898979485566356	0.6287575668893135
J	2	6.82842712474619	0.46272587178047
K	1	3.449489742783178	0.4897801816713282

5.2. Simulation of the proposed algorithm on real-life networks

Fig. 4, and Fig. 5 depicts the final infection scale ($f(t_c)$) with respect to the percentage of spreaders for three real-life data-sets with infection rate (β) as 0.01. We consider the percentage of influential spreaders as the seed nodes in the range of 2%, 4%, 6%, 8%, and 10% to plot the final infection scale. In Fig. **??**, note that the number of nodes affected by the infection is maximum for HookeRank on the US-Airports Network for most percentages of spreaders. In Fig. 4, HookeRank greatly exceeds the performance of other algorithms towards increasing the count of the spreader fraction. In the weighted PowerGrid data, shown in Fig. 5, HookeRank performs better than most other algorithms from an early stage. In the weighted PowerGrid data, shown in Fig. **??**, the increase in the number of spreaders results in WVoteRank becoming marginally close to HookeRank, but our algorithm still performs better than all other algorithms in the simulation.

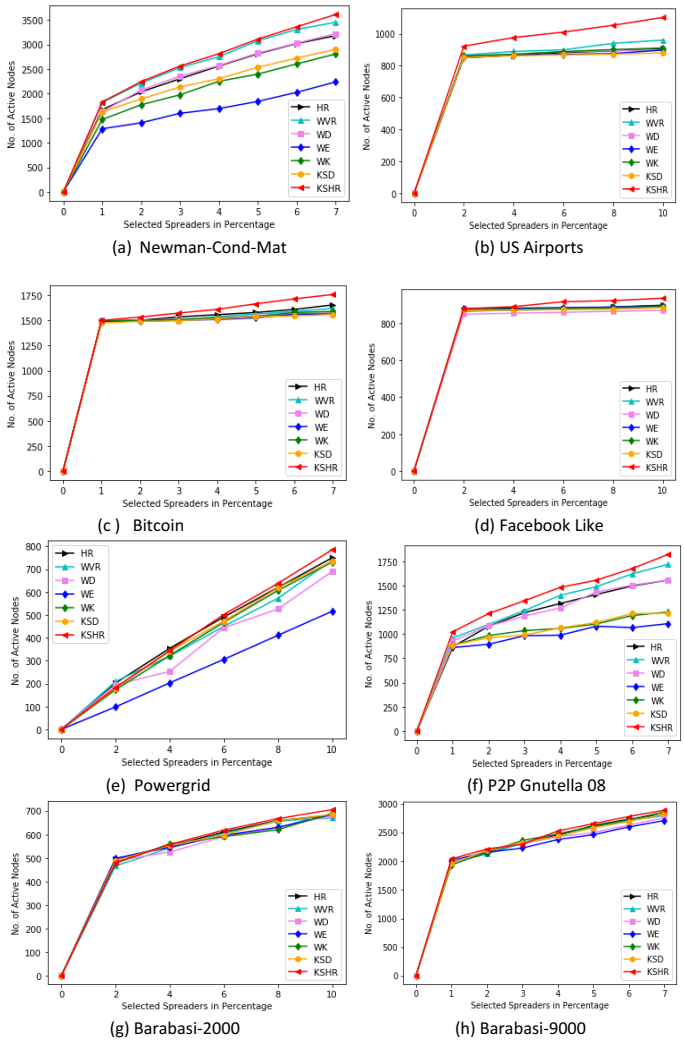

Figure 4: The infection scale with respect to the percentage of spreaders on Facebook-like weighted network with $\beta = 0.01$.

Fig. **??** presents the final infection scale ($f(t_c)$) with respect to the increasing timestamps with infection rate (β) as 0.01 and top 7% influential as seed nodes on US PowerGrid network. Fig. **??** shows the final infection scale ($f(t_c)$) with respect to the increasing timestamps with infection rate (β) as 0.01 and top 5% influential as seed nodes on US PowerGrid network. Fig. **??** displays the final infection scale ($f(t_c)$) with respect to the increasing timestamps with infection rate (β) as 0.01 and top 5% influential as seed nodes on Facebook-like weighted network.

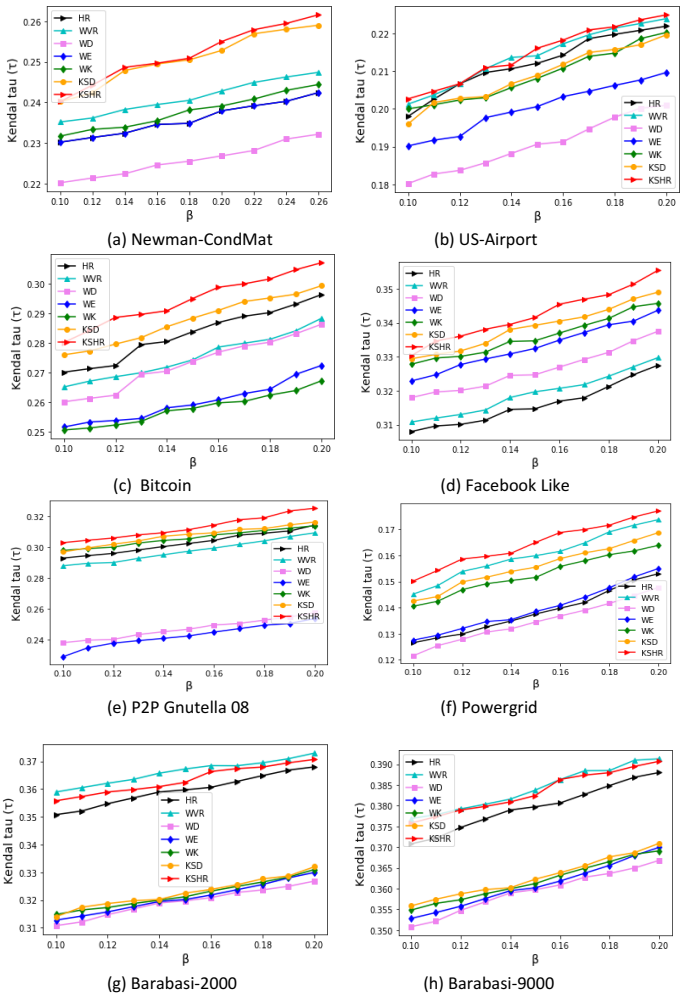

Figure 5: tau vs beta

From above results on three real-life networks, it is evident that HookeRank performs better than state-of-the-art methods like weighted-degree centrality, weighted-betweenness centrality, weighted-eigenvector centrality, and weighted-voteRank, and also stretchedly outperforms recent methods like WVoteRank in terms of final infected scale with respect to time t and spreader fraction p on real-world networks as depicted in Tab. **??**.

Dataset	$L_s(HR)$	$L_s(WVR)$	$L_s(WD)$	$L_s(WE)$	$L_s(WK)$	$L_s(KSD)$	$L_s(KSHR)$
Newman-CondMat	2.80	2.925	2.80	1.18	1.95	2.45	**5.86**
US Airports	1.91	1.82	1.81	1.84	1.72	1.75	**4.02**
Bitcoin	25.02	24.94	24.31	22.41	23.20	24.02	**34.02**
Facebook Like	2.01	1.88	2.02	**2.29**	1.81	1.81	2.05
Powergrid	13.45	14.71	13.45	1.92	5.41	**16.04**	15.17
P2P Gnutella 08	5.46	4.77	5.18	5.39	4.59	4.59	**8.34**
Barabasi-2000	25.62	25.62	25.62	**30.8**	27.10	27.10	26.34
Barabasi-9000	23.62	22.73	22.73	24.11	22.73	22.73	**26.62**

Table 3: Average Shortest Path Length (L_s) values between selected spreaders where HR, WVR, WD, WE, WK, KSD, and $KHSR$ represents HookeRank, weighted VoteRank, weigted degree, weighted Eigenvector, weighted k-shell, weighted k-shell with, and proposed weighted k-shell based HookeRank algorithm respectively.

6. Conclusion

In this paper, we proposed the KSHR method for finding influential nodes in weighted networks by modeling edges of the network as springs and edge weights as spring constants. Initially, we found a measure of the distance between indirect neighbors through the series and parallel combination of edges, by modeling them as springs. Then we proposed a new method of calculating K-shell score on a weighted network. By finding the KSHR value of the nodes, our method locates the top spreaders in the given real-world network to reach a large number of people in the network to maximize the spread of the information. We performed the simulation of the proposed method along with contemporary methods on six real-life data-sets taking the basis of evaluation as the average distance, Kendall tau and Final Infected scale and concluded that the proposed influence maximization KSHR centrality performs considerably well and is effective in real-life scenarios.

References

[1] R. Cohen, S. Havlin, Complex Networks: Structure, Robustness and Function. Cambridge University Press (2010).

[2] M. E. Newman, The structure and function of complex networks. SIAM Review, 45 (2003) 167–256.

[3] M.E. Newman, Analysis of weighted networks. Physical Review E, 70(5) (2004) p.056131.

[4] Granovetter, 1977. The strength of weak ties. In Social networks (pp. 347-367). Academic Press.

[5] T. Opsahl, V. Colizza, P. Panzarasa, J. J. Ramasco, Prominence and control: The weighted rich-club effect. Physical Review Letters 101 (2008) 168702.

[6] D. Kempe, J. Kleinberg, É. Tardos, Maximizing the spread of influence througha social network, Proceedings of the Ninth ACM SIGKDD International Conference on Knowledge Discovery and Data Mining (2003)137–146.

[7] F. Bauer, J. T. Lizier, Identifying influential spreaders and efficiently estimating infection numbers in epidemic models: A walk counting approach, EPL (Europhysics Letters) 99 (2012) 68007.

[8] Zhu, Yu-Xiao, et al. "Social Contagions on Weighted Networks." Physical Review E, American Physical Society, (2017)

[9] B. Doerr, M. Fouz, T. Friedrich, Why rumors spread so quickly in social net-works, Commun. ACM 55(6) (2012) 70–75.

[10] R. Pastor-Satorras, A. Vespignani, Epidemic spreading in scale-free networks, Phys. Rev. Lett. 86 (2001) 3200–3203.

[11] W. Wang, M. Tang, , H.E. Stanley, L.A. Braunstein, Unification of theoretical approaches for epidemic spreading on complex networks. Reports on Progress in Physics, 80(3) (2017) p.036603.

[12] Peng, Sancheng, et al. "Social Influence Modeling Using Information Theory in Mobile Social Networks." Information Sciences, Elsevier, (2016)

[13] Valente, T.W.: Network models of the diffusion of innovations (No. 303.484 V3)(1995)

[14] Chen, W., Wang, C., Wang, Y.: Scalable influence maximization for prevalent viral marketing in large-scale social networks. In Proceedings of the 16th ACM SIGKDD international conference on Knowledge discovery and data mining (pp. 1029-1038). ACM. (2010).

[15] Sun, Y., Liu, C., Zhang, C.X. and Zhang, Z.K.: Epidemic spreading on complex weighted networks. Physics Letters A, 378(7-8), pp.635-640 (2014).

[16] Opsahl, T., Agneessens, F. and Skvoretz, J.: Node centrality in weighted networks: Generalizing degree and shortest paths. Social Networks, 32(3), pp.245-251 (2010).

[17] Prountzos, D. and Pingali, K.: Betweenness centrality. ACM SIGPLAN Notices, 48(8), p.35.(2013).

[18] Wang, H., Hernandez, J., and Van Mieghem, P.: Betweenness centrality in a weighted network (2008).

[19] Zhang, J., Chen, D., Dong, Q. and Zhao, Z.: Identifying a set of influential spreaders in complex networks. Scientific Reports, 6(1) (2016).

[20] Sun, H., Chen, D., He, J. and Ch'ng, E.: A voting approach to uncover multiple influential spreaders on weighted networks. Physica A: Statistical Mechanics and its Applications, 519, pp.303-312. (2019).

[21] Kumar, S. and Panda, B.S.: Identifying influential nodes in Social Networks: Neighborhood Coreness based voting approach. Physica A: Statistical Mechanics and its Applications, p.124215.(2020).

[22] Yu, S., Gao, L., Wang, Y.F., Gao, G., Zhou, C. and Gao, Z.Y.: Weighted H-index for identifying influential spreaders. arXiv preprint arXiv:1710.05272.(2017).

[23] Bihari, A., Pandia, M. K.: Eigenvector centrality and its application in research professionals' relationship network. 2015 International Conference on Futuristic Trends on Computational Analysis and Knowledge Management (ABLAZE).(2015)

[24] Eades, P., Lin, X.: Spring algorithms and symmetry. Theoretical Computer Science, 240(2), 379–405. (2000).

[25] Fruchterman, T.M., Reingold, E.M.: Graph drawing by force-directed placement. Software: Practice and experience, 21(11), pp.1129-1164.(1991)

[26] Kamada, T. and Kawai, S.: An algorithm for drawing general undirected graphs. Information processing letters, 31(1), pp.7-15. (1989).

[27] Slaughter, William S.: The Linearized Theory of Elasticity. Birkhäuser (2001).

[28] Batagelj, V., and M. Zaversnik. "An O(m) Algorithm for Cores Decomposition of Networks." ArXiv.org, 25 Oct. 2003, arxiv.org/abs/cs/0310049.

[29] Eidsaa, Marius. "Core Decomposition Analysis of Weighted Biological Networks." NTNU Open, NTNU, 1 Jan. 1970, ntnuopen.ntnu.no/ntnu-xmlui/handle/11250/2399913.

[30] Al-garadi, Mohammed Ali, et al. "Identification of Influential Spreaders in Online Social Networks Using Interaction Weighted K-Core Decomposition Method." Physica A: Statistical Mechanics and Its Applications, North-Holland, 4 Nov. 2016, www.sciencedirect.com/science/article/pii/S0378437116308068.

[31] Maji, G. (2019). Influential Spreaders Identification in Complex Networks with Potential Edge Weight based k-shell Degree Neighborhood Method. Journal of Computational Science, 101055. doi:10.1016/j.jocs.2019.101055

[32] Wei, Bo, et al. "Weighted k-Shell Decomposition for Complex Networks Based on Potential Edge Weights." Physica A: Statistical Mechanics and Its Applications, North-Holland, 11 Nov. 2014, www.sciencedirect.com/science/article/pii/S0378437114009637.

[33] Hethcote, H.W.: The mathematics of infectious diseases. SIAM Review, 42(4), pp.599-653.(2000).

[34] Yook, S. H., Jeong, H., & Barabási, A. L. (2002). Modeling the Internet's large-scale topology. Proceedings of the National Academy of Sciences, 99(21), 13382-13386.

[35] T. Opsahl and P. Panzarasa: Clustering in Weighted Networks, Social Networks, Vol. 31, No. 2, May, pp. 155-163. doi:10.1016/j.socnet.2009.02.002 (2009).

[36] Newman, M. E. J., 2001. The structure of scientific collaboration networks. PNAS 98, 404-409.

[37] Watts, D. J., Strogatz, S. H.: Collective dynamics of "small-world" networks. Nature 393, 440-442 (1998).

[38] S. Kumar, F. Spezzano, V.S. Subrahmanian, C. Faloutsos. Edge Weight Prediction in Weighted Signed Networks. IEEE International Conference on Data Mining (ICDM), 2016.

[39] Sun, Y., Liu, C., Zhang, C.-X., & Zhang, Z.-K. (2014). Epidemic spreading on weighted complex networks. Physics Letters A, 378(7-8), 635–640. doi:10.1016/j.physleta.2014.01.004

[40] J. Leskovec, J. Kleinberg and C. Faloutsos. Graph Evolution: Densification and Shrinking Diameters. ACM Transactions on Knowledge Discovery from Data (ACM TKDD), 1(1), 2007.

Impact of Reverse Gate Oxide Stacking on Gate All Around Tunnel FET for High Frequency Analog and RF Applications

Amit Das
School of Computational and Integrative Sciences,
Jawaharlal Nehru University,
New Delhi-110067, India.
amitofficial7492@gmail.com

Binod Kumar Kanaujia
School of Computational and Integrative Sciences,
Jawaharlal Nehru University,
New Delhi-110067, India.
bkkanaujia@yahoo.co.in

Vandana Nath
University School Of Information and Communication Technology,
Guru Gobind Singh Indraprastha University,
New Delhi-110078, India.
vandanausit@gmail.com

Sonam Rewari
Department of Electronics and Communication Engineering,
Delhi Technological University,
New Delhi-110042, India.
rewarisonam@gmail.com

R. S. Gupta
Department of Electronics and Communication Engineering,
Maharaja Agrasen Institute of Technology,
New Delhi-110086, India.
rsgupta1943@gmail.com

2020 IEEE 17th India Council International Conference (INDICON) | 978-1-7281-6916-3/20/$31.00 ©2020 IEEE | DOI: 10.1109/INDICON49873.2020.9342175

***Abstract*—We have studied the impact of the reverse gate oxide stacking technique on a typical Gate All Around Tunnel Field Effect Transistor (GAA TFET). For this, we have compared it's performance with the conventional GAA TFET. By reverse gate oxide stacking, we mean that it is a gate oxide stacking technique in which a high-k dielectric constant oxide (k_1) is just fabricated above the channel and another oxide layer with a low-k dielectric constant value (k_2) is formed just above the previous oxide layer where $k_1>k_2$. This significantly improves the device performance. In this paper, DC and AC analysis has been done for both the structures and a detailed comparison has been made for both the structures to demonstrate the usability and efficacy of the proposed reverse gate oxide stacking technique. Various AC performance parameters have been analysed for the proposed reverse gate oxide stacking on the GAA TFET.**

Keywords— Ambipolarity, Band to Band Tunnelling, Gate All Around Tunnel Field Effect Transistor (GAA TFET), Gate Induced Drain Leakage, Metal Oxide Semi-Conductor Field Effect Transistor (MOSFET), Reverse Gate Oxide Stacking and Subthreshold Slope (SS).

I. INTRODUCTION

Tunnel Field-Effect Transistor [1] is the greatest-engineered devices in the field of FET devices. TFET devices came into the existence to overcome the ultra scaling limitations of the MOSFET devices. Various short channel effects such as punch-through, gate induced drain leakage (GIDL), high subthreshold slope, high threshold voltage and a poor high-frequency response became apparent in different MOSFET devices due to their continuous scaling. These shortcomings cannot be removed by using the semiconductors having lower energy band-gap energy or some novel structures using multiple gates because the conventional MOSFET uses the thermionic emission as the carrier transport mechanism. Thus, to overcome the various shortcomings of the conventional MOSFET [2] device, a new device was proposed and came into the picture, i.e. TUNNEL FIELD EFFECT TRANSISTOR (TFET). The carrier transport mechanism of TFET uses band to band tunnelling and also the subthreshold slope (SS) of this device can go below 60mv/decade [3]. The band to band tunnelling in these devices is due to the extremely thin depletion layer at the source-channel and drain-channel interface arising due to the extremely highly doped source and the drain which allows the charge carriers to directly tunnel from the source to drain instead of overcoming the potential barrier. This also leads to lowering of on-state current. High threshold voltage and ambipolar conduction are the few limitations of TFET devices. Now, the main challenge for the engineers was to boost the low on-state current without degrading the other device parameters. Till now, many variants for the TFET have been proposed to overcome the various shortcomings. Variants such as TFET with multiple gates [4,5] and high gate oxide dielectric or a TFET with a thin silicon body were proposed to boost its on-state current. Other variants of TFET with asymmetric drain-source doping or TFET with an underlap gate were proposed to overcome its ambipolarity problem. Ambipolarity is the conduction arising because of both electrons and holes which are predominant in the TFET devices because here doping of the source and the drain are not of the same type (p-type/n-type) which gives rise to the ambipolar conduction. This ambipolar behaviour is highly undesirable in devices because it increases the noise effect and decreases the noise immunity in our FET devices. On the other hand, researchers are concentrating on using high-k gate dielectric material as gate oxide to solve the low on-state current (I_{ON})

978-1-7281-6916-3/20/$31.00 ©2020 IEEE

Authorized licensed use limited to: DELHI TECHNICAL UNIV. Downloaded on February 15,2021 at 10:02:02 UTC from IEEE Xplore. Restrictions apply.

problem of TFET. Using a lower band gap material for the construction of TFET or junctionless TFET devices had shown a great improvement in switching behaviour and low parasitic capacitance at lower voltages [6]. These parasitic or junction capacitance limits the device frequency response which affects the device RF performance. The low band-gap material engineering had shown a great improvement in switching behaviour and a low capacitance at lower voltages. Study shows that using graphene as the alternative material for the channel can drastically increase the ratio of on-current and off-current. A new geometry for TFET was also proposed-Gate All Around (GAA) [7] which further improves the device characteristics. The second geometry feature involves the gate oxide stacking technique. Both these geometries improve the device overall performance. Moreover, observations show that a TFET with a gate oxide stacking and source delta doping [8] can significantly improve the subthreshold slope (SS) characteristics of any device. This paper concentrates meticulously on the reverse gate oxide stacking technique on GAA TFET and analysed its DC & AC behaviour for analog and RF applications. The latest version of ATLAS SILVACO TCAD software has been used for analyzing and simulation [9].

II. STRUCTURAL DESCRIPTION AND SOFTWARE DESCRIPTION

The 3D (three-dimensional) view and the cross-sectional (cut plane) view of a typical GAA TFET has been picturized in fig. 1(a) and fig. 1(b) respectively. Similarly, the 3D (three-dimensional) view and the cut plane view of a typical GAA TFET with the reverse gate oxide stacking has been picturized in fig. 2(a) and fig. 2(b) respectively. The 3D structure shows the cylindrical structure of both the devices whereas the cross-sectional view corresponds to the cut plane view of both the structures.

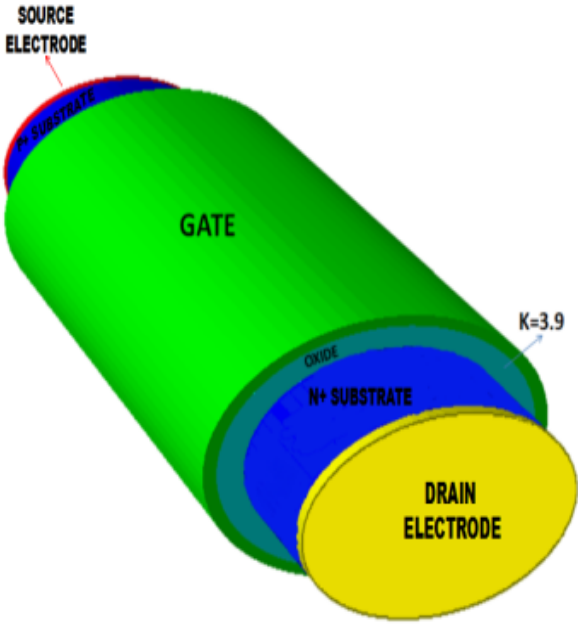

Fig. 1(a). 3D (three-dimensional) view of a typical GAA TFET.

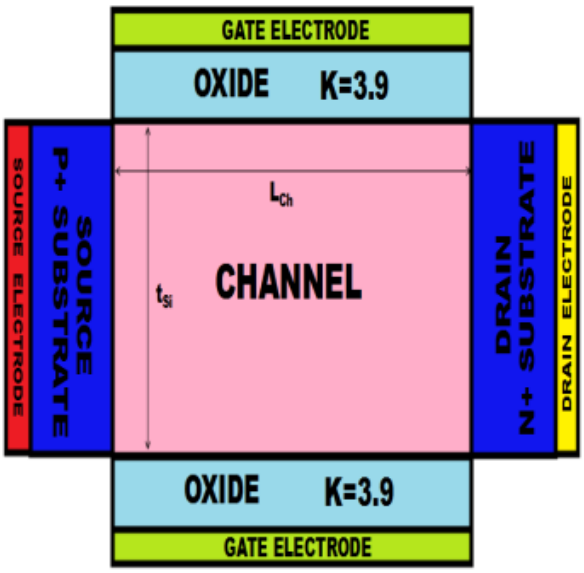

Fig. 1(b). Cut-plane view(two-dimensonal) of a typical GAA TFET.

TABLE I. STRUCTURAL PARAMETERS OF DEVICES

DEVICE PARAMETERS	
PARAMETERS	***VALUES***
Channel Radius (R_{ch})	10 nm
Channel Length (L_{ch})	50 nm
Oxide Dielectric Constant (k)	3.9/21
Source Doping (N_A)	10^{20} cm^{-3}
Channel Thickness (t_{ch})	20 nm
Oxide Thickness (individual layer)	02 nm
Channel Doping	10^{16} cm^{-3}
Electrode Length	01 nm
Source Radius (R_S)	10 nm
Drain Radius (R_D)	10 nm
Gate Work Function (Φ_{Gate})	4.4 ev
Drain Doping (N_D)	10^{18} cm^{-3}

Silicon has been used as a base material for the construction of both the devices and can be considered as a homojunction device because the semiconductor material used for the fabrication of source, channel and drain is same. The individual thickness or the depth of any gate oxide layer used is 2nm for both the simulated devices. Value of the common gate oxide layer has lower dielectric constant value

Authorized licensed use limited to: DELHI TECHNICAL UNIV. Downloaded on February 15,2021 at 10:02:02 UTC from IEEE Xplore. Restrictions apply.

of k=3.9 (low-k value) and that of the other layer has higher dielectric constant value of k=21(high-k value). In the reverse gate oxide stacking, the oxide layer having higher dielectric constant value is kept near to the channel while the oxide layer having lower dielectric constant value is kept near to the gate. The thickness of each electrode is kept 1nm. The permittivity of the SiO_2 layer is 3.9 whereas the permittivity of HfO_2 is 21. The channel length (L_{Ch}) taken under consideration is 50 nm in length. The radius of the channel taken into consideration for the simulation purpose is 10 nm. Radius of the drain and source part is also 10 nm with a depth (length) of 10 nm.

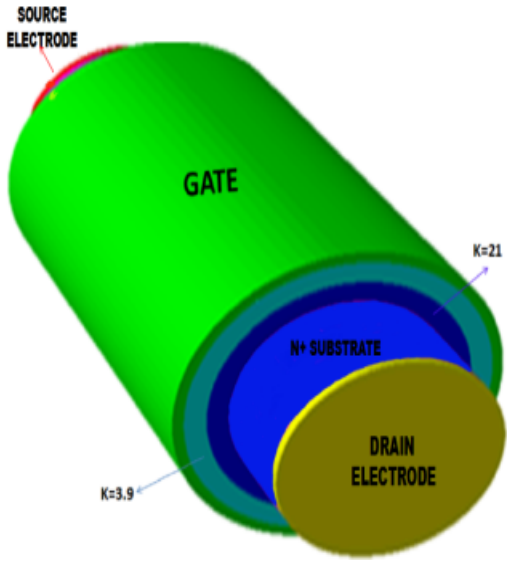

Fig. 2(a). 3D (three-dimensional) view of the GAA TFET with the reverse gate oxide stacking.

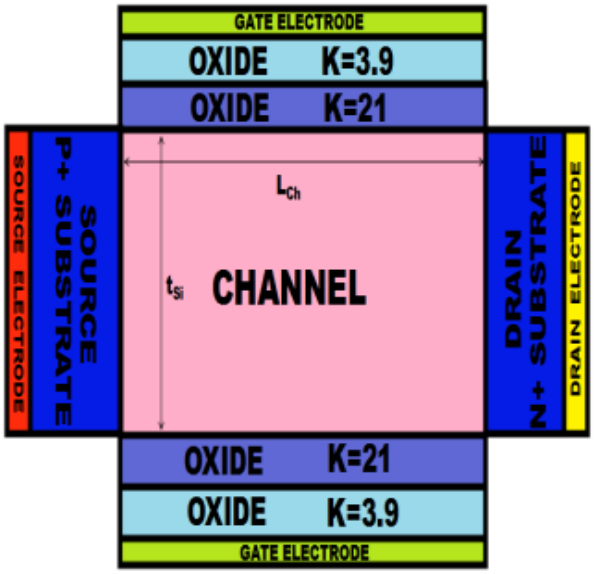

Fig. 2(b). Cut-plane view(two-dimensonal) of the GAA TFET with the reverse gate oxide stacking.

Table 1 summarizes overall framework for both variants in this simulation work. The channel is uniformly doped in both the devices. The doping level of the source is higher than that of the drain. This has been done to suppress the ambipolar behavior which is inherent in any TFET device. Doping of the channel is kept low as compared to the source which has been done to increase the drain current. The latest version of ATLAS SILVACO TCAD software has been used for analyzing and simulation. Generation model that has been used here is BBT.Kl proposed by Klaassen and this model includes both direct and indirect transitions. This is a localized model which is based upon tunneling from band-to-band. The numerical method used here to analyze the complicated mesh equations is based upon Newton-Gummel method.

III. GRAPHS AND RESULT DISCUSSION

This section describes the DC as well as AC performance and analysis of both the variants. Fig. 3 graphically visualizes the drain current (I_{DS}) with the variable potential of drain terminal (V_{DS}) at a constant potential of the gate terminal (V_{GS}=0.5 V) whereas fig. 4 graphically visualizes the drain current with the variable potential of gate terminal at a constant potential of the drain terminal (V_{DS}=1 V).

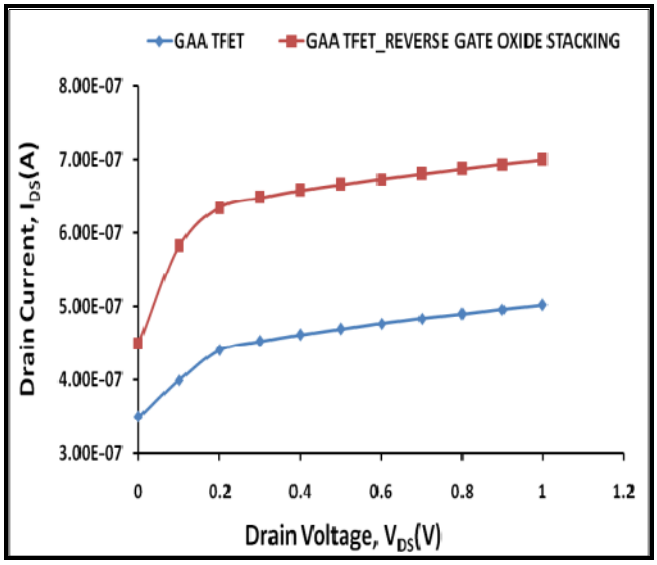

Fig. 3. Drain current (I_{DS}) vs the potential of drain terminal (V_{DS}) in both the variants.

In case of fig. 3, it has to be keeping in mind that the selection of gate voltage is important and a slight variation in the gate voltage can affect the output characteristics. We know that the drain current is dependent on the overdrive voltage and this overdrive voltage reckon on the potential of gate terminal (V_{GS}) and the threshold voltage (V_t). So, selection of gate potential will ostentatiously affect the drain current since this gate voltage is responsible for the channel formation in the GAA TFET device. In case of fig. 4, the potential of drain terminal highly affects the movement of charge carrier flowing across the channel. The improved on-current or drain current is a result due to increased overdrive voltage which is affected by the capacitive stacking. The stacking of gate oxide layer in reverse gate oxide stacking

Authorized licensed use limited to: DELHI TECHNICAL UNIV. Downloaded on February 15,2021 at 10:02:02 UTC from IEEE Xplore. Restrictions apply.

technique allows the same amount of drain current at a lower overdrive voltage. Thus, we can see an improvement in the drain current due to both the gate voltage and the drain voltage.

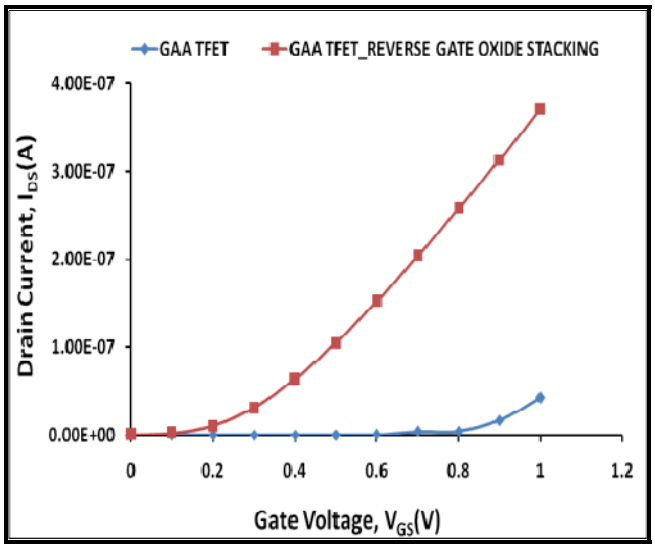

Fig. 4. Drain current (I_{DS}) vs the potential of gate terminal (V_{GS}) in both the variants.

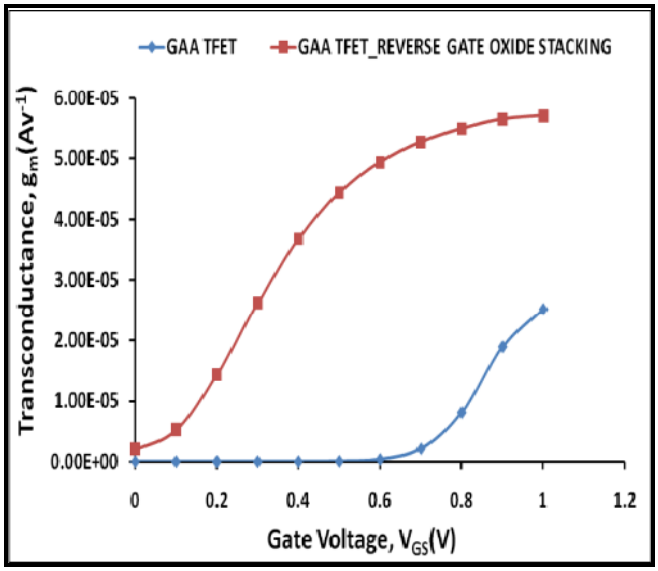

Fig. 5. Transconductance (g_m) vs the potential of gate terminal (V_{GS}) in both the variants.

Fig. 5 shows the graphical variation of transconductance for both the variants of TFET. Transconductance refers to the ratio of on-current or output drain current or drain-to-source current and input gate potential at any constant drain voltage. It's an important device metric for any device to analyze the analog performance. The reverse gate stacking definitely improves the basic features of the conventional TFET. The drain current flowing in a typical TFET device is directly proportional to device transconductance parameter. This device transconductance parameter is directly dependent upon the gate oxide capacitance. Now, adding a gate oxide layer with a high permeability allows us to obtain a relatively high gate oxide capacitance keeping the same thickness. So using a gate oxide layer with a high permeability improves the effective gate oxide capacitance which increases the device transconductance parameter. This improvement in the value of device transconductance value will thereby increase the drain current by a substantial amount. The improvement in the value and the magnitude of on-current or drain current will further improve the transconductance value. A non zero drain current at V_D=0V in the I_D-V_D curve indicates the presence of leakage current due to the short channel. Features like the drain current and transconductance gets improved with the reverse gate stacking technique which is always desirable since high drain current and high transconductance gives high voltage gain for RF and analog applications. A higher value of transconductance ensures large transconductance-generation-factor for any device which is defined as the inherent competency of the device to transmogrify the available DC power efficiently into output AC gain. Higher drain current with minimum channel resistance is always needed for a faithful amplification process since minimum channel resistance enables less hindrance to charge carriers. This minimum channel resistance or on-resistance improves the drain current in the device and a high current can be seen flowing across the channel. The reverse gate oxide stacking technique in GAA TFET helps in minimizing the channel resistance which is evident in the fig. 3, 4 and 5.

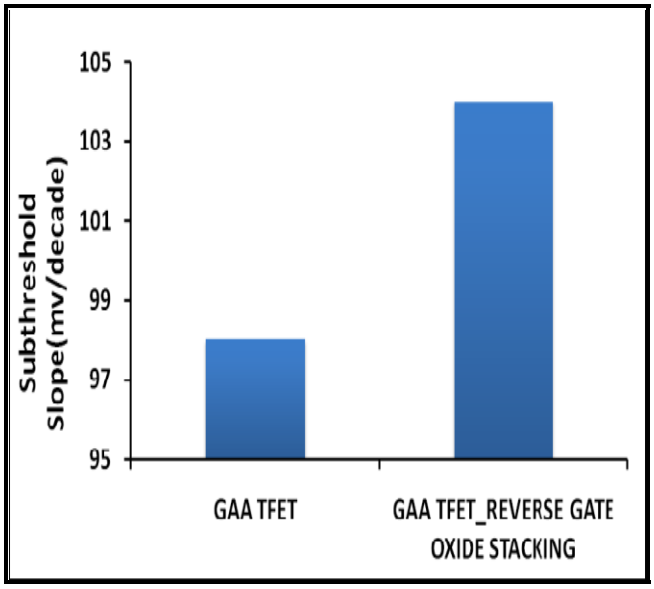

Fig. 6. Comparison of the subthreshold slope (SS) for both the variants.

Fig. 6 and fig. 7 graphically show the column graph comparison of the subthreshold slope and I_{ON}/I_{OFF} ratio for both the variants. Lower sub-threshold slope (SS) leads to low power consumption which is advantageous in low power electronics and a higher I_{ON}/I_{OFF} ratio is desirable for better switching action and high frequency applications. A low subthreshold slope always gives a high value of drain current at low value of gate voltage. The reverse gate oxide

Authorized licensed use limited to: DELHI TECHNICAL UNIV. Downloaded on February 15,2021 at 10:02:02 UTC from IEEE Xplore. Restrictions apply.

stacking increases the SS by a small value with a fractional change less than 0.06 which can be neglected, but the high k dielectric leads to the increment of the I_{ON}/I_{OFF} ratio which indicates high switching speed (needed in switching action for analog applications). I_{ON} current is basically the drain current that is flowing across the channel in both the devices. The reverse gate oxide stacking technique in GAA TFET improves the drain current which ultimately improves the I_{ON}/I_{OFF} ratio of the device.

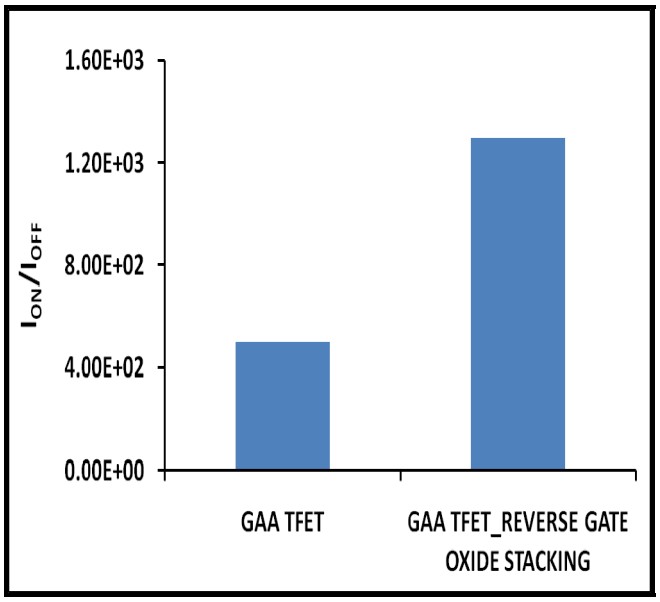

Fig. 7. Comparison of the on-current (I_{ON}) and off-current ratio (I_{OFF}) for both the variants.

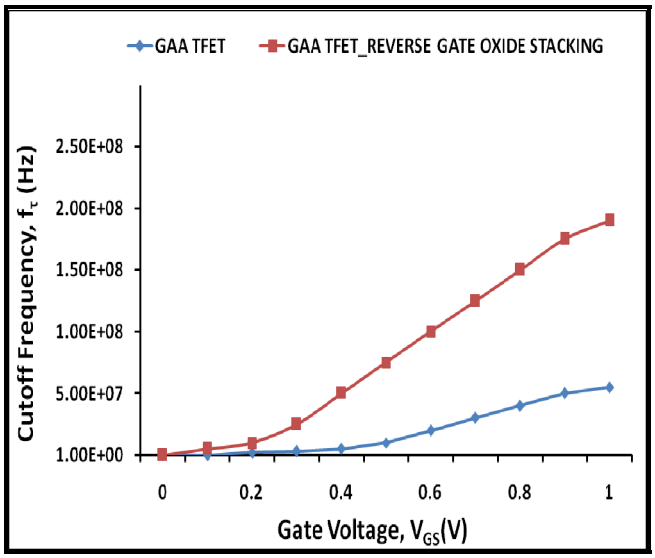

Fig. 8. Variation of the cut-off frequency (f_τ) with the potential of gate terminal (V_{GS}) in GAA TFET and GAA TFET with reverse gate stacking technique.

Fig. 8 shows the graphical variation of cut-off frequency (f_τ) or 3-dB frequency for GAA TFET and GAA TFET with the reverse gate oxide stacking [8-11]. Cut-off frequency limits the high frequency operation of any device, so a high cut-off frequency is always desirable. A larger cut-off frequency indicates that the device can be easily used for wideband applications. And a GAA TFET with the reverse gate oxide stacking gives a high on-current, a high I_{ON}/I_{OFF} ratio and a high 3-dB or cut-off frequency when compared to the conventional structure. The cut-off frequency of a GAA TFET is limited by mainly its junction capacitance and coupling capacitance. Also, this cut-off frequency directly varies with the transconductance and the transconductance improves with the reverse gate oxide stacking technique. Compared to a single layer gate oxide, a double layer gate oxide stacking is much better because of the better electrical response offered by the device. The equivalent gate oxide thickness is much lesser than the actual gate oxide thickness in the case of reverse gate oxide stacking.

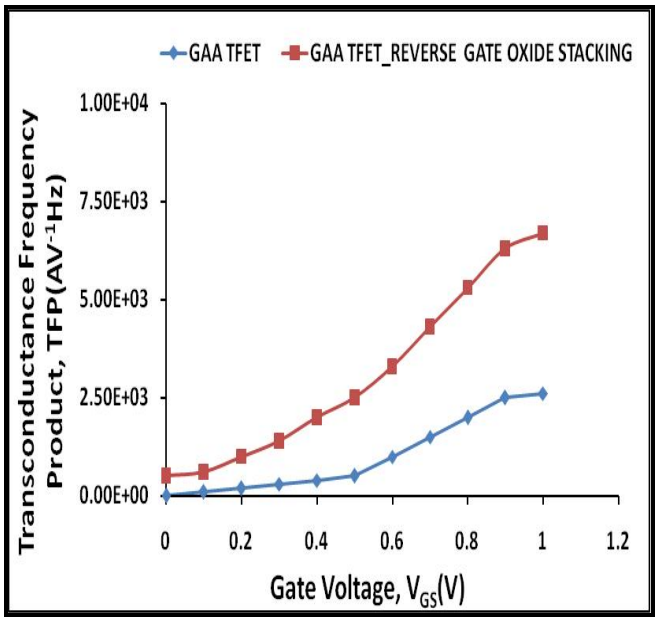

Fig. 9. Variation of the transconductance frequency product (TFP) with the potential of gate terminal (V_{GS}) in GAA TFET and GAA TFET with reverse gate oxide stacking technique.

Fig. 9 shows the graphical plot of the transconductance frequency product (TFP) and the applied potential in the gate terminal for both the device variants. TFP for any device is defined as the product the transconductance and the cut-off frequency and practically, its value must be high. A high TFP is always desirable for analog and RF applications and its value improve with the reverse gate oxide stacking because of the increment in the value of transconductance and cut-off frequency because of the addition of the extra gate oxide layer with high permeability above the body/channel of the variant. This additional layer improves the current flowing in the device and the cut-off frequency, which is responsible for the improvement in the value of TFP. The selection as well as the placement of the gate oxide layer plays a very vital part in influencing the electrical characteristics and the analog performance. The addition of a gate oxide layer in reverse gate oxide stacking

Authorized licensed use limited to: DELHI TECHNICAL UNIV. Downloaded on February 15,2021 at 10:02:02 UTC from IEEE Xplore. Restrictions apply.

has improved the various device metrics of the conventional GAA TFET and hence, this reverse gate oxide technique is useful in improving the device overall performance.

IV. CONCLUSION

This paper proposes a very different reverse gate oxide engineering technique for GAA TFET and the simulation results are juxtaposed, compared and graphically analyzed with the conventional structure of GAA TFET. DC and AC analysis have been done to check its suitability for high frequency analog and RF applications. The simulation results implies that the addition of the reverse gate oxide stacking in the conventional GAA TFET shows a tremendous improvement in the analog performance (f_τ, TFP, I_{ON}/I_{OFF} ratio). Other important parameters like transconductance (g_m) and drain current (I_D) gets improved with the reverse gate oxide stacking used in GAA TFET. Although various parameters got improved but the value of SS degrades by a fractional amount and even the drain current does not get substantially improved with the reverse gate oxide stacking. But considering the overall DC and AC performance of both the devices, these simulation results clearly indicates that the reverse gate oxide stacking is useful in improving the RF analog behaviour of GAA TFET. The result of this DC and AC analysis implies that the reverse gate oxide stacking technique can be used with GAA TFET for various practical analog applications like amplifiers, data storage devices, high speed switching circuits where switching speed must be high, low power electronics , biosensing applications etc.

REFERENCES

[1] G. B. Beneventi, E. Gnani, A. Gnudi, S. Reggiani, and G. Baccarani, "Can interface traps suppress TFET ambipolarity?," *IEEE Electron Device Lett.*, 2013.

[2] S. Strangio *et al.*, "Digital and analog TFET circuits: Design and benchmark," *Solid-State Electronics*. 2018.

[3] W. G. Vandenberghe, A. S. Verhulst, G. Groeseneken, B. Sorée, and W. Magnus, "Analytical model for a tunnel field-effect transistor," in *Proceedings of the Mediterranean Electrotechnical Conference - MELECON*, 2008.

[4] A. Narendiran, K. Akhila, and B. Bindu, "A Physics-Based Model of Double-Gate Tunnel FET for Circuit Simulation," *IETE J. Res.*, 2016.

[5] L. Zhang, X. Lin, J. He, and M. Chan, "An analytical charge model for double-gate tunnel FETs," *IEEE Trans. Electron Devices*, 2012.

[6] B. Ghosh and M. W. Akram, "Junctionless tunnel field effect transistor," *IEEE Electron Device Lett.*, 2013.

[7] M. Kumar, S. Haldar, M. Gupta, and R. S. Gupta, "Impact of gate material engineering(GME) on analog/RF performance of nanowire Schottky-barrier gate all around (GAA) MOSFET for low power wireless applications: 3D T-CAD simulation," *Microelectronics J.*, 2014.

[8] S. Dash, G. S. Sahoo, and G. P. Mishra, "Improved Cut-off Frequency for Cylindrical Gate TFET Using Source Delta Doping," *Procedia Technol.*, 2016.

[9] Silvaco International, ATLAS User Manual 2010 (Silvaco International, Santa Clara, 2010).

[10] Upasana, R. Narang, M. Saxena, and M. Gupta, "Modeling and TCAD assessment for gate material and gate dielectric engineered TFET architectures: Circuit-level investigation for digital applications," *IEEE Trans. Electron Devices*, 2015.

[11] S. Rewari, R. S. Gupta, S. S. Deswal and V. Nath, "Silicon carbide based DSG MOSFET for high power, high speed and high frequency applications," 2014 *IEEE 6th India International Conference on Power Electronics (IICPE),* Kurukshetra, pp. 1-4, 2014.

Authorized licensed use limited to: DELHI TECHNICAL UNIV. Downloaded on February 15,2021 at 10:02:02 UTC from IEEE Xplore. Restrictions apply.

Multimedia Tools and Applications
https://doi.org/10.1007/s11042-021-10643-3

Impulse noise removal in color image sequences using fuzzy logic

Isha Singh[1] · Om Prakash Verma[1]

Received: 26 February 2020 / Revised: 17 January 2021 / Accepted: 4 February 2021
Published online: 17 February 2021
© The Author(s), under exclusive licence to Springer Science+Business Media, LLC part of Springer Nature 2021

Abstract
This paper presents a two-step fuzzy filter to remove impulse noise from a color image sequence in RGB color space. The primary filter recognizes the pixels corrupted by impulse noise. It also computes the extent of noise and afterward rectifies them. The output of the first filter acts as an input to the secondary filter and further refines the outcome to give the final output. Excellent alignment is seen between noise removal and structure conservation of an image due to the classifying nature of the algorithm. To minimize blurring, noisy pixels are exclusively rectified and noise-free pixels remain intact. The proposed filter is a 3-D Spatio-temporal filter that considers spatial, temporal as well as color information. A pixel of one color component is compared to its neighboring pixels within the same frame and with the corresponding pixels in neighboring frames. It is likewise compared with the pixels of the other two color components. Peak Signal to Noise Ratio (*PSNR*) and structural similarity index (*SSIM*), Miss Detection (*MD*), and False Alarm (*FA*) rates are utilized as a performance metric. The experimental result of several color image sequences demonstrates the efficacy of the proposed fuzzy filter both qualitatively and quantitatively.

Keywords Impulse noise · Spatio-temporal filter · Peak signal to noise ratio · Fuzzy filter

1 Introduction

The signal is the intrigued, structured information which is the critical piece of the data that we need to assess. On the contrary, Noise represents itself as the irregular and undesirable variations in the measured signal. Noise in images is an inconsistent, improper deviation in photometric brilliance or color information. With the rise in technology, noise removal has become an

✉ Isha Singh
222ishasingh@gmail.com

Om Prakash Verma
opverma.dce@gmail.com

[1] Department of Information Technology, Delhi Technological University, Delhi, India

important aspect of multimedia devices. It is undesirable and intrusive that yields wrong pixel values. Counter-factual image acquisition and transmission are the two major causes of the introduction of noise in images.

A video sequence is the broadcasting of visual images or frames at a certain frame rate per second unit of time. The number of frames displayed per second depends on the type of application and user requirements. These frames or images get contaminated by image noise as a result of various anomalies. Among many types of image noises [18, 23], impulse noise often degrades the quality of an image. In literature, it is also termed as salt and pepper noise.

Over the years, there is a massive advancement in the technology used for the removal of impulse noise. Various researchers have utilized fuzzy systems to enhance the performance of their algorithms. Along with fuzzy systems, there is a substantial rise in the use of neural networks for noise removal [16]. Both neural networks and fuzzy logic provide exemplary results in the absence of a proper mathematical model of the given problem. E.g. pattern recognition, regression or density estimation, etc. A combination of these two concepts like fuzzy neural networks or Neuro-fuzzy systems is also utilized in various applications for image analysis in various fields. A Neuro-fuzzy system computes the parameters of a fuzzy system with the help of approximation techniques from neural networks. Convolutional Neural Networks [10] are the latest advancements used for image processing. Neural fuzzy methods need to access the entire image for weights assignment, but Convolutional Neural Networks (CNN) can deal with a small section of the image with the least number of weights. All the systems have their pros and cons, but with real-time systems, the algorithm should be of practical use. Despite good results, the formulation of such algorithms based on deep learning, sometimes becomes a tedious task. The computation time rises with the complexity of an algorithm and it is not apt for the real-world environment. Therefore, In our work, we have utilized fuzzy logic to derive an intuitive and efficient algorithm for impulse noise removal with practical computation time. These features make our algorithm more suitable to be used with real-time applications and multimedia devices.

This paper proposes a Spatio-temporal filter that removes impulse noise from the video using fuzzy logic. It is a double-stage filter that calculates the degree to which the pixel is noisy and removes the noise from it accordingly. Hence, only the noisy pixels are corrected and un-corrupted pixels are left untouched. The unique characteristic feature of this filter to exploit the spatial correlation and temporal correlation along with color components in a two-step process makes it work even with high impulse noise presence up to 70%. The video denoising performance is evaluated by the peak signal-to-noise ratio (*PSNR*) and structural similarity index (*SSIM*). Miss detection (MD) and False alarm (FA) rates are also computed. The experimental results on several videos proved the efficacy of the proposed filter as compared to other well-known video filters.

The paper is constituted sequentially. Section 2 presents the literature review and contribution of the paper, Section 3 defines the proposed Spatio-temporal filter to minimize impulse noise. Results and analysis, parameter selection, and comparison with other filters are depicted in Section 4. Lastly, the conclusion is provided in Section 5.

2 Literature review and contribution of the paper

2.1 State of the art filters for impulse noise

Spatial filters play a substantial role to suppress impulse noise from images. They exploit the image plane itself for their processing. Most of the filters developed for video are 2-D spatial

filters that filter the individual frames of the video progressively. To expel impulse noise, assortments of linear and nonlinear filters have been presented by different researchers. It is seen that non-linear techniques outdo the linear procedures in terms of their proficiency in recognizing and expelling noise.

To eliminate noise from images, many filters have employed fuzzy logic in the past [11]. Fuzzy filters provide both edge preservation and precision. Several filters are found in literature like the Fuzzy Directional (FD) filter [38, 40], Fuzzy random impulse noise removal from color image sequences which uses noise adaptive mean absolute difference along with fuzzy logic [35], fuzzy filter with type-2 fuzzy inference systems [50], Fuzzy two-step filter [43], Fuzzy random impulse noise removal [36] and Region adaptive fuzzy filter [42] to name a few. Median (*MED*) filter is a notable non-linear filter utilized as a foundation in numerous filters since it disposes of the noise and performs the filtering process effectively even in the soft area of an image. Various varieties of median filters, namely center-weighted median [26], tri-state median filter [31], direction based adaptive weighted switching median filter [37], vector median filters [8], switching weighted vector median filter [48], modified switching median filter [47], Combination of adaptive vector median filter and weighted mean filter [41], Decision Based Unsymmetric Trimmed Median Filter [17], Iterative grouping median filter [13] and many more. A combination of fuzzy logic and median filter has proved as an efficient tool for noise removal in images. Some state-of-art filters based on this combination are Adaptive fuzzy inference system based directional median filter [20], Fuzzy Directional Median Filter [25], cluster-based adaptive fuzzy switching median filter [22], Fuzzy reasoning-based directional median filter [24], adaptive fuzzy median filter [46, 49] and many more. The use of fuzzy logic and median filters in our work has enhanced the noise removal capacity alongside the conservation of image details.

All the above-mentioned filters are also known as intra-frame filters as they consider only one frame at a time and remove the noise independent of the neighboring frames. By considering only one frame at a time they neglect the temporal relation between frames of the video. On the contrary, temporal filters are inter-frame filters that analyze the relationship between the subsequent frame and neglect the spatial correlation [19, 39]. For the enhanced performance of any filter for noise removal in videos, along with spatial information, there should be some parameters for proper motion estimation as well. In the current scenario of the technology boom, Spatio-temporal filters provide superior results. Spatio-temporal filters are those filters that take into account both the spatial as well as temporal correlation and remove noise from video by considering the current frame as well as the next frame [9, 28]. A study of various filtering schemes to remove noise in the color image frame or video can be found in the paper by Maity et al. [32].

Spatio-temporal filters also employ various systems like fuzzy systems, neural networks, Neuro-fuzzy systems [30], optimization techniques [21], and so on. E.g., a paper by Lee et.al [29], which is a noise adaptive filter designed for low light levels. It requires extra hardware implementation using various modules which increases the overall system cost. Another paper by Szczepanski [45] introduces a Spatio-temporal based on digital paths which provide good results but are quite computation intensive in nature. Chervyakov et.al [14] proposed a method based on the Lorentz function and utilized adaptive filtering for video denoising. These types of algorithms which include double processing stages excel better than other algorithms having a single module for noise detection. Therefore, in our work, we have introduced two-phase detection of impulse noise. The result of the primary filter acts as input to the secondary filter so that results are more refined and accurate.

Researchers utilize the algorithms to clean the images and videos for various applications like astronomical videos [2], to enhance the video technology [15, 34], for military surveillance, medical images, and many more. Noise removal is essential before further processing of images and videos. For different application fields as per user requirements, the algorithms for impulse noise can be combined with other technologies as well for efficient image processing. For example, in medical images, we often need to segment a region of interest and then operate on them. Performing image segmentation techniques and then processing them for noise removal is quite useful. Image segmentation techniques also utilize fuzzy systems and their modifications. Fuzzy logic enhances the segmentation results for medical imagery. The concepts of video noise removal can be incorporated for medical 3-D volumes. Few techniques on 3-D volumes of medical images are [1, 3–6]. Mahmoud et.al integrated the graphics processing unit (GPU) with Fuzzy C-Means (FCM) [1] to form a hybrid filter for 3-D volumes. FCM is established as an efficient tool for clustering unsupervised data and is used in various methods for noise removal and segmentation in images. Other techniques based on FCM, devised for volume reconstruction are by Shadi et.al [3]. The algorithms are robust which provides good results. Image segmentation is altogether a vast research field in which the noise removal techniques can be merged for enhanced results.

Fuzzy systems play an important role in the methodologies devised for image processing. For real-time applications as discussed above, fuzzy logic provides more efficient results and is less computationally intensive as compared to other systems. Therefore, in our work, we propose a Spatio-temporal filter that removes impulse noise from the video using fuzzy logic to enhance the decision making capability of our algorithm. Nevertheless, a variety of methods are present in literature to remove noise from a color image sequence, most of them are either unable to provide desirable results or provide results only with low noise density. The proposed work calculates the degree to which the pixel is noisy and then removes the noise from it accordingly. Hence, only the noisy pixels are processed, which maintains the basic image structure. For noise removal in a color image sequence, along with spatial and temporal information, color information in other bands is required as well. Hence, the noise is corrected by considering the current frame, the neighboring frames, and the values of the other color components. Five membership functions are defined which provide complete spatial, temporal, and color information about the pixel. A Fuzzy rule is then applied to each pixel to check if it is degraded by noise or not. If the pixel is observed to be noisy, it is restored using the median value computed exclusively from the pixels free from noise in their neighborhood otherwise it is not changed. It is a robust technique that can handle the high impulse noise presence of up to 70%. The video denoising performance is evaluated by the peak signal-to-noise ratio (*PSNR*), structural similarity index (*SSIM*), false alarm (FA), and miss detection (MD) rates. The experimental results on several videos proved the efficacy of the proposed filter as compared to other well-known methods.

2.2 Main contributions of the paper

The main contributions of the proposed work are as follows:

- A novel algorithm is proposed using fuzzy logic for color video sequences in RGB color space. For efficient noise removal in videos, along with spatial and temporal information, the color band information is also important. The proposed work examines all the aspects of the processing pixel to provide proper results. It is a Spatio-temporal filter that considers

the current frame, the neighboring frames, and the values of the other color components for efficient impulse noise removal. Five membership functions are defined which provide complete spatial, temporal, and color information about the pixel.

- The use of fuzzy logic has enhanced the decision-making capacity of the filter. The algorithm has double detection stages, which aids in more refined results and provides lower false alarm and miss detection values. With efficient noise removal, the algorithm also maintains the basic structure of the video, and blurring is reduced. The quality of the denoised video is quite impressive both quantitatively and qualitatively.
- The algorithm has a simple structure as compared to complex methods based on neural networks, Neuro-fuzzy, and so on. It can be easily implemented for real-time applications with minimal cost. The computation timings are quite low as compared to other state of art techniques present in literature. This makes our work more apt for practical use in a real-world application, where along with efficient noise removal, the speed of the algorithm is also an important aspect.
- The proposed algorithm is evaluated by four performance metrics namely PSNR, SSIM, MD, and FA rates. Besides the computation timings are also computed for standard video sequences. Sometimes, despite good results at low noise levels, the performance of any filter degrades at high noise levels. The extensive simulation results depict that our work is a robust technique whose performance is not degraded with rising noise densities up to 70%.

3 The Proposed Work

The proposed work is devised for the color image sequence impaired with impulse noise. A pixel of a given color component can be corrupted with noise by some probability '*p*'.The neighboring pixels of the given color component as well as the relating pixels in the other color component can be noisy or noise-free independent of this pixel.

Mathematically, noisy sequence 'f_n' is represented in Eq. (1):

$$f_n\left(v^x, v^y, v^z, N^F\right) = \begin{Bmatrix} f_o\left(v^x, v^y, v^z, N^F\right) : for 1-p \\ N\left(v^x, v^y, v^z, N^F\right) : for\ p \end{Bmatrix} \quad (1)$$

Where the probability 'p' of a pixel being noisy ranges between $[0,1]$, f_n is the noisy sequence, f_o is the original (noise-free) sequence, N is the noise value of the pixel, (v^x, v^y) corresponds to the pixel location in a video sequence, v^z corresponds to one of the three color components, $v^z = 1, 2, 3$ for Red, Blue and Green components respectively and N^F corresponds to the frame number.

E.g. $f\ (v^x, v^y, 1, N^F)$ corresponds to the red component of the pixel at $v^x{}_{th}$ row and $v^y{}_{th}$ column in the current frame N^F. This notation is followed throughout the paper.

The impulse noise from the color image sequence is removed in two progressive steps of filtering. The primary filter detects the noisy pixels alongside the measure of noise present and then rectifies them by utilizing the median computed from pixels free from noise. The output of the primary filter acts as an input to the secondary filter where it is further refined to give the final output. A Fuzzy rule operates on every pixel to check if it is noisy or noise-free. Depending on the outcome, the algorithm proceeds.

3.1 Primary filter

The main objective of the primary filter is the proper detection and rectification of impulse noise. The pixels, altered due to impulse noise are detected in this step along with the amount of noise with which they are corrupted. After detection, the median value calculated from noise-free pixels in the present window restores the noisy pixels.

Consider one color component, say a red component of the current frame N^F in a noisy image sequence. The extent of noise present in a pixel at position (v^x, v^y) is attained via the *fuzzy Rule 1* stated below:

***Rule 1**:*

IF (($f(v^x,v^y,1,N^F)$ - $med(v^x,v^y,1,N^F)$ is ***Big***).

AND (the degree of similarity of $f(v^x, v^y, 1, N^F)$ to its neighboring pixel in N^F is ***Dissimilar***).

AND ($f(v^x, v^y, 1, N^F)$ is ***Terminal***).

AND ((either the difference between the $f(v^x, v^y, 1, N^F)$ in N^F and $f(v^x,v^y,1, N^F -1)$ in $N^F -1$ is ***High***).

OR (the difference between $f(v^x, v^y, 1, N^F)$ in N^F and $f(v^x, v^y, 1, N^F + 1)$ in $N^F + 1$ is ***High***)).

AND (the degree of similarity $f(v^x, v^y, 1, N^F)$ to its neighboring pixels in $N^F -1$ is ***Variant***).

THEN $f(v^x, v^y, 1, N^F)$ is noisy.

Where $f(v^x, v^y, 1, N^F)$ is the central pixel under evaluation, N^F denotes the current frame, $N^F + 1$ is the next frame, and $N^F -1$ is *the* preceding frame. $f(v^x, v^y, 1, N^F -1)$ denotes the comparable pixel in the preceding frame, $f(v^x,v^y, 1, N^F + 1)$ is the relating pixel in the next frame and $med(v^x, v^y, 1, N^F)$ is the median value computed from noise-free pixels in the current window. Mathematically, the amount of noise that exists in the red component of a pixel at position (v^x, v^y) in the current frame N^F is evaluated as:

$$N_1\left(v^x, v^y, 1, N^F\right) = min\left\{\begin{matrix}\mu_b\left(D\left(v^x, v^y, 1, N^F\right)\right), \mu_d\left(v^x, v^y, 1, N^F\right), \mu_{ter}\left(v^x, v^y, 1, N^F\right), \\ \mu_h\left(v^x, v^y, 1, N^F\right), \mu_v\left(v^x, v^y, 1, N^F\right)\end{matrix}\right\} \quad (2)$$

Where μ_b, μ_d, μ_{ter}, μ_h *and* μ_v are the five membership functions that represent the five fuzzy sets Big, Dissimilar, Terminal, High and Variant respectively. '*D*' denotes the distinction between the center pixel and the median value. Mathematically,

$$D\left(v^x, v^y, 1, N^F\right) = \left|f\left(v^x, v^y, 1, N^F\right) - med\left(v^x, v^y, 1, N^F\right)\right| \quad (3)$$

Likewise, to compute the difference in the remaining two color components $v^z = 2, 3$ for Blue and Green components respectively. The same is followed throughout the paper.

The median value is estimated only from the noise-free pixels present within the window to modify the noisy pixel under interest. Unique median values are calculated for all the color components. This median value is used instead of a simple median value due to its superior performance in both qualitative as well as quantitatively. The Algorithm is described below:

Step 1) Select a 3×3 window size to center on the present pixel to be processed in the noisy frame.

Step 2) Every pixel of the window is organized into a vector and is sorted in ascending order to compute the median value.

Step 3) Difference between the obtained median value and every window pixel is computed.
Step 4) Pixels carrying the difference value ≤ parameter δ are organized into a new vector.
Step 5) The new vector is sorted in ascending order to get the new median value (*med*).

3.1.1 Fuzzy set: big

A noisy pixel exhibits a bigger difference with the median value. It is denoted via a membership function μ_b, which is used for the fuzzy set "**Big"**, which illustrates the huge difference. After calculating the difference D, μ_b is calculated for each color component as:

$$\mu_b\left(D\left(v^x, v^y, 1, N^F\right)\right) = \left\{ \begin{array}{cc} 1, & D\left(v^x, v^y, 1, N^F\right) \geq \alpha_2 \\ \frac{D\left(v^x, v^y, 1, N^F\right) - \alpha_1}{\alpha_2 - \alpha_1}, & \alpha_1 \leq D\left(v^x, v^y, 1, N^F\right) < \alpha_2 \\ 0, & D\left(v^x, v^y, 1, N^F\right) < \alpha_1 \end{array} \right\} \quad (4)$$

The parameters α_1 and α_2 in the above equation are obtained experimentally.

3.1.2 Fuzzy set: dissimilar

A pixel with more number of similar neighboring pixels, the less are the chances of a given pixel being noisy. For this, a similarity criterion is used to decide whether the given pixel is similar to its neighboring pixels or not. Also, if we want to find the similarity of a red component of a pixel, we will find its interaction with the other two color components as well to ascertain the extent of the similarity.

To discover whether the red component of a pixel at location (v^x, v^y) matches with its adjacent pixels at the location $(v^x + i, v^y + j)$, we have to find the following differences. The variation amongst the red and green components (d_{rg}) and the red and blue components (d_{rb}) for (v^x, v^y) is estimated using the following equations:

$$\mathrm{d_{rg}}\left(v^x, \mathrm{v}^y, 1, N^F\right) = \left|\mathrm{f}\left(v^x, \mathrm{v}^y, 1, N^F\right) - \mathrm{f}\left(v^x, \mathrm{v}^y, 2, N^F\right)\right| \quad (5)$$

$$\mathrm{d_{rb}}\left(v^x, \mathrm{v}^y, 1, N^F\right) = \left|\mathrm{f}\left(v^x, \mathrm{v}^y, 1, N^F\right) - \mathrm{f}\left(v^x, \mathrm{v}^y, 3, N^F\right)\right| \quad (6)$$

In the same manner, the variations for the neighboring pixels $(v^x + i, v^y + j)$ are estimated using the following equations:

$$\mathrm{d_{rg}}\left(v^x + \mathrm{i}, \mathrm{v}^y + \mathrm{j}, 1, N^F\right) = \left|\mathrm{f}\left(v^x + \mathrm{i}, \mathrm{v}^y + \mathrm{j}, 1, N^F\right) - \mathrm{f}\left(v^x + \mathrm{i}, \mathrm{v}^j + \mathrm{j}, 2, N^F\right)\right| \quad (7)$$

$$\mathrm{d_{rb}}\left(v^x + \mathrm{i}, \mathrm{v}^y + \mathrm{j}, 1, N^F\right) = \left|\mathrm{f}\left(v^x + \mathrm{i}, \mathrm{v}^y + \mathrm{j}, 1, N^F\right) - \mathrm{f}\left(v^x + \mathrm{i}, \mathrm{v}^y + \mathrm{j}, 3, N^F\right)\right| \quad (8)$$

The variation amongst the above-combined components at the pixel locations (v^x, v^y) and $(v^x + i, v^y + j)$ is derived using the following equations:

$$\Delta_{\mathrm{rg}}\left(v^x+\mathrm{i},\mathrm{v}^y+\mathrm{j},1,N^F\right)=\left|\mathrm{d}_{\mathrm{rg}}\left(v^x+\mathrm{i},\mathrm{v}^y+\mathrm{j},1,N^F\right)-\mathrm{d}_{\mathrm{rg}}\left(v^x,\mathrm{v}^y,1,N^F\right)\right| \tag{9}$$

$$\Delta_{\mathrm{rb}}\left(v^x+\mathrm{i},\mathrm{v}^y+\mathrm{j},1,N^F\right)=\left|\mathrm{d}_{\mathrm{rb}}\left(v^x+\mathrm{i},\mathrm{v}^y+\mathrm{j},1,N^F\right)-\mathrm{d}_{\mathrm{rb}}\left(v^x,\mathrm{v}^y,1,N^F\right)\right| \tag{10}$$

Likewise, the variations amongst the central pixel and its adjacent pixels of the red component of the current processing window are computed as**:**

$$\Delta_{\mathrm{r}}\left(v^x+\mathrm{i},\mathrm{v}^y+\mathrm{j},1,N^F\right)=\left|\mathrm{f}\left(v^x+\mathrm{i},\mathrm{v}^y+\mathrm{j},1,N^F\right)-\mathrm{f}\left(v^x,\mathrm{v}^y,1,N^F\right)\right| \tag{11}$$

Now, the red component of a pixel located at position (v^x, v^y) in the present frame N^F is considered similar to that at $(v^x + i, v^y + j)$ within the same frame in process N^F provided that the variations $\Delta_{rg}(v^x + i, v^y + j, 1, N^F)$, $\Delta_{rb}(v^x + i, v^y + j, 1, N^F)$ and $\Delta_r(v^x + i, v^y + j, 1, N^F)$ as computed in Eqs. (9), (10) and (11) respectively have their value below than the parameter λ_1 which is estimated experimentally.

Consider a window of size w × w (say 3 × 3). Then *i* and *j* in Eqs. (7), (8), (9), (10), and (11) will range from -1 *to* $+1$. '*K*' is the number of neighboring pixels that are analogous to the pixel at the center. In the window of size 3 × 3, *K* will range from 0 to 8. More are the count of neighboring pixels with comparable values; less will be the chances of the central pixel being noisy. This number '*K*' is decided by comparing differences calculated in Eqs. (9), (10), and (11) with parameter λ_1.

Now if $\Delta_{rg}(v^x + i, v + j, 1, N^F)$, $\Delta_{rb}(v^x + i, v^y + j, 1, N^F)$ *and* $\Delta_r(v^x + i, v^y + j, 1, N^F)$ are less than a parameter λ_1 we say that condition 'A' meets, then

$$K_r\left(v^x,v^y,1,N^F\right)=\left\{\begin{matrix}K_r\left(v^x,v^y,1,N^F\right)+1,\mathit{condition\,A\,meets}\\K_r\left(v^x,v^y,1,N^F\right),\mathit{otherwise}\end{matrix}\right\} \tag{12}$$

For a window of size 3 × 3, $\mu(K_r(v^x, v^y, N^F))$ can be computed as:

$$\mu\left(K_r\left(v^x,v^y,1,N^F\right)\right)=\left\{\begin{matrix}1,K_r\left(v^x,v^y,1,N^F\right)\le 2\\0.5,K_r\left(v^x,v^y,1,N^F\right)=3\\0,K_r\left(v^x,v^y,1,N^F\right)\ge 4\end{matrix}\right\} \tag{13}$$

A pixel having a high count of comparable neighboring pixels and whose intensity level is similar to the median is more likely to be noise-free. It is denoted by the membership function 'μ_d', which represents the fuzzy set "**dissimilar"**. It indicates the number of neighboring pixels with homogeneous intensity levels. After calculating the difference '*D*' and the amount of the pixels having comparable values for the central pixel in the current window (taking 3 × 3 here), '$\boldsymbol{\mu_d}$' is calculated for each color component as:

$$\mu_{\mathrm{d}}\left(\mathrm{v}^x,\mathrm{v}^y,1,N^F\right)=\max\left(\mu\left(\mathrm{K}_{\mathrm{r}}\left(v^x,\mathrm{v}^y,1,N^F\right)\right),\mu\left(\mathrm{D}\left(v^x,\mathrm{v}^y,1,N^F\right)\right)\right) \tag{14}$$

The membership function $\mu(D(v^x, v^y, 1, N^F))$ is computed as:

$$\mu\left(D\left(v^x,v^y,1,N^F\right)\right)=\left\{\begin{matrix}1, & D\left(v^x,v^y,1,N^F\right)\ge\lambda_2\\\dfrac{D\left(v^x,v^y,1,N^F\right)-\lambda_1}{\lambda_2-\lambda_1}, & \lambda_1\le D\left(v^x,v^y,1,N^F\right)<\lambda_2\\0, & D\left(v^x,v^y,1,N^F\right)<\lambda_1\end{matrix}\right\} \tag{15}$$

Here $D\ (v^x, v^y, 1, N^F)$ is the same as that calculated in Eq. (3) and the '*max*' operator used is the Cartesian co-product. Hence, if the value of a pixel is closer to the greater part of the pixels in the present window as well as compared to the median value, thereupon it is recognized as a noise-free pixel. The parameters λ_1 and λ_2 are obtained experimentally. Similarly, the Eqs. (5)–(15) can be defined for the blue and green color components respectively.

3.1.3 Fuzzy set: terminal

Impulse noise changes the true intensity levels of pixels by terminal values of the dynamic range. For instance, in an 8-bit image, the pixel values will be altered by either 0 or 255. These are the terminal values present in an image. Therefore, for optimized evaluation of noise, it is beneficial to check the presence of terminal values in the neighborhood of the processing pixel. For any window size (say 3 × 3), there will be two-terminal pixels and one median pixel. The 2 terminal pixels are denoted by 'f_{min}' having the smallest intensity value in the window and 'f_{max}' having the highest intensity value in the window respectively. The median pixel is denoted by 'f_{med}'. The closer the value of the central pixel to 'f_{min}' or 'f_{max}', the higher is its probability of being noisy, and if the value of the pixel is nearby to 'f_{med}', its probability of being noise-free rises. This is defined by the third membership function 'μ_{ter}' which represents the fuzzy set "**terminal**". It is calculated for each color component as:

$$\mu_{ter}(f) = \begin{cases} 1, & f = f_{\min} \, or \, f = f_{\max} \\ \dfrac{f - f_{\min}}{f_{med} - f_{\min}}, & f_{\min} < f < f_{med} \\ \dfrac{f_{\max} - f}{f_{\max} - f_{med}}, & f_{med} < f < f_{\max} \\ 0, & f = f_{med} \end{cases} \tag{16}$$

Where 'f' represents the pixel value in the given color component of the selected frame.

Till now we have only focused on the color and spatial information. But since we are removing noise from a color image sequence, we also need to take care of the temporal information. If we need to ascertain the amount of noise existing in a component of a pixel in one frame, we need to consider its neighboring frames (previous and next frame) too. Therefore, the next two membership functions are employed to calculate the amount of noise present in a component of the pixel in one frame by comparing the current frame with its neighboring frames.

3.1.4 Fuzzy set: high

A noisy pixel in the current frame will have a high difference with its neighboring pixels, for a particular color component. Apart from this, it will also have a huge difference to its neighboring pixels, at the equivalent spatial position in the preceding or upcoming frame. This approach is adopted in obtaining the fuzzy set "**High**" defined by the membership function 'μ_h'. That is, if a component (let us say Red) of a pixel at (v^x, v^y) in the ongoing frame 'N^F' has a high difference with either the relating component (Red) of a pixel on the equivalent spatial position (v^x, v^y) in the preceding frame 'N^F -1' or with the relating component (Red) of a pixel on the equivalent spatial position (v^x, v^y) in the later frame '$N^F + 1$', it will be considered as High. The parameters γ_1 and γ_2 are again obtained experimentally. Let,

$$\mu\left(\mathrm{R}_0\left(v^x, v^y, 1, N^F\right)\right) = \left\{ \begin{array}{ll} 1, & \mathrm{R}_0\left(v^x, v^y, 1, N^F\right) \geq \gamma_2 \\ \dfrac{\mathrm{R}_0\left(v^x, v^y, 1, N^F\right) - \gamma_1}{\gamma_2 - \gamma_1}, & \gamma_1 \leq \mathrm{R}_0\left(v^x, v^y, 1, N^F\right) < \gamma_2 \\ 0, & \mathrm{R}_0\left(v^x, v^y, 1, N^F\right) < \gamma_1 \end{array} \right\} \tag{17}$$

Where $R_0\ (v^x, v^y, 1, N^F)$ in Eq. (17) can either be replaced by $R_{11}\ (v^x, v^y, 1, N^F)$ *or* $R_{12}\ (v^x, v^y, 1, N^F)$ as defined below:

$$\mathrm{R}_{11}\left(\mathrm{v}^x, \mathrm{v}^y, 1, N^F\right) = \left|\mathrm{f}\left(v^x, \mathrm{v}^y, 1, N^F\right) - \mathrm{f}\left(v^x, \mathrm{v}^y, 1, N^F - 1\right)\right| \tag{18}$$

$$\mathrm{R}_{12}\left(\mathrm{v}^x, \mathrm{v}^y, 1, N^F\right) = \left|\mathrm{f}\left(v^x, \mathrm{v}^y, 1, N^F\right) - \mathrm{f}\left(v^x, \mathrm{v}^y, 1, N^F + 1\right)\right| \tag{19}$$

R_0, R_{11}, *and* R_{12} represent the current frame, previous frame, and next frame computations for calculating the difference value respectively.

Then, using Eqs. (17), (18), and (19), '$\boldsymbol{\mu_h}$' is calculated for the red color component as:

$$\mu_{\mathrm{h}}\left(v^x, \mathrm{v}^y, 1, N^F\right) = \max\left(\begin{array}{l} \mu\left(\mathrm{R}_{11}\left(v^x, \mathrm{v}^y, 1, N^F\right)\right), \\ \mu\left(\mathrm{R}_{12}\left(v^x, \mathrm{v}^y, 1, N^F\right)\right) \end{array}\right) \tag{20}$$

Using Eqs. (17)–(20), the values of the other two color components are also computed by taking $v^z = 2$ and 3. The Max operator used is the Cartesian co-product.

3.1.5 Fuzzy set: variant

This membership function is used to compute the variations in the central pixel for its adjacent neighboring pixels in the previous and next frames. It is denoted by 'μ_v'. The differences between neighboring pixels $(v^x + i,\ v^y + j)$ of the pixel in the present frame 'N^F' and the neighboring pixels $(v^x + i,\ v^y + j)$ of the relating component of the pixel at the equivalent spatial position within the preceding frame 'N^F -1' is determined as:

$$\mathrm{d}_{\mathrm{r}}\left(v^x + \mathrm{i}, \mathrm{v}^y + \mathrm{j}, 1, N^F\right) = \left|\mathrm{f}\left(v^x + \mathrm{i}, \mathrm{v}^y + \mathrm{j}, 1, N^F\right) - \mathrm{f}\left(v^x + \mathrm{i}, \mathrm{v}^y + \mathrm{j}, 1, N^F - 1\right)\right| \tag{21}$$

The second difference is computed from the following equation:

$$\mathrm{R}_3\left(v^x + \mathrm{i}, \mathrm{v}^y + \mathrm{j}, 1, N^F\right) = \left|\mathrm{d}_{\mathrm{r}}\left(v^x + \mathrm{i}, \mathrm{v}^y + \mathrm{j}, 1, N^F\right) - \mathrm{R}_{11}\left(\mathrm{v}^x, \mathrm{v}^y, 1, N^F\right)\right| \tag{22}$$

Where $R_{11}\ (v^x, v^y, 1, N^F)$ is defined in Eqs. (17) and (18).

The parameter λ_1 has the same value as used in Eq. (15). For the computations of variations among adjacent pixel values in current, next, and previous frames, a window size of w × w (say 3 × 3) is selected.

$$k_r\left(v^x, v^y, 1, N^F\right) = \left\{ \begin{array}{ll} k_r\left(v^x, v^y, 1, N^F\right) + 1, & R_3\left(v^x + i, v^y + j, 1, N^F\right) < \lambda_1 \\ k_r\left(v^x, v^y, 1, N^F\right), & \textit{otherwise} \end{array} \right\} \tag{23}$$

For a window of size 3 × 3 $\mu(\mathrm{k_r}(v^x, \mathrm{v}^y, 1, N^F))$ is formulated as:

$$\mu\left(k_r\left(v^x, v^y, 1, N^F\right)\right) = \left\{ \begin{array}{ll} 1, & k_r\left(v^x, v^y, 1, N^F\right) \leq 2 \\ 0.5, & k_r\left(v^x, v^y, 1, N^F\right) = 3 \\ 0, & k_r\left(v^x, v^y, 1, N^F\right) \geq 4 \end{array} \right\} \tag{24}$$

Similarly, the other two membership functions $\mu(k_g(v^x, v^y, 1, N^F))$ and $\mu(k_b(v^x, v^y, 1, N^F))$can be computed.

If the number of such similar neighboring pixels is more, then the pixel is considered noise-free. Finally 'μ_v' is calculated for the red color component as:

$$\mu_v(x, y, 1, N^F) = min\left(\mu(k_r), max\left(\mu(k_g), \mu(k_b)\right)\right) \tag{25}$$

For simplicity we have used k_r for k_r (v^x, v^y, 1, N^F), k_g for k_g (v^x, v^y, 1, N^F), and k_b for k_b (v^x, v^y, 1, N^F). The Max operator used is the Cartesian co-product and the min operator used is the Cartesian product.

Now, after computing all the membership values for fuzzy sets *Big, Dissimilar, Terminal, High,* and *Variant* using Eqs. (4), (14), (16), (20), and (25) respectively, from Eq. (2), we get the measure of noise $N_1(v^x, v^y, 1, N^F)$.

Its value should be zero for the noise-free pixel and the noisy pixel; it should have some value between 0 and 1. If the pixel is noisy then a '*correction term*' is computed. It is added to the original value of the pixel to make it noise-free. It is '0' for noise-free pixel and any positive or negative value for the noisy pixel. The correction term (Δf) is calculated using the following equation:\

$$\Delta f\left(v^x, v^y, 1, N^F\right) = N_1\left(v^x, v^y, 1, N^F\right) \times \left(\text{med}\left(v^x, v^y, 1, N^F\right) - f\left(v^x, v^y, 1, N^F\right)\right) \tag{26}$$

This correction term obtained is then combined with the original value of the pixel '$f(v^x, v^y, 1, N^F)$'. The pixels free from noise are left untouched and noisy pixels are restored via the median value of the adjacent noise-free pixels. Other pixels having an average noise density are modified according to the extent of noise present in them. Thus, the result of Primary filter '$f_1(v^x, v^y, 1, N^F)$' is:

$$f_1\left(v^x, v^y, 1, N^F\right) = f\left(v^x, v^y, 1, N^F\right) + \Delta f\left(v^x, v^y, 1, N^F\right) \tag{27}$$

3.2 Secondary Filter

The output of the primary filter acts as an input to the secondary filter to give the final output. The objective of the secondary filter is the detection and rectification of residual noisy pixels. This step refines the output of the Primary filter by taking into account the interactions among the color components of the same frame as well as the interaction of the given frame with its previous frame as well as the next frame.

Again in the secondary filter, the degree of noise is calculated by using a fuzzy rule. Consider one color component, say a red component of the current frame 'N^F' in the resulting image sequence 'f_1'. The extent of noise present in a pixel at location (v^x, v^y) is measured by the fuzzy *Rule2*:

Rule 2:

IF ($f_1(v^x, v^y, 1, N^F) - f_1(v^x, v^y, 2, N^F)$ is **Big**).

AND ($f_1(v^x, v^y, 1, N^F) - f_1(v^x, v^y, 3, N^F)$ is **Big**).

AND ((either the difference between $f_1(v^x, v^y, 1, N^F)$ in N^F and $f_1(v^x, v^y, 1, N^F - 1)$ in $N^F - 1$ is **High**).

OR (the difference between $f_1(v^x, v^y, 1, N^F)$ in N^F and $f_1(v^x, v^y, 1, N^F + 1)$ in $N^F + 1$ is **High**)).

THEN $f_1\ (v^x, v^y, 1, N^F)$ is noisy.

Where, $f_1\ (v^x, v^y, 1, N^F)$ is the pixel under evaluation. The differences are computed with the relating pixel in the previous frame and the next frame. These computations are for the red color component.

$f_1(v^x,v^y,2, N^F)$ is the relating pixel from the blue component and $f_1\ (v^x,v^y,3, N^F)$ is the corresponding pixel from the green component.

Mathematically, the amount of noise existing in the red color component of a pixel at position (v^x, v^y) in the current frame N^F is evaluated as:

$$N_2\left(v^x, \mathrm{v}^y, 1, N^F\right) = min\left\{\begin{array}{l}\mu_b\left(\zeta_{rg}\left(\mathrm{v}^x, \mathrm{v}^y, 1, N^F\right)\right),\\ \mu_b\left(\zeta_{rb}\left(\mathrm{v}^x, \mathrm{v}^y, 1, N^F\right)\right),\\ \mu_h\left(\mathrm{v}^x, \mathrm{v}^y, 1, N^F\right)\end{array}\right\} \tag{28}$$

Where 'μ_b' *and* 'μ_h' *are* the fuzzy sets "*Big*" and "*High*" respectively. **'ζ_{rg}'** signifies the distinction between the red and green component and **'ζ_{rb}'** is the distinction between red and blue components. These are calculated in the following equations:

$$\zeta_{rg}\left(\mathrm{v}^x, \mathrm{v}^y, 1, N^F\right) = \left|\mathrm{f}_1\left(v^x, \mathrm{v}^y, 1, N^F\right) - \mathrm{f}_1\left(v^x, \mathrm{v}^y, 2, N^F\right)\right| \tag{29}$$

$$\zeta_{rb}\left(\mathrm{v}^x, \mathrm{v}^y, 1, N^F\right) = \left|\mathrm{f}_1\left(v^x, \mathrm{v}^y, 1, N^F\right) - \mathrm{f}_1\left(v^x, \mathrm{v}^y, 3, N^F\right)\right| \tag{30}$$

After calculating these differences, we will compute the fuzzy membership value 'μ_b' by comparing these differences with parameters 'β_1' and 'β_2'. The values of these 2 parameters are obtained experimentally.

$$\mu_b\left(\zeta_{rg}\left(v^x, \mathrm{v}^y, 1, N^F\right)\right) = \left\{\begin{array}{ll}1, & \zeta_{rg}\left(v^x, \mathrm{v}^y, 1, N^F\right) \geq \beta_2\\ \dfrac{\zeta_{rg}\left(v^x, \mathrm{v}^y, 1, N^F\right) - \beta 1}{\beta 2 - \beta 1}, & \beta_1 \leq \zeta_{rg}\left(v^x, \mathrm{v}^y, 1, N^F\right) < \beta_2\\ 0, & \zeta_{rg}\left(v^x, \mathrm{v}^y, 1, N^F\right) < \beta_1\end{array}\right\} \tag{31}$$

Similarly, $\mu_b(\zeta_{rb}(v^x, \mathrm{v}^y, 1, N^F))$ is derived.

$$\mu\left(\mathrm{R}_1\left(v^x, v^y, 1, N^F\right)\right) = \left\{\begin{array}{ll}1, & \mathrm{R}_1\left(v^x, v^y, 1, N^F\right) \geq \gamma_2\\ \dfrac{\mathrm{R}_1\left(v^x, v^y, 1, N^F\right) - \gamma_1}{\gamma_2 - \gamma_1}, & \gamma_1 \leq \mathrm{R}_1\left(v^x, v^y, 1, N^F\right) < \gamma_2\\ 0, & \mathrm{R}_1\left(v^x, v^y, 1, N^F\right) < \gamma_1\end{array}\right\} \tag{32}$$

Where $R_1\ (v^x, v^y, 1, N^F)$ in Eq. (32) can either be replaced by $R_{21}\ (v^x, v^y, 1, N^F)$ or $R_{22}\ (v^x, v^y, 1, N^F)$ as defined below:

$$\mathrm{R}_{21}\left(\mathrm{v}^x, \mathrm{v}^y, 1, N^F\right) = \left|\mathrm{f}_1\left(v^x, \mathrm{v}^y, 1, N^F\right) - \mathrm{f}_1\left(v^x, \mathrm{v}^y, 1, N^F - 1\right)\right| \tag{33}$$

$$\mathrm{R}_{22}\left(\mathrm{v}^x, \mathrm{v}^y, 1, N^F\right) = \left|\mathrm{f}_1\left(v^x, \mathrm{v}^y, 1, N^F\right) - \mathrm{f}_1\left(v^x, \mathrm{v}^y, 1, N^F + 1\right)\right| \tag{34}$$

Using Eqs. (32), (33) and (34), **'μ_h'** is calculated for the red color component as:

$$\mu_{\mathrm{h}}\left(v^{x}, \mathrm{v}^{y}, 1, N^{F}\right)=\max\begin{pmatrix}\mu\left(\mathrm{R}_{11}\left(v^{x}, \mathrm{v}^{y}, 1, N^{F}\right)\right), \\ \mu\left(\mathrm{R}_{21}\left(v^{x}, \mathrm{v}^{y}, 1, N^{F}\right)\right)\end{pmatrix} \tag{35}$$

The Max operator used is the Cartesian co-product. *'N_1 (v^x, v^y, 1, N^F)'* denotes the amount of noise existing in the red component of a pixel at *(v^x, v^y)* position in the present frame 'N^F'. Again the correction term is derived using Eq. (36) and added to the pixel value after the evaluation of the pixel as noisy or not.

$$\Delta \mathrm{f}_{2}\left(v^{x}, v^{y}, 1, N^{F}\right)=N_{1}\left(v^{x}, v^{y}, 1, N^{F}\right) \times\left(\operatorname{med}\left(v^{x}, v^{y}, 1, N^{F}\right)-\mathrm{f}_{1}\left(v^{x}, v^{y}, 1, N^{F}\right)\right) \tag{36}$$

Thus, the result of the secondary filter is:

$$\mathrm{f}_{2}\left(v^{x}, v^{y}, 1, N^{F}\right)=\mathrm{f}\left(v^{x}, v^{y}, 1, N^{F}\right)+\Delta \mathrm{f}\left(v^{x}, v^{y}, 1, N^{F}\right) \tag{37}$$

4 Results

A color image sequence comprising of '*T*' frames and $M \times N \times 3$ arrays of the pixel at location *(x, y)* can be seen as an assembly of three scale frames analogous with RGB components. *PSNR* is selected as the measure of performance. It is correlated to *MSE* (Mean Square Error) as in Eq. (38):

$$PSNR(u, v)=10 \log\left(\frac{1}{MSE(u, v)}\right) \tag{38}$$

Mean Square Error is measured as

$$MSE(u, v)=\frac{\sum_{t=1}^{T} \sum_{z=1}^{3} \sum_{x=1}^{N} \sum_{y=1}^{M}\left[v\left(x, y, z, N^{F}\right)-u\left(x, y, z, N^{F}\right)\right]^{2}}{3 \times N \times M} \tag{39}$$

Where '*v*' represents the original sequence, '*u*' stands for the output sequence. The dimensions of the sequences are of '*N X M*' size. *MSE* gives the similarity between two image sequences. The higher estimation of the PSNR value depicts the higher uniformity between the two image sequences.

Parameter Selection:

After the evaluation of our work on the following color image sequences: "Salesman", "Tennis", "Bus", "Foreman", "Flower", and "Deadline" for impulse noise level ranging from '*p = 5%* to *p = 80%*'. The values of the membership function parameters were determined experimentally by taking the average of the *PSNR* result of ten frames of these six color image sequences, corrupted by impulse noise at different noise levels. The parameters $\alpha_1 = 10$, $\alpha_2 = 10.5$, $\delta = 5$, $\lambda_1 = 0.1$, $\lambda_2 = 0.3$, $\gamma_1 = 10.5$, $\gamma_2 = 30$, $\beta_1 = 5$ **and** $\beta_2 = 5.5$ were selected experimentally as per the maximum value of the PSNR. These values provide optimal results to remove impulse noise from video sequences while restoring the basic structure of the image.

The other performance metric employed in our work is the structural similarity index (SSIM) [51]. It is described as

$$SSIM = \frac{\left(2\mu_I\mu_f + c_1\right) + \left(2\sigma_{If} + c_2\right)}{\left(\mu_I^2 + \mu_f^2 + c_1\right) + \left(\sigma_I^2 + \sigma_f^2 + c_2\right)} \tag{40}$$

Where 'c_1' and 'c_2' denote the constant values. μ_I, μ_F,σ_I, σ_f, and σ_{If} denote the average intensity, standard deviation, and cross-covariance values. In general, $c_1 = (0.01 \times 255)^2$ and $c_2 = (0.03 \times 255)^2$.

SSIM index results in a decimal value between 0 and 1. The absolute structural similarity in the two images is signified by *'1'*. Lack of structural similarity is denoted by *'0'*. SSIM was postulated on the idea that the human eyes are eminently adapted to derive structural information from visual scenes. SSIM is constituted of 3 components, namely luminance (l), contrast (C), and structure (S).

$$l(v,u) = \frac{2\mu_I\mu_f + c_1}{\mu_I^2 + \mu_f^2 + c_1} \tag{41}$$

$$C(v,u) = \frac{2\sigma_I\sigma_f + c_2}{\sigma_I^2 + \sigma_f^2 + c_2} \tag{42}$$

$$S(v,u) = \frac{\sigma_{If} + c_3}{\sigma_I\sigma_f + c_3} \tag{43}$$

$$c_3 = \frac{c_2}{2} \tag{44}$$

SSIM is expressed by a weighted solution of *l, C,* and *S*:

$$SSIM(v,u) = \left[l(v,u)^{\theta_1} \cdot C(v,u)^{\theta_2} \cdot S(v,u)^{\theta_3}\right] \tag{45}$$

For Eq. (40), $_1$, $_2$, $_3$ = *1, and* $c_1 = c_2$.

The efficacy of the proposed work is analyzed to that of Fuzzy Random Impulse Noise Removal from Color Image Sequence (*FRINR*) [43], Fast averaging peer-group filter for the impulsive noise removal in color images (*FAPG*) [33], Adaptive fuzzy inference system based directional median filter for impulse noise removal (*AFISD*) [20], A denoising model based on convolutional neural networks (*DMCNN*) [27], Structure-Adaptive Fuzzy Estimation for Random-Valued Impulse Noise Suppression (*SAFEIN*) [12], and Fast adaptive switching technique of impulsive noise removal in color images (*HFBFT*) [7]. All the results are simulated on standard image sequences available using MATLAB R2018b.

The proposed algorithm is examined on the following color image sequences: *"Salesman", "Tennis", "Bus", "Foreman", "Flower",* and "*Deadline*" for impulse noise levels *5%, 10%, 15%, 20%, 25%, and 30%* respectively. The result of this experiment in terms of PSNR for the 10th frame of all the standard sequences is presented in Fig. 1. Results deduce that the

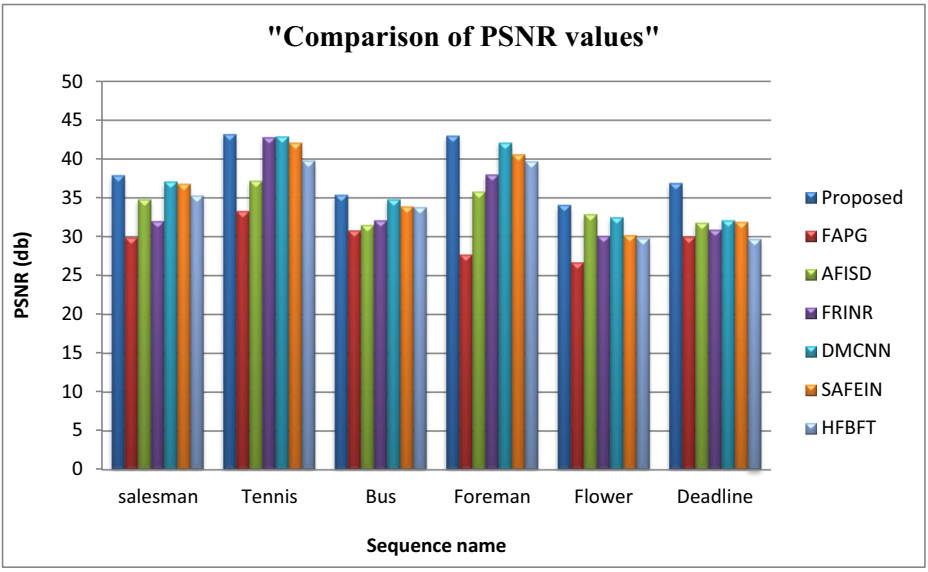

Fig. 1 Comparison graph of the PSNR values of the proposed filter with various methods

proposed method can handle distinct image sequences for varying noise levels. It provides the highest PSNR results as compared to other state of the art techniques.

From 'Fig. 1', we can deduce that with the rise in noise density levels the performance of our work is not degraded. Apart from this, our work can be utilized for various kinds of image sequences in different fields like astrology, medical analysis, satellite imagery, military surveillance, and many more. It is multifunctional in nature. Although the latest advancements in noise removal based on neuro-fuzzy systems and optimization techniques, like DMCNN [27] and SAFEIN [12] excel in terms of good PSNR results, they lag in terms of processing time. In real-world applications along with the noise removal capacity of the filter, the time taken by the algorithm to generate the final result is quite critical. Computation timings are also computed for all the methods in Table 1.

The results in 'Table 1' predict that the proposed method provides rapid output as compared to other methods in terms of processing time. The methods based on fuzzy logic like FAPG [33] provide faster results as compared to other methods. Though the qualitative results of the filters like DMCNN [27] and SAFIN [12] are good, they are slower in computation. This is a

Table 1 Comparison of computation time (in seconds) for various methods

Noise density %						
Method	20%	30%	40%	50%	60%	70%
FRINR [43]	11.73	11.98	12.97	13.80	15.79	17.99
SAFIN [12]	14.20	14.83	15.99	17.50	18.34	19.95
DMCNN [27]	15.52	16.28	18.93	19.52	20.70	21.43
FAPG [33]	10.94	11.46	11.95	13.06	14.13	15.89
HFBFT [7]	12.05	13.15	13.91	14.73	16.23	16.88
AFISD [20]	11.61	12.17	13.70	15.62	16.37	17.13
Proposed	10.01	10.93	11.21	12.18	13.77	14.29

Table 2 Comparison of SSIM values of various filters for different sequences

Noise %	FRINR [43]	SAFEIN [12]	DMCNN [27]	FAPG [33]	HFBFT [7]	AFISD [20]	Proposed
"Salesman"							
30	0.7308	0.7381	0.7601	0.6808	0.7091	0.6944	0.7626
40	0.7261	0.7304	0.7515	0.6771	0.7022	0.6873	0.7592
50	0.7140	0.7229	0.7394	0.6698	0.6945	0.6809	0.7403
60	0.7069	0.7153	0.7202	0.6583	0.6792	0.6793	0.7389
70	0.7002	0.7115	0.7096	0.6439	0.6773	0.6707	0.7311
"Tennis"							
30	0.9799	0.9759	0.9821	0.9792	0.9643	0.9788	0.9887
40	0.9700	0.9643	0.9795	0.9722	0.9611	0.9753	0.9814
50	0.9612	0.9586	0.9610	0.9669	0.9507	0.9667	0.9773
60	0.9514	0.9439	0.9545	0.9549	0.9313	0.9543	0.9744
70	0.9378	0.9403	0.9493	0.9467	0.9217	0.9416	0.9615
"Bus"							
30	0.9773	0.9811	0.9857	0.9761	0.9777	0.9815	0.9893
40	0.9681	0.9765	0.9764	0.9688	0.9706	0.9751	0.9819
50	0.9593	0.9710	0.9668	0.9604	0.9634	0.9644	0.9761
60	0.9516	0.9674	0.9517	0.9413	0.9572	0.9577	0.9591
70	0.9453	0.9501	0.9461	0.9339	0.9484	0.9411	0.9503
"Foreman"							
30	0.9537	0.9508	0.9578	0.9414	0.9479	0.9560	0.9601
40	0.9482	0.9472	0.9473	0.9377	0.9338	0.9513	0.9547
50	0.9407	0.9346	0.9417	0.9284	0.9249	0.9437	0.9501
60	0.9319	0.9279	0.9264	0.9114	0.9216	0.9331	0.9483
70	0.9202	0.9223	0.9202	0.9010	0.9177	0.9300	0.9446
"Deadline"							
30	0.9651	0.9577	0.9699	0.9606	0.9663	0.9689	0.9749
40	0.9518	0.9445	0.9641	0.9569	0.9585	0.9620	0.9698
50	0.9463	0.9389	0.9516	0.9493	0.9504	0.9550	0.9611
60	0.9372	0.9314	0.9437	0.9399	0.9470	0.9467	0.9560
70	0.9288	0.9266	0.9312	0.9318	0.9322	0.9378	0.9515

major drawback for techniques having complex structures and they are not apt for practical use. In the case of neural networks also, there is training difficulty and higher computation timings due to dependence on input qualities. The proposed work has a simple structure and the use of fuzzy logic has enhanced the output of the filter. The computation timings are in practical range and the algorithm can be used with applications used for various multimedia devices.

Another performance metric used for the evaluation of our work is SSIM. The analysis of the SSIM values in 'Table 2', for various sequences predicts that the proposed algorithm is

Table 3 MD & FA rates

Noise%	Miss detection (MD)				False Alarm (FA)			
	SAFEIN [12]	DMCNN [27]	HFBFT [7]	Proposed	SAFEIN [12]	DMCNN [27]	HFBFT [7]	Proposed
10	0	0	0	0	0	0	0	0
30	1	1	2	0	1	0	1	0
50	3	2	4	0	1	1	2	1
70	3	5	5	1	4	3	5	2
90	5	6	7	3	5	4	5	3

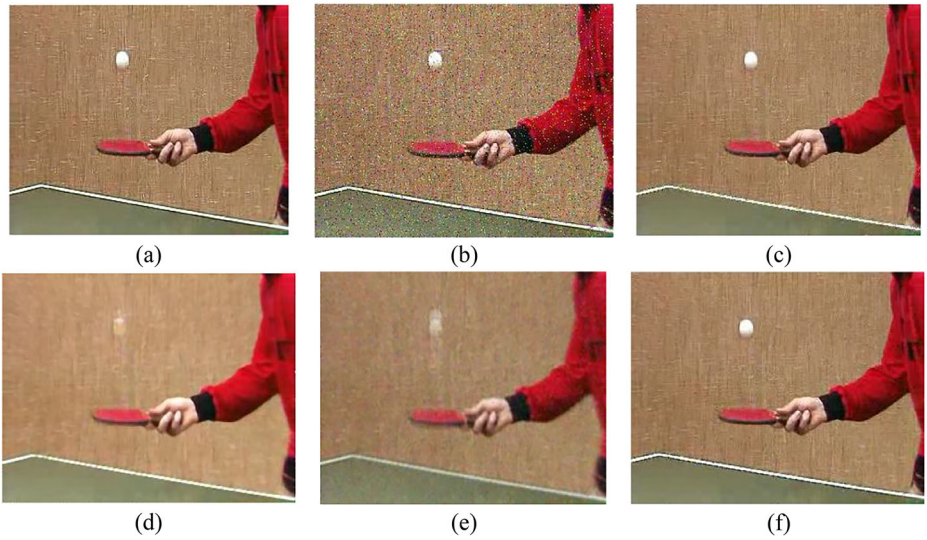

Fig. 2 Results for the 30th frame of the sequel "Tennis"

capable to handle varying amounts of noise levels. It is a robust method that maintains the basic structure of an image. The high SSIM results signify the better reliability of the proposed work. After noise removal, the proposed algorithm can preserve the true image pixels which lead to higher SSIM values.

Various techniques face issues regarding over-detection and under detection of noisy pixels. False Alarm (FA) means when a noise-free pixel is marked as noisy. Miss Detection exists (MD) when a noisy pixel is identified as noisy. MD and FA rates are calculated to analyze the efficacy of our filter in terms of its image conservation feature. False Alarm means when an un-corrupted pixel is marked as noise. Miss detection exists when a pixel with noise is detected as un-corrupted. We have used a difference based method [44] to compute the MD

Fig. 3 Results for the 30th frame of the sequel "Bus"

Fig. 4 Results for the 30th frame of the sequel "Salesman"

Fig. 5 Results using the proposed filter for various frames of a video sequence at noise density 50%

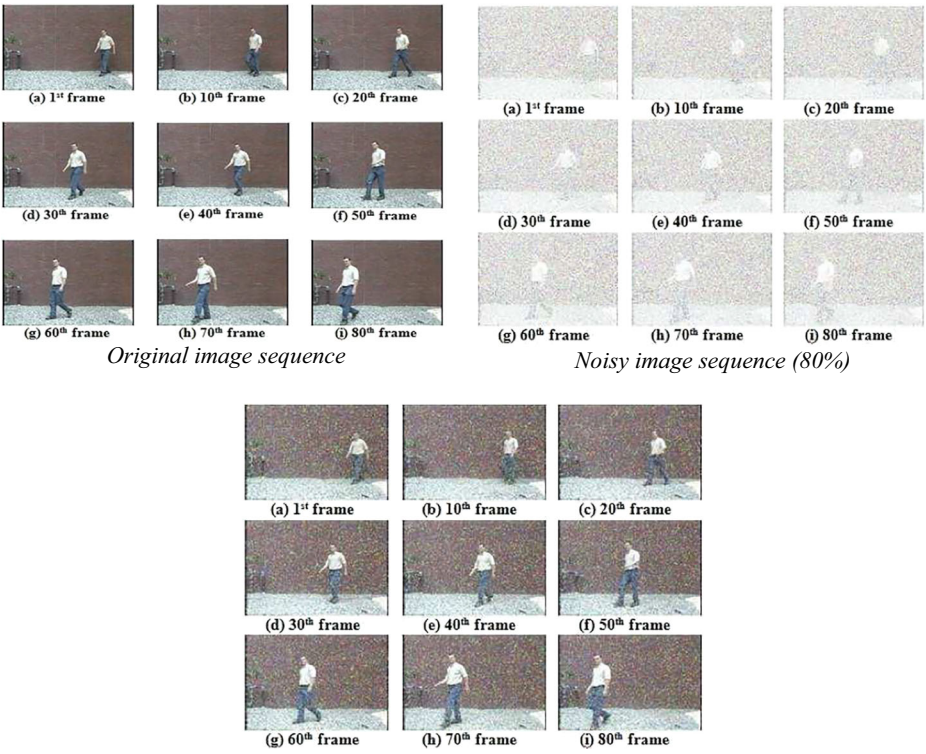

Fig. 6 Results using the proposed filter for various frames of a video sequence at noise density 80%

and FA rates. It generates a noise chart after computing the differences between the original image frame and the noise chart. The results are computed frame by frame with video sequences and average values are presented in this paper. To preserve the original image data, the values of MD and FA should be as low as possible. The results are shown in 'Table 3'.Results show that the proposed method surpasses other methods. The MD and FA rates are quite low which aids in the better reconstruction of the original image sequence. With the rise in noise levels, the chances of Miss detection and false alarm cases rise, but the results depict that the proposed filter is consistent in performance. Even at high noise levels above 50%, the filter detects noise in an optimum manner.

The extensive mathematical simulation results of the proposed work in 'Fig. 1', 'Tables 1, 2 and 3', in terms of *PSNR, Computation time, SSIM*, *MD,* and *FA values* respectively, validate the efficiency of the filter. All the quality metrics employed for the evaluation depict that the proposed filter is a potent method to remove impulse noise from a color image sequence. It can be utilized for various applications in the real world. It is rapid and feature conserving in nature. Simple structure, fast computation time, and high denoising capacity help to reduce the costs as well. It is practical and cheap as compared to other methods, which require separate hardware installations for various modules.

The visual results in the 30th frame are also presented in 'Figs. 2, 3, and 4' for the image sequences *'Tennis'* with 5% impulse noise, *'Bus'* with 10% noise, and *'Salesman'* with 20% noise respectively. These are the standard image sequences tested with MATLAB R2018b.

'Figs. 5 and 6' presents the visual results at noise levels 50% and 80% using the proposed filter. For the evaluation of the proposed work, nine distinct frames of an image sequence are extracted and tested using MATLAB R2018b. At high noise levels of 50% and 80%, the proposed work has practical computation timings of *13.86 s* and *14.79 s*. These are the average computation time of nine frames.

The proposed method outperforms these methods, both in objective measure and optical evaluation.

5 Conclusions

A new filtering schema for color image sequences debased by impulse noise is introduced in this paper. It retains the basic details present in an image sequence and the noise is also expelled in an optimum manner. The assessment of noisy color components depends on fuzzy rules which incorporate the data from spatial and temporal neighbors including other color bands. Every color band is filtered independently. Two fuzzy subfilters are successively used to detect and filter the impulse noise. Since an impressive portion of the noise is filtered in the initial step, the remaining noise is easier to detect in the second step and hence the details are well preserved. Only noisy pixels are modified and noise-free pixels are left untouched, which minimizes the blurring. Furthermore, only noise-free pixels are used for filtering noisy pixels. The proposed method is characterized by superior results and stability. The simple structure and rapid computation timings make it apt for real-world applications and multimedia devices. The experimental results demonstrate that the proposed filter result in an excellent alignment between noise removal and detail preservation. The proposed work surpasses other state-of-the-art techniques, both visually and mathematically.

References

1. Al-Ayyoub M, AlZu'bi S, Jararweh Y, Shehab MA, Gupta BB (2016) Accelerating 3D medical volume segmentation using GPUs. Multimed Tools Appl 77:4939–4958
2. Aliakhmet K, James AP (May 2019) Temporal G-neighbor filtering for Analog domain noise reduction in astronomical videos. in IEEE Transactions on Circuits and Systems II: Express Briefs 66(5):868–872. https://doi.org/10.1109/TCSII.2019.2907817
3. AlZu'bi S, Shehab M, Al-Ayyoub M, Jararweh Y, Gupta B (2020) Parallel implementation for 3D medical volume fuzzy segmentation. Pattern Recognition Letters 130:312–318, ISSN 0167-8655. https://doi.org/10.1016/j.patrec.2018.07.026
4. Al-Zu'bi S, Al-Ayyoub M, Jararweh Y, Shehab MA (2017) Enhanced 3D segmentation techniques for reconstructed 3D medical volumes. Robust and Accurate Intelligent System, Procedia Computer Science 113:531–538, ISSN 1877-0509. https://doi.org/10.1016/j.procs.2017.08.318
5. AlZu'bi, Shadi, Naveed Islam, and Maysam F. Abbod. (2010) 3D multiresolution analysis for reduced features segmentation of medical volumes using PCA. 2010 IEEE Asia Pacific Conference on Circuits and Systems: 604–607.
6. AlZu'bi S, Hawashin B, Mughaid A, Baker T (2020) Efficient 3D medical image segmentation algorithm over a secured multimedia network. Multimed Tools Appl:1–19. https://doi.org/10.1007/s11042-020-09160-6
7. Arnal J, Súcar L (2020) Hybrid filter based on fuzzy techniques for mixed noise reduction in color images. Appl Sci 10(1):243. https://doi.org/10.3390/app10010243 https://www.mdpi.com/2076-3417/10/1/243
8. Astola J, Haavisto P, Neuvo Y (1990) Vector median filters. Proc IEEE 78(4):678–689

9. Balster EJ, Ewing RL (2006) Combined spatial and temporal domain wavelet shrinkage algorithm for video denoising. IEEE Trans Circuits Syst Video Technol 16(2):220–230
10. Browne M, Ghidary SS (2003) Convolutional neural networks for image processing: An application in robot vision. In: Gedeon T..D., Fung L.C.C. (eds) AI 2003: Advances in Artificial Intelligence. AI 2003. Lecture notes in computer science, vol 2903. Springer, Berlin, Heidelberg https://doi.org/10.1007/978-3-540-24581-0_55.
11. Chacón MMI (2006) Fuzzy logic for image processing: definition and applications of a fuzzy image processing scheme. In: Bai Y, Zhuang H, Wang D (eds) Advanced fuzzy logic Technologies in Industrial Applications. Advances in Industrial Control. Springer, London. https://doi.org/10.1007/978-1-84628-469-4_7
12. Chen Y, Zhang Y, Shu H, Yang J, Luo L, Coatrieux JL, Feng Q (Feb. 2018) Structure-adaptive fuzzy estimation for random-valued impulse noise suppression. in IEEE Transactions on Circuits and Systems for Video Technology 28(2):414–427. https://doi.org/10.1109/TCSVT.2016.2615444
13. Chen J, Zhan Y, Cao H, Xiong G (2019) Iterative grouping median filter for removal of fixed value impulse noise. IET Image Processing 13(6)
14. Chervyakov NI, Lyakhov PA, Orazaev AR Valueva MV (2019) A new method of cleaning video from impulse noise. 2019 International conference on engineering and telecommunication (EnT), Dolgoprudny, Russia, pp. 1–5, https://doi.org/10.1109/EnT47717.2019.9030589
15. Chervyakov NI, Lyakhov PA, Orazaev AR (2020) 3D-generalization of impulse noise removal method for video data processing. Comput Opt 44(1):92–100
16. Egmont-Petersen M, de Ridder D, Handels H (2002) Image processing with neural networks—a review. Pattern Recogn 35(10):2279–2301, ISSN 0031-3203. https://doi.org/10.1016/S0031-3203(01)00178-9
17. Esakkirajan S, Veerakumar T, Subramanyam AN, Chand CHP (May 2011) Removal of high density salt and pepper noise through modified decision based unsymmetric trimmed median filter. IEEE Signal Process Lett 18(5)
18. Gonzalez RC, Woods RE (2002) Digital image processing. Second ed. Upper Saddle River: Prentice-Hall, Book.
19. Guo L, Au OC, Ma M, Liang Z (2007) Temporal video denoising based on multi hypothesis motion compensation. IEEE Trans Circuits Syst Video Technol 17(10):1423–1429
20. Habib M, Hussain A, Rasheed S, Ali M (2016) Adaptive fuzzy inference system based directional median filter for impulse noise removal. International Journal of Electronics & Communications 70(5):689–697
21. Huang S, Peng Y, Chang C, Cheng K, Huang S, Chen B (2020) Restoration of images with high-density impulsive noise based on sparse approximation and ant-Colony optimization. IEEE Access 8:99180–99189. https://doi.org/10.1109/ACCESS.2020.2995647
22. Hussain A, Habib (May 2017) A new cluster based adaptive fuzzy switching median filter for impulse noise removal. M Multimedia Tools Appl Springer 76:22001
23. Joshua O, Ibiyemi T, Adu B (2019) A comprehensive review on various types of noise in image processing. International Journal of Scientific and Engineering Research 10:388–393
24. Kang C-C, Wang W-J (2009) Fuzzy reasoning-based directional median filter design. Signal Process 89(3): 344–351
25. Kiani V, Zohrevand A (April 2019) A fuzzy directional median filter for fixed-value impulse noise removal. 7th Iranian Joint Congress on Fuzzy and Intelligent Systems (CFIS)
26. Ko SJ, Lee YH (1991) Center weighted median filters and their applications to image enhancement. IEEE Transactions on Circuits and Systems 38(9):984–993
27. Le T, Lin P, Huang S (2020) LD-net: an efficient lightweight Denoising model based on convolutional neural network. in IEEE Open Journal of the computer society. https://doi.org/10.1109/OJCS.2020.3012757
28. Lee S-W, Maik V, Jang J-H, Shin J, Paik J (2005) Noise-adaptive Spatio-temporal filter for real-time noise removal in low light level images. IEEE Trans Consum Electron 51(2):648–653
29. Lee S-W, Maik V, Jang J, Shin J, Paik J (May 2005) Noise-adaptive Spatio-temporal filter for real-time noise removal in low light level images. in IEEE Transactions on Consumer Electronics 51(2):648–653. https://doi.org/10.1109/TCE.2005.1468014
30. Li Y, Chung F-L, Wang S (2008) A robust neuro-fuzzy network approach to impulse noise filtering for color images. Applied Soft Computing 8:872–884. https://doi.org/10.1016/j.asoc.2007.07.006
31. Ma KK, Chen T, Chen LH (1999) Tri-state median filter for image denoising. IEEE Trans Image Process 8(12):1834–1838
32. Maity A, Chatterjee R (2018) Impulsive noise in images: a brief review. Computer Vision Graphics and Image Processing 4:6–15. https://doi.org/10.19101/TIPCV.2017.39025
33. Malinski L, Smolka B (2015) Fast averaging peer group filter for the impulsive noise removal in color images. J Real-Time Image Process

34. Malinski L, Smolka B (2019) Fast adaptive switching technique of impulsive noise removal in color images. J Real-Time Image Proc 16:1077–1098. https://doi.org/10.1007/s11554-016-0599-6
35. Mélange T, Nachtegael M, Kerre EE (2011) Fuzzy random impulse noise removal from color image sequences. IEEE Trans Image Process 20(4):959–970
36. Mélange T, Nachtegael M, Schulte S, Kerre EE (2011) A fuzzy filter for the removal of random impulse noise in image sequences. Image Vis Comput 29(6):407–419
37. Nair MS, Mol PMA (2013) Direction based adaptive weighted switching median filter for removing high density impulse noise. Comput Electr Eng 39:663–689
38. Ponomaryov V, Gallegos-Funes F, Rosales-Silva A (2010) Fuzzy directional (FD) filter to remove impulse noise from color images. IEICE Trans Fundament Electron Commun Comput Sci E93-A(2):570–572
39. Rajagopalan R, Orchard MT (2002) Synthesizing processed video by filtering temporal relationships. IEEE Trans Image Process 11(1):26–36
40. Rosales-Silva AJ, Gallegos-Funes FJ, Ponomaryov VI (2012) Fuzzy directional (FD) filter for impulsive noise reduction in color video sequences. J Vis Commun Image Represent 23(1):143–149
41. Roy J, Singha L, Manam R, Laskar H (Jan. 2017) Combination of adaptive vector median filter and weighted mean filter for removal of high density impulse noise from color images. IET Image Process 11(6):352–361
42. Roy A, Manam L, Laskar RH (2018) Region adaptive fuzzy filter: an approach for removal of random-valued impulse noise. IEEE Trans Ind Electron 65:7268–7278
43. Schulte S, De Witte V, Nachtegael M, Van der Weken D, Kerre EE (Nov. 2011) Fuzzy two step filter for impulse noise reduction from color images. IEEE Trans Image Process 15(11):3567–3578
44. Singh I, Verma OP (2016) High density impulse noise detection using fuzzy C-means algorithm. Def Sci J 66(1):30–36
45. Szczepanski M (2019) Fast Spatio-temporal digital paths video filter. J Real-Time Image Proc 16:477–489. https://doi.org/10.1007/s11554-016-0561-7
46. Thirilogasundari V, Sureshbabu VS, Janet A (2012) Fuzzy based salt and pepper noise removal using adaptive switching median filter. Procedia Engineering, ScienceDirect 38:2858–2865
47. Wang G, Li D, Pan W, Zang Z (2010) Modified switching median filter for impulse noise removal. Signal Process 90(12):3213–3218
48. Xu J, Wang L, Shi Z (2014) A switching weighted vector median filter based on edge detection. Signal Process 98:359–369
49. Yan Z (2008) Adaptive fuzzy median filter for images corrupted by impulsive noise. In, Congress on Image and Signal Processing
50. Yuksel ME, Basturk A (July 2012) Application of type-2 fuzzy logic filtering to reduce noise in color images. IEEE Comput Intell Mag 7(3):25–35
51. Zhou W, Bovik AC, Sheikh HR, Simoncelli EP (2004) Image quality assessment: from error visibility to structural similarity. IEEE Trans Image Process 13:600–612

Publisher's note Springer Nature remains neutral with regard to jurisdictional claims in published maps and institutional affiliations.

ResearchGate

See discussions, stats, and author profiles for this publication at: https://www.researchgate.net/publication/349053781

Incorporating Teacher's Preferences and Student Time Management in University Course Timetabling

Article · January 2021

CITATIONS
0

READS
16

2 authors:

Seba Susan
Delhi Technological University
80 PUBLICATIONS **431** CITATIONS
SEE PROFILE

Aparna Bhutani
New York University
3 PUBLICATIONS **8** CITATIONS
SEE PROFILE

All content following this page was uploaded by Seba Susan on 05 February 2021.

The user has requested enhancement of the downloaded file.

International Journal of Computer Information Systems and Industrial Management Applications.
ISSN 2150-7988 Volume 13 (2021) pp. 001-009
© MIR Labs, www.mirlabs.net/ijcisim/index.html

Received: 8 July, 2020; Accepted: 4 January, 2021; Published: 28 January, 2021

Incorporating Teacher's Preferences and Student Time Management in University Course Timetabling

Seba Susan[1], and Aparna Bhutani[2]

[1] Department of Information Technology, Delhi Technological University,
Shahbad Daulatpur, Bawana Road, Delhi- 110042
seba_406@yahoo.in

[2] Department of Information Technology, Delhi Technological University,
Shahbad Daulatpur, Bawana Road, Delhi- 110042
bhutaniaparna@gmail.com

***Abstract*: University course timetabling is a challenging task today due to the mushrooming of a variety of courses with flexible timings in different streams and disciplines in global universities. The challenge is to devise non-overlapping class schedules for students enrolled in different courses with the available and limited resources of teachers and classrooms. The task of automated timetable generation is a constrained optimization problem. In any optimization problem, the hard constraints are those that need to be mandatorily satisfied. The soft constraints are the penalties that are sought to be minimized in every iteration of the optimization algorithm. In this paper, we propose a novel set of soft constraints for university course timetabling that in addition to the conventional constraints, incorporates teacher's preferences and student time management as well. The latter constraint takes the form of minimizing student mobility between classrooms and restricting time gaps between classes to ensure that student's time on-campus is fully utilized. The evolutionary algorithms- Genetic Algorithm (GA), Particle Swarm Optimization (PSO), and Simulated Annealing (SA) are used for optimizing the course schedules. The timetables so generated, based on actual university data, are found to be more humanely optimized than the previous work of the authors due to the incorporation of human factor consideration both from the perspective of teachers and students.**

***Keywords*:** University Course Timetabling, Particle swarm optimization, Genetic Algorithm, Simulated Annealing, Teacher's preferences, Student time management

I. Introduction

University course timetabling is a challenging task today due to the mushrooming of a variety of courses with flexible timings in various streams and disciplines in global universities. The challenge is to devise non-overlapping class schedules for students enrolled in different courses with the available and limited resources of teachers and classrooms [1]. The task of automated timetable generation is a constrained optimization problem. The range of optimization algorithms vary from mathematical to evolutionary to heuristic [2]. Genetic Algorithm (GA) is a highly efficient evolutionary algorithm that follows the principle of the evolution of the fittest chromosome [23]. Its application to the timetable scheduling problem can be observed in [3,4]. Highly optimized schedules are generated by the heuristic Simulated Annealing (SA) algorithm, reportedly in minimal time, as per research in [5-8]. The different types of schedules generated by SA in [5-8] range from university course timetables, exam timetables, staff job schedules etc. SA and GA are the most investigated optimization algorithms for scheduling [16, 22] and combinations of GA and SA with local search have also been explored for timetabling problems [17, 21, 19]. Most of the algorithms differ in the initialization routines or variant of SA and GA used. Several variants of GA are found in literature [12]. Particle Swarm Optimization (PSO) which is another population-based evolutionary algorithm has been explored in [18, 20] for timetable scheduling. The penalty or cost function was, in fact, found lower for PSO as compared to GA in [20]. A timetable template satisfying the constraints is initialized in [9] before application of GA to optimize the timetable. In cases where students opt for elective courses, association rule mining is applied for mining student's preferences [10, 22]. In this paper, we extend our recent work on automatic timetable generation in [22] by formulating novel additional soft constraint functions that generate human-friendly optimized schedules both from the perspective of students and teachers. GA, SA and PSO optimization algorithms are investigated for the task. The organization of the paper is as follows: The different optimization algorithms used for our experiments are reviewed in Section II, the hard and soft constraints and the additional soft constraints proposed in this paper as well as the overall methodology are detailed in Section III, the results are discussed in Section IV and the overall conclusions are drawn in Section V.

II. Optimization algorithms

This section reviews three of the most popular optimization algorithms used for scheduling problems especially university

course timetabling, namely, Genetic Algorithm (GA), Particle Swarm Optimization (PSO), and Simulated Annealing (SA) algorithm. GA and PSO are evolutionary approaches that evolve globally optimal solutions over time based on the concept of the 'survival of the fittest'. SA is based on local search heuristics, and like GA and PSO, aims to find globally optimal solutions to the course timetabling problem.

A. *Optimization by SA*

The concept of Simulated Annealing (SA) [24] is borrowed from metallurgy. The metal prone to defects is heated to a high temperature and then cooled under controlled conditions. The resulting metal has lesser defects as compared to the initial condition and hence a lower energy. Optimization problems especially in scheduling are solved quite efficiently by SA in minimal execution time [5-8]. High temperature emulates Random Walk i.e. new possibilities are randomly explored at high temperatures akin to the mutation step in Genetic Algorithm. As the temperature cools with each iteration, the solution converges as the randomness factor reduces. The method is described in more detail below.

The initial temperature is set to a pre-defined high value. In every iteration, a random neighboring node is selected for each current node for possible replacement. The difference of energy levels is computed as

$$\Delta \boldsymbol{E} = \boldsymbol{E}(\boldsymbol{new}) - \boldsymbol{E}(\boldsymbol{current}) \quad (1)$$

where $\boldsymbol{E}(\boldsymbol{new})$ = Energy level for new node

$\boldsymbol{E}(\boldsymbol{current})$ =Energy level for current node

if $\Delta \boldsymbol{E} \le 0$ then we make the move with a probability=1.

if $\Delta \boldsymbol{E} > 0$ then we still allow that move but with a lower probability given by

$$\boldsymbol{P} = \boldsymbol{e}^{-\frac{\Delta \boldsymbol{E}}{\boldsymbol{T}}} \quad (2)$$

Here, $\boldsymbol{P}$ represents the probability with which the new node is selected and $\boldsymbol{T}$ represents the temperature. The temperature is updated in every iteration as

$$\boldsymbol{T}_{i+1} = \boldsymbol{T}_i \times \beta \quad (3)$$

where, β is the cooling rate pre-defined in the algorithm.

B. *Optimization by GA*

Genetic Algorithm (GA) is a highly efficient evolutionary algorithm that follows the principle of the evolution of the fittest chromosome [23]. It is a popular optimization tool in pattern recognition experiments to optimize values of unknown parameters while learning [15]. It involves the steps of initialization of chromosomes, computing the fitness function, selection, crossover and mutation. These steps are described briefly below. The steps are iterated over all the generations, with the maximum number of generations being fixed at the beginning of the algorithm. The steps in a single generation of the Genetic Algorithm are:

i. *Initialization*:

The initial population of chromosomes are randomly initialized at the beginning of the algorithm. Chromosomes indicate single solutions to the problem and are represented as binary strings.

ii. *Computing the Fitness function*:

The fitness or the cost function is that which is optimized in every iteration. Higher the fitness value, the more fit is the chromosome (for a maximization problem).

iii. Selection

This stage emulates the principle of the survival of the fittest. The fittest chromosomes indicated by high values of fitness function are retained and replicated while the ones with lower values of the fitness function are eliminated.

iv. Crossover

In Crossover, new chromosomes are created by mixing the genes of the existing chromosomes.

v. Mutation

Mutation of some genes in the chromosomes induce randomness in the population. This step is the reason why GA is claimed to converge to global optima.

C. *Optimization by PSO*

Particle Swarm Optimization (PSO) proposed by Eberhart and Kennedy [25] is an evolutionary algorithm based on swarm theory. It has been extensively used for optimizing values of unknown parameters in pattern recognition experiments [26]. It does not have the crossover, mutation steps of GA. However, the randomness induced in the position of the particles in the swarm that indicate single solutions, help to converge to global optima. The particle position and velocity are iterated over time to stable values. The steps of PSO algorithm are briefly described below.

i. *Initialization*:

Each particle in the swarm has a position vector and a velocity vector that are randomly initialized at the beginning of the algorithm. Each particle position indicates a possible solution.

ii. *Finding pBest and gBest*:

In each iteration, the local or personal best position (pBest) of each particle is updated and the global best position (gBest) amongst all particles is also updated. The velocity vector in (4) is first updated and the position vector is then updated as per (5). The position and velocity update equations are given below in Eq (4) and (5) respectively.

$$\begin{aligned} \boldsymbol{velocity}[\boldsymbol{i}] &= \boldsymbol{velocity}[\boldsymbol{i}-1] \\ &+ \boldsymbol{c}1 * \boldsymbol{rand}() * (\boldsymbol{pBest} - \boldsymbol{position}[\boldsymbol{i}-1]) \\ &+ \boldsymbol{c}2 * \boldsymbol{rand}() * (\boldsymbol{gBest} - \boldsymbol{position}[\boldsymbol{i}-1]) \end{aligned} \quad (4)$$

$$\boldsymbol{position}[\boldsymbol{i}] = \boldsymbol{position}[\boldsymbol{i}-1] + \boldsymbol{velocity}[\boldsymbol{i}] \quad (5)$$

Here c1 and c2 are constants and the randomness function ***rand***() in (4) introduces a certain randomness in the solutions formed.

III. Proposed Methodology for Constrained Timetable Schedule Optimization

Our previous work in [22] focusses on scheduling open elective courses by association rule mining for student's preferences [13, 14]. In this work, we schedule core subjects, labs and electives (obtained after the association rule mining in [22]) for the same enrolled students as in [22] with real

University data, available at the university website [11], using a novel set of constraints.

A. Proposed hard, soft, and additional soft constraints

A collection of hard and soft constraints is integrated from different research works (sources are cited) and additional soft constraints are added to make the timetable more human centric as shown below in boxed entries.

Hard Constraints (proposed method):

Hard constraints cannot be violated (as per the rules of the Delhi Technological University [11]). Hard constraints are as follows:

i. Electives are arranged to be taught between certain time slots: 08:00 am - 10:00 am
ii. Core Courses are taught between time slots: 10:00 am - 4:00 pm
iii. All students of B.Tech 6th semester from Information Technology department should enroll for the theory and practical courses (Core + Labs + Both Electives)

Soft Constraints (proposed method):

A 10-point penalty is assigned if soft constraints are violated. The soft constraints are as follows:

i. Classroom capacity should be greater than the size of the class. [2]
ii. No room should be assigned to a course or teacher if its already assigned to another course or teacher for that particular time slot.[2]
iii. Every teacher can teach only one class in a particular time slot. [4]
iv. Every course should have a professor to teach it.
v. Classrooms and lab for separate courses should not overlap with each other. [3]
vi. No student is assigned more than one class at a time. [2]

Additional Soft Constraints (proposed method):

A set of additional constraints are added in this paper to incorporate teacher timing preferences and restrict student mobility between classes and avoid time gaps between classes. These are a part of soft constraints only and a 10-point penalty is assigned if they are violated. These additional constraints are:

i. The students of a class are allotted one room in which they will have all the classes. This is done to avoid the time consumed for students while traveling between classrooms.
ii. There should not be empty slots in between classes in a day for the students.
iii. The teacher's preference to teach in a particular time slot is considered.

The soft constraints include teacher's preferences of timings of lectures that were compiled on an individual basis, and also the consideration for student time management in between classes to reduce the mobility of students in between classrooms and to avoid free time gaps between classes. The novel set of constraints- hard constraints (to be mandatorily satisfied) and soft constraints (to be minimized to the best extent possible) are outlined in the text box. For each soft constraint, we have stated, where appropriate, the reference works that have used these constraints before. We have also included three additional soft constraints that consider the human factors of teacher preferences and student time management as a separate box entitled 'Additional soft constraints'. Timetable scheduling is done for 6th semester undergraduate B.Tech (Information Technology) students (strength of 100 in numbers) of Delhi Technological University. The data for students enrolled for various courses is available at [11]. Students of sixth semester are divided into two batches or sections of 6-A and 6-B. The number of classrooms is limited to two- Room numbers: TW2GF2 and TW1TF3, as opposed to three classrooms in our previous work in [22]. The Professors involved are the current staff of Department of Information Technology, Delhi Technological University (names withheld on request).

There are 5 theory courses (Elective + Core subjects) and two laboratory courses (or labs). The two Electives were derived by association rule mining of student's subject preferences as per our recent work in [22].

a. Electives (Selected by students)
   i. Cyber Forensics (CFCC)
   ii. Machine Learning (ML)
b. Core Courses:
   i. Compiler Design (CD)
   ii. Software engineering (SE)
   iii. Artificial Intelligence (AI)
c. Laboratory:
   i. Compiler Design (CD) Lab
   ii. Artificial Intelligence (AI) Lab

B. Step wise procedure for automated timetable generation using GA

- Fitness function = number of penalties (to be minimized)
- Maximum number of generations=1000

Initial Parameters:

- Mutation Rate = 0.01
- Population size = 100
- Crossover Rate= 0.9

Procedure: Applying GA to create optimized timetable

1. Initialize a timetable with given number of professors, time slots, classes and electives
2. Define population size, mutation rate, crossover rate
3. For each chromosome, calculate number of penalties as per constraints not satisfied
4. Calculate fitness of the chromosomes using fitness function=number of penalties
5. Conduct Selection, Crossover and Mutation for the current population of chromosomes
6. Repeat steps 3, 4, 5 for all generations
7. Analyze the performance with respect to following factors:
   a. No of penalties vs generations.
   b. Time taken for execution of each generation with respect to generation number
8. Compare these factors with that of SA and PSO

C. Step wise procedure for automated timetable generation using SA

- Fitness function = number of penalties

- Maximum number of iterations=1000

Initial Parameters:
- Initial Temperature = 1000
- Cooling Rate = 0.05

Procedure: Applying SA to create optimized timetable

1. Initialize the timetable with the number of professors, time slots, classes and subjects.
2. Initialize temperature T to be very high (T=1000).
3. Initialize the cooling_rate.
4. Repeat while (T > 1)
   a. Define current node C and randomly select a neighbor N.
   b. Evaluate ΔE = fitness(N)- fitness(C).

fitness(N)= number of penalties calculated for soft constraint violation in new node

fitness(C)= number of penalties calculated for soft constraint violation in current node

   a. If fitness(N) < fitness(C) i.e. ΔE≤0, choose the neighbor N with a probability = 1.
   b. If fitness(N) > fitness(C) i.e. ΔE >0, choose the neighbor N with a probability P=-ΔE/T.
      [Fitness Function (or cost function) = -ΔE/T]
   c. T =T * cooling_rate; cooling_rate ϵ [0,1]
   d. Stop when T < 1
5. Analyze the performance with respect to following factors:
   a. No of penalties vs iterations.
   b. Time taken for execution of each iteration with respect to iteration number
6. Compare these factors with that of GA and PSO

D. Step wise procedure for automated timetable generation using PSO
- Fitness function = number of penalties
- Maximum number of iterations=1000

Initial Parameters:
Maximum velocity = 100
Learning factors c1=2, c2=2

Procedure: Applying PSO to create optimized timetable

1. Initialize solutions (particle positions in the swarm)
2. Repeat till maximum iterations reached
   a. Calculate fitness value of each particle.
   b. Fitness value= number of penalties
   c. If Current fitness value <pBest , do
      pBest = current fitness value
   d. else
      retain previous pBest
   e. Assign best particle's pBest to gBest (gBest= best {pBest})
   f. Calculate velocity of each particle using (4)
   g. Update Eq (5) using values from Eq (4)
3. Analyze the performance with respect to following factors:
   a. No of penalties vs iterations.
   b. Time taken for execution of each iteration with respect to iteration number
4. Compare these factors with that of GA and SA

IV. Results and discussions

The experiments were conducted in JAVA eclipse and Python 3.7 software on a 1.6 GHz PC. As stated before, the student data is available at the university website at [11]. The timetables are generated by GA, SA and PSO algorithms by ensuring that no hard constraints are violated and the soft constraints are minimized to the maximum extent.

A. Performance Analysis:

Performance of GA:
The graph in Fig. 1 shows that the number of penalties decrease with the increase in generations in GA. Initially there is a huge decrease in penalties and then it becomes almost constant. The optimized fitness function is when the penalties = 40 at 1000 iterations.

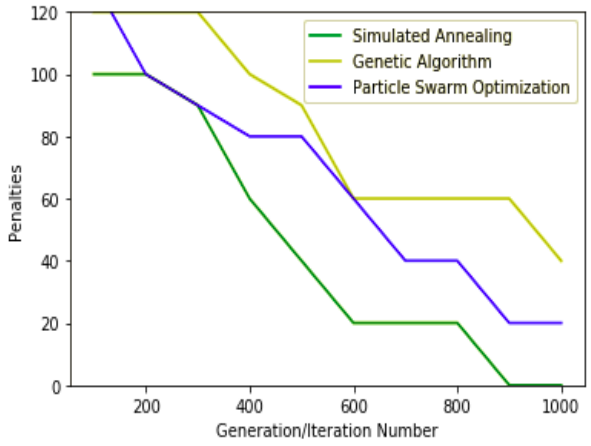

Figure 1. The number of penalties minimized over generation/iteration number (upto 1000) for GA, SA, PSO

Performance of SA:
The graph in Fig. 1 shows that the number of penalties decrease rapidly with the increase in generations in SA. The optimized solution is obtained for iterations close to 900 where number of penalties=0 and an optimized timetable is obtained.

Performance of PSO:
The graph in Fig. 1 shows that the number of penalties decrease with the increase in generations in PSO. The convergence speed is lesser than SA but more than GA. The optimized fitness function is when the penalties =20 at around 900 iterations when an optimized timetable is obtained.

B. Time taken for execution of each generation/iteration
The three algorithms are also compared with respect to their execution time (in ms) for every generation/iteration.

Performance of GA:
Here we study the execution time of each generation with respect to the generation number which is plotted in Fig. 2 for GA. We can observe that for GA, the execution time for consecutive generations decreases consistently with increase in

the number of generations. Initial execution time for GA =50 ms.

Performance of PSO:
Next we study the execution time of each iteration with respect to the iteration number in Fig. 3 for PSO. We can observe that for PSO, the execution time for consecutive iterations decreases (though inconsistently) with increase in the number of iterations. We can also observe that execution time for PSO is less than GA and SA and decreases slowly as compared to GA, SA.

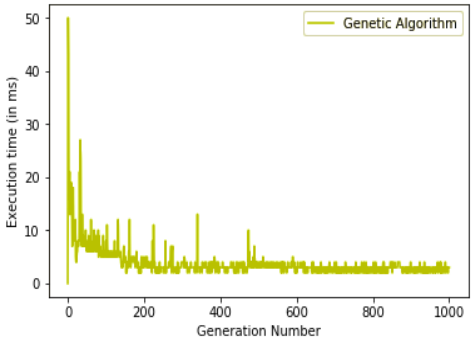

Figure 2. The variation of execution time (ms) over generation/iteration number for GA

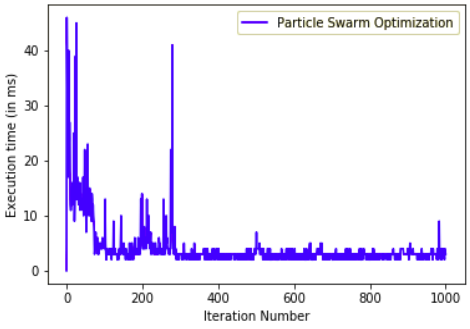

Figure 3. The variation of execution time (ms) over generation/iteration number for PSO

Performance of SA:
Fig. 4 shows the execution time of each iteration with respect to the iteration number for SA. We can observe that for SA, the execution time for consecutive iterations decreases with increase in the number of iterations with last few iterations taking up negligible time. SA has maximum execution time for the initial iterations than either GA and PSO i.e. 250 ms. However, it reduces steeply to less than 50 ms in less than 100 iterations.

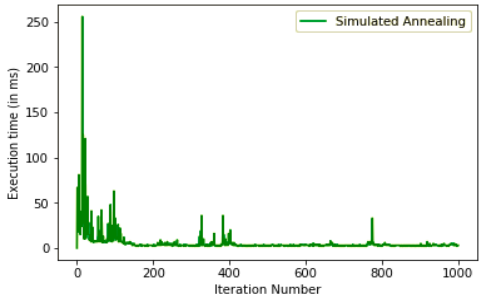

Figure 4. The variation of execution time (ms) over generation/iteration number for SA.

Thus, in summary, SA converges much faster in fewer iterations as compared to PSO and GA as observed from Fig. 1. GA takes more time to converge as compared to the other two algorithms. A comparison of the timing graphs in Figs. 2-4 indicates that initially, PSO followed by GA has lower execution time. However, overall SA has faster execution as observed from the tail end of the graph in Fig. 4. We compare the above graphs with our results in [22] that are shown in Table I for reference. Here also, GA is found to take up more iteration time than SA. The performance analysis for timetable optimization thus establishes the computational efficiency of SA involving local search heuristics. This indicates potential future research directions and would form the basis for incorporating some local search strategies, as in SA, within evolutionary algorithms like GA and PSO for quicker convergence.

C. Timetables generated using GA, PSO and SA

An instance of teacher preference input is shown in Fig. 5. Out of all the professors, two professors of the university gave their choice of slots as in Fig. 5, while the other professors indicated that they were comfortable with all slots. The timetables generated by our method are shown in Tables II and III for GA, Tables IV and V for SA, and Tables VI and VII for PSO, for the two sections 6-A and 6-B. An observation from the timetables is that SA gives a more uniformly distributed schedule than GA and PSO. It satisfies the constraints to a maximum extent such that there are no free gaps in between. PSO, however, creates more free time gaps for students than SA as observed from Tables VI and VII.

We also show for comparison purpose the timetables generated by our previous work in [22]. The timetables generated in [22] are shown for reference in Tables VIII, IX, X for GA, and Tables XI, XII, XIII for SA. Only the open elective courses were scheduled in [22] as seen. The entire core, lab, elective courses are scheduled. As observed from Tables VIII to XIII, the timetables generated for the elective courses, for the same students as in [22], did not incorporate teacher's preferences of slots, and the two classes A batch and B batch were allotted classrooms randomly causing the students to move constantly from one class to the other. In the present set of timetables in Tables II to VII, due to the additional soft constraints introduced, the two professors who requested their respective slots (Fig. 5) had their requests granted. There are not much of free gaps between classes and the student's time is utilized to a great extent. The movement of students from one classroom to the other was also minimized. The A batch was concentrated in classroom no. TW1TF3 while the B batch classes were found scheduled in TW2GF2. We achieved this through the additional soft constraints that are not mandatory, yet their satisfaction in our case proved to be crucial to achieve high efficiency.

Best Case Makespan		Average Case Makespan		Worst Case Makespan	
Generation No.	Time (in ms)	Generation No.	Time (in ms)	Generation No.	Time (in ms)
1	170	7	265	13	413
Simulated Annealing					
Best Case Makespan		Average Case Makespan		Worst Case Makespan	
Iteration No.	Time (in ms)	Iteration No.	Time (in ms)	Iteration No.	Time (in ms)
1	143	5	220	10	311

Table I. Performance analysis for SA and GA for timetables generated in [22]

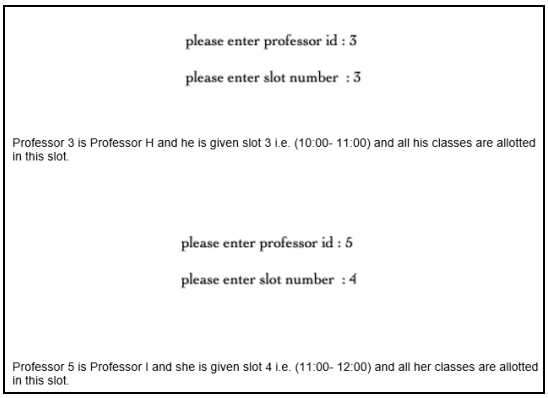

Figure 5. The Graphical User Interface (GUI) for accepting teacher preference against Teacher ID

Room: TW1TF3	6-A							
Time	08:00- 09:00	09:00- 10:00	10:00- 11:00	11:00-12:00	12:00- 13:00	13:00- 14:00	14:00- 15:00	15:00- 16:00
MONDAY	CFCC- A Theory: Prof. B	CFCC- A Theory: Prof. B	SE-A Theory: Prof: E	SE-A Theory: Prof: E			AI Lab - A- G1: Prof: G	AI Lab - A- G1: Prof: G
TUESDAY	ML- A Theory: Prof. A	CFCC- A Theory: Prof. B		SE-A Theory: Prof: E	SE - A - T - G2: Prof: E		AI Lab - A- G2: Prof: A	AI Lab - A- G2: Prof: A
WEDNESDAY	CFCC- T- A- G1: Prof. B	ML- T- A- G1: Prof. A	AI-A Theory: Prof: F	SE - A - T - G1: Prof: E			CD Lab - A- G2: Prof: D	CD Lab - A- G2: Prof: D
THURSDAY	CFCC- T- A- G2: Prof. B	ML- A Theory: Prof. A	AI-A Theory: Prof: F	CD-A Theory: Prof: D		CD Lab - A- G1: Prof: D	CD Lab - A- G1: Prof: D	
FRIDAY	ML- A Theory: Prof. A	ML- T- A- G2: Prof. A	AI-A Theory: Prof: F		CD-A Theory: Prof: D	CD-A Theory: Prof: D		

Table II. Timetable generated by GA for the students of batch 6-A

Room: TW2GF2	6-B							
Time	08:00- 09:00	09:00- 10:00	10:00- 11:00	11:00-12:00	12:00- 13:00	13:00- 14:00	14:00- 15:00	15:00- 16:00
MONDAY	CFCC- B Theory: Prof. C	CFCC- T- B- G2: Prof. B	SE-B Theory: Prof: H		AI Lab - B- G2: Prof: A	AI Lab - B- G2: Prof: A	CD Lab - B- G1: Prof: D	CD Lab - B- G1: Prof: D
TUESDAY	ML- B Theory: Prof. A	CFCC- T- B- G1: Prof. B	SE - B - T - G2: Prof: H	AI-B Theory: Prof: I		CD Lab - B- G2: Prof: D	CD Lab - B- G2: Prof: D	
WEDNESDAY	ML- B Theory: Prof. A	ML- B Theory: Prof. A	SE - B - T - G1: Prof: H	AI-B Theory: Prof: I	CD-B Theory: Prof: J			
THURSDAY	ML- T- B- G1: Prof. A	CFCC- B Theory: Prof. C	SE-B Theory: Prof: H		AI Lab - B- G1: Prof: A	AI Lab - B- G1: Prof: A		
FRIDAY	ML- T- B- G2: Prof. A	CFCC- B Theory: Prof. C	SE-B Theory: Prof: H	AI-B Theory: Prof: I		CD-B Theory: Prof: J	CD-B Theory: Prof: J	

Table III. Timetable generated by GA for the students of batch 6-B

Room: TW1TF3	6-A							
Time	08:00- 09:00	09:00- 10:00	10:00- 11:00	11:00-12:00	12:00- 13:00	13:00- 14:00	14:00- 15:00	15:00- 16:00
MONDAY	ML- A Theory: Prof. A	CFCC- A Theory: Prof. B	CD-A Theory: Prof: D		AI-A Theory: Prof: F	AI Lab - A- G2: Prof: A	AI Lab - A- G2: Prof: A	
TUESDAY	CFCC- A Theory: Prof. B	ML- A Theory: Prof. A	CD-A Theory: Prof: D	CD-A Theory: Prof: D		CD Lab - A- G2: Prof: D	CD Lab - A- G2: Prof: D	
WEDNESDAY	CFCC- T- A- G1: Prof. B	ML- A Theory: Prof. A		AI-A Theory: Prof: F	AI-A Theory: Prof: F			
THURSDAY	CFCC- T- A- G2: Prof. B	ML- T- A- G2: Prof. A	SE - A - T - G1: Prof: E	SE-A Theory: Prof: E	SE-A Theory: Prof: E	CD Lab - A- G1: Prof: D	CD Lab - A- G1: Prof: D	
FRIDAY	ML- T- A- G1: Prof. A	CFCC- A Theory: Prof. B	AI Lab - A- G1: Prof: G	AI Lab - A- G1: Prof: G	SE-A Theory: Prof: E			SE - A - T - G2: Prof: E

Table IV. Timetable generated by SA for the students of batch 6-A

Room: TW2GF2	6-B							
Time	**08:00- 09:00**	**09:00- 10:00**	**10:00- 11:00**	**11:00-12:00**	**12:00- 13:00**	**13:00- 14:00**	**14:00- 15:00**	**15:00- 16:00**
MONDAY	CFCC- B Theory: Prof. C	CFCC- T- B- G2: Prof. B	SE - B - T - G2: Prof: H		CD Lab - B- G1: Prof: D	CD Lab - B- G1: Prof: D	CD Lab - B- G2: Prof: D	CD Lab - B- G2: Prof: D
TUESDAY	CFCC- B Theory: Prof. C	ML- T- B- G2: Prof. A	SE-B Theory: Prof: H	AI-B Theory: Prof: I	CD-B Theory: Prof: J		CD-B Theory: Prof: J	
WEDNESDAY	CFCC- T- B- G1: Prof. B	ML- T- B- G1: Prof. A	SE - B - T - G1: Prof: H	AI-B Theory: Prof: I		CD-B Theory: Prof: J		
THURSDAY	CFCC- B Theory: Prof. C	ML- B Theory: Prof. A	SE-B Theory: Prof: H	AI-B Theory: Prof: I				
FRIDAY	ML- B Theory: Prof. A	ML- B Theory: Prof. A	SE-B Theory: Prof: H		AI Lab - B- G1: Prof: A	AI Lab - B- G1: Prof: A	AI Lab - B- G2: Prof: A	AI Lab - B- G2: Prof: A

Table V. Timetable generated by SA for the students of batch 6-B

Room: TW1TF3	6-A							
Time	**08:00- 09:00**	**09:00- 10:00**	**10:00- 11:00**	**11:00-12:00**	**12:00- 13:00**	**13:00- 14:00**	**14:00- 15:00**	**15:00- 16:00**
MONDAY	ML- T- A- G2: Prof. A	ML- A Theory: Prof. A		AI Lab - A- G2: Prof: A	AI Lab - A- G2: Prof: A		CD-A Theory: Prof: D	
TUESDAY	CFCC- A Theory: Prof. B	CFCC- A Theory: Prof. B		SE-A Theory: Prof: E		CD-A Theory: Prof: D	CD-A Theory: Prof: D	
WEDNESDAY	CFCC- A Theory: Prof. B	ML- A Theory: Prof. A	CD Lab - A- G2: Prof: D	CD Lab - A- G2: Prof: D		AI Lab - A- G1: Prof: G	AI Lab - A- G1: Prof: G	
THURSDAY	CFCC- T- A- G2: Prof. B	ML- A Theory: Prof. A	SE - A - T - G2: Prof: E	AI-A Theory: Prof: F	AI-A Theory: Prof: F		CD Lab - A- G1: Prof: D	CD Lab - A- G1: Prof: D
FRIDAY	CFCC- T- A- G1: Prof. B	ML- T- A- G1: Prof. A	SE-A Theory: Prof: E	SE-A Theory: Prof: E		AI-A Theory: Prof: F	SE - A - T - G1: Prof: E	

Table VI. Timetable generated by PSO for the students of batch 6-A

Room: TW2GF2	6-B							
Time	**08:00- 09:00**	**09:00- 10:00**	**10:00- 11:00**	**11:00-12:00**	**12:00- 13:00**	**13:00- 14:00**	**14:00- 15:00**	**15:00- 16:00**
MONDAY	CFCC- B Theory: Prof. C	ML- T- B- G2: Prof. A	SE-B Theory: Prof: H	AI-B Theory: Prof: I	CD Lab - B- G2: Prof: D	CD Lab - B- G2: Prof: D		
TUESDAY	ML- B Theory: Prof. A	ML- T- B- G1: Prof. A	SE-B Theory: Prof: H		AI Lab - B- G1: Prof: A	AI Lab - B- G1: Prof: A		
WEDNESDAY	CFCC- T- B- G1: Prof. B	CFCC- T- B- G2: Prof. B	SE - B - T - G1: Prof: H	AI-B Theory: Prof: I		AI Lab - B- G2: Prof: A	AI Lab - B- G2: Prof: A	
THURSDAY	ML- B Theory: Prof. A	ML- B Theory: Prof. A	SE-B Theory: Prof: H	AI-B Theory: Prof: I	CD-B Theory: Prof: J			
FRIDAY	CFCC- B Theory: Prof. C	CFCC- B Theory: Prof. C	SE - B - T - G2: Prof: H		CD-B Theory: Prof: J	CD-B Theory: Prof: J	CD Lab - B- G1: Prof: D	CD Lab - B- G1: Prof: D

Table VII. Timetable generated by PSO for the students of batch 6-B

Room: TW2GF2				
Time	**08:00- 09:00**	**09:00- 10:00**	**10:00- 11:00**	**11:00-12:00**
MONDAY	CFCC- B- Theory: Prof. C			
TUESDAY		CFCC- B- Theory: Prof. C	CFCC- B- Theory: Prof. C	
WEDNESDAY			CFCC- A- Theory: Prof. B	CFCC- A- Theory: Prof. B
THURSDAY	CFCC- A- Theory: Prof. B			
FRIDAY				

Table VIII. Timetable generated by GA for the elective subject CFCC in [22] for classroom TW2GF2

Room: TW1TF3				
Time	**08:00- 09:00**	**09:00- 10:00**	**10:00- 11:00**	**11:00-12:00**
MONDAY	CFCC- T- A- G2: Prof. B	CFCC- T- A- G1: Prof. B		
TUESDAY				
WEDNESDAY				
THURSDAY				
FRIDAY			CFCC- T- B- G1: Prof. B	CFCC- T- B- G2: Prof. B

Table IX. Timetable generated by GA for the elective subject CFCC in [22] for classroom TW1TF3

Room: TW3TF3				
Time	08:00- 09:00	09:00- 10:00	10:00- 11:00	11:00-12:00
MONDAY				
TUESDAY		ML- A Theory: Prof. A	ML- A Theory: Prof. A	
WEDNESDAY	ML- T- G3: Prof. A			
THURSDAY			ML- A Theory: Prof. A	ML- T- G4: Prof. A
FRIDAY	ML- T- G1: Prof. A	ML- T- G2: Prof. A		

Table X. Timetable generated by GA for the elective subject ML in [22] for classroom TW3TF3

Room: TW2GF2				
Time	08:00- 09:00	09:00- 10:00	10:00- 11:00	11:00-12:00
MONDAY				
TUESDAY				
WEDNESDAY			CFCC- B- Theory: Prof. C	
THURSDAY		CFCC- T- A- G2: Prof. B		
FRIDAY	CFCC- B- Theory: Prof. C	CFCC- B- Theory: Prof. C		

Table XI. Timetable generated by SA for the elective subject CFCC in [22] for classroom TW2GF2

Room: TW1TF3				
Time	08:00- 09:00	09:00- 10:00	10:00- 11:00	11:00-12:00
MONDAY	CFCC- A- Theory: Prof. B			
TUESDAY	CFCC- T- B- G1: Prof. B	CFCC- A- Theory: Prof. B	CFCC- A- Theory: Prof. B	
WEDNESDAY	CFCC- T- B- G2: Prof. B			
THURSDAY				
FRIDAY			CFCC- T- A- G1: Prof. B	

Table XII. Timetable generated by SA for the elective subject CFCC in [22] for classroom TW1TF3

Room: TW3TF3				
Time	08:00- 09:00	09:00- 10:00	10:00- 11:00	11:00-12:00
MONDAY		ML- T- G2: Prof. A	ML- T- G4: Prof. A	
TUESDAY	ML- A Theory: Prof. A			
WEDNESDAY	ML- A Theory: Prof. A	ML- T- G3: Prof. A		
THURSDAY	ML- A Theory: Prof. A		ML- T- G1: Prof. A	
FRIDAY				

Table XIII. Timetable generated by SA for the elective subject ML in [22] for classroom TW3TF3

We propose to further explore more complex teacher and student preferences for testing the efficiency of our constraint model. This forms the future scope of our work.

V. Conclusions

In this paper, we have investigated genetic algorithm, simulated annealing and particle swarm optimization algorithms for the task of automatically creating an entire timetable (electives + core courses + laboratory sessions) for two separate batches of undergraduate students in a recognized university. We have proposed a novel set of hard constraints and soft constraints suited to the task that incorporate teacher's preferences for slots, and minimizes student movement between classes and the gaps between classes. The three optimization algorithms are compared on the basis of execution time of each generation/iteration with respect to generation/iteration number which decreases most in Simulated Annealing. We also compared the algorithms on the basis of number of penalties vs generations/iterations. With respect to the minimized penalties, the algorithms can be ranked as SA < PSO < GA. Simulated annealing minimizes penalties to the greatest extent and obtains an optimal solution in the least number of iterations.

References

[1] Gür, Şeyda, and Tamer Eren. "Scheduling and Planning in Service Systems with Goal Programming: Literature Review." *Mathematics* 6, no. 11 (2018): 265.

[2] Yazdani, Mehdi, Bahman Naderi, and Esmaeil Zeinali. "Algorithms for university course scheduling problems." *Tehnicki Vjesnik-Technical Gazette* 24 (2017): 241-247.

[3] Akkan, Can, and Ayla Gülcü. "A bi-criteria hybrid Genetic Algorithm with robustness objective for the course timetabling problem." *Computers & Operations Research* 90 (2018): 22-32.

[4] Rozaimee, Azilawati, Adibah Nabihah Shafee, Nurul Anissa Abdul Hadi, and Mohamad Afendee Mohamed. "A Framework for University's Final Exam Timetable Allocation Using Genetic Algorithm." *World Applied Sciences Journal* 35, no. 7 (2017): 1210-1215.

[5] AlHadid, Issam, Khalid Kaabneh, Hassan Tarawneh, and Aysh Alhroob. "Investigation of simulated annealing

components to solve the university course timetabling problem." *Italian Journal of Pure and Applied Mathematics* (2020): 291.

[6] Leite, Nuno, Fernando Melício, and Agostinho C. Rosa. "A fast simulated annealing algorithm for the examination timetabling problem." *Expert Systems with Applications* 122 (2019): 137-151.

[7] Zheng, Shuang, Long Wang, Yueyue Liu, and Rui Zhang. "A simulated annealing algorithm for university course timetabling considering travelling distances." *International Journal of Computing Science and Mathematics* 6, no. 2 (2015): 139-151.

[8] Goh, Say Leng, Graham Kendall, and Nasser R. Sabar. "Simulated annealing with improved reheating and learning for the post enrolment course timetabling problem." *Journal of the Operational Research Society* 70, no. 6 (2019): 873-888.

[9] Wang, Yao-Te, Yu-Hsin Cheng, Ting-Cheng Chang, and S. M. Jen. "On the application of data mining technique and genetic algorithm to an automatic course scheduling system." In *Cybernetics and Intelligent Systems, 2008 IEEE Conference on*, pp. 400-405. IEEE, 2008.

[10] Agrawal, Rakesh, and Ramakrishnan Srikant. "Fast algorithms for mining association rules." In *Proc. 20th int. conf. very large data bases, VLDB*, vol. 1215, pp. 487-499. 1994.

[11] [online] reg.exam.dtu.ac.in/register_all.php [*website: Delhi Technological University, New Delhi, India*]

[12] Sastry, Kumara, David E. Goldberg, and Graham Kendall. "Genetic algorithms." In *Search methodologies*, pp. 93-117. Springer, Boston, MA, 2014

[13] Savasere, Ashok, Edward Robert Omiecinski, and Shamkant B. Navathe. An efficient algorithm for mining association rules in large databases. Georgia Institute of Technology, 1995.

[14] Viktoratos, Iosif, Athanasios Tsadiras, and Nick Bassiliades. "Combining community-based knowledge with association rule mining to alleviate the cold start problem in context-aware recommender systems." *Expert systems with applications* 101 (2018): 78-90.

[15] Susan, Seba, Puneet Sharawat, Sandeep Singh, Ramkesh Meena, Amit Verma, and Mukesh Kumar. "Fuzzy C-means with non-extensive entropy regularization." In *Signal Processing, Informatics, Communication and Energy Systems (SPICES), 2015 IEEE International Conference on*, pp. 1-5. IEEE, 2015.

[16] Shen, Jia-ji, Hui-zhu Dong, Yi-ran Su, and Zhi-gang Zhang. "Application of Genetic Algorithm and Simulated Annealing Algorithm for Course Scheduling Problem." In *2019 International Conference on Modeling, Analysis, Simulation Technologies and Applications (MASTA 2019)*. Atlantis Press, 2019.

[17] Abdullah, Salwani, and Hamza Turabieh. "Generating university course timetable using genetic algorithms and local search." In *Convergence and Hybrid Information Technology, 2008. ICCIT'08. Third International Conference on*, vol. 1, pp. 254-260. IEEE, 2008.

[18] Hossain, Sk Imran, M. A. H. Akhand, M. I. R. Shuvo, Nazmul Siddique, and Hojjat Adeli. "Optimization of university course scheduling problem using particle swarm optimization with selective search." *Expert Systems with Applications* 127 (2019): 9-24.

[19] Susan, Seba, and Aparna Bhutani. "A Novel Memetic Algorithm Incorporating Greedy Stochastic Local Search Mutation for Course Scheduling." In *2019 IEEE International Conference on Computational Science and Engineering (CSE) and IEEE International Conference on Embedded and Ubiquitous Computing (EUC)*, pp. 254-259. IEEE, 2019.

[20] Adrianto, Dennise. "Comparison Using Particle Swarm Optimization and Genetic Algorithm for Timetable Scheduling." *Journal of Computer Science* 10, no. 2 (2014): 341

[21] Zhang, Defu, Yongkai Liu, Rym M'Hallah, and Stephen CH Leung. "A simulated annealing with a new neighborhood structure based algorithm for high school timetabling problems." *European Journal of Operational Research* 203, no. 3 (2010): 550-558.

[22] Susan, Seba, and Aparna Bhutani. "Data Mining with Association Rules for Scheduling Open Elective Courses Using Optimization Algorithms." In *International Conference on Intelligent Systems Design and Applications*, pp. 770-778. Springer, Cham, 2018.

[23] Holland, John Henry. Adaptation in natural and artificial systems: an introductory analysis with applications to biology, control, and artificial intelligence. MIT press, 1992.

[24] Henderson, Darrall, Sheldon H. Jacobson, and Alan W. Johnson. "The theory and practice of simulated annealing." In *Handbook of metaheuristics*, pp. 287-319. Springer, Boston, MA, 2003.

[25] Eberhart, Russell, and James Kennedy. "Particle swarm optimization." In *Proceedings of the IEEE international conference on neural networks*, vol. 4, pp. 1942-1948. 1995.

[26] Susan, Seba, Rohit Ranjan, Udyant Taluja, Shivang Rai, and Pranav Agarwal. "Neural Net Optimization by Weight-Entropy Monitoring." In *Computational Intelligence: Theories, Applications and Future Directions-Volume II*, pp. 201-213. Springer, Singapore, 2019.

.

Author Biographies

Seba Susan received her Ph.D in Image Processing from the Electrical Engineering Department of Indian Institute of Technology (IIT), Delhi in 2014. She is currently Associate Professor in the Department of Information Technology, Delhi Technological University (DTU), India. Her research areas are Machine Learning, Computer Vision, Speech & Natural Language Processing.

Aparna Bhutani completed her B.Tech in Information Technology from Pune University in 2013. She is currently a postgraduate student in Information Systems in the Department of Information Technology, Delhi Technological University (DTU), Delhi, India. Her research area is exploring the use of evolutionary algorithms for scheduling problems.

View publication stats

Journal of Ubiquitous Computing and Communication Technologies (UCCT) (2020)
Vol.02/ No.04
Pages: 219-222
https://www.irojournals.com/jucct/
DOI: https://doi.org/10.36548/jucct.2020.4.005

IoT in Online Banking

Malti Bansal [1,*], Naman Oberoi [2], Mohd. Sameer [1]
[1]Department of Electronics & Communication Engineering,
Delhi Technological University (DTU), Delhi-110042, India

[2]Department of Mathematics,
Delhi Technological University (DTU), Delhi-110042, India

maltibansal@gmail.com

Abstract –As we know, there are so many changes arriving right now ion the banking industries which are really complex industries. Every day, huge amount of data is processed and gathered. With this increase in size, it is becoming more difficult for banking institutions to manage this data and handle other segments of their business. This paper presents the scope of IoT in the banking domain and how various transformations could potentially bring game changing reforms in the traditional methodology. Banking institutions need to integrate IoT in their systems to increase their market share by providing services catered to a clients need based on the data that's being processed in real time. In future, IoT will be able to create such technologies which will be able to connect physical objects so that objects can do their own intelligent decision making.

Keywords –Banking, IoT, Big Data, Analytics, Security and Privacy

I. Introduction

Banking and financial services serve as the backbone for a country's economy and information technology helps power this infrastructure. For a growing economy, its financial systems should be stable. As the technology advances, the scope of Online Banking increases as it is more convenient for people to do banking online then to go physically in the bank. Like, applying for an account online, doing transactions online, verifying all the details online. All of this provides a major convenience to the users. That's why these days most of the banks are providing online services to the users. Banking involves maintaining relationship with customers and trust if of key nature. Customer satisfaction is key for maintaining lifetime business.

In online banking, a person can perform many processes on his account related to finance using the website of financial institution. We can also call it 'Internet Banking'. As we know, banking systems are where a bank employee deals with the customer and solve his queries physically but in Internet Banking, we are trying to connect the main banking systems with Online Banking to make an ease for the customers.

IoT or Internet of things is a network where there is a transfer and communication of data over the internet through objects which are known as smart devices. It has been widely used in various fields ranging from healthcare, agriculture, smart homes, waste management, etc. There are a total of 5 stages in it. 1st is where we tried to connect 2 systems. When WWW(World Wide Web) is created, many computers can be connected at same time which is the next stage. Then, internet is connected to different devices like mobile phones which are followed by social networking platforms known as people-internet. After that comes the IOT where different objects are connected with each other.

In this paper, we are going to study and discuss things regarding how we can connect IoT with Online Banking. That is how we can do the Online Banking processes with the use of Internet of Things so that we can make some processes easier with it. Rest of the paper is divided into sections as follows. Section II presents what developments in the sector are. Section III describes the position of IoT in the online banking sphere. Section IV highlights the challenges that further need to be addressed and what lies ahead for this industry. Section V gives a conclusive statement to the paper.

II. When it started and developments done so far

As far as the online banking domain is concerned, developments are still in a nascent stage with new ideas coming up every day. The existing services can further be enhanced using a standardized framework as proposed by [1].

ISSN: 2582-337X
Submitted: 06.12.2020
Accepted: 31.12.2020
Published: 08.01.2021

Journal of Ubiquitous Computing and Communication Technologies (UCCT) (2020)
Vol.02/ No.04
Pages: 219-222
https://www.irojournals.com/jucct/
DOI: https://doi.org/10.36548/jucct.2020.4.005

This requires the interpretation of a user's income accounts and balances to provide offers based on the financial condition of the individual and his spending pattern. What further needs to be considered is that such information is secure and not misused by the banks for driving its profitability by using unethical means.

A standard architecture across various papers published consists of the following layers

a) Device management layer – consists of IoT devices that gather data and transmits it to the communication layer. This layer continuously interacts with the physical world. Devices include sensors, telematics from wearables or financial statements of the user.

b) Communication layer – performs functions of the network and transport layer of the traditional internet architecture [1]. This supports routing, error control, handles congestion, QoS,etc. The data is transferred to a cloud platform.

c) Integration layer and analytics layer – This layer helps in storing the information and providing an architecture for analytics on data to take place. This also handles the security of the data.

d) Application layer – this acts as an interface for the user where the user is presented with alerts, offers, reports, etc.

An example of this structure employed is fingerprint authentication. Sensors in device management layer capture the fingerprint and communicate it onto the cloud. Here, it is verified with the data in the database and on successful correspondence, the user is granted access to the banking interface [4].

III. Where we stand today

We will now discuss some of the trends that have had a direct impact on the online financial sphere using IoT. In mobile banking, account management has become easier, seamless and can be done instantly and all banking services can be accessed easily. Now, we can access to our bank accounts anywhere anytime. It has become much easier now. To recognise an individual, biometrics is helping a lot because its data is absolutely unique and specific for everyone. Because it uses some advanced techniques. What you need is an account and a platform to access that which is also known as a digital interface.

Removing physical signatures and using 'wet ink technology' is also one of the major achievements. In this, signature of a person is cloned to a paper via a touch screen device so that the need of physical presence of that person is not compulsory.

Monitoring in real time of collaterals and assets is done as a specific identity is provided to the physical objects and hence their tracking and monitoring becomes easier.

Nowadays, everyone wants an instant payment. People are investing in the technologies where physical appearance is not compulsory for transactions. In online banking, you may think there is not enough security but biometrics data is very secure as it is not easy for anyone to access to that data or to understand that data in its original form. So, more and more people are using these online methods now.

There is a platform where you don't need a bank account and you can store and transfer money to other same platforms easily and really fast using 'Wallets of things'. For example, we see PAYTM and PHONEPE apps which have a section known as wallets. Through these sections, we can transfer money to other wallets instantly and in a much easier way.

In future, we can connect an action to a condition. For example, you can take electrical cycles on rent. Suppose you pay rent for 10 km riding. After you ride 10 km, bike will automatically stop. That is an action (bike stopped) occurred automatically when a condition (rent service finished) arrived.

In Crowd-based financing, small amounts of funds are collected from large amount of crowd using a basic internet platform. In earlier times, you have to go to each house for such payments but now it's all become much easier.

ISSN: 2582-337X
Submitted: 06.12.2020
Accepted: 31.12.2020
Published: 08.01.2021

Journal of Ubiquitous Computing and Communication Technologies (UCCT) (2020)
Vol.02/ No.04
Pages: 219-222
https://www.irojournals.com/jucct/
DOI: https://doi.org/10.36548/jucct.2020.4.005

'PM CARES FUND' is one of the best examples of such financings where funds are collected from a large number of people through online banking methods.

VIRTUAL MONEY is also become really common these days, where you have virtual money in your mobile and you can do payments and transactions through those without having some real money with you.

For securities, biometrics is really enough as these are approximately impossible to access through and even if you get the data, it will be very hard to understand. Like, computers only understand binary languages and it has to convert any other language into binary to actually understand that. So that conversion is nearly impossible for anyone. Also, some venous impressions are created to unable transactions which are impossible to duplicate.

KYC means "Know Your Customer" which is done by bank to get a specific identification of its customer. Some processes are done by bank for KYC to protect their customers from frauds. By using IOT, and giving a specific identity to the customer, special services can be given to special customers through his history. Like, you get much more discount on a shop from where you are buying stuff regularly.

Banks have been quick in terms on investing in new technologies and allotting a significant amount for these services. The number of financial frauds has risen in recent times. The public sector banks have been hit the hardest. With various measures initiated through RBI, number of banking fraud cases have decline, but the amount of money lost has increased [2]. The key piece for the effective implementation of the systems is through employing the best analytics to flag accounts that trigger early warning signals as advised by the RBI.

There has been a significant integration of artificial intelligence for modelling and statistics of data and blockchain for the data privacy. Bluetooth based beacons by Barclays has found use in helping disabled passenger navigate to branches. The use of IoT powered devices such as Alexa, wearables like Samsung gear and fit pay has been crucial in the sense that customers can now pay their bills through it. Banks have started to analyse a customers need through the data obtained, to provide them with sound and smart financial decisions.

IV. Future Scope

IoT relies on huge data sets to learn about the users and surrounding to better provide interface. However the processing and collection of this data on a huge scale can lead to concerns regarding security and privacy, as well as the management and authentication of a user's identity.

With the amount of data in hand, it also becomes crucial to remove false conclusions from the interpretation of this data which could lead to false positives or false negatives that could label the system as unreliable.

Targeting promotions and ads to users could lead to modifying their behaviour as seen in the Cambridge Analytica scandal. Monitoring and using statistics is what the upcoming models would need to further consider.

Quick response time using analytics on raw data in real time would help in formulating meaningful data from which results can be obtained for the applications. Edge analytics is an area of research to help improve the response time [3].

Banks would further need to employ Big Data in correspondence to IoT to tackle the issues of variety, volume and velocity. Hadoop and MapReduce prove that there is a enormous scope to decrease the detection and/or processing time to prevent fraud [5-13].

Advancements in available hardware and software has led to the development of new methods for the financial service sector. This would lead to a better customer experience, however this is only possible if big data analytics and cloud accessibility are integrated with the IoT structures [1].

V. Conclusion

With the integration of IoT in the banking sphere, the strain on banking institutions have reduced as they need to address fewer customers physically.From Table I. [3], India remains a largely untapped market in terms of banking online with only 48% of the population engaged. IoT can help capture this untapped market and for its successful

ISSN: 2582-337X
Submitted: 06.12.2020
Accepted: 31.12.2020
Published: 08.01.2021

Journal of Ubiquitous Computing and Communication Technologies (UCCT) (2020)
Vol.02/ No.04
Pages: 219-222
https://www.irojournals.com/jucct/
DOI: https://doi.org/10.36548/jucct.2020.4.005

implementation, banking institutions would need to strive to make a uniform customer interface that is easy for the general public to use. Future banking will circle around IoT being the critical support for the institutions products and services. It will lead to essential developments in the banking sectors and hence we will see more ease in money transactions, creating bank accounts, security of our accounts, etc. As the graph of development in IOTs is exponential, we will see these changes really quickly and we will be able to observe those in our day-to-day lives.

References

[1] Vemula, Dr-Dinesh Reddy & Gangadharan, G R. (2016). Towards an Internet of Things Framework for Financial Services Sector. 10.1109/RAIT.2016.7507897.
[2] R. S. Lande, S. A. Meshram and P. P. Deshmukh, "Smart banking using IoT," *2018 International Conference on Research in Intelligent and Computing in Engineering (RICE)*, San Salvador, 2018, pp. 1-4, doi: 10.1109/RICE.2018.8627903.
[3] H. Ramalingam and V. P. Venkatesan, "Conceptual analysis of Internet of Things use cases in Banking domain," *TENCON 2019 - 2019 IEEE Region 10 Conference (TENCON)*, Kochi, India, 2019, pp. 2034-2039, doi: 10.1109/TENCON.2019.8929473.
[4] A. Taralekar, G. Chouhan, R. Tangade and N. Shardoor, "One touch multi-banking transaction ATM system using biometric and GSM authentication," *2017 International Conference on Big Data, IoT and Data Science (BID)*, Pune, 2017, pp. 60-64, doi: 10.1109/BID.2017.8336574.
[5] Boumlik, Abdeljalil & Bahaj, Mohamed. (2018). Big Data and IoT: A Prime Opportunity for Banking Industry. Lecture Notes in Networks and Systems. 396-407. 10.1007/978-3-319-69137-4_35.
[6] Du, X., Zhou, Z., Zhang, Y. *et al.* Energy-efficient sensory data gathering based on compressed sensing in IoT networks. *J Cloud Comp* **9,** 19 (2020). https://doi.org/10.1186/s13677-020-00166-x
[7] A. Al-Fuqaha, M. Guizani, M. Mohammadi, M. Aledhari and M. Ayyash, "Internet of Things: A Survey on Enabling Technologies, Protocols, and Applications," in *IEEE Communications Surveys & Tutorials*, vol. 17, no. 4, pp. 2347-2376, Fourthquarter 2015, doi: 10.1109/COMST.2015.2444095.
[8] Fadoua Khanboubi, Azedine Boulmakoul, Mohamed Tabaa,Impact of digital trends using IoT on banking processes,Procedia Computer Science,Volume 151,2019,Pages 77-84,ISSN 1877-0509, https://doi.org/10.1016/j.procs.2019.04.014.(http://www.sciencedirect.com/science/article/pii/S1877050919304752)
[9] M. Bansal and Priya, "Application Layer Protocols for Internet of Healthcare Things (IoHT)," *2020 Fourth International Conference on Inventive Systems and Control (ICISC)*, Coimbatore, India, 2020, pp. 369-376, doi: 10.1109/ICISC47916.2020.9171092.
[10] M. Bansal, Priya, "Performance Comparison of MQTT and CoAP Protocols in Different Simulation Environments". G. Ranganathan, J. Chen, A. Rocha (eds) Inventive Communication and Computational Technologies. Lecture Notes in Networks and Systems, vol. 145, pp. 549-560, Springer, Singapore, https://doi.org/10.1007/978-981-15-7345-3_47
[11] M.Bansal, Priya, "Machine Learning Perspective in VLSI Computer Aided Design at Different Abstraction Levels", 2nd Int. Conf. on Mobile Computing and Sustainable Informatics (ICMCSI 2021), Tribhuvan University, Nepal, 2021.
[12] M.Bansal, A. Goyal, A. Choudhary, "Industrial Internet of Things (IIoT): A Vivid Perspective", 5th Int. Conf. on Inventive Systems and Control (ICISC 2021), India, 2021.
[13] M. Bansal, V. Sirpal, M. K. Choudhary, "Advancing e-Government using Internet of Things", ", 2nd Int. Conf. on Mobile Computing and Sustainable Informatics (ICMCSI 2021), Tribhuvan University, Nepal, 2021.

ISSN: 2582-337X
Submitted: 06.12.2020
Accepted: 31.12.2020
Published: 08.01.2021

ResearchGate

See discussions, stats, and author profiles for this publication at: https://www.researchgate.net/publication/349412860

Levofloxacin Detection Using L-Cysteine Capped MgS Quantum Dots via the Photoinduced Electron Transfer Process

Conference Paper · February 2021

DOI: 10.3389/fnano.2021.616186

CITATIONS
0

READS
41

8 authors, including:

Tarun Kumar Dhiman
Jawaharlal Nehru University
11 PUBLICATIONS **18** CITATIONS

SEE PROFILE

Anil Kumar
National Institute of Immunology
11 PUBLICATIONS **22** CITATIONS

SEE PROFILE

Pratima R Solanki
Jawaharlal Nehru University
199 PUBLICATIONS **5,439** CITATIONS

SEE PROFILE

Some of the authors of this publication are also working on these related projects:

Development of Nanobiochip for Oral Cancer Detection View project

Application of Carbon Dots View project

All content following this page was uploaded by Tarun Kumar Dhiman on 19 February 2021.

The user has requested enhancement of the downloaded file.

frontiers in Nanotechnology

ORIGINAL RESEARCH
published: 17 February 2021
doi: 10.3389/fnano.2021.616186

Levofloxacin Detection Using L-Cysteine Capped MgS Quantum Dots *via* the Photoinduced Electron Transfer Process

S. Z. H. Hashmi[1†], *Tarun Kumar Dhiman*[1†], *Navneet Chaudhary*[1,2], *Avinash Kumar Singh*[1,3], *Rahul Kumar*[1,3], *Jai Gopal Sharma*[2], *Anil Kumar*[4*] and *Pratima R. Solanki*[1]

[1]*Special Centre for Nanoscience, Jawaharlal Nehru University, New Delhi, India,* [2]*Department of Biotechnology, Delhi Technological University, New Delhi, India,* [3]*School of Physical Sciences, Jawaharlal Nehru University, New Delhi, India,* [4]*National Institute of Immunology, New Delhi, India*

Antibiotics resistance is becoming one of the biggest problems of the 21st century. The prior detection of antibiotics resistance can help human beings in better treatment of diseases. Here, we have used L-Cysteine capped magnesium sulfide quantum dots (L-Cyst-MgS QDs) to detect Levofloxacin antibiotic. L-Cyst-MgS QDs were synthesized using the hydrothermal method. Transmission electron microscopy study showed monodispersed L-Cyst-MgS QDs of 2–4 nm in size. Energy dispersive x-ray photoemission spectroscopy study confirmed the elemental composition of the L-Cyst-MgS QDs without any impurity. UV-vis absorption study showed a peak centered around 340 nm. The photoluminescence study exhibited the maximum peak at 410 nm for 340 nm of excitation wavelength. L-Cyst-MgS QDs were studied with thirteen antibiotics, namely Thiamphenicol, Gentamicin, Erythromycin, Ofloxacin, Ampicillin, Ciprofloxacin, Tetracycline, Chloramphenicol, Florfenicol, Amoxicillin, Moxifloxacin, Norfloxacin, and Levofloxacin. Among these, Levofloxacin showed the most significant change in the peaks' intensity and was further used for the interaction study. In the interaction study, the peak corresponding to MgS showed a continuous decrease, while the peak corresponding to Levofloxacin showed an increase with the increased concentrations (0–100 μg/ml) of Levofloxacin. Linear behavior was obtained in the range of 1–90 μg/ml. FT-IR study confirmed the interaction of the Levofloxacin with L-Cyst-MgS QDs. The Time-resolved fluorescence spectroscopy showed identical lifetime for both the samples and no spectral overlap confirm the FRET free system. The underlying mechanism is explained based on the electron transfer from the conduction band of the L-Cyst-MgS QDs to the HOMO of Levofloxacin. The limit of detection was found to be 0.21 μg/ml.

Keywords: hydrothermal synthesis, levofloxacin antibiotic, MgS quantum dots, L-cysteine, photo-induced electron transfer

OPEN ACCESS

Edited by:
Kumud Malika Tripathi, Indian Institute of Petroleum and Energy (IIPE), India

Reviewed by:
Seshadri Reddy Ankireddy, Eternal University, India
Sumit Sonkar, Malaviya National Institute of Technology, Jaipur, India

***Correspondence:**
Anil Kumar
anilk@nii.ac.in

[†]*These authors have contributed equally to this work*

Specialty section:
This article was submitted to Biomedical Nanotechnology, a section of the journal Frontiers in Nanotechnology

Received: *11 October 2020*
Accepted: *08 January 2021*
Published: *17 February 2021*

Citation:
Hashmi SZH, Dhiman TK, Chaudhary N, Singh AK, Kumar R, Sharma JG, Kumar A and Solanki PR (2021) Levofloxacin Detection Using L-Cysteine Capped MgS Quantum Dots via the Photoinduced Electron Transfer Process. Front. Nanotechnol. 3:616186. doi: 10.3389/fnano.2021.616186

INTRODUCTION

The population increase in the last two centuries has considerably increased pharmaceuticals use in society because of growing health problems. The discovery of the first antibiotic in 1928 has revolutionized the pharmaceutical industry as antibiotics can cure many diseases (Martinez et al., 2008; Adzitey, 2015). There is a considerable increase in antibiotics use since then in both human and

animal hosts because of two main reasons. Firstly, because of the specific nature against bacteria and fungi (Levy, 1978; Bungau et al., 2015; Ferrone et al., 2017) and secondly, because of their capability to increase the growth rate of animals and improve their feed efficiency (Aarestrup and Wegener., 1999; Cháfer-Pericás et al., 2010; Deng et al., 2014). However, their presence in the environment is equally dangerous and alarming. If a large quantity of antibiotics is introduced in the environment, then it will give rise to bacterial resistance to antibiotics making an adverse effect on the use of antibiotics for treatment of both humans and animals (Martínez, 2008; Bungau et al., 2015; Mahmood et al., 2019). These effects necessitate the need to detect antibiotics in the environment as it is a matter of great concern in modern times. Conventionally, the methods available for detecting antibiotics are chromatography, which requires extensive equipment and preparation. The chromatography process is quite complicated since it requires accurate quantification, simultaneous detection, and high specificity based on the structural information of the analytes (Deng et al., 2014; Dai et al., 2017; Pérez et al., 2017). Other methods for antibiotic determination include electrophoresis (Dai et al., 2017; Jang et al., 2017; Ji et al., 2017), diode array (Bitas and Samanidou, 2016), or enzyme immunosorbent assay (ELISA) (Kong et al., 2017; Váradi et al., 2017), polymerase chain reaction (PCR), or immunologic reactions have been developed. While such well-established techniques are present for the detection of antibiotics, there are also some disadvantages of these techniques like costly equipment, tiring and laborious work for the preparation of samples, and a constant requirement for well-trained human resources (Chauhan et al., 2016; Yadav et al., 2020). These disadvantages give rise to the necessity of economically feasible techniques. Optical sensing of antibiotics is a solution for this significant problem since it requires fewer human resources and instruments and involves less time than other methods.

Fluorescent materials are mostly used for optical sensing applications (Sarkar et al., 2020). Among various fluorescent materials, quantum dots (QDs) have the highest fluorescence. Also, their size can be easily controlled using different capping agents and synthesis parameters. Such tunability of size allows the fluorescence emission between UV and visible range (Garimella et al., 2020; Kujur and Singh., 2020). Quantum dots as QDs only show unique optical properties, such as the dramatic enhancement of photoluminescence (PL) compared with the bulk counterpart of the same material. This happens due to the quantum confinement effect. Size is one of the significant parameters which affect the PL of a material. Several authors have shown that with the decrease in the size of the material, PL properties increases. Also, PL emission can be obtained in either the UV region or visible region. The UV region's PL spectra arise due to the direct transfer of e-from the conduction band to the valence band. The PL spectra in the visible light can be due to the material's surface defect, giving non-radiative recombination. QDs have symmetrical fluorescence emission spectra and broad absorption spectra, having only 25–40 nm of half-width. They can also emit multicolor fluorescence when excited at the same wavelength, making them ideal optical detection materials (Alivisatos et al., 2005). The capping agent also allows for making them specific toward the detection of a particular biomolecule. Magnesium sulfide (MgS) QDs have been synthesized earlier using the hydrothermal method for using as a potential replacement of electrode material in lithium-ion batteries, but this material's optical properties remain unexplored (Zhang et al., 2018). MgS is a well-known material for a potential replacement of electrode material in lithium-ion batteries, but this material's optical properties remain unexplored. Here, we have tried to explore the optical properties of MgS QDs. We have studied the absorption and emission characteristics of extremely small size of L-Cyst-MgS. This also helps us in understanding the effect of reduction in size on optical properties of MgS QDs. In this work, optical sensing of Levofloxacin was carried out by analyzing its interaction with L-Cyst-MgS QDs. In this context, a novel and fully optimized method for the synthesis of L-Cyst capped MgS QDs, and their specific nature antibiotic for the detection of Levofloxacin has been proposed. L-Cyst-MgS QDs were synthesized using the hydrothermal method and characterized using transmission electron microscopy (TEM), energy dispersive x-ray emission (EDX), UV-visible, and fluorescence spectroscopy. L-Cyst-MgS QDs were studied with thirteen antibiotics. Among these, Levofloxacin antibiotics showed the most significant change. Linear detection of Levofloxacin antibiotic was obtained in the 1–90 μg/ml range.

EXPERIMENTAL

Reagents

Magnesium nitrate [$Mg(NO_3)2.H_2O$] (98.99%) and L-cysteine (99.99%) were purchased from Sigma Aldrich, and sodium sulfide pellets [Na_2S] (99.99%) was purchased from SDL. All the antibiotics i.e., Thiamphenicol, Gentamicin, Erythromycin, Ofloxacin, Ampicillin, Ciprofloxacin, Tetracycline, Chloramphenicol, Florfenicol, Amoxicillin, Moxifloxacin, Norfloxacin, Levofloxacin, were purchased from SRL, Hi-media, and Sigma Aldrich. 10 ml of 0.1 millimolar concentration was prepared for each antibiotic.

Characterizations Techniques

The obtained L-Cyst-MgS-QDs were further characterized using high-resolution transmission electron microscopy (HR-TEM; JEOL-TEM-2100F), energy dispersive x-ray spectroscopy (EDX) (Bruker), UV-vis absorption spectroscopy (T-90+UV-vis spectrometer, P. G. Instruments), and fluorescence spectroscopy (Carry Eclipse Spectrophotometer, Agilent Technologies). The interaction of L-Cyst-MgS-QDs with thirteen antibiotics was studied using fluorescence spectroscopy. The interaction study of Levofloxacin with L-Cyst-MgS-QDs was studied at various concentrations in the range of 0–100 μg/ml. These results were further confirmed with Fourier transform infrared (FT-IR-Spectrum 2-Perkin Elmer),

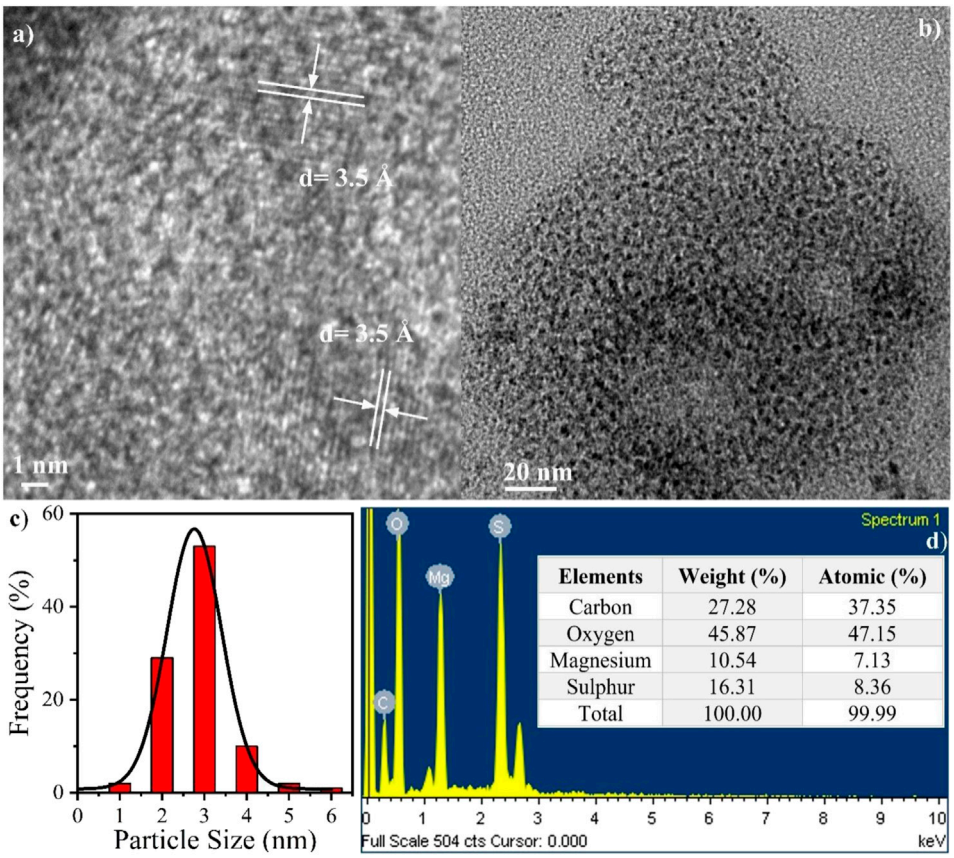

FIGURE 1 | (A) HR-TEM image, **(B)** TEM image, **(C)** size distribution bar plot fitted with Gaussian function, and **(D)** EDX results showing the constituent elements, and the inset Table shows the corresponding weight and atomic distribution.

and Fluorescence life-time decay was recorded in a commercial TCSPC setup FL-920 (Edinburgh Instruments) by exciting the samples at 375 nm using a picosecond diode laser (pulse width ~60 ps).

Synthesis of L-Cyst Capped MgS QDs

Magnesium nitrate [$Mg(NO_3)_2.H_2O$] (98.99%) powder and sodium sulfide pellets [Na_2S] (99.99) were mixed with L-Cysteine in various concentrations till the solution becomes transparent. This solution was placed in a hydrothermal teflon vessel and kept in a steel chamber for hydrothermal synthesis at 200°C for 4 h. The obtained solution was the first centrifuge for 30 min and then dialyzed overnight to remove the impurities.

RESULTS AND DISCUSSIONS

Transmission Electron Microscopy (TEM) Analysis

TEM study was carried out to observe the structure and the particle size of the synthesized QDs. **Figure 1A** shows the HR-TEM image of L-cyst-MgS-QDs. The d spacing calculated from the lattice fringes was found to be 3.5 Å. **Figure 1B** shows images of TEM of L-cyst-MgS-QDs showing uniformly distributed L-Cyst-MgS-QDs. It can be seen from the image that the L-cyst-MgS-QDs size is very small and monodispersed. The size of the QDs was calculated using a histogram and fitted with the gaussian function [**Figure 1C**] and obtained the average size ranging from 2 to 4 nm. TEM study shows that we have synthesized small size quantum dots with high surface area to volume ratio capped with L-Cysteine.

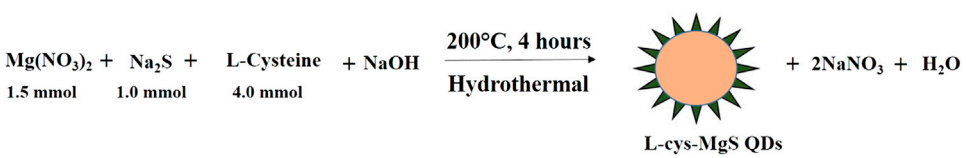

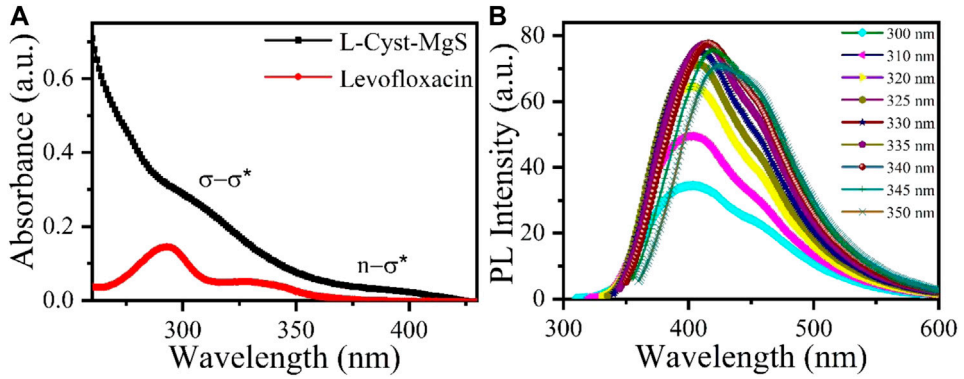

FIGURE 2 | (A) UV-Vis absorption spectra of L-Cyst-MgS-QDs and Levofloxacin and **(B)** shows the fluorescence spectra of L-Cyst-MgS-QDs for varying wavelengths.

Figure 1D shows EDX measurement to find the elemental composition. It can be seen from **Figure 1D** that the elemental composition of L-cyst-MgS-QDs consists of carbon, oxygen, magnesium, and sulfur (Sankararamakrishnan et al., 2019). Carbon and oxygen confirm the L-cysteine presence, while Mg and S confirm the presence of MgS. The inset of **Figure 1D** shows the Table for the elemental composition and their percentage by weight and atomic weight. It can be seen from the Table, the total weight and atomic of all the elements compose of L-cyst-MgS-QDs is 100 and 99.99%, respectively. This shows that the reaction was completed, and no residual precursor was left over after completing the reaction. Also, the atomic ratio of Mg and sulfur is nearly equal in the 1:1 ratio; results confirm the formation of L-cyst-MgS-QDs (Hu et al., 2010). TEM and EDX studies confirm the formation of pure and small size L-cyst-MgS-QDs without any impurity. These L-cyst-MgS-QDs were further studied using a UV-vis spectrometer and fluorescence spectrophotometer to study their optical properties.

UV-Vis Absorption Spectra and Fluorescence Study of L-Cyst-MgS-QDs

UV-VIS absorption spectrum and fluorescence emission spectra of L-Cyst-MgS QDs are shown in **Figure 2**. UV- vis absorption spectrum was recorded in the wavelength range of 270–430 nm. A small hump was obtained in L-Cyst-MgS QDs at a wavelength of 310 nm as shown in **Figure 2A**. The first peak hump around 320 nm is due to the σ - σ transition of an electron from sigma bond between Mg and S. The second hump at around 400 nm is due to the n-σ* transition due to lone pair electron of sulfur and sigma bond of Mg. The UV- vis absorption spectrum of Levofloxacin shows two peaks at 292 nm and 330 nm. Out of which broad peak at 292 nm indicate the n → π* transition while other peak at 330 nm shows the π → π* transition (Mat Amin et al., 2012). **Figure 2B** shows the fluorescence spectra obtained at different excitation wavelengths in the range of 260–360 nm. The fluorescence spectra were recorded for the varying excitation wavelengths of 300–350 nm. The highest emission was obtained at a wavelength of 410 nm for an excitation wavelength of 340 nm. These results indicate that L-Cyst-MgS QDs is an excellent candidate to study antibiotics' interaction using fluorescence spectroscopy. The quantum yield of L-Cyst-MgS QDs was calculated against the reference (quinine sulfate) that's already known. The absorbance and photoluminescence (PL) spectrum of quinine sulfate were obtained using photometry at 340 nm. The quantum yield was found to be 2%.

Response Study of L-Cyst-MgS-QDs With Levofloxacin

L-Cyst-MgS-QDs were studied with thirteen antibiotics using fluorescence spectroscopy as shown in **Figure 3A**. The thirteen antibiotics are Thiamphenicol, Gentamicin, Erythromycin, Ofloxacin, Ampicillin, Ciprofloxacin, Tetracycline, Chloramphenicol, Florfenicol, Amoxicillin, Moxifloxacin, Norfloxacin and Levofloxacin. The experiment was performed by adding 200 µL of L-Cyst-MgS-QDs into a solution of 200 µL of each antibiotic (1 mg/ml) and 2.6 ml of DI and the responses were recorded. The area was calculated for each study and a bar graph was plotted to see the specific detection of the L-Cyst-MgS-QDs toward Levofloxacin. **Figure 3A** shows the area under the curve for the response of the fluorescence signal. The area under the curve for Levofloxacin is considerably higher than that of the other antibiotics. **Figures 3B,C** show the image of all the antibiotics under visible light and UV light, respectively. The most significant change in the intensity can be observed for Levofloxacin. These results demonstrate the high selectivity of L-Cyst-MgS-QDs toward Levofloxacin. **Figure 3B** shows the response study of the L-Cyst-MgS-QDs with varying Levofloxacin concentrations in the physiological range of 0–100 µg/ml. It can be seen from **Figure 3B** that with the increase in the Levofloxacin concentration, the peak corresponding to L-Cyst-MgS-QDs (410 nm) is decreasing; however, the peak corresponding to the Levofloxacin is increasing (480 nm). The inset of **Figure 3B** shows the calibration curve obtained using the area under the curve for each concentration and plotted against the Levofloxacin concentration. Good linearity of 0.95 was obtained from the linear fit of the experimental data. Also, from this curve, it can see that the linear range was obtained from 1 to 90 µg/ml. Using this linearity plot, the limit of detection (LOD) was found to be 0.21 µg/

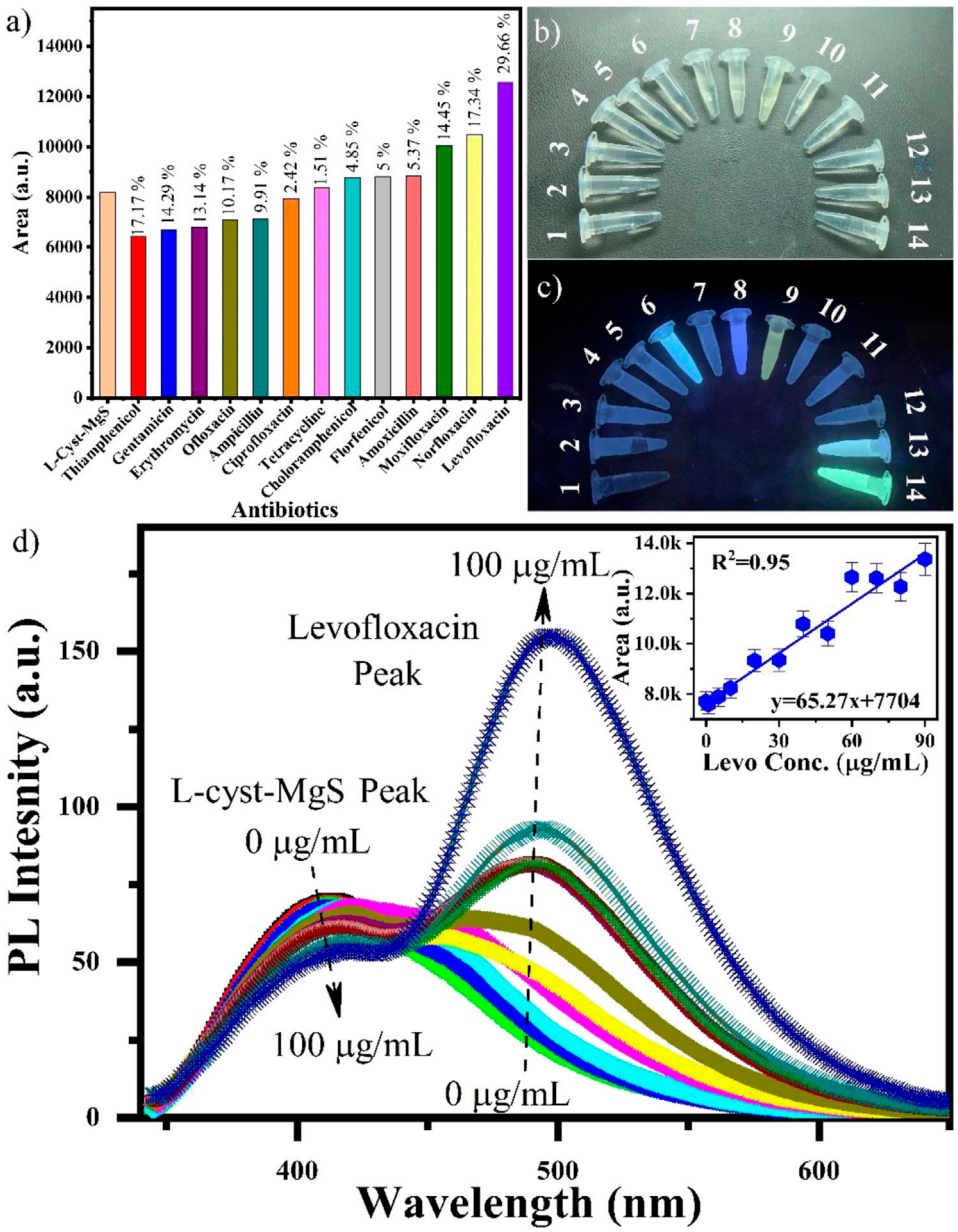

FIGURE 3 | (A) Selectivity study for L-cyst-MgS with thirteen antibiotics, photographic image of all the thirteen antibiotics 1: L-Cyst-MgS, 2: Thiamphenicol, 3: Gentamicin, 4: Erythromycin, 5: Ofloxacin, 6: Ampicillin, 7: Ciprofloxacin, 8: Tetracycline, 9: Chloramphenicol, 10: Florfenicol, 11: Amoxicillin, 12: Moxifloxacin, 13: Norfloxacin, and 14: Levofloxacin under **(B)** visible light, **(C)** UV light and **(D)** response study of L-cyst-MgS with Levofloxacin in the range of 0–100 g/ml concentrtion range. The inset shows the corresponding calibration curve.

ml. These studies suggest that L-Cyst-MgS-QDs is a suitable material for the detection of Levofloxacin.

FT-IR and TCSPC Studies of L-Cyst-MgS-QDs Interaction With Levofloxacin

Figure 4A shows the FT-IR study of L-Cyst-MgS-QDs and Levofloxacin. FTIR measurement was carried out in the wavenumber range between 400 and 4,000 cm^{-1}. **Figure 4A** represents the L-Cysteine capped MgS and having a well-resolved peak at 1,556 and 2,920 cm^{-1} are ascribed the asymmetric stretching vibration of COO- and anti-symmetric stretching of -CH_2. Considering the FTIR spectrum of pure L-Cysteine, the respective peak at 2,548 cm^{-1} corresponding to the stretching vibrations of S-H disappeared, resulting in the cleavage of the S-H bond formation of MgS bonds (Li et al., 2017). In **Figure 4B**, the symmetric stretching carboxylate (-COO-) peak of Levofloxacin was observed at 1,394 cm^{-1}, while in the case of L-Cys-MgS-Levo, this peak was shifted to 1,385 cm^{-1}, which suggests the binding of MgS with Levofloxacin (Qassim., 2015).

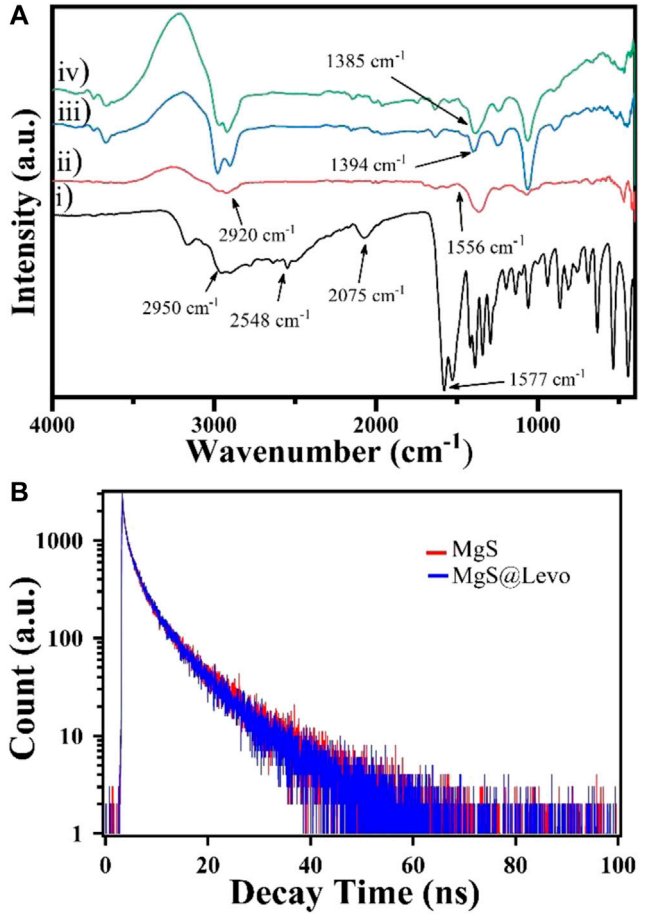

FIGURE 4 | (A) FT-IR spectra of (i) L-cysteine, (ii) L-cyst-MgS, (iii) Levofloxacin and (iv) L-cyst-MgS-levofloxacin; and **(B)** TCSPC plot for L-cyst-MgS and L-cyst-MgS-Levofloxacin.

Figure 4B shows the time-resolved fluorescence plot of L-Cyst-MgS-QDs in the presence and absence of Levofloxacin and fitted with three exponential decay function, which is given below;

$$I(t) = a_1^* \exp\left(-\frac{t}{\tau_1}\right) + a_2^* \exp\left(-\frac{t}{\tau_2}\right) + a_3^* \exp\left(-\frac{t}{\tau_3}\right)$$

The calculated lifetime was obtained nearly 8.43 ns and 7.78 ns for MgS-QDs and Levofloxacin's presence, respectively, by three exponential decay functions. There is a little difference of lifetime among these two systems that showed no spectral overlap. So, there is no fluorescence resonance energy transfer process took place (Yan et al., 2015). From the plotted and calculated life-time data, it is clear that Levofloxacin is not quenching the fluorescence of MgS and this interaction between MgS and Levofloxacin takes place through the electron transfer process.

L-Cyst-MgS Levofloxacin Interaction Mechanism

While studying the UV-absorbance curve of Levofloxacin and L-Cyst-MgS-QDs, Levofloxacin's absorption band is much closer to the UV absorbance curve of L-Cyst-MgS-QDs, allowing the transfer of electron in the L-Cyst-MgS QDs to Levofloxacin. Moreover, time-resolved fluorescence measurement also showed no significant change in the fluorescence life-time of L-Cyst-MgS-QDs-LEVO and L-Cyst-MgS QDs, as shown in **Figure 4B**. This excludes the fluorescence resonance energy transfer mechanism (Yan et al., 2015). **Figures 5A,B** shows the deconvoluted PL spectra of L-cyst-MgS and L-cyst-MgS with 100 µg/ml Levofloxacin. The spectrum was deconvoluted using the Gaussian function, and in both the spectrum, two distinct peaks were obtained. These two peaks PL 1 and PL 2 in **Figure 5A** have been explained according to the band diagram of L-Cyst-MgS explained in **Figure 5C**. The PL 1 peak in L-cyst-MgS arises due to band edge transition of excited e-from conductance band to the valence band. The PL 2 peak in L-cyst-MgS appears due to the surface defect i.e., broadband transition (Pearson., 1963; Garimella et al., 2020). In the mixture of L-Cyst-MgS QDs and Levofloxacin solution, the Levofloxacin molecules tend to come close to the surface L-Cyst-MgS QDs with the help of hydrogen bonds. This bond forms among–NH_2 group of L-Cyst with the carbonyl group of Levofloxacin and similarly carboxylic group L-Cyst with a carboxylic group Levofloxacin as shown in **Figure 5E**. On the exposure of light at a fixed wavelength of 340 nm, the photoluminescence intensity successively decreased at 410 nm (band edge) and increased at 458 nm with the increasing concentration of Levofloxacin as shown in **Figure 3D**. It is because of the absorption of light at 340 nm by L-Cyst-MgS QDs, which create the electron and hole in the valence band and conduction band, respectively. The hole of MgS QDs has more tendency to trap Levofloxacin (electron-rich) because of the vicinity between MgS and Levofloxacin molecules *via* hydrogen bonding as shown in **Figures 5F,G**. Thus electron-hole recombination does not take place between them. As a result, the emission spectra of MgS become quenched as it was coming from 410 nm (PL1) and surface defect (PL2) (**Figure 5D**). At the same time, Levofloxacin molecules were also excited at 340 nm, which generated electron and hole in the valence band (VB) and conduction band (CB), respectively. And therefore, the electron in surface defect of MgS has an alternative route of recombination of electron-hole with HOMO (hole) of Levofloxacin. Thus, emission spectra were observed with enhanced PL intensity at 458 nm (PL3) (**Figure 5D**). The shifting in the PL spectra in **Figure 3D** is due to Levofloxacin's interaction with the MgS molecule as shown in **Figure 5G**. The above results indicate that electron transfer from the MgS-QDs to Levofloxacin is responsible for the increase in Levofloxacin and a slight decrease in the intensity of L-Cyst-MgS-QDs.

CONCLUSION

L-Cyst capped MgS QDS were synthesized using the hydrothermal method. TEM study showed that L-Cyst-MgS

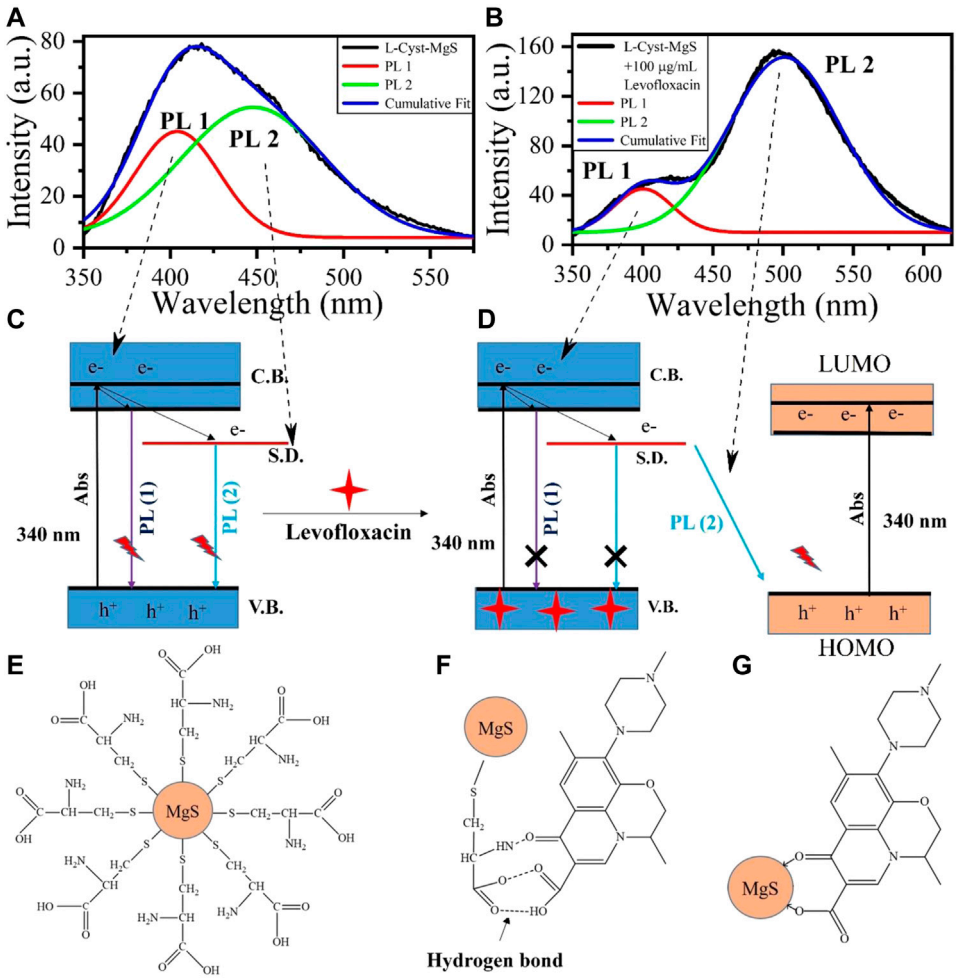

FIGURE 5 | L-Cyst-MgS interaction with Levofloxacin.

QDs have a size distribution from 2 to 4 nm and are very well dispersed. EDX study confirmed the completion of the reaction and formation of L-Cyst-MgS QDs without any impurity. UV absorbance study revealed maximum absorption in the range of 300–350 nm for L-Cyst-MgS. In the photoluminescence (PL) study, maximum emission was obtained at 410 nm for 340 nm of excitation for L-Cyst-MgS. Among Thiamphenicol, Gentamicin, Erythromycin, Ofloxacin, Ampicillin, Ciprofloxacin, Tetracycline, Chloramphenicol, Florfenicol, Amoxicillin, Moxifloxacin, Norfloxacin, Levofloxacin antibiotics, Levofloxacin showed the most significant change in PL spectra. Linear detection of Levofloxacin was obtained in the `range of 1–90 g/ml. The Time-resolved fluorescence spectroscopy showed identical lifetime for both the samples and no spectral overlap confirm the FRET free system. This was further confirmed using Fourier Transform infrared spectroscopy. The underlying mechanism can be explained based on the electron transfer from the conduction band of the L-Cyst-MgS QDs to the HOMO of Levofloxacin. The limit of detection (LOD) was found to be 0.21 µg/ml.

DATA AVAILABILITY STATEMENT

The raw data supporting the conclusions of this article will be provided after corresponding authors consent.

AUTHOR CONTRIBUTIONS

AK and PS have formulated the concept. ZH and TD have carried out the synthesis and characterization experiments. RK has helped in formulating the mechanism. JS helped in drafting the revised manuscript. AS and NC helped during measurements.

ACKNOWLEDGMENTS

The authors would like to thanks the Department of Biotechnology (DBT), India Indo-Russia project (DBT/IC-2/Indo-Russia/2017-19/02), and Department of Science and Technology (DST), India TDP/BDTP/24/2019 and ICMR,

India (34/13/2019-TF Nano/BMS), Government of India, for financial support. The authors also acknowledge the Advanced Instrument Research Facility (AIRF), JNU, New Delhi.

REFERENCES

Aarestrup, F. M., and Wegener, H. C. (1999). The effects of antibiotic usage in food animals on the development of antimicrobial resistance of importance for humans in Campylobacter and Escherichia coli. *Microb. Infect.* 1, 639–644. doi:10.1016/s1286-4579(99)80064-1

Adzitey, F. (2015). *Antibiotic classes and antibiotic susceptibility of bacterial isolates from selected poultry; a mini review*.

Alivisatos, A. P., Gu, W., and Larabell, C. (2005). Quantum dots as cellular probes. *Annu. Rev. Biomed. Eng.* 7, 55–76. doi:10.1146/annurev.bioeng.7.060804.100432

Bitas, D., and Samanidou, V. F. (2016). Effective cleanup for the determination of six quinolone residues in shrimp before HPLC with diode array detection in compliance with the European Union Decision 2002/657/EC. *J. Separ. Sci.* 39, 4805–4811. doi:10.1002/jssc.201600945

Bungau, S., Suciu, R., Bumbu, A., Cioca, G., and Tit, D. (2015). Study on hospital waste management in medical rehabilitation clinical hospital. *J. Environ. Prot. Ecol. Baile Felix.* 16, 980–987.

Cháfer-Pericás, C., Maquieira, Á., and Puchades, R. (2010). Fast screening methods to detect antibiotic residues in food samples. *Trac. Trends Anal. Chem.* 29, 1038–1049. doi:10.1016/j.trac.2010.06.004

Chauhan, R., Singh, J., Sachdev, T., Basu, T., and Malhotra, B. (2016). Recent advances in mycotoxins detection. *Biosens. Bioelectron.* 81, 532–545. doi:10.1016/j.bios.2016.03.004

Dai, T., Duan, J., Li, X., Xu, X., Shi, H., and Kang, W. (2017). Determination of sulfonamide residues in food by capillary zone electrophoresis with on-line chemiluminescence detection based on an Ag(III) complex. *Int. J. Mol. Sci.* 18, 1286. doi:10.3390/ijms18061286

Deng, F. Y., Huang, C. X., and Liu, Y. (2014). Determination of Levofloxacin in chicken tissue, manure and serum by self-ordered ring fluorescent microscopic imaging. *J. Anal. Chem.* 69, 283–289. doi:10.1134/s1061934814030046

Ferrone, V., Cotellese, R., Di Marco, L., Bacchi, S., Carlucci, M., Cichella, A., et al. (2017). Meropenem, Levofloxacin and linezolid in human plasma of critical care patients: a fast semi-automated micro-extraction by packed sorbent UHPLC-PDA method for their simultaneous determination. *J. Pharmaceut. Biomed. Anal.* 140, 266–273. doi:10.1016/j.jpba.2017.03.035

Garimella, L. B. V. S., Dhiman, T. K., Kumar, R., Singh, A. K., and Solanki, P. R. (2020). One-step synthesized ZnO np-based optical sensors for detection of aldicarb via a photoinduced electron transfer route. *ACS Omega* 5 (6), 2552–2560. doi:10.1021/acsomega.9b01987

Hu, J., Chen, Z., Chen, H., Chen, H., Song, Y., Sun, Y., et al. 2010). Single-crystal MgS nanotubes: synthesis and properties. *CrystEngComm* 12, 1286–1289. doi:10.1039/b919643a

Jang, M. G., Jang, M. D., and Park, J. (2017). Doxycycline as a new chiral selector in capillary electrophoresis. *J. Chromatogr. A* 1508, 176–181. doi:10.1016/j.chroma.2017.06.019

Ji, H., Wu, Y., Duan, Z., Yang, F., Yuan, H., and Xiao, D. (2017). Sensitive determination of sulfonamides in environmental water by capillary electrophoresis coupled with both silvering detection window and in-capillary optical fiber light-emitting diode-induced fluorescence detector. *Electrophoresis* 38, 452–459. doi:10.1002/elps.201600364

Kong, D., Xie, Z., Liu, L., Song, S., Kuang, H., and Xu, C. (2017). Development of ic-ELISA and lateral-flow immunochromatographic assay strip for the detection of vancomycin in raw milk and animal feed. *Food Agric. Immunol.* 28, 414–426. doi:10.1080/09540105.2017.1293014

Kujur, V. S., and Singh, S. (2020). Structural, magnetic, optical and photocatalytic properties of GaFeO3 nanoparticles synthesized via non-aqueous solvent-based sol–gel route. *J. Mater. Sci. Mater. Electron.* 31, 17633–17646. doi:10.1007/s10854-020-04318-2

Levy, S. B. (1978). Emergence of antibiotic-resistant bacteria in the intestinal flora of farm inhabitants. *J. Infect. Dis.* 137, 689–690. doi:10.1093/infdis/137.5.688

Li, L., Liao, L., Ding, Y., and Zeng, H. (2017). Dithizone-etched CdTe nanoparticles-based fluorescence sensor for the off-on detection of cadmium ion in aqueous media. *RSC Adv.* 7 (17), 10361–10368. doi:10.1039/c6ra24971j

Mahmood, A. R., Al-Haideri, H. H., and Hassan, F. M. (2019). *Detection of antibiotics in drinking water treatment plants in Baghdad City, Iraq*. Health: Advance Pub.

Martinez, J. L., Fajardo, A., Garmendia, L., Hernandez, A., Linares, J. F., Martínez-Solano, L., et al. (2008). A global view of antibiotic resistance. *FEMS Microbiol. Rev.* 33, 44–65. doi:10.1111/j.1574-6976.2008.00142.x

Martínez, J. L. (2008). Antibiotics and antibiotic resistance genes in natural environments. *Science* 321, 365–367. doi:10.1126/science.1159483

Mat Amin, K. A., Gilmore, K. J., Matic, J., Poon, S., Walker, M. J., Wilson, M. R., et al. (2012). Polyelectrolyte complex materials consisting of antibacterial and cell-supporting layers. *Macromol. Biosci.* 12 (3), 374–382. doi:10.1002/mabi.201100317

Pearson, R. G. (1963). Hard and soft acids and bases. *J. Am. Chem. Soc.* 85 (22), 3533–3539. doi:10.1021/ja00905a001

Pérez, R. A., Albero, B., Férriz, M., and Tadeo, J. L. (2017). Analysis of macrolide antibiotics in water by magnetic solid-phase extraction and liquid chromatography-tandem mass spectrometry. *J. Pharmaceut. Biomed. Anal.* 146, 79–85. doi:10.1016/j.jpba.2017.08.013

Qassim, A. W. (2015). Determination of Levofloxacin in pharmaceutical formulation tavanic by Visible spectrophotometry of its chelating complex with aluminum ion (iii). *Int. J. Dev. Res.* 5 (6), 4702–4706.

Sankararamakrishnan, N., Singh, R., and Srivastava, I. (2019). Performance of novel MgS doped cellulose nanofibres for Cd(II) removal from industrial effluent – mechanism and optimization. *Sci. Rep.* 9, 12639–12648. doi:10.1038/s41598-019-49076-2

Sarkar, T., Dhiman, T., Sajwan, R., Sri, S., and Solanki, P. R. (2020). Studies on carbon-quantum-dot-embedded iron oxide nanoparticles and their electrochemical response. *Nanotechnology* 31 (35), 355502. doi:10.1088/1361-6528/ab925e

Váradi, L., Luo, J. L., Hibbs, D. E., Perry, J. D., Anderson, R. J., Orenga, S., et al. (2017). Methods for the detection and identification of pathogenic bacteria: past, present, and future. *Chem. Soc. Rev.* 46, 4818–4832. doi:10.1039/c6cs00693k

Yadav, A. K., Dhiman, T. K., Lakshmi, G. B. V. S., Berlina, A. N., and Solanki, P. R. (2020). A highly sensitive label-free amperometric biosensor for norfloxacin detection based on chitosan-yttria nanocomposite. *Int. J. Biol. Macromol.* 151, 566–575. doi:10.1016/j.ijbiomac.2020.02.089

Yan, X., Li, H., Han, X., and Su, X. (2015). A ratiometric fluorescent quantum dots based biosensor for organophosphorus pesticides detection by inner-filter effect. *Biosens. Bioelectron.* 74, 277–283. doi:10.1016/j.bios.2015.06.020

Zhang, B., Xia, G., Chen, W., Gu, Q., Sun, D., and Yu, X. (2018). Controlled-size hollow magnesium sulfide nanocrystals anchored on graphene for advanced lithium storage. *ACS Nano* 12, 12741–12750. doi:10.1021/acsnano.8b07770

Conflict of Interest: The authors declare that the research was conducted in the absence of any commercial or financial relationships that could be construed as a potential conflict of interest.

Copyright © 2021 Hashmi, Dhiman, Chaudhary, Singh, Kumar, Sharma, Kumar and Solanki. This is an open-access article distributed under the terms of the Creative Commons Attribution License (CC BY). The use, distribution or reproduction in other forums is permitted, provided the original author(s) and the copyright owner(s) are credited and that the original publication in this journal is cited, in accordance with accepted academic practice. No use, distribution or reproduction is permitted which does not comply with these terms.

View publication stats

2021 International Conference on COMmunication Systems & NETworkS (COMSNETS) | 978-1-7281-9127-0/20/$31.00 ©2021 IEEE | DOI: 10.1109/COMSNETS51098.2021.9352815

mFlameGaze: Mobile-Based Flame Gazing for Improving Sustained Attention

[1]Divyashikha Sethia, [1]Anil Singh Parihar, [1]Aheli Ghosh, [1]Tanish Grover, [2]Deep Diwakar,
[1]Shivam Kumar, [1]Utkarsh Tyagi

[1]*Department of Computer Science & Engineering,* [2]*Department of Electronics & Communication Engineering*
Delhi Technological University
New Delhi - 042, India
divyashikha@dtu.ac.in

***Abstract*—Yogic visual concentration techniques have proved to create a long term effect on mindfulness in adults. However, none of the existing gaze detection platforms actively monitor attention and provide feedback to the users. This paper presents a novel method to correlate and estimate the effect of a short-term candle gaze concentration technique on the sustained attention, by providing feedback to the participants and helping them keep track of their sustained attention. We present the prototype of an Android mobile-based flame gaze application known as mFlameGaze to perform the candle flame test (CFT). The app determines for how long the participants focus on the candle tip in their screens. It also detects the moment in time when the eyes first deflect from the flame. The proposed work uses this app to analyze the impact of candle gaze on sustained attention for a small group of normal, healthy children. The participants' sustained attention is measured before and after conducting the study using a letter cancellation test (LCT) as the benchmark. The results indicate an increase in the performance of participants in the LCT and also an increase in the focused gaze time, as measured by the mFlameGaze mobile app in a short duration of ten days.**

I. Introduction

Sustained attention refers to the ability to focus on a particular activity or stimulus over a long period [1]. It enables us to concentrate on an activity until it finishes, despite the presence of distracting stimuli. Insufficient sustained attention is usually accompanied by fatigue and inefficiency in completing daily activities. Nowadays, the average attention span of a human being is around eight seconds [2]. This age of smartphones, instant gratification and now, a worldwide pandemic situation, has rapidly pushed everyone into digital transformation. Thus today, it is more necessary than ever before, to develop longer attention spans in children. It is a pertinent research question to investigate if technology can assist in building sustained attention.

Prolonged attention translates to better academic performance, developing competences, self-regulation from compulsive action and making better decisions about health and wealth. Yoga can be a useful technique for this. Yogic visual concentration (*Trataka*) is one of the six cleansing techniques mentioned in the ancient Indian yogic text, *Hata Yoga Pradipika* [3]. It involves looking intently with an unwavering gaze at a small point until tears are shed [3]. *Hata Yoga Pradipika* mentions that the practice of *Trataka* eradicates all eye diseases, fatigue, and lethargy. The *Trataka Kriya* strengthens eye muscles and improves vision and memory. *Trataka* practised over a long period improves perception, attention, and cognition. [3].

This paper explores the feasibility of a screen-based candle flame test, and whether it can benefit the participants by improving their sustained attention. The paper proposes the design and implementation of an Android flame gaze mobile app called mFlameGaze [4]. It helps perform the candle flame test (CFT) and also measures the focused time of the participant through eye-gaze detection.

The outcome of the CFT can be gauged and compared with the help of cognitive tests like the letter cancellation test(LCT) [5]. LCT tasks involve sustained attention, concentration, visual scanning, and activation and inhibition of rapid responses [6]. The participants take LCT first and practice CFT using the mFlameGaze app [4] daily for two minutes for ten days. On the last day, they retake LCT.

The results indicate that their focused time duration, as detected by the app, increases over time. Additionally, they perform better on the LCT. Thus, the gaze detection methodology in the mFlameGaze app can be further improved in the future to help improve the sustained attention and predict the improvement over time in sustained attention. To test the scope of the study, the experiment is limited to a small group of children only. There are several challenges as discussed in section VII which limit the scope of the current study. From the positive results of the study, the experiment may extend over more participants, across different age groups.

Contributions of the paper:

- mFlameGaze mobile application: Development of candle flame test based application to help participants gaze at a candle flame and help compute the focused time. It utilizes computer vision-based gaze detection techniques using Python, OpenCV [7] and Dlib libraries [8].
- LCT web application: Enables participants to undertake the LCT.

Authorized licensed use limited to: DELHI TECHNICAL UNIV. Downloaded on February 23,2021 at 06:51:27 UTC from IEEE Xplore. Restrictions apply.

- Study to analyze the impact of the flame gaze using the mFlameGaze app on the focused time and the LCT for sustained attention of a small group of children in the age group of 10-15 years.

Roadmap: The rest of the paper comprises of Section II, which explains the details of LCT; section III, which discusses the pre-existing work in this field and section IV which details the entire testing procedure. Section V explains the algorithm used behind the gaze detection and focus calculation. This section is followed by section VI, which highlights the results of our study, and section VII discusses the challenges faced during our study. At last, section VIII discusses the conclusion and future work.

II. Letter Cancellation Test

Sustained attention is the ability to focus on a stimulus or work over a long time. In order to complete any planned cognitive task with understanding, take any subsequent action, or have any thought, one must use sustained attention. An example is the act of reading a newspaper article.

A cognitive test like the letter cancellation test (LCT) can help also requires sustained attention. Each component of the test measures a different measure and functions of the brain. The total number of cancellations is a measure of motor skill combined with cognitive function. The net score is a measure of sustained attention which is associated with the right frontoparietal cortex. The number of wrong cancellations is a measure of the lack of focused attention and mental distraction [9].

To assist our study, an LCT web application [5] is proposed as the benchmark for measuring an improvement in CFT results. It specifies the target character which the participant selects from an array of characters of the English alphabet arranged randomly in forty columns and six rows. The participants must cancel as many instances of the target character as possible with a timer of three minutes. They can follow a horizontal, vertical, or a random path according to their choice [10]. The participants undertake LCT on the first and the last day of CFT, as mentioned in the study in section V.

III. Related Work

Several previous studies analyze the effect of different aspects of yoga on human attention. Physical postures (asanas), voluntary breathing regulation (pranayama), meditation, cleansing practices (kriyas) and devotional sessions on the theory and philosophy of yoga improve attention span in school children [11].

Sahasi et al. (1989) has demonstrated the effectiveness of yogic techniques in the management of anxiety and reported increased attention and concentration [12]. Two yoga-based relaxation techniques, namely, cyclic meditation (CM) and supine rest (SR) on the six-letter cancellation task (SLCT) reported a significant increase in the attention scores in school students [13]. Sarang et al. (2007) assessed performance on SLCT in forty male subjects immediately before and after yoga-based relaxation techniques of CM and SR with equal duration. Both practices significantly improved net scores, total scores, and score for the wrong cancellation. [14].

Previous studies have shown that candle flame gazing (Trataka) has significant increase over concentration and memory level of the subjects [15]. It increases selective attention, cognitive flexibility, and response inhibition [3]. However,

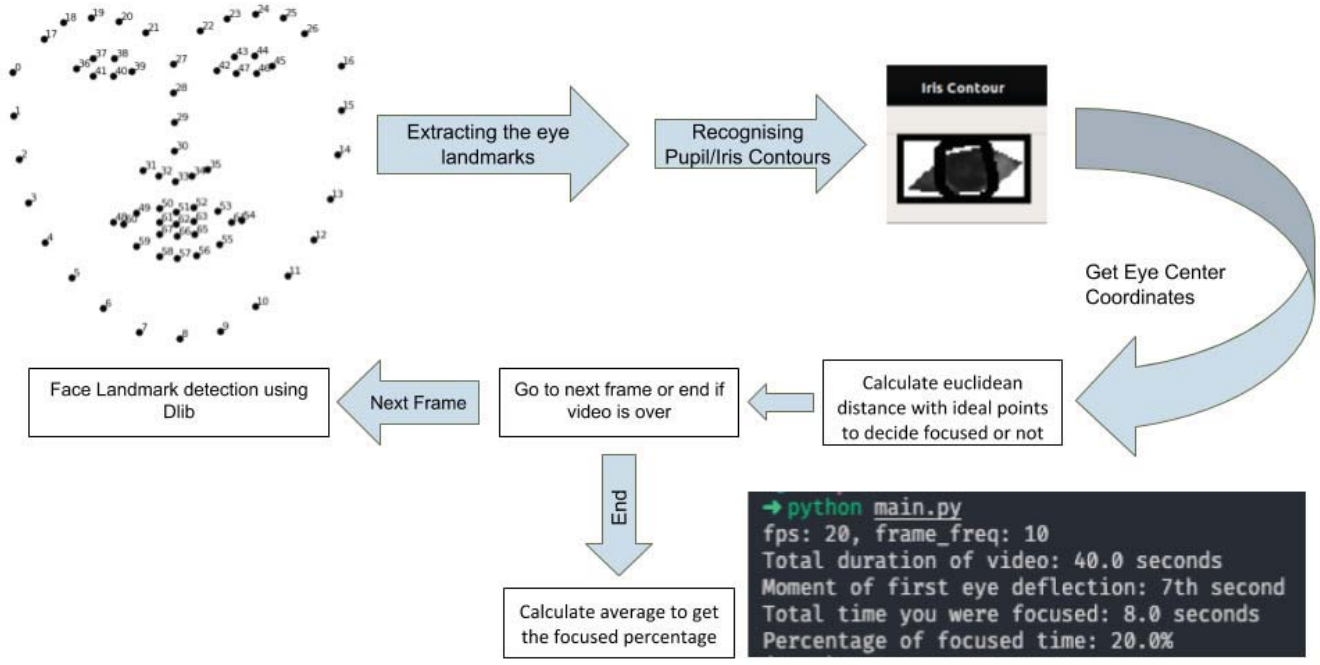

Fig. 1. Sustained Attention Calculation Methodology

Authorized licensed use limited to: DELHI TECHNICAL UNIV. Downloaded on February 23,2021 at 06:51:27 UTC from IEEE Xplore. Restrictions apply.

(a) Isolating Eye Using Face Landmarks.

(b) Isolating Iris By Applying Threshold.

(c) Contour Drawn Around The Iris.

(d) Detected Center Of The Iris.

Fig. 2. Steps For Eye Coordinate Detection For A Single Frame.

none of the studies focus on the short term benefit of candle gaze exercise on sustained attention. There is no existing platform which helps in monitoring the focused attention through gaze detection.

IV. Gaze Detection Methodology for the mFlameGaze App

This paper uses the mFlameGaze app [4] to calculate the sustained attention of the participants. The methodology comprises of two steps - calculating the eye centres in a single frame and calculating the sustained attention from the recorded video. The following subsections explain the details of these processes. Fig. 1 illustrates the overall processing pipeline and Algorithm 1 explains the details of the steps.

A. Eye Coordinates Detection

The gaze detection algorithm uses Python OpenCV [7] and Dlib libraries [8] to calculate the coordinates of the centre of the eyes from a video frame.

1) Convert image from BGR format to Grayscale format.
2) Use the frontal face detector functionality in the Dlib library [8] to get the facial landmarks from the image.
3) The landmarks corresponding to the left and right eyes are [36, 37, 38, 39, 40, 41] and [42, 43, 44, 45, 46, 47] respectively.
4) Using these landmarks, isolate the eyes of the individual by masking the rest of the image, as shown in Fig. 2a.
5) After isolating the eyes, calculate the optimal threshold to isolate the iris from the rest of the eye.
   a) Loop over different threshold values and find out the iris size for each value.
   b) Pick the optimal threshold, which is the threshold for which the absolute difference between the calculated iris size and average iris size is minimum.
6) Use the optimal threshold to isolate the iris in the frame, as shown in Fig. 2b.
7) After the iris is isolated, find the contours of this frame. Fig. 2c depicts the contours drawn on the frame.
8) Finally, calculate the centre of the contour using image moments which gives us the centre of the iris as shown in Fig. 2d.

B. Focus Calculation Algorithm

Algorithm 1 Algorithm for eye coordinate detection and focus calculation

procedure GAZEDETECTION
    // Convert the image into grayscale
    convImage ← *grayscale(image)*
    // Locating facial features using the dlib library
    faceCoords ← *dlibFaceFeatures(convImage)*
    // Single out the features useful in calculating eye coordinates
    eyeFeatures ← *faceCoords[36:41], faceCoords[42:47]*
    // Skip the frame in which the features detect blinking
    if *isBlinking(eyeFeatures)* **then**
        continue
    // Mask out the rest of the image
    isolatedEye ← *maskOutRest(convImage, eye features)*
    // Isolate the iris by applying tested threshold on the image containing the isolated eye
    irisIsolated ← *threshold(isolatedEye)*
    // Use OpenCV to find all the contours in the isolated iris
    contours[] ← *findContours(irisIsolated)*
    // Estimate the iris coordinates by calculating the centre of the contours
    irisCoords ← *centre(contours[])*
    // Focused counter increased if distance of calculated coordinates are within threshold
    if *Dist(irisCoords, idealCoords)* < 0.071 **then**
        focused_frames+=1
    focus ← *(focusedFrames / totalFrames)*100*
    return *focus*

Authorized licensed use limited to: DELHI TECHNICAL UNIV. Downloaded on February 23,2021 at 06:51:27 UTC from IEEE Xplore. Restrictions apply.

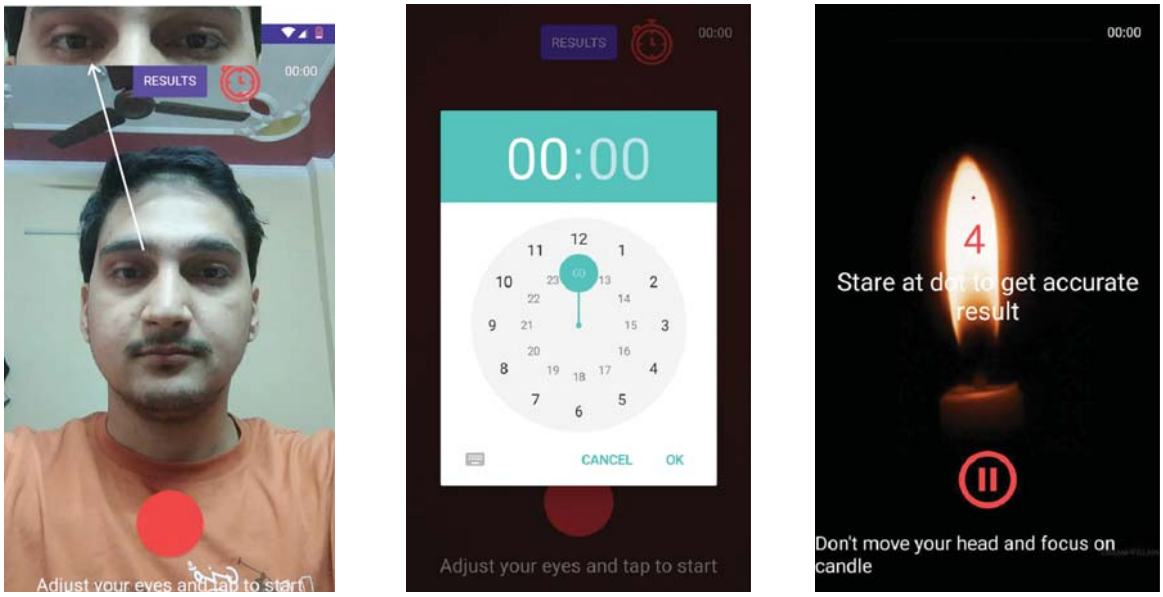

(a) Sample of a well lit environment.

(b) Setting up of gaze timer which will notify after the time is up.

(c) Timer of five seconds.

Fig. 3. Snapshots from mFlameGaze mobile app

This section explains how the eye coordinates detection algorithm calculates the sustained attention of a user.

1) Get the ideal location of eyes.
   a) The algorithm requires that the user is gazing at the candle flame correctly when the video starts recording; otherwise, it returns an invalid video response to the user.
   b) If the above condition is satisfied, the algorithm uses the first frame of the video as the ideal frame. The algorithm refers to the eye coordinates detected from this frame as the ideal eye coordinates.
   c) Use these ideal coordinates to decide if the user is focused or not in the subsequent frames of the video.
   d) Normalise the ideal eye coordinates between 0 and 1.
2) Iterate over the frames of the video with gaps of 0.5s between them.
3) For each frame determine if the user is in focus or not:
   a) Calculate the coordinates for the center of the eye and normalize them between 0 and 1.
   b) Calculate the Euclidean distance between the eye coordinates and the ideal eye coordinates.
   c) Calculate the average of the distance calculated for each eye. This value is termed as the focus value of the specific frame.
   d) After multiple robust tests with the different participants, a threshold Euclidean distance value of 0.071 is selected to decide the focus of eyes in a frame. If the Euclidean distance of eye coordinates from the ideal coordinates is less than this threshold distance, then the user is in focus otherwise not. This threshold value prevents slight deflections in the prediction of coordinates from affecting the overall focus of the user.
4) Finally, calculate the sustained attention (focus percentage) of the participant. The focus percentage is defined as the percentage of focused frames in the video, as shown in the Eq. 1.

$$Focus\% = \frac{No.of Focused Frames}{Total No.of Processed Frames} \times 100 \quad (1)$$

V. Participant Testing Procedure

The subjects consisted of 11 children in the age range of 10–15 years.

A. Steps to use mFlameGaze app [4]

1) Register (first-time users) or sign in (by using login credentials). Allow the displayed permissions.
2) Ensure a well-lit environment (Fig. 3a) before taking CFT with the mFlameGaze app. Align the phone and eyes at the same vertical level with a maximum horizontal distance of 50 cm. Ensure that the eyes are kept wide open and stable as they gaze at the flame.
3) Select time for meditation from the timer dialog available on the screen, as shown in Fig. 3b and start.
4) After clicking on the start button, CFT will start after five seconds, as shown in Fig. 3c.
5) Alter the meditation time by clicking on the timer button on the top.

Authorized licensed use limited to: DELHI TECHNICAL UNIV. Downloaded on February 23,2021 at 06:51:27 UTC from IEEE Xplore. Restrictions apply.

6) End the CFT in case of any discomfort (press the capture button).
7) The mobile app announces completion of the test with a beep sound and a message at the bottom.
8) On completion of CFT, the app sends the recorded video to the server for processing and focus percentage calculation.
9) User can check the previous CFT results using the results button (check center-top).

B. LCT Testing

The subjects access LCT immediately before and after CFT. Section VI presents the details of the result analysis.

VI. Results

On analyzing the data obtained through testing the participants, we observe that there is a significant increase in the average focus level of the participants, as shown in Fig. 4 and Fig. 5. The average focus shows an increase of 3.3%, from 85.27% initially to 88.57% finally. Seven out of the eleven participants show an increase in focus after practising CFT for ten days, as shown in TABLE. I. Participants with a high initial focus rate show a negligible improvement (like P6), or degradation (like P4, P9, P10) due to variable environmental factors. P5 is an anomaly; the algorithm shows a lower focus on the final day, even though his LCT performance improved significantly (+1 incorrect responses and -4 in missed responses). The rest show a high degree of enhancement in sustained attention.

Also, there is an improvement in focus-requiring tasks like the LCT, as shown in Fig. 6. Column I and column II in TABLE. I demonstrate the LCT results, wherein seven out of the eleven participants show improvement in terms of correct and missed responses, respectively. The average increase in correct responses is 0.82, while the number of missed responses decreases by an average value of 1.09. For those whose absolute score did not change after CFT, the LCT web app observed a reduction in time taken to perform the test. The LCT results remained unchanged for those who had a perfect score initially.

The LCT randomly chooses a set of characters and a character to cancel and prompts the user to start the test. Thus, there is no prior learning or memory retention bias for a user in repeating the LCT after ten days of CFT.

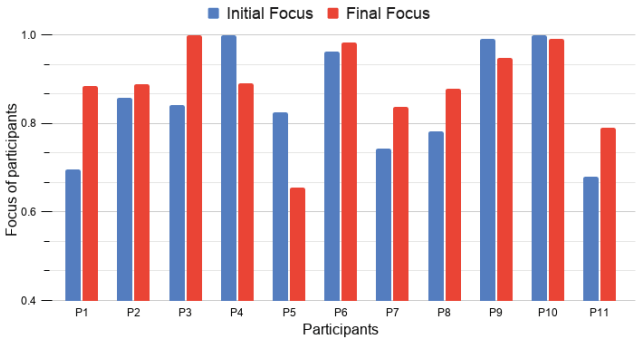

Fig. 4. Candle Flame Test (CFT) Results

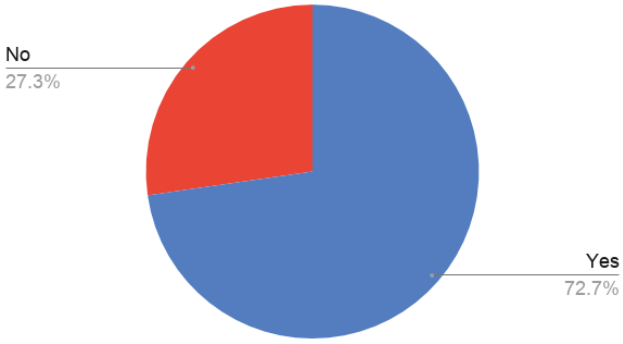

Fig. 5. % Improvement In Focused Time Among Participants

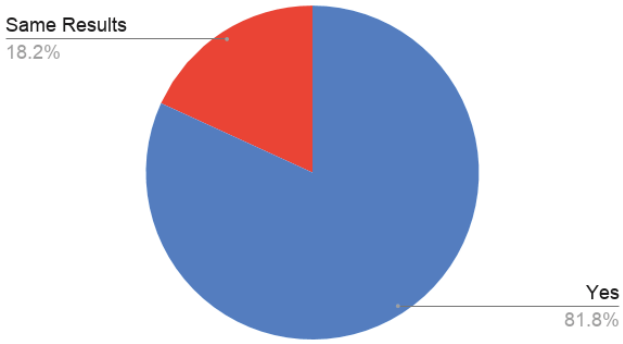

Fig. 6. % Improvement In Cancelled Characters Among Participants

VII. Challenges

There were several challenges faced in using a mobile-based application to help perform the CFT and measure sustained attention.

1) *Limitation of Server-Side Processing:* To calculate the sustained attention of the participants, there is a remote server-based program with REST API to calculate the focus calculation. Firebase [16] provides storage for media. However, video processing is a computationally expensive task. Performing the processing on server-side rather than user devices leads to much longer wait times for the users and massive load on the server.
Bandwidth restriction in the Firebase plan limited the video duration to 2 minutes. A system design change in the future by using on-device processing can overcome the problem and significantly improve the user experience of the application.
2) *Limitations of Image Processing Algorithm:* Eye-tracking using a mobile camera is a complex problem. Unlike deep learning, using OpenCV image techniques

Authorized licensed use limited to: DELHI TECHNICAL UNIV. Downloaded on February 23,2021 at 06:51:27 UTC from IEEE Xplore. Restrictions apply.

TABLE I. candle flame and letter cancellation tests analysis of 11 participants

Participants	Change in focus in CFT(%)	Change in correct responses (LCT)	Change in missed responses (LCT)
1	18.82	3	-3
2	3.056	1	-1
3	15.78	1	-1
4	-11	1	-1
5	-16.98	1	-4
6	1.99	0	0
7	9.29	0	0
8	9.56	0	0
9	-4.258	1	-1
10	-1.0	0	0
11	11.0	1	-1

allows us to break the problem into more straightforward steps and solve it, without collecting large data sets. However, in environments with highly uneven lighting conditions, the current algorithm can sometimes fail to detect the eye centre. In this study, to solve this lighting problem, we review each participant's video manually every day and provide daily feedback after the test to reduce the chances of failure in the next test.

However, the objective of this paper is not to develop a robust eye tracking model, but to prove that a mobile-based candle gazing application with gaze feedback can have a positive impact on the user's sustained attention.

VIII. Conclusion and Future Work

Candle gazing can help strengthen focus. There are several standalone applications which only provide features to gaze without returning any feedback to the user. We successfully conduct a study with a small group of participants and observe that the CFT improves performance in tasks requiring attention and reduces distraction. Results indicate that over a short period, the focused time and the sustained attention with LCT improved for the majority of participants.

The current mFlameGaze app processes videos on the server, which is costly and time taking. The current algorithm for gaze tracking uses on OpenCV for image processing [7], which has a significant dependency on the right lighting environment.

For future studies, usage of a transfer learning approach is proposed. A lightweight, embedded convolutional neural network-based model like MobileNet [17] for gaze tracking will move the computations to the Android device (on-device processing) for focus score calculation. In such a case, the algorithm can use a more efficient threshold value for calculation of gaze.

Due to the limitation of bandwidth overheads of video uploads, processing and the requirement of uniform lighting for the mobile app, the study involved a small group of students. However, with the proposed system design change and previous results based on Trataka kriya on adults [15], the study should provide better results of improvement in sustained attention on a large group. In future, such an app can directly help predict the increase in sustained attention through machine learning with gaze detection, without requiring LCT.

Acknowledgment

We thank Samsung India Electronics Pvt. Ltd. for providing the Samsung Innovation Lab and research devices to Delhi Technological University. We are grateful to Dr Vibha Sharma from Institute of Human Behaviour and Allied Sciences (IHBHAS) for her valuable insight towards the study. Finally, we are grateful to Rachit Bansal for his contributions to the LCT web application and inputs to the gaze detection.

References

[1] A. O. Okunola and M. G. Yusupov, "THE STUDY OF COGNITIVE STATES IN FOREIGN PSYCHOLOGY," in , 2018, pp. 126–133.
[2] N. Georgiou, "Attention span crisis in our schools," *Synergy*, vol. 13, no. 1, 2015.
[3] B. Raghavendra and P. Singh, "Immediate effect of yogic visual concentration on cognitive performance," *Journal of traditional and complementary medicine*, vol. 6, no. 1, pp. 34–36, 2016.
[4] "mflamegaze," https://play.google.com/store/apps/details?id=com.dd.camerax, 2020, last accessed on Oct 2020.
[5] R. Bansal and A. Rana, "Letter_cancellation," https://github.com/aryanrana/Letter_Cancellation, 2020, last accessed on Oct 2020.
[6] Lezak *et al.*, *Neuropsychological assessment*. Oxford University Press, USA, 2004.
[7] I. Corporation, W. Garage, and Itseez, "Opencv," https://github.com/opencv/opencv, 2000, last accessed on Oct 2020.
[8] D. King, "Dlib c++ library," https://github.com/davisking/dlib, 2011, last accessed on Oct 2020.
[9] Rueckert *et al.*, "Sustained attention deficits in patients with right frontal lesions," *Neuropsychologia*, vol. 34, no. 10, pp. 953–963, 1996.
[10] Natu *et al.*, "Testing of stimulant effects of coffee on the psychomotor performance: An exercise in clinical pharmacology," *Indian journal of pharmacology*, vol. 29, no. 1, p. 11, 1997.
[11] Telles *et al.*, "Improvement in static motor performance following yogic training of school children," *Perceptual and Motor Skills*, vol. 76, no. 3_suppl, pp. 1264–1266, 1993.
[12] Sahasi *et al.*, "Effectiveness of yogic techniques in the management of anxiety." *Journal of Personality and Clinical Studies*, 1989.
[13] Pradhan *et al.*, "Immediate effect of two yoga-based relaxation techniques on attention in children," *International journal of yoga*, vol. 3, no. 2, p. 67, 2010.
[14] S. Sarang and S. Telles, "Immediate effect of two yoga-based relaxation techniques on performance in a letter-cancellation task," *Perceptual and Motor Skills*, vol. 105, no. 2, pp. 379–385, 2007.
[15] B. Chowdhary, "Effect of tratak candle flame meditation on concentration and memory level of the college athletics team," *PARIPEX-Indian Journal of Research*, vol. 4, no. 7, 2016.
[16] Firebase. (2020) Cloud storage. https://firebase.google.com/docs/storage. Last accessed on Nov 2020.
[17] A. G. Howard, M. Zhu, B. Chen, D. Kalenichenko, W. Wang, T. Weyand, M. Andreetto, and H. Adam, "Mobilenets: Efficient convolutional neural networks for mobile vision applications," *arXiv preprint arXiv:1704.04861*, 2017.

Authorized licensed use limited to: DELHI TECHNICAL UNIV. Downloaded on February 23,2021 at 06:51:27 UTC from IEEE Xplore. Restrictions apply.

Operational Research in Engineering Sciences: Theory and Applications
Vol. 4, Issue 1, 2021, pp. 38-66
ISSN: 2620-1607
eISSN: 2620-1747
DOI: https://doi.org/10.31181/oresta2040123t

MODELING AND ANALYSIS OF LEAN MANUFACTURING STRATEGIES USING ISM-FUZZY MICMAC APPROACH

Mohit Tyagi [1], Dilbagh Panchal [1]*, Deepak Kumar [2], R. S. Walia [3]

[1]Department of Industrial and Production Engineering, Dr B R Ambedkar National Institute of Technology Jalandhar, Punjab, India
[2] Department of Mechanical Engineering, Delhi Technological University, Delhi, India
[3] Department of Production and Industrial Engineering, PEC University, Chandigarh, India

Received: 01 December 2020
Accepted: 12 February 2021
First online: 20 February 2021

Original scientific paper

Abstract: *The current research work deals with an identification of different lean strategies and extraction to relevant strategies after discussion with experts and gives the answer of a question "how lean manufacturing strategies can help the organization to enhance the efficiency of the organization with great effectiveness?" In this research work, thirty-six lean strategies have been identified and out of which thirteen lean strategies were filtered in respect of highly importance value by factor analysis using software SPSS 21. Further, to identify and analyze the inter-relationship among filtered strategies, an Interpretive Structural Modeling (ISM) with Fuzzy Matriced' Impacts Croise´s Multiplication Applique´e a UN Classement (MICMAC) approach has been used. Fuzzy MICMAC help to understand the dependence and driver's power of the lean strategies. The mutual importance of extracted strategies has been discussed through developing the ISM model and the individual assessment of each strategy with each of the other strategies has been derived using the Fuzzy MICMAC approach.*

Key words: *Lean Manufacturing System (LMS), Lean Strategies; Factor Analysis, SPSS 21, ISM Methodology, Fuzzy MICMAC*

1. Introduction

In the present scenario, it has been observed that the manufacturing firms are facing many challenges worldwide like quality, productivity, time management etc. To overcome these challenges forced the world's manufacturing firms to develop new manufacturing methods and concepts in the competitive market. Among them one of the main concepts is execution of lean manufacturing strategies in the production system. The concept of lean manufacturing system (LMS) was initiated by a Japanese automobile industry Toyota in mid-20th century was well known for production

* Corresponding author: Dilbagh Panchal
e-mail addresses: mohitmied@gmail.com (M. Tyagi), panchald@nitj.ac.in (D. Panchal), dk18102010@gmail.com (D. Kumar), waliaravinder@yahoo.com (R. Walia)

system. The aim of Toyota Production system was to enhance and raise the productivity with cost-reduction of the product by reducing waste or non-value added ventures (Womack et al., 1990; Srinivasaraghavan & Allada, 2006). It defines the production process and procedures to improve the working environment of the shop floor consequently it also helps in increasing the overall productivity of company (Narasimhan et al., 2006; Kusrini et al., 2014). It can provide the essential extended term performance to automobile companies by refining the organization of cost effectiveness, elimination of wastage and also environmental risks over the improvement of experiences for endless organizational progress. Lean manufacturing can implement the various set of activities for better performance of a company (Yusup et al., 2015; Al-Tit, 2017). There are different techniques generally accessing in the industry for effective outcomes. Application of lean manufacturing strategies can lead to continuous improvement in industrial field. The concept of lean can be implemented in any business organization along with the industries. Different types of tool are being used from past several decades in order to get error free production from production unit. It is a tool that provides effective results to withstand the competition in prevailing different segments in the market aiming to remove all others unnecessary parameters from production unit (Schiele & McCue, 2010). It uses very small inventory for manufacturing of product at high productivity. That's why, it can be seen as a very popular tool or technique used by most of big industries and firms.

Lean management is meant for respect of humanity, it does not under estimate the capacity of people working in the company. Moreover, it will help people to be more effective and appreciate their work. Lean management maintains the production and levelise all stages of production in the company (Ahlstrom, 2004; Nenni et al., 2014). Many errors occur during production like breakdown, lot reject etc. it can provide the framework to remove all these errors during the production. It can analyze the production procedure to find out the causes occur during production. Lean can help in maintaining the documentation of work process or procedure of production and establish the standards of the manufacturing for the company for present and future production (Jasti & Kodali, 2016). Many articles have focused on lean manufacturing strategies and lean integrated production system (Hackman & Wageman, 1995; McKone et al., 2001). This research purposes to pinpoint several lean strategies and features through comprehensive textual review to analyze them through interpretive structural modeling (ISM). A model based on ISM technique is developed to frame the immediate connection between various considered strategies. Then the fuzzy MICMAC technique is performed to measure the inter-dependent power of different lean strategies. The results of present effort will assist the managers to improve the efficiency of their firm in this competitive market.

In the current study, an ISM approach with fuzzy MICMAC analysis has been applied due to its various importances over the other MCDM approaches. This approach provides a model based on that the dependence and driving nature of any factor/measures/strategies which is missing with the application of other MCDM approaches. Furthermore, the MICMAC analysis under uncertain environment (fuzzy) provide the cluster based analysis through four sectors (dependent, independent, linkage or individual) which provides a platform to the manager or policy makers to emphasize on strategies or factors according to the policy notion of the concerned organization.

The organization of this research article is as follow: section one gives a brief introduction on the various lean strategies and their importance in present manufacturing scenario, section two encloses the inclusive literature review and the based that important lean strategies have been extracted, section three illustrates the methodology which has been applied on the selected strategies in order to obtain the interrelationship among them, the conclusion drawn from the present research and its managerial implications in manufacturing environment have been expressed in section four and five respectively. In the last, section six shows the limitation and future scope of the present study.

2. Literature review

The goal of LMS is to reduce inventory and increase human efficiency and handling industrial stocks which are in accordance to consumer needs and the products are manufactured effectively and efficiently (Bhim et al., 2010). Increasing resource effectiveness by excluding superfluous consumption denotes the logical extension from lean manufacturing to lean and manufacturing. A simulation based methodology for monetary valuation was studied by Greinacher et al., (2015) of lean and green manufacturing organizations as non-monetary green parameters. Thus, economical efficiency is an indispensable evaluating factor in the application of lean and green manufacturing strategies. Salleh et al., (2012) Studied the forming process for simulation of combined total quality management along with lean manufacturing activities. Wahab et al., (2013) established a theoretical model to evaluate leanness in manufacturing unit. In this research, a concept based model for leanness element in the manufacturing unit has been made and deliberate in two prime levels i.e. dimensions and factors. Additionally, the model also demonstrations how lean parameters of an organization or manufacturing system co- relating different forms of wastes. Hartini & Ciptomulyono (2015) examined the effect of lean and sustainable production system to improve organization performance. Onyeocha et al., (2015) worked on assessment of multi-product lean manufacturing system with assembly and changing demand.

Many of the suggestions recommended that lean production system is favorable for sustainable production system; most influentially, it would help in perspective environment and cost-effective aspects. Duraccio et al., (2014), Arslankaya & Atay (2015) observed and apply the maintenance management with the lean manufacturing methods at the maintenance workshop for removing the losses caused by breakdowns in order to improve production and motivate the personnel. Youssouf et al., (2014) worked on the optimization of strategies lean Six Sigma. Lean manufacturing with ergonomic working environment in the automobile sector is another very effective concept to enhance the working condition, improve productivity, improving production processes, and eliminate the waste (Berlin et al., 2014; Dos Santos et al., 2015). The key area of ergonomics is to improve and relate the man alteration methods to their work and competent and harmless ways in order to enhance the welfare, safety, health, prosperity and thus to accumulate efficiency and productivity of the organization (Dul & Neumann, 2009). Mohammaddust et al., (2017) developed the robust lean model for alternative risk mitigation strategies. Rohani & Zahraee (2015) studied lean manufacturing technique termed as Value Stream Mapping (VSM) for enhancing the assembly line of an industry. To attain this

goal, lean strategies were applied in order to construct VSM for identification, disposal of wastages and improved performance of the organization. Susilawati et al., (2015) used the fuzzy logic based process to quantify the level of lean activity in industry.

Mandal & Deshmukh (1994) researched about the vendor selection procedure of the company dependent on different parameters using ISM. ISM methodology is a very popular technique to define the direct relationship among different enablers or barriers. Lee et al., (2011) analysed that the Lean manufacturing is very popular technique in the field of production system from past several decades. Kanban system among them is the most important lean manufacturing principles for lean production system along with reduced cost and marginal inventories. The objectives are (i) to define the working of the KANBAN system successfully across organizations globally and (ii) categorizing factors obstructing small and medium enterprises from executing Kanban in lean manufacturing system (Rahman et al., 2013). Shah & Ward (2003) observed the outcomes of three dependent issues, plant dimensions, plant life and unionization position, on the chance of applying different manufacturing industrial practices that are main facets of LMS. Lee et al., (2011) analyzed the process-advantages, expenses, and threats for identifying techniques by making use of integrated ISM and fuzzy analytic order of procedure. Shuaib et al., (2016) studied on enablers of smart organization and developed the integrated ISM model with fuzzy MICMAC. Dewangan et al., (2015) examined the enablers for advancement of innovation in the Indian manufacturing segment and direct relationship has been analyzed among different enablers with help of ISM and fuzzy MICMAC. Charan et al., (2008) explored the barriers in supply chain performance measurement system and implementation in Indian context. ISM technique to analysis the enablers and barriers of green supply chain management (GSCM) has been used by many researcher, some of them are as follows (Diabat & Govindan, 2011; Gorane & Kant, 2013; Faisal, 2010; Mudgal et al., 2010; Singh et al., 2010; Talib et al., 2011; Tyagi et al., 2015; Wang et al., 2015; Tyagi et al., 2017). Kannan et al. (2009) applied the combined study of ISM and fuzzy TOPSIS approach to examine and considering the 3-P reverse logistic providers. Diabat & Govindan (2011) have suggested the ISM approach to examination the drivers influencing the application of GSCM. Prasad et al., (2020) developed a novel framework based on lean manufacturing concept for continuous improvement in Indian textile industry. Palang & Dhatrak (2020) implemented Define, Measure, Analysis, Improve and Control (DMAIC), Failure Mode and Effect Analysis (FMEA), Industry 4.0 and Kaizen approaches for developing the lean manufacturing concept based model in order to improve the productivity of the industry. Yadav et al., (2020) proposed hybrid Fuzzy Analytical Hierarchy Process (FAHP) - Decision Making Trial and Evaluation Laboratory (DEMATEL) approaches based lean manufacturing concept for enhancing the improvement capabilities of companies under developing economies. Guillen et al., (2020) proposed a structured methodology based on lean manufacturing principles for improving facility management. Tortorella et al., (2021) proposed lean automation based model for examining improvement pathway of an industry.

From the reviewed literature it has been noted that the application of ISM-MICMAC approaches was not yet been reported by any researcher in order to identify and analyze the inter-relationship among filtered strategies for the considered lean manufacturing case. To bridge this, gap the current work presents the application of

ISM-MICMAC approaches based framework to enhance the efficiency of the considered organization.

3. Research Methodology

On the basis of discussion with experts and literature review lean manufacturing strategies were identified and a developed questionnaire was floated among the experts for the collection of the data. Factor analysis was performed, and appropriate strategies were filtered and further brainstorming session was conducted for their acceptance or rejection. After the acceptance of filtered strategies ISM and fuzzy MICMAC approaches were applied and analysis was carried for reaching appropriate decision. The flow diagram on the research work plan denoted in figure 1 is carried out in unique view. However, a step by step explanation of ISM approach is also given below.

The interpretive structural modeling (ISM) used to create a composite system into an envisioned ordered arrangement. It is used for studying and solving complex problems to help in decision-making (Warfield, 1974; Jain & Raj, 2015). It is based on computer-assisted method that usually used to conclude the multiplex situations by providing a sensible and reasonable path of action (Kannan et al., 2009).

Initial phase of the ISM method is used to pin-point lean strategies, drivers or other alternatives, which concerns the research complication. Then a theoretically feasible derived relation is selected (Thakkar et al., 2006).

ISM methodology involves several steps as follows (Kannan &Haq, 2007; Sharma & Garg, 2010).

Identify and enlist the diverse strategies of lean manufacturing system.

I. Creating a relative relationship between different lean manufacturing strategies.

II. Development of a fundamental self-interaction matrix (SSIM) to lean manufacturing strategies which show interactions among lean manufacturing strategies under the ambit.

III. Creating reachability matrix using SSIM and then transitivity of the matrix is evaluated.

IV. A flow chart is drawn on the basis of reachability matrix.

V. Interpret the subsequent relationship digraph into an ISM by switching lean strategies with statements

Verify for conceptual difference and essential improvements made and contextual correlation was developed among diverse lean manufacturing strategies.

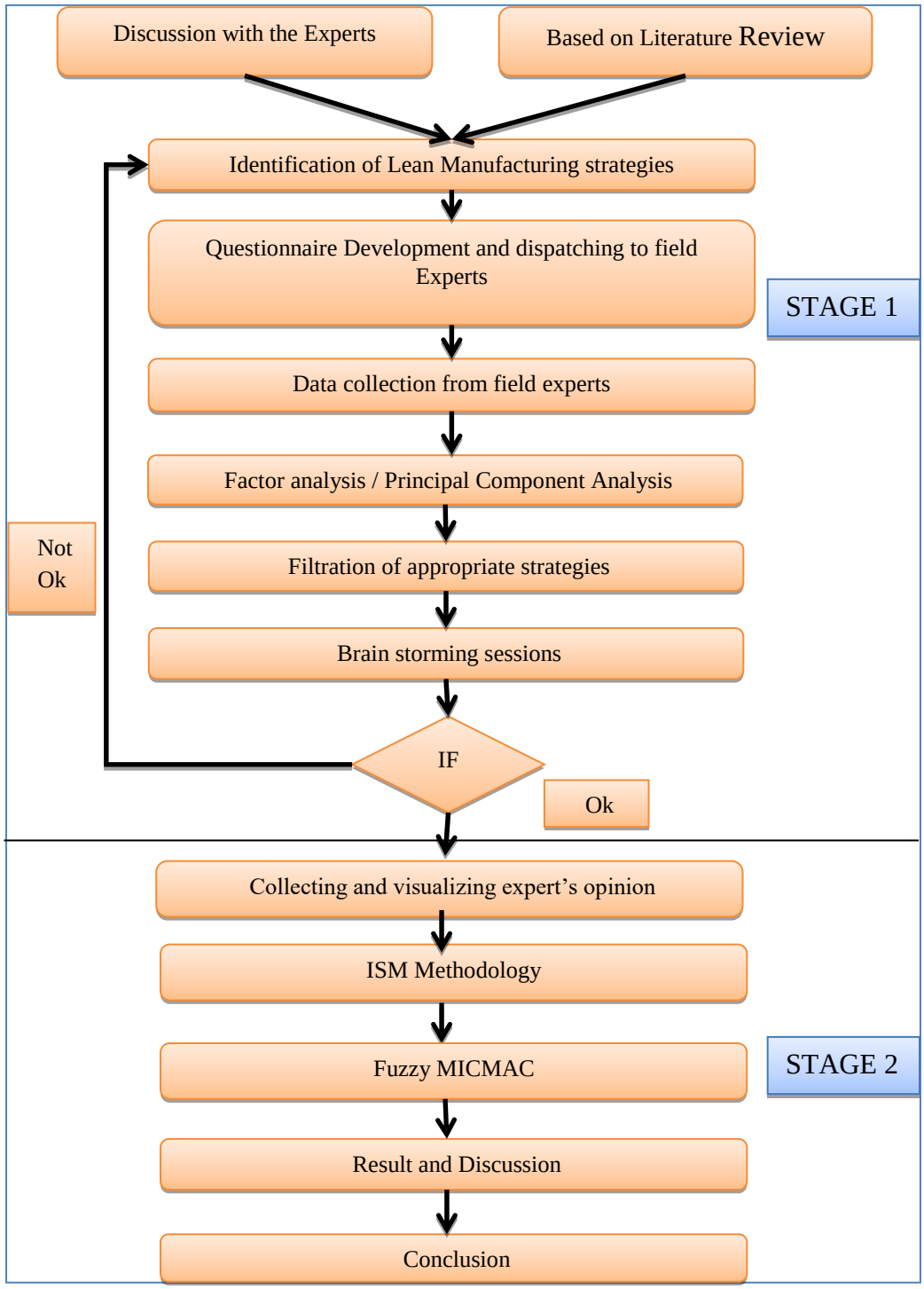

Figure 1. Flow chart illustrating research direction

4. Proposed research methodology implementation based results

In accordance to the literature survey and after consultation with the field professionals, thirty-six lean manufacturing strategies were acknowledged. Then, a questionnaire was designed using Google form and forwarded on Google doc. Numerous views of different field professionals were collected. To analyze the lean strategies, the experts from Indian automobiles companies situated near Delhi NCR and academicians from several organizations were communicated for the view of lean manufacturing strategies. encompassing expertise in the field of manufacturing and strategies formulation have been considered to collect their opinions regarding the implementation of lean strategies in Indian automobile companies in order to improve their performance. To analyze the lean strategies, an ISM approach with fuzzy MICMAC has been applied, for the same qualitative input from the experts (four groups having five to six experts in each group) have been taken to develop the structural self-interaction matrix. Here concept of fuzzy set is used to consider the vagueness of the collected data for high accuracy in the decision results. Before implementing the ISM approach, a factor analysis has also been carried in order to extract the significant strategies based on their factor loading values.

Factor analysis (FA) is a dynamic means for statistical mitigation and conveying the nearby events of diverse strategies by deciding the normal elements in view of the account of perceived correlations (Hayton, 2004). Primarily, a questionnaire has been designed by5-point Likert type scale for thirty-six lean strategies and was send to the one hundred and fifty field professionals to gather their view regarding the significance of lean strategies. Out of one hundred and fifty, fifty-seven replies were acknowledged, which reveals the 38% response rate. When the response rate is greater than 30%, it is appropriate to execute the reliability examination as suggested by Malhotra & Grover (1998).

The received stats are deemed as reliable, only if the cronbach alpha coefficient(α)ranges from0.7to 1. Gliem & Gliem (2003) mentions the rules as follows: $\alpha > 0.9$ signifies Outstanding, $\alpha > 0.8$ signifies Good, $\alpha > 0.7$ signifies Satisfactory, $\alpha > 0.6$ signifies Questionable, $\alpha > 0.5$ signifies Poor, and $\alpha < 0.5$ signifies Unacceptable". In the present research work, score of the cronbach alpha coefficient comes as 0.794, hence the collected data can be considered as reliable. Then factor analysis is done for the clarification of appropriate lean strategies by same software. Table 1 shows cumulative variances of different lean strategies and thirteen lean strategies contributed to about 77.648 % of the total variance and have eigen values greater than threshold value of 1. The component matrix was observed to extract thirteen lean strategies based on the variable loaded in the software. The listed of extracted lean strategies is shown in table 2. To understand the dominance thirteen extracted lean strategies over the total identified strategies a scree plot has been structured, as shown in Figure 2. The scree plot makes an elbow after the thirteenth component, which means that each succeeding factor accounts for smaller and smaller accounts of the total variance.

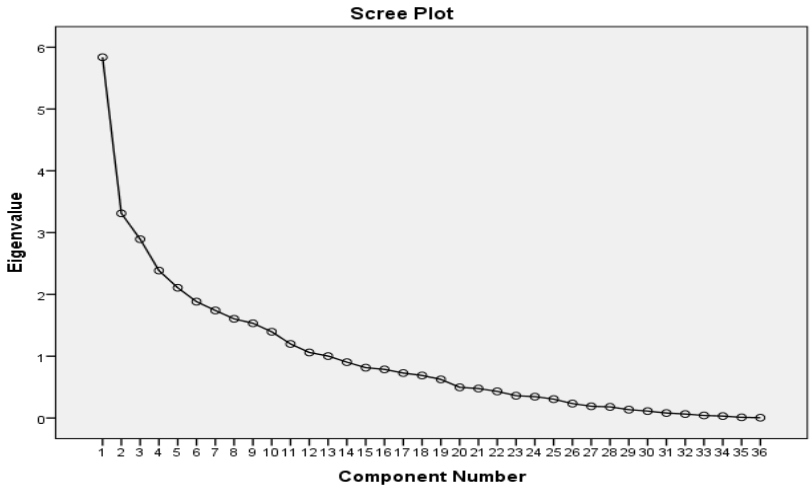

Figure 2 Scree graph for different components

Table 1 Total variance explained

Component	Initial Eigenvalues			Extraction Sums of Squared Loadings			Rotation Sums of Squared Loadings
	Total	% of Variance	Cumulative %	Total	% of Variance	Cumulative %	Total
1	5.838	16.216	16.216	5.838	16.216	16.216	2.764
2	3.311	9.196	25.412	3.311	9.196	25.412	2.745
3	2.894	8.038	33.450	2.894	8.038	33.450	2.608
4	2.386	6.628	40.078	2.386	6.628	40.078	2.557
5	2.107	5.854	45.932	2.107	5.854	45.932	2.547
6	1.882	5.229	51.161	1.882	5.229	51.161	2.420
7	1.741	4.836	55.997	1.741	4.836	55.997	2.220
8	1.604	4.456	60.453	1.604	4.456	60.453	1.971
9	1.533	4.258	64.712	1.533	4.258	64.712	1.750
10	1.396	3.878	68.590	1.396	3.878	68.590	1.742
11	1.198	3.329	71.919	1.198	3.329	71.919	1.595
12	1.060	2.946	74.865	1.060	2.946	74.865	1.578
13	1.002	2.784	77.648	1.002	2.784	77.648	1.458
14	.903	2.510	80.158	-	-	-	-
15	.814	2.261	82.419	-	-	-	-
16	.786	2.184	84.603	-	-	-	-
17	.727	2.019	86.622	-	-	-	-
18	.688	1.911	88.533	-	-	-	-
19	.625	1.735	90.268	-	-	-	-
20	.497	1.380	91.648	-	-	-	-
21	.476	1.323	92.971	-	-	-	-
22	.431	1.197	94.168	-	-	-	-

23	.361	1.002	95.170	-	-	-	-
24	.346	.962	96.131	-	-	-	-
25	.305	.848	96.980	-	-	-	-
26	.233	.649	97.628	-	-	-	-
27	.190	.529	98.157	-	-	-	-
28	.180	.501	98.658	-	-	-	-
29	.135	.375	99.034	-	-	-	-
30	.112	.312	99.346	-	-	-	-
31	.081	.225	99.571	-	-	-	-
32	.065	.180	99.751	-	-	-	-
33	.041	.115	99.866	-	-	-	-
34	.032	.089	99.955	-	-	-	-
35	.011	.031	99.986	-	-	-	-
36	.005	.014	100.000	-	-	-	-

Table 2 Extracted lean strategies

Sr. No.	Lean Strategies	Sources
S1.	Line improvement activity	(Salleh et al., 2012; Chai et al., 2012)
S2.	Ability to adjust capacity rapidly within a short time period	(Stecke& Kim, 1988; Ward &Duray, 2000)
S3.	Alternative supply chain networks	(Harland, 1996; Hugo &Pistikopoulos, 2005; Mohammaddust et al., 2017)
S4.	Focus on Market orientation	(Venkatraman&Ramanujam, 1987)
S5.	Development programs or past performance record	(Brown & Cousins, 2004)
S6.	Proper machine utilization	(Nordin et al., 2010)
S7.	Minimizing Work in progress	(Riezebos et al., 2009; Onyeocha et al., 2015)
S8.	Ability to provide innovation design	(Zhao et al., 2006; Le Dain et al., 2011)
S9.	Recycling of raw materials and defective parts	(Thierry et al., 1995; Wang et al., 2008)
S10	Higher collaboration for better production planning	(Seifert, 2003; Kenne et al., 2007; Chinprateep&Boondiskulchok, 2010)
S11.	Monitoring the implementation schedules step by step	(Ballard & Howell, 1998; Guo et al., 2015; Soroush, 2015)
S12.	Training of employees to develop multi skills	(Wang et al., 2008; Heimerl&Kolisch, 2010)
S13.	Handling of appropriate variations in customer orders	(Anand& Ward, 2004)

Now, after extracting the significant lean manufacturing strategies, a step by step implementation of ISM approach has been made as given below:

4.1 Structural self-interaction matrix (SSIM)

The SSIM is used to understand the related relationship between the diverse identified lean strategies in table 3 by making use of professional's view. The matrix delivers the pair-wise connection of each lean strategy. The signs [V, A, X and O] are applied for linking of lean strategies (a, b).

V - Strategy 'a' will assistance to enhance strategy 'b'

A -Strategy 'a' will assistance to enhance strategy 'b'

X -Strategy 'a' and 'b' will assistance to enhance each other

O - Strategy 'a' and 'b' are independent

Table 3 SSIM lean strategies

S.no.	Lean Strategies	13	12	11	10	9	8	7	6	5	4	3	2	1
S1.	Line improvement activity	V	A	A	A	O	V	V	V	A	V	A	A	-
S2.	Ability to adjust capacity rapidly within a short time period	V	A	A	A	O	A	V	X	O	A	A	-	
S3.	Alternative supply chain networks	V	O	A	O	X	A	V	V	O	A	-		
S4.	Focus on Market orientation	V	V	V	A	V	V	O	V	V	-			
S5.	Development programs or past performance record	V	A	V	X	V	V	V	V	-				
S6.	Proper machine utilization	A	A	A	A	O	O	V	-					
S7.	Minimizing Work in progress	O	A	A	A	V	A	-						
S8.	Ability to provide innovation design	X	A	A	A	O	-							
S9.	Recycling of raw materials and defective parts	A	A	O	O	-								
S10	Higher collaboration for better production	V	A	V	-									

	planning			
S11.	Monitoring the implementation schedules step by step	X	A	-
S12.	Training of employees to develop multi skills	V	-	
S13.	Handling of appropriate variations in customer orders	-		

4.2 Reachability matrix

The formulation of the initial reachability matrix is the subsequent stage in ISM methodology. The transformation into initial reachability matrix as depicted in table 4 is obtained by the dual linking of the lean strategies in SSIM given in table 3 by means of binary system. The transformation is prepared with the assistance of the below mentioned rules:

When (a, b) in the set implies V, assign the value of (a, b) within the reachability matrix as 1 and assign the (b, a) value as 0.

When (a, b) in the set implies A, assign the value of (a, b) within the reachability matrix as 0 and assign the (b, a) value as 1.

When (a, b) in the set implies X, assign the value of (a, b) within the reachability matrix as 1 and assign the (b, a) value as 1.

When (a, b) in the set implies O, then assign the (a, b) result within the reachability matrix as 0 and assign the (b, a) value as 0.

Table 4 Initial reachability matrix

Sr. no.	Lean Strategies	1	2	3	4	5	6	7	8	9	10	11	12	13
S1.	Line improvement activity	1	0	0	1	0	1	1	1	0	0	0	0	1
S2.	Ability to adjust capacity rapidly within a short time period	1	1	0	0	0	1	1	0	0	0	0	0	1
S3.	Alternative supply chain networks	1	1	1	0	0	1	1	0	1	0	0	0	1
S4.	Focus on Market orientation	0	1	1	1	1	1	0	1	1	0	1	1	1
S5.	Development programs or past	1	0	0	0	1	1	1	1	1	1	1	0	1

	performance record													
S6.	Proper machine utilization	0	1	0	0	0	1	1	0	0	0	0	0	0
S7.	Minimizing Work in progress	0	0	0	0	0	0	1	0	1	0	0	0	0
S8.	Ability to provide innovation design	0	1	1	0	0	0	1	1	0	0	0	0	1
S9.	Recycling of raw materials and defective parts	0	0	1	0	0	0	0	0	1	0	0	0	0
S10	Higher collaboration for better production planning	1	1	0	1	1	1	1	1	0	1	1	0	1
S11.	Monitoring the implementation schedules step by step	1	1	1	0	0	1	1	1	0	0	1	0	1
S12.	Training of employees to develop multi skills	1	1	0	0	1	1	1	1	1	1	1	1	1
S13.	Handling of appropriate variations in customer orders	0	0	0	0	0	1	0	1	1	0	1	0	1

By applying the transitivity rule the initial matrix was converted into final matrix in table 5, which suggests that the lean strategy 'L' is interrelated to 'M' and 'M' is interrelated to 'N', it is considered that L will be interrelated to N. The set that indicates the transitivity is noticeable with the symbol (*).

Table 5 Final reachability matrix

Sr. no.	Lean Strategies	1	2	3	4	……..	9	10	11	12	13	S.P
S1.	Line improvement activity	1	1*	1*	1	……..	1*	0	1*	1*	1	12
S2.	Ability to adjust capacity rapidly within a short time period	1	1	0	1*	……..	1*	0	1*	0	1	9

S3.	Alternative supply chain networks	1	1	1	1*	……..	1	0	1*	0	1	10
S4.	Focus on Market orientation	1*	1	1	1	……..	1	1*	1	1	1	13
S5.	Development programs or past performance record	1	1*	1*	1*	……..	1	1	1	0	1	12
S6.	Proper machine utilization	1*	1	0	0	……..	1*	0	0	0	1*	6
S7.	Minimizing Work in progress	0	0	1*	0	……..	1	0	0	0	0	3
S8.	Ability to provide innovation design	1*	1	1	0	……..	1*	0	1*	0	1	9
S9.	Recycling of raw materials and defective parts	1*	1*	1	0	……..	1	0	0	0	1*	7
S10	Higher collaboration for better production planning	1	1	1*	1	……..	1*	1	1	1*	1	13
S11.	Monitoring the implementation schedules step by step	1	1	1	1*	……..	1*	0	1	0	1	10
S12.	Training of employees to develop multi skills	1	1	1*	1*	……..	1	1	1	1	1	13
S13.	Handling of appropriate variations in customer orders	1*	1*	1*	1*	……..	1	1*	1	0	1	12
		12	12	11	9	……..	13	5	10	4	12	

4.3 Level partition

In order to filter out the reachability and antecedent sets, reachability matrix has been partitioned by applying the concept of level partition as shown in tables 6 and 7. In table 6, a complete process has been explained for level partition based on reachability and antecedent sets in respect of each filtered strategy.

However, in table 7, a complete summary of levels has been given. The reachability set includes the lean strategy itself along with lean strategies that it would affect while the antecedent set includes the lean strategy itself along with other lean strategies that may impact it. Then, different levels are obtained by the intersection for all lean strategies of these sets. The lean strategy whose reachability and antecedent set are identical, is placed in the uppermost level of the order. The uppermost level lean strategies are the ones that would not lead other lean strategies to overcome their own level in this order.

After identifying the topmost level of lean strategies, they are uninvolved in contemplation while the same procedure is reiterated to find out the successive levels. This method is applied till the level of each lean strategy is obtained. These levels play a major role in building the ISM model.

Table 6 Level partition (Iteration I)

Lean Strategies	Reachability set	Antecedent set	Interaction	Level
S1.	1,2,3,4,5,6,7,8,9,11,12,13	1,2,3,4,5,6,8,9,10,11,12,13	1,2,3,4,5,6,8,9,11,12,13	-
S2.	1,2,4,6,7,8,9,11,13	1,2,3,4,5,6,8,9,10,11,12,13	1,2,4,6,8,9,11,13	-
S3.	1,2,3,4,6,7,8,9,11,13	1,3,4,5,7,8,9,10,11,12,13	1,3,4,7,8,9,11,13	-
S4.	1,2,3,4,5,6,7,8,9,10,11,12,13	1,2,3,4,5,10,11,12,13	1,2,3,4,5,10,11,12,13	-
S5.	1,2,3,4,5,6,7,8,9,10,11,13	1,4,5,10,13	1,4,5,10,13	-
S6.	1,2,6,7,9,13	1,2,3,4,5,6,8,9,10,11,12,13	1,2,6,9,13	-
S7.	3,7,9	1,2,3,4,5,6,7,8,9,10,11,12,13	3,7,9	I
S8.	1,2,3,6,7,8,9,11,13	1,2,3,4,5,8,10,11,12,13	1,2,3,8,11,13	-
S9.	1,2,3,6,7,9,13	1,2,3,4,5,6,7,8,9,10,11,12,13	1,2,3,6,7,9,13	I
S10	1,2,3,4,5,6,7,8,9,10,11,12,13	4,5,10,12,13	4,5,10,12,13	-
S11.	1,2,3,4,6,7,8,9,11,13	1,2,3,4,5,8,10,11,12,13	1,2,3,4,8,11,13	-
S12.	1,2,3,4,5,6,7,8,9,10,11,12,13	1,4,10,12	1,4,10,12	-
S13.	1,2,3,4,5,6,7,8,9,10,11,13	1,2,3,4,5,6,8,9,10,11,12,13	1,2,3,4,5,6,8,9,10,11,13	-

Table 7 Level partition (Final Iteration)

Lean Strategies	Reachability set	Antecedent set	Interaction	Level
S1.	1,2,3,4,5,6,8,11, 12,13	1,2,3,4,5,6,8,10,11,12, 13	1,2,3,4,5,6,8,11,1 2,13	II
S2.	1,2,4,6,8,11,13	1,2,3,4,5,6,8,10,11,12, 13	1,2,4,6,8,11,13	II
S3.	3,4,8,11,	3,4,5,8,10,11,12	3,4,8,11,	III
S4.	4,5,10,12	4,5,10,12	4,5,10,12	IV
S5.	4,5,10,	4,5,10	4,5,10	IV
S6.	1,2,6,13	1,2,3,4,5,6,8,10,11,12, 13	1,2,6,13	II
S7.	3,7,9	1,2,3,4,5,6,7,8,9,10,11, 12,13	3,7,9	I
S8.	8,11	3,4,5,8,10,11,12	8,11	III
S9.	1,2,3,6,7,9,13	1,2,3,4,5,6,7,8,9,10,11, 12,13	1,2,3,6,7,9,13	I
S10	4,5,10,12	4,5,10,12	4,5,10,12	IV
S11.	3,4,8,11	3,4,5,8,10,11,12	3,4,8,11	III
S12.	12	12	12	V
S13.	1,2,3,4,5,6,8,10, 11,13	1,2,3,4,5,6,8,10,11,12, 13	1,2,3,4,5,6,8,10,1 1,13	II

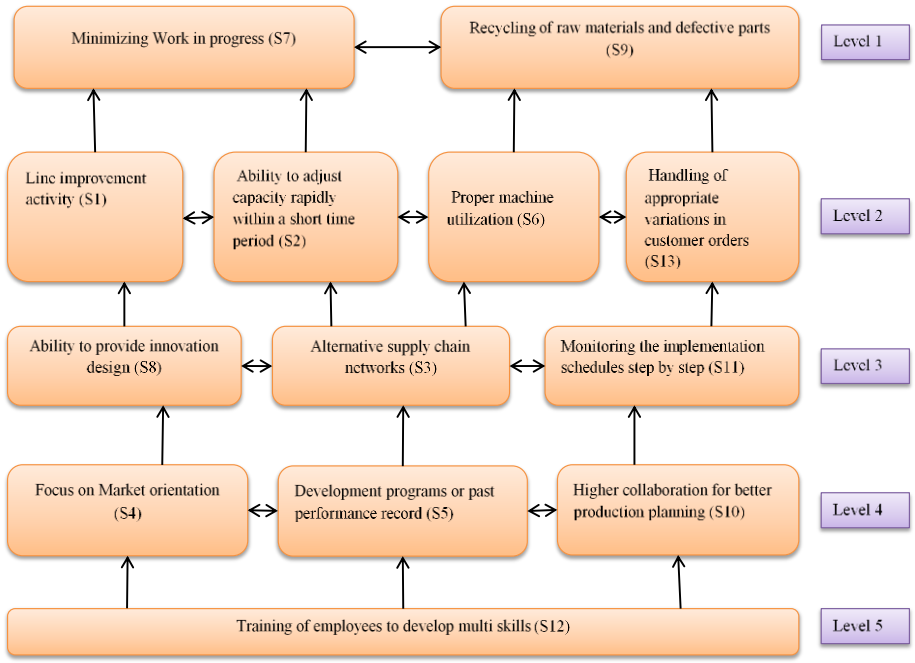

Figure 3 Model based on ISM

The above flow charts illustrated in figure 3 depicts the diverse lean strategies and their inter-dependence. In the flowchart, the adopted influential steps have been distributed into 5 levels for the progress of the organization. Training of employees to develop multi skills (S35) is most significant lean strategy which pushes all the former strategies which effect in positive incorporation of lean and every organization need to focus on this strategy. With continuous and systematic training, personnel become competent in new techniques that assist in building up several abilities which further help to steer the organization at higher level. The foundation of this ISM model is built up by level 5 strategies (S12).

Training of employees to develop multi skills (S12) escorts the three strategies at level 4 i.e. focus on market orientation (S4), development programs or past performance record (S5) and higher collaboration for better production planning (S10). These three strategies have solid connection among them based on the performance data of the past or improvement programs which plays a role in finding out the shortcomings of concluding products or new demands of consumers centered by concentrated on the inclination of the market. This would assist the manufacturing unit in teaming up with other personnel, hence enhancing productivity.

At level 3 strategies, alternative supply chain networks (S3), ability to provide innovation design (S8) and monitoring the implementation schedules step by step (S11) ushered by level 4. Regular training and Focusing on market orientation helps the employees to create the ability of innovative designing according to the demand that further come out to give alternative sully chain networks. This is also helps in monitoring the implementing schedules steps by steps. Level 2 drive the further four strategies i.e. line improvement activity (S1), ability to modify capacity quickly within a short time interval (S2), proper machine utilization (S6) and handling of appropriate variations in customer orders (S13).

Strategies at level 2 have very strong connectivity with each other. If there is proper machine utilization and improved line activity, it can create ability to adjust the capacity quickly within short period of time that helps to handle the variations in customers' orders.

Minimizing work in progress (S7) and recycling of raw materials and defective parts (S9) at first level directed by second level are the preferred products of the figures. Aforementioned two strategies acquiring the uppermost rank of this orderly representation make use of proper machine utilization and improved line activity results in minimizing work in process with minimal defective parts which gives desired best quality products and increases the productivity of the organization.

4.4 Fuzzy MICMAC analysis

MICMAC can be elaborated as "Matriced Impacts croises-multipication applique and classment" or in simple way it is define as "cross-impact matrix multiplication applied to classification" (Jain & Raj, 2016; Qureshi et al., 2008). This analysis involves the different steps as follows:

I: Creating the binary direct relationship matrix

II: Constructing the fuzzy direct reachability matrix

III: Producing the stabilized fuzzy MICMAC matrix

Here, fuzzy concept is used in order to consider the uncertainties or vagueness in the collected data useful for high accuracy in the decision results.

4.5 Creating the binary direct relationship matrix

To make the binary direct relationship matrix, it is required to transform the convectional MICMAC analysis into fuzzy MICMAC analysis using binary system (0 & 1). To make an analysis stronger through considering the uncertainty in the collected raw data, fuzzy set theory (Panchal & Kumar, 2014; Stojić et al., 2018; Chatterjee & Stević, 2019; Panchal et al., 2018; Panchal et al., 2019; Petrović et al.,2019; Đalić et al., 2020; Pająk, 2020; Kushwaha et al., 2020; Zavadskas et al., 2020) has been utilized. The binary direct relationship matrix is shown below in table 8.

Table 8 Binary direct relationship matrix

Sr. no.	Lean Strategies	1	2	3	4	5	6	7	8	9	10	11	12	13	**D.P**
S1.	Line improvement activity	0	0	0	1	0	1	1	1	0	0	0	0	1	**5**
S2.	Ability to adjust capacity rapidly within a short time period	1	0	0	0	0	1	1	0	0	0	0	0	1	**3**
S3.	Alternative supply chain networks	1	1	0	0	0	1	1	0	1	0	0	0	1	**6**
S4.	Focus on Market orientation	0	1	1	0	1	1	0	1	1	0	1	1	1	**9**
S5.	Development programs or past performance record	1	0	0	0	0	1	1	1	1	1	1	0	1	**8**
S6.	Proper machine utilization	0	1	0	0	0	0	1	0	0	0	0	0	0	**2**
S7.	Minimizing Work in progress	0	0	0	0	0	0	0	0	1	0	0	0	0	**1**
S8.	Ability to provide innovation design	0	1	1	0	0	0	1	0	0	0	0	0	1	**4**
S9.	Recycling of raw materials and defective parts	0	0	1	0	0	0	0	0	0	0	0	0	0	**1**
S10	Higher collaboration	1	1	0	1	1	1	1	1	0	0	1	0	1	**9**

	for better production planning													
S11.	Monitoring the implementation schedules step by step	1	1	1	0	0	1	1	1	0	0	0	0	1	**7**
S12.	Training of employees to develop multi skills	1	1	0	0	1	1	1	1	1	1	1	0	1	**10**
S13.	Handling of appropriate variations in customer orders	0	0	0	0	0	1	0	1	1	0	1	0	0	**4**
	Dependence power	6	7	4	2	3	9	9	7	7	2	5	1	9	

Table 9 Possibility of numerical values of the reachability

Possibility of reachability	No	Very low	Low	Medium	High	Very high	Complete
Value	0	0.1	0.3	0.5	0.7	0.9	1

4.6 Constructing the fuzzy direct reachability matrix

The values given in table 9 are made use in the binary direct relationship matrix for developing the fuzzy direct reachability matrix. The understanding of MICMAC analysis is augmented by making use of fuzzy theory which is why possibility of interaction is used to interpret the immediate connection among different lean strategies as represented in table 9. Therefore, fuzzy direct reachability is developed and as depicted in table 10.

Table 10 Fuzzy direct reachability matrix

S.no.	Lean Strategies	1	2	3	4	…..	9	10	11	12	13
S1.	Line improvement activity	0	0	0	0	…..	0	0	0	0	0.1
S2.	Ability to adjust capacity rapidly within a short time period	0	0	0	0	……	0	0	0	0	0.3
S3.	Alternative supply chain networks	0.3	0	0	0	…..	0.9	0	0	0	0.3
S4.	Focus on Market orientation	0	0.9	0.7	0	……	0.9	0	0.3	0	0.5
S5.	Development	0	0	0	0		0	0	0	0	0.1

	programs or past performance record					……					
S6.	Proper machine utilization	0	0	0	0	……	0	0	0	0	0
S7.	Minimizing Work in progress	0	0	0	0	……	0	0	0	0	0
S8.	Ability to provide innovation design	0	0	0	0	……	0	0	0	0	0
S9.	Recycling of raw materials and defective parts	0	0	0	0	……	0	0	0	0	0
S10	Higher collaboration for better production planning	0.5	0.5	0	0	…….	0	0	0.5	0	0.9
S11.	Monitoring the implementation schedules step by step	0.1	0.1	0	0	……..	0	0	0	0	0
S12.	Training of employees to develop multi skills	0.5	0.5	0	0	…….	0	0	0.5	0	0.7
S13.	Handling of appropriate variations in customer orders	0	0	0	0	……..	0.3	0	0	0	0

The subset values are given in table10 is used as the base for constructing stabilized fuzzy MICMAC matrix. Multiplication of the obtained matrix is done many a times unless the orders of dependence and driving power become constant. With reference to the mentioned theory, the result obtained could be a fuzzy matrix, after the multiplication of two fuzzy (Kandasamy et al., 2007) interval values. The Following multiplication method is used to get the required result for multiplying of two fuzzy matrixes,

MN = Max {min (mij, nij)}

Where, M = [mij] and N = [nij] are two fuzzy matrices.

For solving the above equation, the program is written in the 'C' language to attain the accuracy. The result obtained is illustrated in figure 4 and the required stabilized fuzzy MICMAC matrix is given in table 11.

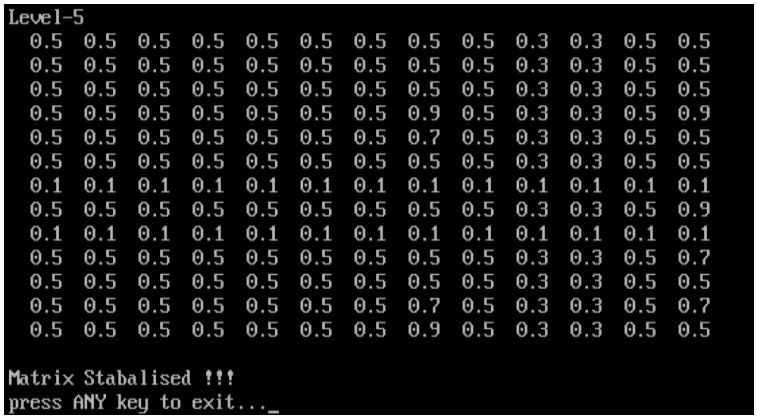

Figure 4 Stabilized fuzzy MICMAC matrix

Table 11 Stabilized fuzzy MICMAC matrix

S.no.	Lean Strategies	1	2	3	4	.....	9	10	11	12	13	Driving power
S1.	Line improvement activity	0.5	0.5	0.5	0.5	.....	0.5	0.3	0.3	0.5	0.5	**6.1**
S2.	Ability to adjust capacity rapidly within a short time period	0.5	0.5	0.5	0.5	.....	0.5	0.3	0.3	0.5	0.5	**6.1**
S3.	Alternative supply chain networks	0.5	0.5	0.5	0.5	.....	0.5	0.3	0.3	0.5	0.5	**6.1**
S4.	Focus on Market orientation	0.5	0.5	0.5	0.5	.....	0.5	0.3	0.3	0.5	0.9	**6.9**
S5.	Development programs or past performance record	0.5	0.5	0.5	0.5	.....	0.5	0.3	0.3	0.5	0.5	**6.3**
S6.	Proper machine utilization	0.5	0.5	0.5	0.5	.....	0.5	0.3	0.3	0.5	0.5	**6.1**
S7.	Minimizing Work in progress	0.1	0.1	0.1	0.1	.....	0.1	0.1	0.1	0.1	0.1	**1.3**
S8.	Ability to provide innovation design	0.5	0.5	0.5	0.5	.....	0.5	0.3	0.3	0.5	0.9	**6.5**
S9.	Recycling of raw materials	0.1	0.1	0.1	0.1	.....	0.1	0.1	0.1	0.1	0.1	**1.3**

	and defective parts											
S10	Higher collaboration for better production planning	0.5	0.5	0.5	0.5	.....	0.5	0.3	0.3	0.5	0.7	**6.3**
S11.	Monitoring the implementation schedules step by step	0.5	0.5	0.5	0.5	.....	0.5	0.3	0.3	0.5	0.5	**6.1**
S12.	Training of employees to develop multi skills	0.5	0.5	0.5	0.5	.....	0.5	0.3	0.3	0.5	0.7	**6.5**
S13.	Handling of appropriate variations in customer orders	0.5	0.5	0.5	0.5	.....	0.5	0.3	0.3	0.5	0.5	**6.5**
Dependence power		**5.7**	**5.7**	**5.7**	**5.7**	**....**	**5.7**	**3.5**	**3.5**	**5.7**	**6.9**	

Stabilized matrix as shown in table 11 is categorized into four cluster in accordance to driving power and dependence power. The summing up values of rows in the stabilized fuzzy MICMAC matrix is driving power and summing up values columns in the stabilized fuzzy MICMAC matrix is the dependence power. The cluster representation is shown in figure 5.

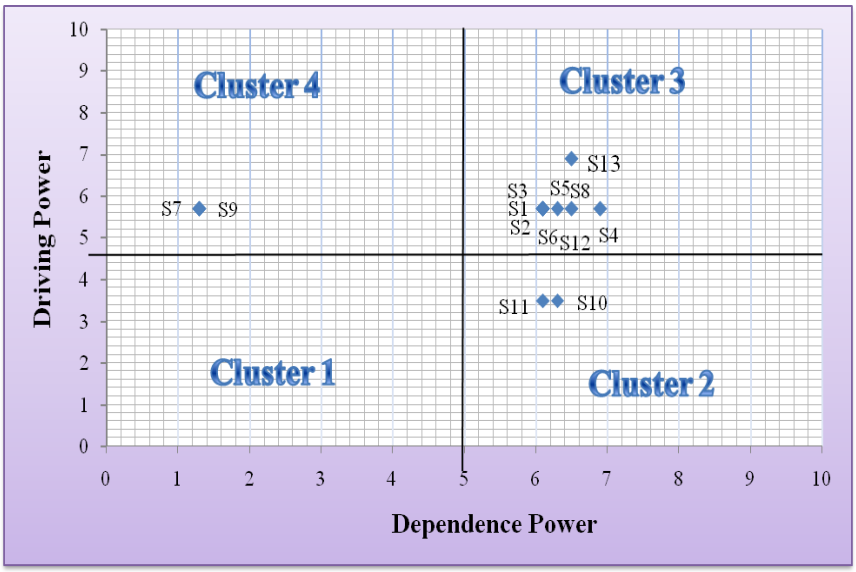

Figure 5 Driving and dependence power graph

Cluster 1: Lean strategies belonging to the particular group should have low driving and dependence power. Strategies in this group have no relation to each other. They are neither influence nor influenced by any others strategies. There is no lean strategy in our research that fall in this cluster. This is called autonomous cluster

Cluster 2: In this cluster, lean strategies are having low driving power and high dependence power. It characterizes lean strategies that are dependent on others strategies. The dependency of these lean strategies shows that they need all other lean strategies for the implementation of lean strategies into the system. Lean strategy (S7) minimizing work in progress and lean strategy (S9) recycling of raw materials and defective parts and are categorized in this cluster. This is called dependence cluster

Cluster 3: Lean strategies in this group are having very high driving power and high dependence power. This cluster denotes lean strategies which have very robust relation to each other's. Most of lean strategies in current research fall in this group. If there is a change in any lean strategy it will immediately affect the other lean strategy. Most of the lean strategies of present study fall in this cluster. Total eight strategies are categorized that are line improvement activity (S1), ability to adjust capacity quickly within a short time period (S2), alternative supply chain networks (S3), focus on Market orientation (S4), development programs or past performance record (S5), proper machine utilization (S6), ability to provide innovation design (S8), training of employees to develop multi skills (S12) and handling of appropriate variations in customer orders (S13). This is called linkage cluster.

Cluster 4: Lean strategies belonging to this group have low dependence power but very high driving power. Lean strategy which are categorized in this group are higher collaboration for better production planning (S10) and monitoring the implementation schedules step by step (S11). This is called Independent Cluster.

5. Managerial implications of the work

To prevail over the various tasks that emerge during production time and to improve the efficiency of their organization, managers require flexible attitudes to take the worthwhile decision for the growth of organization. The current research reveals that manager is required to emphasize on diverse lean strategies liable on the condition at different level. Training of employees is the primary need of the organization which accelerates the others strategies effectively in every field. Apart from this strategy, managers need to focus on secondary strategies at different level also as illustrated in figure 2. Driving and dependence graph illustrated in figure 3 would help the managers to decide whether the applied strategies are driving in nature or dependent on others. Most of strategies fall in cluster 3 managers have to focus more on this category. Strategies in this category are very crucial for application of lean manufacturing in the organization. Also, each and every strategy serves its role in the performance of the organization at its level. Therefore, this study helps the managers for implementation of various lean strategies into the organization.

6. Conclusion

It is understood that no single strategy is enough for implementation of lean manufacturing for enhancement of the efficiency organization. After factor analysis out of thirty-six lean strategies thirteen were extracted using software SPSS 21 and analyzed by structural modeling and then used to construct the ISM based model which helps to understand the direct relationship among various lean strategies. "Training of employees to develop multi skills(S12)" has been identified as the most crucial strategy which drives all the other strategies for the success of lean. Minimizing Work in progress (S7) and recycling of raw material and defective parts (S9) were level one, strategies whose success is dependent on other factors. Apart from the relationship among various lean strategies, it was also essential to express the role of individual strategy also. It was observed that most of the selected strategies have very high driving power and dependence power as well. No lean strategy was identified which fall in the autonomous cluster. Higher collaboration for better production planning (S10) and monitoring the implementation schedules step by step (S11) have been identified as the independent strategies which have high driving power and low dependence power. Also, minimizing work in progress (S7) and recycling of raw materials and defective parts (S9) were categorized in dependence cluster as they have low driving power and high dependence power. Organization across the globe now wants to make their system more define for every aspect. The present research contribution gives the optimistic correlation between different lean strategies to maintain their organization systematically. The present research assists the managers or industrialists in decision making for the implication of particular lean strategy during the production. The outcomes of this research may also be helpful for managers to comprehend the indirect and direct relationship among various lean strategies in order to provide a path to improve the efficiency of their enterprise in this competitive market. As an advantage of lean system in manufacturing organization, it is most valuable to identify and asses the importance of strategies related to lean system but it is not easy or feasible to implement the all strategies at a time in any industry or organization. For the same, a need arises to explore the strategies based on their dependence and driving behavior in order to implement and improve the lean manufacturing system of an organization. By keeping this view in mind, this study has been performed.

6.1 Limitations and future scope of the work

In this study, initially thirty-six lean strategies were identified on the basis of literature review; however, thirteen lean strategies have been extracted by using factor analysis. In ISM approach, there is no restriction in consideration on numbers of lean strategies, therefore more numbers of lean strategies can also be considered. Moreover, as the numbers of lean strategies increases, ISM model will become more complex. To drive the analysis, data have been gathered only from the automobiles industries situated at Delhi NCR. In future, data can also be gathered from the automobile industries situated at different locations of India and comprehensive study can also be implemented. To compare the outcomes of present research, the other multi-faceted decision building approaches like Fuzzy DEMATEL and SEM can be considered.

References

Ahlstrom, P. (2004). Lean service operations: translating lean Pro principles to service operations. International Journal of Services Technology and Management, 5(5-6): 545-564.

Al-Tit, A. A. (2017). Factors affecting the organizational performance of manufacturing firms. International Journal of Engineering Business Management, 9: 1-9.

Anand, G., & Ward, P. T. (2004). Fit, flexibility and performance in manufacturing: coping with dynamic environments. Production and Operations Management, 13(4): 369-385.

Arslankaya S & Atay H. (2015). Maintenance Manage and Lean Manufacturing Practices in a Firm Which Produces Dairy Products. Procedia-Social and Behavioral Sciences, 207: 214-224.

Ballard, G., & Howell, G. (1998). Shielding production: essential step in production control. Journal of Construction Engineering and management, 124(1): 11-17.

Berlin, C., Neumann, W. P., Theberge, N., &Örtengren, R. (2014). Avenues of entry: how industrial engineers and ergonomists access and influence human factors and ergonomics issues. European Journal of Industrial Engineering, 8(3): 325-348.

Brown, S., & Cousins, P. D. (2004). Supply and operations: parallel paths and integrated strategies. British Journal of Management, 15(4): 303-320.

Chai, S. F., Luo, S. J., & Zhang, L. J. (2012). Study on simulation of the main shaft production line. In Advanced Materials Research, 472: 2076-2079.

Charan, P., Shankar, R., & Baisya, R. K. (2008). Analysis of interactions among the variables of supply chain performance measurement system implementation. Business Process Management Journal, 14(4): 512-529.

Chatterjee, P., & Stević, Ž. (2019). A two-phase fuzzy AHP-fuzzy TOPSIS model for supplier evaluation in manufacturing environment. Operational Research in Engineering Sciences: Theory and Applications, 2(1): 72-90.

Chinprateep, S., & Boondiskulchok, R. (2011). Heuristic for integrated purchasing and production planning. European Journal of Industrial Engineering, 5(1): 64-80.

Đalić, I., Ateljević, J., Stević, Ž., & Terzić, S. (2020). An integrated swot–fuzzy piprecia model for analysis of competitiveness in order to improve logistics performances. FactaUniversitatis, Series: Mechanical Engineering, 18(3): 439-451.

Dewangan, D. K., Agrawal, R., & Sharma, V. (2015). Enablers for competitiveness of Indian manufacturing sector: An ISM-fuzzy MICMAC analysis. Procedia-Social and Behavioral Sciences, 189: 416-432.

Diabat, A., & Govindan, K. (2011). An analysis of the drivers affecting the implementation of green supply chain management. Resources, conservation and recycling, 55(6): 659-667.

Dos Santos, Z. G., Vieira, L., & Balbinotti, G. (2015). Lean Manufacturing and ergonomic working conditions in the automotive industry. Procedia Manufacturing, 3: 5947-5954.

Dul, J., & Neumann, W. P. (2009). Ergonomics contributions to company strategies. Applied ergonomics, 40(4): 745-752.

Duraccio, V., Forcina, A., Silvestri, A., & Bona, G. D. (2014). Assessment of the Effectiveness of Maintenance-oriented Design. International Journal of Engineering Business Management, 6: 6-19.

Faisal, M. N. (2010). Sustainable supply chains: a study of interaction among the enablers. Business Process Management Journal, 16(3): 508–529.

Gliem, J. A., & Gliem, R. R. (2003). Calculating, interpreting, and reporting Cronbach's alpha reliability coefficient for Likert-type scales. Midwest Research-to-Practice Conference in Adult, Continuing, and Community Education.

Gorane, S. J., & Kant, R. (2013). Supply chain management: modeling the enablers using ISM and fuzzy MICMAC approach. International Journal of Logistics Systems and Management, 16(2): 147-166.

Greinacher, S., Moser, E., Hermann, H., & Lanza, G. (2015). Simulation based assessment of lean and green strategies in manufacturing systems. Procedia CIRP, 29: 86-91.

Guo, Z., Ngai, E., Yang, C., & Liang, X. (2015). An RFID-based intelligent decision support system architecture for production monitoring and scheduling in a distributed manufacturing environment. International journal of production economics, 159: 16-28.

Guillen, D., Gomez, D., Hernandez, I., Charris, D., Gonzalez, J., Leon, D., & Sanjuan, M. (2020). Integrated methodology for industrial facilities management and design based on FCA and lean manufacturing principles. Facilities, 38 (7/8): 523-538.

Hackman, J. R., & Wageman, R. (1995). Total quality management: Empirical, conceptual, and practical issues. Administrative science quarterly, 40(2): 309–342.

Harland, C. M. (1996). Supply chain management: relationships, chains and networks. British Journal of management, 7(s1): S63-S80.

Hartini, S., & Ciptomulyono, U. (2015). The relationship between lean and sustainable manufacturing on performance: literature review. Procedia Manufacturing, 4: 38-45.

Hayton, J. C., Allen, D. G., & Scarpello, V. (2004). Factor retention decisions in exploratory factor analysis: A tutorial on parallel analysis. Organizational research methods, 7(2): 191-205.

Heimerl, C., & Kolisch, R. (2010). Work assignment to and qualification of multi-skilled human resources under knowledge depreciation and company skill level targets. International Journal of Production Research, 48(13): 3759-3781.

Hugo, A., & Pistikopoulos, E. N. (2005). Environmentally conscious long-range planning and design of supply chain networks. Journal of Cleaner Production, 13(15): 1471-1491.

Jain, V., & Raj, T. (2015). Modeling and analysis of FMS flexibility factors by TISM and fuzzy MICMAC. International Journal of System Assurance Engineering and Management, 6(3): 350-371.

Jain, V., & Raj, T. (2016). Modeling and analysis of FMS performance variables by ISM, SEM and GTMA approach. International journal of production economics, 171: 84-96.

Jasti, N. V. K., & Kodali, R. (2016). Validity and reliability of lean enterprise frameworks in Indian manufacturing industry. Proceedings of the institution of mechanical engineers, Part B: Journal of engineering manufacture, 230(2): 354-363.

Kandasamy, W. V., Smarandache, F., & Ilanthenral, K. (2007). Elementary fuzzy matrix theory and fuzzy models for social scientists. Infinite Study, Published by Automaton, Los Angeles, USA.

Kannan, G., & Haq, A. N. (2007). Analysis of interactions of criteria and sub-criteria for the selection of supplier in the built-in-order supply chain environment. International Journal of Production Research, 45(17): 3831-3852.

Kannan, G., Pokharel, S., & Kumar, P. S. (2009). A hybrid approach using ISM and fuzzy TOPSIS for the selection of reverse logistics provider. Resources, conservation and recycling, 54(1): 28-36.

Kenné, J. P., Gharbi, A., & Beit, M. (2007). Age-dependent production planning and maintenance strategies in unreliable manufacturing systems with lost sale. European Journal of Operational Research, 178(2): 408-420.

Kushwaha, D. K., Panchal, D., & Sachdeva, A. (2020). Risk analysis of cutting system under intuitionistic fuzzy environment. Reports in Mechanical Engineering, 1(1): 162-173.

Kusrini, E., Subagyo, & Masruroh, N. A. (2014). Good criteria for supply chain performance measurement. International Journal of Engineering Business Management, 6(9): 1-19.

Le Dain, M. A., Calvi, R., & Cheriti, S. (2011). Measuring supplier performance in collaborative design: proposition of a framework. R&d Management, 41(1): 61-79.

Lee, A. H., Kang, H. Y., & Chang, C. C. (2011). An integrated interpretive structural modeling–fuzzy analytic network process–benefits, opportunities, costs and risks model for selecting technologies. International Journal of Information Technology & Decision Making, 10(05): 843-871.

Malhotra, M. K., & Grover, V. (1998). An assessment of survey research in POM: from constructs to theory. Journal of operations management, 16(4): 407-425.

Mandal, A., & Deshmukh, S. G. (1994). Vendor selection using interpretive structural modeling (ISM). International journal of operations & production management, 14(6): 52-59.

McKone, K. E., Schroeder, R. G., & Cua, K. O. (2001). The impact of total productive maintenance practices on manufacturing performance. Journal of operations management, 19(1): 39-58.

Mohammaddust, F., Rezapour, S., Farahani, R. Z., Mofidfar, M., & Hill, A. (2017). Developing lean and responsive supply chains: A robust model for alternative risk mitigation strategies in supply chain designs. International Journal of Production Economics, 183: 632-653.

Mudgal, R. K., Shankar, R., Talib, P., & Raj, T. (2010). Modeling the barriers of green supply chain practices: An Indian perspective. International Journal of Logistics Systems and Management, 7(1): 81-107.

Narasimhan, R., Swink, M., & Kim, S. W. (2006). Disentangling leanness and agility: an empirical investigation. Journal of operations management, 24(5): 440-457.

Nenni, M. E., Giustiniano, L., & Pirolo, L. (2014). Improvement of manufacturing operations through a lean management approach: a case study in the pharmaceutical industry. International Journal of Engineering Business Management, 6(1): 24.

Nordin, N., Deros, B. M., & AbdWahab, D. (2010). A survey on lean manufacturing implementation in Malaysian automotive industry. International Journal of Innovation, Management and Technology, 1(4): 374.

Onyeocha, C. E., Khoury, J., & Geraghty, J. (2015). Evaluation of multi-product lean manufacturing systems with setup and erratic demand. Computers & Industrial Engineering, 87: 465-480.

Pająk, M. (2020). Fuzzy model of the operational potential consumption process of a complex technical system. Facta Universitatis, Series: Mechanical Engineering, 18(3): 453-472.

Panchal, D., & Kumar, D. (2014). Reliability analysis of CHU system of coal fired thermal power plant using fuzzy λ-τ approach. Procedia Engineering, 97: 2323-2332.

Panchal, D., Jamwal, U., Srivastava, P., Kamboj, K., & Sharma, R. (2018). Fuzzy methodology application for failure analysis of transmission system. International Journal of Mathematics in Operational Research, 12(2): 220-237.

Prasad, M. M., Dhiyaneswari, J. M., Jamaan, J. R., Mythreyan, S., & Sutharsan, S. M. (2020). A framework for lean manufacturing implementation in Indian textile industry. Materials Today: Proceedings, 33: 2986-2995.

Palange, A., & Dhatrak, P. (2021). Lean manufacturing a vital tool to enhance productivity in manufacturing. Materials Today: Proceedings: doi.org/10.1016/j.matpr.2020.12.193

Panchal, D., Singh, A. K., Chatterjee, P., Zavadskas, E. K., & Keshavarz-Ghorabaee, M. (2019). A new fuzzy methodology-based structured framework for RAM and risk analysis. Applied Soft Computing, 74: 242-254.

Petrović, G., Mihajlović, J., Ćojbašić, Ž., Madić, M., & Marinković, D. (2019). Comparison of three fuzzy MCDM methods for solving the supplier selection problem. Facta Universitatis, Series: Mechanical Engineering, 17(3): 455-469.

Qureshi, M. N., Kumar, D., & Kumar, P. (2008). An integrated model to identify and classify the key criteria and their role in the assessment of 3PL services providers. Asia Pacific Journal of Marketing and Logistics, 20(2): 227-249.

Rahman, N. A. A., Sharif, S. M., & Esa, M. M. (2013). Lean manufacturing case study with Kanban system implementation. Procedia Economics and Finance, 7: 174-180.

Riezebos, J., Klingenberg, W., & Hicks, C. (2009). Lean production and information technology: connection or contradiction? Computers in industry, 60(4): 237-247.

Rohani, J. M., & Zahraee, S. M. (2015). Production line analysis via value stream mapping: a lean manufacturing process of color industry. Procedia Manufacturing, 2: 6-10.

Salleh, N. A. M., Kasolang, S., & Jaffar, A. (2012). Simulation of integrated total quality management (TQM) with lean manufacturing (LM) practices in forming process using Delmia Quest. Procedia Engineering, 41: 1702-1707.

Schiele, J. J., & McCue, C. P. (2010). A framework for the adoption of lean thinking within public procurement. International Journal of Procurement Management, 3(4): 379-396.

Seifert, D. (2003). Collaborative planning, forecasting, and replenishment: How to create a supply chain advantage. AMACOM Div American Mgmt Assn.

Shah, R., & Ward, P. T. (2003). Lean manufacturing: context, practice bundles, and performance. Journal of operations management, 21(2): 129-149.

Sharma, R., & Garg, S. (2010). Interpretive structural modeling of enablers for improving the performance of automobile service centre. International Journal of Services Operations and Informatics, 5(4): 351-372.

Shuaib, M., Khan, U., & Haleem, A. (2016). Modeling knowledge sharing factors and understanding its linkage to competitiveness. International Journal of Global Business and Competitiveness, 11(1): 23-36.

Singh, B., Garg, S. K., Sharma, S. K., & Grewal, C. (2010). Lean implementation and its benefits to production industry. International journal of lean six sigma, 1(2): 157-168.

Singh, R. K., Sharma, H. O., & Garg, S. K. (2010). Interpretive structural modeling for selection of best supply chain practices. International Journal of Business Performance and Supply Chain Modelling, 2(3): 237-257.

Soroush, H. M. (2015). Scheduling with job-dependent past-sequence-dependent setup times and job-dependent position-based learning effects on a single processor. European Journal of Industrial Engineering, 9(3): 277-307.

Srinivasaraghavan, J., & Allada, V. (2006). Application of mahalanobis distance as a lean assessment metric. The International Journal of Advanced Manufacturing Technology, 29(11-12): 1159-1168.

Stecke, K. E., & Kim, I. (1988). A study of FMS part type selection approaches for short-term production planning. International Journal of Flexible Manufacturing Systems, 1(1): 7-29.

Stojić, G., Sremac, S., & Vasiljković, I. (2018). A fuzzy model for determining the justifiability of investing in a road freight vehicle fleet. Operational Research in Engineering Sciences: Theory and Applications, 1(1): 62-75.

Susilawati, A., Tan, J., Bell, D., & Sarwar, M. (2015). Fuzzy logic based method to measure degree of lean activity in manufacturing industry. Journal of Manufacturing Systems, 34: 1-11.

Talib, F., Rahman, Z., & Qureshi, M. N. (2011). An interpretive structural modelling approach for modelling the practices of total quality management in service sector. International Journal of Modelling in Operations Management, 1(3): 223-250.

Thakkar, J., Deshmukh, S. G., Gupta, A. D., & Shankar, R. (2007). Development of a balanced scorecard, An integrated approach of interpretive structural modeling (ISM) and analytic network process (ANP). International Journal of Productivity and Performance Management, 56(1): 25-59.

Thierry, M., Salomon, M., Van Nunen, J., & Van Wassenhove, L. (1995). Strategic issues in product recovery management. California management review, 37(2): 114-136.

Tyagi, M., Kumar, P., & Kumar, D. (2015). Analysis of interactions among the drivers of green supply chain management. International Journal of Business Performance and Supply Chain Modelling, 7(1): 92-108.

Tyagi, M., Kumar, P., & Kumar, D. (2017). Modelling and analysis of barriers for supply chain performance measurement system. International Journal of Operational Research, 28(3): 392-414.

Tortorella, G. L., Narayanamurthy, G., & Thurer, M. (2021). Identifying pathways to a high-performing lean automation implementation: An empirical study in the manufacturing industry. International Journal of Production Economics, 231: 107918.

Venkatraman, N., & Ramanujam, V. (1987). Measurement of business economic performance: an examination of method convergence. Journal of management, 13(1): 109-122.

Wahab, A. N. A., Mukhtar, M., & Sulaiman, R. (2013). A conceptual model of lean manufacturing dimensions. Procedia Technology, 11: 1292-1298.

Wang, G., Wang, Y., & Zhao, T. (2008). Analysis of interactions among the barriers to energy saving in China. Energy Policy, 36(6): 1879-1889.

Wang, Z., Subramanian, N., Gunasekaran, A., Abdulrahman, M. D., & Liu, C. (2015). Composite sustainable manufacturing practice and performance framework: Chinese auto-parts suppliers′ perspective. International Journal of Production Economics, 170: 219-233.

Ward, P. T., & Duray, R. (2000). Manufacturing strategy in context: environment, competitive strategy and manufacturing strategy. Journal of operations management, 18(2): 123-138.

Warfield, J. N. (1974). Developing interconnection matrices in structural modeling. IEEE Transactions on Systems, Man, and Cybernetics, 1: 81-87.

Womack, J.P., Jones D.T. & Roos D. (1990). The machine that changed the World: The triumph of lean Production. New York: Rawson Macmillan.

Youssouf, A., Rachid, C., & Ion, V. (2014). Contribution to the optimization of strategy of maintenance by lean six sigma. Physics procedia, 55: 512-518.

Yusup, M. Z., Mahmood, W. H. W., & Salleh, M. R. (2015). Basic formation in streamlining lean practices in manufacturing operations-a review. International Journal of Advanced Operations Management, 7(4): 255-273.

Yadav, G., Luthra, S., Huisingh, D., Mangla, S. K., Narkhede, B. E., & Liu, Y. (2020). Development of a lean manufacturing framework to enhance its adoption within manufacturing companies in developing economies. Journal of Cleaner Production, 245: 118726.

Zavadskas, E. K., Turskis, Z., Stević, Ž., & Mardani, A. (2020). Modelling procedure for the selection of steel pipes supplier by applying fuzzy AHP method. Operational Research in Engineering Sciences: Theory and Applications, 3(2): 39-53.

Zhao, X., Flynn, B. B., & Roth, A. V. (2006). Decision sciences research in China: a critical review and research agenda—foundations and overview. Decision Sciences, 37(4): 451-496.

© 2021 by the authors. Submitted for possible open access publication under the terms and conditions of the Creative Commons Attribution (CC BY) license (http://creativecommons.org/licenses/by/4.0/).

Multimedia Systems
https://doi.org/10.1007/s00530-020-00747-5

SPECIAL ISSUE PAPER

Multimodal cyberbullying detection using capsule network with dynamic routing and deep convolutional neural network

Akshi Kumar[1] · **Nitin Sachdeva**[1]

Received: 13 April 2020 / Accepted: 28 December 2020
© The Author(s), under exclusive licence to Springer-Verlag GmbH, DE part of Springer Nature 2021

Abstract
Cyberbullying is the use of information technology networks by individuals' to humiliate, tease, embarrass, taunt, defame and disparage a target without any face-to-face contact. Social media is the 'virtual playground' used by bullies with the upsurge of social networking sites such as Facebook, Instagram, YouTube and Twitter. It is critical to implement models and systems for automatic detection and resolution of bullying content available online as the ramifications can lead to a societal epidemic. This paper presents a deep neural model for cyberbullying detection in three different modalities of social data, namely textual, visual and info-graphic (text embedded along with an image). The all-in-one architecture, CapsNet–ConvNet, consists of a capsule network (CapsNet) deep neural network with dynamic routing for predicting the textual bullying content and a convolution neural network (ConvNet) for predicting the visual bullying content. The info-graphic content is discretized by separating text from the image using Google Lens of Google Photos app. The perceptron-based decision-level late fusion strategy for multimodal learning is used to dynamically combine the predictions of discrete modalities and output the final category as bullying or non-bullying type. Experimental evaluation is done on a mix-modal dataset which contains 10,000 comments and posts scrapped from YouTube, Instagram and Twitter. The proposed model achieves a superlative performance with the AUC–ROC of 0.98.

Keywords Cyberbullying · Multimodal · Deep learning · Convolution neural network · Capsule network

1 Introduction

Bullying is an adverse societal issue which is rising at an alarming rate. In general, a bullying behavior can be categorized on the basis of type of behavior (verbal, social and physical), the environment (in-person and online), its mode (direct and indirect), the visibility (overt and covert), the damage caused (physical and psychological) and the context in terms of place of occurrence (home, workplace and school).[1] Cyberbullying is typically a social behavior bullying within the online setting done covertly by direct or indirect means causing short-term and long-term psychological harm. The increasing availability of reasonable data services and social media [1] presence has given some uninhibited effects where online users have discovered wrong and unlawful ways to harm and humiliate individuals through hateful comments on online platforms or apps. The persistence, audience size and damage speed make cyberbullying even more damaging than face-to-face bullying causing serious mental health and wellbeing issues to victims and making them feel totally overwhelmed. Cyberbullying can result in increased distress for the victims along with low self-esteem, increased anger, frustration, depression, social withdrawal and in some cases, developing violent or suicidal traits [2–4].

Technology allows the bullies to be anonymous, hard to trace and insulated from confrontation. To the targets of cyberbullying, it feels invasive and never-ending. With the amount of emotional and psychological distress caused to victims, it is urgently required to find appropriate provisions which can detect and prevent it. Effective prevention relies on the timely and satisfactory detection of potentially toxic posts [5]. The information overload on the chaotic and complex social media portals necessitates advanced automatic

✉ Akshi Kumar
akshikumar@dce.ac.in

Nitin Sachdeva
nits.usit@gmail.com

[1] Department of Computer Science and Engineering, Delhi Technological University, Delhi, India

[1] https://bullyingnoway.gov.au/WhatIsBullying/Pages/Types-of-bullying.aspx.

Published online: 02 February 2021

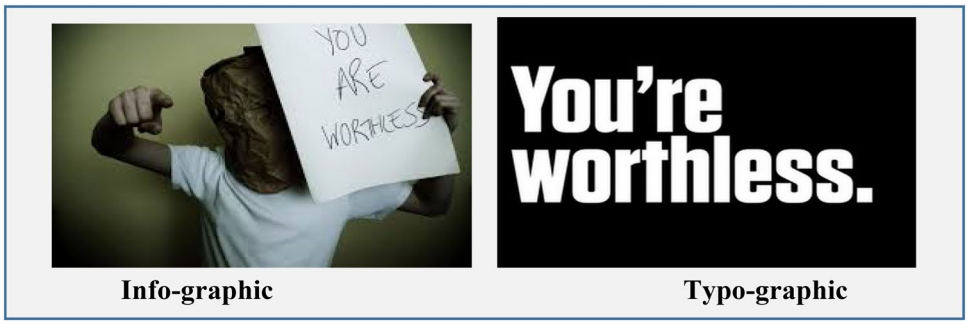

Fig. 1 Types of visual content

systems to identify potential risks pro-actively. Researchers worldwide have been trying to develop new ways to detect cyberbullying, manage it and reduce its prevalence on social media. Advanced analytical methods and computational models for efficient processing, analysis and modeling for detecting such bitter, taunting, abusive or negative content in images, memes or text messages are imperative. More recently, as memes, online videos and other image-based, inter-textual content has become customary in social feeds; typo-graphic and info-graphic visual content (Fig. 1) has become a considerable element of social data [6, 7].

Cyberbullying through varied content modalities is very common. Social media specificity, topic dependence and variety in hand-crafted features currently define the bottlenecks in detecting online bullying posts [3]. Deep learning methods are proving useful and obtaining state-of-the-art results for various natural language tasks with end-to-end training and representation learning capabilities [8–10]. Pertinent studies report the use of deep learning models like CNN, RNN and semantic image features for bullying content detection by analyzing textual, image-based and user features [3, 11]. But most of the research on online cyber-aggression, harassment detection and toxicity has been limited to text-based analytics. Few related studies have also re-counted analysis of images to determine bullying content but the domain of visual text which combines both text and image has been least explored in the literature. The combination can be observed in two variants: typo-graphic (artistic way of text representation) or info-graphic (text embedded along with an image). This paper presents a deep neural model for bullying content prediction, where the content, c ε, {text, image, info-graphic}. The primary contribution of the work is:

- The all-in-one hybrid deep architecture, CapsNet–ConvNet, consists of CapsNet with dynamic routing [12, 13] for predicting the textual bullying content and ConvNet [14] for predicting the visual bullying content.
- The info-graphic content is discretized by separating text from the image using Google Lens of Google Photos App.[2]
- The processing of textual and visual components is carried out using the hybrid architecture and late fusion decision layer is then used to output the final prediction.
- The performance of CapsNet–ConvNet is validated on 10,000 comments and posts (text, image, and info-graphic) prepared using three social media sites YouTube, Instagram and Twitter. The results of textual processing module are compared against state-of-the-art *toxic comment classification challenge* dataset[3] from Kaggle competition, whereas the results of the visual processing module are compared with baseline machine learning classifiers.

This unifying model thus considers modalities of content and processes each modality type using a deep neural learning technique for an efficient decision support for cyberbullying detection. The paper organization is as follows: Sect. 2 discusses the related work followed by the description of the proposed CapsNet–ConvNet model for cyberbullying detection in multimodal online content in Sect. 3. Section 4 presents the results and finally, the conclusion is given in Sect. 5.

2 Related work

Cyberspace is 'Virtual Society' where we can get huge information and also share information [15]. Most importantly we express ourselves—our understanding, our opinions and our views. Given the amount of increasing users and reach of cyberspace, cyberbullying is a definitely serious social concern. The recent literature accounts the use of machine learning methods for classifying hate speech, aggression, comment

[2] https://photos.google.com/.

[3] https://www.kaggle.com/c/jigsaw-toxic-comment-classification-challenge.

toxicity and bullying content on social forums. Dinakar et al. [16] constructed a common sense knowledge base that analyzed knowledge about bullying situations and the messages on Formspring website. Hinduja et al. [17] explored the relationship between cyberbullying and suicide among adolescents. The characteristic profile of wrongdoers and victims and conceivable strategies for its preventions was introduced in [18]. Till now, the majority of the work is devoted to text analysis [19–31].

The use of deep learning models has also been reported [11]. Agrawal et al. [32] experimented with four deep neural models for cyberbullying detection which included CNN, LSTM, BLSTM and BLSTM with attention on multiple social networks such as Twitter, Formspring and Wikipedia. Huang et al. [33] concatenated social network features with textual features for improved performance of cyberbullying detection. Authors analyzed features such as number of friends, network embeddedness and relationship centrality with the textual features and observed significant improvement in performance. Some rule-based classifications for the identification of bullies have also been done in [23] using Formspring data set. A new sentence-level filtering model was established by Xu et al. [34] which semantically eliminates bullying words in texts by utilizing grammatical relations among words on the YouTube dataset. Works have been done where pictures are utilized for the discovery of cyberbullying utilizing deep learning models like CNN, RNN or where semantic image features are utilized for identifying bullying [35–38].

The pertinent literature reports automated models of mono-modal (primarily text only) cyberbullying detection in social media. Few recent studies also report multimodal cyberbullying detection in online platforms. A framework was proposed by Kansara et al. [39] with bag-of-visual-word (BoVW) model, local binary pattern (LBP) and SVM classification for image analysis and bag-of-word (BoW) model with Naïve Bayesian classification for text analysis. Singh et al. [40] used some visual features along with textual features to improve the accuracy results. Yang et al. [41] classified the posts with images using deep multimodal fusion techniques, including simple concatenation, bilinear transformation, gated summation and attention mechanism. The work in this paper aims to build a three-in-one modality model based on deep learning which not only predicts cyberbullying in textual or visual content but also mix-modal infographic content. The details of the proposed CapsNet–ConvNet model are given next.

3 The proposed CapsNet–ConvNet model

The proposed deep neural model comprehends the complexities of natural language and deals with different modalities of data in online social media content where the representations of data in different forms, such as text and image, are learned as real-valued vectors. In addition to text, we examine the image as well as utilize info-graphic property of the image (information which is the content/text embedded on that picture) to predict bullying content. The proposed CapsNet–ConvNet model consists of four modules, namely modality discretization module, textual processing module, visual processing module and prediction module (Fig. 2).

The details of each module are as follows:

3.1 Modality discretization module

Depending on the input modality that is text only or image only, the content is forwarded to the respective processing modules. If the input is an info-graphic post/comment, which is the image with text embedded on it, the CapsNet–ConvNet model utilizes a Google Photos app to extract text from an image. This visual analysis tool separates the text from the image and sent to the respective textual processing and visual processing modules for analysis. The Google Lens feature has the ability to recognize texts in the images recorded utilizing the optical character recognition (OCR). The Google Cloud's Vision API offers powerful pre-trained machine learning models which can detect and extract text from images. There are *two* annotation features that support OCR, namely TEXT_DETECTION that detects and extracts text from any image and DOCUMENT_TEXT_DETECTION which extracts text from an image, but the response is optimized for dense text and documents.

3.2 Textual processing module: CapsNet with dynamic routing

CapsNet belongs to the class of deep neural networks comprising of set of capsules [42]. These are further composed of groups of neurons arranged in a layer and do the actual internal computations in order to predict instantiation parameters of any feature, such as orientation and color at any given location. The pertinent literature reports the use of many routing techniques for text classification such as dynamic, attention-based, clustering and static, where dynamic routing reported major applicability. In this research, the workflow of CapsNet [4] involves the following steps:

- The embedding layer of a neural network converts an input from a sparse representation into a distributed or dense representation. In this research, we use the state-of-the-art pre-trained ELMo 5.5B word embeddings model [43] to generate the word vectors. We preferred ELMo over the conventional embedding models such as Word-2Vec or GloVe, as ELMo offers contextualized word

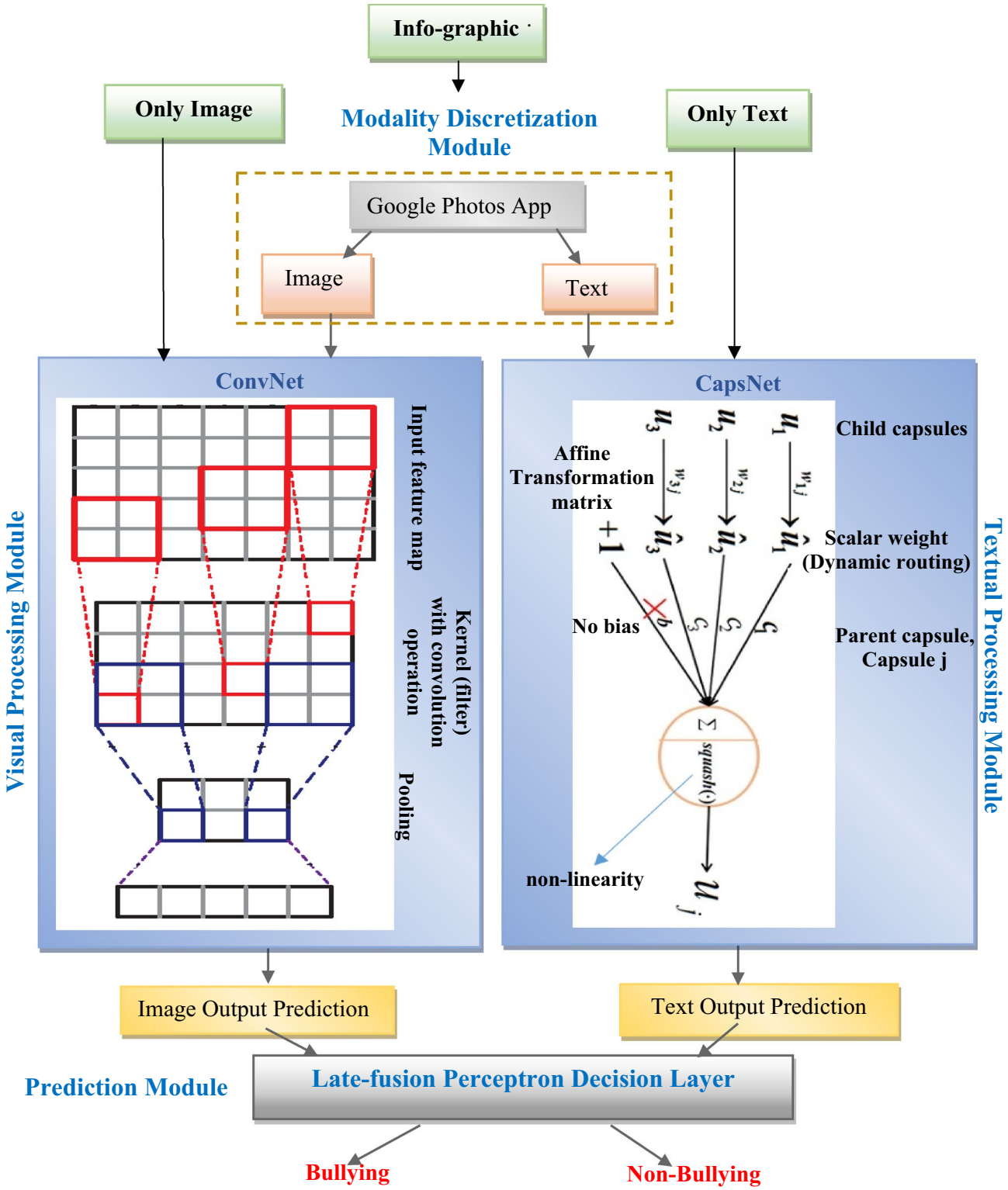

Fig. 2 The proposed CapsNet–ConvNet model

representations, which essentially means that the representation for each word depends on the entire context in which it is used. The same word can have two different vector representations based on different contexts. ELMo creates vectors on the go by passing words through the deep learning model rather than having a dictionary of

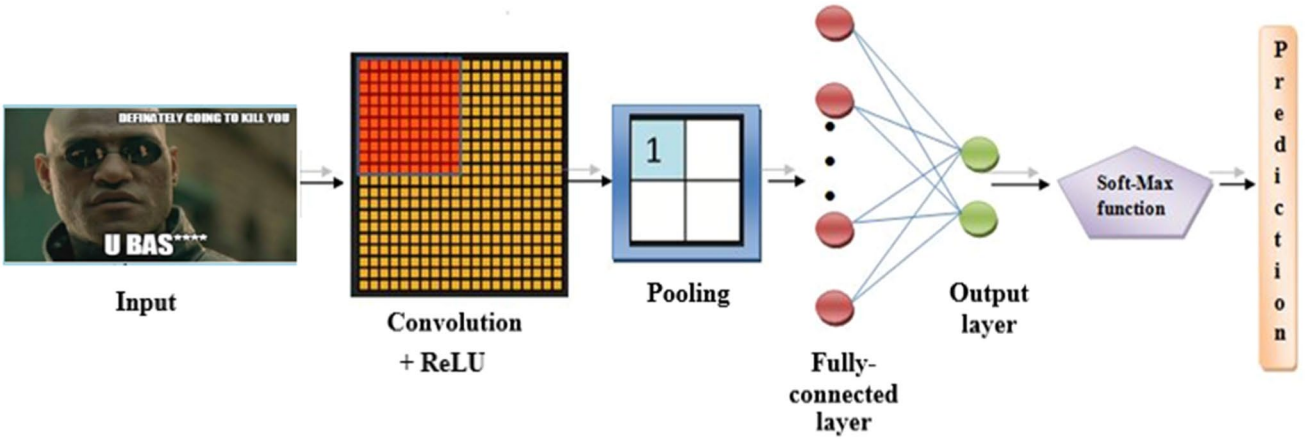

Fig. 3 Visual processing module

words and their corresponding vectors, as is the case with traditional word embedding models. Also, ELMo representations are purely character-based, which allows the network to form representations for words that are not seen in training. All this motivated us to use the ELMo 5.5B model for implementing the embedding layer.

- Encoding layer, thereafter, reshapes the word vector matrix into feature vectors of single dimension, where this encoding layer is executed as capsule network. This network comprises of convolution, primary caps and class caps layers. Here, the scalar outputs of each convolution layer are fed as input to primary caps layer that generates capsules.
- It must be noted that the output of a capsule is a vector that exhibits the object's existence, whereas the vector's orientation represents the object's properties. The vector is passed to all the possible parents in the network.
- These capsules work toward detecting the parts of the object under consideration in order to associate the random parts of the object to the whole.
- For accomplishing this, CapsNet uses non-linear dynamic routing algorithm in order to capture the capsules part-whole relationship dynamics. Thus, ensuring that the output of the capsule is sent to the possible and relevant parent.
- Lower-level capsule vectors are multiplied with weight matrices in order to encode spatial and other relationships between features of lower and higher level using Eq. (1)

$$u_{j|i} = W_{ij} u_i, \tag{1}$$

where 'i' is low-level capsule, 'j' is high-level capsule and W_{ij} is the translation matrix.

- Lower-level capsule knows which upper level capsule accommodates its results in an efficient way and therefore adjust it coupling coefficient. Thus, previous step output is multiplied with coupling coefficients using Eq. (2):

$$s_j = \sum_i c_{ij} u_{j|i}, \tag{2}$$

where c_{ij} is coupling coefficient and $u_{j|i}$ is output vector from Eq. (1).

- Post this, squashing is applied for normalizing the length of each capsule's output vector in the range of [0, 1] using Eq. (3):

$$v_j = \frac{\left|\left|s_j\right|\right|^2}{1 + \left|\left|s_j\right|\right|^2} \frac{s_j}{\left|\left|s_j\right|\right|}. \tag{3}$$

3.3 Visual processing module: *ConvNet*

To analyze visual bullying content, the model uses a ConvNet [14]. A ConvNet is a deep neural architecture which works using multiple copies of the same neuron in different places. It has the power of self-tuning and learning skills by generalizing from the training data. The visual processing is shown in Fig. 3.

A ConvNet convolves learned features with input data and uses 2D convolutional layers. It usually consists of several convolutional networks with filters (kernels) in combination with non-linear and pooling layers [44]. The image is passed through convolution layers such that the output of the primary layer becomes the input for the subsequent layer.

Convolution is a linear operation but images are non-linear. Therefore, non-linearity is added post every convolution operation using an activation function such as ReLU, Leaky_ReLU, tanh or sigmoid. Each non-linear layer is followed by a pooling layer which reduces the spatial size of the image and performs a downsampling operation. Pooling

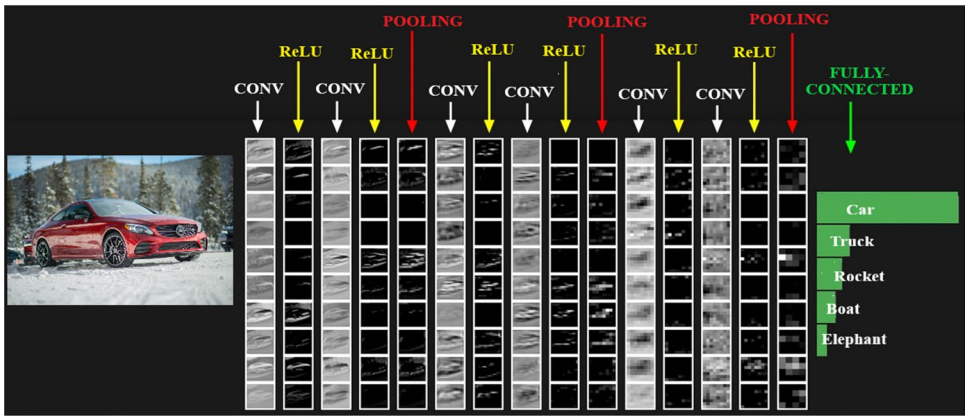

Fig. 4 Working of a typical ConvNet

operation thus helps to progressively reduce the size of the input representation and control overfitting too. We can either use max, average or sum pooling. A fully connected layer is then attached to this series of convolution, non-linear and pooling layers which outputs the information from the convolutional networks. The working of a typical ConvNet is shown in Fig. 4.

In this work, the visual processing module has three convolutional layers followed by three max-pooling layers to extract the features of images, a flatten layer which takes the output from the previous max-pooling layer and convert it to a 1D array such that it can be feed into the dense layers and finally, two dense layers. The dense layer is a standard layer of neurons where the actual learning is done by adjusting the weights. Here we have two such dense layers and since this is a binary classification only one neuron there is in the output layer. The details of the layers are as follows:

- Convolution layer: The convolution layer transforms the input image to extract the features. This is done by convolving the image with a filter (kernel) which is specialized to extract certain features. Mathematically, the convolution operation (a.k.a. scalar product) is the summation of the element-wise product of two matrices (filter-sized patch of the input and filter) which results in a single value.
- Activation layer and pooling layer: The activation (ReLU) layer is intended to introduce non-linearity to the system and produces a rectified feature map which is inserted into the pooling layer where a max-pooling operation is applied to each convolution $c_{\max} = \max(c)$. The max-pooling operation extracts the 'k' most important features for each convolution. The output of the final convolution layer, that is, the pooled feature map is a representation of the original image.
- Fully connected layer: A fully connected neural network is a feed-forward network that will have the feature vector of n dimension obtained after concatenating every c_i obtained by the application of n filters. Now, we train the network using back-propagation algorithm. Gradients are back propagated and when we reach at the convergence, we finally stop the algorithm. A softmax function is used to classify the post as bullying (+1) or non-bullying (− 1).

3.4 Prediction module

The final prediction is done using an additional decision layer implementing multimodal classification fusion. Typically, there are two strategies to multimodal fusion: model-free and model-level. Model-free fusion can be further classified into early fusion (feature-level) and late fusion (decision-level). In early fusion, the different types of input features are firstly concatenated and then fed into a classifier, whereas in late fusion, the predictions of different classifiers trained for distinct input types are combined to provide us with the final output. Model-level fusion combines the advantages of both of these strategies by concatenating high-level feature representations from different classifiers. In this work, late fusion strategy for multimodal learning is used, that is, the bullying content prediction of mono-modalities (text and image separately) is done by the respective classification models. Late fusion allows the use of different models on different modalities, thus allowing more flexibility. It is easier to handle a missing modality as the predictions are made separately. The class probabilities are thus fused together to join information from the two modalities to perform a final prediction task. We use a multi-layer perceptron (MLP) neural network with sigmoid activation function to implement the decision-level fusion.

MLP can be thought of as a linear classifier, which means that it can segregate two different entities or classes from each other using a straight line. The input to a perceptron is usually a feature vector x, which is multiplied to a weight w and then finally added to a bias b as given in Eq. (4)

$$y = w \times x + b. \tag{4}$$

A perceptron is a shallow neural network and thus incapable of solving classification problems in which the number

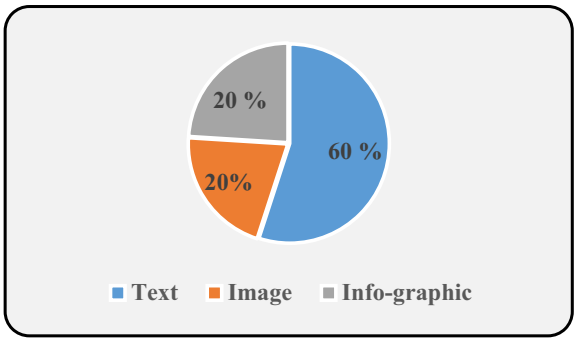

Fig. 5 Modality distribution in dataset

Table 1 Categorization of data used for training

Type of modality	Number of instances	
	Bullying	Non-bullying
Image only	1260	740
Text only	3000	3000
Info-graphic	1440	560

of classes is more than two. It takes in a number of inputs and generates an output by forging a linear coalition by utilizing the weights of its inputs. It also, sometimes, passes the output through a non-linear activation function. This can be shown using Eq. (5):

$$y = \varphi\left(\sum_{i=1}^{n} w_i x_i + b\right), \tag{5}$$

where, w stands for the weight vector, x stands for the input vector, b stands for the bias, and phi represents the non-linear activation function.

4 Results and discussion

The dataset prepared for experiments contains 10,000 comments and posts (text, image and info-graphic) prepared using three social media sites YouTube, Instagram and Twitter. The modalities within the dataset were 60% textual, 20% visual and 20% info-graphic (Fig. 5).

Table 1 below shows the actual distribution of data in numbers.

We performed tenfold cross-validation and calculated the AUC–ROC curve. We used the scikit-learn library and Keras deep learning library with Theano backend. Since two different models were used based on the input-type, the tuning of each model's respective hyperparameters was performed. The choice of model hyperparameters considered is given in Table 2.

Table 2 Model hyperparameters

	Hyperparameter	Value
Word embeddings	ELMo 5.5B	
CapsNet	No. of convolution layers	1
	Batch size	64
	No. of filters	32
	Activation	ReLU
	Learning rate	0.001
	Kernel_size	3
	No. of capsule in PrimaryCaps layer	8
	No. of nodes in PrimaryCaps layer	64
	Routing time	2
	Dimension of each capsule	8
	Length of PrimaryCaps	2
	Length of Digi Caps	2
	Optimizer	Adam
ConvNet	Number of filters	150 of each size
	Filter size	2, 3, 4 and 5
	Drop out	0.5
	Epochs	5
	Non-linearity function	ReLU

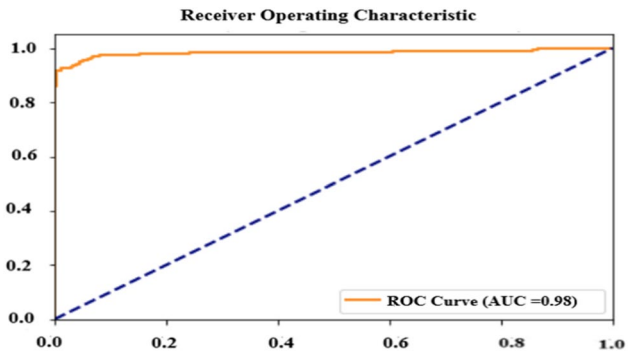

Fig. 6 Performance of CapsNet–ConvNet model

The proposed model achieves a performance of 0.98 (Fig. 6).

Confusion matrices for all type of modalities are shown in Fig. 7.

As we proposed training a CapsNet model for textual content, it was imperative to evaluate the robustness of this module. In our previous work [4], we proposed a multi-input integrative learning model based on deep neural networks (MIIL-DNN) which combined information from three sub-networks to detect and classify bully content in real-time code-mix data. It took three inputs, namely English language features, Hindi language features (transliterated Hindi converted to Hindi language) and typo-graphic

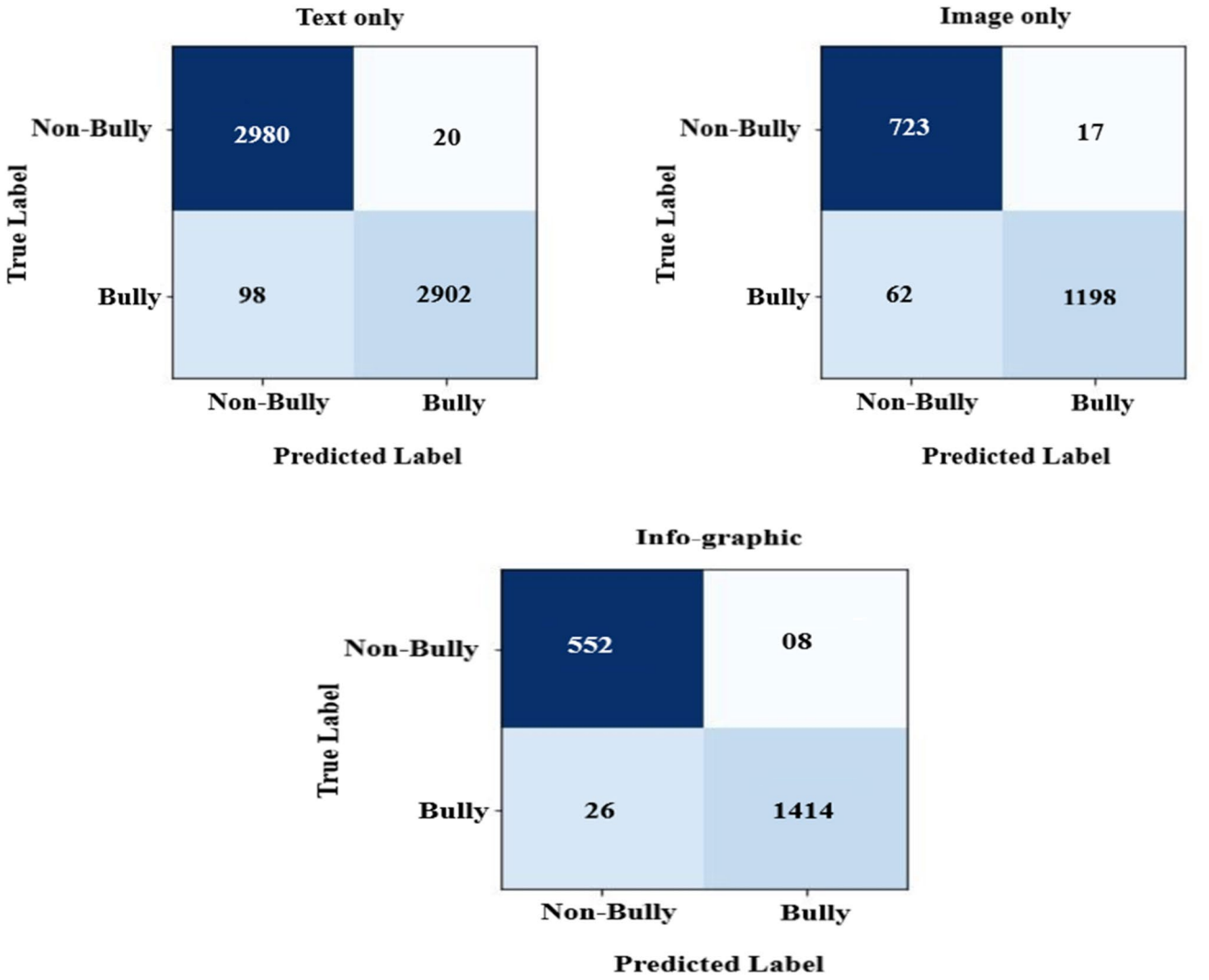

Fig. 7 Confusion matrices for all modalities

features, which are learned separately using sub-networks (Capsule network for English, Bi-LSTM for Hindi and MLP for typo-graphic). The CapsNet sub-network for English was trained using GloVe pre-trained embeddings and the results were compared with the existing state-of-the-art *Toxic Comment Classification Challenge* dataset[4] from a Kaggle competition. The dataset contained 159,571 Wikipedia manually labeled comments categorized as: *toxic; severe toxic; obscene; threat; insult*; and *identity hate*. All these categories accounted for cyberbullying, whereas any comment with value = 0 in all fields indicated non-cyberbullying, i.e., non-toxic comments. As per http://www.kaggle.com, the first place solution reported a performance of 0.9885 using a Bi-GRU with the pseudo-labeling technique. The performance of the best single model of the competition was around 0.9869 and a single layer RNN-Capsule Network with GRU cell performed at 0.9857. In 2019, Srivastava et al. [45] used capsule network with focal loss and achieved an ROC–AUC of 0.9846 on the Kaggle toxic comment dataset. The performance of the proposed CapsNet was comparable at 0.9841. In this work, as we used ELMo, the results further improved and achieved a ROC–AUC of 0.9924.

Three machine learning classifiers, namely K-nearest neighbor (K-NN) and Naïve Bayesian (NB) and support vector machine (SVM), were compared with deep neural ConvNet image classifier. The bag-of-visual words (BoVW) approach [46] was used to extract the features and train the three machine learning classifiers. It was observed that the ConvNet outperformed the other classifiers. Comparative analysis of the image classification algorithms is given in Table 3.

[4] https://www.kaggle.com/c/jigsaw-toxic-comment-classification-challenge.

Table 3 Comparative analysis of different classifiers used for image modality

Classifier	Precision	Recall	Accuracy
K-NN	71.3	71.8	65.8
NB	67	69.2	64.4
SVM	76.86	79.17	73.2
ConvNet	**98.6**	**95.08**	**97.05**

Bold indicates that the CNN model (deep learning) obtained highest accuracy for image modalities in comparison to other machine learning techniques

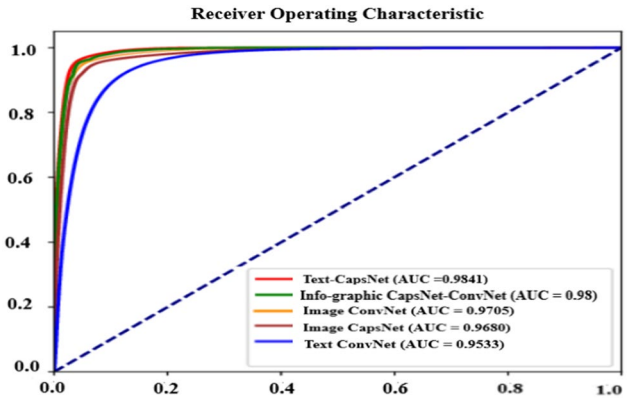

Fig. 8 Performance results of model reversal

We also implemented reversed the hybrid by using a ConvNet for the textual processing module and the CapsNet for the visual processing module and it was observed that the original set-up achieved superlative results. The ROC–AUC curve for this variation is shown in Fig. 8.

5 Conclusion

Social media and the internet have unlocked innovative modes to communication, empowerment and oppression. Meaningful engagement has transformed into a detrimental avenue where individuals are often vulnerable targets to online ridiculing. Cyberbullying is a rising predicament linked to the use of social media due to the increased consequential mental health risks associated. Predictive models to detect this cyberbullying in online content are imperative and this research proffered a prototype model for the same. The uniqueness of the proposed hybrid deep learning model, CapsNet–ConvNet is that it deals with different modalities of content, namely textual, visual (image) and info-graphic (text with image). The results have been evaluated and compared with various baselines and it is observed the proposed model gives superlative performance accuracy.

The limitations of the model arise from the characteristics of real-time social data which are inherently 'high-dimensional,' 'imbalanced or skewed,' 'heterogeneous' and 'cross-lingual.' The growing use of micro-text (wordplay, creative spellings and slangs) and emblematic markers (punctuations and emoticons) further increase the complexity of real-time cyberbullying detection. Other content modalities such as audio, GIFs and videos are open to research too. Also recently, the transformer-based methods, namely BERT, ELECTRA, XLNet, RoBERTa and DistilBERT have been used within the NLP landscape, outperforming the state-of-the-art on several tasks, and therefore, their use for cyberbullying detection can be probed.

References

1. Kumar, A., Sharma, H.: PROD: A potential rumour origin detection model using supervised machine learning. In: International Conference on Intelligent Computing and Smart Communication 2019, Springer, pp. 1269–1276 (2020)
2. Campbell, M.A.: Cyber bullying: an old problem in a new guise? J. Psychol. Couns. Sch. **15**(1), 68–76 (2005)
3. Kumar, A., Sachdeva, N.: Cyberbullying detection on social multimedia using soft computing techniques: a meta-analysis. Multimed. Tools Appl. **78**(17), 23973–24010 (2019)
4. Kumar, A., Sachdeva, N.: Multi-input integrative learning using deep neural networks and transfer learning for cyberbullying detection in real-time code-mix data. Multimed. Syst. (2020). https://doi.org/10.1007/s00530-020-00672-7
5. Sangwan, S.R., Bhatia, M.P.S.: D-BullyRumbler: a safety rumble strip to resolve online denigration bullying using a hybrid filter-wrapper approach. Multimed. Syst. (2020). https://doi.org/10.1007/s00530-020-00661-w
6. Kumar, A., Srinivasan, K., Cheng, W.H., Zomaya, A.Y.: Hybrid context enriched deep learning model for fine-grained sentiment analysis in textual and visual semiotic modality social data. Inf. Process. Manag. **57**(1), 102141 (2020)
7. Kumar, A.: Using cognition to resolve duplicacy issues in socially connected healthcare for smart cities. Comput. Commun. **152**(2020), 272–281 (2020). https://doi.org/10.1016/j.comcom.2020.01.041
8. Kumar, A., Jaiswal, A.: A deep swarm-optimized model for leveraging industrial data analytics in cognitive manufacturing. IEEE Trans. Ind. Inform. (2020)
9. Nimmi, K., Menon, V.G., Janet, B., Kumar, A.: Deep Learning for Next-Generation Inventive Wireless Networks: Issues, Challenges, and Future Directions. Handbook of Research on Emerging Trends and Applications of Machine Learning, pp. 183–199. IGI Global, Philadelphia (2020)
10. Young, T., Hazarika, D., Poria, S., Cambria, E.: Recent trends in deep learning based natural language processing. IEEE Comput. Intell. Mag. **13**(3), 55–75 (2017)
11. Dadvar, M., & Eckert, K.: Cyberbullying detection in social networks using deep learning based models; a reproducibility study. arXiv preprint arXiv:1812.08046 (2018)
12. Zhao, W., Ye, J., Yang, M., Lei, Z., Zhang, S., Zhao, Z.: Investigating capsule networks with dynamic routing for text classification. arXiv preprint arXiv:1804.00538 (2018)

13. Kim, J., Jang, S., Park, E., Choi, S.: Text classification using capsules. Neurocomputing **376**, 214–221 (2019)
14. Rawat, W., Wang, Z.: Deep convolutional neural networks for image classification: a comprehensive review. Neural Comput. **29**(9), 2352–2449 (2017)
15. Tripathi, A.K., Sharma, K., Bala, M., Kumar, A., Menon, V.G., Bashir, A.K.: A parallel military dog based algorithm for clustering big data in cognitive industrial internet of things. IEEE Trans. Ind. Inform. (2020)
16. Dinakar, K., Jones, B., Havasi, C., Lieberman, H., Picard, R.: Common sense reasoning for detection, prevention, and mitigation of cyberbullying. ACM Trans. Interact. Intell. Syst. (TiiS) **2**(3), 18 (2012)
17. Hinduja, S., Patchin, J.W.: Bullying, cyberbullying, and suicide. Arch. Suicide Res. **14**(3), 206–221 (2010)
18. Kokkinos, C.M., Antoniadou, N., Markos, A.: Cyber-bullying: an investigation of the psychological profile of university student participants. J. Appl. Dev. Psychol. **35**(3), 204–214 (2014)
19. Dadvar, M., Jong, F.D., Ordelman, R., Trieschnigg, D.: Improved cyberbullying detection using gender information. In: Proceedings of the Twelfth Dutch-Belgian Information Retrieval Workshop (DIR 2012). University of Ghent, (2012)
20. Dadvar, M., Trieschnigg, D., Ordelman, R., de Jong, F.: Improving cyberbullying detection with user context. In: European Conference on Information Retrieval, pp. 693–696. Springer, Berlin (2013)
21. Nahar, V., Unankard, S., Li, X., Pang, C.: Sentiment analysis for effective detection of cyber bullying. In: Asia-Pacific Web Conference, pp. 767–774. Springer, Berlin (2012)
22. Nahar, V., Al-Maskari, S., Li, X., Pang, C.: Semi-supervised learning for cyberbullying detection in social networks. In: Australasian Database Conference, pp. 160–171. Springer, Cham (2014)
23. Reynolds, K., Kontostathis, A., Edwards, L.: Using machine learning to detect cyberbullying. In: 2011 10th International Conference on Machine learning and applications and workshops, vol. 2, pp. 241–244. IEEE. (2011)
24. Michal, P., Pawel, D., Tatsuaki, M., Fumito, M., Rafal, R., Kenji, A., Yoshio, M.: In the service of online order: tackling cyberbullying with machine learning and affect analysis. Int. J. Comput. Linguist. Res. **1**(3), 135–154 (2010)
25. Yin, D., Xue, Z., Hong, L., Davison, B.D., Kontostathis, A., Edwards, L.: Detection of harassment on web 2.0. Proc. Content Anal. WEB **2**, 1–7 (2009)
26. Van Hee, C., Lefever, E., Verhoeven, B., Mennes, J., Desmet, B., De Pauw, G., Daelemans, W., Hoste, V.: Automatic detection and prevention of cyberbullying. In: International Conference on Human and Social Analytics (HUSO 2015), pp. 13–18. IARIA (2015)
27. Van Hee, C., Lefever, E., Verhoeven, B., Mennes, J., Desmet, B., De Pauw, G., Daelemans, W., Hoste, V.: Detection and fine-grained classification of cyberbullying events. In: Proceedings of the International Conference Recent Advances in Natural Language Processing, pp. 672–680. (2015)
28. Al-garadi, M.A., Varathan, K.D., Ravana, S.D.: Cybercrime detection in online communications: the experimental case of cyberbullying detection in the Twitter network. Comput. Hum. Behav. **63**, 433–443 (2016)
29. Xu, J.M., Jun, K.S., Zhu, X., Bellmore, A.: Learning from bullying traces in social media. In: Proceedings of the 2012 Conference of the North American Chapter of the Association for Computational Linguistics: Human Language Technologies, pp. 656–666. Association for Computational Linguistics (2012)
30. Zhao, R., Zhou, A., Mao, K.: Automatic detection of cyberbullying on social networks based on bullying features. In: Proceedings of the 17th International Conference on Distributed Computing and Networking, p. 43. ACM. (2016)
31. Raisi, E., Huang, B.: Cyberbullying detection with weakly supervised machine learning. In: Proceedings of the 2017 IEEE/ACM International Conference on Advances in Social Networks Analysis and Mining 2017, pp. 409–416. ACM. (2017)
32. Agrawal, S., Awekar, A.: Deep learning for detecting cyberbullying across multiple social media platforms. In: European Conference on Information Retrieval, pp. 141–153. Springer, Cham (2018)
33. Huang, Q., Singh, V.K., Atrey, P.K.: Cyber bullying detection using social and textual analysis. In: Proceedings of the 3rd International Workshop on Socially-Aware Multimedia, pp. 3–6. (2014)
34. Xu, Z., Zhu, S.: Filtering offensive language in online communities using grammatical relations. In: Proceedings of the Seventh Annual Collaboration, Electronic Messaging, Anti-Abuse and Spam Conference, pp. 1–10. (2010)
35. Cheng, L., Guo, R., Silva, Y., Hall, D., Liu, H.: Hierarchical attention networks for cyberbullying detection on the Instagram social network. In: Proceedings of the 2019 SIAM International Conference on Data Mining, pp. 235–243. Society for Industrial and Applied Mathematics. (2019)
36. Al-Hashedi, M., Soon, L.K., Goh, H.N.: Cyberbullying detection using deep learning and word embeddings: an empirical study. In: Proceedings of the 2019 2nd International Conference on Computational Intelligence and Intelligent Systems, pp. 17–21. (2019)
37. Founta, A.M., Chatzakou, D., Kourtellis, N., Blackburn, J., Vakali, A., Leontiadis, I.: A unified deep learning architecture for abuse detection. In: Proceedings of the 10th ACM Conference on Web Science, pp. 105–114. (2019)
38. Mahlangu, T., Tu, C.: Deep learning cyberbullying detection using stacked embbedings approach. In: 2019 6th International Conference on Soft Computing and Machine Intelligence (ISCMI), pp. 45–49. IEEE. (2019)
39. Kansara, K.B., Shekokar, N.M.: A framework for cyberbullying detection in social network. Int. J. Curr. Eng. Technol. **5**(1), 494–498 (2015)
40. Singh, V.K., Ghosh, S., Jose, C.: Toward multimodal cyberbullying detection. In: Proceedings of the 2017 CHI Conference Extended Abstracts on Human Factors in Computing Systems, pp. 2090–2099. (2017)
41. Yang, F., Peng, X., Ghosh, G., Shilon, R., Ma, H., Moore, E., Predovic, G.: Exploring deep multimodal fusion of text and photo for hate speech classification. In: Proceedings of the Third Workshop on Abusive Language Online, pp. 11–18. (2019)
42. Sabour, S., Frosst, N., Hinton, G.E.: Dynamic routing between capsules. In: Advances in neural information processing systems, pp. 3856–3866. (2017)
43. Peters, M.E., Neumann, M., Iyyer, M., Gardner, M., Clark, C., Lee, K., Zettlemoyer, L.: Deep contextualized word representations. arXiv preprint arXiv:1802.05365. (2018)
44. Caldeira, M., Martins, P., Costa, R.L.C., Furtado, P.: Image Classification Benchmark (ICB). Expert Syst. Appl. **142**, 112998 (2020)
45. Srivastava, S., Khurana, P., Tewari, V.: Identifying aggression and toxicity in comments using capsule network. In: Proceedings of the First Workshop on Trolling, Aggression and Cyberbullying (TRAC-2018), pp. 98–105. (2018)
46. Alkhawlani, M., Elmogy, M., Elbakry, H.: Content-based image retrieval using local features descriptors and bag-of-visual words. Int. J. Adv. Comput. Sci. Appl. **6**(9), 212–219 (2015)

Publisher's Note Springer Nature remains neutral with regard to jurisdictional claims in published maps and institutional affiliations.

Materials Today: Proceedings xxx (xxxx) xxx

Contents lists available at ScienceDirect

Materials Today: Proceedings

journal homepage: www.elsevier.com/locate/matpr

Numerical study for dynamic fracture toughness of AA7075-T651 under dynamic loading

Sanjay Kumar [a], Anoop Kumar Pandouria [b], Purnashis Chakraborty [b], Vikrant Tiwari [b]

[a] Delhi Technological University, Delhi 110042, India
[b] Indian Institute of Technology Delhi, Hauz Khas, New Delhi 110016, India

ARTICLE INFO

Article history:
Available online xxxx

Keywords:
AA7075-T651
ABAQUS
Load point displacement
Crack mouth opening displacement
Modified Hopkinson pressure bar
Digital image correlation

ABSTRACT

Finite element simulations for three-point bend specimens of aluminium AA7075-T651 were performed by using ABAQUS software. The simulation parameters, load point displacement and crack mouth opening displacement obtained, were used to evaluate the dynamic stress intensity factor. Three-point bend specimens impacted with an incident bar at three different striker velocities on modified Hopkinson pressure bar (MHPB) used to evaluate load point displacements and crack mouth opening displacements during the experiment were simulated. Load point displacements and crack mouth opening displacements were obtained using finite element simulation with maintaining same experimental conditions and it was found a good agreement between experimental and numerical results. These results were used to evaluate dynamic initiation fracture toughness at different loading rates using dynamic stress intensity factor and the time of initiation of fracture obtained with an experimental method using MHPB conjugation with digital image correlation (DIC) method.

© 2021 Published by Elsevier Ltd Second International Conference on Aspects of Materials Science and Engineering (ICAMSE 2021).

1. Introduction

Due to light weight alloy of aluminium, designer prefer it for many structural applications including transport industry [1]. It was found by Miller et al. [2] that the use of aluminium alloys had been increased up to 85% between 1985 and 2000 for manufacturing of automotive body. Mechanical properties used for design can be obtained with experiments but it is costly and time consuming, so researchers are using numerical technique to obtain the mechanical properties. This study presents the numerical simulation of aluminium alloy AA7075-T651 specimens for dynamic loading. The specimen was a three-point bend type and drawn according to the ASTM E399 standard. The finite element simulation had been carried out to evaluate the parameters used to assess the dynamic fracture toughness. These parameters can also be obtained using experimental and analytical methods, but each method has some limitations. The establishment of an experimental setup needs a lot of time and money; hence, it restricts the researcher's dependency on impact analysis experiments. On the other hand, analytical models used for impact problems implement some assumptions to simplify the problems. An analytical solution's accuracy depends on how it can be modeled to represent an actual practical problem [3]. In the present study, the three-point bend specimen, along with the incident bar, is simulated, and the obtained results are compared with experimental results. The commercial software ABAQUS of 6.12 version [4] is used during the finite element simulation.

1.1. Finite element method formulation

The finite element method (FEM) is used in computational mechanics to solve engineering problems such as impact, elasticity, plasticity, metal forming, fluid mechanics, etc. [5].

The FEM used effectively to obtain solutions for different engineering problems was developed a few decades ago. However, its results cannot be relied on, like any other numerical method, without assessing its reliability. During simulation with FEM any structural problem of the complex domain, which has an infinite degree of freedom, is considered a collection of subdomains with a finite number of degrees of freedom. The complex domain problem is discretized into several simple subdomains, called finite elements, having a finite number of degrees of freedom. The finite elements are connected at specific points called nodes. During meshing, the complex structure is discretized into several finite elements [6]. Subsequently, the shape of elements such as brick, triangular, or shell elements is used according to the analysis requirements. Using the material properties and geometry of elements the stiffness and mass matrix are derived which is used to describe the

E-mail address: sanjaykumar@dtu.ac.in (S. Kumar)

https://doi.org/10.1016/j.matpr.2021.01.374
2214-7853/© 2021 Published by Elsevier Ltd Second International Conference on Aspects of Materials Science and Engineering (ICAMSE 2021).

Please cite this article as: S. Kumar, A. Kumar Pandouria, P. Chakraborty et al., Numerical study for dynamic fracture toughness of AA7075-T651 under dynamic loading, Materials Today: Proceedings, https://doi.org/10.1016/j.matpr.2021.01.374

force–displacement relationship. After the stiffness matrix's derivation, the loading conditions such as pressure, force, and velocities are defined along with the boundary conditions at specified nodes. Finally, the stiffness matrix and applied loads are assembled in the form of equations following which, the boundary conditions are used. The equations are then converted in the form of a matrix for application in software code, and the set of equations are solved numerically for the unknown values. The stresses, strain, and other quantities of interest can be calculated based on the resulting nodal displacements. For a general linear and/or nonlinear static problem, the equilibrium equation for finite element analysis is expressed as [K][U] = [F].

The numerical simulation, based on finite element methods for impact problems, uses numerical inputs such as material models and failure models. The numerical formulations are solved by using different time integration techniques such as explicit and implicit techniques. All the steps discussed are summarized in a chart and presented in Fig. 1(a).Fig. 2.

1.2. Finite element codes

Two techniques which are used to determine the nodal displacements at different time intervals for a dynamic system are called implicit and explicit. Both are described separately in two separate sections, 1.2.1and 1.2.2.

1.2.1. Implicit code

The important points related to implicit code are given as follows.

- Two direct integration techniques, such as the Newmark-Beta method and Wilson –Theta methods, are used in implicit code.
- Implicit code solves equilibrium equations, which are in matrix form, at every time step. In this method, iteration at each step needs formulation as well as a solution of linear equations.
- The implicit finite element method may develop convergence problems whenever unexpected changes in contact conditions exist between two surfaces.
- A significant time increment is taken, and the equilibrium condition must be fulfilled when time steps end.
- Each time step requires several equilibrium iterations, and a set of linear equations is solved in each iteration.
- The implicit code is generally used for relatively slow problems where loads are applied slowly.

1.2.2. Explicit code

The salient features of the explicit code are outlined as follows.

- The explicit method uses direct time integration to solve the equilibrium at time t. This technique is conditionally stable since the iterative procedure is not implemented to reach equilibrium and is limited by natural time.
- The time increment used for this problem should be of small size so that the unbalanced force lies within tolerance.
- This code is used for deformation dependent contact problem, as the solution procedure is stable.
- Explicit code is generally preferred for impact and explosion problems.

2. Nonlinear problem

Three main types of nonlinearities encountered during the analysis of the impact problems are followings: -

2.1. Material nonlinearity

The stress and strain relation, which is called the constitutive equation, is nonlinear [7]. In this nonlinear problem, material behaviour is not elastic after the elastic limit. The stress–strain curve of the material becomes nonlinear.

2.2. Geometric Nonlinearity

The equations that relate strain and displacements comprise higher-order terms, leading to nonlinear problems. This nonlinearity during analysis is produced due to large strain or large displacement. The geometric nonlinearity has either a stiffening effect or a softening effect on the structure's overall load–displacement response.

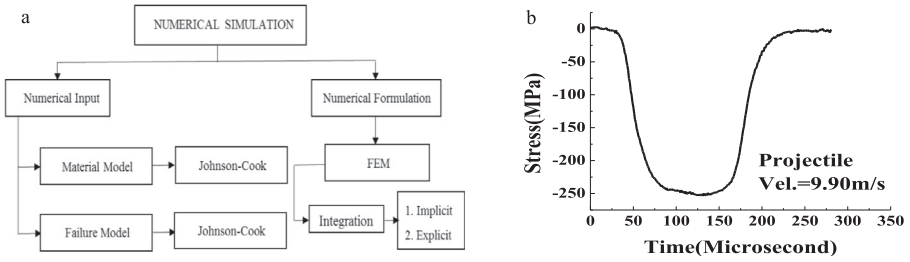

Fig. 1. (a) Input parameters for numerical simulation; (b) Stress wave at impact velocity 9.90 m/s.

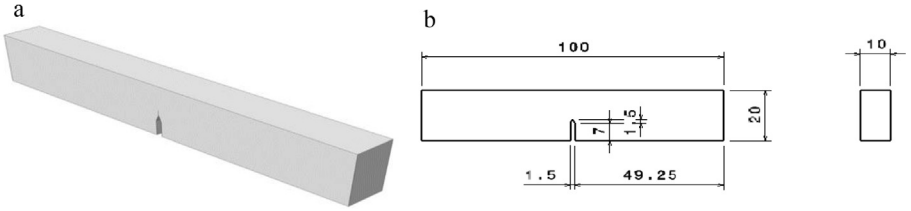

Fig. 2. (a) Three-point Bend Specimen; (b) Drawing of Three-point Bend Specimen.

2.3. Contact nonlinearity or boundary nonlinearity

During analysis, if boundary conditions change, the response of the structure is no longer linear, and it is considered a nonlinear problem.

3. Different stages used for finite element simulation

Commercially available software ABAQUS of 6.12 version has been used for simulating a three-point bend specimen subjected to impact loading through the input bar. The solver used for the simulation is explicit dynamic. The complete simulation takes place in the following stages:

1. Pre-processing (modeling)
2. Simulation (analysis)
3. Post-processing (outputs)

4. Results and discussion

4.1. Load point displacement along the longitudinal direction of incident bar

The commercial software ABAQUS of 6.12 version was used to simulate the three-point bend experiment in dynamic conditions. Various steps mentioned in section 3 were used during finite element modeling. Two deformable parts, the three-point bend specimen and the incident bar, of different shapes and sizes were created and assigned with different mechanical properties. The conditions used for the experimental setup were provided to the finite element model to match the results obtained with experiments. The following boundary conditions (Uy = 0, Uz = 0, URx = 0, URy = 0) were applied at the locations where rollers were used to support the specimen. The incident bar was constrained to move in the opposite direction of the Y-axis. During the simulation, the pressure impulse wave, obtained with modified Hopkinson pressure bar, was used to match the simulated result with the experimental result. The pressure applied to the input bar was directly obtained from incident strain pulse induced on the incident bar. The stress pulse for the experiment, which was conducted at 0.5 bar pressure, and corresponding striker bar velocity at 9.90 m/s, is shown in Fig. 1(b). The duration of pressure pulse was 300 microseconds, whereas its magnitude was 250Mpa in compression.

The finite model consists of two parts: the three-point bend single notched specimen and incident bar shown in figures (2(a), (b)), and 3(a), respectively. The specimen was discretized such that the number of nodes and elements (8-noded linear brick C3D8R) in the specimen were 34,755 and 31200, respectively. The incident bar was discretized into 217,038 nodes and 199,456 elements, and each element was C3D8R. The assembled view of the specimen with the incident bar is shown in Fig. 3(b).

To validate the results obtained with finite element analysis, the experimental load point displacement–time curve of a three-point bend test [8] on the specimen is superimposed on the finite element displacement diagram, as shown in Fig. 4(a) at striker velocity 9.90 m/s. In the figure, the legend experimental (SG) represents the load point displacement (LPD) obtained using strain gauges. It is seen that both curves match approximately.

Similarly, finite element analysis is carried out for a three-point bend experiment at a striker velocity of 12.8 m/s. Its load point displacement curve with time is shown in Fig. 4(b). This is achieved by merely replacing incident pressure pulse wave obtained during the experiment at striker velocity 12.8 m/s. Except for the change in incident pressure pulse, all conditions are similar, as mentioned in the previous investigation.

It is observed that load point displacement obtained with FEM simulation closely matches that obtained with an experiment using strain gauges. However, LPD obtained at striker velocity 12.8 m/s is higher than that obtained at 9.90 m/s. The result of the experiment, which is conducted at striker velocity 14.1 m/s, which is also higher than those of previous impact velocities, is shown in Fig. 5(a). The results of both experimental and FEM simulation show good agreement.

Fig. 5(b) compares FEM simulation results obtained at three different striker velocities 9.9 m/s, 12.8 m/s, and 14.1 m/s. It is observed that the load point displacement obtained at higher stri-

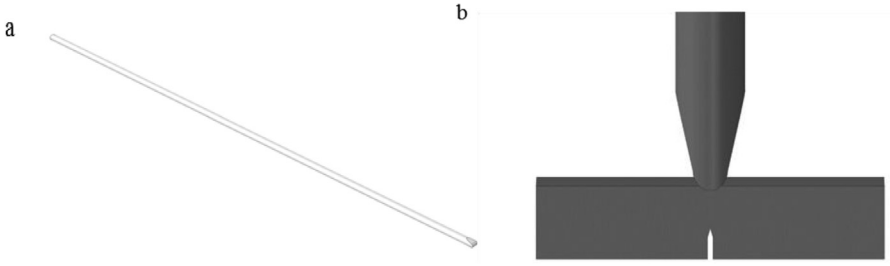

Fig. 3. (a) Incident bar (b) Assembly of input bar with assembly.

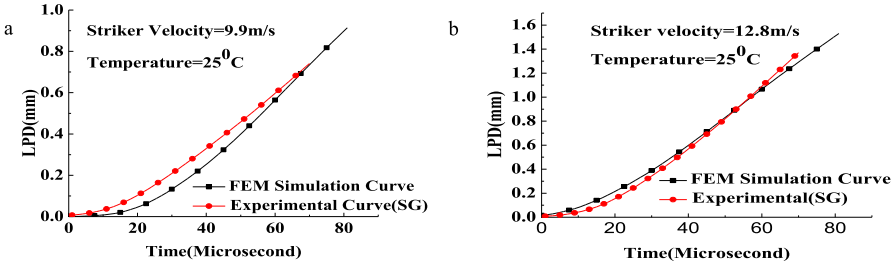

Fig. 4. (a) LPD at impact velocity 9.9 m/s. (b) LPD at impact velocity 12.8 m/s.

ker velocity, 14.1 m/s, is greater than that obtained at the other two velocities.

4.2. Crack mouth opening displacement of specimen

. Figs. 6 to 7 show a comparison of crack mouth opening displacements (CMODs) obtained from finite element simulation and experiments using digital image correlation (DIC). Details of experimental set up consisting modified Hopkinson pressure bar conjugation with digital image correlation is mentioned in reference [8]. Fig. 6(a) represents the CMOD acquired using finite element simulation and experiment conducted at striker velocity 9.90 m/s. This figure shows good agreement between results obtained by both methods. Fig. 6(b) and 7(a) represent the CMOD acquired using finite element simulation and experiment conducted at striker velocity 12.8 m/s and 14.1 m/s, respectively. The results obtained by both methods have a good agreement for two different velocities.

Fig. 7(b) compares FEM simulation results obtained at three different striker velocities 9.9 m/s, 12.8 m/s, and 14.1 m/s. It is observed that the crack mouth opening displacement obtained at higher striker velocity, 14.1 m/s, is greater than those obtained from the other two different velocities.

5. Dynamic initiation fracture toughness

Dynamic initiation fracture toughness of AA7075-T651 was obtained from dynamic stress intensity factor (DSIF), obtained in terms of load point displacements and crack mouth opening displacements, and time of initiation of fracture [9]. Three-point bend experimental set up ,MHPB, used during experiments at different impact velocities was procured from engineers and builders company [10] and installed at Impact Mechanics Lab in Applied Mechanics Department, Indian Institute of Technology, Delhi. Time of initiation of fractures was obtained from digital image correlation software at different impact velocities 9.90, 12.8, and 14.1 m/s. Digital image processed images at different impact velocities are shown in Figs. 8, 9, and 10, respectively. The time of initiation of fractures was obtained 40 μs for impact velocity 9.90 m/s, whereas the time of initiation at 14.1 m/s was 30 μs. The time of initiations was obtained by counting different images after loading started on the specimen.

The time of initiation at impact velocity 12.80 m/s was obtained by interpolating time at which experiments conducted at two others velocities 9.9 and 14.1 m/s. The time of initiation obtained at impact velocity 12.80 m/s is 33.1 μs. Using this time of initiations and stress intensity factor using the formula mentioned in the appendix, dynamic fracture initiation toughness's are obtained and shown in Fig. 11.

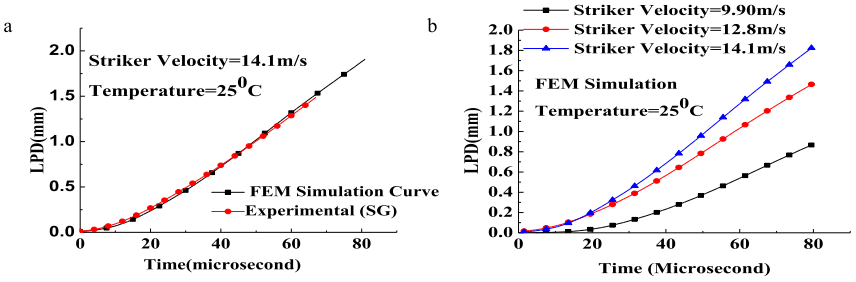

Fig. 5. (a) LPD at impact velocity 14.1 m/s; (b) LPD at impact velocities 9.90, 12.8 and 14.1 m/s.

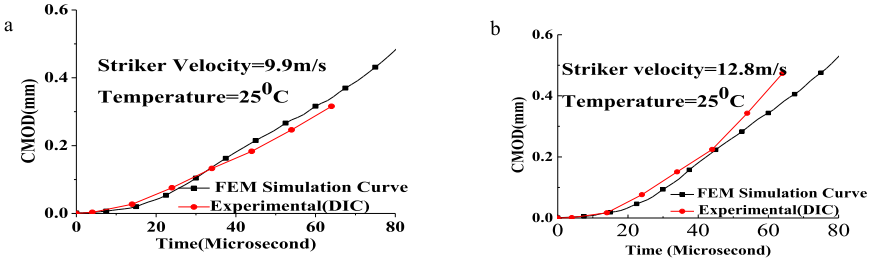

Fig. 6. (a) CMOD at impact velocity 9.9 m/s. (b) CMOD at impact velocity 12.8 m/s.

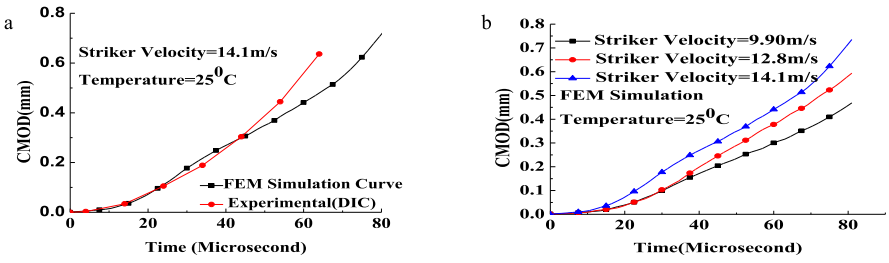

Fig. 7. (a) CMOD at impact velocity 14.1 m/s; (b)CMOD impact velocities 9.90, 12.8 and 14.1 m/s.

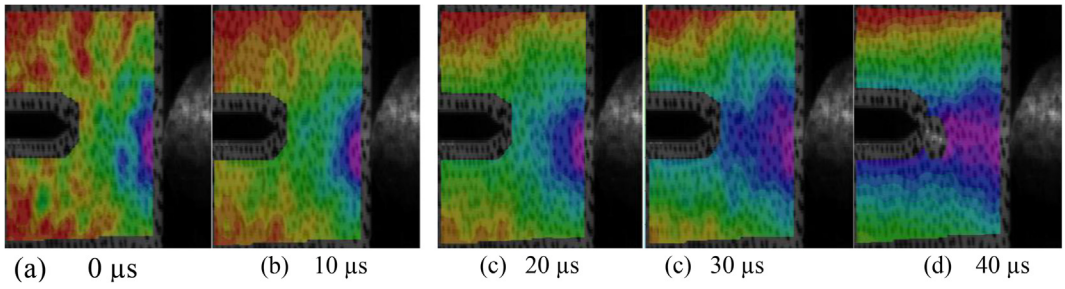

Fig. 8. DIC processed images ((a) 0 μs, (b) 10 μs, (c) 20 μs, (d) 30 μs, and (e) 40 μs) and impact velocity of 9.90 m/s.

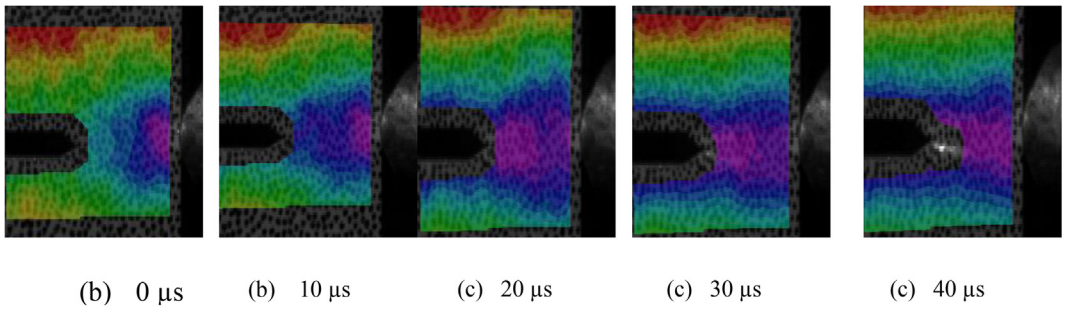

Fig. 9. DIC processed images ((a) 0 μs, (b) 10 μs, (c) 20 μs, (d) 30 μs, and (e) 40 μs) and impact velocity of 12.8 m/s.

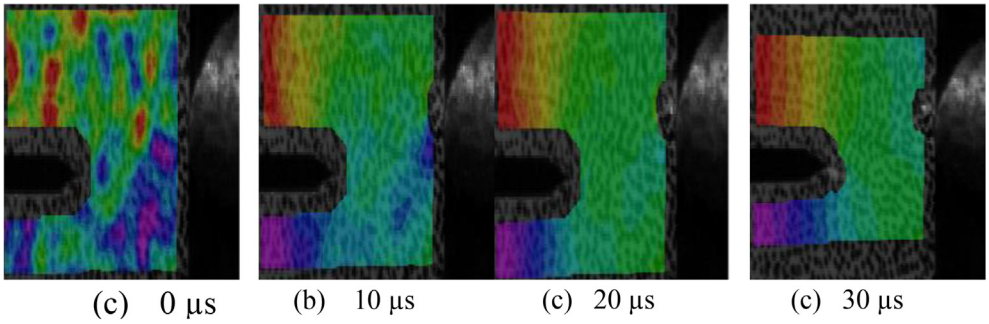

Fig. 10. DIC processed images ((a) 0 μs, (b) 10 μs, (c) 20 μs, and (d) 30 μs) and impact velocity of 14.1 m/s.

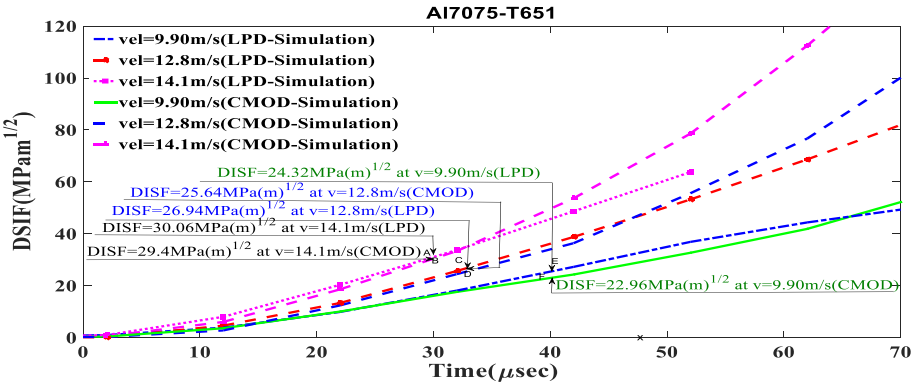

Fig. 11. Dynamic initiation fracture toughness's at different impact velocities.

The value of dynamic initiation fracture toughness's at different impact velocities are mentioned in table 1. The loading rates obtained at different impact velocities 9.90, 12.8, and 14.1 m/s, are $6.2X10^6$, $7.87X10^{6,}$ and $10.1X10^{6,}$ respectively.

6. Summary

The following observations are made from the present finite element simulation.

Table 1
Dynamic initiation fracture toughness at different loading rates.

Velocity of projectile(m/s)	Time of initiation (t_f)(μs)	DFIT(LPD)MPa$\sqrt{m}$	DFIT(CMOD)MPa$\sqrt{m}$	Loading ratesMPa$\sqrt{m}$/s
9.90	40	24.32	22.96	6.2X10^6
12.8	33.1	26.94	25.96	7.87X10^6
14.1	30	30.06	29.40	10.1X10^6

- The load point displacements are obtained at three different impact velocities, and results are compared with those obtained through experiments. It is found that results obtained by both methods are closely matched.
- The crack mouth opening displacements are obtained at three different impact velocities, and results are compared those obtained with experiments. There is good agreement in results obtained by both techniques.
- The load point displacements at different striker velocities are shown simultaneously in Fig. 5(b), and it is found that at higher striker velocity, the load point displacement is more.
- The crack mouth opening displacements at different striker velocities are shown simultaneously the Fig. 7(b), and it is found that at higher striker velocity, the crack mouth opening displacement is more.
- The time of initiation of fractures is obtained at different impact velocities by using digital image correlation software.
- Dynamic initiation fracture toughness at different impact velocities are obtained at different loading rates and mentioned in table 1.

CRediT authorship contribution statement

Sanjay Kumar: Conceptualization, Methodology, Writing - original draft. **Anoop Kumar Pandouria:** Software. **Purnashis Chakraborty:** Writing - review & editing. **Vikrant Tiwari:** Supervision.

Declaration of Competing Interest

The authors declare that they have no known competing financial interests or personal relationships that could have appeared to influence the work reported in this paper.

Acknowledgements

The authors are indebted to the Applied Mechanics Department of Indian Institute of Technology, Delhi, India, and Delhi Technological University, Delhi, India, for their support to perform experiments and simulation work.

Appendix

Dynamic initiation fracture Toughness, (K_{1d})

Load point displacement is obtained from equation (1) , where

$$u_p(t) = c\int_0^{\tau}(\varepsilon_i(t) - \varepsilon_r(t))\,dt \tag{1}$$

Where $\varepsilon_i(t)$ and $\varepsilon_r(t)$ represent incident and reflected strain and C is wave velocity.

The dynamic stress intensity factor

$$K_I(t) = \frac{3\beta u_p(t)}{2B\sqrt{W}C(\alpha)}k_\beta(\alpha) \tag{2}$$

$$Here\,,\ \ k_\beta(\alpha) = \frac{\sqrt{a}}{(1-\alpha)^{3/2}(1+3\alpha)}\left(1.9 + 0.41\alpha + 0.51\alpha^2 - 0.17\alpha^3\right)$$

$$C(\alpha) = C_o + C_c(\alpha)$$

$$C_o = \frac{L^3}{48EI}\left(1 + \frac{24(1+\nu)}{k}\frac{I}{AL^2}\right)$$

$$C_c(\alpha) = \frac{1}{EB}\left(h_1(\alpha) + \beta h_2(\alpha) + \beta^2 h_3(\alpha)\right)$$

$$h_1(\alpha) = -0.378\alpha^3\ln(1-\alpha) + \alpha^2\frac{(0.29 + 1.39\alpha - 1.62\alpha^2)}{(1 + 0.54\alpha - 0.84\alpha^2)}$$

$$h_2(\alpha) = 1.1\alpha^3\ln(1-\alpha) + \alpha^2\frac{(-3.22 - 16.4\alpha + 28.1\alpha^2 - 11.4\alpha^3)}{(1-\alpha)(1 + 4.7\alpha - 4\alpha^2)}$$

$$h_3(\alpha) = -0.176\alpha^3\ln(1-\alpha) + \alpha^2 \times \frac{(8.91 - 4.88\alpha - 0.435\alpha^2 + 0.26\alpha^3)}{(1-\alpha)^2(1 + 2.9\alpha)}$$

Here, the compliance of the cracked specimen,$C(\alpha)$, is related to SIF,$K_I(t)$, in equation (2).

Dynamic Initiation Fracture Toughness, (K_{1d}), is also obtained in terms of CMOD [9]. In this method, the SIF, $K_I(t)$, is obtained in terms of,w_m, which denotes CMOD and shown in equation (3).

$$K_I(t) = \frac{Ew_m k_\beta(\alpha)}{4\sqrt{a\alpha}\,v_\beta(\alpha)} \tag{3}$$

$$v_\beta(\alpha) = 0.76 - 2.28\alpha + 3.87\alpha^2 - 2.04\alpha^3 + \frac{0.66}{(1-\alpha)^2}$$

The expression $k\beta\,(\alpha)$ is the same as used in equation (2).

References

[1] R. Smerd, S. winkler, C. Salisbury, M. Worswick, D. Lloyd, M. Finn, High strain rate tensile testing of automotive alloy sheet", International Journal of Impact Engineering 32 (2005) 541–560.
[2] W.S. Miller, L. Zhuang, J. Bottema, A.J. Wittebrood, P Smet De, A Haszler, " Recent development in aluminium alloys for automotive industry"J Mater sci, Engg. 280 (2000) 37–49.
[3] V. Narayanamurthy, C.L. Rao, B.N. Rao, Def. Sci. J. 64 (2014) 55–61.
[4] V.C. Babu, Experimental and numerical studies on the mechanical behaviour of bovine cortical bone using rectangular miniature specimens, Ph.D. Thesis, Department Applied Mech. IIT, Delhi no (2010).
[5] C. Lakshmana Rao, V. Narayanamurthy, K.R.Y. Simha, "Applied Impact Mechanics" Ane Books Pvt. Ltd. (2016).
[6] M. A. Bhatti, "Advanced topics in finite element analysis of structures : with Mathematica and MATLAB computations," 2006.
[7] R. D. Cook, D. S. Malkus, M. E. Plesha, and R. J. W. Concepts, "Robert D. Cook, David S. Malkus, Michael E. Plesha, Robert J. Witt ' Concepts and Applications of Finite Element Analysis ' Wiley student edition, 4," 2007.
[8] S. Kumar, Experimental and numerical investigation on dynamic fracture of aluminium alloys, Ph.D Thesis, *Department Applied Mech. IIT, Delhi* (2020 Submitted 2020.).
[9] L. Rubio, J. FernáNdez-Sáez, C. Navarro, Determination of Dynamic Fracture-Initiation Toughness Using Three-Point Bending Tests in a Modified Hopkinson Pressure Bar, Exp. Mech. 43 (4) (Dec. 2003) 379–386.
[10] Standard and tools and techniques for dynamic characterization of materials. Design book of Engineers and Builders. http://www.engineersandbuilders.com, 2017.

Journal of Electronics and Informatics (2020)
Vol.02/ No.04
Pages: 202-210
https://www.irojournals.com/iroei/
DOI: https://doi.org/10.36548/jei.2020.4.002

Phototransistor: The Story So Far

Malti Bansal, Raaghav Raj Maiya
Department of Electronics & Communication Engineering
Delhi Technological University, Delhi-110042, India
maltibansal@gmail.com

Abstract— The research paper prospects the theory of phototransistor ranging from the history of the device to its application in the real world. The research paper deep dives into the characteristics of the phototransistor while discussing its dependence on bias drive, bias voltage, and illumination intensity. The research paper includes a comparative study between the various types of phototransistors based on optical gain, spectral range, and efficiency. It also concludes the best illumination method for the phototransistor based on the optical gain parameter.

Keywords: BJT; phototransistor; illumination; intensity; current gain; base current; optical

I. INTRODUCTION

There are numerous events in which it is helpful to supplant the human eye with some kind of electronic gadget to perform the desired task. For instance, in gas-or oil heaters where fire outbreak would establish a serious peril, it isn't monetary to use a human, only to recognize the fire and raise the alarm. This is where the optical-electronic devices come in handy. These devices detect the light in the surrounding and control the working of the electronic circuitry. One such optical device is a phototransistor. The phototransistor comes under the category of photoconductive electronic devices. The phototransistor is an electronic switching and amplification device whose working depends on the exposure to light. The phototransistor is a combination of a traditional transistor and a photodiode, in which the base current of the transistor depends on the intensity of light falling on the photodiode. The phototransistor has a slower response speed as compared to a photodiode but it is much more efficient in operation.

II. HISTORY

The phototransistor was invented by John Shive in the year 1948 in Bell Laboratories. Shive joined the laboratory in the year 1939 and started his research on physical components initially. Later he was shifted to the training and education department where Shive started working on developing transistor. This later became the main principle in the development of a transistor. He then tried to use the disclosure to build a point-contact semiconductor whose contacts were made of bronze on the front and back part of the germanium. Through this, he was able to demonstrate that the gaps can also diffuse from mass germanium rather than just the surface. In that very year, Shive used a light emission rather than a live wire to create electron-hole pairs to flow to the collector. After some more developments and research, the Bell laboratories announced this invention in the year 1950. The other scientists were pretty confident that after some strong developments, the phototransistor will have some serious application and will completely transform the real world. While the phototransistor was being announced its was proposed to use the transistor in a then developing ‘toll dialing machine’ in which the telephone operator dials a distant telephone automatically.

III. PHOTOTRANSISTOR AND ITS FABRICATION

Phototransistors are basically a combination of photodiode and amplifier integrated on a single silicon strip. It has been designed to overcome the major limitation of the photodiode that is the unity gain. The use of a single phototransistor turns out to be much more cost-effective and simple as compared to using a photodiode and an Op-amp in the circuit.

ISSN: 2582-3825 (online)
Submitted: 25.11.2020
Accepted: 19.12.2020
Published: 26.12.2020

Journal of Electronics and Informatics (2020)
Vol.02/ No.04
Pages: 202-210
https://www.irojournals.com/iroei/
DOI: https://doi.org/10.36548/jei.2020.4.002

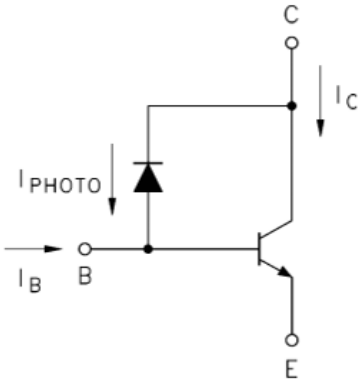

Fig. 1: Phototransistor Equivalent Circuit [7]

A. FABRICATION

The phototransistor is very similar to that of a traditional transistor just instead of a voltage source connected through a wire. The collector and the emitter are connected to a voltage source like a normal transistor but to generate the base current we take the help of the detector that is photo one.. The current that comes from a place known as base is generated by the light falling on the base which is made of a photosensitive material. The phototransistor package is provided with a window to allow light to fall on the photosensitive base region. The phototransistor in the active region acts as an amplifier in which the collector current is dependent on the value of base current which is further dependent on the intensity of illumination. So we can easily conclude the emitter and the collector current of the transistor is dependent on the intensity of illumination. The current coming from a place known as base is somewhat proportional that to directly to the parameter intensity. Higher the intensity, higher is the value of base current. The phototransistor can either have two-pin or three-pin configuration. In a two pin configutraion, the base current is generated by illumination while in the case of three-pin the base current can be generated by either voltage source or through illumination.

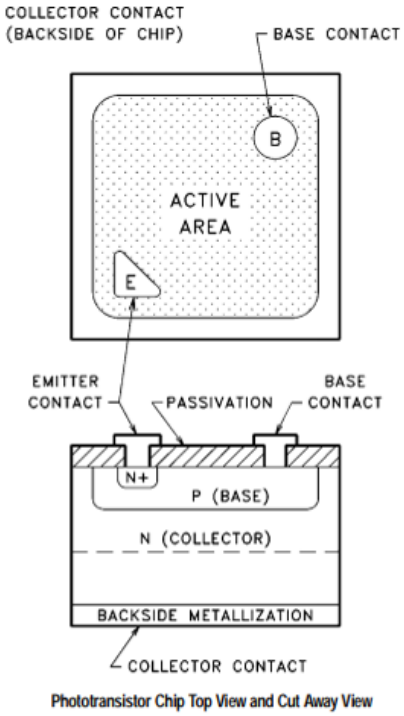

Fig. 2: Top view and Front view of Phototransistor [7]

ISSN: 2582-3825 (online)
Submitted: 25.11.2020
Accepted: 19.12.2020
Published: 26.12.2020

Journal of Electronics and Informatics (2020)
Vol.02/ No.04
Pages: 202-210
https://www.irojournals.com/iroei/
DOI: https://doi.org/10.36548/jei.2020.4.002

IV. WORKING OF PHOTOTRANSISTOR

The photo-transistor has similar working like a traditional transistor and has the same operation modes which are the region that is when it is in cut-off, the active region, the reverse active region, and the region in which it is in the saturation. Just like the traditional transistor, the emitter of a photo transistor is connected to a voltage source but in case of the base, it is provided with a window for illumination instead of a voltage source. The base current is generated by the illumination of the photosensitive base region which further becomes the deciding factor for the output current. For the illumination of the phototransistor the transistor is provided with a window for the base to trap the incoming light. When no light falls on the window of the phototransistor, no light is incident on the base region of the transistor, hence there is no base current. Only a small current flows due to movement of the minority of charge carries which is the reverse flowing which is in the wire is which is current also termed as dark current. The it is a current which is highly temperature-dependent. This mode of operation is the cut off region mode of the photo-transistor in which the collector or the output current like the base current is zero because of zero illumination. The phototransistor in the active region acts as an amplifier in which the collector current is dependent on the value of base current which is further dependent on the intensity of illumination. So we can easily conclude the emitter and the collector current of the transistor is dependent on the intensity of illumination. In the saturation region, the value of the collector current is at its maximum for the given values of the transistor and cannot increase any further on the increase of base current. In the reverse active region, the emitter of the transistor which plays the role or what we can say is act collector of the active state phototransistor and the collector acts as the emitter of the active state phototransistor. It is to the equal sum of the emitter and base current. This state is not useful as the current gain is very high in this case as compared to the active state photo-transistor.

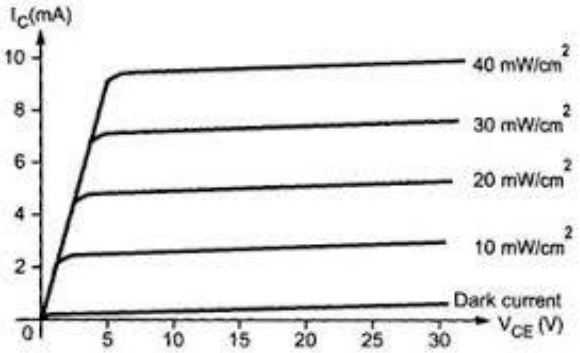

Fig. 3: I-V curve of phototransistor [3]

V. CHARACTERISTICS OF PHOTOTRANSISTOR

A. Spectral response:-

The output depends upon the 'Frequency'/'Wavelength' of the incident light. Just like any other optical device, phototransistor responds to the wavelength spectrum ranging from the near UV to the IR region of the wavelength spectrum. Over the range of wavelength the phototransistor show varying spectral response and thus varying efficiency. It is at the peak of it graph or what we can say is value is around the near IR region at approximately 840mm which is somewhat at a shorter wavelength as compared to a typical photodiode. Sources of light but show poor coupling efficiencies, this essentially is more clear visible when they are seen with Infrared Light ED.

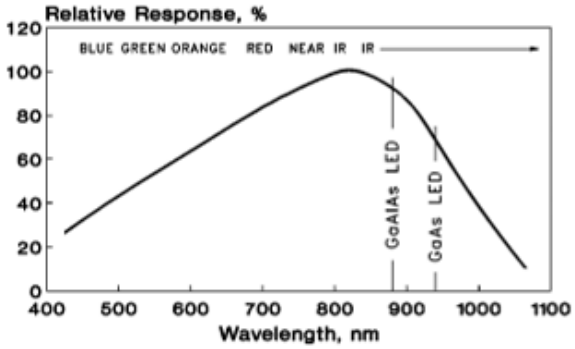

Fig. 4: Sensitivity of the phototransistor [7]

ISSN: 2582-3825 (online)
Submitted: 25.11.2020
Accepted: 19.12.2020
Published: 26.12.2020

Journal of Electronics and Informatics (2020)
Vol.02/ No.04
Pages: 202-210
https://www.irojournals.com/iroei/
DOI: https://doi.org/10.36548/jei.2020.4.002

B. Dependence on the area of base region

Just like other photoelectric devices the output of the phototransistor changes with changing the area exposed to illumination. In the case of phototransistor, the area exposed to illumination is the emitter-base junction, it acts as a photodiode. The base current flow soon as the emitter-base junction is exposed to the appropriate lighting condition. With the increase in the area of the base region, the base current also increases (make are somewhat double of base region and what we see is doubling the base current). The phototransistor base current then gets amplified according to the current gain of the transistor to give the output current.

C. Transistor gain

The current gain is dependent upon the base drive, bias voltage, and temperature. The current gain is low at low light and increases with increasing illumination and reaches a peak value and then again somewhat goes down or decrease and reaches its low but not that low.

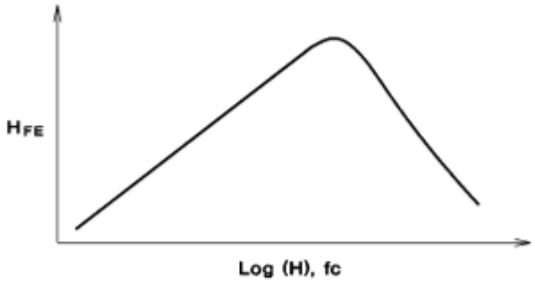

Fig. 5: Transistor gain vs light intensity [7]

The current gain is also dependent on the potential between collector and emitter region (Vce). The increase in potential between the collector and emitter leads to an increase in the voltage gain. The Current gain also increases with the increase in temperature.

D. Speed of response

The speed of response of the phototransistor is the time it takes to respond to the change in intensity of light. It is completely. So for a device with the same active region, the speed of response decreases with an increase in gain of the phototransistor. The response of the transistor is usually expressed in terms of rise and fall time.

VI. TYPES OF PHOTOTRANSISTOR

A. BJT phototransistor

The BJT transistor triggered by photos is similar to a simple BJT transistor in the construction According to the type of material used and structure, the BJT phototransistor is further classified into two types.

1)Homo-junction:

A homo-junction could be a semiconductor having equal band gaps with somewhat different doping level or like that only. The entire structure is made up of the same material, to increase the efficiency they are dopes with other material. The homo-junction is used more as compared to a hetero-junction transistor.

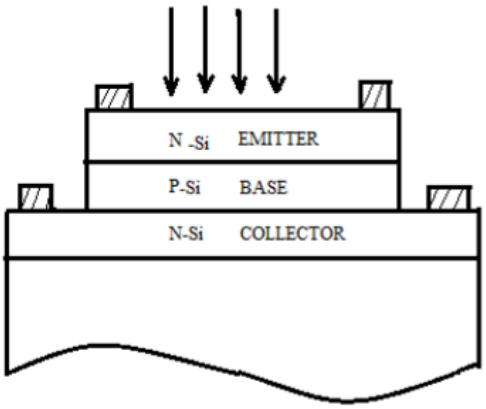

Fig. 6: Homo-junction Phototransistor [8]

ISSN: 2582-3825 (online)
Submitted: 25.11.2020
Accepted: 19.12.2020
Published: 26.12.2020

Journal of Electronics and Informatics (2020)
Vol.02/ No.04
Pages: 202-210
https://www.irojournals.com/iroei/
DOI: https://doi.org/10.36548/jei.2020.4.002

2) Heterojunction:

The hetero-junction phototransistor uses different materials to make the emitter-base and the collector junction of the semiconductor. This increases the performance of the transistor to several frequency ranges. The materials which can be used to make the hetero-junction phototransistor are AlGaAs, InP, InGaAs, Si-SiGe.

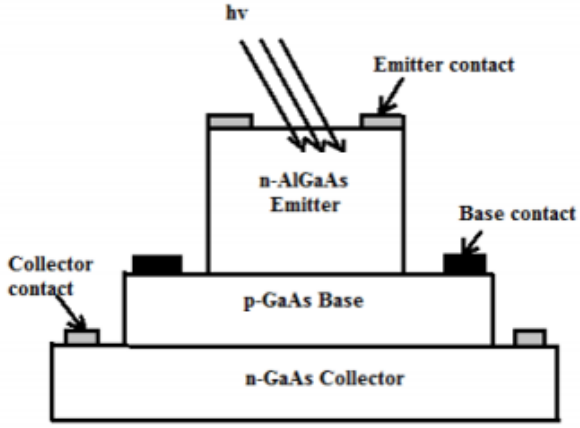

Fig. 7: Hetero-junction Phototransistor [4]

The characteristic curve of hetero-junction phototransistor is shown in fig. 8, the graph shows the active, cut-off, and saturation region of the hetero-junction transistor. It clearly shows the active region is higher in hetero-junction as compared to the homo-junction transistor.

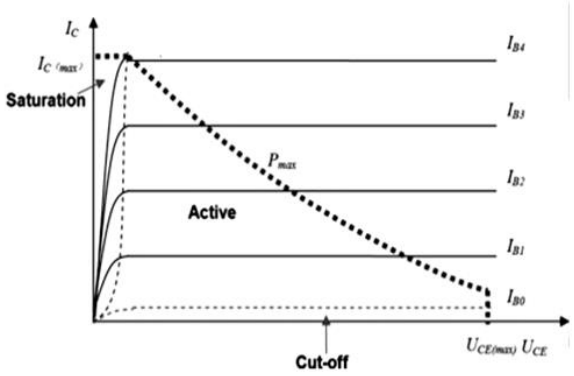

Fig. 8: Characteristic curve of the hetero-junction phototransistor [2]

B. FET Phototransistor –

The field effect phototransistor or the field effect transistor triggered by photo has bascically a source drain and a gate the current flows from the sourse to the drain. In FET phototransistor the only diffrence is that the gate current is generatede through light. This the control the current flowing between gate and source. The FET phototransistor are generally more sensitive as compared to BJT phototransistor. With increase in light intensity the gate current and hence the biasing increases, this increases the currrent between source and drain but decrease the width simultaneously. This leads to saturation of source current. According to the material of which the transistor is constructed, there are two type of transistor- P-channel and N-channel. In p-channel, the phototransitor is constructed, the tranistor is constructed of n-type semicoductor. The channel is the path between source and drain through which current flows.

ISSN: 2582-3825 (online)
Submitted: 25.11.2020
Accepted: 19.12.2020
Published: 26.12.2020

Journal of Electronics and Informatics (2020)
Vol.02/ No.04
Pages: 202-210
https://www.irojournals.com/iroei/
DOI: https://doi.org/10.36548/jei.2020.4.002

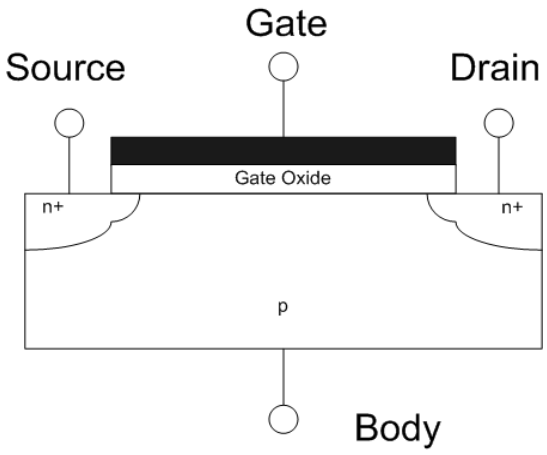

Fig. 9: FET Phototransistor

C. Photo-darlington

Photo-darlington just like a darlington transistor is a combination of two transistors in which the emitter current of one transistor is fed as base current into the other. The only difference is that in the case of Photo-darlington, a phototransistor is used instead of a traditional transistor. The first phototransistor which is basically what u can say acting as the photo-detector which is coupled in the place which is known of the base of the studied second transistor through an emitter.

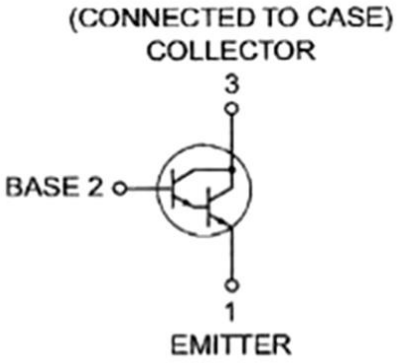

Fig. 10: Photo-darlington transistor symbol

Photo-darlington is only used where low frequencies are required in the circuit. The lower frequency response of the phototransistor may only have a bandwidth of a few tens of kHz. It has a higher active emitter and collector voltage as compared to other transistors.

VII. TYPES OF ILLUMINATION:-

A transparent window is used in the encapsulation of the light that falls on the phototransistor. Based upon the direction of illumination there are three different types of illumination based upon which the transistor performs to different efficiency levels. The different types of illumination are as follows.

a> Vertical face illumination,
b> Rear face illumination
c> Lateral face illumination.

All three illuminations are studied under ideal conditions whereby the electron and holes are generated uniformly all over the body when the lights fall on it.

ISSN: 2582-3825 (online)
Submitted: 25.11.2020
Accepted: 19.12.2020
Published: 26.12.2020

Journal of Electronics and Informatics (2020)
Vol.02/ No.04
Pages: 202-210
https://www.irojournals.com/iroei/
DOI: https://doi.org/10.36548/jei.2020.4.002

A. Vertical surface illumination

It is the most basic method or what we can say is that it is the most traditional method of illuminating the surface of the transistor. The light essentially falls directly and vertically on the base and obviously fight fall on it will create electron hole pairs which will essentially create current and hence the current will start flowing tin the transistor and it will start operating in either of the three mode of or region of operation in which generally transistor operates. But it may also operate in the fourth operating region that is essentially the reverse active region which is essentially the opposite of active region.

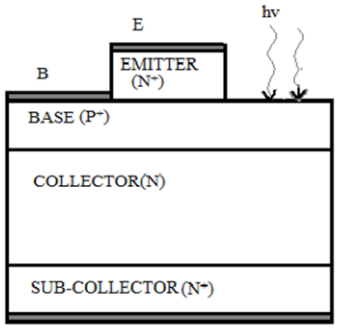

Fig. 11: Vertical face illumination [8]

B. Rear –face illumination

The rear face illumination in the BJT phototransistor takes place at the collector. The photo-carriers generation takes place in the active region of the transistor. Its efficiency and current gain are a bit higher as compared to vertical illumination but lower than lateral face illumination. The current gain is also dependent on the potential between collector and emitter region (Vce). The increase in potential between the collector and emitter leads to an increase in the voltage gain. The Current gain also increases with the increase in temperature

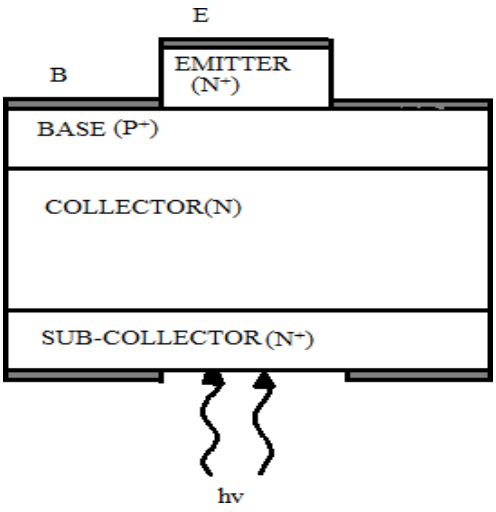

Fig. 12: Rear face illumination [8]

C. Lateral illumination

In this illumination technique, the light falls parallel to the layer of the transistor. The current gain is also dependent on the potential between collector and emitter region (Vce). Like in the vertical illumination, the photons and the charge carriers no longer move in the same direction. The biasing is provided when the electron pairs are created due to illumination. The lateral illumination method has a better speed response as compared to rear face or vertical face illumination. The injection efficiency of the lateral face illuminated transistor is around 50-90%. In the case of lateral illumination, the absorption volume is higher and each photon can interact with more silicon atoms due to which it has a higher current gain and efficiency as compared to the other two cases.

ISSN: 2582-3825 (online)
Submitted: 25.11.2020
Accepted: 19.12.2020
Published: 26.12.2020

Journal of Electronics and Informatics (2020)
Vol.02/ No.04
Pages: 202-210
https://www.irojournals.com/iroei/
DOI: https://doi.org/10.36548/jei.2020.4.002

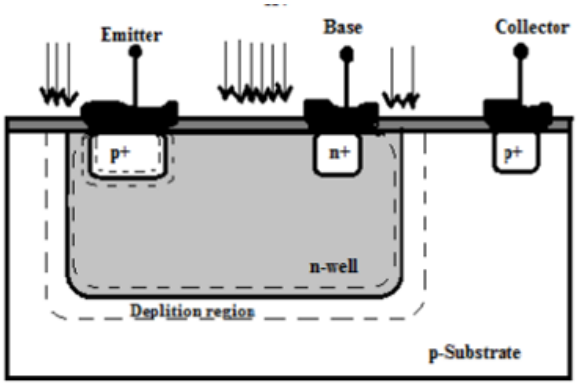

Fig. 13: Lateral face illumination [8]

According to the experimental data, there is the highest current gain in lateral face illumination followed by rear face illumination and then vertical face illumination. The above results hold for all frequency ranges. This proves the efficiency of lateral face illumination over other illumination methods. For better understanding, the results have been plotted in the following graph

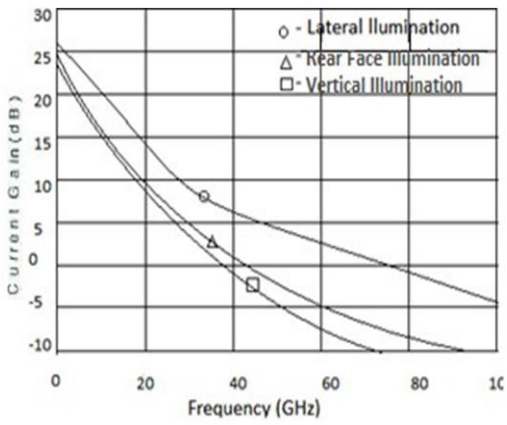

Fig. 14: Current gain for lateral, rear-face, and vertical Face illumination [5]

VIII. APPLICATIONS

The phototransistor has transformed the human world due to its numerous applications. The phototransistor is used in every field of life, ranging from industries and hospital to our day to day activities.

A.Industrial

The phototransistor is used in the security system. Here the phototransistor detects the presence of a person based on interruption in the path of light falling on it from the source. The Phototransistor is also used in the counter circuit in industries and banks for counting coins, currency, and any such stuff. It is used as an encoder for measuring speed and direction. It is also used in the Opto-coupler.

B. Medical

The phototransistor is used in medical devices for efficient and light controlled performance. The phototransistor is used to provide an electrical isolation between the patients and hospital equipments. The phototransistor is also used in the radiation monitor which is based on its variation in performance depending upon the frequency of light. The phototransistor also finds its application in hospitals as counters where they are used to monitor and keep an exact count of rates of intravenous injections

C. Other Applications:

Apart from these, the phototransistor has several other applications in our day to day life. The phototransistor is used in the remote controller of toys, audio-video appliances. It is used to monitor the position of the joystick. It

ISSN: 2582-3825 (online)
Submitted: 25.11.2020
Accepted: 19.12.2020
Published: 26.12.2020

Journal of Electronics and Informatics (2020)
Vol.02/ No.04
Pages: 202-210
https://www.irojournals.com/iroei/
DOI: https://doi.org/10.36548/jei.2020.4.002

is also used as laser tags in gaming. It is used to indicate the level of a working system that plays an important role in relays and punch cards.

IX. CONCLUSION

The phototransistor is a revolutionary invention in the history of mankind. A device that found its application while being in its developing stage proves the strong potential it withholds. The phototransistor is similar to traditional phototransistor to all extent except that the base current is generated by illumination. Out of the various phototransistor available in the market, the hetero-junction phototransistors made from group III-V elements are the most efficient when it comes to performance. In the case of types of illumination techniques, the lateral illumination out-performs the vertical and the rear face illuminated phototransistor in both current gain and efficiency. In a nutshell, even after having numerous applications, the phototransistor still has several pages to unfold and possess immense scope of research in the coming future.

REFERENCES

[1] S.Chand, Everything about Semiconductors, Dharma Publicatios, 1996

[2] 2. M.S.Tyagi, Introduction to Semiconductor Material And devices. India: Wiley, 1991.

[3] Didier Decoster and Joseph Harari, Optoelectronic sensors. USA: Wiley, 2002.

[4] 5.Shailendra Bansropun, R. C. Woods, and John Stuart Roberts, “Evidence of Optical Gain Improvement in AlGaAs/GaAs Heterojunction Phototransistors Using an Emitter Shoulder Structure”. IEEE Transactions On Electron Devices, vol. 48, no. 7, July 2001.

[5] Noureddine CHENNAFI, Christian RUMELHARD, Carmen GONZALEZ, Julien THURET, “Modelling The Photoresponse Charecteristics of InP/InGaAs Heterojunction Phototransistor With Different Incident direction of Beam Light” CNET, GAAS 98, Amsterdam, 1998.

[6] Ottfried Madelung Semiconductors: Data Handbook, 3rd edition Springer (2004)

[7] Phototransitor and IRED data book.

[8] Chandrika Shamra, Nidhi Sharma, Poornima Sharma, Veerendraa Kumar, “A Review of BJT Based Phototransistor” IJERT, vol. 03. issue 04, April 2014.

ISSN: 2582-3825 (online)
Submitted: 25.11.2020
Accepted: 19.12.2020
Published: 26.12.2020

PI and Fuzzy Logic Control of Single Phase Grid Connected Inverter Serving Two PV Panels

Dhruv Bhatia
Department of Electrical engineering
Delhi Technological University
Delhi, India
dhruv4uvd@gmail.com

Alka Singh
Department of Electrical Engineering
Delhi Technological University
Delhi, India
alkasingh@dce.ac.in

Ankita Arora
Department of Electrical Engineering
Delhi Technological University
Delhi, India
aroraankita@dtu.ac.in

2020 IEEE 17th India Council International Conference (INDICON) | 978-1-7281-6916-3/20/$31.00 ©2020 IEEE | DOI: 10.1109/INDICON49873.2020.9342393

***Abstract*— In this paper, two serially connected solar photovoltaic panels operating under different irradiance and temperature levels are tied to the grid with a one phase transformerless inverter. The proposed method has been simulated in MATLAB with Proportional Integral Control and Fuzzy Logic Control scheme. Results of the two controllers has been compared with parameters such as PV voltage, PV current and PV power. The THD% for the grid current has also been compared for the two control schemes.**

***Keywords*— Single Stage Grid Connected Inverter, Maximum Power Point Tracking, Varying operating conditions, Fuzzy logic.**

I. INTRODUCTION

The grid connected PV systems are divided into Single Stage and Dual Stage systems. In the dual-stage systems the flow of power from the PV array to the grid is split into two stages. The first stage is used to mark the Maximum Power Point (MPP) of the PV array and boost this tracked voltage using DC- DC power electronic converters. Stage two comprises of an inverter which converts the DC to AC power. While the multi-stage technique is time tested and work very well but it suffers from the disadvantage of large initial cost, low efficiency and bulky size [1]. The above drawbacks can be solved using the following techniques.

1.To only use the inverter stage i.e. H-bridge inverter with transformer [2].

2.Using large numbers of serially and parallel connected PV cells developing a high output voltage with an inverter [3] [4].

These options have the drawback that they are bulky and raises the cost of the designed system and large PV arrays suffers from creation of hotspots and increased leakage current from the parasitic capacitor [5][6].

With the above discussion we can conclude that the PV systems with one power stage is advantageous as it makes the system cost effective and more compact. It is also needed that in a power stage the devices used should be minimized to cater the modern needs [8][9].

In this paper, two half bridge inverters have been combined with their individual AC bypasses. In the input side of the inverter two PV panels are connected in series. Both the PV panels are able to measure the MPP. The inverter is controlled by the conventional PI controller [7] and Fuzzy Logic Controller (FLC).

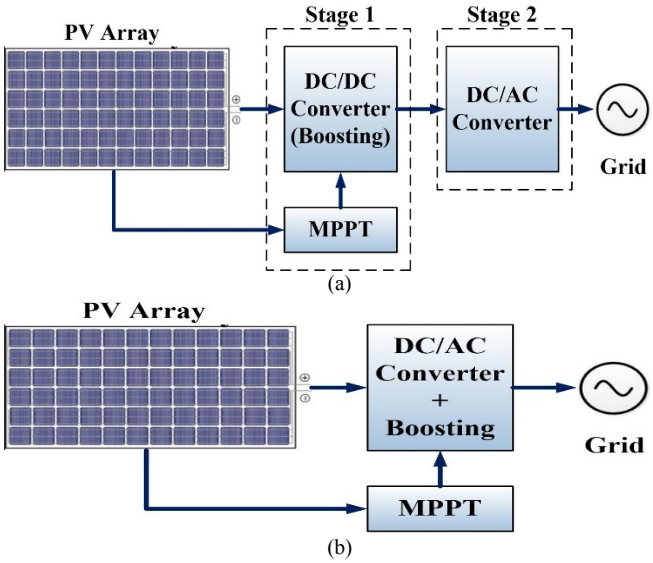

Fig. 1. PV System: (a) Dual Syage System and (b) Single Stage System

The principle of operation of the inverter topology has been explained in Section II and the controlling strategy is discussed in Section III and the results of the simulation with both the control strategies are compared in Section IV.

II. OPERATING PRINCIPLE

In this paper, the designed circuit diagram of a dual H-bridge inverters with their individual AC Bypasses topology is simulated [7]. The first half bridge is designed using switches S1 and S3 and its AC bypass consists of the switches S5 and S6. Similarly to second half bridge is designed using switches S2 and S4 while its AC bypass consists of the switches S7 and S8. L1, Co1, L2, and Co2 forms the output filters of the bridge 1 and bridge 2 respectively.

PV1 and PV2 are the two PV subarrays with Cf1 and Cf2 as their input side filter capacitors. Cpv0, Cpv1, Cpv2 are the

978-1-7281-6916-3/20/$31.00 ©2020 IEEE

Authorized licensed use limited to: DELHI TECHNICAL UNIV. Downloaded on February 15,2021 at 09:55:08 UTC from IEEE Xplore. Restrictions apply.

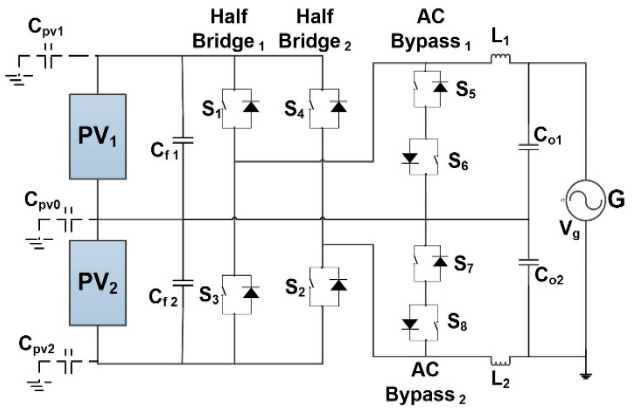

Fig. 1. Power Circuit Diagram of the Designed Topology

parasitic ground capacitors. The parasitic ground capacitors have been taken into account for the simulation part but have been neglected for the analysis part of the scheme.

In the positive half cycle, S1 and S2 switches operate with a sinusoidally varying duty cycle d1 and d2 and the AC bypass switches S5 and S6 are always on. Similarly in the negative half cycle the S3 and S4 switches are varied with sinusoidal duty cycles d3 and d4 and the switches S7 and S8 are always kept on. This change in the sinusoidal duty cycle ensures that under the unity power factor condition the Ig (grid current) is in synchronism with Vg (grid voltage).

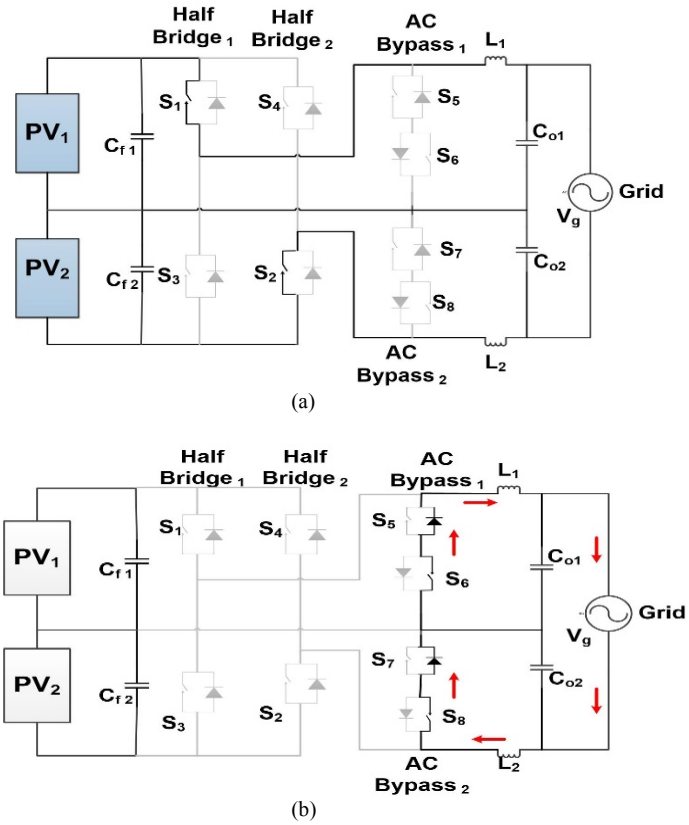

Fig. 2. Stages of Inverter in Positive Half Cycle: (a) Active Stage, (b) Freewheeling Stage [7].

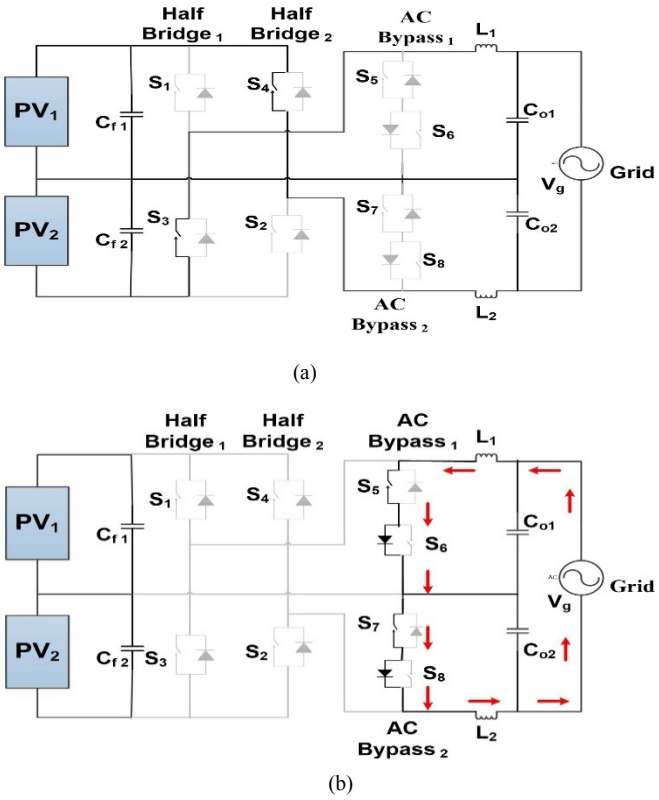

Fig. 3. Stages of Inverter in Negative Half Cycle: (a) Active Stage, (b) Freewheeling Stage [7].

The analysis of the scheme can be simplified with Fig. 3 and Fig. 4. Since the PV subarrays are subjected to varying insolation level and temperature level the output power, output DC voltage and the current for both the subarrays would be different. P_{MPP1}, V_{MPP1} and I_{MPP1} are the maximum power, voltage and current for PV subarray 1 and P_{MPP2}, V_{MPP2} and I_{MPP2} is for the PV subarray 2. During the positive half cycle the power from PV_1 and PV_2 is given to C_{o1} and C_{o2} while in the negative half cycle the power from PV_1 and PV_2 are dumped at C_{o2}, C_{o1}.

The power fed to the grid at steady state condition can be expressed as the sum of the powers across the capacitors C_{o1} and C_{o2} given by (1).

$$P_{Grid} = P_{Co1} + P_{Co2} \quad (1)$$

Further we can add,

$$v_g = v_{co1} + v_{co2} \quad (2)$$

A. During Positive Half Cycle:

The power extracted from the PV_1 is given to C_{o1} and from PV_2 is given to C_{o2} as shown in the Fig. 3(a) [7]. Hence,

$$P_{co1} = P_{MPP1} \text{ and } P_{co2} = P_{MPP2} \quad (3)$$

From (2) it can be concluded that the voltages across the capacitors C_{o1} and C_{o2} are in phase with the grid voltage and

Authorized licensed use limited to: DELHI TECHNICAL UNIV. Downloaded on February 15,2021 at 09:55:08 UTC from IEEE Xplore. Restrictions apply.

since the inverter is made to be operated at unity power factor the grid current is also in phase with the above voltages.

$$P_{co1} = \frac{1}{\pi}\int_0^{\pi} V_{co1m}\sin(wt)\, I_{gm}\sin(wt)d(wt) = \frac{V_{co1m}I_{gm}}{2} \quad (4)$$

$$P_{co2} = \frac{1}{\pi}\int_0^{\pi} V_{co2m}\sin(wt)\, I_{gm}\sin(wt)d(wt) = \frac{V_{co2m}I_{gm}}{2} \quad (5)$$

Combining (3), (4) and (5) the amplitude for the voltage across filter capacitors V_{co1m} and V_{co2m} can be obtained.

$$V_{co1m} = \frac{\sqrt{2}V_g P_{mpp1}}{P_{MPP1} + P_{MPP2}} \quad (6)$$

$$V_{co2m} = \frac{\sqrt{2}V_g P_{mpp2}}{P_{MPP1} + P_{MPP2}} \quad (7)$$

It can be concluded from (6) and (7) that the amplitude of the voltages across the grid is proportional to the maximum power extracted from the PV modules P_{MPP1} and P_{MPP2} [7].

Since in the positive half cycle switch S_1 controls the voltage V_{co1} and switch S_3 controls the voltage V_{co2} and shown in Fig. 3(a) therefore the duty ratios of the switches are varied sinusoidally with amplitudes proportional to V_{co1m} and V_{co2m}.

B. During Negative Half Cycle

In the negative half cycle the power from PV_1 is given to C_{o2} and the power from PV_2 is given to C_{o1} as shown in Fig. 4(a). Therefore the amplitude of V_{co1} is proportional to P_{MPP2} and the amplitude of V_{co2} is proportional to P_{MPP1} which is given by (8) and (9).

$$V_{co1m} = \frac{\sqrt{2}V_g P_{MPP2}}{P_{MPP1} + P_{MPP2}} \quad (8)$$

$$V_{co2m} = \frac{\sqrt{2}V_g P_{MPP1}}{P_{MPP1} + P_{MPP2}} \quad (9)$$

Similarly the switch S_4 controls the voltage V_{co2} with PV_1 and input and switch S_3 controls the voltage V_{co1} with PV_2 as input as shown in Fig. 4(a). Hence switches S_3 and S_4 have duty cycles varied sinusoidally with amplitude proportional to V_{co1m} and V_{co2m} respectively.

III. CONTROL SCHEME

A. Using Conventional PI Controller

The simulated control strategy is shown in Fig. 5, Fig. 6 and Fig. 7. Here the two subarrays are able to monitor the MPP with the help of Incremental Conductance MPPT Algorithm. The obtained voltages at MPP are then compared with the actual PV voltages to generate an error which is then processed to PI controllers [7].

A PLL is used to track the frequency of the voltage v_g. This grid frequency is imposed on a unity amplitude sinusoidal function to generate the signal X. The signal X is basically a sinusoidal signal with unity amplitude and the frequency of this signal is equal to the grid frequency and changes with the change in grid frequency.

The output of the PI controllers and signal X are multiplied to generate the reference currents I_{ref1} and I_{ref2}. These reference currents are used to control the filter currents I_{L1} and I_{L2} which eventually controls the grid current I_g.

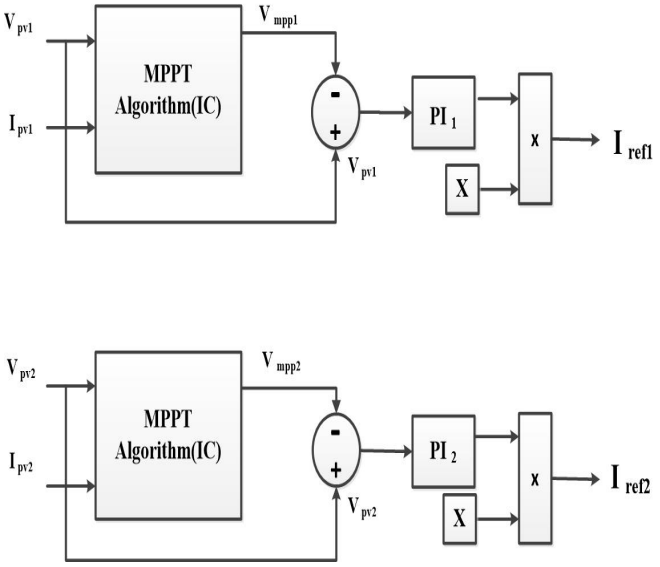

Fig. 4. Reference Current Generation

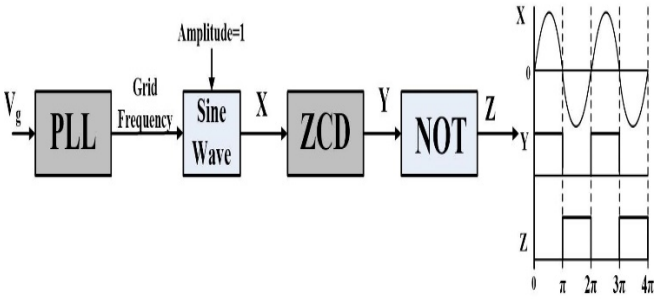

Fig. 5. Grid voltage synchronism with PLL

During the positive half cycle as shown in Fig. 3(a) the module PV1 controls the current in inductor L1 through switch S1 and module PV2 controls the current in inductor L2 through switch S2. Hence it is shown in Fig. 7 when X > 0 (i.e. positive half cycle) Iref1 is compared with iL1 and Iref2 is compared with iL2.

During negative half cycle as shown in Fig. 4(a) module PV1 controls the current in inductor L2 through the switch S4 and module PV2 controls the current in inductor L1 through switch S3. Hence it is shown in Fig. 7 when X<0 (i.e. negative half cycle) Iref2 is compared with iL1 and Iref1 is compared with current iL2.

The errors generated with the above comparisons are then given to two separate PI controllers to generate the duty ratios for the switches S1-S4.

Authorized licensed use limited to: DELHI TECHNICAL UNIV. Downloaded on February 15,2021 at 09:55:08 UTC from IEEE Xplore. Restrictions apply.

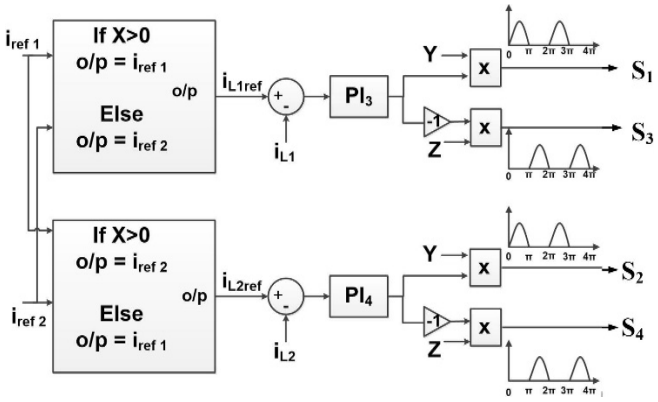

Fig. 6. Duty ratio generation for the switches

B. Using Fuzzy Logic Controller (FLC)

The FLC scheme is given in Fig. 8. Here the two inputs given to the controller are the error and its derivative. The fuzzy controller consists of the fuzzification, the rule based system and deffuzification. The rule based system is the main brain of the system which contains the membership function [10].

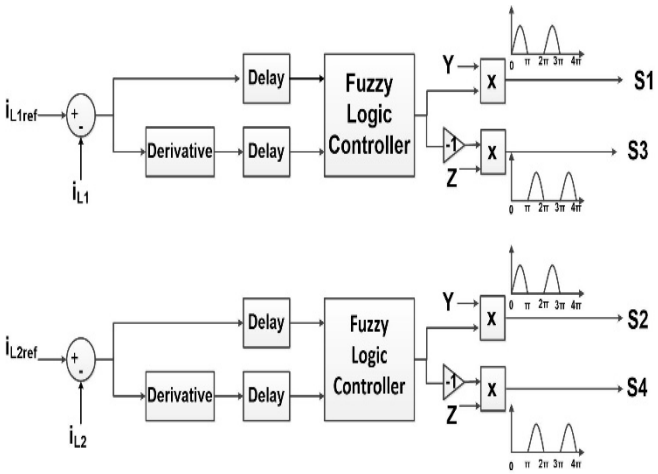

Fig. 7. Fuzzy Control Scheme

For the fuzzy logic controller error and its derivative are taken as the two inputs. The two inputs have 3 Gaussian Membership functions. The membership functions have a standard deviation of 0.4247. The linguistic variables are "Negative" [N], "Positive [P] and "Zero" [Z]. The mean value for these functions are -1,1 and 0 respectively.

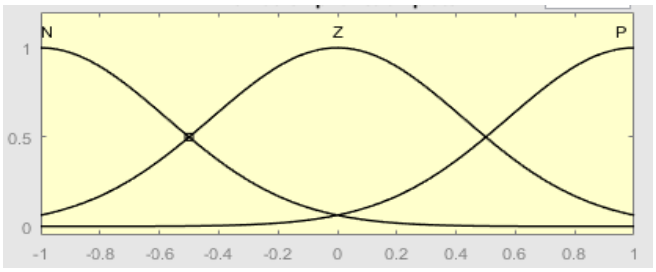

Fig. 8. Membership functions for the input variables of the Fuzzy Logic Controller.

The control action is then defuzzified with a five membership functions to a unity value as shown in Fig. 10. The output variables are taken as "Big Negative" [BN], "Negative" [N], "Zero" [Z], "Positive" [P] and "Big Positive" [BP].

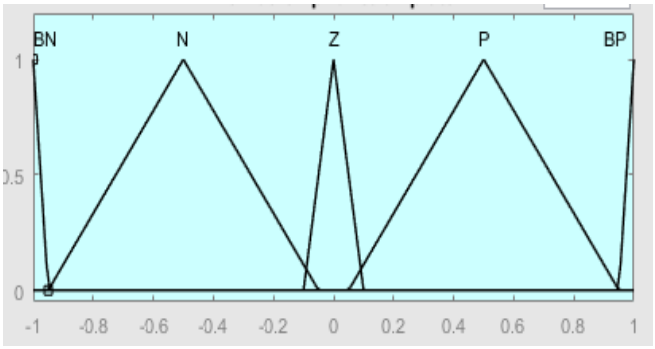

Fig. 9. Output Variables for the Fuzzy System after applying the rules

The ruling system for the FLC is derived from the input error signal and its derivation and the behavior of the system. The rule bases of the fuzzy logic for output variables are seen in Table I.

TABLE I. RULES FOR FUZZY SYSTEM

E / dE/dt	N	Z	P
N	BN	BN	BN
Z	P	Z	N
P	BP	BP	BP

IV. SIMULATION AND RESULTS

The simulation has been designed in MATLAB- Simulink to compare the two control schemes. The changes in insolation and temperature levels with time is provided in Table III. The changes in V_{MPP}, I_{MPP}, P_{MPP}, V_g and I_g are plotted and compared for both control schemes.

TABLE II. PARAMETERS OF THE DESIGNED SYSTEM

Parameter	Value
Single Phase Grid Voltage (V_g)	230 V, 50 Hz
V_{oc}[a] and V_{mpp} of subarrays at STC[b]	270 V and 217 V
I_{sc}[c] and I_{mpp} of subarrays at STC	3.58 A and 3.22 A
P_{mpp1} and P_{mpp2} at STC	780 W
Total Power	1.5 KW Approx
L_1 and L_2	5 mH
C_{o1} and C_{o2}	5 µF
C_{f1} and C_{f2}	3300 µF
Deployed MPPT Methodology	Incremental Conductance

STC[b] = Standard test condition,
Insolation = 1KW/m^2 and
Temperature = 25^o.

Authorized licensed use limited to: DELHI TECHNICAL UNIV. Downloaded on February 15,2021 at 09:55:08 UTC from IEEE Xplore. Restrictions apply.

TABLE III. CHANGES IN SOLAR DENSITY AND TEMPERATURE LEVELS WITH TIME

Time (sec)	0-1	1-2	2-3	3-4	4-6	6-8
PV1 Insolation , Kw/m^2	0.7	0.8	0.9	1	1	1
PV2 Insolation , Kw/m^2	0.9	0.9	0.9	0.9	0.9	0.9
Temperature in PV_1 , ^{0}C	25	25	25	25	30	35
Temperature in PV_2 , ^{0}C	25	25	25	25	25	25

A. Conventional PI Controller

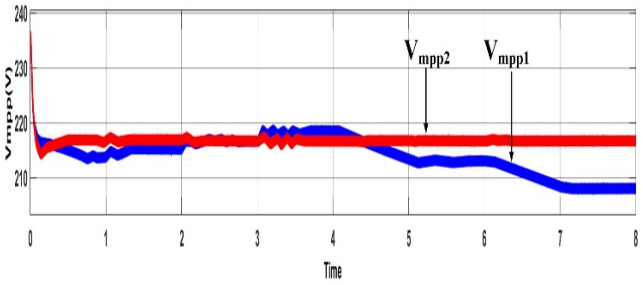

(a)

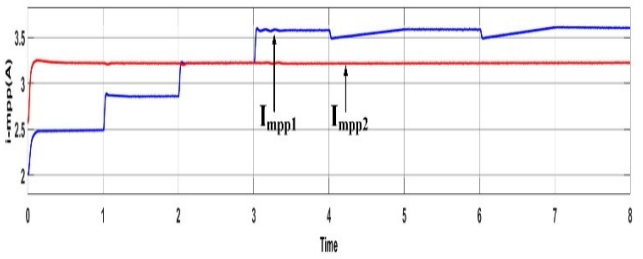

(b)

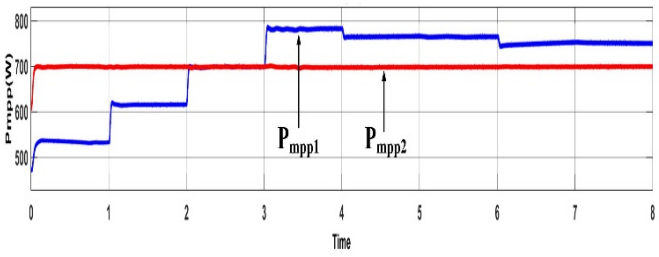

(c)

Fig. 10. PI Controller: (a) DC Voltage , (b) DC Current and (c) Power of PV1 and PV2

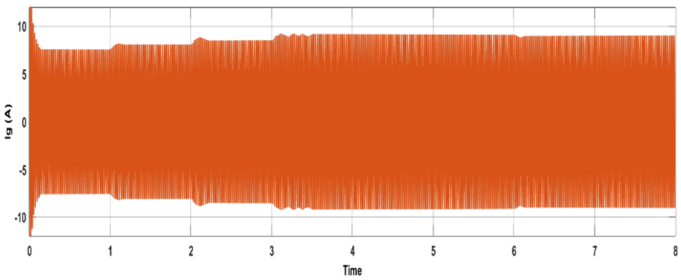

Fig. 11. Variation in Grid Current with changes in insolation and temperature levels.

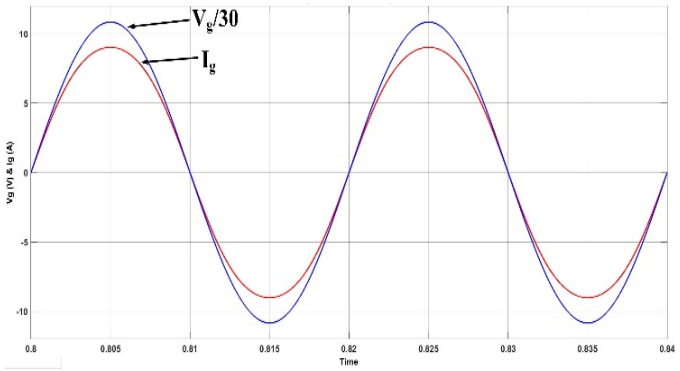

Fig. 12. Magnified Version of Grid Current and Voltage taken for 2 cycles (0.8-0.84 sec) : PI Controller

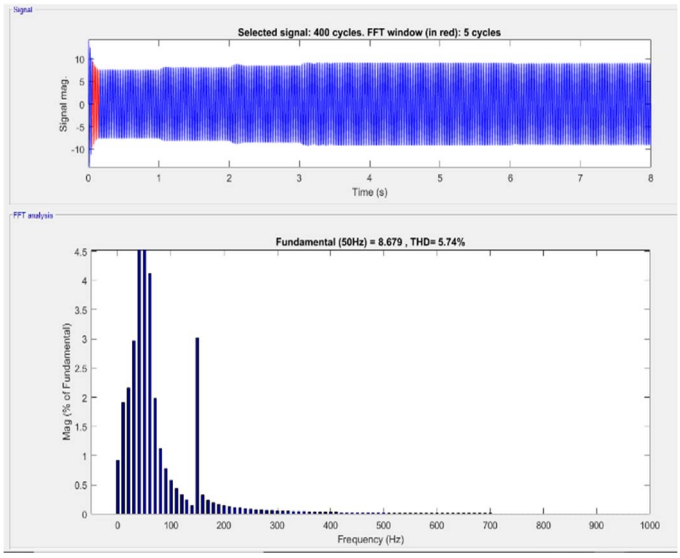

Fig. 13. THD% for the injected grid current using PI Controller : 5.74%

B. Fuzzy Logic Controller

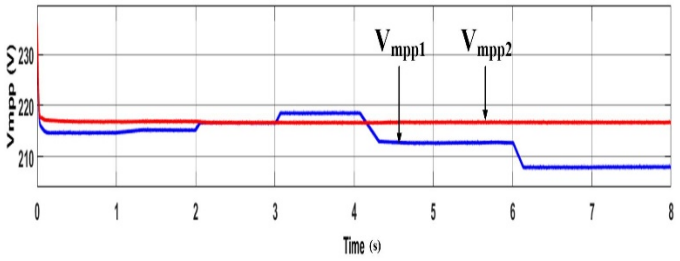

(a)

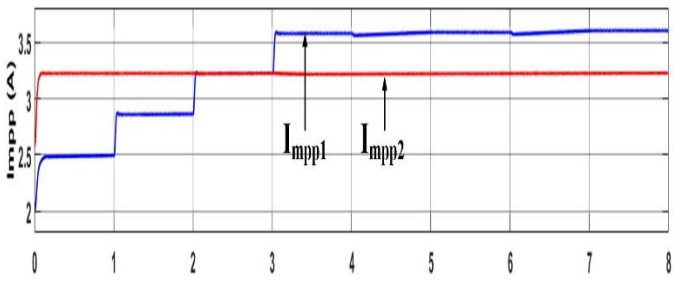

(b)

Authorized licensed use limited to: DELHI TECHNICAL UNIV. Downloaded on February 15,2021 at 09:55:08 UTC from IEEE Xplore. Restrictions apply.

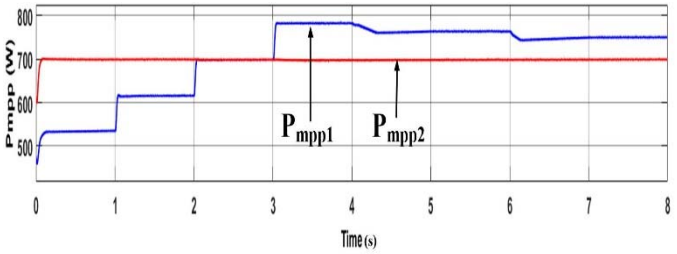

(c)

Fig. 15. Fuzzy Controller: (a) DC Voltage, (b) DC Current and (c) Power of PV1 and PV2.

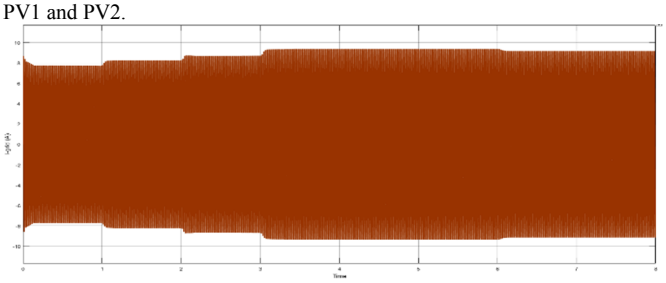

Fig. 16. Variation in Grid Current with changes in insolation and temperature levels for FLC.

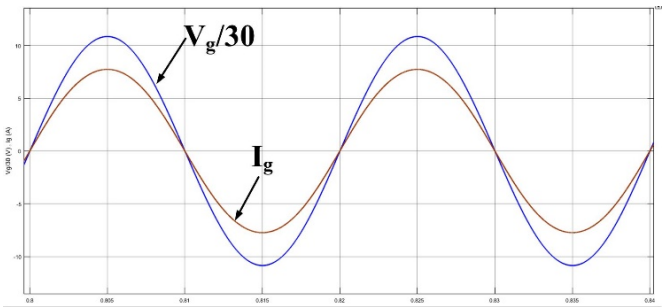

Fig. 17. Magnified Version of Grid Current and Voltage taken for 2 cycles (0.8-0.84 sec): Fuzzy Logic Controller.

It can be concluded from Fig. 16. that v_g and i_g are in phase and hence the inverter is working with unity power factor.

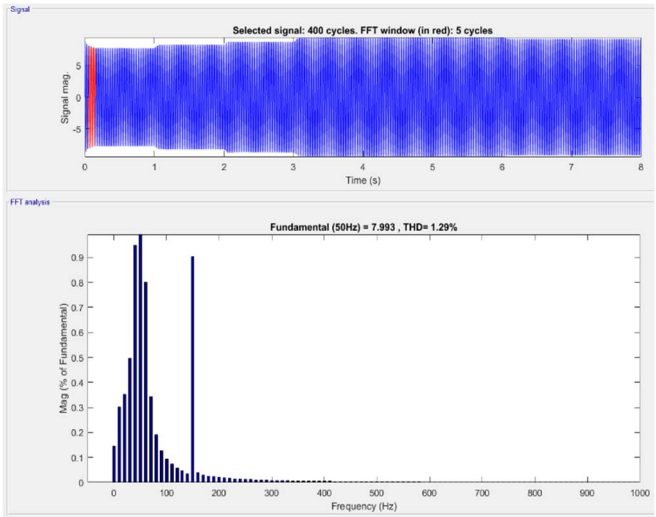

Fig. 18. THD% for the injected grid current using FLC: 1.29%

The results for the comparison of the two controllers have been tabulated in Table IV.

TABLE IV. COMPARISON OF CONTROLLERS

CONTROLLER / PARAMETER	SETTLING TIME(Vmpp1) (4-6sec)	THD% (Injected Grid Current)
CONVENTIONAL PI CONTROLLER [7]	1 sec	5.74%
FUZZY LOGIC CONTROLLER	0.3 sec	1.29%

V. CONCLUSION

A single stage inverter serving two PV panels which is connected to the grid has been presented in this paper. It is ensured with the control scheme that the two PV panels are operated at their maximum power point. The control scheme has been derived using a conventional Proportional Integral (PI) and Fuzzy Logic controller (FLC) and it is concluded that the FLC is fast as shown in Table IV. The settling time for FLC is smaller than the PI controller. The THD% for the injected grid current has also been compared for both the controllers and it has been concluded that the FLC provides better THD result of 1.29% while the PI controller gives a THD of 5.74%.

REFERENCES

[1] S. Jain and V. Agarwal, "A Single-Stage Grid Connected Inverter Topology for Solar PV Systems With Maximum Power Point Tracking," in IEEE Transactions on Power Electronics, vol. 22, no. 5, pp. 1928-1940, Sept. 2007.

[2] F. S. Kang, S. Cho, S. J. Park, C. U. Kim, and T. Ise, "A new control scheme of a cascaded transformer type multilevel PWM inverter for a residential photovoltaic power conditioning system," Solar Energy, vol. 78, no. 6, pp. 727–738, 2005.

[3] T. J. Liang, Y. C. Kuo, and J. F. Chen, "Single-stage photovoltaic energy conversion system," Proc. Inst. Elect. Eng., vol. 148, no. 4, pp. 339–344, 2001.

[4] Y. Chen and K. Ma-Smedley, "A cost-effective single-stage inverter with maximum power point tracking," IEEE Trans. Power Electron., vol. 19, no. 5, pp. 1289–1294, Sep. 2004.

[5] F. Blaabjerg, Z. Chen, and S. B. Kjaer, "Power electronics as efficient interface in dispersed power generation Systems," IEEE Trans. Power Electron., vol. 19, no. 5, pp. 1184–1194, Sep. 2004.

[6] S. B. Kjaer, J. K. Pedersen, and F. Blaabjerg, "A review of single-phase grid-connected inverters for photovoltaic Modules," IEEE Trans. Ind. Appl., vol. 41, no. 5, pp. 1292–1306, Sep./Oct. 2005.

[7] S. Dutta, D. Debnath and K. Chatterjee, "A Grid-Connected Single-Phase Transformerless Inverter Controlling Two Solar PV Arrays Operating Under Different Atmospheric Conditions," in IEEE Transactions on Industrial Electronics, vol. 65, no. 1, pp. 374-385, Jan. 2018.

[8] T. Kerekes, R. Teodorescu, P. Rodriguez, G. Vazquez, and E. Aldabas, "A new high-efficiency single-phase transformerless PV inverter topology," IEEE Trans. Industrial Electronics, vol. 58, no. 1, pp. 184-191, Jan. 2011.

[9] S. V. Araujo, P. Zacharias, and R. Mallwitz, "Highly efficient singlephase transformerless inverters for grid-connected photovoltaic systems," IEEE Trans. Industrial Electronics, vol. 57, no. 9, pp. 3118- 3128, Sep. 2010.

[10] M. A. Hannan, Z. A. Ghani, M. M. Hoque, P. J. Ker, A. Hussain and A. Mohamed, "Fuzzy Logic Inverter Controller in Photovoltaic Applications: Issues and Recommendations," in IEEE Access, vol. 7, pp. 24934-24955, 2019.

Authorized licensed use limited to: DELHI TECHNICAL UNIV. Downloaded on February 15,2021 at 09:55:08 UTC from IEEE Xplore. Restrictions apply.

Power Gated ECRL Adiabatic Logic Based Optimized Two-Input Multiplexer

Aarushi Mann[1]
Department of Electronics and Communication
Delhi Technological University, Delhi, India
aarushimann36dtu@gmail.com

Naman Malhotra[2]
Department of Electronics and Communication
Delhi Technological University, Delhi, India
naman16malhotra@gmail.com

Abhishek Wadhwa[3]
Department of Electronics and Communication
Delhi Technological University, Delhi, India
wahabhi@gmail.com

Neeta Pandey[4]
Department of Electronics and Communication
Delhi Technological University, Delhi, India
n66pandey@rediffmail.com

2020 IEEE 17th India Council International Conference (INDICON) | 978-1-7281-6916-3/20/$31.00 ©2020 IEEE | DOI: 10.1109/INDICON49873.2020.9342133

***Abstract*- In this paper, the effect of header and footer power gating techniques is examined in the context of Efficient Charge Recovery Logic (ECRL) based two input multiplexer (MUX). These power gating methodologies have been successful in mitigating the power dissipated through the conventional adiabatic circuits. The functionality and efficacy of the circuits designed using MUX are examined through simulations in Tanner tool wherein 32 nm PTM models are used. The effect of supply voltage, load capacitance and frequency of the power clock signal is investigated on power dissipation. The results illustrate that the header gated ECRL based MUX consumes more power in the awake state. On the other hand, there is a significant power saving in the idle state.**

Keywords- Adiabatic logic, ECRL, Header Gating, Footer Gating, Multiplexer Power Efficient Circuits, Power Gating

I. INTRODUCTION

The ever-growing usage of modern portable electronic gadgets like smart-phones, laptops and tablets, has led to sleeker and thinner designs with every new generation having lightning fast data computations and minimal amount of heating, thereby making minimization of power dissipation an integral part of VLSI design. Latest technologies have been focusing on putting a larger number of transistors on a single chip but as feature size is scaled down, area power density continues to increase.

The CMOS, most widely used and popular, logic family suffers from three main factors of power dissipation- dynamic (switching activity), static (idle) and short circuit. As the input frequency increases, the power dissipated from the circuits also increases [1]. Nowadays, electronic devices are designed to operate at high frequencies for fast operations thus, subjected to increased power dissipation [2] and various research works have been carried out to minimize it. The adiabatic logic family is capable of reducing power dissipation beyond the limit established by static CMOS [3]. It works on four-phase trapezoidal power clock and is based on the principle of charge recovery from the load capacitance [3].

With increase in the functionality and usage of electronics in modern life, their design is now more intricate and time consuming, hence a modular approach has been employed in modern circuit designing, where many different circuits combine and function as a complete device [4]. All these subparts or modules are not active concurrently, hence can be switched off when not needed by employing power gating; this further minimizes the power dissipation in the adiabatic logic circuits. Two different power gating methods, header and footer gating are investigated in context of Efficient Charge Recovery Logic (ECRL) adiabatic logic family [5]. The logic gates have been simulated and analyzed using ECRL based two-input multiplexer (MUX). The MUX is a universal circuit i.e., it can be used to design all combinational circuits by varying the inputs and the select lines of the MUX [6]. It is a combinational circuit wherein one of the 'n' given data inputs is selected and routed to the output [7].

This paper is structured as follows. Section I dealt with introduction and vision of this paper. Preliminaries are discussed in Section II as follows: ECRL adiabatic logic and the power gating techniques. The logic gates' design using two input MUX is evaluated in section III. Section IV comprises of functional verification and the power consumption analysis. It also presents the performance evaluation of the circuits. The conclusions and future scope have been mentioned in the fifth section. The references have been provided in the last section.

II. PRELIMINARIES

The term 'adiabatic' originates from the field of thermodynamics and describes a process where energy exchange does not take place with the surroundings leading to no energy loss [3]. This has motivated researchers to work on adiabatic logic circuits. Various adiabatic logic families like, Positive Feedback Adiabatic Logic (PFAL) [8], Efficient Charge Recovery Logic (ECRL) [9], Modified Positive Feedback Adiabatic Logic (MPFAL) [10], Diode Feedback Adiabatic Logic (DFAL) [11], Split Charge Recovery Logic (SCRL) [12] have been suggested in literature for improvement in power dissipation.

A. Efficient Charge Recovery Logic (ECRL)

ECRL, for its flexibility and simplicity, is a popular adiabatic family which provides potent reduction in power dissipation. It is a quasi-static and differential logic using two PMOS as the latch while the NMOS trees as the pull-down networks for realizing different functions. Figure 1(a) depicts the generic block of ECRL [13], in which the logic function F and its complement $\overline{F}$ are implemented using only NMOSs as pull-down networks alongside the two cross coupled PMOS as pull up networks which drive the two complementary outputs of the circuit. It requires presence of dual nature of input and creates dual nature of output as well, hence increasing its flexibility [14]. The V_{CLK} mentioned in Fig.1(a) is a four-phase trapezoidal power clock. Figure 1(b) depicts the four sections of the power clock, Evaluate, Hold, Recovery and Wait.

978-1-7281-6916-3/20/$31.00 ©2020 IEEE

Authorized licensed use limited to: DELHI TECHNICAL UNIV. Downloaded on February 15,2021 at 09:53:21 UTC from IEEE Xplore. Restrictions apply.

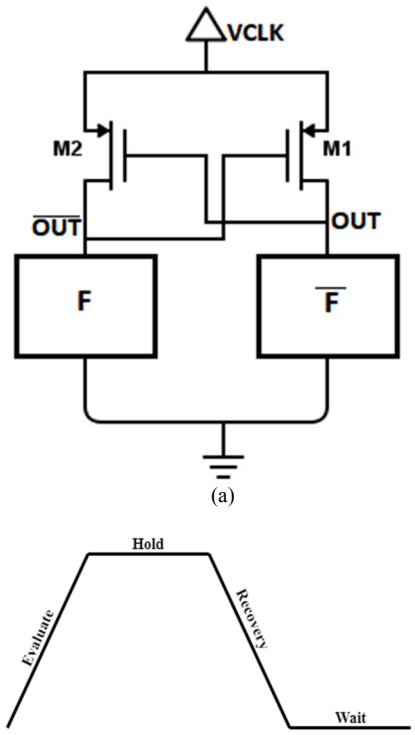

Fig.1. (a) Generic Block Diagram of ECRL
(b) power clock

B. Gated ECRL

Various methods have been utilized to further reduce power dissipation in adiabatic circuits, like transistor sizing [15], technology scaling [16] and power gating [17]. This research work discusses the power gating in a detailed fashion; a methodology of turning off or putting the circuits in sleep or idle state when they are not required. In order to accomplish power gating, the circuit is segregated from the any one of the power rails by introducing sleep state control transistors between the circuit and power rails [18]. When the sleep transistors are inactive, the power supply at V_{DD} across the function block will be collapsing towards the middle. As a result, the voltage difference across the transistor gate as well as source and drain is decreased, which reduces the leakage significantly [5].

Figure 2 shows a general power gated ECRL logic block, where supply rails can be isolated using Header or footer gating. A transmission gate (TG) is used in the header circuitry while the footer makes use of a single NMOS transistor. As the power clock switches from high (V_{DD}) to low (0V) and vice versa every period, hence the header sleep state control unit is a transmission gate which passes both a strong high (V_{DD}) and a strong low (0V), which enables the node N1 to follow the power clock when the circuit is in awake state and is left floating otherwise.

Similarly, footer sleep state control unit passes a strong low (0V) as it isolates the circuit from ground, therefore a NMOS (M5) connected between the pull down network and ground functions as the footer. In the awake state the gated virtual ground at node N2 is at a low (0V) level and left floating in sleep state.

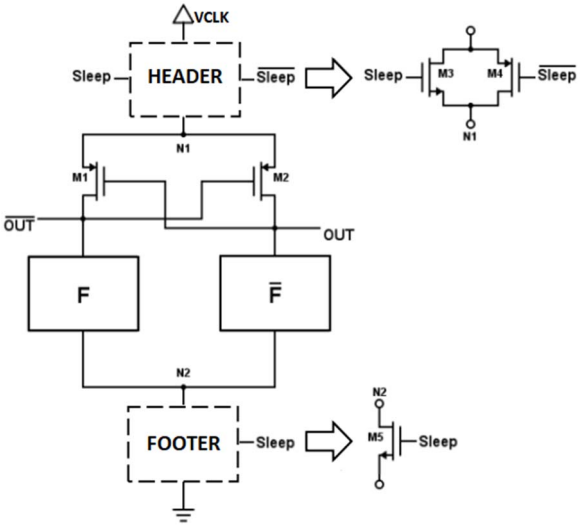

Fig.2. Generic Block Diagram of Gated ECRL

III. Multiplexer Implementation Using ECRL Variants

The block diagram of ECRL based MUX depicted in Fig. 3, has two inputs (and their complements) and one select line. Equation (1) is the governing equation of the mentioned two-input MUX.

$$(1)\quad OUT = X1.\overline{SELECT} + X2.SELECT$$
$$(2)\quad \overline{OUT} = X1.\overline{SELECT} + X2.SELECT$$

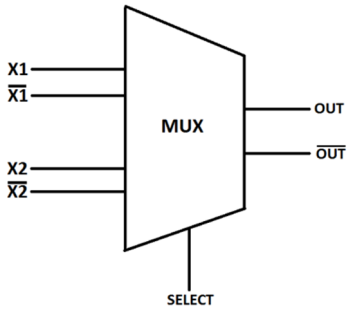

Fig.3. Block Diagram of ECRL based Multiplexer

The ECRL based multiplexer is shown below in Fig.4 (a) [19]. Figures 4(b) and 4(c) represent the header and footer gated variants of Fig. 4(a). The NMOSs M3, M4, M5 and M6 act as pull down network for the output node $\overline{OUT}$ and M7, M8, M9 and M10 for the output node OUT and similarly M1 and M2 are the pull up networks for $\overline{OUT}$ and OUT output nodes respectively.

Authorized licensed use limited to: DELHI TECHNICAL UNIV. Downloaded on February 15,2021 at 09:53:21 UTC from IEEE Xplore. Restrictions apply.

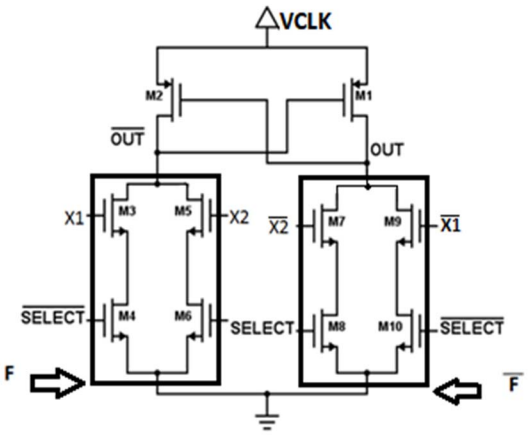

(a)

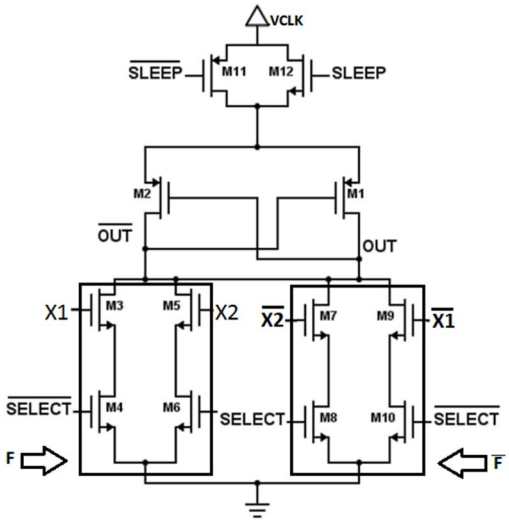

(b)

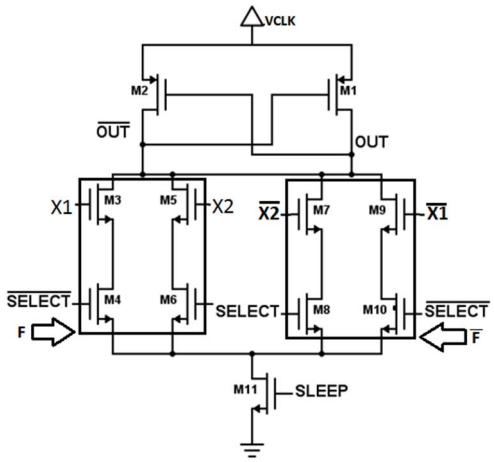

(c)

Fig.4. (a) ECRL based Multiplexer and its (b) header and (c) footer gated variants

The universal nature of MUX has been exploited in designing basic types of logic gates such as, NOT, NAND, NOR and XNOR along with their respective complements, BUFFER, AND, OR and XOR [19]. Logic gates are the rudimentary building blocks of digital circuits. They are utilized to realize various logic functions and are a major part of numerous Boolean expressions. The input combinations for realizing all logic gates employing the above-mentioned MUX have been summarized in the Table I.

TABLE I. INPUT COMBINATIONS FOR ECRL BASED MUX FOR REALIZING LOGIC GATES

SELECT	X1	X2	OUT	$\overline{OUT}$
X	$\bar{X}$	$\bar{X}$	NOT	BUFFER
Y	Y	X	NAND	AND
Y	X	Y	NOR	OR
Y	X	$\bar{X}$	XNOR	XOR

IV. SIMULATION RESULTS

The following section delineates the functional verification of the ECRL based MUX and its gated variants. The technology node of 32 nm PTM CMOS is considered along with the trapezoidal power clock of frequency 200MHz. The aspect ratio of MOSFETs employed for simulation purposes in this paper is W/L= 115n/32n. The simulations have been performed for all three ECRL variants of the MUX circuit.

A. Functional Verification Of MUX

Figure 5 showcases the transient response of ECRL based MUX. As seen in the graph when SELECT is low (high) the input X1 (X2) is routed to the output, thereby verifying the functionality of ECRL based MUX.

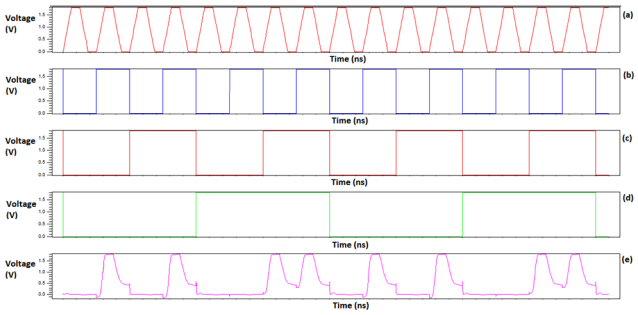

Fig.5. Transient response of ECRL based MUX and the waveforms of(a) Power clock (b) Input X1, (c) Input X2, (d) Select Signal and(e) Output

The transient response of ECRL based footer gated MUX is depicted in Fig. 6. The simulation waveforms highlights that the circuit functions as a MUX for high on Sleep and the output nodes are in a floating state otherwise (sleep/idle state). In the idle state there is no discharging path therefore the output node rises in the hold state of the four phase power clock and equilibrates at a value of V_{DD}-$|V_{tp}|$, where V_{tp} corresponds to the PMOS threshold voltage.

Authorized licensed use limited to: DELHI TECHNICAL UNIV. Downloaded on February 15,2021 at 09:53:21 UTC from IEEE Xplore. Restrictions apply.

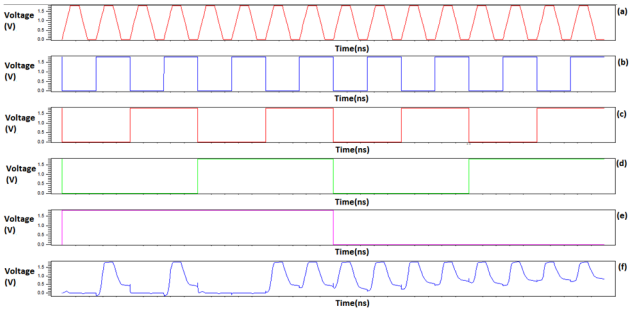

Fig.6. Transient response of ECRL based MUX and the waveforms of (a) Power clock (b) Input X1, (c) Input X2, (d) Select Signal, (e) sleep signal and (f) Output waveform

Figure 7 depicts the transient response of ECRL based header gated MUX. As observed in the simulation, the circuit works as a MUX in awake state and output nodes remain low/discharged in the sleep state.

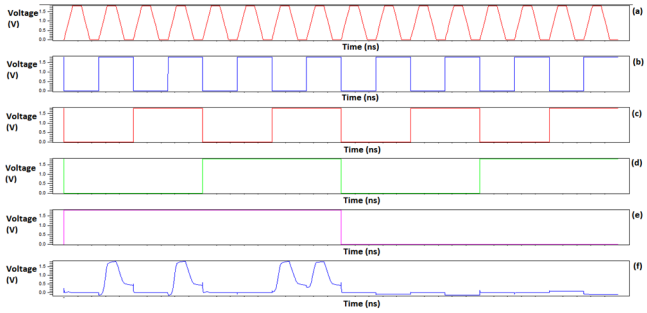

Fig.7. Transient response of ECRL based MUX and the waveforms of (a) Power clock (b) Input X1, (c) Input X2, (d) Select Signal, (e) sleep signal and (f) Output

B. *Impact of Load Capacitance Variation on Power Dissipation*

In this section, the impact of capacitance variation is examined on power dissipation for ungated, footer sleep, footer awake, header sleep and header awake state of the circuit with power supply of 1V and input frequency of 200MHz. The load capacitance has been varied from 10fF to 50fF in a step of 10fF. The observations are summarized in Fig. 8.

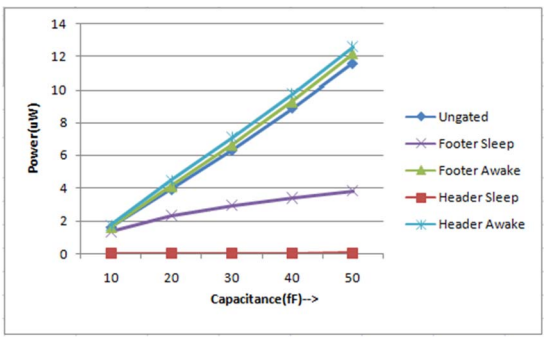

Fig.8. ECRL based MUX Power Dissipation w.r.t Load Capacitance

Figure 8 clearly displays that as the load capacitance increases, the power dissipation also increases. Power dissipated in footer gated circuit (when active i.e. awake) is more than its ungated counterpart throughout the range of capacitance. This is due to an extra transistor in the circuitry. Similarly, when the header gated circuit is awake it has two more transistors than ungated hence has more power dissipation than both footer and ungated topology. When header circuit is idle due to the absence of four phase clock signal, there is no switching of the output node value in the circuit, henceforth the power dissipation is negligible. Whereas, for the footer circuit, in idle state, the switching at the output node due to the presence of VCLK, is equilibrating due to the lack of discharging path, as discussed in section A. Thus, it has significantly more power consumption than in header asleep but less than that in the footer awake through the range of load capacitance.

C. *Impact Of Power Supply Variation On Power Dissipation*

This subsection showcases the power dissipation analysis by varying the power clock from 0 to V_{DD} where V_{DD} has been varied from 0.8V to 1.2V in the steps of 0.1V. The input frequency and load capacitance are kept at 200MHz and 10fF respectively. The observations are summarized in Fig. 9 which clearly illustrates that there is an upward trend in the power dissipated as the supply voltage increases. A similar trend is noticed for all awake circuits at lower voltage except header gated circuits which have quite minimal power dissipation throughout the voltage range (when in idle state). The header awake circuit has highest power dissipation. The footer gated circuit, though, has a significant power dissipation in sleep mode, the power dissipation in the awake state is less than the header gated and closer to the power dissipation of the ungated counterpart.

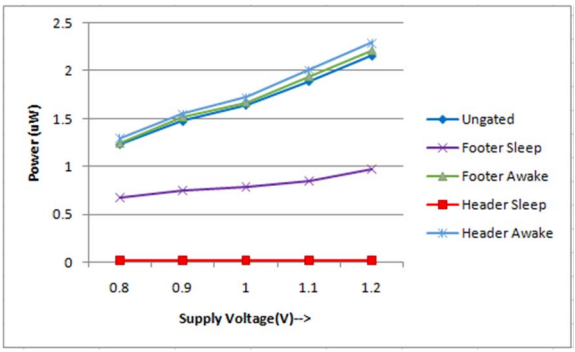

Fig.9. ECRL based MUX Power Dissipation w.r.t Power Supply

D. *Impact Of Frequency Variation On Power Dissipation*

In this subsection the power dissipation analysis has been performed over the range of 10MHz to 200MHz of input frequency wherein the load capacitance and supply voltage has been kept as 10fF and 1V respectively. Figure 10 details out the results graphically. The power dissipation demonstrates an upward trend with the increase in the input frequency.

Authorized licensed use limited to: DELHI TECHNICAL UNIV. Downloaded on February 15,2021 at 09:53:21 UTC from IEEE Xplore. Restrictions apply.

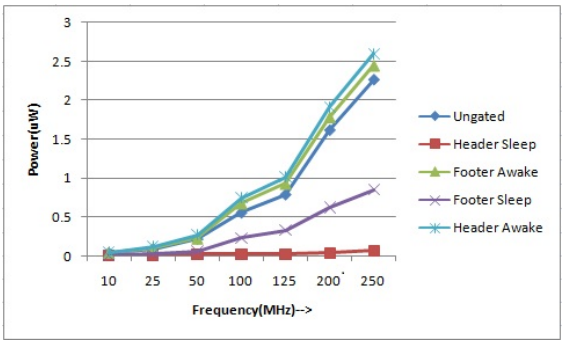

Fig.10. ECRL based MUX gate Power Dissipation w.r.t Frequency

Due to no switching the header gated circuit, idle mode, have negligible power dissipation and possess highest power consumption, when awake. Footer gated circuits although have a significant power dissipation in sleep or idle state yet the power dissipation in awake state is less than that in the header gated state. It is closer to the power consumed in the ungated circuit.

E. Further Analysis

The NAND/AND, NOR/OR and XOR/XNOR gates had been successfully implemented; simulated and verified for their functionality using two input ECRL based MUX. The simulation results for the power dissipation with respect to load capacitance, supply voltage and input frequency were observed similar to the deductions drawn from figures 5 to 9. The simulation results have not been shown in the paper for the sake of brevity.

V. CONCLUSION

In this paper ECRL based two input MUX circuit has been implemented employing both header and footer power gated and ungated design methodologies. Since, the power consumption is almost negligible in header sleep state, thus the blocks which operate majorly in sleep mode can employ this gating topology. On the other hand, the circuits which function more in the active mode can utilize footer gating for minimal power consumption overhead in active state. Furthermore, designs which have critical area constraints can opt footer gating to achieve power gating with minimal increase in the area requirements. The performance of the circuits is evaluated under different simulation criterion. The gated counterparts of the ECRL result in better power analysis for high input frequency, high load capacitance and high power supply voltages. It has been observed from the simulation results discussed in section IV, that power dissipation in header and footer gated variants of MUX is 9-17% and 5-14% of their ungated counterparts respectively. However, in sleep state there is a significant power saving of approximately 99% in header gated MUX and 70% in footer gated MUX. Henceforth, it is concluded that the gated variant of ECRL based MUX circuit shows noteworthy power saving in sleep state.

REFERENCES

[1] J. M. Rabaey, A. Chandrakasan and B. Nikolic, Digital Integrated Circuits, A Design Perspective, Second Edition, 2003.

[2] N. Nitish, N. Pandey, R. Pandey and K. Gupta, "DFAL based implementation of frequency divider-by-3," Annual IEEE India Conference (INDICON), pp. 1-6, 2015.

[3] P. Teichmann, Adiabatic Logic in Future Trend and System Level Perspective, Springer Series in Advance Microelectronics, 2012.

[4] K. Zhang, "Challenges and opportunities in nano-scale VLSI design", IEEE VLSI-TSA International Symposium on VLSI Design, Automation and Test, pp. 6-7, 2005.

[5] W. Morell and A. Srivastava, "Evaluation of Four Power Gating Schemes Applied to ECRL Adiabatic Logic", in 61st International Midwest Symposium on Circuits and Systems (MWSCAS), 2018, pp. 1012-1015.

[6] M. Mano and M. D. Ciletti, Digital Design, With an Introduction to the Verilog HDL, 5th ed., pp. 158-164 2013.

[7] R.V. Anugraha, D. S. Durga, and R. Avudaiammam, "Design and performance analysis of 2:1 multiplexer using multiple logic families at 180 nm technology", in 2nd IEEE International Conference on Recent Trends in Electronics, Information & Communication Technology, pp. 1341-1345, 2017.

[8] S. Machanooru and N. Bandi, "A novel low power high speed positive feedback adiabatic logic", in International Conference on Innovations in Information, Embedded and Communication Systems, pp. 1-5, 2017.

[9] M. L. Keote and P. T. Karule, "Design and implementation of energy efficient Adiabatic ECRL and basic gates", in International Conference on Soft Computing Techniques and Implementations, pp. 87-91, 2015.

[10] S. P. S. Kushawahaand and T. N. Sasamal, "Modified positive feedback adiabatic logic for ultra-low power VLSI", in International Conference on Computer, Communication and Control, pp. 1-5, 2015.

[11] V. Grover, V. Gosain, N. Pandey and K. Gupta, "Arithmetic Logic Unit Using Diode Free Adiabatic Logic and Selection Unit for Adiabatic Logic Family", in 5th International Conference on Signal Processing and Integrated Networks, pp. 777-781, 2018.

[12] S. D. Kumar and S. K. N. Mahammad, "A novel adiabatic SRAM cell implementation using split level charge recovery logic", in 19th International Symposium on VLSI Design and Test, pp. 1-2, 2015.

[13] A. K. Bakshi and M. Sharma, "Design of basic gates using ECRL and PFAL", in International Conference on Advances in Computing, Communications and Informatics, pp. 580-585, 2013.

[14] A. Mondal, A. Chowdhury, S. Mal, A. Podderand and M. Chanda, "Analysis of adiabatic ECRL NAND/NOR for ultra-low power near-threshold computing", Devices for Integrated Circuit, pp. 456-461, 2017.

[15] M. Borah, R.M. Owens and M.J. Irwin, "Transistor Sizing for Low Power CMOS Circuits", IEEE

Authorized licensed use limited to: DELHI TECHNICAL UNIV. Downloaded on February 15,2021 at 09:53:21 UTC from IEEE Xplore. Restrictions apply.

Transactions on Computer-Aided Designed of Integrated Circuits and Systems, pp. 665-671, 1996.
[16] Z. Chen, J. Shott, J. Burr, J.D. Plummer, "CMOS technology scaling for low voltage low power applications", in Proceedings of 1994 IEEE Symposium on Low Power Electronics, pp. 56-57, 1994.
[17] K. K. Sahu, Adiabatic Logic Design for Low Power VLSI Applications, 111EI0259, 2014-2015.
[18] P. Teichmann, J. Fischer and S. Henzler, Power clock Gating in Adiabatic Logic Circuits, Proc. PATMOS, pp. 638–646, 2005.
[19] A. Kumar and M. Sharma, "Design and analysis of Mux using adiabatic techniques ECRL and PFAL", in International Conference on Advances in Computing, Communications and Informatics, pp. 1341-1345, 2013.

Authorized licensed use limited to: DELHI TECHNICAL UNIV. Downloaded on February 15,2021 at 09:53:21 UTC from IEEE Xplore. Restrictions apply.

Profit Maximization of Multiple Active Distribution Networks Using a Fuzzy Based Approach

Avirup Maulik
Department of Electrical Engineering
Delhi Technological University
Delhi, India
avirupmaulik@gmail.com

Debapriya Das
Department of Electrical Engineering
Indian Institute of Technology
Kharagpur, India
ddas@ee.iitkgp.ac.in

2020 IEEE 17th India Council International Conference (INDICON) | 978-1-7281-6916-3/20/$31.00 ©2020 IEEE | DOI: 10.1109/INDICON49873.2020.9342162

***Abstract*—This paper proposes a novel fuzzy multi-objective approach for finding the economic operating point in an active distribution network comprising multiple utilities in a deregulated environment. Post-deregulation, different utilities in a distribution network compete for maximizing their profit and do not share sensitive information like generator cost characteristics with other utilities. Thus, a central optimal power flow program is no longer relevant in a deregulated environment. Hence, we need to apply an algorithm that individually solves the economic dispatch problem of each utility while yields a trade-off solution agreeable to all the concerned entities. In the algorithm proposed in this paper, we have formulated a multi-objective optimization problem taking the individual profits of different utilities as the objectives. The objectives are then translated into a fuzzy domain and solved using a particle swarm optimization algorithm. The proposed algorithm is validated in a case study.**

***Keywords*—profit maximization, economic dispatch, deregulation, fuzzy domain**

I. Introduction

For optimal operation of an active distribution network, proper co-ordination between the main grid and distributed generation (DG) units in the microgrid is imperative. The optimal operation of a microgrid is carried out by a smart energy management system (SEMS). An EMS calculates and provides the necessary voltage and power set-points to all the DG units for optimal operation of the microgrid. Several approaches for optimal functioning of a microgrid have been proposed in the literature [1]–[10]. Although many studies on the economic operation of the distribution system and microgrids (MGs) have been reported in the literature, research on the economic operation of an active distribution network considering deregulated environment are few. Solving the economic dispatch problem before and after deregulation of electricity markets are quite different from the following aspect:

Before deregulation, all the DG units present in an active distribution network belonged to a single utility. Therefore, a central optimal power flow (COPF) used to be formulated and solved. After deregulation of the electricity market, multiple microgrids and distribution companies (DISCOs) work in tandem to feed power to a single distribution system. These utilities (microgrids and DISCOs) have different ownerships and therefore are administratively and operationally independent entities. They compete for maximizing their profits and do not share information like DG unit cost characteristics. At the same time, the utilities collaborate to feed the total load in the distribution network.

978-1-7281-6916-3/20/$31.00 ©2020IEEE

Therefore, a COPF program for overall profit maximization of the distribution network is no longer relevant under a deregulated environment. Rather, we require an algorithm that independently solves the economic dispatch problem of each utility, but at the same time yields a trade-off solution acceptable to all stakeholders. Modeling of such a deregulated distribution network comprising multiple utilities using "systems of system" (SoS) approach has been presented in [11]. A solution methodology based on "analytical target cascading" (ATC) is also presented in the same paper. The above method requires the use of vectors of multipliers to solve the problem. But, vectors of multipliers are sensitive parameters, and their choices significantly affect the accuracy and convergence of the algorithm. However, choices of the values of vectors of multipliers are not unique but depend on the system parameters. The contributions of this paper are the following: 1) In this paper, a fuzzy multi-objective approach based technique is presented as an alternative to the ATC based approach for solving the economic dispatch problem of an active distribution network under a deregulated environment. 2) The proposed method does not involve any sensitive parameter that affects the accuracy and/or convergence of the algorithm. Therefore, the proposed method overcomes the shortcomings of the ATC based approach. 3) The proposed method is much simpler to code in comparison to the ATC approach.

The proposed method is validated on a test distribution system comprising two microgrids and one DISCO. A comparison of the results with the ATC approach is also presented. The organization of the rest of the paper is as follows. In section II, we have introduced the mathematical formulation, followed by the modeling of the problem in the fuzzy domain in section III. The test system and simulation results are presented in section IV, followed by conclusions in section V.

II. Mathematical formulation

For a microgrid n interacting with a DISCO, the optimization problem can be formulated as follows:

Authorized licensed use limited to: DELHI TECHNICAL UNIV. Downloaded on February 15,2021 at 10:06:23 UTC from IEEE Xplore. Restrictions apply.

A. Optimization problem for microgrids

A microgrid n tries to minimize it's expense minus its earnings. It is mathematically given as:

$$Min \sum_{i \in MG_n} f_i.(Pg_i) - \sum_{j \in MG_n} C_n.PL_j - C_{nd}.P_{nd} \quad (1)$$

$fi(.)$ is the fuel cost of power generation, and Pg_i is the active power generation of the i^{th} unit. C_n is the retail power price in the area of microgrid n, PL_j is the j^{th} load power demand. C_{nd} is the price of power exchange and the active between microgrid n and the DISCO, P_{nd} is the power exported by microgrid n to DISCO. The first term of (1) represents the fuel cost of the DG units in the microgrid; the second term represents the earnings of the microgrid by selling power to its retail customers; the third term represents the earnings of the MG by selling power to the DISCO (if the MG purchases electricity from the DISCO, P_{nd} will have negative value).

B. Optimization problem for DISCO

The DISCO tries to minimize it's expense minus it's earnings. It is mathematically given as:

$$Min \sum_{i \in DISCO} f_i.(Pg_i) - \sum_{j \in DISCO} C_d.PL_j + \sum_{n=1}^{NMG} C_{nd}.P_{nd} + C_{ID}.P_{ID} \quad (2)$$

C_d is the retail power price in DISCO, C_{ID} is the wholesale power price, P_{ID} is the power purchased by DISCO from independent system operator (ISO). The first term of (2) represents the fuel cost of the DG units in the DISCO; the second term represents the earnings of the DISCO by selling power to its retail customers; the third term represents the expenditure incurred by the DISCO in purchasing power from the MGs (if the DISCO sells electricity to the MG n, P_{nd} will have negative value); the fourth term represents the cost of power purchase from the independent system operator (ISO).

C. System constraints

1) Power balance constraint of each microgrid:

$$\sum_{i \in MG_n} Pg_i - \sum_{j \in MG_n} PL_j - P_{nd} = 0 \forall n \quad (3)$$

2) Power balance constraint of DISCO:

$$\sum_{i \in DISCO} Pg_i - \sum_{j \in DISCO} PL_j + \sum_{n=1}^{NMG} P_{nd} + P_{ID} = 0 \quad (4)$$

3) Generation limits of each DG unit:

$$Pg_i^{min} \leq Pg_i \leq Pg_i^{max} \quad (5)$$

4) Power exchange limits between utilities:

$$P_{nd}^{min} \leq P_{nd} \leq P_{nd}^{max} \quad (6)$$

5) Power exchange limit between DISCO and ISO:

$$P_{ID}^{min} \leq P_{ID} \leq P_{ID}^{max} \quad (7)$$

$()^{min}$ and $()^{max}$ represent the minimum and maximum limits of the quantity, respectively.

III. Modeling of active distribution network for solution using fuzzy multi-objective PSO

The given problem of maximizing the profit of individual microgrids and DISCO can be considered as a multi-objective optimization problem, where each objective is to maximize the profit of each autonomous utility. We have used a "fuzzy max-min" approach to solving the problem. We have assigned a linear membership function to each objective for going from the crisp to the fuzzy domain. The membership value can take any value between zero and unity. The membership functions are described below:

A. Membership functions for profit maximization of microgrids

Calculation of the profit of microgrid n ($n = 1, 2, \cdots NMG$, NMG is the number of MGs), i.e., $profit_n$, is carried out using the negative of (1) and translated to the following linear membership function:

$$\begin{aligned} fit_n &= 0.5.(\frac{profit_n}{profit_n^{max}}) + 0.5 \\ &: -profit_n^{max} \leq profit_n \leq profit_n^{max} \\ &= 0 : otherwise \end{aligned} \quad (8)$$

B. Membership function for profit maximization of DISCO

Calculation of $profit_{DISCO}$ is carried out using the negative of (2). The membership function of the profit for the DISCO is given by the following:

$$\begin{aligned} fit_{DISCO} &= 0.5.(\frac{profit_{DISCO}}{profit_{DISCO}^{max}}) + 0.5 \\ &: -profit_{DISCO}^{max} \leq profit_{DISCO} \\ &\leq profit_{DISCO}^{max} \\ &= 0 : otherwise \end{aligned} \quad (9)$$

C. Representation of the system variables

The proposed method uses particle swarm optimization (PSO) to solve the optimization problem [12]. The optimization problem can be mathematically represented as follows:

$$Maximize fit_n : n = 1, 2, \cdots NMG; Maximize fit_{DISCO} \quad (10)$$

Constraints given by (3) - (7) should be satisfied. A population vector X of dimension $(NPOP) \times (NMG+1)$ is formed at each iteration step, where $NPOP$ is the population size in the PSO program. Structure of the population vector X is given below:

$$X = \begin{pmatrix} x_{11} & \cdots & x_{1j} & \cdots & x_{1NMG+1} \\ \vdots & \vdots & \ddots & \vdots & \vdots \\ x_{NPOP1} & \cdots & x_{NPOPj} & \cdots & x_{NPOPNMG+1} \end{pmatrix} \quad (11)$$

Authorized licensed use limited to: DELHI TECHNICAL UNIV. Downloaded on February 15,2021 at 10:06:23 UTC from IEEE Xplore. Restrictions apply.

Algorithm 1: Proposed Algorithm

Set $IT = 0$;
Find $profit_n^{max}$ for $n = 1, 2, \ldots, NMG$ and $profit_{DISCO}^{max}$;
while $IT \leq ITMAX$ **do**
  if $IT = 0$ **then**
    MGs randomly initialize power exchanges between MGs and DISCO;
    MGs calculate (1) and (8) and convey the information to the DISCO;
    DISCO randomly generates power exchange values between DISCO and ISO;
    DISCO calculates (2) and (9);
  else
    MGs update power exchange values by position and velocity update formula;
    MGs calculate (1) and (8) and convey the information to the DISCO;
    DISCO updates power exchange value between DISCO and ISO;
    MGs DISCO calculates (2) and (9);
  end
  DISCO finds $D = Min[fit_1, fit_2, \ldots, fit_n, fit_{DISCO}]$;
  $E = max\{D\}$;
  DISCO finds local and global best;
  DISCO communicates power exchange values corresponding to the local and global best to all MGs;
  $IT = IT + 1$;
end

Here, each row stands for a member of the population. The genotype of an element of the population, say the i^{th} element of the population (represented by the i^{th} row of vector X) is illustrated below:

$$X_i = \left[x_{i1} \cdots x_{ij} \cdots x_{iNMG+1}\right] = \left[P_{i1d} \cdots P_{ijd} \cdots P_{iID}\right] \tag{12}$$

In the row vector X_i, the first NMG elements represent the power exchange between microgrids and DISCO, i.e. say the j^{th} element ($1 \leq NMG$) represents the power flow from the microgrid number j to the $DISCO$. The last element in the row vector, i.e. the $(NMG+1)^{th}$ element represents the power drawn by the DISCO from the ISO.

The elements of j^{th} column of vector X is given as:

$$Z_j = \left[x_{1j}, x_{2j}, \cdots x_{ij}, \cdots x_{NPOPj}\right]^T \tag{13}$$

For $1 \leq j \leq NMG$, this represents the power delivered by MG j to DISCO corresponding to different population members. For $j = NMG+1$, this represents the power drawn from ISO by DISCO corresponding to different population members.

D. Optimization in fuzzy environment

Solution strategy to carry out a multi-objective optimization problem using a "fuzzy max-min" composition is available in [10] and is not reiterated here for brevity. The algorithm to implement the "fuzzy max-min" approach for tackling the given problem is given below:

1) Determine the maximum possible profit $profit_n^{max}$ for each microgrid and also the maximum possible profit for DISCO $profit_{DISCO}^{max}$.
2) Each microgrid will randomly create a set of numbers(within specified limits) representing the power exchange values between the microgrid and the DISCO. Each microgrid also calculates its profit (1) and the corresponding fitness value as per (8) for each power exchange value.
3) Each microgrid communicates the set of power exchange values and the corresponding fitness function magnitudes to the DISCO.
4) DISCO also generates a random set of power exchange values (within specified limits) between DISCO and the ISO such that all the constraints are satisfied. DISCO calculates its profit for different sets of power exchange values between the microgrids, DISCO and ISO as per (2) and also finds the corresponding fitness function values as per (9).
5) DISCO finds the minimum fitness function value (of all microgrids and DISCO) for every member of the population and stores it in a vector D. The vector D contains $NPOP$ numbers of the elements. DISCO finds the maximum of D and stores it in a variable E. The objective is to maximize the value of E.
6) DISCO also finds the local best and global best members (as per PSO convention).
7) DISCO communicates the power exchange values (between a given microgrid and the DISCO) corresponding to the local best and global best member to each MG.
8) Microgrids and DISCO update the power exchange values using the velocity and position update formulas of PSO technique to get a new set of population members.
9) Convergence criteria (maximum number of iterations) is checked. If convergence is not achieved, then go back to step 3; else go to step 10.
10) Terminate the program and print the results.

The algorithm is shown in algorithm 1.

IV. Case Study

A. Test system

The test system comprises two operationally and administratively autonomous MGs and one DISCO. DISCO and MG2, both contain four (04) numbers of dispatchable DG units; whereas MG1 has three (03) numbers of dispatchable DG units. A schematic representation of the test system is shown in Fig.1. The DG unit cost characteristics are derived from cost characteristics given in [13]. The DG unit parameters are given in Table I. Loads of DISCO, MG1, and MG2 are 3.30

Authorized licensed use limited to: DELHI TECHNICAL UNIV. Downloaded on February 15,2021 at 10:06:23 UTC from IEEE Xplore. Restrictions apply.

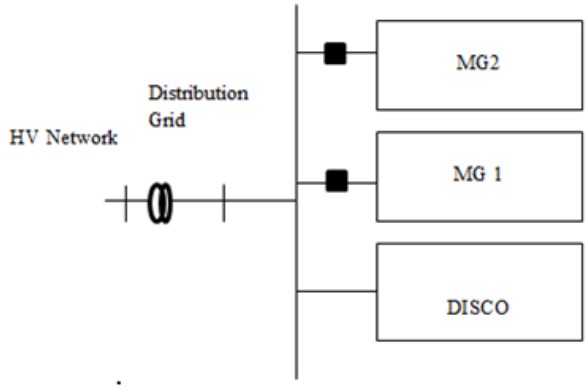

Fig. 1. A schematic representation of the test system used for simulation studies

TABLE I
PARAMETERS OF DISPATCHABLE DG UNITS

Control Area	DG No.	a ($)	b($/MWh)	c($/MWh^2)	Pmin(MW)	Pmax(MW)
DISCO	1	145.26	103.20	10.00	0.35	3.0
	2	152.39	79.20	16.67	0.60	3.0
	3	175.31	65.60	20.00	0.60	1.0
	4	10.63	68.90	72.00	0.1250	1.0
MG1	5	61.47	30.10	36.67	0.60	3.0
	6	48.08	142.50	6.67	0.15	3.0
	7	103.15	34.60	16.67	0.72	3.0
MG2	8	21.26	68.90	36.00	0.25	2.0
	9	101.59	79.20	25.00	0.40	2.0
	10	56.75	13.40	54.00	0.50	2.0
	11	40.07	142.50	8.00	0.1250	2.50

TABLE II
DG UNIT OUTPUTS BY VARIOUS METHODS: CASE 1

Control Area	DG No.	DG power outputs (MW)			
		ATC	Proposed Method	Central Optimization	Individual optimization
DISCO	1	3.00	3.00	3.00	3.00
	2	3.00	3.00	3.00	3.00
	3	2.8601	2.8444	2.8601	2.8601
	4	0.7716	0.7672	0.7716	0.7716
Total Generation		9.6317	9.6116	9.6317	9.6317
MG1	5	1.88	1.88	1.88	1.88
	6	1.91	1.91	1.91	1.91
	7	3.00	3.00	3.00	3.00
Total Generation		6.79	6.79	6.79	6.79
MG2	8	1.5756	1.5756	1.5756	1.5431
	9	2.0	2.0	2.0	2.0
	10	1.5643	1.5643	1.5643	1.5426
	11	2.4901	2.4901	2.4901	2.3438
Total Generation		7.63	7.63	7.63	7.4295

MW, 1.79 MW, and 2.63 MW, respectively. The maximum permissible limits of power exchange between each microgrid and the DISCO is 5 MW. The maximum permitted value of power exchange between the DISCO and the ISO is 50 MW.

The codes are written in MATLAB on a Core i5, 1.6 GHz laptop with 8 GB RAM. Parameters used in PSO are as follows: $c1 = c2 = 2$, initial weight $= 0.9$, final weight $= 0.4$, population size $= 60$, maximum iterations $= 50$.

B. Results and discussions

Three different cases are considered.

1) Case 1: In the first case, the retail and wholesale prices are as follows: C_n=216 \$/MWh and C_{nd}=180 \$/MWh: $\forall n = 1, 2, \cdots NMG$; C_d=216 \$/MWh; C_{ID}=180 \$/MWh. With the above values, the results obtained are given in Table II, Table III, Table IV, and Table V. Central optimization has an objective to maximize the total profit of all the DG units in the active distribution network, i.e., it does not take into account the profit or loss of the individual utilities. Therefore, central optimization applies to a pre-deregulation conventional environment, where all generators have single ownership.

TABLE III
POWER EXCHANGES BETWEEN UTILITIES BY DIFFERENT METHODS: CASE1

Utilities	Power exchanges (MW)		
	ATC	Proposed Method	Central Optimization
MG1-DISCO	5.00	5.00	5.00
MG2-DISCO	5.00	5.00	5.00
ISO-DISCO	-16.3317	-16.3116	-16.3317

TABLE IV
POWER EXCHANGES BETWEEN UTILITIES FOR INDIVIDUAL OPTIMIZATION: CASE 1

Utilities	Power exchanges (MW)		
	DISCO	MG1	MG2
MG1-DISCO	2.26	5.00	-
MG2-DISCO	-2.1346	-	4.7995
ISO-DISCO	-6.4570	-	-

When optimizations are carried out to maximize the profits of individual utilities separately, it is observed that DISCO can make a maximum profit of \$ 134.45, MG1 can earn a maximum profit of \$ 337.46, and MG2 can make a maximum profit of \$ 234.77 in the hour for the given load (see Table V). When only profit of DISCO is optimized, DISCO generates a total power of 9.6317 MW in the given hour (see Table II). It imports a power of 2.26 MW from MG1 and exports a power of 2.1346 MW to MG2 (see Table III). After feeding its area load of 3.30 MW, it also exports 6.4570 MW power to the ISO (see Table III). While this ensures maximum possible profit for DISCO and may be acceptable to MG1 (since it is earning by selling electricity to DISCO), this solution will be unacceptable to MG2, since it has to purchase power from DISCO and incur an expense on that account.

If only the profit MG1 is to be optimized, then MG1 generates a total power of 6.79 MW (see Table II). After feeding its area load of 1.79 MW, it exports a power of 5 MW to the DISCO (see Table IV). Generators in MG1 generate electricity at a relatively lower fuel cost, and therefore it generates maximum possible power without violating the system constraint. In this case, the limiting constraint is the maximum magnitude of power exchange possible between DISCO and MG1, which has a value of 5 MW. But, DISCO, for its profit maximization, has already found out that it should purchase power of 2.26 MW from MG1 (see Table II). Therefore, while this is the best possible solution for profit maximization of MG1, it may not be acceptable to DISCO if it impacts its profit-making adversely.

Again, optimization of profit of MG2 suggests that DGs in MG2 should generate 7.4295 MW (see Table II). After feeding its area load of 2.63 MW, it exports 4.7995 MW to DISCO (see Table IV). While this ensures maximum profit for MG2,

Authorized licensed use limited to: DELHI TECHNICAL UNIV. Downloaded on February 15,2021 at 10:06:23 UTC from IEEE Xplore. Restrictions apply.

TABLE V
PROFITS OF UTILITIES BY VARIOUS METHODS: CASE 1

Utilities	Profits ($)			
	ATC	Proposed Method	Central Optimization	Individual optimization
DISCO	134.43	134.43	134.43	134.45
MG1	337.41	337.46	337.41	337.46
MG2	234.53	234.77	234.53	234.77
Total	706.37	706.36	706.37	706.69

TABLE VI
DG UNIT OUTPUTS BY VARIOUS METHODS: CASE 2

Control Area	DG No.	DG power outputs (MW)		
		Proposed Method	Central Optimization	Individual optimization
DISCO	1	2.84	2.84	2.84
	2	2.424	2.424	2.424
	3	2.36	2.36	2.36
	4	0.6326	0.6326	0.6326
Total Generation		8.2566	8.2566	8.2566
MG1	5	0.60	1.88	1.88
	6	0.15	1.91	1.91
	7	1.0031	3.00	3.00
Total Generation		1.7531	6.79	6.79
MG2	8	0.344	1.2653	1.5431
	9	0.40	1.616	2.0
	10	0.7432	1.3574	1.5426
	11	0.125	1.0937	2.3438
Total Generation		1.6122	5.3324	7.4295

TABLE VII
POWER EXCHANGES BETWEEN UTILITIES BY DIFFERENT METHODS: CASE 2

Utilities	Power exchanges (MW)	
	Proposed Method	Central Optimization
MG1-DISCO	-0.0369	5.00
MG2-DISCO	-1.0178	2.7024
ISO-DISCO	-3.9019	-12.659

TABLE VIII
POWER EXCHANGES BETWEEN UTILITIES FOR INDIVIDUAL OPTIMIZATION: CASE 2

Utilities	Power exchanges (MW)		
	DISCO	MG1	MG2
MG1-DISCO	-5.00	5.00	-
MG2-DISCO	-5.00	-	4.7995
ISO-DISCO	5.0434	-	-

TABLE IX
PROFITS OF UTILITIES BY VARIOUS METHODS: CASE 2

Utilities	Profits ($)		
	Proposed Method	Central Optimization	Individual optimization
DISCO	41.07742	-134.065	219.9978
MG1	63.03095	337.4077	337.4603
MG2	43.83723	213.6421	234.7724
Total	147.9456	416.9852	792.2305

it may not be acceptable to DISCO, since it has already found out that it should sell 2.1346 MW to MG2 (see Table IV).

Therefore, it is evident that the target values of power exchanges for individual profit maximization of different utilities are all different. Therefore a mechanism needs to be developed, which gives a solution acceptable to all the stakeholders.

As per the proposed method, DISCO should generate a total power of 9.6116 MW, MG1 should generate 6.79 MW, and MG2 should generate 7.63 MW (see Table II). While power generation values obtained by the proposed method are

TABLE X
DG UNIT OUTPUTS BY VARIOUS METHODS: CASE 3

Control Area	DG No.	DG power outputs (MW)		
		Proposed Method	Central Optimization	Individual optimization
DISCO	1	3.00	3.00	3.00
	2	3.00	3.00	3.00
	3	2.8601	2.8601	2.8601
	4	0.7716	0.7716	0.7716
Total Generation		9.6317	9.6317	9.6317
MG1	5	1.88	1.88	1.88
	6	1.91	1.91	1.91
	7	3.00	3.00	3.00
Total Generation		6.79	6.79	6.79
MG2	8	1.4522	1.5756	1.2653
	9	1.8751	2.00	1.6160
	10	1.4774	1.5643	1.3574
	11	1.9034	2.4901	1.0937
Total Generation		6.7011	7.63	5.3324

TABLE XI
POWER EXCHANGES BETWEEN UTILITIES BY DIFFERENT METHODS: CASE 3

Utilities	Power exchanges (MW)	
	Proposed Method	Central Optimization
MG1-DISCO	5.00	5.00
MG2-DISCO	4.0711	5.00
ISO-DISCO	-15.4028	-16.3317

TABLE XII
POWER EXCHANGES BETWEEN UTILITIES FOR INDIVIDUAL OPTIMIZATION: CASE 3

Utilities	Power exchanges (MW)		
	DISCO	MG1	MG2
MG1-DISCO	5.00	4.2938	-
MG2-DISCO	5.0	-	2.7024
ISO-DISCO	-16.3316	-	-

TABLE XIII
PROFITS OF UTILITIES BY VARIOUS METHODS: CASE 3

Utilities	Profits ($)		
	Proposed Method	Central Optimization	Individual optimization
DISCO	315.8511	334.4291	334.4539
MG1	237.4077	237.4077	240.2732
MG2	150.7286	134.5311	159.6004
Total	703.9874	706.3679	734.3275

close to those obtained by individual optimization, the power exchange values between utilities are quite different. As per the proposed method, DISCO should purchase 5 MW from MG1 and 5 MW from MG2, and sell 16.3116 MW to ISO (see Table III). Therefore, DISCO makes a profit of $ 134.42, MG1 makes a profit of $ 337.41, and MG2 makes a profit of $ 234.53 (see Table V). These values are close to the maximum possible profits that all these utilities can make. Hence, this solution is acceptable to all stakeholders.

Since the wholesale power price and price of power exchange between DISCO and MGs are the same; DISCO agrees to purchase maximum possible power from MGs. While this makes sure that the MGs make a profit by selling maximum allowed power to the DISCO, DISCO offsets its cost of power purchase from the MGs by selling that power to ISO at the same price. Further, it is observed that the results obtained by the ATC method are similar to those obtained by the proposed method. With a central optimization, DISCO generates a total

Authorized licensed use limited to: DELHI TECHNICAL UNIV. Downloaded on February 15,2021 at 10:06:23 UTC from IEEE Xplore. Restrictions apply.

power of 9.6317 MW, MG1 generates 6.79 MW, and MG2 generates 7.63 MW (see Table II). DISCO purchases 5 MW power each from MG1 and MG2 and sells 16.3317 MW to ISO (see Table III). DISCO, MG1, and MG2 make profits of $ 134.43, $ 337.41, and $ 234.77 respectively so that the total profit of three utilities taken together is $ 706.37 (see Table V).

2) Case 2: Next, the following retail and wholesale prices are considered: C_n=216 $/MWh and C_{nd}=180 $/MWh: $\forall n = 1, 2, \cdots NMG$; C_d=216 $/MWh; C_{ID}=160 $/MWh. Results with the above power prices are given in Table VI, Table VII, Table VIII, and Table IX. The total generation of DISCO should be 8.2566 MW for maximizing the profit of the DISCO (see Table VI). It can make a maximum profit of $ 219.998 (see Table IX), and it sells 5 MW each to MG1 and MG2, while it buys 5.0434 MW from ISO (see Table VIII). It is explained by the fact that wholesale power price is lower than the retail power price, and therefore DISCO seeks to sell maximum power to MGs while buying cheap power from ISO. Individual profit maximization of MG1 advocates that MG1 should generate 6.79 MW (see Table VI) and sell 5 MW to DISCO (see Table VIII), translating into a profit of $ 337.46 for MG1 (see Table IX). Similarly, individual profit optimization of MG2 advocates that it should generate 7.4295 MW (see Table VI)and sell 4.7995 MW to DISCO (see Table VIII), bringing a profit of $ 234.77 for MG2 (see Table IX).

With the above situation, evidently optimization of MGs and DISCO leads to conflicting power exchange targets. Therefore, in this case, a trade-off solution acceptable to all the utilities is to be obtained. The use of the proposed method suggests that DISCO, MG1, and MG2 should generate 8.2566 MW, 1.7531 MW, and 1.6122 MW, respectively. DISCO sells 0.0369 MW, 1.0177 MW, and 3.9020 MW respectively to MG1, MG2, and ISO. Profits made by DISCO, MG1, and MG2 are $ 41.08, $ 63.31, and $ 43.84, respectively. The values are 18.672 %, 18.678 %, and 18.672 % respectively of their maximum possible profits. The profits as a percentage of maximum possible values are almost the same for all the utilities. Thus, the proposed method hands out a fair solution for all the utilities, and none get any undue advantage or disadvantage. Therefore, all the utilities have a level playing ground, and the solution naturally is acceptable to all.

A central optimization seeking to maximize the profit of all the DG units suggests that DISCO, MG1, and MG2 should generate 8.2566 MW, 6.79 MW, and 5.3324 MW respectively. DISCO should purchase 5 MW and 2.7024 MW power from MG1 and MG2, respectively, and it should sell 12.659 MW to ISO. It gives a total profit of $ 416.99. But, while this means that MG1 and MG2 are making profits of $ 337.41 and $ 213.64 respectively, DISCO is incurring a loss of $ 134.065. Therefore, although this solution maximizes the total profit in a conventional environment, it is not acceptable to DISCO in a deregulated scenario. Therefore, a trade-off solution obtained by the proposed method is the fair proposition.

3) Case 3: We consider the following retail and wholesale prices: C_n=216 $/MWh and C_{nd}=160 $/MWh: $\forall n = 1, 2, \cdots NMG$; C_d=216 $/MWh; C_{ID}=180 $/MWh. Results with the above power prices are given in Table X, Table XI, Table XII, and Table XIII. For maximizing the profit of DISCO only, DISCO should generate power of 9.6317 MW (see Table X). It should purchase 5 MW power each from the MGs and sell 16.3316 MW to ISO (see Table XII). It is because DISCO purchases as much power as permissible at a relatively lower price from MGs and sells it at a higher price to the ISO. The maximum profit that the DISCO can make is $ 334.45 (see Table XIII). For maximization of profit of MG1, it should generate 6.0833 MW (see Table X), and it sells 4.2938 MW to DISCO (see Table XII). Since the cost of power exchange between MGs and DISCO is relatively lower in this case, earnings by selling more power to DISCO, say 5 MW is more than offset by the cost of generation. Therefore, it intends to sell 4.2938 MW and not 5 MW. The maximum possible profit for MG1 is $ 240.27 (see Table XIII). Similarly, MG2, for its maximum profit, has to sell 2.7024 MW power to DISCO (see Table XII) and generates 5.3324 MW (see Table X). Again, it intends to sell only 2.7024 MW to DISCO due to a relatively lower power exchange cost between MG and DISCO.

In this case also, we have different targets of power exchange values between utilities, requiring a solution acceptable to all the stakeholders. Now the proposed method suggests that DISCO, MG1, and MG2 should generate 9.6317 MW, 6.79 MW, and 6.7011 MW, respectively (see Table X). DISCO purchases 5 MW and 4.0711 MW from MG1 and MG2 respectively and sells 15.4028 MW to ISO (see Table XI). Profits are $ 315.85, $ 237.41, and $ 150.73 respectively for DISCO, MG1, and MG2 (see Table XIII). The profit values are 94.44%, 98.81%, and 94.44%, respectively, of the maximum possible profits for DISCO, MG1, and MG2. All the entities get a fair and unbiased deal by the proposed method, and hence the proposed solution is acceptable to all.

With a central optimization, DISCO, MG1, and MG2 generate 9.6317 MW, 6.79 MW, and 7.63 MW (see Table X). DISCO purchases 5 MW from MG1 and 5 MW from MG2 and sells 16.3317 MW to ISO (see Table XI), making the total profit of the distribution system $ 706.37. DISCO, MG1, and MG2 individually make profits of $ 334.43, $ 237.41, and $ 134.53, respectively (see Table XIII). These are 99.99%, 98.81%, and 84.29%, respectively, of the maximum profit values for DISCO, MG1, and MG2. While this is acceptable to DISCO and MG1, MG2 may not accept this solution. Therefore, the proposed method gives a more unbiased solution satisfactory to all the utilities.

V. Conclusions

In this paper, a PSO based multi-objective optimization technique in a fuzzy framework has been proposed for profit maximization of multiple utilities with different ownerships in an active distribution network. The proposed method considers the profits of the utilities as objective functions and translates them to the fuzzy domain. Then, it uses the max-min principle to find a trade-off solution. The proposed method is free

Authorized licensed use limited to: DELHI TECHNICAL UNIV. Downloaded on February 15,2021 at 10:06:23 UTC from IEEE Xplore. Restrictions apply.

from the requirement of choice of parameters that significantly affect the results. The proposed method has been applied to a test active distribution network. Numerical results for different values of wholesale power price and inter-utility power exchange prices have been presented. It has been observed that in all the cases, the utilities are treated in an unbiased fashion.

REFERENCES

[1] A. Maulik and D. Das, "Optimal operation of microgrid using four different optimization techniques," *Sustainable Energy Technologies and Assessments*, vol. 21, pp. 100–120, 2017.

[2] E. Grover-Silva, M. Heleno, S. Mashayekh, G. Cardoso, R. Girard, and G. Kariniotakis, "A stochastic optimal power flow for scheduling flexible resources in microgrids operation," *Applied energy*, vol. 229, pp. 201–208, 2018.

[3] B. Dey and B. Bhattacharyya, "Dynamic economic and emission dispatch of large scale renewable integrated microgrids for varying loads and seasons," in *2018 2nd International Conference on Power, Energy and Environment: Towards Smart Technology (ICEPE)*. IEEE, 2018, pp. 1–6.

[4] K. Gholami and E. Dehnavi, "A modified particle swarm optimization algorithm for scheduling renewable generation in a micro-grid under load uncertainty," *Applied Soft Computing*, vol. 78, pp. 496–514, 2019.

[5] M. A. Ramli, H. Bouchekara, and A. S. Alghamdi, "Efficient energy management in a microgrid with intermittent renewable energy and storage sources," *Sustainability*, vol. 11, no. 14, p. 3839, 2019.

[6] B. Lokeshgupta and S. Sivasubramani, "Optimal operation of a residential microgrid with demand side management," in *2019 IEEE PES Innovative Smart Grid Technologies Europe (ISGT-Europe)*. IEEE, 2019, pp. 1–5.

[7] A. N'Goran, B. Daugrois, M. Lotteau, and S. Demassey, "Optimal engagement and operation of a grid-connected pv/battery system," in *2019 IEEE PES Innovative Smart Grid Technologies Europe (ISGT-Europe)*. IEEE, 2019, pp. 1–5.

[8] A. Maulik and D. Das, "Optimal operation of a droop-controlled dcmg with generation and load uncertainties," *IET Generation, Transmission & Distribution*, vol. 12, no. 12, pp. 2905–2917, 2018.

[9] ——, "Determination of optimal reserve requirement for fuel cost minimization of a microgrid under load and generation uncertainties," *Arabian Journal for Science and Engineering*, vol. 44, no. 3, pp. 2003–2031, 2019.

[10] A. Maulik, D. Das, and A. Jain, "Optimal scheduling of an islanded microgrid with complex impedances considering load demand and renewable power uncertainties," in *2019 21st International Middle East Power Systems Conference (MEPCON)*. IEEE, 2019, pp. 20–25.

[11] A. K. Marvasti, Y. Fu, S. DorMohammadi, and M. Rais-Rohani, "Optimal operation of active distribution grids: A system of systems framework," *IEEE Transactions on Smart Grid*, vol. 5, no. 3, pp. 1228–1237, 2014.

[12] J. Kennedy and R. Eberhart, "Particle swarm optimization," in *Proceedings of ICNN'95-International Conference on Neural Networks*, vol. 4. IEEE, 1995, pp. 1942–1948.

[13] S.-J. Ahn, S.-R. Nam, J.-H. Choi, and S.-I. Moon, "Power scheduling of distributed generators for economic and stable operation of a microgrid," *IEEE Transactions on Smart Grid*, vol. 4, no. 1, pp. 398–405, 2013.

Authorized licensed use limited to: DELHI TECHNICAL UNIV. Downloaded on February 15,2021 at 10:06:23 UTC from IEEE Xplore. Restrictions apply.

Hindawi
Security and Communication Networks
Volume 2021, Article ID 7940103, 21 pages
https://doi.org/10.1155/2021/7940103

Research Article

S²NOW: Secure Social Network Ontology Using WhatsApp

Rahul Johari,[1] **Sawan Kalra**,[1] **Sonika Dahiya**,[2] **and Kalpana Gupta**[3]

[1]*SWINGER: Security, Wireless, IoT Network Group of Engineering and Research Lab, University School of Information, Communication Technology (USICT), Guru Gobind Singh Indraprastha University, Sector-16C, Dwarka, Delhi, India*
[2]*Department of Computer Science and Engineering, Delhi Technological University, Delhi, India*
[3]*Academics Division, Centre for Development of Advanced Computing (C-DAC), Noida, India*

Correspondence should be addressed to Rahul Johari; rahuljohari@hotmail.com

Received 21 January 2019; Accepted 28 December 2020; Published 31 January 2021

Academic Editor: Rohit Ranchal

Copyright © 2021 Rahul Johari et al. This is an open access article distributed under the Creative Commons Attribution License, which permits unrestricted use, distribution, and reproduction in any medium, provided the original work is properly cited.

Communicating and sharing the ideas and feelings between human beings form the basis of social network. With the advent of different social network tools and applications, the task of networking between people has reached to next level, crossing bridges and boundaries. However, is there a connection or linkage between the frequent and sometime just random exchange of text messages between people using social network-based tools and applications and also are these messages secure? Or are they vulnerable to threat and attacks? Literature survey shows that very little work has been done in this direction. With this intention, in the current research work, a real-time case study has been taken identifying the creation of the social network between a group of persons who frequently chat using the WhatsApp Messenger application based on their common hobbies, choices, and areas of interest and applying cryptographic techniques to ensure the security of data (chats). The proposed study uses the Caesar Cipher Cryptographic Technique and newly proposed Block Quadra Crypto Technique for encrypting the chats and showcases a comparison between the two techniques. The results are encouraging and exceed the expectation.

1. Introduction

Social network is the network that get established when a group of people share common interest with each other, bond with each other, share the feelings and sentiments with each other, and connect with each other digitally towards sharing common and mutually acceptable thoughts, feelings, and emotions. This is a reason that why various social networking platforms such as Facebook, WhatsApp, Instagram, Vine, Tumblr, Meetup, and ClassMates all have bombed our social life. In today's digital world, bonding on social platform is quite common. Every day, every person spends quality time of his life by devoting hour(s) on these social networking sites, tools, and applications (STA) searching for old peers, new friends, and acquaintances. The bonding happens naturally between the people that have some common point-of-interest (PoI) such as connection between individuals that are a part of college football clubs, movie and theatre societies, career-oriented women (CoW), and recreation clubs. With more digitization going to happen in the coming years, these sites, tools, and applications are here to stay and would definitely impact the way we live, think, express, and bond with fellow human beings. In this current research work, an effort has been made to identify the social network link by taking into consideration the contents of the messages and chat exchanged on the WhatsApp Messenger application of different persons for the duration of one month (or 30 days). The study not only tries to detect connections between chats and formulate a social inclination between the selected sample size but also provide security to the chats by applying encryption techniques to the chats, thereby ensuring data privacy. In the current research work, the two encryption techniques that have been used for securing chats are Caesar Cipher and the newly proposed Block Quadra Crypto Technique. A comparison is also showcased between the two encryption techniques.

Cryptographic encryption is of two types: symmetric encryption and asymmetric encryption. Symmetric encryption in turn can be implemented through cryptographic

techniques, which include techniques such as Caesar Cipher, Vigenere Cipher, Monoalphabetic Cipher, Polyalphabetic Cipher, and Transposition Cipher, and through cryptographic algorithms, which include RSA, DES, and AES algorithms.

To show the effectiveness of the proposed work, the crypto technique has been coded in C# Programming Language in the front end whereas MongoDB has been used in the back end as it is a vital component of MEAN Software Stack.

The novelty of the work is that, to the best of our knowledge, understanding, and wisdom, the current study is first of its kind where a social networking tool such as WhatsApp has been undertaken as a single source of study where end-to-end user chats are made safe and secure using symmetric cipher techniques and newly postulated Block Quadra Crypto Technique. Not only this, the study focuses on the integration and mapping of WhatsApp with the Big Data tools and technologies, which were always viewed separately and never have been integrated in the past. It is believed that the security aspect of proposed work would throw challenges to the research community leading further pathway to the devise and develop the new, effective, and efficient cryptographic techniques.

For the sake of clarity and simplification, the rest of the paper is organised as follows: Section 2 describes the related work on social media data mining. Section 3 describes the motivation for pursuing current research work, Section 4 describes the problem statement, Section 5 illustrates the methodology adopted, Section 6 describes the procedure that was adopted, followed by the flowchart and mathematical modeling of the S^2NOW algorithm, Section 7 describes the results obtained, Section 8 describes the conclusion and future work, and Section 9 describes acknowledgment followed by references.

2. Related Work

In [1], authors have presented elaborated details about the advantages and disadvantages of Big Data tools and techniques. In [2], authors have presented a workflow to bring together collectively both qualitative analysis and important data mining techniques. In [3], authors commented that it is challenging for traditional databases following hierarchical and network model approach to modify and then organize the data in a form that the web user generates on daily basis while performing social activities such as online-chatting, liking, poking and pinging, and tweeting on social media which over period of time have become a huge source of semistructured and unstructured data. In [4], authors have illustrated a framework to improve the throughput of the system. In this paper, two issues related to quick access of real-time data are presented; first issue deals with indexing, and the second one deals with handling of data. Based on these concepts, RTSEs (real-time search engines) were analysed.

In [5], authors comment that students of Polytechnics in Ghana are dependent on the WhatsApp application for their daily exchange of messages as compared to using mobile voice calls or phone calls. Economical, fast, easy, and effective modes of communication are some of the prominent features that influenced the decision of the students. To illustrate it further, a student survey was carried out from January 2014 to June 2014 where a questionnaire was designed to compile data from a sample of 600 odd students from three polytechnic institutions of Ghana. The study revealed the students' attention in switching to WhatsApp application as their most preferred mode of social network tools and applications.

In [6], authors have analysed the performance of numerous algorithms such FCM, IFCM, and T2FCM on noise free and noisy data (also linearly and on nonlinearly separable data). In [7], the author describes how the usage of WhatsApp in smart phones has led to significant effect on writing, usage of vocabulary word choice, and voice of Saudi students studying in College. In [8], authors describe a study that seeks to empirically identify the impact and magnitude of social network application such as WhatsApp Messenger on the overall performance of the students in Ghana. In [9], authors focus on the use of mobile phones as a platform to pursue high-quality collaborative and coordinated research work amongst a selected group of third-year UG Computer Science students. The students used a WhatsApp application to have collaborative group conversations about their ongoing research project. In [10], the author describes the effectiveness of using mobile tools and technologies and STA such as WhatsApp to show how mobile learning activities are guided by activity theory using students' knowledge management system.

In [11], authors discuss the usage of WhatsApp in the effective learning of a group of 37 students of B. Ed. (Bachelor in Education) programme during session 2013-2014. In [12], authors conducted an extensive study to explore and understand classroom interaction between teachers and students of school using WhatsApp. To achieve it, the authors carried out twelve half-structured interviews with faculty members who use the WhatsApp application in order to effectively interact with their students. In [13], authors compared the communication practices done by the users using textese and other ways of online writing in WhatsApp across two eras of generations. The authors comment that failing to communicate using a variety of languages cannot be systematically associated with their communicative practices. In [14], the authors examined the undergraduate students at Universiti Brunei Darussalam depicting the convenience of WhatsApp in their everyday lives and some critical issues arising with it. In [15], authors described how the texters mobilize transcribed laughter (i.e., hahaha) by focusing on the position of smiled and laughter in the message and its course of actions including unilateral laughter and when the user laughs before producing a message. In [16], the authors showcased how information was spread through WhatsApp during the search and rescue operation of three youths kidnapped and detected that 9 out of the 13 rumours circulating on WhatsApp were true.

3. Motivation

WhatsApp is a social network based online instant messaging application that runs on a variety of heterogeneous operating systems such as BlackBerry, Android, or iOS. As a

result, the motivation of undertaking the current research work is to mine the conversations and figure out social interests between individuals as a major time of everyone's life is now spent on communicating these messages on STA. The social conduct of the individuals coupled with the topics of interest and the intensity/gravity or the seriousness of the topics provided valuable information to establish an understanding of the customer base who extensively uses STA such as WhatsApp. This could also find application in the corporate world as official chats can be analysed for social interests or sentiment that brings together certain category of corporate honchos together in social groups. This unexplored area acted as motivation to work in this direction and attain the plausible results. The current exchange of chats over STA is majorly insecure, often vulnerable to threats and attacks. Recent work performed by security experts highlights the case as in [17] as per the market survey mobile-based communication apps and platforms such as Skype and WhatsApp have far less or almost no protection against app-based phishing as compared to e-mail.

In [18], researchers comment that all the users who access web versions of WhatsApp are likely to get cyber-attacked. They have detected a vulnerability which has not been patched yet and that could allow hackers to gain control over end-user accounts, thereby gaining access to personal data using a malware-laced image resulting in customer privacy violation.

As per [19], the WhatsApp suffered a massive cyber-attack resulting in downtime of around 120 minutes affecting more than 175 million users. As per [20], software architects pointed out various bugs such as "quote" feature in a group-oriented conversation to change the identity of the source, even if that individual may not be a member of that particular social group or modifying the text of someone else's reply or transmitting a private message to fellow cogroup participant, being disguised as a full-view public message for everyone, so when the targeted individual replies back, it is visible to all in the conversation.

In [21], new research from Check Point reveals that WhatsApp vulnerabilities enable attackers to manipulate, tamper, and modify messages (MTM) both in public and private conversations. This type of MTM usually makes it easy for intruder to spread fake messages and misinformation. In [22], authors claim that engineers and researchers detected three prominent WhatsApp vulnerabilities that enable users to not only intercept and intrude but also manipulate messages in private and group chats. These WhatsApp vulnerabilities enable hackers to tamper messages, launch vicious online scams, and spread artificial rumours and fake news resulting in what is now popularly called as "FakesApp."

In [23], technical writers' comments that Facebook owned WhatsApp has major problem with the widespread circulation of fake news and rumours. With a result, they had to put control and restrictions on the number of times a specific message could be forwarded to the other users on the group.

This acted as a great zeal of inspiration to work in this direction, and the newly proposed Block Quadra Crypto Technique is the outcome of the same.

4. Problem Statement

In the current social networking scenario, no research work has been done till date on social networking application "WhatsApp," leading to its linkage or connection to social network as no authentic reports or publications could be traced on the web. The current research work focuses on social networking in WhatsApp, providing security to the chats using symmetric cipher technique that means the study focuses on the integration and mapping of WhatsApp with the Big Data tools and technologies, which were always viewed separately and had never have been integrated in the past.

Will the social networking through WhatsApp provide intriguing results upon which various graphical analytics can be applied and whether the graph having nodes/vertices representing a person's WhatsApp chat and edges that define how strong a connection between two persons or nodes can be plotted? Also, in the graph, the weights on the edges increase as the number of common words exchanged between two chats (nodes) increases, and does this hypothesis hold true in all the environments? This is something that needs to be ascertained.

5. Methodology Adopted

5.1. Mapping Table. Proposed Table 1 is used for conversions that were required in securing the chats both while encrypting as well as decrypting.

5.2. Caesar Cipher. In the field of cryptography, it is one the naive and simplest encryption technique. It is an additive cryptographic technique. Each letter of the plain text is replaced. The cryptographic equation followed, here, is

$$\mathbf{C} = (\mathbf{P} + \mathbf{K}) \bmod 95, \tag{1}$$

where $\boldsymbol{C}$ is the cipher text, $\boldsymbol{P}$ is the plain text, $\boldsymbol{K}$ is the key (**3**), and "95" is the total number of characters in the mapping table.

For example, the plain text is "This is in Caesar Cipher."

After the application of Caesar Cipher, the cipher text obtained will be as follows: "Wklv#lv#lq#Fdhvdu#Flskhu" (an addition of 3 letters in the plain text and the new positional value according to the mapping table, as listed in Table 1).

For instance, character "T" has the positional value 52 in the mapping table.

So, $(52 + 3) \bmod 95 = 55 \bmod 95$.

$55 \bmod 95 = 55$.

Value at 55 in the mapping table is "W." So, "T" will be replaced by "W."

Similarly, character "}" has the positional value 93 in the mapping table.

So, $(93 + 3) \bmod 95 = 96 \bmod 95$.

$96 \bmod 95 = 1$.

Value at 1 in the mapping table is "!." So, "}" will be replaced by "!."

Table 1: Mapping table.

Code	Value	Code	Value	Code	Value
0	SPACE	37	E	74	J
1	!	38	F	75	K
2	“	39	G	76	L
3	#	40	H	77	M
4	$	41	I	78	N
5	%	42	J	79	O
6	&	43	K	80	P
7	’	44	L	81	Q
8	(	45	M	82	R
9	)	46	N	83	S
10	*	47	O	84	T
11	+	48	P	85	U
12	,	49	Q	86	V
13	-	50	R	87	W
14	.	51	S	88	X
15	/	52	T	89	Y
16	0	53	U	90	Z
17	1	54	V	91	{
18	2	55	W	92	|
19	3	56	X	93	}
20	4	57	Y	94	~
21	5	58	Z	—	—
22	6	59	[	—	—
23	7	60	\	—	—
24	8	61	]	—	—
25	9	62	^	—	—
26	:	63	_	—	—
27	;	64	`	—	—
28	<	65	A	—	—
29	=	66	B	—	—
30	>	67	C	—	—
31	?	68	D	—	—
32	@	69	E	—	—
33	A	70	F	—	—
34	B	71	G	—	—
35	C	72	H	—	—
36	D	73	I	—	—

5.3. Block Quadra Crypto Technique. In this newly proposed technique, additive shift cipher is applied to the plain text and then these are read character by character, and each character’s binary equivalent value is fed into different quadrants sequentially.

For example, the plain text is “This is Block Quadra Crypto Technique.”

After the application of additive shift, the text will be as follows:

“rs}*s}∗Lvymu*[kn|k*M|$z ~ y*omrxs{ o.”

Now, the text obtained is fed into 4 different quadrants as shown in Figure 1 (in binary) and Figure 2 (in characters).

Since the distribution provides an unequal number of characters in each quadrant, a space is padded at the end of each quadrant (Table 2).

The values in these quadrants will be as follows:

1st quadrant:

00111110,00001010,00101100,01010101,01001011,00001010,01011010,00111110,01011000 and 01001111 (which are equivalent to ^, *, L, u, k, *, z, ^, x and o).

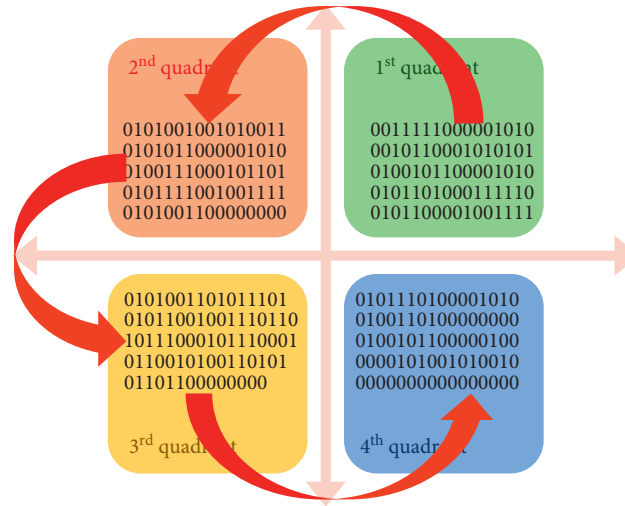

Figure 1: Depiction of the values (in binary) in each quadrant.

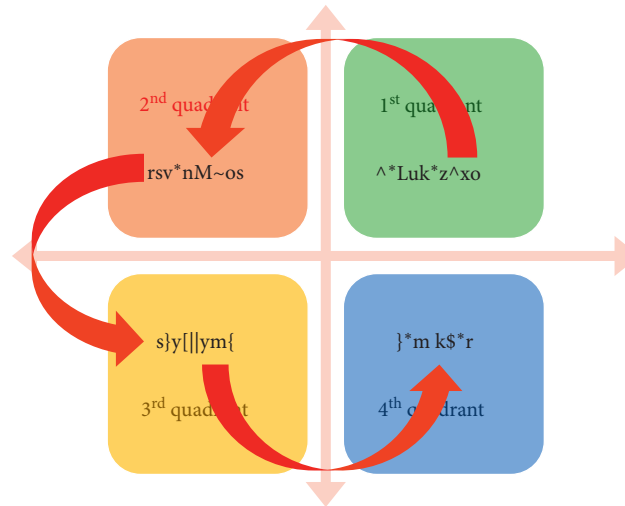

Figure 2: Depiction of the values (character equivalent) in each quadrant.

2nd quadrant:

01010010, 01010011, 01010110, 00001010, 01001110, 00101101, 01011110, 01001111, 01010011 and 00000000. (which are equivalent to r, s, v, *, n, M, ~, o, s and “).

3rd quadrant:

01010011, 01011101, 01011001, 00111011, 01011100, 01011100, 01011001, 01001101, 01011011 and 00000000. (which are equivalent to s, }, y, [, |, |, y, m, { and “).

4th quadrant:

01011101, 00001010, 01001101, 00000000, 01001011, 00000100, 00001010, 01010010, 00000000 and 00000000 (which are equivalent to }, *, m,“, k, $, *, r,“and “).

Now, the cipher text will be the contents of each quadrant read sequentially from 1st quadrant to 4th quadrant, that is, “00111110000010100010110001010101010010110000101001011010001111100101100001001111010100100101001101010110 0

Table 2: An example depicting the distribution of characters into 4 different quadrants.

Q1	^	*	L	u	k	*	z	^	X	o
Q2	R	S	V	*	n	M	~	o	S	SPC
Q3	S	}	Y	[	|	|	y	m	{	SPC
Q4	}	*	M	SPC	k	$	*	r	SPC	SPC

^	*	L	U	K
00111110	00001010	00101100	01010101	01001011
*	Z	^	X	O
00001010	01011010	00111110	01011000	01001111

r	s	V	*	N
01010010	01010011	01010110	00001010	01001110
M	~	O	S	SPC
00101101	01011110	01001111	01010011	00000000

s	}	y	[	|
01010011	01011101	01011001	00111011	01011100
|	y	m	{	SPC
01011100	01011001	01001101	01011011	00000000

}	*	m	SPC	K
01011101	00001010	01001101	00000000	01001011
$	*	r	SPC	SPC
00000100	00001010	01010010	00000000	00000000

000101001001110001011010101111001001111010100110000000010100110101110101011001001110110101110001011100101100101001101010110110000000001011101000010100100110100000000010010110000010000001010010100100000000000000000" (which is equivalent to "*Luk*ẑxorsv*nM ~ os s}y[||ym { }*m k$*r, " when mapped from the mapping table).

5.4. Mechanism Adopted. WhatsApp chats of different individuals for a duration of one month (March, 2018) were taken as part of study. The chats were obtained in text file format, that is, for each WhatsApp chat, a different text file was obtained. These chats were directly imported into Microsoft Excel application, wherein each and every chat was splitted into different columns such as time, date, and message. Then, the file was saved in .CSV (comma-separated values delimited) file format.

Now, after saving the WhatsApp chats in CSV format, each file was encrypted using a C# program, which encrypted the text in the WhatsApp messages. The chats were encrypted through both the encryption techniques and in an entirely new file.

After the application of the encryption, all the chats including original and encrypted were imported into the database, namely, MongoDB using the command (as depicted in Figures 3–5): mongoimport -d database -c collection --type .CSV --file filename.csv –-headerline.

After these chats were imported in the MongoDB database, these chats were fetched through a program, coded in C# Programming Language.

Now, these encrypted messages were received, decryption was applied on them, and the chats were obtained back in its original text or plain text form.

After the chats were obtained, analysis was performed over these and a graph was made which depicted the social inclination between all these people and along with this time taken by both the encryption techniques was compared.

6. Procedure

The procedure adopted for pursuing current research work has been showcased with the help of Figures 6–15, which are detailed as follows:

(1) Open WhatsApp and Select Options > More > Email chat (Figure 6).

(2) The text file received as attachment in the mail, Figure 7.

(3) Open Microsoft Excel and select the Data tab and click on From Text. Select Delimited as shown in Figure 8.

(4) Follow the steps in the wizard and select Comma and Other (specify "-") (Figure 9 followed by Figure 10).

(5) Now, the data looked as shown in Figure 11.

(6) Final sheet obtained was as shown in Figure 12.

(7) Save this spreadsheet in .CSV (Comma delimited) file format (Figure 13).

(8) The steps as detailed with the help of screenshots from Figures 6–13 were repeated for every chat, and a separate .CSV file was saved for each chat.

(9) These chats were encrypted in Caesar Cipher and Block Quadra Crypto Technique and imported into the MongoDB database. The chats when fetched from the database were in the form as shown in Figures 14 and 15 (Block Quadra Crypto Technique).

6.1. Algorithm Formulated. Text analytics (text mining) indicate the extraction of the information from textual data. Information extraction (IE) techniques extract/fetch structured data from unstructured text. To achieve it, the S^2NOW algorithm has been devised, S^2NOW algorithm, Secure Social Network Ontology using WhatsApp; in this, a framework/strategy is presented and results are showcased that show how a popular social media tool such as WhatsApp chat can relate two or more people by their common interest on the basis of words they had used in their respective chat. These are the various steps that are involved in the process of data mining from data collection to decision making.

Sequential procedure adopted to understand the working of the S^2NOW algorithm is detailed as follows:

Figure 3: Snapshot showing the importing of original WhatsApp chat file (.CSV) in MongoDB.

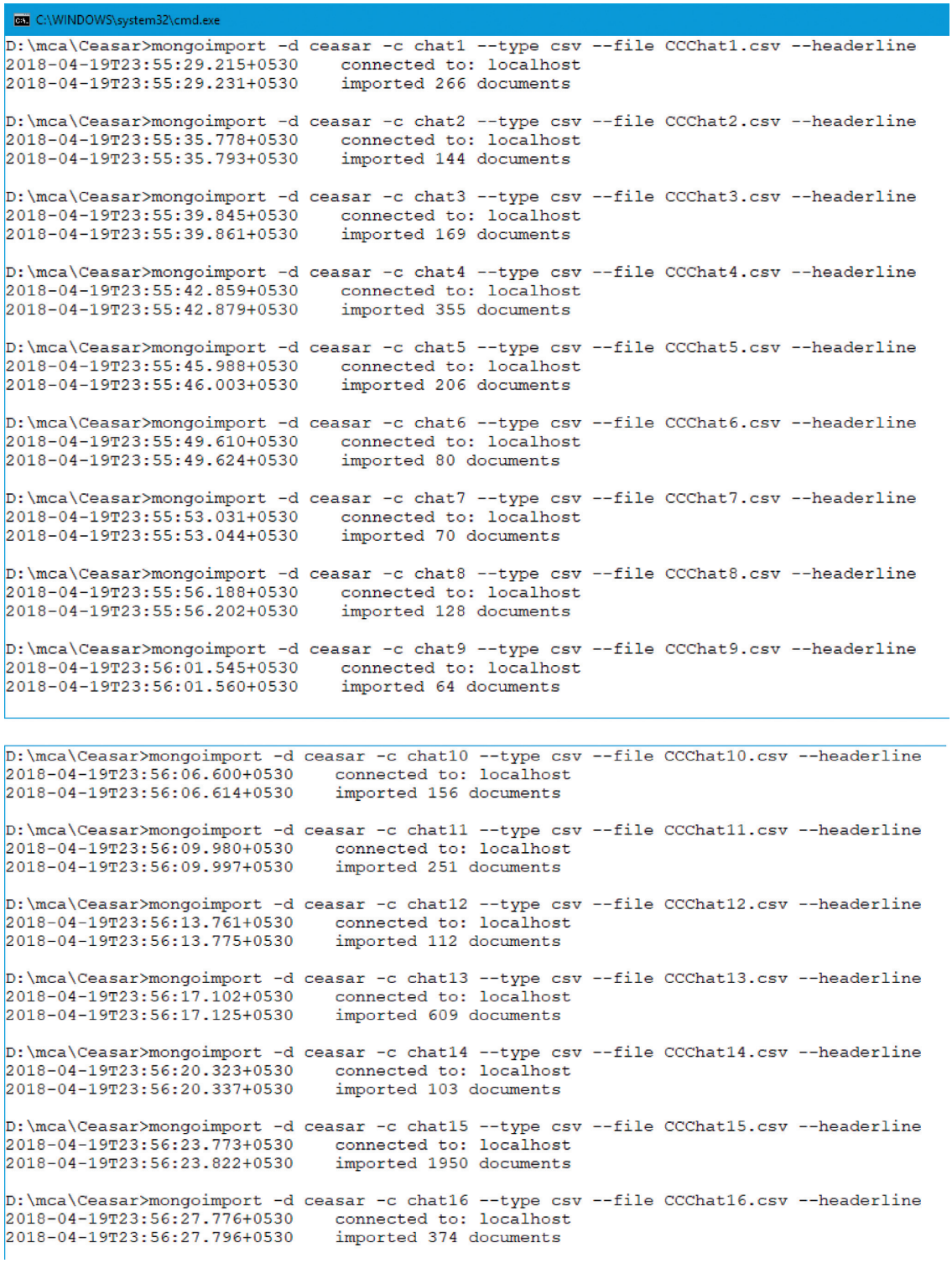

Figure 4: Snapshot showing the importing of Caesar Cipher encrypted chat file (.CSV) in MongoDB.

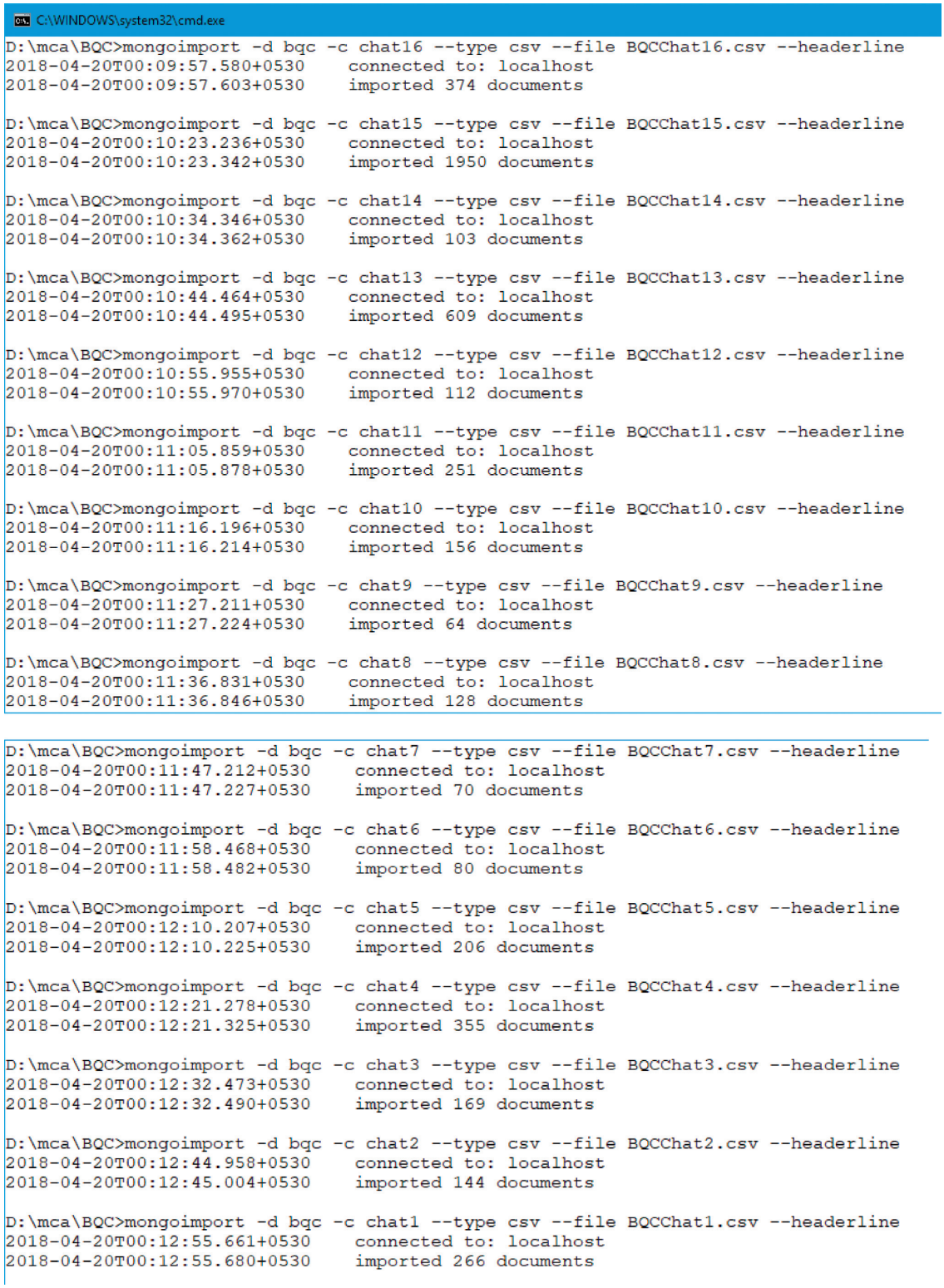

```
C:\WINDOWS\system32\cmd.exe
D:\mca\BQC>mongoimport -d bqc -c chat16 --type csv --file BQCChat16.csv --headerline
2018-04-20T00:09:57.580+0530    connected to: localhost
2018-04-20T00:09:57.603+0530    imported 374 documents

D:\mca\BQC>mongoimport -d bqc -c chat15 --type csv --file BQCChat15.csv --headerline
2018-04-20T00:10:23.236+0530    connected to: localhost
2018-04-20T00:10:23.342+0530    imported 1950 documents

D:\mca\BQC>mongoimport -d bqc -c chat14 --type csv --file BQCChat14.csv --headerline
2018-04-20T00:10:34.346+0530    connected to: localhost
2018-04-20T00:10:34.362+0530    imported 103 documents

D:\mca\BQC>mongoimport -d bqc -c chat13 --type csv --file BQCChat13.csv --headerline
2018-04-20T00:10:44.464+0530    connected to: localhost
2018-04-20T00:10:44.495+0530    imported 609 documents

D:\mca\BQC>mongoimport -d bqc -c chat12 --type csv --file BQCChat12.csv --headerline
2018-04-20T00:10:55.955+0530    connected to: localhost
2018-04-20T00:10:55.970+0530    imported 112 documents

D:\mca\BQC>mongoimport -d bqc -c chat11 --type csv --file BQCChat11.csv --headerline
2018-04-20T00:11:05.859+0530    connected to: localhost
2018-04-20T00:11:05.878+0530    imported 251 documents

D:\mca\BQC>mongoimport -d bqc -c chat10 --type csv --file BQCChat10.csv --headerline
2018-04-20T00:11:16.196+0530    connected to: localhost
2018-04-20T00:11:16.214+0530    imported 156 documents

D:\mca\BQC>mongoimport -d bqc -c chat9 --type csv --file BQCChat9.csv --headerline
2018-04-20T00:11:27.211+0530    connected to: localhost
2018-04-20T00:11:27.224+0530    imported 64 documents

D:\mca\BQC>mongoimport -d bqc -c chat8 --type csv --file BQCChat8.csv --headerline
2018-04-20T00:11:36.831+0530    connected to: localhost
2018-04-20T00:11:36.846+0530    imported 128 documents

D:\mca\BQC>mongoimport -d bqc -c chat7 --type csv --file BQCChat7.csv --headerline
2018-04-20T00:11:47.212+0530    connected to: localhost
2018-04-20T00:11:47.227+0530    imported 70 documents

D:\mca\BQC>mongoimport -d bqc -c chat6 --type csv --file BQCChat6.csv --headerline
2018-04-20T00:11:58.468+0530    connected to: localhost
2018-04-20T00:11:58.482+0530    imported 80 documents

D:\mca\BQC>mongoimport -d bqc -c chat5 --type csv --file BQCChat5.csv --headerline
2018-04-20T00:12:10.207+0530    connected to: localhost
2018-04-20T00:12:10.225+0530    imported 206 documents

D:\mca\BQC>mongoimport -d bqc -c chat4 --type csv --file BQCChat4.csv --headerline
2018-04-20T00:12:21.278+0530    connected to: localhost
2018-04-20T00:12:21.325+0530    imported 355 documents

D:\mca\BQC>mongoimport -d bqc -c chat3 --type csv --file BQCChat3.csv --headerline
2018-04-20T00:12:32.473+0530    connected to: localhost
2018-04-20T00:12:32.490+0530    imported 169 documents

D:\mca\BQC>mongoimport -d bqc -c chat2 --type csv --file BQCChat2.csv --headerline
2018-04-20T00:12:44.958+0530    connected to: localhost
2018-04-20T00:12:45.004+0530    imported 144 documents

D:\mca\BQC>mongoimport -d bqc -c chat1 --type csv --file BQCChat1.csv --headerline
2018-04-20T00:12:55.661+0530    connected to: localhost
2018-04-20T00:12:55.680+0530    imported 266 documents
```

Figure 5: Snapshot showing the importing of Block Quadra Crypto encrypted chat file (.CSV) in MongoDB.

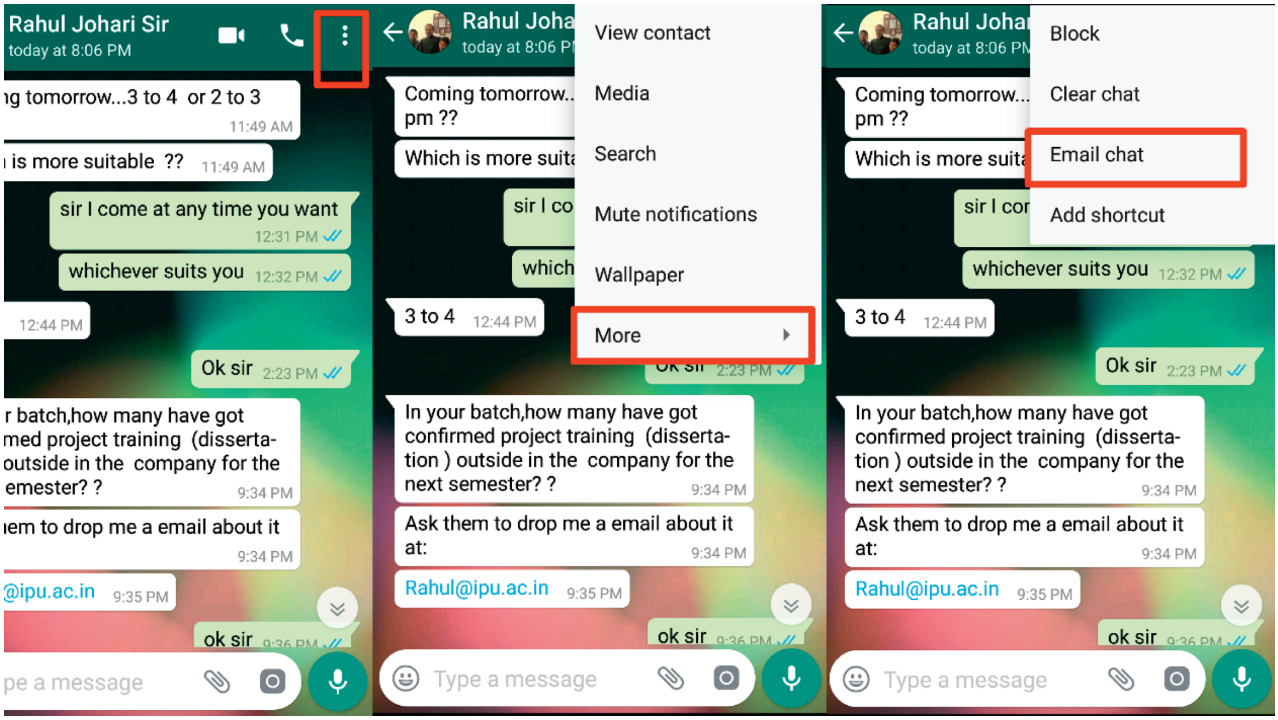

Figure 6: Steps to be followed on WhatsApp to get the data.

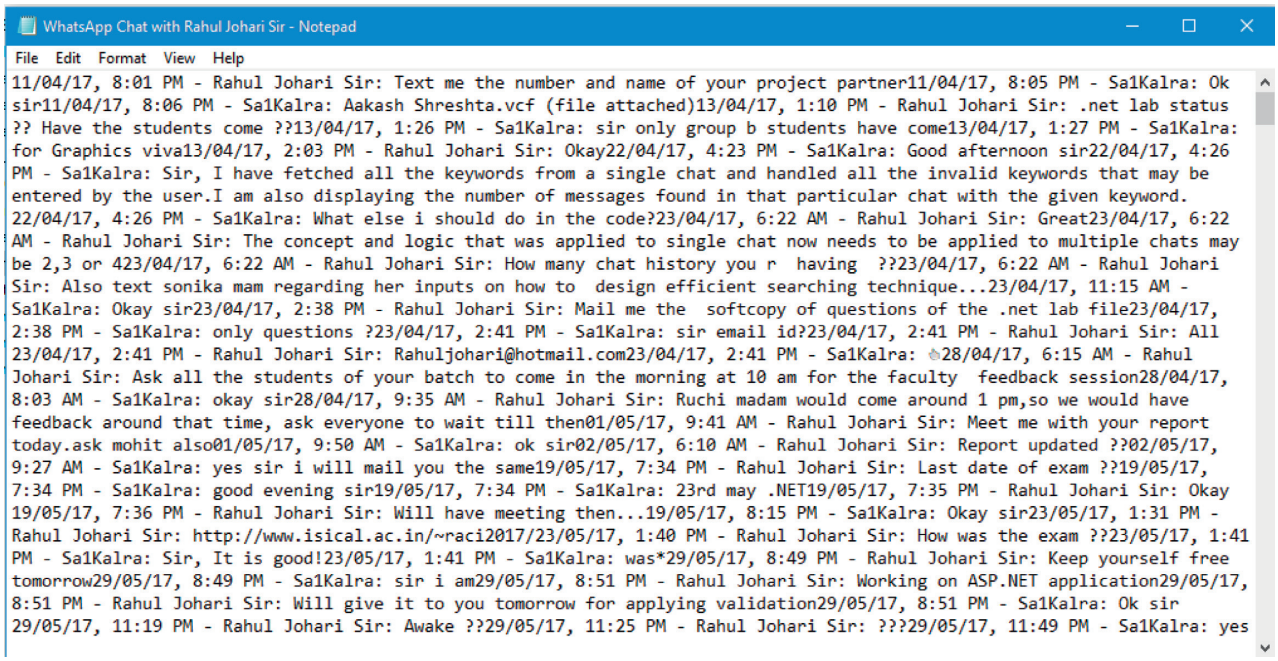

Figure 7: Contents of the text file obtained.

(1) Select the WhatsApp chat of 16 persons for a defined date and time, and let us say of 1-month duration

(2) Encrypt the chats using Caesar Cipher and Block Quadra Crypto Technique

(3) Start the MongoDB database server

(4) Fetch and decrypt the chats

(5) Take a WhatsApp chat

(5.1) Iterate/start scanning from first word to the EOF

(5.2) To remove frequently used English language connecting words such as I, we, and, if, are, and if

(5.3) To ignore all the words whose word length $(W_L) <= 6$

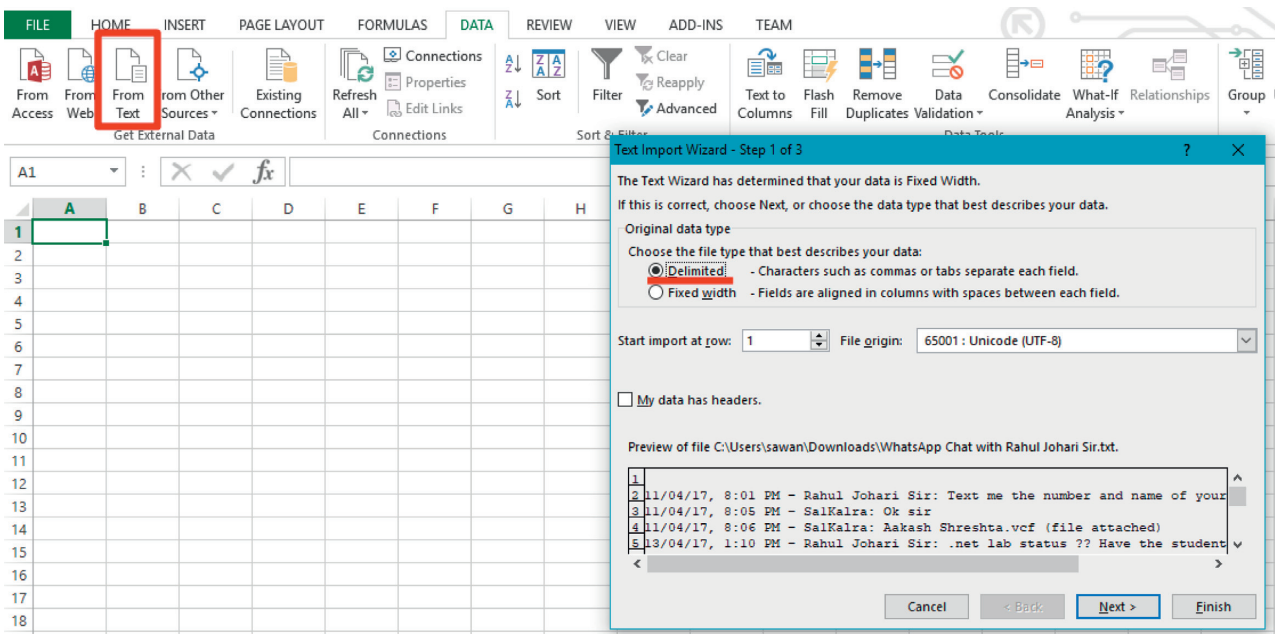

Figure 8: Importing of the text file into MS Excel.

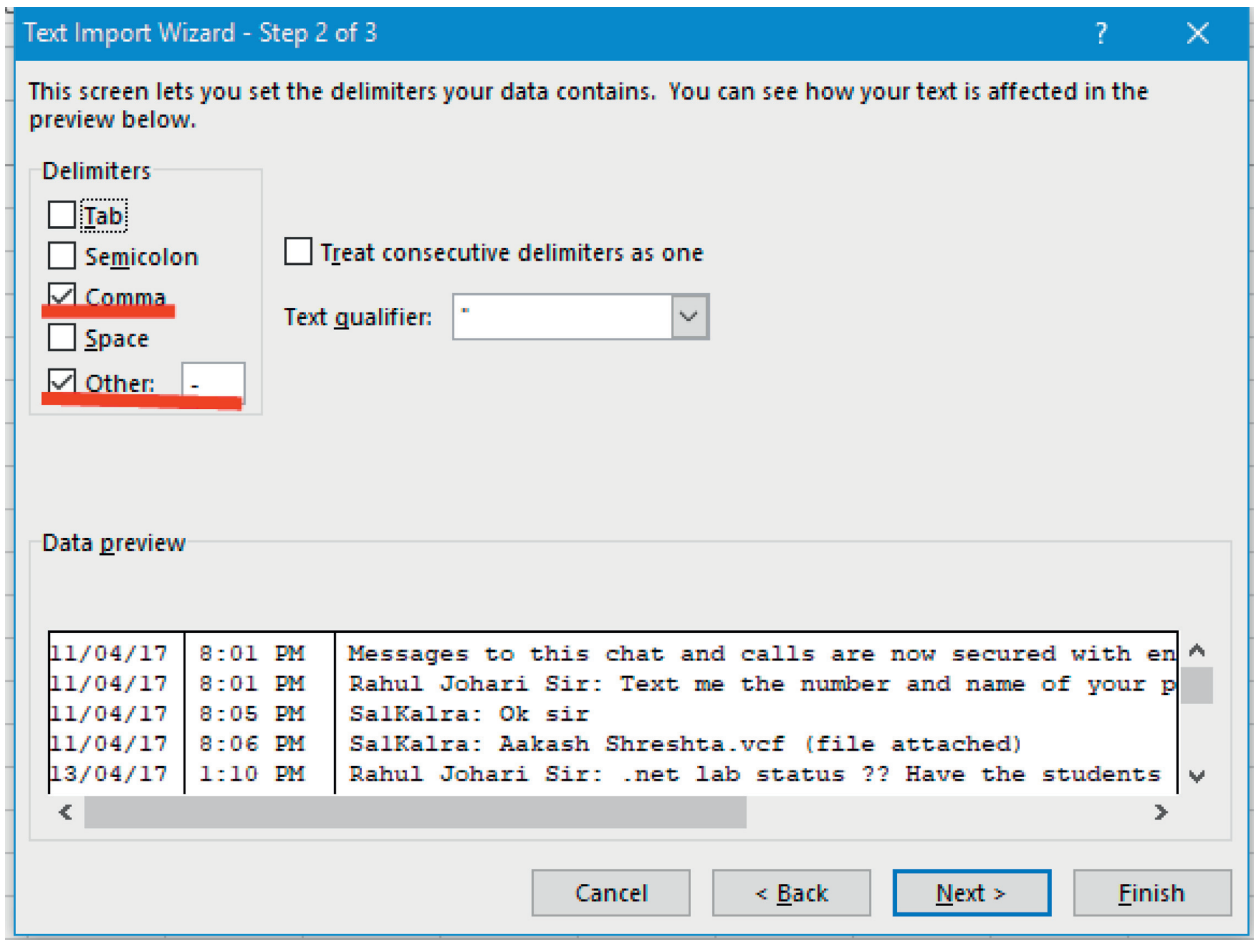

Figure 9: Text Import Wizard, selecting Comma and "-."

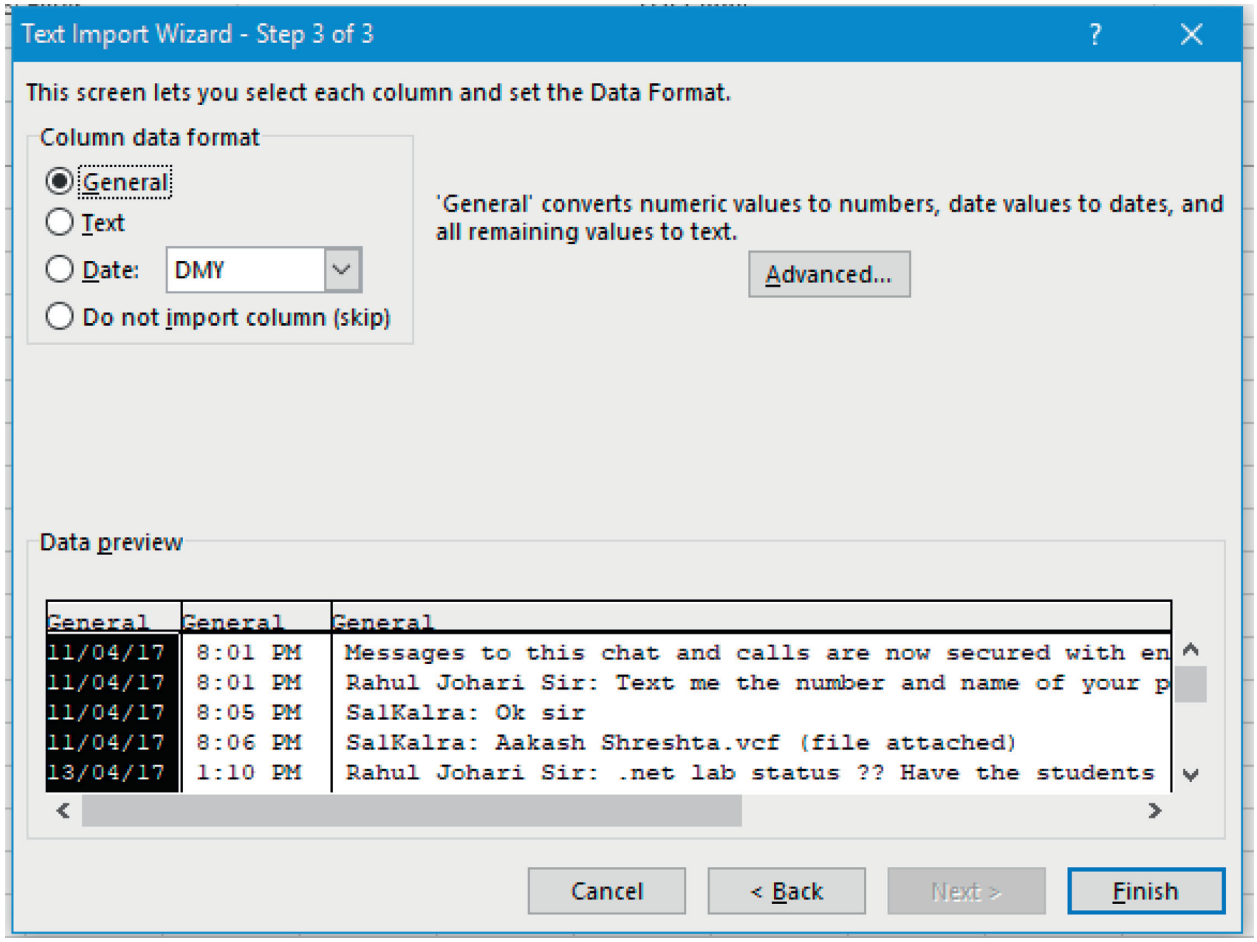

Figure 10: Text Import Wizard (step 3 of 3).

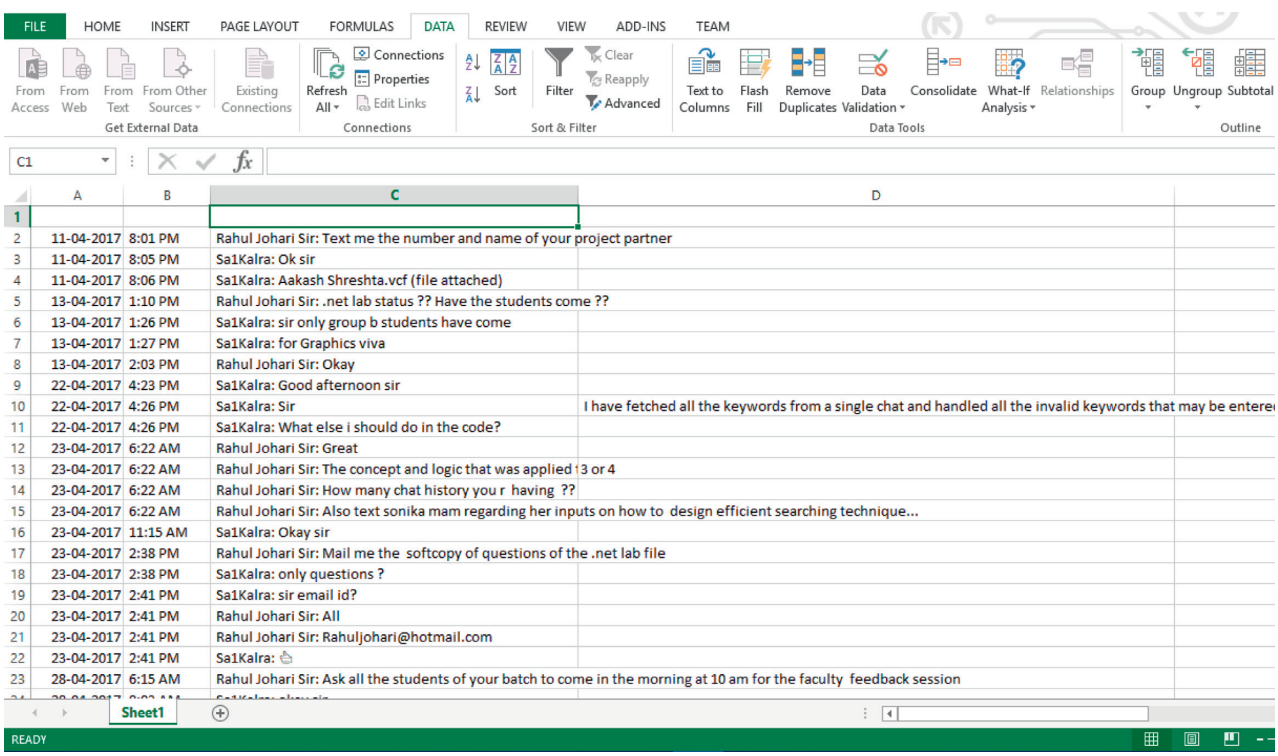

Figure 11: Text data separated into columns.

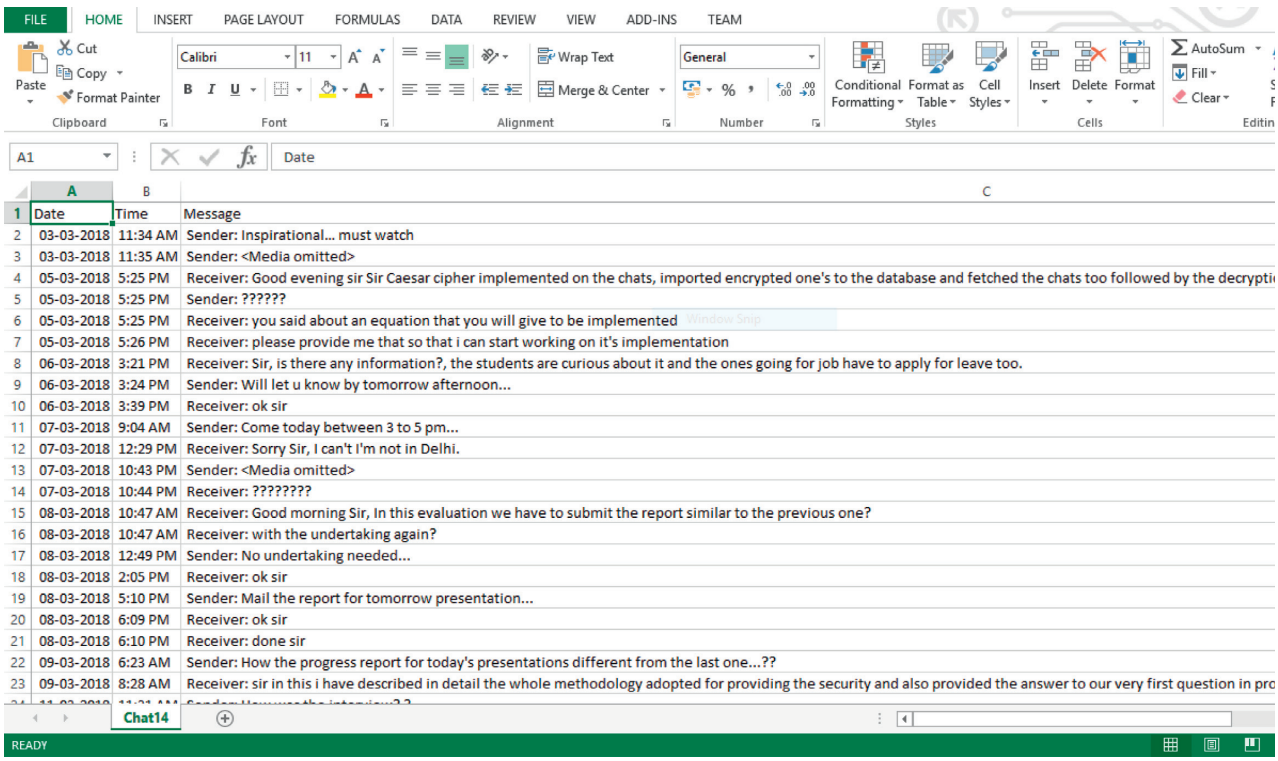

	A	B	C
1	Date	Time	Message
2	03-03-2018	11:34 AM	Sender: Inspirational... must watch
3	03-03-2018	11:35 AM	Sender: <Media omitted>
4	05-03-2018	5:25 PM	Receiver: Good evening sir Sir Caesar cipher implemented on the chats, imported encrypted one's to the database and fetched the chats too followed by the decrypti
5	05-03-2018	5:25 PM	Sender: ??????
6	05-03-2018	5:25 PM	Receiver: you said about an equation that you will give to be implemented
7	05-03-2018	5:26 PM	Receiver: please provide me that so that i can start working on it's implementation
8	06-03-2018	3:21 PM	Receiver: Sir, is there any information?, the students are curious about it and the ones going for job have to apply for leave too.
9	06-03-2018	3:24 PM	Sender: Will let u know by tomorrow afternoon...
10	06-03-2018	3:39 PM	Receiver: ok sir
11	07-03-2018	9:04 AM	Sender: Come today between 3 to 5 pm...
12	07-03-2018	12:29 PM	Receiver: Sorry Sir, I can't I'm not in Delhi.
13	07-03-2018	10:43 PM	Sender: <Media omitted>
14	07-03-2018	10:44 PM	Receiver: ????????
15	08-03-2018	10:47 AM	Receiver: Good morning Sir, In this evaluation we have to submit the report similar to the previous one?
16	08-03-2018	10:47 AM	Receiver: with the undertaking again?
17	08-03-2018	12:49 PM	Sender: No undertaking needed...
18	08-03-2018	2:05 PM	Receiver: ok sir
19	08-03-2018	5:10 PM	Sender: Mail the report for tomorrow presentation...
20	08-03-2018	6:09 PM	Receiver: ok sir
21	08-03-2018	6:10 PM	Receiver: done sir
22	09-03-2018	6:23 AM	Sender: How the progress report for today's presentations different from the last one...??
23	09-03-2018	8:28 AM	Receiver: sir in this i have described in detail the whole methodology adopted for providing the security and also provided the answer to our very first question in pro

Figure 12: Naming columns as date, time, and message.

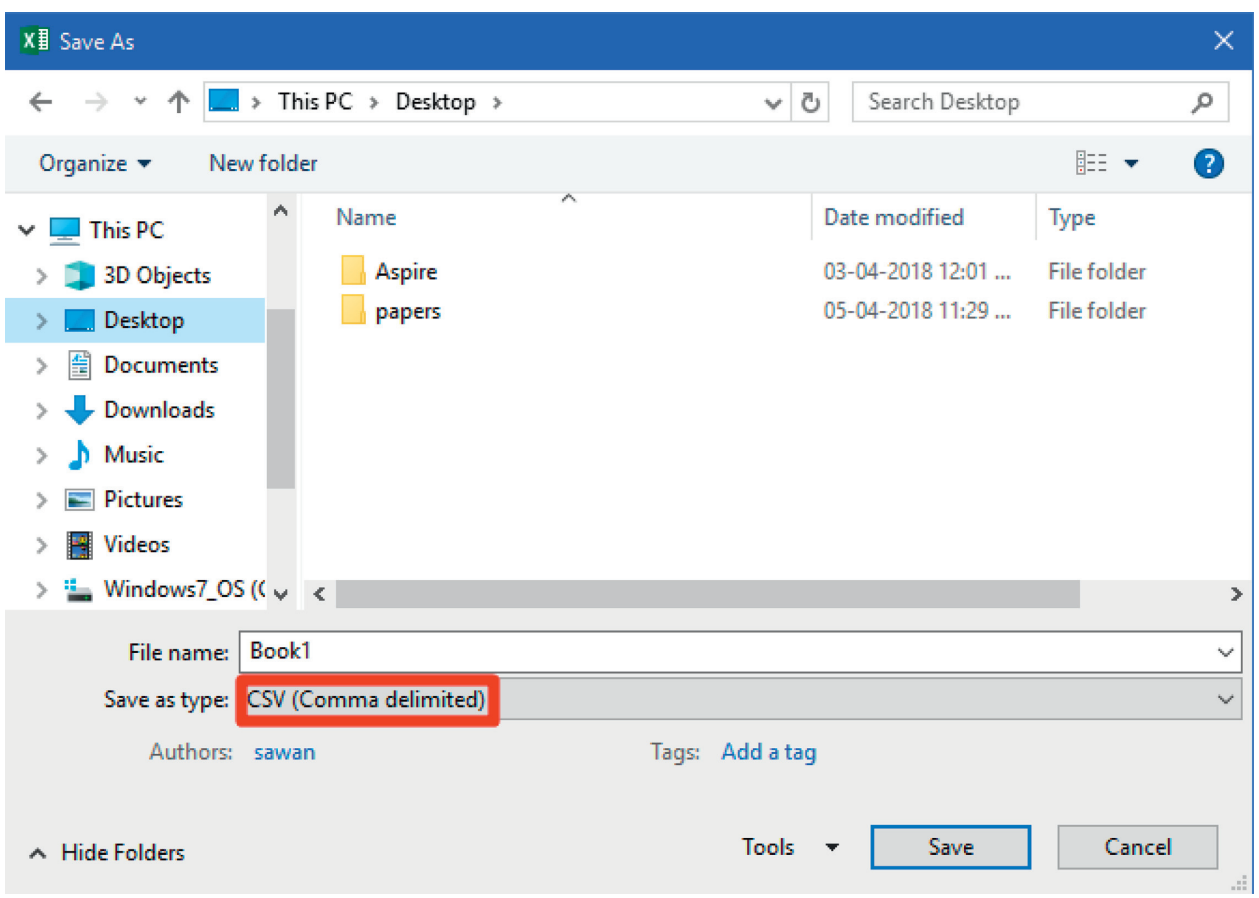

Figure 13: Saving of the spreadsheet in .CSV file format.

```
C:\WINDOWS\system32\cmd.exe - mongo
> use ceasar
switched to db ceasar
> db.chat1.find().pretty()
{
        "_id" : ObjectId("5ad8df198aacfa05fd2c1f5f"),
        "Date" : "01-03-2018",
        "Time" : "2:11 PM",
        "Message" : "Receiver:#?Phgld#rplwwhgA"
}
{
        "_id" : ObjectId("5ad8df198aacfa05fd2c1f60"),
        "Date" : "01-03-2018",
        "Time" : "2:11 PM",
        "Message" : "Receiver:#wkhhn#kdl#qd#ekdlBB"
}
{
        "_id" : ObjectId("5ad8df198aacfa05fd2c1f61"),
        "Date" : "01-03-2018",
        "Time" : "2:11 PM",
        "Message" : "Sender:#BBBBBB"
}
{
        "_id" : ObjectId("5ad8df198aacfa05fd2c1f62"),
        "Date" : "01-03-2018",
        "Time" : "2:12 PM",
        "Message" : "Sender:#\\h#ewd"
}
{
        "_id" : ObjectId("5ad8df198aacfa05fd2c1f63"),
        "Date" : "01-03-2018",
        "Time" : "2:12 PM",
        "Message" : "Sender:#Pmkh#hduskrqh#ohqh#k"
}
{
        "_id" : ObjectId("5ad8df198aacfa05fd2c1f64"),
        "Date" : "01-03-2018",
        "Time" : "2:12 PM",
        "Message" : "Receiver:#hydoxdwlrq#nd#pdw#sxfkqd#nxfk#edv"
```

Figure 14: Contents in the Caesar Cipher encrypted chat.

(5.4) Insert the words that have been selected into the respective dictionary with the number of occurrences of each and every unique word

(6) Repeat step 5 for left over fifteen WhatsApp chats numbered 2 to 16

(7) Create a complete connected weighted graph with 16 vertices, where each vertex represents a particular dictionary, and set the weight of edges to be zero

(8) At the end of step 6, it would be as in Figure 16

Now, 16 dictionaries were obtained, and one for each individual contains at least 10 words which are unique and whose length is greater than 6 along with the number of occurrences of that word. Out of 16 dictionaries, four random dictionaries are shown in step 4.

(9) From 1st dictionary, select the first word and search for its occurrence in dictionary 02 to 16

(10) If occurrence of the word is found in dictionary 02 to 16, then

increase weight by 1 of the edge between node representing dictionary 1 and node representing respective dictionary, where the word is found,

else

repeat step 9 and step 10 with the next word from dictionary 1 until all words in dictionary 1 are considered

Figure 15: Contents in the Block Quadra Crypto encrypted chat.

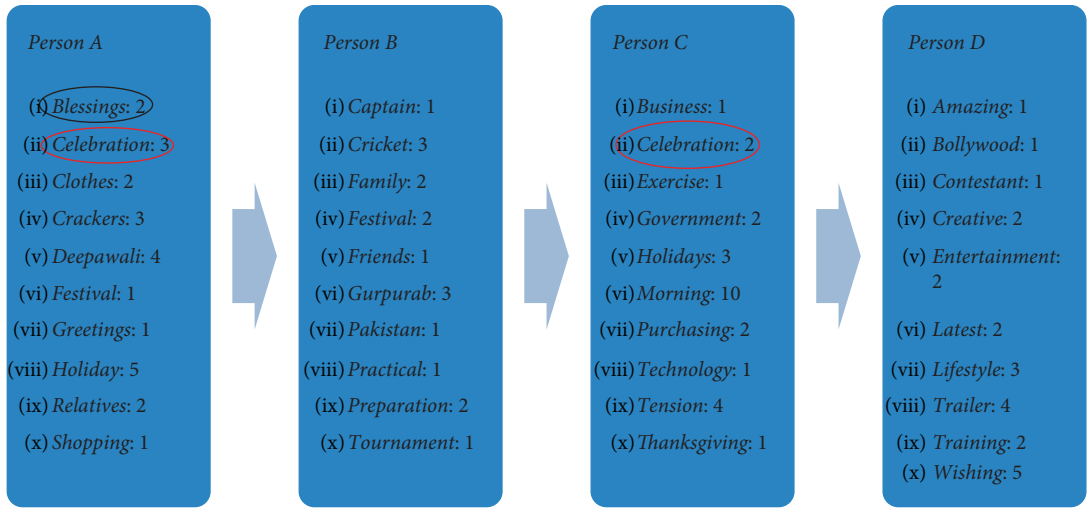

Figure 16: Words into the respective dictionary with the number of occurrences of each and every unique word.

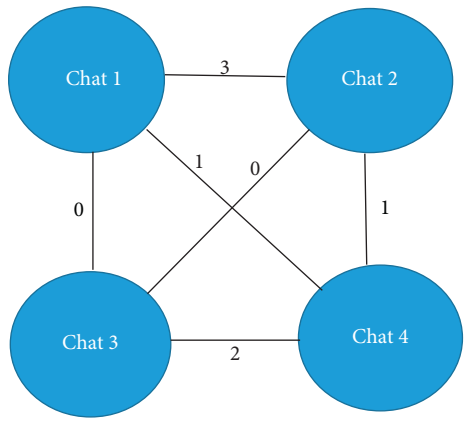

Figure 17: Sample graph to show the connection and linkages amongst chats.

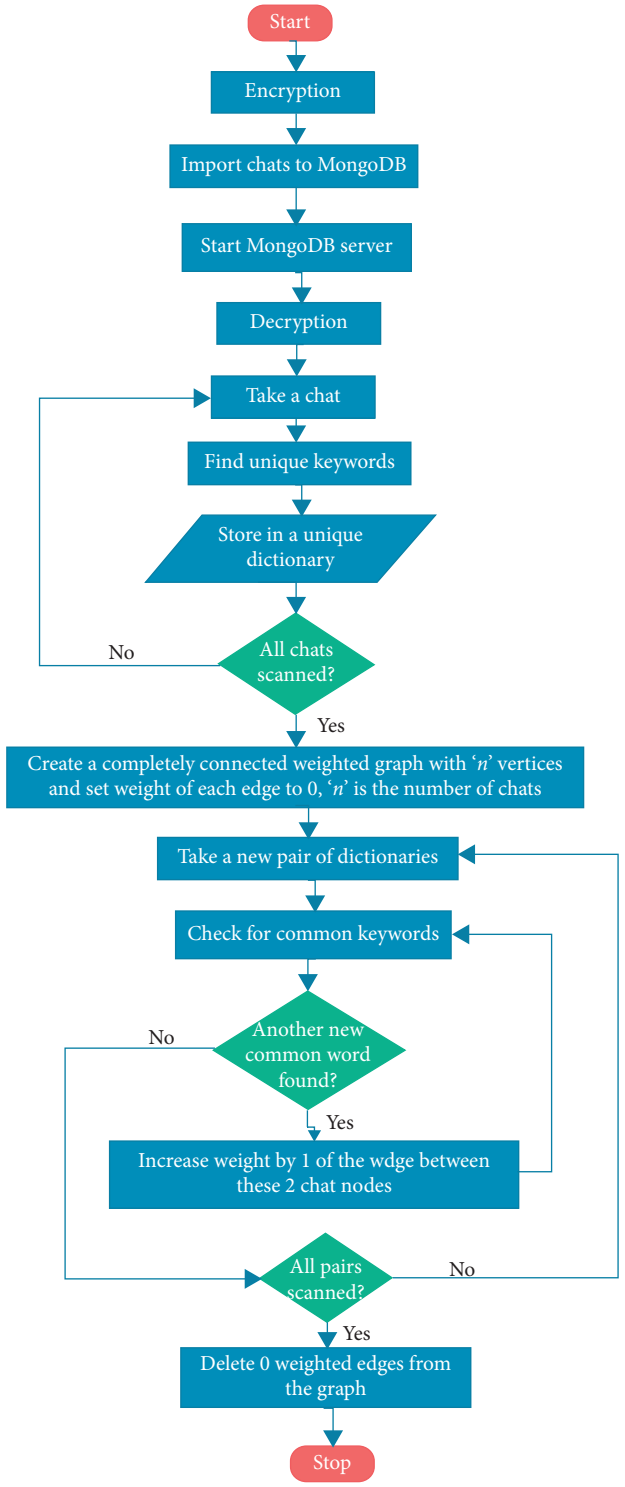

Figure 18: Flowchart indicating methodical procedure adopted for the efficient working of the S^2NOW algorithm.

(11) Repeat step 9 and step 10 for other dictionaries one by one, that is, from dictionary 02 to dictionary 16

(12) Delete zero weight edges

To conclude, primary focus is to detect social pattern amongst the selected sample dataset of 16 (sixteen) WhatsApp chats and it can amicably be concluded that greater the weight of edge, stronger is the bond.

6.2. Flowchart. Working steps of the S^2NOW algorithm, Secure Social Network Ontology using WhatsApp, are indicated in the flowchart depicted in Figure 18.

6.3. Mathematical Modeling. Notations:

WAC_i: WhatsApp chat of i^{th} person for a period of approximately 30 days/1 month

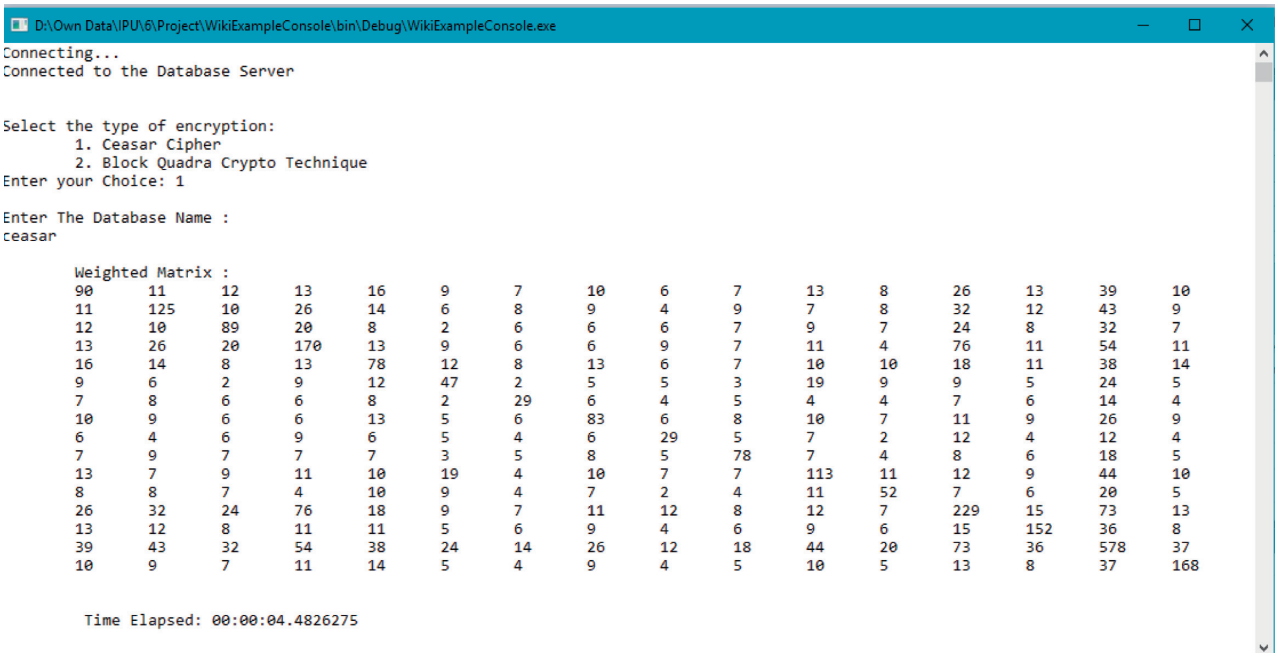

Figure 19: Resultant Weighted Matrix obtained on chats encrypted in Caesar Cipher.

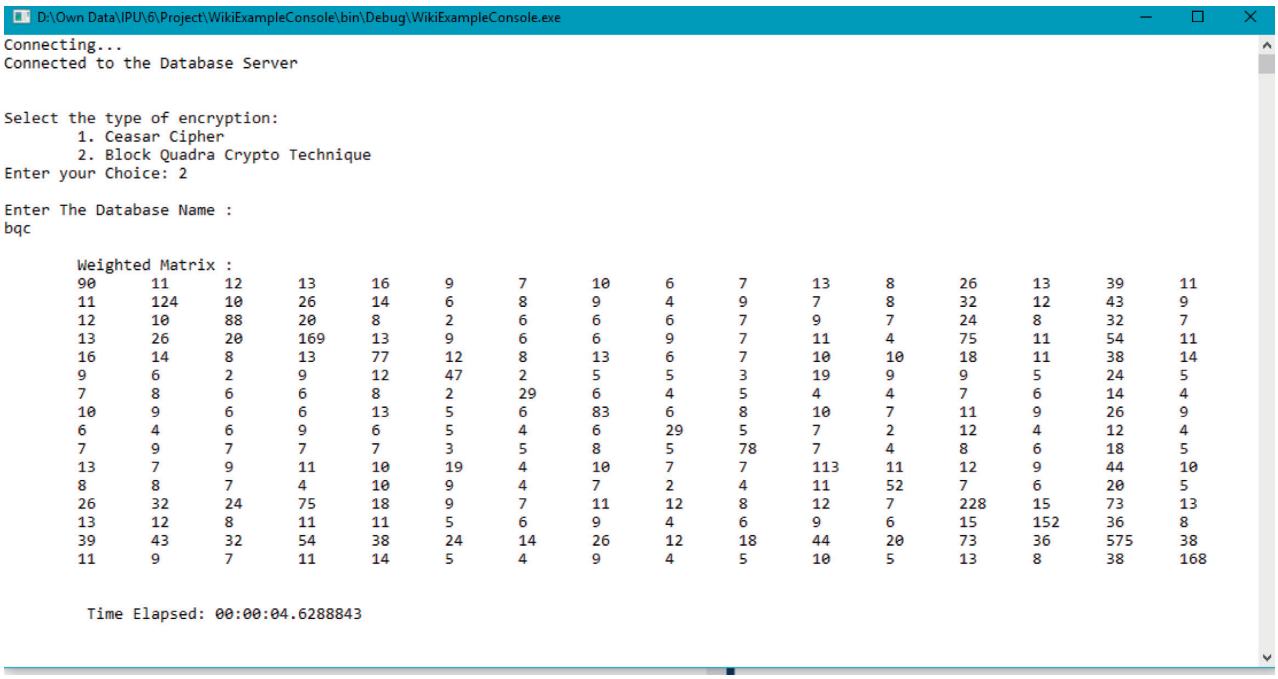

Figure 20: Resultant Weighted Matrix obtained on chats encrypted in Block Quadra Crypto Technique.

n: number of WhatsApp chats, one per person

Dict_i: a dictionary belonging to i^{th} WhatsApp chat, used for storing unique words

w_d: word in any WAC_i

l_w: length of w_d

INPUT: WhatsApp chats for n persons (WAC_i)

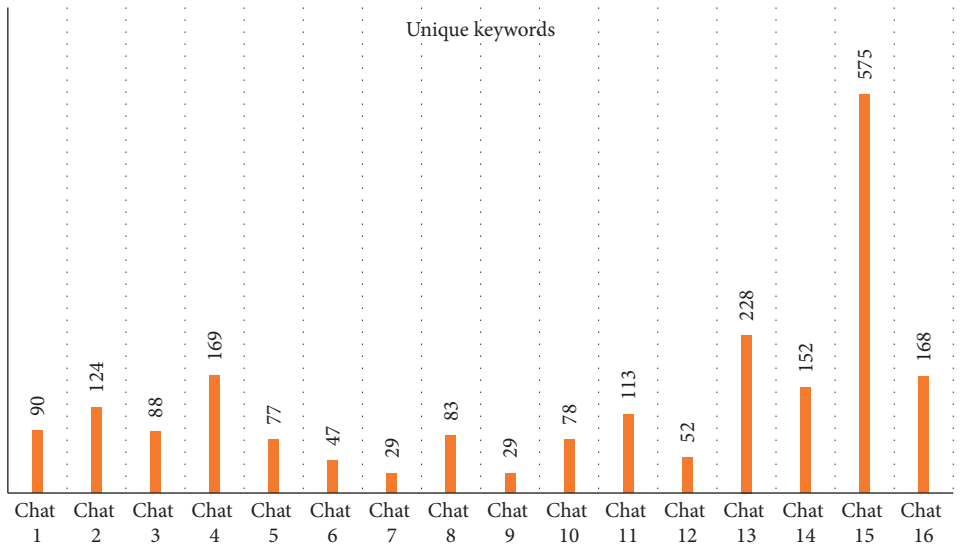

Figure 21: Bar chart showing the number of unique keywords found in the WhatsApp Chat of 16 persons.

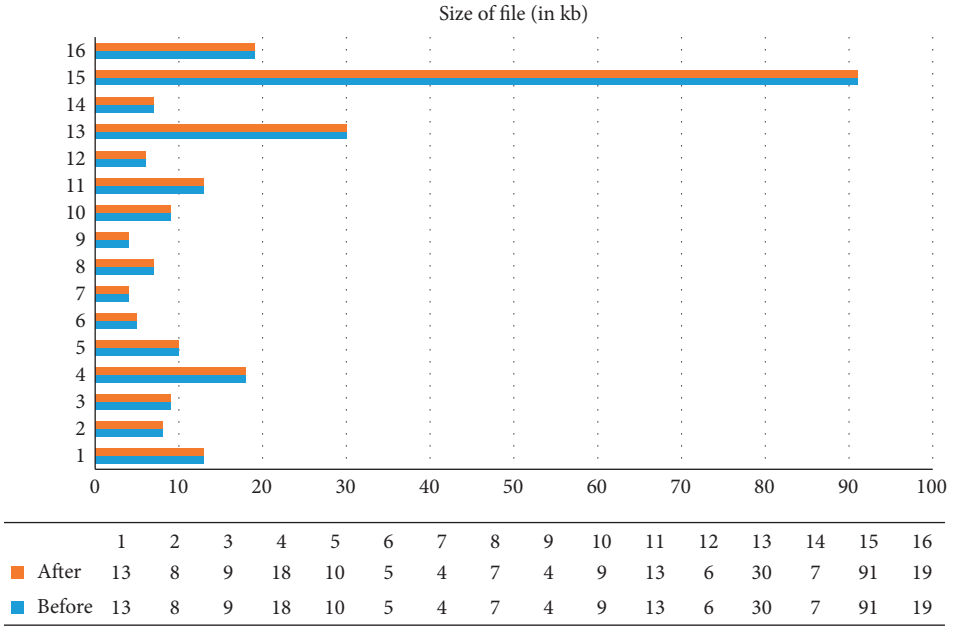

Figure 22: Bar chart showing the size of file before and after the application of Caesar Cipher.

OUTPUT: Weighted Graph with n vertices (G=(V,E))

(1) Set all Dict_i ϕ. $1 \le i \le n$

(2) Collect Sample WhatsApp chats of n persons for a defined date and time, say of a month

(3) Create weighted connected graph, G with $||V|| = n$. Set weight of each edge to zero

(4) **for** $i \leftarrow 1$ **to** n

do Start scanning from first letter of WAC_i.

for each wd $\in \text{WAC}_i$

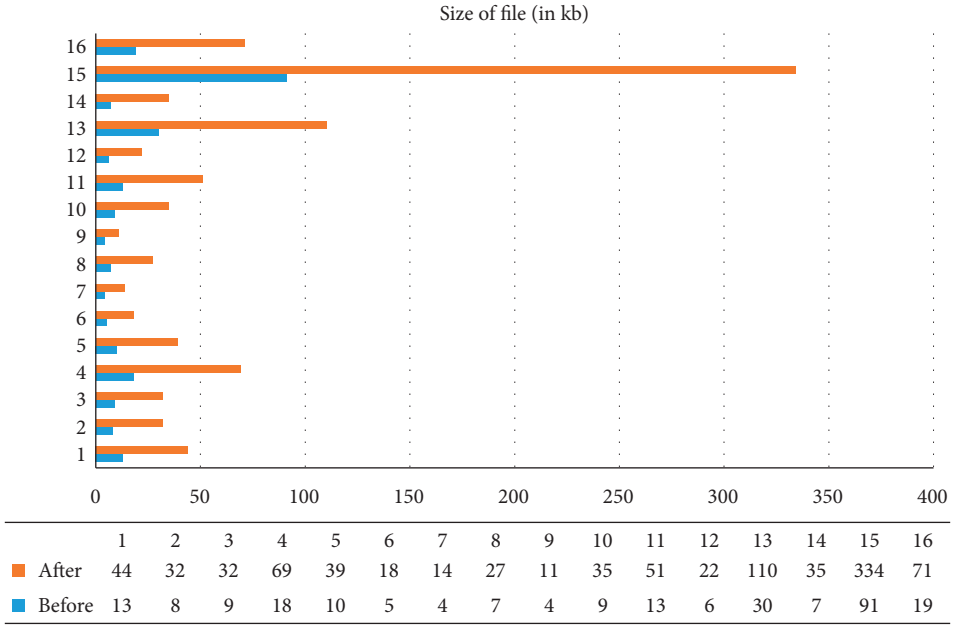

Figure 23: Bar chart showing the size of file before and after the application of Block Quadra Crypto Technique.

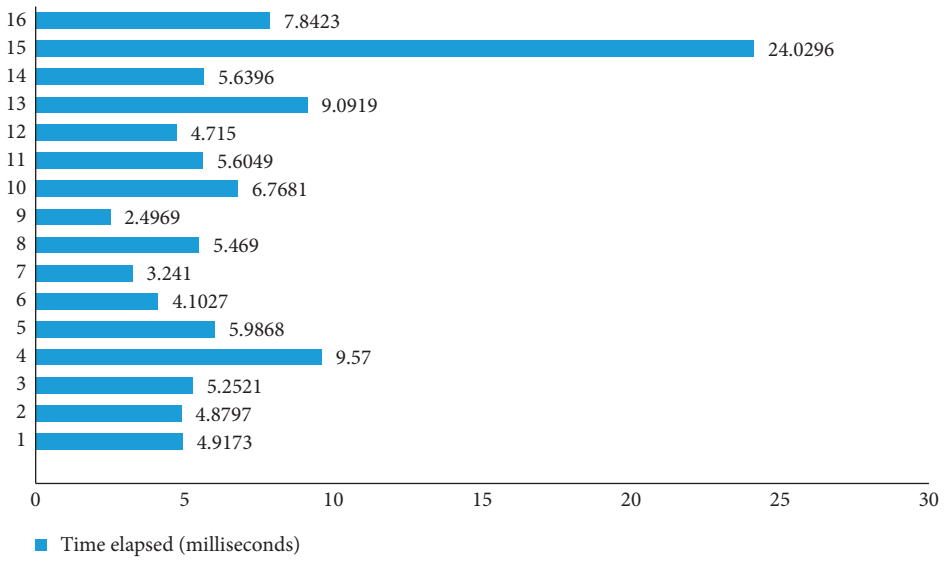

Figure 24: Bar chart showing the time consumed in encryption (Caesar Cipher).

do if ($l_w \geq 6$ and $w_d \in Dict_i$)
then continue
else if ($l_w \geq 6$ and $w_d \notin Dict_i$)
then $Dict_i \leftarrow w_d \cup Dict_i$

(5) **for** $i \leftarrow 1$ **to** n
do $j \leftarrow i + 1$
while $j < n$
do Check for each w_d from $Dict_i$
if (FIND(w_d, $Dict_j$))
do Increment weight of the edge between $Node_i$(representing $Dict_i$) and $Node_j$ (representing $Dict_j$) by one.

(6) Delete zero weight edges from the weighted graph

*FIND(w_d, $Dict_j$) returns true if $w_d \in Dict_j$ else false

7. Results

Social Network Resultant Weighted Matrix was created (Figure 19 with chats in Caesar Cipher and Figure 20 with chats in Block Quadra Crypto Technique) which shows the number of unique common words between 2 chats. For example, matrix position [1, 2] gives the number of unique common words in Chat 1 and Chat 2. The principle diagonal elements in the resultant weighted matrix represent the number of unique keywords in that chat; for instance, matrix position [2, 2] gives the number of unique keywords in Chat

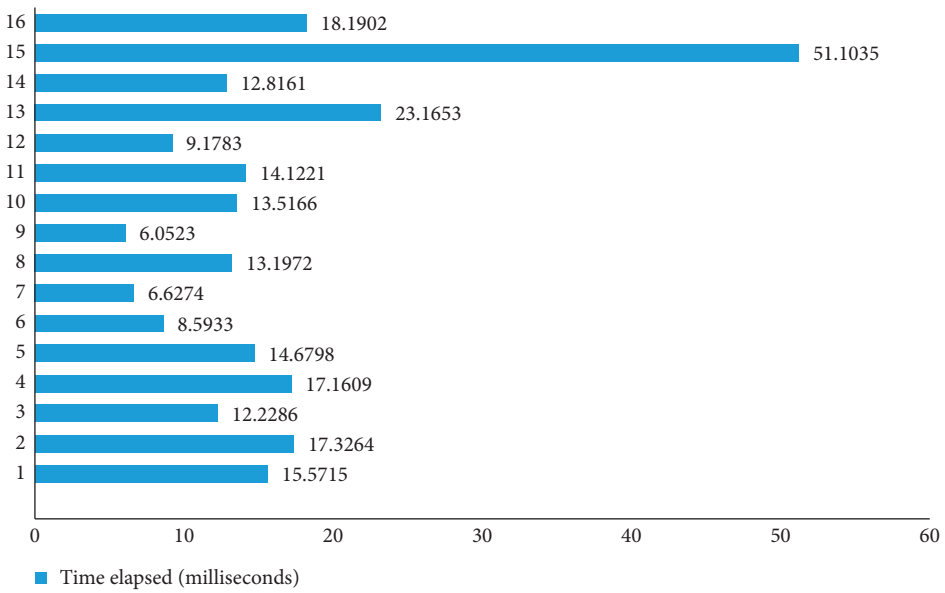

Figure 25: Bar chart showing the time consumed in encryption (Block Quadra Crypto Technique).

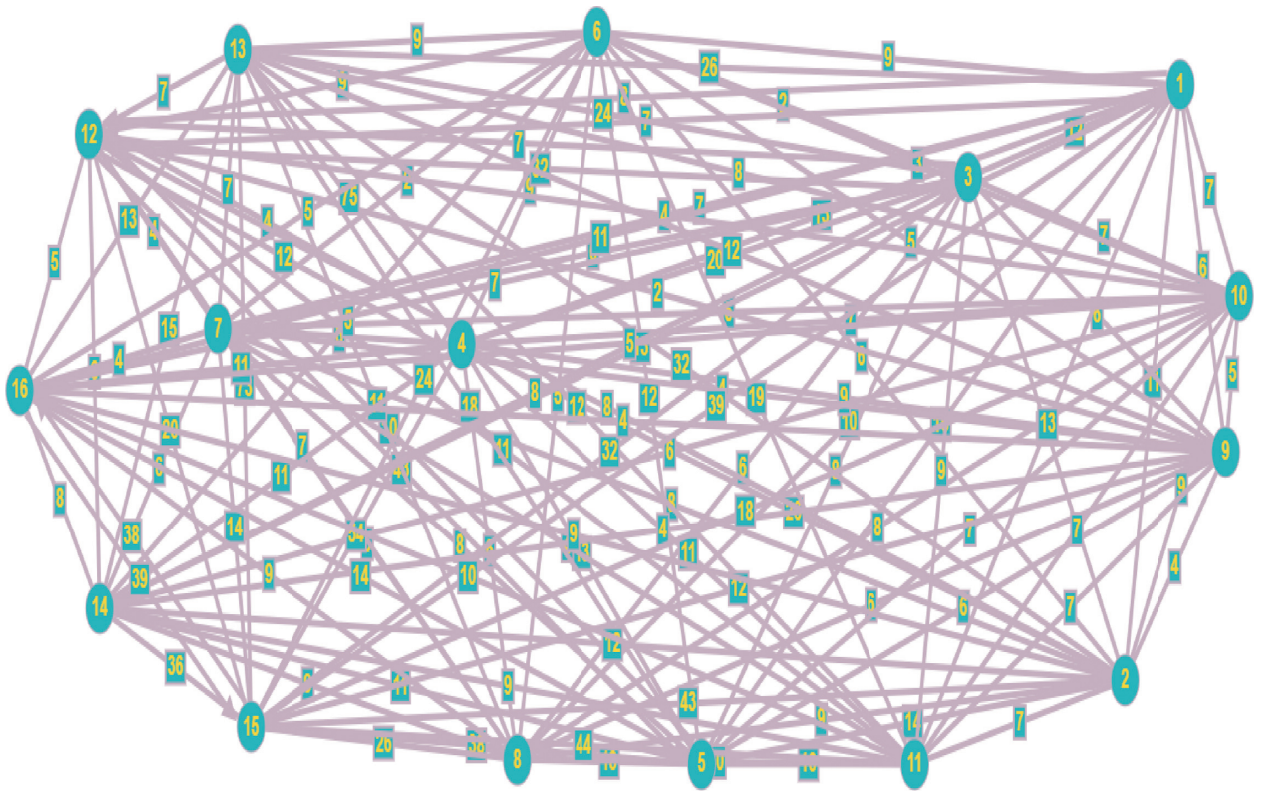

Figure 26: Node graph showing common words between 16 persons.

2. Figure 21 shows the total number of unique keywords found in the respective chats. Figures 22 and 23 show the change in the size of the .CSV (comma-separated value delimited) file before and after the application of the respective encryption technique; that is, the file size remains the same on the application of Caesar Cipher Technique, but

Figure 27: Node graph showing social inclination between groups of 16 selected persons.

on the other hand, the file size increases (approximately 4 times) on the application of Block Quadra Crypto Technique. Figures 24 and 25 show the time taken in milliseconds to encrypt the chat .csv files. Figures 26 and 27 depict some of the many ways of the node graph that can be represented where the nodes represent the persons and the edges represent the weights.

8. Conclusion and Future Work

This proposed work is in continuation of the previous work done in "WAPiS, WhatsApp Pattern Identification Algorithm indicating Social Connection" [24] wherein all the chats were imported into the MongoDB database and a connectivity program in C# was made.

In the current research work, the WhatsApp chats after encryption were imported into the MongoDB database and were then decrypted, before analyzing and the results were obtained. The implementation of cipher techniques was achieved, and the results as elaborated in Section 7 were achieved which are encouraging and exceed the expectations. However, it would be interesting to explore and enhance the asymmetric encryption cryptographic techniques and algorithms that facilitate the usage of the public and private key pair and would definitely provide a pretty large scope to work upon in the time to come.

In future, it also proposed to integrate the concept of community creation, identification, and detection in the current research work of collection and aggregation of the WhatsApp chats of different persons. This work would give insight into Ego Network and help in the quick identification of those nodes/persons who are quite active in the sharing and exchange of WhatsApp chats, popularly referred to as "Hub Nodes" in social network.

The results achieved are also proposed to be compared with other cryptographic techniques such as SCLCT, secured cross language cipher technique [25], C^3T, cloud-based cyclic cryptographic technique [26], and LBCLCT, location-based cross language cipher technique [27]. It is also proposed to extend the Block Quadra Crypto Technique with its successor symmetric cipher techniques such as Tri-Quadrant Cryptographic Technique (TQCT), Odd-Even Block-Based Cryptographic Technique (OEBBCT), and Quad-Quadrant Cryptographic Technique (QQCT). Also, effort would be made to enhance the level of security by adding a pair of public and private keys in the proposed cipher technique.

Data Availability

The data used to support the findings of this study are included within the article.

Conflicts of Interest

The authors declare that they have no conflicts of interest.

Acknowledgments

The authors are thankful to Director (Research and Consultancy), Guru Gobind Singh Indraprastha University, Dwarka, Delhi, India, for providing APC (article-processing charges) towards publication of this research paper.

References

[1] S. Bajaj and R. Johari, "Big data: a boon or bane-the big question," in *Proceedings of the 2016 Second International Conference on Computational Intelligence & Communication Technology (CICT)*, pp. 106–110, IEEE, Ghaziabad, India, February 2016.

[2] X. Chen, M. Vorvoreanu, and K. Madhavan, "Mining social media data for understanding students' learning experiences," *IEEE Transactions on Learning Technologies*, vol. 7, no. 3, pp. 246–259, 2014.

[3] S. Gole and B. Tidke, "A survey of big data in social media using data mining techniques," in *Proceedings of the 2015 International Conference on Advanced Computing and Communication Systems*, January 2015.

[4] N. Z. Quazilbash, S. M. H. Qadri, and S. Khoja, "Improved user RTSE experience on the web through fast retrieval of social media content," in *Proceedings of the 2012 15th International Multitopic Conference (INMIC)*, December 2012.

[5] Y. S. Tawiah, H. E. Nondzor, and A. Alhaji, "Usage of WhatsApp and voice calls (phone call): preference of polytechnic students in Ghana," *Science Journal of Business and Management*, vol. 2, no. 4, pp. 103–108, 2014.

[6] A. Gosain and S. Dahiya, "Performance analysis of various fuzzy clustering algorithms: a review," *Procedia Computer Science*, vol. 79, pp. 100–111, 2016.

[7] B. I. A. Alsaleem, "The effect of "WhatsApp" electronic dialogue journaling on improving writing vocabulary word choice and voice of EFL undergraduate Saudi students," *Arab World English Journal*, vol. 4, no. 3, pp. 213–225, 2013.

[8] J. Yeboah and G. D. Ewur, "The impact of WhatsApp messenger usage on students performance in Tertiary Institutions in Ghana," *Journal of Education and Practice*, vol. 5, no. 6, pp. 157–164, 2014.

[9] A. Ngaleka and W. Uys, "M-learning with WhatsApp: a conversation analysis," in *Proceedings of the 8th International Conference on e-Learning ICEL-2013*, p. 282, Academic Conferences International Limited, Cape Town, South Africa, June 2013.

[10] C. Barhoumi, "The effectiveness of WhatsApp mobile learning activities guided by activity theory on students' knowledge management," *Contemporary Educational Technology*, vol. 6, no. 3, pp. 221–238, 2015.

[11] T. Bansal and D. Joshi, "A study of students experiences of WhatsApp mobile learning," *Global Journal of Human-Social Science Research*, vol. 14, no. 4, 2014.

[12] D. Bouhnik and M. Deshen, "WhatsApp goes to school: mobile instant messaging between teachers and students," *Journal of Information Technology Education: Research*, vol. 13, pp. 217–231, 2014.

[13] A. Sánchez-Moya and O. Cruz-Moya, "WhatsApp, textese, and moral panics: discourse features and habits across two generations," *Procedia - Social and Behavioral Sciences*, vol. 173, pp. 300–306, 2015.

[14] A. D. Ahad and S. M. A. Lim, "Convenience or nuisance?: the 'WhatsApp' dilemma," *Procedia - Social and Behavioral Sciences*, vol. 155, pp. 189–196, 2014.

[15] C. Petitjean and E. Morel, ""Hahaha": laughter as a resource to manage WhatsApp conversations," *Journal of Pragmatics*, vol. 110, pp. 1–19, 2017.

[16] T. Simon, A. Goldberg, D. Leykin, and B. Adini, "Kidnapping WhatsApp - rumors during the search and rescue operation of three kidnapped youth," *Computers in Human Behavior*, vol. 64, pp. 183–190, 2016.

[17] https://www.darkreading.com/endpoint/whatsapp-mobile-phishings-newest-%20attack-target/a/d-id/1332652.

[18] https://www.cybersecurity-insiders.com/millions-of-whatsapp-and-telegram-%20users-are-vulnerable-to-cyber-attacks/.

[19] https://www.cybersecurity-insiders.com/cyber-attack-on-whatsapp-leads-to-a-%202-hour-major-outage/.

[20] https://research.checkpoint.com/fakesapp-a-vulnerability-in-whatsapp/.

[21] https://searchsecurity.techtarget.com/news/252446722/WhatsApp-%20vulnerabilities-let-hackers-alter-messages.

[22] https://searchsecurity.techtarget.com/answer/How-did-WhatsApp-%20vulnerabilities-get-around-encryption.

[23] https://www.bleepingcomputer.com/news/security/whatsapp-vulnerability-%20allows-attackers-to-alter-messages-in-chats/.

[24] R. Johari, S. Kalra, S. Dahiya, and P. Yadav, "WAPiS: WhatsApp pattern identification algorithm indicating social connection," in *Proceedings of the International Conference on Advanced Computational and Communication Paradigms – 2017 (ICACCP-2017)*, pp. 595–603, Springer, Sikkim, India, September 2017.

[25] S. Kumar, R. Johari, L. Singh, and K. Gupta, "SCLCT: secured cross language cipher technique," in *Proceedings of the 2017 International Conference on Computing, Communication and Automation (ICCCA)*, pp. 545–550, IEEE, Greater Noida, India, May 2017.

[26] S. Gupta, R. Johari, P. Garg, and K. Gupta, "C^3T: cloud based cyclic cryptographic technique and it's comparative analysis with classical cipher techniques," in *Proceedings of the 2018 5th International Conference on Signal Processing and Integrated Networks (SPIN)*, pp. 332–337, IEEE, Noida, India, February 2018.

[27] V. Gupta, R. Johari, and K. Gupta, S. Seth, LBCLCT: location based cross language cipher technique," in *Smart Cities Performability, Cognition, & Security*, pp. 221–234, Springer, Switzerland, 2020.

This article has been accepted for publication in a future issue of this journal, but has not been fully edited. Content may change prior to final publication. Citation information: DOI 10.1109/TTE.2021.3049559, IEEE Transactions on Transportation Electrification

Second Order Ripple Minimization in Single Phase Single Stage On-Board PEV Charger

Aakash Kumar Seth and Mukhtiar Singh, *Member, IEEE*

Abstract— **This paper presents a single phase, single stage on-board Plug-in Electric Vehicle (PEV) charger. The single phase PEV chargers have inherent problem of introducing second order ripple component on DC side. This problem is further exaggerated during vehicle-to-grid (V2G) mode of operation where it may be normally controlled to supply both active as well as reactive power. During the V2G reactive power compensation, the second order harmonics ripple component at DC side will increase which further reduces the life cycle and performance of battery pack. Therefore, a second order ripple component compensation technique is proposed by pre-compensating the reference current itself. The resultant reference current is periodic in nature and accordingly, repetitive controller (RC) is used which is well known for its capability of tracking the periodic signals. The PEV charger is controlled in both grid to vehicle (G2V) and V2G mode. Here, the performance of the controller has been tested in eight different modes on active-reactive (P-Q) power plane and found that ripple minimization technique successfully reduced second order ripple component on DC side. The PEV charger controller has been simulated in MATLAB/Simulink environment and implemented on the scaled down experimental setup.**

***Index Terms*— Battery Energy storage, ripple minimization, Power electronics, Battery chargers, Charge Controller**

I. INTRODUCTION

With depletion of oil reserve, a paradigm shift is required from fossil fuel vehicle to zero emission, more efficient and sustainable electric vehicle (EV). Generally, EV can be classified as Battery Electric Vehicle (BEV), Hybrid Electric Vehicle (HEV) and Fuel Cell Electric Vehicle (FCEV) [1]. Due to the demerits in FCEVs such as high fuel cell cost, hydrogen storage, transportation and production of hydrogen and life cycle of fuel cell, these vehicles are not much popular [2]. In HEV, a utility grid is required for supplying electricity and thereby such vehicles are well known as gridable electric vehicle (GEV). To discourage the use of fossil fuel usage in order to get rid of pollution and greenhouse emission, the PEV and HEV are gaining lot of popularity very recently. Further, the rolling battery pack in PEV can act as the distribution energy storage units and may be helpful in the widespread grid integration of renewable energy sources (RES). The PEVs are highly responsive, provide a high torque and may save more than 80% on fuel consumption in comparison with petrol vehicle [3]. The major barriers that has stagnated the overall success of PEVs are high cost, battery life, energy storage capacity, charging complications, short driving range and lack of charging infrastructure [4]-[5].

Some of the EVs use lead acid battery because of low cost, simple in manufacturing, high cell voltage (i.e. 2.1 V) and higher reliability. It has good discharging rate which makes it preferable for quick acceleration applications and also capable to respond fast for load variations. It has very low self-discharging rate i.e. 3-20% per month [6].

The life of battery is measured by two ways i.e. minimum calendar year and number of charger/discharge cycles. However, it is mainly depends on the amount of ripple in battery current. This unfavorable low frequency ripple component of current adversely affect the battery lifetime because of internal heating [7]-[8], and also raises the count of charge/discharge micro cycles of the battery pack which deplete the lifetime more rapidly. This ripple component may diminish by using the large filter circuit or a proper control design. The allowable amount of current ripple in lead-acid battery without affecting the lifetime is different and varies with the manufacturers. Some of the manufacturers allow the amount of current ripple is *C*/10 or *C*/20, where *C* is the charging current of battery [9]. It means if a battery is charging current is 100 Amps then the allowable ripple is 10 Amps for *C*/10 type of battery and 5 Amps for *C*/20. Therefore, ripple in output of the charger must be within that permissible limits to prevent the battery from overheating and life degradation.

Generally, two-stage charger is utilized to minimizing the ripple current component. This consist two power converters to charge the battery pack. Here, the second stage i.e. DC-DC conversion provides the galvanic isolation between grid and battery [10]-[11]. However, the use of this stage will increase the hardware cost, with decreased efficiency and increased component count. With the controller of DC-DC converter, the ripple component in battery current can be minimized easily. Moreover, the control design of two stage charger is quite complex as it requires two separate controllers for both the converters. Therefore, to overcome the limitation of two stage charger, a fully controlled single phase, single stage converter-

Aakash Kumar Seth is research scholar in Department of Electrical Engineering, Delhi Technological University, Delhi, India (e-mail: akrseth@gmail.com)
(*corresponding author*: Mukhtiar Singh) is professor in Department of Electrical Engineering, Delhi Technological University, Delhi, India (e-mail: smukhtiar_79@yahoo.co.in)

2332-7782 (c) 2020 IEEE. Personal use is permitted, but republication/redistribution requires IEEE permission. See http://www.ieee.org/publications_standards/publications/rights/index.html for more information.
Authorized licensed use limited to: DELHI TECHNICAL UNIV. Downloaded on February 15,2021 at 10:24:35 UTC from IEEE Xplore. Restrictions apply.

This article has been accepted for publication in a future issue of this journal, but has not been fully edited. Content may change prior to final publication. Citation information: DOI 10.1109/TTE.2021.3049559, IEEE Transactions on Transportation Electrification

based charger may be used. However, these types of single stage chargers suffer from higher amount of second-order harmonic ripple current component and require large value of DC link capacitor or tuned LC filter or by involving pre-compensating terms in control design [12]. This results into the increase in capacitor size, cost and overall higher order of system for which controller design becomes very complex task.

Several control techniques for vehicle charging have been discussed in literature by many researchers [10]-[11], [13]-[17]. Generally, the control design of charger has two loops, where the current control (i.e. inner loop) is much faster than the outer slower loop. The outer loops mainly deal with regulation of DC signals in terms of active power (*P*), reactive power (*Q*) or DC voltage regulations which may be easily handled by normal *PI* regulator. The inner current loop may also involve the control of DC signals, but finally complicated transformations are applied in order to generate the equivalent AC reference signal. The *d-q* transformation is very much suitable for three phase system. However, the conversion accuracy suffers in case of single phase transformation [13]. Therefore, the reference signal of inner control loop is directly realized by multiplying the *cos* and *sin* terms to the output of outer *P* and *Q* control loops, respectively.

Among the various control strategies available in the literature for the tracking of inner current loop of charger, most of them are based on proportional plus integral (*PI*), proportional plus resonant (*PR*), hysteresis and unified controller. Here, *PI* is the simple and exhibits satisfactory performance under steady state conditions, but they fail to track the periodic signals [11], [15]. The *PR* controller has tuning issues and can be tuned only for selective frequencies and cannot diminish the lower order harmonics [10], [16]. The hysteresis control may have the issue of resonance due to fluctuating switching frequency [10]. The unified controller may take much time due to conversion stages in control loop [18].

Since, the reference signal of inner current control in present case is periodic in nature, a repetitive controller (RC) which is based on internal model principle theory (IMPT) has been utilized due to its well-known capability of tracking the periodic signals [19]-[23]. This approach of current control is found to be very helpful in seamless exchange of power in G2V and V2G mode of operation. Further, this reference control signal is modified by involving the pre-compensating terms for the reduction of DC-ripple current component. The nature of such resultant control signal is periodic in nature and very difficult to track with normal *PI* regulators [15].

Therefore, the main aim of proposed work is to develop a robust control system for single phase, single stage EV charger to operate it in wide range of G2V and V2G mode of operations while minimizing the second-order ripple current component on DC side. The proposed charger may supply active power to grid if required and compensate reactive power (inductive or capacitive) if a battery charge at slower rate. In that case, the remaining rating of charger is utilized for compensating the reactive power for optimally utilization of charger's rating. Moreover, if the battery is not connected to the charger then the proposed charger can work as an active power filter and improves the power quality. Supporting reactive power by charger can curtails the installation and maintenance cost of reactive power compensators such as static synchronous compensators, static VAR compensators, and capacitor banks [24]. However, the reactive power compensation while charging may put lot of stress on battery and reduce its life cycle due to the presence of unwanted ripple current component in charger as explained in [25]-[26].

The proposed control strategy is designed in MATLAB/Simulink. The simulation results have been provided for eight different modes of charger under dynamic exchange of active and reactive power. The proposed control approach has been validated through the scaled down experimental setup.

The structure of the paper is as follows. The system description is presented in section II. The section III presented the different modes of operation and system control. The proposed RC is described in section IV. The simulation and experimental results are presented in section V and VI respectively. Finally, the conclusion of paper is summarized in section VII.

II. System Description

The proposed system consists of insulated gate bipolar transistor (IGBT) with antiparallel diode based single phase h-bridge converter and can easily perform four quadrant operation due to its bidirectional capability as shown in Fig. 1. Each switch has the blocking capacity of DC-link voltage (V_{dc}) and peak current during conduction is $\sqrt{2}I_s$, where I_s is the rated RMS value of grid current. When the upper switch of phase leg (S_1) and lower switch of neutral leg (S_4) are on, lower switch of phase leg (S_2) and upper switch of neutral leg (S_3) are off, and vice versa. The EV charger is directly connected to the single-phase AC supply through interfacing inductor (L_f) to compensate harmonic of grid current and achieve sinusoidal current waveform. On the DC side EV battery pack is connected in parallel with DC link capacitor.

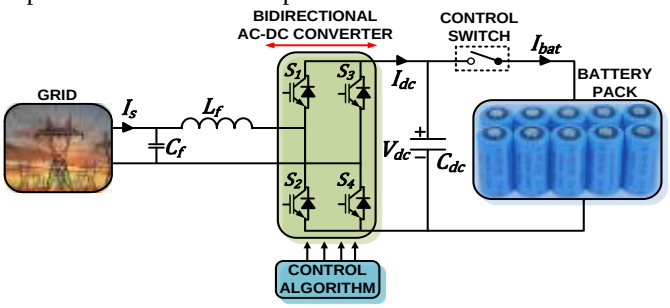

Fig.1. On Board Plug-in Electric Vehicle Charger

The main focus of this paper is to design and implementation of the PEV charger controller and validates the controller performance during all four-quadrant operation on active-reactive power plane as well as reduction in second order harmonic ripple current component at DC side. Moreover, the total harmonic distortion (THD) level must be contained to 5% irrespective of battery charging level and size of battery pack [27].

III. System Operation And Control Development

The main purpose of bidirectional PEV charger is to have the exchange of active as well as reactive power between grid and

2332-7782 (c) 2020 IEEE. Personal use is permitted, but republication/redistribution requires IEEE permission. See http://www.ieee.org/publications_standards/publications/rights/index.html for more information.
Authorized licensed use limited to: DELHI TECHNICAL UNIV. Downloaded on February 15,2021 at 10:24:35 UTC from IEEE Xplore. Restrictions apply.

This article has been accepted for publication in a future issue of this journal, but has not been fully edited. Content may change prior to final publication. Citation information: DOI 10.1109/TTE.2021.3049559, IEEE Transactions on Transportation Electrification

vehicle. Thus, the PEV may supply active power to grid whenever there is sudden increase in demand and may also absorb it in case of availability of surplus power. Therefore, the large amount of PEVs in distribution network may not only help in absorbing the mismatch in demand and supply but also very useful in the large-scale integration of intermittent renewables in to the grid. Moreover, the controlled exchange of reactive power further reduces the chances of voltage fluctuation.

Here, it is worthwhile to mention that in four quadrant operation with exchange of active and reactive power, only eight modes of operation are possible. The different combinations of active-reactive power exchange are shown in Fig. 2. The reactive power is positive in mode- 1, 5 and 7, negative in mode- 2, 6 and 8 and zero in mode-3 and 4.

Similarly, active power is positive in mode- 3, 5 and 6, negative in mode- 4, 7 and 8 and zero in mode 1 and 2. Note that the power transfer from the grid to vehicle takes positive sign and vice versa.

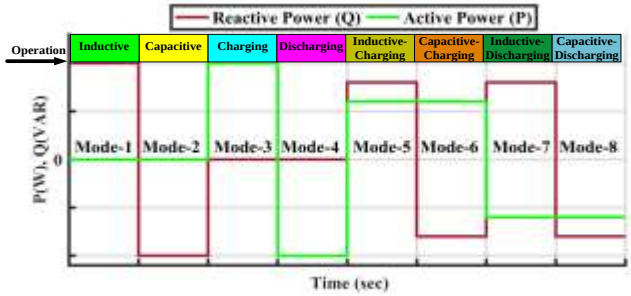

Fig. 2. Operating modes of charger.

The positive active power (P) indicates the charging operation as power is transferred to the vehicle while the negative power shows the discharging operation. For inductive operation, reactive power (Q) is positive and in capacitive operation, it is taken as negative. Mode 1 and 2 shows the exchange of inductive and capacitive reactive power, respectively, while the active power is kept at zero. Therefore, the current lags behind exactly 90° in mode 1 and leads by 90° in mode 2. Similarly, the charging and discharging operation without exchange of reactive power are related to mode 3 and 4, respectively. In that case, the current is exactly in phase with voltage during mode 3 and exactly out of phase during mode 4. Mode 5 and 6 are associated with the exchange of reactive power (i.e. inductive and reactive respectively) with charging of battery simultaneously. Since, being a G2V mode, the active power flows from grid to battery while the reactive power supplied may be inductive or capacitive. Accordingly, the current lags or leads the voltage while having phase difference less than 90°, respectively. Similarly, during V2G mode, the active power is supplied back from battery to grid while the reactive power may be inductive or capacitive. Accordingly, the current lags or leads the voltage while having phase difference more than 90°, respectively.

The layout of proposed on-board PEV charger with its control is shown in Fig. 3. Here, the outer control loops are used to regulate the P and Q which are inherently DC quantities and therefore, the simple PI regulator is used to track them. Since, the inner loop control signal in proposed method is periodic and accordingly RC is utilized to track this periodic signal. Here, the main aim is to set the reference signal for inner loop while pre-compensating the second order ripple current harmonics. Therefore, it is very important to analyze the power equations on AC side which are responsible for the introduction of ripple current harmonics on the DC side. Let us assume that the AC side voltage and current are as follows,

$$v = v_m \cos \omega t \tag{1}$$

$$i = i_m \cos(\omega t - \emptyset) \tag{2}$$

Where, v_m and i_m are peak value of AC voltage and current respectively, and $\emptyset$ is phase angle between them.

AC power can be calculated by multiplying (1) and (2).

$$P_{ac} = v \cdot i = v_m \cos \omega t \cdot i_m \cos(\omega t - \emptyset)$$

$$= \frac{v_m}{\sqrt{2}} \cdot \frac{i_m}{\sqrt{2}} \cos \emptyset + \frac{v_m}{\sqrt{2}} \cdot \frac{i_m}{\sqrt{2}} \cos(2\omega t - \emptyset)$$

$$= v_r \cdot i_r \cdot \cos \emptyset + v_r \cdot i_r \cdot \cos(2\omega t - \emptyset) \tag{3}$$

Here v_r and i_r are the root mean square (RMS) value of AC side voltage and current respectively.

The first term of P_{ac} represents the active power and second term represents the reactive power of the AC side.

$$P = v_r \cdot i_r \cdot \cos \emptyset = k_r \cos \emptyset \tag{4}$$

$$Q = v_r \cdot i_r \cdot \cos(2\omega t - \emptyset) = k_r \cos(2\omega t - \emptyset) \tag{5}$$

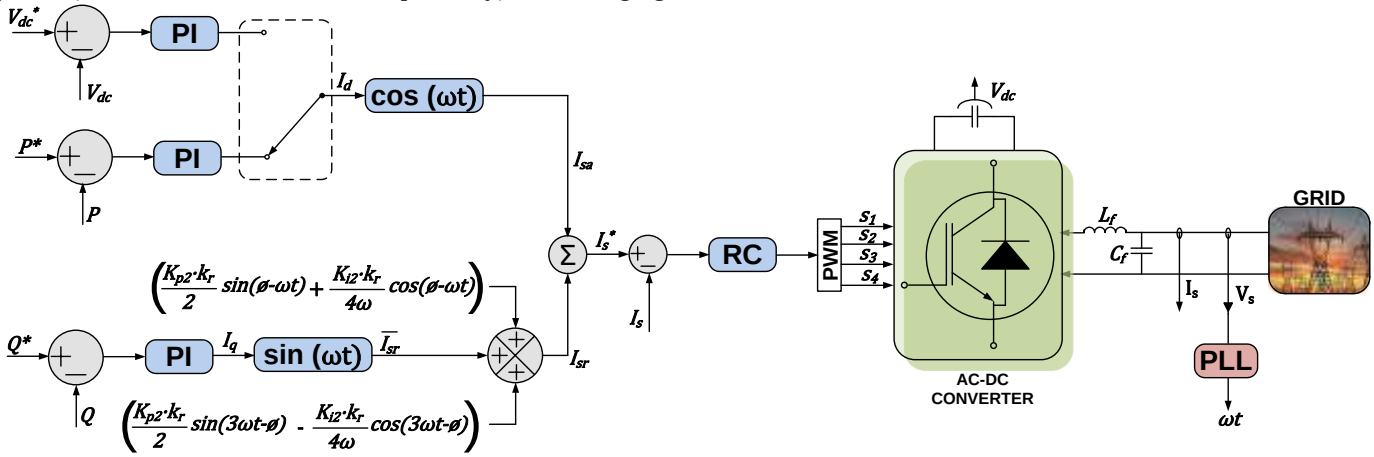

Fig. 3. Control Description of single stage on board EV charger.

2332-7782 (c) 2020 IEEE. Personal use is permitted, but republication/redistribution requires IEEE permission. See http://www.ieee.org/publications_standards/publications/rights/index.html for more information.
Authorized licensed use limited to: DELHI TECHNICAL UNIV. Downloaded on February 15,2021 at 10:24:35 UTC from IEEE Xplore. Restrictions apply.

This article has been accepted for publication in a future issue of this journal, but has not been fully edited. Content may change prior to final publication. Citation information: DOI 10.1109/TTE.2021.3049559, IEEE Transactions on Transportation Electrification

Here, $k_r = v_r \cdot i_r$

The active component of current may be determined as

$$I_d = K_{p1}(P^* - P) + K_{i1}\int (P^* - P)\,dt$$

$$= K_{p1}(P^* - k_r \cos\emptyset) + K_{i1}\int (P^* - k_r \cos\emptyset)\,dt$$

$$= K_{p1} \cdot P^* - K_{p1} \cdot k_r \cos\emptyset + K_{i1}\, P^*\, t - K_{i1}\, k_r\, \cos\emptyset \cdot t \quad (6)$$

Similarly, the reactive component of current may be determined as

$$I_q = K_{p2}(Q^* - Q) + K_{i2}\int (Q^* - Q)\,dt$$

$$= K_{p2}[Q^* - k_r \cos(2\omega t - \emptyset)] + K_{i2}\int [Q^* - k_r \cos(2\omega t - \emptyset)]\,dt$$

$$= K_{p2}\, Q^* - K_{p2}\, k_r\, \cos(2\omega t - \emptyset) + K_{i2}\, Q^*\, t - K_{i2}\, k_r \cdot \frac{1}{2\omega}\sin(2\omega t - \emptyset) \quad (7)$$

Furthermore, the instantaneous value of active current component is,

$$I_{sa} = I_d \cdot \cos\omega t$$

$$= \left[K_{p1} \cdot P^* - K_{p1} \cdot k_r \cos\emptyset + K_{i1}\, P^*\, t - K_{i1}\, k_r\, \cos\emptyset \cdot t\right] \cdot \cos\omega t$$

$$= \left(K_{p1} + K_{i1} \cdot t\right)[P^* - k_r \cdot \cos\emptyset]\cos\omega t \quad (8)$$

Similarly, the instantaneous value of reactive current component is,

$$\overline{I_{sa}} = I_q \cdot \sin\omega t$$

$$= \left[K_{p2}\, Q^* - K_{p2}\, k_r\, \cos(2\omega t - \emptyset) + K_{i2}\, Q^*\, t - K_{i2}\, k_r \cdot \frac{1}{2\omega}\sin(2\omega t - \emptyset)\right] \cdot \sin\omega t$$

$$= Q^*\left(K_{p2} + K_{i2} \cdot t\right)\sin\omega t - \underbrace{\left[\frac{K_{p2} \cdot k_r}{2}\sin(\emptyset - \omega t) + \frac{K_{i2} \cdot k_r}{4\omega}\cos(\emptyset - \omega t)\right]}_{\text{A}} - \underbrace{\left[\frac{K_{p2} \cdot k_r}{2}\sin(3\omega t - \emptyset) - \frac{K_{i2} \cdot k_r}{4\omega}\cos(3\omega t - \emptyset)\right]}_{\text{B}} \quad (9)$$

From eq. (9) it can be seen that the reactive current component having three terms, where the first term is associated with fundamental frequency component, where the term A comprises the reactive and active lossy component and term B represents the 3rd harmonic component. Here, the term B can be easily eliminated by any low pass filter (LPF) with appropriate cut-off frequency, but it is not advisable to eliminate the term A by LPF because it has fundamental frequency component. Therefore, in the proposed method, both the ripple component terms (i.e. term A & B) have been pre-compensated in the reactive part of reference current itself.

Hence, the modified reference current is the combination of active component (I_{sa}) and modified reactive component(I_{sr}).

$$I_s^* = I_{sa} + I_{sr} \quad (10)$$

IV. Controller Design

The main objective of proposed work is to develop a versatile control law for the proposed system. For the sake of understanding, the simplified diagram of the system is as shown in Fig. 4. Here, PWM driven single phase converter is connected through filtering resistance R_f, inductance L_f, and filtering capacitance C_f. The grid, which may act as both source and load depending on mode of operation (i.e. G2V, V2G) and accordingly, the grid inductance is taken as L_l and grid resistance as R_l.

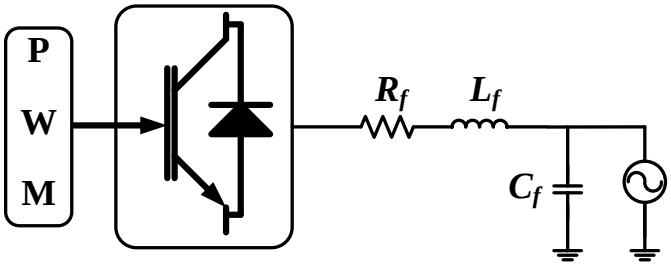

Fig. 4. Single Line System Diagram.

The equivalent control diagram of the system as discussed above is shown in Fig. 5. Here, the control is performed in two stages, where the outer loop deals with *P*, *Q* regulation and being DC signals, these can be easily tracked by the *PI* regulator. Since, the inner current control loop has to deal with the periodic signal which cannot be handled by *PI* controller and accordingly a *RC* is used for inner control loop.

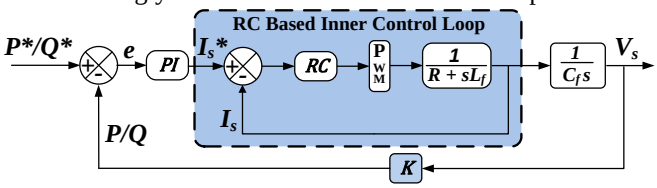

Fig. 5. System Control.

The RC is primarily based on internal model principle theory (IMPT). According to this theory, if a fixed time delay of a given system is associated in closed loop for any periodic signal, asymptotic tracking ability with rejection of harmonic can be achieved.

The general form of RC is shown in Fig. 6.

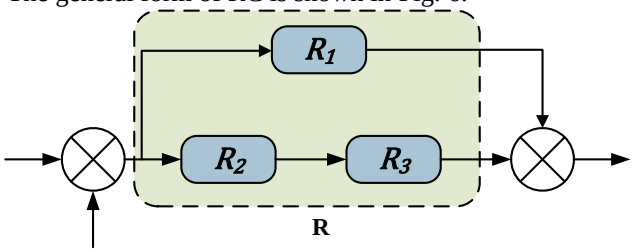

Fig. 6. Generalized RC.

$$R(s) = R_1(s) + R_2(s) \cdot R_3(s) \quad (11)$$

Where $R_3(s)$ is internal model for periodic reference input, $R_1(s)$ and $R_2(s)$ are internally stabilizing controller (ISC) and pre-compensator, respectively. For any repetitive reference signal, internal model may be depicted by feedback time delay with LPF.

$$R_3(s) = \frac{1}{1 + q(s)e^{-Ts}} \quad (12)$$

2332-7782 (c) 2020 IEEE. Personal use is permitted, but republication/redistribution requires IEEE permission. See http://www.ieee.org/publications_standards/publications/rights/index.html for more information.
Authorized licensed use limited to: DELHI TECHNICAL UNIV. Downloaded on February 15,2021 at 10:24:35 UTC from IEEE Xplore. Restrictions apply.

This article has been accepted for publication in a future issue of this journal, but has not been fully edited. Content may change prior to final publication. Citation information: DOI 10.1109/TTE.2021.3049559, IEEE Transactions on Transportation Electrification

Where T represents the time period of fundamental signal and $q(s)$ is LPF.

According to [28], to have stabilized operation of a given plant with unity feedback, the ISC, $R_1(s)$ may be expressed as:

$$R_1(s) = \frac{X(s) + Z(s) * D_P(s)}{Y(s) - Z(s) * N_P(s)}\Big|_{Y(s)-Z(s)*N_P(s)\neq 0} \quad (13)$$

Where $D_P(s)$ and $N_P(s)$ are the co-prime factors of the plant $P(s)$, such that

$$P(s) = \frac{N_P(s)}{D_P(s)} \quad (14)$$

and $X(s)$ and $Y(s)$ are RH_∞ functions satisfying

$$X(s)\,N(s) + Y(s)\,D(s) = 1 \quad (15)$$

Here, the equation (15) is known as Bezout's identity. The term $Z(s)$ in eqn. 13 is known as rational function whose value is selected in such a way that the ISC has maximum gain at fundamental frequency. However, this kind of approach results in to increased impact of disturbance on output. Therefore, the value of $Z(s)$ must be selected in such a way that it should exhibit maximum gain of ISC while ensuring maximum attenuation to the external disturbances and that can be taken as

$$Z(s) = \frac{q(s)}{N(s)}\left(Y(s) - \frac{1}{D(s)\,W_1(s)}\right) \quad (16)$$

Where $W_1(s)$ is the weighing function and selected in order to shape the selectivity function $S(s)$ for a given perturbation bandwidth [25]. Here, the selectivity function is expressed as:

$$S(s) = \frac{1}{1 + P(s)R(s)} \quad (17)$$

Similarly, the complimentary sensitivity function T(s) which sets the upper band of R(s) is expressed as

$$T(s) = \frac{P(s)R(s)}{1 + P(s)R(s)} \quad (18)$$

And for the desired band width from $T(s)$, the $Z(s)$ may be expressed as

$$Z(s) < \frac{1}{N(s)}\left(Y(s) - \frac{1}{D(s)}\left(1 - \frac{1}{W_2(s)}\right)\right) \quad (19)$$

Here, $W_2(s)$ is the frequency dependent weighing function. For the robust performance of controller, the mixed sensitivity constraints are taken as

$$\left\|\begin{bmatrix} W_1(s)\,S(s) \\ W_2(s)\,T(s) \end{bmatrix}\right\|_\infty \leq 1 \quad (20)$$

Now for the present case, the plant transfer function for inner current control loop is expressed as

$$P(s) = \frac{1}{R_f + sL_f} \quad (21)$$

and the co-prime factors of the plant are taken as

$$N(s) = \frac{1/L_f}{(s + R_f/L_f)} \quad (22)$$

and $D(s) = 1$

For the simplicity of control design, the various factors have been taken as $X(s) = 0$, $Y(s) = 1$, $W_1(s) = \frac{s+\omega}{s}$, Since, the plant is strictly proper and has higher order frequency attenuation, the $W_2(s)$ is taken as unity. On using equation (16) the $Z(s)$ is calculated and it is further utilized in equation (13) to find out the higher order ISC, $R_1(s)$. In order to reduce the order of ISC up to 2nd order, a balanced truncation method is applied by calculating the error bond of Hankel's singular value as

$$\|R_1(s) - R_1(s)\|_\infty \leq 2\sum_{k+1}^{n} \sigma_i \quad (23)$$

Where k is the order up to which ISC has to be reduced and σ_i is Hankel's singular values. The approximated reduced order ISC is as follows:

$$R_1(s)^{2nd} = \frac{0.995s^2 + 130.5s + 3985}{s(s + 63.25)} \quad (24)$$

The frequency response of the RC is shown in Fig. 7, where, the RC is the combination of ISC, pre-compensator and feedback delay with low pass filter. Here, the pre-compensator is taken as unity while the time delay of 20ms have been considered for LPF. From the Bode diagram of proposed system, it is evident that the controller offers sufficiently high gain at multiple fundamental frequencies in order to reject their correlated disturbances.

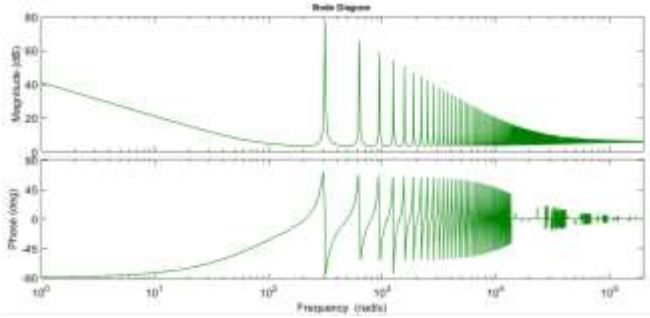

Fig. 7. Frequency response of inner current RC

V. Simulation Results & Discussion

TABLE I
SIMULATION SCENARIO

Mode	Active Power (KW)	Reactive Power (KVAR)	Apparent Power (KVA)	Time (sec)
1	0	1.4	1.4	0-3
2	0	-1.4	1.4	3-6
3	1.4	0	1.4	6-9
4	-1.4	0	1.4	9-12
5	1.1	0.8	1.4	12-15
6	0.8	-1.1	1.4	15-18
7	-1.1	0.8	1.4	18-21
8	-0.8	-1.1	1.4	21-24

The proposed PEV charger with its control design is simulated in MATLAB/Simulink. The Li-ion battery model and

2332-7782 (c) 2020 IEEE. Personal use is permitted, but republication/redistribution requires IEEE permission. See http://www.ieee.org/publications_standards/publications/rights/index.html for more information.
Authorized licensed use limited to: DELHI TECHNICAL UNIV. Downloaded on February 15,2021 at 10:24:35 UTC from IEEE Xplore. Restrictions apply.

This article has been accepted for publication in a future issue of this journal, but has not been fully edited. Content may change prior to final publication. Citation information: DOI 10.1109/TTE.2021.3049559, IEEE Transactions on Transportation Electrification

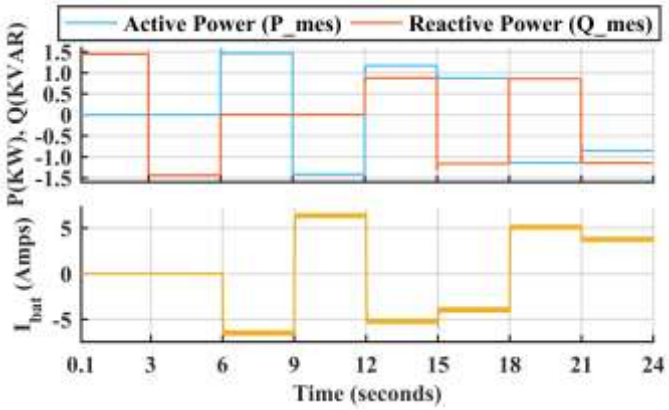

Fig. 8. Measured active, reactive power and Battery Current during all operating modes.

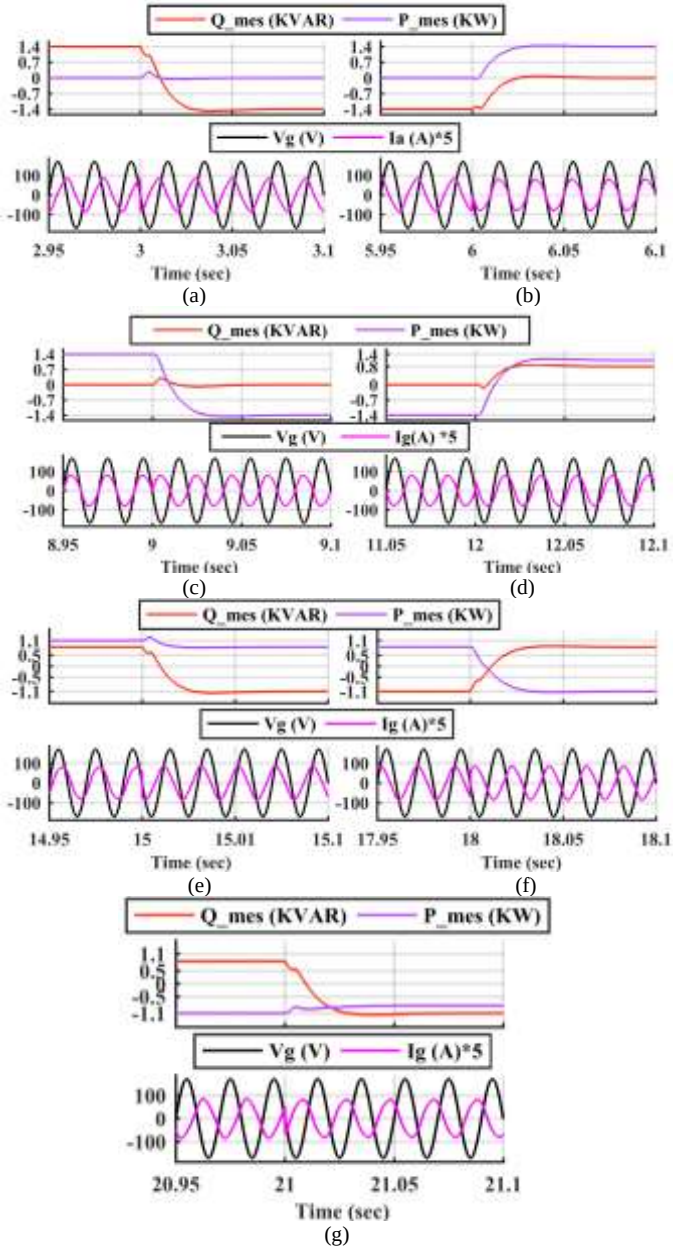

Fig. 9. Measured Current and Voltage relation during change in operating mode (a) mode-1 to mode-2 (b) mode-2 to mode-3 (c) mode-3 to mode-4 (d) mode-4 to mode-5 (e) mode-5 to mode-6 (f) mode-6 to mode-7 (g) mode-7 to mode-8.

two IGBT legs with antiparallel diode based converter is used in simulation. Initially, the battery's SOC level is taken as 50% at 208 V. The battery terminal voltage may be lower or higher than the nominal voltage depending on the SOC level and configuration of cells. The simulations are carried out for the different operating modes of the charger as listed in table I.

The simulation results of measured active (P_mes), reactive (Q_mes) power and battery current (I_{bat}) during all the modes of operation are shown in Fig. 8. During the first four modes, only the exchange of either active or reactive power is performed. Then in next four modes, the exchange of both of the active and reactive is performed simultaneously. During mode 5 and 7, the active and reactive power transfer is limited only up to 78% and 57% of rated power, respectively just to limit the net power exchange within the nominal KVA rating of charger. Similarly, in mode 6 and 8 the, the limit of active and reactive power exchange is interchanged and again the net power exchange remains below the nominal rating.

The simulation results have been presented for both steady state as well as dynamic operating conditions, where the controller shows the tremendous performance. The battery pack voltage level is kept to 208 V, whereas the active and reactive power demand is varied to simulate all the eight mode of operations. The P_mes and Q_mes are calculated at the AC side of the converter and fed to the controller which in turn, tracks the active and reactive power command successfully within the settling time of less than three grid cycles. Note that, the grid current remains same during all operating mode (i.e. $I_g = 1440/120 = 12$ A) since the apparent power is kept constant.

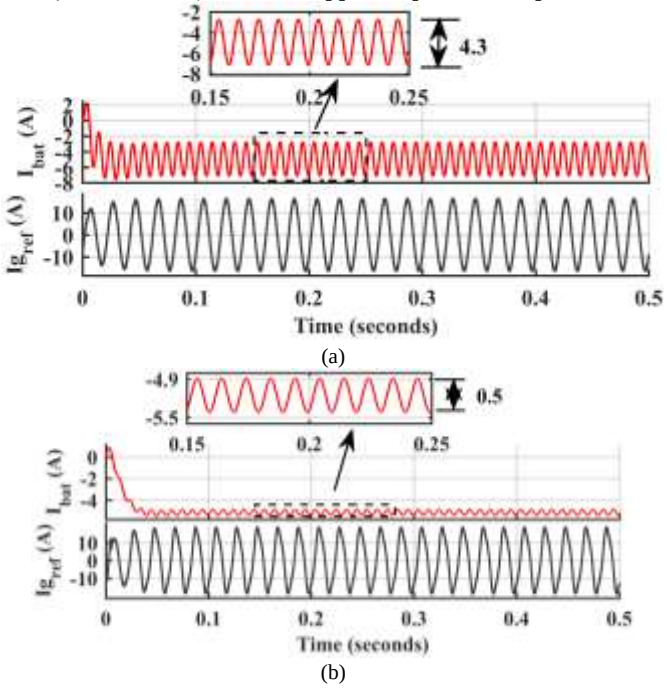

Fig. 10. Simulation Results of DC side current (a) without ripple reduction (b) with ripple reduction method.

The controller performance is shown in expended version of simulation result as shown in Fig. 9. Fig. 9 (a) shows the transition after the reactive power command changes from 1.4 to -1.4 KVAR with active power command is kept to 0. Similarly, Fig. 9 (c) shows the change of active power command from 1.4 to -1.4 KW while keeping the reactive

2332-7782 (c) 2020 IEEE. Personal use is permitted, but republication/redistribution requires IEEE permission. See http://www.ieee.org/publications_standards/publications/rights/index.html for more information.
Authorized licensed use limited to: DELHI TECHNICAL UNIV. Downloaded on February 15,2021 at 10:24:35 UTC from IEEE Xplore. Restrictions apply.

This article has been accepted for publication in a future issue of this journal, but has not been fully edited. Content may change prior to final publication. Citation information: DOI 10.1109/TTE.2021.3049559, IEEE Transactions on Transportation Electrification

power to 0. Fig. 9 (d), (e), (f), (g) shows the various possible cases of battery charger with non-zero active and reactive power command simultaneously.

Fig. 10 (a) and (b) represents the simulation results of DC side and reference grid current without and with reduction of second order ripple current harmonics, respectively. The most challenging battery charger operation is under mode 5 (i.e. EV battery is charging from the grid and charger is compensating reactive power) and accordingly, the results for ripple current reduction methods have been presented for this mode only. It can be clearly seen that the ripples in DC side current have been reduced to almost 1/3rd of their original level.

From the simulation results, it can be analyze that controller successfully reduce the ripple in DC side current and takes less than three grid cycles to respond active and reactive power command during all the possible transition. Furthermore, the modification in reference grid current increases the THD but it is within the permissible limit of IEEE std. 519 i.e. 5%. The proposed battery charger controller algorithm is then designed and tested on experimental setup.

VI. Experimental Results & Discussion

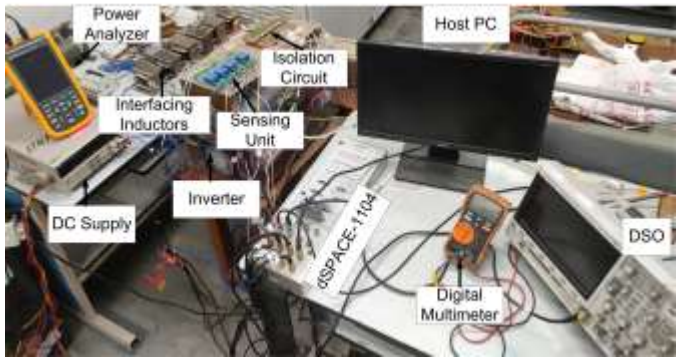

(a)

(b)

Fig. 11. (a) Experimental Setup (b) Battery Bank.

TABLE II
EXPERIMENTAL SCENARIO

Mode	Active Power (W)	Reactive Power (KVAR)	Apparent Power (KVA)
1	0	350	350
2	0	-350	350
3	350	0	350
4	-350	0	350
5	280	210	350
6	280	-210	350
7	-280	210	350
8	-280	-210	350

A scaled hardware prototype of battery charger is also designed to validate the proposed control approach as shown in Fig. 11. For this purpose, two Semikron *IGBT* leg (each having two *IGBT* with antiparallel diode) converter is used and eight 12 V, 7Ahr Lead acid batteries are connected in series to make a 96 V battery pack. The experimental setup parameters are listed in table III. The experimental study has been carried out in real time using *dSPACE 1104*.

The performance of the charger controller is tested as per the scenario listed in table II and the results are shown in Fig. 12. The experimental results have been presented in compliance of simulation results, where the maximum KVA is limited to 350 while the maximum active power and reactive power are restri-

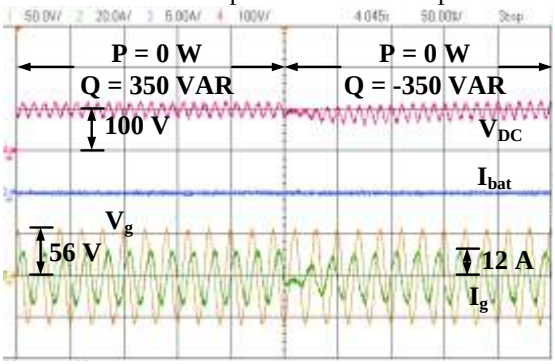

(a)

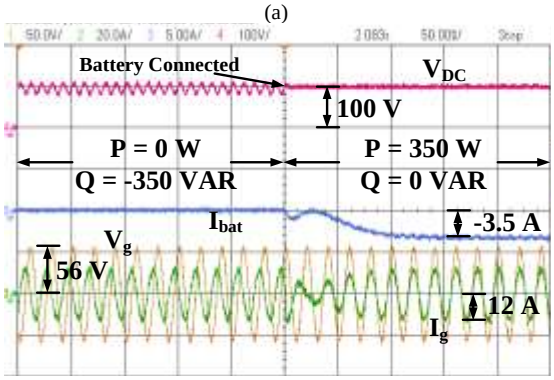

(b)

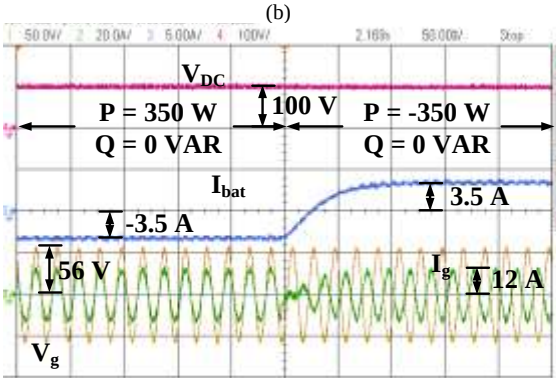

(c)

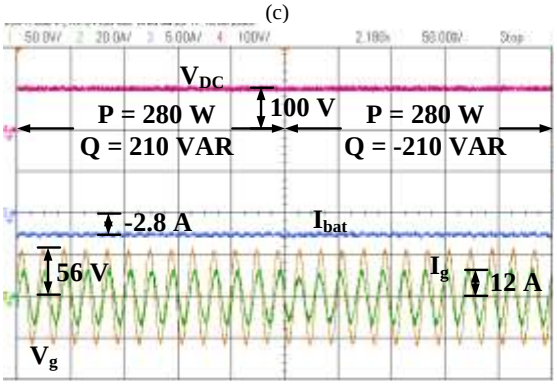

(d)

2332-7782 (c) 2020 IEEE. Personal use is permitted, but republication/redistribution requires IEEE permission. See http://www.ieee.org/publications_standards/publications/rights/index.html for more information.
Authorized licensed use limited to: DELHI TECHNICAL UNIV. Downloaded on February 15,2021 at 10:24:35 UTC from IEEE Xplore. Restrictions apply.

This article has been accepted for publication in a future issue of this journal, but has not been fully edited. Content may change prior to final publication. Citation information: DOI 10.1109/TTE.2021.3049559, IEEE Transactions on Transportation Electrification

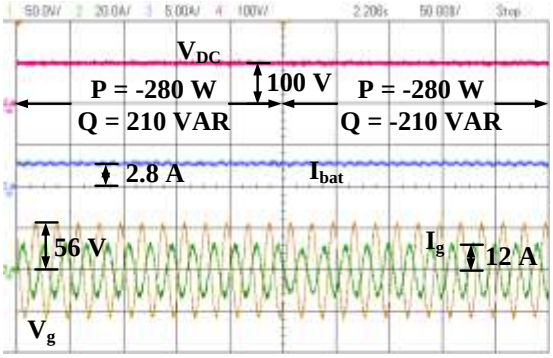

(e)

Fig. 12. Transition from (a) mode-1 to 2 (b) mode-2 to 3 (c) mode-3 to 4 (d) mode-5 to 6 (e) mode-7 to 8

cted to 280 W and 210 VAR, respectively. The on-board charger initially feeds the inductive reactive power only as shown in Fig. 12 (a) without any active power support and accordingly, the current lags the voltage by 90º. After some time, the charger is controlled to supply the capacitive reactive power in compliance of mode 2 and now the current leads the voltage by 90º. Here, it can be seen that the battery current is almost constant during this transition.

In mode-3 and 4 only the exchange of active power takes place without any reactive power support as shown in Fig. 12 (b). During the transition from mode-3 to 4 the current changes its phase from being in phase to out of phase with respect to voltage and accordingly, the battery current changes its polarity from positive to the negative charging current as shown in Fig. 12 (c). Later, the exchange of both active and reactive power is tested simultaneously. During mode-5 and 6, 280 W active power is supplied from the grid side as shown in Fig. 12 (d) and during mode-7 and 8 same amount of active power is injected in to the grid from battery pack as shown in Fig. 12 (e). Similarly, during mode-5 and 7, 210 VAR reactive power is drawn from the grid and supplied back to the grid during mode-6 and 8. According to the amount of active and reactive power being exchanged, the grid current lags behind the grid voltage by about 36º initially and just after the changeover of power flow direction, the current start leading the grid voltage by same angle as shown in Fig. 12 (d). Later, in discharging mode (mode-7) the grid current lags behind the grid voltage about 143º and leads the grid voltage by same angle during mode-8 as shown in Fig. 12 (e). The battery current during the transition from mode-5 to 6 is almost constant because the battery is being charged by constant amount of power in both modes. Similarly, battery current is constant in mode-7 and 8 because it is supplying same amount of power to the grid.

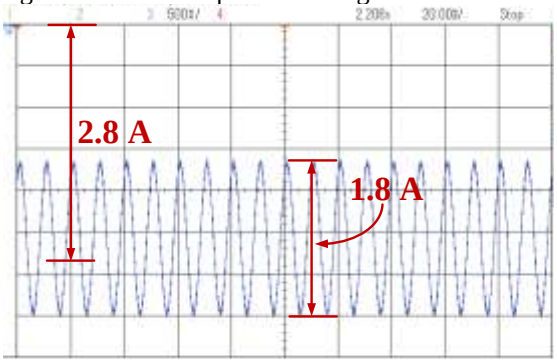

(a)

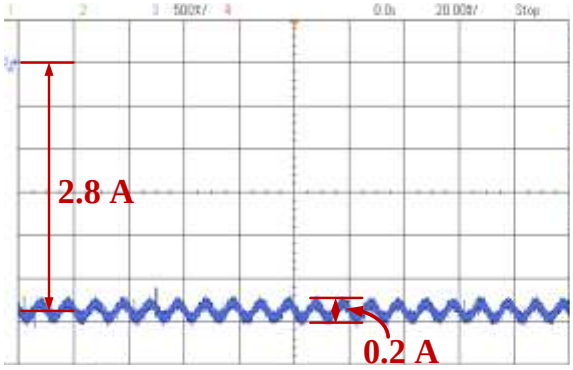

(b)

Fig. 13. Inverter DC side current (a) without ripple reduction method (b) with ripple reduction method

Fig. 13 shows the experimental results of converter DC side current during the mode-5, where the current without ripple compensation is shown in Fig. 13 (a) and with compensation is shown in Fig. 13 (b). Here, on comparing both the results, it can be easily observed that the ripple current harmonics have been reduced to considerably lower level.

The THD of grid current during mode 5, 6, 7 and 8 is given in table III. Since, last modes are associated with both active and reactive power operation therefore the THD in grid current is given with and without ripple minimization technique applied. It can be seen that the ripple minimization technique has not increase the THD too much and it is within the permissible limit of IEEE standard 519 i.e. 5%.

TABLE III
THD with and without minimization technique

Mode	With minimization	Without minimization
5	3.87%	1.44%
6	4.09%	1.52%
7	4.19%	1.41%
8	4.46%	1.45%

Moreover, the proposed control technique is compared with other ripple minimization existing techniques. In proposed technique the ripple in battery current is minimized up to around 11% which is lesser than other techniques as presented in [29], [30].

TABLE IV
Comparison with other techniques

#	Ref. [29]	Ref. [30]	Proposed
Ripple Reduction	12.5%	13.2%	11.6%

VII. Conclusion

The focus of this paper is on the controller design and implementation of single-phase single stage bidirectional on-board PEV charger. The proposed PEV charger is able to operate in all four quadrants of active-reactive power plane. The proposed charger controller diminishes the second order ripple current harmonics component on DC side and hence up to 11%, may be very helpful in extending the lifetime of battery which having acceptable ripple of C/10. For the inner current loop, a RC has been designed and implemented successfully. From the control performance prospective, it has been observed that the proposed PEV charger controller is fast enough in comparison to other existing controllers and takes less than three grid cycles

2332-7782 (c) 2020 IEEE. Personal use is permitted, but republication/redistribution requires IEEE permission. See http://www.ieee.org/publications_standards/publications/rights/index.html for more information.
Authorized licensed use limited to: DELHI TECHNICAL UNIV. Downloaded on February 15,2021 at 10:24:35 UTC from IEEE Xplore. Restrictions apply.

This article has been accepted for publication in a future issue of this journal, but has not been fully edited. Content may change prior to final publication. Citation information: DOI 10.1109/TTE.2021.3049559, IEEE Transactions on Transportation Electrification

to settle down any external disturbance. Along with the fast-dynamic response it has good steady state performance too. To confirm these facts, various cases of the step-changes in reactive power (inductive/capacitive) and active power (charging/discharging) have been presented. Furthermore, the proposed technique increases the THD in grid current but it is within the limit of 5%. Simulation and experimental results have been presented to verify the claims. The thorough simulation study supported by experimental results has been provided to validate the claims.

APPENDIX

Table. V
SYSTEM PARAMETERS

Parameters	Symbol	Value (Simulation)	Value (Experimental)
Charger Apparent Power	S	1.4 KVA	350 VA
Grid Voltage	V_g	120 V(rms)	40 V(rms)
Grid Frequency	f	50 Hz	50 Hz
Interfacing Inductance	L_s	1 mH	1 mH
DC Link Capacitance	C_{dc}	330 μF	330 μF
Converter Switching Frequency	f_s	20 KHz	10 KHz
Battery Voltage	V_{bat}	208 V	96 V

REFERENCES

[1] C. C. Chan, "The State of the Art of Electric, Hybrid, and Fuel Cell Vehicles," in *Proceedings of the IEEE*, vol. 95, no. 4, pp. 704-718, April 2007.

[2] Ronald Jurgen, "Fuel-Cell Hybrid Evs," in Electric and Hybric-Electric Vehicles: Fuel Cell Hybrid EVs , SAE, pp.9-9, 2011.

[3] EECA. Energy Efficiency & Conservation Authority: April 2019. [online]. Available: https://www.energywise.govt.nz/on-the-road/electric-vehicles/ev-running-costs/.

[4] S. Habib, M. M. Khan, F. Abbas, L. Sang, M. U. Shahid and H. Tang, "A Comprehensive Study of Implemented International Standards, Technical Challenges, Impacts and Prospects for Electric Vehicles," in IEEE Access, vol. 6, pp. 13866-13890, 2018.

[5] Iqbal Husain, "Electric and Hybrid Vehicles: Design Fundamentals," CRC Press, 2010.

[6] Sharma, S., Panwar, A.K., Tripathi, M.M., Storage technologies for electric vehicles, Journal of Traffic and Transportation Engineering (English Edition), 2020.

[7] Isidor Buchmann, "Batteries in a Portable World: a handbook on rechargeable batteries for non-engineers," Cadex Electronics Inc., 2011.

[8] S. Bala, T. Tengner, P. Rosenfeld, and F. Delince, "The effect of low frequency current ripple on the performance of a Lithium Iron Phosphate (LFP) battery energy storage system," in Proc. IEEE Energy Convers. Congr. Expo., pp. 3485–3492, 2012.

[9] Kisacikoglu, Mithat Can, "Vehicle-to-grid (V2G) Reactive Power Operation Analysis of the EV/PHEV Bidirectional Battery Charger. " PhD diss., University of Tennessee, 2013

[10] M. C. Kisacikoglu, M. Kesler, and L. M. Tolbert, Single-phase on-board bidirectional PEV charger for V2G reactive power operation, IEEE Trans. Smart Grid, vol. 6, no. 2, pp. 767–775, Mar. 2015.

[11] D. B. Wickramasinghe Abeywardana, P. Acuna, B. Hredzak, R. P. Aguilera and V. G. Agelidis, "Single-Phase Boost Inverter-Based Electric Vehicle Charger With Integrated Vehicle to Grid Reactive Power Compensation," in IEEE Transactions on Power Electronics, vol. 33, no. 4, pp. 3462-3471, April 2018.

[12] Linlin Gu; Xinbo Ruan; Ming Xu; Kai Yao, "Means of Eliminating Electrolytic Capacitor in AC/DC Power Supplies for LED Lightings," Power Electronics, IEEE Transactions on , vol.24, no.5, pp.1399,1408, May 2009

[13] V. Khadkikar, M. Singh, A. Chandra and B. Singh, "Implementation of single-phase synchronous d-q reference frame controller for shunt active filter under distorted voltage condition," 2010 Joint International Conference on Power Electronics, Drives and Energy Systems & 2010 Power India, New Delhi, pp. 1-6, 2010.

[14] T. Tanaka, T. Sekiya, H. Tanaka, E. Hiraki and M. Okamoto, "Smart charger for electric vehicles with power quality compensator on single-phase three-wire distribution feeders," 2012 IEEE Energy Conversion Congress and Exposition (ECCE), Raleigh, NC, pp. 3075-3081, 2012.

[15] M. Restrepo, J. Morris, M. Kazerani and C. A. Cañizares, "Modeling and Testing of a Bidirectional Smart Charger for Distribution System EV Integration," in IEEE Transactions on Smart Grid, vol. 9, no. 1, pp. 152-162, Jan. 2018.

[16] A. K. Seth and M. Singh, "Resonant controller of single-stage off-board EV charger in G2V and V2G modes," in *IET Power Electronics*, vol. 13, no. 5, pp. 1086-1092, 8-4-2020.

[17] M. C. Kisacikoglu, B. Ozpineci, and L. M. Tolbert, "Examination of a PHEV bidirectional charger for V2G reactive power compensation," in Proc. IEEE APEC Expo., Palm Springs, CA, USA, Feb. 21–25, pp. 458–465, 2010.

[18] A. Arancibia, K. Strunz and F. Mancilla-David, "A Unified Single- and Three-Phase Control for Grid Connected Electric Vehicles," in IEEE Transactions on Smart Grid, vol. 4, no. 4, pp. 1780-1790, Dec. 2013.

[19] A. Trivedi, and M. Singh, "Repetitive Controller for VSIs in Droop Based AC-Microgrid," IEEE Trans. Power Electronics, Vol. 32, No. 8, pp. 6595-6604, Aug.-2017.

[20] Qingzeng Yan, Xiaojie Wu, X. Yuan, and Y. Geng, "An Improved Grid-Voltage Feedforward Strategy for High-Power Three-Phase Grid-Connected Inverters Based on the Simplified Repetitive Predictor," IEEE Trans. Power Electronics, Vol. 31, No. 5, pp. 3880-3897, May. 2016.

[21] G. Pandove, A. Trivedi, and M. Singh, "Repetitive control-based single-phase bidirectional rectifier with enhanced performance," IET Trans. Power Electronics., vol. 9, no.5, pp. 1029-1036, Apr. 2016.

[22] B. G. Sun, Y. X. Xie, H. Ma and L. Cheng, "Analysis and application of repetitive control scheme for three-phase active power filter with frequency adaptive capability," Journal of Electrical Engineering and Technology, vol. 11, no. 3, pp. 618-628, May. 2016.

[23] B. A. Francis and W. M. Wonham, "The internal model principle for linear multivariable regulators," J. Appl. Math. Optim., vol. 2, pp. 170–194, 1975.

[24] M. C. Kisacikoglu, B. Ozpineci and L. M. Tolbert, "EV/PHEV Bidirectional Charger Assessment for V2G Reactive Power Operation," in IEEE Transactions on Power Electronics, vol. 28, no. 12, pp. 5717-5727, Dec. 2013.

[25] S. S. Williamson, A. K. Rathore and F. Musavi, "Industrial Electronics for Electric Transportation: Current State-of-the-Art and Future Challenges," in IEEE Transactions on Industrial Electronics, vol. 62, no. 5, pp. 3021-3032, May 2015.

[26] K. J. Dyke, N. Schofield and M. Barnes, "The Impact of Transport Electrification on Electrical Networks," in *IEEE Transactions on Industrial Electronics*, vol. 57, no. 12, pp. 3917-3926, Dec. 2010.

[27] IEEE Recommended Practices and Requirements for Harmonic Control in Electrical Power Systems, IEEE Std. 519-1992, 1993, updated in 2002.

[28] M. Morimoto, T. Zanma, M. Ishida, G. Pipeleers, and J. Swevers, "Suppression of harmonic current for IPMSM using generalized repetitive control," in Proc. 36th Annu. Conf. IEEE Ind. Electron. Soc., Glendale, AZ, USA, pp. 2270–2275, 2010.

[29] G. Zhu, S. Tan, Y. Chen and C. K. Tse, "Mitigation of Low-Frequency Current Ripple in Fuel-Cell Inverter Systems Through Waveform Control," in *IEEE Transactions on Power Electronics*, vol. 28, no. 2, pp. 779-792, Feb. 2013.

[30] D. B. W. Abeywardana, B. Hredzak and V. G. Agelidis, "A Rule-Based Controller to Mitigate DC-Side Second-Order Harmonic Current in a Single-Phase Boost Inverter," in IEEE Transactions on Power Electronics, vol. 31, no. 2, pp. 1665-1679, Feb. 2016.

2332-7782 (c) 2020 IEEE. Personal use is permitted, but republication/redistribution requires IEEE permission. See http://www.ieee.org/publications_standards/publications/rights/index.html for more information.
Authorized licensed use limited to: DELHI TECHNICAL UNIV. Downloaded on February 15,2021 at 10:24:35 UTC from IEEE Xplore. Restrictions apply.

Stability of fractional order fuzzy cellular neural networks with distributed delays via hybrid feedback controllers [1]

Ajendra singh [a*], Jitendra Nath Rai [b]
[a] Research scholar, Electrical Engineering Department, Delhi Technological University, New Delhi-110042, India
[b] Professor, Electrical Engineering Department, Delhi Technological University, New Delhi -110042, India.

1. Abstract

This article studies the global Mittag-Leffler stability of fractional order fuzzy cellular neural networks via hybrid feedback controllers. Based on hybrid feedback control technique Lyapunov approach, and some novel analysis techniques of fractional calculation, some sufficient conditions are obtained to guarantee the Global Mittag-lefflers stability. Finally, two simulation example are given to illustrate the effectiveness of the proposed method.

Keywords: fractional order, distributed delays, global mittag-leffler stability, hybrid feedback controllers, fuzzy cellular neural networks.

2. Introduction

Fractional-order calculus have a very long history in pure mathematics. The study of fractional calculus can be dated back to 1695, the fractional operator concept has been put forward by Leibnitz. Fractional calculus as an extension of usual calculus dates from the late seventeenth century and it is regarded as a generalization of derivation and integration of arbitrary order. Over the past few days, the fractional order dynamical system attracts many researchers in different branches, especially science and engineering. Comparing to the traditional integer order dynamical system, the main distinguished influence of fractional order is that infinite memory and more degrees of freedom because it has nonlocal and weakly singular kernels. For the description of memory and hereditary properties of various materials and processes, fractional order models have been proven to be an excellent instrument in comparison with classical integer order models [1]. Actually, the behavior of real world processes generally or most likely is governed by fractional-order systems[2]-[6]. Moreover, fractional-order systems are more likely to be used to describe most of the real-world behaviors than integer-order ones because they can provide more practical value and accurate results. Therefore, many researchers have paid close attention to studying the dynamical behaviors of fractional-order systems and have drawn some wonderful results in the literature [7]-[8].

Stability has been a hot research topic that has drawn much attention from mathematicians, physicists, and computer scientists, and a large amount of results have been available in the literature [9]-[39]. However, most of these results are of integer-order networks. Recently, the various kinds of stability problems for fractional-order differential systems including global stability [40], Exponential stability[41] and Robust stability [42] have been widely discussed. As we all know, the stability problem is a very important performance measure for any dynamical system. [43] investigated the Mittag-Leffler stability of nonlinear fractional neutral singular systems under Caputo and Riemann–Liouville derivatives. Mittag-Leffler stability is a relatively new concept related deeply to fractional calculus. In [44], conditions on the Stability of fractional-order nonlinear dynamic systems: Lyapunov direct method and generalized Mittag-Leffler stability are established.

So far, there were three basic CNN structures being proposed. The first one is traditional CNN [45] which is a dynamical and analogical computational network using analog weights, inputs, states and

[1] *E-mail address: ajendradu@gmail.com*
* *Corresponding author*

Research Square
Preprints are preliminary reports that have not undergone peer review. They should not be considered conclusive, used to inform clinical practice, or referenced by the media as validated information.

outputs. The second one is delay-type CNN [46] which introduces delayed weights into the traditional CNN and uses analog weights, inputs, states and outputs. The last one is discrete-time CNN [47] which uses analog weights, inputs, states, and digital outputs. Unlike the traditional CNNs structure, FCNNs implements fuzzy logic between its template input and/or output besides the sum of product operations. Different from the cellular neural networks, fuzzy cellular neural networks integrate fuzzy logic into the structure of customary cell neural systems and keeps up nearby connectedness among cells. Fuzzy cellular neural networks (FCNNs), introduced by Yang et al. [48]-[49]. such as thinking and reasoning, [50], [51] white blood cell detection, [52] and pattern recognition. On the other hand, outer synchronization between two coupled networks has been extensively studied. Similar to the traditional CNNs, the stability of the system is very important in the design of FCNNs. We note that several conditions for FCNNs have been proposed [53]-[54].

Between multiple performance objectives using a single feedback function, whereas hybrid control seeks to achieve multiple performance objectives in a locally adaptive sense by exchanging between individuals from a from the earlier determined group of input capacities. There are numerous outcomes on half breed frameworks and cross breed control in the distributed writing. Conferences have been held with published proceedings [55]-[56], and special issues of archival publications have been devoted to hybrid systems and control [57] - [61]. In addition, the literature on hybrid control systems is very large; a number of references to this literature are identified throughout this paper. Tutorial papers [62]-[64], a monograph [65], and doctoral dissertations that treat hybrid control systems have been written. Examples of hybrid controllers in the automotive field include applications for automated highway systems [66], motion planning [67]-[69], and so on. Despite the fact that, examine in half breed control has been the article of an extraordinary and gainful exertion in the ongoing years in the car field, from the best of our knowledge, this is the first time that benefits of both FOC and hybrid control are used for ACC maneuvers.

Motivated by the above discussions, the objective of this paper is to study the global Mittag-Leffler stability of fractional order fuzzy cellular neural networks with distributed delays via hybrid feedback controllers. To the best of authors knowledge global Mittag-Leffler stability of fractional order fuzzy cellular neural networks with distributed delays via hybrid feedback controllers is not yet fully studied. By constructing a suitable Lyapunov functional, Stability criteria are derived to ensure the stability of concerned fractional order systems. Caputo definition are applied. An effective controller is achieved for synchronization of master and slave systems considered. A numerical examples is illustrated to show the correctness of proposed method.

The novelties of the study are given below:

- We studied the global Mittag-Leffler stability of fractional order fuzzy cellular neural networks.
- Constructed a novel Lyapunov functional for check the stabilty of the fractional order system.
- Stability criteria are derived to ensure the stability of concerned fractional order systems.
- An effective hybrid feedback controller is applied for synchronization of master and slave systems.

The paper is organized as follows. In section 3, model description of fractional order neural networks and preliminaries are presented. In section 4, main results are drawn. In section 5, numerical example is performed to verify the effectiveness of our method. Finally, conclusion results are drawn.

3. MODEL DESCRIPTION AND PRELIMINARIES

In the present section, we introduce some basic definitions and the corresponding results will be used later.

Definition 1.([70]) Suppose that $\beta > 0$ for a function $f(t)$ is defined as

$$J^{\beta} f(t) = \frac{1}{\Gamma(\beta)} \int_b^t (t-\tau)^{\beta-1} f(\tau) d\tau, \tag{1}$$

where $t \geq b$, $t \in \mathbb{R}$, $\Gamma(\cdot)$ is the gamma function, given by $\Gamma(\beta) = \int_0^{\infty} t^{s-1} e^{-t} dt$.
Definition 2.([70]) The Caputo fractional derivative of order β for a function $f(t)$ is defined as

$$D^{\beta} f(t) = \frac{1}{\Gamma(n-\beta)} \int_b^t (t-\tau)^{n-\beta-1} f^{(n)}(\tau) d\tau, \tag{2}$$

in which $t \geq b$, $t \in \mathbb{R}$, $n-1 < \beta < n \in \mathbb{N}$.
Definition 3([71]). The one-parameter Mittag-Leffler function is defined as

$$E_{\phi}(x) = \sum_{l=0}^{\infty} \frac{x^l}{\gamma(l\phi + 1)}. \tag{3}$$

Definition 4([71]). The two-parameter Mittag-Leffler function is defined as

$$E_{\phi,\psi}(x) = \sum_{l=0}^{\infty} \frac{x^l}{\gamma(l\phi + \psi)}. \tag{4}$$

Definition 5([71]). Moreover, the Laplace transform of Mittag-Leffler function in two parameters is

$$\mathbb{L}\{t^{\psi-1} E_{\phi,\psi}(-\lambda t^{\phi})\} = \frac{s^{\phi-\psi}}{s^{\phi} + \lambda}, (R(s) > |\lambda|^{\frac{1}{\phi}}), \tag{5}$$

where s is the variable in Laplace domain, $R(s)$ denotes the real part of s, $\lambda \in R$ and $L\cdot$ stands for the Laplace transform.
Lemma 1([72]).Let a vector-value function $p(t) \subset \mathbb{R}^n$ is differentiable. Then, for any $t > 0$, one has

$$\frac{1}{2} D^{\beta} p^2(t) \leq p(t) D^{\beta} p(t) \tag{6}$$

when $0 < \beta < 1$.
Lemma 2([73]). Suppose that $x, y \in \mathbb{R}^n$ be the two states of the system (1). Then, one has

$$|\bigwedge_{j=1}^{n} u_{ij} f_j(\vartheta_j) - \bigwedge_{j=1}^{n} u_{ij} f_j(\zeta_j)| \leq \sum_{j=1}^{n} |u_{ij}||f_j(\vartheta_j) - f_j(\zeta_j)|,$$
$$|\bigvee_{j=1}^{n} v_{ij} f_j(\vartheta_j) - \bigvee_{j=1}^{n} v_{ij} f_j(\zeta_j)| \leq \sum_{j=1}^{n} |v_{ij}||f_j(\vartheta_j) - f_j(\zeta_j)|.$$

Lemma 3([74]). Let $k_1 > 0$, $k_2 > 0$, $k_3 > 0$, $k_4 > 1$, and $(\frac{1}{k_3}) + (\frac{1}{k_4}) = 1$. Then for any $\epsilon > 0$, we have

$$k_1 k_2 \leq \frac{1}{k_3} (k_1 \epsilon)^{k_3} + \frac{1}{k_4} (k_2 \frac{1}{\epsilon})^{k_4}$$

The equality holds if and only if $(k_1\epsilon)^{k_3} = (k_2(\frac{1}{\epsilon}))^{k_4}$.
Lemma 4([75]). Let V(t) be a continuous function on $[0, \infty)$ satisfying

$${}^{C}D^{\alpha} V(t) \leq -\gamma V(t), \alpha \in (0, 1), \tag{7}$$

for some constant γ. Then

$$V(t) \leq V(0) E_{\alpha}(-\gamma t^{\alpha}), t \geq 0. \tag{8}$$

Lemma 5([76]). Let $u > 0$, $v > 0$, $1 < p < +\infty$, and $\frac{1}{p} + \frac{1}{q} = 1$, then the following relationship holds

$$uv \leq \frac{1}{p} u^p + \frac{1}{q} v^q, \tag{9}$$

the equality holds if and only if $u = v^{p-1}$.

Assumption 1. The neuron activation functions f_j are Lipschitz continuous and satisfy for

$$|f_j(\vartheta_j) - f_j(\zeta_j)| \leq F_j|\vartheta_j - \zeta_j|.$$

positive constants $F_j > 0$.

4. Main results

In this section, we will derive some criteria to guarantee the Global Mittag-Leffler stability between drive system (10) and response system (11).

In this paper, we consider the following n-dimensional FCNNs with distributed delay:

$$\begin{aligned} {}^{C}D^{\alpha}\zeta_i(t) = &-d_i\zeta_i(t) + \sum_{j=1}^{n} c_{ij}f_j(\zeta_j(t)) + \sum_{j=1}^{n} a_{ij}f_j(\zeta_j(t-\tau)) + \sum_{j=1}^{n} h_{ij}\mu_j \\ &+ \bigwedge_{j=1}^{n} u_{ij}\int_0^{\infty} k_j(s)f_j(\zeta_j(s-\tau))ds + \bigwedge_{j=1}^{n} P_{ij}\mu_j + \bigvee_{j=1}^{n} v_{ij}\int_0^{\infty} k_j(s)f_j(\zeta_j(s-\tau))ds \\ &+ \bigvee_{j=1}^{n} Q_{ij}\mu_j + I_i, i = 1, 2, ..., n, \end{aligned} \tag{10}$$

where, ${}^{C}D^{\alpha}$ is the Caputo's fractional derivative and $0 < \alpha < 1$, $d_i > 0$ denote the rate with which the ith neuron, $\zeta_i(t)$ corresponds to the state variable of the ith unit at time t, c_{ij}, a_{ij} are elements of feedback and feed forward template h_{ij} is the feed-forward template. u_{ij}, v_{ij}, P_{ij}, Q_{ij} are elements of fuzzy feedback MIN template, fuzzy feedback MAX template, respectively. $\bigvee$ and $\bigwedge$ denote the fuzzy AND and fuzzy OR operation, respectively. I_i denote state, input and bias of the ith neuron, respectively. f_i is the activation function.

In this paper, we refer to model (10) as the drive system, the response system is given as follows

$$\begin{aligned} {}^{C}D^{\alpha}\vartheta_i(t) = &-d_i\vartheta_i(t) + \sum_{j=1}^{n} c_{ij}f_j(\vartheta_j(t)) + \sum_{j=1}^{n} a_{ij}f_j(\vartheta_j(t-\tau)) + \sum_{j=1}^{n} h_{ij}\mu_j \\ &+ \bigwedge_{j=1}^{n} u_{ij}\int_0^{\infty} k_j(s)f_j(\vartheta_j(s-\tau))ds + \bigwedge_{j=1}^{n} P_{ij}\mu_j + \bigvee_{j=1}^{n} v_{ij}\int_0^{\infty} k_j(s)f_j(\vartheta_j(s-\tau))ds \\ &+ \bigvee_{j=1}^{n} Q_{ij}\mu_j + I_i + u_i(t), \end{aligned} \tag{11}$$

where $\vartheta_i(t)$ corresponds to the state variable of the ith neuron of the response system and $u_i(t)$ indicates the control input.

Suppose that $\zeta_i(t)$, $\vartheta_i(t)$ are arbitrary solutions of system (10) and system (11) respectively, and let $e_i(t) = \vartheta_i(t) - \zeta_i(t)$ for $i \in I$, then from system (10) and system (11), the error dynamical system can be derived as

$$\begin{aligned} \xi_i(t) = &-d_i\xi_i(t) + \sum_{j=1}^{n} c_{ij}[f_j(\vartheta_j(t)) - f_j(\zeta_j(t))] + \sum_{j=1}^{n} a_{ij}[f_j(\vartheta_j(t-\tau))) - f_j(\zeta_j(t-\tau))] \\ &+ \bigwedge_{j=1}^{n} u_{ij}\int_0^{\infty} k_j(s)[f_j(\vartheta_j(t-\tau)) - f_j(\zeta_j(t-\tau))]ds \\ &+ \bigvee_{j=1}^{n} v_{ij}\int_0^{\infty} k_j(s)[f_j(\vartheta_j(t-\tau)) - f_j(\zeta_j(t-\tau))]ds + u_i(t) \end{aligned} \tag{12}$$

Now we introduce the hybrid feedback controls are
$u_i(t) = u_{1i}(t) + u_{2i}(t)$, where $u_{1i}(t) = -\phi_i(t)\xi_i(t)$ and $u_{2i}(t) = -\Psi_i(t)\xi_i(t)$.

$$\begin{aligned}\xi_i(t) = &-d_i\xi_i(t) + \sum_{j=1}^{n} c_{ij}[f_j(\vartheta_j(t)) - f_j(\zeta_j(t))] + \sum_{j=1}^{n} a_{ij}[f_j(\vartheta_j(t-\tau)) - f_j(\zeta_j(t-\tau))] \\ &+ \bigwedge_{j=1}^{n} u_{ij} \int_0^{\infty} k_j(s)[f_j(\vartheta_j(t-\tau)) - f_j(\zeta_j(t-\tau))]ds \\ &+ \bigvee_{j=1}^{n} v_{ij} \int_0^{\infty} k_j(s)[f_j(\vartheta_j(t-\tau)) - f_j(\zeta_j(t-\tau))]ds - \phi_i(t)\xi_i(t) - \Psi_i(t)\xi_i(t) \end{aligned} \tag{13}$$

Remark 4.1. *Motivated by the success of the applications of the Mittag-Leffler functions in many areas of science and engineering, we present our work here. Applications of Mittag-Leffler functions in certain areas of physical and applied sciences are also very common. Very recently Chen et al.* [77] *formulated and investigated the global Mittag-Leffler stability and synchronization of fractional-order memristor NNs. Stamova and Stamov* [78] *studied the impulsive and linear controllers on Mittag-Leffler synchronization of fractional-order NNs with time-varying delays. For extending the application of fractional calculus in nonlinear systems, we propose the Mittag–Leffler stability and the Lyapunov direct method with a view to enrich the knowledge of both system theory and fractional calculus.*

Theorem 4.2. Assume that Assumption (1) and Lemma (4) hold, then the system (10) is Globally mittag-leffler stable, provided the following conditions holds:

$$\begin{aligned}&\eta_1(t) > \eta_2(t), \\ &\eta_1(t) = \min_{1\le i\le}[(d_i + \phi_i(t) + \Psi_i(t)) - \sum_{j=1}^{n} c_{ij}F_j\rho^{-1} - \sum_{j=1}^{n} c_{ji}F_i\rho - \sum_{j=1}^{n} a_{ij}F_j\rho^{-1} \\ &\qquad + \sum_{j=1}^{n} |u_{ij}|F_j\rho^{-1} + \sum_{j=1}^{n} |v_{ij}|F_j\rho^{-1}] > 0 \\ &\eta_2(t) = \max_{1\le i\le n}[\sum_{j=1}^{n} a_{ji}F_i\rho + \sum_{j=1}^{n} |u_{ji}|F_i\rho + \sum_{j=1}^{n} |v_{ji}|F_i\rho] > 0 \end{aligned} \tag{14}$$

Proof: Let us consider the Lyapunov function is

$$V(t) = \sum_{i=1}^{n} \frac{1}{2}\xi_i^2(t) \tag{15}$$

According to the Caputo fractional-order derivative definition, we have

$$\begin{aligned}{}^{C}D^{\alpha}V(t,\xi(t)) &\le \sum_{i=1}^{n} \xi_i(t)\,{}^{C}D^{\alpha}\xi_i(t) \\ &\le \sum_{i=1}^{n} \xi_i(t)[-d_i\xi_i(t) + \sum_{j=1}^{n} c_{ij}[f_j(\vartheta_j(t)) - f_j(\zeta_j(t))] \\ &+ \sum_{j=1}^{n} a_{ij}[f_j(\vartheta_j(t-\tau)) - f_j(\zeta_j(t-\tau))] \\ &+ \bigwedge_{j=1}^{n} |u_{ij}| \int_0^{\infty} k_j(s)[f_j(\vartheta_j(t-\tau)) - f_j(\zeta_j(t-\tau))]ds \end{aligned}$$

$$
\begin{aligned}
&+\bigvee_{j=1}^{n}|v_{ij}|\int_0^\infty k_j(s)[f_j(\vartheta_j(t-\tau))-f_j(\zeta_j(t-\tau))]ds-\phi_i(t)\xi_i(t)-\Psi_i(t)\xi_i(t)]\\
&=-\sum_{i=1}^{n}d_i\xi_i^2(t)+\sum_{i=1}^{n}\sum_{j=1}^{n}c_{ij}F_j|\xi_i(t)||\xi_j(t)|+\sum_{i=1}^{n}\sum_{j=1}^{n}a_{ij}F_j|\xi_i(t)||\xi_j(t-\tau)|\\
&+\sum_{i=1}^{n}\sum_{j=1}^{n}|u_{ij}|\int_0^\infty k_j(s)F_j|\xi_i(s)||\xi_j(s-\tau)|ds\\
&+\sum_{i=1}^{n}\sum_{j=1}^{n}|v_{ij}|\int_0^\infty k_j(s)F_j|\xi_i(s)||\xi_j(s-\tau)|ds-\sum_{i=1}^{n}\phi_i(t)\xi_i^2(t)-\sum_{i=1}^{n}\Psi_i(t)\xi_i^2(t)\\
&\le-\sum_{i=1}^{n}d_i\xi_i^2(t)+\sum_{i=1}^{n}\sum_{j=1}^{n}c_{ij}F_j[\frac{\rho^{-1}}{2}\xi_i^2(t)+\frac{\rho}{2}\xi_j^2(t)]\\
&+\sum_{i=1}^{n}\sum_{j=1}^{n}a_{ij}F_j[\frac{\rho^{-1}}{2}\xi_i^2(t)+\frac{\rho}{2}\xi_j^2(t-\tau)]\\
&+\sum_{i=1}^{n}\sum_{j=1}^{n}|u_{ij}|\int_0^\infty k_j(s)F_j[\frac{\rho^{-1}}{2}\xi_i^2(s)+\frac{\rho}{2}\xi_j^2(s-\tau)]ds\\
&+\sum_{i=1}^{n}\sum_{j=1}^{n}|v_{ij}|\int_0^\infty k_j(s)F_j[\frac{\rho^{-1}}{2}\xi_i^2(s)+\frac{\rho}{2}\xi_j^2(s-\tau)]ds-\sum_{i=1}^{n}\phi_i(t)\xi_i^2(t)-\sum_{i=1}^{n}\Psi_i(t)\xi_i^2(t)\\
&\le-\sum_{i=1}^{n}d_i\xi_i^2(t)+\sum_{i=1}^{n}\sum_{j=1}^{n}c_{ij}F_j[\frac{\rho^{-1}}{2}\xi_i^2(t)]+\sum_{i=1}^{n}\sum_{j=1}^{n}c_{ij}F_j[\frac{\rho}{2}\xi_j^2(t)]\\
&+\sum_{i=1}^{n}\sum_{j=1}^{n}a_{ij}F_j[\frac{\rho^{-1}}{2}\xi_i^2(t)]+\sum_{i=1}^{n}\sum_{j=1}^{n}a_{ij}F_j[\frac{\rho}{2}\xi_j^2(t-\tau)]\\
&+\sum_{i=1}^{n}\sum_{j=1}^{n}|u_{ij}|\int_0^\infty k_j(s)F_j[\frac{\rho^{-1}}{2}\xi_i^2(s)]ds+\sum_{i=1}^{n}\sum_{j=1}^{n}|u_{ij}|\int_0^\infty k_j(s)F_j[\frac{\rho}{2}\xi_j^2(s-\tau)]ds\\
&+\sum_{i=1}^{n}\sum_{j=1}^{n}|v_{ij}|\int_0^\infty k_j(s)F_j[\frac{\rho^{-1}}{2}\xi_i^2(s)]ds+\sum_{i=1}^{n}\sum_{j=1}^{n}|v_{ij}|\int_0^\infty k_j(s)F_j[\frac{\rho}{2}\xi_j^2(s-\tau)]ds\\
&-\sum_{i=1}^{n}\phi_i(t)\xi_i^2(t)-\sum_{i=1}^{n}\Psi_i(t)\xi_i^2(t)\\
&\le-\sum_{i=1}^{n}d_i\xi_i^2(t)+\sum_{i=1}^{n}\sum_{j=1}^{n}c_{ij}F_j[\frac{\rho^{-1}}{2}\xi_i^2(t)]+\sum_{i=1}^{n}\sum_{j=1}^{n}c_{ji}F_i[\frac{\rho}{2}\xi_i^2(t)]\\
&+\sum_{i=1}^{n}\sum_{j=1}^{n}a_{ij}F_j[\frac{\rho^{-1}}{2}\xi_i^2(t)]+\sum_{i=1}^{n}\sum_{j=1}^{n}a_{ji}F_i[\frac{\rho}{2}\xi_i^2(t-\tau)]\\
&+\sum_{i=1}^{n}\sum_{j=1}^{n}|u_{ij}|\int_0^\infty k_j(s)F_j[\frac{\rho^{-1}}{2}\xi_i^2(s)]ds+\sum_{i=1}^{n}\sum_{j=1}^{n}|u_{ji}|\int_0^\infty k_j(s)F_i[\frac{\rho}{2}\xi_i^2(s-\tau)]ds\\
&+\sum_{i=1}^{n}\sum_{j=1}^{n}|v_{ij}|\int_0^\infty k_j(s)F_j[\frac{\rho^{-1}}{2}\xi_i^2(s)]ds+\sum_{i=1}^{n}\sum_{j=1}^{n}|v_{ji}|\int_0^\infty k_j(s)F_i[\frac{\rho}{2}\xi_i^2(s-\tau)]ds\\
&-\sum_{i=1}^{n}\phi_i(t)\xi_i^2(t)-\sum_{i=1}^{n}\Psi_i(t)\xi_i^2(t)
\end{aligned}
$$

$$
\begin{aligned}
&\leq \sum_{i=1}^{n}[-(d_i+\phi_i(t)+\Psi_i(t))+\sum_{j=1}^{n}c_{ij}F_j\frac{\rho^{-1}}{2}+\sum_{j=1}^{n}c_{ji}F_i\frac{\rho}{2}+\sum_{j=1}^{n}a_{ij}F_j[\frac{\rho^{-1}}{2}]]\xi_i^2(t)\\
&+\sum_{i=1}^{n}[\sum_{j=1}^{n}a_{ji}F_i[\frac{\rho}{2}]]\xi_i^2(t-\tau)+\sum_{i=1}^{n}[\sum_{j=1}^{n}|u_{ij}|\int_0^{\infty}k_j(s)F_j[\frac{\rho^{-1}}{2}]ds\\
&+\sum_{j=1}^{n}|v_{ij}|\int_0^{\infty}k_j(s)F_j[\frac{\rho^{-1}}{2}]]\xi_i^2(s)ds+\sum_{i=1}^{n}[\sum_{j=1}^{n}|u_{ji}|\int_0^{\infty}k_j(s)F_i[\frac{\rho}{2}]ds\\
&+\sum_{j=1}^{n}|v_{ji}|\int_0^{\infty}k_j(s)F_i[\frac{\rho}{2}]]\xi_i^2(s-\tau)ds\\
&\leq -\sum_{i=1}^{n}[(d_i+\phi_i(t)+\Psi_i(t))-\sum_{j=1}^{n}c_{ij}F_j\frac{\rho^{-1}}{2}-\sum_{j=1}^{n}c_{ji}F_i\frac{\rho}{2}-\sum_{j=1}^{n}a_{ij}F_j[\frac{\rho^{-1}}{2}]]\xi_i^2(t)\\
&+\sum_{i=1}^{n}[\sum_{j=1}^{n}a_{ji}F_i[\frac{\rho}{2}]]\xi_i^2(t-\tau)+\sum_{i=1}^{n}[\sum_{j=1}^{n}|u_{ij}|\int_0^{\infty}k_j(s)F_j[\frac{\rho^{-1}}{2}]ds\\
&+\sum_{j=1}^{n}|v_{ij}|\int_0^{\infty}k_j(s)F_j[\frac{\rho^{-1}}{2}]]\xi_i^2(s)ds+\sum_{i=1}^{n}[\sum_{j=1}^{n}|u_{ji}|\int_0^{\infty}k_j(s)F_i[\frac{\rho}{2}]ds\\
&+\sum_{j=1}^{n}|v_{ji}|\int_0^{\infty}k_j(s)F_i[\frac{\rho}{2}]]\xi_i^2(s-\tau)(s)ds\\
&\leq -\eta_1 V(t,\xi(t))+\eta_2\max_{t-\tau\leq s\leq t}V(s,\xi(s)),
\end{aligned}
\tag{16}
$$

where,

$$
\begin{aligned}
\eta_1(t) &= \min_{1\leq i\leq n}[(d_i+\phi_i(t)+\Psi_i(t))-\sum_{j=1}^{n}c_{ij}F_j\rho^{-1}-\sum_{j=1}^{n}c_{ji}F_i\rho-\sum_{j=1}^{n}a_{ij}F_j\rho^{-1}\\
&\quad+\sum_{j=1}^{n}|u_{ij}|F_j\rho^{-1}+\sum_{j=1}^{n}|v_{ij}|F_j\rho^{-1}]>0,\\
\eta_2(t) &= \max_{1\leq i\leq n}[\sum_{j=1}^{n}a_{ji}F_i\rho+\sum_{j=1}^{n}|u_{ji}|F_i\rho+\sum_{j=1}^{n}|v_{ji}|F_i\rho]>0.
\end{aligned}
\tag{17}
$$

From this estimate, for any solution (13), which satisfies the Razumichin condition

$$V(s,\xi(s))\leq V(t,\xi(t)), t-\tau\leq s\leq t,$$

we have

$${}^{C}D^{\alpha}V(t,\xi(t))\leq -(\eta_1-\eta_2)V(t,\xi(t)), t\geq 0. \tag{18}$$

According to Lemma 5, the claim of Theorem 4.1 follows.

$$V(t,\xi(t))\leq V(0,\xi(0))E_{\alpha}(-\gamma t^{\alpha}), t\geq 0 \tag{19}$$

By Lemma 4 and inequality (19), this proves system (10) can be achieved globally Mittag-Leffler stabilization under the designed control law.
Hence complete the proof.

Theorem 4.3. Assume that Assumption (1) and Lemma (4) hold, then the system (10) is Globally mittag-leffler stable, provided the following conditions holds:

$$\theta_1(t)>\theta_2(t),$$

$$\theta_1(t) = \min_{1\le i\le n}[\omega(d_i + |\phi_i(t)| + |\Psi_i(t)|) - \sum_{j=1}^{n}|c_{ij}|F_j\delta_1(\omega-1) - \sum_{j=1}^{n}|c_{ji}|F_i\frac{1}{\delta_1^{\omega-1}}$$
$$-\sum_{j=1}^{n}|a_{ij}|F_j(\omega-1)\delta_2 + |u_{ij}|F_j(\omega-1)\delta_3 + |v_{ij}|F_j(\omega-1)\delta_3]\frac{|\xi_i(t)|^\omega}{\omega} > 0,$$
$$\theta_2(t) = \max_{1\le i\le n}[\sum_{j=1}^{n}|a_{ji}|F_i\frac{1}{\delta_2^{\omega-1}} + \sum_{j=1}^{n}|u_{ji}|F_i\frac{1}{\delta_3^{\omega-1}} + \sum_{j=1}^{n}|v_{ji}|F_i\frac{1}{\delta_3^{\omega-1}}]\frac{|\xi_i(t-\tau)|^\omega}{\omega} > 0.$$

Proof: we define a Lyapunov function

$$V(t,\xi(t)) = \sum_{i=1}^{n}\frac{1}{\omega}|\xi_i(t)|^\omega \tag{20}$$

According to the Caputo fractional-order derivative definition, we have

$$\begin{aligned}
{}^{C}D^{\alpha}V(t,\xi(t)) &\le \sum_{i=1}^{n}|\xi_i(t)|^{\omega-1}[-d_i|\xi_i(t)| + \sum_{j=1}^{n}|c_{ij}|[f_j(\vartheta_j(t)) - f_j(\zeta_j(t))]\\
&+\sum_{j=1}^{n}|a_{ij}|[f_j(\vartheta_j(t-\tau)) - f_j(\zeta_j(t-\tau))]\\
&+\bigwedge_{j=1}^{n}|u_{ij}|\int_0^\infty k_j(s)[f_j(\vartheta_j(s-\tau)) - f_j(\zeta_j(t-\tau))]ds\\
&+\bigvee_{j=1}^{n}|v_{ij}|\int_0^\infty k_j(s)[f_j(\vartheta_j(s-\tau)) - f_j(\zeta_j(t-\tau))]ds + |\phi_i(t)||\xi_i(t)| + |\Psi_i(t)||\xi_i(t)|]\\
&\le \sum_{i=1}^{n}|\xi_i(t)|^{\omega-1}[-d_i|\xi_i(t)| + \sum_{j=1}^{n}|c_{ij}|F_j|\xi_j(t)| + \sum_{j=1}^{n}|a_{ij}|F_j|\xi_j(t-\tau)|\\
&+\sum_{j=1}^{n}|u_{ij}|\int_0^\infty k_j(s)F_j|\xi_j(s-\tau)|ds + \sum_{j=1}^{n}|v_{ij}|\int_0^\infty k_j(s)F_j|\xi_j(s-\tau)|ds\\
&+|\phi_i(t)||\xi_i(t)| + |\Psi_i(t)||\xi_i(t)|]\\
&\le -\sum_{i=1}^{n}(d_i + |\phi_i(t)| + |\Psi_i(t)|)|\xi_i(t)|^\omega + \sum_{i=1}^{n}\sum_{j=1}^{n}|c_{ij}|F_j|\xi_i(t)|^{\omega-1}|\xi_j(t)|\\
&+\sum_{i=1}^{n}\sum_{j=1}^{n}|a_{ij}|F_j|\xi_i(t)|^{\omega-1}|\xi_j(t-\tau)| + \sum_{i=1}^{n}\sum_{j=1}^{n}|u_{ij}|\int_0^\infty k_j(s)F_j|\xi_i(s)|^{\omega-1}|\xi_j(s-\tau)|ds\\
&+\sum_{i=1}^{n}\sum_{j=1}^{n}|v_{ij}|\int_0^\infty k_j(s)F_j|\xi_i(s)|^{\omega-1}|\xi_j(s-\tau)|ds
\end{aligned} \tag{21}$$

From Lemma 3 we have

$$\begin{aligned}
|\xi_i(t)|^{\omega-1}|\xi_j(t)| &\le \frac{\omega-1}{\omega}[|\xi_i(t)|^{\omega-1}\delta_1^{\frac{\omega-1}{\omega}}]^{\frac{\omega}{\omega-1}} + \frac{1}{\omega}[|\xi_j(t)|\delta_1^{\frac{-\omega-1}{\omega}}]^\omega\\
&= \frac{\omega-1}{\omega}|\xi_i(t)|^\omega\delta_1 + \frac{1}{\omega}|\xi_j(t)|^\omega\frac{1}{\delta_1^{\omega-1}}\\
|\xi_i(t)|^{\omega-1}|\xi_j(t-\tau)| &\le \frac{\omega-1}{\omega}[|\xi_i(t)|^{\omega-1}\delta_2^{\frac{\omega-1}{\omega}}]^{\frac{\omega}{\omega-1}} + \frac{1}{\omega}[|\xi_j(t-\tau)|\delta_2^{\frac{-\omega-1}{\omega}}]^\omega
\end{aligned}$$

$$
\begin{aligned}
&= \frac{\omega-1}{\omega}|\xi_i(t)|^{\omega}\delta_2 + \frac{1}{\omega}|\xi_j(t-\tau)|^{\omega}\frac{1}{\delta_2^{\omega-1}} \\
\int_0^{\infty}|\xi_i(s)|^{\omega-1}|\xi_j(s-\tau)|ds &\leq \int_0^{\infty}\frac{\omega-1}{\omega}[|\xi_i(s)|^{\omega-1}\delta_3^{\frac{\omega-1}{\omega}}]^{\frac{\omega}{\omega-1}} + \frac{1}{\omega}[|\xi_j(s-\tau)|\delta_3^{\frac{-\omega-1}{\omega}}]^{\omega} \\
&= \int_0^{\infty}\frac{\omega-1}{\omega}|\xi_i(s)|^{\omega}\delta_3 + \frac{1}{\omega}|\xi_j(s-\tau)|^{\omega}\frac{1}{\delta_3^{\omega-1}}
\end{aligned} \tag{22}
$$

Now substitute the above values in the above equation we get

$$
\begin{aligned}
{}^{C}D^{\alpha}V(t,\xi(t)) \leq &-\sum_{i=1}^{n}(d_i+|\phi_i(t)|+|\Psi_i(t)|)|\xi_i(t)|^{\omega} + \sum_{i=1}^{n}\sum_{j=1}^{n}|c_{ij}|F_j[\frac{\omega-1}{\omega}|\xi_i(t)|^{\omega}\delta_1 \\
&+\frac{1}{\omega}|\xi_j(t)|^{\omega}\frac{1}{\delta_1^{\omega-1}}] + \sum_{i=1}^{n}\sum_{j=1}^{n}|a_{ij}|F_j[\frac{\omega-1}{\omega}|\xi_i(t)|^{\omega}\delta_2 + \frac{1}{\omega}|\xi_j(t-\tau)|^{\omega}\frac{1}{\delta_2^{\omega-1}}] \\
&+\sum_{i=1}^{n}\sum_{j=1}^{n}|u_{ij}|\int_0^{\infty}k_j(s)F_j[\frac{\omega-1}{\omega}|\xi_i(s)|^{\omega}\delta_3 + \frac{1}{\omega}|\xi_j(s-\tau)|^{\omega}\frac{1}{\delta_3^{\omega-1}}]ds \\
&+\sum_{i=1}^{n}\sum_{j=1}^{n}|v_{ij}|\int_0^{\infty}k_j(s)F_j[\frac{\omega-1}{\omega}|\xi_i(s)|^{\omega}\delta_3 + \frac{1}{\omega}|\xi_j(s-\tau)|^{\omega}\frac{1}{\delta_3^{\omega-1}}]ds \\
\leq &-\sum_{i=1}^{n}[d_i+|\phi_i(t)|+|\Psi_i(t)|]|\xi_i(t)|^{\omega} + \sum_{i=1}^{n}\sum_{j=1}^{n}|c_{ij}|F_j[\frac{\omega-1}{\omega}|\xi_i(t)|^{\omega}\delta_1] \\
&+\sum_{i=1}^{n}\sum_{j=1}^{n}|c_{ij}|F_j[\frac{1}{\omega}|\xi_j(t)|^{\omega}\frac{1}{\delta_1^{\omega-1}}] + \sum_{i=1}^{n}\sum_{j=1}^{n}|a_{ij}|F_j[\frac{\omega-1}{\omega}|\xi_i(t)|^{\omega}\delta_2] \\
&+\sum_{i=1}^{n}\sum_{j=1}^{n}|a_{ij}|F_j][\frac{1}{\omega}|\xi_j(t-\tau)|^{\omega}\frac{1}{\delta_2^{\omega-1}}] + \sum_{i=1}^{n}\sum_{j=1}^{n}|u_{ij}|\int_0^{\infty}k_j(s)F_j[\frac{\omega-1}{\omega}|\xi_i(s)|^{\omega}\delta_3]ds \\
&+\sum_{i=1}^{n}\sum_{j=1}^{n}|u_{ij}|\int_0^{\infty}k_j(s)F_j[\frac{1}{\omega}|\xi_j(s-\tau)|^{\omega}\frac{1}{\delta_3^{\omega-1}}]ds \\
&+\sum_{i=1}^{n}\sum_{j=1}^{n}|v_{ij}|\int_0^{\infty}k_j(s)F_j[\frac{\omega-1}{\omega}|\xi_i(s)|^{\omega}\delta_3]ds \\
&+\sum_{i=1}^{n}\sum_{j=1}^{n}|v_{ij}|\int_0^{\infty}k_j(s)F_j[\frac{1}{\omega}|\xi_j(s-\tau)|^{\omega}\frac{1}{\delta_3^{\omega-1}}]ds \\
\leq &-\sum_{i=1}^{n}[d_i+|\phi_i(t)|+|\Psi_i(t)|]|\xi_i(t)|^{\omega} + \sum_{i=1}^{n}\sum_{j=1}^{n}|c_{ij}|F_j[\frac{\omega-1}{\omega}|\xi_i(t)|^{\omega}\delta_1] \\
&+\sum_{i=1}^{n}\sum_{j=1}^{n}|c_{ji}|F_i[\frac{1}{\omega}|\xi_i(t)|^{\omega}\frac{1}{\delta_1^{\omega-1}}] \\
&+\sum_{i=1}^{n}\sum_{j=1}^{n}|a_{ij}|F_j[\frac{\omega-1}{\omega}|\xi_i(t)|^{\omega}\delta_2] + \sum_{i=1}^{n}\sum_{j=1}^{n}|a_{ji}|F_i][\frac{1}{\omega}|\xi_i(t-\tau)|^{\omega}\frac{1}{\delta_2^{\omega-1}}] \\
&+\sum_{i=1}^{n}\sum_{j=1}^{n}|u_{ij}|\int_0^{\infty}k_j(s)F_j[\frac{\omega-1}{\omega}|\xi_i(s)|^{\omega}\delta_3]ds
\end{aligned}
$$

$$
\begin{aligned}
&+\sum_{i=1}^{n}\sum_{j=1}^{n}|u_{ji}|\int_0^{\infty}k_j(s)F_i[\frac{1}{\omega}|\xi_i(s-\tau)|^{\omega}\frac{1}{\delta_3^{\omega-1}}]ds\\
&+\sum_{i=1}^{n}\sum_{j=1}^{n}|v_{ij}|\int_0^{\infty}k_j(s)F_j[\frac{\omega-1}{\omega}|\xi_i(s)|^{\omega}\delta_3]ds\\
&+\sum_{i=1}^{n}\sum_{j=1}^{n}|v_{ji}|\int_0^{\infty}k_j(s)F_i[\frac{1}{\omega}|\xi_i(s-\tau)|^{\omega}\frac{1}{\delta_3^{\omega-1}}]ds\\
\le&\sum_{i=1}^{n}[-\omega(d_i+|\phi_i(t)|+|\Psi_i(t)|)+\sum_{j=1}^{n}|c_{ij}|F_j\delta_1(\omega-1)\\
&+\sum_{j=1}^{n}|c_{ji}|F_i\frac{1}{\delta_1^{\omega-1}}+\sum_{j=1}^{n}|a_{ij}|F_j\delta_2(\omega-1)]\frac{|\xi_i(t)|^{\omega}}{\omega}+\sum_{i=1}^{n}[\sum_{j=1}^{n}|a_{ji}|F_i\frac{1}{\delta_2^{\omega-1}}]\frac{|\xi_i(t-\tau)|^{\omega}}{\omega}\\
&+\sum_{i=1}^{n}\sum_{j=1}^{n}\int_0^{\infty}k_j(s)[|u_{ij}|F_j(\omega-1)\delta_3+|v_{ij}|F_j(\omega-1)\delta_3]\frac{|\xi_i(s)|^{\omega}}{\omega}ds\\
&+\sum_{i=1}^{n}\sum_{j=1}^{n}\int_0^{\infty}k_j(s)[|u_{ji}|F_i(\frac{1}{\delta_3^{\omega-1}})+|v_{ji}|F_i(\frac{1}{\delta_3^{\omega-1}})]\frac{|\xi_i(s-\tau)|^{\omega}}{\omega}ds\\
\le&-\sum_{i=1}^{n}[\omega(d_i+|\phi_i(t)|+|\Psi_i(t)|)-\sum_{j=1}^{n}|c_{ij}|F_j\delta_1(\omega-1)\\
&-\sum_{j=1}^{n}|c_{ji}|F_i\frac{1}{\delta_1^{\omega-1}}-\sum_{j=1}^{n}|a_{ij}|F_j\delta_2(\omega-1)]\frac{|\xi_i(t)|^{\omega}}{\omega}+\sum_{i=1}^{n}[\sum_{j=1}^{n}|a_{ji}|F_i\frac{1}{\delta_2^{\omega-1}}]\frac{|\xi_i(t-\tau)|^{\omega}}{\omega}\\
&+\sum_{i=1}^{n}\sum_{j=1}^{n}\int_0^{\infty}k_j(s)[|u_{ij}|F_j(\omega-1)\delta_3+|v_{ij}|F_j(\omega-1)\delta_3]\frac{|\xi_i(s)|^{\omega}}{\omega}ds\\
&+\sum_{i=1}^{n}\sum_{j=1}^{n}\int_0^{\infty}k_j(s)[|u_{ji}|F_i(\frac{1}{\delta_3^{\omega-1}})+|v_{ji}|F_i(\frac{1}{\delta_3^{\omega-1}})]\frac{|\xi_i(s-\tau)|^{\omega}}{\omega}ds\\
&\le-\theta_1(t)V(t,\xi(t))+\theta_2\max_{t-\tau\le s\le t}V(s,\xi(s)).
\end{aligned}
\tag{23}
$$

where

$$
\begin{aligned}
\theta_1(t)=&\min_{1\le i\le n}[\omega(d_i+|\phi_i(t)|+|\Psi_i(t)|)-\sum_{j=1}^{n}|c_{ij}|F_j\delta_1(\omega-1)-\sum_{j=1}^{n}|c_{ji}|F_i\frac{1}{\delta_1^{\omega-1}}\\
&-\sum_{j=1}^{n}|a_{ij}|F_j(\omega-1)\delta_2+|u_{ij}|F_j(\omega-1)\delta_3+|v_{ij}|F_j(\omega-1)\delta_3]\frac{|\xi_i(t)|^{\omega}}{\omega}\\
\theta_2(t)=&\max_{1\le i\le n}[\sum_{j=1}^{n}|a_{ji}|F_i\frac{1}{\delta_2^{\omega-1}}+\sum_{j=1}^{n}|u_{ji}|F_i\frac{1}{\delta_3^{\omega-1}}+\sum_{j=1}^{n}|v_{ji}|F_i\frac{1}{\delta_3^{\omega-1}}\frac{|\xi_i(t-\tau)|^{\omega}}{\omega}
\end{aligned}
$$

From this estimate, for any solution (13), which satisfies the Razumichin condition

$$V(s,\xi(s))\le V(t,\xi(t)),t-\tau\le s\le t,$$

we have

$${}^{C}D^{\alpha}V(t,\xi(t))\le-(\eta_1-\eta_2)V(t,\xi(t)),t\ge0. \tag{24}$$

According to Lemma 5, the claim of Theorem 4.2 follows.

$$V(t,\xi(t))\le V(0,\xi(0))E_{\alpha}(-\gamma t^{\alpha}),t\ge0 \tag{25}$$

By Lemma 4 and inequality (25), this proves the system (10) can be achieved globally Mittag-Leffler stabilization under the designed control law. Hence complete the proof.

Theorem 4.4. Assume that Assumption (1) and Lemma (4) hold, then the system (10) is Globally mittag-leffler stable, provided the following conditions holds:

$$\begin{aligned}
&\eta_1(t) > \eta_2(t)\\
&\eta_1(t) = \min_{1\leq i\leq}[(d_i+\phi_i+\Psi_i) - \sum_{j=1}^{n} c_{ij}F_j\rho^{-1} - \sum_{j=1}^{n} c_{ji}F_i\rho - \sum_{j=1}^{n} a_{ij}F_j\rho^{-1}\\
&\qquad + \sum_{j=1}^{n}|u_{ij}|F_j\rho^{-1} + \sum_{j=1}^{n}|v_{ij}|F_j\rho^{-1}] > 0\\
&\eta_2(t) = \max_{1\leq i\leq n}[\sum_{j=1}^{n} a_{ji}F_i\rho + \sum_{j=1}^{n}|u_{ji}|F_i\rho + \sum_{j=1}^{n}|v_{ji}|F_i\rho] > 0
\end{aligned} \tag{26}$$

Proof:Let us consider the Lyapunov function is

$$V(t) = \sum_{i=1}^{n}\frac{1}{2}\xi_i^2(t) + \sum_{i=1}^{n}\frac{1}{2q_i}(\phi_i(t)-\phi_i)^2 + \sum_{i=1}^{n}\frac{1}{2r_i}(\Psi_i(t)-\Psi_i)^2 \tag{27}$$

$$^{C}D^{\alpha}\phi_i(t) = q_i\xi_i^2(t), \quad ^{C}D^{\alpha}\Psi_i(t) = r_i\xi_i^2(t)$$

According to the Caputo fractional-order derivative definition, we have

$$\begin{aligned}
^{C}D^{\alpha}V(t,\xi(t)) &\leq \sum_{i=1}^{n}\xi_i(t)^{C}D^{\alpha}\xi_i(t) + \sum_{i=1}^{n}\frac{1}{q_i}(\phi_i(t)-\phi_i)^{C}D^{\alpha}\phi_i(t) + \sum_{i=1}^{n}\frac{1}{r_i}(\Psi_i(t)-\Psi_i)^{C}D^{\alpha}\psi_i(t)\\
&\leq \sum_{i=1}^{n}\xi_i(t)[-d_i\xi_i(t) + \sum_{j=1}^{n}c_{ij}[f_j(\vartheta_j(t)) - f_j(\zeta_j(t))]\\
&+ \sum_{j=1}^{n}a_{ij}[f_j(\vartheta_j(t-\tau)) - f_j(\zeta_j(t-\tau))]\\
&+ \bigwedge_{j=1}^{n}|u_{ij}|\int_0^{\infty}k_j(s)[f_j(\vartheta_j(t-\tau)) - f_j(\zeta_j(t-\tau))]ds\\
&+ \bigvee_{j=1}^{n}|v_{ij}|\int_0^{\infty}k_j(s)[f_j(\vartheta_j(t-\tau)) - f_j(\zeta_j(t-\tau))]ds - \phi_i(t)\xi_i(t)\\
&- \Psi_i(t)\xi_i(t)] + \sum_{i=1}^{n}\frac{1}{q_i}(\phi_i(t)-\phi_i)q_i\xi_i^2(t) + \sum_{i=1}^{n}\frac{1}{r_i}(\Psi_i(t)-\Psi_i)r_i\xi_i^2(t)\\
&= -\sum_{i=1}^{n}d_i\xi_i^2(t) + \sum_{i=1}^{n}\sum_{j=1}^{n}c_{ij}F_j|\xi_i(t)||\xi_j(t)| + \sum_{i=1}^{n}\sum_{j=1}^{n}a_{ij}F_j|\xi_i(t)||\xi_j(t-\tau)|\\
&+ \sum_{i=1}^{n}\sum_{j=1}^{n}|u_{ij}|\int_0^{\infty}k_j(s)F_j|\xi_i(s)||\xi_j(s-\tau)|ds\\
&+ \sum_{i=1}^{n}\sum_{j=1}^{n}|v_{ij}|\int_0^{\infty}k_j(s)F_j|\xi_i(s)||\xi_j(s-\tau)|ds - \sum_{i=1}^{n}\phi_i(t)\xi_i^2(t) - \sum_{i=1}^{n}\Psi_i(t)\xi_i^2(t)\\
&+ \sum_{i=1}^{n}(\phi_i(t)-\phi_i)\xi_i^2(t) + \sum_{i=1}^{n}(\Psi_i(t)-\Psi_i)\xi_i^2(t)
\end{aligned}$$

$$
\begin{aligned}
&\leq -\sum_{i=1}^{n} d_i\xi_i^2(t) + \sum_{i=1}^{n}\sum_{j=1}^{n} c_{ij}F_j[\frac{\rho^{-1}}{2}\xi_i^2(t) + \frac{\rho}{2}\xi_j^2(t)] \\
&+ \sum_{i=1}^{n}\sum_{j=1}^{n} a_{ij}F_j[\frac{\rho^{-1}}{2}\xi_i^2(t) + \frac{\rho}{2}\xi_j^2(t-\tau)] \\
&+ \sum_{i=1}^{n}\sum_{j=1}^{n} |u_{ij}| \int_0^{\infty} k_j(s)F_j[\frac{\rho^{-1}}{2}\xi_i^2(s) + \frac{\rho}{2}\xi_j^2(s-\tau)]ds \\
&+ \sum_{i=1}^{n}\sum_{j=1}^{n} |v_{ij}| \int_0^{\infty} k_j(s)F_j[\frac{\rho^{-1}}{2}\xi_i^2(s) + \frac{\rho}{2}\xi_j^2(s-\tau)]ds - \sum_{i=1}^{n}\phi_i(t)\xi_i^2(t) - \sum_{i=1}^{n}\Psi_i(t)\xi_i^2(t) \\
&+ \sum_{i=1}^{n}\phi_i(t)\xi_i^2(t) - \sum_{i=1}^{n}\phi_i\xi_i^2(t) + \sum_{i=1}^{n}\Psi_i(t)\xi_i^2(t) - \sum_{i=1}^{n}\Psi_i\xi_i^2(t) \\
&\leq -\sum_{i=1}^{n} d_i\xi_i^2(t) + \sum_{i=1}^{n}\sum_{j=1}^{n} c_{ij}F_j[\frac{\rho^{-1}}{2}\xi_i^2(t)] + \sum_{i=1}^{n}\sum_{j=1}^{n} c_{ij}F_j[\frac{\rho}{2}\xi_j^2(t)] \\
&+ \sum_{i=1}^{n}\sum_{j=1}^{n} a_{ij}F_j[\frac{\rho^{-1}}{2}\xi_i^2(t)] + \sum_{i=1}^{n}\sum_{j=1}^{n} a_{ij}F_j[\frac{\rho}{2}\xi_j^2(t-\tau)] \\
&+ \sum_{i=1}^{n}\sum_{j=1}^{n} |u_{ij}| \int_0^{\infty} k_j(s)F_j[\frac{\rho^{-1}}{2}\xi_i^2(s)]ds + \sum_{i=1}^{n}\sum_{j=1}^{n} |u_{ij}| \int_0^{\infty} k_j(s)F_j[\frac{\rho}{2}\xi_j^2(s-\tau)]ds \\
&+ \sum_{i=1}^{n}\sum_{j=1}^{n} |v_{ij}| \int_0^{\infty} k_j(s)F_j[\frac{\rho^{-1}}{2}\xi_i^2(s)]ds + \sum_{i=1}^{n}\sum_{j=1}^{n} |v_{ij}| \int_0^{\infty} k_j(s)F_j[\frac{\rho}{2}\xi_j^2(s-\tau)]ds \\
&- \sum_{i=1}^{n}\phi_i\xi_i^2(t) - \sum_{i=1}^{n}\Psi_i\xi_i^2(t) \\
&\leq -\sum_{i=1}^{n} d_i\xi_i^2(t) + \sum_{i=1}^{n}\sum_{j=1}^{n} c_{ij}F_j[\frac{\rho^{-1}}{2}\xi_i^2(t)] + \sum_{i=1}^{n}\sum_{j=1}^{n} c_{ji}F_i[\frac{\rho}{2}\xi_i^2(t)] \\
&+ \sum_{i=1}^{n}\sum_{j=1}^{n} a_{ij}F_j[\frac{\rho^{-1}}{2}\xi_i^2(t)] + \sum_{i=1}^{n}\sum_{j=1}^{n} a_{ji}F_i[\frac{\rho}{2}\xi_i^2(t-\tau)] \\
&+ \sum_{i=1}^{n}\sum_{j=1}^{n} |u_{ij}| \int_0^{\infty} k_j(s)F_j[\frac{\rho^{-1}}{2}\xi_i^2(s)]ds + \sum_{i=1}^{n}\sum_{j=1}^{n} |u_{ji}| \int_0^{\infty} k_j(s)F_i[\frac{\rho}{2}\xi_i^2(s-\tau)]ds \\
&+ \sum_{i=1}^{n}\sum_{j=1}^{n} |v_{ij}| \int_0^{\infty} k_j(s)F_j[\frac{\rho^{-1}}{2}\xi_i^2(s)]ds + \sum_{i=1}^{n}\sum_{j=1}^{n} |v_{ji}| \int_0^{\infty} k_j(s)F_i[\frac{\rho}{2}\xi_i^2(s-\tau)]ds \\
&- \sum_{i=1}^{n}\phi_i\xi_i^2(t) - \sum_{i=1}^{n}\Psi_i\xi_i^2(t) \\
&\leq \sum_{i=1}^{n}[-(d_i + \phi_i + \Psi_i) + \sum_{j=1}^{n} c_{ij}F_j\frac{\rho^{-1}}{2} + \sum_{j=1}^{n} c_{ji}F_i\frac{\rho}{2} + \sum_{j=1}^{n} a_{ij}F_j[\frac{\rho^{-1}}{2}]]\xi_i^2(t) \\
&+ \sum_{i=1}^{n}[\sum_{j=1}^{n} a_{ji}F_i[\frac{\rho}{2}]]\xi_i^2(t-\tau) + \sum_{i=1}^{n}[\sum_{j=1}^{n} |u_{ij}| \int_0^{\infty} k_j(s)F_j[\frac{\rho^{-1}}{2}]ds \\
&+ \sum_{j=1}^{n} |v_{ij}| \int_0^{\infty} k_j(s)F_j[\frac{\rho^{-1}}{2}]]\xi_i^2(s)ds + \sum_{i=1}^{n}[\sum_{j=1}^{n} |u_{ji}| \int_0^{\infty} k_j(s)F_i[\frac{\rho}{2}]ds
\end{aligned}
$$

$$
\begin{aligned}
&+\sum_{j=1}^{n}|v_{ji}|\int_0^{\infty}k_j(s)F_i[\frac{\rho}{2}]]\xi_i^2(s-\tau)ds\\
&\leq-\sum_{i=1}^{n}[(d_i+\phi_i+\Psi_i)-\sum_{j=1}^{n}c_{ij}F_j\frac{\rho^{-1}}{2}-\sum_{j=1}^{n}c_{ji}F_i\frac{\rho}{2}-\sum_{j=1}^{n}a_{ij}F_j[\frac{\rho^{-1}}{2}]]\xi_i^2(t)\\
&+\sum_{i=1}^{n}[\sum_{j=1}^{n}a_{ji}F_i[\frac{\rho}{2}]]\xi_i^2(t-\tau)+\sum_{i=1}^{n}[\sum_{j=1}^{n}|u_{ij}|\ int_0^{\infty}k_j(s)F_j[\frac{\rho^{-1}}{2}]ds\\
&+\sum_{j=1}^{n}|v_{ij}|\int_0^{\infty}k_j(s)F_j[\frac{\rho^{-1}}{2}]]\xi_i^2(s)ds+\sum_{i=1}^{n}[\sum_{j=1}^{n}|u_{ji}|\int_0^{\infty}k_j(s)F_i[\frac{\rho}{2}]ds\\
&+\sum_{j=1}^{n}|v_{ji}|\int_0^{\infty}k_j(s)F_i[\frac{\rho}{2}]]\xi_i^2(s-\tau)(s)ds\\
&\leq-\eta_1V(t,\xi(t))+\eta_2\max_{t-\tau\leq s\leq t}V(s,\xi(s)),
\end{aligned}
\tag{28}
$$

where,

$$
\begin{aligned}
\eta_1(t)=&\min_{1\leq i\leq n}[(d_i+\phi_i+\Psi_i)-\sum_{j=1}^{n}c_{ij}F_j\rho^{-1}-\sum_{j=1}^{n}c_{ji}F_i\rho-\sum_{j=1}^{n}a_{ij}F_j\rho^{-1}\\
&+\sum_{j=1}^{n}|u_{ij}|F_j\rho^{-1}+\sum_{j=1}^{n}|v_{ij}|F_j\rho^{-1}]>0,\\
\eta_2(t)=&\max_{1\leq i\leq n}[\sum_{j=1}^{n}a_{ji}F_i\rho+\sum_{j=1}^{n}|u_{ji}|F_i\rho+\sum_{j=1}^{n}|v_{ji}|F_i\rho]>0.
\end{aligned}
\tag{29}
$$

From this estimate, for any solution (13), which satisfies the Razumichin condition

$$V(s,\xi(s))\leq V(t,\xi(t)),t-\tau\leq s\leq t,$$

we have

$${}^{C}D^{\alpha}V(t,\xi(t))\leq-(\eta_1-\eta_2)V(t,\xi(t)),t\geq0. \tag{30}$$

According to Lemma 5, the claim of Theorem 4.3 follows.

$$V(t,\xi(t))\leq V(0,\xi(0))E_{\alpha}(-\gamma t^{\alpha}),t\geq0 \tag{31}$$

By Lemma 4 and inequality (31), this proves system (10) can be achieved globally Mittag-Leffler stabilization under the designed control law.
This completes the proof.

Theorem 4.5. Assume that Assumption (1) and Lemma (4) hold, then the system (10) is Globally mittag-leffler stable, provided the following conditions holds:

$$
\begin{aligned}
&\theta_1(t)>\theta_2(t)\\
&\theta_1(t)=\min_{1\leq i\leq n}[\omega(d_i+|\phi_i(t)|+|\Psi_i(t)|)-\sum_{j=1}^{n}|c_{ij}|F_j\delta_1(\omega-1)-\sum_{j=1}^{n}|c_{ji}|F_i\frac{1}{\delta_1^{\omega-1}}\\
&-\sum_{j=1}^{n}|a_{ij}|F_j(\omega-1)\delta_2+|u_{ij}|F_j(\omega-1)\delta_3+|v_{ij}|F_j(\omega-1)\delta_3]\frac{|\xi_i(t)|^{\omega}}{\omega}\\
&+\min_{1\leq i\leq n}[\rho(d_i+|\phi_i(t)|+|\Psi_i(t)|)-\sum_{j=1}^{n}|c_{ij}|F_j\delta_1(\rho-1)-\sum_{j=1}^{n}|c_{ji}|F_i\frac{1}{\delta_1^{\rho-1}}
\end{aligned}
$$

$$-\sum_{j=1}^{n}|a_{ij}|F_j(\rho-1)\delta_2+|u_{ij}|F_j(\rho-1)\delta_3+|v_{ij}|F_j(\rho-1)\delta_3]\frac{|\xi_i(t)|^\rho}{\rho}>0,$$

$$\theta_2(t)=\max_{1\le i\le n}[\sum_{j=1}^{n}|a_{ji}|F_i\frac{1}{\delta_2^{\omega-1}}+\sum_{j=1}^{n}|u_{ji}|F_i\frac{1}{\delta_3^{\omega-1}}+\sum_{j=1}^{n}|v_{ji}|F_i\frac{1}{\delta_3^{\omega-1}}]\frac{|\xi_i(t-\tau)|^\omega}{\omega}$$
$$+\max_{1\le i\le n}[\sum_{j=1}^{n}|a_{ji}|F_i\frac{1}{\delta_2^{\rho-1}}+\sum_{j=1}^{n}|u_{ji}|F_i\frac{1}{\delta_3^{\rho-1}}+\sum_{j=1}^{n}|v_{ji}|F_i\frac{1}{\delta_3^{\rho-1}}]\frac{|\xi_i(t-\tau)|^\rho}{\rho}>0.$$

Proof: we define a Lyapunov function

$$V(t,\xi(t))=\sum_{i=1}^{n}\frac{1}{\omega}|\xi_i(t)|^\omega+\sum_{i=1}^{n}\frac{1}{\rho}|\xi_i(t)|^\rho \tag{32}$$

According to the Caputo fractional-order derivative definition, we have

$$\begin{aligned}
{}^{C}D^{\alpha}V(t,\xi(t))\le&\sum_{i=1}^{n}|\xi_i(t)|^{\omega-1}[-d_i|\xi_i(t)|+\sum_{j=1}^{n}|c_{ij}|[f_j(\vartheta_j(t))-f_j(\zeta_j(t))]\\
&+\sum_{j=1}^{n}|a_{ij}|[f_j(\vartheta_j(t-\tau))-f_j(\zeta_j(t-\tau))]\\
&+\bigwedge_{j=1}^{n}|u_{ij}|\int_0^\infty k_j(s)[f_j(\vartheta_j(s-\tau))-f_j(\zeta_j(t-\tau))]ds\\
&+\bigvee_{j=1}^{n}|v_{ij}|\int_0^\infty k_j(s)[f_j(\vartheta_j(s-\tau))-f_j(\zeta_j(t-\tau))]ds+|\phi_i(t)||\xi_i(t)|+|\Psi_i(t)||\xi_i(t)|]\\
&+\sum_{i=1}^{n}|\xi_i(t)|^{\rho-1}[-d_i|\xi_i(t)|+\sum_{j=1}^{n}|c_{ij}|[f_j(\vartheta_j(t))-f_j(\zeta_j(t))]\\
&+\sum_{j=1}^{n}|a_{ij}|[f_j(\vartheta_j(t-\tau))-f_j(\zeta_j(t-\tau))]\\
&+\bigwedge_{j=1}^{n}|u_{ij}|\int_0^\infty k_j(s)[f_j(\vartheta_j(s-\tau))-f_j(\zeta_j(t-\tau))]ds\\
&+\bigvee_{j=1}^{n}|v_{ij}|\int_0^\infty k_j(s)[f_j(\vartheta_j(s-\tau))-f_j(\zeta_j(t-\tau))]ds+|\phi_i(t)||\xi_i(t)|+|\Psi_i(t)||\xi_i(t)|]\\
&\le\sum_{i=1}^{n}|\xi_i(t)|^{\omega-1}[-d_i|\xi_i(t)|+\sum_{j=1}^{n}|c_{ij}|F_j|\xi_j(t)|+\sum_{j=1}^{n}|a_{ij}|F_j|\xi_j(t-\tau)|\\
&+\sum_{j=1}^{n}|u_{ij}|\int_0^\infty k_j(s)F_j|\xi_j(s-\tau)|ds+\sum_{j=1}^{n}|v_{ij}|\int_0^\infty k_j(s)F_j|\xi_j(s-\tau)|ds\\
&+|\phi_i(t)||\xi_i(t)|+|\Psi_i(t)||\xi_i(t)|]\\
&+\sum_{i=1}^{n}|\xi_i(t)|^{\rho-1}[-d_i|\xi_i(t)|+\sum_{j=1}^{n}|c_{ij}|F_j|\xi_j(t)|+\sum_{j=1}^{n}|a_{ij}|F_j|\xi_j(t-\tau)|\\
&+\sum_{j=1}^{n}|u_{ij}|\int_0^\infty k_j(s)F_j|\xi_j(s-\tau)|ds+\sum_{j=1}^{n}|v_{ij}|\int_0^\infty k_j(s)F_j|\xi_j(s-\tau)|ds\\
&+|\phi_i(t)||\xi_i(t)|+|\Psi_i(t)||\xi_i(t)|]
\end{aligned}$$

$$
\begin{aligned}
&\leq -\sum_{i=1}^{n}(d_i+|\phi_i(t)|+|\Psi_i(t)|)|\xi_i(t)|^{\omega}+\sum_{i=1}^{n}\sum_{j=1}^{n}|c_{ij}|F_j|\xi_i(t)|^{\omega-1}|\xi_j(t)|\\
&+\sum_{i=1}^{n}\sum_{j=1}^{n}|a_{ij}|F_j|\xi_i(t)|^{\omega-1}|\xi_j(t-\tau)|+\sum_{i=1}^{n}\sum_{j=1}^{n}|u_{ij}|\int_0^{\infty}k_j(s)F_j|\xi_i(s)|^{\omega-1}|\xi_j(s-\tau)|ds\\
&+\sum_{i=1}^{n}\sum_{j=1}^{n}|v_{ij}|\int_0^{\infty}k_j(s)F_j|\xi_i(s)|^{\omega-1}|\xi_j(s-\tau)|ds\\
&-\sum_{i=1}^{n}(d_i+|\phi_i(t)|+|\Psi_i(t)|)|\xi_i(t)|^{\rho}+\sum_{i=1}^{n}\sum_{j=1}^{n}|c_{ij}|F_j|\xi_i(t)|^{\rho-1}|\xi_j(t)|\\
&+\sum_{i=1}^{n}\sum_{j=1}^{n}|a_{ij}|F_j|\xi_i(t)|^{\rho-1}|\xi_j(t-\tau)|+\sum_{i=1}^{n}\sum_{j=1}^{n}|u_{ij}|\int_0^{\infty}k_j(s)F_j|\xi_i(s)|^{\rho-1}|\xi_j(s-\tau)|ds\\
&+\sum_{i=1}^{n}\sum_{j=1}^{n}|v_{ij}|\int_0^{\infty}k_j(s)F_j|\xi_i(s)|^{\rho-1}|\xi_j(s-\tau)|ds
\end{aligned}
\tag{33}
$$

From Lemma 3 we have

$$
\begin{aligned}
|\xi_i(t)|^{\omega-1}|\xi_j(t)| &\leq \frac{\omega-1}{\omega}[|\xi_i(t)|^{\omega-1}\delta_1^{\frac{\omega-1}{\omega}}]^{\frac{\omega}{\omega-1}}+\frac{1}{\omega}[|\xi_j(t)|\delta_1^{\frac{-\omega-1}{\omega}}]^{\omega}\\
&=\frac{\omega-1}{\omega}|\xi_i(t)|^{\omega}\delta_1+\frac{1}{\omega}|\xi_j(t)|^{\omega}\frac{1}{\delta_1^{\omega-1}}\\
|\xi_i(t)|^{\omega-1}|\xi_j(t-\tau)| &\leq \frac{\omega-1}{\omega}[|\xi_i(t)|^{\omega-1}\delta_2^{\frac{\omega-1}{\omega}}]^{\frac{\omega}{\omega-1}}+\frac{1}{\omega}[|\xi_j(t-\tau)|\delta_2^{\frac{-\omega-1}{\omega}}]^{\omega}\\
&=\frac{\omega-1}{\omega}|\xi_i(t)|^{\omega}\delta_2+\frac{1}{\omega}|\xi_j(t-\tau)|^{\omega}\frac{1}{\delta_2^{\omega-1}}\\
\int_0^{\infty}|\xi_i(s)|^{\omega-1}|\xi_j(s-\tau)|ds &\leq \int_0^{\infty}\frac{\omega-1}{\omega}[|\xi_i(s)|^{\omega-1}\delta_3^{\frac{\omega-1}{\omega}}]^{\frac{\omega}{\omega-1}}+\frac{1}{\omega}[|\xi_j(s-\tau)|\delta_3^{\frac{-\omega-1}{\omega}}]^{\omega}\\
&=\int_0^{\infty}\frac{\omega-1}{\omega}|\xi_i(s)|^{\omega}\delta_3+\frac{1}{\omega}|\xi_j(s-\tau)|^{\omega}\frac{1}{\delta_3^{\omega-1}}\\
|\xi_i(t)|^{\rho-1}|\xi_j(t)| &\leq \frac{\rho-1}{\rho}[|\xi_i(t)|^{\rho-1}\delta_1^{\frac{\rho-1}{\rho}}]^{\frac{\rho}{\rho-1}}+\frac{1}{\rho}[|\xi_j(t)|\delta_1^{\frac{-\rho-1}{\rho}}]^{\rho}\\
&=\frac{\rho-1}{\rho}|\xi_i(t)|^{\rho}\delta_1+\frac{1}{\rho}|\xi_j(t)|^{\rho}\frac{1}{\delta_1^{\rho-1}}\\
|\xi_i(t)|^{\rho-1}|\xi_j(t-\tau)| &\leq \frac{\rho-1}{\rho}[|\xi_i(t)|^{\rho-1}\delta_2^{\frac{\rho-1}{\rho}}]^{\frac{\rho}{\rho-1}}+\frac{1}{\rho}[|\xi_j(t-\tau)|\delta_2^{\frac{-\rho-1}{\rho}}]^{\rho}\\
&=\frac{\rho-1}{\rho}|\xi_i(t)|^{\rho}\delta_2+\frac{1}{\rho}|\xi_j(t-\tau)|^{\rho}\frac{1}{\delta_2^{\rho-1}}\\
\int_0^{\infty}|\xi_i(s)|^{\rho-1}|\xi_j(s-\tau)|ds &\leq \int_0^{\infty}\frac{\rho-1}{\rho}[|\xi_i(s)|^{\rho-1}\delta_3^{\frac{\rho-1}{\rho}}]^{\frac{\rho}{\rho-1}}+\frac{1}{\rho}[|\xi_j(s-\tau)|\delta_3^{\frac{-\rho-1}{\rho}}]^{\rho}\\
&=\int_0^{\infty}\frac{\rho-1}{\rho}|\xi_i(s)|^{\rho}\delta_3+\frac{1}{\rho}|\xi_j(s-\tau)|^{\rho}\frac{1}{\delta_3^{\rho-1}}
\end{aligned}
\tag{34}
$$

Now substitute the above values in the above equation we get

$$
\begin{aligned}
{}^{C}D^{\alpha}V(t,\xi(t)) \leq & -\sum_{i=1}^{n}(d_i+|\phi_i(t)|+|\Psi_i(t)|)|\xi_i(t)|^{\omega}+\sum_{i=1}^{n}\sum_{j=1}^{n}|c_{ij}|F_j[\frac{\omega-1}{\omega}|\xi_i(t)|^{\omega}\delta_1 \\
& +\frac{1}{\omega}|\xi_j(t)|^{\omega}\frac{1}{\delta_1^{\omega-1}}]+\sum_{i=1}^{n}\sum_{j=1}^{n}|a_{ij}|F_j[\frac{\omega-1}{\omega}|\xi_i(t)|^{\omega}\delta_2+\frac{1}{\omega}|\xi_j(t-\tau)|^{\omega}\frac{1}{\delta_2^{\omega-1}}] \\
& +\sum_{i=1}^{n}\sum_{j=1}^{n}|u_{ij}|\int_0^{\infty}k_j(s)F_j[\frac{\omega-1}{\omega}|\xi_i(s)|^{\omega}\delta_3+\frac{1}{\omega}|\xi_j(s-\tau)|^{\omega}\frac{1}{\delta_3^{\omega-1}}]ds \\
& +\sum_{i=1}^{n}\sum_{j=1}^{n}|v_{ij}|\int_0^{\infty}k_j(s)F_j[\frac{\omega-1}{\omega}|\xi_i(s)|^{\omega}\delta_3+\frac{1}{\omega}|\xi_j(s-\tau)|^{\omega}\frac{1}{\delta_3^{\omega-1}}]ds \\
& -\sum_{i=1}^{n}(d_i+|\phi_i(t)|+|\Psi_i(t)|)|\xi_i(t)|^{\rho}+\sum_{i=1}^{n}\sum_{j=1}^{n}|c_{ij}|F_j[\frac{\rho-1}{\rho}|\xi_i(t)|^{\rho}\delta_1 \\
& +\frac{1}{\rho}|\xi_j(t)|^{\rho}\frac{1}{\delta_1^{\rho-1}}]+\sum_{i=1}^{n}\sum_{j=1}^{n}|a_{ij}|F_j[\frac{\rho-1}{\rho}|\xi_i(t)|^{\rho}\delta_2+\frac{1}{\rho}|\xi_j(t-\tau)|^{\rho}\frac{1}{\delta_2^{\rho-1}}] \\
& +\sum_{i=1}^{n}\sum_{j=1}^{n}|u_{ij}|\int_0^{\infty}k_j(s)F_j[\frac{\rho-1}{\rho}|\xi_i(s)|^{\rho}\delta_3+\frac{1}{\rho}|\xi_j(s-\tau)|^{\rho}\frac{1}{\delta_3^{\rho-1}}]ds \\
& +\sum_{i=1}^{n}\sum_{j=1}^{n}|v_{ij}|\int_0^{\infty}k_j(s)F_j[\frac{\rho-1}{\rho}|\xi_i(s)|^{\rho}\delta_3+\frac{1}{\rho}|\xi_j(s-\tau)|^{\rho}\frac{1}{\delta_3^{\rho-1}}]ds \\
\leq & -\sum_{i=1}^{n}[d_i+|\phi_i(t)|+|\Psi_i(t)|]|\xi_i(t)|^{\omega}+\sum_{i=1}^{n}\sum_{j=1}^{n}|c_{ij}|F_j[\frac{\omega-1}{\omega}|\xi_i(t)|^{\omega}\delta_1] \\
& +\sum_{i=1}^{n}\sum_{j=1}^{n}|c_{ji}|F_i[\frac{1}{\omega}|\xi_i(t)|^{\omega}\frac{1}{\delta_1^{\omega-1}}] \\
& +\sum_{i=1}^{n}\sum_{j=1}^{n}|a_{ij}|F_j[\frac{\omega-1}{\omega}|\xi_i(t)|^{\omega}\delta_2]+\sum_{i=1}^{n}\sum_{j=1}^{n}|a_{ji}|F_i][\frac{1}{\omega}|\xi_i(t-\tau)|^{\omega}\frac{1}{\delta_2^{\omega-1}}] \\
& +\sum_{i=1}^{n}\sum_{j=1}^{n}|u_{ij}|\int_0^{\infty}k_j(s)F_j[\frac{\omega-1}{\omega}|\xi_i(s)|^{\omega}\delta_3]ds \\
& +\sum_{i=1}^{n}\sum_{j=1}^{n}|u_{ji}|\int_0^{\infty}k_j(s)F_i[\frac{1}{\omega}|\xi_i(s-\tau)|^{\omega}\frac{1}{\delta_3^{\omega-1}}]ds \\
& +\sum_{i=1}^{n}\sum_{j=1}^{n}|v_{ij}|\int_0^{\infty}k_j(s)F_j[\frac{\omega-1}{\omega}|\xi_i(s)|^{\omega}\delta_3]ds \\
& +\sum_{i=1}^{n}\sum_{j=1}^{n}|v_{ji}|\int_0^{\infty}k_j(s)F_i[\frac{1}{\omega}|\xi_i(s-\tau)|^{\omega}\frac{1}{\delta_3^{\omega-1}}]ds \\
& -\sum_{i=1}^{n}[d_i+|\phi_i(t)|+|\Psi_i(t)|]|\xi_i(t)|^{\rho}+\sum_{i=1}^{n}\sum_{j=1}^{n}|c_{ij}|F_j[\frac{\rho-1}{\rho}|\xi_i(t)|^{\rho}\delta_1] \\
& +\sum_{i=1}^{n}\sum_{j=1}^{n}|c_{ji}|F_i[\frac{1}{\rho}|\xi_i(t)|^{\rho}\frac{1}{\delta_1^{\rho-1}}]
\end{aligned}
$$

$$
\begin{aligned}
&+\sum_{i=1}^{n}\sum_{j=1}^{n}|a_{ij}|F_j[\frac{\rho-1}{\rho}|\xi_i(t)|^{\rho}\delta_2]+\sum_{i=1}^{n}\sum_{j=1}^{n}|a_{ji}|F_i[\frac{1}{\rho}|\xi_i(t-\tau)|^{\rho}\frac{1}{\delta_2^{\rho-1}}]\\
&+\sum_{i=1}^{n}\sum_{j=1}^{n}|u_{ij}|\int_0^{\infty}k_j(s)F_j[\frac{\rho-1}{\rho}|\xi_i(s)|^{\rho}\delta_3]ds\\
&+\sum_{i=1}^{n}\sum_{j=1}^{n}|u_{ji}|\int_0^{\infty}k_j(s)F_i[\frac{1}{\rho}|\xi_i(s-\tau)|^{\rho}\frac{1}{\delta_3^{\rho-1}}]ds\\
&+\sum_{i=1}^{n}\sum_{j=1}^{n}|v_{ij}|\int_0^{\infty}k_j(s)F_j[\frac{\rho-1}{\rho}|\xi_i(s)|^{\rho}\delta_3]ds\\
&+\sum_{i=1}^{n}\sum_{j=1}^{n}|v_{ji}|\int_0^{\infty}k_j(s)F_i[\frac{1}{\rho}|\xi_i(s-\tau)|^{\rho}\frac{1}{\delta_3^{\rho-1}}]ds\\
\le&\sum_{i=1}^{n}[-\omega(d_i+|\phi_i(t)|+|\Psi_i(t)|)+\sum_{j=1}^{n}|c_{ij}|F_j\delta_1(\omega-1)\\
&+\sum_{j=1}^{n}|c_{ji}|F_i\frac{1}{\delta_1^{\omega-1}}+\sum_{j=1}^{n}|a_{ij}|F_j\delta_2(\omega-1)]\frac{|\xi_i(t)|^{\omega}}{\omega}+\sum_{i=1}^{n}[\sum_{j=1}^{n}|a_{ji}|F_i\frac{1}{\delta_2^{\omega-1}}]\frac{|\xi_i(t-\tau)|^{\omega}}{\omega}\\
&+\sum_{i=1}^{n}\sum_{j=1}^{n}\int_0^{\infty}k_j(s)[|u_{ij}|F_j(\omega-1)\delta_3+|v_{ij}|F_j(\omega-1)\delta_3]\frac{|\xi_i(s)|^{\omega}}{\omega}ds\\
&+\sum_{i=1}^{n}\sum_{j=1}^{n}\int_0^{\infty}k_j(s)[|u_{ji}|F_i(\frac{1}{\delta_3^{\omega-1}})+|v_{ji}|F_i(\frac{1}{\delta_3^{\omega-1}})]\frac{|\xi_i(s-\tau)|^{\omega}}{\omega}ds\\
&+\sum_{i=1}^{n}[-\rho(d_i+|\phi_i(t)|+|\Psi_i(t)|)+\sum_{j=1}^{n}|c_{ij}|F_j\delta_1(\rho-1)\\
&+\sum_{j=1}^{n}|c_{ji}|F_i\frac{1}{\delta_1^{\rho-1}}+\sum_{j=1}^{n}|a_{ij}|F_j\delta_2(\rho-1)]\frac{|\xi_i(t)|^{\rho}}{\rho}+\sum_{i=1}^{n}[\sum_{j=1}^{n}|a_{ji}|F_i\frac{1}{\delta_2^{\rho-1}}]\frac{|\xi_i(t-\tau)|^{\rho}}{\rho}\\
&+\sum_{i=1}^{n}\sum_{j=1}^{n}\int_0^{\infty}k_j(s)[|u_{ij}|F_j(\rho-1)\delta_3+|v_{ij}|F_j(\rho-1)\delta_3]\frac{|\xi_i(s)|^{\rho}}{\rho}ds\\
&+\sum_{i=1}^{n}\sum_{j=1}^{n}\int_0^{\infty}k_j(s)[|u_{ji}|F_i(\frac{1}{\delta_3^{\rho-1}})+|v_{ji}|F_i(\frac{1}{\delta_3^{\rho-1}})]\frac{|\xi_i(s-\tau)|^{\rho}}{\rho}ds\\
\le&-\sum_{i=1}^{n}[\omega(d_i+|\phi_i(t)|+|\Psi_i(t)|)-\sum_{j=1}^{n}|c_{ij}|F_j\delta_1(\omega-1)\\
&-\sum_{j=1}^{n}|c_{ji}|F_i\frac{1}{\delta_1^{\omega-1}}-\sum_{j=1}^{n}|a_{ij}|F_j\delta_2(\omega-1)]\frac{|\xi_i(t)|^{\omega}}{\omega}+\sum_{i=1}^{n}[\sum_{j=1}^{n}|a_{ji}|F_i\frac{1}{\delta_2^{\omega-1}}]\frac{|\xi_i(t-\tau)|^{\omega}}{\omega}\\
&+\sum_{i=1}^{n}\sum_{j=1}^{n}\int_0^{\infty}k_j(s)[|u_{ij}|F_j(\omega-1)\delta_3+|v_{ij}|F_j(\omega-1)\delta_3]\frac{|\xi_i(s)|^{\omega}}{\omega}ds\\
&+\sum_{i=1}^{n}\sum_{j=1}^{n}\int_0^{\infty}k_j(s)[|u_{ji}|F_i(\frac{1}{\delta_3^{\omega-1}})+|v_{ji}|F_i(\frac{1}{\delta_3^{\omega-1}})]\frac{|\xi_i(s-\tau)|^{\omega}}{\omega}ds
\end{aligned}
$$

$$
\begin{aligned}
&-\sum_{i=1}^{n}[\rho(d_i+|\phi_i(t)|+|\Psi_i(t)|)-\sum_{j=1}^{n}|c_{ij}|F_j\delta_1(\rho-1)\\
&-\sum_{j=1}^{n}|c_{ji}|F_i\frac{1}{\delta_1^{\rho-1}}-\sum_{j=1}^{n}|a_{ij}|F_j\delta_2(\rho-1)]\frac{|\xi_i(t)|^\rho}{\rho}+\sum_{i=1}^{n}[\sum_{j=1}^{n}|a_{ji}|F_i\frac{1}{\delta_2^{\rho-1}}]\frac{|\xi_i(t-\tau)|^\rho}{\rho}\\
&+\sum_{i=1}^{n}\sum_{j=1}^{n}\int_0^\infty k_j(s)[|u_{ij}|F_j(\rho-1)\delta_3+|v_{ij}|F_j(\rho-1)\delta_3]\frac{|\xi_i(s)|^\rho}{\rho}ds\\
&+\sum_{i=1}^{n}\sum_{j=1}^{n}\int_0^\infty k_j(s)[|u_{ji}|F_i(\frac{1}{\delta_3^{\rho-1}})+|v_{ji}|F_i(\frac{1}{\delta_3^{\rho-1}})]\frac{|\xi_i(s-\tau)|^\rho}{\rho}ds\\
&\le-\theta_1(t)V(t,\xi(t))+\theta_2\max_{t-\tau\le s\le t}V(s,\xi(s)).
\end{aligned}
\tag{35}
$$

where

$$
\begin{aligned}
\theta_1(t)=&\min_{1\le i\le n}[\omega(d_i+|\phi_i(t)|+|\Psi_i(t)|)-\sum_{j=1}^{n}|c_{ij}|F_j\delta_1(\omega-1)-\sum_{j=1}^{n}|c_{ji}|F_i\frac{1}{\delta_1^{\omega-1}}\\
&-\sum_{j=1}^{n}|a_{ij}|F_j(\omega-1)\delta_2+|u_{ij}|F_j(\omega-1)\delta_3+|v_{ij}|F_j(\omega-1)\delta_3]\frac{|\xi_i(t)|^\omega}{\omega}\\
&+\min_{1\le i\le n}[\rho(d_i+|\phi_i(t)|+|\Psi_i(t)|)-\sum_{j=1}^{n}|c_{ij}|F_j\delta_1(\rho-1)-\sum_{j=1}^{n}|c_{ji}|F_i\frac{1}{\delta_1^{\rho-1}}\\
&-\sum_{j=1}^{n}|a_{ij}|F_j(\rho-1)\delta_2+|u_{ij}|F_j(\rho-1)\delta_3+|v_{ij}|F_j(\rho-1)\delta_3]\frac{|\xi_i(t)|^\rho}{\rho}\\
\theta_2(t)=&\max_{1\le i\le n}[\sum_{j=1}^{n}|a_{ji}|F_i\frac{1}{\delta_2^{\omega-1}}+\sum_{j=1}^{n}|u_{ji}|F_i\frac{1}{\delta_3^{\omega-1}}+\sum_{j=1}^{n}|v_{ji}|F_i\frac{1}{\delta_3^{\omega-1}}\frac{|\xi_i(t-\tau)|^\omega}{\omega}\\
&+\max_{1\le i\le n}[\sum_{j=1}^{n}|a_{ji}|F_i\frac{1}{\delta_2^{\rho-1}}+\sum_{j=1}^{n}|u_{ji}|F_i\frac{1}{\delta_3^{\rho-1}}+\sum_{j=1}^{n}|v_{ji}|F_i\frac{1}{\delta_3^{\rho-1}}\frac{|\xi_i(t-\tau)|^\rho}{\rho}
\end{aligned}
$$

From this estimate, for any solution (13), which satisfies the Razumichin condition

$$V(s,\xi(s))\le V(t,\xi(t)),t-\tau\le s\le t,$$

we have

$${}^{C}D^{\alpha}V(t,\xi(t))\le-(\eta_1-\eta_2)V(t,\xi(t)),t\ge0. \tag{36}$$

According to Lemma 5, the claim of Theorem 4.4 follows.

$$V(t,\xi(t))\le V(0,\xi(0))E_\alpha(-\gamma t^\alpha),t\ge0 \tag{37}$$

By Lemma 4 and inequality (37), this proves the system (10) can be achieved globally Mittag-Leffler stabilization under the designed control law. Hence complete the proof.

Remark 4.6. *In the FCNNs, the fuzzy minimum feed-forward refers to taking the minimum value of the connection parameters with the fuzzy AND operation, and the fuzzy maximum feed-forward refers to taking the maximum value of the connection parameters with the fuzzy OR operation. The fuzzy minimum feedback refers to taking the minimum value of the delay connection parameter with the fuzzy AND operation, and the fuzzy maximum feedback refers to the maximum value of the delay connection parameter with the fuzzy OR operation. There are many other fuzzy logics, such as fuzzy AND, fuzzy OR, fuzzy NOT, fuzzy NAND, fuzzy NOR, fuzzy XOR, fuzzy XNOR, complex fuzzy logic and etc. It is worth highlighting that our work can be applied to FCNNs with more complex fuzzy logic.*

Remark 4.7. *Neural networks usually have a spatial extension due to the presence of a multitude of parallel pathways with a variety of axon sizes and length and hence there is a distribution of propagation delays over a period of time. It is worth noting that although the signal propagation is sometimes instantaneous and can be modelled with discrete delays, it may also be distributed during a certain time period, so the distributed delays should be incorporated in the model. In other words, it is often the case that the neural network model possesses both discrete and distributed delays. In recent years, the stability of Hopfield neural networks, cellular neural networks and bidirectional associative memory neural networks with distributed delays has been discussed (see* [40, 59] *and refernces threin).*

Remark 4.8. *In recent days, stability analysis of fuzzy cellular neural networks have been extensively studied by te researchers. Stability analysis of fuzzy cellular neural networks with time delay in the leakage term and impulsive perturbations investigated in* [79]*. Finite-time synchronization of delayed fuzzy cellular neural networks with discontinuous activations is studied (see* [80] *and refernces there in). In these works integer order is considered in our paper fractional order is consideered. Great efforts have been made in study of fractional order neural networks bythe researchers. See for example, Adaptive control for fractional order induced chaotic fuzzy cellular neural networks* [81]*, asymptotic stability of delayed fractional-order fuzzy neural networks with impulse effects* [82]*, Mittag-Leffler stability of fractional-order Hopfield neural networks* [83]*, Synchronization of fractional fuzzy cellular neural networks with interactions* [84] *have been invesitgated. In our paper stability fractional order fuzzy cellular neural networks with hybrid control is investigated.*

Remark 4.9. *In* [85]*, Xu et al. investigated complete synchronization of fractional order complex networks via pinning adaptive and impulsive control strategy. In the past few years, due to the limited theory to deal with finite time stability of fractional order systems, synchronization research of fractional order systems is only the beginning* [86] - [87]*. In* [88]*, Velmurugan et al. studied synchronization of fractional order neural networks by employing linear feedback control strategy. In* [89]*, Ding et al. designed a novel controller based on feedback control strategy and discontinuous control strategy, and investigated stability of the considered fractional order neural networks. As is known to all, it is more perfect if the designed controller both realize the network synchronization objective and reduce the corresponding control cost. Motivated by the above discussions, we designed a novel hybrid feedback controller, which is based on a simple discontinuous control strategy and study stability problem of fractional order cellular neural networks networks.*

Remark 4.10. *It is well known that every control strategy has its own advantages and disadvantages. Therefore, in some cases, hybrid control strategies are necessary to control some complex systems to achieve synchronization or other properties. Since fuzzy cellular neural networks may experience instantaneous perturbation or abrupt changes at certain instances, hybrid impulsive and other control strategies could be used to control them to the synchronous state. However, to authors' knowledge, there have few research achievements on the stability of fuzzy cellular neural networks by means of hybrid control strategies at present. It is still an open problem that deserves further investigation, which motivated our research in this paper.*

5. Numerical Example

In this section, two examples are given to illustrate the effectiveness of proposed Global Mittag-Leffler stability schemes.

Example 1: For n=4, consider the following fractional-order fuzzy cellular neural networks,

$$
\begin{aligned}
{}^{C}D^{\alpha}\zeta_i(t) = -d_i\zeta_i(t) + \sum_{j=1}^{2} c_{ij} f_j(\zeta_j(t)) + \sum_{j=1}^{2} a_{ij} f_j(\zeta_j(t-\tau) + \sum_{j=1}^{2} h_{ij}\mu_j \\
+ \bigwedge_{j=1}^{2} u_{ij} \int_0^{\infty} k_j(s) f_j(\zeta_j(s-\tau))ds + \bigwedge_{j=1}^{2} p_{ij}\mu_j + \bigvee_{j=1}^{n} v_{ij} \int_0^{\infty} k_j(s) f_j(\zeta_j(s-\tau))ds
\end{aligned}
$$

$$+\bigvee_{j=1}^{2} Q_{ij}\mu_j + I_i, i = 1, 2, \tag{38}$$

The parameters of (13) error system are assumed that $a_{11} = 0.4$, $a_{12} = 0.6$, $a_{13} = 0.9$, $a_{14} = 1.2$, $a_{21} = 0.8$, $a_{22} = 0.9$, $a_{23} = 2.3$, $a_{24} = 1.5$, $a_{31} = 0.7$, $a_{32} = 1.8$, $a_{33} = 0.5$, $a_{34} = 0.7$ $a_{41} = 1.3$, $a_{42} = 0.5$, $a_{43} = 0.2$, $a_{44} = 0.9$, $c_{11} = 1.5$, $c_{12} = 1.8$, $c_{13} = 0.7$, $c_{14} = 1.3$ $c_{21} = 2.9$, $c_{22} = 2.8$, $c_{23} = 0.9$ $c_{24} = 0.7$ $c_{31} = 1.8$, $c_{32} = 1.5$, $c_{33} = 0.7$, $c_{34} = 0.9$ $c_{41} = 2.8$, $c_{42} = 2.9$, $c_{43} = 0.7$, $c_{44} = 1.3$, $u_{11} = 0.9$, $u_{12} = 1.2$, $u_{13} = 2.1$, $u_{14} = 3.4$, $u_{21} = 2.1$, $u_{22} = 3.4$, $u_{23} = 1.2$, $u_{24} = 0.9$, $u_{31} = 2.1$, $u_{32} = 1.2$, $u_{33} = 0.9$, $c_{34} = 1.7$ $u_{41} = 1.7$, $u_{42} = 1.7$, $u_{43} = 1.2$, $u_{44} = 0.9$, $v_{11} = 1.8$, $v_{12} = 2.2$, $v_{13} = 0.7$, $v_{14} = 2.7$, $v_{21} = 2.2$, $v_{22} = 0.9$, $v_{23} = 0.5$, $v_{24} = 1.2$, $v_{31} = 1.7$, $v_{32} = 2.2$, $v_{33} = 0.7$, $v_{34} = 0.9$ $v_{41} = 0.9$, $v_{42} = 0.5$, $v_{43} = 1.8$, $v_{44} = 1.7$, $d_1 = 5$, $d_2 = 7$, $d_3 = 7$, $d_4 = 5$, $\Psi_1 = 0.6$, $\Psi_2 = 0.7$, $\Psi_3 = 0.5$, $\Psi_4 = 0.4$, $\phi_1 = 1.4$, $\phi_2 = 3.1$,$\phi_3 = 2.7$, $\phi_4 = 3.7$, $\alpha = 0.97$, $f(t) = tanh(t)$.
The corresponding response system is described by

$$\begin{aligned}
{}^{C}D^{\alpha}\vartheta_i(t) &= -d_i\vartheta_i(t) + \sum_{j=1}^{2} c_{ij}f_j(\vartheta_j(t)) + \sum_{j=1}^{2} a_{ij}f_j(\vartheta_j(t-\tau) + \sum_{j=1}^{2} h_{ij}\mu_j \\
&+ \bigwedge_{j=1}^{2} u_{ij}\int_0^{\infty} k_j(s)f_j(\vartheta_j(s-\tau))ds + \bigwedge_{j=1}^{2} p_{ij}\mu_j + \bigvee_{j=1}^{2} v_{ij}\int_0^{\infty} k_j(s)f_j(\vartheta_j(s-\tau))ds \\
&+ \bigvee_{j=1}^{2} Q_{ij}\mu_j + I_i + u_i(t),
\end{aligned} \tag{39}$$

where a_{ij}, u_{ij}, v_{ij}, d_i, c_{ij}, and I_i are the same as in system (39), and the hybrid feedback controllers is as follows: $u_i(t) = u_{1i}(t) + u_{2i}(t)$, where $u_{1i}(t) = -\phi_i(t)\xi_i(t)$ and $u_{2i}(t) = -\Psi_i(t)\xi_i(t)$. where $\xi_i(t) = \vartheta_i(t) - \zeta_i(t)$ for i=1,2. According to the developed idea in Theorem 4.1, it asks that

$$\begin{aligned}
\eta_1(t) &= \min_{1\le i\le n}[(d_i + \phi_i(t) + \Psi_i) - \sum_{j=1}^{n} c_{ij}F_j\rho^{-1} - \sum_{j=1}^{n} c_{ji}F_i\rho - \sum_{j=1}^{n} a_{ij}F_j\rho^{-1} \\
&+ \sum_{j=1}^{n} u_{ij}F_j\rho^{-1} + \sum_{j=1}^{n} v_{ij}F_j\rho^{-1}] = 12.33 > 0, \\
\eta_2(t) &= \max_{1\le i\le n}[\sum_{j=1}^{n} a_{ji}F_i\rho + u_{ji}F_i\rho + \sum_{j=1}^{n} v_{ji}F_i\rho] = 12.18 > 0.
\end{aligned}$$

Then it follows from Theorem 4.1 that system (38) can be achieved global Mittag-Leffler stabilization under the designed hybrid feedback control law.

Example 2: For n=2, consider the following fractional-order fuzzy cellular neural networks,

$$\begin{aligned}
{}^{C}D^{\alpha}\zeta_i(t) &= -d_i\zeta_i(t) + \sum_{j=1}^{2} c_{ij}f_j(\zeta_j(t)) + \sum_{j=1}^{2} a_{ij}f_j(\zeta_j(t-\tau) + \sum_{j=1}^{2} h_{ij}\mu_j \\
&+ \bigwedge_{j=1}^{2} u_{ij}\int_0^{\infty} k_j(s)f_j(\zeta_j(s-\tau))ds + \bigwedge_{j=1}^{2} p_{ij}\mu_j + \bigvee_{j=1}^{n} v_{ij}\int_0^{\infty} k_j(s)f_j(\zeta_j(s-\tau))ds \\
&+ \bigvee_{j=1}^{2} Q_{ij}\mu_j + I_i, i = 1, 2,
\end{aligned} \tag{40}$$

where $\alpha = 0.97$, $f(t) = tanh(t)$

The parameters of (13) error system are assumed that $a_{11} = 0.9$, $a_{12} = 0.8$, $a_{13} = 0.4$, $a_{14} = 0.6$, $a_{21} = 0.4$, $a_{22} = 0.8$, $a_{23} = 0.7$, $a_{24} = 0.3$, $a_{31} = 0.3$, $a_{32} = 0.7$, $a_{33} = 0.7$, $a_{34} = 0.5$ $a_{41} = 0.5$, $a_{42} = 0.8$, $a_{43} = 0.3$, $a_{44} = 0.5$, $c_{11} = 0.4$, $c_{12} = 0.5$, $c_{13} = 0.4$, $c_{14} = 1.3$ $c_{21} = 0.7$, $c_{22} = 0.8$, $c_{23} = 0.5$

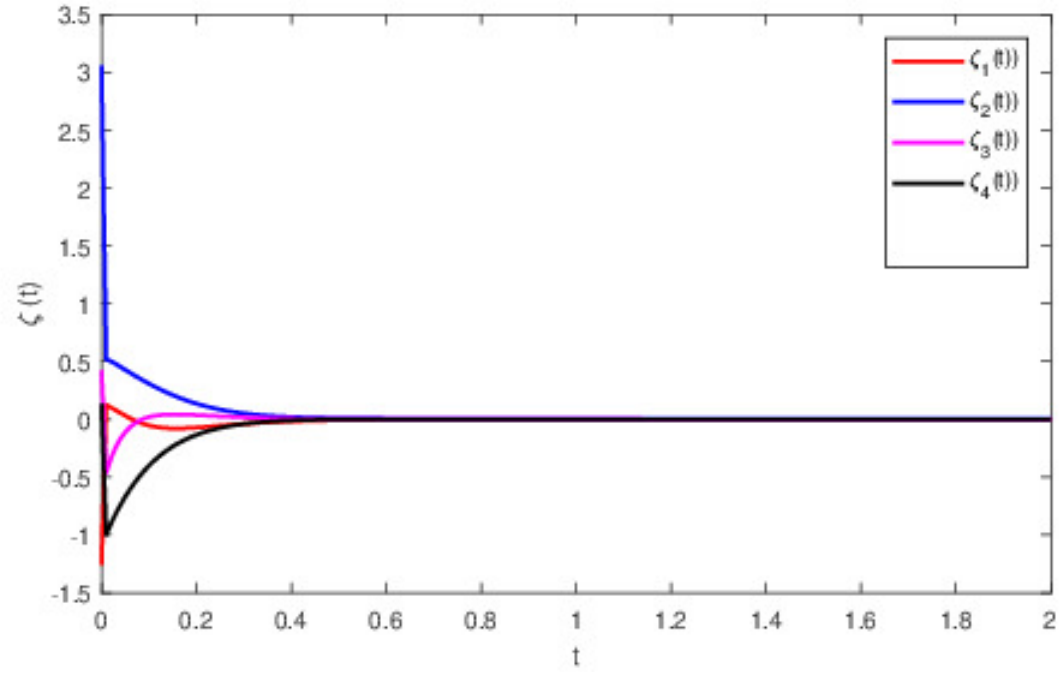

FIGURE 1. State trajectories of the FCNN system in Example 1

$c_{24} = 0.7$ $c_{31} = 0.4$, $c_{32} = 0.7$, $c_{33} = 0.9$, $c_{34} = 0.3$ $c_{41} = 0.3$, $c_{42} = 0.8$, $c_{43} = 0.5$, $c_{44} = 0.7$, $u_{11} = 0.9$, $u_{12} = 1.1$, $u_{13} = 1.3$, $u_{14} = 0.7$, $u_{21} = 1.3$, $u_{22} = 0.9$, $u_{23} = 0.8$, $u_{24} = 1.2$, $u_{31} = 1.2$, $u_{32} = 0.7$, $u_{33} = 1.1$, $u_{34} = 1$ $u_{41} = 1.3$, $u_{42} = 1$, $u_{43} = 0.5$, $u_{44} = 0.3$, $v_{11} = 0.7$, $v_{12} = 1.1$, $v_{13} = 1$, $v_{14} = 1.3$, $v_{21} = 1$, $v_{22} = 0.3$, $v_{23} = 0.7$, $v_{24} = 0.2$, $v_{31} = 0.4$, $v_{32} = 0.8$, $v_{33} = 0.9$, $v_{34} = 1.2$ $v_{41} = 1.1$, $v_{42} = 0.2$, $v_{43} = 0.7$, $v_{44} = 1.2$, $d_1 = 9$, $d_2 = 9$, $d_3 = 7$, $d_4 = 7$, $\Psi_1 = 2.7$, $\Psi_2 = 3.1$, $\Psi_3 = 4.5$, $\Psi_4 = 2.5$, $\phi_1 = 5.3$, $\phi_2 = 4.7$,$\phi_3 = 5.3$, $\phi_4 = 5.1$, $\alpha = 0.97$, $f(t) = tanh(t)$.
$\omega = 2$, $\delta_1 = \delta_2 = \delta_3 = 1, F_i = 1, (i = 1, 2, 3, 4)$.
The corresponding response system is described by

$$
\begin{aligned}
{}^{C}D^{\alpha}\vartheta_i(t) = &-d_i\vartheta_i(t) + \sum_{j=1}^{2} c_{ij} f_j(\vartheta_j(t)) + \sum_{j=1}^{2} a_{ij} f_j(\vartheta_j(t-\tau) + \sum_{j=1}^{2} h_{ij}\mu_j \\
&+ \bigwedge_{j=1}^{2} u_{ij} \int_0^{\infty} k_j(s) f_j(\vartheta_j(s-\tau))ds + \bigwedge_{j=1}^{2} p_{ij}\mu_j + \bigvee_{j=1}^{2} v_{ij} \int_0^{\infty} k_j(s) f_j(\vartheta_j(s-\tau))ds \\
&+ \bigvee_{j=1}^{2} Q_{ij}\mu_j + I_i + u_i(t), \qquad (41)
\end{aligned}
$$

where a_{ij}, u_{ij}, v_{ij}, d_i, c_{ij}, and I_i are the same as in system (41), and the hybrid feedback controllers is as follows: $u_i(t) = u_{1i}(t) + u_{2i}(t)$, where $u_{1i}(t) = -\phi_i(t)e_i(t)$ and $u_{2i}(t) = -\Psi_i(t)e_i(t)$. where $\xi_i(t) = \vartheta_i(t) - \zeta_i(t)$ for i=1,2. According to the developed idea in Theorem 4.2, it asks that

$$
\theta_1(t) = \min_{1\le i\le n}[(d_i + |\phi_i(t)| + |\Psi_i(t)|) - \sum_{j=1}^{n} |c_{ij}|F_j\delta_1(\omega-1) - \sum_{j=1}^{n} |c_{ji}|F_i \frac{1}{\delta_1^{\omega-1}}
$$

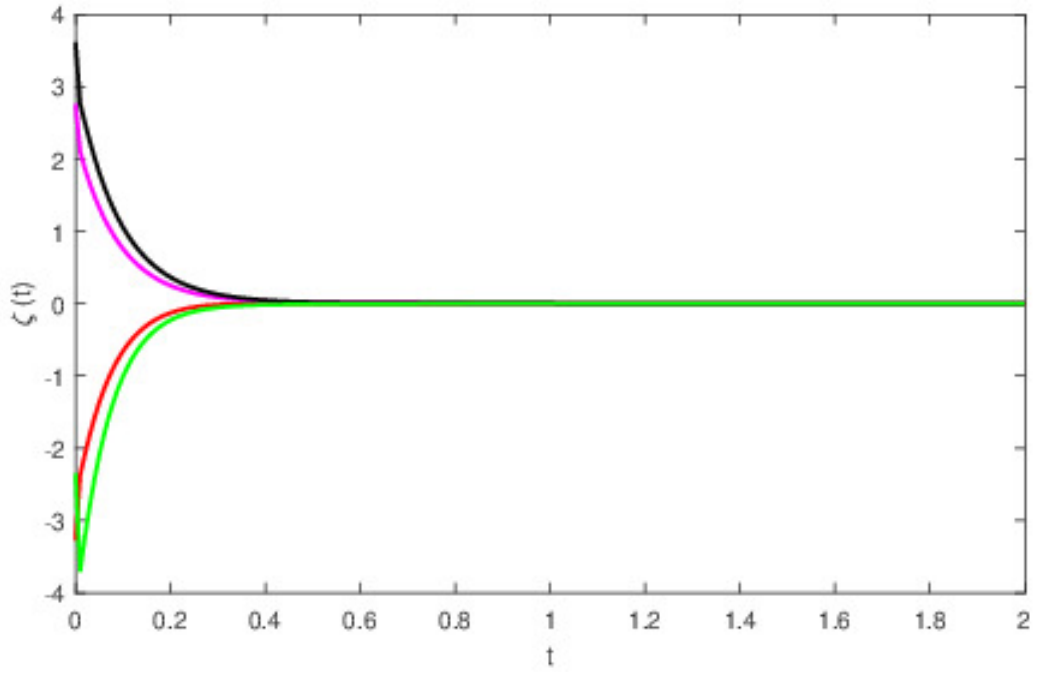

FIGURE 2. State trajectories of the FCNN system in Example 2

$$+\sum_{j=1}^{n}|a_{ij}|F_j(\omega-1)\delta_2+|u_{ij}|F_j(\omega-1)\delta_3+|v_{ij}|F_j(\omega-1)\delta_3]=10.40>0.$$

$$\theta_2(t)=\max_{1\le i\le n}[\sum_{j=1}^{n}|a_{ji}|F_i\frac{1}{\delta_2^{\omega-1}}+\sum_{j=1}^{n}|u_{ji}|F_i\frac{1}{\delta_3^{\omega-1}}+\sum_{j=1}^{n}|v_{ji}|F_i\frac{1}{\delta_3^{\omega-1}}]=10>0.$$

Then it follows from Theorem 4.2 that system (40) can be achieved global Mittag-Leffler stabilization under the designed hybrid feedback control law.

6. Conclusion

In this paper, Global Mittag-Leffler stability of fractional order fuzzy cellular neural networks with distributed delays via hybrid feedback controllers is addressed. We proposed the definition of Global Mittag-Leffler stability and the fractional Lyapunov direct method, which enriches the knowledge of both the system theory and the fractional calculus. This papers serves as a first step in presenting sufficient conditions for global Mittag-Leffler stability for a generalized fuzzy cellular fractional-order neural network with distributed delay. The main theoretical findings of this paper are that hybrid feedback control law. We extend the concept of Lyapunov functions for a fuzzy cellular fractional-order neural network. Under the assumption of Lipschitz continuity of activation functions, we have proved the Global Mittag-Leffler stability of the proposed model, which implies faster convergence rate of the network model than the Lyapunov convergence. An illustrative examples was provided to demonstrate the applicability of the proposed approach.

References

[1] E. S. A. Shahri, S. Balochian, Analysis of fractional-order linear systems with saturation using Lyapunov's second method and convex optimization, *International Journal of Automation and Computing* **12(4)**(2015)440–447.

[2] P. Arena, R. Caponetto, L. Fortuna, D. Porto, Bifurcation and chaos in non integer order cellular neural networks, *International Journal of Bifurcation and Chaos,* **8**(1998)1527 – 1539.

[3] M. Syed Ali, L Palanisamy, J Yogambigai, L Wang, Passivity-based synchronization of Markovian jump complex dynamical networks with time-varying delays, parameter uncertainties, reaction–diffusion terms, and sampled-data control *Journal of Computational and Applied Mathematics* **352** (2019) 79–92.

[4] M. Syed Ali, J Yogambigai, S Saravanan, S Elakkia, Stochastic stability of neutral-type Markovian-jumping BAM neural networks with time varying delays, *Journal of Computational and Applied Mathematics* **349** (2019) 142–156

[5] M. Syed Ali, J Yogambigai Extended dissipative synchronization of complex dynamical networks with additive time-varying delay and discrete-time information *Journal of Computational and Applied Mathematics* **348** (2019) 328–341

[6] I. Stamova, Global Mittag-Leffler stability and synchronization of impulsive fractional-order neural networks with time-varying delays, *Nonlinear Dynamics,* **77** (2014) 1251 – 1260.

[7] H. Q. Li, X. F. Liao, and M. W. Luo, A novel non-equilibrium fractional-order chaotic system and its complete synchronization by circuit implementation, *Nonlinear Dynamics,* **68** (2012) 137 – 149.

[8] L. P. Chen, Y. Chai, R. C. Wu, T. D. Ma, and H. Z. Zhai, Dynamic analysis of a class of fractional-order neural networks with delay, *Neurocomputing,* **111** (2013) 190 – 194.

[9] Z, Quanxin, S. Shiyun, T. Tianren, Mean square exponential stability of stochastic nonlinear delay systems of *International Journal of Control,* **90** (2017) 2384 – 2393.

[10] X. Li, X. Yang, T. Huang, Persistence of delayed cooperative models , *Impulsive control method, Applied Mathematics and Computation*, **342** (2019) 130-146.

[11] X. Li, J. Shen, R. Rakkiyappan, Persistent impulsive effects on stability of functional differential equations with finite or infinite delay , *Applied Mathematics and Computation*, **329** (2018) 14-22

[12] M.Syed Ali, G.Narayanana, S. Sevgen, V. Shekher, S. Arik, Global stability analysis of fractional-order fuzzy BAM neural networks with time delay and impulsive effects, *Communications in Nonlinear Science and Numerical Simulation*, **78** (2019) Article ID 104853.

[13] E. Yucel, M.Syed Ali, N. Gunasekaran, S. Arik, Sampled-data filtering of Takagi-Sugeno fuzzy neural networks with interval time-varying delays, *Fuzzy Sets and Systems*, **316** (2017) 69-81.

[14] N. Ozcan, M.Syed Ali, J. Yogambigai, Q. Zhu, S. Arik, Robust synchronization of uncertain Markovian jump complex dynamical networks with time-varying delays and reaction-diffusion terms via sampled-data control, *Journal of the Franklin Institute*, **355** 3 (2018) 1192-1216.

[15] C. Song, S. Fei, J. Cao, C. Huang, Robust synchronization of fractional-order uncertain chaotic systems based on output feedback sliding mode control, *Mathematics* **7(7)** (2019) 599.

[16] X. Yang, S. Wen, Z. Liu, C. Li, C. Huang, Dynamic Properties of Foreign Exchange Complex Network, *Mathematics* **7** (2019) 832.

[17] F. Wang, Z. Yao, Approximate controllability of fractional neutral differential systems with bounded delay. *Fixed Point Theory.* **17** (2016) 495-507.

[18] G. Rajchakit, A. Pratap, R.Raja, J.Cao, J. Alzabut, C. Huang, Hybrid control scheme for projective lag synchronization of Riemann-Liouville sense fractional order memristive BAM neural networks with mixed delays. *Mathematics* **7(8)** (2019) 759 .

[19] X. Yang, S. Wen, Z. Liu, C. Li, C. Huang, Dynamic properties of foreign exchange complex network, *Mathematics*, **7** (2019) 832.

[20] C. Huang, S. Wen, L. Huang, Dynamics of anti-periodic solutions on shunting inhibitory cellular neural networks with multi-proportional delays, *Neurocomputing* **357** (2019) 47-52.

[21] J. Zhang, C. Huang, Dynamics analysis on a class of delayed neural networks involving inertial terms, *Advances in Difference Equations* (2020) Article 120.

[22] C. Qian, Y. Hu ,Novel stability criteria on nonlinear density-dependent mortality Nicholson's blowflies systems in asymptotically almost periodic environments, *Journal of Inequalities and Applications* (2020) Article number: 13.

[23] J. Zhang , C. Huang, Dynamics analysis on a class of delayed neural networks involving inertial terms, *Advances in Difference Equations* (2020) Article number: 120.

[24] M. Shi, J. Guo, X. Fang , C. Huang , Global exponential stability of delayed inertial competitive neural networks, *Advances in Difference Equations* (2020) Article number: 87.

[25] Q. Cao,G. Wang, C. Qian, New results on global exponential stability for a periodic Nicholson's blowflies model involving time-varying delays, **Advances in Difference Equations** (2020) Article number: 43.

[26] C. Huang ,R. Su, Y. Hu, Global convergence dynamics of almost periodic delay Nicholson's blowflies systems , **Journal of Biological Dynamics 14** (2020) 633-655.

[27] J. Wang, X. Chen, L. Huang, The number and stability of limit cycles for planar piecewise linear systems of node–saddle type, **Journal of Mathematical Analysis and Applications**, *469* (1) (2019) 405-427.

[28] J. Wang, C. Huang, L. Huang, Discontinuity-induced limit cycles in a general planar piecewise linear system of saddle–focus type, *Nonlinear Analysis: Hybrid Systems*, **33** (2019) 162-178.

[29] W. Wang, Finite-time synchronization for a class of fuzzy cellular neural networks with time-varying coefficients and proportional delays, *Fuzzy Sets and Systems*, **338** (2018) 40-49.

[30] C. Huang and H. Zhang, Periodicity of non-autonomous inertial neural networks involving proportional delays and non-reduced order method, *International Journal of Biomathematics*,**12(2)** (2019) 1950016.

[31] H. Yang, Weighted pseudo almost periodicity on neutral type CNNs involving multi-proportional delays and D operator, *AIMS Mathematics* **(6)** (2021) 1865-1879.

[32] C. Huang, L. Yang, J. Cao Asymptotic behavior for a class of population dynamics, *AIMS Mathematics*, **5** (2020) 3378-3390.

[33] C. Huang, X. Long,L. Huang and Si Fu, Stability of Almost Periodic Nicholson's Blowflies Model Involving Patch Structure and Mortality Terms *Canadian Mathematical Bulletin* , **63** (2) (2020) 405 – 422.

[34] C. Huang, J. Wang, L. Huang, Asymptotically almost periodicity of delayed Nicholson-type system involving patch structure, *Electron. J. Differential Equations***61** (2020) 1-17.

[35] H. Hu, T. Yi and X. Zou., On spatial-temporal dynamics of a Fisher-KPP equation with a shifting environment, *Proc. Amer. Math. Soc.* **148** (2020) 213-221.

[36] HJ Hu, XP Yuan, LH Huang, CX Huang, Global dynamics of an SIRS model with demographics and transfer from infectious to susceptible on heterogeneous networks. *Math. Biosci. Eng.* **16(5)** (2019) 5729-5749.

[37] H. Hu and X. Zou. Existence of an extinction wave in the Fisher equation with a shifting habitat *Proc. Amer. Math. Soc.* **145** (2017) 4763-4771.

[38] SM. Lee, OM. Kwon, SH. Lee, Improved stability criteria for sampled-data systems using modified free weighting matrix *Journal of the Franklin Institute,* **356** (2019) 2198 – 2211.

[39] P. Balasubramaniam, M. Syed Ali Robust stability of uncertain fuzzy cellular neural networks with time-varying delays and reaction diffusion terms, *Neurocomputing,* **74**(2010) 439 – 446.

[40] X. Li and S. Song, Impulsive control for existence, uniqueness and global stability of periodic solutions of recurrent neural networks with discrete and continuously distributed delays, *IEEE Transactions on Neural Networks and Learning Systems,* **24** (2013) 868 – 877.

[41] Y. Du, S. Zhong, N. Zhou, K. Shi, J. Cheng, Exponential stability for stochastic Cohen-Grossberg BAM neural networks with discrete and distributed time-varying delays, *Neurocomputing,* **127** (2014) 144 – 151.

[42] M. Syed Ali, N. Gunasekaran, ME. Rani, Robust stability of hopfield delayed neural networks via an augmented LK functional, *Neurocomputing,* **234** (2017) 198 – 204.

[43] S. Liu, XY. Li, W. Jiang, XF. Zhou, Mittag–Leffler stability of nonlinear fractional neutral singular systems, *Communications in Nonlinear Science and Numerical Simulation,* **17**(2012)3961 – 3966.

[44] Y. Li, Y.Q. Chen, I. Podlubny, Stability of fractional-order nonlinear dynamic systems: Lyapunov direct method and generalized Mittag-Leffler stability, *Computers and Mathematics with Applications,* **24** (2010) 1429 – 1468.

[45] L. O. Chua and L. Yang, Cellular neural networks: Theory, *IEEE Transactions on Circuits and Systems,* **35** (1988) 1257 – 1272.

[46] T. Roska and L. O. Chua, Cellular neural networks with nonlinear and delay-type template elements and nonuniform grids, *International Journal of Circuit Theory and Applications,* **20** (1992) 469 – 481.

[47] H. Harrer and J. A. Nossek, Discrete-time cellular neural networks, *International Journal of Circuit Theory and Applications,* **20** (1992)453 – 467.

[48] T. Yang, LB. Yang, CW. Wu, LO. Chua, Fuzzy cellular neural networks:theory, *International Journal of Circuit Theory and Applications,* (1996)181 – 186.

[49] T. Yang, LB. Yang, CW. Wu, LO. Chua, Fuzzy cellular neural networks:applications *Fourth IEEE International Workshop on Cellular Neural Networks and their Applications Proceedings,* (1996)225 – 230.

[50] Z. D. Huang, Almost periodic solutions for fuzzy cellular neural networks with multi-proportional delays, *International Journal of Machine Learning and Cybernetics,* **78**(2016) 1323 –1331.

[51] S. T. Wang and M. Wang, A new detection algorithm based on fuzzy cellular neural networks for white blood cell detection, *IEEE Transactions on Information Technology in Biomedicine,* **10** (2006) 5 – 10.

[52] W. Y. Ma, C. P. Li, and Y. J. Wu, Impulsive synchronization of fractional Takagi-Sugeno fuzzy complex networks, *Chaos,* **26** (2016)084311.

[53] H. Shen, F. Li, H. Yan, H. R. Karimi and H. K. Lam, Finite-time event-triggered H_∞ control for T-S fuzzy Markov jump systems, *IEEE Transactions on Fuzzy Systems,* **26** (2018)3122 – 3135.

[54] H. Shen,F. Li, Z. Wu, J. H. Park, Victor Sreeram. Fuzzy-model-based non-fragile control for nonlinear singularly perturbed systems with semi-Markov jump parameters, *IEEE Transactions on Fuzzy Systems,* **26** (2018)3428 – 3439.

[55] M S. Branicky, Introduction to Hybrid Systems *Springer,* (2005)91 – 116.

[56] A. S. Morse, Control Using Logic-Based Switching, *Springer,* (1997)1– 276.

[57] P. J. Antsaklis, Special issue on hybrid systems: Theory and applications - A brief introduction to the theory and applications of hybrid systems, *Proceedings of the IEEE,* **88** (2000)879 – 887.

[58] X. Li, J. Shen, H. Akca, R. Rakkiyappan, LMI-based stability for singularly perturbed nonlinear impulsive differential systems with delays of small parameter, *Applied Mathematics and Computation*, **250** (2015) 798-804.

[59] X. Li, Donal O'Regan, H. Akca, Global exponential stabilization of impulsive neural networks with unbounded continuously distributed delays, *IMA Journal of Applied Mathematics*, **80(1)** (2015) 85-99.

[60] X. Li, T. Caraballo, R. Rakkiyappan, Xiuping Han, On the stability of impulsive functional differential equations with infinite delays, *Mathematical Methods in the Applied Sciences*, **38(14)** (2015) 3130-3140.

[61] Y. Wardi, M. Egerstedt, B. Lennartson, P. Tabuada Hybrid Systems, *Nonlinear Analysis,* (2019).

[62] M. Syed Ali, J. Yogambigai, Synchronization of complex dynamical networks with hybrid coupling delays on time scales by handling multitude Kronecker product terms, *Applied Mathematics and Computation,* **291** (2016) 244 – 258.

[63] A. Feuer, G. C. Goodwin, and M. Salgado, Potential benefits of hybrid control for linear time invariant plants, *Proceedings of the 1997 American Control Conference,* **5** (1997)2790 – 2794.

[64] N. H. McClamroch, C. Rui, I. Kolmanovsky, and M. Reyhanoglu, Hybrid closed loop systems: A nonlinear control perspective, *Proceedings of the 36th IEEE Conference on Decision and Control,* **1** (1997) 114 – 119.

[65] A. J. van der Schaft and J. M. Schumacher, An Introduction to Hybrid Dynamical Systems, *Springer,* **251**(1999)1 –174.

[66] J. Lygeros, D. Godbole, and S. Sastry, Verified hybrid controllers for automated vehicles, *IEEE Transactions on Automatic Control,* **43** (1998)522 – 539.

[67] E. Frazzoli, Robust hybrid control for autonomous vehicle motion planning, *Proceedings of the IEEE Conference on Decision and Control,* **1**(2000)821 – 826.

[68] E. Frazzoli, M. A. Dahleh, and E. Feron, A maneuver-based hybrid control architecture for autonomous vehicle motion planning, *Information Technology for Dynamical Systems,* (2005)299 – 323.

[69] A. Balluchi, P. Soueres, and A. Bicchi, Hybrid feedback control for path tracking with a bounded-curvature vehicle, *Proceedings of the fourth International Workshop on Hybrid Systems,* (2001)133 – 146.

[70] K. Diethelm, N J. Ford, Analysis of Fractional Differential Equations, *Journal of Mathematical Analysis and Applications,* **265** (2002)229 – 248.

[71] C. Li, F. Zhang, A survey on the stability of fractional differential equations, *The European Physical Journal Special Topics,* **193**(2011) 27 – 47.

[72] M. A. Duatte-Mermoud, N. Aguila-Camacho, J. A. Gallegos, R. Castro-Limares, Using general quadratic Lyapunov functions to prove Lyapunov uniform stability for fractional order systems, *Communications in Nonlinear Science and Numerical Simulation,* **22** (2015) 650 – 659.

[73] S. H. Maboobi, M. Shahrokhi, H. N. Pishkenari, Observer-based control design for three well-known chaotic systems, *Chaos Solitions and Fractals,* **29**(2006) 381 –392.

[74] A. Wu, Z. Zeng, Global Mittag-Leffler stabilization of fractional-order memristive neural networks, *IEEE Transactions on Neural Networks and Learning Systems,* **28** (2015)1 – 12.

[75] J. Chen, Z. Zeng, P. Jiang, Global Mittag–Leffler stability and synchronization of memristor-based fractional-order neural networks, *Neural Network: the official journal of the International Neural Network Society* **51** (2013) 1 – 8.

[76] J. Kuang, Applied inequalities, *Shandong Science and Technology Press,* (2004).

[77] J. Chen, Z. Zeng, P. Jiang, Global Mittag-Leffler stability and synchronization of memristor-based fractional-order neural networks, *Neural Networks* ,**51** (2014) 1-8.

[78] I . Stamova, G. Stamov, Mittag-Leffler synchronization of fractional neural networks with time-varying delays and reaction-diffusion terms using impulsive and linear controllers, , *Neural Networks* , **96** (2017) 22-32.

[79] S. Long Q. Song, X. Wang D. Li, Stability analysis of fuzzy cellular neural networks with time delay in the leakage term and impulsive perturbations, *Journal of the Franklin Institute* , **349 (7)** (2012) 2461—2479.

[80] L. Duan, H. Wei, L. Huang, Finite-time synchronization of delayed fuzzy cellular neural networks with discontinuous activations *Fuzzy Sets and Systems* **361** (2019) 56—70.

[81] P. Mani, R. Rakkiyappan , S. Lakshmanan , Y. H. Joo, Adaptive control for fractional order induced chaotic fuzzy cellular neural networks and its application to image encryption, *Information Sciences*, **491** (2019) 74—89.

[82] J. Chen, C. Li, X.Yang, Asymptotic stability of delayed fractional-order fuzzy neural networks with impulse effects, *Journal of the Franklin Institute* **355 (15)** (2018) 7595-7608

[83] S. Zhang, Y. Yu, H . Wang, Mittag-Leffler stability of fractional-order Hopfield neural networks, *Nonlinear Anal. Hybrid Syst.* **16** (2015) 104-121.

[84] W. Ma, C. Li, Y. Wu, Y. Wu, Synchronization of fractional fuzzy cellular neural networks with interactions, *Chaos* **27** (2017) 103106.

[85] H. Li, C. Hu, Y. Jiang, Z. Wang, Z. Dong, Pinning adaptive and impulsive synchronization of fractional-order complex dynamical networks, *Chaos Solitons Fract.* **92** (2016) 142-149.

[86] L. Wang, Q. Song, Y. Liu, Z. Zhao, F. Alsaadi, Finite-time stability analysis of fractional-order complex-valued memristor-based neural networks with both leakage and time-varying delays, *Neurocomputing* **245** (2017) 86-101.

[87] J. Xiao, S. Zhong, Y. Li, F. Xu, Finite-time Mittag-Leffler synchronization of fractional-order memristive BAM neural networks with time delays, *Neurocomputing* **219** (2017) 431-439.

[88] G. Velmurugan, R. Rakkiyappan, J. Cao, Finite-time synchronization of fractionalorder memristor-based neural networks with time delays, *Neural Netw.* **73** (2016) 36-46.

[89] Z. Ding, Z. Zeng, L. Wang, Robust finite-time stabilization of fractional-order neural networks with discontinuous and continuous activation functions under uncertainty, *IEEE Trans. Neural Netw. Learn. Syst.* **29** (2018) 1477-1490.

arXiv:2101.11513v1 [physics.flu-dyn] 27 Jan 2021

STATE ESTIMATION WITH LIMITED SENSORS – A DEEP LEARNING BASED APPROACH

A PREPRINT

Yash Kumar
Department of Mechanical Engineering
Delhi Technological University
Shahbad Daulatpur, Main Bawana Road, Delhi-110042, India
yashk8481@gmail.com

Pranav Bahl
Department of Mechanical Engineering
Delhi Technological University
Shahbad Daulatpur, Main Bawana Road, Delhi-110042, India
bahlpranav24@gmail.com

Souvik Chakraborty
Department of Applied Mechanics
Indian Institute of Technology Delhi
Hauz Khas - 110042, New Delhi, India
souvik@am.iitd.ac.in

January 28, 2021

ABSTRACT

The importance of state estimation in fluid mechanics is well-established; it is required for accomplishing several tasks including design/optimization, active control, and future state prediction. A common tactic in this regards is to rely on reduced order models. Such approaches, in general, use measurement data of one-time instance. However, oftentimes data available from sensors is sequential and ignoring it results in information loss. In this paper, we propose a novel deep learning based state estimation framework that learns from sequential data. The proposed model structure consists of the recurrent cell to pass information from different time steps enabling utilization of this information to recover the full state. We illustrate that utilizing sequential data allows for state recovery from only one or two sensors. For efficient recovery of the state, the proposed approached is coupled with an auto-encoder based reduced order model. We illustrate the performance of the proposed approach using two examples and it is found to outperform other alternatives existing in the literature.

Keywords state estimation · autoencoder · recurrent neural network · limited sensors

1 Introduction

The integration of deep learning has benefited modern algorithms in modeling, data processing, prediction, and control of various engineering systems. In fluid mechanics, work on machine learning implementation started last decade and has grown since then. Milano & Koumoutsakos [1] used a neural network to reconstruct turbulence flow fields and the flow in the near-wall region of a channel flow using wall information. Ling et al. [2] and Geneva & Zabaras [3], in two separate works, used deep learning algorithms to improve a Reynolds-averaged Navier–Stokes turbulence model. Recently, Geneva & Zabaras [4] proposed a multi-fidelity deep learning framework for turbulent flow. Erichson et al. [5] used a shallow network for estimating 2D state from measurements over cylinder surface. In this paper, we are particularly interested in applying deep learning for state estimation in fluid mechanics, and hence, the discussion hereafter is focused on the same.

State estimation is the ability to recover flow based on a few noisy measurements. It is an inverse problem and arises in many engineering applications such as remote sensing, medical imaging, ocean dynamics, reservoir modeling, and blood flow modeling. Controlling the flow and optimizing machine design in these applications depend upon the ability to predict the state with given sensors. The challenge associated with state estimation is two-fold. Firstly, for almost all

practical cases, state-estimation is an ill-posed problem, and hence, a unique solution to the problem does not exist [6]. Secondly, for practical problems, the number of sensors available is often limited. As a consequence, one has to deal with a sparse data set [7].

Attempts for state estimation dates back to 1960 when the Kalman filter based approaches were used for state estimation [8]. This method assumes the system's dynamics to produce full state and updates it based on new measurements to reduce estimation error forming a closed feedback loop. However, the classical Kalman filter based approaches are only applicable for linear dynamical systems [9]. Improvements to Kalman filter algorithms, such as Extended Kalman filter [10] and Unscented Kalman filter [11] algorithms can also be found in the literature. Nayek et al. [12] attempts to generalize Kalman filters by using the Gaussian process. Approaches based on observer dynamical system uses a reduced-order model to predict the future based on the past while simultaneously corrected by receiving measurements. Tu et al. [13] applies dynamic mode decomposition as a reduced-order model to Kalman smoother estimate to identify coherent structures. Buffoni et al. [14] used a nonlinear observer-based on Galerkin projection of Navier-Stokes equation to estimate POD coefficients. The use of Bayes filters, such as the Kalman and particle filters, in conjugation with POD based ROM on various flow problems, can also be found in the literature [15–17].

Another major category of approaches includes library-based approaches and stochastic approaches. Library-based approaches use offline data, and the library consists of generic modes such as Fourier, wavelet, discrete cosine transform basis or data specific POD or DMD modes, or training data. Library based approaches using sparse representation assumes state can be expressed as the combination of library elements. Sparse coefficients are obtained by solving pursuit problem [18,19]. Callaham et al. [20] used sparse representation and training data as the library with localized reconstruction for reconstructing complex fluid flows. Gappy POD [21] estimates POD coefficients in a least-square sense and uses a library of POD modes. However, it is prone to ill-conditioning and is dealt with using the best sensor placements [22] to improve the condition number [23].

The most explored approach for state estimation is perhaps the one based on stochastic estimation. The idea was first proposed by Adrian [24] for a turbulence study where the conditional mean was approximated using a power series. In a linear setting, coefficients are computed using a two-point, second-order correlation tensor. Other variants like quadratic stochastic estimation [25] and spectral linear stochastic estimation [26] can also be found in the literature. Guezennec [27] proposed to include time delayed measurements to further improve accuracy. . Bonnet et al. [28] extended stochastic approach to estimate POD coefficients. A linear mapping between sensors and coefficients was assumed. Recently, Nair & Goza [29] used a neural network to learn a non-linear mapping between sensor measurements and POD coefficients. These approaches allow more flexibility in sensor placements and have been applied for flow control over airfoil [30] and analyzing isotropic turbulence [31, 32] and turbulent boundary layers [25, 27].

One limitation associated with all the approaches mentioned above resides in the fact that spatial information of a single sample is used to recover the full state, but often, data is sequential. Ignoring the sequence of the data during state information invariably results in information loss. To address this apparent shortcoming, we propose a deep learning-based non-intrusive framework for state estimation that learns from sequential data. The proposed framework couples recurrent neural network (RNN) with auto-encoder (AE). While AE is used to learn the nonlinear manifold, RNN is employed to take advantage of the time series data. We illustrate that by utilizing sequential data, the proposed framework is able to estimate the state in a more accurate fashion. Perhaps, more importantly, the number of sensors required is significantly less. For showcasing the performance of the proposed framework, two benchmark problems involving periodic vortex shedding and transient flow past a cylinder are considered. Results obtained are compared with those obtained using other state-of-the-art techniques.

The remainder of the paper is organized as follows. In Section 2, details on the problem statement is provided. A brief review of RNN and AE are furnished in Section 3. Details on the proposed approach are provided in Section 4. Section 5 presents two numerical examples to illustrate the performance of the proposed approach. Finally, Section 6 provides the concluding remarks.

2 Problem statement

We consider a dynamical system obtained by partial discretization of the governing differential equations:

$$\dot{\boldsymbol{w}} = \boldsymbol{f}\left(\boldsymbol{w}, t; \boldsymbol{\theta}\right), \quad \boldsymbol{w}(t_n, \boldsymbol{\theta}) = \boldsymbol{w}^n\left(\boldsymbol{\theta}\right), \tag{1}$$

where $\boldsymbol{w} \in \mathbb{R}^{N_w}$ represents the high-dimensional state vector that depends on parameters $\boldsymbol{\theta} \in \mathbb{R}^{N_d}$ and time $t \in [0, t_{max}]$. $\boldsymbol{f}$ in Eq. (1) is a nonlinear function that governs the dynamical evolution of the state vector $\boldsymbol{w}$. Note that for brevity of representation, we have not shown the dependence of the state $\boldsymbol{w}$ on t and $\boldsymbol{\theta}$, and the dependence of $\boldsymbol{f}$ on $\boldsymbol{w}, t$ and $\boldsymbol{\theta}$.

We note that the state vector $\boldsymbol{w}$ is high-dimensional in nature and it is extremely difficult to directly work with $\boldsymbol{w}$. A commonly used strategy in this regards is to approximate the high-dimensional state vector $\boldsymbol{w}$ on a low-dimensional

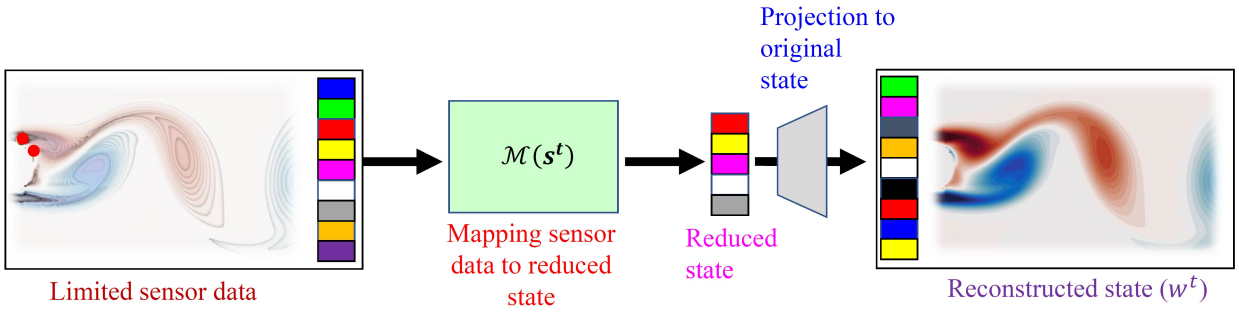

Figure 1: Schematic representation of state estimation framework. It consists of two components, (a) $\mathscr{M}(\boldsymbol{s})$ - it maps the sensor data to a reduced state and (b) a projection operator - it maps the predicted reduced state to the original state. Performance of a state estimation framework is dependent on performance of this two components and the quality and quantity of data.

manifold,

$$\boldsymbol{w}(t;\boldsymbol{\theta}) \approx \boldsymbol{w}_r(t;\boldsymbol{\theta}) = \boldsymbol{\Phi}(\boldsymbol{a}(t;\boldsymbol{\theta})), \tag{2}$$

where $\boldsymbol{a}(t;\boldsymbol{\theta}) \in \mathbb{R}^{N_a}$ represents the reduced space and $\boldsymbol{\Phi}(\cdot) : \boldsymbol{a}(t;\boldsymbol{\theta}) \mapsto \boldsymbol{w}(t;\boldsymbol{\theta})$ is the manifold. N_a in Eq. (2) represent the dimension of reduced space such that $N_a \ll N_w$. Substituting Eq. (2) into Eq. (1), we obtain

$$\dot{\boldsymbol{a}} = \boldsymbol{\Psi}(\boldsymbol{f}(\boldsymbol{\Phi}(a), t;\boldsymbol{\theta})), \; \boldsymbol{a}(t_n;\boldsymbol{\theta}) = \boldsymbol{a}^n(\boldsymbol{\theta}), \tag{3}$$

where $\boldsymbol{\Psi}(\cdot) = \left(\boldsymbol{\Lambda}\boldsymbol{\Gamma}^{-1}\right) \circ \boldsymbol{\Lambda}(\cdot)$ and $\boldsymbol{\Lambda} : \mathbb{R}^{N_w} \mapsto \mathbb{R}^{N_a}$. In Eq. (3), we have assumed that $\boldsymbol{\Phi}(\boldsymbol{a})$ is continuously differentiable such that $\boldsymbol{\Gamma}(\dot{\boldsymbol{a}}) = \dot{\boldsymbol{\Phi}}(\boldsymbol{a})$; $\boldsymbol{\Gamma} : \mathbb{R}^{N_a} \mapsto \mathbb{R}^{N_w}$. $a^n(\boldsymbol{\theta})$ in Eq. (3) represents the initial condition. With this representation, the objective in state-estimation reduces to estimating the reduced order state variable $\boldsymbol{a}^n(\boldsymbol{\theta})$. Generally, this is achieved by determining a mapping $\mathscr{M} : \mathbb{R}^{N_s} \mapsto \mathbb{R}^{N_a}$ between the sensor measurements and reduced state,

$$\boldsymbol{a}^n = \mathscr{M}(\boldsymbol{s}^n(\boldsymbol{\theta})), \tag{4}$$

where $\boldsymbol{s}^n \in \mathbb{R}^{N_s}$ represents the sensor measurements at time-step n and N_s indicates the number of sensors present. A schematic representation of the same is shown in Fig. 1.

The state estimation framework discussed above has two major limitations.

- We note that the state estimation framework only relies on sensor responses at the current step for predicting the state variables. In other words, the sequential nature of the sensor measurements is ignored. This invariably results in loss of information, and hence, the accuracy of the state estimation is compromised.
- Secondly, as shown in Eq. (2), the use of reduced-order model results in information loss. While completely avoiding this information loss is unavoidable, it is necessary to ensure that this information loss is minimized.

This paper aims to develop a deep learning-based framework for state estimation that addresses the two limitations discussed above.

3 A brief review of AE and RNN

This section briefly reviews two poplar deep learning approaches, namely auto-encoders (AE) and recurrent neural networks (RNN). It is to be noted that AE and RNN form the backbone of the proposed approach.

3.1 Auto-encoders

AE is a class of unsupervised deep learning techniques trained to copy the inputs to the output. It consists of a latent space/hidden layer $\boldsymbol{h} \in \mathbb{R}^h$ that represents a compressed representation of the input; this is often referred to as the bottleneck layer. The network architecture for an AE can be viewed as having two parts, an encoder that maps the input to the latent space $\boldsymbol{h}$ and a decoder that reconstructs the inputs from the latent space. Mathematically, this is represented as

$$\boldsymbol{h} = \boldsymbol{\omega}(\boldsymbol{\xi}), \; \hat{\boldsymbol{\xi}} = \boldsymbol{g}(\boldsymbol{h}), \tag{5}$$

where $\boldsymbol{\omega}$ represents the encoder network and $\boldsymbol{g}$ represents the decoder network. $\boldsymbol{\xi} \in \mathbb{R}^N$ in Eq. (5) represents the input variables with N being the number of variables. A schematic representation of AE is shown in Fig. 2.

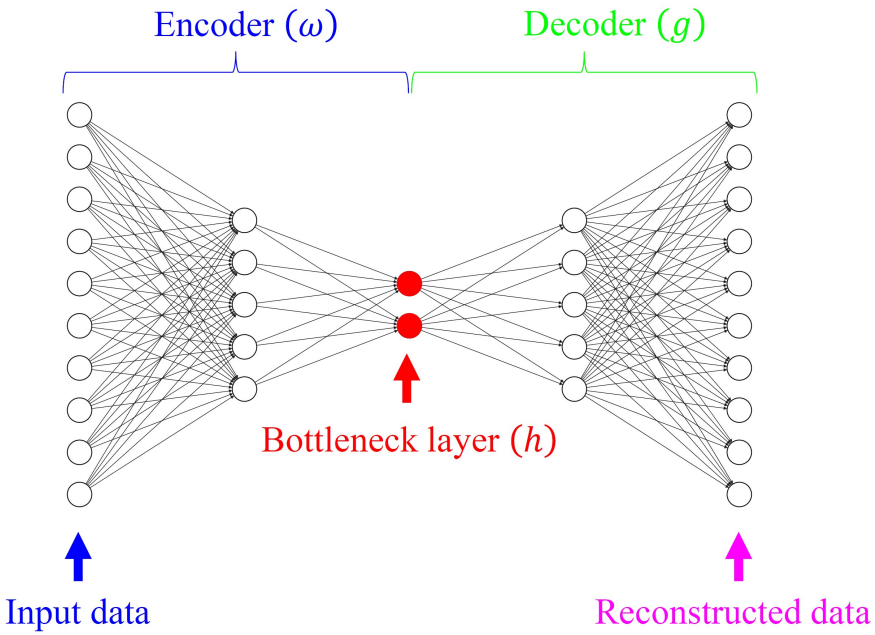

Figure 2: Schematic representation of an auto-encoder (AE). It consists of encoder (ω) and (g). The red nodes represents the bottleneck layer.

AE is integral to the neural network landscape and was initially developed for model reduction and feature extraction. As far as training an AE is concerned, an adaptive learning rate optimization algorithm(ADAM) is a popular choice. The learning in AE is generally expressed as

$$\boldsymbol{\alpha} = \arg\min_{\boldsymbol{\alpha}} \mathscr{L}(\boldsymbol{\xi}_t, \boldsymbol{g}(\boldsymbol{\omega}(\boldsymbol{\xi})); \boldsymbol{\alpha}), \tag{6}$$

where $\mathscr{L}(\boldsymbol{\xi}_t, \boldsymbol{g}(\boldsymbol{\omega}(\boldsymbol{\xi})); \boldsymbol{\alpha})$ represents the loss-function and $\boldsymbol{\alpha} = [\boldsymbol{\alpha}_e, \boldsymbol{\alpha}_d]$ are the hyperparameters (weights and biases) of the neural network. $\boldsymbol{\alpha}_e$ corresponds to the hyperparameters of the encoder while $\boldsymbol{\alpha}_d$ corresponds to the hyperparameters of the decoder. Some important remarks on AE are furnished below

Remark 1: A situation where $\boldsymbol{g}(\boldsymbol{\omega}(\boldsymbol{\xi})) = \boldsymbol{\xi}$ everywhere needs to be avoided [33]. In other words, the training algorithm is designed in such a way to restrict direct copying of the input.

Remark 2: In AE, the dimensionality of the latent space $\boldsymbol{h} \in \mathbb{R}^h$ is generally much smaller than the dimensionality of the input variable $\boldsymbol{\xi} \in \mathbb{R}_N$, $h \ll N$. Therefore, $\boldsymbol{h}$ can be thought of as a reduced-order representation of $\boldsymbol{\xi}$.

Remark 3: When the decoder $\boldsymbol{g}$ is linear, and $\mathscr{L}$ is a mean-squared error, an AE learns to span the same subspace as principal component analysis.

Remark 4: AE with nonlinear encoder $\boldsymbol{\omega}$ and nonlinear decoder $\boldsymbol{g}$ learns a nonlinear reduced-order manifold; however, an AE with too much expressive capacity learns to copy the inputs (Remark 1).

It is to be noted that researchers are still working on developing AE for various types of tasks. Some of the popular AE available in the literature includes variational AE [34], sparse AE [35], stochastic AE [36] and capsule AE [37] among other. For further details on different types of AE, interested readers may refer [33].

3.2 Recurrent neural networks

Many of the learning tasks involved in artificial intelligence necessitate handling data that are sequential in nature. Examples of sequential data include image captioning, time-series forecasting, and speech synthesis, among others. A recurrent neural network (RNN) is a type of neural network that is particularly suitable for sequential data. RNN captures the time dynamics by using cycles in the graph. Consider $\boldsymbol{\xi}$ to be inputs and $\boldsymbol{y}_t$ to be the output at time t. The output $\boldsymbol{y}_t$ in RNN is expressed as a function of $\boldsymbol{\xi}$ and $\boldsymbol{h}_t$; however, owing to the cyclic graph in RNN, the hidden state $\boldsymbol{h}_t$ is continuously updated as the sequence is processed. A schematic representation of a simple RNN is shown in Fig. 3. Note that different variants to the classical RNN can be found in the literature. In this work, we have used a Long

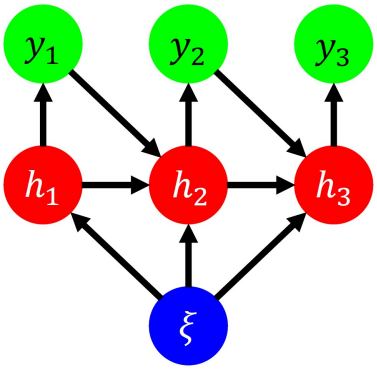

Figure 3: Schematic representation of a typical RNN. ξ (blue node) represents the input, $h_i, \forall i$ (red node) represents the hidden layer and y_i (green node) is the output sequence.

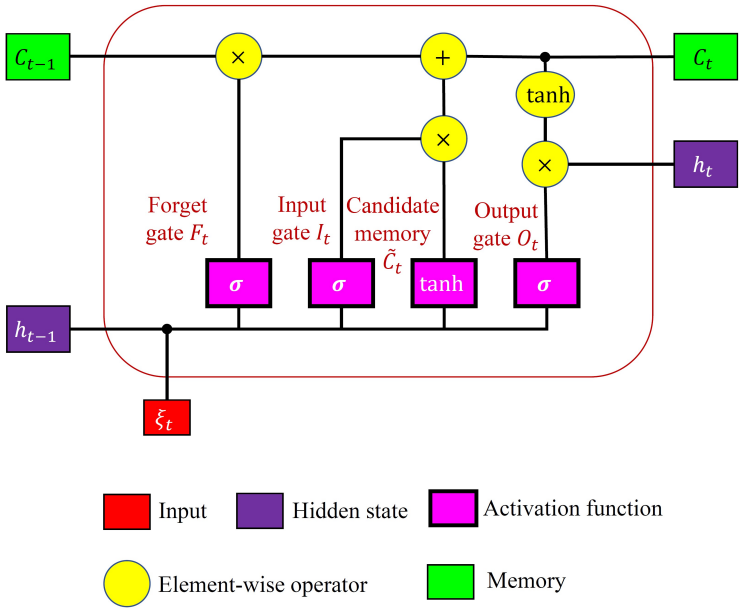

Figure 4: Schematic of the LSTM cell

Short-Term Memory [38], and hence, the discussion hereafter is focused on the same. Readers interested in other types of RNN may refer to [39].

LSTM, first proposed by [38], is a type of gated RNN cell that overcomes the well-know issue of vanishing gradient with the help of the gates that control the flow of information, i.e., differentiates between the information to be updated and that to be deleted [40–42]. LSTM cell comprises a forget gate, input gate, output gate, and a cell state. Each of these has its significance. The cell state refers to the information that has to be transferred in the sequence, and the respective gates determine the information that has to updated or deleted from the cell state [43]. The output of the current cell, also referred to as the hidden state, helps retain the short-term memory, and the cell state, on the other hand, is used to retain the Long-term Memory. Cell state in LSTM is multiplied with the forget gate in each cell along with the addition from the input gate, and this provides the opportunity for forgetting gate to eradicate the unimportant information and input gate to enhance state with useful information [43]. A schematic representation of LSTM cell is shown in Fig. 4. Mathematical, the operations being carried out inside a LSTM cell is represented using the following equations.

$$C_t = \mathbf{F}_t \odot \mathbf{C}_{t-1} + \mathbf{I}_t \odot \tilde{\mathbf{C}}_t \tag{7a}$$

$$\tilde{\mathbf{C}}_t = \tanh(\xi_t \mathbf{W}_{xc} + \mathbf{h}_{t-1}\mathbf{W}_{hc} + \mathbf{b}_c \tag{7b}$$

$$\mathbf{I}_t = \sigma(\xi_t \xi_{xi} + \mathbf{h}_{t-1}\mathbf{W}_{hi} + \mathbf{b}_i \tag{7c}$$

$$\mathbf{F}_t = \sigma(\xi_t \xi_{xf} + \mathbf{h}_{t-1}\mathbf{W}_{hf} + \mathbf{b}), \tag{7d}$$

where $\mathbf{I}_t$, $\mathbf{F}_t$ and $\tilde{\mathbf{C}}_t$ are respectively the input gate, forget gate, and a candidate cell state. Note that the update is carried out is additive in nature; this allows long-term information to pass through and avoids the gradient from vanishing. The short term state in LSTM is calculated as

$$\mathbf{O}_t = \sigma\left(\xi_t \xi_{xo} + \mathbf{h}_{t-1}\mathbf{W}_{ho} + \mathbf{b}_o\right) \tag{8a}$$

$$\mathbf{h}_t = \mathbf{O}_t \odot \tanh(\mathbf{C}_t), \tag{8b}$$

where $\mathbf{O}_t$ represents the output gate. It is to be noted that $\mathbf{h}_t$ is used as the output of the cell as well as the hidden state for the next time-step; this is responsible for the short term memory of LSTM. $\mathbf{C}_t$ on the other hand is responsible for long term memory.

The use of RNN for complex dynamical systems has attracted significant interest from the research community; this is primarily because of its capability in capturing temporal dependencies [40]. Multiple architectures have been proposed for using RNN for accomplishing the task future state prediction of a dynamical system. Recently Geneva & Zabara [44] and Eivazi et al. [45] used LSTM and transformers as time integrator to predict flow evolution state. Hosseinyalamdary [46] used simple RNN for IMU modeling in deep Kalman filter. Otto & Rowley [47] used autoencoder with linear recurrence to learns important dynamical features. In this work also, we use LSTM for extracting useful information from sequential sensor data. The next section provides more details on the same.

4 Proposed approach

In this section, we propose a novel deep learning based framework for state estimation. The proposed approach integrates the two deep learning approaches discussed in Section 3, namely AE and RNN. Within the proposed framework, AE learns the reduced nonlinear subspace. It helps in reducing the information loss due to the compressed representation. RNN, on the other hand, extends the capability of the proposed approach and allows it to reuse sensor data collected at previous time-steps. AE (by reducing the state variable) and RNN (by incorporating information from the past) also helps address the ill-posedness associated with solving a state estimation problem.

Consider $\boldsymbol{s} = [\boldsymbol{s}_1, \boldsymbol{s}_2, \ldots, \boldsymbol{s}_n] \in \mathbb{R}^{N_t \times N_s}$ represents the measurement data obtained from N_s sensors over N_t time-steps. Also consider $\boldsymbol{w} \in \mathbb{R}_{N_w}$ to be state variables. We can express the state variable $\boldsymbol{w}^t$ at time t as

$$\boldsymbol{w}^t = g\left(\mathscr{M}\left(\boldsymbol{s}^{t-k:t}; \boldsymbol{\theta}_M\right); \boldsymbol{\theta}_g\right) \tag{9}$$

where $\mathscr{M}(\cdot; \boldsymbol{\theta}_M)$ represents a mapping between the sensor data and the reduced state variable and $g(\cdot; \boldsymbol{\theta}_g)$ projects the reduced state variable back to the original space. $\boldsymbol{\theta}_M$ and $\boldsymbol{\theta}_g$ represent parameters associated with $\mathscr{M}(\cdot; \boldsymbol{\theta}_M)$ and $g(\cdot; \boldsymbol{\theta}_g)$, respectively. Unlike existing methods, sensor data corresponding to current and previous time-steps have been used for predicting $\boldsymbol{w}^t$ in Eq. (9). A schematic representation of the same is shown in Fig. 5. We also note that the sensor data is sequential and hypothesize that modeling this sequential nature of the sensor data will improve the predictive capability of model $\mathscr{M}(\cdot; \boldsymbol{\theta}_M)$. Therefore, we propose to model $\mathscr{M}(\cdot; \boldsymbol{\theta}_M)$ by using RNN. As stated in Section 3.2, RNN is suited explicitly for modeling such sequential data. Another aspect in Eq. (9) is associated with the projection operator $g(\cdot; \boldsymbol{\theta}_g)$. We reiterate that accuracy and efficiency of Eq. (9) is significantly dependent on $g(\cdot; \boldsymbol{\theta}_g)$. One popular choice among researchers is to use proper orthogonal decomposition for computing the projection operator g. However, proper orthogonal decomposition being a linear projection scheme has limited expressive capability. In this work, we propose to use AE as $g(\cdot; \boldsymbol{\theta}_g)$. Owing to the fact that AE is a nonlinear reduced order model, we expect the accuracy to enhance. However, one must note that training AE demands more computational effort as compared to proper orthogonal decomposition. Hereafter, we refer to the proposed framework as Auto-encoder and Recurrent neural network based state Estimation (ARE) framework. Next, details on network architecture and training algorithm for ARE are furnished.

4.1 Network architecture and training

The ARE architecture proposed in this paper involves an AE and an RNN. For state estimation, the trained AE is split into the encoder and the decoder parts. The encoder part is used during training the RNN within the ARE framework. The decoder part is used while estimating the state variable. The AE and RNN networks are trained separately, with the

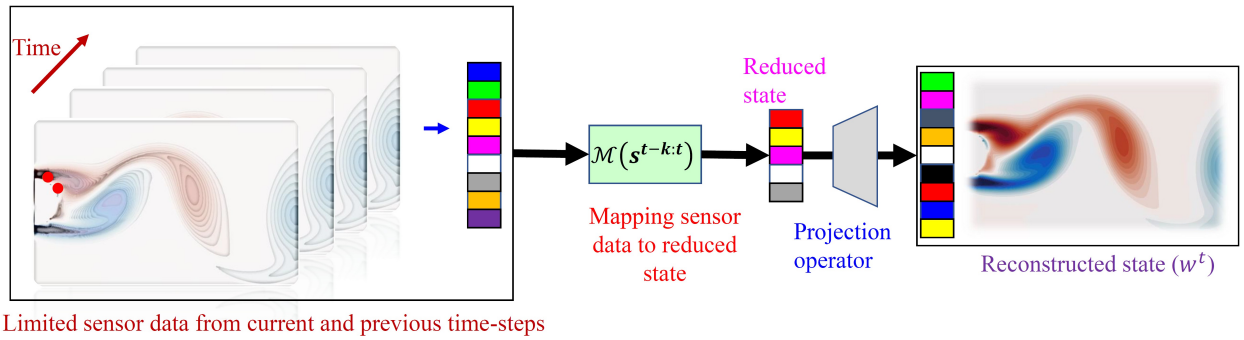

Figure 5: Schematic representation of the proposed approach. The difference with Fig. 1 resides in the fact that information from previous time-steps are also utilized within the proposed framework. We propose to model $\mathscr{M}(\cdot;\boldsymbol{\theta}_M)$ using RNN and $g(\cdot;\boldsymbol{\theta}_g)$ by using AE.

latter following the former (see Fig. 6). The AE architecture considered in this paper consists of 5 hidden layers, with the 3rd layer being the bottleneck layer. The flow-field is vectorized before providing it as an input to the AE. Rectified linear unit (ReLU) activation function has been used for all but the last layer. For the last layer, a linear activation function is used. For training the network, ADAM [48] optimizer with a learning rate of 0.0007 is used. We denote the trained parameters of the AE as $\boldsymbol{\theta}_{AE} = [\boldsymbol{\theta}_w, \boldsymbol{\theta}_g]$, where $\boldsymbol{\theta}_w$ and $\boldsymbol{\theta}_g$ corresponds to the network parameters for encoder and decoder part respectively. For making the model robust to noisy data, two batch-norm layers and one dropout layer is added to AE. Batch normalization [49] is used to normalizes the activation distribution. It reduces the model's sensitivity to learning rate [50], reduces training time, and increases stability. Additionally, this also acts as a regularizer. Dropout [51] is also an effective regularization technique that works by dropping connections between neurons during training with a specified probability p. Using the dropout layer just before the second hidden layer proved to be most efficient in increasing the robustness of the network to noise as it simulates the noise in latent vector from the RNN network. A dropout probability of 0.35 is used in the network. Considering *Li* to be the *i*-th layer of AE, BN to be the batch normalization and DR to be the dropbout, the architecture used in this paper is as follows:

$$L1 \rightarrow BN \rightarrow L2 \rightarrow BN \rightarrow DR \rightarrow L3 \rightarrow L4 \rightarrow L5 \rightarrow L5 \rightarrow Output$$

Once the AE trains, we proceed to train the RNN part. The objective here is to learn a mapping between the sequential sensor data and the reduced state variable obtained by using the encoder part of the trained AE. First, the sensor data passes through RNN. It helps in capturing information from the sequential data. After that, the RNN outputs are mapped to the reduced states by using a feed-forward neural network. Reduced states of the training outputs are obtained by using the trained AE (encoder part). The parameters $\boldsymbol{\theta}_M$ (see Eq. (9)) corresponds to the RNN and the feedforward neural network and are obtained by solving the following optimization problem

$$\boldsymbol{\theta}_M^* = \arg\min_{\boldsymbol{\theta}} \sum_{i=1}^{N_{\text{samp}}} \left\| h^t - \mathscr{N}\left(s^{t-k:t};\boldsymbol{\theta}_M\right) \right\| + \lambda \left\|\boldsymbol{\theta}_M\right|_2^2, \tag{10}$$

Where $\mathscr{N}$ represents the combined RNN and feed-forward neural network mapping. The second term in Eq. (10) represents L^2 regularization and is adopted to avoid overfitting. λ is a tuning parameter and needs to be tuned manually. Similar to AE, the optimization problem is solved by using ADAM optimizer [48]. We have used weight decay of 10^{-5} and a learning rate of 0.0008. Early stopping is used, which also acts as a regularizer [52]. RNN training is schematically shown in Fig. 6(b). The steps involved in training the proposed (ARE) are shown in Algorithm 1.

4.2 State estimation using the proposed approach

Once the proposed ARE is trained by following the procedure detailed in Algorithm 1, one can use it for estimating the state. A trained ARE performs state estimation in two simple steps. In the first step, the trained RNN is used for estimating the reduced state based on the sensor measurement. Once the reduced state has been estimated, the decoder part of the AE is used to project the reduced state onto the original state. For clarity of readers, the steps for predicting state using ARE are shown in Algorithm 2. A schematic representation of the same is also shown in Fig. 7.

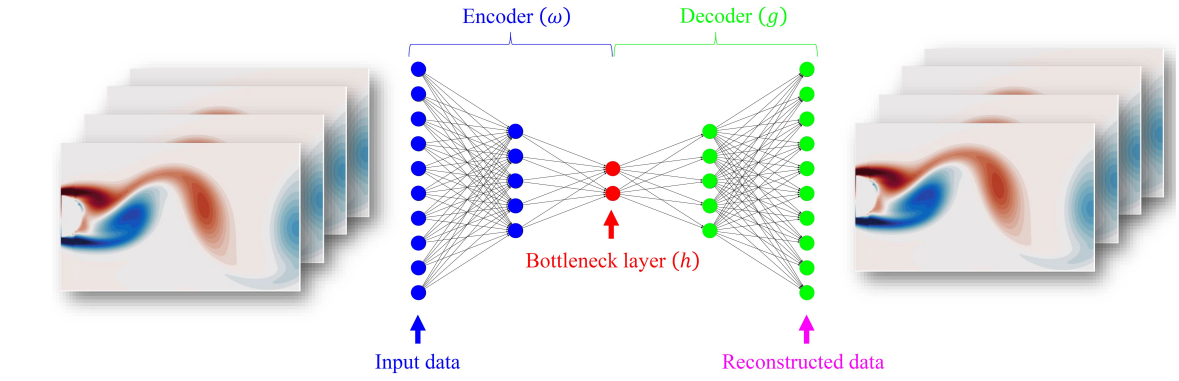

(a)

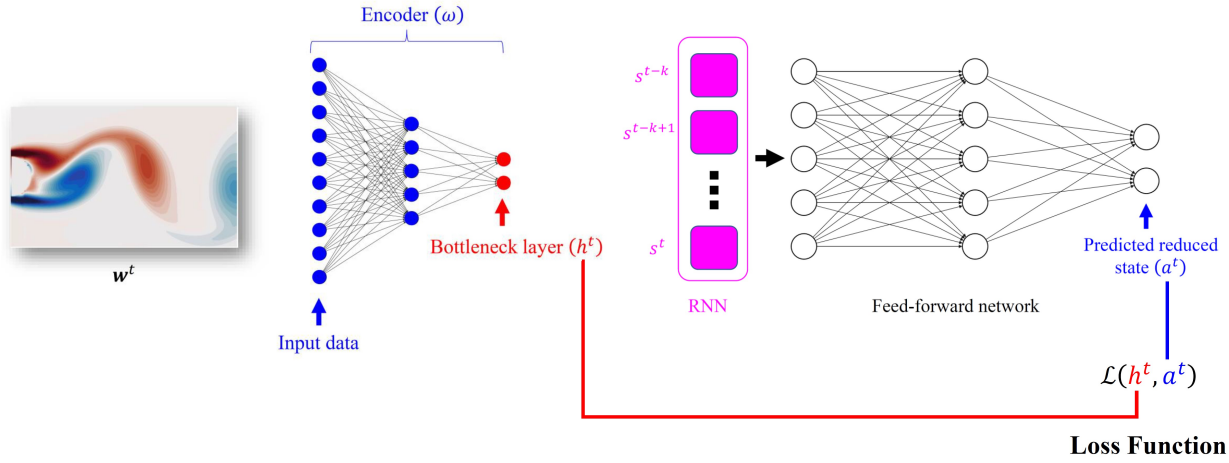

(b)

Figure 6: Schematic representation of ARE (training phase) - (a) Training AE for reconstructing the flow-field. (b) Training the RNN for mapping the sensor data to the reduced state.

Algorithm 1: Training ARE

1 **Library data generation:** Perform experiment or run CFD simulations to generate a library of data, $\mathscr{D} = [\boldsymbol{s}, \boldsymbol{w}]$ where,

$$\boldsymbol{s} = [\boldsymbol{s}^1_{1:N_s}, \ldots, \boldsymbol{s}^{N_t}_{1:N_s}], \quad \boldsymbol{w} = \left[\boldsymbol{w}^1, \ldots, \boldsymbol{w}^{N_t}\right],$$

where $\boldsymbol{w}^i \in \mathbb{R}^{N_w}$.

2 **Initialize:** Initialize $\boldsymbol{\theta}_g$ and $\boldsymbol{\theta}_M$. Provide sequence length $k+1$ for RNN, learning rate parameters, network architectures and number of training epochs.

3 Train AE for $\boldsymbol{w} = \left[\boldsymbol{w}^1, \ldots, \boldsymbol{w}^{N_t}\right]$.

4 $\boldsymbol{a}^t \leftarrow \boldsymbol{\omega}(\boldsymbol{w}^t; \boldsymbol{\theta}_w)$; ▷ Reducing dimensionality using AE

5 Train RNN for sequence length $k+1$; ▷ Eq. (10)

Algorithm 2: State estimation using ARE

1 **Pre-requisite:** Trained ARE model, $\boldsymbol{\theta} = [\boldsymbol{\theta}_M, \boldsymbol{\theta}_g]$ and sensor data $\boldsymbol{s}^{t-k:t}_*$.

2 $\boldsymbol{a}^t_* \leftarrow \mathscr{N}(\boldsymbol{s}^{t-k:t}_*; \boldsymbol{\theta}_M)$; ▷ Reduced state prediction using RNN

3 $\boldsymbol{w}^t_* \leftarrow = g(\boldsymbol{a}^t_*; \boldsymbol{\theta}_g)$; ▷ Full-state estimation using decoder part of AE

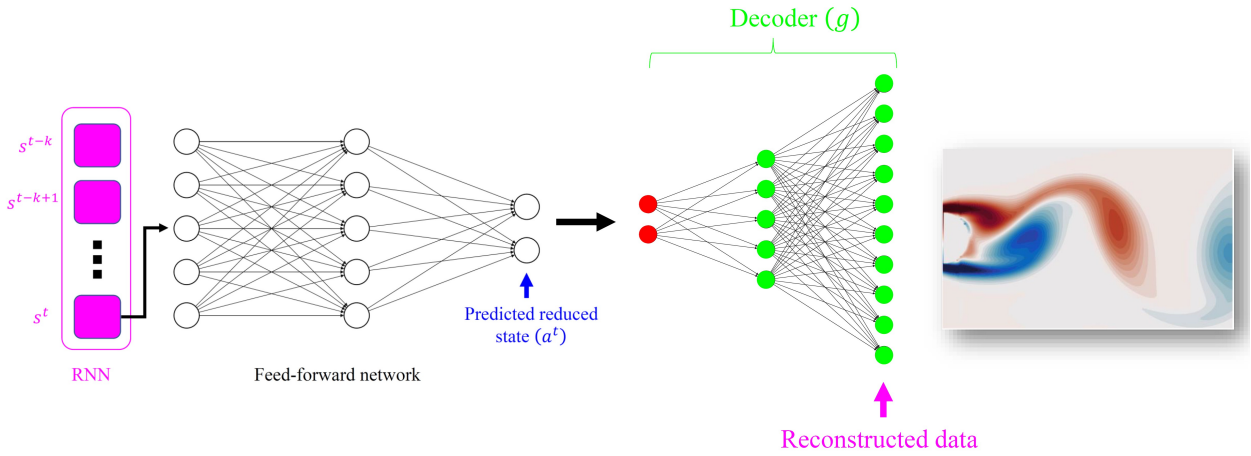

Figure 7: Schematic representation of the proposed ARE for state estimation

5 Numerical experiments

In this section, two examples are presented to illustrate the performance of the proposed approach. The examples selected are well-known benchmark problems in the fluid mechanic's community. For both examples, we have considered that the sensor measures vorticity, and the objective is to reconstruct the vorticity field. We present case studies by varying the number of sensors and the number of sequences available. To illustrate the excellent performance of our approach, a comparison with another state-of-the-art method has been provided. Comparison among results is carried out based on a qualitative and quantitative metric. To be specific, visual inspection is used as a qualitative metric, and the relative error is used as a quantitative metric,

$$\varepsilon = \frac{\|\boldsymbol{\omega}^n(\boldsymbol{\theta}^*) - \boldsymbol{\omega}_r^n(\boldsymbol{\theta}^*)\|_2}{\|\boldsymbol{\omega}^n(\boldsymbol{\theta}^*)\|_2} \times 100. \tag{11}$$

where ε represents the error, $\boldsymbol{\omega}^n(\boldsymbol{\theta}^*)$ is the true state and $\boldsymbol{\omega}_r^n(\boldsymbol{\theta}^*)$ is the state vector predicted using the proposed approach. $\|\cdot\|_2$ represents the l_2 norm. The dataset for solving the state estimation problems is generated using OpenFoam [53]. The proposed approach has been implemented using PyTorch [54]. The software associated with the proposed approach, along with the implementation of both the examples, will be made available on acceptance of the paper.

5.1 Periodic Vortex shedding past a cylinder

As the first example, we consider two-dimensional flow past a circular cylinder at Reynolds's number $Re = 190$. It is a well known canonical problem and is characterized by periodic laminar flow vortex shedding.

A schematic representation of the computational domain is shown in Fig. 8. The circular cylinder is considered to have a diameter of 1 unit. The center of the cylinder is located at a distance of 8 units from the inlet. The outlet is located at a distance of 25 units from the center of the cylinder. The sidewalls are at 4 units distance from the center of the cylinder. At the inlet boundary, a uniform velocity of 1 unit along the X-direction is applied. Pressure boundary condition with $P = 0$ is considered at the outlet. A no-slip boundary at the cylinder surface is considered.

The dataset necessary for training the proposed model is generated by using Unsteady Reynolds's Average Navier Stokes (URANS) simulation in OpenFoam [53]. The overall problem domain is discretized into 63420 elements with finer mesh near the cylinder. Time step $\delta t = 0.02$ units is considered.

For training the model, a library of 180 snapshots is generated by running OpenFoam. Additional 120 snapshots, 60 for validation and 60 for testing, have also been generated. Two consecutive snapshots are separated by $10\delta t$. Coordinate of the snapshot cutout stretches from $[0,-2] \times [6,2]$ which is discretized into 168×251 points in x and y directions (see Fig. 8(b)). The objective here is to recover the complete vorticity-field in the cutout by using the sensor measurements. Details on the network architecture are provided in Table 1.

To illustrate the superiority of the proposed approach, the results obtained using the proposed approach are compared with those obtained using proper orthogonal decomposition-based deep state estimation (PDS) proposed by [29]. In PDS, the first 25 modes are used, which is the same as the number of neurons in the bottleneck layer of the proposed

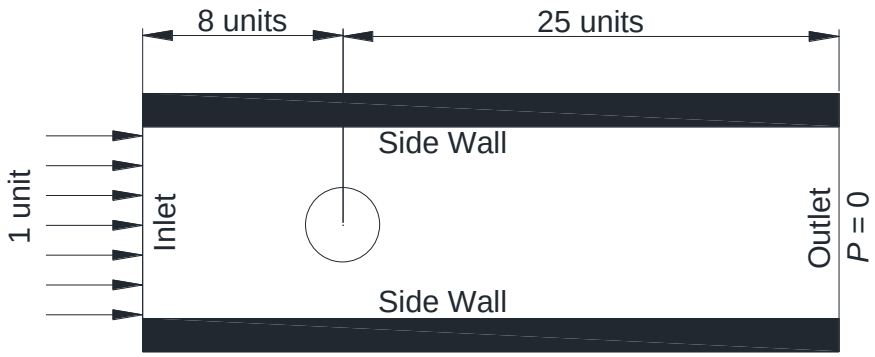

(a)

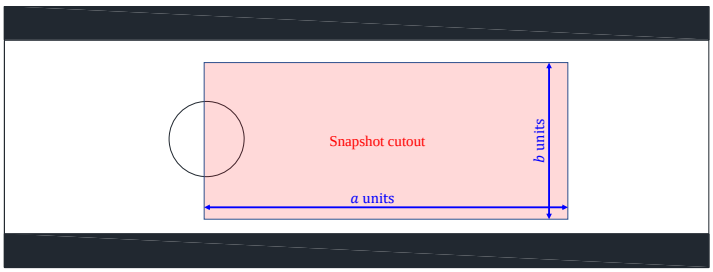

(b)

Figure 8: (a) Schematic representation of the computational domain with boundary conditions at the inlet and the outlet. The cylinder is having a diameter of 1 unit. A no-slip boundary is considered at the cylinder wall. Zero pressure gradient at the inlet and zero velocity gradient at the outlet are considered. (b) Schematic of the problem domain with snapshot cutout of $a \times b$. For periodic vorticity problem, $a = 6$ units and $b = 4$ units. For transient flow problem, $a = 12$ units and $b = 6$ units. *The schematics are not to scale.*

Table 1: Network architecture of proposed ARE for periodic vortex shedding problem. BN indicates batch normalization and DR represents dropout. In case of noise-free data, BN and DR are not used. A DR rate of 0.35 is used.

Network component	Architecture
AE	$251 \times 168 \rightarrow BN \rightarrow 1024 \rightarrow BN \rightarrow DR \rightarrow 256 \rightarrow 25 \rightarrow 256 \rightarrow 1024 \rightarrow 168 \times 251$
RNN	RNN $\rightarrow 50 \rightarrow 50 \rightarrow 25$

approach. The feed-forward neural network used in PDS for mapping the sensor measurements to the latent state is the same as the feed-forward network used in ARE. Note that comparison with other popular approaches such as gappy-POD and linear stochastic estimation is not shown as it is already established in [29] that PDS outperforms both the approaches. Brief details on PDS, gappy-POD, and linear stochastic estimation are provided in Appendix A.

Fig. 9 shows the results obtained using different approaches. It is an idealized case where we have considered the sensor data to be noise free. The sequence length of four is used for training ARE. We have considered the extreme case where data from only one sensor is available. We observe that the proposed ARE, with only one senor, is able to recover the full state accurately. PDS, on the other hand, yields less accurate results. Fig. 10 shows results corresponding to the case where the sensor is corrupted by white Gaussian noise. This is a more realistic case. Again, a sequence length of 4 is considered and it is assumed that data from only one sensor is available. In this case also, we observe that ARE yields highly accurate results and outperforms PDS. The effect of noise on the proposed ARE is shown in Fig. 11. We observe that the proposed approach is robust to the noise in the sensor measurements.

Next, we investigate the effect of varying the number of sensors. Fig. 12 shows the performance of different methods with the increase in the number of sensors. Cases corresponding to one, two, five, and ten sensors are presented. We observe that as the number of sensors increases, PDS starts yielding better results. The proposed ARE found to yield the best result for all four cases.

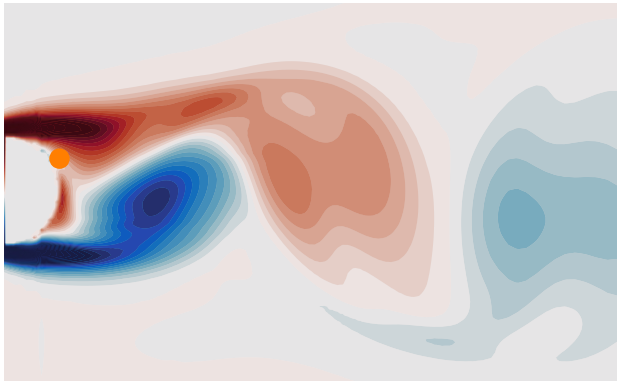

(a) PDS

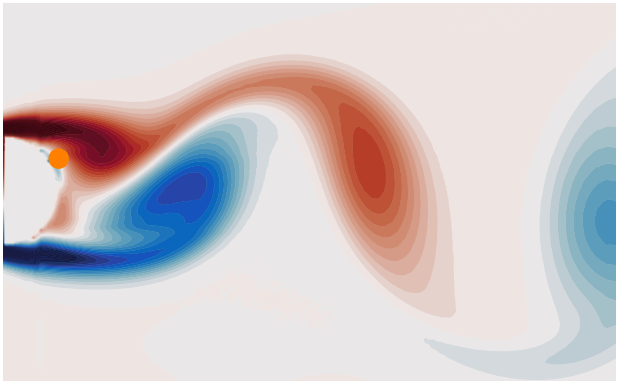

(b) ARE

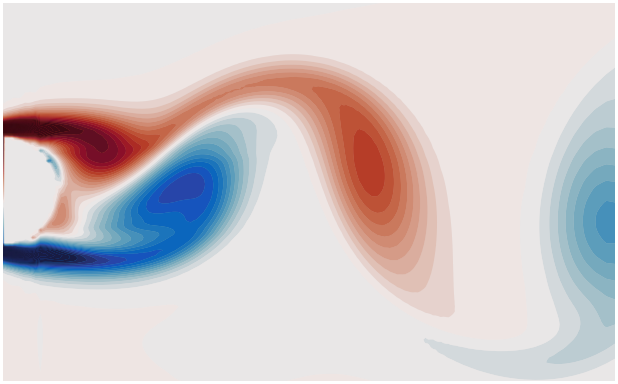

(c) Ground Truth

Figure 9: Figure depicts results of periodic vortex shedding for one sensor. Orange dots in the images represents the location of sensor. (First row -PDS, Second row -ARE, Third row -Ground truth) SEQ-LEN used for ARE model is 4.

We also carried out an additional case study where we considered that sensor data from both past and future is available. A bi-directional RNN (B-RNN) based ARE developed for the same. However, due to the paucity of space, the same is not presented here. Those interested can refer to Appendix B for details on the same.

5.2 Transient Flow past a cylinder

As the second example, we consider the problem involving transient flow past a cylinder. Because of the transient nature of the flow, this is much more challenging than the periodic vortex shedding problem in Section 5.1. The problem domain, meshing, and solution strategy for this problem are considered the same as the periodic vortex shedding problem. However, unlike the previous problem, we have varied the training, and test data corresponds to different Reynolds numbers. It exponentially increases the complexity of the problem.

The training library for this problem was created by running URANS in OpenFoam. Total 1200 snapshots consisting of 400 snapshots at $Re = [180, 190, 200]$ were generated. Validation and test set consists of 400 sequential snapshots at $Re = [185, 195]$. Similar to the previous problem, the snapshots were separated by a time interval of $10\delta t$. Co-ordinate of snapshot cutout stretches from $[0, -3] \times [12.0, 3.0]$ (see Fig. 8(b)). The cutout is discretized into 252 and 502 points in the x and y direction, respectively. Similar to the previous example, the objective here is to recover the vorticity field based on sensor measurements. Similar to the previous example, results obtained have been compared with PDS (with a similar setup as before). Details on the network architecture used for this problem are provided in Table 2.

Fig. 13 shows the reconstructed vorticity field using ARE and PDS. Ground truth has also been reported. It is an idealized case where we have considered the sensor data to be noise-free. A sequence length of four is used for ARE. We have considered the extreme case where data from only one sensor is available. For this problem also, the proposed is able to recover the full vorticity field accurately. PDS, on the other hand, fails to recover the vorticity field accurately. Next, we consider a more realistic scenario where the sensor data is corrupted by noise. Fig. 14 shows the results corresponding to noisy sensor measurement. For this case also, the results obtained using the proposed ARE is found

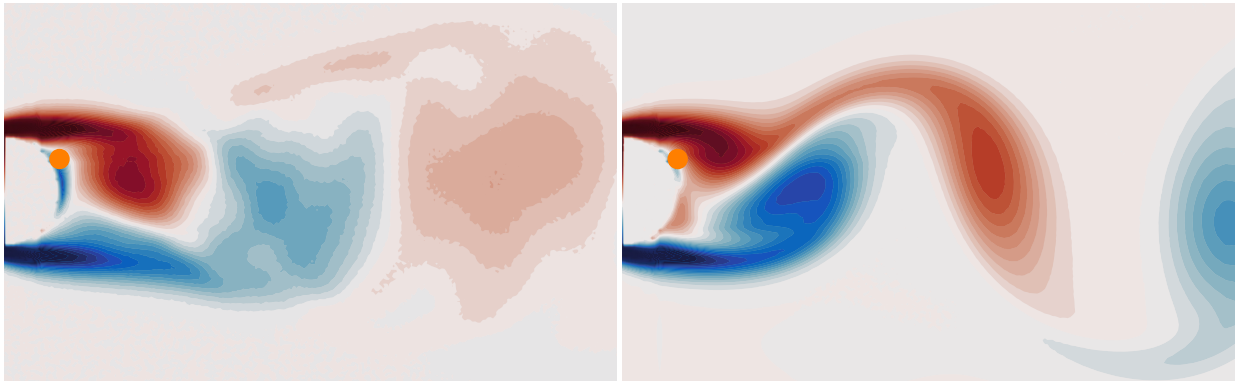

(a) PDS (b) ARE

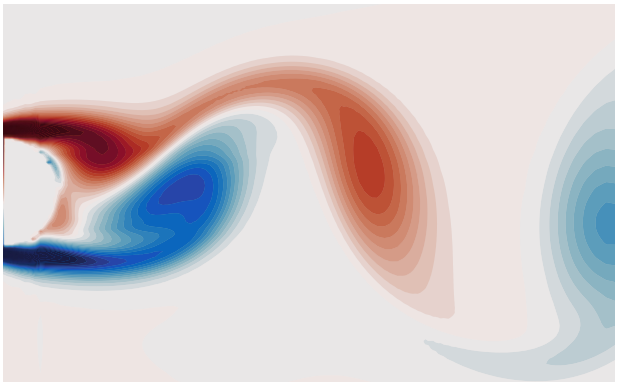

(c) Ground Truth

Figure 10: Figure depicts results of periodic vortex shedding for one sensor. The data is corrupted with white Gaussian noise having SNR = 20. Orange dots in the images represents the location of sensor. SEQ-LEN used for ARE model is 4.

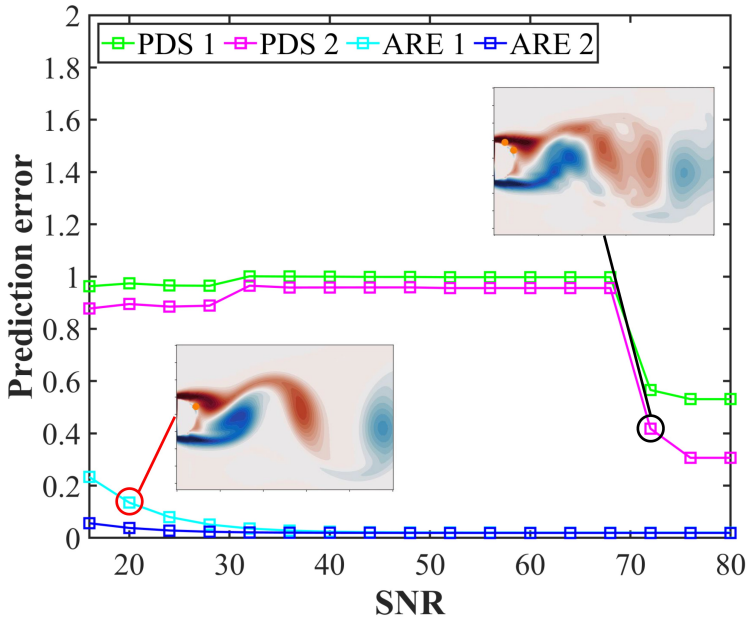

Figure 11: Performance of the proposed approach (ARE) and PDS for periodic vortex shedding problem at different noise level. For both ARE and PDS, results corresponding to one and two sensors are presented.

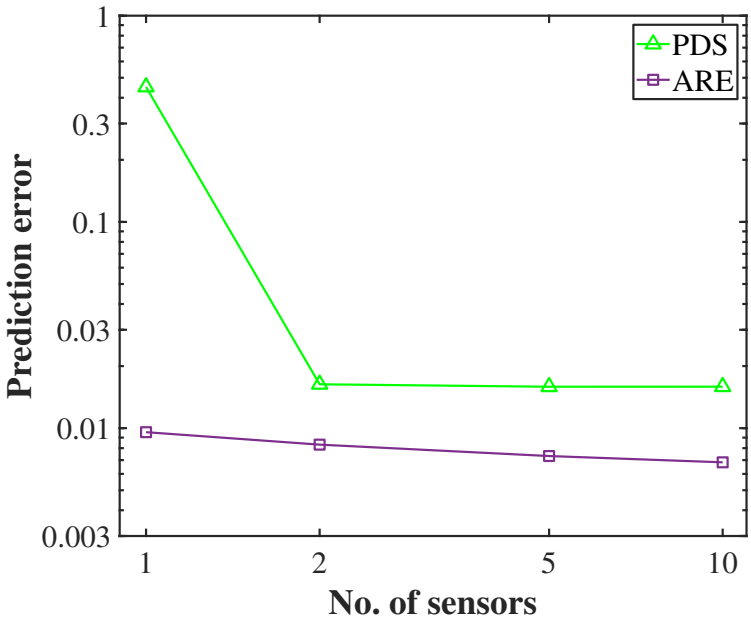

Figure 12: Performance of proposed ARE and PDS with increase in number of sensors.

Table 2: Network architecture of proposed ARE for transient flow problem. Dropout rate of 0.35 is used.

Network component	Architecture
AE	$252 \times 502 \rightarrow BN \rightarrow 2000 \rightarrow BN \rightarrow DR \rightarrow 300 \rightarrow 25 \rightarrow 300 \rightarrow 2000 \rightarrow 252 \times 502$
RNN	RNN $\rightarrow 50 \rightarrow 50 \rightarrow 25$

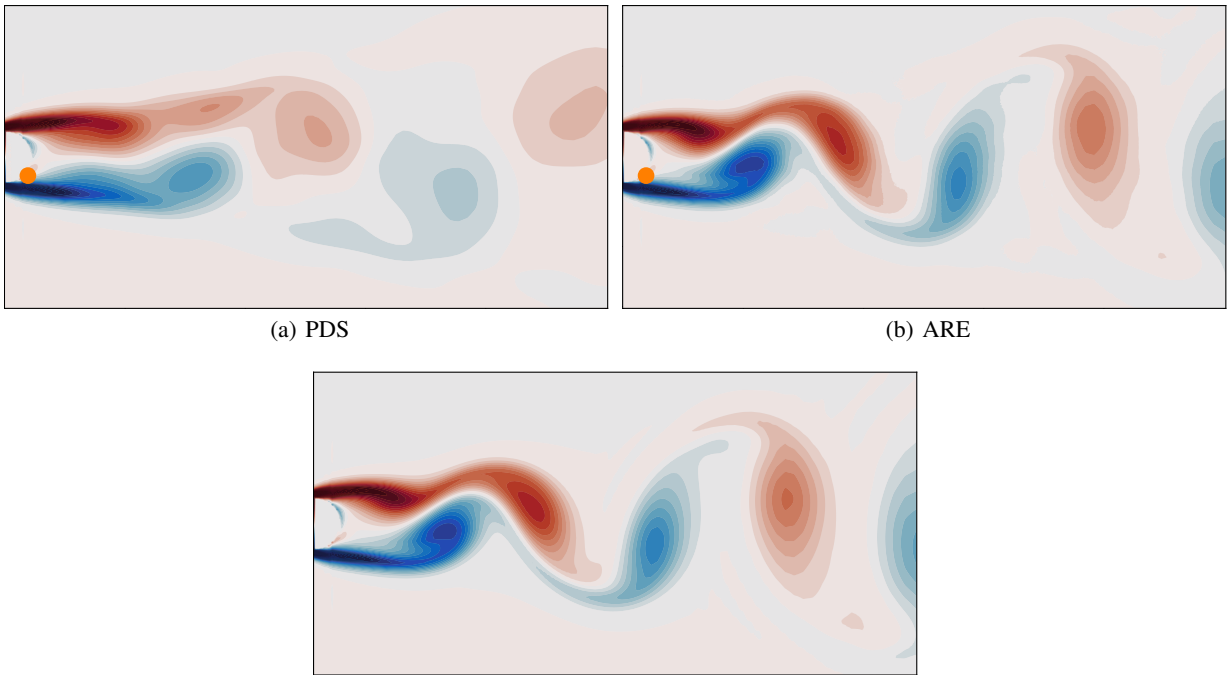

(a) PDS

(b) ARE

(c) Ground truth

Figure 13: Figure depicts results of Transient Flow for one sensor. Orange dots in the images represents the location of sensor. SEQ-LEN used for ARE model is 4

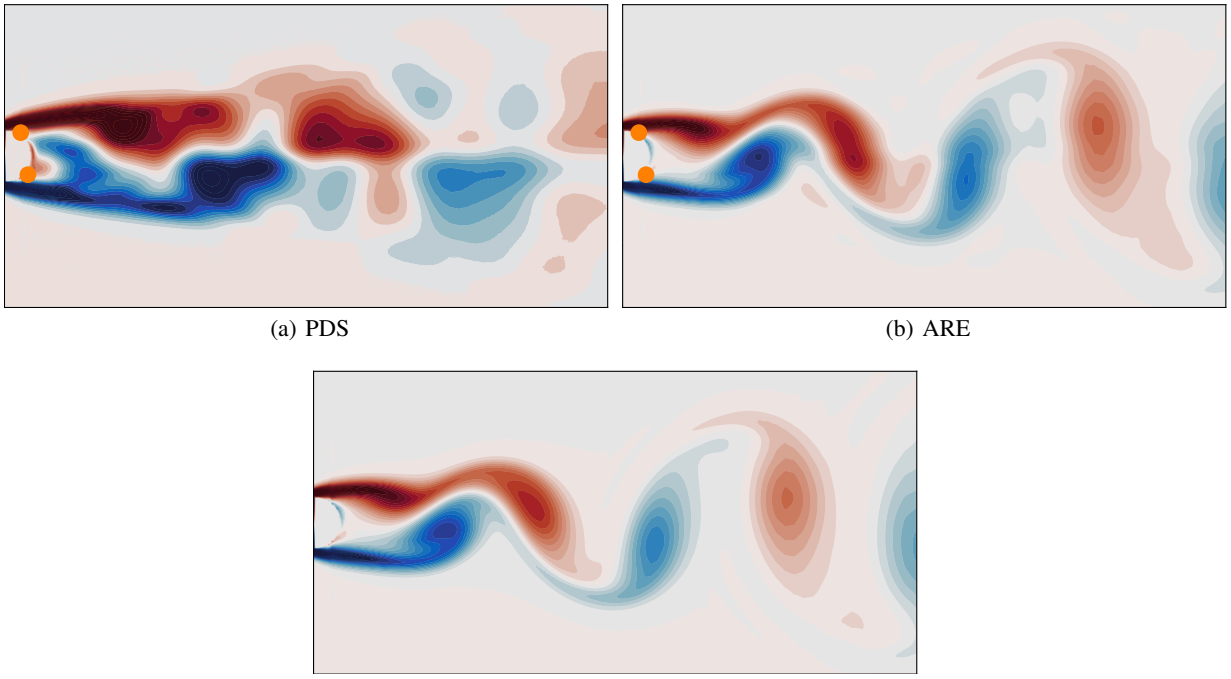

(a) PDS (b) ARE

(c) Ground truth

Figure 14: Figure depicts results of Transient Flow for two sensors. The data is corrupted with white Gaussian noise with SNR = 28. Orange dots in the images represents the location of sensor. SEQ-LEN used for ARE model is 4

to be superior as compared to those in the literature. The effect of noise on the performance of the proposed ARE is shown Fig. 15. ARE is found to be robust to the noise in the sensor measurements.

Next, we investigate the effect of a number of sensors and sequence length considered in the proposed approach. Fig. 16 shows the performance of different methods with an increase in the number of sensors. Cases corresponding to one, two, five, and ten sensors are presented. We observe that as the number of sensors increases, PDS starts yielding better results. The proposed approach is found to yield the best result for all four cases. Fig. 17 illustrates the performance of the proposed approach corresponding to the different sequence length. As expected, initially, the results are found to improve with an increase in the sequence length. ARE reaches a saturation point at sequence length three, and no significant improvement in results is observed on further increasing the sequence length.

Lastly, for details on B-RNN based ARE for this problem, interested readers may refer Apendix B

6 Conclusions

In this work, we introduced a novel deep learning based approach for state estimation. The proposed approach uses an auto-encoder as a reduced-order model and recurrent neural network to map the sensor measurements to the reduced state. The proposed framework is superior to existing state estimation frameworks in two aspects. First, auto-encoder, being a nonlinear manifold learning framework, is superior to the usually used proper orthogonal decomposition. Secondly, unlike existing state estimation frameworks, the proposed approach utilizes present and past sensor measurements using the recurrent neural network. It results in improved accuracy, specifically for cases where limited sensors are deployed. Experiments performed on simulation of flow past a cylinder illustrated the capability of the proposed approach in learning from sequential data. Comparison carried out with respect to proper orthogonal decomposition-based deep state estimation showed the superior accuracy of the proposed approach. Moreover, The proposed approach was also found to be robust to the noise in the sensor measurements.

Utilizing sequential information can prove beneficial in many other state estimation tasks. Future work can be aimed at exploiting effects of other models used on sequential information such as transformers, comparing between other auto-encoder network variations, the effect of varying time step between measurements, developing models capable of

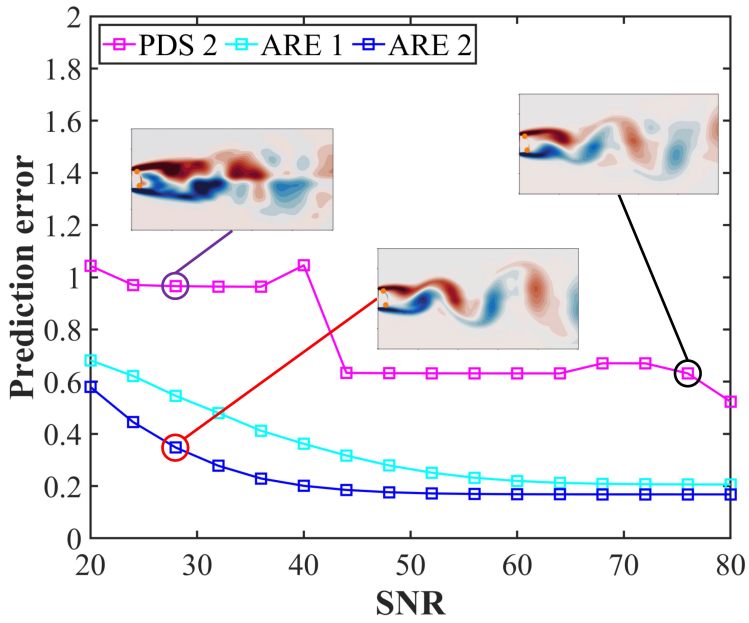

Figure 15: Performance of the proposed approach (ARE) and PDS for the transient flow problem at different noise level. ARE1 corresponds to results with one sensor and ARE2 corresponds to results with 2 sensors.

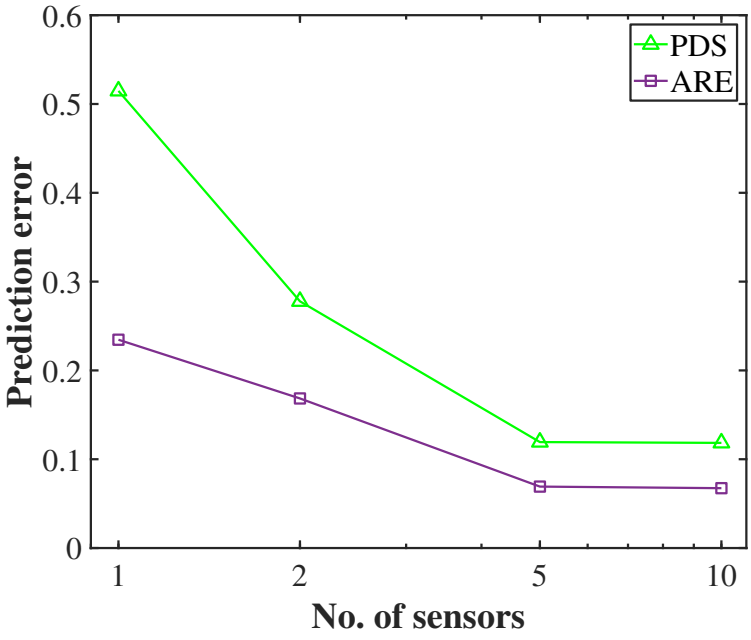

Figure 16: Performance of PDS and proposed ARE with increase in number of sensors.

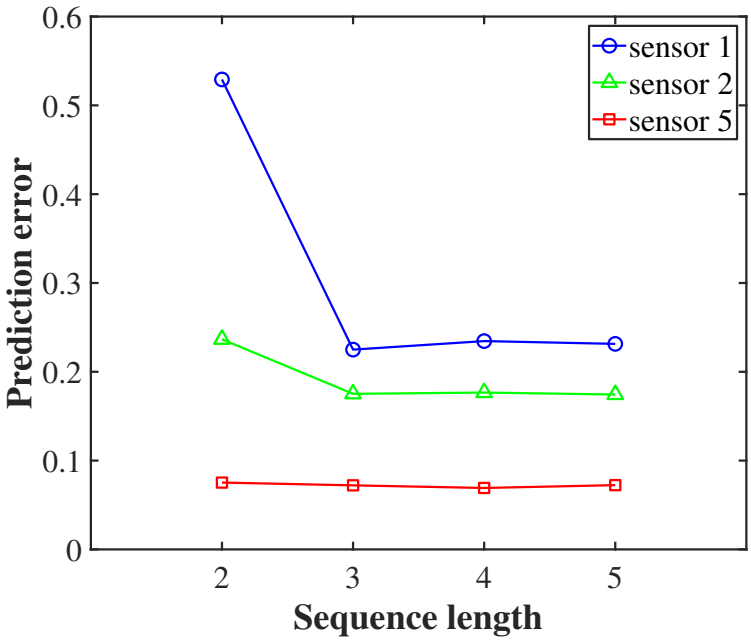

Figure 17: Performance of proposed ARE with increase in sequence length.

transfer learning, i.e., trained on smaller time step but can use larger time step. Work on utilizing, recently developed a physics-informed neural network for solving such problems can also be pursued in the future.

Acknowledgements: The authors would like to thank Dr. Arghya Samanta and Nirmal J Nair for the useful discussions during this paper's preparation. SC acknowledges the financial support of the I-Hub Foundation for Cobotics (IHFC) and seed grant provided through Faculty initiation grant, IIT Delhi.

References

[1] Michele Milano and Petros Koumoutsakos. Neural network modeling for near wall turbulent flow. *Journal of Computational Physics*, 182(1):1 – 26, 2002.

[2] Julia Ling, Andrew Kurzawski, and Jeremy Templeton. Reynolds averaged turbulence modelling using deep neural networks with embedded invariance. *Journal of Fluid Mechanics*, 807:155–166, 2016.

[3] Nicholas Geneva and Nicholas Zabaras. Quantifying model form uncertainty in reynolds-averaged turbulence models with bayesian deep neural networks. *Journal of Computational Physics*, 383:125–147, 2019.

[4] Nicholas Geneva and Nicholas Zabaras. Multi-fidelity generative deep learning turbulent flows. *arXiv preprint arXiv:2006.04731*, 2020.

[5] N. Benjamin Erichson, Lionel Mathelin, Zhewei Yao, Steven L. Brunton, Michael W. Mahoney, and J. Nathan Kutz. Shallow learning for fluid flow reconstruction with limited sensors and limited data, 2019.

[6] Lorenzo Rosasco, Andrea Caponnetto, Ernesto Vito, Francesca Odone, and Umberto Giovannini. Learning, regularization and ill-posed inverse problems. *Advances in Neural Information Processing Systems*, 17:1145–1152, 2004.

[7] Rajdip Nayek, Suparno Mukhopadhyay, and Sriram Narasimhan. Mass normalized mode shape identification of bridge structures using a single actuator-sensor pair. *Structural Control and Health Monitoring*, 25(11):e2244, 2018.

[8] Simo Särkkä. *Bayesian filtering and smoothing*. Number 3. Cambridge University Press, 2013.

[9] Christopher M Bishop. *Pattern recognition and machine learning*. springer, 2006.

[10] Konrad Reif, Stefan Gunther, Engin Yaz, and Rolf Unbehauen. Stochastic stability of the discrete-time extended kalman filter. *IEEE Transactions on Automatic control*, 44(4):714–728, 1999.

[11] Eric A Wan, Rudolph Van Der Merwe, and Simon Haykin. The unscented kalman filter. *Kalman filtering and neural networks*, 5(2007):221–280, 2001.

[12] Rajdip Nayek, Souvik Chakraborty, and Sriram Narasimhan. A gaussian process latent force model for joint input-state estimation in linear structural systems. *Mechanical Systems and Signal Processing*, 128:497–530, 2019.

[13] Jonathan Tu, John Griffin, Adam Hart, Clarence Rowley, Louis Cattafesta, and Lawrence Ukeiley. Integration of non-time-resolved piv and time-resolved velocity point sensors for dynamic estimation of velocity fields. *Experiments in Fluids*, 54, 01 2012.

[14] M. Buffoni, S. Camarri, A. Iollo, E. Lombardi, and M.V. Salvetti. A non-linear observer for unsteady three-dimensional flows. *Journal of Computational Physics*, 227(4):2626 – 2643, 2008.

[15] Ryota Kikuchi, Takashi Misaka, and Shigeru Obayashi. Assessment of probability density function based on POD reduced-order model for ensemble-based data assimilation. *Fluid Dynamics Research*, 47(5):051403, sep 2015.

[16] V. Mons, J.-C. Chassaing, T. Gomez, and P. Sagaut. Reconstruction of unsteady viscous flows using data assimilation schemes. *Journal of Computational Physics*, 316:255 – 280, 2016.

[17] Andre Fernando De Castro da Silva and Tim Colonius. Ensemble-based state estimator for aerodynamic flows. *AIAA Journal*, 56:1–11, 06 2018.

[18] J. A. Tropp and A. C. Gilbert. Signal recovery from random measurements via orthogonal matching pursuit. *IEEE Transactions on Information Theory*, 53(12):4655–4666, 2007.

[19] S. G. Mallat and Zhifeng Zhang. Matching pursuits with time-frequency dictionaries. *IEEE Transactions on Signal Processing*, 41(12):3397–3415, 1993.

[20] Jared L. Callaham, Kazuki Maeda, and Steven L. Brunton. Robust flow reconstruction from limited measurements via sparse representation. *Physical Review Fluids*, 4(10), Oct 2019.

[21] Richard Everson and Lawrence Sirovich. Karhunen–loève procedure for gappy data. *JOSA A*, 12, 08 1995.

[22] Kelly Cohen, Stefan Siegel, and Thomas McLaughlin. A heuristic approach to effective sensor placement for modeling of a cylinder wake. *Computers & Fluids*, 35:103–120, 01 2006.

[23] K. Willcox. Unsteady flow sensing and estimation via the gappy proper orthogonal decomposition. *Computers & Fluids*, 35(2):208 – 226, 2006.

[24] Ronald Adrian. On the role of conditional averages in turbulence theory. -1:323–332, 01 1977.

[25] A. M. Naguib, C. E. Wark, and O. Juckenhöfel. Stochastic estimation and flow sources associated with surface pressure events in a turbulent boundary layer. *Physics of Fluids*, 13(9):2611–2626, 2001.

[26] Dan Ewing and Joseph H. Citriniti. Examination of a lse/pod complementary technique using single and multi-time information in the axisymmetric shear layer. In J. N. Sørensen, E. J. Hopfinger, and N. Aubry, editors, *IUTAM Symposium on Simulation and Identification of Organized Structures in Flows*, pages 375–384, Dordrecht, 1999. Springer Netherlands.

[27] Y. G. Guezennec. Stochastic estimation of coherent structures in turbulent boundary layers. *Physics of Fluids A: Fluid Dynamics*, 1(6):1054–1060, 1989.

[28] J. P. Bonnet, D. R. Cole, J. Delville, M. N. Glauser, and L. S. Ukeiley. Stochastic estimation and proper orthogonal decomposition: Complementary techniques for identifying structure. *Experiments in Fluids*, 17(5):307–314, Sep 1994.

[29] Nirmal J. Nair and Andres Goza. Leveraging reduced-order models for state estimation using deep learning. *Journal of Fluid Mechanics*, 897:R1, 2020.

[30] Jeremy Pinier, Julie Ausseur, Mark Glauser, and Hiroshi Higuchi. Proportional closed-loop feedback control of flow separation. *Aiaa Journal - AIAA J*, 45:181–190, 01 2007.

[31] Ronald Adrian. Conditional eddies in isotropic turbulence. *Physics of Fluids*, 22, 11 1979.

[32] T. C. Tung and R. J. Adrian. Higher-order estimates of conditional eddies in isotropic turbulence. *The Physics of Fluids*, 23(7):1469–1470, 1980.

[33] Kevin P Murphy. *Machine learning: a probabilistic perspective*. MIT press, 2012.

[34] Ilyes Khemakhem, Diederik Kingma, Ricardo Monti, and Aapo Hyvarinen. Variational autoencoders and nonlinear ica: A unifying framework. In *International Conference on Artificial Intelligence and Statistics*, pages 2207–2217. PMLR, 2020.

[35] Xavier Glorot, Antoine Bordes, and Yoshua Bengio. Deep sparse rectifier neural networks. In *Proceedings of the fourteenth international conference on artificial intelligence and statistics*, pages 315–323. JMLR Workshop and Conference Proceedings, 2011.

[36] Hareesh Bahuleyan, Lili Mou, Hao Zhou, and Olga Vechtomova. Stochastic wasserstein autoencoder for probabilistic sentence generation. *arXiv preprint arXiv:1806.08462*, 2018.

[37] Adam R Kosiorek, Sara Sabour, Yee Whye Teh, and Geoffrey E Hinton. Stacked capsule autoencoders. *arXiv preprint arXiv:1906.06818*, 2019.

[38] Sepp Hochreiter and Jürgen Schmidhuber. Long short-term memory. *Neural computation*, 9:1735–80, 12 1997.

[39] Zachary C Lipton, John Berkowitz, and Charles Elkan. A critical review of recurrent neural networks for sequence learning. *arXiv preprint arXiv:1506.00019*, 2015.

[40] Suraj Pawar, Shady E. Ahmed, Omer San, Adil Rasheed, and Ionel M. Navon. Long short-term memory embedded nudging schemes for nonlinear data assimilation of geophysical flows. *Physics of Fluids*, 32(7):076606, 2020.

[41] José del Águila Ferrandis, Michael S. Triantafyllou, Chryssostomos Chryssostomidis, and George Em Karniadakis. Learning functionals via LSTM neural networks for predicting vessel dynamics in extreme sea states. *CoRR*, abs/1912.13382, 2019.

[42] Sepp Hochreiter. The vanishing gradient problem during learning recurrent neural nets and problem solutions. *International Journal of Uncertainty, Fuzziness and Knowledge-Based Systems*, 06(02):107–116, 1998.

[43] Hamidreza Eivazi, Hadi Veisi, Mohammad Hossein Naderi, and Vahid Esfahanian. Deep neural networks for nonlinear model order reduction of unsteady flows. *Physics of Fluids*, 32(10):105104, 2020.

[44] Nicholas Geneva and Nicholas Zabaras. Transformers for modeling physical systems, 2020.

[45] Hamidreza Eivazi, Hadi Veisi, Mohammad Hossein Naderi, and Vahid Esfahanian. Deep neural networks for nonlinear model order reduction of unsteady flows. *Physics of Fluids*, 32(10):105104, Oct 2020.

[46] Siavash Hosseinyalamdary. Deep kalman filter: Simultaneous multi-sensor integration and modelling; a gnss/imu case study. *Sensors*, 18(5), 2018.

[47] Samuel E. Otto and Clarence W. Rowley. Linearly-recurrent autoencoder networks for learning dynamics, 2019.

[48] Diederik Kingma and Jimmy Ba. Adam: A method for stochastic optimization. *International Conference on Learning Representations*, 12 2014.

[49] Sergey Ioffe and Christian Szegedy. Batch normalization: Accelerating deep network training by reducing internal covariate shift, 2015.

[50] Sanjeev Arora, Zhiyuan Li, and Kaifeng Lyu. Theoretical analysis of auto rate-tuning by batch normalization, 2018.

[51] Nitish Srivastava, Geoffrey Hinton, Alex Krizhevsky, Ilya Sutskever, and Ruslan Salakhutdinov. Dropout: A simple way to prevent neural networks from overfitting. *Journal of Machine Learning Research*, 15(56):1929–1958, 2014.

[52] Jeffrey Heaton. Ian goodfellow, yoshua bengio, and aaron courville: Deep learning: The mit press, 2016, 800 pp, isbn: 0262035618. *Genetic Programming and Evolvable Machines*, 19, 10 2017.

[53] Hrvoje Jasak. Openfoam: open source cfd in research and industry. *International Journal of Naval Architecture and Ocean Engineering*, 1(2):89–94, 2009.

[54] Adam Paszke, Sam Gross, Soumith Chintala, Gregory Chanan, Edward Yang, Zachary DeVito, Zeming Lin, Alban Desmaison, Luca Antiga, and Adam Lerer. Automatic differentiation in pytorch. 2017.

[55] M. Schuster and K. K. Paliwal. Bidirectional recurrent neural networks. *IEEE Transactions on Signal Processing*, 45(11):2673–2681, 1997.

[56] Pierre Baldi, Søren Brunak, Paolo Frasconi, Giovanni Soda, and Gianluca Pollastri. Exploiting the past and the future in protein secondary structure prediction. *Bioinformatics (Oxford, England)*, 15:937–46, 12 1999.

A Proper orthogonal decomposition based deep state estimation (PDS)

In this section, we briefly provide the theoretical background of PDS. We note that development of PDS is motivated from gappy-POD and linear stochastic estimation and hence, the discussion in this section also starts from gappy-POD and then proceeds to PDS via linear stochastic estimation.

Let training set consist of N_t flattened data images, $\mathbf{W} = (\boldsymbol{w}_1, \boldsymbol{w}_2, \ldots, \boldsymbol{w}_{N_t})$, where $\boldsymbol{w}_t \in \mathbb{R}^{N_w}$ and corresponding sensor measurements $\boldsymbol{s} = (\boldsymbol{s}_1, \boldsymbol{s}_2, \ldots, \boldsymbol{s}_{N_t})$. As already state in Section 2, the aim in state estimation is to recover full state $\boldsymbol{w}$ via sensor measurements $\boldsymbol{s}$.

A.1 Gappy-POD

Consider, $\mathbf{H} \in \mathbb{R}^{N_s \times N_w}$ is measurement operator that maps full state to measurements and have ones as sensor location and zeros otherwise. Mathematically,

$$\boldsymbol{s} = \mathbf{H}\boldsymbol{w}, \tag{12}$$

where $\boldsymbol{w}$ can be approximated by linear combination of k modes. Modes used here are k most dominant modes, $\boldsymbol{\Phi}$, and are obtained by proper orthogonal decomposition of training data $\mathbf{W}$ and selecting first k singular vectors,

$$\boldsymbol{w} \approx \sum_{i=1}^{k} \phi_i a_i = \boldsymbol{\Phi}\boldsymbol{A}, \tag{13}$$

where

$$\mathbf{W} \approx \boldsymbol{\Phi} D B^*, truncated \;\; k-rank, \tag{14}$$

and

$$\boldsymbol{s} \approx \mathbf{H}\boldsymbol{\Phi} a. \tag{15}$$

In Eq. (14), $\boldsymbol{\Phi} \in \mathbb{R}^{N_w \times k}$. During testing $\boldsymbol{a}$ is obtained by solving the following minimization problem.

$$\boldsymbol{a} \in \arg\min_{\tilde{\boldsymbol{a}}} \| \boldsymbol{s} - \mathbf{H}\boldsymbol{\Phi}\tilde{\boldsymbol{a}} \| \, |_2^2. \tag{16}$$

Solution to this problem is obtained by taking Moore-Penrose pseudo inverse

$$\boldsymbol{a} = (\mathbf{H}\boldsymbol{\Phi})^{+}\boldsymbol{s} \tag{17}$$

This approach requires previous knowledge of operator $\mathbf{H}$. This operator is only available for simple systems but is often unknown for systems of practical interest.

A.2 Linear stochastic estimation

Linear Stochastic Estimation overcomes this issue by defining another operator which will map latent state to sensor. Operator $P : \mathbb{R}^k \mapsto \mathbb{R}^{N_s}$ is learned from training data via the following minimization problem.

$$P \in \arg\min_{\tilde{P}} ||\boldsymbol{s} - \tilde{P}\boldsymbol{A}||_2^2, \tag{18}$$

where $\mathbf{S} \in \mathbb{R}^{N_s \times N_t}$ and $A \in \mathbb{R}^{k \times N_t}$. This approach completely skips over the operator $\mathbf{H}$; instead, P is considered to be the empirical estimate of the linear operator $\mathbf{H}\Phi$. Subsequently, $\boldsymbol{a}$ is obtained as

$$\boldsymbol{a} \in \arg\min_{\tilde{\boldsymbol{a}}} ||\boldsymbol{s} - P\tilde{\boldsymbol{a}}||_2^2 \tag{19}$$

A.3 Deep state estimation

Deep state estimation [29] approache replaces the linear mapping between latent state and sensors with nonlinear mapping to further generalize the approach. It uses a neural network $G : \mathbb{R}^{N_s} \mapsto \mathbb{R}^{bn}$ parametrized by θ for nonlinear mapping of sensor measurements to approximate embeddings.

$$\boldsymbol{a} = G(\boldsymbol{s}, \boldsymbol{\theta}) \tag{20}$$

The neural network is trained as

$$\boldsymbol{\theta} \in \arg\min_{\tilde{\boldsymbol{\theta}}} \sum_{i=1}^{N_t} ||\boldsymbol{a}^{(i)} - G(\boldsymbol{s}^{(i)}, \tilde{\boldsymbol{\theta}})||_2^2, \tag{21}$$

where

$$\boldsymbol{a} \in \arg\min_{\tilde{\boldsymbol{a}}} ||\boldsymbol{w} - \boldsymbol{\Phi}\tilde{\boldsymbol{a}}||_2^2. \tag{22}$$

$\boldsymbol{\Phi}$ as before are the POD-modes. During testing trained neural network G approximate embeddings for sensor measurements which is used to recover full state. We refer to this method as POD based deep state estimation (PDS).

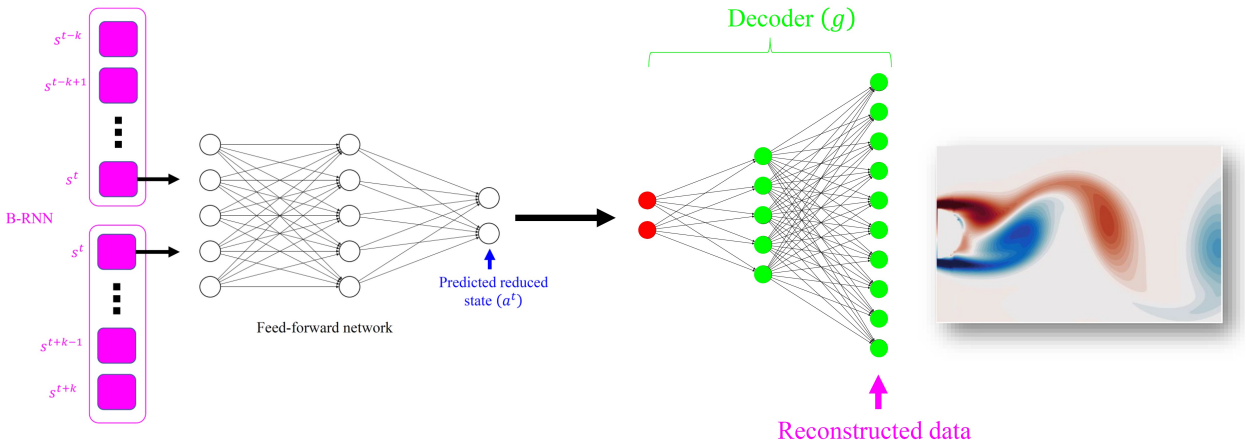

Figure 18: Schematic representation of bi-directional ARE. This is useful when both past and future sensor measurements are available.

B Bi-directional RNN

The basic idea of bidirectional recurrent neural nets (B-RNN) [55, 56] is to present each training sequence to two separate recurrent nets namely forward and backward, both of which are connected to the same output layer. (In some cases a third network is used in place of the output layer, but here we have used the simpler model). This means that for every point in a given sequence, the BRNN has complete, sequential information about all points before and after it. In this work, we have used B-RNN for solving a special state estimation problem where sensor measurements from both past and future states are available.

A Schematic representation of B-RNN used is shown in the Fig. 18. It is modified to stop propagating information after the middle time step in forward and backward network. This lowers computational time and reduce number of training weights. Thus architecture proposed is capable of using information from both ahead and behind in time. To feed sensor measurements $s^{t-k,\ldots,t+k}$ into network, data is splitted into $s^{t-k,\ldots,t}$ and $s^{t,\ldots,t+k}$ as shown in the Fig. 18. Note that although more accurate, this network can use only be used when delay in time of reconstruction is acceptable also it uses odd sequence length of sensor measurements. Output of forward and backward network is concatenated and passed to feedforward network which yields the final estimated latent representation of middle sensor measurement s^t. Thus training of $\mathscr{N}$ can be formulated as follows

$$\boldsymbol{\theta}_M^* = \arg\min_{\boldsymbol{\theta}} \sum_{i=1}^{N_{\text{samp}}} \left\| h^t - \mathscr{N}\left(\boldsymbol{s}^{t-k:t+k}; \boldsymbol{\theta}_M\right) \right\| + \lambda \left\|\boldsymbol{\theta}_M\right|_2^2, \tag{23}$$

where θ_M are parameters of combined RNN and feed-forward network $\mathscr{N} : \mathbb{R}^{N_s*(2k+1)} \mapsto \mathbb{R}^h$.

B.1 Results

The state estimation results obtained using the B-RNN based ARE is shown in Figs. 19 (periodic vortex shedding) and 20 (transient flow). For both the examples, results obtained using one and two sensors are presented. Compared to PDS, the states obtained using ARE are found to be superior. This is expected as unidirectional RNN was already providing superior results as compared to PDS. Fig. 21 shows a comparative assessment between B-RNN based ARE, and RNN based ARE. Results corresponding to one, two, five, and ten sensors are presented. For one sensor, results obtained using B-RNN based ARE significantly outperforms those obtained using RNN based ARE. However, as the number of sensors increases, the results obtained using the two approaches becomes identical. One counter-intuitive result is obtained for the periodic vortex shedding problem where the result obtained using B-RNN based ARE found to be worse than that obtained using RNN based ARE. It is probably because the neural network parameters for B-RNN has converged to a local minimum.

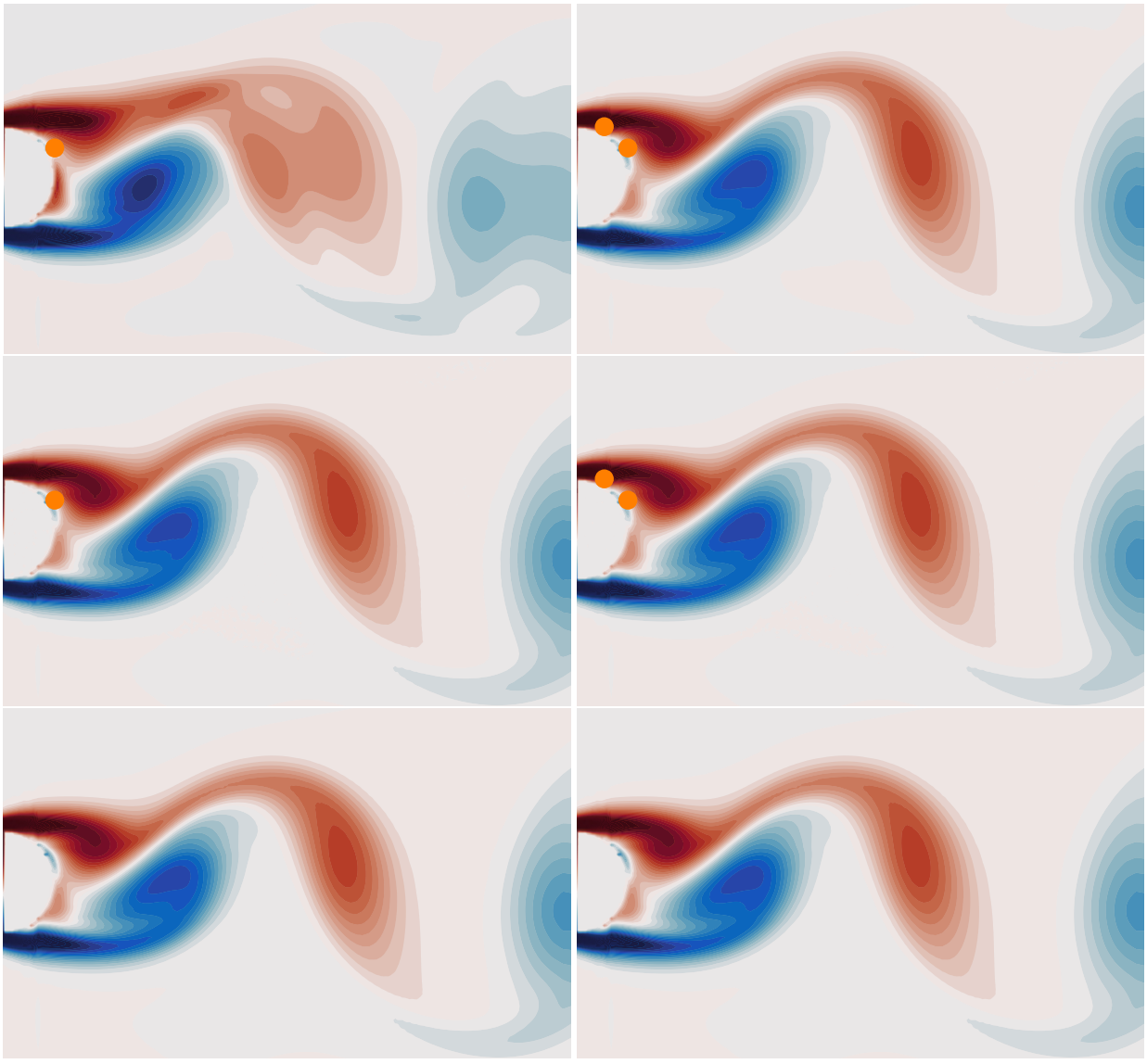

Figure 19: Figure depicts results of periodic vortex shedding for sensors=1,2. Orange dots in the images represents the location of sensor. (First row -PDS, Second row -ARE-Bidirectional, Third row -Ground truth) SEQ-LEN used for ARE model is 7

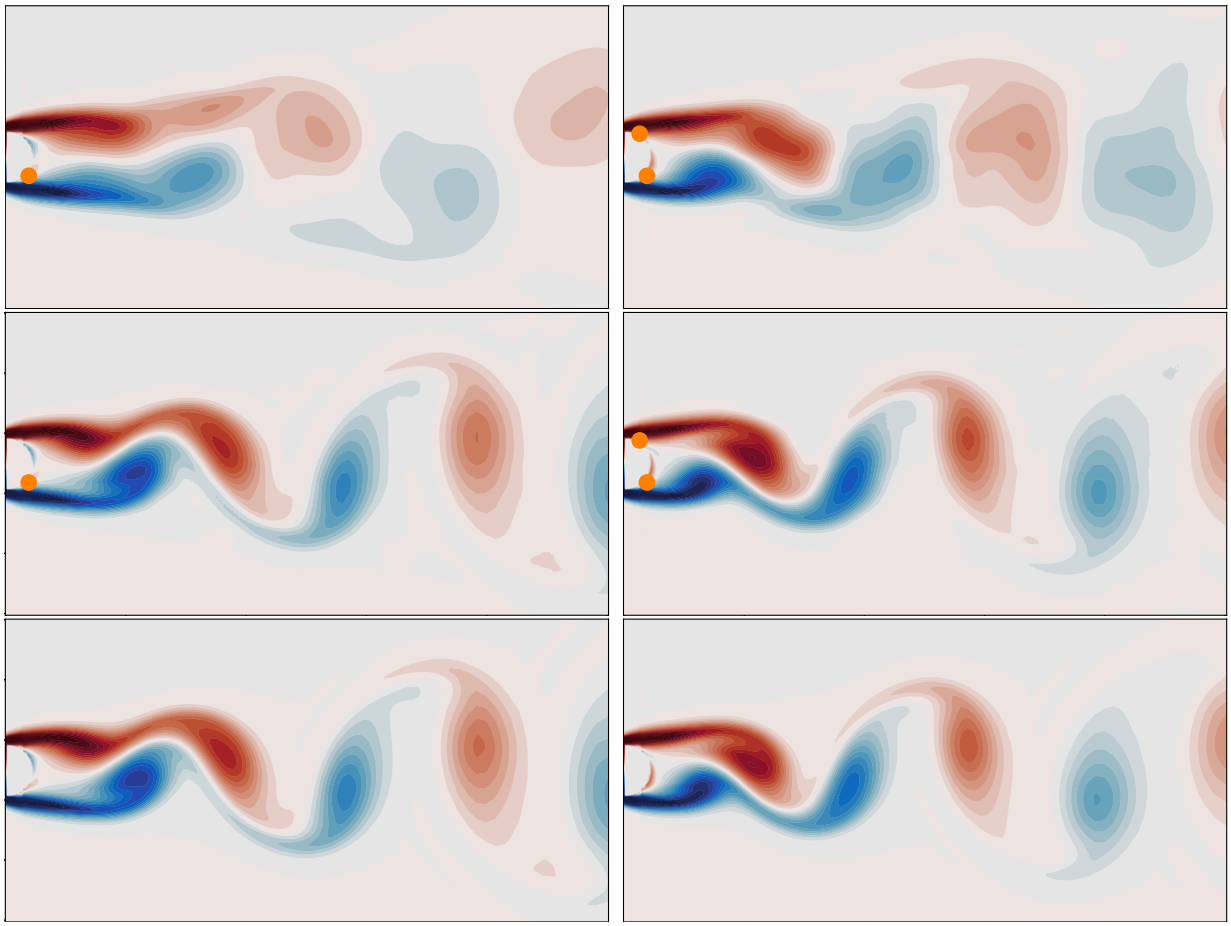

Figure 20: Figure depicts results of Transient Flow for sensors=1,2. Orange dots in the images represents the location of sensor. (First row -PDS, Second row -ARE-Bidirectional, Third row -Ground truth) SEQ-LEN used for ARE model is 11

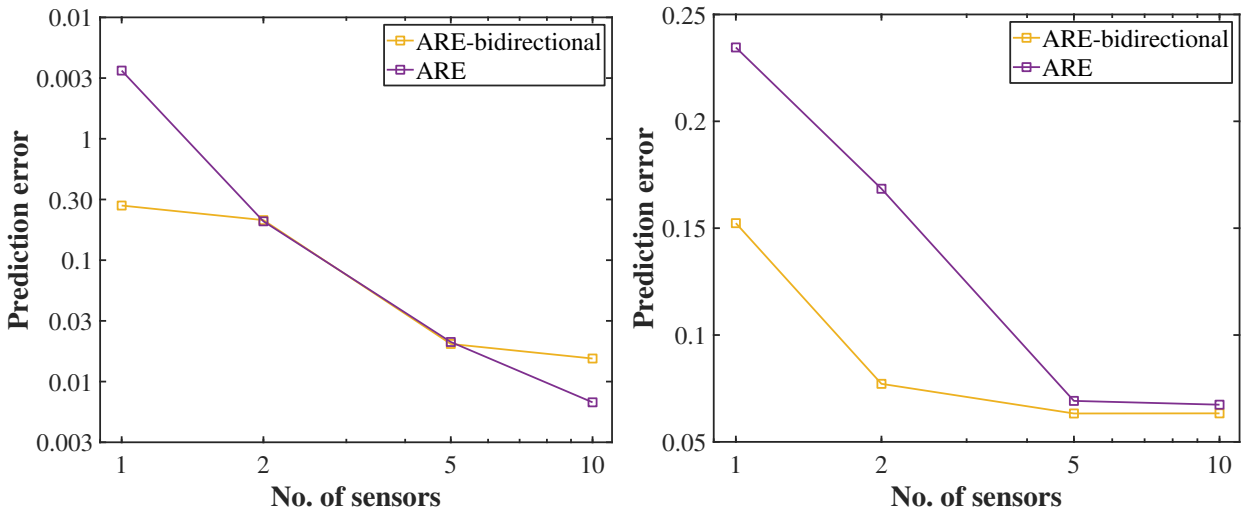

(a) Periodic vortex shedding

(b) Transient flow

Figure 21: Comparison between B-RNN based ARE and RNN based ARE

Step-down Fibonacci switched capacitor converters- a topological design method

2020 IEEE 17th India Council International Conference (INDICON) | 978-1-7281-6916-3/20/$31.00 ©2020 IEEE | DOI: 10.1109/INDICON49873.2020.9342146

Arvind Gupta
Delhi, India
arvind31297@gmail.com

Shirish Raizada
Electrical Engineering Department
Delhi Technological University
Delhi, India
raizada.shirish@gmail.com

***Abstract*— Fibonacci step down converters are an attractive proposition in the realm of integrable switching power management as they give a very high step-down ratio per capacitor as compared to other switched capacitor topologies such as series parallel, ladder. This paper puts forth a generalized method of synthesizing and describing step-down Fibonacci converters. Based on charge conservation a simplistic theoretical proof of the proposed synthesis procedure is also presented. Useful closed form expressions for parameters such as flying capacitor voltage ripple and equivalent output resistance have also been derived.**

Keywords—switched capacitor, fibonacci, step-down

I. Introduction

Reducing the size of switching power supplies is an area of research that is seeing immense activity. The majority of switching power supplies are inductor based such as (Buck, Boost, LLC etcetera). Isolation requirements make the use of a transformer a must and thus further bulk up the power processing stage. Non-isolated power supplies on the other hand require no such techniques and only use a combination of passives such as inductors, coupled inductors, and capacitors. As magnetic components take most of the space in these power supplies, scaling down their size is a quick way to bring down the overall volume of the converter. High frequency power conversion was thus adopted although with a small caveat of dominant switching losses. Switched capacitor converter, on the other hand, do away with bulky magnetics altogether. Thus, by removing magnetic components we suddenly have a drastic reduction in volume and further scope of moving towards integrated switched power solutions [8]-[14]. There are multiple papers in the literature focusing on design of switched capacitor converters [1]-[4],[15]-[18]. Of which [1]-[3],[16] focus on Fibonacci switched capacitor converters while [4],[17],[18] present charge balancing procedures for evaluating switched capacitor converters. In [2], higher order Fibonacci series in power conversion techniques is introduced while complex mathematical approach for synthesis of step-down Fibonacci converters based on the Zeckendorf Theorem is described in [3]. A comprehensive performance comparison of different SC topologies is presented in [4] and [18]. Owing to a lack of quick and straightforward approach for synthesis of step-down Fibonacci converters, a simple procedure is illustrated herein. This work was arrived at by finding a common pattern between various step-down Fibonacci topologies already presented by various authors.

This paper is divided into 4 sections. The second section provides an overview of the proposed synthesis procedure and the relevant results. The third section deals with a thorough treatment of the theoretical proof. The fourth section contains simulation results and pertinent graphical illustrations.

II. Synthesis Procedure

Fibonacci switched capacitor converters present us with step-down or step-up voltage conversion ratios that follow the Fibonacci series (1,1,2,3,5,8…..). Such switched capacitor networks give the highest conversion ratio for a given number of capacitors and operate in two phases [1]. Each phase sees the capacitor connections being altered in order to produce sub-topologies in both phases.

The synthesis procedure can be laid out in the following simple steps.

- For the desired step-down conversion 1/F(k), where F(k) is the k^{th} Fibonacci number starting from 1,1,2,3,5,8……, choose the number of capacitors as equal to k-1 [1].
- Annotate the positive and negative nodes of all the capacitors as n+ and n- respectively. The DC supply

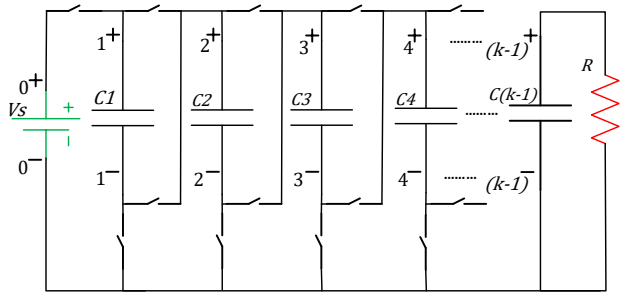

Fig. 1. Step-Down Fibonacci Switched Capacitor Converter.

978-1-7281-6916-3/20/$31.00 ©2020 IEEE

Authorized licensed use limited to: DELHI TECHNICAL UNIV. Downloaded on February 15,2021 at 10:05:07 UTC from IEEE Xplore. Restrictions apply.

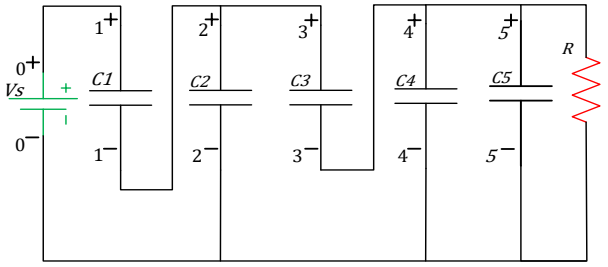

Fig. 2. k=6, phase I, Step-Down Ratio 1/8.

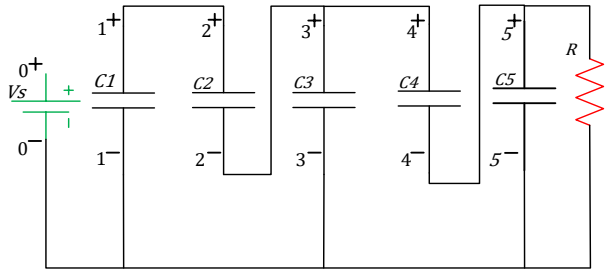

Fig. 3. k=6, phase II, Step-Down Ratio 1/8.

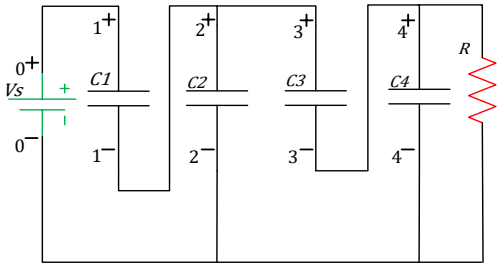

Fig. 4. k=5, phase I, Step-Down Ratio 1/5.

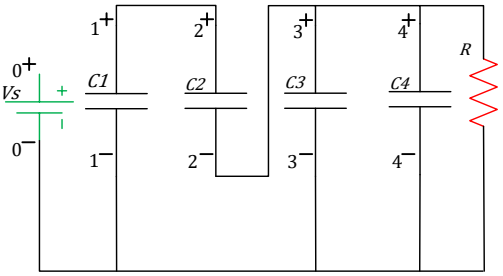

Fig. 5. k=5, phase II, Step-Down Ratio 1/5.

voltage can be annotated as 0+ and 0- whereas the capacitors starting from 1+ and 1- upto (k-1)+ and (k-1)- for the sake of clarity. This step leads to a network as shown in Fig. 1 along with the switches.

- For an even k: In the first phase, for an odd natural number 'n' where n=1,3,5,…(k-1), connect all the (n-1)+ nodes to n+ nodes, n- nodes to (n+1)+ nodes and all the (n-1)- nodes to the (k-1)- node. Connect the (k-1)+ node to the (k-2)+ node as shown in Fig. 2.

  In the second phase, for an even natural number 'n' where n=2,4,6,…(k-2), connect all the (n-1)+ nodes to n+ nodes, connect all the n- nodes to (n+1)+ nodes and all the (n-1)- nodes to the (k-1)- node. Connect the (k-1)+ node to the (k-2)- node as shown in Fig. 3.

- For an odd k: In the first phase, for an even natural number 'n' where n=2,4,6,…(k-1), connect all the (n-2)+ nodes to (n-1)+ nodes, (n-1)- nodes to n+ nodes, connect all the (n-2)- nodes to the (k-1)- node as shown in Fig. 4.

  In the second phase, for an odd natural number 'n' where n=3,5,…(k-2), connect all the (n-2)+ nodes to (n-1)+ nodes, connect all the (n-1)- nodes to n+ nodes, connect all the (n-2)- nodes to the (k-1)- node. Connect the (k-2)- node to the (k-1)- node as shown in Fig. 5.
- These steps have to be repeated for every F(k)= 1, 1,2, 3,5,8,13 …….
- All the phases will have an equal duty ratio of 50% [1].

The result of the above synthesis is a step-down switched capacitor network whose step-down ratios is summarized below in table II.

Apart from the steady state voltages across the flying capacitors and the load capacitor, their respective voltage ripple and the SC converter's equivalent output resistance also follow a pattern very similar to the Fibonacci sequence as summarized in table I and (1) respectively. Here ΔV_n is the n^{th} flying capacitor's voltage ripple, F(k) is the k^{th} Fibonacci number, I_o is the average load current, C is the capacitance value of all capacitors, f is the switching frequency and R_{on} is the switch ON resistance.

TABLE I

Flying Capacitor Voltage Ripple	Closed Form Expression
ΔV_1	$(F(1)\times I_o)/(F(k)\times C\times f)$
ΔV_2	$(F(2)\times I_o)/(F(k)\times C\times f)$
ΔV_3	$(F(3)\times I_o)/(F(k)\times C\times f)$
ΔV_4	$(F(4)\times I_o)/(F(k)\times C\times f)$
ΔV_5	$(F(5)\times I_o)/(F(k)\times C\times f)$
ΔV_6	$(F(6)\times I_o)/(F(k)\times C\times f)$
ΔV_{k-2}	$(F(k-2)\times I_o)/(F(k)\times C\times f)$

Authorized licensed use limited to: DELHI TECHNICAL UNIV. Downloaded on February 15,2021 at 10:05:07 UTC from IEEE Xplore. Restrictions apply.

TABLE II

k	Fibonacci Step-Down Ratio
4	1/3
5	1/5
6	1/8
7	1/13
8	1/21

$$R_{eq}=\frac{2R_{on}}{(F(k))^2}\left\{\left(3\sum_{n=1}^{k-2}(F(n))^2\right)+(F(k-1))^2\right\} \quad (1)$$

III. Theoretical Proof

A. Steady State Capcitor Voltages

In this section, a charge balancing procedure will be followed for each and every capacitor in the sequence. This procedure is followed because it gives a clear proof of the fact that the voltages across all the capacitors in a Fibonacci converter also follow the Fibonacci sequence as mentioned in [1]. The proof will be shown for k=7 (i.e. for 6 capacitors). Given below in Fig. 6 and Fig. 7 are topological views of the six-capacitor circuit in its two phases.

Before we start, we would like the reader to keep in mind the following assumptions that have been made so as to arrive at gross results having practical significance:

1. Odd numbered capacitors undergo charging in the first phase and even numbered capacitors in the second phase.

2. The frequency of operation and the value of capacitances are assumed to be high enough so as to render a near linear voltage ripple on the capacitors.

3. The time period of the switching operation of the SC converter is small in comparison to the RC time constant of the load.

4. All capacitors have the same value C.

Capacitor voltages are represented by V_{np} for the n^{th} capacitor (C_n) at the end of the p^{th} phase. In steady state, the charge (Q_{np}) gained by a capacitor in one phase is simultaneously lost in the next phase. Thus, looking at C_1 we have for phase I:

$$Q_{11}=C\times(V_{11}-V_{12}) \quad (2)$$

For phase II, this same charge is lost by C_1.

Thus, we have:

$$Q_{11}=-Q_{12}=C\times(V_{22}-V_{21}) \quad (3)$$

Using the above two equations, we have:

$$C\times(V_{11}-V_{12})=-C\times(V_{21}-V_{22}) \quad (4)$$

From Fig. 6 we see that:

$$V_{21}=V_s-V_{11} \quad (5)$$

And from Fig. 7, using the voltage divider rule:

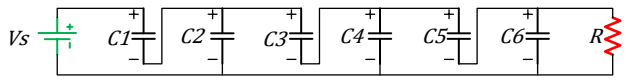

Fig. 6. k=7, phase I, Step-Down Ratio 1/13.

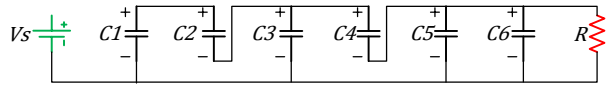

Fig. 7. k=7, phase II, Step-Down Ratio 1/13.

$$V_{22}=\frac{5}{8}\times V_{12} \quad (6)$$

Substituting the above two in (4), we have:

$$V_{11}-V_{12}=-V_s+V_{11}+\frac{5}{8}V_{12} \quad (7)$$

We can rewrite V_{np} as:

$$V_{np}=V_{n,avg}\pm\frac{\Delta V_n}{2} \quad (8)$$

Where the '+' or '-' sign depends on 'n'.

Now, going back to (7), we see that:

$$\Delta V_1=-V_s+\frac{13}{8}V_{1,avg}+\frac{3}{16}\Delta V_1 \quad (9)$$

Solving, we get:

$$V_{1,avg}-\frac{1}{2}\Delta V_1=\frac{8}{13}V_s \quad (10)$$

We will assume $\Delta V_1 \ll V_{1,avg}$, and thus, finally for capacitor C_1 we have:

$$V_{1,avg}=\frac{8}{13}V_s \quad (11)$$

In the same manner, the average capacitor voltages for the remaining five capacitors can be found and they are listed below:

$$V_{2,avg}+\frac{\Delta V_2}{2}=\frac{5}{13}V_s \quad (12)$$

$$V_{3,avg}+\frac{\Delta V_3}{2}=\frac{3}{13}V_s \quad (13)$$

$$V_{4,avg}-\frac{\Delta V_4}{2}=\frac{2}{13}V_s \quad (14)$$

$$V_{5,avg}+\frac{\Delta V_5}{2}=\frac{V_s}{13}+\frac{Q_{o2}}{C} \quad (16)$$

$$V_{6,avg}-\frac{\Delta V_6}{2}=\frac{V_s}{13}-\frac{Q_{o1}}{C} \quad (17)$$

Where Q_{o2} and Q_{o1} are the charges transferred to the load in the second and first phase respectively as in Fig. 9 and Fig. 10, and $Q_{o2}+Q_{o1}=Q_o$ (total charge flowing through load per switching cycle).

And in a similar manner to (11):

$$V_{2,avg}=(5/13)V_s \quad (18)$$

$$V_{3,avg}=(3/13)V_s \quad (19)$$

$$V_{4,avg}=(2/13)V_s \quad (20)$$

$$V_{5,avg}=\frac{V_s}{13} \quad (21)$$

$$V_{6,avg}=\frac{V_s}{13} \quad (22)$$

This procedure when extended for other values of k yields the same result: The voltage across the flying capacitors of a Fibonacci switched capacitor converter follow the Fibonacci sequence, albeit in a reversed manner.

B. Equivalent Output Resistance

SC converters can be represented by an ideal DC transformer, as shown in Fig. 8, and a series resistance [1]. For the topic of this discussion, invoking third assumption makes it easier for us to relate this output resistance to the switch ON resistances R_{on} [4]-[6]. As a 1/N voltage transformer transforms current as $I_o = N \times I_{in}$, the charge also follows the same conversion ratio: $Q_{in}=Q_o/N$. Referring to Fig. 8, it is seen that the resultant load voltage V_o would be lower than the ideal

Authorized licensed use limited to: DELHI TECHNICAL UNIV. Downloaded on February 15,2021 at 10:05:07 UTC from IEEE Xplore. Restrictions apply.

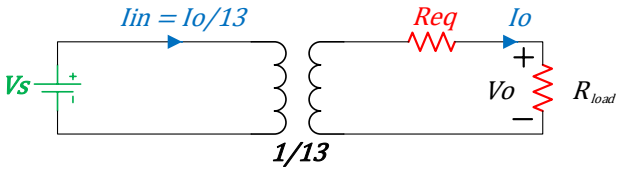

Fig. 8. DC Transformer Model of a 1/13 Switched capacitor converter.

$V_s/13$ but the load current I_o would be exactly equal to $13\times I_{in}$. Using the charge conservation theorem, the two topological states in the two phases of the 1/13 Fibonacci converter are shown below in Fig. 9 and Fig. 10, this time including the switch ON resistances also. Note the charge shown flowing through each capacitor is the total charge that has flown through each capacitor till the conclusion of each phase. For a charge Q flowing through a resistor R for a time T (frequency f), the average resistive power loss P will be equal to:

$$P=R\times\left(\frac{Q}{T}\right)^2=R\times(Q\times f)^2 \tag{23}$$

And thus, going back to Fig. 9 and Fig. 10, we see that:

$$P_1=4\times R_{on}\left(\frac{f}{13}\right)^2\begin{Bmatrix}3\times(Q_o)^2+2\times(2Q_o)^2\\+(3Q_o)^2+2\times(5Q_o)^2\end{Bmatrix} \tag{24}$$

$$P_2=4\times R_{on}\left(\frac{f}{13}\right)^2\begin{Bmatrix}3\times(Q_o)^2+(2Q_o)^2+\\2\times(3Q_o)^2+(5Q_o)^2+(8Q_o)^2\end{Bmatrix} \tag{25}$$

Where P_1 and P_2 are average resistive power losses in the respective phases. The total average power loss over the two phases can be written as: $P_{L,avg}=(P_1+P_2)/2$.

Using (24) and (25), we see that:

$$P_{L,avg}=2R_{on}\left(\frac{f}{13}\right)^2\begin{Bmatrix}6\times(Q_o)^2+3\times(2Q_o)^2\\+3\times(3Q_o)^2+3\times(5Q_o)^2\\+(8Q_o)^2\end{Bmatrix} \tag{26}$$

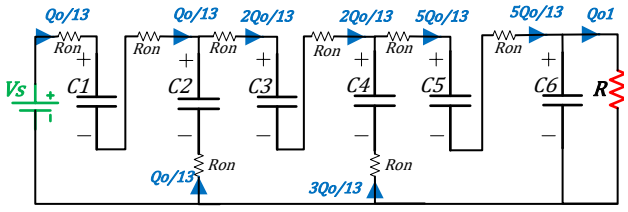

Fig. 9. k=7, phase I.

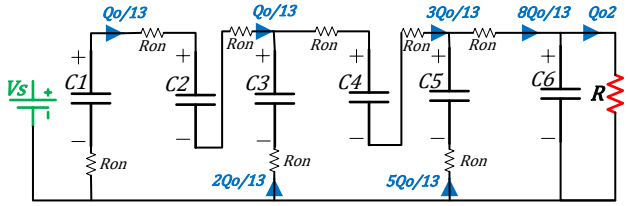

Fig. 10. k=7, phase II.

Equating this total average power loss to that through an equivalent resistance in the transformer model of Fig. 8 for an 1/13 SC converter, we have:

$$P_{L,avg}=R_{eq}(f\times Q_o)^2 \tag{27}$$

And, thus from (26) and (27):

$$R_{eq}=2R_{on}\left(\frac{1}{13}\right)^2\begin{Bmatrix}6+3(2)^2\\+3(3)^2\\+3(5)^2\\+(8)^2\end{Bmatrix}=\frac{368}{169}R_{on} \tag{28}$$

This result will also be obtained by plugging k=7 in (1).

C. *Voltage Ripple on Flying Capacitors*

For voltage stringent POL applications, the voltage ripple on each capacitor starts to play an important role [7].

Referring to Fig. 9 and Fig. 10 we see that:

$$\Delta V_1=\frac{Q_o}{13C}=\frac{I_o}{13Cf} \tag{29}$$

$$\Delta V_2=\frac{I_o}{13Cf} \tag{30}$$

$$\Delta V_3=\frac{2I_o}{13Cf} \tag{31}$$

$$\Delta V_4=\frac{3I_o}{13Cf} \tag{32}$$

$$\Delta V_5=\frac{5I_o}{13Cf} \tag{33}$$

Again, the same result is obtained by substituting k=7 in table I.

IV. Simulation Results

A. *Equivalent Output Resistance*

Using (1), given in Fig. 11 is a stem graph showing the variation of the normalized equivalent output resistance R_{eq}/R_{on} with the step-down ratio F(k).

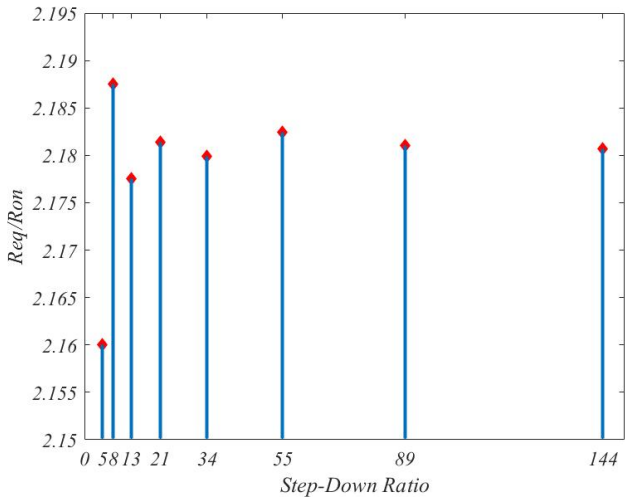

Fig. 11. Normalized output resistance vs Step-Down Ratio.

Authorized licensed use limited to: DELHI TECHNICAL UNIV. Downloaded on February 15,2021 at 10:05:07 UTC from IEEE Xplore. Restrictions apply.

B. Load Steady State Voltage

Fig. 12 – Fig. 14 shows the MATLAB simulation results for a fixed supply voltage V_s=13 V, F(k)=13 and R_{on}=2.43 mΩ comparing the theoretical work with simulation. The theoretical load voltage V_o is calculated using the voltage divider rule in Fig. 8:

$$V_o=\left(\frac{V_s}{13}\right)\left(\frac{R_{load}}{R_{eq}+R_{load}}\right) \tag{34}$$

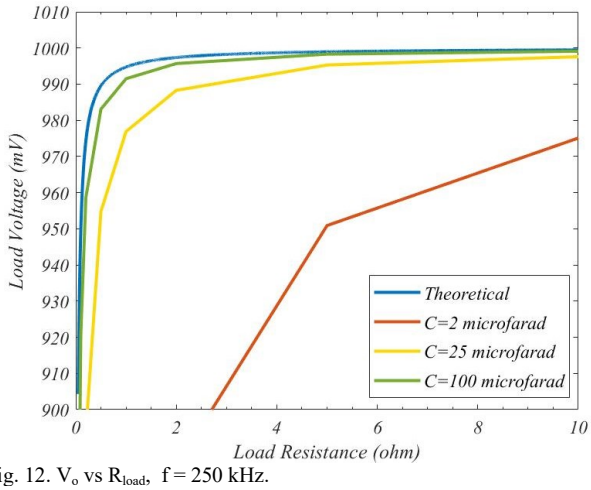

Fig. 12. V_o vs R_{load}, f = 250 kHz.

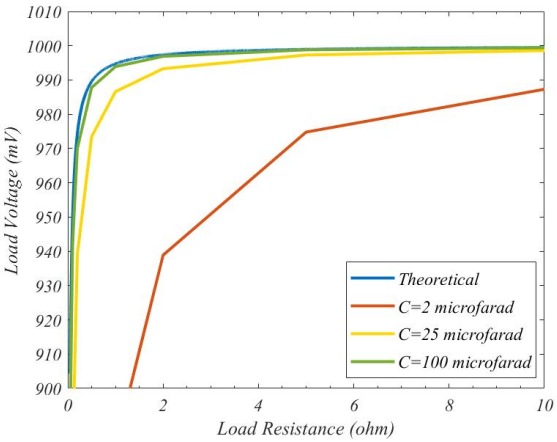

Fig. 13. V_o vs R_{load}, f = 500 kHz.

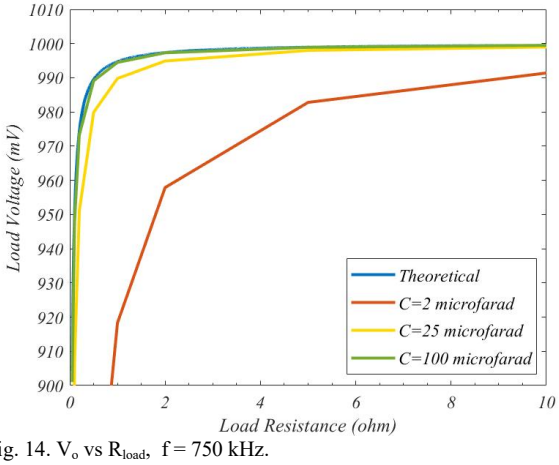

Fig. 14. V_o vs R_{load}, f = 750 kHz.

Note that in accordance with our assumptions, the simulated and theoretical results follow each other closely for values of T=1/f very small than τ (the load RC time constant).

C. Flying Capacitor Voltage Ripple

For illustrative purposes, the theoretical and simulated voltage ripple on C_2 for a 1/13 Fibonacci SC converter, for V_s=13V, is shown in Fig. 15 – Fig. 17. As can be seen, the theoretical and simulated results are in excellent agreement for the switching time period small as compared to τ.

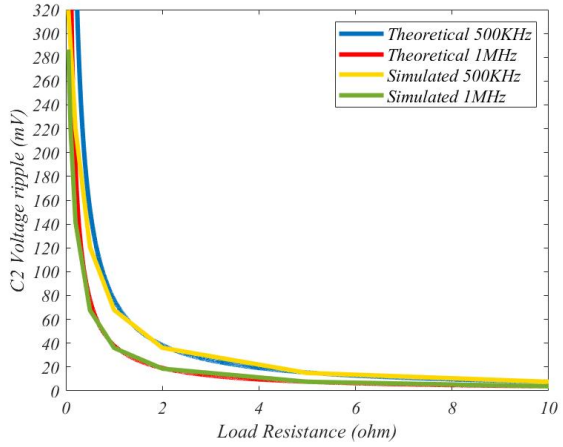

Fig. 15. ΔV_2 vs R_{load}, C = 2 µF.

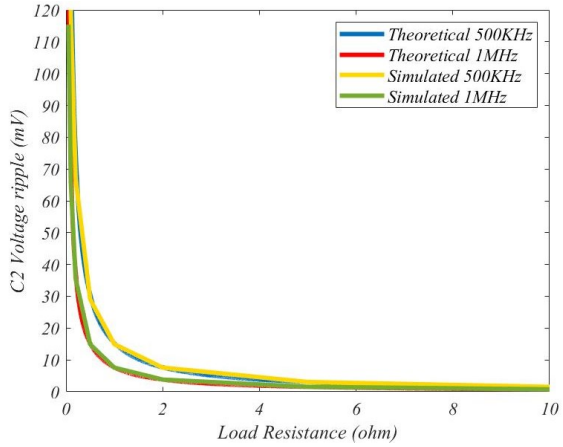

Fig. 16. ΔV_2 vs R_{load}, C = 10 µF.

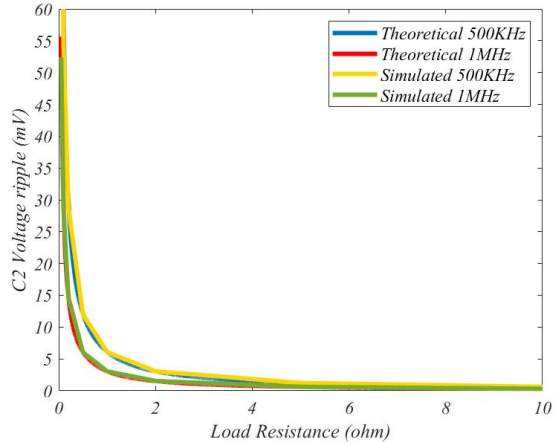

Fig. 17. ΔV_2 vs R_{load}, C = 25 µF.

Authorized licensed use limited to: DELHI TECHNICAL UNIV. Downloaded on February 15,2021 at 10:05:07 UTC from IEEE Xplore. Restrictions apply.

D. Output Voltage For Various Step-Down Ratios

The results in Fig. 18 – Fig. 19 are presented for f=750kHz, C=25µF, $V_{k\text{-}1,avg}$=1V, R_{on}=2.43mΩ. The parameters were chosen so as to showcase the RC time constant conditions under which the theoretical results hold.

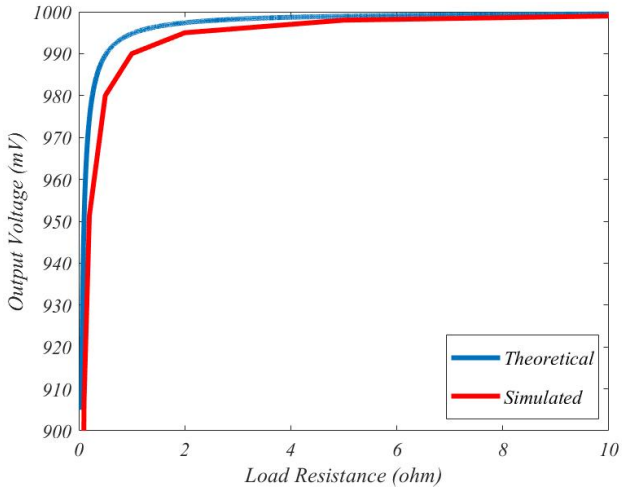

Fig. 18. V_o vs R_{load}, Step-Down Ratio 1/5.

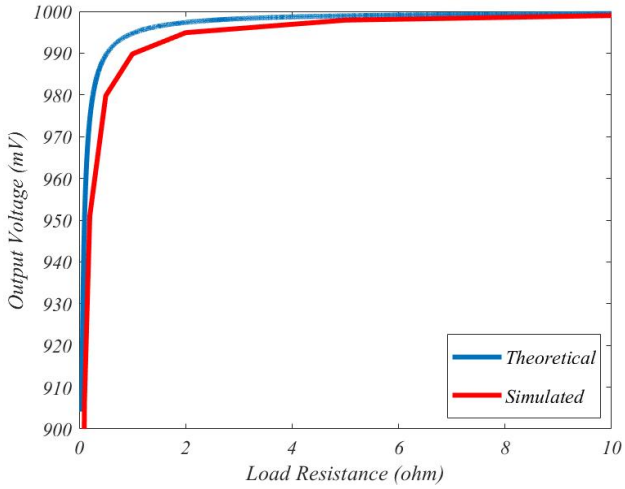

Fig. 19. V_o vs R_{load}, Step-Down Ratio 1/8.

CONCLUSION

A topological synthesis method for step-down switched capacitor Fibonacci converters was presented. The proofs for steady state capacitor voltages, flying capacitor voltage ripple and equivalent output resistance were presented. It was noted that the above state parameters follow the Fibonacci sequence as well. Finally, it is shown through various simulation results that the simulated results and predicted results will be in good agreement if the switching time period is small compared to the RC time constant of the load.

REFERENCES

[1] Marek S.Makowski and Dragan Maksimovic, "Performance Limits of Switched Capacitor DC-DC converters," IEEE Power Electronics Specialists Conf. (PESC), Vol. 2, pp. 1215-1221, June 1995.

[2] Kei Eguchi, Motoki Shimoji, Satsuki Hirata and Hongbing Zhu, "Design of a Step-Up/Step-Down *k* (= 2, 3, ···)-Fibonacci DC-DC Converter Designed by Switched-Capacitor Techniques," IEEE International Conference on Intelligent Networks and Intelligent Systems, pp. 170-173, 2012.

[3] Alexander Kushnerov and Sam Ben Yaakov, "Algebraic Synthesis of Fibonacci Switched Capacitor Converters," IEEE International Conf. on Microwaves, Communictions, Antennas and Electronic Systems, pp. 170-173, Nov. 2011.

[4] Michael Douglas Seeman, "A Design Methodology for Switched-Capacitor DC-DC Converters," Phd Dissertation UC Berkeley, Spring 2009.

[5] Sam Ben Yakov, "Behavioral Average Modeling and Equivalent Circuit Simulation of Switched Capacitors Converters," IEEE Transactions On Power Electronics, Vol. 27, No. 2, pp. 632-636, Feb. 2012

[6] T. Souvignet, B. Allard and X. Lin-shi, "Sampled-Data Modeling of Switched-Capacitor Voltage Regulator With Frequency-Modulation Control," IEEE Transactions on Circuits and Systems, Vol.62, No.4, pp. 957-966, April 2015.

[7] Philip T.Krein, "Data Center Challenges and Their Power Electronics," CPSS Transactions On Power Electronics And Applications, Vol. 2, No. 1, pp. 39-46, March 2017.

[8] Leland Chang, Robert K. Montoye, Brian L. Ji, Alan J. Weger, Kevin G. Stawiasz, and Robert H. Dennard "A Fully-Integrated Switched-Capacitor 2:1 Voltage Converter with Regulation Capability and 90% Efficiency at 2.3A/mm2," IEEE Symposium on VLSI Circuits/Technical Digest of Technical Papers, pp. 55-56, 2010.

[9] Toke M. Andersen, Florian Krismer, Johann W. Kolar, Thomas Toifl, Christian Menolfi, Lukas Kull, Thomas Morf, Marcel Kossel, Matthias Brandli, Peter Buchmann, Pier Andrea Francese, "A 4.6W/mm2 Power Density 86% Efficiency On-Chip Switched Capacitor DC-DC Converter in 32nm SOI CMOS," IEEE Applied Power Electronics Conf. and Exposition (APEC), pp. 692-699, Mar. 2013.

[10] S. M. Ahsanuzzaman, Aleksandar Prodic and David A. Johns, "An Integrated High-Density Power Management Solution for Portable Applications Based on a Multioutput Switched-Capacitor Circuit," IEEE Transactions On Power Electronics, Vol. 31, No. 6, pp. 4305-4323, June 2016.

[11] John F. Dickson, "On-Chip High-Voltage Generation in MNOS Integrated Circuits Using an Improved Voltage Multiplier Technique," IEEE Journal Of Solid-State Circuits, Vol. SC-11, No. 3, pp.374-378, June 1976.

[12] T.M Andersen, F. Krismer, J.W Kolar, T. Toifl, C. Menolfi, L. Kull, T.Morf, M. Kossel, M. Brändli, P. Buchmann, P.A Francese, "Sub-ns Response On-Chip Switched-Capacitor DC-DC Voltage Regulator Delivering 3.7W/mm2 at 90% Efficiency Using Deep-Trench Capacitors in 32nm SOI CMOS," IEEE International Solid State Conference, pp. 90-92, Feb. 2014.

[13] H.P Le, M. Seeman, Seth R. Sanders, Visvesh Sathe, Samuel Naffziger, Elad Alon, "A 32nm Fully Integrated Reconfigurable Switched Capacitor DC-DC Converter Delivering 0.55W/mm2 at 81% Efficiency," IEEE International Solid State Conference, pp. 210-212, Feb. 2010.

[14] H.P Le, S.R Sanders, Elad Alon, "Design Techniques for Fully Integrated Switched-Capacitor DC-DC Converters," IEEE Journal Of Solid-State Circuits,Vol.46, No.9, pp. 2120-2131, Sept. 2011.

[15] Gaetano Palumbo and Domenico Pappalardo,"Charge Pump Circuits: An Overview on Design Strategies and Topologies," IEEE Circuits And Systems Magazine, pp. 31-45, First Quarter 2010.

[16] Ratanaubol Rubpongse, Wanglok Do and Kei Eguchi, "The Development of K^N Voltage Gain Switched Capacitor DC-DC Converter Based on Parallel Fibonacci-Type Converter," IEEE Conf. on Engineering Applied Sciences and Technology (ICEAST), 2019.

[17] P.M Lin and Leon O.Chua, "Topological Generation and Analysis of Voltage Multiplier Circuits," IEEE Transactions On Circuits And Systems, Vol. CAS-24, No. 10, pp. 517-530 Oct. 1977

[18] Michael D. Seeman and Seth R. Sanders, "Analysis and Optimization of Switched-Capacitor DC–DC Converters," IEEE Transactions On Power Electronics, Vol. 23, NO. 2, pp. 841-851, March 2008.

Authorized licensed use limited to: DELHI TECHNICAL UNIV. Downloaded on February 15,2021 at 10:05:07 UTC from IEEE Xplore. Restrictions apply.

Digital Signal Processing ••• (••••) ••••••

Contents lists available at ScienceDirect

Digital Signal Processing

www.elsevier.com/locate/dsp

Stochastic filtering based transmissibility estimation of novel coronavirus

Rahul Bansal [a], Amit Kumar [b], Amit Kumar Singh [c], Sandeep Kumar [d,*]

[a] ECE Department, Ajay Kumar Garg Engineering College, Ghaziabad, India
[b] CS Department, Dyal Singh College, University of Delhi, Delhi, India
[c] CS Department, Ramanujan College, University of Delhi, Delhi, India
[d] Central Research Laboratory, BEL, Ghaziabad, Uttar Pradesh, India

ARTICLE INFO

Article history:
Available online xxxx

Keywords:
Novel coronavirus
Extended Kalman filter
State space model
Transmissibility estimation

ABSTRACT

In this study, the transmissibility estimation of novel coronavirus (COVID-19) has been presented using the generalized fractional-order calculus (FOC) based extended Kalman filter (EKF) and wavelet transform (WT) methods. Initially, the state-space representation for the bats-hosts-reservoir-people (BHRP) model is obtained using a set of fractional order differential equations for the susceptible-exposed-infectious-recovered (SEIR) model. Afterward, the EKF and Kronecker product based WT methods have been applied to the discrete vector representation of the BHRP model. The main advantage of using EKF in this system is that it considers both the process and the measurement noise, which gives better accuracy and probable states, which are the Markovian (processes). The importance of proposed models lies in the fact that these models can accommodate conventional EKF and WT methods as their special cases. Further, we have compared the estimated number of contagious people and recovered people with the actual number of infectious people and recovered people in India and China.

© 2021 Elsevier Inc. All rights reserved.

UNCORRECTED PROOF

1. Introduction

The novel coronavirus (COVID-19) disease has emerged as the world's biggest outbreak of the century. It is a positive sensed group of the single-standard ribonucleic acid (RNA) virus, which belongs to the coronavirdae family. These viruses cause a mild infectious disorder that leads to severe acute respiratory syndrome (SARS) in mammals [1–3]. Since the infection of COVID-19 is spreading faster, and until now, there is no approved vaccine available for its prevention and control, its transmissibility estimation is of utmost importance. Several methods have been proposed in the literature for the transmissibility estimation of COVID-19 [4–8]. In [4], Zhao et al. estimated the reproduction rate of coronavirus in China, and they found out that the early outbreak data largely follows the exponential. Li et al. [5] presented a mathematical model for estimating the reproduction number regarding coronavirus's confirmed cases. Lauer et al. [6] presented an incubation period estimation of coronavirus disease and studied its implication on public health. The method proposed in [6] gives good results for mild cases, but its performance falls with the patients' severity. The susceptible-exposed-infectious-recovered (SEIR) is one of the most popular estimation models in the literature, and Tang et al. [7] estimated the transmission risk of COVID-19 disease using this method. In [8], Fanelli et al. Fanelli et al. proposed susceptible infected recovered dead (SIRD) model-based estimation of COVID-19.

Several parametric Bayesian methods are useful for the parameter estimation of Gaussian and non-Gaussian systems in which states are Markov process. Different parametric Bayesian estimation methods are available in the literature [9–32] are described in Table 1. For the non-Gaussian systems, Bayesian computation of conditional probabilities has been used for updating the weights involved in the state estimation. This method can be applied for Markovian state dynamics, i.e., the input is represented using the Ornstein-Uhlenbeck (O.U.) process; further, it is added to the state process to get a non-Gaussian Markov process of larger size. Using the extended Kalman filter (EKF) method, a more accurate estimation of COVID-19 can be performed as the nonlinear dynamical system is modeled as an O.U. process that accounts for both white noise and the Brownian process. EKF is derived from a real-time estimator, i.e., Kushner Kallainpur filter, and

* Corresponding author.
E-mail addresses: rahulbansal1591@gmail.com (R. Bansal), amitbansal06@gmail.com (A. Kumar), amit.scss@gmail.com (A.K. Singh), sann.kaushik@gmail.com (S. Kumar).

https://doi.org/10.1016/j.dsp.2021.103001
1051-2004/© 2021 Elsevier Inc. All rights reserved.

Table 1
State estimation literature survey.

Method	Merits	Limitations	Applications
WLS*	Real-time modeling.	(i) Inaccurate estimations. (ii) Limited to static systems.	Electrical power systems [9].
KF**	(i) Least computational burden. (ii) Accurate estimation for linear systems. (iii) Real-time estimation.	(i) Limited to linear systems but fails for nonlinear systems. (ii) Applicable for Gaussian noise.	(i) Electrocardiogram [10]. (ii) Epidemic model of chronic disease [11]. (iii) Power system state estimation [12]. (iv) Electromagnetic field estimation [13].
H_∞ filter	(i) Accurate estimation even for strongly nonlinear system. (ii) Considers process and measurement noise as non-Gaussian process.	(i) Real-time implementation constraints. (ii) Fundamental time domain behavior is not addressed when deals with frequency domain.	(i) Optimal control method for bioneuron [14]. (ii) Blood glucose level optimal control [15]. (iii) Multi-agent financial models [16].
PF***	(i) Better estimation for strongly nonlinear system. (ii) State process is non-Gaussian process which gives improved accuracy.	(i) Particle degradation results in estimation error.	(i) Electrocardiogram denoising [17]. (ii) Cancer patient treatment systems [18] (iii) Heart rate estimation [19].
EKF	(i) Real-time estimations (ii) Moderate computational complexity. (iii) Ideal for weakly and mildly nonlinear systems	(i) Fails for strongly nonlinear system.	(i) Electronics engineering [20], [21]. (ii) Biomedical engineering [22], [23]. (iii) Wireless communication [24].
WT	(i) Lesser data stored. (ii) Compressed data. (iii) Better for weakly and mildly nonlinear systems	(i) Fails for strongly nonlinear system. (ii) Not real time estimation.	(i) Electronics engineering [21], [27]. (ii) Biomedical engineering [28], [29].
UKF	(i) Accurate estimations (ii) Moderate computational complexity. (iii) It can be used with discontinuous transformation.	(i) Larger computational time.	(i) Electrical power systems [30]. (ii) Power plant [31]. (iii) Human arm motion tracking [32].

* Weighted least squares.
** Kalman filter.
*** Particle filter.

has several applications in electronics engineering and biomedical engineering. The main advantage of EKF is that it uses the stochastic approach for estimation; i.e., it considers measurement noise and process noise; consequently, it provides better accuracy. EKF gives the joint evaluation of conditional mean and conditional error covariance; therefore, it provides better estimates than the conventional SEIR model. Recently, the wavelet transform (WT) method has been used in state and parameter estimation of various systems [21][27–29]. In this method, different minimum and maximum frequencies are used for each time slot.

Recently, fractional-order calculus (FOC) has been popular amongst researchers in the arena of mathematical analysis [33][34]. FOC has several advantages over conventional calculus, and therefore several phenomena can better be explained using the FOC. The main advantage of FOC based model representation is that it can be considered as a superset of integer-order calculus. The FOC based model is more accurate than the other integer-order modeling methods presented in the literature. Moreover, the fractional-order process has a simplified model structure and less computational complexity without compromising the model's accuracy. Furthermore, estimation and prediction of transmissibility of any disease can be investigated in a more generalized way using the fractional-order differential equations due to its property of huge global memory. Recently, fractional-order calculus theory has been used in the mathematical modeling of biological systems [35–43] as shown in Table 2. Given the several advantages of FOC-based models in terms of the generalized and flexible solution with high accuracy, it is important to investigate the accuracy of these models for the COVID-19 case. Although there are many works in the literature related to the transmutability estimation of COVID-19, none of the previous works have investigated the performance of the prediction model using FOC based EKF and WT methods by transforming the dynamical state equations using Kronecker product (tensor product) [44][45] into a form, where the gradient algorithm can be applied. The importance of these models lies in the fact that these models can accommodate conventional EKF [26] and WT methods as their special cases. We have also considered bats-hosts-reservoir-people (BHRP) transmission modes [46] for our study. We obtained a continuous-time BHRP based SEIR deterministic mathematical model. This continuous-time deterministic model is converted to a stochastic model by introducing noise to the state-space equations. Then, it is discretized using the Euler-Maruyama method to obtain discrete-time state-space equations to apply the EKF algorithm. Such investigation is essential in the estimation of resources required to fight against this epidemic. Motivated by this, we have performed a detailed analysis of FOC-based EKF and WT methods for the transmissibility estimation of COVID-19. We can summarize the key contributions of the paper as

- We have proposed the FOC based EKF and WT nonlinear system for transmissibility estimation of COVID-19.
- To improve the accuracy of nonlinear systems in WT method, Kronecker product-based fractional-order system is presented.
- We extensively analyzed the developed models and their special cases for different values of the parameters to estimate the COVID-19 contagious and recovered people.
- The comparison between the transmissibility estimation of COVID-19 using real-time EKF algorithm and block processing based WT method has been provided for different values of the system parameters.

UNCORRECTED PROOF

Table 2
Recent fractional order calculus applications in biomedical science.

S. No.	Applications	References
1.	Electrocardiogram	Miljkovic et al. [35], Popovic et al. [36]
2.	Epidemic model	Rihan et al. [37], Rihan et al. [38], Latha et al. [39]
3.	State/parameter estimation	Mawonou et al. [40], Hidalgo et al. [41], Wang et al. [42], Huang et al. [43]

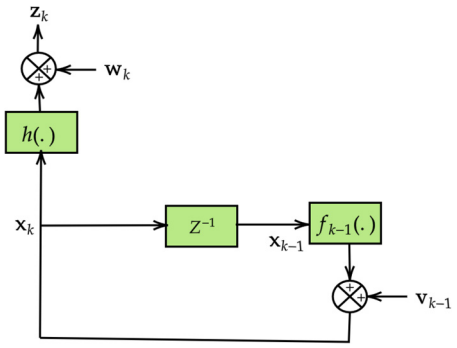

Fig. 1. Representation of dynamical system.

The rest of the paper is organized as follows: A brief introduction to EKF and FOC is presented in Section 2 and Section 3. Section 4 presents the state-space modeling of SEIR based BHRP transmission network model. The application of EKF to the BHRP transmission network model is given in Section 5. Kronecker product based fractional-order system representation using the WT method is presented in Section 6. Discussion on results and concluding remarks are given in Section 7 and Section 8, respectively.

2. Extended Kalman filter

Following notations have been used throughout the paper:-

(i) Cap on the bold lower case letters denotes estimated value e.g. $\hat{\mathbf{x}}$.
(ii) Random variables ($\mathbf{x}_k, \mathbf{z}_k, \mathbf{v}_k, \mathbf{w}_k$) are denoted using bold lower case letters.
(iii) Bold italic lower case letters denote deterministic vectors ($\boldsymbol{u}_k$).
(iv) Bold italic capital letters denote matrices ($\boldsymbol{F}_k, \boldsymbol{H}_k, \boldsymbol{Q}_k, \boldsymbol{R}_k, \boldsymbol{B}_k, \boldsymbol{P}_k, \boldsymbol{L}_k, \boldsymbol{M}_k$).

Consider a nonlinear dynamical system as shown in Fig. 1. Mathematically, it can be represented as

$$\mathbf{x}_k = \mathbf{f}_{k-1}(\mathbf{x}_{k-1}, \boldsymbol{u}_{k-1}, \mathbf{v}_{k-1}), \tag{1}$$

$$\mathbf{z}_k = \mathbf{h}_k(\mathbf{x}_k, \mathbf{w}_k), \tag{2}$$

where $\mathbf{x}_k \in \mathbb{R}^n$ denotes the state vector and $\mathbf{z}_k \in \mathbb{R}^p$ is the measurement vector at time k, $\mathbf{f}_k(.) : \mathbb{R}^n \times \mathbb{R}^d \to \mathbb{R}^n$ and $\mathbf{h}_k(.) : \mathbb{R}^n \times \mathbb{R}^l \to \mathbb{R}^p$ are the nonlinear functions of the nonlinear dynamical system. $\mathbf{u}_k$ is the known input vector. $\mathbf{v}_k \in \mathbb{R}^d$ and $\mathbf{w}_k \in \mathbb{R}^l$ are the process noise and measurement noise respectively, having zero mean white Gaussian noise with covariance $\boldsymbol{Q}_k$ and $\boldsymbol{R}_k$ respectively. Expand equations (1) and (2) using Taylor series expansion, we have

$$\mathbf{x}_k \approx f_{k-1}(\hat{\mathbf{x}}_{k-1|k-1}) + \boldsymbol{F}_{k-1}(\mathbf{x}_{k-1} - \hat{\mathbf{x}}_{k-1|k-1}) + \boldsymbol{L}_{k-1}(\Delta\mathbf{v}_{k-1}), \tag{3}$$

$$\mathbf{z}_k \approx h_k(f_{k-1}(\hat{\mathbf{x}}_{k-1|k-1})) + \boldsymbol{H}_k(\mathbf{x}_k - f_{k-1}(\hat{\mathbf{x}}_{k-1|k-1})) + \boldsymbol{M}_k(\Delta\mathbf{w}_k), \tag{4}$$

where $\Delta\mathbf{x}_{k-1} = \mathbf{x}_{k-1} - \hat{\mathbf{x}}_{k-1|k-1}$ and $\Delta\mathbf{x}_k = \mathbf{x}_k - \hat{\mathbf{x}}_{k|k-1} = \mathbf{x}_k - f_{k-1}(\hat{\mathbf{x}}_{k-1|k-1})$ for every $\Delta\mathbf{x}_{k-1}$, $\Delta\mathbf{v}_{k-1}$, $\Delta\mathbf{x}_k$ and $\Delta\mathbf{w}_k$, where

$$\boldsymbol{F}_{k-1} = \frac{\partial f_{k-1}(\hat{\mathbf{x}}_{k-1|k-1})}{\partial \mathbf{x}_{k-1}}, \tag{5}$$

$$\boldsymbol{L}_{k-1} = \frac{\partial \mathbf{f}_{k-1}(\hat{\mathbf{x}}_{k-1|k-1})}{\partial \mathbf{v}_{k-1}}, \tag{6}$$

$$\boldsymbol{H}_k = \frac{\partial \mathbf{h}_k(\mathbf{f}_{k-1}(\hat{\mathbf{x}}_{k-1|k-1}))}{\partial \mathbf{x}_k}, \tag{7}$$

$$\boldsymbol{M}_k = \frac{\partial h_k(\mathbf{f}_{k-1}(\hat{\mathbf{x}}_{k-1|k-1}))}{\partial \mathbf{w}_k}. \tag{8}$$

Steps involved in EKF algorithm are as shown in Table 3.

The EKF algorithm gives the best estimates if following assumptions are fulfilled:

- Matrices $\mathbf{w}_k$ and $\mathbf{v}_k$ have small norms;

UNCORRECTED PROOF

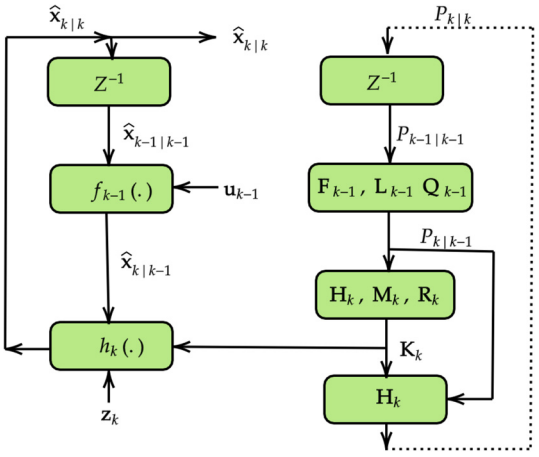

Fig. 2. EKF algorithm flowchart.

Table 3
Summary of EKF algorithm for nonlinear dynamical system.

Algorithm 1: Extended Kalman filter.
Initialization:
Initialize $\boldsymbol{P}_{k-1\|k-1}$, $\hat{\mathbf{x}}_{k-1\|k-1}$, $\boldsymbol{Q}_{k-1}$ and $\boldsymbol{R}_k$.
Prediction step:
Calculate $\boldsymbol{F}_{k-1}$ and $\boldsymbol{L}_{k-1}$ using (5) and (6) respectively.
Calculate predicted mean $\hat{\mathbf{x}}_{k\|k-1}$
$\hat{\mathbf{x}}_{k\|k-1} = \mathbf{f}_{k-1}(\hat{\mathbf{x}}_{k-1\|k-1}, \boldsymbol{u}_{k-1})$.
Evaluate the predicted covariance $\boldsymbol{P}_{k\|k-1}$:
$\boldsymbol{P}_{k\|k-1} = \boldsymbol{F}_{k-1}\boldsymbol{P}_{k-1\|k-1}\boldsymbol{F}_{k-1}^T + \boldsymbol{L}_{k-1}\boldsymbol{Q}_{k-1}\boldsymbol{L}_{k-1}^T$.
Update step:
Calculate $\boldsymbol{H}_k$ and $\boldsymbol{M}_k$ using (7) and (8) respectively.
Compute the Kalman gain $\boldsymbol{K}_k$:
$\boldsymbol{K}_k = \boldsymbol{P}_{k\|k-1}\boldsymbol{H}_k^T\left[\boldsymbol{H}_k\boldsymbol{P}_{k\|k-1}\boldsymbol{H}_k^T + \boldsymbol{M}_k\boldsymbol{R}_k\mathbf{M}_k^T\right]^{-1}$.
Compute estimated mean $\hat{\mathbf{x}}_{k\|k}$:
$\hat{\mathbf{x}}_{k\|k} = \hat{\mathbf{x}}_{k\|k-1} + \boldsymbol{K}_k[\mathbf{z}_k - \mathbf{h}_k(\hat{\mathbf{x}}_{k\|k-1})]$.
Compute the estimated covariance $\boldsymbol{P}_{k\|k}$:
$\boldsymbol{P}_{k\|k} = [\boldsymbol{I} - \boldsymbol{K}_k\boldsymbol{H}_k]\,\boldsymbol{P}_{k\|k-1}$.

- Initial estimates are equal to actual state of the system;
- Nonlinear functions $\mathbf{f}_k(.)$ and $\mathbf{h}_k(.)$ are mildly nonlinear functions;

where $(k|k-1)$ and $(k|k)$ denote a prior estimate and post estimate, respectively. I is the identity matrix. The time prediction step consists of computing the state projection and error covariance estimation. Measurement update step (correction step) consists of computing the Kalman gain, state correction, and covariance update. Kalman gain is used to correct the expected state. In this step, observed measurements and expected values are compared for state correction and covariance estimation. The steps involved in the EKF algorithm using flowchart are as shown in Fig. 2.

3. Fractional-order calculus

Fractional order calculus was introduced in 1695 by Leibniz, and it attracted several researchers due to its various advantages. In the literature, mainly, Grünwald-Letnikov, Riemann-Liouville, and Caputo defined fractional-order calculus integral form [33]. Amongst these three, Grünwald-Letnikov definition for fractional-order derivative can be used for state estimation of any nonlinear dynamical system due to its compatibility with various filtering methods [34]. Mathematically, it can be expressed as

$$\mathcal{D}^{\alpha}\mathbf{x}(t) = \lim_{\tau\to 0}\frac{1}{\tau^{\alpha}}\sum_{j=0}^{\frac{t}{T}}(-1)^{\alpha}\langle\alpha, j\rangle\mathbf{x}(t-j\tau), \tag{9}$$

where $\mathcal{D}^{\alpha}$ and α denote the integral-differential operator and integral-differential order, respectively. $\frac{t}{T}$ is the memory length. $\langle\alpha, j\rangle$ is the Newton Binomial coefficient which is formulated as

$$\langle\alpha, j\rangle = \frac{\Gamma(\alpha+1)}{\Gamma(j+1)(\alpha-j+1)}, \tag{10}$$

where $\Gamma(.)$ is the Gamma function, mathematically it is expressed as

$$\Gamma(\alpha) = \int_{\zeta=0}^{\infty}\zeta^{\alpha-1}e^{-\zeta}d\zeta. \tag{11}$$

UNCORRECTED PROOF

Table 4
State variable description.

Source	State variable	Description
Bat	$\mathbf{x}_1$	Susceptible bats
	$\mathbf{x}_2$	Exposed bats
	$\mathbf{x}_3$	Infected bats
	$\mathbf{x}_4$	Removed bats
Hosts	$\mathbf{x}_5$	Susceptible hosts
	$\mathbf{x}_6$	Exposed hosts
	$\mathbf{x}_7$	Infected hosts
	$\mathbf{x}_8$	Removed hosts
People	$\mathbf{x}_9$	Susceptible people
	$\mathbf{x}_{10}$	Exposed people
	$\mathbf{x}_{11}$	Symptomatic infected people
	$\mathbf{x}_{12}$	Removed people
	$\mathbf{x}_{13}$	Asymptomatic infected people
	$\mathbf{x}_{14}$	SARS-CoV-2 in reservoir

Table 5
Parameter description.

Source	Parameter	Description
Bats	n_B	Birth rate of bats
	m_B	Death rate of bats
	μ_B	Number of newborn bats
	$\frac{1}{\omega_B}$	The incubation period of bats
	$\frac{1}{\gamma_B}$	Infectious period of bats
Hosts	n_H	Birth rate of hosts
	m_H	Death rate of hosts
	μ_H	Number of new hosts
	$\frac{1}{\omega_H}$	The incubation period of hosts
	$\frac{1}{\gamma_H}$	Infectious period of hosts
People	$\frac{1}{\omega'_P}$	Latent period of people
	m_P	Death rate of people
	$\frac{1}{\omega_P}$	The incubation period of people
	$\frac{1}{\gamma'_P}$	Infectious period symptomatic infection of people
	$\frac{1}{\gamma_P}$	Infectious period asymptomatic infection of people
Transmission from one source to another source	β_B	Transmission rate from infectious bats to susceptible bats
	β_{BH}	Transmission rate from infectious bats to susceptible hosts
	β_H	Transmission rate from infectious hosts to susceptible hosts
	β_P	Transmission rate from infectious people to susceptible people
	β_W	Transmission rate from infectious people from reservoir to susceptible people
	β_W	Transmission rate from infectious people from reservoir to susceptible people
	$\frac{1}{\epsilon}$	Virus lifetime in reservoir

Continuous time Grünwald-Letnikov fractional-order derivative has the disadvantage that it can not be operated and implemented on computer software as it is infinite dimensional. To get over infinite dimensionality, Grünwald-Letnikov fractional-order derivative is converted to discrete form and reduced to finite dimensional form. Therefore, equation (9) is formulated as

$$\mathcal{D}^{\alpha}\mathbf{x}_k = \frac{1}{\tau^{\alpha}}\mathbf{x}_k + \frac{1}{\tau^{\alpha}}\sum_{j=0}^{L}(-1)^{\alpha}\langle\alpha, j\rangle\mathbf{x}_{k-j}. \tag{12}$$

4. State space modeling of BHRP transmission network model

Fig. 3 shows SEIR compartmental model [47], which is based on the clinical progression of the COVID-19. The SEIR model is parameterized in accordance with increase in the number of confirmed cases. The stability of fractional-order SEIR is presented in [48]. Reproduction number R_0 denotes the estimated transmission of the disease.

BHRP model is based on the fact that viruses are transmitted among the bats, and it is transmitted to unknown hosts. These hosts were sent to the seafood market, which was called the reservoir of the COVID-19. Then, it is transmitted to local people, as shown in Fig. 4. Description of state variables $\mathbf{x}_1$, $\mathbf{x}_2$...$\mathbf{x}_{14}$ and parameters is as shown in Table 4 and Table 5 respectively. In the proposed generalized SEIR based model, there is the potential presence of unparameterized disease thresholds for both the infected and infectious populations. It should be noted that the total people and infectious people can be directly known by inspecting the day-to-day disease effects by directly taking the required data.

Based on the SEIR model, BHRP model may be obtained. Nonlinear dynamic equations for the SEIR model for bats are

$$\frac{d^{\alpha}\mathbf{x}_1}{dt^{\alpha}} = \mu_B - m_B\,\mathbf{x}_1 - \beta_B\,\mathbf{x}_1\,\mathbf{x}_3, \tag{13}$$

UNCORRECTED PROOF

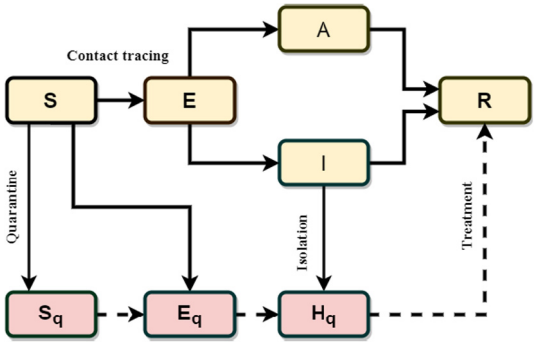

Fig. 3. SEIR model.

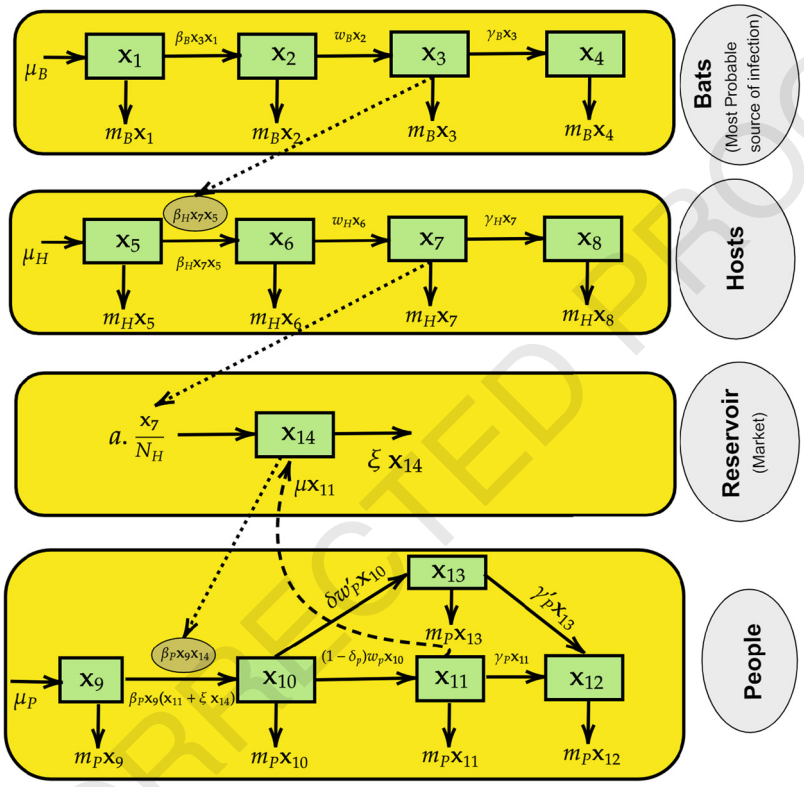

Fig. 4. BHRP model.

$$\frac{d^{\alpha}\mathbf{x}_2}{dt^{\alpha}} = \mathbf{x}_2(-w_B - m_B) + \beta_B\,\mathbf{x}_1\,\mathbf{x}_3, \tag{14}$$

$$\frac{d^{\alpha}\mathbf{x}_3}{dt^{\alpha}} = \mathbf{x}_3(-\gamma_B + m_B) + w_B\,\mathbf{x}_2, \tag{15}$$

$$\frac{d^{\alpha}\mathbf{x}_4}{dt^{\alpha}} = -\mathbf{x}_4 m_B + \gamma_B\,\mathbf{x}_3. \tag{16}$$

Similarly, dynamic equations for hosts are

$$\frac{d^{\alpha}\mathbf{x}_5}{dt^{\alpha}} = \mu_H - m_H\,\mathbf{x}_5 - \beta_{BH}\,\mathbf{x}_5\,\mathbf{x}_3 - \beta_H\,\mathbf{x}_5\,\mathbf{x}_7, \tag{17}$$

$$\frac{d^{\alpha}\mathbf{x}_6}{dt^{\alpha}} = \mathbf{x}_6(-w_H - m_H) + \beta_{SH}\,\mathbf{x}_5\,\mathbf{x}_3 + \beta_H\,\mathbf{x}_5\,\mathbf{x}_8, \tag{18}$$

$$\frac{d^{\alpha}\mathbf{x}_7}{dt^{\alpha}} = \mathbf{x}_7(-\gamma_H - m_H) + w_B\,\mathbf{x}_2, \tag{19}$$

$$\frac{d^{\alpha}\mathbf{x}_8}{dt^{\alpha}} = -\mathbf{x}_8 m_H + \gamma_H\,\mathbf{x}_7. \tag{20}$$

Dynamic equations for transmissibility from people are

$$\frac{d^{\alpha}\mathbf{x}_9}{dt^{\alpha}} = \mu_P - m_P\,\mathbf{x}_9 - \beta_w\,\mathbf{x}_9\,\mathbf{x}_{14} - \beta_P\,\mathbf{x}_9\,(\mathbf{x}_{11} + \xi\,\mathbf{x}_{13}), \tag{21}$$

UNCORRECTED PROOF

$$\frac{d^{\alpha}\mathbf{x}_{10}}{dt^{\alpha}} = \mathbf{x}_{10}(-w'_P - m_P) + \beta_w\, \mathbf{x}_9\mathbf{x}_{14} + \beta_P\, \mathbf{x}_9\mathbf{x}_{11} + \beta_P\,\xi\,\mathbf{x}_9\mathbf{x}_{13} - w_P(1-\delta_P), \tag{22}$$

$$\frac{d^{\alpha}\mathbf{x}_{11}}{dt^{\alpha}} = \mathbf{x}_{11}(-\gamma_P - m_P) + w_P(1-\delta_P)\mathbf{x}_{10}, \tag{23}$$

$$\frac{d^{\alpha}\mathbf{x}_{12}}{dt^{\alpha}} = -\mathbf{x}_{12}m_P + \gamma_P\,\mathbf{x}_{11} + \gamma'_P\,\mathbf{x}_{13}, \tag{24}$$

$$\frac{d^{\alpha}\mathbf{x}_{13}}{dt^{\alpha}} = \mathbf{x}_{13}(-\gamma'_P - m_P) + w'_P\delta_P\mathbf{x}_{10}, \tag{25}$$

$$\frac{d^{\alpha}\mathbf{x}_{14}}{dt^{\alpha}} = \alpha\,\mathbf{x}_{14}\frac{\mathbf{x}_7}{N_H} + w'_P\,\delta_P\,\mathbf{x}_{10} + \mu_P\mathbf{x}_{11} + \mu'_P\mathbf{x}_{13} - \epsilon\mathbf{x}_{14}. \tag{26}$$

SIER based model consists of susceptible people ($\mathbf{x}_9$), exposed people ($\mathbf{x}_{10}$), symptomatic infected people ($\mathbf{x}_{11}$), asymptomatic infected people ($\mathbf{x}_{13}$), and removed people ($\mathbf{x}_{12}$) including recovered and death people. The birth rate and death rate of people were defined as n_P and m_P. In this model, we set $\mu_P = n_P \times N_P$ where N_P denotes the total number of people. The incubation period and latent period of people infection was defined as $\frac{1}{\omega_P}$ and $\frac{1}{\omega'_P}$.

Total number of infected people due to the COVID-19 are

$$\mathbf{z} = \mathbf{x}_{11} + \mathbf{x}_{13} + \mathbf{x}_{14}. \tag{27}$$

The above dynamic equations (13) to (27) combined to give BHRP model. Vector form of above BHRP model based fractional-order differential equations are

$$\frac{d^{\alpha}\mathbf{x}(t)}{dt^{\alpha}} = \boldsymbol{F}\mathbf{x}(t) + \boldsymbol{B}^{(1)}\boldsymbol{u}_1(t) + \boldsymbol{B}^{(2)}\boldsymbol{u}_2(t) + \boldsymbol{B}^{(3)}\boldsymbol{u}_3(t) + \mathcal{Z}(t), \tag{28}$$

$$\mathbf{z} = \boldsymbol{H}\mathbf{x}(t), \tag{29}$$

where $\mathbf{x} = \begin{bmatrix} \mathbf{x}_1 & \mathbf{x}_2 & \mathbf{x}_3 & \mathbf{x}_4 & \mathbf{x}_5 & \mathbf{x}_6 & \mathbf{x}_7 & \mathbf{x}_8 & \mathbf{x}_9 & \mathbf{x}_{10} & \mathbf{x}_{11} & \mathbf{x}_{12} & \mathbf{x}_{13} & \mathbf{x}_{14} \end{bmatrix}^T$,

$$\boldsymbol{F} = \begin{bmatrix}
F_1 & 0 & 0 & 0 & 0 & 0 & 0 & 0 & 0 & 0 & 0 & 0 & 0 & 0 \\
\beta_B\mathbf{x}_3 & F_2 & 0 & 0 & 0 & 0 & 0 & 0 & 0 & 0 & 0 & 0 & 0 & 0 \\
0 & w_B & F_3 & 0 & 0 & 0 & 0 & 0 & 0 & 0 & 0 & 0 & 0 & 0 \\
0 & 0 & \gamma_B & F_4 & 0 & 0 & 0 & 0 & 0 & 0 & 0 & 0 & 0 & 0 \\
0 & 0 & 0 & 0 & F_5 & 0 & 0 & 0 & 0 & 0 & 0 & 0 & 0 & 0 \\
0 & 0 & 0 & 0 & \beta_{BH}\mathbf{x}_3 + \beta_H\mathbf{x}_8 & F_6 & 0 & 0 & 0 & 0 & 0 & 0 & 0 & 0 \\
0 & w_B & 0 & 0 & 0 & 0 & F_7 & 0 & 0 & 0 & 0 & 0 & 0 & 0 \\
0 & 0 & 0 & 0 & 0 & 0 & \gamma_H & F_8 & 0 & 0 & 0 & 0 & 0 & 0 \\
0 & 0 & 0 & 0 & 0 & 0 & 0 & 0 & F_9 & 0 & 0 & 0 & 0 & 0 \\
0 & 0 & 0 & 0 & 0 & 0 & 0 & 0 & F_{10} & F_{11} & 0 & 0 & 0 & 0 \\
0 & 0 & 0 & 0 & 0 & 0 & 0 & 0 & 0 & w_P(1-\delta_P) & F_{12} & 0 & 0 & 0 \\
0 & 0 & 0 & 0 & 0 & 0 & 0 & 0 & 0 & 0 & \gamma_P & F_{13} & \gamma'_P & 0 \\
0 & 0 & 0 & 0 & 0 & 0 & 0 & 0 & 0 & w'_P\,\delta_P & 0 & 0 & F_{14} & 0 \\
0 & 0 & 0 & 0 & 0 & 0 & 0 & 0 & 0 & w'_P\,\delta_P & \mu_P & 0 & \mu'_P & F_{15}
\end{bmatrix},$$

where $F_1 = -m_B - \beta_B\mathbf{x}_3$, $F_2 = -w_B - m_B$, $F_3 = -\gamma_B + m_B$, $F_4 = -m_B$, $F_5 = -m_H - \beta_{BH}\mathbf{x}_3 - \beta_H\mathbf{x}_7$, $F_6 = -w_H - m_H$, $F_7 = -\gamma_H - m_H$, $F_8 = -m_H$, $F_9 = -m_P - \beta_w\,\mathbf{x}_{14} - \beta_P\,(\mathbf{x}_{11} + \xi\,\mathbf{x}_{13})$, $F_{10} = \beta_w\mathbf{x}_{14} + \beta_P\mathbf{x}_{11} + \beta_P\,\xi\mathbf{x}_{13}$, $F_{11} = (-w'_P - m_P)$, $F_{12} = (-\gamma_P - m_P)$, $F_{13} = -m_P$, $F_{14} = (-\gamma'_P - m_P)$, $F_{15} = -\epsilon + \alpha\,\frac{\mathbf{x}_7}{N_H}$.

$$\boldsymbol{B}_1 = \begin{bmatrix} 1 & 0 & 0 & 0 & 0 & 0 & 0 & 0 & 0 & 0 & 0 & 0 & 0 & 0 \end{bmatrix}^T,$$

$$\boldsymbol{B}_2 = \begin{bmatrix} 0 & 0 & 0 & 0 & 1 & 0 & 0 & 0 & 0 & 0 & 0 & 0 & 0 & 0 \end{bmatrix}^T,$$

$$\boldsymbol{B}_3 = \begin{bmatrix} 0 & 0 & 0 & 0 & 0 & 0 & 0 & 0 & 1 & 0 & 0 & 0 & 0 & 0 \end{bmatrix}^T,$$

$$\boldsymbol{u}_1 = \mu_B, \qquad \boldsymbol{u}_2 = \mu_H, \qquad \boldsymbol{u}_3 = \mu_P,$$

$$\mathcal{Z} = \begin{bmatrix} 0 & 0 & 0 & 0 & 0 & 0 & 0 & 0 & 0 & -w_P(1-\delta_P) & 0 & 0 & 0 & 0 \end{bmatrix}^T,$$

$$\boldsymbol{H} = \begin{bmatrix} 0 & 0 & 0 & 0 & 0 & 0 & \mathbf{x}_7 & 0 & 0 & 0 & 1 & 0 & 1 & 1 \end{bmatrix}^T.$$

Consider $\mathbf{R}_0$ as reproduction number of infected people of the COVID-19. Using next generation matrix method, we can express $\mathbf{R}_0$ for the BHRP model as

$$\mathbf{R}_0 = \beta_P\frac{\mu_P}{m_P}\frac{(1-\delta_P)w_P}{(w_P+m_P)(\gamma_P+m_P)} + \beta_P\xi\frac{\mu_P}{m_P}\frac{\delta_P w_P}{(w_P+m_P)(\gamma'_P+m_P)} + \beta_w\frac{\mu_P}{m_P}\frac{(1-\delta_P)\xi w_P}{(\gamma_P+m_P)(\gamma_w+m_P)\epsilon}. \tag{30}$$

Euler-Maruyama method has been used to obtain discrete time state space equation using $t_k - t_{k-1} = T_S$ such that

$$\boldsymbol{F}_k = e^{\boldsymbol{F}(t_k - t_{k-1})} \approx \boldsymbol{I} + \boldsymbol{F}T_S, \tag{31}$$

UNCORRECTED PROOF

$$\boldsymbol{B}_k = \int_{t_{k-1}}^{t_k} e^{\boldsymbol{F}(t_k-\tau)}\boldsymbol{B}d\tau \approx \boldsymbol{B}T_S, \tag{32}$$

where T_s is the sampling time [49].

5. Applying EKF to BHRP transmission network model

Discrete time equations of (13)-(26) and (30) in the form of state space model can be formulated as

$$\mathbf{x}_k = \mathbf{f}_{k-1}(\mathbf{x}_{k-1}, \boldsymbol{u}_{k-1}), \tag{33}$$

$$\mathbf{z}_k = \mathbf{h}_k(\mathbf{x}_k), \tag{34}$$

where

$$\boldsymbol{F}_{k-1} = \frac{\partial^\alpha \mathbf{f}_{k-1}(\hat{\mathbf{x}}_{k-1|k-1}, \boldsymbol{u}_{k-1})}{\partial \mathbf{x}_{k-1}^\alpha}$$

$$= \begin{bmatrix}
\alpha+T_s^\alpha F_1 & 0 & 0 & 0 & 0 & 0 & 0 & 0 & 0 & 0 & 0 & 0 & 0 & 0 \\
\beta_B \mathbf{x}_3 & \alpha+T_s^\alpha F_2 & 0 & 0 & 0 & 0 & 0 & 0 & 0 & 0 & 0 & 0 & 0 & 0 \\
0 & w_B & 1+T_s^\alpha F_3 & 0 & 0 & 0 & 0 & 0 & 0 & 0 & 0 & 0 & 0 & 0 \\
0 & 0 & \gamma_B & \alpha+T_s^\alpha F_4 & 0 & 0 & 0 & 0 & 0 & 0 & 0 & 0 & 0 & 0 \\
0 & 0 & 0 & 0 & \alpha+T_s^\alpha F_5 & 0 & 0 & 0 & 0 & 0 & 0 & 0 & 0 & 0 \\
0 & 0 & 0 & 0 & \beta_{BH}\mathbf{x}_3+\beta_H \mathbf{x}_8 & \alpha+T_s^\alpha F_6 & 0 & 0 & 0 & 0 & 0 & 0 & 0 & 0 \\
0 & w_B & 0 & 0 & 0 & 0 & \alpha+T_s^\alpha F_7 & 0 & 0 & 0 & 0 & 0 & 0 & 0 \\
0 & 0 & 0 & 0 & 0 & 0 & \gamma_H & \alpha+T_s^\alpha F_8 & 0 & 0 & 0 & 0 & 0 & 0 \\
0 & 0 & 0 & 0 & 0 & 0 & 0 & 0 & \alpha+T_s^\alpha F_9 & 0 & 0 & 0 & 0 & 0 \\
0 & 0 & 0 & 0 & 0 & 0 & 0 & 0 & F_{10} & \alpha+T_s^\alpha F_{11} & 0 & 0 & 0 & 0 \\
0 & 0 & 0 & 0 & 0 & 0 & 0 & 0 & 0 & w_P(1-\delta_P) & \alpha+T_s^\alpha F_{12} & 0 & 0 & 0 \\
0 & 0 & 0 & 0 & 0 & 0 & 0 & 0 & 0 & 0 & \gamma_P & \alpha+T_s^\alpha F_{13} & \gamma_P' & 0 \\
0 & 0 & 0 & 0 & 0 & 0 & 0 & 0 & 0 & w_P'\delta_P & 0 & 0 & \alpha+T_s^\alpha F_{14} & 0 \\
0 & 0 & 0 & 0 & 0 & 0 & 0 & 0 & 0 & w_P'\delta_P & \mu_P & 0 & \mu_P' & \alpha+T_s^\alpha F_{15}
\end{bmatrix},$$

$$\boldsymbol{B}_{k-1}^{(1)} = \frac{\partial^\alpha \mathbf{f}_{k-1}(\hat{\mathbf{x}}_{k-1|k-1}, \boldsymbol{u}_{k-1})}{\partial \boldsymbol{u}_1^\alpha}$$

$$= \begin{bmatrix} T_s^\alpha & 0 & 0 & 0 & 0 & 0 & 0 & 0 & 0 & 0 & 0 & 0 & 0 & 0 \end{bmatrix}^T,$$

$$\boldsymbol{B}_{k-1}^{(2)} = \frac{\partial^\alpha \mathbf{f}_{k-1}(\hat{\mathbf{x}}_{k-1|k-1}, \boldsymbol{u}_{k-1})}{\partial \boldsymbol{u}_2^\alpha}$$

$$= \begin{bmatrix} 0 & 0 & 0 & 0 & T_s^\alpha & 0 & 0 & 0 & 0 & 0 & 0 & 0 & 0 & 0 \end{bmatrix}^T,$$

$$\boldsymbol{B}_{k-1}^{(3)} = \frac{\partial^\alpha \mathbf{f}_{k-1}(\hat{\mathbf{x}}_{k-1|k-1}, \boldsymbol{u}_{k-1})}{\partial \boldsymbol{u}_3^\alpha}$$

$$= \begin{bmatrix} 0 & 0 & 0 & 0 & 0 & 0 & 0 & 0 & T_s^\alpha & 0 & 0 & 0 & 0 & 0 \end{bmatrix}^T,$$

$$\mathbf{Z}_{k-1} = \begin{bmatrix} 0 & 0 & 0 & 0 & 0 & 0 & 0 & 0 & 0 & -T_s^\alpha w_P(1-\delta_P) & 0 & 0 & 0 & 0 \end{bmatrix}^T.$$

EKF algorithm has been implemented to the discrete equations by adding process noise $\mathbf{v}_k$ and measurement noise $\mathbf{w}_k$ to (33) and (34) respectively,

$$\mathbf{x}_k = \boldsymbol{F}_{k-1}\mathbf{x}_{k-1} + \boldsymbol{B}_{k-1}^{(1)}\boldsymbol{u}_1 + \boldsymbol{B}_{k-1}^{(2)}\boldsymbol{u}_2 + \boldsymbol{B}_{k-1}^{(3)}\boldsymbol{u}_3 + \mathcal{Z}_{k-1} + \sum_{l=2}^{L}(-1)^l \Phi_l^\alpha \mathbf{x}_{k-l+1} + \mathbf{v}_k, \tag{35}$$

$$\mathbf{z}_k = \boldsymbol{H}_k\mathbf{x}_k + \mathbf{w}_k. \tag{36}$$

6. Kronecker product based fractional-order system representation using WT method

Formalism of the measurement model is

$$\frac{d\mathbf{z}(t)}{dt} = \mathcal{H}\mathbf{x}(t) + \sigma\mathbf{N}(t), \tag{37}$$

where

UNCORRECTED PROOF

$$\mathcal{H} = \begin{bmatrix} 1 & 0 & 0 & 0 & 0 & 0 & 0 & 0 & 0 & 0 & 0 & 0 & 0 & 0 \\ 0 & 1 & 0 & 0 & 0 & 0 & 0 & 0 & 0 & 0 & 0 & 0 & 0 & 0 \\ 0 & 0 & 1 & 0 & 0 & 0 & 0 & 0 & 0 & 0 & 0 & 0 & 0 & 0 \\ 0 & 0 & 0 & 1 & 0 & 0 & 0 & 0 & 0 & 0 & 0 & 0 & 0 & 0 \\ 0 & 0 & 0 & 0 & 1 & 0 & 0 & 0 & 0 & 0 & 0 & 0 & 0 & 0 \\ 0 & 0 & 0 & 0 & 0 & 1 & 0 & 0 & 0 & 0 & 0 & 0 & 0 & 0 \\ 0 & 0 & 0 & 0 & 0 & 0 & 1 & 0 & 0 & 0 & 0 & 0 & 0 & 0 \\ 0 & 0 & 0 & 0 & 0 & 0 & 0 & 1 & 0 & 0 & 0 & 0 & 0 & 0 \\ 0 & 0 & 0 & 0 & 0 & 0 & 0 & 0 & 1 & 0 & 0 & 0 & 0 & 0 \\ 0 & 0 & 0 & 0 & 0 & 0 & 0 & 0 & 0 & 1 & 0 & 0 & 0 & 0 \\ 0 & 0 & 0 & 0 & 0 & 0 & 0 & 0 & 0 & 0 & 1 & 0 & 0 & 0 \\ 0 & 0 & 0 & 0 & 0 & 0 & 0 & 0 & 0 & 0 & 0 & 1 & 0 & 0 \\ 0 & 0 & 0 & 0 & 0 & 0 & 0 & 0 & 0 & 0 & 0 & 0 & 1 & 0 \\ 0 & 0 & 0 & 0 & 0 & 0 & 0 & 0 & 0 & 0 & 0 & 0 & 0 & 1 \end{bmatrix},$$

$\mathbf{N}(t)$ denotes the zero mean white Gaussian process. $\mathbf{x}(t)$ can be expanded using wavelet basis as

$$\mathbf{x}(t) = \sum_{N_1 \le i \le N_2, k_{\min}(i) \le k \le k_{\max}(i)} c(i,k)\psi_{i,k}(t), \tag{38}$$

where resolution range $[N_1, N_2]$ depends on frequency of operation and the measured time duration and the mother wavelet $\psi_{i,k}(t)$ is given by

$$\psi_{i,k}(t) = 2^{\frac{i}{2}}\psi(2^i t - k). \tag{39}$$

Mother wavelet in WT method can be reconstructed from the 'scaling sequence' for different type of wavelets (Daubechies wavelet, Haar wavelet, Shannon wavelet etc.) which have specific properties required for specific kinds of applications. Daubechies wavelets are discrete time orthogonal wavelets in which the scaling and the wavelet functions have longer supports, which offers improved capability of these transformations. These transformations offer powerful tool for various signal processing such as compression, noise removal, image enhancement etc. Let mother wavelet range is [a, b], ω_1 and ω_2 denote the lowest and the highest frequency of operation. Consider $[0, \tau]$ is the measurement time span. Then, for a specified resolution index i, the extent of the transition index k is chosen such that $a \le 2^i t - k \le b, t \in [0, \tau]$. Therefore, $2^i t - b \le k \le 2^i, t - a, t \in [0, \tau]$ or $-b \le k \le 2^i T - a, t \in [0, \tau]$. Wavelet frequency $\Psi_{n,k}(t)$ is mathematically expressed as

$$\left|\frac{\frac{d\psi_{n,k}(t)}{dt}}{\psi_{n,k}(t)}\right| = \frac{2^n\left|\psi'(2^n t - k)\right|}{|\psi(2^n t - k)|} \in [2^n\zeta_{\min}, 2^n\zeta_{\max}], \tag{40}$$

where

$$\zeta_{\max} = \max_t \frac{|\psi'(t)|}{|\psi(t)|}, \tag{41}$$

$$\zeta_{\min} = \min_t \frac{|\psi'(t)|}{|\psi(t)|}, \tag{42}$$

so the resolution indexes N_1, N_2 must be chosen such that

$$2^{N_2}\zeta_{\max} \approx \frac{\omega_2}{2\pi}, \tag{43}$$

$$2^{N_1}\zeta_{\min} \approx \frac{\omega_1}{2\pi}, \tag{44}$$

or

$$N_1 \approx \log_2\left(\frac{\omega_1}{2\pi\zeta_{\min}}\right), \tag{45}$$

$$N_2 \approx \log_2\left(\frac{\omega_2}{2\pi\zeta_{\max}}\right). \tag{46}$$

Now, resolution index range is selected using this method enables us to reserve lesser data for estimation purpose i.e., estimation is done using compression. The wavelet method is applied either directly to estimate the entire set of the state variables or another way is to formulate a square non-singular matrix. The latter case is formulated as

$$\mathbf{x}(t) \approx \mathcal{H}^{-1}\mathcal{D}^{\alpha}\mathbf{z}(t), \tag{47}$$

and so

$$\begin{aligned}\mathcal{D}^{2\alpha}\mathbf{z}(t) &\approx \mathcal{H}\mathcal{D}^{\alpha}\mathbf{x}(t) \\ &\approx \mathcal{H}\boldsymbol{F}\mathbf{x}(t) + \mathcal{H}(\boldsymbol{B}_1\boldsymbol{u}_1(t) + \boldsymbol{B}_2\boldsymbol{u}_2(t) + \boldsymbol{B}_3\boldsymbol{u}_3(t)) + \mathcal{H}\mathcal{Z}(t).\end{aligned} \tag{48}$$

UNCORRECTED PROOF

The signals $\mathcal{D}^{\alpha}\mathbf{z}(t)$ and $\mathcal{D}^{2\alpha}\mathbf{z}(t)$ are expressed using wavelets as

$$\mathcal{D}^{\alpha}\mathbf{z}(t) \approx \sum_{i,k} c_{\mathcal{D}^{\alpha}\mathbf{z}(t)}[i,k]\psi_{i,k}(t), \tag{49}$$

$$\mathcal{D}^{2\alpha}\mathbf{z}(t) \approx \sum_{i,k} c_{\mathcal{D}^{2\alpha}\mathbf{z}(t)}[i,k]\psi_{i,k}(t). \tag{50}$$

Substituting (49) and (50) into (48) and neglecting noise terms, we get

$$\sum_{i,k} c_{\mathcal{D}^{2\alpha}\mathbf{z}(t)}[i,k]\psi_{i,k}(t) \approx \sum_{i,k} \mathcal{H}\boldsymbol{F}\mathcal{H}^{-1} c_{\mathbb{D}^{\alpha}\mathbf{z}(t)}[i,k]\psi_{i,k}(t) + \mathcal{H}\boldsymbol{B}_1\boldsymbol{u}_1(t) + \mathcal{H}\boldsymbol{B}_2\boldsymbol{u}_2(t) + \mathcal{H}\boldsymbol{B}_3\boldsymbol{u}_3(t) + \mathcal{H}\mathcal{Z}(t), \tag{51}$$

where

$$c_{\mathcal{D}^{\alpha}\mathbf{z}(t)}[i,k] \approx \int_0^T \mathcal{D}^{\alpha}\mathbf{z}(t)\psi_{i,k}(t)dt = <\mathcal{D}^{\alpha}\mathbf{z}, \psi_{i,k}> = \mathcal{D}^{\alpha}\mathbf{z}[i,k]. \tag{52}$$

Now, the inner product is computed with $\psi_{p,q}$ on (51) can be written as

$$\begin{aligned}\sum_{i,k} c_{\mathcal{D}^{2\alpha}\mathbf{z}}[i,k] <\psi_{i,k}, \psi_{p,q}> \approx \sum_{i,k} \mathcal{H}\boldsymbol{F}\mathcal{H}^{-1} c_{\mathcal{D}^{\alpha}\mathbf{z}}[i,k] <\psi_{i,k}, \psi_{p,q}> + \mathcal{H}\boldsymbol{B}_1\boldsymbol{u}_1[p,q] + \mathcal{H}\boldsymbol{B}_2\boldsymbol{u}_2[p,q] \\ + \mathcal{H}\boldsymbol{B}_3\boldsymbol{u}_3[p,q] + \mathcal{H}\mathcal{Z}[p,q],\end{aligned} \tag{53}$$

where the input $\boldsymbol{u}(t) = \sum \boldsymbol{u}[i,k]\psi_{i,k}(t)$, i.e. $\boldsymbol{u}[i,k] = <\boldsymbol{u}, \psi_{i,k}>$. Equation (53) can be formulated as

$$c_{\mathcal{D}^{2\alpha}\mathbf{z}}[p,q] = \sum_{i,k} m_1[p,q|i,k]\, c_{\mathcal{D}^{\alpha}\mathbf{z}}[i,k] + \delta \sum_{i,k,m,r} m_2[p,q|i,k,m,r](c_{\mathcal{D}^{\alpha}\mathbf{z}}[i,k] \otimes c_{\mathcal{D}^{\alpha}\mathbf{z}}[m,r]) + \sum_{i,k} m_3[p,q|i,k]\boldsymbol{u}[i,k], \tag{54}$$

where m_1, m_2 and m_3 are formulated in terms of $\mathcal{H}$, $\boldsymbol{F}$, $\boldsymbol{B}_1$, $\boldsymbol{B}_2$, $\boldsymbol{B}_3$. m_1, m_2 depend on Θ, so we write

$$c_{\mathcal{D}^{2\alpha}\mathbf{z}}[p,q] = \sum_{i,k} m_1[p,q|i,k,\Theta] c_{\mathcal{D}^{\alpha}\mathbf{z}}[i,k] + \delta \sum_{i,k,m,r} m_2[p,q|i,k,m,r,\Theta](c_{\mathcal{D}^{\alpha}\mathbf{z}}[i,k] \otimes c_{\mathcal{D}^{\alpha}\mathbf{z}}[m,r]) + \sum_{n,k} m_3[p,q|i,k]\mathbf{u}[i,k]. \tag{55}$$

Now, the perturbation method is used to retain $\mathcal{O}(\delta^2)$ terms as

$$c_{\mathcal{D}^{2\alpha}\mathbf{z}}[i,k] = c^{(0)}_{\mathcal{D}^{2\alpha}\mathbf{z}}[i,k] + \delta c^{(1)}_{\mathcal{D}^{2\alpha}\mathbf{z}}[i,k] + \delta^2 c^{(2)}_{\mathcal{D}^{2\alpha}\mathbf{z}}[i,k] + \mathcal{O}(\delta^3). \tag{56}$$

Comparing the coefficients of $\delta^{(0)}$, $\delta^{(1)}$, $\delta^{(2)}$ respectively gives

$$c^{(0)}_{\mathcal{D}^{2\alpha}\mathbf{z}}[p,q] = \sum_{i,k} m_1[p,q|i,k,\Theta] c^{(0)}_{\mathcal{D}^{\alpha}\mathbf{z}}[i,k] + \sum_{i,k} m_3[p,q|i,k,\Theta]\boldsymbol{u}[i,k], \tag{57}$$

$$\begin{aligned}c^{(1)}_{\mathcal{D}^{2\alpha}\mathbf{z}}[p,q] &= \sum_{i,k,m,r} m_2[p,q|i,k,m,r](c^{(0)}_{\mathcal{D}^{\alpha}\mathbf{z}}[i,k] \otimes c^{(0)}_{\mathcal{D}^{\alpha}\mathbf{z}}[m,r]) + m_1 c^{(1)}_{\mathcal{D}^{\alpha}\mathbf{z}}[p,q|i,k] \\ &\triangleq m_2(c^{(0)}_{\mathcal{D}^{\alpha}\mathbf{z}} \otimes c^{(0)}_{\mathcal{D}^{\alpha}\mathbf{z}})[p,q] + m_1 c^{(1)}_{\mathcal{D}^{\alpha}\mathbf{z}}[p,q],\end{aligned} \tag{58}$$

$$c^{(2)}_{\mathcal{D}^{2\alpha}\mathbf{z}}[p,q] = m_1 c^{(2)}_{\mathcal{D}^{\alpha}\mathbf{z}}[p,q] + m_2(c^{(0)}_{\mathcal{D}^{\alpha}\mathbf{z}} \otimes c^{(1)}_{\mathcal{D}^{\alpha}\mathbf{z}} + c^{(1)}_{\mathcal{D}^{\alpha}\mathbf{z}} \otimes c^{(0)}_{\mathcal{D}^{\alpha}\mathbf{z}})[p,q], \tag{59}$$

where $c^{(0)}_{\mathcal{D}^{\alpha}\mathbf{z}}[i,k]$, $c^{(1)}_{\mathcal{D}^{\alpha}\mathbf{z}}[i,k]$ and $c^{(2)}_{\mathcal{D}^{\alpha}\mathbf{z}}[i,k]$ are obtained from WT of $\mathcal{D}^{\alpha}\mathbf{z}^{(0)}[i,k]$, $\mathcal{D}^{\alpha}\mathbf{z}^{(1)}[i,k]$ and $\mathcal{D}^{\alpha}\mathbf{z}^{(2)}[i,k]$ respectively by equating $\mathcal{O}(\delta^0)$, $\mathcal{O}(\delta^1)$ and $\mathcal{O}(\delta^2)$ variations expressed in $\mathbf{z}(t)$. $\otimes$ is the Kronecker product of two matrices.

Thus, we can use gradient search algorithm to estimate Θ to minimize

$$\begin{aligned}\xi(\Theta) = \sum_{p,q} ||c_{\mathcal{D}^{2\alpha}\mathbf{z}}[p,q] - \sum_{n,k} m_1[p,q|i,k,\Theta] c_{\mathcal{D}^{\alpha}\mathbf{z}}[i,k] - \sum_{i,k,m,r} m_2[p,q|i,k,m,r,\Theta] \\ \times (c_{\mathcal{D}^{\alpha}\mathbf{z}}[i,k] \otimes c_{\mathcal{D}^{\alpha}\mathbf{z}}[m,r]) - \sum_{i,k} m_3[p,q|i,k]\boldsymbol{u}[i,k]||^2.\end{aligned} \tag{60}$$

7. Results and discussion

The mathematical model proposed here is a generalized method that can be applied to any population under different scenarios. In this work, we have applied the proposed model to estimate the number of infected and the recovered people due to COVID-19 in India and China. Figs. 5 to 11 depict the number of estimated infected people and recovered people using FOC-based EKF method and WT method, and it is compared with the actual number of infected people and recovered people [50]. The values of the parameters used for the estimation are: The incubation period is set to 5.2 days, i.e. 95% confidence interval is 4.1-7.0, $\omega_P = \omega'_P = 0.1923$, the mean infectious period of the cases as 5.8 days i.e. $\gamma_P = 0.076$, $\delta_P = 0.50$. The transmission rate from infectious people to susceptible people (β_P) is 0.31. Transmissibility of symptomatic infection is considered to be twice the transmissibility of asymptomatic infection; thus, $\xi = 0.5$. $\epsilon = 0.1$. The reproduction number during this period for India and China is found to be 3.85 and 2.74, respectively. Parameters γ_P and

UNCORRECTED PROOF

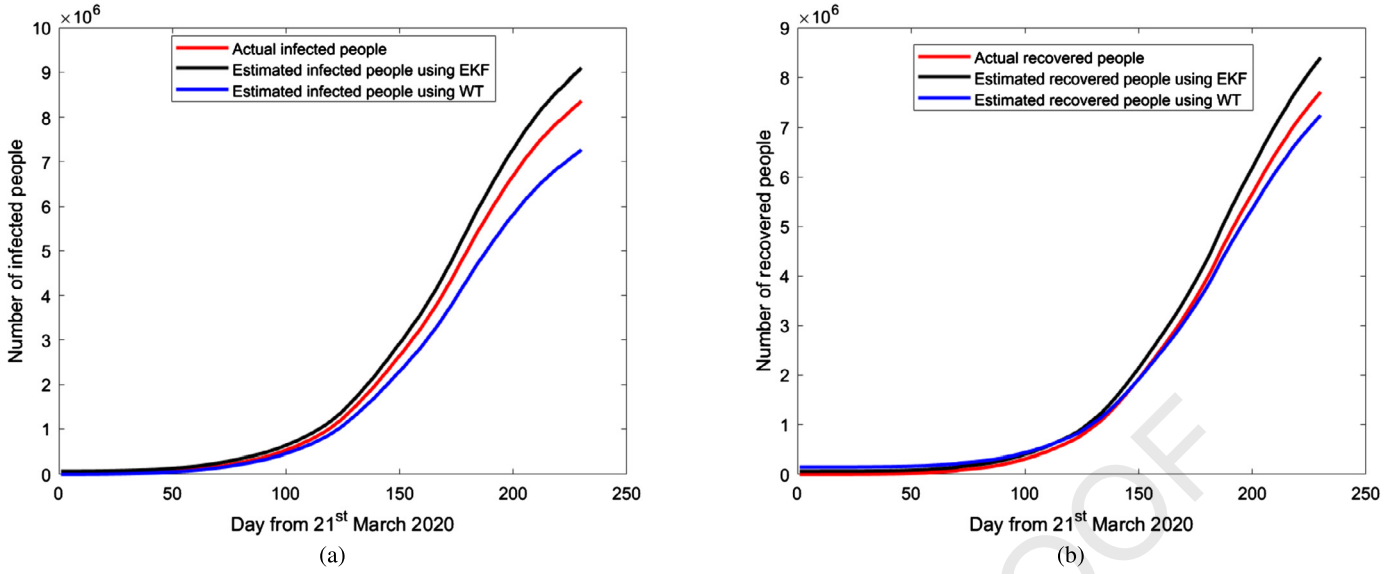

Fig. 5. Estimation of infected and recovered people in India using SEIR model based EKF and WT method for $\gamma_P = 0.076$, $\beta_P = 0.31$. Fractional parameter $\alpha = 1$. (For interpretation of the colors in the figure(s), the reader is referred to the web version of this article.)

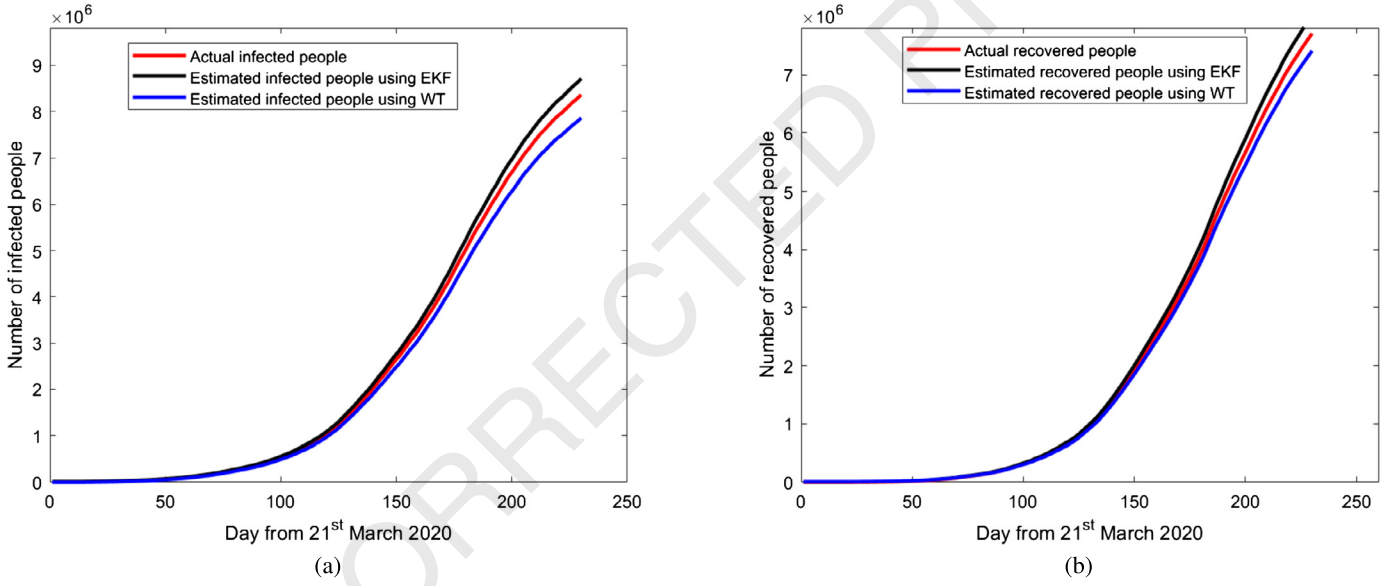

Fig. 6. Estimation of infected and recovered people in India using SEIR model based EKF and WT method for $\gamma_P = 0.076$, $\beta_P = 0.31$. Fractional parameter $\alpha = 1.82$.

β_P are controlling the estimation of the infected and the recovered population using EKF and WT method and any change in these parameter values leads to a significant change in the infected and the recovered population. The about fact is as shown in Fig. 5 and Fig. 7, which depict the estimation of infected people and recovered people using EKF and WT method as γ_P and β_P change from 0.076 to 0.042 and 0.31 to 0.25, respectively. Change in fractional order parameter value also affecting the estimation as shown in Fig. 6 and Fig. 8.

The comparison of estimation using different values of fractional parameter α is presented in Fig. 9. The fractional-order parameter value $\alpha = 1.82$ gives better estimates as compared to $\alpha = 1.0$ (conventional EKF and WT method). Fig. 10 shows the estimation of infected and recovered people in China using EKF and WT methods for a fixed value of $\gamma_P = 0.002$, $\beta_P = 0.16$, and $\alpha = 1.82$. It is observed that the EKF method gives better estimates than the WT method. A comparison of the proposed BHRP-based SEIR model with the conventional SEIR model for China has been demonstrated in Fig. 11. It is noted that the proposed model outperforms the standard SEIR model for the initial estimation, which further merges with the standard model. This is because, initially, the spreading of coronavirus in China was due to bats, host, and reservoir, so their parameters' effect was more significant. This effect of bats, host, and reservoir parameters got diminished in further spreading of COVID-19 due to the dominance of human transmission. The estimation accuracy of the methods discussed in the preceding sections can be calculated in terms of symmetric mean absolute percentage error (SMAPE) [51] as

$$\text{SMAPE}[k] = \frac{1}{N}\sum_{i=1}^{N}\frac{|\mathbf{z}_i[k] - \hat{\mathbf{z}}_i[k]|}{(\mathbf{z}_i[k] + \hat{\mathbf{z}}_i[k])/2}, \tag{61}$$

UNCORRECTED PROOF

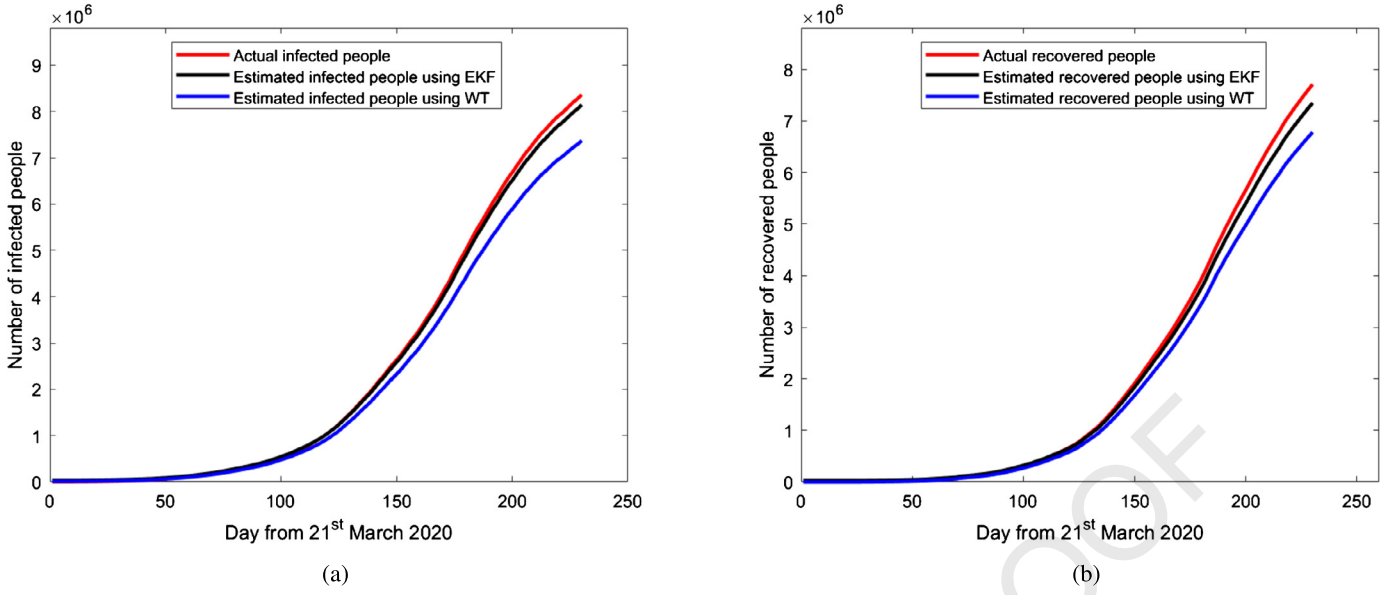

Fig. 7. Estimation of infected and recovered people in India using SEIR model based EKF and WT method for $\gamma_P = 0.042$, $\beta_P = 0.25$. Fractional parameter $\alpha = 1$.

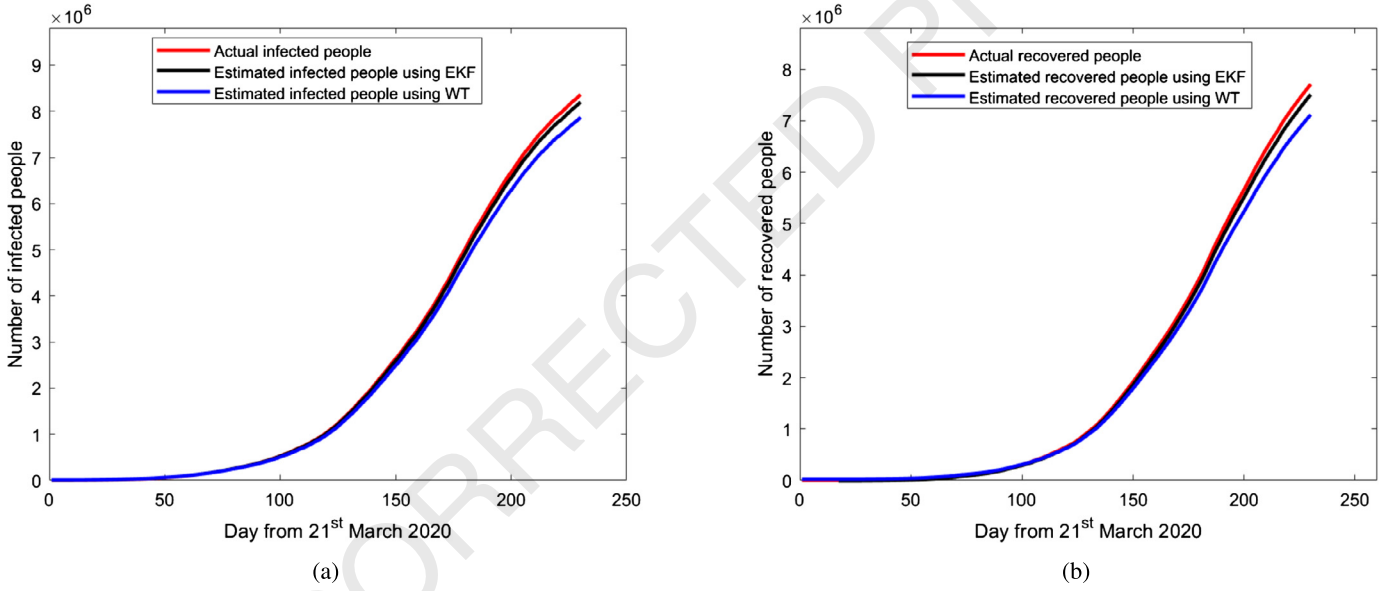

Fig. 8. Estimation of infected and recovered people in India using SEIR model based EKF and WT method for $\gamma_P = 0.042$, $\beta_P = 0.25$. Fractional parameter $\alpha = 1.82$.

Table 6
SMAPE for the estimation of infected people using EKF and WT method.

Country	Parameter values	EKF method			WT method		
		$\alpha = 1$	$\alpha = 1.50$	$\alpha = 1.82$	$\alpha = 1$	$\alpha = 1.50$	$\alpha = 1.82$
India	$\gamma_P = 0.042$, $\beta_P = 0.25$	0.00143	0.00138	0.00131	0.00157	0.00154	0.00148
India	$\gamma_P = 0.076$, $\beta_P = 0.31$	0.00145	0.00140	0.00136	0.00161	0.00162	0.00151
India	$\gamma_P = 0.090$, $\beta_P = 0.40$	0.00148	0.00145	0.00140	0.00166	0.00164	0.00161
China	$\gamma_P = 0.003$, $\beta_P = 0.16$	0.00126	0.00118	0.00110	0.00252	0.00248	0.00262
China	$\gamma_P = 0.005$, $\beta_P = 0.19$	0.00135	0.00120	0.00113	0.00261	0.00257	0.00261
China	$\gamma_P = 0.007$, $\beta_P = 0.22$	0.00144	0.00131	0.00128	0.00266	0.00264	0.00262

where N is the number of samples, $\mathbf{z}_i[k]$ and $\hat{\mathbf{z}}_i[k]$ are the cumulative number of cases and estimated number of cases, respectively, for region i at time k. Table 6 and Table 7 show the SMAPE for the estimation of infected and recovered people using EKF and WT methods for India and China for various values of system parameters. It is clear from the results that the FOC-based EKF method gives better performance than the conventional EKF and the WT methods. This is due to the fact that EKF uses the stochastic approach for the estimation; i.e., it considers both the measurement noise and the process noise in which states are Markov process. Moreover, EKF gives the joint evaluation of conditional mean and conditional error covariance; therefore, it gives better estimates.

UNCORRECTED PROOF

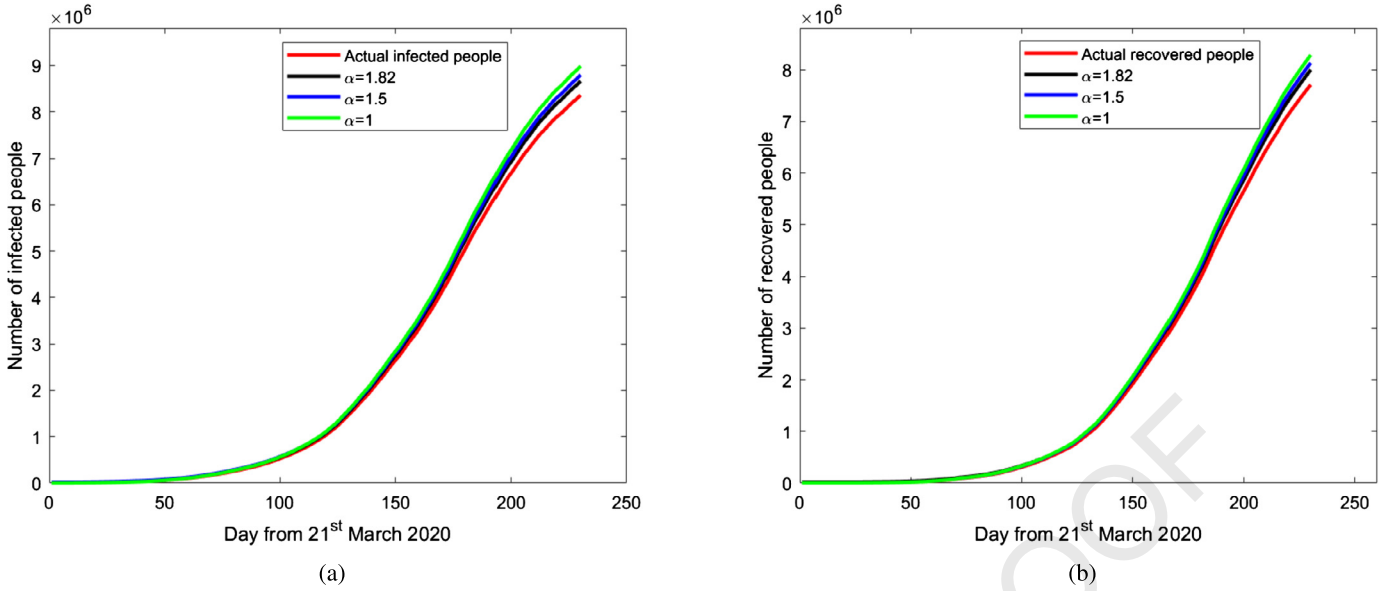

Fig. 9. Estimation of infected and recovered people in India using SEIR model based EKF for different value of fractional parameter.

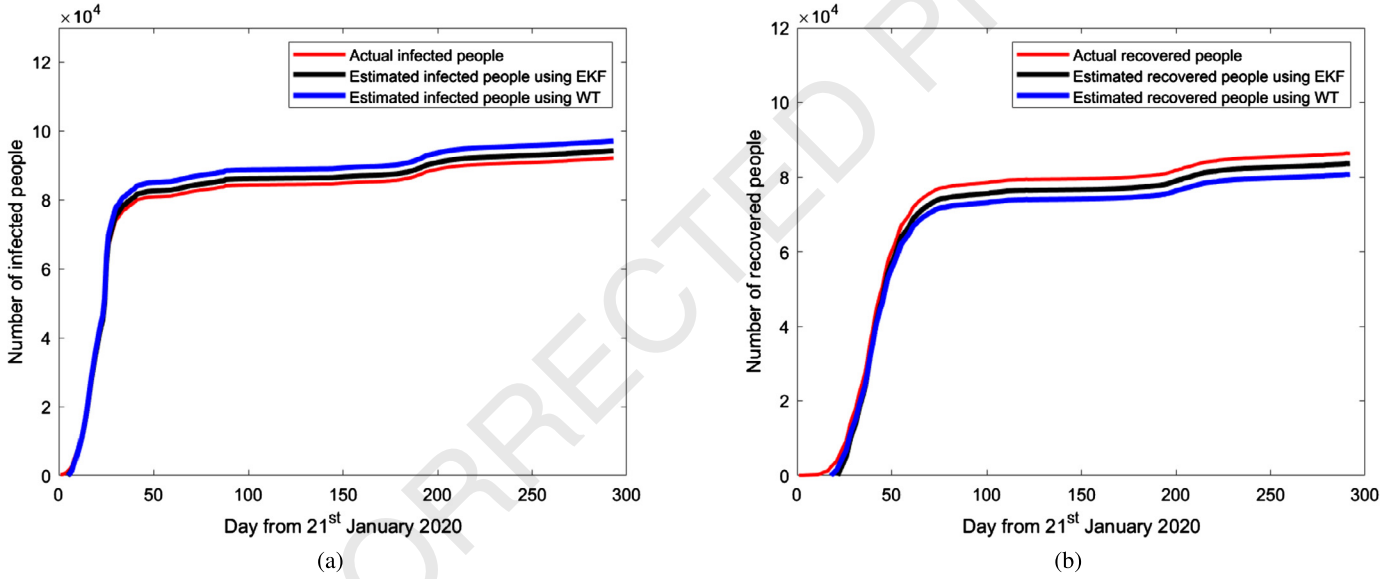

Fig. 10. Estimation of infected and recovered people in China using SEIR model based EKF and WT method for $\gamma_P = 0.002$, $\beta_P = 0.16$. Fractional parameter $\alpha = 1.82$.

Table 7
SMAPE for the estimation of recovered people using EKF and WT method.

Country	Parameter values	EKF method			WT method		
		$\alpha = 1$	$\alpha = 1.50$	$\alpha = 1.82$	$\alpha = 1$	$\alpha = 1.50$	$\alpha = 1.82$
India	$\gamma_P = 0.042$, $\beta_P = 0.25$	0.00150	0.00149	0.00145	0.00170	0.00167	0.00160
India	$\gamma_P = 0.076$, $\beta_P = 0.31$	0.00153	0.00151	0.00148	0.00173	0.00165	0.00162
India	$\gamma_P = 0.090$, $\beta_P = 0.40$	0.00160	0.00158	0.00155	0.00175	0.00173	0.00170
China	$\gamma_P = 0.003$, $\beta_P = 0.16$	0.00137	0.00130	0.00122	0.00264	0.00260	0.00273
China	$\gamma_P = 0.005$, $\beta_P = 0.19$	0.00145	0.00132	0.00124	0.00269	0.00268	0.00265
China	$\gamma_P = 0.007$, $\beta_P = 0.22$	0.00156	0.00140	0.00139	0.00276	0.00275	0.00272

General remarks

1. When non-Gaussian component is added with the Gaussian distribution of measurement noise, it is called as outlier. EKF can be formulated for this condition also. As EKF is derived from Kushner filter's equation for which the states are Markovian and the measurement noise considered as Gaussian process. When the measurement noise is non-white Gaussian process, nonlinear EKF can be formulated which is based on the Bayesian method for computing the conditional probabilities using non-Gaussian probability

UNCORRECTED PROOF

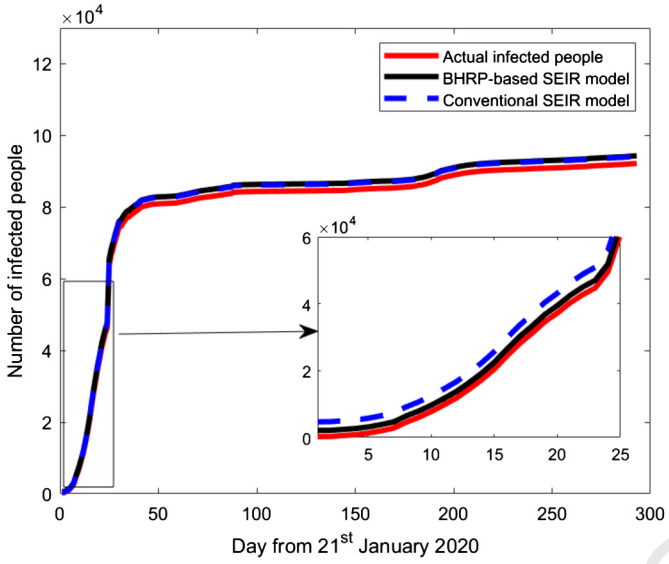

Fig. 11. Estimation of infected people using EKF method based on conventional SEIR model and BHRP-based SEIR model.

density functions. This follows the fact, for non-Gaussian measurement noise, the states are Markovian. First discretize the state model as

$$\boldsymbol{\chi}_{n+1} = \mathbf{f}(\boldsymbol{\chi}_n, \boldsymbol{u}_{n+1}) + \mathbf{v}_{n+1}, \tag{62}$$

$$\mathbf{y}(n) = \mathbf{h}(\boldsymbol{\chi}_n) + \mathbf{w}_n, \tag{63}$$

$$\mathbf{y}_n = \{\mathbf{y}(n) : \quad k \leq n\}, \tag{64}$$

$$p(\boldsymbol{\chi}_{n+1}|\mathbf{y}_{n+1}) = \frac{p(\boldsymbol{\chi}_{n+1}, \mathbf{y}_{n+1})}{p(\mathbf{y}_{n+1})} = \frac{p(\mathbf{y}(n+1), \mathbf{y}_n, \chi_{n+1})}{p(\mathbf{y}_{n+1})} \tag{65}$$

$$= \frac{\int p(\mathbf{y}(n+1)|\boldsymbol{\chi}_{n+1}) p(\boldsymbol{\chi}_{n+1}|\boldsymbol{\chi}_n) p(\boldsymbol{\chi}_n|\mathbf{y}_n) d\boldsymbol{\chi}_n}{\int p(\mathbf{y}(n+1)|\boldsymbol{\chi}_{n+1}) p(\boldsymbol{\chi}_{n+1}|\boldsymbol{\chi}_n) p(\boldsymbol{\chi}_n|\mathbf{y}_n) d\boldsymbol{\chi}_n d\boldsymbol{\chi}_{n+1}} \tag{66}$$

$$= \frac{\int p_{\mathbf{w}_{n+1}}(\mathbf{y}(n+1) - h(\boldsymbol{\chi}_{n+1})) p_{\mathbf{v}_{n+1}}(\boldsymbol{\chi}_{n+1} - \mathbf{f}(\boldsymbol{\chi}_n, \boldsymbol{u}_{n+1})) p(\boldsymbol{\chi}_n|\mathbf{y}_n) d\boldsymbol{\chi}_n}{\int p_{\mathbf{w}_{n+1}}(\mathbf{y}(n+1) - h(\boldsymbol{\chi}_{n+1})) p_{\mathbf{v}_{n+1}}(\boldsymbol{\chi}_{n+1} - \mathbf{f}(\boldsymbol{\chi}_n, \boldsymbol{u}_{n+1})) p(\boldsymbol{\chi}_n|\mathbf{y}_n) d\boldsymbol{\chi}_n d\boldsymbol{\chi}_{n+1}} \tag{67}$$

$$\hat{\boldsymbol{\chi}}_{n+1|n+1} = \underset{\boldsymbol{\chi}}{\operatorname{argmax}} \int p_{\mathbf{w}_{n+1}}(\mathbf{y}(n+1) - \mathbf{h}(\boldsymbol{\chi})) p_{\mathbf{v}_{n+1}}(\boldsymbol{\chi} - \mathbf{f}(\boldsymbol{\chi}_n, \boldsymbol{u}_{n+1})) p(\boldsymbol{\chi}_n|\mathbf{y}_n) d\boldsymbol{\chi}_n. \tag{68}$$

Using these Bayesian arguments, we can develop the nonlinear filter, when states are arbitrary Markovian process and measurement noise is non-Gaussian process. It should be noted that in our notation, $\mathbf{y}(n)$ is the instantaneous measurement at the time n, while $\mathbf{y}_n = \{\mathbf{y}_k : k \leq n\}$ is the aggregate of all measurements taken up to time n.

2. Large measurement noise ($\boldsymbol{R}$) leads to bad estimates in EKF method. However, small value of $\boldsymbol{R}$ leads to large $\boldsymbol{R}^{-1}$ which cause numerical instability. On the other hand, application of gradient search algorithm has computational limitations as matrix $\boldsymbol{F}(\Theta)$ is highly nonlinear dependence of parameter Θ.

8. Conclusions

This paper presents the transmissibility and recovery estimation of COVID-19 using the FOC-based EKF and WT methods. The EKF considers measurement and process noise into consideration, which gives better accuracy, while Kronecker product-based WT utilizes the property of scaling/resolution over different-time slots, which results in the compression of data. The importance of proposed models lies in the fact that these models can accommodate conventional EKF and WT methods as their special cases. Further, the estimated number of infected people and recovered people has been compared with the actual number of infected people and recovered people in India and China. Furthermore, the estimation accuracy of the proposed models is obtained in terms of SMAPE forecast errors. It is concluded that the FOC-based EKF method gives better performance than the conventional EKF and WT methods.

CRediT authorship contribution statement

All authors have participated in (a) conception and design, or analysis and interpretation of the data; (b) drafting the article or revising it critically for important intellectual content; and (c) approval of the final version. All the authors have contributed equally to the work reported in the manuscript (e.g., technical help, writing and editing assistance, general support), but who do not meet the criteria for authorship, are named in the Acknowledgements and have given us their written permission to be named. The corresponding author is responsible for ensuring that the descriptions are accurate and agreed by all authors.

UNCORRECTED PROOF

Declaration of competing interest

The authors declare that they have no known competing financial interests or personal relationships that could have appeared to influence the work reported in this paper.

References

[1] Y. Chen, Q. Liu, D. Guo, Emerging coronaviruses: genome structure, replication, and pathogenesis, J. Med. Virol. 92 (4) (2020) 418–423.
[2] W.G. Carlos, C.S. Dela Cruz, B. Cao, S. Pasnick, S. Jamil, Novel Wuhan (2019-nCoV) coronavirus, Am. J. Respir. Crit. Care Med. (2020), https://doi.org/10.1164/rccm.2014P7.
[3] L.E. Gralinski, V.D. Menachery, Return of the coronavirus: 2019-nCoV, Viruses 12 (2) (2020), https://doi.org/10.3390/v12020135.
[4] S. Zhao, Q. Lin, J. Ran, et al., Preliminary estimation of the basic reproduction number of novel coronavirus (2019-nCoV) in China, from 2019 to 2020: a data-driven analysis in the early phase of the outbreak, Int. J. Infect. Dis. 92 (2020) 214–217.
[5] J. Li, Y. Wang, S. Gilmour, et al., Estimation of the epidemic properties of the 2019, novel coronavirus: a mathematical modeling study.
[6] S.A. Lauer, K.H. Grantz, Q. Bi, et al., The incubation period of coronavirus disease 2019 (COVID-19) from publicly reported confirmed cases: estimation and application, Ann. Intern. Med. 172 (9) (2020) 577–583.
[7] B. Tang, X. Wang, Q. Li, et al., Estimation of the transmission risk of the 2019-nCoV and its implication for public health interventions, J. Clin. Med. 9 (2) (2020) 462.
[8] D. Fanelli, F. Piazza, Analysis and forecast of COVID-19 spreading in China, Italy and France, Chaos Solitons Fractals 134 (2020) 109761.
[9] A. Monticelli, State Estimation in Electric Power Systems: A Generalized Approach, Springer Science & Business Media, 2012.
[10] Z. Zhang, Q. Yu, Q. Zhang, et al., A Kalman filtering based adaptive threshold algorithm for QRS complex detection, Biomed. Signal Process. Control 58 (2020) 101827.
[11] M.L. Diouf, A. Iggidr, M.O. Souza, Stability and estimation problems related to a stage-structured epidemic model.
[12] M. Netto, L. Mili, A robust data-driven Koopman Kalman filter for power systems dynamic state estimation, IEEE Trans. Power Syst. 33 (6) (2018) 7228–7237.
[13] R. Bansal, S. Majumdar, H. Parthasarthy, Stochastic filtering in electromagnetics, IEEE Trans. Antennas Propag. (2020), https://doi.org/10.1109/TAP.2020.3027054.
[14] G. Rigatos, P. Wira, A. Melkikh, Nonlinear optimal control for the synchronization of biological neurons under time-delays, Cogn. Neurodyn. 13 (1) (2019) 89–103.
[15] G. Rigatos, P. Siano, A. Melkikh, A nonlinear optimal control approach of insulin infusion for blood glucose levels regulation, Intell. Ind. Syst. 3 (2) (2017) 91–102.
[16] G. Rigatos, Statistical validation of multi-agent financial models using the H-infinity Kalman filter, Comput. Econ. (2020) 1–22.
[17] H.D. Hesar, M. Mohebbi, Implementation of a square root filtering approach in marginalized particle filters for mixed linear/nonlinear state space models, Int. J. Adapt. Control Signal Process. 33 (3) (2019) 493–511.
[18] B. Lamien, L.A. Varon, H.R. Orlande, et al., State estimation in bioheat transfer: a comparison of particle filter algorithms, Int. J. Numer. Methods Heat Fluid Flow 27 (3) (2017) 615–638.
[19] Y. Fujita, M. Hiromoto, T. Sato, PARHELIA: particle filter-based heart rate estimation from photoplethysmographic signals during physical exercise, IEEE Trans. Biomed. Eng. 65 (1) (2017) 189–198.
[20] L. Feng, J. Ding, Y. Han, Improved sliding mode based EKF for the SOC estimation of lithium-ion batteries, Ionics (2020) 1–8.
[21] R. Bansal, S. Majumdar, Parthasarathy H. Extended, Kalman filter based nonlinear system identification described in terms of Kronecker product, AEÜ, Int. J. Electron. Commun. 108 (2019) 107–117.
[22] M. Yakoubi, R. Hamdi, M.B. Salah, EEG enhancement using extended Kalman filter to train multi-layer perceptron, Biomed. Eng., Appl. Basis Commun. 31 (01) (2019) 1950005.
[23] O. Brovko, D.M. Wiberg, L. Arena, et al., The extended Kalman filter as a pulmonary blood flow estimator, Automatica 17 (1) (1981) 213–220.
[24] I. Ullah, S. Qian, Z. Deng, J.H. Lee, Extended Kalman Filter-based localization algorithm by edge computing in Wireless Sensor Networks, Dig. Commun. Netw. (2020).
[25] D. Ndanguza, I.S. Mbalawata, H. Haario, et al., Analysis of bias in an Ebola epidemic model by extended Kalman filter approach, Math. Comput. Simul. 142 (2017) 113–129.
[26] A. Gomez-Exposito, J.A. Rosendo-Macias, M.A. Gonzalez-Cagigal, Monitoring and tracking the evolution of a viral epidemic through nonlinear Kalman filtering: application to the Covid-19 case, medRxiv, 2020 Jan. 1.
[27] S. Majumdar, H. Parthasarathy, Wavelet-based transistor parameter estimation, Circuits Syst. Signal Process. 29 (5) (2010) 953–970.
[28] R. Cartas-Rosado, B. Becerra-Luna, R. Martinez-Memije, O. Infante-Vazquez, C. Lerma, H. Perez-Grovas, J.M. Rodriguez-Chagolla, Continuous wavelet transform based processing for estimating the power spectrum content of heart rate variability during hemodiafiltration, Biomed. Signal Process. Control 62 (2020) 102031.
[29] T. Tuncer, S. Dogan, Subasi A. Surface, EMG signal classification using ternary pattern and discrete wavelet transform based feature extraction for hand movement recognition, Biomed. Signal Process. Control 58 (2020) 101872.
[30] C. Wu, M.E. Magana, E. Cotilla-Sanchez, Dynamic frequency and amplitude estimation for three-phase unbalanced power systems using the unscented Kalman filter, IEEE Trans. Instrum. Meas. 68 (9) (2018) 3387–3395.
[31] S. Metia, Q.P. Ha, H.N. Duc, M. Azzi, Estimation of power plant emissions with unscented Kalman filter, IEEE J. Sel. Top. Appl. Earth Obs. Remote Sens. 11 (8) (2018) 2763–2772.
[32] A. Atrsaei, H. Salarieh, A. Alasty, M. Abediny, Human arm motion tracking by inertial/magnetic sensors using unscented Kalman filter and relative motion constraint, J. Intell. Robot. Syst. 90 (1–2) (2018) 161–170.
[33] D. Baleanu, K. Diethelm, E. Scalas, J.J. Trujillo, Fractional Calculus: Models and Numerical Methods, World Scientific, Singapore, 2010.
[34] X. Hu, H. Yuan, C. Zou, Z. Li, L. Zhang, Co-estimation of state of charge and state of health for lithium-ion batteries based on fractional-order calculus, IEEE Trans. Veh. Technol. 67 (11) (2018) 10319–10329.
[35] N. Miljkovic, N. Popovic, O. Djordjevic, L. Konstantinovic, T.B. Sekara, ECG artifact cancellation in surface EMG signals by fractional order calculus application, Comput. Methods Programs Biomed. 140 (2017) 259–264.
[36] N.B. Popovic, N. Miljkovic, T.B. Sekara, Electrogastrogram and electrocardiogram interference: Application of fractional order calculus and Savitzky-Golay filter for biosignals segregation, in: 2020 19th International Symposium INFOTEH-JAHORINA, INFOTEH, IEEE, 2020, pp. 1–5, Mar 18.
[37] F.A. Rihan, Q.M. Al-Mdallal, H.J. AlSakaji, A. Hashish, A fractional-order epidemic model with time-delay and nonlinear incidence rate, Chaos Solitons Fractals 126 (2019) 97–105.
[38] F.A. Rihan, D. Baleanu, S. Lakshmanan, R. Rakkiyappan, On fractional SIRC model with salmonella bacterial infection, in: Abstract and Applied Analysis, Hindawi, 2014 Apr 1 (Vol. 2014).
[39] V.P. Latha, F.A. Rihan, R. Rakkiyappan, G. Velmurugan, A fractional-order model for Ebola virus infection with delayed immune response on heterogeneous complex networks, Am. J. Comput. Appl. Math. 339 (2018) 134–146.
[40] K.S. Mawonou, A. Eddahech, D. Dumur, D. Beauvois, E. Godoy, Improved state of charge estimation for Li-ion batteries using fractional order extended Kalman filter, J. Power Sources 435 (2019) 226710.
[41] J.I. Hidalgo-Reyes, J.F. Gomez-Aguilar, V.M. Alvarado-Martinez, M.G. Lopez-Lopez, R.F. Escobar-Jimenez, Battery state-of-charge estimation using fractional extended Kalman filter with Mittag-Leffler memory, Alex. Eng. J. (2019).
[42] Y. Wang, G. Gao, X. Li, Z. Chen, A fractional-order model-based state estimation approach for lithium-ion battery and ultra-capacitor hybrid power source system considering load trajectory, J. Power Sources 449 (2020) 227543.
[43] X. Huang, Z. Gao, C. Yang, F. Liu, State estimation of continuous-time linear fractional-order systems disturbed by correlated colored noises via Tustin generating function, IEEE Access 8 (2020) 18362–18373.
[44] J. Brewer, Kronecker products and matrix calculus in system theory, IEEE Trans. Circuits Syst. 25 (9) (1978) 772–781.
[45] W.H. Greub, Multilinear Algebra, Springer, Berlin, Heidelberg, 1967.
[46] T. Chen, J. Rui, Q. Wang, Z. Zhao, J-A. Cui, L. Yin, A mathematical model for simulating the transmission of Wuhan novel Coronavirus, bioRxiv, 2020, 2020.2001.2019.911669 (Accessed 13 February 2020).
[47] W.T. Zha, F.R. Pang, N. Zhou, B. Wu, Y. Liu, Y.B. Du, X.Q. Hong, Y. Lv, Research about the optimal strategies for prevention and control of varicella outbreak in a school in a central city of China: based on an SEIR dynamic model, Epidemiol. Infect. (2020) 148.

UNCORRECTED PROOF

[48] Y. Yang, L. Xu, Stability of a fractional order SEIR model with general incidence, Appl. Math. Lett. 24 (2020) 106303.
[49] B. Xiong, J. Zhao, Z. Wei, et al., Extended Kalman filter method for state of charge estimation of vanadium redox flow battery using thermal-dependent electrical model, J. Power Sources 262 (2014) 50–61.
[50] World Health Organization, Novel Coronavirus, World Health Organization, 2020, Available at: https://www.who.int/.
[51] R.J. Hyndman, A.B. Koehler, Another look at measures of forecast accuracy, Int. J. Forecast. 22 (4) (2006) 679–688.

Rahul Bansal received Ph.D. degree from Delhi Technological University (Formerly Delhi College of Engineering), New Delhi, India, in 2020. He was the recipient of Junior Research Fellowship and Senior Research Fellowship from Council for Scientific and Industrial Research (CSIR), India. He received Research Excellence Award from Delhi Technological University, Delhi, India in March 2020. He is a reviewer of several international journals. He is currently working as an Assistant Professor with the Department of Electronics and Communication Engineering, Ajay Kumar Garg Engineering College, Ghaziabad, India. His research interests include nonlinear filtering, state and parameter estimation of the systems, nonlinear analysis of systems, stochastic filtering.

Amit Kumar received his Bachelor of Computer Application (BCA) from Dr. Bhimrao Ambedkar University, Agra, India and Master of Computer Application (MCA) from Amity University, Noida, India. Currently, he is working as an Assistant Professor in Dyal Singh College, Delhi University, India. His research interests include parameter estimation of the systems, nonlinear analysis of systems etc.

Amit Kumar Singh received his M.Tech. and Ph.D. degree in Computer Science from Jawaharlal Nehru University, New Delhi, India. He was a postdoc fellow in National Tsing Hua University, Taiwan. He is currently an assistant professor with the department of Computer Science at Ramanujan College, University of Delhi, India. His research interests include performance modeling of wireless networks, information theory, and queueing systems.

Sandeep Kumar received his B. Tech. in electronics and communication from Kurukshetra University, India in 2004 and Master of Engineering in Electronics and Communication from Thapar University, Patiala, India in 2007. He received his PhD. from Delhi Technological University, Delhi, India in 2018. He is currently working as Member (Research Staff) at Central Research Laboratory, Bharat Electronics Limited Ghaziabad, India. His research interests include the study of wireless channels, performance modeling of fading channels and cognitive radio networks. He is also serving as a reviewer for several international journals IEEE, Springer, Elsevier etc.

UNCORRECTED PROOF

Cognitive Computation
https://doi.org/10.1007/s12559-020-09813-6

Survey on Machine Learning and Deep Learning Applications in Breast Cancer Diagnosis

Gunjan Chugh[1] · **Shailender Kumar**[1] · **Nanhay Singh**[2]

Received: 4 September 2020 / Accepted: 28 December 2020
© The Author(s), under exclusive licence to Springer Science+Business Media, LLC part of Springer Nature 2021

Abstract
Cancer is a fatal disease caused due to the undesirable spread of cells. Breast carcinoma is the most invasive tumors and is the main reason for cancer deaths in females. Therefore, early diagnosis and prognosis have become necessary to increase survivability and reduce death rates in the long run. New artificial intelligence technologies are assisting radiologists in medical image scrutiny, thereby improving cancer patients' status. This survey enrolls peer-reviewed, newly developed computer-aided diagnosis (CAD) systems implementing machine learning (ML) and deep learning (DL) techniques for diagnosing breast carcinoma, compares them with previously established methods, and provides technical details with the pros and cons for each model. We also discuss some open issues, research gaps, and future research directions for the advanced CAD models in medical image analysis. Over the past decade, machine learning and deep learning have emerged as a subfield of artificial intelligence (AI), whose healthcare industry applications have provided excellent results with reduced cost and improved efficiency. This survey analyzes different classifiers of machine learning and deep learning approaches for breast cancer diagnosis. Results from previous studies proved that deep learning outperforms conventional machine learning for diagnosing breast carcinoma when the dataset is broad. Research gaps from the recent studies depict that practical and scientific research is an urgent necessity for improving healthcare in the long run.

Keywords Breast cancer · Machine learning · Deep learning · Convolution neural network (CNN) · Computer-aided diagnosis (CAD)

Introduction

Our bodies have millions of cells. Cancer starts when cellular changes cause these cells to grow excessively, creating a lump called a primary tumor [1]. According to data reported in Cancer Statistics, 2018 [2], approximately 2.25 million people live with this disease. New registered cancer patients exceed 1,157,294, and nearly 784, 821 cancer-related deaths are reported annually. The risk of dying from cancer is approximately 7.34% in males and 6.28% in females. In males, 25% of cancer deaths were reported for oral cavity and lung cancer, whereas breast and oral cavity cancer accounts for 25% of cancers in females [2].

Figure 1 shows a detailed description of cancer statistics for the year 2018. As we can see, breast cancer is the most frequent carcinoma and constitutes 14% of all cancers in women. Globocan 2018 study [2] reported approximately 162,468 new breast cancer cases and 87,090 deaths.

Incidences of breast carcinoma are increasing at a startling rate in India, particularly in younger age groups—30s and 40s (Fig. 2). Women aged 20–59 years are most often affected by breast cancer [4]. In India, detection occurs very late, which is the main reason for low survival rates for breast carcinoma [5]. Over the last few decades, cancer-related research is being performed. Scientists have applied different methods to predict disease before they cause symptoms. Therefore, accurate diagnosis and prognosis of breast cancer are regarded as exciting and challenging tasks for physicians in the medical and healthcare communities [6].

✉ Shailender Kumar
shailenderkumar@dce.ac.in

[1] Department of Computer Science and Engg, Delhi Technological University, Delhi, India

[2] Department of Computer Science, Ambedkar Institute of Advanced Communication Technologies and Research, Delhi, India

Published online: 30 January 2021

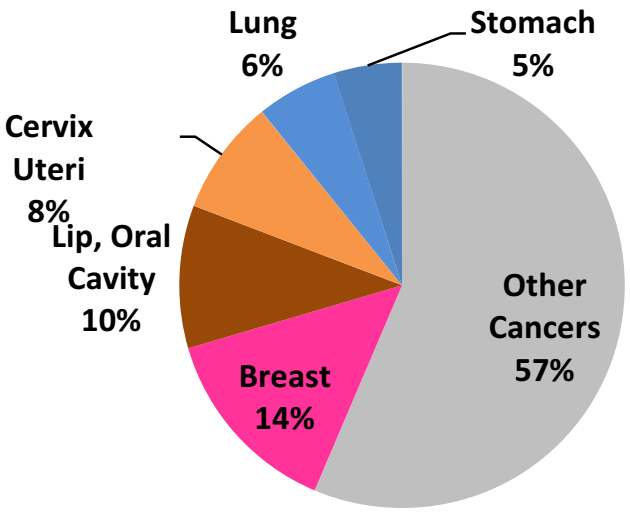

Fig. 1 Cancer Statistics 2018[3]

Manual diagnosis of breast cancer is tedious and time-consuming; thus, there arises a need for automatic diagnosis. The current healthcare systems have proven to be helpful, but they are prone to errors. Therefore, medical image classification using CAD has emerged as an efficient tool that can help doctors classify medical images in different categories, leading to early diagnosis and treatment [8–10]. In this context, ML and DL have come up with algorithms capable of more accurately diagnosing the disease at an earlier stage and thus diminishing the number of readmissions in hospitals and clinics. AI techniques can thus boost the procurement of new fidelity protocols in medicine and reduce healthcare costs due to misdiagnosis [11].

This survey focuses on recent research developments for early diagnosis of breast carcinoma using ML & DL techniques. It highlights the strengths and weaknesses of various research methods distinguishing this survey paper from other existing surveys. Challenges and future directions are also discussed that would guide a new researcher in this field.

The paper is structured in the following way: "Breast Cancer" introduces breast cancer with its categorization, evolution stages, imaging modalities, and performance measures. "Computer-Aided Diagnosis [18]" focuses on medical image analysis using CAD and outlines machine learning and deep learning-based CAD models. Literature survey for diagnosing breast carcinoma is summarized in "Literature Survey". "Research Gaps and Future Directions" discusses research gaps and future research recommendations for the advanced CAD system in the field. Finally, the conclusion is outlined in "Conclusion".

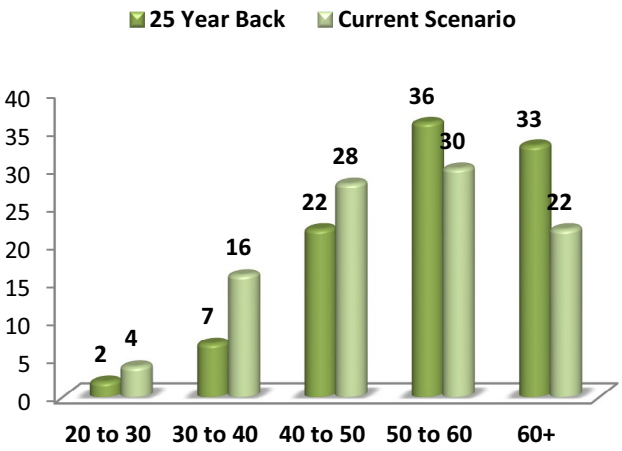

Fig. 2 Incidences of breast cancer in India [7]

Breast Cancer

Lobules (i.e., milk-producing glands) or the ducts (i.e., canals for carrying the milk from the lobules to the mammilla) of the breast are the primary regions where breast cancer initiates. The unbounded evolution of cancer cells can spread to other robust breast tissue and transit to the arms' lymph glands. The lymphatic nodes are responsible for moving the tumor cells to further body parts.

Physical signs of breast carcinoma include breast tenderness, irritation, nipple discharge besides breast milk, inverted nipple, change in breast size, soreness, or blister under your arm. Risk factors associated with breast cancer may include age, overweight, low physical activity, excessive alcohol consumption, dense breast, genes, early menstruation, and advanced maternal age [12]. S. Simsek et al. [13] evaluated the impact of several factors that contribute to breast cancer at various time intervals (1 year, 5 years, and 10 years). The authors used two algorithms, artificial neural network (ANN) and logistic regression (LR), and also show how the significance of such parameters changes over time. Researchers concluded that the factors that are considered relevant for cancer at an initial stage might not contribute equally to predicting patients' survivability over the long term. For example, age is regarded as an essential factor for forecasting survivability, but its potentiality drops with time, maybe due to the empowerment of other factors such as grade, lymph nodes positive, etc. Therefore, the importance of all such elements must be considered when developing a model for predicting breast cancer survivability in the future.

Categorization

Breast carcinoma is investigated by distinguishing tumors as malignant and benign. The medical practitioner and pathologists need a reliable diagnostic procedure to differentiate these two classes of tumors [14].

It can be categorized into two classes: invasive and non-invasive/in situ. Invasive cancer starts in the milk ducts (canals) and can spread to the surrounding breast tissue and other breast parts, whereas non-invasive cancer cannot escalate within or to other body parts.

Invasive and non-invasive breast carcinomas are further categorized as follows:

1. **Ductal carcinoma in situ:** It is non-invasive carcinoma where cancer cells have not transmitted in the neighboring breast tissue and are limited to the breast ducts.
2. **Lobular carcinoma in situ:** In this carcinoma also, cancer cells have not infected nearby tissues, but cells spread in the milk-producing glands of the breast.
3. **Invasive ductal carcinoma:** This is the most prevalent category of cancer. It initiates in milk ducts of the breast and can then spread to neighboring tissues of the breast. This might extend to adjacent tissues in the body once it starts spreading beyond the breast ducts.
4. **Invasive lobular carcinoma:** This cancer starts in lobules and then infects adjacent tissues.

Some less frequent categories of breast cancer include:

1. **Phyllodes tumor:** This category of breast cancer is infrequent and mostly benign but can be malignant too. It can grow in the connected tissues of the breast.
2. **Angiosarcoma:** Blood vessels or lymph vessels are the primary sources where this carcinoma grows in the breast.
3. **Inflammatory breast carcinoma:** It is the rarest of a rare case and accounts for 1 to 5% of all cases. Having this carcinoma causes the breast to swell, felt very hot, and becomes red.
4. **Triple-negative breast carcinoma:** It accounts for 10 to 20% of all cases. This type of carcinoma occurs when a tumor does not have extra human epidermal growth factor receptor (HER2) proteins on its surface and lacks estrogen and progesterone receptors. Hormonal therapy for breast cancer is not sufficient, so this type of carcinoma is difficult to treat.

Evolution Stages

Stages of breast carcinoma can be divided based on the tumor size and how much it has grown in the nearby tissues. Table 1 shows the categorization of breast cancer in four main stages [15].

Imaging Modalities

Different modalities can be used to diagnose breast carcinoma. The following are some of the commonly used modalities used by the researchers in recent years:

1. Screen Film Mammography (SFM)[16, 17]

SFM shows an X-ray picture of the breast.
Pros:

- Detects cancer at an early stage
- Standard modality
- High sensitivity for breast with fatty tissue
- Cost-effective

Cons:

- Low sensitivity with dense breast
- Not digital

2. Full field digital mammography (FFDM)/digital mammography (DM) [16, 17]

Here, X-ray films are converted into mammographic photographs of the breast (digital images) by digital detectors.
Pros:

- Detects cancer at an early stage
- Effective and standard modality
- Reduce cancer rate by 15%

Cons:

Table 1 Breast carcinoma evolution stages

Stages	Description
Stage 0	Abnormal cells are present but not grown in neighboring tissues
Stage 1: In situ	Cancer cells are confined only in the lobules and ducts of the breast
Stage 2: Localized	Some lymph nodes are involved, and the size of the tumor is confined between 20 and 50 mm
Stage 3: Regional	Tumor size is greater than 50 mm, and cancer grows in skin or chest wall with more involvement of lymph nodes
Stage 4: Distant	The tumor can spread further to any part of the body and can be of any size

- High false-positive and false-negative findings
- High radiation exposure
- High cost compared with SFM
- Low specificity thus leads to unnecessary biopsies

3. Digital breast tomosynthesis (DBT)/3D mammography [16, 17]

Similar to mammogram, here, breast images are acquired at multiple angles and thus create 2D and 3D-like pictures of the breasts.

Pros:

- Detects cancer in women with dense breast
- Reduce no. of false positive and false negative
- Multiple 3D images with a single screening

Cons:

- Expensive
- Average radiation dose is 1 to 2 times higher than DM

4. Ultrasound (US) [16, 17]

US images are also called sonograms. It uses high-frequency sound waves.

Pros:

- No radiation involved
- It can be used for pregnant women and women with dense breast
- It is the best way to figure out whether the anomaly is solid or fluid-filled.
- Safe, accurate, and low-cost

Cons:

- Operator dependent
- Many false-positive and false-negative results

5. Magnetic resource imaging (MRI) [16, 17]

Another modality to diagnose breast carcinoma is MRI. Here, powerful magnetization and radio signals generate high-quality pictures of the breast.

Pros:

- Used for high-risk patients
- High sensitivity as compared with the US
- Identifies incredulous areas that can further be used for biopsy

Cons:

- Expensive compared with US and DM
- Low specificity
- Risk of a false-positive result
- Body temperature may increase during long MRI

6. Histopathology (HP) images [16, 17]

These are Hematoxylin & Eosin-stained images. In this, samples are taken from abnormal breast regions (called a biopsy) and are observed under the microscope.

Pros:

- Diagnose different breeds of cancer instead of detecting only malignancy because of multi-color images
- A comprehensive study of tissues is possible
- Fewer chances of missing cancer in the initial stages because multiple region-of-interest (ROI) images are created from whole slide images

Cons:

- High proficiency is required as the manual analysis is tedious and time-consuming
- Color variation and different staining procedures can cause misdiagnosis

Performance Measures

The confusion metric is one of the estimates used for evaluating the performance of a model. It indicates the relationship between predicted and actual values (Table 2).

True positive (TP)—patients diagnosed positive and are genuinely positive.

True negative (TN)—patients diagnosed negative and are actually negative.

False positive (FP)—patients diagnosed positive but are truly negative.

False negative (FN)—patients diagnosed negative and are genuinely positive.

Other metrics for evaluating the effectiveness of a model are discussed below:

Table 2 Confusion matrix

	Predicted positive	Predicted negative
Actual positive	True positive	False negative
Actual negative	False positive	True negative

1. Accuracy: It is the ratio of correctly categorized samples to the total number of samples and is interpreted as:

$$\text{Accuracy} = \frac{TP+TN}{TP+TN+FP+FN}$$

2. Sensitivity/recall/true positive rate (TPR): It evaluates what percentage of patients are correctly identified to have a particular disease (+ve instances) and illustrated as:

$$\text{Sensitivity (recall)} = \frac{TP}{TP+FN}$$

3. Specificity/true negative rate (TNR): Determines what percentages of patients are correctly identified not to have a particular disease (−ve instances) and elucidated as:

$$\text{Specificity} = \frac{TN}{TN+FP}$$

4. Precision/positive predicted value (PPV): Specifies what percentage of patients are actually relevant (+ve) and described as:

$$\text{Precision} = \frac{TP}{TP+FP}$$

5. F-measure: Interpreted as the harmonic mean of precision and recall and is defined as:

$$\text{F-measure} = \frac{2\times\text{Precision}\times\text{Recall}}{\text{Precision}+\text{Recall}}$$

6. False-positive rate (FPR): It predicts a positive value when the result is negative. Thus, FPR is 1-specificity and is given as:

$$\text{FPR} = \frac{FP}{TN+FP}$$

7. Area under the receiver operating characteristic curve (AUC-ROC): It defines a model's capability to distinguish between different classes. It is drawn by plotting sensitivity on the *y*-axis (true positive rate) and 1-specificity on the *x*-axis (false-positive rate). Thus, model performance is evaluated by calculating the area under this curve, whose value lies from 0 to 1. The higher the value, the more powerful and reliable the model is at distinguishing positive patients as positive and negative patients as negative.

Computer-Aided Diagnosis [18]

Earlier, medical image processing was done manually. Still, it faces three main issues—firstly, the unavailability of more than one pathologist in one place. Secondly, manual image analysis is a very laborious and stressful operation, and thirdly, the professional experience and domain knowledge of pathologists are very crucial for breast carcinoma diagnosis. Thus, to overcome misdiagnosis in the early stages, CAD has emerged, which acts as a "second notion" for solving breast cancer multi-classification problems [16].

CAD systems require processing on medical images; thus, extensive computational algorithms must be developed to process those images. CAD is reasonably good at detecting invasive breast cancers in their early stages but increases the peril of false positive results. Thus, accuracy and workflow efficiency must be considered before implementing CAD in clinical practice, and secondly, to avoid improper use, user training is equally important to understand the limitations and capabilities of CAD systems (Fig. 3) [19].

CAD systems are categorized into two categories [21]:

Computer-aided detection (CADe) systems: Provides computerized detection and localization of anomalies in medical images

Computer-aided diagnosis (CADx) systems: Serve to determine the class of anomalies to classify them as benign or malignant. It can be used as a step further to the detection model, to provide additional information and further help in decision making.

CAD Using Machine Learning

CAD system implementing machine learning comprises of the following stages:

(1) Image preprocessing, i.e., removing the noise and thus cleaning the image and preparing it for the subsequent stage [22]

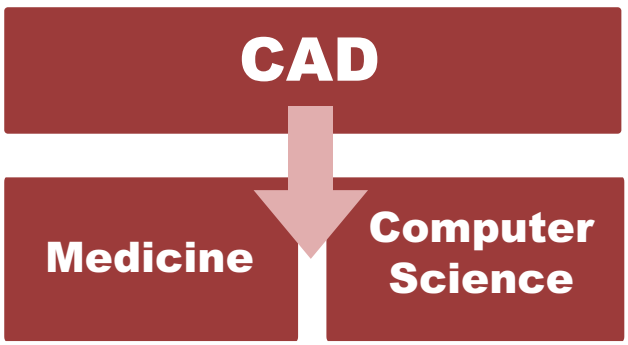

Fig. 3 CAD acts as a mediator connecting medicine with computer science [20]

(2) Image segmentation, i.e., partitioning the image into several parts, to work only on the segmented regions called regions of interest (ROI) [22]
(3) Feature extraction and selection, i.e., extracting relevant features from the pre-processed images. Feature selection provides many advantages that include cost reduction, lesser learning time, and increased accuracy [23]
(4) Classification, i.e., assigning labels or classes to different groups using several classifiers such as support vector machine (SVM), K-nearest neighbor (KNN), Naïve Bayes (NB), decision tree (DT), random forest (RF), logistic regression (LR), etc.

CAD Using Deep Learning

Before classifying the entire image, neural networks are competent in learning transitional, hierarchical, and more intellectual characterization of the data [24], and thus, deep learning is categorized as a representation learning technique. Deep learning learns characteristics directly from the data using several non-linear computation layers [9]. Contemporary research communicated that "convolutional neural network (CNN)" attains remarkable performance in cancer detection and diagnosis [25]. Layers adjoining the input layer learn low-level features and are more generic. In contrast, layers adjoining the output layer learn distinctive features of the input image and, thus, are more specific [26]. Figure 4 shows the ML- and DL-based CAD systems. CAD system based on CNN implements the following layers:

(1) Convolutional layers for performing convolution operation that automatically extract features from the image
(2) Pooling layer for reducing the dimensionality of features
(3) Fully connected and Softmax layer for performing classification.

When inadequate data is available to train a generalizable model, data augmentation is executed for enlarging statistics of data points. Operations performed for augmentation involve rotation, noise inclusion, image cropping, and other geometrical activities [27].

Two ways to implement CNN are

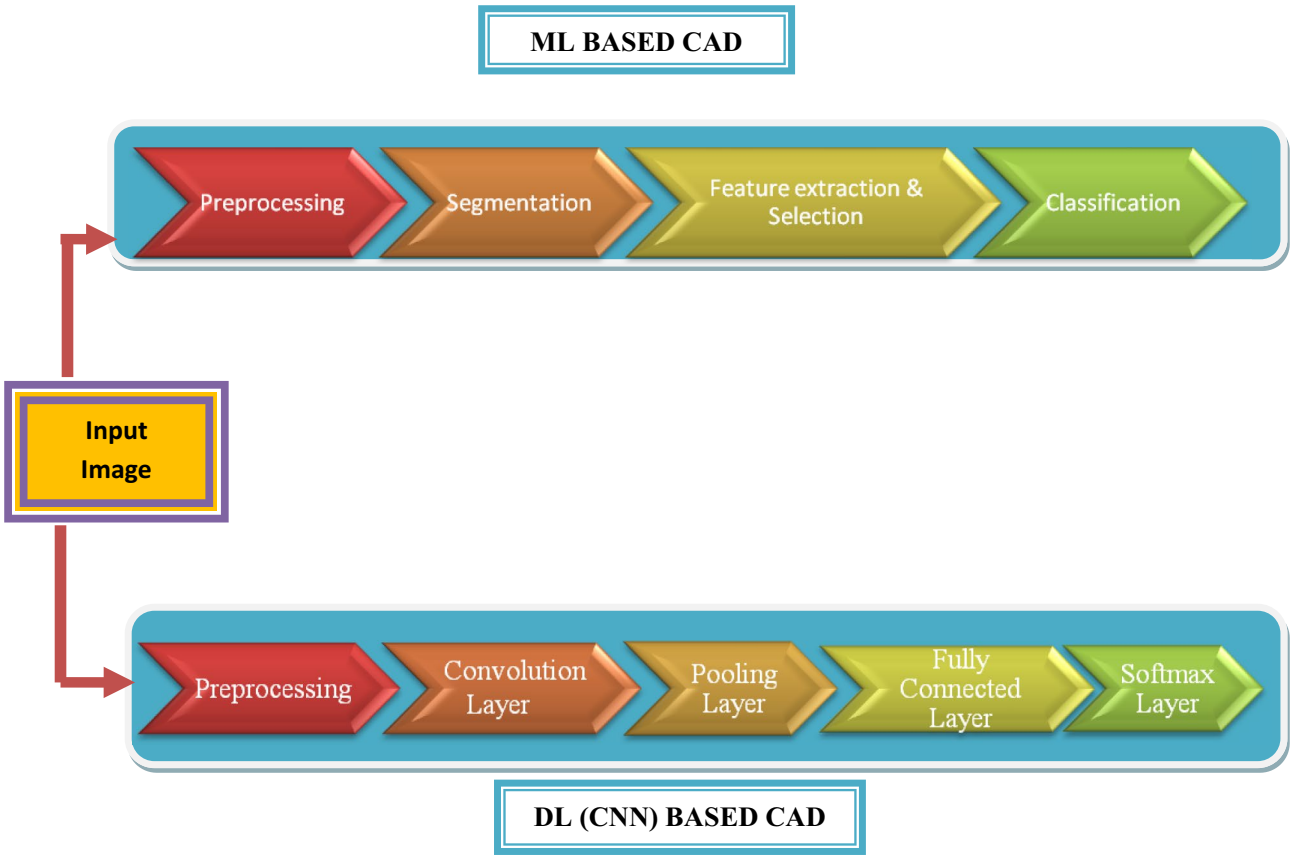

Fig. 4 ML-based and DL (CNN)-based CAD systems

(1) Training from scratch*:* CNN can be trained from scratch by providing enough training examples as input. When creating CNN from scratch, considerable skill and experience are required. Selecting suitable hyperparameters such as the learning rate, the size of convolutional filters, the number of layers, etc., is challenging. Thus, the entire process is time-consuming and is usually implemented on powerful GPUs with high processing power.[28].

(2) Transfer learning: Training a CNN on a small database affects the model's generalizability and usually results in overfitting. Transfer learning involves transferring the knowledge from the source domain, which has extensive samples of data, to the target domain, where data is comparably significantly less for training a deep CNN. Pretrained models, i.e., models trained on non-medical images, which usually have large datasets, can prepare the models for medical images with smaller datasets. Pretrained networks can be used in three approaches, which are discussed below:

- As the baseline model: This approach exploits only the architecture of the pre-trained network. Thus, the complete model is built from scratch by random initialization of weights. [29].
- As feature extractor: Here, convolutional base is frozen, and the pre-trained weights remain unaltered, i.e., the output from the convolutional base is fed directly to the classifier [29]. The pre-trained model is used to excerpt the essential features from the input dataset.
- Fine tuning: Through this method, weights are passed into the intended network from a pre-trained network. This can be implemented in two ways: fine-tuning the system—layer-wise—and secondly, performing partial training of the network [29].

Literature Survey

Papers Reviewed

This survey explores 81 peer-reviewed papers, of which 23 articles diagnose breast carcinoma using classification algorithms of machine learning while the rest implements deep learning techniques. Figures 5 and 6 show the statistical distribution of ML and DL articles and imaging modalities used in the survey.

Databanks

The list of publicly available datasets used by the researchers in recent years is given in Table 3

Electronic Repositories

This survey paper analyzes several studies on machine learning and deep learning classifiers to diagnose and classify breast carcinoma. Searching criteria for inclusion and exclusion of the peer-reviewed journal paper are based on the following keywords: breast cancer, computer-aided diagnosis, machine learning, deep learning, classification, detection, computer-assisted diagnosis, and computer-aided detection. The researchers' electronic databases used in the survey include Elsevier, Springer, IEEE, Wiley, Oxford, Plos One, Hindwai, etc.

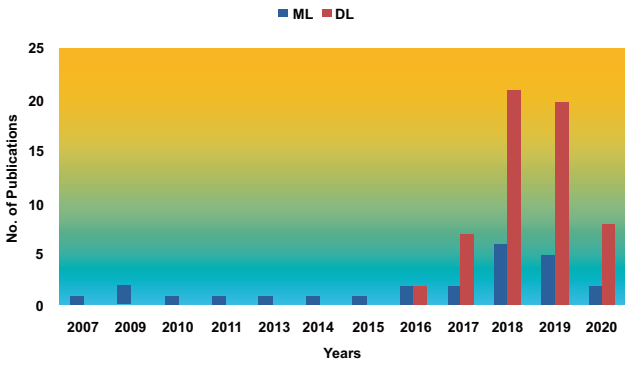

Fig. 5 A statistical distribution of ML and DL papers analyzed in the survey

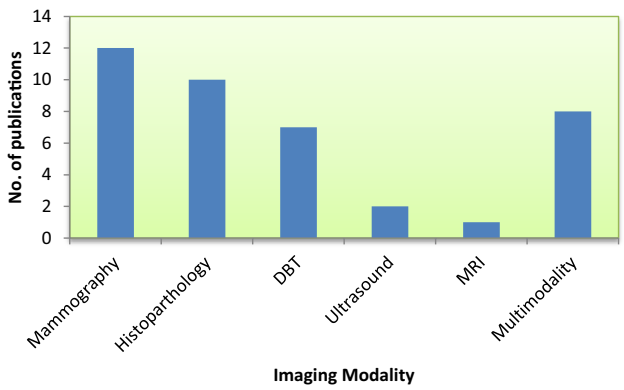

Fig. 6 A statistical distribution of imaging modalities used in the survey

Table 3 Databanks

Digital repository	Dataset name	Dataset description
UCIMLR/University of California Irvine Machine Learning Repository [30]	WBCD/Wisconsin Breast Cancer Dataset	WBCD is a commonly used dataset among researchers working on machine learning research. It contains 569 instances with 32 attributes
BCDR/Breast Cancer Digital Repository[31]	(a) BCDR-FM/ Film Based Digital Repository (b) BCDR–DM/ Full Field Digital Mammography based Digital Repository	It comprises mammography and ultrasound images of 1734 patients(1010 BCDR-FM and 724 BCDR-DM) along with their clinical history
MIAS /Mammography Image Analysis Society[32]	MIAS/Mammography Image Analysis Society	It has 322 digital mammography breast images at 50-micron resolution
Mini-MIAS[33]	Mini-MIAS	Here, the resolution of mammographic images (MIAS) has been reduced to 200 microns, and the image size is 1024 × 1024 pixels
The University of South Florida [34]	DDSM/Digital Database for Screening Mammography	It comprises 2620 cases which are annotated in 3 categories—normal, benign, malignant
BreakHis [35]	BreakHis/Breast Cancer Histopathological Database	It consists of a total of 7909 microscopic images of breast tissue collected at different magnifying factors. 7909 cases are divided into 2480 benign samples and 5429 malignant samples
SEER[36]	SEER/ Surveillance Epidemiology and End Result	SEER dataset provides stage-wise survivability statistics of breast cancer data
InBreast [37]	InBreast	This database consists of 115 cases with 410 images
IRMA [38]	IRMA/Image Retrieval in Medical Applications	It consists of 10,509 reference breast images

Comparative Research Using Classification Algorithms of Machine Learning

This section presents a comparative study from various authors implementing diverse machine learning classifiers for diagnosing breast cancer.

Osareh and Shadgar [39] categorized benign and malignant tumors on fine needle aspirates of breast lumps (FNAB) and Gene Microarray datasets. The authors performed feature extraction using principal component analysis (PCA), feature ranking using signal to noise ratio (SNR), and feature selection using a wrapper-based approach, i.e., sequential forward selection (SFS). Finally, classification was done using three classifiers—SVM, KNN, and probabilistic neural network (PNN). The authors concluded that the best results could be obtained by appropriate selection of kernels and classifiers. SVM with the RBF kernel attains the accuracy of 98.80% on FNAB and 96.33% on the microarray dataset after applying SFS and PCA. Their work suggested that SVM models with radial basis function (RBF) kernel could be further explored as a diagnostic aid for breast carcinoma diagnosis.

Feature selection and reduction are very crucial parameters that affect classifier performance. The finest classifier will perform worse if features are not chosen wisely. Karabatak and Ince [40] used association rules (AR) on WBCD and reduced feature dimensions from nine to four. The authors obtained 95.6% and 97.4% accuracy with 4-inputs and 8-inputs, respectively, by performing classification using neural network (NN). In contrast, the rough set (RS) reduction algorithm eliminates redundant attributes and identifies essential features relevant to the model [41]. Chen et al. [41] implemented the RS algorithm on WBCD along with the SVM classifier and obtained 99.41% accuracy for a subset with five critical features. K. Goyal et al. [1] implemented seven different algorithms—Bagging, Ada Boost, LR, SVM, RF, NB, and DT on WBCD. The authors compared classifiers' results by implementing various feature selection techniques such as PCA, subset evaluation using best first, and correlation attribute evaluation. Ada Boost and LR classifier attained significant performance using PCA with an accuracy of 97.92% for the reduced dataset.

Similarly, Shaikh et al. [42] implemented four classifiers, namely, NB, KNN, J48, and SVM, on WBCD and BCDR. 'WrapperSubsetEval,' the wrapper feature selection technique provided by the Weka tool, was applied to both datasets. Results show that the best results were given by SVM with an accuracy of 97.91% and 95.10% on WBCD and BCDR. Some of the well-known research on breast carcinoma diagnosis is summarized in Table 4.

Table 4 Summarization of distinguished work on breast cancer diagnosis using machine learning classifiers

Data set used	Method adopted	Accuracy achieved	Pros	Cons	Reference
UCI machine learning repository	Feature selection: *genetic algorithm (GA)* Classification: *SVM*	Small scale—GA + linear SVM *bagging: 98%* GA + RBF SVM *boosting: 98.28%* Large scale—RBF + SVM *boosting: 99.52%*	• SVM ensemble model performs better than single SVM classifier • Feature reduction using GA reduces computation time to a large extent in small datasets	• SVM ensemble model based on boosting took a long time in construction	[12]
2301 patients (clinical data records)	Support vector regression ((SVR) with RBF, linear and poly kernel, decision tree regression (DTR) model, stochastic gradient descent model	Best accuracy—*SVR-linear and DTR*	• SVR linear model and DTR model best suited for survival time prediction • Tumor integrated clinical feature(TICF) performs better than the Nottingham prognostic index (NPI)	-	[14]
SEER	NB, LR, DT	Survivability prediction on all stages together can cause overestimation of performance	• The stage-specific model performs better than the joint model	• Distant summary stage shows the worst performance due to lesser instances of training data	[15]
WBCD	Least square–support vector machine (LS-SVM)	*98.53%*	• Used a set of linear equations for training; therefore, calculation became easier	• Feature Selection not combined with the classification	[48]
	Hybrid of K-means with SVM (K-SVM)	*97.38%*	• Reduces training time by reducing input features from *thirty-two to six* • Feature selection during training and validation phase not required	-	[49]
	SVM, Decision Tree-C4.5, Naive Bayes, KNN	*97.13%*	• SVM is manifested to be the finest classifier with the least error rate and highest correctly classified instances on WBCD		[50]
UCI machine learning repository	SVM, DT-J48, NB, LR	Dermatology—*NB + LR (97%)* Breast cancer-*SVM-PCA (97%)* Chronic kidney Disease-*J48 (99%)*	• High accuracy • Accuracy could be improved by considering more data and parameters such as age, sex, locality • CNN could be used in the future to automate feature extraction.		[51]

Sometimes, the results from individual classifiers can be improved by combining several classifiers using different methods, thus producing an ensemble model. In [43], the authors proposed an ensemble framework using four machine learning classifiers—KNN, SVM, DT, and LR and obtained 97.88% accuracy. The sequential least square programming method (SLSQP) was used for assigning weights to each classifier. The findings show that the ensemble model outperforms a standalone machine learning classifier. In Table 4, we discuss another work on SVM ensemble classifiers [12].

Kashif et al. [44] performed image processing, segmentation, and feature extraction on the MIAS dataset using several ML algorithms—SVM, Ada Boost, DT, LR, RF, Gradient Boost, and KNN. Results proved that SVM performs best with an accuracy of 90%. In contrast, the worst performance was given by Gradient Boost classifier with an accuracy of 52%. Another work on the MIAS dataset was proposed in [45], where authors applied discrete wavelet transform (DWT) for feature extraction and PCA for dimension reduction of feature space. The classification was performed using SVM. The combination of DWT, PCA, and SVM approach attains an accuracy of $82.85 + -2.21\%$. The proposed work could be continued in the future by applying other variants of wavelength transform, such as stationary wavelet or wavelet package transform. The authors also suggested using deep learning methods on large datasets in the future to obtain high accuracy and precision for prediction and classification.

Cancer prognosis refers to the probability of success of treatment leading to recovery. A lot of work on cancer prognosis has been conducted in the past few years. Similar work was proposed in [46] by evaluating eight different classifiers, firstly, by comparing their AUC value for the prognosis period of 2, 5, 8, and 11 years, and secondly, based on the importance of different variables. The authors concluded that, on average, a 5-year prognosis period shows the overall best performance. Out of eight models, overall RF, Boosted Trees, partial least square, and generalized linear model (GLM Net) classifiers provided the best results with an AUC value of approximately 0.75. In contrast, the KNN model performed worst with an AUC value of 0.67. In the future, their work could be extended by including bagging, boosting, and other ensemble techniques.

Many times, oncologists face difficulties in the identification of the disease through the naked eye. In those cases, radiomics, a branch of medicine, is used to analyze radiological images and thus extract radiomic features to uncover disease characteristics. Sakai et al. [47] classified benign and malignant masses on DBT images using machine learning and radiomic features. Seventy radiomic features relevant to lesion shape, specula existence, and texture information were extracted and fed to different classifiers. The authors selected six features using the least absolute shrinkage and a selection operator (LASSO) because of lesser training data. Results were evaluated based on the presence and absence of dimension reduction. In the case of 70 radiomic features, SVM shows the best results with a 55% correct recognition rate for a benign tumor and 84% for malignant tumors with an AUC value of 0.798. In contrast, NB attained an AUC value of 0.808 for six radiomic features selected by LASSO. Feature extraction could be automated in the future by implementing deep learning techniques.

Comparative Analysis Using the Strategies of Deep Learning

This section presents the contributions of researchers in recent years for diagnosing breast carcinoma through deep learning techniques.

Al-antari et al. [52] drafted a CAD system on the In-Breast database and implemented the "You Look Only Once (YOLO)" model for detection. The authors proposed a "full resolution convolutional network (Fr-CN)" and a deep convolutional neural network (DCNN) for segmentation and classification, respectively. Compared with other CAD models, the presented method attains significant performance with a testing time per image of only 12.23 s. The model achieved an accuracy of 95.64% after detection, segmentation, and classification of masses with an AUC value of 0.94. In [53], the authors utilized YOLO for the simultaneous detection and categorization of breast masses on the DDSM dataset. Results show that YOLO achieves remarkable performance with effective mass detection existing over pectoral muscle and dense tissues. Another mass detection model proposed by authors in [54] is based on one stage object detector, i.e., Retina Net. The model gave a higher value of sensitivity w.r.t. False-positive per image (FPPI). The model was implemented on a publicly available dataset, i.e., in breast, and an in-house dataset, i.e., GURO. The authors concluded that performance could be improved by integrating large datasets using transfer learning. Ting et al. [55] utilized an "interactive detection based lesion locator (IDBLL)" and proposed an improved CNN model for breast cancer classification. The authors attained an accuracy value of 90.50% on the MIAS dataset.

In [56], the authors presented an efficient approach for classifying mass lesions on BCDR-FM using a convolutional neural network. The stated framework attains an AUC value of 0.826 and outperforms other state-of-art methods by combining learned and hand-crafted features. Their work could be continued in the future to high-resolution images provided by BCDR-DM. In [57], the authors performed a three-class mammogram classification, i.e., normal, benign, and malignant, on the IRMA dataset by applying a convolutional neural network discrete wavelet (CNN-DW)

and convolutional neural network curvelet transform (CNN-CT). Results have shown that using SVM instead of the Softmax layer can improve classifier performance. CNN-CT outperforms CNN-DW with an accuracy value of 83.74, 83.11, and 81.49 using the SVM layer, SVM layer with tenfold cross-validation, and Softmax layer. Their performance can be enhanced by applying different CNN architectures and various deep learning techniques in the future. H. Li et al. [58] proposed Dense Net II architecture for classifying mammograms. The authors substituted the first convolutional layer with the inception framework. The proposed model shows significant performance when compared with other pre-trained models—Alex Net, VGG Net, Dense Net, and Google Net—and attains an accuracy of 94.55% and AUC of 0.91. Therefore, the model improves speed and efficiency and solves pre-trained models' gradient descent by reducing parameters and enhancing feature re-use. In [59], the authors proposed a supervised approach for evaluating percentage density (PD) and compared the DCNN approach with the statistical learning approach. PD is defined as the proportion of dense area to the breast area on digital mammograms. They concluded that, for PD evaluation, the DCNN method is superior and powerful to a feature-based learning approach. In the future, their system can be extended by including mammograms from the different vendors, using various imaging modalities, and implementing transfer learning.

Pectoral muscles hinder the detection process and should be removed before diagnosis. Mughal et al. [60] proposed a hybrid technique to eliminate pectoral muscle using a curve stitching technique. The adaptive hysteresis thresholding segmentation technique identifies the region of interest (ROI) and segments the breast region of a digital mammogram. Results have shown that this method obtains the loftiest recall of 96.6% on MIAS and 96.4% on the DDSM dataset when compared with other revolutionary methods. As discussed in "Imaging Modalities", FFDM offers low detection sensitivity, and MRI, on the other hand, provides high costs with longer scanning time. "Contrast-enhanced digital mammography (CEDM)" combines the advantages of both, offers four times faster scanning, and is only 1/6 the price. CEDM generates low energy images similar to FFDM and recombined images comparable with breast MRI [61]. For improving the diagnosis of breast carcinoma, "shallow-deep CNN (SD-CNN)" was proposed by authors in [61] by utilizing CEDM. The authors used deep CNN for comparing the results obtained through low energy (LE) image and by the combination of LE and recombined image. Secondly, due to the restricted availability of CEDM, the authors applied shallow CNN (S-CNN) and obtained a 'virtual' recombined image from FFDM images. After evaluation, with virtual recombined imaging features, results show an increase in the model's performance.

Breast calcifications are minute deposits of calcium on the breasts. They commonly appear as white specks or dots on the mammograms. Calcifications are generally non-cancerous, but microcalcification clusters can be an initial symptom of cancer. In [62], the authors performed breast micro-calcification diagnosis using a deep convolutional neural network (DCNN) by utilizing hand-crafted and deep learning features on digital mammograms. They attained 86.89% recall and 89.32% precision using filtered deep features. Researchers concluded that although deep features surpass hand-crafted (morphological) features, on the other hand, hand-crafted features could guide CNN for attaining higher accuracy by providing additional information.

On the other hand, authors in [26] classify multi-view mammograms and segmentation maps using pre-trained deep learning models. As opposed to classifying individual lesions, this holistic approach classifies the whole mammogram containing "Craniocaudal (CC)" and "Mediolateral oblique (MLO)" views. Results show that this semi-automated approach achieves excellent results on In-Breast and DDSM dataset with volume under the ROC surface (VUS) over 0.9 for the three-class problem (normal, benign, malignant) and AUC also over 0.9 for the two-class problem (benign, cancerous). In contrast, a fully automated approach attains VUS and AUC over 0.7 for three-class and two-class problems, respectively.

In medical imaging, multiple instance learning (MIL) provides room for weakly labeled data and reduces the effort and cost of marking all the dataset images. Instead of taking a group of labeled instances, it considers the set of labeled bags comprising multiple instances. P.J. Sudharshan [63] used MIL and implemented several methods on the Break His database. The authors proposed two ways for implementing the process. The first method considers patients as bags and instances are the patches extracted from images, and the second assumes images as bags and instances are the patches. Non-parametric MIL and multiple instance learning convolutional neural network (MILCNN) attain significant results with an accuracy of 92.1%. The authors concluded that MIL outperforms other methods for classifying cancer on histopathology images.

Similarly, Samala et al. [64] concluded that when training samples from one modality are inadequate, multi-task learning is a competent technique for implementing deep networks in medical image processing. Another work on MIL was proposed in [65] for mass detection in DBT images. The authors proposed a framework based on deep CNN (DCNN)) with multiple instances learning random forest approach(MILRF), i.e., DCNN-MILRF, and compared the presented structure with two other proposals—first based on hand-crafted features, i.e., MIL-CAD, and second based on deep cardinality restricted Boltzmann machine (deep CaRBM). Results show that the DCNN-MILRF outperforms

the other two approaches with 86.8% accuracy. In the future, their work could be explored with a larger DBT dataset by combining 3D imaging information with 2D information.

In [66], the authors proposed a model for lesion detection on ultrasound images on two datasets, A&B with 306 and 163 images. The authors used three deep learning approaches, patch-based Le-Net & U-Net, and transfer learning-based pre-trained fully convolutional network-AlexNet (FCN-AlexNet). Results show that FCN-AlexNet gave the best performance on dataset A and patch-based Le-Net on dataset B in terms of F-measure and false-positive/image but at the cost of increased training time. Their work could be extended by increasing training data and implementing segmentation and classification on ultrasound lesions. Another similar work on ultrasonographic images was proposed in [67]. The authors used a deep CNN and aimed two frameworks called "Mt-Net" and "Sn-Net" to classify cancerous tumors and solid nodules in the breast lesions. Results reveal that the presented approach surpasses other revolutionary methods and can be elaborated in the future by combining several imaging modalities. Table 5 summarizes some of the well-known research on breast cancer diagnosis using deep learning models.

For training CAD models using deep learning techniques, training data is required in bulk. But the collection of the labeled dataset is a challenging job in the health sector. Different augmentation strategies can be applied to increase dataset size. In recent years, many researchers have used the Break-His dataset to categorize histopathology images due to the widespread availability of a large set of images. In [68, 69], the authors have attained significant performance on classifying breast cancer using histopathology image by comparing the results separately on patch-wise and image-wise classification. In addition to data augmentation, transfer learning can also be utilized when the dataset is not enough for diagnosis. Li Y et al. and Deniz E et al. [70, 71] discussed histology image classification using several pre-trained networks such as Res-Net50, Alex-Net, VGG16, and obtained satisfactory results. In another research, Brancati et al. [72] detected invasive ductal carcinoma. The researchers also performed multi-classification of lymphoma in histological images, using residual convolutional auto-encoder (CAE), i.e., Fusion-Net. Authors implemented two approaches—firstly, classification by reconstruction, i.e., training CAE in an unsupervised manner, and secondly, supervised classification, i.e., guiding only the encoder part of Fusion-Net called Supervised Encoder Fusion-Net (SEF). The authors compared results obtained using SEF with other existing deep learning networks (Fusion-Net, U-Net, Res-Net) under the same conditions and on the same datasets. They concluded that SEF provides outstanding results for the considered cases and can be used in the future for other histopathology image analysis cases.

Jiang et al. [73] proposed a new model, i.e., Breast Cancer Histopathology Image Classification network (BHC Net). The authors reduced training parameters by designing a new module called the small Squeeze and Excitation Residual network (SE-ResNet) and prevented the model from the risk of overfitting. The proposed method attained an accuracy of 98.87 to 99.34% for binary classification and 90.66 to 93.81% for multi-class classification. Their work can be elaborated to study cell duplication and irregular distribution of color in pathological images in the future. Nahid et al. [74] proposed three models for histopathology image classification—CNN, long-short-term-memory (LSTM), and a combination of CNN and LSTM. The authors found unseen structured and statistical information from the data using two unsupervised clustering techniques—K-Means and Mean shift. CNN with Softmax classifier outperforms the other two models with an accuracy of 91%. The authors in [75] presented a hybrid deep learning approach, i.e., multi-modal data fusion by combining structured data from Electronic Medical Record (EMR) with pathological images. Results show significant improvement in diagnostic accuracy by fusing high dimensional and low dimensional data. Sharma and Mehra [29] suggested a framework for the multi-classification of histopathology images on the Break His dataset. The authors, firstly, employed traditional classifiers for performing classification using hand-crafted features. Secondly, transfer learning was implemented, where pre-trained models "VGG16," "VGG19," and "ResNet50" were used as feature extractors and as baseline models. Outcomes show that the approach based on pre-trained models as a feature extractor outperforms the baseline and hand-crafted approach. VGG16 model with a linear SVM classifier attained the highest accuracy. Their work could be elaborated further to perform layer-wise fine-tuning of the model and implement an ensemble model with a pre-trained network.

Bevilacqua et al. [28] perform a supervised classification of breast tomosynthesis images by comparing shallow and deeper neural networks. The authors proposed two frameworks: the first framework was based on hand-crafted (morphological/textual) features, i.e., classification by ANN, and the second was a non-neural classifier (i.e., automatic feature extraction by CNN) in which different CNN models (Google Net, ResNet, Alex Net, and VGG Net) were evaluated. Results evinced that the CNN-based model outperforms the ANN approach. In [76], the authors classify mammograms and DBT images on an in-house dataset by evaluating ten different models using pre-trained Alex Net. In this research, 2D mammography outperforms 3D tomosynthesis models in classifying cancer. However, 3D tomosynthesis has proven to be robust in manual cancer detection. The variation in result might be due to memory limitations; as a result of which the authors considered

Table 5 Summarization of distinguished work on breast cancer diagnosis using deep learning techniques

Data set used	Method adopted	Performance	Pros	Cons	Reference
Mammograms (mini-MIAS)	CNN, Sparse Auto-Encoder (SAE) and Stacked Sparse Auto-Encoder(SSAE)	Accuracy: *CNN: 97%* *SAE: 98.5%* *SSAE: 98.9%*	• Best Result by Stacked Sparse Auto-encoder • Helps to identify smaller masses more accurately	-	[9]
Mammograms (labeled and unlabeled)	CNN with Semi-Supervised Learning (SSL) algorithm	Accuracy: *0.8243* AUC: *0.8818* (labeled and unlabeled data)	• Best result obtained using mixed labeled and unlabeled data • Useful when the labeled data is not available in bulk • Performance of the system increases using unlabeled data	-	[82]
MRI images	DCNN	Accuracy: *98.33*	• User Independent and time saving as it took only 36 s. to distinguish 59 cancerous regions out of 60 correctly • Reduces unnecessary biopsies • An optimum system for breast MRI	-	[83]
	Inception network, DCNN, gradient boosting tree classifier	Accuracy: *4-class–96.4* *2-class–99.5*	• Gradient Boosting tree algorithm performs well even in imbalanced training data and limited samples, thus avoiding overfitting. • Improves performance when DCNN is fused with gradient boosting tree	-	[84]
Histopathological images	Pretrained Xception Network	Pre-eminent performance	• Multi-task CNN outperforms single task CNN. • Fine-tuned CNN performs better than CNN trained from scratch • Inclusion of prior knowledge in feature extraction step overcomes intra-class variance problem in pathological images.	-	[85]
SFM, DM, and DBT	Multi-stage transfer learning	ROI-based & View-Based AUC *Single-stage: 0.84 and 0.85* *Multi-stage: 0.90 and 0.91*	• A supplementary phase of transfer learning from a similar related domain provides an improvement in learning.	• Hyper-parameters such as momentum, learning rate, no. of iterations, and the batch size were not optimized due to smaller datasets and less computational cost. • Did not compare performance with conventional feature engineering methods	[86]

Table 5 (continued)

Data set used	Method adopted	Performance	Pros	Cons	Reference
DBT and FFDM	Pretrained VGG16 network	-	• Transfer learning based DBT model outperforms model based on FFDM • Integrating imaging modalities such as FFDM and DBT, increases classification accuracy.	• It did not include breast density and other parameters such as breast asymmetry, retraction of mammilla, etc.	[87]
DDSM, BCDR, In-Breast, MIAS	Pretrained VGG16, ResNet50, Inception v3	Inception v3 models perform best *on MIAS(test dataset)* *Accuracy: 98.23* *AUC-0.99*	• End-to-end learning maximize overall performance • Fine-tuning performs well till two fully connected (FC) layers after that performance degrades	• Mammography fails in the case of the dense breast; thus, performance could be further improved by including other modalities-ultrasound, MRI	[88]
FFDM, US, dynamic contrast-enhanced MRI (DCE-MRI)	Pretrained VGG19 model	AUC (Max pooled features) *FFDM: 0.81* *US: 0.87* *MRI: 0.87* *AUC (Fusion classifier) –* *FFDM: 0.86* *US: 0.90, MRI: 0.89*	• Max- pooled features performed better as compared to fully connected features with or without pre-processing • Fusion classifier outperforms CNN and convolutional CAD classifier	-	[89]

the subset of 3D frames, and thus, significant information loss might have occurred in 3D images. For achieving optimal performance, their research could be extended in the future for developing an ensemble classifier integrating 2D mammography with 3D tomosynthesis images. Samala et al. [77] proposed a DCNN model for mass detection in DBT images and showed a comparison between DCNN and feature-based CAD. Unlike other research, where pictures of natural scenes were utilized for pre-training a DCNN, the authors firstly used mammography images for training a DCNN, and then, this pre-trained model is used for mass detection in DBT images using transfer learning. Results have shown that the AUC value increases from 0.81 to 0.90 after transfer learning with DBT. Secondly, DCNN-based CAD surpasses feature-based CAD and thus improves sensitivity from 83 to 91%. Another work on mass detection on DBT images was proposed in [78] using a "Faster Region-Based Convolutional Neural Network (Faster-RCNN)." The authors modified the DCNN proposed in [66] and compared it with the RCNN. Results show that RCNN outperforms DCNN with an AUC value of 0.96 with a reduced false-positive rate. Thus, the false-positive rate is diminished, but at the sake of cost and speed, i.e., RCNN is sluggish and costly as compared with DCNN.

D. Zhang et al. [79] integrated feature selection and feature extraction techniques on gene expression datasets for anticipating clinical outcomes of breast carcinoma. The classification task consists of two phases—unsupervised feature learning, i.e., combining PCA and auto-encoder, and, second, supervised classifier learning, i.e., constructing ensemble classifier based on the Ada-Boost algorithm. Experimental results proved that the proposed method, i.e., PCA-AE-Ada-Boost, gave AUC of 0.714 and accuracy of 0.85 and performed better than other state-of-art methods. Despite its advantages, the authors highlighted some limitations—firstly, difficulty identifying essential features for prediction tasks; secondly, increasing generalization capability of the proposed method by including more publicly available datasets. Deep learning methods can also be utilized for extracting extensive clinical information for breast carcinoma from multiple categories of clinical notes in Chinese [80]. In [80], the authors proposed a system with two constituents—named entity recognition (NER) and relation recognition component. The bi-directional encoder representations from transformers (BERT) language model was fine-tuned for extracting the notion and features from clinical breast cancer documents. Results have shown that fine-tuned BERT outperforms traditional bi-directional long-short-memory-conditional random fields (Bi-LSTM-CRF) algorithms. The method attains precision, recall, and F-measure of 0.927, 0.939, and 0.935 for NER and 0.976, 0.959, and 0.967 for relation extraction, respectively. For information extraction, the proposed approach considered

only 100 patients; therefore, additional data annotation could be done to increase dataset size in the future. Secondly, the proposed model could be enhanced to integrate data from alternative imaging modalities such as computed tomography (CT), MRI, and pathological microscopic images.

Deep learning can also be utilized for nucleus detection and semantic segmentation in human epidermal growth factor receptor-2 (HER2)-colored images of breast carcinoma. In [4], the authors proposed a framework called Her2Net, which consisted of a deep network along with a trapezoidal long short-term memory (TLSTM) structure. Findings suggest that the stated framework is highly efficient and robust in contrast to other recent methods. Generalization error is another critical parameter that needs to be considered when using transfer learning with limited training data. DCNN can memorize the training data due to millions of parameters and trainable weights. Thus, memorization, over-fitting, and a classifier model with enormous specifications may result in generalization error [81]. Samala et al. [81] considered the effect of learning capacity and transfer learning on the generalization error by plotting ROC curves as an evaluation parameter. The noise was introduced by corrupting image labels and the input image. The authors evaluated the correspondence between learning and memorization of deep networks by freezing convolutional layers of pre-trained networks such as Alex-Net and Google-Net. Results show that generalization error increases when training is done with noisy data. The authors also concluded that a proper strategy should be chosen based on available training data and classification tasks to minimize overfitting and improve the model's generalizability when implementing transfer learning.

Research Gaps and Future Directions

Incidences of breast cancer are increasing at a startling rate around the world. In contrast to developed countries, fatality estimates are comparably high in low-wage and middle-wage countries [22]. Early detection and diagnosis play a crucial role and boost long-term survivability [26]. Evaluating medical images using CAD has been confirmed to be the most effective way for early diagnosis and treatment. The symptomatic potentialities of training methods are impending the degree of personal competence using deep learning. Thus, the CAD paradigm of the "second opinion" tool is now being shifted to a more collaborative utility [27].

In the past few years, artificial intelligence has come with advanced methods for the practical examination of medical images to aid doctors and physicians at varying disease diagnosis levels [19]. Deep learning models learn high-level and low-level features directly from the input and facilitate multi-modality input [26]. The authors widely use deep learning in most of the studies because it reduces the need for feature engineering, especially in processing redundant data. Secondly, existing deep learning architectures can easily be adapted or modified on new applications [25]. But its computation and storage cost hinder its real-time execution and deployment to hospitals and clinics. Samala et al. [90] perform network pruning using an evolutionary method. It reduces the count of neurons by 87%, count of parameters by 34%, and total multiply-and-add operations by 95% without reducing performance. Thus, the pruned DCNN requires lesser memory and computation for refining an anonymous image and thus increases the model's capability and robustness. Features can be extracted from any layer in DCNN. Still, authors in [90] used the third fully connected layer, and future work is thus required for analyzing the peculiarity of features in various layers.

Experimental results from studies by different authors have proven that breast cancer diagnosis is better using deep learning than conventional machine learning. Deep learning is beneficial for handling complex, heterogeneous, unstructured, and poorly annotated data, but it needs improvement in data integration, interpretability, security, temporal modeling, and incorporating expert knowledge [91]. Despite its advantages, the following are some crucial challenges that need to be addressed when using deep learning for breast cancer diagnosis:

- Less availability of large-scale reliable datasets from expert doctors for breast cancer diagnosis

Deep learning models need a considerable amount of training images. Most of the authors have used publicly available datasets instead of independent datasets. Independent datasets usually do not have many images from expert doctors, so most authors prefer to use publicly available datasets instead of other ones. But the models developed on public datasets are less reliable as these datasets are already pre-processed. Thus, the health industry could be improved if researchers are provided with large annotated datasets from expert doctors [16].

- Less availability of models pre-trained on medical images

As discussed in "Computer-Aided Diagnosis [18]", CNN can be implemented in several strategies: training from scratch, adopting a transfer learning approach, and as a feature extractor. Most of the selected studies have utilized pre-trained models that are trained on an enormous amount of non-medical images. In the second step, fine-tuning is performed to re-train the pre-trained model on medical images. Thus, this process is time-consuming, costly, complicated, and requires a massive set of resources. In recent years, very few researchers have

focused on training a model on medical images and, thus, utilizing these models further for transfer learning. If the dataset is too narrow, i.e., lesser than 1000 images, pre-trained networks experience overfitting issues. Thus, there arises a demand for domain-specific pre-trained models that are specially trained on medical images that would take less time, fewer resources, and are cost-effective.

- Using different imaging modalities and multiple modalities for breast carcinoma classification [16]

Most researchers have used mammography and histopathology images for breast cancer diagnosis, and very few studies have focused on DBT, US, and MRI. Although DBT has given outstanding results in detecting tumors, it is costly, requires a vast amount of data and extra memory capacity for training. Thus, the same patient could be diagnosed using different modalities to enhance the models' classification ability, thus improving efficiency and reliability. In the literature, few studies have utilized multiple modalities [21, 22, 24, 75, 76, 87, 89, 92], and therefore, more research needs to be focused on this area.

- Mammography craniocaudal (CC) and mediolateral oblique (MLO) views

Arefan et al. [93] evaluated the results using CC and MLO views on mammography patients and estimated that the CC view shows superior performance than the MLO view. The authors also observed an increase in AUC value when the two views are used in combination with dense breasts, but the results are reversed in the whole breast region. Thus, additional research is required for evaluating the performance of both views on dense breasts and the entire breast region individually.

- Unsupervised approaches for breast cancer classification [16]

The majority of the selected studies have implemented supervised deep learning, i.e., CNN, that requires a large annotated dataset for breast cancer diagnosis. But in the medical domain, the collection of labeled datasets is challenging, and most of the available datasets are unlabeled. Therefore, more research is needed for developing CAD models that utilize these unlabeled images, which are an essential source of information.

- Stage-specific breast cancer survivability prediction

Kleinlein and Riaño in [94] used data-driven knowledge for predicting 5-year breast cancer survival on the SEER database on all the BC instances in 1988–2009. The authors compared stage-specific (in situ, localized, regional, distant) and joint predictive models for three distinct machine learning algorithms—naive Bayes, logistic regression, and decision tree. Authors concluded that summary stage predictive models achieve superior results compared with the joint model; secondly, it is essential to collaborate all the knowledge attained from various stages with its validity time. More research is thus needed for predicting stage-wise and year-wise survival rates for breast cancer patients.

- Integrating non-imaging information with imaging data

Till now, there are very few CAD models that integrate radiomic features with the imaging data. Geras et al. [24] discussed that in the future, many such models must be developed that could combine non-imaging attributes such as analytical information, cancer history, genetic information, along with image data, to provide early diagnosis for women at high risk of cancer.

- Imbalanced dataset

Another challenge for deep neural networks is the class imbalance problem, i.e., the proportion of positive and negative samples. Many available datasets are still imbalanced. The prediction may be biased towards the more common class when models are trained on an imbalanced dataset and have a pessimistic effect on the classifier's behavior [29]. Thus, the unavailability of balanced datasets is another issue that needs to be addressed [25].

- Future of CAD in medicine

Yanase and Triantaphyllou [20] addressed some crucial issues discussing CAD future in medical science. That includes various approaches such as data acquisition and quality estimation, advanced segmentation, feature extraction/selection, trading with big data, and cultivating essential performance evaluation for all developed models.

- Training deep models using smaller datasets in medical applications

Many studies utilize pre-trained models on large image datasets in recent years, but none uses these models on a smaller dataset. As medical datasets are not abundant in numbers, thus, new algorithms should be developed to train deep models on smaller medical image datasets [17].

- Feature extraction from small medical image datasets

Feature extraction enacts a remarkable role in medical image classification. Lai and Deng [10] address two challenges in this regard that need to be considered. Firstly, extract useful features from the small medical image datasets and, secondly, expertly fuse them from different models.

- Generalizability of deeply learned models

Most of the studies discussed in the survey have used small training datasets. Moreover, trained models were not being exposed to meticulous validation on massive testing data that may increase false positives and false negatives due to overfitting and memorizing training data. Data augmentation reduces the risk of overfitting due to small training set by introducing variations or jittering to the original data, thus improving generalizability. But augmenting the training set is not equivalent to independent training samples of comparable size. Therefore, many such models' generalizability to unseen data of new patients is still unknown and is an important parameter to be considered [19].

Conclusion

Breast carcinoma is the premier category of deadliest cancer reported in females. There arises an urgency for early diagnosis and treatment for reducing the mortality rate. Medical image analysis using CAD has cropped up as an essential field for early diagnosis and prognosis in the healthcare domain. Our survey communicates the present state of the art research disseminated in breast cancer using machine learning and deep learning techniques. Although malignancy cannot be proven without biopsy, early carcinoma detection using imaging modalities is an hour of need. Mammography is used as the "gold standard" for breast carcinoma diagnosis due to its widespread availability compared with others. But it is also being criticized because of its low effectiveness for women with dense breasts. Thus, extensive research needs to be addressed by combining various imaging modalities such as ultrasound, MRI, DBT, and mammography to achieve significant results.

This survey also highlights research challenges and future recommendations for the new researchers in this field. Research in machine learning manifested SVM to be the finest classifier for diagnosing breast carcinoma. Deep learning methods also exhibited an outstanding performance for varied evaluation parameters such as accuracy, sensitivity, specificity, F-measure, etc. High-level and low-level features can be learned automatically from the input image using DCNN. Training deep learning models from scratch is time-consuming and requires extensive resources. As a result, many studies have utilized pre-trained models and attained remarkable performance. Results have proven that deep learning outperforms conventional machine learning in diagnosing breast carcinoma when the dataset is broad. Research gaps from the recent studies depict that practical and scientific research is an urgent necessity for improving healthcare in the long run.

Abbreviations

AI	Artificial intelligence
ML	Machine learning
DL	Deep learning
CAD	Computer-aided diagnosis
ANN	Artificial neural network
CNN	Convolutional neural network
DCNN	Deep convolutional neural network
SFM	Screen film mammography
FFDM	Full-field digital mammography
DBT	Digital breast tomosynthesis
MRI	Magnetic resonance imaging
HP	Histopathology
US	Ultrasound
UCI	University of California Irvine
WBCD	Wisconsin Breast Cancer Dataset
MIAS	Mammography Image Analysis Society
DDSM	Digital Database for Screening Mammography
PCA	Principal component analysis
SVM	Support vector machine
KNN	K-nearest neighbor
LR	Logistic regression
RBF	Radial basis function
NB	Naïve Bayes
DT	Decision tree
GPU	Graphical processing unit
LASSO	Least absolute shrinkage and a selection operator
ROI	Region of interest

Declarations

Ethics approval and informed consent The article does not contain any studies with human participants or animals performed by any of the authors.

Informed consent This is not required as no human participants are involved.

Conflict of Interest The authors declare that they have no conflict of interest.

References

1. Goyal K, Prakriti S, Preeti A, Mukesh K. Comparative Analysis of Machine Learning Algorithms for Breast Cancer Prognosis. 2nd International Conference on Communication, Computing and Networking. Springer Singapore; 2019;46:93–102. https://doi.org/10.1007/978-981-13-1217-5.
2. Cancer Statistics-Indian against cancer. Statistics - India Against Cancer [Internet]. 2018 [cited 2020 May 26]. http://cancerindia.org.in/cancer-statistics/.
3. Globocan IAC. Globocan 2018_ India factsheet - India Against Cancer [Internet]. 2018 [cited 2020 May 26]. http://cancerindia.org.in/globocan-2018-india-factsheet/.
4. Saha M, Chakraborty C. Her2Net: a deep framework for semantic segmentation and classification of cell membranes and nuclei in breast cancer evaluation. IEEE Trans Image Process. 2018;27(5):2189–200.
5. Comparison G. Statistics of breast cancer in india. 2019 [cited 2020 May 26];1–10. https://cytecare.com/blog/statistics-of-breast-cancer/.
6. Kourou K, Exarchos TP, Exarchos KP, Karamouzis MV, Fotiadis DI. Machine learning applications in cancer prognosis and prediction. Comput Struct Biotechnol J. 2015;1(13):8–17. https://doi.org/10.1016/j.csbj.2014.11.005.
7. PBCR. Trends of Breast Cancer in India [Internet]. 2020 [cited 2020 May 26]. https://www.breastcancerindia.net/statistics/trends.html.
8. Khuriwal N, Mishra N. Cancer Diagnosis Using Deep Learning. Proc- IEEE 2018 Int Conf Adv Comput Commun Control Networking, ICACCCN. 2018;98–103.
9. Selvathi D, Poornila AA. Deep Learning Techniques for Breast Cancer Detection Using Medical Image Analysis. Biol Ration Comput Tech Image Process Appl [Internet]. 2018;25:85–109. https://doi.org/10.1007/978-3-319-61316-1.
10. Lai Z, Deng H. Medical image classification based on deep features extracted by deep model and statistic feature fusion with multilayer perceptron. Comput Intell Neurosci. 2018.
11. Duggento A, Scimeca M, Urbano N, Bonanno E, Aiello M, Cavaliere C, et al. A random initialization deep neural network for discriminating malignant breast cancer lesions. Proc Annu Int Conf IEEE Eng Med Biol Soc EMBS. 2019;912–5.
12. Huang MW, Chen CW, Lin WC, Ke SW, Tsai CF. SVM and SVM ensembles in breast cancer prediction. PLoS One [Internet]. 2017;12(1):1–14. https://doi.org/10.1371/journal.pone.0161501.
13. Simsek S, Kursuncu U, Kibis E, AnisAbdellatif M, Dag A. A hybrid data mining approach for identifying the temporal effects of variables associated with breast cancer survival. Expert Syst Appl [Internet]. 2020;139:112863. https://doi.org/10.1016/j.eswa.2019.112863.
14. Mihaylov I, Nisheva Ma, Vassilev D. Machine Learning Techniques for Survival Time Prediction in Breast Cancer [Internet]. Springer International Publishing; 2018;1:286–290 .https://doi.org/10.1007/978-3-319-99344-7_17.
15. Kate RJ, Nadig R. Stage-specific predictive models for breast cancer survivability. Int J Med Inform [Internet]. 2017;97:304–11. https://doi.org/10.1016/j.ijmedinf.2016.11.001.
16. Murtaza G, Shuib L, Abdul Wahab AW, Mujtaba G, Mujtaba G, Nweke HF, et al. Deep learning-based breast cancer classification through medical imaging modalities: state of the art and research challenges. Artif Intell Rev [Internet]. 2020;53(3):1655–720. https://doi.org/10.1007/s10462-019-09716-5.
17. Debelee TG, Schwenker F, Ibenthal A, Yohannes D. Survey of deep learning in breast cancer image analysis. Evol Syst [Internet]. 2020;11(1):143–63. https://doi.org/10.1007/s12530-019-09297-2.
18. Zou L, Yu S, Meng T, Zhang Z, Liang X, Xie Y. A Technical Review of Convolutional Neural Network-Based Mammographic Breast Cancer Diagnosis. Comput Math Methods Med. 2019(Dm).
19. Chan HP, Samala RK, Hadjiiski LM, Zhou C. Deep Learning in Medical Image Analysis. Adv Exp Med Biol. 2020;1213:3–21.
20. Yanase J, Triantaphyllou E. The seven key challenges for the future of computer-aided diagnosis in medicine. Int J Med Inform [Internet]. 2019;129:413–22. https://doi.org/10.1016/j.ijmedinf.2019.06.017.
21. Jalalian A, Mashohor SBT, Mahmud HR, Saripan MIB, Ramli ARB, Karasfi B. Computer-aided detection/diagnosis of breast cancer in mammography and ultrasound: A review. Clin Imaging [Internet]. 2013;37(3):420–6. https://doi.org/10.1016/j.clinimag.2012.09.024..
22. Yassin NIR, Omran S, El Houby EMF, Allam H. Machine learning techniques for breast cancer computer aided diagnosis using different image modalities: A systematic review. Comput Methods Prog Biomed [Internet]. 2018;156:25–45. https://doi.org/10.1016/j.cmpb.2017.12.012..
23. Turgut S, Dagtekin M, Ensari T. Microarray breast cancer data classification using machine learning methods. Electr Electron Comput Sci Biomed Eng Meet EBBT. 2018;1–3.
24. Geras KJ, Mann RM, Moy L. Artificial intelligence for mammography and digital breast tomosynthesis: current concepts and future perspectives. Radiology. 2019;293(2):246–59.
25. Hu Z, Tang J, Wang Z, Zhang K, Zhang L, Sun Q. Deep learning for image-based cancer detection and diagnosis − A survey. Pattern Recognit [Internet]. 2018;83:134–49. https://doi.org/10.1016/j.patcog.2018.05.014.
26. Carneiro G, Nascimento J, Bradley AP. Automated analysis of unregistered multi-view mammograms with deep learning. IEEE Trans Med Imaging. 2017;36(11):2355–65.
27. Burt JR, Torosdagli N, Khosravan N, Raviprakash H, Mortazi A, Tissavirasingham F, et al. Deep learning beyond cats and dogs: Recent advances in diagnosing breast cancer with deep neural networks. Br J Radiol. 2018;91(1089):20170545.
28. Bevilacqua V, Brunetti A, Guerriero A, Trotta GF, Telegrafo M, Moschetta M. A performance comparison between shallow and deeper neural networks supervised classification of tomosynthesis breast lesions images. Cogn Syst Res [Internet]. 2019;53:3–19. https://doi.org/10.1016/j.cogsys.2018.04.011.
29. Sharma S, Mehra R. Conventional Machine Learning and Deep Learning Approach for Multi-Classification of Breast Cancer Histopathology Images—a Comparative Insight. J Digit Imaging 2020.
30. Worlberg W, Street WN, Mangasarian O. UCI Machine Learning Repository: Breast Cancer Wisconsin (Diagnostic) Data Set [Internet]. http://archive.ics.uci.edu/ml/datasets/Breast+Cancer+Wisconsin+%2528Diagnostic%2529. 2011 [cited 2020 Dec 11]. https://archive.ics.uci.edu/ml/datasets/breast+cancer+wisconsin+(diagnostic).
31. University of Aveiro. Breast Cancer Digital Repository [Internet]. 2018 [cited 2020 Dec 11]. https://bcdr.eu/information/about.
32. Suckling J, Parker J, Dance D, Astley S, Hutt I, Boggis C, et al. Mammographic Image Analysis Society (MIAS) database v1.21. 2015 Aug 28 [cited 2020 Dec 12]; https://www.repository.cam.ac.uk/handle/1810/250394.
33. Suckling J, Boggis CRM, Hutt I, Astley S, Betal D, Cerneaz N, et al. The mini-MIAS database of mammograms [Internet]. The Mammographic Image Analysis Society Digital Mammogram Database Exerpta Medica. International Congress Series 1069. [cited 2020 Dec 12]. 1994;375–8. http://peipa.essex.ac.uk/info/mias.html.
34. Heath M, Bowyer K, Kopans D, Moore R, Kegelmeyer P. The Digital Database for Screening Mammography.

35. Spanhol, F., Oliveira, L. S., Petitjean, C. and Heutte L. Breast Cancer Histopathological Database (BreakHis) – Laboratório Visão Robótica e Imagem [Internet]. 2016 [cited 2020 Dec 12]. https://web.inf.ufpr.br/vri/databases/breast-cancer-histopathological-database-breakhis/.
36. Accessing the Data - SEER Datasets [Internet]. [cited 2020 Dec 12]. https://seer.cancer.gov/data/access.html.
37. Moreira IC, Amaral I, Domingues I, Cardoso A, Cardoso MJ, Cardoso JS. INbreast: toward a full-field digital mammographic database. Acad Radiol. 2012;19(2):236–48.
38. Oliveira JEE, Gueld MO, de A. Araújo A, Ott B, Deserno TM. Toward a standard reference database for computer-aided mammography. In: Medical Imaging 2008: Computer-Aided Diagnosis [Internet]. 2008;[cited 2020 Dec 13]: 69151Y. http://marathon.csee.usf.edu/mammography/database.html
39. Osareh A, Shadgar B. Machine learning techniques to diagnose breast cancer. 2010 5th Int Symp Heal Informatics Bioinformatics. 2010;114–20.
40. Karabatak M, Ince MC. An expert system for detection of breast cancer based on association rules and neural network. Expert Syst Appl [Internet]. 2009;36(2):3465–9. https://doi.org/10.1016/j.eswa.2008.02.064.
41. Chen HL, Yang B, Liu J, Liu DY. A support vector machine classifier with rough set-based feature selection for breast cancer diagnosis. Expert Syst Appl [Internet]. 2011;38(7):9014–22. https://doi.org/10.1016/j.eswa.2011.01.120.
42. Shaikh TA, Rashid A. Applying Machine Learning Algorithms for Early Diagnosis and Prediction of Breast Cancer Risk [Internet]. 2nd International Conference on Communication, Computing and Networking. Springer Singapore; 2019;46:93–102. https://doi.org/10.1007/978-981-13-1217-5.
43. Gupta M, Gupta B. An Ensemble Model for Breast Cancer Prediction Using Sequential Least Squares Programming Method (SLSQP). 2018 11th Int Conf Contemp Comput IC3. 2018;1–3.
44. Kashif M, Malik KR, Jabbar S, Chaudhry J. Application of machine learning and image processing for detection of breast cancer [Internet]. Innovation in Health Informatics. Elsevier Inc.; 2020;145–162. https://doi.org/10.1016/B978-0-12-819043-2.00006-X.
45. Liu F, Brown Mackenzie. Breast Cancer Recognition by Support Vector Machine Combined with Daubechies Wavelet Transform and Principal Component Analysis [Internet]. Vol. 2018. Springer International Publishing; 2018;377–388. https://doi.org/10.1007/978-3-030-00665-5_39.
46. Boughorbel S, Al-Ali R, Elkum N. Model comparison for breast cancer prognosis based on clinical data. PLoS One [Internet]. 2016;11(1):1–15. https://doi.org/10.1371/journal.pone.0146413.
47. Sakai A, Onishi Y, Matsui M, Adachi H, Teramoto A, Saito K, et al. A method for the automated classification of benign and malignant masses on digital breast tomosynthesis images using machine learning and radiomic features. Radiol Phys Technol [Internet]. 2020;13(1):27–36. https://doi.org/10.1007/s12194-019-00543-5.
48. Polat K, Güneş S. Breast cancer diagnosis using least square support vector machine. Digit Signal Process A Rev J. 2007;17(4):694–701.
49. Zheng B, Yoon SW, Lam SS. Breast cancer diagnosis based on feature extraction using a hybrid of K-means and support vector machine algorithms. Expert Syst Appl [Internet]. 2014;41(4):1476–82. https://doi.org/10.1016/j.eswa.2013.08.044.
50. Asri H, Mousannif H, Al Moatassime H, Noel T. Using Machine Learning Algorithms for Breast Cancer Risk Prediction and Diagnosis. Procedia Comput Sci [Internet]. 2016;83:1064–9. https://doi.org/10.1016/j.procs.2016.04.224.
51. Ram S, Gupta S. Building Machine Learning Based Diseases Diagnosis System Considering Various Features of Datasets [Internet]. Emerging Trends in Expert Applications and Security. Springer Singapore; 2019;841:357–363. https://doi.org/10.1007/978-981-13-2285-3_17.
52. Al-antari MA, Al-masni MA, Choi MT, Han SM, Kim TS. A fully integrated computer-aided diagnosis system for digital X-ray mammograms via deep learning detection, segmentation, and classification. Int J Med Inform [Internet]. 2018;117:44–54. https://doi.org/10.1016/j.ijmedinf.2018.06.003.
53. Al-masni MA, Al-antari MA, Park JM, Gi G, Kim TY, Rivera P, et al. Simultaneous detection and classification of breast masses in digital mammograms via a deep learning YOLO-based CAD system. Comput Methods Programs Biomed [Internet]. 2018;157:85–94. https://doi.org/10.1016/j.cmpb.2018.01.017.
54. Jung H, Kim B, Lee I, Yoo M, Lee J, Ham S, et al. Detection of masses in mammograms using a one-stage object detector based on a deep convolutional neural network. PLoS One. 2018;13(9):1–16.
55. Ting FF, Tan YJ, Sim KS. Convolutional neural network improvement for breast cancer classification. Expert Syst Appl [Internet]. 2019;120:103–15. https://doi.org/10.1016/j.eswa.2018.11.008.
56. Arevalo J, González FA, Ramos-Pollán R, Oliveira JL, Guevara Lopez MA. Representation learning for mammography mass lesion classification with convolutional neural networks. Comput Methods Programs Biomed. 2016;127:248–57.
57. Jadoon MM, Zhang Q, Haq IU, Butt S, Jadoon A. Three-Class Mammogram Classification Based on Descriptive CNN Features. Biomed Res Int. 2017.
58. Li H, Zhuang S, Li D ao, Zhao J, Ma Y. Benign and malignant classification of mammogram images based on deep learning. Biomed Signal Process Control [Internet]. 2019;51:347–54. https://doi.org/10.1016/j.bspc.2019.02.017
59. Li S, Wei J, Chan HP, Helvie MA, Roubidoux MA, Lu Y, et al. Computer-aided assessment of breast density: Comparison of supervised deep learning and feature based statistical learning. Phys Med Biol. 2018.
60. Mughal B, Muhammad N, Sharif M. Adaptive hysteresis thresholding segmentation technique for localizing the breast masses in the curve stitching domain. Int J Med Inform [Internet]. 2019;126:26–34. https://doi.org/10.1016/j.ijmedinf.2019.02.001.
61. Gao F, Wu T, Li J, Zheng B, Ruan L, Shang D, et al. SD-CNN: A shallow-deep CNN for improved breast cancer diagnosis. Comput Med Imaging Graph [Internet]. 2018;70:53–62. https://doi.org/10.1016/j.compmedimag.2018.09.004.
62. Cai H, Huang Q, Rong W, Song Y, Li J, Wang J, et al. Breast Microcalcification Diagnosis Using Deep Convolutional Neural Network from Digital Mammograms. Comput Math Methods Med. 2019.
63. Sudharshan PJ, Petitjean C, Spanhol F, Oliveira LE, Heutte L, Honeine P. Multiple instance learning for histopathological breast cancer image classification. Expert Syst Appl [Internet]. 2019;117:103–11. https://doi.org/10.1016/j.eswa.2018.09.049.
64. Samala RK, Chan HP, Hadjiiski LM, Helvie MA, Cha K, Richter C. Multi-task transfer learning deep convolutional neural network: application to computer-aided diagnosis of breast cancer on mammograms. Phys Med Biol. 2017;8894–8908.
65. Yousefi M, Krzyżak A, Suen CY. Mass detection in digital breast tomosynthesis data using convolutional neural networks and multiple instance learning. Comput Biol Med. 2018;96(February):283–93.
66. Yap MH, Pons G, Martí J, Ganau S, Sentís M, Zwiggelaar R, et al. Automated breast ultrasound lesions detection using convolutional neural networks. IEEE J Biomed Heal Informatics. 2018;22(4):1218–26.
67. Qi X, Zhang L, Chen Y, Pi Y, Chen Y, Lv Q, et al. Automated diagnosis of breast ultrasonography images using deep neural networks. Med Image Anal [Internet]. 2019;52:185–98. https://doi.org/10.1016/j.media.2018.12.006.

68. Araujo T, Aresta G, Castro E, Rouco J, Agular P, Eloy C, et al. Classification of breast cancer based on histology images using convolutional neural networks. PLoS One. 2017;6:24680–93.
69. Roy K, Banik D, Bhattacharjee D, Nasipuri M. Patch-based system for Classification of Breast Histology images using deep learning. Comput Med Imaging Graph [Internet]. 2019;71:90–103. https://doi.org/10.1016/j.compmedimag.2018.11.003.
70. Li Y, Wu J, Wu Q. Classification of breast cancer histology images using multi-size and discriminative patches based on deep learning. IEEE Access. 2019;7:21400–8.
71. Deniz E, Şengür A, Kadiroğlu Z, Guo Y, Bajaj V, Budak Ü. Transfer learning based histopathologic image classification for breast cancer detection. Heal Inf Sci Syst [Internet]. 2018;6(1). https://doi.org/10.1007/s13755-018-0057-x.
72. Brancati N, De Pietro G, Frucci M, Riccio D. A Deep Learning Approach for Breast Invasive Ductal Carcinoma Detection and Lymphoma Multi-Classification in Histological Images. IEEE Access. 2019;7(c):44709–20.
73. Jiang Y, Chen L, Zhang H, Xiao X. Breast cancer histopathological image classification using convolutional neural networks with small SE-ResNet module. PLoS One. 2019;14(3):1–21.
74. Nahid A Al, Mehrabi MA, Kong Y. Histopathological breast cancer image classification by deep neural network techniques guided by local clustering. Biomed Res Int. 2018.
75. Yan R, Ren F, Rao X, Shi B, Xiang T, Zhang L, et al. Integration of Multimodal Data for Breast Cancer Classification Using a Hybrid Deep Learning Method [Internet]. LNCS, Lecture Notes in Computer Science (including subseries Lecture Notes in Artificial Intelligence and Lecture Notes in Bioinformatics). Springer International Publishing; 2019;11643:460–469. https://doi.org/10.1007/978-3-030-26763-6_44.
76. Zhang X, Zhang Y, Han EY, Jacobs N, Han Q, Wang X, et al. Classification of whole mammogram and tomosynthesis images using deep convolutional neural networks. IEEE Trans Nanobioscience. 2018;17(3):237–42.
77. Samala RK, Chan HP, Hadjiiski L, Helvie MA, Wei J, Cha K. Mass detection in digital breast tomosynthesis: deep convolutional neural network with transfer learning from mammography. Med Phys. 2016;43(12):6654–66.
78. Fan M, Li Y, Zheng S, Peng W, Tang W, Li L. Computer-aided detection of mass in digital breast tomosynthesis using a faster region-based convolutional neural network. Methods [Internet]. 2019;166:103–11. https://doi.org/10.1016/j.ymeth.2019.02.010.
79. Zhang D, Zou L, Zhou X, He F. Integrating feature selection and feature extraction methods with deep learning to predict clinical outcome of breast cancer. IEEE Access. 2018;6(8):28936–44.
80. Zhang X, Zhang Y, Zhang Q, Ren Y, Qiu T, Ma J, et al. Extracting comprehensive clinical information for breast cancer using deep learning methods. Int J Med Inform [Internet]. 2019;132:103985. https://doi.org/10.1016/j.ijmedinf.2019.103985.
81. Samala RK, Chan HP, Hadjiiski LM, Helvie MA, Richter CD. Generalization error analysis for deep convolutional neural network with transfer learning in breast cancer diagnosis. Phys Med Biol. 2020;in press.
82. Sun W, Tseng TLB, Zhang J, Qian W. Enhancing deep convolutional neural network scheme for breast cancer diagnosis with unlabeled data. Comput Med Imaging Graph [Internet]. 2017;57:4–9. https://doi.org/10.1016/j.compmedimag.2016.07.004.
83. Yurttakal AH, Erbay H, İkizceli T, Karaçavuş S. Detection of breast cancer via deep convolution neural networks using MRI images. Multimed Tools Appl. 2019.
84. Vo DM, Nguyen NQ, Lee SW. Classification of breast cancer histology images using incremental boosting convolution networks. Inf Sci (Ny) [Internet]. 2019;482:123–38. https://doi.org/10.1016/j.ins.2018.12.089.
85. Li L, Pan X, Yang H, Liu Z, He Y, Li Z, et al. Multi-task Deep Learning for Fine-Grained Classification and grading in Breast Cancer Histopathological Images. Multimed Tools Appl. 2018.
86. Samala RK, Chan HP, Hadjiiski L, Helvie MA, Richter CD, Cha KH. Breast cancer diagnosis in digital breast tomosynthesis: effects of training sample size on multi-stage transfer learning using deep neural nets. IEEE Trans Med Imaging. 2019;38(3):686–96.
87. Li X, Qin G, He Q, Sun L, Zeng H, He Z, et al. Digital breast tomosynthesis versus digital mammography: integration of image modalities enhances deep learning-based breast mass classification. Eur Radiol. 2020;30(2):778–88.
88. Chougrad H, Zouaki H, Alheyane O. Deep Convolutional Neural Networks for breast cancer screening. Comput Methods Programs Biomed [Internet]. 2018;157:19–30. https://doi.org/10.1016/j.cmpb.2018.01.011.
89. Antropova N, Huynh BQ, Giger ML. A deep feature fusion methodology for breast cancer diagnosis demonstrated on three imaging modality datasets. Med Phys. 2017;44:5162–71.
90. Samala RK, Chan HP, Hadjiiski LM, Helvie MA, Richter C, Cha K. Evolutionary pruning of transfer learned deep convolutional neural network for breast cancer diagnosis in digital breast tomosynthesis. Phys Med Biol. 2018;63.
91. Miotto R, Wang F, Wang S, Jiang X, Dudley JT. Deep learning for healthcare: review, opportunities and challenges. Brief Bioinform. 2017;19(6):1236–46.
92. Hamidinekoo A, Denton E, Rampun A, Honnor K, Zwiggelaar R. Deep learning in mammography and breast histology, an overview and future trends. Med Image Anal [Internet]. 2018;47:45–67. https://doi.org/10.1016/j.media.2018.03.006.
93. Arefan D, Mohamed AA, Berg WA, Zuley ML, Sumkin JH, Wu S. Deep learning modeling using normal mammograms for predicting breast cancer risk. Med Phys. 2020;47(1):110–8.
94. Kleinlein R, Riaño D. Persistence of data-driven knowledge to predict breast cancer survival. Int J Med Inform [Internet]. 2019;129(June):303–11. https://doi.org/10.1016/j.ijmedinf.2019.06.018.

The current issue and full text archive of this journal is available on Emerald Insight at:
https://www.emerald.com/insight/0368-492X.htm

The role of motivation theories in knowledge sharing: an integrative theoretical reviews and future research agenda

Asha Thomas
Department of Management, Jagan Institute of Management Studies, Delhi, India and Delhi School of Management, Delhi Technological University, Delhi, India, and
Vikas Gupta
Delhi School of Management, Delhi Technological University, Delhi, India

Received 21 July 2020
Revised 13 September 2020
9 November 2020
19 December 2020
Accepted 29 December 2020

Abstract

Purpose – The purpose of this study is to identify and explain the role of motivation in facilitating knowledge sharing (KS). This study explains the connection between "motivation" and "knowledge sharing" or KS. Research finding offers significant theoretical and practical suggestions. Theoretically, the study provides clarity on various motivation theories and important constructs in KS.

Design/methodology/approach – This research reviews the literature on knowledge management in detail along with other published works. A search was conducted using online databases on the Web of Science (WoS) and Google Scholar. An analysis was done with the help of qualitative software NVivo 12 to critically analyze literature.

Findings – This theoretical review offers a retrospective view of theories, context, methods, antecedents or enablers to understand the motivation theories used in knowledge sharing research and provides a guideline for upcoming researches to contemplate and examine numerous motivation theories and also choose the most significant motivation theory and their construct in the researches on KS.

Originality/value – This theoretical review contributes toward knowledge sharing and motivation literature. There are no reviews on knowledge sharing relating to contemporary motivational theories to the best of our knowledge.

Keywords Self-determination theory (SDT), Social cognitive theory (SCT), Goal-oriented theory (GOT), Expectancy value theory (EVT), Attribution theory (AT), Knowledge sharing (KS), Nvivo 12, Review

Paper type Literature review

1. Introduction

In the transforming environment of business, an organization's competitive benefits depend on its capacity to create and organize fresh solutions to knowledge (Sahibzada *et al.*, 2020a, 2020c). One of the primary processes for knowledge management is knowledge sharing (KS) (Bock and Kim, 2002; Del Giudice *et al.*, 2017). Also, KS directs toward the use of the current knowledge. This also provides a solution to the creation and improvement of knowledge (Nonaka, 1994). It was further mentioned by Rutten *et al.* (2016) that "knowledge sharing" and "knowledge capture" are necessary for improving the performance of organizations. Thus, KS is "the dissemination of ideas, information, expertise, and suggestions among individuals in organizations to solve problems, develop new ideas or implement policies or procedures." (Liu and Li, 2018, p. 1331)

Kybernetes
0368-492X
DOI 10.1108/K-07-2020-0465
© Emerald Publishing Limited

Motivation is an important subject of study because it influences one's action and it is used to explain the type of behavior that people perform. Human motivation is explained by many theories (Cook and Artino, 2016), including the traditional theories such as Maslow Hierarchy of Needs, Herzberg's Motivation Hygiene Theory (Maslow, 1970; Herzberg, 1968; Deci and Ryan, 1985; Udechukwu, 2009; Imlawi and Gregg, 2020; Sahibzada *et al.*, 2020d, 2020e, 2020b) and contemporary motivation theories such as self-determination theory (SDT), social cognitive theory (SCT), attribution theory (AT), expectancy value theory (EVT), goal-oriented theory (GOT) (Cook and Artino, 2016). Nonetheless, it is evident that recent studies in KS have moved well beyond these traditional motivational theories (Bock *et al.*, 2005; Ko *et al.*, 2005; Chiu *et al.*, 2006; Hsu *et al.*, 2007; Chang and Chuang, 2011; Hung *et al.*, 2011; Sedighi *et al.*, 2016; Serenko and Bontis, 2016; Llopis and Foss, 2016; Eid and Al-Jabri, 2016; Zhang *et al.*, 2018; Park and Gabbard, 2018. Cook and Artino, 2016) conducted research and presented five contemporary motivational theories in "health profession education." This research is encouraged by motivators' role in KS. This can be supported by considering contemporary theories on motivation and gaining a better clarity on the same. The present theoretical review adopts a comparative and composed approach and will lead to a more complicated picture of the motivators for KS. Theories were chosen based on their occurrence in current reviews (Graham and Weiner, 2012; Cook and Artino, 2016). There are no broadly identified contemporary theories.

According to the present study, a review that explains and compares the various contemporary motivation theories will support more comprehensive principles of motivation and assist in further investigation. There are fewer efforts in identifying the most primary factors that affect the KS, even though there is the depth and robustness of factors of motivation that influence the KS.

The objective of this theoretical review is to reassess motivation theories in KS. The research reviewed and coded 30 published empirical studies on KS using NVivo 12 software. These were picked from 20-year publications. The theoretical review presents a systematized retrospective examination relating to the antecedents, context and methods. Following are the four main review objectives discussed:

(1) Which motivational theories were accepted in the KS research?

(2) What "research contexts" were considered?

(3) What methods of research were used?

(4) Which antecedents were used in the KS and under which theories of motivation?

With answers to the above-mentioned questions, the authors were able to create an upcoming direction. Authors acknowledge that this is the first review that amalgamates literature studies for investigating the motivational role in the KS.

The structure of this research is as follows. The focus of Section 2 is on the Theoretical Underpinning for the research, whereas Section 3 talks about the research methods taken by the authors. Section 4 (review of literature) and (theories of contemporary and their forms in knowledge management) provide a complete review and related discussions on antecedents, theories and their outcomes. Section 5 states the conclusion, implication and future directions.

2. Theoretical underpinning

2.1 Knowledge sharing

Explicit and tacit are two types of knowledge. Explicit or formal knowledge is the "codified information" that is changed to some tangible form such as database or documents and is

cautiously imparted for broad distribution and use, whereas, tacit knowledge is private information and deals with a combination of training, skills, education and experiences. This type of knowledge is exclusively based on beliefs, emotions, attitudes and intuition of an individual. Researchers have synonymously used "knowledge sharing" with terms such as knowledge contribution, knowledge transfer, and so on. (Hsu and Wang, 2008; Cruz *et al.*, 2009). However, according to Tangaraja *et al.* (2016) and Wang and Noe (2010), KS differs from the similar term "knowledge transfer." Tangaraja *et al.* (2016) summarized that KS is an entirely behavioral concept because it involves observable actions, whereas, KT is not entirely a behavioral concept since it encompasses both behavioral and nonbehavioral features through various processes. KT and KS are two varied concepts, even though they are interlinked in some ways and KS is a component of KT. This study uses only KS literature.

2.2 Historical overview of contemporary theories of motivation

There are many contemporary theories of motivation. These are discussed later.

2.2.1 Social cognitive theory. Miller and Dollard (1941) suggested the social learning theory and this theory led to SCT. According to social cognitive theory, personal communications with other individuals would affect each others opinion, emotion and behavior (Bandura, 2001). Since individual behavior studies accept SCT, it provides a structure for recognizing, predicting and changing the behavior of people. According to this theory, factors such as personal, behavioral and situational affect individual behavior simultaneously. This theory further states that a person will take personal cognition action in social surroundings. Two factors establish a person's cognition to work in a particular manner. These are self-efficacy and outcome expectations. Self-efficacy is a significant factor that affects the choice to share information. It is faith in one's ability to arrange and execute actions that are required to administer future circumstances (Bock and Kim, 2002; Kankanhalli *et al.*, 2005). Recently, self-efficacy has been employed in knowledge management to authenticate personal efficacy belief in KS self-efficacy (KSSE) (Kwahk and Park, 2016). SCT emphasizes self-efficacy and elucidates that the usual positive result of behavior will be futile if we hesitate to execute the behavior successfully. The decision on KS is also impacted by the resultant beliefs connected to rewards (Bartol and Srivastava, 2002). Outcome expectations can be personal or team-related. This includes pleasure or the advantage that is derived from KS, improved performance of a project, and so on. In making contributions, if there are no incentives, people are rarely keen to spend time and effort. Thus, people who expect higher outcomes are less likely to be idle on a cognitively engaging task. It is observed by many researchers (Lin and Huang, 2008; Chang *et al.*, 2013) that there is a connection between KS and the outcome of a team. According to them, the outcome of a team was improved by KS.

2.2.2 Self-determination theory In a social context, the SDT, a macro theory, is based on incentive, feeling and traits (Deci and Ryan, 2000). The SDT of motivation is again subdivided into six mini theories, which include:

(1) Cognitive Evaluation Theory (CET): CET was based on a wide investigation on the active interaction between external events. Cognitive evaluation connects to inherent motivation that is the source of the contentment of behaving in a particular manner. CET specifically talks about social context's effects on inherent motivation or how inherent motivation is affected by factors such as incentive, interpersonal controls and ego.

(2) Organismic Integration Theory (OIT): people are involved in activities that are not necessarily attractive and pleasant, but they engage in such practices to fulfill their obligations. Thus, it can be safely stated that the inherent motivation is less applicable or irrelevant to a few practices where extrinsic motivation (EM) is both favored and needed. This led to the emergence of the OIT of SDT. Both Deci and Ryan (1985) and Gilal (2019) have documented in their study that this theory deals with the individual's EM and observed locus of causality. Extrinsically motivated behavior provides a feeling of satisfaction that is achieved after attaining an external goal to the behavior itself. EM includes rules relating to outside laws, introjections, recognized statutes and combined regulations (Deci and Ryan, 1985). A controlled motivation composite comprises the external regulation and introjected regulation, whereas an autonomous motivation composite consists of the identified regulation and integrated regulation. Where the locus of causality is external to an individual it is referred to as external regulation. This includes the offer of compensation. Introjected regulation is the behavior that takes in regulation, but it is not fully accepted as one's own. The example includes assured rewards. Identified regulation happens when an individual values the behavior and identifies with and accepts the regulatory process. The individual becomes a part of the self completely. Integrated regulation entails releasing an activity choice and amalgamating it with the person's rational sense of self, such as values, needs and identities completely (Deci and Ryan, 1991).

(3) Causality Orientation Theory (COT): COT focuses on differences between individuals in overall motivational orientations (Deci and Ryan, 1985). Human or psychological behaviors such as autonomy orientation, controlled orientation and motivation form the basis for COT (Vansteenkiste *et al.*, 2010). Individuals who have major self-esteem problems and undergo low force of guilt have a highly autonomous orientation (Gilal *et al.*, 2019). However, people under the "controlled orientation," act according to external or internal demands. They clarify that external events operate as force and thus it manages their behavior with an experience (Vansteenkiste *et al.*, 2010). Finally, "amotivation" tends to make people realize that their different experiences of life are beyond their control; rather, they think that their experiences are the consequence of fortune or destiny.

(4) Basic Psychological Needs Theory (BPNT): according to BPNT "psychological well-being" and "optimal human functioning" are rooted in three universal psychological requirements. These are "autonomy," "competence," and "relatedness" (Deci and Ryan, 2002). The occurrence of "volition" and "psychological freedom" relates to the need for autonomy. The competence need is associated with the "understanding of effectiveness" in the individual quest, and lastly, the need for relatedness devalues individual wish to feel associated with other people.

(5) Goal Contents Theory (GCT): GCT has developed from the differences between an intrinsic goal and extrinsic goal and their effect on people's psychological well-being and motivation. Kasser and Ryan (1996) documented in their study intrinsic life goals, which according to them are related to personal growth, close relationships, community contribution, physical health, and these can be distinguished from the extrinsic life goals that include wealth, reputation and image. They further opined that intrinsic life goals fulfill the basic needs for autonomy, competence and relatedness. Extrinsic life aspirations are unrelated to

basic needs satisfaction. Finally, relatedness refers to how one develops and maintains close personal relationships.

(6) Relationships Motivation Theory (RMT): RMT suggests that for the best human functioning and well-being, a certain level of close individual association is required. These associations accomplish the need for relatedness (Deci and Ryan, 2014).

2.2.3 Expectancy value theory. The Expectancy Value Theory (EVT) stemmed in the 1950s and 1960s. Vroom's (1964) suggested that motivation functions because of expectancy, instrumentality and valence. *Expectancy* is a brief faith that results in a specific outcome. The expectancy range varies from zero to one. *Instrumentality* is the perception of a person that specific performance will show the way to a certain outcome. Finally, *valence* means "affective orientations toward particular outcomes." Vroom (1964) stated that the above-mentioned factors impact motivation in many ways. There is a criticism of the early EVTs due to their excessive rationalistic and mechanistic postulations about how people move toward solving problems and decision-making in day-to-day circumstances (Steel and König, 2006). No calculations are made by the people to recognize the best amalgamation of expectancy, instrumentality and valence. People are pleased if they find a good solution to problems. Contemporary EVTs have further expanded components of expectancy and value by concentrating on affective and contextual factors as well. This is done to avoid rationalistic bias. According to the contemporary EVTs, success expectancy is formed by motivational beliefs that can be categorized into goals, self-concept and subjective task value (Eccles and Wigfield, 2002). The first form is the goals that are the specific short- and long-term purpose of behavior. Self-concept is the feeling of personal capacity in a task domain. Finally, diverse components constituted subjective task value by specifying that a person's enjoyment is the result of activity performance, the importance of getting involved in a KS and relative costs included.

2.2.4 Goal-oriented theory. Educational psychologists such as Dweck (1975) and Eison (1979) introduced the idea of goal orientations in the 1970s. According to Dweck (1986) individuals in achievement conditions pursue "dispositional goal orientations." These are learning (mastery) goals or performance goals. Recently, the idea of learning goal orientation is associated with presentation (Dweck, 1986). Learning goal imitates a desire to connect with demanding behavior, readiness to improve self and a tendency inclination to calculate the personal presentation from past performances (Button *et al.*, 1996). The focus of learning goal oriented individuals is on new skill development, the mastery of new circumstances and to give importance to the process of learning. They know the fact that if new practices are developed, there is a need for a certain amount of effort. Evading challenges and declining performances faced with obstacles categorizes performance goal orientation (Button *et al.*, 1996). Performance-oriented people make the slightest attempt for their presentations in demanding circumstances as they attempt to surpass others, display their capability and achieve success. Subsequently, situations that show a need for competence are avoided by performance-oriented employees.

2.2.5 Attribution theory. There are numerous approaches to Attribution Theory (AT) (Savolainen, 2013). According to attribution theorists, the main source of motivation is information or knowledge of the fundamental environment arrangement. Bernard Weiner is the well-known theorist of attribution since the 1970s. According to Weiner's theory (2010), outcomes, whether positive or negative, lead to common positive and negative feelings. The look for fundamental factors such as capability, attempt, job difficulty and fortune is advanced by undesired and/or unexpected events. The key causal dimensions are *locus*,

stability and control. Causal *locus* is associated with pride and self-worth. Causal stability partly establishes expectancy shifts and the limit or level of expectation, despair and powerlessness. Causal control is associated with effects that include disgrace (to unmanageable causality) and fault as well as feel sorry (to manageable causality).

3. Research method

This research is based on numerous earlier studies that are organized in the manner described briefly in this section. First, the authors widely searched for important contemporary motivation theories and their connection with knowledge management. They critically analyzed the crucial constructs for knowledge management – explicit .This study talks about primary contemporary theories of motivation, spanning diverse countries and industries. "knowledge sharing," "knowledge management," "knowledge contribution," "motivation theory" "contemporary motivation" "self-determination theory," "social cognitive theory," "expectancy-value theory," "goal-orientation theory," "attribution theory," "predictors" and "contemporary theories of motivation" were the keywords used to conduct the research. This research reviews the literature on knowledge management in detail along with other published works. A search was conducted using online databases on Web of Science (WoS) and Google Scholar (Gupta and Thomas, 2019; Sharma *et al.*, 2020; Thomas and Chopra, 2020). An analysis was done of research papers so derived and these were assessed profoundly. In all, 30 empirical papers were selected and critically evaluated, coded (open and axial code) and analyzed to drive a complete understanding with the help of qualitative software Nvivo12.

4. Review of studies

The study conducted a cluster analysis using VOSviewer to reach the relevant clusters examined in the selected papers and gave a graphical representation (Figure 1) of the contemporary motivation theories employees in KS studies.Table 1 indicates the top journals used in this research. *Journal of Knowledge Management* is the top contributor in the field. A project map coded in Nvivo (Figure 2) is

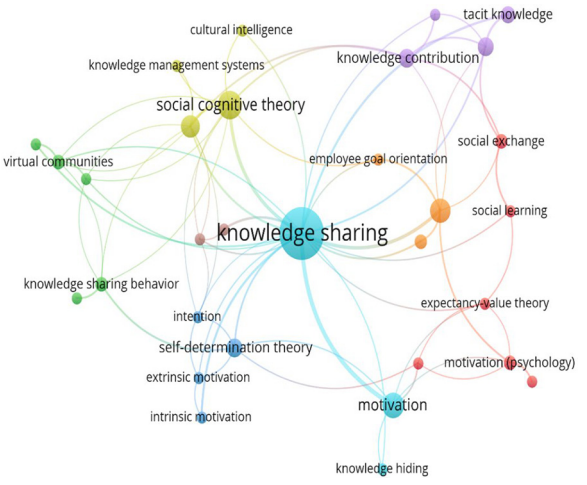

Figure 1.
Clusters of keywords used by the reviewed literature

List of top ten journals	H-index
Journal of Knowledge Management	106
Information and management	153
Human Resource Management	87
Internet Research	80
MIS quarterly	216
Cross Cultural and Strategic Management	37
European Management Journal	99
Journal of Organizational Behavior	164
Academy of Management Journal	260
Aslib Journal of Information Management	39

Table 1.
Top contributing journals

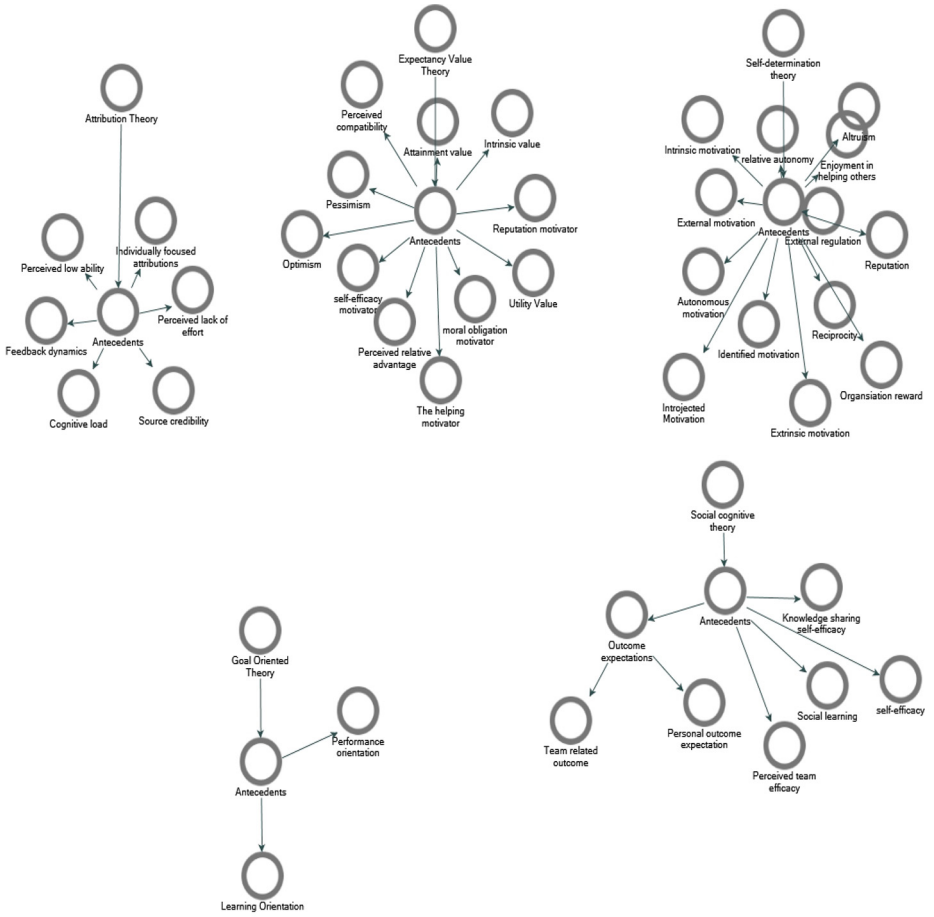

Source: Coded and created by author(S) in Nvivo12

Figure 2.
Project map of antecedents

represented in the graphical representation of all antecedents used under different motivation theories and KS.

5. Theories of motivation used in knowledge sharing

5.1 Knowledge sharing under self-determination theory

5.1.1 Most well-known motivation theory is self-determination theory. (Cockrell and Stone, 2010, Llopis and Foss, 2016). It is extensively adopted to examine how and why the specific behavior of an individual is caused. SDT forms the basis for several types of research that studies "motivated behavior." This covers the studies relating to KS (Razmerita *et al.*, 2016). Current empirical studies take in to account the effect of an important key factor, that is, "intrinsic motivation" on KS (Bock *et al.*, 2005; Razmerita *et al.*, 2016). Intrinsic motivators (such as the pleasure gained in helping other people) play a vital role in clarifying KS attitude (Lin, 2007; Razmerita *et al.*, 2016). Research conducted by Cavaliere *et al.* (2015) depicts the great enjoyment derived from helping other people to maintain KS among workers. According to Hwang (2011), using the SDT in empirical findings of data analysis, great pleasure is the most noteworthy feature in behavior toward the KS by email. Further, Gagné *et al.* (2019) also found that sharing and hiding of knowledge might be inspired differentially and that the description of work design might impact the motivation to share knowledge with coworkers. Their research showed that cognitive job demands and job autonomy were connected to reports of KS regularly and the value through self-directed motivation to KS. According to Liou *et al.* (2016), KS attitude factors are directly and positively impacted by "anticipated reciprocity relationship, the norm of reciprocity, and anticipated extrinsic rewards and also anticipated extrinsic rewards." Another crucial element was reputation (Chang and Chung, 2011). The KS attitude is also impacted by "knowledge sharing self-efficacy," which means the confidence of knowledge sharers' in providing essential knowledge to other individuals in a particular circumstance.

5.2 Knowledge sharing under the social cognitive theory

Researchers have applied social cognitive theory (SCT) to expand knowledge of determinants that impact KS. According to this theory, an action is taken by an individual if the same has cognition in a social environment. Two basic determinants make an individual's cognition to operate in a particular manner. These are self-efficacy and outcome expectations (Jin *et al.*, 2015). Self-efficacy is faith in personal abilities to arrange and achieve courses of actions that are needed to control future circumstances (Bandura, 1997). According to Cai and Shi (2020), research SCT is applicable to explain the KS questions and answers in a community. A model of the fundamental methods relating to the "virtual community climate" on the purpose of sharing knowledge can be created and the same can recommend that KS self-efficacy and its expected result play a mediation role in "community climate" and the KS relationship. Another research conducted by Chen and Lin (2013) presents a descriptive and realistic example to show how SCT can be employed for understanding KS in "cross-cultural teaming" circumstances. They suggest that KS is impacted by "metacognitive, cognitive, and motivational cultural intelligence." They further recommended that metacognitive and behavioral cultural intelligence affects KS indirectly with the perceived team effective mediation. According to Kim *et al.* (2015), personal factors such as self-efficacy and outcome expectations as well as environmental factors are important interpreters of information sharing on social media. According to SCT, user's outcome anticipation of their knowledge contribution behavior is promoted by high social exposure based on which Guan *et al.* (2018) also assumed that there is a positive effect on user's knowledge contribution behavior in social communities, as users are free to express

their own opinions (Chiu *et al.*, 2006). Another significant sign in SCT is the expected result that can be categorized into two aspects, namely, personal-related and community-related expectations. Personal-related expectations are related to the beliefs of a person, such as individual reputation and rank, making friends or bringing more stable KS collaborations, whereas community-related expectations are the impact of KS by an individual on communities such as community expanding objective, improving community knowledge and aid in the development of a community (Hsu and Lin, 2008). Shan *et al.* (2013) mentioned that members do KS relating to emergency occurrences, the expected results positively promote the impact on the value and magnitude of KS. It impacts on the endorsement of KS attitudes. Team relationship commitment and team relational norms are significant motivational forces derived from the social cognitive perspective. This plays an important role in knowledge contribution barriers management by promoting and supporting behaviors that contribute to knowledge (Chang *et al.*, 2013). Eid and Al-Jabri (2016) used SCT for understanding the fact that KS is a strong forecaster of learning performance and two significant knowledge-sharing predictors of Saudi Arabia students are chatting and discussion as well as file-sharing. Thus, it can be stated that SCT is a capable way to explain unlike motives for predicting KS.

5.3 Knowledge sharing under goal-oriented theory

Numerous studies have used the goal-oriented theory (GOT) to comprehend KS. In the four-factor model by Swift *et al.* (2010), individuals' behavior on KS will differ based on the acceptance of goal orientation. The goal orientation is probably joined to increase the level of individual behavior on the sharing of their knowledge in learning-prove whereas, in performance-avoidance, goal orientation is expected to be related to "less knowledge-sharing behavior" than based on the other goal orientations. Scholars with "learning-prove" goal orientation vision "knowledge collecting" and "knowledge donating" opportunities as circumstances to enlarge their abilities instead of situations to exhibit their knowledge or emphasize on the lack of knowledge. This results in a vigorous connection with the available chances to share knowledge. Alternatively, researchers with performance avoid goal orientation and are involved with incompetence that results in staying away from the behavior of KS circumstances. They are indecisive or uncertain about how other people react to their knowledge or the likelihood of successful transmits of KS. Kim and Lee (2013) found goal orientation as a KS predictor leading to service innovative behavior between the five-star hotel workers. According to Kankanhalli *et al.* (2005) and Lu *et al.* (2012), individuals high in learning goal orientation do not withdraw from KS in their mission. This is similar to the earlier-mentioned view. Matzler and Mueller (2011) discussed that there is a positive impact of learning orientation on the KS, whereas a negative influence includes performance orientation. They further talked about traits of personality forming a background for goal orientations. Shamim *et al.* (2017) examined how at an individual level, knowledge management can be improved by managers between front line employees of a hotel. This can be done by influencing the goal orientations of an employee with the help of "supervisory orientations." Also, important is the positive effect of learning goal orientation of an employee or worker on knowledge management. The impact of performance goal orientation on knowledge management, however, is irrelevant. The indirect positive supervisory result impact and capability orientations on knowledge management from the mediation of goal orientation are supported by results.

5.4 Knowledge sharing under expectancy value theory

Individuals can augment their motivation if they have high and positive expectations relating to the outcome value according to expectancy value theory (EVT). KS of employees' expectations are affected by optimism (the cognitive propensity to assume the best in numerous things) and pessimism (the cognitive propensity to anticipate adverse outcomes). Chiu *et al.* (2018) investigated the growth of KS from the viewpoint of expectancy theory and it was verified that the association between optimism and KS is partly intervened positively and the association between pessimism and KS is mediated completely. The EVT was employed by Imlawi and Gregg (2020) for recognizing the features that might impact intentions of health professionals to add information relating to health in online health communities (OHCs). Intrinsic motivators (aiding motivator, self-efficacy and moral obligation) and EMs (reputation) aid health professionals to continue contributing to OHCs. The result recommends that OHC member's contentment is derived from "helping motivator, self-efficacy motivator, and reputation motivator." According to earlier literature, it has been proved that an employee's positive mood can augment learning and their tendency to participate is intended KS (Lin, 2007). The EVT further proposes that the triggering factors include person's faith about one's ability to implement a given mission comprising the "expected utility value" from the result achieved after the completion of the mission. As proposed by the expectancy-value framework, a member of a team's obligation to attain the goal of the team is based on the expectation that the said goal is possible to be attained (Liu and Li, 2018). Thus, leaders can effectively enhance the commitment of a follower toward team goals in two ways – vision articulation and high-performance expectation and intellectual stimulation. Follower team objectives worth is increased by vision articulation, whereas high-performance expectation and intellectual stimulation impel a follower to solve issues by using novel and creative standards, thereby strengthening his/her belief in the achievement of team goals. Liu and Li (2018) further expanded the literature to detect the interceding roles of "team goal commitment" and "team identification" on the alliance of transformational leadership with KS. Hashim and Tan (2018) observed the determining factors relating to the worth of the online community relating to "predicting continuous knowledge-sharing intentions" among the online commercial communities. The research further conceived that constant KS intention of a person or an individual is affected by the way they perceive the value of an online community. They suggested that the value of this online community is affected by attainment, inherent and usefulness values.

5.5 Knowledge sharing under attribution theory

Attribution theory assumes that a persons' attempt and capability can aid in boosting their inspiration by helping them connect in various "self-regulatory behaviors." This, in turn, results in interceding cognitions that decide the attitude of an individual such as putting suitable and attainable objectives as well as observing and assessing the growth toward these goals. The AT has been used in the KS study. Lekhawipat *et al.* (2018) researched on the attempt and capability beliefs of an individual that has psychological consequences for the improved consideration of the growth of the KS behavior attitude. Causal impediments were used by them to investigate how inner acknowledgments dishearten the KS attitude and it was recommended that the observed low capability is important to obstruct the KS behavior, and the need for attempt relates to the fundamental awareness of low capability. Cramton (2001) conducted a research on the breakdown of joint knowledge in separate associations and under what conditions do acknowledgments "individual, categorical, or situational" effect communication and associations in the future. According to Cramton (2001) "hidden profiles" comprises unrecognized dissimilarity in the circumstances,

background and restraints of scattered coworkers that can help augment "dispositional" instead of "situational" acknowledgments and result in consistency and knowledge. Studies relating to AT recommend that groups are prejudiced toward their accomplishments relating to internal factors in a group. Two types of acknowledgments are internal to the group, but these are different theoretically in the present research. These are acknowledgments that distinguish between the input made by an individual member of the group and acknowledgments that concentrate on the complete group. Goncalo and Duguid (2008) forecasted that there will be diverse results for different acknowledgments to attain excellent "group decision-making." Their Experiment 1 focused on the earlier success attained acknowledgments that aided groups to believe in different options before coming to a joint decision. In Experiment 2, "individually focused" acknowledgments for the earlier achievements helped in contributing to exclusive knowledge and aided in making precise decisions. These results recommend that the "group-serving tendency to internalize success" may impact the results in group performance.

6. Motivation theories and their constructs in knowledge sharing

6.1 Antecedents and outcomes

The comprehensive table and figures supported by the theories of contemporary motivation were tested by researchers of knowledge management to tackle tacit and explicit KS. Usually, the review of the article presents that the forerunner in Table 2 significant theories of contemporary motivation such as the SCT, SDT, GOT, EVT and AT. These were extensively related to the research of knowledge management as an independent variable to deal with issues in KS. Based on the review, significant factors and outcomes were recognized by employing all the vital contemporary motivation theories.

6.2 Top cited research papers

6.3 Important theories integrated with motivation theories in knowledge sharing research

Previous scholars applied the social exchange theory, social capital theory and the theory of planned behavior to interpret KS behavior (Liou *et al.*, 2016; Akhavan *et al.*, 2015; Gupta and Thomas, 2019). Figure 3 depicts that SCT of motivation has incorporated social capital theory for studying the knowledge sharing in four publications (it is prevalent that such integration is used with SCT of motivation) followed by expectancy-value theory integrated with social exchange theory in two publications. Most theories combined with SDT of motivation for studying KS. In KS literature, the most used theory with a motivation theory is social capital theory. Social capital has been theoretically framed as the aggregate of assets/resources encapsulated in the network of social relationships among social participants (Tsai and Ghoshal, 1998; Nahapiet and Ghoshal, 1998; Thomas *et al.*, 2021). It is viewed as a valuable asset that encourages reforms by enabling a closer interpersonal relationship between individuals and incorporates a range of incentives for social participants, ranging from people to organization (Gupta and Thomas, 2019; Thomas and Paul, 2019). Nahapiet and Ghoshal (1998) identified three dimensions of social capital. These are structural, cognitive and relational.

6.4 Publication trend

The publication trend (Figure 4) clearly shows that the year 2016 was the turning point for the SDT of motivation. The SDT was mentioned in five publications followed by two publications in 2011 and 2015 in relation to KS. There were two publications on the SCT of

Table 2.
Theories of motivation and their constructs used in the sphere of knowledge sharing

Self-determination theory (SDT)	Social cognitive theory (SCT)	Attribution theory (AT)	Expectancy value theory (EVT)	Goal-oriented theory (GOT)
Altruism	Knowledge sharing self-efficacy	Cognitive load	Attainment value	Learning orientation
Antecedents				
Autonomous motivation	Outcome expectations	Feedback dynamics	Intrinsic value	Performance orientation
Enjoyment in helping others	Personal outcome expectation	Individually focused attributions	Moral obligation motivator	
External motivation	Team-related outcome	Perceived lack of effort	Optimism	
External regulation	Perceived team efficacy	Perceived low ability	Perceived compatibility	–
Extrinsic motivation	Self-efficacy	Source credibility	Perceived relative advantage	–
Identified motivation	Social learning	–	Pessimism	–
Intrinsic motivation	–	–	Reputation motivator	–
Introjected motivation	–	–	Self-efficacy motivator	–
Organizational reward	–	–	The helping motivator	–
Reciprocity	–	–	Utility value	–
Relative autonomy	–	–	–	–
Reputation	–	–	–	–
Outcomes				
Knowledge hiding	Knowledge acquisition	Knowledge sharing behavior	Knowledge sharing	Knowledge sharing
Knowledge sharing	Knowledge contribution	Mutual knowledge problem	Knowledge contribution	–
Knowledge sharing behavior	Knowledge sharing	Sharing unique information	–	–
Tacit knowledge sharing	Knowledge sharing behavior	–	–	–
–	Knowledge sharing intention	–	–	–

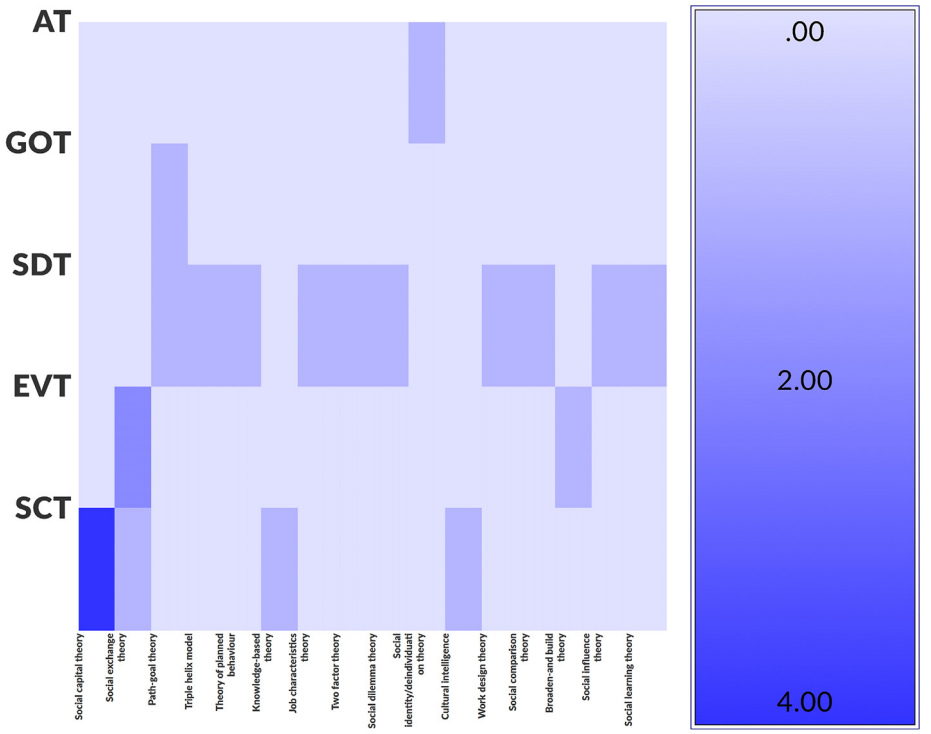

Notes: SDT = SELF-DETERMINATION THEORY, *SCT = SELF COGNITIVE THEORY, *AT = ATTRIBUTION THEORY, *EVT = EXPECTANCY-VALUE THEORY, *GOT = GOAL ORIENTED THEORY
Source: Created by author(S) in Nvivo12

Figure 3. Integration of other important theories with motivation theories in knowledge sharing*Source*: Created by author in Nvivo12

motivation in 2019 and 2013. The year 2019 showed an increase in the number of studies in contemporary theory of motivation with two publication on SDT, one publication on SCT, two publication on EVT, and one publication on GOT.

6.5 Methods employed in research

The particular study used both qualitative (focus group and interviews) and quantitative (surveys and experiments) measures to recognize KS. Figure 5 depicts numerous research studies that used quantitative methods (regressions, structural equation modeling), while a small number of researches employed qualitative methods (case study). These results show that quantitative methods lead research theories of motivation in KS. The number of publications that used more quantitative method (Figure 5) is thirteen in SDT, seven in SCT, three in EVT, two in AT, and one in GOT. Qualitative methods were used maximum in SCT and there are two publications available.

6.6 Research context and country studied

Research settings were assessed, and five significant theories of motivation covered twelve countries. Major research was done in China, followed by Taiwan and the United States.

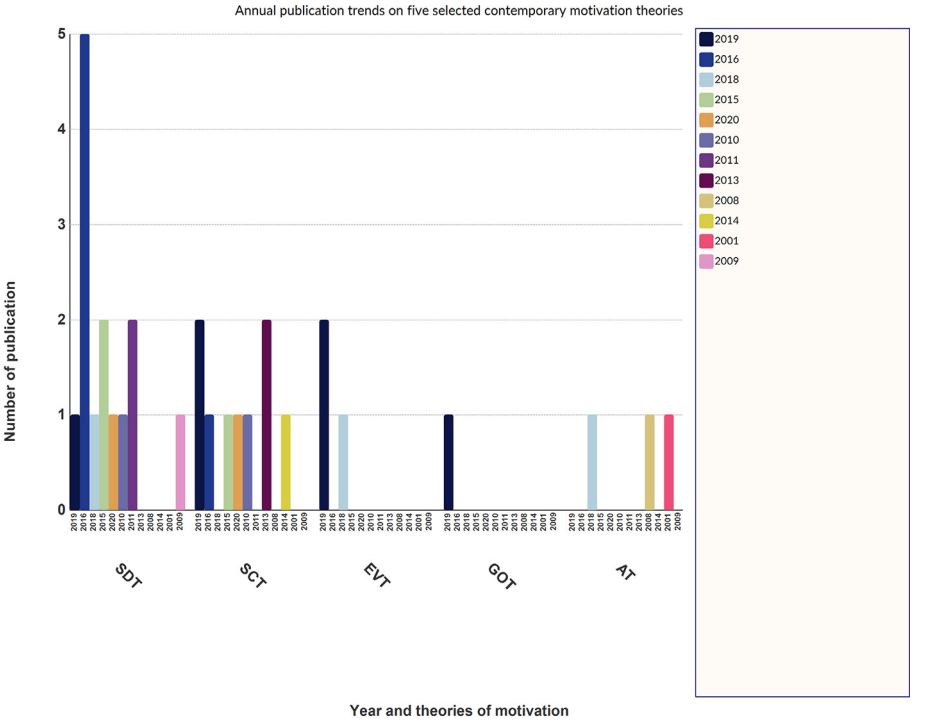

Figure 4.
Annual publication trend based on five selected contemporary motivation theories

Notes: SDT = SELF-DETERMINATION THEORY, *SCT = SELF COGNITIVE THEORY, *AT = ATTRIBUTION THEORY, *EVT = EXPECTANCY-VALUE THEORY, *GOT = GOAL ORIENTED THEORY
Source: Created by author(S) in Nvivo12

Table 3 presents the most regular countries that are studied. The further review (Figure 6) helped in recognizing that the bulk of studies were done in the online communities, multinational companies and knowledge-intensive organizations. Four publications were focused on online communities using SCT of motivation. This was followed by two studies, each from multinational companies and knowledge-intensive organizations using the SDT of motivation under KS. Very restricted studies are conducted in pharmaceutical organizations, telecommunication, university and information technology (Table 4).

7. Conclusion and future research agenda

Motivational drivers are recognized on the basis of significant motivation theory that can suggest how managers can motivate workers to interact and share their knowledge relating to work with other coworkers (Figure 7). The hierarchy chart coded in Nvivo12 presents that researchers of knowledge management used the SDT and SCT to deal with and appreciate "knowledge-sharing enablers" and KS literature.

According to the SDT, workers are intrinsically and extrinsically inspired to share information. The KS attitude is impacted by enjoyment in helping others. KS is an essential part of work and to share knowledge for providing value to the company and its workers or

Author(s)/year	Title	Citation
Cramton (2001)	The mutual knowledge problem and its consequences for dispersed collaboration	832
Reinholt *et al.* (2011)	Why a central network position is not enough: The role of motivation and ability for knowledge sharing in employee networks	215
Foss *et al.* (2009)	Encouraging knowledge sharing among employees: How job design matters	195
Razmerita *et al.* (2016)	What factors influence knowledge sharing in organizations? A social dilemma perspective of social media communication	79
Lin *et al.* (2010)	Withholding effort in knowledge contribution: The role of social exchange and social cognitive on project teams	82

Note: In descending order of the number of citations
Source: Web of science (WoS)

Table 3.
List of the top five cited articles under the theme

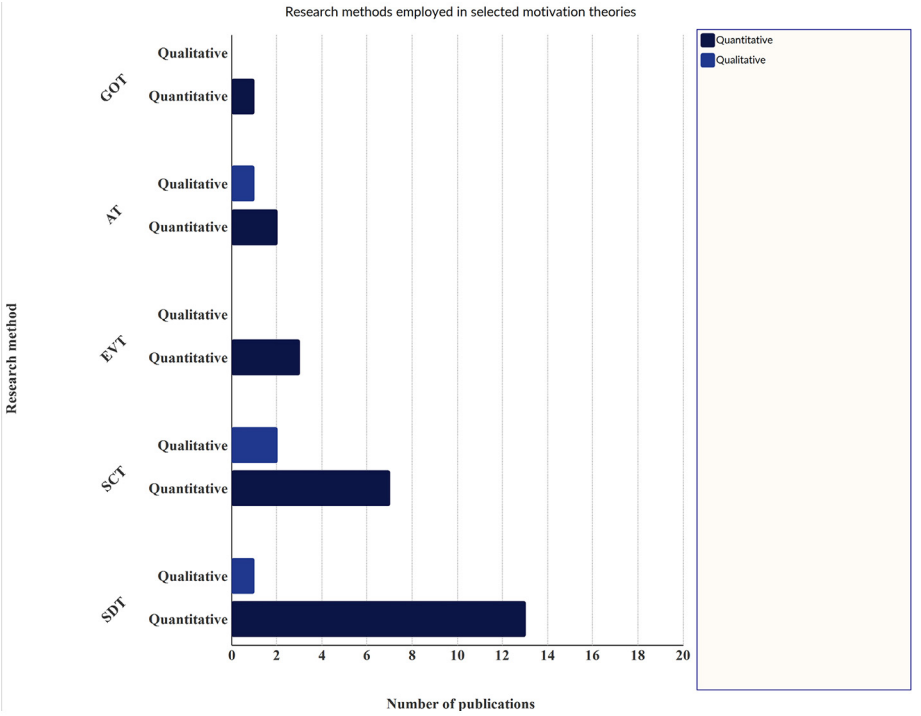

Notes: *SDT = SELF-DETERMINATION THEORY, *SCT = SELF COGNITIVE THEORY, *AT = ATTRIBUTION THEORY, *EVT = EXPECTANCY-VALUE THEORY, *GOT = GOAL ORIENTED THEORY
Source: Created by author(S) in Nvivo12

Figure 5.
Research methods employed in selected motivation theories

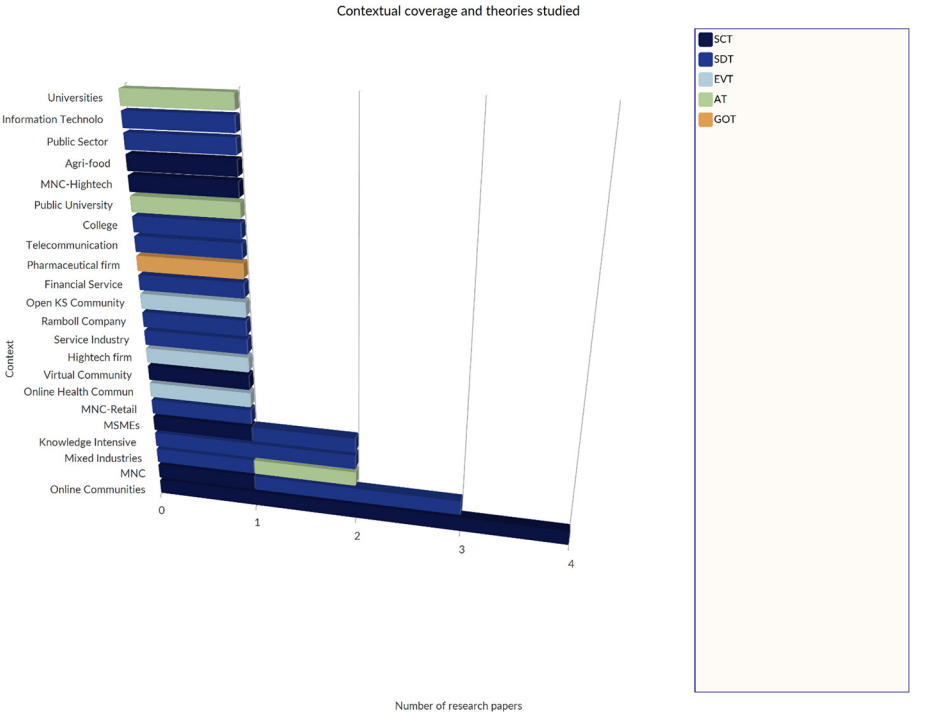

Figure 6.
Contextual coverage and theories studied

Notes: *SDT = SELF-DETERMINATION THEORY, *SCT = SELF COGNITIVE THEORY, *AT = ATTRIBUTION THEORY, *EVT = EXPECTANCY-VALUE THEORY, *GOT = GOAL ORIENTED THEORY
Source: Created by author(S) in Nvivo12

employees. Managers should consider that supporting capability and association helps in attracting intrinsic motivation, and it is recommended to encourage formal meetings on the KS, encouraging associations and knowledge. Managers are required to be cautious while awarding rewards as the outcome is not well-appreciated in KS. A few studies conducted on the KS depict the bad impact of economic rewards for motivating people in the long-term (Osterloh and Frey, 2000; Bock *et al.*, 2005). The current theoretical review presents that for promoting high levels of KS among employees there is a need for managers to cherish autonomous motivation of employees for such sharing. Managers can use numerous ways to aid employees' capabilities and "autonomous motivation" for KS. Thus, there is a need to design jobs to not only aid the openings in KS but also the autonomous motivation of employees to benefit from such openings (Reinholt *et al.*, 2011). According to the SCT, organizations need to aid and assist employees in shaping awareness of the KS. This is possible by boosting their self-efficacy and offering more organizational assistance (Wang and Noe, 2010). There is a need to motivate, design and enable "outcome expectation" by managers and more research is required in this. According to theoretical view, other important enablers are "personal outcome expectations, social outcome expectations, social exposure, altruism, organizational reward, reciprocity, reputation, goal-oriented learning,

Author(s)	Context	Country	Method	Theory
Bavik *et al.* (2018)	MNC-Retail	Hongkong	Quantitative	SDT
Cai and Shi (2020)	Online communities	China	Quantitative	SCT
Cavaliere *et al.* (2015)	Knowledge intensive firms	Italy	Quantitative	SDT
Chen and Lin (2013)	MNC-high-tech	Taiwan	Quantitative	SCT
Chiu *et al.* (2018)	High-tech firm	Taiwan	Quantitative	EVT
Cockrell and Stone (2010)	Service industry	USA	Quantitative	SDT
Cramton (2001)	Universities	Multiple Counties	Qualitative	AT
de Almeida *et al.* (2016)	Telecommunication	USA	Qualitative	SDT
Duarte Alonso *et al.* (2019)	MSMEs	Multiple Counties	Qualitative	SCT
Fait *et al.* (2019)	Agri-food	Italy	Qualitative	SCT
Foss *et al.* (2009)	MNC	Denmark	Quantitative	SDT
Gagné *et al.* (2019)	Knowledge intensive firms	Australia	Quantitative	SDT
Goncalo and Duguid (2008)	Public University	Multiple Counties	Quantitative	AT
Hwang (2011)	College	USA	Quantitative	SDT
Imlawi and Gregg (2020)	Online health communities	Arab countries	Quantitative	EVT
Jin *et al.* (2015)	Online communities	China	Quantitative	SCT
Lekhawipat *et al.* (2018)	Mixed industries	Taiwan	Quantitative	AT
Lin and Huang (2010)	MNC	Taiwan	Quantitative	SCT
Liou *et al.* (2016)	Online communities	Taiwan	Quantitative	SCT
Llopis and Foss (2016)	MNC	Denmark	Quantitative	SDT
Razmerita *et al.* (2016)	MSMEs	Danish	Quantitative	SDT
Reinholt *et al.* (2011)	Ramboll Company	Multiple Counties	Quantitative	SDT
Shan *et al.* (2013)	Virtual community	China	Quantitative	SCT
Shariq *et al.* (2019)	Pharmaceutical firm	Pakistan	Quantitative	GO
Stenius *et al.* (2016)	Public sector	Finland	Quantitative	SDT
Wang and Hou (2015)	Financial service	Taiwan	Quantitative	SDT
Wu *et al.* (2019)	Open KS Community	China	Quantitative	EVT
Zhang *et al.* (2020)	Mixed industries	China	Quantitative	SDT
Zhao *et al.* (2016)	Information technology	China	Quantitative	SDT
Zhou *et al.* (2014)	Online communities	China	Quantitative	SCT

Notes: *SDT = SELF-DETERMINATION THEORY, *SCT = SELF COGNITIVE THEORY, *AT = ATTRIBUTION THEORY, *EVT = EXPECTANCY-VALUE THEORY, *GOT = GOAL ORIENTED THEORY

Table 4.
Contextual coverage, country, method and theory

goal-oriented performance, optimism, pessimism, attainment value, utility value, and social exposure." These were identified as "precursors of knowledge sharing." These theories relating to motivation have a high-level of aptitude to increase motivators' in the area of KS.

This study can be used by researchers and managers to choose the significant factors based on their industry and research. These studies concentrate only on one motivation theory, but the comparative viewpoint needs to be widened after arguing the potential of other psychological approaches that clarify motivator's nature for sharing knowledge. These studies may help to recognize more widely the significant predictors that promote KS. This research helps in getting an insight into motivation theories in KS with the aid of a review to show an association between "motivation" and "knowledge sharing behavior."

This research further identifies important antecedents that affect the motivation on KS. Thus, this research contributes significantly to the theory of motivation and literature relating to the management of knowledge. Accordingly, the research expands the theoretical literature and provides a guideline for upcoming researches to contemplate and examine numerous motivation theories and also choose the most significant construct in the researches on KS.

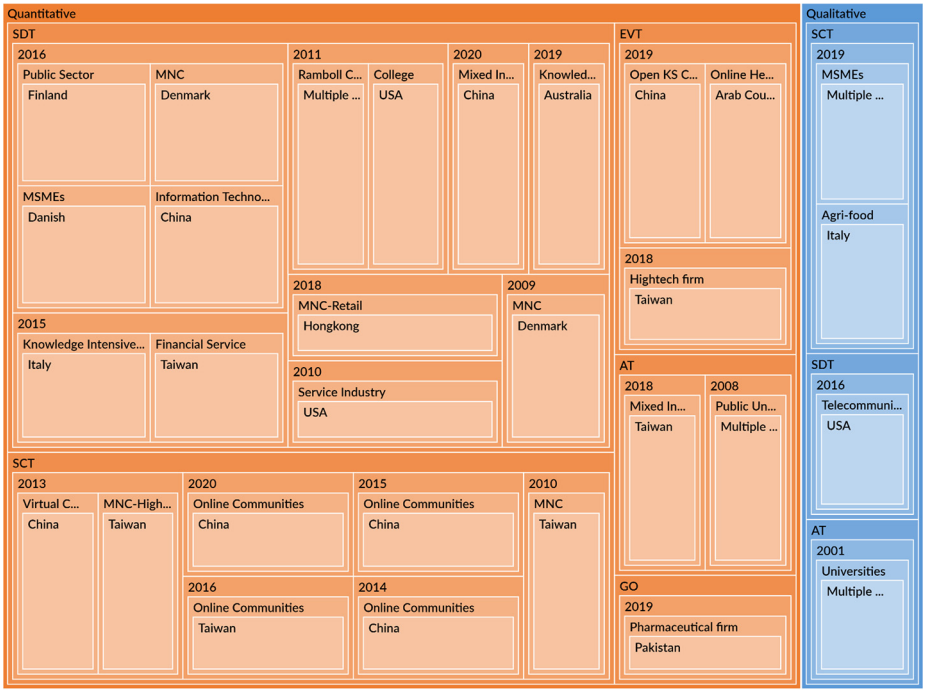

Figure 7.
Hierarchical comprehensive map of literature

Notes: *SDT = SELF-DETERMINATION THEORY, *SCT = SELF COGNITIVE THEORY, *AT = ATTRIBUTION THEORY, *EVT = EXPECTANCY-VALUE THEORY, *GOT = GOAL ORIENTED THEORY
Source: Created by author(S) in Nvivo12

Formal and informal attitude promotes efficient KS behaviors. Organizations that look for institutionalizing the KS behavior need to promote easy work contexts (Bock *et al.*, 2005). Findings of this research depict the significance of numerous motivational theories and promote efficient KS. Findings of this research can be used in future researches by using empirical research in developed and developing countries. Also, the nature of the knowledge shared was not contemplated and separated (tacit or explicit) and the same can be studied separately in future researches to recognize which is the most significant motivation driver for tacit and explicit KS. It is highly recommended to conduct further in-depth study or research. This research (though with limitations) can be used for reference purposes or as a guide to research scholars of sharing knowledge, rousing and tackling further study. Finally, future research can expand insight into what demotivates the KS.

References

Akhavan, P., Hosseini, S.M., Abbasi, M. and Manteghi, M. (2015), "Knowledge-sharing determinants, behaviors, and innovative work behaviors", *Aslib Journal of Information Management*, Vol. 67 No. 5, pp. 562-591, doi:10.1108/AJIM-02-2015-0018.

Bandura, A. (1997), *Self-Self Efficacy: The Exercise of Control.*

Bandura, A. (2001), "Social cognitive theory: an agentic perspective", *Annual Review of Psychology*, Vol. 52 No. 1, pp. 1-26.

Bartol, K.M. and Srivastava, A. (2002), "Encouraging knowledge sharing: the role of organizational reward systems", *Journal of Leadership and Organizational Studies*, Vol. 9 No. 1, pp. 64-76.

Bavik, Y.L., Tang, P.M., Shao, R. and Lam, L.W. (2018), "Ethical leadership and employee knowledge sharing: exploring dual-mediation paths", *The Leadership Quarterly*, Vol. 29 No. 2, pp. 322-332, doi:10.1016/j.leaqua.2017.05.006.

Bock, G.W. and Kim, Y.G. (2002), "Breaking the myths of rewards: an exploratory study of attitudes about knowledge sharing", *Information Resources Management Journal* (IRMJ), Vol. 15 No. 2, pp. 14-21.

Bock, G.W., Zmud, R.W., Kim, Y.G. and Lee, J.N. (2005), "Behavioral intention formation in knowledge sharing: examining the roles of extrinsic motivators, social-psychological forces, and organizational climate", *MIS Quarterly*, pp. 87-111.

Button, S.B., Mathieu, J.E. and Zajac, D.M. (1996), "Goal orientation in organizational research: a conceptual and empirical foundation", *Organizational Behavior and Human Decision Processes*, Vol. 67 No. 1, pp. 26-48.

Cai, Y. and Shi, W. (2020), "The influence of the community climate on users' knowledge-sharing intention: the social cognitive theory perspective", *Behaviour & Information Technology*, pp. 1-17, doi: 10.1080/0144929X.2020.1808704.

Cavaliere, V., Lombardi, S. and Giustiniano, L. (2015), "Knowledge sharing in knowledge-intensive manufacturing firms. An empirical study of its enablers", *Journal of Knowledge Management*.

Chang, H.H. and Chuang, S.S. (2011), "Social capital and individual motivations on knowledge sharing: participant involvement as a moderator", *Information and Management*, Vol. 48 No. 1, pp. 9-18.

Chang, K.C., Yen, H.W., Chiang, C.C. and Parolia, N. (2013), "Knowledge contribution in information system development teams: an empirical research from a social cognitive perspective", *International Journal of Project Management*, Vol. 31 No. 2, pp. 252-263.

Chen, M.L. and Lin, C.P. (2013), "Assessing the effects of cultural intelligence on team knowledge sharing from a socio-cognitive perspective", *Human Resource Management*, Vol. 52 No. 5, pp. 675-695, doi: 10.1002/hrm.21558.

Chiu, C.M., Hsu, M.H. and Wang, E.T. (2006), "Understanding knowledge sharing in virtual communities: an integration of social capital and social cognitive theories", *Decision Support Systems*, Vol. 42 No. 3, pp. 1872-1888.

Chiu, C.K., Lin, C.P., Tsai, Y.H. and Teh, S.F. (2018), "Enhancing knowledge sharing in high-tech firms: the moderating role of collectivism and power distance", *Cross Cultural and Strategic Management*, Vol. 25 No. 3, pp. 468-491.

Cockrell, R.C. and Stone, D.N. (2010), "Industry culture influences pseudo-knowledge sharing: a multiple mediation analysis", *Journal of Knowledge Management*, Vol. 14 No. 6, pp. 841-857, doi: 10.1108/13673271011084899.

Cook, D.A. and Artino, A.R. Jr, (2016), "Motivation to learn: an overview of contemporary theories", *Medical Education*, Vol. 50 No. 10, pp. 997-1014.

Cramton, C.D. (2001), "The mutual knowledge problem and its consequences for dispersed collaboration", *Organization Science*, Vol. 12 No. 3, pp. 346-371, doi: 10.1287/orsc.12.3.346.10098.

Cruz, N.M., Perez, V.M. and Cantero, C.T. (2009), "The influence of employee motivation on knowledge transfer", *Journal of Knowledge Management*, Vol. 13 No. 6, pp. 478-490.

de Almeida, F.C., Lesca, H. and Canton, A.W. (2016), "Intrinsic motivation for knowledge sharing–competitive intelligence process in a telecom company", *Journal of Knowledge Management*, Vol. 20 No. 6, pp. 1282-1301.

Deci, E.L. and Ryan, R.M. (1985), *Intrinsic Motivation and Self-Determination in Human Behavior: perspectives in Social Psychology*, Plenum. New York, NY.

Deci, E.L. and Ryan, R.M. (1985), "Self-determination and intrinsic motivation in human behavior", *EL Deci, RM Ryan.–1985*.

Deci, E.L. and Ryan, R.M. (1991), "A motivational approach to self: integration in personality", in *Nebraska Symposium on Motivation: Perspectives on Motivation*, Dienstbier, R. (Ed.), Vol. 38. University of Nebraska Press, Lincoln, pp. 237-288.

Deci, E.L. and Ryan, R.M. (2000), "The' what' and' why' of goal pursuits: human needs and the self-determination of behavior", *Psychological Inquiry*, Vol. 11 No. 4, pp. 227-268.

Deci, E.L. and Ryan, R.M. (2002), "Overview of self-determination theory: an organismic dialectical perspective", *Handbook of Self-Determination Research*, pp. 3-33.

Deci, E.L. and Ryan, R.M. (2014), "Autonomy and need satisfaction in close relationships: relationships motivation theory", in *Human Motivation and Interpersonal Relationships*, Springer, Dordrecht, pp. 53-73.

Del Giudice, M., Carayannis, E.G. and Maggioni, V. (2017), "Global knowledge intensive enterprises and international technology transfer: emerging perspectives from a quadruple helix environment", *The Journal of Technology Transfer*, Vol. 42 No. 2, pp. 229-235.

Duarte Alonso, Kok, S., Sakellarios, N. and O'Brien, S. (2019), "Micro enterprises, self-efficacy and knowledge acquisition: evidence from Greece and Spain", *Journal of Knowledge Management*, Vol. 23 No. 3, pp. 419-438, doi: 10.1108/JKM-02-2018-0118.

Dweck, C.S., (1986), "Motivational processes affecting learning", *American Psychologist*, Vol. 41 4. No. 10, pp. 1040-4048.

Dweck, C.S. (1975), "The role of expectations and attributions in the alleviation of learned helplessness", *Journal of Personality and Social Psychology*, Vol. 31 No. 4, pp. 674-685.

Eccles, J.S. and Wigfield, A. (2002), "Motivational beliefs, values, and goals", *Annual Review of Psychology*, Vol. 53 No. 1, pp. 109-132.

Eid, M.I. and Al-Jabri, I.M. (2016), "Social networking, knowledge sharing, and student learning: the case of university students", *Computers and Education*, Vol. 99, pp. 14-27.

Eison, J.A. (1979), "The development and validation of a scale to assess different student orientations towards grades and learning", Unpublished doctoral dissertation. University of Tennessee, Knoxville.

Fait, M., Scorrano, P., Mastroleo, G., Cillo, V. and Scuotto, V. (2019), "A novel view on knowledge sharing in the agri-food sector", Journal of Knowledge Management, Vol. 23 No. 5, pp. 953-974, doi: 10.1108/JKM-09-2018-0572.

Foss, N.J., Minbaeva, D.B., Pedersen, T. and Reinholt, M. (2009), "Encouraging knowledge sharing among employees: how job design matters", *Human Resource Management*, Vol. 48 No. 6, pp. 871-893.

Gagné, M., Tian, A.W., Soo, C., Zhang, B., Ho, K.S.B. and Hosszu, K. (2019), "Different motivations for knowledge sharing and hiding: the role of motivating work design", *Journal of Organizational Behavior*, Vol. 40 No. 7, pp. 783-799. doi: 10.1002/job.2364.

Gilal, F.G., Zhang, J., Paul, J. and Gilal, N.G. (2019), "The role of self-determination theory in marketing science: an integrative review and agenda for research", *European Management Journal*, Vol. 37 No. 1, pp. 29-44.

Goncalo, J.A. and Duguid, M.M. (2008), "Hidden consequences of the group-serving bias: causal attributions and the quality of group decision making", *Organizational Behavior and Human Decision Processes*, Vol. 107 No. 2, pp. 219-233.

Graham, S. and Weiner, B. (2012), "Motivation: past, present, and future", in Harris K.R Graham, S. Urdan, T. McCormick, C.B. Sinatra, G.M and Sweller, J. (Eds), *APA Handbooks in Psychology®. APA Educational Psychology Handbook*, Vol. *1*. Theories, constructs, and critical issues, American Psychological Association, p. 367-397, doi: 10.1037/13273-013.

Guan, T., Wang, L., Jin, J. and Song, X. (2018), "Knowledge contribution behavior in online Q&A communities: an empirical investigation", *Computers in Human Behavior*, Vol. 81, pp. 137-147.

Gupta, V. and Thomas, A. (2019), "Fostering tacit knowledge sharing and innovative work behaviour: an integrated theoretical view", *International Journal of Managerial and Financial Accounting*, Vol. 11 Nos 3/4, pp. 320-346.

Hashim, K.F. and Tan, F.B. (2018), "Examining the determinant factors of perceived online community usefulness using the expectancy value model", *Journal of Systems and Information Technology*, Vol. 20 No. 2, pp. 152-167.

Herzberg, F. (1968), "One more time: how do you motivate employees?", *Harv Bus Rev*, Vol. 46, pp. 53-62.

Hsu, C.L. and Lin, J.C.C. (2008), "Acceptance of blog usage: the roles of technology acceptance, social influence and knowledge sharing motivation", *Information & Management*, Vol. 45 No. 1, pp. 65-74.

Hsu, I.C. and Wang, Y.S. (2008), "A model of intraorganizational knowledge sharing", *Journal of Global Information Management*, Vol. 16 No. 3, pp. 45-73.

Hsu, M.H., Ju, T.L., Yen, C.H. and Chang, C.M. (2007), "Knowledge sharing behavior in virtual communities: the relationship between trust, self-efficacy, and outcome expectations", *International Journal of Human-Computer Studies*, Vol. 65 No. 2, pp. 153-169, doi: 10.1016/j.ijhcs.2006.09.003.

Hung, S.Y., Durcikova, A., Lai, H.M. and Lin, W.M. (2011), "The influence of intrinsic and extrinsic motivation on individuals' knowledge sharing behavior", *International Journal of Human-Computer Studies*, Vol. 69 No. 6, pp. 415-427.

Imlawi, J. and Gregg, D. (2020), "Understanding the satisfaction and continuance intention of knowledge contribution by health professionals in online health communities", *Informatics for Health and Social Care*, Vol. 45 No. 2, pp. 151-167, doi: 10.1080/17538157.2019.1625053.

Jin, J., Li, Y., Zhong, X. and Zhai, L. (2015), "Why users contribute knowledge to online communities: an empirical study of an online social Q&A community", *Information & Management*, Vol. 52 No. 7, pp. 840-849.

Kankanhalli, A., Tan, B.C. and Wei, K.K. (2005), "Contributing knowledge to electronic knowledge repositories: an empirical investigation", *MIS Quarterly*, No. 1, p. 29.

Kasser, T. and Ryan, R.M. (1996), "Further examining the american dream: differential correlates of intrinsic and extrinsic goals", *Personality and Social Psychology Bulletin*, Vol. 22 No. 3, pp. 280-287.

Kim, J., Lee, C. and Elias, T. (2015), "Factors affecting information sharing in social networking sites amongst university students", *Online Information Review*, Vol. 39 No. 3, pp. 290-309, doi: 10.1108/OIR-01-2015-0022.

Kim, T.T. and Lee, G. (2013), "Hospitality employee knowledge-sharing behaviors in the relationship between goal orientations and service innovative behavior", *International Journal of Hospitality Management*, Vol. 34, pp. 324-337.

Ko, D.G., Kirsch, L.J. and King, W.R. (2005), "Antecedents of knowledge transfer from consultants to clients in enterprise system implementations", *MIS Quarterly*, pp. 59-85.

Kwahk, K.Y. and Park, D.H. (2016), "The effects of network sharing on knowledge-sharing activities and job performance in enterprise social media environments", *Computers in Human Behavior*, Vol. 55, pp. 826-839.

Lekhawipat, W., Wei, Y.H. and Lin, C. (2018), "How internal attributions affect knowledge sharing behavior", *Journal of Knowledge Management*, Vol. 22 No. 4, pp. 867-886, doi: 10.1108/JKM-02-2017-0081.

Lin, H.F. (2007), "Effects of extrinsic and intrinsic motivation on employee knowledge sharing intentions", *Journal of Information Science*, Vol. 33 No. 2, pp. 135-149.

Lin, T.C. and Huang, C.C. (2008), "Understanding knowledge management system usage antecedents: an integration of social cognitive theory and task technology fit", *Information and Management*, Vol. 45 No. 6, pp. 410-417.

Lin, T.C. and Huang, C.C. (2010), "Withholding effort in knowledge contribution: the role of social exchange and social cognitive on project teams", *Information and Management*, Vol. 47 No. 3, pp. 188-196, doi: 10.1016/j.im.2010.02.001.

Liou, D.K., Chih, W.H., Yuan, C.Y. and Lin, C.Y. (2016), "The study of the antecedents of knowledge sharing behavior", *Internet Research*, Vol. 26 No. 4, pp. 845-868, doi: 10.1108/IntR-10-2014-0256.

Liu, H. and Li, G. (2018), "Linking transformational leadership and knowledge sharing: the mediating roles of perceived team goal commitment and perceived team identification", *Frontiers in Psychology*, Vol. 9, p. 1331.

Llopis, O. and Foss, N.J. (2016), "Understanding the climate–knowledge sharing relation: the moderating roles of intrinsic motivation and job autonomy", *European Management Journal*, Vol. 34 No. 2, pp. 135-144.

Lu, L., Lin, X. and Leung, K. (2012), "Goal orientation and innovative performance: the mediating roles of knowledge sharing and perceived autonomy", *Journal of Applied Social Psychology*, Vol. 42, pp. E180-E197.

Maslow, A.H. (1970), *Motivation and Personality*, New York, NY: Harper and Row Publishers, Inc.

Matzler, K. and Mueller, J. (2011), "Antecedents of knowledge sharing – examining the influence of learning and performance orientation", *Journal of Economic Psychology*, Vol. 32 No. 3, pp. 317-329.

Miller, N.E. and Dollard, J. (1941), *Social Learning and Imitation*, New Haven, CT: Yale University Press.

Nahapiet, J. and Ghoshal, S. (1998), "Social capital, intellectual capital, and the organizational advantage", *Academy of Management Review*, Vol. 23 No. 2, pp. 242-266, doi: 10.5465/amr.1998.533225.

Nonaka, I. (1994), "A dynamic theory of organizational knowledge creation", *Organization Science*, Vol. 5 No. 1, pp. 14-37.

Osterloh, M. and Frey, B.S. (2000), "Motivation, knowledge transfer, and organizational forms", *Organization Science*, Vol. 11 No. 5, pp. 538-550, doi: 10.1287/orsc.11.5.538.15204.

Park, J. and Gabbard, J.L. (2018), "Factors that affect scientists' knowledge sharing behavior in health and life sciences research communities: differences between explicit and implicit knowledge", *Computers in Human Behavior*, Vol. 78, pp. 326-335.

Razmerita, L., Kirchner, K. and Nielsen, P. (2016), "What factors influence knowledge sharing in organizations? A social dilemma perspective of social media communication", *Journal of Knowledge Management*, Vol. 20 No. 6, pp. 1225-1246.

Reinholt, M.I.A., Pedersen, T. and Foss, N.J. (2011), "Why a central network position isn't enough: the role of motivation and ability for knowledge sharing in employee networks", *Academy of Management Journal*, Vol. 54 No. 6, pp. 1277-1297.

Rutten, W., Blaas-Franken, J. and Martin, H. (2016), "The impact of (low) trust on knowledge sharing", *Journal of Knowledge Management*, Vol. 20 No. 2, pp. 199-214.

Sahibzada, U.F., Cai, J., Latif, K.F. and Sahibzada, H.F. (2020a), "Knowledge management processes, knowledge worker satisfaction, and organizational performance: symmetric and asymmetrical analysis", *Aslib Journal of Information Management*, Vol. 72 No. 1, pp. 112-129.

Sahibzada, U.F., Jianfeng, C., Latif, K.F. and Sahibzada, H.F. (2020b), "Fueling knowledge management processes in chinese higher education institutes (HEIs): the neglected mediating role of knowledge worker satisfaction", *Journal of Enterprise Information Management*, Vol. 33 No. 6, pp. 1395-1417.

Sahibzada, U.F., Latif, K.F., Xu, Y. and Khalid, R. (2020c), "Catalyzing knowledge management processes towards knowledge worker satisfaction: fuzzy-set qualitative comparative analysis", *Journal of Knowledge Management*, Vol. 24 No. 10, pp. 2373-2400.

Sahibzada, U.F., Cai, J., Latif, K.F., Shafait, Z. and Sahibzada, H.F. (2020d), "Interpreting the impact of knowledge management processes on organizational performance in chinese higher education:

Mediating role of knowledge worker productivity", *Studies in Higher Education*, doi: 10.1080/03075079.2020.1793930.

Sahibzada, U.F., Cai, J., Latif, K.F., Shah, S.A. and Sahibzada, H.F. (2020e), "Refuelling knowledge management processes towards organisational performance: mediating role of creative organisational learning", *Knowledge Management Research Practice*, doi: 10.1080/14778238.2020.1787802.

Savolainen, R. (2013), "Approaching the motivators for information seeking: the viewpoint of attribution theories", *Library and Information Science Research*, Vol. 35 No. 1, pp. 63-68.

Sedighi, M., van Splunter, S., Brazier, F., van Beers, C. and Lukosch, S. (2016), "Exploration of multi-layered knowledge sharing participation: the roles of perceived benefits and costs", *Journal of Knowledge Management*, Vol. 20 No. 6, pp. 1247-1267.

Serenko, A. and Bontis, N. (2016), "Negotiate, reciprocate, or cooperate? The impact of exchange modes on inter-employee knowledge sharing", *Journal of Knowledge Management*, Vol. 20 No. 4, pp. 687-712.

Shan, S., Xin, T., Wang, L., Li, Y. and Li, L. (2013), "Identifying influential factors of knowledge sharing in emergency events: a virtual community perspective", *Systems Research and Behavioral Science*, Vol. 30 No. 3, pp. 367-382.

Shariq, S.M., Mukhtar, U. and Anwar, S. (2019), "Mediating and moderating impact of goal orientation and emotional intelligence on the relationship of knowledge oriented leadership and knowledge sharing", *Journal of Knowledge Management*, Vol. 23 No. 2, pp. 332-350, doi: 10.1108/JKM-01-2018-0033.

Sharma, G.D., Thomas, A. and Paul, J. (2020), "Reviving tourism industry post-COVID-19: a resilience-based framework", *Tourism Management Perspectives*, Vol. 37, p. 100786, doi: 10.1016/j.tmp.2020.100786.

Steel, P. and König, C.J. (2006), "Integrating theories of motivation", *Academy of Management Review*, Vol. 31 No. 4, pp. 889-913.

Stenius, M., Hankonen, N., Ravaja, N. and Haukkala, A. (2016), "Why share expertise? A closer look at the quality of motivation to share or withhold knowledge", *Journal of Knowledge Management*, Vol. 20 No. 2, pp. 181-198, doi: 10.1108/JKM-03-2015-0124.

Swift, M., Balkin, D.B. and Matusik, S.F. (2010), "Goal orientations and the motivation to share knowledge", *Journal of Knowledge Management*, Vol. 14 No. 3, pp. 378-393.

Tangaraja, G., MohdRasdi, R., Abu Samah, B. and Ismail, M. (2016), "Knowledge sharing is knowledge transfer: a misconception in the literature", *Journal of Knowledge Management*, Vol. 20 No. 4, pp. 653-670.

Thomas, A. and Chopra, M. (2020), "On how big data revolutionizes knowledge management", in *Digital Transformation in Business and Society*, Palgrave Macmillan, Cham, pp. 39-60.

Thomas, A. and Paul, J. (2019), "Knowledge transfer and innovation through university-industry partnership: an integrated theoretical view", *Knowledge Management Research and Practice*, Vol. 17 No. 4, pp. 436-448.

Thomas, A., Cillo, V., Caggiano, V. and Vrontis, D. (2021), "Drivers of social capital in enhancing team knowledge sharing and team performance: moderator role of manager's cultural intelligence", *International Journal of Managerial and Financial Accounting (IJMFA)*, Vol. 12 Nos 3/4, doi: 10.1504/IJMFA.2020.112358.

Tsai, W. and Ghoshal, S. (1998), "Social capital and value creation: the role of intrafirm networks", *Academy of management Journal*, Vol. 41 No. 4, pp. 464-476.

Udechukwu, I.I. (2009), "Correctional officer turnover: of Maslow's needs hierarchy and Herzberg's motivation theory", *Public Personnel Management*, Vol. 38 No. 2, pp. 69-82.

Vansteenkiste, M., Niemiec, C.P. and Soenens, B. (2010), "The development of the five mini-theories of self-determination theory: an historical overview, emerging trends, and future directions", *In the*

Decade Ahead: Theoretical Perspectives on Motivation and Achievement, Emerald Group Publishing Limited, pp. 105-165.

Vroom, V.H. (1964), *Work and Motivation*.

Wang, W.T. and Hou, Y.P. (2015), "Motivations of employees' knowledge sharing behaviors: a self-determination perspective", *Information and Organization*, Vol. 25 No. 1, pp. 1-26.

Wang, S. and Noe, R.A. (2010), "Knowledge sharing: a review and directions for future research", *Human Resource Management Review*, Vol. 20 No. 2, pp. 115-131, doi: 10.1016/j.hrmr.2009. doi: 10.001.

Wu, M., Kang, L., Shi, Y., Zhao, J.L. and Liang, L. (2019), "Why people are involved in and committed to online knowledge-sharing communities: an expectancy-value perspective", *Journal of Global Information Management (JGIM)*, Vol. 27 No. 2, pp. 78-101, doi: 10.4018/JGIM.2019040105.

Zhang, X., Jinpeng, X. and Khan, F. (2020), "The influence of social media on employee's knowledge sharing motivation: a two-factor theory perspective", *SAGE Open*, Vol. 10 No. 3, p. 2158244020942495.

Zhang, X., Zhang, Y., Sun, Y., Lytras, M., Ordonez de Pablos, P. and He, W. (2018), "Exploring the effect of transformational leadership on individual creativity in e-learning: a perspective of social exchange theory", *Studies in Higher Education*, Vol. 43 No. 11, pp. 1964-1978.

Zhao, L., Detlor, B. and Connelly, C.E. (2016), "Sharing knowledge in social Q&A sites: the unintended consequences of extrinsic motivation", *Journal of Management Information Systems*, Vol. 33 No. 1, pp. 70-100.

Zhou, J., Zuo, M., Yu, Y. and Chai, W. (2014), "How fundamental and supplemental interactions affect users' knowledge sharing in virtual communities? A social cognitive perspective", *Internet Research*.

Further reading

Chen, C.J. and Hung, S.W. (2010), "To give or to receive? Factors influencing members' knowledge sharing and community promotion in professional virtual communities", *Information and Management*, Vol. 47 No. 4, pp. 226-236.

Cummings, J.N. (2004), "Work groups, structural diversity, and knowledge sharing in a global organization", *Management Science*, Vol. 50 No. 3, pp. 352-364, doi: 10.1287/mnsc.1030.0134.

Deci, E.L., Connell, J.P. and Ryan, R.M. (1989), "Self-determination in a work organization", *Journal of Applied Psychology*, Vol. 74 No. 4, p. 580.

Del Giudice, M. and Maggioni, V. (2014), "Managerial practices and operative directions of knowledge management within inter-firm networks: a global view", *Journal of Knowledge Management*, Vol. 18 No. 5, pp. 841-846.

Del Giudice, M., Della Peruta, M.R. and Maggioni, V. (2015), "A model for the diffusion of knowledge sharing technologies inside private transport companies", *Journal of Knowledge Management*, Vol. 19 No. 3, pp. 611-625.

Dweck, C.S. and Leggett, E.L. (1988), "A social-cognitive approach to motivation and personality", *Psychological Review*, Vol. 95 No. 2, pp. 256-273.

Hau, Y.S., Kim, B., Lee, H. and Kim, Y.G. (2013), "The effects of individual motivations and social capital on employees' tacit and explicit knowledge sharing intentions", *International Journal of Information Management*, Vol. 33 No. 2, pp. 356-366.

Hewett, R., Shantz, A., Mundy, J. and Alfes, K. (2018), "Attribution theories in human resource management research: a review and research agenda", *The International Journal of Human Resource Management*, Vol. 29 No. 1, pp. 87-126.

Huang, C.C., Lin, T.C. and Lin, K.J. (2009), "Factors affecting pass-along email intentions (PAEIs): integrating the social capital and social cognition theories", *Electronic Commerce Research and Applications*, Vol. 8 No. 3, pp. 160-169.

Kim, J., Lee, C. and Elias, T. (2015), "Factors affecting information sharing in social networking sites amongst university students: application of the knowledge-sharing model to social networking sites", *Online Information Review*, Vol. 39 No. 3, pp. 290-309.

Lam, A. and Lambermont-Ford, J.P. (2010), "Knowledge sharing in organisational contexts: a motivation-based perspective", *Journal of Knowledge Management*, Vol. 14 No. 1, pp. 51-66.

Lin, M.J.J., Hung, S.W. and Chen, C.J. (2009), "Fostering the determinants of knowledge sharing in professional virtual communities", *Computers in Human Behavior*, Vol. 25 No. 4, pp. 929-939.

Martin-Perez, V. and Martin-Cruz, N. (2015), "The mediating role of affective commitment in the rewards–knowledge transfer relation", *Journal of Knowledge Management*, Vol. 19 No. 6, pp. 1167-1185.

Nonaka, I. (2008), "The knowledge-creating company", *Harvard Business Review Press*, Vol. 85 Nos 7/8, p. 162.

Nonaka, I. and Konno, N. (1998), "The concept of 'ba': building a foundation for knowledge creation", *California Management Review*, Vol. 40 No. 3, pp. 40-54.

Rhee, Y.W. and Choi, J.N. (2017), "Knowledge management behavior and individual creativity: goal orientations as antecedents and in-group social status as moderating contingency", *Journal of Organizational Behavior*, Vol. 38 No. 6, pp. 813-832.

Ryan, R.M. and Deci, E.L. (2000), "Self-determination theory and the facilitation of intrinsic motivation, social development, and well-being", *American Psychologist*, Vol. 55 No. 1, p. 68.

Savolainen, R. (2018), "Self-determination and expectancy-value: comparison of cognitive psychological approaches to motivators for information seeking about job opportunities", *Aslib Journal of Information Management*, Vol. 70 No. 1, pp. 123-140.

Shamim, S., Cang, S. and Yu, H. (2017), "Supervisory orientation, employee goal orientation, and knowledge management among front line hotel employees", *International Journal of Hospitality Management*, Vol. 62, pp. 21-32.

Stenius, M., Hankonen, N., Haukkala, A. and Ravaja, N. (2015), "Understanding knowledge sharing in the work context by applying a belief elicitation study", *Journal of Knowledge Management*, Vol. 19 No. 3, pp. 497-513.

Tsai, M.T. and Cheng, N.C. (2012), "Understanding knowledge sharing between IT professionals – an integration of social cognitive and social exchange theory", *Behaviour and Information Technology*, Vol. 31 No. 11, pp. 1069-1080.

Vansteenkiste, V., Lens, W., De Witte, H. and Feather, N.T. (2005), "Understanding unemployed people's job search behaviour, unemployment experience and well-being: a comparison of expectancy-value theory and self-determination theory", *British Journal of Social Psychology*, Vol. 44 No. 2, pp. 269-287.

Wasko, M.M. and Faraj, S. (2005), "Why should I share? Examining social capital and knowledge contribution in electronic networks of practice", *MIS Quarterly*, pp. 35-57.

Weiner, B. (2010), "The development of an attribution-based theory of motivation: a history of ideas", *Educational Psychologist*, Vol. 45 No. 1, pp. 28-36.

Yoon, C. and Rolland, E. (2012), "Knowledge-sharing in virtual communities: familiarity, anonymity and self-determination theory", *Behaviour and Information Technology*, Vol. 31 No. 11, pp. 1133-1143.

Corresponding author
Asha Thomas can be contacted at: mailashaat@gmail.com

For instructions on how to order reprints of this article, please visit our website:
www.emeraldgrouppublishing.com/licensing/reprints.htm
Or contact us for further details: **permissions@emeraldinsight.com**

International Journal of Scientific Research in Multidisciplinary Studies
Vol.7, Issue.1, pp.43-46, January (2021)

Survey Paper
E-ISSN: 2454-9312
P-ISSN: 2454-6143

Thermodynamic Analysis of Waste to Wealth Conversion

M. Kumar[1*], S.K. Singh[2]

[1]Physics Department, SSNC, University of Delhi, Delhi, India
[2]Dept. of Environmental Engineering, Delhi Technological University, Delhi, India

[*]*Corresponding Author: mukeshrana@ss.du.ac.in Tel.: +00-12345-54321*

Available online at: www.isroset.org

Received: 28/Dec/2020, Accepted: 15/Jan/2021, Online: 31/Jan/2021

***Abstract*—** Thermodynamics most important contribution is in deciding whether or not a given imaginable mechanism is feasible. Its famous first and second laws offers insights into the technological / marketing impact on waste production as well as conversion processes. Thermodynamics responds to this question through the concept of entropy and its related variables. Thermodynamics addresses this issue through harvesting energy from produce waste. This Waste to Wealth can be viewed not only as a potential alternative source of energy to feed energy greed, but also is an alternative way to protect environment from any harm from created waste. This paper explores how the potential utility of the Waste to Wealth - based chain method is required to resolve the increasing energy demands and also can lead to major environmental problems being solved. These thermodynamic variables impact study suggested a low entropy change based chain technological process, which does not only help in energy demand but also environmentally friendly and economically feasible. The quantity of residue produced in such a process is either can be reuse or have impact under environment tolerance limits.

Keywords—Waste Management, Waste to Wealth, Thermodynamics, Energy Resource

I. INTRODUCTION

Technical or economic development is that the basic characteristic of human beings and energy is one among the pillar of such development. The development in the form of human need industrial production is a necessity and ineluctable scenario. The demand for such products is related to the production of waste, an inevitable by-product of industrial production. While waste is shown to be a non-essential qualitative component of industrial production, the extent of the quantitative waste differs within certain limits depending on the degree of (in) efficiency with which these processes are operated. The ability of technological equipment to absorb and release energy controls development as well as the surrounding environment. Various energy resources compete for our energy needs and an acceptable choice of energy resources will play a major role in mitigating the deterioration of the environment associated with such growth. The urban areas witness the constantly increasing waste production to follow the everlasting increase in energy desire. Such thrust for energy requires technological exploitation of wastes to recover more energy, as well as to decrease the consumption rate of fossil fuels, and reduction in waste disposal. Uncontrolled waste disposal and unsustainable waste management do not solely harm the atmosphere, however co-jointly affect human health [1,7,8].

This associated waste is because of scientific limitations and less technological disposal focus. The degree of this (in) efficiency is regulated by thermodynamic laws and waste appears to be an inevitable requirement of industrial development. In certain cases, waste and its disposal constitute an external marketing influence, and the issue of waste is actually to some degree due to a failure of the market (and policy). Society metabolism process recast waste in energetic and material terms [13]. This reveals a different relevant aspect of waste production, the presence of waste tends to be an inevitable requirement for industrial development. It can provide an empirical context within which the effects of the metabolism of society in energetic and material terms can be rigorously deduced.

Thermodynamics may address environmental concerns associated with energy usage in terms of the technical mechanism involved. It shows that all possible real processes are within the limits imposed by thermodynamic laws and have an environmental effect. This article explores the relationship between production, technological waste, and the effect on the environment in general and, in particular, the limitations imposed by thermodynamic laws. This work also emphasizes how generated energy resources from waste, which implicitly rely on the availability, technical appropriateness, and socio-cultural acceptability, aid in this respect. These are also critical because they not only support our energy demand, but also help maintain environmental thermodynamic equilibrium. There is no alternative to technological product desire itself; however, the introduction of thermodynamics variables into waste-producing systems relies on environmental effect limitations. It is inferred that the possible utility of

© 2021, IJSRMS All Rights Reserved

thermodynamic variables resulted in a major approach to the output of waste amounts.

II. INSPIRATION FROM NATURE

The Energy and matter are main constituents of nature and obeys various laws of conservations. The famous Einstein mass relation correlate them and through light on their conversion. The natural ecosystem is an exclusive example of such laws / conversions where the energy / solar radiance drive many material processes or vice versa. On the one side solar radiation transformed into chemical or mechanical energy in order to sustain a material cycle of plants / animals and on the other hands at the end plants / animals revert back to energy through decomposer in various steps. The various plants, animals and microbes are involved in matter conversion through various cycles. The cyclic process like synthesis, respiration which involves elements - water, carbon, nitrogen, phosphorus and sulphur, are involved in material cycle process [3-6,13]. Based on their conversion role, can be classified as:

1. Producers: Producers use natural energy as sunlight to produce complex and energy-rich molecules by the photosynthesis process. It is an example of a factory that builds complex elements of life from basic components taken from the earth or the air.

2. Consumers: These utilize producer product so as to perform desired task. The unutilized type of matter and energy offers waste as the by-product of such consumptions.

3. Decomposers: These are known for reutilizing left over matter and energy to bring back into main cycle. This are utilizing energy be in the form of chemical energy or in other form of energy to support natural cycle.

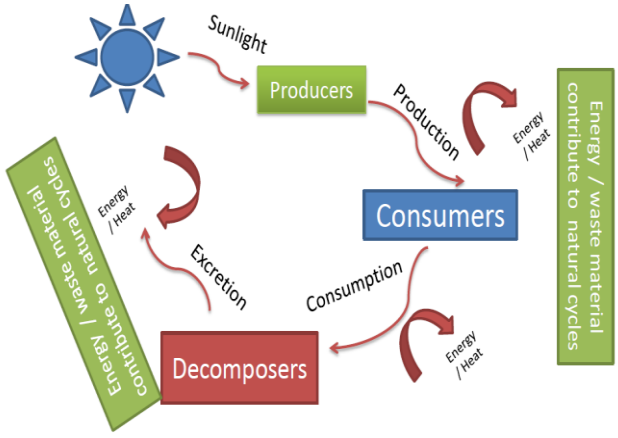

Fig 1: Matter and Energy Cycle

All these show energy and matter are inseparable. They in association with surrounding so called environment form a closed thermo dynamical system and make life possible through various chemical / structural transform. Almost every process output is associated with a waste which is being utilized as a raw input for other structural processes. So our various element stays in closed natural cycles and most of waste is being utilized in various cycle process. The excessive use of sunlight by different component of earth is best example of matter and energy cyclic process utilization.

Therefore to develop a better waste management system, it is important us to understand the basic scientific mechanism on energy and matter behaviour in the environment and in living things.

III. WASTE THERMODYNAMICS

The various study on the interaction between living being and their physical environment appreciate that the principles and lows of physics in many different study and govern life dynamics on the Earth. This refers even to the situation of both natural and human processes. Energy conversions play a central role in driving the dynamics of living as well as industrial processes. Many energy-characterized thermodynamic entities flow both inside the body and between the body and its environment. The variety of thermodynamic laws and principles of physics govern the rate of these energy transfers and the mechanism of thermal control. The first and the second law of thermodynamics governs these energy conversions. Energy conversions and the related dissipative processes are enabled by the entropy exchange in the system and are limited by the second law of natural systems. Any transition mechanism away from thermodynamic balance requires entropy change [2,4,7]

The laws of thermodynamics further put fundamental conversion limits when the work is performed inside the system. The consequences of the work need to be taken into account in the formulation of such thermodynamic limits. Such limit are mathematically well define in Carnot theorem and defined the energy conversion limit as system efficiency. Thermodynamically it depends on system and surrounding temperature and its gap. useful work is not possible. The maximum work obtained is known as EXERGY and the destructed part of energy as ANERGY. In order to minimize ANERGY, one need no temperature gap or infinite environmental sink which is theoretically impossible [8] . This fundamental conversion limits in technology term as the dissipative energy limits so called waste generated capability of the process.

This is essentially the limit on the rate by that work may be performed through time, that is, the facility that's related to the conversion of input kind of energy into another kind. The randomness standing of the system is said to a another construct referred to as entropy and if the overall entropy amendment for any conceivable method is negative, we will make sure that it's not possible in observe unless outside energy is dropped at bear. This indirectly showing that every one potential real processes area unit among the bounds obligatory by the laws of natural philosophy, and have some impact on the setting. Like different thermo-dynamic principles, the index referred to as "free energy"

© 2021, IJSRMS All Rights Reserved

combines each the system's energy and entropy at the same time. It refers to the number of labour from a tool which will be removed. Since a recent product's free energy is commonly quite its product of decay, it seems to be convenient thanks to describe every kind of waste referred to as ANERGY. Therefore, unavailable energy continues to rise, so we can conclude that entropy continues to increase [8].

Since anything that is not available for work has disappeared as waste, we may conclude that waste is unavailable energy and thus entropy is linked to waste.

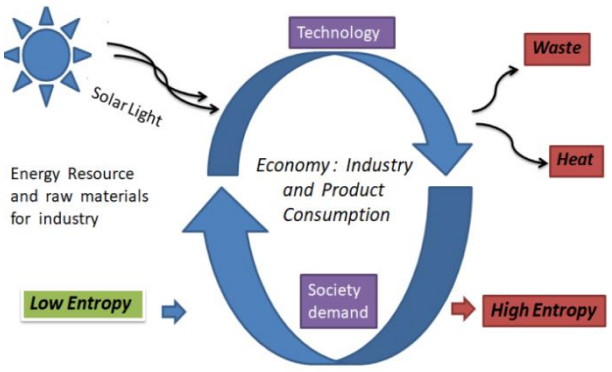

Fig 2 : Irreversible Process : Laws of Thermodynamics

Entropy and associate variables like enthalpy, energy change, free energy etc are associated with dynamics of involved system. The entropy change defines the equilibrium status of the system.

IV. WASTE TO WEALTH

All thermodynamic parameters indicates that no single mechanical machine is capable to accommodate all energy/ matter intake, but output always associated with some unwanted form, so called waste which have some impact on the environment. The concept of zero environment impact is need to be readdress. The above concept of physics provide some indication to minimize such waste production, so that it will be remains under the limit of environmental tolerance. Such minimization is possible either by use of high efficiency machine or the use of a series of machine in order to maintain low entropy changes. The concept of various natural cycles, concept of conversion role as discuss in section 2, provide some indication about natural way to minimize such waste or entropy change. They recommended those almost every process output is associated with a waste which is being utilized as a raw input for other structural / energy processes. This cycles process utilized most of waste is being utilized in previous cycle process and minimize waste production. This push us to use waste to wealth and Wealth-from-waste is a method of energy harvesting and adopt the key elements of waste hierarchy as refuse, reduce, reuse, recycle and recover. By recycling waste to the supply of electricity and/or heat, waste to wealth / Wealth-from-waste (WtW) helps to generate energy [7-9].

The composting and combustion are one of the oldest methods for WtE but limited to organic waste like food / plant material. Various new WtE methodologies have evolved with rapid technology development, from gasification, incineration, pyrolysis to plasma technology [9-11]. All WtE itself needs additional material and energy resources and waste as a resource and leads to an absolute decrease in per capita waste produced. Such utilization establishes waste as resources and contributes to the circular economy as a key.

In order to incorporate this environmentally favourable strategy, criteria such as the investment, the payback period and generated revenue therefore represent obstacles to be addressed. These are thermal conversion methodologies with the benefit of generating sub-product residual quantities such as ash and gaseous emissions [7, 8]. This aid in avoiding toxic pollutants such as NO_x, SO_x etc. These heating systems create synthetic gasses (SYNGAS) that can be used to generate a range of goods, such as fuelling, electrical energy and chemicals. Inputs components, temperature and pressure, as well as the chemical value of the manufactured waste, are the deciding factor in reducing productivity in the environment.

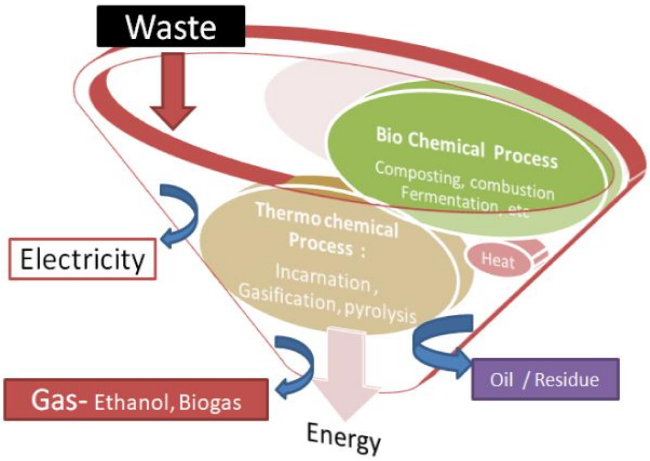

Fig 3: Waste to Energy Technology

The Integration of the advantages of conventional thermal conversion process methodologies with a high-performance SYNGAS cleaning phase results in plasma gasification. More friendly methods are developed. This not only reduces gaseous emissions but also provide economic value product.

V. THERMODYNAMIC ANALYSIS OF WASTE TO WEALTH

The previous section discusses whether a given waste conversion mechanism can be made or not. The main contribution of thermodynamics is decided In response to this issue, thermodynamics utilizes its famous entropy change and offers insights into minimal environmental consequences. Multi-stage waste management with a minimum entropy stage transition may be possible waste management solution.

© 2021, IJSRMS All Rights Reserved

The most of WtE technology perform waste-to-electricity and performance depends on generated heat flow. The integration of heat flow process and heat loss during transfer measures the energy performances of the studied WtW. It will be difficult to achieve for a single WtW, but can be improve by the integration with other WtW such in way that waste output of one process to feed the other as nature does. The performance of such hybrid system will be better than any individual WtW. By integrating the WtW system with other process can also enhance waste-to-electricity efficiency. In addition, this strategy is entirely capable of achieving a hybrid system through the use of adequate energy sources, which can play an important role in resolving waste management and environmental degradation issues. WtW combination selection relies on availability, technical adequacy and socio-cultural acceptability.

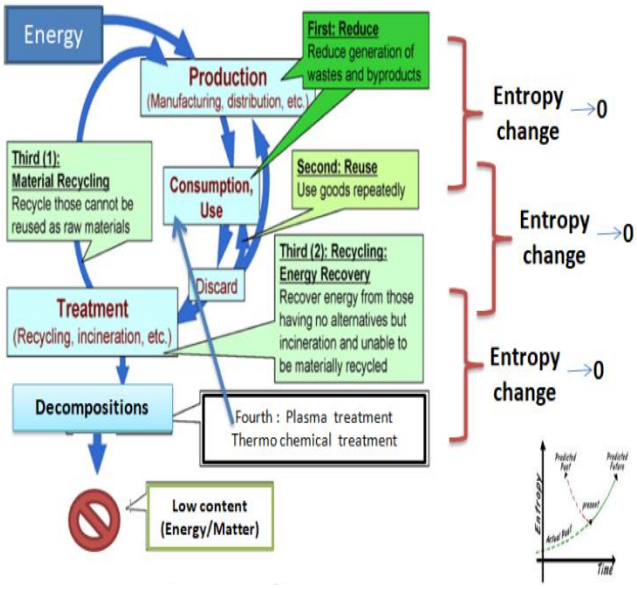

Fig 4: Cycle waste treatment

Life cycle assessment is one of the important tools to assess the environmental impact of thermal Waste-to-Wealth technologies: incineration, combustion, pyrolysis and gasification etc. The various experiments on Waste-to-Wealth technologies were analyzed by many researchers with following crucial factors [8,10-13] :

- Goals and scope definitions (e.g. operative processes, device limits, time period and geographical range),
- Detailed technology parameters (e.g. waste composition, technology, gas cleaning, waste management and inventory data),)
- Rules for simulation (e.g. energy / mass estimation standards, energy cleaning, energy recovery data.

Based on the above factors, one of the main quality characteristics of Waste to Wealth LCA technology studies is the thermodynamic portion. All these show that Waste-to-Wealth technologies are considered an alternative, cost-effective and environmentally sustainable energy supply.

VI. CONCLUSION

In deciding whether or not a certain theoretical mechanism is feasible, thermodynamics is of utmost significance. Thermodynamics addresses this question by applying its famous first and second laws and offering insights into the effect on technology for waste conversion. To meet the increasing need for energy sustainably, the Waste-to-wealth / Wealth-from-waste technologies is appropriate. However, maintaining their low entropy change performance is also essential. The thermodynamics alone have no alternative but the WtW technology chain or WtW technology integration with the minimum entropy transaction relies on the environmental impact limits of waste. It is concluded that the potential usefulness of multiple WtE / energy process results in substantial solution of waste environmental problems. The WtE / energy combination depends on technology appropriateness, waste composition, process parameters and socio-cultural acceptability.

REFERENCES

[1] Central pollution control board (cpcb), Management of municipal solid waste, Ministry of environment and forests, new delhi, India. **2004**.

[2] Elias l. Khalil, The three laws of thermodynamics and the theory of production, Journal of economic issues, vol. **38**, no. **1** (Mar., **2004**), pp. 201-226.

[3] Frank n. Egerton, History of ecological sciences, part 59,bulletin of the ecological society of America, vol. **98**, no. 4 (october **2017**), pp. 298-337

[4] Herman e. Daly , Is the entropy law relevant to the economics of natural resource scarcity?- yes, of course it is!' Journal of environmental economics and management **23**, (**1992**) 91-95.

[5] Jaya R, Srinivasulu K, Vivek R, Gokak D.T., Sanjay B, Environmental friendly ways to generate renewable energy from municipal solid waste, Procedia environmental sciences.35, **2016**:483-490.

[6] K. Bisson and J. Proops (eds), Waste in ecological economics, Edward Elgar, Cheltenham, UK, and nothampton, ma, USA, **2002**.

[7] Kümmel, R., 'Energy as a factor of production and entropy as a pollution indicator in macroeconomic modelling', *Ecological Economics*, **1, 161-180. 1989.**

[8] M. Kumar. Taming waste via laws of physics "International journal of sustainable energy and environmental research, **3(3): 164-170, 2312-5764, 2014.**

[9] M. Kumar, S. Kumar, S.K. Singh, Plasma technology as waste to energy : a review, Int. J. Adv. Res. **8(12), 464-473 2020.**

[10] Peiyuan Pan and others, Thermodynamic and Economic Analyses of a New Waste-to-Energy System Incorporated with a Biomass-Fired Power Plant, Energies **13(17), 4345, 2020**.

[11] Ramos A, Rouboa A., Renewable energy from solid waste: life cycle analysis and social welfare, environ impact assess rev. **2020** nov;85:106469. Doi: 10.1016/j.eiar.2020.106469. Epub 2020 sep 15.pmid: 32952252

[12] S Bansal, SK Singh, Recycling and reuse of construction & demolition (C&D) waste: Technology and equipments- 6th Engineering Conference in the Asian Region **2013.**

[13] Srinivas, Hari, "The 3R Concept and Waste Minimization". GDRC Reseaarch Output - Concept Note Series E-093. Kobe, Japan: Global Development Research Center **2020**.

[14] Stefan Baumgärtner, Thermodynamics of waste generation´ book: Waste in Ecological Economics. Publisher: Edward Elgar, Cheltenham, January **2002**.

© 2021, IJSRMS All Rights Reserved

Towards the Law Enforcement of Firearms

Kushagra Yadav
Computer Science & Engineering
Delhi Technological University
Delhi, India
kushagra_bt2k17@dtu.ac.in

Ravneet Punia
Electronics & Communication Engineering
Delhi Technological University
Delhi, India
ravneet.dtu@gmail.com

NS Raghava
Electronics & Communication Engineering
Delhi Technological University
Delhi, India
nsraghava@dce.ac.in

2020 IEEE 17th India Council International Conference (INDICON) | 978-1-7281-6916-3/20/$31.00 ©2020 IEEE | DOI: 10.1109/INDICON49873.2020.9342202

***Abstract*—The rate of violence in the world has increased tremendously in the last 15 years. Using and even carrying firearms in public places is not legal in most countries, but still Legal and illegal guns play a significant role in violence incidents across the globe on the streets. In the paper, we propose a computer vision-based approach to detect the people carrying firearms in public places using the CCTV camera system. Our approach also classifies the potential threat that can be caused by firearms with adequate quantitative and qualitative analysis. Along with the paper, we also release the high-quality corpora of guns that can be used for various detection and classification tasks by the researcher community for further experimentation. Apart from usage in cities and towns, the army can employ these systems to keep a check on the cross-border connecting roads and high tension areas.**

***Keywords*—Computer-Vision, Firearms, Law Enforcement, Residual Network, Transfer Learning**

I. Introduction

With the advancement of technology, mass shootings incidents are increasing tremendously in recent years. With the introduction of automatic and semi-automatic rifles, these events have risen without a doubt. Some studies indicate that the rate at which public mass shootings occur has tripled since 2011 [1]. According to some sources, 434 mass shootings took place in the year 2019 in the United States. In these incidents, 1,643 people were injured, and the death toll was 517, summing up a total of 2,160 victims. With the increasing crime these days, there is a need for a system to locate guns and weapons in public to ensure safety norms. These incidents have a severe effect on society in terms of casualties and emotional suffering. For instance, in the 2008 Mumbai attacks, there were 166 deaths, and 293 were injured. The property damage in the Mumbai attacks was over 4,000 crore rupees[1]. Recently, there was an attack on the Christchurch mosque in New Zealand in 2019. There were 51 casualties and 49 wounded[2]. There were around 244 fatalities in the Moscow theatre hostage crisis in 2002[3]. Terrorism and alt-right extremism are some of the reasons behind these mass shootings and executions.

[1]https://www.businesstoday.in/magazine/cover-story/the-cost-of-terror/story/3521.html

[2]https://en.wikipedia.org/wiki/Christchurch_mosque_shootings

[3] https://www.history.com/this-day-in-history/hostage-crisis-in-moscow-theater

978-1-7281-6916-3/20/$31.00 ©2020 IEEE

The Gun Laws in various countries also aid these terror attacks in one way or another. For instance, the 'right to keep and bear arms' in the US sometimes supports the terrorists in their motives and can be problematic for public safety. These kinds of shooting attacks could be prevented by framing inflexible gun laws in these countries. To avoid these casualties, we could deploy systems and software beforehand to efficiently detect the firearms in real-time and alert the concerned authorities in the area. Apart from usage in cities and towns, these systems can be employed by the army for their benefit as well. The military can deploy these on borders, forests, and other unreachable areas for enemy surveillance. The system's objective to detect firearms in real-time can support manual monitoring on national borders. It can further help to capture fugitives in the forest as the system can be deployed on wireless cameras and drones to detect any suspicious weapons in the view.

In this paper, we are trying to introduce an initial step towards real-time and better performing weapon-detection systems in public places for better law enforcement. We propose a model for firearm classification utilizing the method of transfer learning proposed by Weiss et al. in [2]. Transfer learning is the improvement of a pre-trained network trained on one task and employing this network for a different task. It repurposes the learned features and targets them to the second network, set to be trained on the target dataset.

We used the pre-trained neural network and fine-tuned it on our custom dataset for our task of classification. Our model categorizes the firearm explicitly in the scene into three classes, viz. big guns such as rifles, small guns like pistols and revolvers, and other weapons like knives. The network uses ResNet-34 [3] and ResNet-50 [3] as the base architecture to implement transfer learning. We intend to employ our model to ensure public safety in an area. There is no public dataset available for the task at hand, so we created a custom dataset to train our classification network. We trained the network on the dataset and achieved notable results. We report our results on this custom dataset for both our ResNet-34 and ResNet-50 models. We reached well over 90% accuracy on both our models. We have also applied an explainability method on our network to produce an interpretation of the classification decision made by our algorithm. For that purpose, we use a technique discussed by

Authorized licensed use limited to: DELHI TECHNICAL UNIV. Downloaded on February 15,2021 at 09:53:58 UTC from IEEE Xplore. Restrictions apply.

Lin et al. in [23] known as GSInquire. It is a direct strategy that considers the network's internal behavior directly and then surfaces it as a probable explanation.

The rest of the paper proceeds as: In Section 2, we discuss the work related to neural networks, transfer learning and firearm classification. In Section 3, we explains about the custom dataset we created for our work. Section 4 goes through the process to fulfill the objective of firearm classification. We describe our experimental setup in Section 5 and experimental results in Section 6. Finally, Section 7 concludes our paper.

II. Related Work

The most substantial work in Computer Vision was developed in 1959, describing the core properties of visual cortical neurons [4]. In 1982, the introduced the hierarchical features of vision was a milestone in the research field [5]. A framework was proposed for a vision where low-level detection algorithms, including edge, curve, and corner detection, contributed to a high-level understanding of visual data. After some time, researchers developed a self-organizing artificial neural network consisting of simple and complex neuron-like cells, capable of recognizing features and unaffected by shift in object position [6]. It introduced various convolutional layers constituting a network where receptive fields have weight vectors, called filters. Technologies like Optical Character recognition and commercial zip codes readers became famous too [7].

Around 1999, researchers made quite a progress in the domain of feature-based object recognition [8]. They described an image recognition system utilizing invariant local features to the rotation, location, and illumination. Soon after that, they introduced the very first face detection framework [9], specializing in localizing faces. With the computer vision advancements, the research community felt an urgent need to introduce an image dataset and standard evaluation metrics to serve as a benchmark for a models' performance. As a result, Deng et al. proposed the ImageNet dataset [10], containing over a million images, became a benchmark in object category classification and detection across 21 various object categories. Recently, Microsoft Research submitted a paper [3] that achieved top results for object detection with localization tasks with their Residual Network or ResNet. An ensemble model of these ResNets achieved a 3.57% error rate on the ImageNet test set.

Manually setting the appropriate learning rate hyperparameter requires great effort. Leslie N. Smith [11] introduced cyclical learning rates for estimating global learning rates to train deep neural networks. Thus, eliminating the necessity to carry various attempts to find the best values.

The idea of automated image perception with video input data is well known and well explored in many domains, especially for public security purposes. Jang and Turk used the concept of the SURF feature detection algorithm to implement a system for vehicle recognition [12].

In 2007, Darker et al. proposed the primary concept of automated detection for gun committed crimes. This concept served as a support to the United Kingdom-based MEDUSA project [13]. Their also suggested a work to indicate the possibility of an individual carrying a concealed firearm [14]. The same team conducted experiments to employ CCTV as an automatic sensor in for gun and firearm detection [15]. Furthermore, Arslan et al. introduced the concept of visual hierarchy and conceptual firearms ontology as an approach for threat assessment [16].

Moreover, it should be pointed out that there are other safe and reliable approaches to detect deadly weapons in dangerous scenarios. In Yong et al. introduced the concept of using microwave swept-frequency radar for detecting metal objects like guns and knives. Mery et al. also showed that using X-ray imaging for object detection in real-time is a promising approach [17], [18]. The practical applications of such methods are limited because of their high cost and hazardous health issues. Besides, Video-based gun detection serves as a precaution in relation to the detection of acoustic fire and can be combined with this [19], [20].

III. Dataset

The goal of the paper is to classify the weapons on the basis of their destructiveness. There is no open dataset available that can be used to train and evaluate the network for this classification task. Therefore, we proposed a dataset that should serve the purpose of firearms classification. Our proposed dataset consists of 5,071 224x224 color images split into three different categories. The three different categories include *big guns*, *small guns*, and *other weapons*, including knives. The dataset contains two subsets named, train and valid containing 4,590 training and 481 validation images, respectively. There are 1530 training images of each class.

A. Data Collection

The first stage of constructing our weapon classification dataset involves the collection of candidate images for each class. The mean accuracy of image search results for each category from the Internet is around 10% [21]. After cleaning the images for each class, we obtained around 1680 images on average. We collected the class images from the Internet by querying the Google Image search engine. Since the dataset is small, we manually entered the search keyword in the query. For the big guns class, we searched for guns that are described as big including rifles, machine guns, rocket launchers, etc. Similarly, for the small gun category, we searched for pistols and revolvers and for other weapon categories, we entered 'knives' and their related keyword in the query. Some of the images for the dataset were obtained from a gun dataset on github[4].

B. Data Preprocessing

To collect a highly accurate dataset, manual verification of individual candidate images is crucial. We manually cleaned and organized the collected images into the three classes.

[4]https://github.com/SasankYadati/Guns-Dataset

Authorized licensed use limited to: DELHI TECHNICAL UNIV. Downloaded on February 15,2021 at 09:53:58 UTC from IEEE Xplore. Restrictions apply.

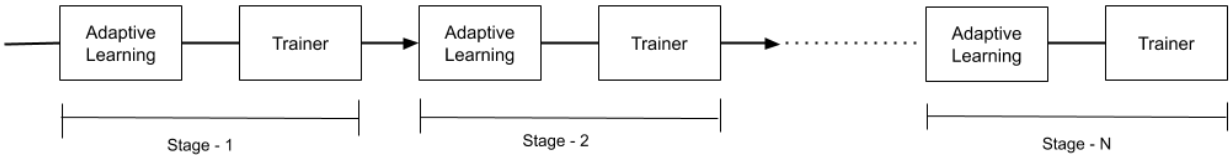

Fig. 1: N-Stage Learning Methodology for any Neural Network training

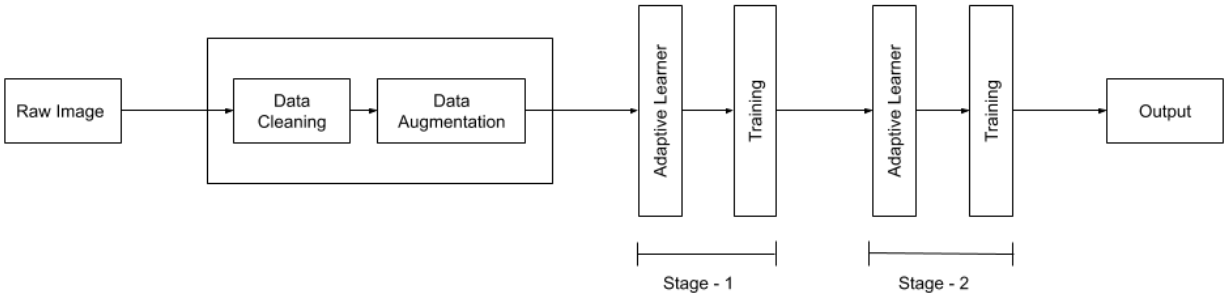

Fig. 2: Schematic representation of the experimental setup established for Gun detection and classification

After obtaining the images, we investigated all the samples in the dataset and deleted the duplicate images. We then manually distributed the image samples into the three defined classes: big guns, small guns, and other weapons. We then converted all the candidate images into a fixed size of 224 x 224 with the image at the center and utilizing the padding around them. Finally, we split the dataset into a training set for model training and validation set for evaluation. The clean dataset is available for the research community at: https://github.com/RavneetDTU/Gun-Detection-Dataset.git

IV. Proposed Methodology

A. N-Stage Learning

Along with architecture, an efficient training procedure is also essential to achieve state of the art results. Hyperparameter such as learning rate plays a crucial role in the training of a neural network. A good starting value of learning rate is necessary, for low too values training process can be inefficient and time-consuming, for the too-high value of learning rate loss function can show divergent behavior [22]. Figure 1 represents an N-Stages training paradigm, where each stage consists of two blocks, an Adaptive Learner block followed by a Trainer block, which trains the implemented Neural Network model for several epochs.The most common approach to select the value of the learning rate is using hit and trial method, which can be tricky and not efficient. Our methodology is inspired by a technique called ADADELTA [11]. This N-Stage Learning method can be used to train any Neural Network model effectively as compare to the standard training procedure.

Adaptive Learner block takes a batch of 16 images; it trained them for 1 epoch and computed the Training loss on learning rate values ranging from 1e-6 to 1 on a logarithmic scale. The learning rate value for which training loss value is minimum is selected as the best value. Figure 3 represents the plot generated by Adaptive Learner for ResNet-34 discussed in the next subsection. By using this method, the layer can be released in between training, and gradually changing the learning rate can help in training efficient and robust prediction models.

B. Deep Learning Algorithm

As already discussed in section 3, the dataset consists of 5,071 images and is not sufficient to train a 34 or 50 layered Residual Network. But using technique transfer learning can be very helpful to achieve state of the art classification result on a small dataset. In Transfer Learning, an already trained deep learning model is used as a parent model; its knowledge is used to improve the performance on a related task. The newly derived model for the related task is reffed as the child model. For the Gun classification task, we two different parent models, 34 layered Residual Network and 50 layer Residual Network. Both these model were already trained on ImageNet dataset [21] which consist of 3 million images with 10000 classes to classify. Both models were trained with a dual-stage training mechanism.

V. Experiments

A. Experimental Setup

Figure 2 represents the overview of the complete pipeline for the Gun detection pipeline. Pretrained ResNet-34 and ResNet - 50 were further trained with Adam Optimizer. Figure 3 depicts the plot of learning rate versus Loss function calculated on the logarithmic scale, and the best learning rate value = 0.1 is selected by Adaptive Learner for the first stage. Further, both models were trained for 25 epochs for the Trainer block. For the second stage, the initial layer of the

Authorized licensed use limited to: DELHI TECHNICAL UNIV. Downloaded on February 15,2021 at 09:53:58 UTC from IEEE Xplore. Restrictions apply.

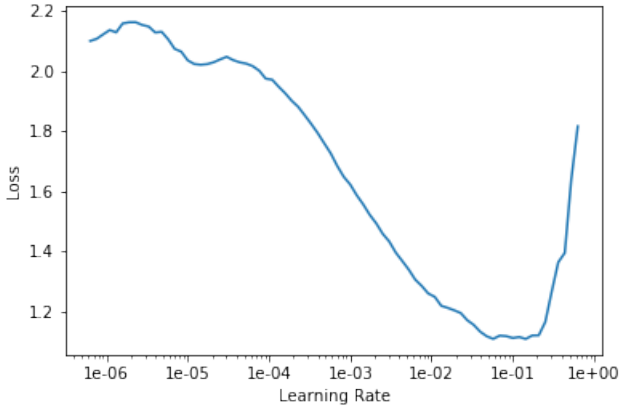

Fig. 3: Loss v/s Learning rate plot for Stage 1

network unfreezes to change the value of the learning rate by Adaptive Learner Block.

For the Second stage, learning rate value = 0.001 selected with the plot represented by Figure 4, which was generated by Adaptive Learner in 2nd stage.

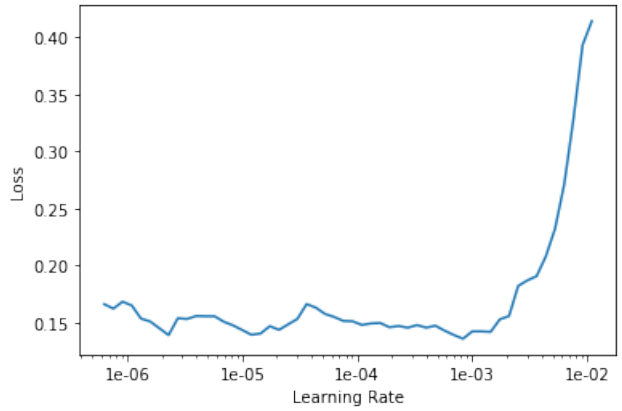

Fig. 4: Loss v/s Learning rate plot for Stage 2

At last, both the model were again trained for 25 epochs and results by both models discussed in the next section. For the data cleaning and Data augmentation, a python script was used with the OpenCV Library for image manipulation, and Pytorch Framework was used for implementing the Deep Learning models. The experimental setup was performed on Linux workstation with Nvidia GPUs for efficient training.

VI. Result & Discussion

Table 1 shows the classification accuracies of our network with both ResNet-34 and ResNet-50 as base architectures, on the dataset we created for the firearm classification task. The network with ResNet-34 as the base architecture showed 92.72% accuracy on the validation set when using the pre-training and 95.010% accuracy when pre-training is not used. Figure 5 shows the confusion martix for the ResNet-34 predictions in the case when the network learned features from scratch. The confusion matrix of ResNet-34 clearly demonstrate the significant results achieved by our network on the validation dataset. On the other hand, the ResNet-50 network achieved 95.011% accuracy when using pre-training and 91.268% without pre-training. Furthermore, figure 6 represents the confusion matrix for the ResNet-50 predictions on the validation set. The matrix shows the result from the time when the network was using pre-trained weights.

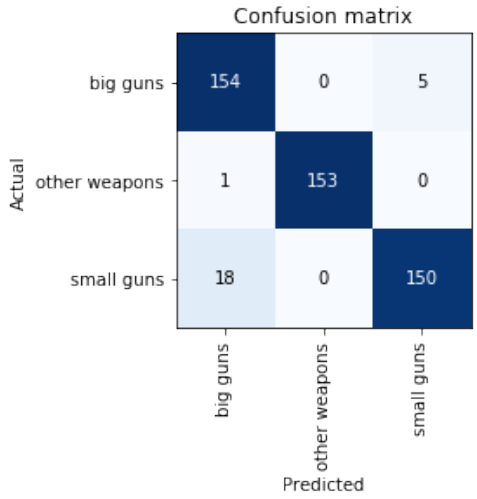

Fig. 5: Confusion Matrix for ResNet-34 Architecture.

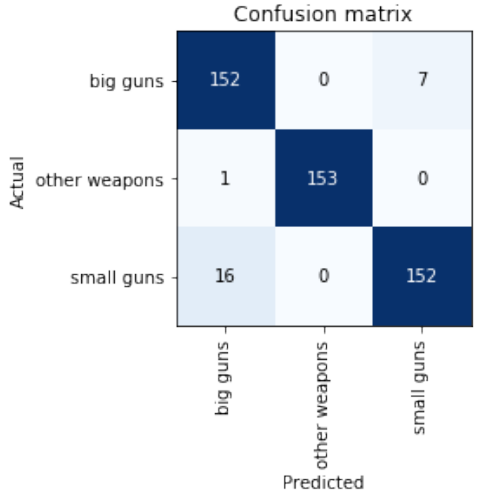

Fig. 6: Confusion Matrix for ResNet-50 Architecture.

TABLE I: Accuracy Score for their respective models

Architecture	With Pre-Training	Without Pre-Training
1. ResNet-34	92.723	95.01
2. ResNet-50	**95.011**	91.268

The results demonstrate that our network in which we used ResNet-50 as the base architecture for transfer learning

Authorized licensed use limited to: DELHI TECHNICAL UNIV. Downloaded on February 15,2021 at 09:53:58 UTC from IEEE Xplore. Restrictions apply.

and with using pretraining achieves the best accuracy among the others. Initially, when using the pre-trained network, the accuracy was 95.011%. However, after unfreezing the initial layers, the accuracy of the model was reduced by a significant percentage point to 91.26%. One reason behind this reduction is the unavailability of sufficient amount of data to train the unfrozen ResNet-50 network. Additionally, since there are more number of network parameters to train in the later method, it suffers from a reduction in overall accuracy .

(a) Output: Small Guns (b) Output: Small Guns

(c) Output: Big Guns (d) Output: Big Guns

Fig. 7: Identified critical features for classification decision made by the network on test images.

Additionally, we have applied an explainability method on our deep neural network to identify the critical features utilized in the decision made by our network for image classification. We use GSInquire [23], a method explained by Lin et al. as the explainability model. They demonstrated in [23] that GSInquire is the best among several explainability methods. This method is based on a generative model described by Wong et. al in [24]. Figure 7 shows the results of applying the GSInquire method on some example test images. The area around the gun has been marked as a critical factor for firearm classification in the test images.

VII. Conclusion & Future Work

In this paper, we have explored the task of firearm classification using the ResNet architectures, particularly, ResNet-34 and ResNet-50, both with and without using pre-training. The method classifies the given weapon image into big, small, and other weapons, based on their fatality. We use the concept of transfer learning for this task. Using ResNet as the base architecture, we try to train our model on a new dataset, created by our team, for the classification of firearms. We used the cyclic learning method to find the appropriate learning rate for model training. The experimented results showed that our method achieves 92.723% accuracy with pre-training and 95.01% without pre-training with the ResNet-34 architecture. Considering the ResNet-50 architecture, our model achieves 95.011% accuracy when using pre-trained model with freezed weights and 91.26% when the network was trained from scratch.

For future work, we can modify the image dataset for firearm detection by annotating the position of bounding boxes for the weapons in the training dataset. We can implement the model to correctly localize the guns or any other weapons in the image using state-of-the-art object detection techniques like SSD, YOLO, etc.

References

[1] Cohen, A.P., Azrael, D. and Miller, M., 2014. Rate of mass shootings has tripled since 2011, Harvard research shows. Mother Jones, 15, p.14.

[2] Weiss, K., Khoshgoftaar, T.M. & Wang, D. A survey of transfer learning. J Big Data 3, 9 (2016). https://doi.org/10.1186/s40537-016-0043-6.

[3] He, K., Zhang, X., Ren, S. and Sun, J., 2016. Deep residual learning for image recognition. In Proceedings of the IEEE conference on computer vision and pattern recognition (pp. 770-778).

[4] Hubel, D.H. and Wiesel, T.N., 1959. Receptive fields of single neurones in the cat's striate cortex. The Journal of physiology, 148(3), pp.574-591.

[5] Marr, D., 1982. Vision: A computational investigation into the human representation and processing of visual information, henry holt and co. Inc., New York, NY, 2(4.2).

[6] Fukushima, K., 1988. Neocognitron: A hierarchical neural network capable of visual pattern recognition. Neural networks, 1(2), pp.119-130.

[7] LeCun, Y., Boser, B.E., Denker, J.S., Henderson, D., Howard, R.E., Hubbard, W.E. and Jackel, L.D., 1990. Handwritten digit recognition with a back-propagation network. In Advances in neural information processing systems (pp. 396-404).

[8] Lowe, D.G., 1999, September. Object recognition from local scale-invariant features. In Proceedings of the seventh IEEE international conference on computer vision (Vol. 2, pp. 1150-1157). Ieee.

[9] Viola, P. and Jones, M.J., 2004. Robust real-time face detection. International journal of computer vision, 57(2), pp.137-154.

[10] Krizhevsky, A., Sutskever, I. and Hinton, G.E., 2012. Imagenet classification with deep convolutional neural networks. In Advances in neural information processing systems (pp. 1097-1105).

[11] Smith, L.N., 2017, March. Cyclical learning rates for training neural networks. In 2017 IEEE Winter Conference on Applications of Computer Vision (WACV) (pp. 464-472). IEEE.

[12] Jang, D.; Turk, M. Car-Rec: A real time car recognition system. In Proceedings of the IEEE Workshop on Applications of Computer Vision (WACV), Kona, HI, USA, 5–7 January 2011; pp. 599–605.

[13] Darker, I., Gale, A., Ward, L. and Blechko, A., 2007, October. Can CCTV reliably detect gun crime?. In 2007 41st Annual IEEE International Carnahan Conference on Security Technology (pp. 264-271). IEEE.

[14] Blechko, A., Darker, I. and Gale, A., 2008, October. Skills in detecting gun carrying from CCTV. In 2008 42nd Annual IEEE International Carnahan Conference on Security Technology (pp. 265-271). IEEE.

[15] Darker, I.T., Gale, A.G. and Blechko, A., 2008, October. CCTV as an automated sensor for firearms detection: Human-derived performance as a precursor to automatic recognition. In Unmanned/Unattended Sensors and Sensor Networks V (Vol. 7112, p. 71120V). International Society for Optics and Photonics.

[16] Attardo, S.; Blount, G.P.; Sirakov, N.M. Threat assessment using visual hierarchy and conceptual firearms ontology. Opt. Eng. 2015, 54, 105–109.

[17] Li, Y., Tian, G.Y., Bowring, N. and Rezgui, N., 2008, October. A microwave measurement system for metallic object detection using swept-frequency radar. In Millimetre Wave and Terahertz Sensors and Technology (Vol. 7117, p. 71170K). International Society for Optics and Photonics.

[18] Mery, D., Riffo, V., Zuccar, I. and Pieringer, C., 2013. Automated X-ray object recognition using an efficient search algorithm in multiple views. In Proceedings of the IEEE conference on computer vision and pattern recognition workshops (pp. 368-374).

Authorized licensed use limited to: DELHI TECHNICAL UNIV. Downloaded on February 15,2021 at 09:53:58 UTC from IEEE Xplore. Restrictions apply.

[19] Maher, R.C., 2006, September. Modeling and signal processing of acoustic gunshot recordings. In 2006 IEEE 12th Digital Signal Processing Workshop & 4th IEEE Signal Processing Education Workshop (pp. 257-261). IEEE.

[20] Chacon-Rodriguez, A., Julian, P., Castro, L., Alvarado, P. and Hernández, N., 2010. Evaluation of gunshot detection algorithms. IEEE Transactions on Circuits and Systems I: Regular Papers, 58(2), pp.363-373.

[21] J. Deng, W. Dong, R. Socher, L.-J. Li, K. Li, and L. Fei-Fei. ImageNet: A Large-Scale Hierarchical Image Database. In CVPR09, 2009.

[22] Behera, L., Kumar, S. and Patnaik, A., 2006. On adaptive learning rate that guarantees convergence in feedforward networks. IEEE transactions on neural networks, 17(5), pp.1116-1125.

[23] Lin, Z. Q. et al. Do explanations reflect decisions? a machine-centric strategy to quantify the performance of explainability algorithms. arXiv preprint arXiv:1910.07387 (2019).

[24] Alexander Wong, Mohammad Javad Shafiee, Brendan Chwyl, and Francis Li. Ferminets: Learning generative machines to generate efficient neural networks via generative synthesis. arXiv preprint arXiv:1809.05989, 2018.

Authorized licensed use limited to: DELHI TECHNICAL UNIV. Downloaded on February 15,2021 at 09:53:58 UTC from IEEE Xplore. Restrictions apply.

e-ISSN : 2620 3502
p-ISSN : 2615 3785

Virtual screening of natural compounds as combinatorial agents from indian medicinal plants against estrogen positive breast cancer

Shaleen Jain[1], Dr. Asmita Das[2]
[1,2]Corresponding Author,Department of Biotechnology, Delhi Technological University, Main Bawana Road, Delhi-110042
Email: asmitadas1710@dce.ac.in
asmita1710@gmail.com

Abstract

Facing worldwide challenges associated with multifactorial etiology of breast cancer, designing of combinatorial therapies using natural compounds is currently the emergent way of treating several cancers including breast cancer in a synergistic way, which may mitigate several problems associated with multiple receptor targeting. In this research, Estrogen receptor positive breast cancer was taken as prototype and several key receptors associated with this particular disease were targeted by virtual screening of natural compounds found in Indian originated medicinal plants using Computer aided Drug Designing (CADD) strategies. We found the combination of Carpusin, Paulownin Cornigerine, Nororientaline, Oryzalexin B, Romucosine H and Colchicine as effective against six potential receptors i.e. FGFR2, ESR1, PIK3CA, PIK3CB, PIK3CD and AR in Estrogen receptor positive breast cancer with their binding energies in the range of $\Delta G \leq -8.0$ Kcal/mol as well as significant number of common amino acid binding residues as compared with binding sites of receptors. Thus this research holds significant implications for the designing of combinatorial therapeutic agents against breast cancer which can be further tested in-vitro and in-vivo to prove their synergistic efficiency.

Key words: CADD, FGFR2, ESR1, Combinatorial therapies, PIK3, AR

1. INTRODUCTION

The occurrence of cancer is related to several factors to which human expose, the complexity of which is an arduous challenge in the field of epidemiology due to which many epidemiologists around the world have been understanding and determining cancer's multifactorial etiology. [1]

The complex interplay of several genetic and non-genetic factors have been clearly assessed in several researches that predispose to development of cancer. In this research, breast cancer was taken as a prototype due to its prevalence at a large scale worldwide and in major areas of India. Breast cancer has been described as multifactorial in occurrence in several epidemiological studies in which 90% cases occur due to the involvement of non-genetic factors, like environmental factors, major biological, chemical carcinogenic agents. [2]–[4]

To date, many researches have shown that a dysregulation of several molecular and signaling pathways occur due to the multifactorial effects pf breast cancer. Nevertheless, several potential therapies are needed for targeting multiple receptors and pathways to serve as an effective treatment against its proliferation and metastasis. [5]

Breast Cancer being an important concern of health and cause of deaths due to cancer among women worldwide has shown increased trends of prevalence and incidence, resulting in a high mortality rate globally. There has been a sharp increase in breast cancer cases in recent past. [6] [7]. According to 'Global Burden of Disease Cancer Collaboration', 2017, the data showed an increment by 33% overall cancer cases from 2005-2015 worldwide. [8] [9]. The total cancer cases are likely to go up to 1,148,757 cases in 2020. [6]

The age standardized prevalence data of cancer cases shows 97 per one lakh individuals according to recent trends. According to a report by WHO, the present data of 6% total deaths due to cancer in India might be harmful in near future which is estimated to show an increment up to 9 million deaths by 2030. [9]–[11]

Improvements in cancer therapies have shown a remarkable success in recent past. Modern therapies have been developed which varies from DNA therapies based on DNA-excision repairing and modifying cell-apoptotic pathways etc. to other potential treatments like hormone-based therapies like tamoxifen (Estrogen synthesis blocking agent) has been developed for breast cancer. Monoclonal antibody based treatment, Immune-based therapies (ICIs, CART therapies) etc. are other potential therapies. [12] [13]

Drug delivery systems like nanoparticles have also been developed in a past decade for targeted delivery in several cancers including breast cancer to avoid by-stander killing of tumor cells. [14] [15]. They include Doxorubicin, ThermoDox (Temperature based release of doxorubicin), SPIONs (Supermagnetic iron oxide nanoparticles), Nanotherm etc. [16] [17]

In the recent Covid-19 pandemic due to novel coronavirus (SARS COV-2), started out around December 2019, there has been a declination in cancer research worldwide and a high chances of increasing comorbidities in patients during this era. Cancer patients have been found vulnerable to Covid-19 infection according to some Chinese studies. Moreover consequences like delayed treatment, distraction in healthcare for cancer patients

e-ISSN : 2620 3502
p-ISSN : 2615 3785

during pandemic conditions pose fatal consequences for cancer patients. [18]. Remarkable efforts have been made uptil now for overcoming the therapeutic and diagnostic challenges in this vulnerable population. According to recent safe guidelines of Canadian Association of Breast Imaging, delaying of breast cancer imaging and screening is needed to be avoid along with prevention of infection to the patients in Covid-19 pandemic. [18] [19]

Combinatorial therapies for cancer have been designed in many researches for overcoming challenges of cross-talk inhibition, signaling feedback etc. The rationale behind using multiple drugs is to suppress multiple receptors and pathways in a particular tumor to eradicate it in a synergistic way as compared with monotherapies. [20] [21]. Uptil now, different combinations of drugs including natural compound-based drugs, synthetic drugs, monoclonal antibodies etc. have been designed. [9] [22]. Examples include, USFDA approved Ipilimumab and nivolumab for unresectable melanoma. [23]. Combinatorial therapies have also been designed in Breast cancer. Eg. Combinations of Gemcitabine and Paclitaxel with Cyclophosphamide and Epirubicin in breast cancer. [24] , combination of Fulvestrant and Anastrozole in hormone receptor positive breast cancer. [25].

Natural compounds has attained enormous benefits in therapeutics like stability, enhancement in efficacy, reduced toxicity, bioavailability, etc. In cancer treatment, many natural compound-based medicines have been designed as monotherapeutics and in combinations as well as in combination with synthetic compounds. [26]–[28]. Examples- Cyclophosphamide and Paclitaxel (Synthetic) in combination with curcumin (Natural), has been used in MDA-MB-231, MCF-12F and MCF-7 cancer cell lines. [29]–[33]. Combinations of natural compounds in breast cancer have been documented in several researches. [34] [31].

Nanoparticles in conjugation with natural compounds and their combinations have been tailored in different cancers including breast cancer, to act as an efficient targeted drug delivery tool to enhance the specificity and preventing bystander killing. [14]–[17].

Breast Cancer as a prototype

Breast Cancer has been found as the most frequently diagnosed cancer in India. The incidence rate has been estimated to 25.8/100000 individuals. In this project, estrogen receptor positive breast cancer was taken as a prototype. Estrogen receptor positive breast cancer accounts for approximately 80% breast cancer cases. Uptil now, various therapies have been designed for ER positive BC. [35]. They include, endocrine therapies under which GnRHa (Gonadotropin releasing hormone agonists), SERMSs (Selective estrogen receptor modulators, eg. Tamoxifen), SERDs (Selective estrogen receptor down-regulators, eg. Fulvestrant) in combination with AIs (Aromatase inhibitors) are given as combinatorial drug therapies. [36] [37].

Although a vast majority of receptors are associated with the expression of ER(+)BC, but in this research, some potential receptors of ER(+)BC in human were screened using a database which have been found to play an important role in its progression. Here, FGFR2 gene (encode protein from fibroblast growth receptor family), ESR1gene (encode estrogen receptor and a transcription factor), AR gene (encode androgen receptor), PIK3CA, PIK3CB and PIK3CD genes (encoding three catalytic isoforms i.e. p110α, p110β and p110δ of phosphatidylinositol 4,5-bisphosphate 3-kinase respectively) were taken into consideration.

FGFRs play an important role in the progression of several cancers whose structures composed of different domains like 3 immunoglobulin-like domain, cytoplasmic tyrosine kinase domain, extra-cellular domain. [38]. FGFR2 has been reported as a crucial biomarker in breast cancer. In a research, its differently expressed genes (namely CXCL8, BMP7, CD44, MMP9) have been found between FGFR2 silenced breast cancer cell lines. FGFR2 also plays an important role in the progression of ER(+)BC. N550K and M5381 mutations of FGFR2 has been observed to offer resistance to CDK4/6, SERDs inhibitors in ER(+)BC patients. [38] [39]

ESR1 gene that encodes for estrogen receptor (ER) is an important biomarker in ER(+)BC which localizes to nucleus and forms homodimer or heterodimer with ESR2. [40]. In a research, patients with circulating ESR1 mutations have been found resistant to endocrine therapy which is given in ER BC treatment. In another research, these ESR1 mutations have been validated using ct-DNA (circulating tumor DNA) detection method in ER(+)BC. [41] [42]

Androgen receptor (encoded by AR gene) which have 3 functional domains and function as a transcription factor activated by steroid hormone act as a potential prognostic biomarker in breast cancers including ER(+)BC. [43]. Overexpression of AR as a key molecule has been seen in aromatase inhibitors (eg. exemestane) resistant ER(+)BC. Therefore, AR antagonism may serve as a promising strategy in ER(+)BC which may in turn target several AR associated pathways like ERK1/2 signaling pathway, PI3K pathways etc. [44], [45]

The pathways of Phosphoinositide 3-kinase PIK (composed of a regulatory and catalytic subunits) shows an emerging prevalence and are responsible for frequent alterations in breast cancers including ER(+)BC. [46]. The three genes i.e. PIK3CA, PIK3CB and PIK3CD encode three catalytic isoforms i.e. p110α, p110β and p110δ respectively and treatments using RNAi has been designed to target these isoforms. [47]–[49]. PIK3CA mutations have been reported crucial in fulvestrant resistant ER(+)BC using circulating tumor DNA (ct DNA), therefore PIK3CA has been found as an important regulator in progression and migration in ER(+)BC. [50]–[53]

In-silico approach in drug development

e-ISSN : 2620 3502
p-ISSN : 2615 3785

Currently, In-silico approach has emerged as a promising strategy which ensures fruitful insights in the various fields like drug designing, target profiling, drug repurposing, polypharmacology, etc. [54]. Conventional pipeline remain centered on time-taking experiments and high delivery cost. Computer aided drug discovery (CADD) on other hand has exhibited as an effective technology for significant drug designing at a faster and cheaper rate in several diseases including cancers. [55]–[57]. Virtual screening, High throughput screening, Molecular docking etc. are emergent techniques for screening of drugs against particular protein receptors involved in various diseases as well as their structural and binding analysis. [58], [59]. Many useful tools have been developed for virtual screening and CADD. Autodock 4 [60], Autodock Vina [60], PyRx [61], PyMol [62], etc. are some of the open source online softwares available for studying the affinities between ligands and proteins and their binding poses, crystallographic analysis, molecular dynamics evaluation etc.

There are many databases available for ligand library screening like ZINC 15, PubChem, etc. IMPPAT (Indian Medicinal Plants, Phytochemistry and Therapeutics) is an online curated database (developed by The Institute of Mathematical Sciences, IMSc, India) which has many useful in-built webservers like admetSAR, FAF-Drugs4, FAF-QED, Open Babel, RDKit, etc. There is a huge library of 1742 medicinal plants of Indian origin, 9596 phytochemicals present in this database which have been used in traditional Indian medicines since time immemorial. [63]

2. MATERIALS AND METHODS

1. Receptors selection

510 genes associated with ER(+)BC were identified using DisGeNET, a curated database for genes associated with human diseases and variants. [64]. Then those 510 genes were filtered on the basis of Gene-disease association score ($Score_{gda} \geq 0.1$), probability of being loss of function intolerant ($pLI \geq 0.99$), total no. of PMIDs supporting association ($N.\ PMIDs \geq 7$) and identified top hits were further evaluated.

2. Protein-Protein Interaction study

Types of protein-protein interactions and their interaction scores between the selected receptors were calculated using STRING (11.0), a database for identification of proteins and their functional interactions. [65]. The strength of associations among them was evaluated from the number of nodes, PPI enrichment value, number of edges, average node degree, average local clustering coefficient and expected number of edges.

3. Binding site analysis

Binding sites of receptors were identified using Discovery Studio Visualizer (DSV), a software for analyzing sequences, modeling molecular structures and other data. [66], [67]**.** It locates all surrounding amino acid residues of a bounded ligand to the protein within a distance under defined threshold and forms a 2-D image which depicts all the amino acid residues and type of bonds through which they were attached to the ligand. In this research, high resolution crystal structures of proteins with their previously experimentally identified inhibitors/drugs were used and their drug sites were evaluated using DSV to which our concerned ligand was supposed to bind.

4. Protein Dataset

Minimum resolution X-ray crystallographic structures of **FGFR2** (PDB Id: 3RI1- catalytic domain of fibroblast growth factor receptor 2 kinase in complex with ARQ069, Resolution- 2.10 Å**,** R-Value Free: 0.247)**, ESR1** (PDB Id: 5ACC- Estrogen receptor 1 in complex with AZD9496, Resolution- 2.10 Å, R-Value Free: 0.247), **AR** (PDB Id: 1E3G- Androgen receptor in complex with metribolone, Resolution- 2.10 Å, R-Value Free: 0.247), **PIK3CA** (PDB Id: 3ZIM- Lipid kinase of Phosphatidylinositol 4,5-bisphosphate 3-kinase catalytic subunit alpha isoform in complex with covalent inhibitor $C_{30}\ H_{35}\ N_7\ O_3\ S$, Resolution- 2.10 Å, R-Value Free: 0.247), **PIK3CB** (PDB Id: 4BFR- Phosphatidylinositol 4,5-bisphosphate 3-kinase catalytic subunit beta isoform in complex with $C_{19}\ H_{22}\ N_4\ O_3$, Resolution- 2.10 Å, R-Value Free: 0.247) and **PIK3CD** (PDB Id: 4XE0- Phosphatidylinositol 4,5-bisphosphate 3-kinase catalytic subunit delta isoform in complex with Idelalisib, Resolution- 2.10 Å, R-Value Free: 0.247) were retrieved from PDB.

5. Protein preparation

Before docking of concerned ligands with selected proteins, proteins were prepared by deleting the hetatoms (co-crystallized water molecules, nonstandard residues, nonpolar hydrogens, small molecules and lone pairs) using DSV. Later gasteiger charges and polar hydrogens were added and merged using PyRx. Here, a file in pdbqt format is generated which is required for docking via Autodock.

6. Ligand library preparation

IMPPAT database was used for literature analysis of natural compounds using in-built webservers admetSAR, FAF-Drugs4, FAF-QED, RDKit. Initially all 9596 phytochemicals were primarily screened and filtered on the basis of zero Lipinski RO5 violations, zero Oral PhysChem Score (Traffic lights) which indicates good oral bioavailability, good GlaxoSmithKline's (GSK's) 4/400 score which indicates log P (octanol-water partition coefficient) ≤ 4 and M_w (Molecular weight) ≤ 400 Dalton, Pfizer's 3/75 rule's good values which indicates small molecules with values of TPSA (Topological polar surface area) > 75 and logP <3 $Å^2$ indicating more drug likeliness and less toxicity, Egan rule's good values ($-1.0 \leq$logP ≤ 5.8 and TPSA ≤ 130 $Å^2$) which indicates good oral bioavailability, veber rule's good value (TPSA<140 and number of

e-ISSN : 2620 3502
p-ISSN : 2615 3785

rotatable bonds ≤ 10) which satisfies good oral bioavailability, good QEDw (Quantitative estimate of drug-likeness) score (≥ 0.8) which evaluates the weighted geometric mean of log P, number of hydrogen donors (≤5) and acceptors (≤10), molecular weight, No. Of rotatable bonds, TPSA, number of structural alerts and number of aromatic rings. QEDw ≥ 0.8 signifies high druggability of compounds. Later, the primarily screened compounds were further secondarily screened on the basis of good PK properties like positive for BBB (Blood Brain Barrier) permeability, positive for HIA (Human intestinal absorption), good solubility. After screening, ligands were prepared finally for docking after energy minimization for 200 conjugate gradient steps with an UFF force field using PyRx.

7. Molecular docking

After secondary screening and preparation of ligands and receptors, they were subjected to structure-based drug designing through molecular docking using PyRx (with in-built Autodock tool). After selecting the binding sites manually, a grid box of dimension 60×60×60 Å was generated with grid spacing 0.375 Å which confines the active sites of protein to which the concerned ligand was supposed to bind within a specific shortened area. Then, after completion of docking within the specific sites, the binding energies i.e. ΔG (in Kcal/mol) were noted and the compounds were selected on the basis of top hits/ autodock vina good scores. It is considered that lower the ΔG, more effective the binding is (in the range of ΔG ≤ -8.0 Kcal/mol).

8. Screening of drug likeliness and ADMET properties evaluation

The drug likeliness was analyzed using admetSAR open-source tool. The docked ligands having good ΔG were again filtered through extensive ADMET properties such as good PK and PD properties like positive BBB permeability, positive HIA, positive calcium carbonate permeability, Non-inhibition of P-glycoprotein protein substrate and inhibitors, Non-inhibition of CYP 450 (Cytochrome P450) substrate and inhibitors (including 2C9, 2D6, 3A4, 1A2, 2C9, 2D6, 2C19, 3A4), low CYP 450 inhibitory promiscuity (CYP IP), Non-ames test toxicity. P-glycoproteins and CYP enzymes substrate play a fundamental role in metabolism of drugs, so their inhibition affects the drug likeliness property of drugs. After assessing binding scores, important ADMET properties, obtained drugs were subjected to binding amino acid residues evaluation using PyRx and PyMol and proposed as combinatorial therapeutic agents.

9. Binding amino acid residues evaluation

After molecular docking and extensive ADMET analysis, the binding amino acid residues of finally selected docked ligands and the type of bonds through which they are attached were observed by generating a 2-D image using DSV. Later PyMol was used for depicting the bounded ligands in the binding pocket of receptors.

Results and discussion

In this research, natural compounds from Indian medicinal plants were screened against potent receptors of ER(+)BC. Further, they were assessed on the basis of good ADMET properties. The 7 top natural compounds having excellent ADMET properties were found to have multi-targeting effects with efficient binding energies and similar binding residues against the binding pockets of selected receptors in ER(+)BC. (Work flow in figure: 1).

1. Receptors selection

The associated genes for ER(+)BC were screened using DisGenet in which we found total 510 associated genes, out of which 6 top genes (FGFR2, ESR1, PIK3CA, PIK3CB, PIK3CD, AR) were filtered on the basis of parameters like pLI, **Score$_{gda}$**, N.PMIDs as mentioned previously. These genes are basically responsible for translation of mentioned receptors/proteins. Moreover, it was found that these six genes were of 'kinase' and 'nuclear receptor' protein class and have a large number of other associated diseases. Table showing 6 potent receptors of ER(+)BC assessed using DisGenet database. All six genes were found to have DSIg (Disease specificity index) ≥ 0.29, out of which FGFR2 showed highest DSIg = 0.38. Their DPIg (Disease pleiotropy index) was found ≥ 0.8, pLi 0.99, **Score$_{gda}$** ≥ 0.1, **EI$_{gda}$** (Evidence index) ≥ 0.9, although out of 6, only FGFR2 and ESR1 were found to have 2 and 1 SNPs (Single nucleotide polymorphisms) respectively. (Table 1). So, on the basis of above parameters, these 6 receptors were found potent to regulate the biological behavior of ER(+)BC, therefore proposed for further evaluation.

2. Protein- protein interactions

Types and strength of protein-protein associations between the selected 6 receptors were assessed using STRING (11.0) database (Figure 2) which defines PPI (protein-protein interaction) with confidence ranges for obtained data scores (low confidence scores <0.4; medium confidence: 0.4-0.7; high confidence: >0.7). All 6 were found to have firm interactions among themselves with significant interaction scores as mentioned in Table 2. Moreover, 6 nodes, 10 edges, average node degree = 3.33, average local clustering coefficient = 0.806, 2 expected number of edges and PPI enrichment p-value = 3.48e-05 were found. These values are strong enough to elucidate the significant interactions among receptors. Therefore, targeting these receptors was considered very useful in targeting associated pathways simultaneously for an effective multi-targeted effect of drugs. These receptors were further evaluated for molecular docking simulations.

3. Protein retrieval and binding sites evaluation

Binding sites or inhibitory sites of proteins after retrieving their crystal structures from PDB in complex

e-ISSN : 2620 3502
p-ISSN : 2615 3785

with different experimentally identified inhibitors were assessed through DSV. The surrounding amino acid residues (which are considered as binding sites) of bounded ligand were noted from DSV which generates a 2-D image of bounded inhibitor/ligand and its surrounding amino acid residues within a distance of threshold value. As shown in Figure: 3, FGFR2, ESR1, PIK3CA, PIK3CB, PIK3CD, AR were found to have 10, 15, 11, 10, 11, 10 residues respectively.

4. **Ligands screening**

In this research, natural compounds from medicinal plants of Indian origin were assessed through IMPPAT database of 9596 phytochemicals. Initially they were filtered using FAF-Drugs4 and FAF-QED open-source cheminformatics platforms on the basis of LRo5 violations, Oral PhysChem score (traffic lights), GSK's 4/400, Pfizer's 3/75, Veber's rule, Egan's rule, QEDw as mentioned previously. At this stage, we found 99 natural compounds satisfying above mentioned properties. Then out of them, 42 Natural compounds were filtered on the basis of PK and PD properties (BBB permeability preferentialy) using admetSAR open source tool. (Table: 4-6)

5. **Molecular docking evaluations**

In this research, Structure-based Drug Designing (SBDD) through molecular docking was undertaken using PyRx (with in-built Autodock). After molecular docking of 42 ligands at the selected binding sites. Here, 25 natural compounds out of 42 were found to have promising binding energies in the range of $\Delta G \leq$ -8.0 kcal/mol with RMSD lower bound and RMSD upper bound values = 0. These 25 selected compounds were further evaluated through extensive ADMET analysis using admetSAR. (Table: 3-6)

6. **Prediction of ADMET properties**

After getting the screening done on the basis of ΔG (in the range $\leq$ -8 kcal/mol), 23 natural compounds were assessed for ADMET properties for identification of likelihood of compounds using admetSAR online server on the basis of CYP450 inhibitory promiscuity, ames toxicity, as mentioned before. Here, top 7 natural compounds were found to possess mentioned desired properties (preferentially CYP inhibitory promiscuity) as shown in table 6. On other hand, compounds like 4-Hydroxysesamin (CID: CID:16745513), Pinoresinol (CID:17750970), Irilone (CID:5281779) among 23 compounds were refuted besides having very good ΔG score, due to not fulfilling the criteria of CYP inhibition. (Table: 3-6). Then these 7 natural compounds were finally selected and subjected for binding amino acid residues evaluation using DSV and PyMol, within the particular domain (kinase or nuclear receptor domain) of concerned receptor. (Figure: 4-9)

7. **Molecular docking studies of receptors**

Having good binding efficiencies (indicating good stability and longer half-life) with 6 receptors, promising ADMET properties and significant number of common interacting amino acid residues as compared with binding sites of receptors, 7 natural compounds compounds whose 2-D structures were taken from PubChem as shown in Figure 6, were finally proposed on the basis of receptor based drug screening or Structure-based Drug Designing (SBDD). Here, we found that among top 7 compounds, some of them showed highest binding energies (as shown in table 3), ΔG (in the range $\leq$ -8 kcal/mol), as well as significant number of common amino acid residues with binding AA residues of protein. (Figure: 4,5,7-9). Besides this, it was also observed that some ligands like **Paulownin-CID:3084131** which showed ΔG of -9.7 Kcal/mol with PIK3CD receptor **and** ΔG of -8.7Kcal/mol with PIK3CA receptor; **Cornigerine-CID:100188** which showed ΔG of -8.3 Kcal/mol with PIK3CD receptor were refuted as no common amino residues were found. The various types of molecular interactions (H-bonds, π-sigma, alkyl, π-alkyl, π-Sulfur, etc.) among the ligand and binding residues were also studied as shown in Tables (7-12) . Finally proposed and their combinations are believed to be promising in inhibiting the potential receptors of ER(+)BC in a multi-targeted way. Furthermore, their synergistic effects can be evaluated further in in-vitro studies on ER(+)BC cell lines.

3.Conclusion

In this research, virtual screening of natural compounds found in Indian medicinal plants was done against the key receptors of Estrogen positive breast cancer. Ligand library was created using IMPPAT database followed by molecular docking simulations and ADMET predictions using PyRx and admetSAR tools respectively. We hereby conclude that the combination of Carpusin-CID:134369, Paulownin-CID:3084131, Cornigerine-CID:100188, Nororientaline-CID:440632, Oryzalexin B-CID:176496, Romucosine H-CID:5320994 and Colchicine-CID:6167 are potential natural compounds against key receptors in clinical expression of Estrogen positive breast cancer. Among them, Carpusin, Paulownin, Oryzalexin B and colchicine showed excellent ADMET properties. These seven compounds which possess good PK, PD, Physiochemical properties as well as high drug likeliness shows efficient binding with these key receptors. Therefore, they can be further explored for their synergistic efficiency in molecular dynamics studies to prove their potential to act as combinatorial therapeutic agents against estrogen receptor positive breast cancer.

LIST OF FIGURES:

e-ISSN : 2620 3502
p-ISSN : 2615 3785

1. Figure 1: Figure showing methodology of virtual screening used in research.
2. Figure 2: Protein-Protein interactions of selected receptors for ER(+)BC using STRING (11.0) database. Colored lines depict edges and types of interactions as shown in key alongside.
3. Figure 3: Binding sites of (A) FGFR2 (PDB Id: 3RI1- catalytic domain of fibroblast growth factor receptor 2 kinase in complex with ARQ069), (B) ESR1 (PDB Id: 5ACC- Estrogen receptor 1 in complex with AZD9496), (C) PIK3CA (PDB Id: 3ZIM- Lipid kinase of Phosphatidylinositol 4,5-bisphosphate 3-kinase catalytic subunit alpha isoform in complex with covalent inhibitor C_{30} H_{35} N_7 O_3 S), (D) PIK3CB (PDB Id: 4BFR- Phosphatidylinositol 4,5-bisphosphate 3-kinase catalytic subunit beta isoform *in complex with* C_{19} H_{22} N_4 O_3 *), (E) PIK3CD (PDB Id: 4X*E0- *Phosphatidylinositol 4,5-bisphosphate 3-kinase catalytic subunit delta isoform in complex with Idelalisib), (F)* AR (PDB Id: 1E3G-Androgen receptor in complex with metribolone).
4. Figure 4: Figure showing 2-D image of binding amino acid residues of ligands and 3-D molecular surface representation of binding pocket of FGFR2 receptor. Ligands are shown in stick format bounded in receptor's pocket (Green cyan). (A) Paulownin-CID:3084131, (B) Cornigerine-CID:100188, (C) Oryzalexin B-CID:176496.
5. Figure 5: Figure showing 2-D image of binding amino acid residues of ligands and 3-D molecular surface representation of binding pocket of ESR1 receptor. Ligands are shown in stick format bounded in receptor's pocket (Green). (A) Carpusin-CID:134369, (B) Nororientaline-CID:440632, (C) Oryzalexin B-CID:176496.
6. Figure 6: Chemical structures of natural compounds taken from PubChem, shown with their respective PubChem IDs and plants. (A) Carpusin-CID:134369 found in *Petrocarpus marsupium* and *Rheum austral*, (B) Paulownin-CID:3084131 found in *Gmelina arborea*, (C) Cornigerine-CID:100188 found in *Gloriosa superba*, (D) Nororientaline-CID:440632 found in *Erythrina fusca*, (E) Oryzalexin B-CID:176496 found in *Oryza sativa*, (F) Romucosine H-CID:5320994 found in *Annona cherimola*, (G) Colchicine-CID:6167 found in *Colchicum autumnale, Colchicum luteum, Crocus sativus* and *Gloriosa superba*.
7. Figure 7: Figure showing 2-D image of binding amino acid residues of ligands and 3-D molecular surface representation of binding pocket of PIK3CA receptor. Ligands are shown in stick format bounded in receptor's pocket (Yellow). (A) Cornigerine-CID:100188, (B) Nororientaline-CID:440632, (C) Romucosine H-CID:5320994
8. Figure 8: Figure showing 2-D image of binding amino acid residues of ligands and 3-D molecular surface representation of binding pocket of PIK3CD receptor. Ligands are shown in stick format bounded in receptor's pocket (Grey). (A) Romucosine H-CID:5320994, (B) Colchicine-CID:6167
9. Figure 9: Figure showing 2-D image of binding amino acid residues of ligands with their type of interactions and 3-D molecular surface representation of binding pocket of PIK3CB and AR receptors. Ligands are shown in stick format bounded in receptor's pocket (Golden yellow- PIK3CB, Red- AR). (A) Carpusin-CID:134369 with PIK3CB, (B) Carpusin-CID:134369 with AR.

LIST OF TABLES:

1. Table 1: Table: Table showing potential associated genes in Estrogen receptor positive breast cancer using DisGeNET database screened on the basis of parameters like pLI (Probability of gene disease association) ≥0.99, $Score_{gda}$ (Score of gene disease association)≥0.1, N.PMIDs (No. of PMIDs)≥7. Abbreviations: DSIg (Disease specificity index), DPIg (Disease pleiotropy index), EI_{gda} (Evidence index), EL_{gda} (Evidence level), $N_diseases_{g}$ (No. of associated diseases to gene), N. $SNPs_{gda}$ (No. of single nucleotide polymorphisms associated with gene).
2. Table 2: Protein-Protein interaction score obtained from STRING (11.0) database.
3. Table 3: Binding energy scores of 7 top ligands with selected receptors. Scores highlighted in red were selected as best ligands with top binding energies with significant number of common interacting amino acid residues with receptor' binding sites.
4. Table 4: Druggability properties of top 7 selected natural compounds. Computed via FAF-Drugs4 and FAF-QED.
5. Table 5: Physicochemical properties of top 7 selected ligands. Computed via FAF-Drugs4 and RDKit
6. Table 6: ADMET analysis of top 7 selected ligands. Computed via admetSAR.
7. Table 7: Types of molecular interactions of top 3 ligands with FGFR2. Binding amino acid residues highlighted in red indicate similarity with the binding sites of receptor.
8. Table 8: Types of molecular interactions of top 3 ligands with ESR1. Binding amino acid residues highlighted in red indicate similarity with the binding sites of receptor.
9. Table 9: Types of molecular interactions of top 3 ligands with PIK3CA. Binding amino acid residues highlighted in red indicate similarity with the binding sites of receptor.
10. Table 10: Types of molecular interactions of top 1 ligands with PIK3CB. Binding amino acid residues highlighted in red indicate similarity with the binding sites of receptor.
11. Table 11: Types of molecular interactions of top 2 ligands with PIK3CD. Binding amino acid residues highlighted in red indicate similarity with the binding sites of receptor.

e-ISSN : 2620 3502
p-ISSN : 2615 3785

12. Table 12: Types of molecular interactions of top 3 ligands with AR. Binding amino acid residues highlighted in red indicate similarity with the binding sites of receptor.

Abbreviations:

ER(+)BC: Estrogen Receptor Positive Breast CANCER
WHO: World Health Organization
DNA: Deoxyribonucleic acid
ICIs: Immune Checkpoint Inhibitors
CART: Chimeric Antigen Receptor T-Cell Therapy
SPIONs: Supermagnetic iron oxide nanoparticles
SARS COV-2: Severe Acute Respiratory Syndrome Coronavirus 2
USFDA: United States Food and Drug Administration
GnRHa: Gonadotropin releasing hormone agonists
SERMSs: Selective estrogen receptor modulators
SERDs: Selective estrogen receptor down-regulators
FGFR2: Fibroblast Growth Factor Receptor 2
ESR1: Estrogen Receptor 1
PIK3CA: Phosphatidylinositol 4,5-bisphosphate 3-kinase Catalytic subunit alpha
PIK3CB: Phosphatidylinositol 4,5-bisphosphate 3-kinase Catalytic subunit beta
PIK3CD: Phosphatidylinositol 4,5-bisphosphate 3-kinase Catalytic subunit delta
AR: Androgen Receptor
CXCL8: C-X-C Motif Chemokine Ligand 8
BMP7: Bone Morphogenetic Protein 7
MMP9: Matrix Metallopeptidase 9
CD44: A Multifunctional Cell Surface Adhesion Receptor
ESR2: Estrogen Receptor 2
CDK 4/6: Cyclin-dependent kinase 4/6
ct-DNA: circulating tumor DNA
ERK1/2: Extracellular signal-regulated protein kinase ½
CADD: Computer aided drug discovery
IMSc: The Institute of Mathematical Sciences
IMPPAT: Indian Medicinal Plants, Phytochemistry and Therapeutics
PMID: Unique identifier number used in PubMed
STRING: Search Tool for the Retrieval of Interacting Genes/Proteins
FAF-Drugs4: Free ADME-Tox Filtering Tool
QEDw: Weighted quantitative Estimate of Drug-likeness
DisGeNET: Database of gene-disease associations
$Score_{gda:}$ Gene-disease association score
pLI: Probability of being loss of function intolerant
N.PMIDs: No. of PMIDs)
DSIg: Disease specificity index),
DPIg: Disease pleiotropy index),
EI_{gda}: Evidence index),
EL_{gda}: Evidence level),
$N_diseases_{g:}$ No. of associated diseases to gene),
N. $SNPs_{gda}$: No. of single nucleotide polymorphisms associated with gene).
DSV: Discovery Studio Visualizer
TPSA: Topological polar surface area
GSK: GlaxoSmithKline
log P: octanol-water partition coefficient
BBB: Blood Brain Barrier
HIA: Human intestinal absorption
ADMET: Absorption, Distribution, Metabolism, Excretion and Toxicity
CYP 450: Cytochrome P450
DSIg: Disease specificity index
DPIg: Disease pleiotropy index
PPI: Protein-Protein Interaction
PK: Pharmacokinetic properties
PD: Pharmacodynamic properties
RMSD: Root Mean Square Deviation
SBDD: Structure-based Drug Designing
LRo5: Lipinski Rule of five
LD50: Lethal Dose, 50%

Author's declaration:

We authors of the above titled paper hereby declare that work included in the above paper is original and both authors share equal responsibilities.

REFERENCES

1. T. N. Toporcov and V. Wünsch Filho, "Epidemiological science and cancer control," *Clinics*, vol. 73, no. Suppl 1. Universidade de Sao Paulo, 2018, doi: 10.6061/clinics/2018/e627s.
2. Z. Momenimovahed and H. Salehiniya, "Epidemiological characteristics of and risk factors for breast cancer in the world," *Breast Cancer: Targets and Therapy*, vol. 11. Dove Medical Press Ltd., pp. 151–164, 2019, doi: 10.2147/BCTT.S176070.
3. S. De Silva, K. H. Tennekoon, and E. H. Karunanayake, "Overview of the genetic basis toward early detection of breast cancer," *Breast Cancer: Targets and Therapy*, vol. 11. Dove Medical Press Ltd., pp. 71–80, 2019, doi: 10.2147/BCTT.S185870.
4. J. Clavel, "Progress in the epidemiological understanding of gene-environment interactions in major diseases: cancer," *Comptes Rendus - Biologies*, vol. 330, no. 4. Inserm, pp. 306–317, Apr. 2007, doi: 10.1016/j.crvi.2007.02.012.
5. M. L. Wan *et al.*, "Colorectal cancer (CRC) as a multifactorial disease and its causal correlations with multiple signaling pathways," *Bioscience Reports*, vol. 40, no. 3. Portland Press Ltd, 2020, doi:

e-ISSN : 2620 3502
p-ISSN : 2615 3785

10.1042/BSR20200265.
6. "Projections of number of cancer cases in India (2010-2020) by cancer groups - PubMed." https://pubmed.ncbi.nlm.nih.gov/21133622/ (accessed Aug. 16, 2020).
7. "WHO | Breast cancer: prevention and control," *WHO*, 2016, Accessed: Aug. 16, 2020. [Online]. Available: http://www.who.int/cancer/detection/breastcancer/en/.
8. N. Azamjah, Y. Soltan-Zadeh, and F. Zayeri, "Global trend of breast cancer mortality rate: A 25-year study," *Asian Pacific J. Cancer Prev.*, vol. 20, no. 7, pp. 2015–2020, 2019, doi: 10.31557/APJCP.2019.20.7.2015.
9. S. Rajpal, A. Kumar, and W. Joe, "Economic burden of cancer in India: Evidence from cross-sectional nationally representative household survey, 2014," *PLoS One*, vol. 13, no. 2, Feb. 2018, doi: 10.1371/journal.pone.0193320.
10. G. Mathew *et al.*, "Community-based burden, warning signs, and risk factors of cancer using public-private partnership model in Kerala, India," *J. Fam. Med. Prim. Care*, vol. 9, no. 2, p. 745, 2020, doi: 10.4103/jfmpc.jfmpc_1030_19.
11. P. Mathur *et al.*, "Cancer Statistics, 2020: Report From National Cancer Registry Programme, India.," *JCO Glob. Oncol.*, vol. 6, no. 6, pp. 1063–1075, Jul. 2020, doi: 10.1200/GO.20.00122.
12. J. Zhang, Y. Deng, and B. L. Khoo, "Fasting to enhance Cancer treatment in models: The next steps," *Journal of Biomedical Science*, vol. 27, no. 1. BioMed Central Ltd., May 05, 2020, doi: 10.1186/s12929-020-00651-0.
13. K. L. Cheung, "Treatment strategies and survival outcomes in breast cancer," *Cancers*, vol. 12, no. 3. MDPI AG, Mar. 01, 2020, doi: 10.3390/cancers12030735.
14. S. Y. Wang, H. Z. Hu, X. C. Qing, Z. C. Zhang, and Z. W. Shao, "Recent advances of drug delivery nanocarriers in osteosarcoma treatment," *Journal of Cancer*, vol. 11, no. 1. Ivyspring International Publisher, pp. 69–82, 2020, doi: 10.7150/jca.36588.
15. W. Scarano, P. De Souza, and M. H. Stenzel, "Dual-drug delivery of curcumin and platinum drugs in polymeric micelles enhances the synergistic effects: A double act for the treatment of multidrug-resistant cancer," *Biomater. Sci.*, vol. 3, no. 1, pp. 163–174, Jan. 2015, doi: 10.1039/c4bm00272e.
16. Q. Mu *et al.*, "Novel drug combination nanoparticles exhibit enhanced plasma exposure and dose-responsive effects on eliminating breast cancer lung metastasis," *PLoS One*, vol. 15, no. 3, 2020, doi: 10.1371/journal.pone.0228557.
17. J. Y. Choi, R. K. Thapa, C. S. Yong, and J. O. Kim, "Nanoparticle-based combination drug delivery systems for synergistic cancer treatment," *Journal of Pharmaceutical Investigation*, vol. 46, no. 4. Springer Netherlands, pp. 325–339, Jul. 01, 2016, doi: 10.1007/s40005-016-0252-1.
18. E. Moujaess, H. R. Kourie, and M. Ghosn, "Cancer patients and research during COVID-19 pandemic: A systematic review of current evidence," *Critical Reviews in Oncology/Hematology*, vol. 150. Elsevier Ireland Ltd, p. 102972, Jun. 01, 2020, doi: 10.1016/j.critrevonc.2020.102972.
19. H. Vatansev, C. Kadiyoran, M. Cumhur Cure, and E. Cure, "COVID-19 infection can cause chemotherapy resistance development in patients with breast cancer and tamoxifen may cause susceptibility to COVID-19 infection," *Medical Hypotheses*, vol. 143. Churchill Livingstone, p. 110091, Oct. 01, 2020, doi: 10.1016/j.mehy.2020.110091.
20. A. M. L. Seca and D. C. G. A. Pinto, "Plant secondary metabolites as anticancer agents: Successes in clinical trials and therapeutic application," *International Journal of Molecular Sciences*, vol. 19, no. 1. MDPI AG, Jan. 16, 2018, doi: 10.3390/ijms19010263.
21. A. Agbarya, N. Ruimi, R. Epelbaum, E. Ben-Arye, and J. Mahajna, "Natural products as potential cancer therapy enhancers: A preclinical update," *SAGE Open Med.*, vol. 2, p. 205031211454692, Jan. 2014, doi: 10.1177/2050312114546924.
22. S. S. Bashraheel, A. Domling, and S. K. Goda, "Update on targeted cancer therapies, single or in combination, and their fine tuning for precision medicine," *Biomedicine and Pharmacotherapy*, vol. 125. Elsevier Masson SAS, May 01, 2020, doi: 10.1016/j.biopha.2020.110009.
23. A. F. Herrera *et al.*, "Safety and activity of ibrutinib in combination with durvalumab in patients with relapsed or refractory follicular lymphoma or diffuse large B-cell lymphoma," *Am. J. Hematol.*, vol. 95, no. 1, pp. 18–27, Jan. 2020, doi: 10.1002/ajh.25659.
24. F. A. Fisusi and E. O. Akala, "Drug Combinations in Breast Cancer Therapy," *Pharm. Nanotechnol.*, vol. 7, no. 1, pp. 3–23, Jan. 2019, doi: 10.2174/2211738507666190122111224.
25. T. K. Burki, "Fulvestrant plus anastrozole for metastatic breast cancer," *The Lancet. Oncology*, vol. 20, no. 5. NLM (Medline), p. e247, May 01, 2019, doi: 10.1016/S1470-2045(19)30217-7.
26. K. H. Jung *et al.*, "Targeted therapy of triple negative MDA-MB-468 breast cancer with curcumin delivered by epidermal growth factor-conjugated phospholipid nanoparticles," *Oncol. Lett.*, vol. 15, no. 6, pp. 9093–9100, Jun. 2018, doi: 10.3892/ol.2018.8471.
27. B. Noel, S. K. Singh, J. W. Lillard, and R. Singh, "Role of natural compounds in preventing and treating breast cancer," *Front. Biosci. - Sch.*, vol. 12, no. 1, pp. 137–160, Mar. 2020, doi: 10.2741/S544.
28. A. Lodi *et al.*, "Combinatorial treatment with natural compounds in prostate cancer inhibits prostate tumor growth and leads to key modulations of cancer cell metabolism," *npj Precis. Oncol.*, vol. 1, no. 1,

e-ISSN : 2620 3502
p-ISSN : 2615 3785

Dec. 2017, doi: 10.1038/s41698-017-0024-z.
29. V. Shriram, T. Khare, R. Bhagwat, R. Shukla, and V. Kumar, "Inhibiting bacterial drug efflux pumps via phyto-therapeutics to combat threatening antimicrobial resistance," *Front. Microbiol.*, vol. 9, no. DEC, Dec. 2018, doi: 10.3389/fmicb.2018.02990.
30. I. Górniak, R. Bartoszewski, and J. Króliczewski, "Comprehensive review of antimicrobial activities of plant flavonoids," *Phytochemistry Reviews*, vol. 18, no. 1. Springer Netherlands, pp. 241–272, Feb. 15, 2019, doi: 10.1007/s11101-018-9591-z.
31. L. Wang *et al.*, "Wnt1-inducible signaling protein 1 regulates laryngeal squamous cell carcinoma glycolysis and chemoresistance via the YAP1/TEAD1/GLUT1 pathway," *J. Cell. Physiol.*, vol. 234, no. 9, pp. 15941–15950, Sep. 2019, doi: 10.1002/jcp.28253.
32. A. Moore and R. Pinkerton, "Vincristine: Can its therapeutic index be enhanced?," *Pediatr. Blood Cancer*, vol. 53, no. 7, pp. 1180–1187, Dec. 2009, doi: 10.1002/pbc.22161.
33. S. R. Lin *et al.*, "Natural compounds as potential adjuvants to cancer therapy: Preclinical evidence," *British Journal of Pharmacology*, vol. 177, no. 6. John Wiley and Sons Inc., pp. 1409–1423, Mar. 01, 2020, doi: 10.1111/bph.14816.
34. S. Mitra and R. Dash, "Natural Products for the Management and Prevention of Breast Cancer," *Evidence-based Complementary and Alternative Medicine*, vol. 2018. Hindawi Limited, 2018, doi: 10.1155/2018/8324696.
35. R. Dembinski *et al.*, "Estrogen Receptor Positive and Progesterone Receptor Negative Breast Cancer: the Role of Hormone Therapy," *Horm. Cancer*, vol. 11, no. 3–4, pp. 148–154, Aug. 2020, doi: 10.1007/s12672-020-00387-1.
36. F. Lumachi, "Current medical treatment of estrogen receptor-positive breast cancer," *World J. Biol. Chem.*, vol. 6, no. 3, p. 231, 2015, doi: 10.4331/wjbc.v6.i3.231.
37. D. Lüftner *et al.*, "Update Breast Cancer 2020 Part 2 - Advanced Breast Cancer: New Treatments and Implementation of Therapies with Companion Diagnostics," *Geburtshilfe Frauenheilkd.*, vol. 80, no. 4, pp. 391–398, Apr. 2020, doi: 10.1055/a-1111-8775.
38. "FGFR2 fibroblast growth factor receptor 2 [Homo sapiens (human)] - Gene - NCBI." https://www.ncbi.nlm.nih.gov/gene/2263 (accessed Aug. 14, 2020).
39. S. Navid, C. Fan, P. O. Flores-Villanueva, D. Generali, and Y. Li, "The fibroblast growth factor receptors in breast cancer: From oncogenesis to better treatments," *International Journal of Molecular Sciences*, vol. 21, no. 6. MDPI AG, Mar. 02, 2020, doi: 10.3390/ijms21062011.
40. "ESR1 estrogen receptor 1 [Homo sapiens (human)] - Gene - NCBI." https://www.ncbi.nlm.nih.gov/gene/2099 (accessed Aug. 14, 2020).
41. F. Clatot *et al.*, "Risk of early progression according to circulating ESR1 mutation, CA-15.3 and cfDNA increases under first-line anti-aromatase treatment in metastatic breast cancer," *Breast Cancer Res.*, vol. 22, no. 1, May 2020, doi: 10.1186/s13058-020-01290-x.
42. A. Zundelevich *et al.*, "ESR1 mutations are frequent in newly diagnosed metastatic and loco-regional recurrence of endocrine-treated breast cancer and carry worse prognosis," *Breast Cancer Res.*, vol. 22, no. 1, p. 16, Feb. 2020, doi: 10.1186/s13058-020-1246-5.
43. "AR androgen receptor [Homo sapiens (human)] - Gene - NCBI." https://www.ncbi.nlm.nih.gov/gene/367 (accessed Aug. 14, 2020).
44. C. Amaral, T. V. Augusto, M. Almada, S. C. Cunha, G. Correia-da-Silva, and N. Teixeira, "The potential clinical benefit of targeting androgen receptor (AR) in estrogen-receptor positive breast cancer cells treated with Exemestane," *Biochim. Biophys. Acta - Mol. Basis Dis.*, vol. 1866, no. 5, May 2020, doi: 10.1016/j.bbadis.2019.165661.
45. K. H. Kensler *et al.*, "Prognostic and predictive value of androgen receptor expression in postmenopausal women with estrogen receptor-positive breast cancer: Results from the Breast International Group Trial 1-98," *Breast Cancer Res.*, vol. 21, no. 1, p. 30, Feb. 2019, doi: 10.1186/s13058-019-1118-z.
46. H. Qin *et al.*, "The impact of PI3K inhibitors on breast cancer cell and its tumor microenvironment," *PeerJ*, vol. 2018, no. 6, 2018, doi: 10.7717/peerj.5092.
47. "PIK3CA phosphatidylinositol-4,5-bisphosphate 3-kinase catalytic subunit alpha [Homo sapiens (human)] - Gene - NCBI." https://www.ncbi.nlm.nih.gov/gene/5290 (accessed Aug. 14, 2020).
48. "PIK3CB phosphatidylinositol-4,5-bisphosphate 3-kinase catalytic subunit beta [Homo sapiens (human)] - Gene - NCBI." https://www.ncbi.nlm.nih.gov/gene/5291 (accessed Aug. 14, 2020).
49. "PIK3CD phosphatidylinositol-4,5-bisphosphate 3-kinase catalytic subunit delta [Homo sapiens (human)] - Gene - NCBI." https://www.ncbi.nlm.nih.gov/gene/5293 (accessed Aug. 14, 2020).
50. R. J. Crowder *et al.*, "PIK3CA and PIK3CB inhibition produce synthetic lethality when combined with estrogen deprivation in estrogen receptor-positive breast cancer," *Cancer Res.*, vol. 69, no. 9, pp. 3955–3962, May 2009, doi: 10.1158/0008-5472.CAN-08-4450.
51. D. Huang, L. Tang, F. Yang, J. Jin, and X. Guan, "PIK3CA mutations contribute to fulvestrant resistance in ER-positive breast cancer.," *Am. J. Transl. Res.*, vol. 11, no. 9, pp. 6055–6065, 2019, Accessed: Aug. 12, 2020. [Online]. Available: http://www.ncbi.nlm.nih.gov/pubmed/31632573.

e-ISSN : 2620 3502
p-ISSN : 2615 3785

52. B. Verret, J. Cortes, T. Bachelot, F. Andre, and M. Arnedos, "Efficacy of PI3K inhibitors in advanced breast cancer," *Annals of oncology : official journal of the European Society for Medical Oncology*, vol. 30, no. 10. NLM (Medline), pp. x12–x20, Dec. 01, 2019, doi: 10.1093/annonc/mdz381.
53. J. S. Chen *et al.*, "PIK3CD induces cell growth and invasion by activating AKT/GSK-3β/β-catenin signaling in colorectal cancer," *Cancer Sci.*, vol. 110, no. 3, pp. 997–1011, Mar. 2019, doi: 10.1111/cas.13931.
54. E. G. Puigjané, "A new ligand-based approach to virtual screening and profiling of large chemical libraries," p. 172, 2008.
55. W. Cui, A. Aouidate, S. Wang, Q. Yu, Y. Li, and S. Yuan, "Discovering Anti-Cancer Drugs via Computational Methods," *Frontiers in Pharmacology*, vol. 11. Frontiers Media S.A., May 20, 2020, doi: 10.3389/fphar.2020.00733.
56. T. Bintener, M. P. Pacheco, and T. Sauter, "Towards the routine use of in silico screenings for drug discovery using metabolic modelling," *Biochem. Soc. Trans.*, vol. 48, no. 3, pp. 955–969, Jun. 2020, doi: 10.1042/BST20190867.
57. Z. Zhang *et al.*, "Overcoming cancer therapeutic bottleneck by drug repurposing," *Signal Transduction and Targeted Therapy*, vol. 5, no. 1. Springer Nature, Dec. 01, 2020, doi: 10.1038/s41392-020-00213-8.
58. A. H. Ananth *et al.*, "Design, Synthesis, and Biological Evaluation of 2-(2-Bromo-3-nitrophenyl)-5-phenyl-1,3,4-oxadiazole Derivatives as Possible Anti-Breast Cancer Agents," *Chem. Biodivers.*, vol. 17, no. 2, Feb. 2020, doi: 10.1002/cbdv.201900659.
59. X. Lu *et al.*, "A new class of 1,3,5-triazine-based selective estrogen receptor degraders (SERDs): Lead optimization, molecular docking and dynamic simulation," *Bioorg. Chem.*, vol. 97, Apr. 2020, doi: 10.1016/j.bioorg.2020.103666.
60. N. T. Nguyen *et al.*, "Autodock Vina Adopts More Accurate Binding Poses but Autodock4 Forms Better Binding Affinity," *J. Chem. Inf. Model.*, vol. 60, no. 1, pp. 204–211, Jan. 2020, doi: 10.1021/acs.jcim.9b00778.
61. S. Dallakyan and A. J. Olson, "Small-molecule library screening by docking with PyRx," *Methods Mol. Biol.*, vol. 1263, pp. 243–250, 2015, doi: 10.1007/978-1-4939-2269-7_19.
62. B. H. M. Mooers, "Simplifying and enhancing the use of PyMOL with horizontal scripts," *Protein Sci.*, vol. 25, no. 10, pp. 1873–1882, Oct. 2016, doi: 10.1002/pro.2996.
63. K. Mohanraj *et al.*, "IMPPAT: A curated database of Indian Medicinal Plants, Phytochemistry and Therapeutics," *Sci. Rep.*, vol. 8, no. 1, Dec. 2018, doi: 10.1038/s41598-018-22631-z.
64. P. J *et al.*, "DisGeNET: a comprehensive platform integrating information on human disease-associated genes and variants," *Nucleic Acids Res.*, vol. 45, no. D1, 2017, doi: 10.1093/NAR/GKW943.
65. D. Szklarczyk *et al.*, "STRING v11: Protein-protein association networks with increased coverage, supporting functional discovery in genome-wide experimental datasets," *Nucleic Acids Res.*, vol. 47, no. D1, pp. D607–D613, Jan. 2019, doi: 10.1093/nar/gky1131.
66. W. Liu *et al.*, "Discovery, Identification and Comparative Analysis of Non-Specific Lipid Transfer Protein (nsLtp) Family in Solanaceae," *Genomics, Proteomics Bioinforma.*, vol. 8, no. 4, pp. 229–237, Dec. 2010, doi: 10.1016/S1672-0229(10)60024-1.
67. "Vina output analysis using Discovery Studio visualizer - Bioinformatics Review." https://bioinformaticsreview.com/20191101/vina-output-analysis-using-discovery-studio-visualizer/ (accessed Aug. 15, 2020).

sustainability

MDPI

Article

Women's Participation and Factors Affecting Their Academic Performance in Engineering and Technology Education: A Study of Ethiopia

Addissie Melak [1,2,*,†] and Seema Singh [1,†]

[1] Department of Humanities, Delhi Technological University, Delhi 110042, India; seemahumanitiesdtu@gmail.com
[2] Department of Economics, Debre Tabor University, Debre Tabor 6300, Ethiopia
* Correspondence: addmelak24@gmail.com
† These authors contributed equally to this work.

Abstract: Academic performance is one of the reasons for gender imbalance in STEM education. This study has two objectives: analyzing women's participation in STEM education and investigating the factors affecting women's achievements in Engineering and Technology university majors in Ethiopia. Secondary data have been analyzed to establish women's involvement in STEM education using enrollment and graduation data and to observe the gender gap. Primary data were collected from 376 women students of engineering and technology. The OLS multiple regression model results reveal that the academic performance of women in engineering and technology education is positively influenced by students' capabilities to gather information about the institution before joining the university. Interventions followed by institutions for supporting women students, peer learning habits of students, and the accessibility of university infrastructure also positively affect women's academic performance. In contrast, sexual harassment and the existence of engineering and technology professionals in the family negatively influence the academic performance of women. Hence, educational organizations, governments, and other stakeholders should work to enhance women's academic performance and reduce the gender gap in STEM education. Engineering colleges must also give attention to students' psychological, economic, and educational support, try to fulfill infrastructure and learning equipment, and protect students from sexual harassment through strong commitment and regulations.

Keywords: women's academic performance; engineering and technology education; Ethiopia

check for updates

Citation: Melak, A.; Singh, S. Women's Participation and Factors Affecting Their Academic Performance in Engineering and Technology Education: A Study of Ethiopia. *Sustainability* **2021**, *13*, 2246. https://doi.org/10.3390/su13042246

Academic Editor: Carmen Botella-Mascarell
Received: 31 December 2020
Accepted: 29 January 2021
Published: 19 February 2021

Publisher's Note: MDPI stays neutral with regard to jurisdictional claims in published maps and institutional affiliations.

Copyright: © 2021 by the authors. Licensee MDPI, Basel, Switzerland. This article is an open access article distributed under the terms and conditions of the Creative Commons Attribution (CC BY) license (https://creativecommons.org/licenses/by/4.0/).

1. Introduction

As the technological intensity domains have increased in recent years, developing human capital in engineering and technology has become an essential aspect of sustainable development. The Agenda of Sustainable Development Goals adopted by the United Nations in 2015 includes sustainable development Goals (SDGs) four on quality education, five on gender equality, and ten on reduced inequality within and among countries [1]. These goals emphasize the importance of increasing opportunities for progress and promoting individuals, families, and communities to ensure sustainable development and improve all human beings' living standards [2]. As Sustainable Development Goals (SDGs) four and five focused on quality education and gender equality such that many developed and developing countries always consider education a crucial tool in their development. Being a developing country, Ethiopia needs many projects, such as road and housing constructions, building manufacturing factories, etc. The government, therefore, requires highly qualified professionals in engineering and technology [3]. As a result, it is necessary to produce students with high academic performance, including women, to reduce the gender gap in STEM education [4], and women have to be encouraged to increase individual

and national income [5]. However, women's education in Science, Technology, Engineering, and Mathematics (STEM) has demonstrated gender gaps, and low representation of women in STEM is universally acknowledged due to a lack of recognition of achievements and fewer promotions [6].

1.1. Women's Participation in STEM Education

The education of females contributes to various aspects of their lives, such as increased longevity, family health, and nutrition. In Ethiopia, women's education was strongly influenced by socio-cultural norms and attitudes, leading to a minimum share of women in higher education and STEM fields. Singh and Sarah have grouped all the countries of the world into four groups to discuss women's participation, based on the similarity of characteristics, and found that Ethiopia falls in the fourth group, which comprises developing countries with traditionally low participation of women in engineering education; however, recently, participation has increased [7].

In another paper [8], Mahajan found that STEM education is male-dominated in other countries of the world. Engineering is considered a male profession, and women's participation is low. He also discussed the reasons for this, such as gender stereotypes, social and cultural values of the society, women's educational background in science subjects, lack of role models, and women undermining the perception of employer companies. Women are usually under-represented in the academic and professional fields of engineering and technology, even though many of them have greatly contributed once they have joined the area [8,9].

A study by Sikora and Pokropek [10] investigated the existence of gender difference in computing, engineering, and mathematics by using survey data from 50 countries. Their findings shows that males are more interested in engaging in these fields than their female counterpart. The idea is also supported by a study [11] which found that only 18% of women who are students in higher education institutions throughout the world pursue STEM fields compared to 35% of men. A study by Botella et al. [12] discussed the problems of gender gaps in Spain in STEM education. They argued that institutional encouragement and support, increasing the professional support network, promoting and supporting leadership, and increasing female role models' feasibility could encourage women in STEM education. These instruments could increase the percentage of graduated female students from information and communications technology studies.

Rodríguez-Rivero et al. [13] also found the existence of gender gaps in STEM education in Spain, that 24.8% women are enrolled in undergraduate engineering and architecture field of study in 2018–2019, whereas 75.2% are men. The same is happening in Master's and Ph.D degree programs. Moreover, López-Iñesta et al. [14] discussed a shortage of STEM talent in areas with a broad range of job positions and fair working conditions. Simultaneously, technology forecasting predicts that big data, artificial intelligence, and advanced communications systems drive us towards a Digital Society with a profound transformation of the job market. Thus, women's participation in future communities is mandatory.

Benavent et al. [15] conducted a project in Spain to link student participation in STEM education and Sustainable Development Goals (SDGs). This project was focused on breaking the stereotypes in STEM fields and maintaining women's role models for female students in STEM disciplines, which helps educate children as future citizens and enables a more sustainable future in equity, inclusion, diversity, prosperity, and justice. The project also focused on SDG4 and SDG5 through outreach activities where students, families, teachers, and STEM professional women were involved. They found that, out-of-school time spent on STEM activities and informal learning environments (campuses, camps, etc.) have been shown to be important factors that [16–19] increase, up to 1–8 times, the chances of a student to enrolling in a STEM degree. However, other research indicates that, despite the numerous initiatives and efforts, outreach activities have a much smaller impact on girls, especially in the field of engineering [20].

There is also a significant imbalance in the distribution between the two genders in Africa, as it happens in other parts of the world. Women engineers are few and unable to fully participate in national development. Masanja [21] indicates that, in sub-Saharan African countries, education statistics show that less women continue their education in general compared to men and specifically in science, mathematics, and technology. He investigated examination results and the selection of students to tertiary level institutions from 10 countries. He found that fifty males had the chance to go to a public university for every one hundred who passed the secondary school examination. In contrast, for every one hundred females who passed the test and were eligible, only seven got a chance.

The UN also shows that in sub-Saharan Africa, girls of primary education continue to significantly lag behind boys in mathematical achievement. The same has happened in South-East Asia [22].

According to Rathgeber [23], in Africa, women are not interested in studying sciences and engineering, resulting in low participation in academic positions in science-related subjects. Oanda and Akudol [24] further claim that there are fewer female sub-Saharan African students enrolled in STEM subjects and that their completion rates are lower than those of male students. There is a similar situation in Asian countries. One study, conducted in Pakistan by Malik and Courtney [25], shows that there are few women in higher education participation, as parents prefer to send their son and spend money on him, rather than doing the same for their daughters. Their finding shows that 80% of respondents believe that parents do not spend similar amounts of money on educating their daughters as they do on their sons.

According to UNESCO, women account for fewer than 30% of the world's researchers, and female representation in engineering and computer science is much lower, which is around 10%. A study from 14 countries also found that the probability for a female student graduating with an undergraduate degree in a science-related field is 18%, compared to 37% for male students [26].

The finding of Melak and Singh [27] confirms this low participation of women in engineering and technology education in Ethiopia. According to their conclusion, in the regular undergraduate degree program, the average number of women enrollment in public universities during 2007 to 2016 was 23.34%. In the same year, 13.4% women were enrolled in a postgraduate degree program. Moreover, the average number of women graduates from the total graduate cohort was only 14.5% during the same year. Therefore, increasing the participation of women students is one of the present policy objectives of higher institutions in a country [28].

1.2. Why do We Need to Study Women's Participation in STEM Education?

There is a need to increase women in engineering and technology fields to find solutions for problems. Women professionals in engineering and technology are necessary to solve climatic change, accessibility of water supply, disease control, etc. Moreover, lower-performing men are frequently selected when women are not well represented in these fields [29]. According to Nishii, creating a heterogeneous labor force in terms of race, ethnicity, gender, religion, etc., is widely linked to enhancing productivity [30]. The women professionals in engineering and technology have an opportunity to engage in high-quality jobs in the field, leading to earning a better salary than other areas [31].

According to UNICEF [11], STEM education improves women's awareness and capacity to participate in actions that protect the environment, position them as leaders in their communities, and actively engaged in a more sustainable society. Women who develop STEM skills are better prepared to contribute to scientific research and technological development initiatives leading to innovative solutions in the industrial sector. STEM knowledge can equip women with the tools to transition from education to employment so that young women improve their livelihoods and contribute to poverty reduction and economic growth. Access to STEM education contributes to women's opportunities to develop transferable, technical, and vocational skills for employment, decent jobs, and

entrepreneurship has the potential to accelerate the elimination of gender disparities in access to digital technologies and digital learning. Such activities lead to women as capable players in promoting sustainable development and gender equality in all areas of life. Thus, STEM knowledge and skills can empower women to decide about their maternal health and their children. The STEM fields offer people job opportunities and offer a higher return on educational investment [32]. Yet women remain less well represented in engineering than in any other STEM field [33]. Therefore, studying women's participation in STEM education is an important issue.

Since Ethiopia is among low income and developing countries globally, there is a need for more women in STEM to lift innovation in one step in poverty reduction, social, economic, and environmental development. Hence, conducting more valuable research in the field and preparing policy implications for the concerned stakeholders is an important issue to increase women's number and quality in engineering and technology. Regarding this issue, UNESCO [26] stated that the lack of women in the technology sectors has significant socio-economic consequences, with women losing a vital tool for personal and economic empowerment. According to United Nations Women's Deputy Executive Director Lakshmi Puri, estimates have shown in energy and agriculture, 2.5 million engineers and technicians will be needed in sub-Saharan Africa to achieve improved access to clean water and sanitation [26]. These reasons push to do more research on the participation of women in STEM.

1.3. Factors Affecting Academic Performance of Women in STEM Education

1.3.1. Socio-Cultural Factors

Women's enrollment in education is better today than ever before. Still, they do not always have the same opportunities as boys to complete and benefit from an education of their choice. They are significantly under-represented in STEM education and careers due to low academic performance, which is affected by several factors [34]. According to Almukhambetova and Kuzhabekova [35], most women are challenged by various socio-cultural factors, labor markets, and regional differences, contributing to women's under-representation in STEM fields in Kazakhstan. The concept was also verified by Mamo and Hailu [36]. They studied factors affecting female students' academic performance and competency in Ethiopia by collecting data from 135 female students at Dire Dawa University and found socio-cultural factors, students' behavior, and commitment related factors were significant reasons for women students' poor academic performance and competency. Another finding [37] also shows, country-level socio-economy, cultural and political factors, number of women in parliament, gender inequality, overall equality, and religion are examined as a possible factors affecting girl's achievement in Poland's STEM education. Balakrishnan and Low [38] also examined socio-cultural factors on female engineering perspectives on engineering courses and careers. The study was focused on the Japanese female students' perception of learning by looking at their intention to pursue careers in engineering fields. The findings revealed that socio-cultural values of a society and self-efficacy have strong influences on students' motivation to pursue careers in engineering.

Regarding this self-efficacy and social perception, Lin and Tsai [39] examined the source of gender difference in science learning self-efficacy of high school students in Taiwan. Their finding reveals that society's positive attitudes and any other groups are the sources for strengthened students' science learning self-efficacy dimension of higher-order cognitive skill and science communication. These lead to improving science learning confidence and better academic performance of students in STEM education. They also found that there is a significant difference in social perception between genders. Male students had encouraging experiences through other sounds than their female counterparts. On the other hand, the female students experienced more negative feelings such as stress, anger, and fear than the male students, leading to low academic performance.

The study conducted by Lytle and Shin [40] explored the correlation among incremental beliefs, STEM efficacy, and STEM interest with the help of 1201 participants from undergraduate students in the USA. They found that students who have optimistic thoughts lead to greater STEM efficacy, leading to greater interest in STEM education to achieve better academic performance.

Fernández-Cézar et al. [41] also studied stereotypes in science education concerning pre-university students using 404 participants in Spain. They explored whether the students are stereotyped in perceptions of gender, science, scientists, and the school's rurality. The finding shows that 95% of the sample are agreed as women and men should equally be considered in the scientific profession's egalitarian perception. They also reported that more than 10% sample is stereotyped with different perceptions according to sex and rurality factors. They also found no differences between boys and girls in terms of gender perspective regarding sex. However, they observe the influence of the sense of belonging that women agreed less than men on those items that indicate women's inferiority to men in all situations. They also found the perception of stereotype is declined with increasing age and school level of students. At the same time, stereotyped ideas of gender in science are affected by the school's rurality.

1.3.2. High School Education Background and University Infrastructure

Mersha et al. [42] studied factors affecting women students' academic achievement at Bahir Dar University using data collected from 200 male and 400 female students studying in 6 faculty, including engineering. The finding shows that high school academic background is the main factor for their low academic performance. He also finds that personal characteristics and university environment contribute to their low conducting. Mamo and Hailu [36] also examined institutional factors that can affect women's academic performance and competency.

Another study by Muhammed [4] found that university entrance exam score is the primary determinant of students' academic performance. Yigermal [43] also proved a significant relationship between their previous educational background (university entrance exam) and students' academic performance. A recent study by Raquel et al. [44] also confirmed other studies that can obtain students' understanding and motivation by knowing their educational background.

1.3.3. Teaching Methodology Followed by Teachers and Peer Learning Habit of Students

Riegle-Crumb and Moore [45] examined 2000 students who enrolled in challenge-based engineering courses in Texas. The finding reveals that compared to males, females reported lower interest and less confidence in engineering class since the class is not participatory. Van den Hurk et al. [46] also found that STEM teachers tend to favor men more than women.

Patall et al. [47] also studied students' gender difference in motivational experience during science class at high school education from 208 participants in the USA. They found that compared to male students, women high school students may experience less daily encouragement from teachers in engineering courses, which leads to lower academic performance in STEM subjects except for biology and biomedical science.

Hosaka [48] also studied women's experiences in the engineering laboratory in Japan; this qualitative study examines Japanese women undergraduate engineering students' experiences of interacting with departmental peers laboratory setting. Findings show that women generally had a discouragement experience while working with their male peers. They participated less and lost confidence by comparing with men who appeared to be confident and competent. According to Hosaka's finding, women were not interested in learning in groups with their friends, which is a crucial factor for experience and knowledge sharing, leading to low academic performance. Balakrishnan and Low [38] also focused on the Japanese female students learning experience in engineering programs. The findings

revealed that female students' intention to pursue a career in engineering was directly related to the learning experiences.

1.3.4. Academic Curriculum and Sexual Harassment

Garcia Villa [49] studied women students in engineering in Mexico. The study found that academic curriculum was a crucial problem of women's academic performance in engineering. When the engineering program's duration is so long that it discourages learning motivation, it leads to low performance. Molla and Cuthbert [50] investigated women's higher education experience in Ethiopia by taking qualitative data from two government universities. The finding shows that sexual violence and bias contrary to women, indicates inequality in the university. The result suggests that this violence and prejudice can affect the psychological and academic performance of women students. The World Economic Forum and UN also identified some reasons women and girls participate in STEM fields at lower rates, such as discouragement experience, lack of role models, negative peer pressure, and sexual violence. Ability is not an issue, as indicated by several studies. Women from under-represented groups face twice over harassment according to their gender and race. Girls are still struggling for necessary access to education and then for acceptance into the workplace in some countries in the developing world [22,51].

1.3.5. Interventions Followed by Institutions for Supporting Women Students

Van den Hurk et al. [46] studied the effectiveness of interventions applied in STEM education and found that some effective interventions prevent the dropout of initially motivated and most intelligent students in STEM areas. Making institutions a conducive environment for learning can lead to better achievement rather than a dropout. In some countries, including Ethiopia, there is an affirmative action policy for girls to support their education achievement [52]. However, there is an argument about this affirmative action provided for females at the university level. For example, Molla and Cuthbert [50] argued that affirmative action policies slightly benefit females at entry point only not in academic achievement.

1.3.6. Annual Income of the Family and Residence Place

Family income situation is an essential factor in determining the academic performance of children. Muhammedhussen [4] found that family economic situation, sleep time, and habit of study are the main determinants of students' academic performance, while the residential place was insignificant. Lin and Lv [53] also found that family income has a significant influence on child education. According to their finding, increasing family income plays a more substantial role in enhancing children's education in China. Tomul and Çelik [54] carried out a study and found that family income affects academic performance. A recent study by Li and Qiu [55] also considered that urban students' academic performance was more affected by their family socioeconomic status than rural students.

On the other hand, Gobena [56] carried out a study by taking data from Education and Behavioral Science students at Haramaya University, Ethiopia. The finding indicates there is no any effect of family income on students' academic performance. There is a controversy about whether family income affects a student's academic performance or not, which needs further investigation from these reviewed studies.

1.3.7. Educational Background of the Family and the Role Model

Learners will need the full support of their families and other stakeholders to maximize their academic performance potential. Buchmann and Diprete [57] find female superior academic performance in college completion remains the largest in families with a low-educated, but currently extends to all family types. Li and Qiu [55] also found that families who have high-quality education backgrounds and understanding educational opportunities leads to better academic performance. Furthermore, parental education support for their children encourages children's learning behaviors and affects academic

performance. Tomul and Çelik [54] also conducted a study in Turkey and confirms parent education affects students' academic achievement. Similarly, Gobena [56] obtained a positive and significant relationship between family educational level and students' academic achievement. Carnasciali et al. [58] also found parental educational achievement levels affect students' performance. Choudhury [59] argued that since children mostly follow their family, educated parents (also other educated adults in the household) are more aware of the benefit of education and invest more in providing quality education.

There are also studies regarding role models that have an impact on women's academic performance. Corbett and Hill [33] concluded that women role models reinforce the perceptions and self-concepts of young women's in mathematics and increase the willingness of women to perceive STEM fields as career opportunities. Sjaastad [60] studied and found teachers are models by displaying how STEM might bring forward someone's success by providing a positive experience with the field. Leavey [61] also reported that women in STEM prefer to have women mentors. The finding supports a study conducted by Shin et al. [62] which indicates women were reported as more interested in STEM after reading biographies of successful STEM role models and reading letters of encouragement women role models.

We have reviewed many papers related to factors affecting women's academic performance in engineering and technology in the context of different countries in the world. Therefore, we found that the previous studies did not study a family profession, year of university establishment, and students' accessibility of information about universities before joining. Therefore, we want to research factors affecting women's academic performance in engineering and technology education, including these three factors with primary data collected from Ethiopia. These can add value to the scope of the literature on women in STEM education. There is also a rationale for more women's participation in engineering and technology in Ethiopia's development and poverty reduction.

2. Materials and Methods

2.1. Objective of the Study

The objectives of this study are:

I To analysis the gender gaps in STEM education with the help of enrollment and graduation data collected from UNESCO and Ethiopian Ministry of Education; and

II To investigate whether (a) peer learning habits of students, (b) interventions followed by institutions for supporting women students, (c) accessibility of university infrastructure, (d) sexual harassment, (e) students having prior information about the university, (f) teaching methodology followed by teachers, (g) accessibility of role model, (h) family educational background, (i) duration of the program or curriculum to study engineering and technology, (j) residence place of students, (k) year of establishment of universities, (l) annual income of the family, and (m) existence of engineering and technology professionals in the family are factors affecting academic performance of women in engineering and technology education.

2.2. Hypothesis of the Study

The study has the following hypothesis based on the objective of analyzing factors affecting women's academic performance in engineering and technology education. These are:

1. Women students who have higher scores on the result of the grade 12 exam will present higher academic performance in engineering and technology education at the university level [43,44];
2. Students who provided academic, financial, and psychological support by the university will have better academic performance [46];
3. Students affected by sexual harassment will present lower academic performance [50];
4. Students who are comfortable with teaching methodology followed by their teachers will record high academic performance [45];

5. Students having a habit of learning in groups will present high academic performance [48,63];
6. Better accessibility of university infrastructure will have a positive impact on students' academic performance [36,42];
7. Students who have the accessibility to information about the university before joining will increase the academic performance of students;
8. Students who have family educational background will score good academic performance [55,56,58];
9. Students who studied the same profession as their family will have better academic performance;
10. Students who have the accessibility of role model will present high academic performance [61];
11. The student who came from the urban area of residence place will score higher academic performance [4];
12. Students who have a better annual income of the family will have high-performance [53];
13. Students will be discouraged with a long time duration of education curriculum that declines their performance [49];
14. Students who studied in old-established and most experienced universities will score high performance.

2.3. Study Area

This study has been conducted based on women's primary and secondary data in engineering and technology education from Ethiopia. There are nine states and two city administrations in a country. In Ethiopia, higher education started in the 1950s following the establishment of the first higher education institution, Addis Ababa University. The number of higher education institutions before the 1990s was only 5. Little progress has been observed in expanding higher education institutions until introducing the current education and training policy in 1994 [64]. Presently, around 44 public universities/colleges provide all types of courses after 2000. Mostly, engineering and technology universities, which is 26% of the total, are found in Addis Ababa, followed by Oromia and Amhara.

2.4. Procedure, Data Collection and Sampling

Primary data have been collected through stratified sampling. Firstly, the Amhara region was randomly selected as a sample state, one of among nine states in a country. The state has ten public higher institutions. Secondly, we categorized ten public higher institutions into four-groups based on the establishment year. The first group includes Bahir Dar University and Gondar University, established as a college in 1954 and recognized as a university in 2000. The second group comprises Debre Birhan University, Debre Markos University, and Wollo universities, which were founded in 2005. The third category includes Debre Tabor University and Woldia University, established in 2008. Finally, Injibara University, Mekdela Amba University, and Debark University, established in 2015, are included in the fourth category.

Thirdly, we select three universities from each group except the fourth category. These are Bahir Dar University, Wollo University, and Debre Tabor University. The selection of sample universities from each group has been made purposively. Since universities established at different times can have different experiences, universities' choice within group was random. Data not collected from 4th group universities since they are new and started working in the 2017/2018 academic year, so that they may not have sufficient data for this study. In Ethiopia, higher education costs such as hostel fees, food, etc., are covered by the government via cost-sharing agreements. Most students are placed to go to university according to their grade 12 marks through placement by the education ministry. Students come from all country directions representing different economic statuses, religions, cultures, languages, and so on. Hence, the sample is representative.

Fourthly, we determine the sample size. For this determination of the number of respondents, we follow procedures. Thus, we have got the total population of women students in engineering and technology in the selected universities during 2018 was 3668. From these entire populations, we have determined 376 sample respondents based on equation one [65].

$$n = \frac{Z^2.p.q.N}{e^2(N-1) + Z^2.p.q} \quad (1)$$

It is valid where n is the sample size, $N = 3668$ (population size), Z^2 is standard variate at the desired confidence level of 95.5% $= (2.01)^2$, $e = 45\%(0.045)$ is the desired level of precision (acceptable error), the range in which the actual value of the population is estimated to be. Whereas p is the estimated proportion of an attribute present in the people taken as 30% and q is $(1 - p)$.

Fifth, we did proportions according to total women students in each sample university. Hence, 227 (60%) respondents from Bahir Dar University, 96 (26%) respondents from Debre Tabor University, and 53 (14%) respondents from Wollo University, a total of 376 respondents have been selected for the study as given in Table 1. Based on this procedure, primary data have been collected from 376 women students enrolled in engineering and technology faculty through structured questionnaires. These students study from 1st year to 5th year during May 2018.

Table 1. Selected total sample respondents.

	Bahir Dar University	**Debre Tabor University**	**Wollo University**	**Total**
	Engineering and Technology	**Engineering and Technology**	**Engineering and Technology**	
No. of students	2212	935	521	3668
No. of respondents	227	96	53	376
Percentage	60%	26%	14%	100%

2.5. Sample Description

As shown in Table 2, the respondents' cumulative GPA is categorized into three levels since CGPA is standardized from zero to four in the Ethiopian grading system of students' academic results. In this background, 64 respondents have below 2.5 score marks; 139 students have scored 2.5 and above but below 3; most respondents have 3-grade points and more. Students' high school performance is a proxy of grades 12 exam results that 40 respondents obtain below half out of 700 marks from around seven subjects, whereas 336 respondents have got 350 and above. Out of 376 samples, 241 have family educational background while 135 respondents have not such family. Out of the total sample, 183 respondents rate accessibility of adequate university infrastructure (i.e., laboratory, library, hostel etc.) as suitable manner, whereas 48 respondents rate it as below satisfaction. From the total respondents, 234 have got the chance of university support directly and indirectly. Regarding sexual harassment, most of the students, especially women, are affected by this problem in any direction from the staff, their peers, but they do not want to talk due to fear and feeling dishonor. Thus, the sample's response shows only 111 students said, "yes, I am harassed". However, we believe that the actual figure will be more than this number (see Table 2).

Table 2. Summary of demographic and socio-economic status of respondents.

Demographic and Socio-Economic Variables	Responses	
Cumulative GPA	<2.5 ≥2.5 and <3 ≥3	64 139 173
High school education performance	<350 = 40	≥ 350 = 336
Family educational background	No = 135	Yes = 241
Pre-informed about the university they have joined	No = 124	Yes = 254
Accessibility of university infrastructure	low = 48 good= 183	medium = 145
Interventions followed by institutions for supporting women students	No = 142	Yes = 234
Sexual harassment	No = 265	Yes = 111
Having engineering and technology professionals in the family	No = 189	Yes = 187
Number of family members	Less than five = 85 Between 5 and 10 = 283	More than 10 = 8
Income of the family	< 50,000 = 184	≥ 50,000 = 192
Place of residence	Rural = 133	Urban = 243
Access of role model	No = 143	Yes = 233
Effect of duration of the program	No = 227	Yes = 149
Teaching methodology	Partly = 119	Yes = 257
Peer learning	No = 118	Yes = 258

2.6. Definition of Variables and Instruments

Academic performance has been measured by cumulative marks of women obtained from the faculty of engineering and technology in the duration of a five year study period. Cumulative marks in higher education are ranging from zero to four scale awards A = 4, B = 3, C = 2, D = 1, and F for 0 with a "plus" or "minus" grade awarded. *A* and A^+ have the same grade point, and 2 points average score is a minimum graduation criterion. Hence, academic achievement is measured by the student's average score mark. Witherspoon and Christian [66] also examine gender difference in educational attainment by taking this GPA as a measure of academic performance.

Students peer learning habits are also measured as 1 = "yes, I have an experience of learning with other students outside the classroom," and 0 = if not. Riegle-Crumb and Moore [45] measured this variable through five Likert scales from strongly disagree to strongly agree through the questionnaire. Such as "would you relate yourself with the people around you in this class," and "could you think that most of the skills learned from outside the class would be useful to you in engineering?" Based on these previous studies, this study also incorporated peer learning habits of the student, which will impact the academic performance of women students.

Interventions followed by institutions for supporting women students were also measured by yes = one if students obtain university support and 0 = if not. Van den Hurk et al. [46] measured this variable through investigating research literature that "What kind of interventions are should take in raising interest and sense of belonging in STEM education among women and men?" Accessibility of university infrastructure is also valued in three levels; low, medium, and good, using the questionnaire "How do you rate infrastructural accessibility and services provided in your university?" [67]. Sexual harassment is another variable considered dichotomous and measured by asking whether students have an experience of any sexual harassment or not [22,51].

Students having prior information about the university is also considered and measured using a questionnaire "Do you have gathered general information about the institu-

tion which you have joined before entering?" Similarly, the existence of engineering and technology professionals in the family has measured using the questionnaire, "Do you have a person in your family who graduated in engineering and technology filed of study?"

Riegle-Crumb and Moore [45] measured teachers' teaching methodology via a Likert scale with the question of "Do you think that your instructors are encouraging you in engineering class?" Patall et al. [47] also measured teacher's encouragement of students in daily class by five items with five Likert scales. It is also estimated as one = "yes I am comfortable with teaching methodology followed by the teacher," and 0 = "I am partly comfortable".

High school education performance is measured through the final semester of the grade 12 Entrance Examination, provided for countrywide Ethiopian University in seven natural science subjects. Exam performance is graded as zero to hundred point scale with a total possible scoring of 700 in seven subjects. Minimum scores for university admission decided by the Ministry of Education of Ethiopia. Therefore, high school educational performance is a continuous variable measured by the grade 12 exam [4,44].

Family educational background is measured as 1 = yes, there is an educated person in the respondent's family, and 0 = if not. Riegle-Crumb and Moore [45] measured family education background by four groups: secondary school level, special occupational training, college level, or advanced degree. In this study, family education background has been taken as a dummy variable whether all family members are illiterate or educated.

Access to role model is also a variable valued as 1 = yes; 0 = I have no role model [33]. The previous studies [4] measured the residence place by kilometer from students home to universities. However, in this study, residence place is categorized into two. Students who belong to rural areas are denoted by 0, and 1 represents students from urban areas. The family's annual income is another continuous variable measured in thousands of Ethiopian Birr [4].

Duration of the program or curriculum to study engineering and technology has been measured through the questionnaire "Have you feeling tired with staying five-year study to complete your degree in engineering and technology?" [49]. This study also considers the establishment of universities as a factor affecting the academic performance of students. It is measured whether students are studying in first group universities or not since senior educational institutions are more experienced and will have a better learning environment.

2.7. Data Analysis

Women students' academic performance in engineering and technology education is a dependent variable affected by independent factors. These are peer learning habits of students, interventions followed by institutions for supporting women students, accessibility of university infrastructure, sexual harassment, students having prior information about the university, existence of engineering and technology professionals in the family, role model, the annual income of the family, high school education performance of students, duration of the program(curriculum), family educational background, and year of establishment of universities.

Checking the reliability of data is an essential issue during primary data analysis. One of the most used reliability estimators is Cronbach's Alpha [68]. This reliability test has computed that shows data are reliable with a scale reliability coefficient of 0.7. The correlation of each independent factor with women students' academic performance in engineering and technology has also computed using Spearman's rank correlation coefficient as given in Table 3. From this table, the correlation coefficient of family income ($p = 0.6$), duration of the program ($p = 0.07$), teaching methodology ($p = 0.3$), high school educational performance (0.2), and year of establishment of universities ($p = 0.29$) are more than standard significant level $p \leq 0.05$ and being insignificant.

Ordinary Least Squire Multiple Linear Regression Analysis also conducted to analyze the most important factors affecting women's academic performance in engineering and technology, which are the reason for the gender imbalance in STEM education. Diagnostic

tests, such as multicollinearity, heteroscedasticity, and link test of the model specification, were computed. Moreover, a normality test of residuals is conducted to check the estimated coefficients and model fitting unbiasedness. Secondary data have also been analyzed through descriptive methods. All analyses were carried out with the STATA 14 software.

Table 3. Spearman's rank correlation coefficient test and statistical summary of variables.

Variables	Correlation Coefficient	Sg.Level	Mean	Std. Dev.
Family educational background (FEDUC)	0.1254	0.0150	0.6409574	0.4803589
Existence of engineering and technology professionals in the family (FP)	0.2267	0.0000	0.4973404	0.5006591
Role Mode (RM)	0.2096	0.0000	0.6196809	0.4861121
Residence Place (RP)	−0.1281	0.0129	0.6462766	0.4787617
Family Income (INC)	0.0231	0.6558	73357.98	105802.1
Duration of the program (DP)	0.0926	0.0728	0.3962766	0.4897749
Teaching methodology (TM)	0.0527	0.3084	0.6835106	0.465726
Peer Learning (PL)	0.4253	0.0000	0.6861702	0.4646664
Accessibility of university infrastructure (AUIF)	0.6045	0.0000	1.359043	0.6976709
Sexual harassment (SH)	−0.5487	0.0000	0.2952128	0.4567461
Interventions followed by institutions for supporting women students (Usport)	0.5628	0.0000	0.6223404	0.4854478
Pre informed about the institution before joining (PI)	0.6942	0.0000	0.6702128	0.4707622
High school education performance (HEP)	0.0628	0.2243	391.9707	42.80644
Year of establishment of universities (YE)	−0.0542	0.2948	0.6037234	0.4897749

Sg.level = significant level (*p*-value), Std. Dev. = standard deviation.

2.8. Model Specification

The factors affecting academic performance were analyzed through Multiple Linear Regression Analysis, which allows many elements in the model. According to Wooldridge [69], the variable's linear function is specified in equation two, and regression estimation has been conducted based on this equation.

$$CGPA = \beta_0 + \beta_1 Usport + \beta_2 SH + \beta_3 PL + \beta_4 AUIF + \beta_5 PI + \beta_6 FEDUC + \beta_7 FP + \beta_8 RM + \beta_9 RP + \epsilon_i \quad (2)$$

where $CGPA$ = cumulative marks, $Usport$ = interventions followed by institutions for supporting women students, SH = sexual harassment, PL = peer learning, $AUIF$ = accessibility of university infrastructure, PI = students prior information about the university they have joined, $FEDUC$ = is family educational background, FP = existence of engineering and technology professionals in the family, RM = role model, RP = residence place of students, β_0 is the intercept(constant term), $\beta_1, \ldots, \beta_9$ are parameters associated with variables, and ϵ_i a disturbance term which is not observable but it can affect a dependent variable.

3. Results

3.1. Descriptive Results

As already mentioned in the second section, the first objective of this study is to explain the gender gaps in STEM education. Based on available data from the Ethioia's Ministry of Education [70], and UNESCO [71], the participation of men and women in STEM was portrayed using graphical diagrams.

Figure 1 shows the percentage share of women's and men's enrollment in engineering and technology progress in the last decades. However, there is a wide gender gap. To solve this under-representation of women, the Ethiopian Ministry of Education adopts a new policy whereby 70% of overall university enrollment registers in a science field, and the remaining 30% in the social sciences and business economics. This policy was built on the bases of the goal of Ethiopia to generate more graduates in science, technology, engineering,

and mathematics and to increase the number of women in the field, helping to secure the countries sustainable development [27].

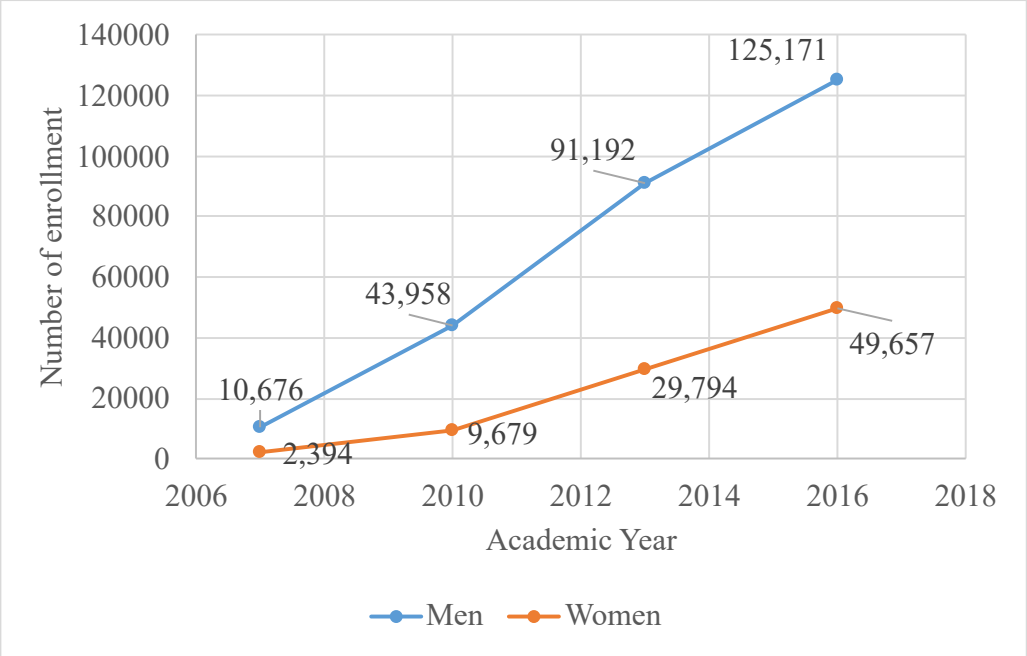

Figure 1. Students enrolled in engineering and technology education in Ethiopia.

Students enrollment in STEM education such as in mathematics, chemistry, physics, biology, and statistics in Ethiopia has given in Figure 2. Again this figure shows a gender imbalance though the gap is narrowing recently [27].

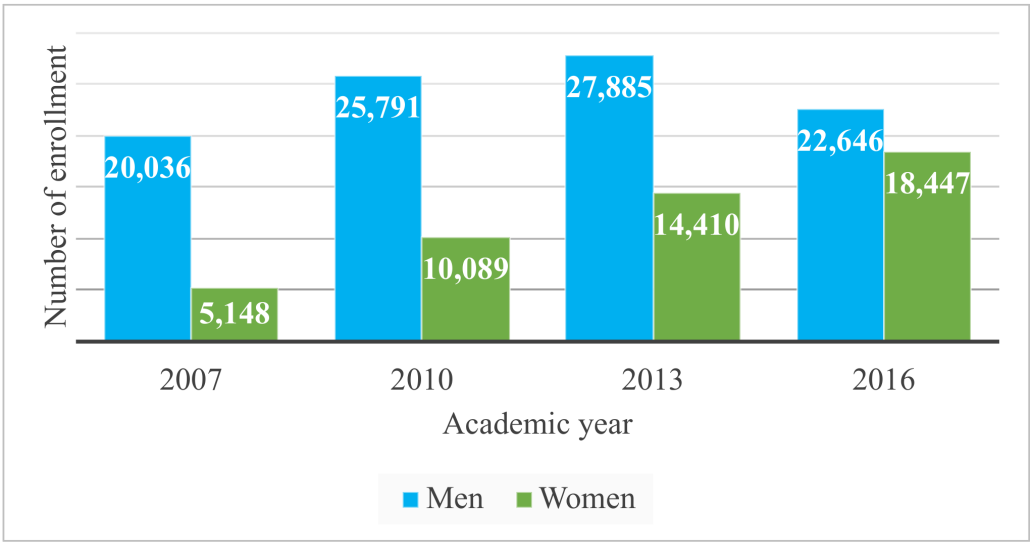

Figure 2. Students enrollment in STEM education excluding engineering and technology in Ethiopia.

Figure 3 shows the number of graduated students in engineering and technology education in Ethiopia from 1999 to presently. Again, there is a huge imbalance, and the gap is increasing over time due to dropout. Since most female students are dismissed and drop out from universities after learning some times due to low academic performance and related issues leads to a wide gender gap in STEM fields [27].

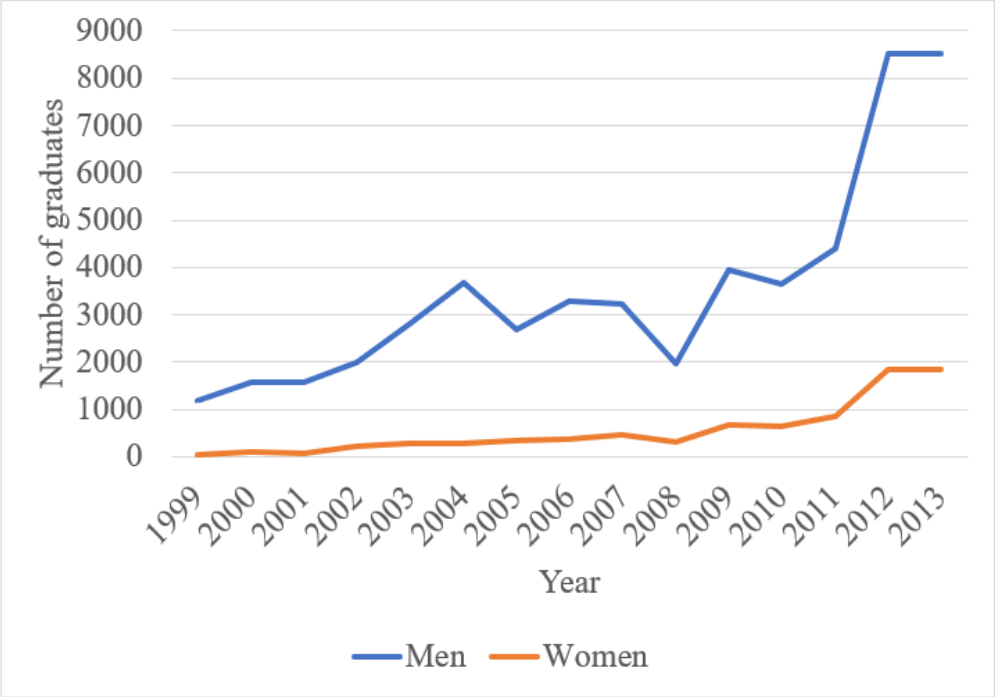

Figure 3. Students graduated in engineering and technology education in Ethiopia.

The participation of women in STEM education for three consecutive years in Africa has also been given in Figure 4, which indicates most countries have below 20% share of women who graduated in STEM education. However, Mauritania and Algeria have done better than others [7,72].

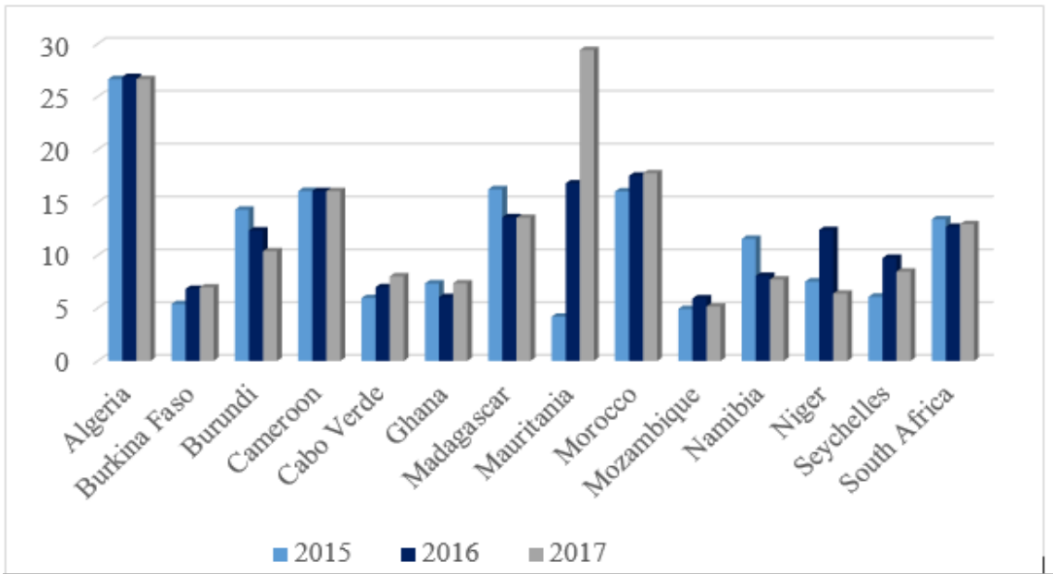

Figure 4. Percentage of women graduates in STEM education in Africa.

Women enrollment in engineering, manufacturing, and construction fields is below 14% in various countries, as shown in Figure 5. From this Figure, Romania, Tunisia, and Portugal have better performance during 2016 and 2017, whereas statistics for Burundi, Burkinafaso, the USA, and the UK show a low proportion. Cebr Analysis of Royal Academy also conducted a study using cross-sectional data from 90 countries that offer the gender gap in STEM education in most parts of the world, supporting the current study [7,72].

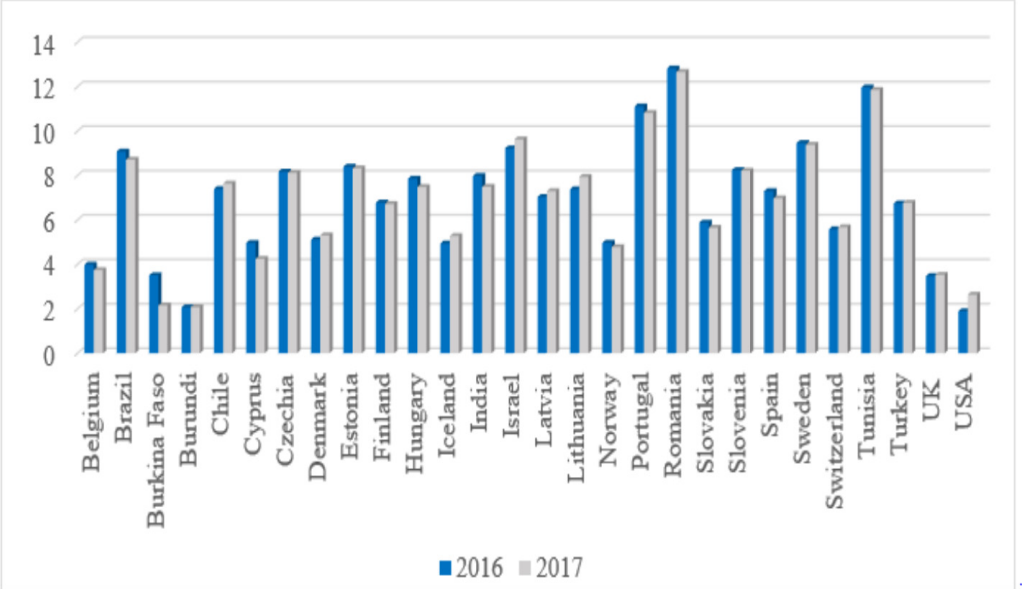

Figure 5. Status of women enrollment in engineering, manufacturing and construction field.

Similarly, Figure 6 shows the percentage of women graduates in science, technology, engineering, and mathematics areas of study in three consequent academic years worldwide. We can see that Oman and India [7,72,73] have better performance. In general, these given Figures indicate the existence of low representation of women in STEM education worldwide [74].

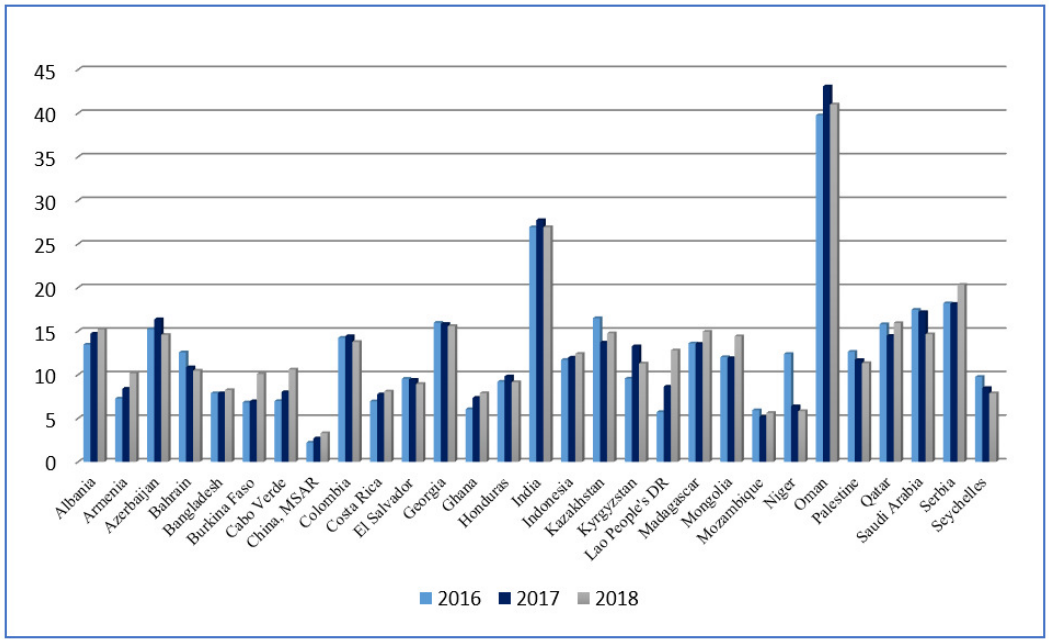

Figure 6. Percentage of women graduates in STEM education in various world countries.

3.2. OLS Regression Analysis

OLS linear regression was used to identify the factors that affect women's academic performance, which is the primary reason for the under-representation of women in STEM education. As explained in the second section of the paper, the dependent variable is women's academic performance, measured by the cumulative grade point. After checking Spearman's rank correlation test, nine independent variables were included in the model,

and various diagnostic tests were conducted. The value of R^2 64.9% shows the model fit. The Shapiro-Wilk normality test of residuals is also one of the tests which confirm residuals are normally distributed with a *p*-value of 0.61283. Furthermore, supported by the link test, a *p*-value of residual square 0.226 leads to accepting the null hypothesis stated that the model is well specified.

A multicollinearity problem among independent variables is also conducted by the Variance Inflation Factor test, where a Mean VIF of 1.72 shows no such problem among the explanatory variables. The Robust test has also checked the assumption of constant variance in the model to avoid heteroscedasticity if any.

Scatter diagram and histogram were also made in the residual of variable and found that the error has a normal distribution, which is mean zero, homoscedasticity, and independent of each other. Presented in Figure A1a,b, which shows the residual's variation stays much the same across the data, apart from the one outlier. Hence, the residual variance can be treated as constant, and the mean of residuals is approximately zero as presented in the histogram.

Corresponding to all of these diagnostic tests of regression coefficients, students having prior information about the institution is an important variable that has a significant and positive impact at 1% level. A unit increase in students gathering preliminary information about the university leads to 0.375 unit increases in their academic performance than others on average, as given in Table 4.

The interventions of universities in supporting women positively and significantly affects women students' academic performance in engineering and technology education at 1% level. A one-unit increase in university support yields 0.187 unit improvement in women's academic performance.

Peer learning is also an essential variable with a positive and significant influence at 1% level. A unit increase in this variables leads to a 0.132 unit that increases averagely on women students' academic performance in engineering and technology education.

Similarly, accessibility of university infrastructure has a positive and significant impact at 1% level that on average, 1 unit increase in the supply of these infrastructure related to 0.168- and 0.39-unit improvement, respectively when the supply is medium and a good standard on academic performance of women students in engineering and technology education.

The existence of engineering and technology professionals in the family or family profession has a negative and significant impact at 10%. On average, a unit increase in the existence of engineering and technology family professionals leads to a 0.063-unit decline in women students academic performance. Sexual harassment also has a significant and negative impact at 1% level that, on average, a unit increase in sexual harassment leads to a 0.136-unit decline in women students' academic performance.

Table 4. Significant variables in the OLS regression model

CGPA (Academic Performance)	Coef.	Robust SE	*t*-Value	*p*-Value	95% Conf. Interval	
					Lower	Upper
Interventions followed by institutions for supporting women students	0.1878082	0.0365764	5.13	0.000	0.1158813	0.259735
Sexual harassment	−0.1365386	0.0386175	−3.54	0.000	−0.2124793	−0.060598
Peer learning habit of students	0.1318955	0.0361807	3.65	0.000	0.0607467	0.2030442
Accessibility of university infrastructure						
Medium	0.1685265	0.0490086	3.44	0.001	0.0721519	0.2649012
Good	0.3924886	0.0547922	7.16	0.000	0.2847406	0.5002367
Students having prior information about the university	0.3752453	0.0406874	9.22	0.000	0.2952342	0.4552564
Family profession	−0.0630425	0.0342077	−1.84	0.066	−0.1303114	0.0042263
cons	2.233827	0.0608458	36.71	0.000	2.114175	2.35348

coef. = coefficents, Robust SE = robust standared error, *p*-value = significance level.

4. Discussion

The developing economy needs academically qualified STEM professionals, including women, to contribute crucial sustainable development roles and achieve the 2030 Agenda of SDGs. These can be considered to promote women's empowerment, mainstream gender equality, and achieve peaceful societies with full human potential [1,2,5,15]. In this background, the paper under discussion analyzes women's enrollment and graduation in STEM education. The statistical analysis of secondary data shows women under-represented in STEM education in Ethiopia and the world, even though some countries have better trends.

This study also attempted to identify factors associated with women students' academic performance in engineering and technology with all diagnostic tests. The result indicates that students having prior information about the institution is the most significant variable that positively impacts academic performance. When the students have previous general information about the institution before joining, they will have psychological readiness, which improves academic performance. The prior knowledge can be about courses, curriculum, administration, examination system, etc., which are performing in the universities. Thus, a variable was not studied by existing studies in the literature as factors that affect students' academic performance. Hence, this factor's finding, which positively influences educational performance, will add value to the existing literature.

Additionally, the result confirms the hypothesis of the positive relationship between the accessibility of university infrastructure (i.e., library, laboratory, dormitory, internet access, water sanitation, food supply, security, etc). Furthermore, women students' academic performance in engineering and technology education, as supported by the previous studies, found that the university environment contributes to students' academic performance [36,42].

The result also confirms that interventions followed by institutions for supporting women students like the (academic, financial, and psychological treatment) given to girls by the university community are another significant variable that can improve women's academic performance. The previous study also finds and confirms the effectiveness of interventions applied in STEM education associated with academic successes [46]. Robsan Margo [52] argued that students capability to complete their studies is related to the sustainable supports of universities.

Students' learning habits are a significant variable that affects women students' academic performance in engineering and technology. It is consistent with the finding of Chachashvili-Bolotin et al. [63] states that the STEM learning experience positively associates with students' interest in pursuing and achieving STEM fields in tertiary education.

A finding by Hosaka [48] also confirmed as there is a link between students' learning experience and academic performance. He found that women were not interested in learning in groups with their friends (which is an essential factor for experience and knowledge sharing), leading to low academic performance.

The hypothesis of the negative impact of sexual harassment on women's academic performance has been confirmed in this study. Several existing studies confirm these results. Molla and Cuthbert [50] found women experience of sexual violence and bias affects women students' psychological and academic performance. The World Economic Forum and UN also identified negative peer pressure and harassment as reasons women's academic performance remains low-level [22,51].

Furthermore, result of this study indicates that the existence of engineering and technology professionals in the family has a negative and significant impact on women's academic performance in engineering and technology education. Which may happen: if the family members who graduated in this profession may not have a job due to a shortage of employment opportunity, STEM professionals in the family may provide exaggerated pessimistic information about STEM education that will create tension in the students mined, the student may observe lack of freedom from their STEM professional families due to the challenging nature of STEM courses that need more effort for success, if students observe discouraging experience of their family who holds STEM profession by government or others bodies on the bases of political perception, race, religion, gender, etc., and if professionals in STEM have an unsuccessful life. As far as our knowledge, this variable did not study by existing research. The previous studies in the literature mostly take the family's academic background, which affects academic successes but not considering the existence of engineering and technology professionals in the family specifically.

The previous studies [4,42–44,63] found that high school educational background impacts students' future academic performance. However, the Spearman's rank correlation test shows that high school education performance is insignificant. It may happen due to maladministration of grade 12 examination that is highly exposed to cheating, which leads to high score recording without their skill and knowledge. Additionally, there may be limited access to employment opportunities and a highly corrupted government system during recruitment, leading students to be hopeless and careless in their academic performance.

Having such results, the finding of this study concludes: students having prior information about the university before joining, better accessibility of university infrastructure, interventions followed by institutions for supporting women students, peer learning habit of students, sexual harassment, and the existence of engineering and technology professional in the family are an essential factor which affects the academic performance of women according to ranking the strength of the impacts of the variable based on the value of t-statistics in the regression result given in Table 4.

The finding implies that women students themselves, educational organizations, government, and other stakeholders should enhance women's academic performance, reducing gender gaps in STEM education and promoting sustainable development [2,5,15]. Students must have peer learning experience, and should have information about the universities (system, rules, regulations, etc). Engineering colleges must pay attention to students' psychological, economic, and academic support, try to arrange infrastructure and learning facilities, and protect students through strong commitment and regulations from sexual harassment. The government must enhance education quality by paying more attention to the examination system, recruiting professionals according to their ability rather than through corruption, race, gender, religion, etc. that leads to discouraging students' academic achievement.

There is a limitation of the present study that leads us to propose future works. In the first place, this research has been carried out by considering only students studied in government universities. Therefore, it would be necessary to extend these studies by including private institutions also.

Supplementary Materials: The supplementary file including diagnostic tests are available online at https://www.mdpi.com/2071-1050/13/4/2246/s1 the datasets generated for this study are available on request to the corresponding author.

Author Contributions: Conceptualization, A.M. and S.S.; methodology, A.M. and S.S.; software, A.M.; validation, A.M. and S.S.; formal analysis, A.M. and S.S.; investigation, A.M. and S.S.; resources, A.M.; data curation, A.M. and S.S.; writing—original draft preparation, A.M.; writing—review and editing, A.M. and S.S.; visualization, A.M. and S.S.; supervision, A.M. and S.S. All authors have read and agreed to the published version of the manuscript.

Funding: This research received no external funding.

Data Availability Statement: The secondary data have been obtained from http://data.uis.unesco.org/, and http://www.moe.gov.et/statistics online. The primary data are from authors own survey.

Conflicts of Interest: The authors declare no conflict of interest.

Appendix A

Appendix A.1

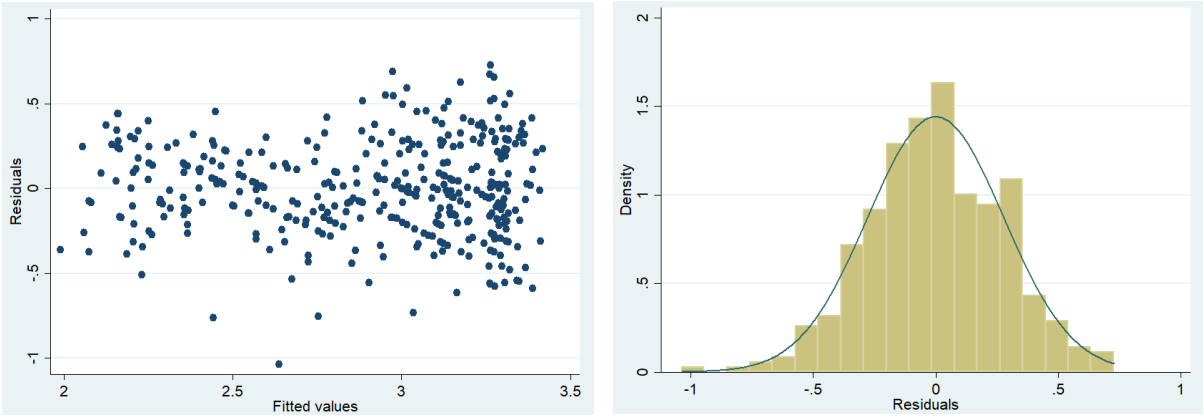

(**a**) (**b**)

Figure A1. Normality test of residual presenting (**a**) scatter plot and (**b**) histogram with normal distribution.

References

1. United Nations. 17 Goals to Transform Our World 2020. Available online: https://www.un.org/sustainabledevelopment/inequality/(accessed on 26 January 2021)
2. Di Fabio, A. The psychology of sustainability and sustainable development for well-being in organizations. *Front. Psychol.* **2017**, *8*, 1534.
3. Gebreluel, G. Ethiopia's Grand Renaissance Dam: ending Africa's oldest geopolitical rivalry? *Wash. Q.* **2014**, *37*, 25–37.
4. Muhammedhussen, M. Determinants of economics students' academic performance: Case study of Jimma University, Ethiopia. *Int. J. Sci. Res. Publ.* **2016**, *6*, 566–571.
5. Robert, K.W.; Parris, T.M.; Leiserowitz, A.A. What is sustainable development? Goals, indicators, values, and practice. *Environ. Sci. Policy Sustain. Dev.* **2005**, *47*, 8–21.
6. Zorzano, M.P. Gender Balance in Mars Exploration: Lessons Learned from the Mars Science Laboratory. *Sustainability* **2020**, *12*, 10658.
7. Singh, S.; Peers, S.M.C. Where are the Women in the Engineering Labour Market? A Cross-Sectional Study. *Int. J. Gender, Sci. Technol.* **2019**, *11*, 203–231.
8. Mahajan, P. Engineering a Woman: Marketing Opportunities and Challenges. *Turk. Online J. Educ. Technol.* **2017**, *2*, 11–22.
9. Wang, M.T.; Degol, J.L. Gender gap in science, technology, engineering, and mathematics (STEM): Current knowledge, implications for practice, policy, and future directions. *Educ. Psychol. Rev.* **2017**, *29*, 119–140.
10. Sikora, J.; Pokropek, A. Gender segregation of adolescent science career plans in 50 countries. *Sci. Educ.* **2012**, *96*, 234–264.
11. UNICEF. ITU, Towards an Equal Future: Reimagining Girls' Education through STEM. 2020. Available online: https://www.unicef.org/media/84046/file/Reimagining-girls-education-through-stem-2020.pdf (accessed on 17 December 2020).
12. Botella, C.; Rueda, S.; López-Iñesta, E.; Marzal, P. Gender diversity in STEM disciplines: A multiple factor problem. *Entropy* **2019**, *21*, 30.

13. Rodríguez-Rivero, R.; Yáñez, S.; Fernández-Aller, C.; Carrasco-Gallego, R. Is It Time for a Revolution in Work–Life Balance? Reflections from Spain. *Sustainability* **2020**, *12*, 9563.
14. López-Iñesta, E.; Botella, C.; Rueda, S.; Forte, A.; Marzal, P. Towards breaking the gender gap in Science, Technology, Engineering and Mathematics. *IEEE Rev. Iberoam. Tecnol. Del Aprendiz.* **2020**, *15*, 233–241.
15. Benavent, X.; de Ves, E.; Forte, A.; Botella-Mascarell, C.; López-Iñesta, E.; Rueda, S.; Marzal, P. Girls4STEM: Gender diversity in STEM for a sustainable future. *Sustainability* **2020**, *12*, 6051.
16. Kitchen, J.A.; Sonnert, G.; Sadler, P.M. The impact of college-and university-run high school summer programs on students' end of high school STEM career aspirations. *Sci. Educ.* **2018**, *102*, 529–547.
17. Mohr-Schroeder, M.J.; Jackson, C.; Miller, M.; Walcott, B.; Little, D.L.; Speler, L.; Schroeder, D.C. Developing Middle School Students' Interests in STEM via Summer Learning Experiences: See Blue STEM Camp. *Sch. Sci. Math.* **2014**, *114*, 291–301.
18. Roberts, T.; Jackson, C.; Mohr-Schroeder, M.J.; Bush, S.B.; Maiorca, C.; Cavalcanti, M.; Cremeans, C. Students' perceptions of STEM learning after participating in a summer informal learning experience. *Int. J. Stem Educ.* **2018**, *5*, 1–14.
19. Demetry, C.; Sontgerath, S. A middle school engineering outreach program for girls yields STEM undergraduates. In Proceedings of the American Society of Engineering Education Annual Conference & Exposition ASEE, Columbus, OH, USA, 25–28 June 2017.
20. Legewie, J.; DiPrete, T.A. The high school environment and the gender gap in science and engineering. *Sociol. Educ.* **2014**, *87*, 259–280.
21. Masanja, V.G. Increasing women's participation in science, mathematics and technology education and employment in Africa. In *United Nations Division for the Advancement of Women: Expert Group Meeting: Gender, Science, and Technology*; National University of Rwanda and University of Dares Salaam: Butare, Rwanda, 2010.
22. United Nation. The World for Women and Girls Annual Report 2020. Available online: https://www.unwomen.org/en/digital-library/publications/2020/06/annual-report-2019-2020 (accessed on 17 December 2020)
23. Rathgeber, E.M. Women in Universities and University-Educated Women: The Current Situation in Africa. In *African Higher Education: An International Reference Handbook*; Indiana University Press: Bloomington, Indiana, 2003.
24. Oanda, I.; Akudolu, L. Addressing Gender inequality in higher education through targeted institutional responses: Field evidence from Kenya and Nigeria. In *Higher Education in Africa: Equity, Access Opportunity*; Institute Of International Education (IIE): New York, NY, USA, 2010; p. 23.
25. Malik, S.; Courtney, K. Higher education and women's empowerment in Pakistan. *Gend. Educ.* **2011**, *23*, 29–45.
26. UNESCO. UNESCO's role in encouraging girls and women to be leaders in science, technology, engineering, art/design, and math fields. In Proceedings of the Conference: UNESCO Executive Board of 199th, Paris, France, 6 April 2016.
27. Melak, A.; Singh, S. The status of women participation in engineering and technology profession and their challenges in working institutions. *Int. J. Manag.* **2020** , *11*, 122.
28. Federal Ministry of Education. *Education Sector Development Programme V (ESDP V) 2008–2012 E.C. 2015/16–2019/20 G.C*; Federal Ministry of Education: Addis Ababa, Ethiopia, 2015. Avilable online: https://www.unicef.org/ethiopia/media/1396/file/Education%20Sector%20Development%20Programme%20V%20(ESDP%20V).pdf (accessed on 04 December 2020)
29. Reuben, E.; Sapienza, P.; Zingales, L. How stereotypes impair women's careers in science. *Proc. Natl. Acad. Sci. USA* **2014**, *111*, 4403–4408.
30. Nishii, L.H. The benefits of climate for inclusion for gender-diverse groups. *Acad. Manag. J.* **2013**, *56*, 1754–1774.
31. Carnevale, A.P.; Smith, N.; Melton, M. *STEM: Science Technology Engineering Mathematics*; Georgetown University Center on Education and the Workforce: Washington, DC, USA, 2011.
32. Landivar, L.C. Disparities in STEM employment by sex, race, and Hispanic origin. *Educ. Rev.* **2013**, *29*, 911–922.
33. Corbett, C.; Hill, C. *Solving the Equation: The Variables for Women's Success in Engineering and Computing*; American Association of University Women: Washington, DC, USA, 2015.
34. UNESCO. Girls' and Women's Education in Science, Technology, Engineering and Mathematics (STEM). 2019. Available online: https://en.unesco.org/stemed (accessed on 17 December 2020).
35. Almukhambetova, A.; Kuzhabekova, A. Factors affecting the decision of female students to enroll in undergraduate science, technology, engineering and mathematics majors in kazakhstan. *Int. J. Sci. Educ.* **2020**, *112*, 1–21.
36. Mamo, H.; Gosa, G.; Hailu, B. Perception of University Female Students on Factors Affecting Their Academic Performance and Competency: A Study from Dire Dawa University, Ethiopia. *Sci. J. Educ.* **2017**, *5*, 211.
37. Hanson, S.L.; Krywult-Albańska, M. Gender and access to STEM education and occupations in a cross-national context with a focus on Poland. *Int. J. Sci. Educ.* **2020**, doi:10.1080/09500693.2020.1737341.
38. Balakrishnan, B.; Low, F.S. Learning experience and socio-cultural influences on female engineering students' perspectives on engineering courses and careers. *Minerva* **2016**, *54*,219–239.
39. Lin, T.J.; Tsai, C.C. Differentiating the sources of Taiwanese high school students' multidimensional science learning self-efficacy: An examination of gender differences. *Res. Sci. Educ.* **2018**, *48*, 575–596.
40. Lytle, A.; Shin, J.E. Incremental Beliefs, STEM Efficacy and STEM Interest Among First-Year Undergraduate Students. *J. Sci. Educ. Technol.* **2020**, *29*, 1–10, doi:10.1007/s10956-020-09813-z.
41. Fernández-Cézar, R.; Garrido, D.; García-Moya, M.; Gómezescobar, A.; Solano-Pinto, N. Equity or Stereotypes in Science Education? Perspectives from Pre-University Students. *Sustainability* **2020**, *12*, 9354.

42. Mersha, Y.; Bishaw, A.; Tegegne, F. Factors affecting female students' academic achievement at Bahir Dar University. *J. Int. Coop. Educ.* **2013**, *15*, 135–148.
43. Yigermal, M.E. Determinant of Academic Performance of Under Graduate Students: In the Cause of Arba Minch University Chamo Campus. *J. Educ. Pract.* **2017**, *8*, 155–166.
44. Gilar-Corbi, R.; Pozo-Rico, T.; Juan-Luis, C.; Sánchez, T.; Sandoval-Palis, I.; Vidal, J. Academic Achievement and Failure in University Studies: Motivational and Emotional Factors. *Sustainability* **2020**, *12*, 9798.
45. Riegle-Crumb, C.; Moore, C. Examining gender inequality in a high school engineering course. *Am. J. Eng. Educ.* **2013**, *4*, pii:7858.
46. Van den Hurk, A.; Meelissen, M.; van Langen, A. Interventions in education to prevent STEM pipeline leakage. *Int. J. Sci. Educ.* **2019**, *41*, 150–164.
47. Patall, E.A.; Steingut, R.R.; Freeman, J.L.; Pituch, K.A.; Vasquez, A.C. Gender disparities in students' motivational experiences in high school science classrooms. *Sci. Educ.* **2018**, *102*, 951–977.
48. Hosaka, M. Women's experiences in the engineering laboratory in Japan. *Eur. J. Eng. Educ.* **2014**, *39*, 424–431.
49. García Villa, C.; González y González, E.M. Women students in engineering in Mexico: exploring responses to gender differences. *Int. J. Qual. Stud. Educ.* **2014**, *27*, 1044–1061.
50. Molla, T.; Cuthbert, D. Qualitative inequality: Experiences of women in Ethiopian higher education. *Gend. Educ.* **2014**, *26*, 759–775.
51. World Economic Forum. Why We Need More Women in Technology by 2030 and How to Do It 2017. Available online: https://www.weforum.org/agenda/2017/11/women-in-tech-engineering-ellen-stofan/ (accessed on 17 December 2020)
52. Egne, R.M. Gender equality in public higher education institutions of Ethiopia: The case of science, technology, engineering, and mathematics. *Discourse Commun. Sustain. Educ.* **2014**, *5*, 3–21.
53. Lin, T.; Lv, H. The effects of family income on children's education: An empirical analysis of CHNS data. In Proceeding of the 4th International Conference on Information Technology and Career Education Asian, Hangzhou, China, 15–16 April 2017; pp. 49–54.
54. Tomul, E.; Çelik, K. The relationship between the students' academic achievement and their socioeconomic level: cross regional comparison. *Procedia-Soc. Behav. Sci.* **2009**, *1*, 1199–1204.
55. Li, Z.; Qiu, Z. How does family background affect children's educational achievement? Evidence from Contemporary China. *J. Chin. Sociol.* **2018**, *5*, 13.
56. Gobena, G.A. Family Socio-Economic Status Effect on Students' Academic Achievement at College of Education and Behavioral Sciences, Haramaya University, Eastern Ethiopia. *J. Teach. Educ. Educ.* **2018**, *7*, 207–222.
57. Buchmann, C.; DiPrete, T.A. The growing female advantage in college completion: The role of family background and academic achievement. *Am. Sociol. Rev.* **2006**, *71*, 515–541.
58. Carnasciali, M.I.; Thompson, A.E.; Thomas, T.J. Factors influencing students' choice of engineering major. *Inf. Syst. Educ. J.* **2013**, *134*, 31–36.
59. Choudhury, P.K. Explaining gender discrimination in the employment and earnings of engineering graduates in India. *J. Educ. Plan. Adm.* **2015**, *29*, 225–246.
60. Sjaastad, J. Sources of Inspiration: The role of significant persons in young people's choice of science in higher education. *Int. J. Sci. Educ.* **2012**, *34*, 1615–1636.
61. Leavey, N.J. Mentoring Women in STEM: A Collegiate Investigation of Mentors and Protégés. Doctoral Dissertation, The Graduate School, Stony Brook University, Stony Brook, NY, USA, 2016.
62. Shin, J.E.L.; Levy, S.R.; London, B. Effects of role model exposure on STEM and non-STEM student engagement. *J. Appl. Soc. Psychol.* **2016**, *46*, 410–427.
63. Chachashvili-Bolotin, S.; Milner-Bolotin, M.; Lissitsa, S. Examination of factors predicting secondary students' interest in tertiary STEM education. *Int. J. Sci. Educ.* **2016**, *38*, 366–390.
64. Ethiopia Ministry of Education. *Education and Training Policy*; George Printing Press: Addis Ababa, Ethiopia, 1994. Available online: https://www.cmpethiopia.org/media/education_and_training_policy_ethiopia_1994 (accessed on 4 December 2020)
65. Del Águila, M.R.; González-Ramírez, A.R. Sample size calculation. *Allergol. Immunopathol.* **2014**, *42*, 485–492.
66. Witherspoon, E.B.; Schunn, C.D. Locating and understanding the largest gender differences in pathways to science degrees. *Sci. Educ.* **2020**, *104*, 144–163.
67. Eccles, J.S.; Wang, M.T. What motivates females and males to pursue careers in mathematics and science?. *Int. J. Behav. Dev.* **2016**, *40*, 100–106.
68. Mohamad, M.M.; Sulaiman, N.L.; Sern, L.C.; Salleh, K.M. Measuring the validity and reliability of research instruments. *Procedia Soc. Behav. Sci.* **2015**, *204*, 164–171.
69. Wooldridge, J.M. *Introductory Econometrics: A Modern Approach*; Nelson Education Ltd.: Toronto, ON, Canada, 2016.
70. Ethiopia Ministry of Education; Fedral Democratic Republic of Ethiopia; Ministry of Education. Educational Statistics Annual Abstract Report 2016. Available online: http://www.moe.gov.et/statistics (acceded on 19 August 2020).
71. UNESCO. Education Database 2020. Available online: http://data.uis.unesco.org/ (acceded on 21 June 2020).
72. Cebr for the Royal Academy of Engineering. Engineering and Economic Growth: A Global View 2016. Available online: https://www.raeng.org.uk/publications/reports/engineering-and-economic-growth-a-global-view (accessed on 15 January 2021).

73. Gupta, N. Women undergraduates in engineering education in India: A study of growing participation. *Gender Technol. Dev.* **2012**, *16*, 153–176.
74. National Science Foundation. Women, Minorities, and Persons with Disabilities in Science and Engineering 2017. Available online: https://ncses.nsf.gov/pubs/nsf19304/ (accessed on 15 January 2021).